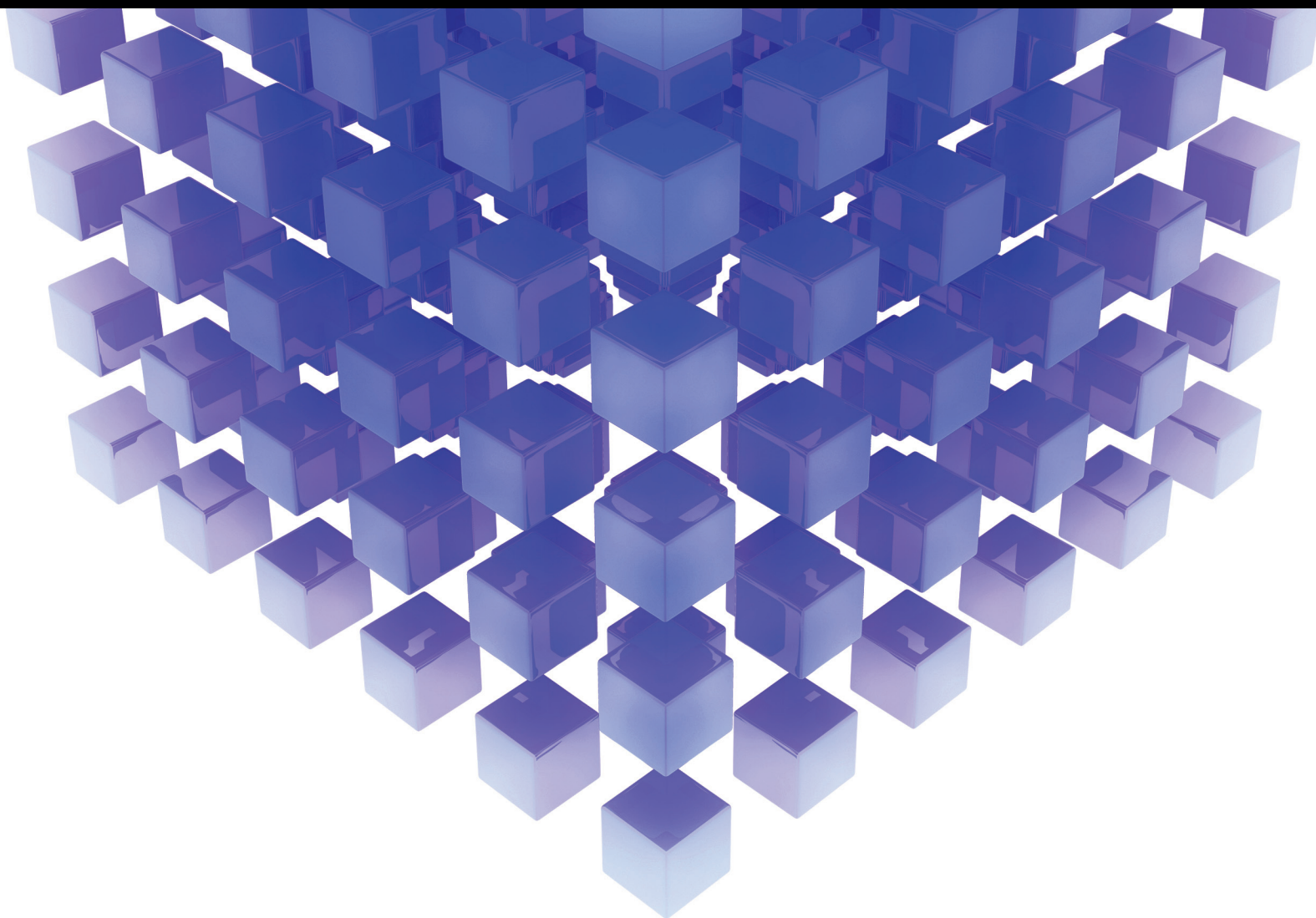


MATHEMATICAL PROBLEMS IN ENGINEERING

SELECTED PAPERS FROM THE INTERNATIONAL CONFERENCE ON INFORMATION, COMMUNICATION, AND ENGINEERING 2013

GUEST EDITORS: TEEN-HANG MEEN, STEPHEN D. PRIOR, KUEI-SHU HSU,
AND ARTDE DONALD KIN-TAK LAM





**Selected Papers from the International
Conference on Information, Communication,
and Engineering 2013**

Mathematical Problems in Engineering

**Selected Papers from the International
Conference on Information, Communication,
and Engineering 2013**

Guest Editors: Teen-Hang Meen, Stephen D. Prior,
Kuei-Shu Hsu, and Artde Donald Kin-Tak Lam



Copyright © 2014 Hindawi Publishing Corporation. All rights reserved.

This is a special issue published in “Mathematical Problems in Engineering.” All articles are open access articles distributed under the Creative Commons Attribution License, which permits unrestricted use, distribution, and reproduction in any medium, provided the original work is properly cited.

Editorial Board

Mohamed Abd El Aziz, Egypt
Eihab M. Abdel-Rahman, Canada
Rashid K. Abu Al-Rub, USA
Sarp Adali, South Africa
Salvatore Alfonzetti, Italy
Igor Andrianov, Germany
Sebastian Anita, Romania
W. Assawinchaichote, Thailand
Erwei Bai, USA
Ezzat G. Bakhoum, USA
José Manoel Balthazar, Brazil
R. K. Bera, India
Christophe Bérenguer, France
Jonathan N. Blakely, USA
Stefano Boccaletti, Spain
Stephane P.A. Bordas, USA
Daniela Boso, Italy
M. Boutayeb, France
Michael J. Brennan, UK
Salvatore Caddemi, Italy
Piermarco Cannarsa, Italy
Jose E. Capilla, Spain
Carlo Cattani, Italy
Marcelo Moreira Cavalcanti, Brazil
Diego J. Celentano, Chile
Mohammed Chadli, France
Arindam Chakraborty, USA
Yong-Kui Chang, China
Michael J. Chappell, UK
Kui Fu Chen, China
Xinkai Chen, Japan
Kue-Hong Chen, Taiwan
Jyh-Horng Chou, Taiwan
Slim Choura, Tunisia
Cesar Cruz-Hernandez, Mexico
Swagatam Das, India
Filippo de Monte, Italy
Antonio Desimone, Italy
Yannis Dimakopoulos, Greece
Baocang Ding, China
Joao B. R. Do Val, Brazil
Daoyi Dong, Australia
B. Dubey, India
Horst Ecker, Austria
M. Onder Efe, Turkey
Elmetwally Elabbasy, Egypt
A. Elías-Zúñiga, Mexico
Anders Eriksson, Sweden
Vedat S. Erturk, Turkey
Moez Feki, Tunisia
Ricardo Femat, Mexico
Robertt A. Fontes Valente, Portugal
Claudio R. Fuerte-Esquivel, Mexico
Zoran Gajic, USA
Ugo Galvanetto, Italy
Xin-Lin Gao, USA
Furong Gao, Hong Kong
Behrouz Gatmiri, Iran
Oleg V. Gendelman, Israel
Didier Georges, France
Paulo Batista Gonçalves, Brazil
Oded Gottlieb, Israel
Fabrizio Greco, Italy
Quang Phuc Ha, Australia
M. R. Hajj, USA
Tony Sheu Wen Hann, Taiwan
Thomas Hanne, Switzerland
K. R. (Stevanovic) Hedrih, Serbia
M.I. Herreros, Spain
Wei-Chiang Hong, Taiwan
Jaromir Horacek, Czech Republic
Gordon Huang, Canada
Huabing Huang, China
Chuangxia Huang, China
Yi Feng Hung, Taiwan
Hai-Feng Huo, China
Asier Ibeas, Spain
Anuar Ishak, Malaysia
Reza Jazar, Australia
Zhijian Ji, China
Jun Jiang, China
J. J. Judice, Portugal
Tadeusz Kaczorek, Poland
Tamas Kalmar-Nagy, USA
Tomasz Kapitaniak, Poland
Hamid Reza Karimi, Norway
Metin O. Kaya, Turkey
Nikolaos Kazantzis, USA
Farzad Khani, Iran
Kristian Krabbenhoft, Australia
Ren-Jieh Kuo, Taiwan
Jurgen Kurths, Germany
Claude Lamarque, France
Usik Lee, Korea
Marek Lefik, Poland
Stefano Lenci, Italy
Roman Lewandowski, Poland
Shihua Li, China
Ming Li, China
Jian Li, China
Shanling Li, Canada
Teh-Lu Liao, Taiwan
Panos Liatsis, UK
Jui-Sheng Lin, Taiwan
Yi-Kuei Lin, Taiwan
Shueei M. Lin, Taiwan
Wanquan Liu, Australia
Yuji Liu, China
Bin Liu, Australia
Paolo Lonetti, Italy
Vassilios C. Loukopoulos, Greece
Junguo Lu, China
Chien-Yu Lu, Taiwan
Alexei Mailybaev, Brazil
Manoranjan K. Maiti, India
Oluwole Daniel Makinde, South Africa
Rafael Martinez-Guerra, Mexico
Driss Mehdi, France
Roderick Melnik, Canada
Xinzhu Meng, China
Yuri Vladimirovich Mikhlin, Ukraine
Gradimir Milovanovic, Serbia
Ebrahim Momoniat, South Africa
Trung Nguyen Thoi, Vietnam
Hung Nguyen-Xuan, Vietnam
Ben T. Nohara, Japan
Sotiris K. Ntouyas, Greece
Gerard Olivar, Colombia
Claudio Padra, Argentina
Bijaya Ketan Panigrahi, India
Francesco Pellicano, Italy
Matjaz Perc, Slovenia
Vu Ngoc Phat, Vietnam
Maria do Rosário Pinho, Portugal
Alexander Pogromsky, The Netherlands

Seppo Pohjolainen, Finland
Stanislav Potapenko, Canada
Sergio Preidikman, USA
Carsten Proppe, Germany
Hector Puebla, Mexico
Justo Puerto, Spain
Dane Quinn, USA
K. R. Rajagopal, USA
Gianluca Ranzi, Australia
Sivaguru Ravindran, USA
G. Rega, Italy
Pedro Ribeiro, Portugal
J. Rodellar, Spain
Rosana Rodriguez-Lopez, Spain
Alejandro J. Rodriguez-Luis, Spain
Ignacio Romero, Spain
Hamid Ronagh, Australia
Carla Roque, Portugal
Rubén Ruiz García, Spain
Manouchehr Salehi, Iran
Miguel A. F. Sanjuán, Spain
Ilmar Ferreira Santos, Denmark
Nickolas S. Sapidis, Greece
Evangelos J. Sapountzakis, Greece
Bozidar Sarler, Slovenia
Andrey V. Savkin, Australia
Massimo Scalia, Italy
Mohamed A. Seddeek, Egypt
Alexander P. Seyranian, Russia
Leonid Shaikhet, Ukraine
Cheng Shao, China
Bo Shen, Germany
Zhan Shu, UK
Jian-Jun Shu, Singapore
Dan Simon, USA
Luciano Simoni, Italy
Grigori M. Sisoiev, UK
Christos H. Skiadas, Greece
Davide Spinello, Canada
Sri Sridharan, USA
Rolf Stenberg, Finland
Changyin Sun, China
Jitao Sun, China
Xi-Ming Sun, China
Andrzej Swierniak, Poland
Yang Tang, Germany
Allen Tannenbaum, USA
Cristian Toma, Romania
Irina N. Trendafilova, UK
Alberto Trevisani, Italy
Jung-Fa Tsai, Taiwan
Kuppalapalle Vajravelu, USA
Victoria Vampa, Argentina
Josep Vehi, Spain
Stefano Vidoli, Italy
Xiaojun Wang, China
Dan Wang, China
Youqing Wang, China
Cheng C. Wang, Taiwan
Yijing Wang, China
Yongqi Wang, Germany
Moran Wang, China
Gerhard-Wilhelm Weber, Turkey
Jeroen A.S. Witteveen, The Netherlands
Kwok-Wo Wong, Hong Kong
Ligang Wu, China
Zhengguang Wu, China
Gongnan Xie, China
Wang Xing-yuan, China
Xuping Xu, USA
Xi Frank Xu, USA
Jun-Juh Yan, Taiwan
Xing-Gang Yan, UK
Suh-Yuh Yang, Taiwan
Mahmoud T. Yassen, Egypt
Mohammad I. Younis, USA
Bo Yu, China
Huang Yuan, Germany
S.P. Yung, Hong Kong
Ion Zaballa, Spain
Ashraf M. Zenkour, Saudi Arabia
Jianming Zhan, China
Xu Zhang, China
Yingwei Zhang, China
Lu Zhen, China
Liancun Zheng, China
Jian Guo Zhou, UK
Zexuan Zhu, China
Mustapha Zidi, France

Contents

Selected Papers from the International Conference on Information, Communication, and Engineering 2013, Teen-Hang Meen, Stephen D. Prior, Kuei-Shu Hsu, and Artde Donald Kin-Tak Lam
Volume 2014, Article ID 460848, 1 page

Design Pattern Retrieval and Style Analysis for Content Creation of Comic Figures, Bor-Shen Lin and Shang-Te Tsai
Volume 2014, Article ID 497634, 12 pages

Solving Reality Problems by Using Mutual Information Analysis, Chia-Ju Liu, Chin-Fei Huang, Ray-Ying Huang, Ching-Sen Shih, Ming-Chung Ho, and Hsing-Chung Ho
Volume 2014, Article ID 631706, 4 pages

A Study of Classics-Reading Curriculum, Classics-Reading Promotion, and Classics-Reading Effect Modeling Exploration in Elementary Schools, Chuen-An Tang, Kuang-Ming Chen, Li-Chuan Chang, and Deng-Shun Lin
Volume 2014, Article ID 367659, 9 pages

Analyzing Lifestyle and Consumption Pattern of Hire Groups under Product Service Systems in Taiwan, Jui-Che Tu, Yu-Chen Huang, Chuan-Ying Hsu, and Yu-Wen Cheng
Volume 2013, Article ID 710981, 15 pages

Rough Set Theory Based Fuzzy TOPSIS on Serious Game Design Evaluation Framework, Chung-Ho Su, Ken T.-K. Chen, and Kuo-Kuang Fan
Volume 2013, Article ID 407395, 13 pages

Exploring the Effects of Multidimensional Context on Human Performance in Personal Bookmark Management, Siu-Tsen Shen
Volume 2013, Article ID 932586, 8 pages

An Extensive QFD and Evaluation Procedure for Innovative Design, Chang-Tzuoh Wu, Tien-Szu Pan, Ming-Hui Shao, and Chang-Shiann Wu
Volume 2013, Article ID 935984, 7 pages

Analyzing PSU's Performance: A Case from Ministry of Petroleum and Natural Gas of India, Chia-Nan Wang, Lei-Chuan Lin, and Dhanabalan Murugesan
Volume 2013, Article ID 802690, 9 pages

Vision Servo Motion Control and Error Analysis of a Coplanar XXY Stage for Image Alignment Motion, Hau-Wei Lee and Chien-Hung Liu
Volume 2013, Article ID 592312, 12 pages

An Achievement Prediction Model of Meaningful Learning, Motivation, and Cognitive on SPANI: Partial Least Square Analysis, Kuo-Kuang Fan, Chung-Ho Su, Shuh-Yeuan Deng, and Wei-Jhung Wang
Volume 2013, Article ID 961963, 11 pages

DSP- and FPGA-Based Stair-Climbing Robot Design, Ming-Shyan Wang, Che-Min Mi, Shih-Yu Wu, and Yi-Ming Tu
Volume 2013, Article ID 243094, 9 pages

Fairness Time-Slot Allocation and Scheduling with QoS Guarantees in Multihop WiMAX Mesh Networks, Chien-Yu Wu, Hann-Jang Ho, Sing-Ling Lee, and Liang Lung Chen
Volume 2013, Article ID 293962, 14 pages

Designing a Single-Stage Inverter for Photovoltaic System Application, M. T. Tsai, C. L. Chu, C. M. Mi, J. Y. Lin, and Y. C. Hsueh
Volume 2013, Article ID 912487, 8 pages

FPGA Realization of Sensorless PMSM Speed Controller Based on Extended Kalman Filter, Ying-Shieh Kung, Nguyen Vu Quynh, Nguyen Trung Hieu, and Jin-Mu Lin
Volume 2013, Article ID 919318, 13 pages

Minimum Porosity Formation in Pressure Die Casting by Taguchi Method, Quang-Cherng Hsu and Anh Tuan Do
Volume 2013, Article ID 920865, 9 pages

A Data Transmission Technique for Personal Health Systems, Jih-Fu Tu and Chih-yung Chen
Volume 2013, Article ID 496043, 7 pages

Numerical Analysis of Indoor Sound Quality Evaluation Using Finite Element Method, Yu-Tuan Chou and Shao-Yi Hsia
Volume 2013, Article ID 420316, 8 pages

An Innovative Design Methodology KKBDCA for Affective Product Development, Kun-Chieh Wang and Fang-Rong Ju
Volume 2013, Article ID 629708, 10 pages

An Objective Approach to Identify Spectral Distinctiveness for Hearing Impairment, Yeou-Jiunn Chen and Jiunn-Liang Wu
Volume 2013, Article ID 760258, 9 pages

Developments of Machine Learning Schemes for Dynamic Time-Wrapping-Based Speech Recognition, Ing-Jr Ding, Chih-Ta Yen, and Yen-Ming Hsu
Volume 2013, Article ID 542680, 10 pages

Optimization of Microextrusion Preforming Using Taguchi Method, Shao-Yi Hsia
Volume 2013, Article ID 305797, 9 pages

Construction of the Control System of Cleaning Robots with Vision Guidance, Tian-Syung Lan, Long-Ji Yeh, Min-Chie Chiu, and You-Xiang Hwang
Volume 2013, Article ID 283795, 6 pages

Influential Factors and Strategy of Sustainable Product Development under Corporate Social Responsibility in Taiwan, Jui-Che Tu, Pi-Lien Chiu, Yu-Chen Huang, and Chuan-Ying Hsu
Volume 2013, Article ID 303850, 15 pages

Study on the Wind Environment of the Architecture Communities: Traditional Typical Min Nan Human Settlements' Case, Yuan Miao and Shang-Chia Chiou
Volume 2013, Article ID 467076, 11 pages

The Use of a Brain Computer Interface Remote Control to Navigate a Recreational Device,

Shih Chung Chen, Aaron Raymond See, Yeou Jiunn Chen, Chia Hong Yeng,
and Chih Kuo Liang

Volume 2013, Article ID 823736, 8 pages

Empirical Analysis of Server Consolidation and Desktop Virtualization in Cloud Computing,

Bao Rong Chang, Hsiu-Fen Tsai, and Chi-Ming Chen

Volume 2013, Article ID 947234, 11 pages

Analyzing Taiwan IC Assembly Industry by Grey-Markov Forecasting Model,

Lei-Chuan Lin and Shan-Yau Wu

Volume 2013, Article ID 658630, 6 pages

An Indoor Video Surveillance System with Intelligent Fall Detection Capability,

Ming-Chih Chen and Yang-Ming Liu

Volume 2013, Article ID 839124, 8 pages

A Novel Cloud Computing Algorithm of Security and Privacy, Chih-Yung Chen and Jih-Fu Tu

Volume 2013, Article ID 871430, 6 pages

Traffic Noise Propagating from Vibration of Railway Wagon, Shao-Yi Hsia and Yu-Tuan Chou

Volume 2013, Article ID 651797, 7 pages

Thrust Reduction of Magnetic Levitation Vehicle Driven by Long Stator Linear Synchronous Motor,

Wan-Tsun Tseng

Volume 2013, Article ID 850615, 8 pages

A Karaoke System with Real-Time Media Merging and Sharing Functions for a

Cloud-Computing-Integrated Mobile Device, Her-Tyan Yeh, Juing-Shian Chiou,
and Ting-Jun Zhou

Volume 2013, Article ID 713589, 8 pages

Low-Cost Design of an FIR Filter by Using a Coefficient Mapping Method,

Ming-Chih Chen and Hong-Yi Wu

Volume 2013, Article ID 495207, 6 pages

Implementation of Fall Detection and Localized Caring System, Ming-Chih Chen, Yi-Wen Chiu,

Chien-Hsing Chen, and Ei-Jo Chen

Volume 2013, Article ID 217286, 5 pages

An 8-Bit ROM-Free AES Design for Low-Cost Applications, Ming-Chih Chen and Wei-Ting Li

Volume 2013, Article ID 696717, 5 pages

Impacts of Light Rail Transit Tram on the Voltage and Unbalance of the Distribution System,

Cheng-Ting Hsu, Hung-Ming Huang, Tsun-Jen Cheng, and Lian-Jou Tsai

Volume 2013, Article ID 478637, 8 pages

Performance Enhancement of Optical CDMA by Differential-Phase Method for Radio-over-Fiber

Transmissions, Hsu-Chih Cheng, Chih-Ta Yen, and Ing-Jr Ding

Volume 2013, Article ID 901871, 6 pages

Strategic Bidding Behaviors in Nondecreasing Sponsored Search Auctions, Chen-Kun Tsung,
Hann-Jang Ho, and Sing-Ling Lee
Volume 2013, Article ID 206386, 8 pages

An Innovative Direct-Interaction-Enabled Augmented-Reality 3D System,
Sheng-Hsiung Chang and Tsair-Chun Liang
Volume 2013, Article ID 984509, 4 pages

Design and Analysis of a Novel Speed-Changing Wheel Hub with an Integrated Electric Motor for Electric Bicycles, Yi-Chang Wu and Zi-Heng Sun
Volume 2013, Article ID 369504, 8 pages

Fast Facial Detection by Depth Map Analysis, Ming-Yuan Shieh and Tsung-Min Hsieh
Volume 2013, Article ID 694321, 10 pages

A Novel Dual-Electrode Plug to Achieve Intensive Electric Field for High Performance Ignition,
Chih-Lung Shen, Jye-Chau Su, and Tsair-Chun Liang
Volume 2013, Article ID 351594, 7 pages

Delay Pressure Detection Method to Eliminate Pump Pressure Interference on the Downhole Mud Pressure Signals, Yue Shen, Ling-Tan Zhang, Shi-Li Cui, Li-Min Sheng, Lin Li, and Yi-Nao Su
Volume 2013, Article ID 797549, 6 pages

A Study of Developing a System Dynamics Model for the Learning Effectiveness Evaluation,
Tian-Syung Lan, Yu-Hua Lan, Kai-Ling Chen, Pin-Chang Chen, and Wen-Cheng Lin
Volume 2013, Article ID 298621, 6 pages

A Fast Image Stitching Algorithm via Multiple-Constraint Corner Matching, Minchen Zhu,
Weizhi Wang, Binghan Liu, and Jingshan Huang
Volume 2013, Article ID 157847, 6 pages

Investigation of Dispersion and Performance Based on Ring Cavity by Birefringent Interleaver for DWDM Transmission Systems, Tsair-Chun Liang and Chun-Ting Chen
Volume 2013, Article ID 740412, 5 pages

Design and Implementation of a High-Voltage Generator with Output Voltage Control for Vehicle ER Shock-Absorber Applications, Chih-Lung Shen and Tsair-Chun Liang
Volume 2013, Article ID 324590, 6 pages

Editorial

Selected Papers from the International Conference on Information, Communication, and Engineering 2013

Teen-Hang Meen,¹ Stephen D. Prior,² Kuei-Shu Hsu,³ and Artde Donald Kin-Tak Lam⁴

¹ Department of Electronic Engineering, National Formosa University, Yunlin 632, Taiwan

² Department of Aeronautics, Astronautics and Engineering, University of Southampton, Southampton SO17 1BJ, UK

³ Department of Applied Geoinformatics, Chia Nan University of Pharmacy & Science, Tainan City 717, Taiwan

⁴ College of Physics and Information Engineering, Fuzhou University, Fuzhou, Fujian 350116, China

Correspondence should be addressed to Teen-Hang Meen; thmeen@nfu.edu.tw

Received 6 April 2014; Accepted 6 April 2014; Published 8 May 2014

Copyright © 2014 Teen-Hang Meen et al. This is an open access article distributed under the Creative Commons Attribution License, which permits unrestricted use, distribution, and reproduction in any medium, provided the original work is properly cited.

2013 International Conference on Information, Communication and Engineering (ICICE 2013) is organized by China University of Petroleum (Huadong, East China) and Taiwanese Institute of Knowledge Innovation and held in Qingdao, Shandong, People's Republic of China on October 26–November 1, 2013. ICICE 2013 has received 653 submitted papers from 10 countries, whereby 214 papers have been selected by the committees to be presented in the ICICE 2013. The conference provides a unified communication platform for researchers in a wide area of topics from information technology, communication science, applied mathematics, computer science, advanced material science, and engineering. ICICE 2013 enables interdisciplinary collaboration between science and engineering technologists in the academic and industrial fields as well as networking internationally.

Mechanical engineering and design innovations are both an academic and practical engineering field that involves systematic technological materialization through scientific principles and engineering designs. Technological innovation by mechanical engineering includes IT-based intelligent mechanical systems, mechanics, and design innovations. IT-based intelligent mechanical systems, which implant intelligence to machine systems, are an interdisciplinary area combining conventional mechanical technology and new

information technology. The main goal of IT-based intelligent mechanical systems is to develop fundamental technologies and to apply them to the industry field as follows:

- (i) computer-based design;
- (ii) intelligent manufacturing system;
- (iii) virtual manufacturing system;
- (iv) core parts and devices for intelligent systems;
- (v) computational engineering science;
- (vi) design methodology and optimization;
- (vii) machine diagnostics & reliability;
- (viii) human-machine interaction/virtual reality and entertainment.

This special issue selects 47 papers from ICICE 2013. This special issue enables interdisciplinary collaboration between material science and engineering technologists in the academic and industrial fields.

*Teen-Hang Meen
Stephen D. Prior
Kuei-Shu Hsu
Artde Donald Kin-Tak Lam*

Research Article

Design Pattern Retrieval and Style Analysis for Content Creation of Comic Figures

Bor-Shen Lin and Shang-Te Tsai

Department of Information Management, National Taiwan University of Science and Technology, Taipei 106, Taiwan

Correspondence should be addressed to Bor-Shen Lin; bslin@cs.ntust.edu.tw

Received 7 November 2013; Accepted 29 December 2013; Published 9 March 2014

Academic Editor: Teen-Hang Meen

Copyright © 2014 B.-S. Lin and S.-T. Tsai. This is an open access article distributed under the Creative Commons Attribution License, which permits unrestricted use, distribution, and reproduction in any medium, provided the original work is properly cited.

Placement of objects within a constrained space is a common challenge for designers; it is associated with decisions regarding the furnishing of a space with furniture, collocation of dressings, flower arrangement, and design of comic figures. Though many design elements can be shared on the Internet in the current age of technology, it is still not easy to compare or search for design patterns based on these elements. Thus, it is difficult for designers to efficiently retrieve similar patterns designed by others, to compare them, or to learn from them. This paper proposes the architecture of representing, comparing, retrieving, and analyzing the design patterns of digital contents for design support. This scheme can help the designers to explore the huge space of design patterns efficiently, to analyze and summarize the design styles quickly, and to improve design skills and stimulate imaginations effectively during the process of learning or creating. The proposed scheme has been verified with a design support system for the content creation of comic figures. It is generally applicable to the creation of digital contents and shows potential for applications in the fields of design and education.

1. Introduction

Placement of objects within a constrained space is a common challenge for designers; it is associated with decisions regarding the furnishing of a space with furniture, collocation of dressings, flower arrangement, and design of comic figures [1–8]. In such design tasks, users' goals are usually vague or implicit and require clarifications again and again through self-exploration or through the interaction between the customer and the designer for multiple turns. This is mainly because personal tastes and design styles are often implicit, not easy to describe, and difficult to match. For the collocation of dressings, for example, a lady might have simply rough ideas about what she needs. She might have some preferences of choices on color, style, or accessory due to fashion or simply would like to buy a shirt to match a coat or a pair of shoes. In such cases, it often takes much time for the clerks to suggest the candidates of dressings because the preferences of the customers can seldom be described explicitly. If the patterns of collocation can be represented

digitally and retrieved efficiently, the cycles of customer-designer interaction could be reduced effectively and the services might be delivered more efficiently.

With the advances of computer and network technologies, more and more design elements are digitized and become accessible on the Internet, such as photos, icons, sounds, or 3D models. It could be expected that design elements and patterns of various types, such as hair, garment, or comic styles, will be produced, shared, and reused in the future [9–12]. In some researches, for example, design patterns can be represented with specific data structure [13, 14] so as to be reusable for further design or creation. However, the lack of effective comparison and search methods for high-level structural patterns makes it difficult for the designers to refer to similar patterns designed by others, to compare them, or to learn the design skills or styles from them. Provided that the patterns can be compared and retrieved responsively through network, the learning of design can be facilitated largely, and the cocreation or resource sharing among designers becomes feasible [15–21]. In addition, the

style analysis for the design patterns is still a complex problem nowadays. Traditionally, the design styles can be analyzed or summarized only by experienced designers or experts manually through observing a large amount of samples. If the styles can be analyzed and summarized automatically, the tutors could instruct and inspire the learners more efficiently.

In this paper, the architecture for representing, comparing, retrieving, and analyzing structural design patterns of digital contents was proposed, as shown in Figure 1. Based on this scheme, design support systems can be built to assist the content creation and facilitate the sharing of patterns among the designers. Designers, for example, can view patterns that are similar to their own works and see how the elements used in their own works are utilized differently and innovatively by others. These observations can help the designers to improve their skills and stimulate their imaginations for creation. Since design patterns can be clustered, main styles of clusters can be analyzed and summarized automatically. Consequently, designers may browse patterns in an orderly manner, and they can obtain a broader view of design styles quickly. The proposed scheme has been verified with a design support system for the content creation of comic figures; thus, the design elements, which include objects of various types, can be searched, edited, and assembled into patterns. Subsequently, these patterns can be compared, retrieved, and clustered, while the design styles can be analyzed and summarized efficiently. This scheme is generally applicable to the creation of digital contents, and it shows potential for applications in the fields of design and education.

The organization for the rest of this paper is as follows. Section 2 describes how to create the digital contents of comic figures using shared design elements in a network environment. Section 3 illustrates how a pattern can be represented as the feature, based on which similarity and distance can be measured and the comparison of patterns can be performed. Section 4 depicts how the patterns are clustered with agglomerative clustering or k -means clustering and how the style of each cluster can be analyzed and summarized automatically. Section 5 shows how the proposed scheme can be applied to the retrieval and style analysis for the design patterns of comic figures so as to improve the process of learning or creating. Section 6 finally concludes the contributions of this paper.

2. Content Creation of Comic Figures

In Figure 1, the design patterns are composed by the designers with the shared design elements in a library through a web application. Here in this paper a web application for composing comic figures is taken as an example for illustration. A library of design elements, which contains about 8,000 colored images, has been built using image editing tools and is shared and used for design. The images can be classified into a few types according to their contents, including the heads of famous stars or politicians, the bodies with different poses, actions or dressings, the shadows, the props, and the background scenes, as shown in Figure 2. In addition, each image was tagged manually with several keywords. The image

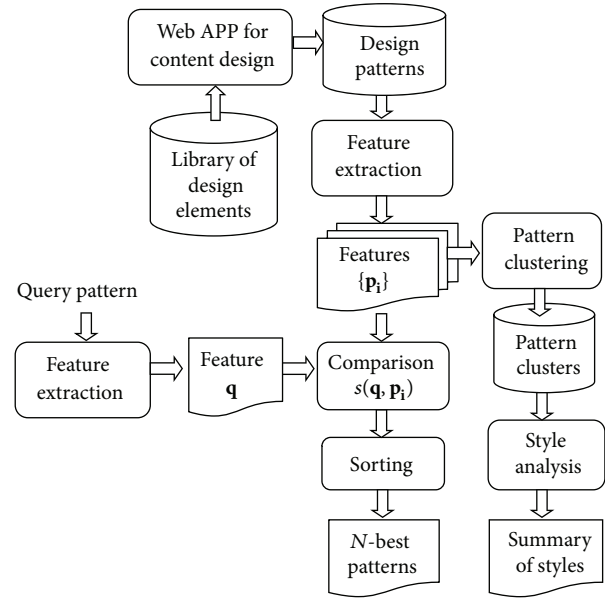


FIGURE 1: Architecture for design pattern retrieval and style analysis.

of Michael Jackson, for example, could be tagged with “pop,” “rock,” and “star,” while the image of Obama could be tagged with “U.S.,” “president,” and “politician.” In addition to the shared elements in the library, images can be imported for design from other sources, such as the camera, the drawing panel, and the web sites like Google or Flickr.

A web application based on the client and server architecture is further provided for the designers to compose the comic figures with the elements. An example of the user interface of the web application for assembling and editing the comic figures is shown in Figure 3. During composition, the designers can adjust the attributes of the design elements such as the size, location, transparency, font text, and font type, while adding the special effects such as rotation or mirror. In addition, the designer can search for desired elements with the keywords, such as *iron man*, or according to the categories, such as *politician*. Each output pattern contains a set of layered image objects of various types with respective attributes.

Figure 4 shows a few output patterns of comic figures composed with the web application. As can be observed in this figure, the example on the top right contains the head of Obama, the body with a nice suit, a luxury car, two shadows, a background scene containing the White House, and a caption with the title of “Yes! We Can.” The example on the bottom left of Figure 4, on the other hand, contains two photos, two cartoon figures, a prop of crown, and a caption. These patterns were composed and saved as the records in the database and used for retrieval and clustering later on.

3. Feature Representation and Pattern Retrieval

To compare the design patterns, the feature of each pattern, which includes the attributes of various objects, needs first



FIGURE 2: Samples of design elements with various types of content, including heads, bodies, shadows, props, fonts, and background scenes.



FIGURE 3: Example of user interface for composing comic figures.

to be extracted and represented in a structural form. This is accomplished in the procedure of “feature extraction” as shown on the top or left part of Figure 1. With the features, the similarities between the query pattern and the target patterns in the database can be measured and then sorted to obtain the

most similar patterns, as depicted in Figure 1 and discussed as follows.

3.1. Feature Extraction. In order to compare the design patterns, the attributes for every pattern need to be extracted and represented structurally. As can be seen from the examples in Figure 4, every pattern contains a variable number of heterogeneous image objects with respective attributes, so conventional feature representation based on the popular bag-of-words model [22] for information retrieval appears too simple and imprecise to be applicable. In this paper, the keywords of the image objects and the attributes of the image objects assigned during composition, such as the location, size, and transparency, were extracted to represent the feature of the pattern. A pattern can then be described with a set of heterogeneous objects with variable attributes.

Figure 5 shows an example of attributes extracted from an image object. In Figure 5, the attribute table on the right hand side corresponds to the head object on the left hand side. On the other hand, the caption on the left hand side has the attributes of x , y , $size$, $font\ text$, $font\ type$, and $font\ color$. Since each pattern contains a variable number of heterogeneous objects, it is necessary to consider the types of the objects when matching two patterns, which will be discussed in the following section.



FIGURE 4: Example design patterns containing the elements of various types from different sources.



Attribute	Value
id	P0320081016195102
Type	Picture/head
Size	50
x	19 px
y	57 px
Transparency	0
Special effect	No
Rotation angle	0
Mirror effect	No
Tags	Uncle Mau (role name) Cape no. 7 (movie name)

FIGURE 5: An example of extracted attributes corresponding to the head object.

3.2. *Similarity Measure and Pattern Retrieval.* Similarity or dissimilarity measures are critical for quite a few tasks on information retrieval and machine learning [23, 24]. Because the feature of a comic pattern in this study is structural and contains a set of heterogeneous objects, it is inappropriate to compute the similarity between two patterns based on

the classical cosine similarity. Assume the features of two patterns are \mathbf{p} and \mathbf{q} , where $\mathbf{p} = \{p_i\}$, $\mathbf{q} = \{q_j\}$, and p_i 's and q_j 's are the image objects in the two patterns, respectively. The numbers of elements in \mathbf{p} and \mathbf{q} and the types of image objects, p_i and q_j , may be different, as depicted in Figure 6(a). Different symbols in Figure 6(a) stand for different types of

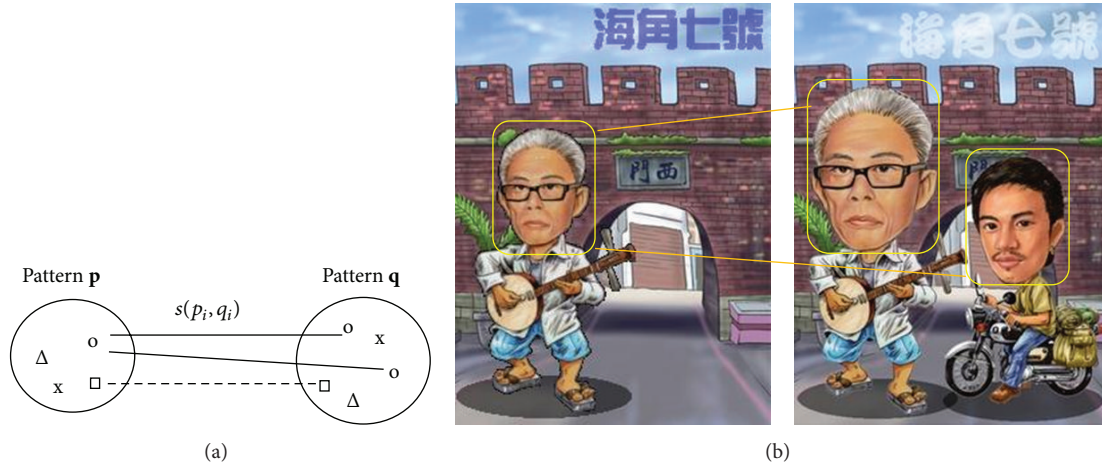


FIGURE 6: Match between two patterns.

image objects, such as head, body, or font. Since there might be more than one object for a type, for an object in one pattern it is reasonable to find the most matched object of the same type in the other pattern. The similarity between the two matched objects then contributes to the similarity of the two patterns. In this way, the similarity between the two patterns \mathbf{p} and \mathbf{q} can be accumulated for all matched pairs of objects. Figure 6(b) is further used to illustrate how two patterns are compared. The pattern on the left hand side of Figure 6(b) contains one head and one body, but the pattern on the right hand side contains two heads (elder and younger) and two bodies. It is intuitive to find the most matched head object on the right hand side of Figure 6(b) for the head object on the left hand side. When two patterns are compared, every object in one pattern is used to find the most matched object of the same type in the other pattern individually, as shown in Figure 6(a), and the similarities of all matched pairs are accumulated into the similarity of the two patterns.

However, how should the similarity between two objects be defined to measure the degree that they are similar to each other? Intuitively, the similarity should be 0 if p_i and q_j are of different types and could be the degree of similarity for all attributes between the two objects, otherwise, as follows:

$$s(p_i, q_j) = \sum_k \text{hit}(p_i[k], q_j[k]) \quad (1)$$

if type (p_i) equals type (q_j),

0 otherwise.

Here p_i and q_j are the objects in the two patterns, respectively, k signifies the attribute index, and $p_i[k]$ and $q_j[k]$ signify the values of attribute k for p_i and q_j , respectively. In addition, $\text{hit}(p_i[k], q_j[k])$ gives a positive score that indicates that the values of attribute k meet the criteria of similarity for that attribute and is 0 elsewhere. In other words, the score is positive when the two objects are similar enough on that attribute and 0 if they are not. The criteria of similarity can be defined flexibly according to the characteristic of the

TABLE 1: Criteria for attribute similarity.

Attribute	Criteria for similarity
id	The same image
Location	Distance less than 30 pixels
Size	Difference smaller than 10 pixels
Transparency	Difference of alpha smaller 30 (0–255)
Color change	Difference for specific band of RGB is lower than 30 (0–255)
Name/tags	Contains the same keyword
Mirror	Mirror effect applied for both
Font size	Difference smaller than 8 points
Font type	The same font type
Font text	Contains the same keyword
Font color	Euclidean distance in RGB space smaller than 30 (0–255).

attribute, as shown in Table 1. For the attribute *location*, for instance, the criteria could be whether the two objects are close enough spatially, while that for the attribute *font color* could be whether the difference between two font colors in color space is small enough. In addition, higher weights of similarity could be assigned to more important attributes. In this study, doubled weight is imposed on the attribute *id* because the image itself is very distinguishable visually. For the attribute *tags* containing a list of keywords, the number of common keywords is taken into account so as to increase the weight of the attribute. In this way, the similarity between two objects can be measured numerically by accumulating the similarities for all attributes.

With the similarity of objects, $s(p_i, q_j)$, depicted in (1), the most matched image object q_i^* in \mathbf{q} corresponding to the object p_i in \mathbf{p} can be computed as

$$q_i^* = \operatorname{argmax}_{q_j \in \mathbf{q}} s(p_i, q_j), \quad (2)$$

where the object q_i^* and the object p_i are of the same type. Table 2 shows an example for illustrating the computation of similarities between the head object on the left hand side of Figure 6(b) and the two objects (elder head and younger head) on the right hand side of Figure 6(b), respectively. As can be seen from Table 2, the total similarities for the elder head and the younger head are 5 and 2, respectively, so the elder head is the most matched object, and the similarity score 5 is accumulated into the similarity between the two patterns in Figure 6(b).

The similarity between the two patterns, \mathbf{p} and \mathbf{q} , can thus be computed by accumulating the similarities for all most matched pairs of objects as follows:

$$s(\mathbf{p}, \mathbf{q}) = \sum_{p_i \in \mathbf{p}} s(p_i, q_i^*). \quad (3)$$

Based on this definition, the similarities between a query pattern with the feature \mathbf{q} and the target patterns with the features \mathbf{p}_i 's can be computed one by one, as shown in the middle of Figure 1. All the similarities can be further sorted to obtain the most similar patterns for the query pattern, which can be formulated as

$$P = nbest_i s(\mathbf{q}, \mathbf{p}_i), \quad (4)$$

where $nbest$ denotes the function of finding N -best patterns that have the highest similarities with the query pattern. Note that the similarity defined in (3) is asymmetric, which is valid for pattern retrieval since all the similarities can be accumulated based on the query pattern. However, when applied to the pattern clustering, the similarity or the distance should be symmetric, so the following definitions are used instead:

$$s'(\mathbf{p}, \mathbf{q}) = \frac{1}{2} [s(\mathbf{p}, \mathbf{q}) + s(\mathbf{q}, \mathbf{p})], \quad (5)$$

$$d(\mathbf{p}, \mathbf{q}) = 1 - \frac{s'(\mathbf{p}, \mathbf{q})}{s'_{\max}}. \quad (6)$$

The processing stages for retrieving the N -best patterns are summarized as a flowchart shown in Figure 7. The query pattern and target patterns are first extracted from the database and represented as features, denoted as \mathbf{q} and \mathbf{p}_i 's, respectively. The similarities between query feature (\mathbf{q}) and the target features (\mathbf{p}_i 's) can be computed according to (1)–(3) one by one and sorted according to (4) such that N -best patterns for the query pattern can be obtained.

4. Pattern Clustering and Style Analysis

Traditionally, design style usually refers to a prominent group of similar patterns in which implicit rules of attributes exist. To analyze the design styles therefore implies to find out the groups of design patterns and to summarize the styles over them. In this section, clustering algorithms were used to generate the clusters of design patterns, based on which the summarization for design styles could be performed, as shown on the right hand side of Figure 1.

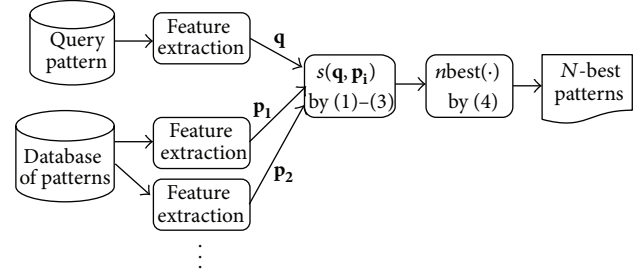


FIGURE 7: Flowchart of retrieving N -best patterns for a query pattern.

TABLE 2: Example for the computation of similarities.

Attribute	Elder head	Younger head
id	2	0
Location	0	0
Size	0	1
Transparency	1	1
Color change	0	0
Name/tags	2	0
Mirror	0	0
Font size	0	0
Font type	0	0
Font text	0	0
Font color	0	0
Total	5	2

4.1. Clustering Design Patterns. Since the distance between two patterns has been defined in (6), it is not difficult to conduct agglomerative clustering for all the patterns [25, 26]. In agglomerative clustering, each pattern initially belongs to a cluster individually. The distances among all pairs of clusters are then computed so as to decide the closest pair of clusters and merge them. This procedure is executed iteratively, and smaller clusters are merged gradually to produce larger clusters according to the distances, as shown in Figure 8(a). Finally, all clusters are merged into one cluster, and a tree structure called *dendrogram* is constituted, as shown in Figure 8(a). Afterwards, a threshold of distance can be set to split the dendrogram into clusters. For the case shown in Figure 8(a), for instance, the threshold can split the dendrogram into three clusters, $\{\mathbf{p}_1, \mathbf{p}_2\}$, $\{\mathbf{p}_3, \mathbf{p}_4, \mathbf{p}_5\}$, and $\{\mathbf{p}_6\}$, respectively.

In agglomerative clustering, the distance between two clusters could typically be the maximum distance, the minimum distance, or the average distance, among the distances of all pairwise patterns [25]. Here in this study the maximum distance is utilized, as illustrated in Figure 8(b), because it can strictly constrain the similarity for the patterns within every cluster and produces more compact clusters [26]. In addition, the threshold of distance stands for the maximum allowable distance among patterns within every cluster and can be adjusted to obtain different numbers of clusters flexibly. The limitation of agglomerative clustering is that, it may require a

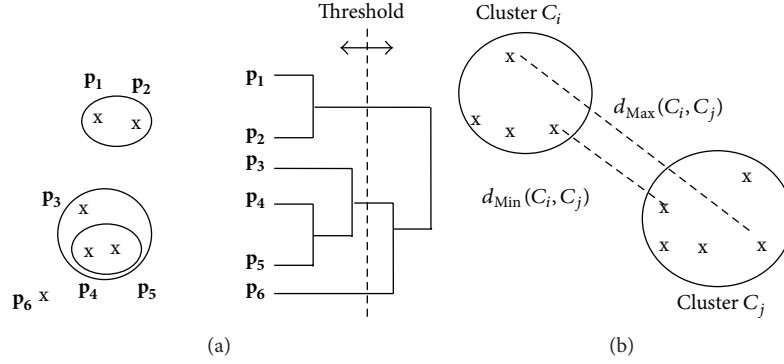


FIGURE 8: Agglomerative clustering (a) agglomeration and dendrogram (b) distance computation.

lot of computations for computing the pairwise distances and is therefore suitable for moderate amount of data only.

In addition to agglomerative clustering, k -means clustering is the most commonly used clustering algorithm. It is popular mainly because it is simple and efficient. Also, it works fairly well for quite a few applications. Conventional k -means clustering is based on square-error criterion,

$$E_k = \sum_{x_i \in C_k} (x_i - m_k)^2, \quad (7)$$

and the centroid of each cluster is computed as

$$m_k = \frac{1}{|C_k|} \sum_{x_i \in C_k} x_i. \quad (8)$$

However, for the structural design patterns studied in this paper, it is impossible to compute the centroid for a cluster of patterns according to (8), because each pattern contains a set of objects whose attributes are perhaps categorical instead of numerical (e.g., *font type* or *tags*). To deal with this issue, here a *pseudo centroid* based on the minimization of average distance is proposed. Note that the conventional centroid in (8) is a point that minimizes the within-cluster variance and the average distance. Though it is infeasible to find the average for nonnumerical data, it is possible to compute the pairwise distance of patterns according to (3). Hence, the pseudo centroid for a cluster can be defined as the pattern that achieves the minimum average (or total) distance in a cluster, as follows:

$$\widehat{m}_k = \operatorname{argmin}_i \left(\sum_{\substack{j \\ \mathbf{p}_j \in C_k}} d(\mathbf{p}_i, \mathbf{p}_j) \right). \quad (9)$$

Accordingly, the k -means clustering can be modified and conducted for the structural patterns in this study. Note the pseudo centroid here is not the *average* of the patterns in fact, but a pattern that is selected from the cluster and regarded as close to the *center* of the cluster relatively. Therefore, the criterion of minimizing the square error for k -means clustering does not hold for the modified version.

4.2. Style Analysis. After the clustering was performed, a few clusters of patterns were produced. Since every cluster contains a set of patterns that are similar to one another, it is possible to collect the statistics of the attributes for each cluster so as to find out the key attributes that contribute mostly to the similarity of the patterns within the cluster. This is actually the issue of summarization in data mining. However, because some attributes of image objects here are categorical variables (e.g., *font type* or *tags*) instead of continuous or numerical variable, it is infeasible to summarize a cluster according to the means, variances, or ranges for the attributes. In this section, an analysis approach based on the attribute similarity was proposed, based on which summarization can be performed.

As depicted in (1), the similarity between objects can be accumulated for all attributes such that the similarity between two patterns can be obtained, as illustrated in (3). To summarize the style on a cluster, the similarity between pairwise patterns within the cluster in (2) and (3) could be computed once again to collect the statistics of the attributes. Let \mathbf{p} and \mathbf{q} denote two patterns within a cluster, C . The statistics of the attributes can then be collected based on the procedure of Algorithm 1, in which q_i^* is the most matched object in pattern \mathbf{q} for the object p_i in pattern \mathbf{p} , as depicted in (2), and k is the attribute index for the objects p_i and q_i^* . It can be seen from Algorithm 1 that the count of attribute k is increased when the attribute values of p_i and q_i^* meet the criteria of similarity for the attribute. Moreover, when the attribute is *name*, *tags*, or *font text* that contains perhaps multiple keywords, the content strings need to be further parsed such that the statistics of the keywords can be collected to summarize the main topics for the cluster.

5. Experiments and Analysis

5.1. Retrieval of Similar Patterns. The web application described in Section 2 was used to compose 709 comic figures by 66 designers. These patterns were extracted from the database, represented as the features according to the attributes of objects, and used for retrieval. Query patterns were also selected randomly from these patterns and used to

```

for every  $\mathbf{p}, \mathbf{q} \in C$  and  $\mathbf{p} \neq \mathbf{q}$ 
  for every  $p_i \in \mathbf{p}$  and  $q_i^* \in \mathbf{q}$  as the most matched pair
    for each attribute  $k$  for  $p_i$  and  $q_i^*$ 
      if (hit ( $p_i [k], q_i^* [k]$ ) > 0)
        count [ $k$ ] += hit ( $p_i [k], q_i^* [k]$ )
        if ( $k$  is name, tag or font text)
          parse the strings of  $p_i [k]$  and  $q_i^* [k]$  and
          collect the statistics of the keywords
        end if
      end if
    end for
  end for
end for

```

ALGORITHM 1: Procedure of collecting the statistics of attributes and keywords for a cluster of patterns.

TABLE 3: Average of means and standard deviations for pairwise similarities for all clusters.

Clustering	<i>K</i> -means partitioning clustering						Agglomerative clustering	
	50	100	150	200	250	300	253 (6.0)	305 (6.5)
Number of clusters	50	100	150	200	250	300	253 (6.0)	305 (6.5)
Average of means	5.34	6.40	6.95	7.29	7.63	8.04	8.09	8.4
Average of standard deviations	1.81	1.61	1.40	1.36	1.17	0.97	0.61	0.49

retrieve 10-best patterns that are most similar to the query pattern, according to the flowchart depicted in Figure 7. The retrieval results are shown in Figure 9. In both Figures 9(a) and 9(b), the top-left icons are the query patterns and the rest icons are the corresponding retrieved patterns. As can be seen from this figure, the proposed scheme is able to find out visually similar patterns, which contain either common elements or the elements with similar attributes of size, location, name, tags, and so on. In addition, it can be seen that the icons with higher similarity look more similar to the query pattern in general. The patterns in the upper row, for example, are more similar than those patterns in the lower row visually. This implies that the proposed similarity measure based on the attributes can achieve quite adequate discriminative capability for the structural patterns.

Moreover, it can be observed that a few elements are commonly used in the 10-best patterns when compared with the query pattern. Therefore, the designers can learn efficiently from the retrieval results how the elements used in their works are utilized differently or innovatively by other designers. For example, they may learn how a character (head object) can be accompanied with different background scenes, props, or bodies, and what their relative locations are. This may help the designers to improve the design skills and inspire them for creation. It can also encourage the exchange of ideas and facilitate the sharing of such resources as the patterns in a design support system.

5.2. Analysis of Pattern Clusters. The patterns can be further clustered by the algorithms depicted in Section 4.1. First, the *k*-means clustering was performed. Note that for *k*-means clustering, if the clusters are initially selected randomly, its performance is unstable and very sensitive to the initial selection. Therefore, here in this study the largest cluster was

selected to split into two clusters iteratively so as to increase the cluster number gradually. In addition, the clustering is performed based on pairwise similarity, so the mean and variance of pairwise similarities for each cluster can be defined as

$$\begin{aligned}
m_{PS} &= \frac{1}{C_2^n} \sum_{i \neq j} s(\mathbf{p}_i, \mathbf{p}_j), \\
\sigma_{PS}^2 &= \frac{1}{C_2^n} \sum_{i \neq j} (s(\mathbf{p}_i, \mathbf{p}_j) - m_{PS})^2,
\end{aligned} \tag{10}$$

respectively, where n denotes the number of patterns in the cluster, C_2^n with the value of $n(n-1)/2$ denotes the number of unequal pairs of patterns in the cluster, and \mathbf{p}_i and \mathbf{p}_j are two patterns within a cluster. The average of the means and standard deviations for pairwise similarities for all clusters can then be used to measure the overall closeness for all clusters.

In addition, since the space of the structural patterns is sparse, large number of clusters is necessary in order to obtain visually similar clusters. Therefore, *k*-means clustering was conducted on the 709 patterns for the group number from 50 to 300 with a step of 50, and the results are displayed in Table 3. It can be seen from Table 3 that the average of means increases as the number of clusters is increased from 50 to 300. However, the average of standard deviations decreases slowly because the pairwise similarities within every cluster are not constrained strictly and more outliers are included. Figure 10 further shows two examples of clusters obtained from *k*-means clustering with 200 clusters. As can be seen from this figure, the *k*-means clustering tends to produce the clusters with outliers that are visually less similar to the other patterns.



(a)



(b)

FIGURE 9: Two examples of retrieval results for the query patterns on top-left corner.

Furthermore, agglomerative clustering depicted in Section 4.1 was conducted for the patterns, and a strict threshold of distance was selected such that every pairwise similarity within a cluster must be above a similarity threshold. Note that the maximum distance applied during agglomeration as depicted in Figure 8(b) also imposes the constraint of minimum pairwise similarity according to (6). Therefore, agglomerative clustering can constrain all pairwise similarities within every cluster strictly. The averages of means and standard deviations for minimum similarities of 6.0 and 6.5, corresponding to 253 and 305 clusters are 8.09/0.61 and 8.40/0.49, respectively, as can be

seen from Table 3. Such result means that, for structural patterns, agglomerative clustering is more effective than *k*-means clustering in average for obtaining visually similar patterns within every cluster. 46 large clusters with more than three patterns and 173 small chunks can be obtained finally when excluding 86 outliers from the dendrogram for the 305 clusters. A few patterns in four large clusters are displayed in Figure 11, in which every row corresponds to a cluster. As can be observed in this figure, the patterns in every cluster show high degree of similarity and the styles can be easily discriminated visually. The topics of the patterns for the four clusters are mainly the horse-riding dance in a Korean

TABLE 4: Contributions of the attributes to pattern similarity within every cluster.

Attribute	Cluster 1	Cluster 2	Cluster 3	Cluster 4
id	24.36%	20.23%	23.08%	21.71%
Location	5.95%	5.84%	7.69%	7.75%
Size	12.18%	14.01%	23.08%	24.03%
Name	12.18%	13.23%	11.54%	10.85%
Tags	42.78%	40.08%	34.62%	32.56%
Font size	1.42%	0.78%	0	0.78%
Font type	0.85%	0.39%	0	0
Font color	0.28%	5.45%	0	2.33%
Keywords with high frequency	Keywords relevant to a Korean show: Jiang-Nan (role), Pu Jae-Shiang (actor), suits of horse-riding dance, horse-riding dance.	Keywords relevant to the movie "Iron Man": space base, Iron Man II, Iron man.	Keywords relevant to a comic star in a Chinese drama: God of wealth, Stephen Chou (actor), hat for God of wealth.	Keywords relevant to pop music: male singer, A-Shin (singer), Mayday (band), with suit and microphone.

FIGURE 10: Example of clusters generated by k -means clustering with 200 clusters.

show, the scenes in the movies *iron man* and *iron man II*, a comic movie star in a Chinese drama, and a Taiwanese rock band, respectively. The visual clues are so prominent that the designers can make conclusions on the topics of the clusters by themselves instinctively.

In addition, the cooccurrences of image objects with high frequency imply the preference of collocation or the correlation that might be socially and culturally meaningful. The character and the body in the first cluster, for example, are from a Korean show, and the character and the prop in the third cluster are from a Chinese drama. Therefore, such analysis for patterns could help to discover the public images, designers' behaviors, or cultural knowledge that might be delivered implicitly in the designed patterns. Moreover, the main clusters can give the designers a quick and broad view of

the design works in an orderly manner and make them avoid being overwhelmed by a lot of disordered patterns. Therefore, it can also be used for browsing the patterns structurally and systematically, which can potentially improve the user experiences for design support systems.

5.3. Automatic Style Analysis. When the style analysis proposed in Section 4.2 was further applied to the clusters, the contributions of the attributes to the similarity for each cluster could be estimated according to the statistics computed from the procedure of Algorithm 1. The statistics of the attributes and the summary of important keywords with high frequency corresponding to the four clusters in Figure 11 are further displayed in Table 4. As can be observed from this table, clusters 3 and 4 have relatively higher ratio of similarity

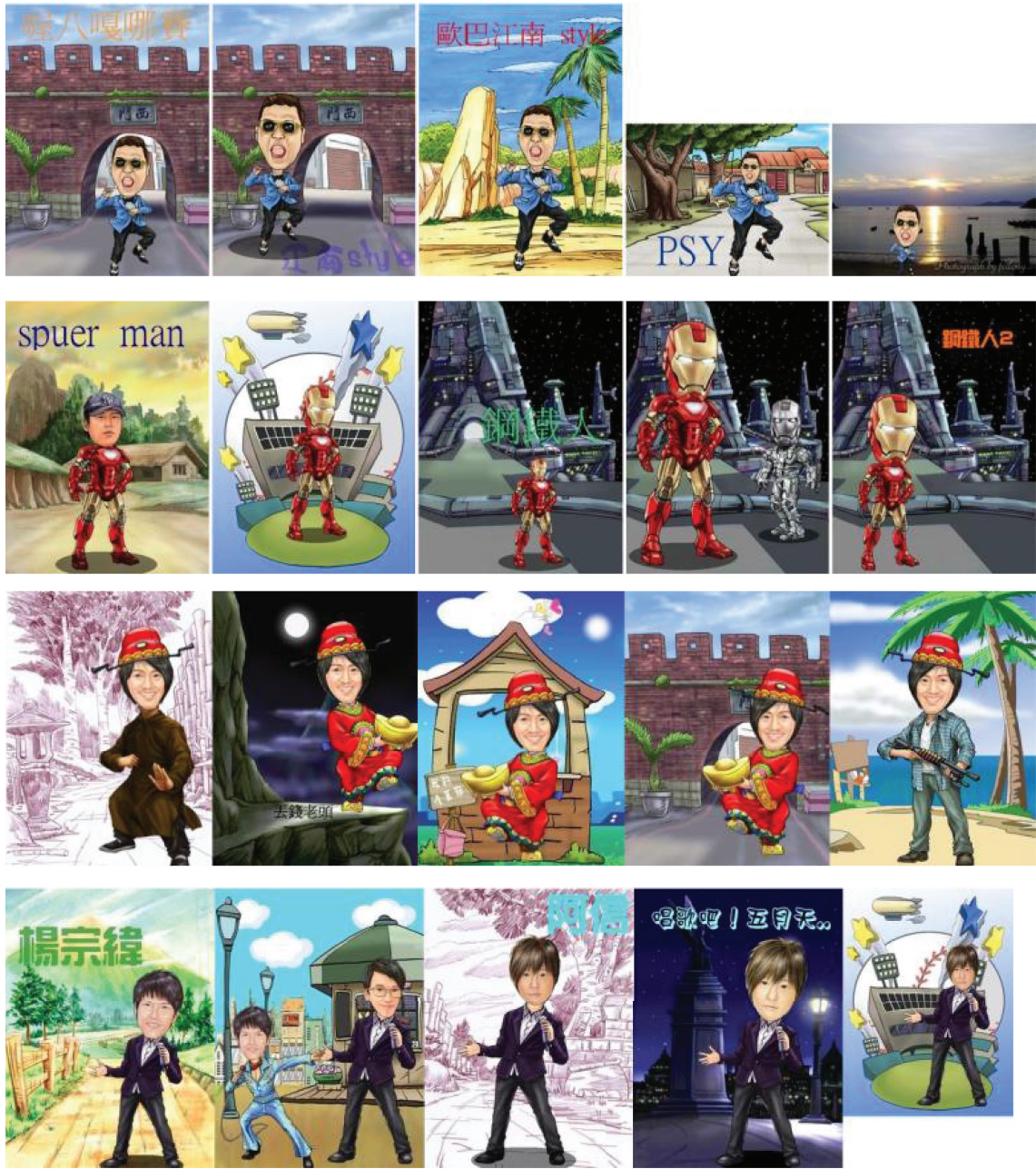


FIGURE 11: Three examples of clusters with a part of patterns.

on the attribute of *size*, and cluster 1 has the highest similarity on the attribute of *tags* due to more common head and body. The most relevant keywords for each cluster can be summarized automatically according to their occurrence counts, as shown in Table 4, and used to indicate the main topics of the cluster. Through the proposed approach, it becomes possible to perform style analysis and summarization on pattern clusters automatically at a significantly lower cost than conventional summarization by experts. The analysis results may be helpful for both the learners and the tutors and applicable to design learning systems.

6. Conclusions

In this paper, the architecture for representing, comparing, retrieving, and analyzing the design patterns of digital contents was proposed. Based on this scheme, design support systems can be built to assist the content creation and facilitate the sharing of patterns among the designers. Designers can view the design patterns similar to their works efficiently and see how the design elements used in their works are utilized differently and innovatively by others. These observations can help the designers to enhance their skills and stimulate their imaginations during

the process of learning or creating. The proposed scheme has been verified with a design support system for the content creation of comic figures; thus, the design elements, which include objects of various types, can be searched, edited, and assembled into patterns. Subsequently, these patterns can be compared, retrieved, and clustered, while the design styles can be analyzed and summarized efficiently. This scheme is generally applicable to the creation of digital contents, and it shows potential for applications in the fields of design and education.

Conflict of Interests

The authors declare that there is no conflict of interests regarding the publication of this paper.

References

- [1] K. Honda and F. Mizoguchi, "Constraint-based approach for automatic spatial layout planning," in *Proceedings of the 11th Conference on Artificial Intelligence for Applications*, pp. 38–45, 1995.
- [2] L.-F. Yu, S.-K. Yeung, C.-K. Tang, D. Terzopoulos, T. F. Chan, and S. J. Osher, "Make it home: automatic optimization of furniture arrangement," *ACM Transactions on Graphics*, vol. 30, no. 4, article 86, 2011.
- [3] P. Merrell, E. Schkufza, Z. Li, M. Agrawala, and V. Koltun, "Interactive furniture layout using interior design guidelines," *ACM Transactions on Graphics*, vol. 30, no. 4, article 87, 2011.
- [4] Y. -C. Lin, Y. Kawakita, E. Suzuki, and H. Ichikawa, "Personalized clothing recommendation system based on a modified Bayesian network," in *Proceedings of the 12th International Symposium on Applications and the Internet (SAINT '12)*, pp. 414–417, 2012.
- [5] Y. Kalatidis, L. Kennedy, and L.-J. Li, "Getting the look: clothing recognition and segmentation for automatic product suggestions in everyday photos," in *Proceedings of the International Conference on Multimedia Retrieval (ACM ICMR '13)*, pp. 105–112, 2013.
- [6] L. Bossard, M. Dantone, C. Leistner, C. Wengert, T. Quack, and L. V. Gool, "Apparel classification with style," in *Proceedings of the Computer Vision (ACCV '12)*, vol. 7727 of *Lecture Notes in Computer Science*, pp. 321–335, 2013.
- [7] K. Arai and H. Tolle, "Automatic e-comic content adaptation," *International Journal of Ubiquitous Computing*, vol. 1, no. 1, pp. 1–11, 2010.
- [8] H. Tobita, "Comic computing: Creation and communication with comic," in *Proceedings of the 29th ACM International Conference on Design of Communication (SIGDOC '11)*, pp. 91–98, October 2011.
- [9] J.-K. Chou and C.-K. Yang, "Simulation of face/hairstyle swapping in photographs with skin texture synthesis," *Multimedia Tools and Applications*, vol. 63, no. 3, pp. 729–756, 2013.
- [10] X. Wang and K. Li, "Pattern recognition based on fuzzy cluster for recognizing garment style in the photo," in *Proceedings of the 9th International Conference on Computer-Aided Industrial Design and Conceptual Design: Multicultural Creation and Design (CAIDCD '08)*, pp. 250–254, November 2008.
- [11] C. Zhang, G. Liu, and Z. Wang, "Cartoon face synthesis based on Markov Network," in *Proceedings of the 18th International Symposium on Intelligent Signal Processing and Communication Systems (ISPACS '10)*, December 2010.
- [12] C. Sauvaget and V. Boyer, "Comics stylization from photographs," in *Proceedings of the 4th International Symposium on Visual Computing (ISVC '08)*, pp. 1125–1134, 2008.
- [13] D. Jung, Y. K. Hui, H.-K. Lee, J. Nam, and W. H. Jin, "Development of a packaging storage format for electronic comic services with metadata," in *Proceedings of the 26th IEEE International Conference on Consumer Electronics, The Mobile Consumer (ICCE '08)*, pp. 1–12, January 2008.
- [14] K. Arai and T. Herman, "Method for automatic E-comic scene frame extraction for reading comic on mobile devices," in *Proceedings of the 7th International Conference on Information Technology—New Generations (ITNG '10)*, pp. 370–375, April 2010.
- [15] T. Kohler, J. Fueller, K. Matzler, and D. Stieger, "CO-creation in virtual worlds: The design of the user experience," *MIS Quarterly*, vol. 35, no. 3, pp. 773–788, 2011.
- [16] R. Fruchter, "Internet-based web-mediated collaborative design and learning environment," in *Artificial Intelligence in Structural Engineering*, pp. 133–145, Springer, 1998.
- [17] Ö. Özyurt, H. Özyurt, and A. Baki, "Design and development of an innovative individualized adaptive and intelligent e-learning system for teaching-learning of probability unit: details of UZWEBMAT," in *Expert Systems with Applications*, vol. 4, pp. 2914–2940, 2012.
- [18] D. Romero and A. Molina, "Collaborative networked organizations and customer communities: value co-creation and co-innovation in the networking era," *Production Planning and Control*, vol. 22, no. 5–6, pp. 447–472, 2011.
- [19] M. Gilbert and M. Zachry, "Sharing time: engaging students as co-designers in the creation of an online knowledge sharing application," in *Proceedings of the 30th International Conference on Design of Communication (ACM SIGDOC '12)*, pp. 121–126, 2012.
- [20] I. Alkholy, "Using hypermedia in teaching baroque Interior design as seen in Dutch paintings," *International Journal of Emerging Technologies in Learning*, vol. 5, no. 3, pp. 37–41, 2010.
- [21] J. Xiao, M. Wang, L. Wang, X. Zhu, and J. Ng, "Design and implementation of a cloud-learning service platform," in *Proceedings of the International Conference on Web Intelligence and Intelligent Agent Technology (WI-IAT '12)*, pp. 296–300, 2012.
- [22] B. Liu, *Web Data Mining: Exploring Hyperlinks, Contents and Usage Data*, Springer, 2011.
- [23] J. Zobel and A. Moffat, "Exploring the similarity space," *SIGIR Forum*, vol. 32, no. 1, pp. 18–34, 1998.
- [24] R. P. W. Duin and E. Pçkalska, "The dissimilarity space: bridging structural and statistical pattern recognition," *Pattern Recognition Letters*, vol. 33, no. 7, pp. 826–832, 2012.
- [25] M. Kantardzic, *Data Mining: Concepts, Models, Methods, and Algorithms*, Wiley Inter-Science, Piscataway, NJ, USA, 2003.
- [26] E. Alpaydin, *Hierarchical Clustering. Introduction to Machine Learning*, MIT Press, 2004.

Research Article

Solving Reality Problems by Using Mutual Information Analysis

**Chia-Ju Liu,¹ Chin-Fei Huang,¹ Ray-Ying Huang,¹ Ching-Sen Shih,¹
Ming-Chung Ho,² and Hsing-Chung Ho¹**

¹ Graduate Institute of Science Education, National Kaohsiung Normal University, Kaohsiung 824, Taiwan

² Department of Physics, National Kaohsiung Normal University, Kaohsiung 824, Taiwan

Correspondence should be addressed to Ming-Chung Ho; t1603@nknuc.nknu.edu.tw

Received 8 November 2013; Accepted 4 December 2013; Published 10 February 2014

Academic Editor: Teen-Hang Meen

Copyright © 2014 Chia-Ju Liu et al. This is an open access article distributed under the Creative Commons Attribution License, which permits unrestricted use, distribution, and reproduction in any medium, provided the original work is properly cited.

Cross-mutual information (CMI) can calculate to time series for thousands of sampled points from corticocortical connection among different functional states of brain in Alzheimer's disease (AD) patients. The aim of this study was to use mutual information analysis in the multichannel EEG to predict the probability of AD disease. Considering the correlation between AD disease and ageing effect, the participants were 9 AD patients and 45 normal cases involving teenagers, young people and elders. This data revealed that both right frontal and temporo-parietal are differences between normal and AD participants. Besides, this study found the theta band is the main frequency to separate AD patients from all participants. Furthermore, this study suggested a higher distinguishable method by mutual information to predict the possibility AD patients.

1. Introduction

Alzheimer's disease (AD) is one of the most prevalent neurodegenerative diseases in recent years [1]. In 2000, there were 7.6 million people being reported as Alzheimer's disease (AD) in Europe [2], and there were 26.6 million cases of AD worldwide in 2006. It has been forecasted that AD will be 106.8 million in 2050 [3]. Therefore, predicting which individuals will progress as an AD patient is an important issue in clinical diagnosis and researches [4]. However, the rate of correctly identified AD cases in early AD stages only within a range between 29% and 42% by electrophysiological methods [5]. Two approaches to estimate AD disease are generally accepted: one is temporal resolution such as Event-Related Potentials (ERPs), and another is spatial resolution such as Functional Magnetic Resonance Imaging (fMRI) [6].

Many studies addressed that ERPs is the more reliable and sensitive method to diagnose AD disease [3, 4]. They also advised different ERPs components to diagnose mild AD disease such as P3, CNV, C145, C250, later components and so forth [4]. However, the individual ERPs component can not show the complex mutual connection of each electrode of EEG data. To combine with conventional and quantification

of EEG data can enhance the analysis of brain's functional properties [5].

The quantification EEG analysis included linear and nonlinear analysis, several studies indicated the mathematics of nonlinear dynamical systems are advantaged to interpret the dynamic processing of brain work [5], and the other studies concerned the linear calculation of characteristics of EEG data. Na et al. [7] mentioned that cross mutual information does not matter if the signal is chaotic or not, it just calculate to time series for thousands of sampled points from different functional states of brain. Jeong et al. [8] also indicated that cross mutual information is a good way to assess the cortico-cortical connection between different cortical areas in AD patients. Hence, the main purpose of this study was to use mutual information analysis in the multichannel EEG to assess the cross-interaction of information between each electrode of AD patients and normal cases.

According to the quantitative ERPs analysis, auditory oddball might be a useful way to predict the conversion of AD, because the task spent a few time to collect EEG of AD patients, and it is simple but more accurate to know the brain work [9]. Therefore, this study used pure auditory of ERPs to elicit participants' response, and this study wanted

to establish a higher distinguishable method to predict the possibility AD patients.

2. Methods

2.1. Subjects. In this study, the data of subjects are the reality brain wave from human beings. There are 54 volunteers who participated in this research including normal and AD patients. AD disease is a continuous progressive degenerative disease, and it might be started in healthy young individuals and developed into a terminal stage of AD disease in elder [6]. Hence, this study collected the normal cases involving teenagers ($N = 28$, age: 17.5 ± 0.8), young people ($N = 13$, age: 21.7 ± 0.9), and elder ($N = 4$, age: 81.8 ± 7.3). Besides, this study collected the AD patients ($N = 9$, age: 80.7 ± 9.5) identified by doctor of Kaohsiung Veterans General Hospital.

None of the participants reported hearing loss or psychological diseases, and all were naive to electrophysiological studies. All participants gave informed consents and need to join the diagnosis of three tests included minimal state examination (MMSE), clinical dementia rating (CDR) and cognitive abilities screening instrument (CASI). In EEG data, the average accuracy rate of normal cases is 98% and of the AD cases is 92.8%. That means all participants can response to the tasks well. In normal group ($N = 45$), the average MMSE scores are 30 (SD = 0), the average CASI scores are 100 (SD = 0), and the CDR scores estimated as "normal". In AD group, the average MMSE scores are 16.9 (SD = 6.7), the CASI scores are 57.7 (SD = 19.4), and the CDR scores are 1.3 (SD = 0.7).

2.2. Data Acquisition. The auditory oddball was presented to two pure auditory: one was 2000 Hz, and the other was 1000 Hz that occurred regularly with a 0.20 probability. The participants need to press the response button when they heard the 1000 Hz sound, but no response is required when hearing the 2000 Hz sound.

EEG was recorded with the SynAmps/SCAN 4.4 hardware and software (NeuroScan, Inc., Herndon, VA) from 32 tin electrodes mounted in a commercial electrocap (ElectroCap International, Eaton, OH), and electrode impedance was always kept below 5 k Ω . The common reference electrode for EEG measurements was placed on the mastoids behind the ears. Stimulus presentation was generated by Neuroscan Stim 3.3 Software. EEG channels were continuously digitized at a rate of 10000 Hz by a SynAmpTM amplifier. The signal was analog filtered (0.1–200 Hz), and A/D converted with a sampling rate of 10000 Hz and 14 bit precision and digitally filtered in the range 0.1–50 Hz. The EEG was segmented into 2048 ms epochs. Sweeps exceeding $\pm 80 \mu\text{V}$ were excluded by automatic artifact rejection, which was followed by visual artifact screening.

2.3. Data Analyses. EEG cross mutual information analysis was performed in the following frequency bands: delta band (1–4 Hz), alpha band (7–13 Hz), beta band (13–25 Hz), and

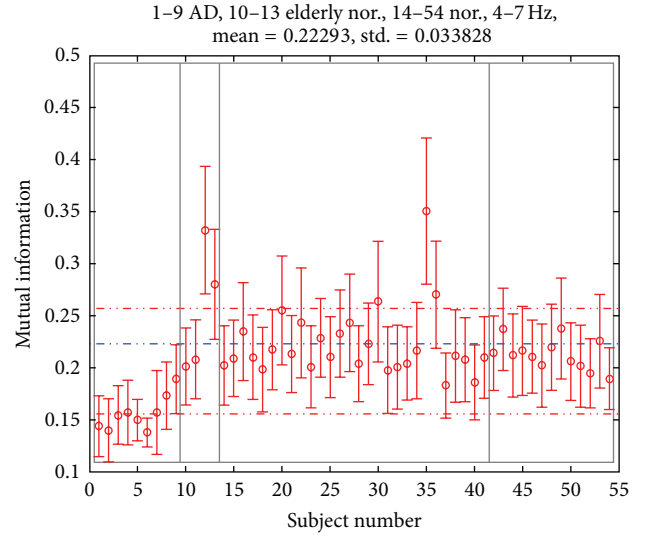


FIGURE 1: The theta band of right frontal and temporo-parietal area by cross mutual information analysis.

gamma band (25–50 Hz) and was defined as (Jeong et al., 2001 [8])

$$I_{XY_\tau} = \sum_{x(t), y(t+\tau)} P_{XY_\tau}(x(t), y(t+\tau)) \times \log_2 \frac{P_{XY_\tau}(x(t), y(t+\tau))}{P_X(x(t)) P_Y(y(t+\tau))}. \quad (1)$$

The cross mutual information I_{XY_τ} is between time serials data $x(t)$ and $y(t+\tau)$. The τ of y function is time delayed. $P_X(x(t))$, $P_Y(y(t+\tau))$, and $P_{XY_\tau}(x(t), y(t+\tau))$ are the normalized histogram of the distribution of values observed for the measurement $x(t)$ and $y(t+\tau)$. Based on the theory, this study analyzed all electrodes by mutual information methods from all participants, which involved the mean values between electrodes located over frontal and anterotemporal, temporal, parietal, and occipital regions. Also, this study calculated between the pairs of electrodes across the central line. Time serials data is 6000 data points, and sampling frequency is 1000 Hz (the average time delays of $\tau = 3$).

3. Results and Discussion

3.1. Analysis on Right Frontal and Temporoparietal. This study calculated the average cross mutual information of all normal participants. In addition, this study analyzed all electrodes by mutual information methods from all participants, which involved the mean values between electrodes located over frontal and anterotemporal, temporal, parietal, and occipital regions. Previous studies supported that EEG data which collected information from cortex is validity and sensitivity to predict the attention and semantic memory differences between normal and AD patients by using different instruments.

In this study, Figure 1 presented that the average cross mutual information is about 0.225, and all normal cases'

mutual information analyses are located within 2 times of standard deviation. But 78.8% AD cases' mutual information analyses are located without 2 times of standard deviation. The results showed that theta bands (4–7 Hz) of right frontal and temporo-parietal are higher differentiate from normal and AD cases. In other words, this study increased the percentage of AD predictability by analyzing the EEG data with cross mutual information.

Khachaturian [10] mentioned that number of neurofibrillary tangles (NFT) in brain regions could be a definite diagnosis in AD disease. Almkvist [6] also indicated that the first clinical stage of AD could be defined by NFT in the cortex. These studies supported that EEG data which collected information from cortex is validity and sensitivity. Almkvist's review paper mentioned that the medial temporal lobe could show the differences between normal and AD cases with NFT analysis. Then, Johannsen et al. [11] using Positron Emission Tomography (PET) to investigate sustained attention of AD patients which indicated the right middle frontal gyrus showed significant differences between normal and AD cases. To sum up, the right medial temporal lobe and the right and inferior frontal and the temporo-parietal regions are important factors to predict the attention and semantic memory differences between normal and AD cases by using different instruments.

In this study, we found both right frontal and temporo-parietal are higher differences than other brain areas between normal and AD cases, especially in F4 and CP3 electrodes. In other words, the results of this study contained a lot of important predictable factors of attention and semantic memory about AD disease.

3.2. Analysis on Theta Band. This paper analyzed different frequency included delta band (1–4 Hz), theta band (4–7 Hz), alpha band (7–13 Hz), beta band (13–25 Hz), and gamma band (25–50 Hz). The results revealed that theta band (4–7 Hz) of F4 and CP3 electrodes are higher differentiate from normal and AD cases. Although this study analyzed by 1–50 frequency band, delta band (1–4 Hz), alpha band (7–13 Hz), beta band (13–25 Hz), and gamma band (25–50 Hz), there are no significant differences on normal and AD cases. The results of this study showed that theta band is the main frequency to separate AD cases from all participants. Scheeringa et al. [12] mentioned that frontal theta activity is less pronounced than the alpha activity. But frontal theta power has been reported for increasing with working memory loading [13, 14].

4. Conclusion

The findings of this study support a lot of important predictable factors of attention and semantic memory about AD disease. Moreover, this study increased the percentage of AD predictability by analyzing the EEG data with cross mutual information.

The results showed that AD patients eliminate from 2 times standard deviation of average by calculating EEG theta power of normal participants in right frontal and temporo-parietal area by cross mutual information analysis. Frontal

theta power has been reported for increasing with working memory loading [13, 14]. Nevertheless, Scheeringa et al. [12] mentioned that frontal theta activity is less pronounced than the alpha activity. This study preferred finding both right frontal and temporo-parietal are higher differences than other brain areas between normal and AD cases more accurate. This study supposed that in auditory oddball task testing, participants need to expend working memory loading to remember the different sounds and pay attention to response to different stimuli to induce participants' EEG.

The implication of this study is to prove that the reality nonlinear problems such as brain waves could be solved by using mathematical analysis such as mutual information. Furthermore, these mathematical analyses could provide predictions of the reality of AD disease.

Conflict of Interests

The authors declare that there is no conflict of interests regarding the publication of this paper.

References

- [1] B. Czigler, D. Csikós, Z. Hidasi et al., "Quantitative EEG in early Alzheimer's disease patients—power spectrum and complexity features," *International Journal of Psychophysiology*, vol. 68, no. 1, pp. 75–80, 2008.
- [2] K. Blennow, M. J. de Leon, and H. Zetterberg, "Alzheimer's disease," *The Lancet*, vol. 368, no. 9533, pp. 387–403, 2006.
- [3] C. E. Jackson and P. J. Snyder, "EEG and ERP as biomarkers of mild cognitive impairment and mild Alzheimer's disease," *Alzheimer's and Dementia*, vol. 4, no. 1, pp. S137–S143, 2008.
- [4] R. M. Chapman, M. Mapstone, A. P. Porsteinsson et al., "Diagnosis of Alzheimer's disease using neuropsychological testing improved by multivariate analyses," *Journal of Clinical and Experimental Neuropsychology*, vol. 32, no. 8, pp. 793–808, 2010.
- [5] C. J. Stam, B. Jelles, H. A. M. Achtereekte, J. H. Van Birgelen, and J. P. J. Slaets, "Diagnostic usefulness of linear and nonlinear quantitative EEG analysis in Alzheimer's disease," *Clinical EEG Electroencephalography*, vol. 27, no. 2, pp. 69–77, 1996.
- [6] O. Almkvist, "Functional brain imaging as a looking-glass into the degraded brain: reviewing evidence from Alzheimer disease in relation to normal aging," *Acta Psychologica*, vol. 105, no. 2-3, pp. 255–277, 2000.
- [7] S. H. Na, S.-H. Jin, S. Y. Kim, and B.-J. Ham, "EEG in schizophrenic patients: mutual information analysis," *Clinical Neurophysiology*, vol. 113, no. 12, pp. 1954–1960, 2002.
- [8] J. Jeong, J. C. Gore, and B. S. Peterson, "Mutual information analysis of the EEG in patients with Alzheimer's disease," *Clinical Neurophysiology*, vol. 112, no. 5, pp. 827–835, 2001.
- [9] D. S. Goodin, "Event-related potentials," in *Electrodiagnosis in Clinical Neurology*, M. J. Aminoff, Ed., pp. 575–595, Churchill Livingstone, New York, NY, USA, 1986.
- [10] Z. S. Khachaturian, "Diagnosis of Alzheimer's disease," *Archives of Neurology*, vol. 42, no. 11, pp. 1097–1105, 1985.
- [11] P. Johannsen, J. Jakobsen, P. Bruhn et al., "Cortical sites of sustained and divided attention in normal elderly humans," *NeuroImage*, vol. 6, no. 3, pp. 145–155, 1997.

- [12] R. Scheeringa, K. M. Petersson, A. Kleinschmidt, O. Jensen, and M. C. Bastiaansen, "EEG alpha power modulation of fMRI resting state connectivity," *Brain Connectivity*, vol. 2, pp. 254–264, 2012.
- [13] A. Gevins, M. E. Smith, L. McEvoy, and D. Yu, "High-resolution EEG mapping of cortical activation related to working memory: effects of task difficulty, type of processing, and practice," *Cerebral Cortex*, vol. 7, no. 4, pp. 374–385, 1997.
- [14] O. Jensen and C. D. Tesche, "Frontal theta activity in humans increases with memory load in a working memory task," *European Journal of Neuroscience*, vol. 15, no. 8, pp. 1395–1399, 2002.

Research Article

A Study of Classics-Reading Curriculum, Classics-Reading Promotion, and Classics-Reading Effect Modeling Exploration in Elementary Schools

Chuen-An Tang,¹ Kuang-Ming Chen,² Li-Chuan Chang,³ and Deng-Shun Lin²

¹ Graduate Institute of Education, National Cheng Kung University, Tainan 701, Taiwan

² Department of Chinese Language and Literature, National University of Tainan, Tainan 700, Taiwan

³ Department of Nursing, Tajen University, Pingtung 907, Taiwan

Correspondence should be addressed to Deng-Shun Lin; linem@mail.nutn.edu.tw

Received 14 September 2013; Accepted 29 November 2013; Published 2 January 2014

Academic Editor: Teen-Hang Meen

Copyright © 2014 Chuen-An Tang et al. This is an open access article distributed under the Creative Commons Attribution License, which permits unrestricted use, distribution, and reproduction in any medium, provided the original work is properly cited.

The purposes of this study are to test reliabilities and validities of classics-reading curriculum (CRC) scale, classics-reading promotion (CRP) scale, and classics-reading effect (CRE) scale and to examine the relationships between CRC, CRP, and CRE in elementary schools through applying CORPS framework. The pilot sample and formal sample contain 141 and 500 participants from elementary school faculties and classics-reading volunteers in the north, central, south, and east regions of Taiwan. The findings indicate that Cronbach α coefficients of curriculum cognition (CC), curriculum teaching (CT), inside-school promotion (IP), outside-school promotion (EP), learning effect (LE), and class management effect (CME) subscales are .88, .85, .93, .91, .91, .94, respectively, through exploratory factor analysis and they have good internal reliabilities and construct validities, respectively, through confirmatory factor analysis. Moreover, CC, CT, IP, and EP have positive influences on LE (standardized coefficients .34, .25, .14, and .22) and on CME (standardized coefficients .41, .14, .14, and .20), respectively. CC, CT, IP, and EP can explain 69% of LE and 61% of CME. The model is supported by the data. Lastly, this study proposes some suggestions regarding the classics-reading education for elementary schools.

1. Introduction

Since mandarin text books were written in vernacular Chinese no longer in classical Chinese in elementary schools (ESs) in 1920, the trend of classics-reading (CR) has been going down [1]. In 1994, Tsai-Kui Wang in hopes of opening children's pure hearts through great ancient books in the Chinese culture and laying good foundations for developing wonderful personalities under the gradual changes and influences started to promote CR for children, so that the traditions of the Chinese culture can be passed on [2]. He has been giving speeches everywhere for propagation of the philosophy of CR education and held CR workshops for teachers annually to pass on the methods and skills of CR teaching during 19 years.

In 1989, UNESCO holds for the twenty-first century conference and points out that the challenges of morality, ethics,

and values will be the first one that people face in the twenty-first century [3]. Character Counts offers six pillars of character in 1992 [4]. New century's education is that becoming good is more important than getting smart for the students. Global Education Council points out that the new education is characterized by that. Building noble-character citizens will be a focus point of education in the world.

Because the education philosophy of Confucian is concerned about character training, the trend of the new education helps to promote the CR education in the society and school. The twenty-first century is an era that English supports and competes against Chinese mutually, and Chinese ability cannot easily be ignored [5]. The CR education has flourished not only in the society but also in the schools since Wang and the numerous nongovernmental CR organizations struggled to promote CR education from 1994 to the present. Although there has been an ongoing debate of the CR

education [1, 6–8], the CR education workshops for teachers [9–11], the promotion of CR education in all Hualien County's primary schools [12], the national CR examination, and so on indicate that the CR education for ESs still develops and grows sustainably in the practice of educational reform.

There are about 1.5 million children participated in CR until 2007 [13]. The trend of CR has led to many studies regarding CR for children. In the National Digital Library of Theses and Dissertations in Taiwan, there are at least 53 master's theses and doctoral dissertations regarding CR education, dated from 1999 to Jan 2013. The keys to whether CR education for children can succeed include insights of, emphases on, plans for, and implementation and effects of CR education for the first-line school faculties and CR volunteers. In other words, CR philosophy, degrees of understanding CR, CR teaching, and planning CR activities of school faculties and CR volunteers determine effects of CR education for children. Moreover, there have not been enough studies about CR education with elementary school faculties and CR volunteers being the research subjects. Therefore, it is necessary to explore the degrees of understanding CR ideals, CR teaching, plans about CR activities, and CR effect for school faculties and CR volunteers.

Firstly, the specific educational objectives of the CR education plans implemented by many ESs include inspiring humanity, passing on the Chinese culture, developing humanistic spirit, and discovering potentials. CR teachers should not only know the importance of CR and realize the values of CR [14, 15] but also must understand the basic principles of CR education: one purpose, two natures, three principles, four standards, and five characteristics [16].

The findings of the empirical studies indicate that over 77% of teachers believed that CR teachers can recognize the values of classics, and over 35% of teachers believed that children should start reading classics as early as possible [17]. The basic principle of CR teaching for children is allowing children to contact, read, and recite classics more often [1]. Currently, most teachers usually develop various recitation methods in the ESs, such as fan-tan, taking turns, and passing challenges. Teachers always have different practices to interpret contents of classics. In the aspect of rewards and punishments, verbal praises instead of material rewards and encouragement instead of punishments are stressed [18, 19]. Above those, this study creates a classics-reading curriculum (CRC) scale including curriculum cognition (CC) and curriculum teaching (CT). The former represents the degree of understanding the CR philosophy and the later represents the teaching methods for CR.

Secondly, ESs often invite experts or scholars to give speeches regarding CR education in order to clear up teachers' and parents' doubts about CR education and to offer teachers and parents a chance to further understand the importance of CR education, so that they would then accept and recognize CR education [15]. CR achievement exhibitions are usually held for the purposes of offering community residents to know CR, increasing teachers' willingness to engage in CR, increasing parents' willingness to become CR volunteers, and even improving schools' enrollment rates [12, 20–22]. ESs implement various CR activities, such as CR

webpage [12], CR volunteer trainings or summer/winter CR camps [22], CR education parenting seminars, parent-child CR curriculums or adult CR curriculums, CR education workshops for teachers [9–11], cross-school CR exchange activities, Cross-Strait CR Seminar [20], and the Suzhou-Taipai Chinese Classic Poems and Prose Exchange Activity Series [23]. Above those, this study creates a classics-reading promotion (CRP) scale, including intramural promotion (IP) and extramural promotion (EP). The former represents various inside-school CR activities and plans promoting CR and the later represents various outside-school CR activities and plans promoting CR.

Thirdly, the findings of many empirical studies show that there are not only positive views on CR education for children but also affirmation to the overall effects of promoting CR education for children, such as improving memory [21–27], enhancing concentration [28], understanding more about the culture [29, 30], reducing ill behaviors and fighting, avoiding arguments, accepting advises, showing understanding for others, improving interpersonal interactions, becoming more mature [15, 19, 25, 28, 30], having harmonious class atmosphere, making class management easier [17, 24, 31, 32], helping to promote moral education [26, 28], increasing close parent-child interactions [24, 28], and increasing teacher-student interactions [17, 28, 32]. In other words, CR can not only improve the effects of students' learning but also enhance the effects of teachers' class management. Above those, this study creates a classics-reading effect (CRE) scale including learning effect (LE) and class management effect (CME). The former represents the effects about moral, concentration, memory, and so on, and the later represents the effects about class order, class atmosphere, teacher-student relationship, parent-child relationship, and so on.

Fourthly, the nonprofit organization originated in the United States of America. The school is a nonprofit organization of education [33, 34]. Seetoo [35] constructs CORPS framework for nonprofit organization's management. CORPS consists of five basic factors and is an acronym for Client, Operation, Resource, Participant, and Service. The Client factor (C) means service objects. The Operation factor (O) contains plan, execution and control of the activities. The Resource factor (R) includes financial resources, material resources, and resource providers. The Participant factor (P) consists of full-time staff and volunteers. The Service factor (S) means that the organization provides services for objects. Further, the CORPS operation model means that an organization provides some valuable services (S) for some people in society (C) through implementing numerous organized activities (O) and combining with the participants (P), financial resources, material resources, and resource providers (R) (see Figure 1).

The research directions of 34 empirical studies are roughly classified into six aspects including participant, resource, curriculum, promotion, effect, and client. They are categorized according to the characters of the CORPS factors. Because school staffs and CR volunteers are the central executors in the CR education for ESs, the P contains principals, directors, teachers, and CR volunteers. The financial

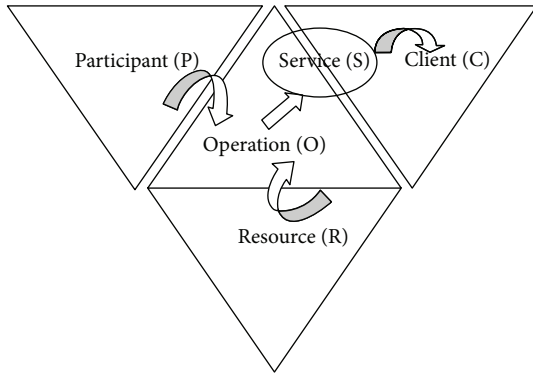


FIGURE 1: CORPS operation model (graph source from Seetoo [35]).

resources and material resources are needed in the implementation of CR education for ESs. Those resources always are provided by the school or parents association or parents. Thus, the R consists of financial resources, material resources, and resource providers. The O contains CRC including CC and CT and CRP including IP and EP. The S consists of CRE including LE for students and CME for teachers. Because CRE is aimed at students and teachers mainly the C includes students and teachers.

The CRE can be affected separately by principals, directors, teachers, CR volunteers, and various resources [15, 26, 36, 37]. In other words, the Participant factor and the Resource factor should influence the Operation factor. The CR aim and philosophy for the teachers can affect the implementation of CR education in the school and then can affect CRE [19, 22, 38]. Therefore, CRC should relate to CRE. If the school wants to reach the aim and effect for CR education, and there should be a comprehensive implementation plan and activities for CR education in the school [35]. Therefore, CRP should relate to CRE. In other words, the Operation factor should influence the Service factor. Further, the CORPS operation model for CR education in the school means that the CR education of the school provides CRE (S) for students and teachers in the school (C) through the CRC and CRP (O), combining with the principals, directors, teachers, CR volunteers (P), various financial resources, material resources, and resource providers (R).

The research directions of 34 empirical studies all focus on certain selected aspects. The growing effects of CR are slow because CR must be carried out for a long time [15, 26, 27, 30, 39]. And it is not easy for the effects of CR to last. One of the key reasons is that there is no overall plan for CR education [36]. Therefore, it is essential to explore the influences of degrees of understanding the CR philosophy, CR teaching, and CR activity planning of school faculties and CR volunteers on CR effects.

In addition, because there is the lack of overall management concept for the combination of those aspects about CR education's research, it is important to integrate those aspects. However, the literatures about the principals, directors, teachers, CR volunteers, and resources having influence on CRE for CR education in ESs are insufficient, this study only examines

the relationships between CRC, CRP, and CRE for the principals, directors, teachers, and CR volunteers through applying CORPS framework constructed by Seetoo [35] for nonprofit organization's management (see Figure 2). In other words, this study only investigates the influence of Operation factor on Service factor. Lastly, some related suggestions are proposed for CR education in ESs.

Above those, the research questions are as follows.

- (1) Dose each of CRC scale, CRP scale, and CRE scale has a good internal reliability?
- (2) Dose each of CRC scale, CRP scale, and CRE scale has a good construct validity?
- (3) Dose CRC and CRP influence CRE? (see Figure 2).

2. Method

2.1. Participants and Procedure. Because CR education is not yet a part of the formal elementary school education system, this study adopts the purposive sampling method. H. E. Tinsley and D. J. Tinsley [40] suggest that 10 subjects or 5 subjects at a minimum are required for every variable being analyzed. Although there is no correct rule for estimating sample size for SEM, recommendations are for a size ranging between 100 and 200 [41]. Reisinger and Turner [42] showed that the sample size should be as a rule of thumb at least 5 times the number of parameters. Thus, according to the statistics regarding the numbers of elementary school faculties in northern, central, southern, and eastern Taiwan [43, 44] and 82 estimated parameters in the model 1 of this study, the pilot sample of 150 subjects and the formal sample of 515 subjects are selected from principals, directors, teachers, and CR volunteers of ESs in the northern, central, southern, and eastern Taiwan from Oct 2012 to Jan 2013. With the response rate over 93%, there are 141 valid pilot samples and 500 valid formal samples.

2.2. Measure. This study adapts CRC scale, CRP scale, and CRE scale developed by Tang [45] and retests the validity and reliability of each of the three scales. The pretest questionnaire contained 40 items, 11 items of CRC scale, 12 items of CRP scale, 12 items of CRE scale, and 5 demographic items. Responses are judged on 6-point Likert type scales for each item (1 = strongly disagree and 6 = strongly agree).

2.3. Exploratory Factor Analysis. 141 records are used to identify factor structures of each of CRC scale, CRP scale, and CRE scale. 11, 12, 11 items are remained in each of them, respectively, through exploratory factor analysis (EFA) using SPSS 17.0. CRC scale contains CC subscale (5 items) and CT subscale (6 items), CRP scale contains IP subscale (6 items) and EP subscale (6 items), and CRE scale contains LE subscale (5 items) and CME subscale (6 items) through exploratory factor analysis (EFA) using SPSS 17.0. Each total variance explained of three scales is 63.18%, 72.52%, and 76.38%. Cronbach [46] claims that $.8 \leq \text{Cronbach } \alpha < .9$ represents a good internal consistency. Each Cronbach α coefficient of CC, CT, IP, EP, LE, and CME subscales is .88, .85, .93,

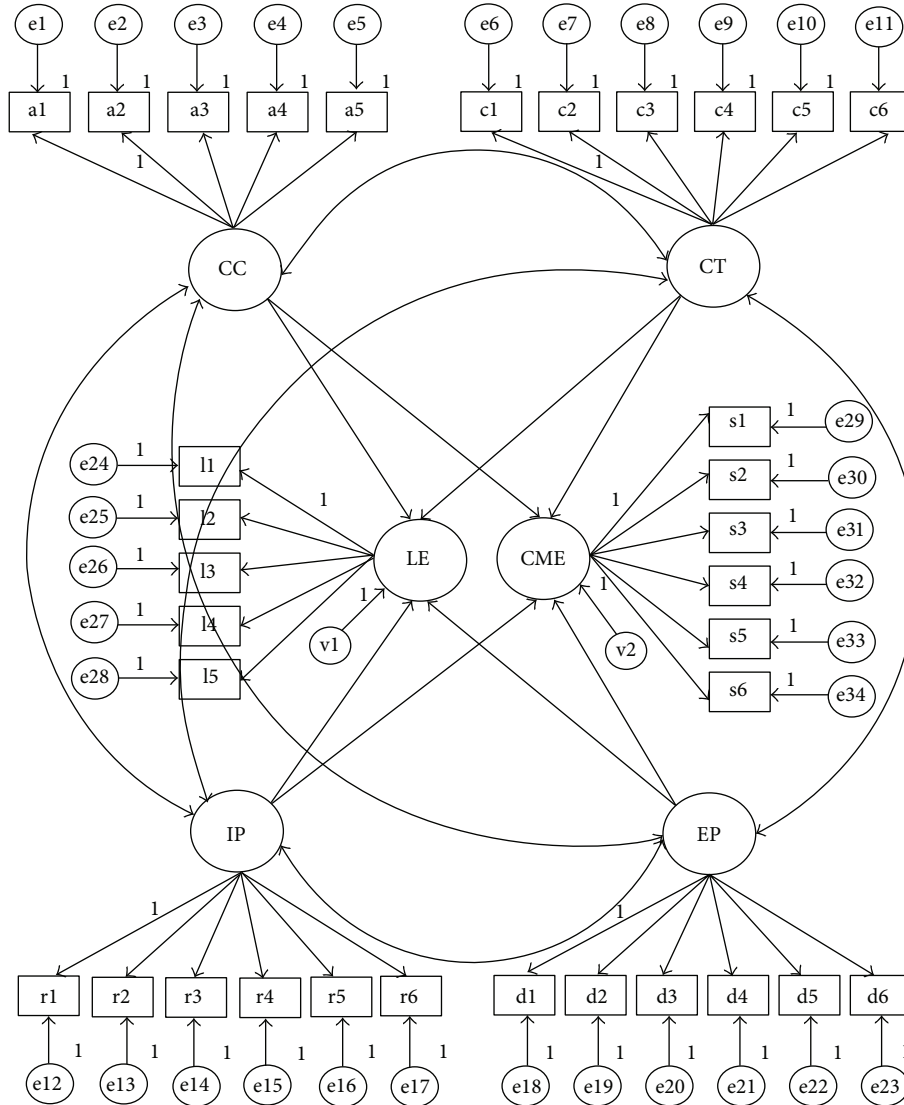


FIGURE 2: The hypothetical constructs of relationships between CRC, CRP, and CRE in model 1.

.91, .91, and .94. Those indicate that all subscales are with good internal reliabilities.

2.4. Confirmatory Factor Analysis and Structural Equation Modeling. 500 records are used to test reliability and validity of each of CRC scale, CRP scale, and CRE scale through confirmatory factor analysis (CFA) and to examine model 1 (see Figure 2) using Amos 17.0. Eleven fit indices criteria are chosen: chi-square ratio (χ^2/df) < 5 [47], goodness of fit index (GFI) > .90, adjusted goodness of fit index (AGFI) > .9, normed incremental fit index (NFI) > .90, comparative fit index (CFI) > .90, parsimony normed fit index (PNFI) > .5, parsimony goodness of fit index (PGFI) > .5, value of saturated model < expected cross-validation index (EVC) < value of independent model, value of saturated model < Akaike information criteria (AIC) < value of independent model [48], root mean square (RMR) < .05 [47], and root mean square error of approximation (RMSEA) < .08 [49].

TABLE 1: Mean, SD, and correlation coefficients of all subscales (N = 500).

Subscale	Mean (SD)	CC	CT	IP	EP	LE	CME
CC	5.00 (.63)	1					
CT	5.07 (.60)	.64**	1				
IP	4.80 (.67)	.62**	.61**	1			
EP	4.75 (.66)	.53**	.56**	.73**	1		
LE	5.07 (.67)	.68**	.63**	.66**	.62**	1	
CME	4.77 (.75)	.64**	.57**	.63**	.58**	.72**	1

Note. SD: standard deviation **P < .01.

3. Results and Discussion

3.1. Descriptive Statistics and Correlations. As shown in Table 1, each mean of CC, CT, IP, EP, LE, and CME from 500 records is >4.70. It indicates that most of principals, directors,

TABLE 2: Each of fit indices of CRC scale, CRP scale, and CRE scale (N = 500).

Index	χ^2/df <5	GFI >.9	AGFI >.9	NFI >.9	CFI >.9	RMR <.05	RMSEA <.08	PNFI >.5	PGFI .5
CRC	4.01***	.94	.91	.94	.95	.03	.078	.74	.61
CRP	4.62***	.92	.88	.94	.95	.028	.085	.73	.63
CRE	12.66***	.82	.73	.89	.89	.035	.154	.70	.54

Note. ***P < .001.

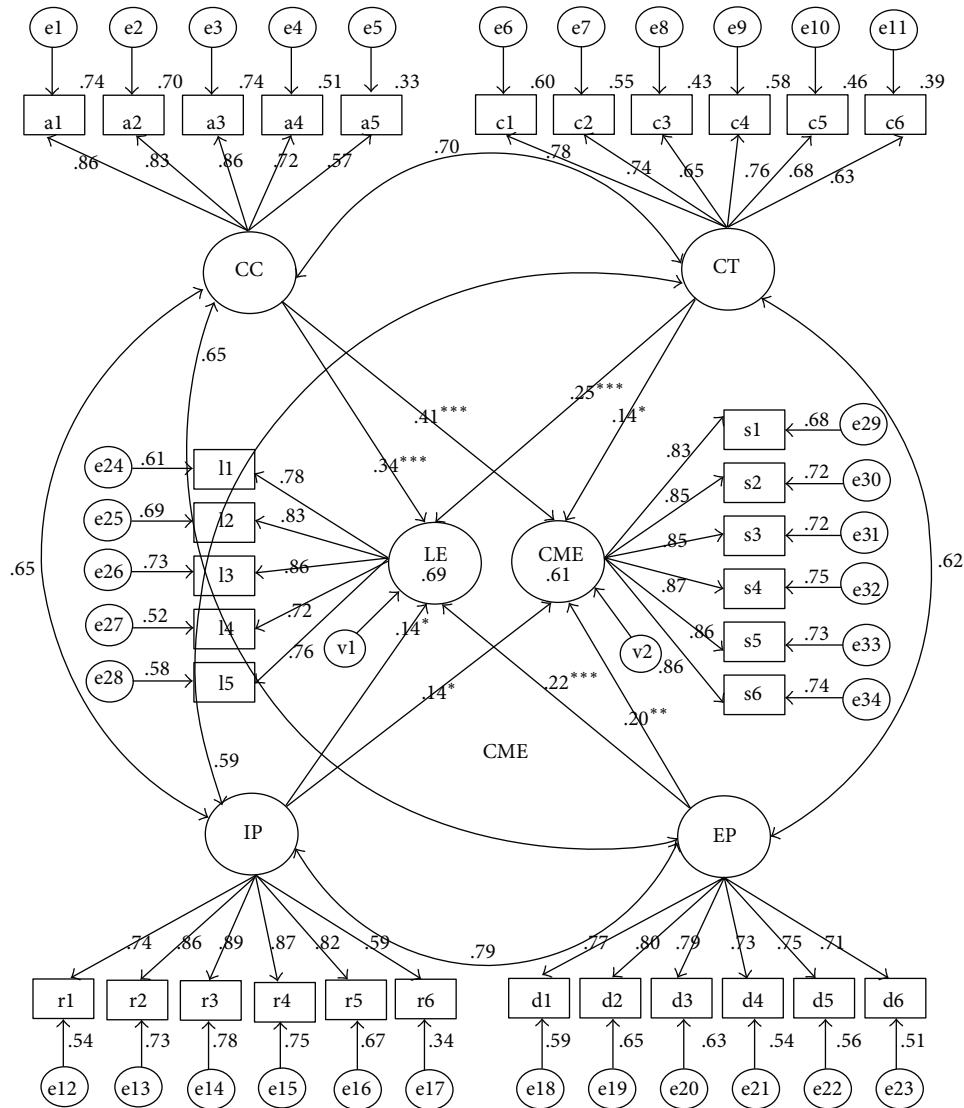


FIGURE 3: Standardized coefficients of CRC and CRP to CRE in model 1.

teachers, and CR volunteers of ESS have the degree of understanding the CR philosophy, accept teaching methods for CR, promote roughly various CR related inside-school and outside-school activities and plans, and indentify effects of CR for students and teachers. Any two of CC, CT, IP, EP, LE, and CME are significantly and positively correlated, and all correlation coefficients are between .53 and .73.

3.2. CFA. CFA is applied with the 500 valid formal samples. As shown in Table 2, the internal quality and external quality

of CRC and CRP and the internal quality of CRE are good. Although the external quality of CRE is not ideal, it is better than moderate and is acceptable.

As shown in Table 3, it indicates the following: (1) because each composite reliability (C.R.) of the all latent variables is >.60 [50], there is a good internal reliability for each of CRC scale, CRP scale, and CRE scale. (2) Because each standardized factor loading (SFL) of the all observable variables is $\geq .50$ and all P values are significant and each average variance extracted (AVE) of the all latent variables is between .50

TABLE 3: Parameters estimation for CC, CT, IP, EP, LE, and CME subscales (N = 500).

Subscale	SFL ≥.5	SMC ≥.3	C.R. >.6	AVE >.5	Subscale	SFL ≥.5	SMC ≥.3	C.R. >.6	AVE >.5	CORR. COEF.
CC			.88	.61	CT			.86	.50	CC and CT
a1	.87***	.77			c1	.79***	.62			.69
a2	.84***	.71			c2	.74***	.55			
a3	.86***	.74			c3	.64***	.41			
a4	.71***	.50			c4	.78***	.61			
a5	.51***	.26			c5	.67***	.45			
					c6	.60***	.36			
IP			.90	.64	EP			.89	.58	IP and EP
r1	.73***	.64			d1	.77***	.58			.79
r2	.86***	.74			d2	.81***	.66			
r3	.89***	.79			d3	.79***	.62			
r4	.86***	.74			d4	.74***	.55			
r5	.82***	.67			d5	.75***	.56			
r6	.58***	.34			d6	.71***	.50			
LE			.89	.63	CME			.94	.73	LE and CME
l1	.78***	.63			s1	.83***	.73			.78
l2	.81***	.66			s2	.85***	.72			
l3	.86***	.74			s3	.85***	.72			
l4	.75***	.56			s4	.87***	.76			
l5	.77***	.59			s5	.85***	.72			
					s6	.86***	.74			

Note. SFL: standardized factor loading; SMC: squared multiple correlation. C.R.: composite reliability; AVE: average variance extracted. CORR. COEF.: correlation coefficient; *** P < .001.

TABLE 4: Summary of the overall fit indices for model 1 (N = 500).

Absolute fit measures		Accept or not
χ^2	1706.79	
df	513	
$\chi^2/df < 5$	3.33	○
P value > .05	<.001	X
RMR < .05	.034	○
RMSEA < .08	.068	○
GFI > .9	.83	X
AGFI > .9	.80	X
Value of saturated model < EVCI < value of independent model	2.39 < 3.75 < 26.54	○
Incremental fit measures		Accept or not
NFI > .9	.87	X
IFI > .9	.91	○
CFI > .9	.91	○
Parsimonious fit measures		Accept or not
PNFI > .5	.80	○
PGFI > .5	.71	○
Value of saturated model < AIC < value of independent model	1190.00 < 1870.79 < 13241.07	○

and .73, there is a good convergent validity for each of CRC scale, CRP scale, and CRE scale. (3) Because the correlation coefficients among CRC, CRP, and CRE are .69, .79, and .78 and because each of them is under .85 [51], there is a discriminant validity for each of the three scales.

3.3. Structure Model

3.3.1. Estimation Method. Because the skew coefficients and kurtosis coefficients of all variables are between $-.73$ and $-.14$ and between $-.74$ and $.91$, this study chooses to adopt

the method of maximum likelihood to estimate the parameters of model 1.

3.3.2. *Offending Estimation.* All the standardized parameter estimations are between .14 and .89, not too close to 1, and the plus or minus signs of the estimations of parameters are consistent. All the standard errors of the estimations are between .012 and .048, not very large. There is no negative error variable and all the error variables are significant. Therefore, model 1 meets the 5 preliminary fit criteria [52].

3.3.3. *Evaluation of the Overall Goodness-of-Fit.* As shown in Table 4, the values of χ^2/df , RMR, RMSEA, ECVI, IFI, CFI, PNFI, PGFI, and AIC are all acceptable, but *P* value is significant. The values of GFI, AGFI, and NFI are nearly accepted. Therefore, the empirical data are fitted in model 1.

3.3.4. *To Test Goodness-of-Fit for Internal Structure.* As shown in Table 5, the parameter estimations of the 34 observed indices are all significant, each SEL of them is $\geq .5$, each AVE of the six latent variables is $> .5$, and each C. R. of them is $> .6$ [50]. Therefore, the internal quality of model 1 is good.

3.4. *Direct and Total Effect.* As shown in Figure 3, the effects of CC on LE and CT on LE are .34***, .25***. Those results are consistent with the findings of many studies which had pointed out that CRC would influence LE [15, 22, 24, 26, 28, 29]. The effects of CC on CME and CT on CME are .41***, .14*. Those results are consistent with the findings of many studies which had pointed out that CRC would further influence CME [17, 19, 24, 25, 30–32, 53]. The effects of IP on LE and EP on LE are .14*, .22***. The effects of IP on CME and EP on CME are .14*, .20**. Those results are consistent with the findings of which had pointed out that CRP would influence LE and CME [17, 22, 36, 54]. CC, CT, IP, and EP can explain 69% of LE and 61% of CME.

Above those, the influences of CC on LE and on CME are both the largest. It indicates that CC is the main factor influencing LE and CME. The influences of CC and CT on LE and CC on CME are larger than the influences of IP and EP on LE and on CME. It implies that to promote CR, CR philosophy plays an important role. The influences of IP on LE and on CME are both rather small. The main reason may be that teachers do not entirely believe that CR achievement exhibitions are helpful for their teaching [36], and then the influences on LE are not strong. The influences of IP on LE and on CME are smaller than the influences of EP on LE and on CME. The reasons may be that because CR education is not a part of the formal education system, CR education policies are not compulsory; because manpower and resources of ESs are limited and there are a lot of school activities other than CR activities, teachers do not want to participate in promoting CR actively, and then those limit to promote CR activities and lead to a rather small influences of IP on LE and CME [17]. Although those reasons may lead to a smaller influence of CRP on CRE, CRP cannot be ignored for the classics-reading education in the school.

TABLE 5: SEL, R^2 , AVE, and C. R. in model 1.

L.V.	O.V.	SEL $\geq .5$	SMC (R^2)	AVE $> .5$	C.R. $> .6$
CC	a1	.86***	.74	.60	.88
	a2	.83***	.70		
	a3	.86***	.74		
	a4	.72***	.51		
	a5	.57***	.33		
CT	c1	.78***	.60	.50	.86
	c2	.74***	.55		
	c3	.65***	.43		
	c4	.76***	.58		
	c5	.68***	.46		
	c6	.63***	.39		
IP	r1	.74***	.54	.64	.91
	r2	.86***	.73		
	r3	.89***	.78		
	r4	.87***	.75		
	r5	.82***	.67		
	r6	.59***	.34		
EP	d1	.77***	.59	.58	.89
	d2	.80***	.65		
	d3	.79***	.63		
	d4	.73***	.54		
	d5	.75***	.56		
	d6	.71***	.51		
LE	l1	.78***	.61	.63	.89
	l2	.83***	.69		
	l3	.86***	.73		
	l4	.72***	.52		
	l5	.76***	.58		
CME	s1	.83***	.68	.73	.94
	s2	.85***	.72		
	s3	.85***	.72		
	s4	.87***	.75		
	s5	.86***	.73		
	s6	.86***	.74		

Note. L.V.: latent variable; O.V.: observed variable; SFL: standardized factor loading. SMC (R^2): square multiple correlation. AVE: average variance extracted; C.R.: composite reliability; *** $P < .001$.

As shown in Table 5, a1 and a3 are the max ($R^2 = .74$) among 10 observed variables' R^2 of CRC, and they means that CR can inspire human nature and has far-reaching implication for people. Perennialism education also emphasized those [55]. Thus, those results are similar to the view on Perennialism education. r3 is the max ($R^2 = .78$) among 12 observed variables' R^2 of CRP, and it means that CR achievement exhibitions are usually held for the purposes of offering community residents to know CR. Bagin and Gallagher [56] claim that there is a school public relation between the school and community. Thus, the school wants to establish relationships with the community through CR achievement exhibitions. s4 is the max ($R^2 = .75$) among 12 observed variables' R^2 of CRE, and it means that CR contributes to

practice life education. Bandura [57] shows that individual behaviors change through observational learning or modeling. The students always regard sages as models in CR teaching and then their behaviors change in a positive direction gradually through observational learning or modeling.

4. Conclusion

The fit of the external and internal structure of model 1 is good. It indicates that CRC and CRP positively influence CRE from Figure 3. In other words, the Operation factor influences the Service factor for CR education's CORPS model. The results of the SEM construction and verification of this study are consistent with the CR literature and CORPS framework. The results of this study can not only conducive to facilitating CRC, CRP, and CRE but also provide the management policy for the CR education in ESs. This study also shows that both CORPS framework can apply to CR education management and the overall CR plans play an important role for CR education in ESs. Especially, the findings of this study contribute to achieving the sustainable management for the CR education in ESs.

Furthermore, this study suggests that the educational institutions or ESs should always hold the CR education workshops for school faculties and CR volunteers to enhance their CR philosophy and CR teaching; ESs should plan more CR activities inside/outside schools to promote CR education; ESs should increase manpower and resources about CR education. Finally, the further research is to investigate the influences of manpower and resources on CRE.

Conflict of Interests

The authors declare that there is no conflict of interests regarding the publication of this paper.

Acknowledgments

The authors are grateful to Global Classics-Reading Education Foundation, Professor Tsai-Kui Wang, Miss Shu-Kui Tsai, and numerous principals, directors, teachers, and classics-reading volunteers for their kind assistance.

References

- [1] T. K. Wang, *The Handbook of Classics for Children Education*, Language Teaching & Research Center, National Taichung University of Education, Taichung, Taiwan, 1995, (Chinese).
- [2] International Cultural Institute, *A Guide for Children's Classics-Reading: Global Promotion of Classics-Reading Education for Children by Mr. Nan Huai-Chin*, Laoku, Taipei, Taiwan, 2007, (Chinese).
- [3] H. Zhou, "The first lesson of the new century: character decided win and lose-future talented person's secret," *CommonWealth Magazine*, vol. 14, 2004 (Chinese).
- [4] Character Counts, "The six pillars of character," 2008, <http://charactercounts.org/sixpillars.html>.
- [5] R. B. Cooter Jr., "Teacher "capacity-building" helps urban children succeed in reading," *Reading Teacher*, vol. 57, no. 2, pp. 198–205, 2003.
- [6] X. D. Liu, *Blind and Save: Evaluation of Children's Classics-Reading*, Education, Jiangsu, China, 2009, (Chinese).
- [7] T. T. Pan, "Analysis of Tsai-Kuei Wang's theory of childhood education centered on the recitation of Chinese ancient classics," *Studies in the Humanities and Social Science*, vol. 9, pp. 55–96, 2008 (Chinese).
- [8] J. Q. Guo, "The requirement for children to read classics is abreast of the times," *Journal of Educational Studies*, vol. 3, no. 2, pp. 29–34, 2007 (Chinese).
- [9] Department of Education and Hualien County Government, "2012 Workshop of promotion of classics-reading education for teachers" (Chinese), 2011, http://www.yam.ks.edu.tw/joomla01/index.php?option=com_content&view=article&id=627&Itemid=544.
- [10] Department of Education, Hualien County Government, "2012 workshop of promotion of classics-reading education for teachers," 2011, (Chinese), <http://teacher.hlc.edu.tw/imain9.asp?id=365&sid=448>.
- [11] Ministry of Education, "The 2009 implementation plan for the teacher training seminars in 7 counties/cities in Southern Taiwan during the summer vacation," 2009, (Chinese), <http://163.32.48.5/data/pub/200906031026070.doc>.
- [12] Department of Education, Hualien County Government, "The implementation plan for promoting classics-reading for children in Hualien County," 2010, (Chinese), <http://teacher.hlc.edu.tw/imain9.asp?id=365&sid=448>.
- [13] Epoch Times, "Founding of the classics-reading foundation, propagating classics-reading to the world: classics-reading can help students learn more about the Chinese culture, increase their concentration, improve their behaviors, and treat their learning disabilities," 2007, (Chinese), <http://hk.epochtimes.com/7/1/8/37905.htm>.
- [14] Fu Chih Cultural and Educational Foundation, *Explanation of Classics-Reading*, Fu Chih, Taipei, Taiwan, 1999, (Chinese).
- [15] C. J. Yang, *A Case Study of the Application of Reading Chinese Classics Approach in Elementary School*, Graduate Institute of Education, National Taitung University, Taitung, Taiwan, 2005, (Chinese).
- [16] T. K. Wang, "The basic principles of classics-reading education," 2012, (Chinese), <http://bbs.gsr.org.tw/cgi-bin/topic.cgi?forum=14&topic=476&show=0>.
- [17] Y. H. Weng, *The Research of Teacher's Teaching Beliefs in the Children's Classics-Memorizing Programs*, Graduate Institute of Educational Entrepreneurship and Management, National University of Tainan, Tainan, Taiwan, 2008, (Chinese).
- [18] H. R. Chang, *The Learning Process of Classics Education [M.S. thesis]*, Graduate Institute of Curriculum and Instruction, Mingdao University, Taichung, Taiwan, 2012, (Chinese).
- [19] Y. F. Wang, *Research on the Attitude, Teaching Process and Effect of the Children Poem Study Class-the Example of Three Primary Schools in Taichung County*, Institute of National Education, National Hualian Teachers College, Hualian, Taiwan, 1999, (Chinese).
- [20] Shihchuan Elementary School, "Shihchuan classics-reading website," 2009, (Chinese), http://classweb.scps.kh.edu.tw/Homepage.php?teacher_id=123.
- [21] Ruimeit Elementary School, "The implementation plan for characteristic development of new ways to read classics," 2010, (Chinese), <http://host.rmes.tyc.edu.tw/~cer2/01/02.doc>.
- [22] Y. H. Chen, *The Study of Applying Classics-Reciting Education Programs in Elementary Schools*, Department of Language and

- Literacy Education, National Taichung University of Education, Taichung, Taiwan, 2009, (Chinese).
- [23] C. Y. Chen, L. F. Cheng, and C. J. Jiang, *The Business Trip Report to Mainland China (Type of Trip: Visiting)*, Suzhou-Taipei Chinese Classic Poems and Prose Exchange Activity Series, Dalong Elementary School, Taipei, Taiwan, 2011, (Chinese).
- [24] D. S. Lin, "Study on classics-reading education in curriculum of the elementary school," in *Proceedings of the 2nd Taiwan International Symposium of Confucianism*, 1999, (Chinese).
- [25] S. C. Chang, *A Study on the Effect of Chinese Classics Reading Teaching for the Elementary Students*, Graduate School of Curriculum and Instruction, National Taipei University of Education, Taipei, Taiwan, 2001, (Chinese).
- [26] C. Y. Yen, *A Case Study of Child Classics-Reciting Education Implemented in Zheng Dian Elementary School in Taichung*, Department of Education, National Taichung University of Education, Taichung, Taiwan, 2012, (Chinese).
- [27] T. P. Huang, *A Study of Children's School Achievements in Classics-Reading [M.S. thesis]*, Department of Education, National Taichung University of Education, Taichung, Taiwan, 2012, (Chinese).
- [28] D. L. Tsui, *Effects of Children's Classical Reading Classes on the Character Development of Elementary School Students*, Department of Adult & Continuing Education, National Taiwan Normal University, Taipei, Taiwan, 2011, (Chinese).
- [29] C. H. Chen, *A Case Study: The Effects on Reading Motivation of Children's Reading-Classics at Home Schooling*, Graduate Institute of Education, National Sun Yat-Sen University, Kaohsiung, Taiwan, 2006, (Chinese).
- [30] H. W. Tsai, *Social Observation on Child Classics-Reciting—Three Examples in Chiayi Classics-Reciting Classes*, Department of Applied Sociology and Institute of Sociology, Chiayi, Taiwan, 2011, (Chinese).
- [31] A. B. Chu, "Report of the achievements of implementing classics-reading education," *Classics-Reading Magazine*, vol. 12, 1998 (Chinese).
- [32] B. R. Yao, "The educational reflexive meaning on the movement of memorization of traditional classics in childhood (I)," in *Education and Society: Introspection of Sociology of Education in the Coming Age of Information*, pp. 51–81, Yang-Chih Book, Taipei, Taiwan, 2000, (Chinese).
- [33] B. J. Bitter and K. R. George, "The exemption of nonprofit organizations from federal income taxation," *Yale Law Journal*, vol. 85, pp. 229–358, 1976.
- [34] B. A. Weisbrod, *To Profit or Not to Profit: The Commercial Transformation of the Nonprofit Sector*, Cambridge University Press, Cambridge, UK, 2003.
- [35] D. H. Seetoo, *The Nongovernmental Organization's Management*, Commonwealth Publishing, Taipei, Taiwan, 1999, (Chinese).
- [36] M. H. Chen, *Study on Current Situation Obstacles and Solutions of Reading Classics in Childhood in Primary Schools in Penghu County [M.S. thesis]*, Master's Program of Curriculum and Instruction, Department of Education, National University of Tainan, Tainan, Taiwan, 2008, (Chinese).
- [37] H. W. Xie, *The Study of Classics-Reading Education for Shitan Junior High School in Miaoli Country*, Department of Chinese Literature, National Taiwan University, Taipei, Taiwan, 2009, (Chinese).
- [38] M. F. Yang, *The Teaching Beliefs of Five Teachers in the Classics-Memorizing Programs*, Graduate Institute of Education, National Chung Cheng University, Chiayi, Taiwan, 2001, (Chinese).
- [39] R. S. Chuang, *An Observational Study of a Children's Class with Classics-Reading Implemented*, Graduate Institute of Compulsory Education, National Chiayi University, Chiayi, Taiwan, 2002, (Chinese).
- [40] H. E. Tinsley and D. J. Tinsley, "Uses of factor analysis in counseling psychology research," *Journal of Counseling Psychology*, vol. 34, no. 4, pp. 414–424, 1987.
- [41] J. Hair, R. Anderson, R. Tatham, and W. Black, *Multivariate Data Analysis with Readings*, Prentice-Hall International, Englewood Cliffs, NJ, USA, 4th edition, 1995.
- [42] Y. Reisinger and L. Turner, "Structural equation modeling with Lisrel: application in tourism," *Tourism Management*, vol. 20, no. 1, pp. 71–88, 1999.
- [43] Department of Statistics and Ministry of Education, "Important educational statistics information" (Chinese), 2011, <https://stats.moe.gov.tw/files/gender/302-2.xls>.
- [44] Ministry of the Interior, "Monthly bulletin of interior statistics," 2012, (Chinese), <http://sowf.moi.gov.tw/stat/month/list.htm>.
- [45] C. A. Tang, "A study of the current situation of classics-reading education in Taiwan and China," *Journal of Cultural and Creative Industries Research*, vol. 2, no. 3, pp. 243–254, 2012 (Chinese).
- [46] L. J. Cronbach, "Coefficient alpha and the internal structure of tests," *Psychometrika*, vol. 16, no. 3, pp. 297–334, 1951.
- [47] K. A. Bollen, *Structural Equations with Latent Variables*, John Wiley & Sons Inc., New York, NY, USA, 1989.
- [48] L. T. Hu and P. Bentler, "Evaluating model fit," in *Structural Equation Modeling: Concepts, Issues, and Applications*, R. H. Hoyle, Ed., pp. 76–99, Sage, London, UK, 1995.
- [49] M. W. Browne and R. Cudeck, "Alternative ways of assessing model fit," in *Testing Structural Equation Models*, K. A. Bollen and J. S. Long, Eds., pp. 136–162, Sage, Kern County, Calif, USA, 1993.
- [50] C. R. Fornell and F. F. Larcker, "Structural equation models with unobservable variables and measurement error," *Journal of Marketing Research*, vol. 18, pp. 39–51, 1981.
- [51] R. B. Kline, *Principles and Practice of Structural Equation Modeling*, Guilford Press, New York, NY, USA, 2005.
- [52] R. P. Bagozzi and Y. Yi, "On the evaluation of structural equation models," *Journal of the Academy of Marketing Science*, vol. 16, no. 1, pp. 74–94, 1988.
- [53] C. M. Liao, *A Study of the Influences of Implementing Classics-Reading Education in Elementary Schools on Improving Children's Self-Concept*, Department of Language and Literacy Education, National Taichung University of Education, Taichung, Taiwan, 2003, (Chinese).
- [54] Y. P. Song, *The Action Research of the Effects of Classics-reading Lessons on the Learning Methods, Learning Attitudes, and Scholastic Achievements in Mandarin Chinese for the Pupils in a Rural Elementary School*, Department of Education, National Kaohsiung Normal University, Kaohsiung, Taiwan, 2008, (Chinese).
- [55] A. Ornstein and F. Hunkins, *Curriculum: Foundation, Principles, and Issues*, Pearson, Boston, Mass, USA, 2004.
- [56] D. Bagin and D. R. Gallagher, *The School and Community Relations*, Allyn and Bacon, Needham Heights, Mass, USA, 7th edition, 2001.
- [57] A. Bandura, *Social Learning Theory*, Prentice Hall, Englewood Cliffs, NJ, USA, 1985.

Research Article

Analyzing Lifestyle and Consumption Pattern of Hire Groups under Product Service Systems in Taiwan

Jui-Che Tu,¹ Yu-Chen Huang,¹ Chuan-Ying Hsu,² and Yu-Wen Cheng³

¹ Graduate School of Design Doctoral Program, National Yunlin University of Science and Technology, Yunlin 64002, Taiwan

² Department of Business Administration, Dayeh University, Changhua 51591, Taiwan

³ Graduate School and Department of Creative Design, National Yunlin University of Science and Technology, Yunlin 64002, Taiwan

Correspondence should be addressed to Jui-Che Tu; tujc@yuntech.edu.tw

Received 14 September 2013; Accepted 20 October 2013

Academic Editor: Teen-Hang Meen

Copyright © 2013 Jui-Che Tu et al. This is an open access article distributed under the Creative Commons Attribution License, which permits unrestricted use, distribution, and reproduction in any medium, provided the original work is properly cited.

This study explores the characteristics of rental goods, integrates the green concept in the design and development, and introduces the concept of product service into the rental consumption trend in Taiwan. This study takes the questionnaire survey to collect various opinions of the consumers to rental consumption and also classifies the Taiwanese consumers into five clusters based on the life styles, and the names of clusters are simple financial management cluster, environment and taste cluster, fashionable and flexible cluster, careful purchase cluster, and smart consumption cluster. Finally, conclusions are as follows. (1) The green consumption cognition and attitude of the consumers to the environmental goods can help to master the factor of green consumption property for developing the rental commodities. (2) The market segmentation of the rental consumption market can be enhanced by the variables of available life styles. (3) The applications with product service rental characteristics should take the opinion feedback of the consumers into the sustainable product development conditions and expand the service property of the product. (4) As the cost of cradle-to-cradle recycling pattern is high, the support and promotion of the government can help to construct the business model of product service rental consumption and develop the rental economy.

1. Introduction

Human plunder and the destruction of nature are closely related to consumption patterns. The purpose of consumption is to satisfy needs; however, in a society of capitalism, in order to sell more products, capitalists stimulate need through the use of various kinds of marketing measures that result in unnecessary consumption [1–3]. With the rise of environmental consciousness, green consumption has been proposed in response to unsustainable crisis in economic development. According to Marx, consumption is not only the end but also the start of production. Consumption both fulfills and enhances production. It also influences exchange and distribution [4–8]. Critical positions of consumption suggest that, in order to avoid the crisis of unsustainable development, human beings must change the current consumption model, which is destroying the environment [9, 10]. Leasing changes the consumption habit of manufacturers

and consumers. Purchase has changed into leasing. The sold products are changed as services [11, 12]. Consumers benefit from functions of products, but the ownership still belongs to manufacturers. Thus, manufacturers not only satisfy customers' needs of product functions, but also reduce product output and sales by services provided [13–15]. It will decrease resource consumption and pollutant output and control the total volume.

According to WRAP of the UK, in 2009, every year in the UK 143 billion GBP of usable goods are disposed. Using clothing as an example, the current average utilization rate is only 66%. If goods can be fully used until the end of product life, it will save 47 billion GBP for consumers every year. According to the data, with environmental protection, by means of rental, hire groups are becoming the new green consumption group [11, 13, 14].

When consumption trends change from buying-selling consumption to that of rental consumption, rental behavior

will enhance the circular consumption. It will not only save their product resources but also their social public resources. Leases can be divided into capital leases and operating leases. Capital leases are financial leases. The lessees authorize the purchase of new machines and equipment to the lessors and then rent the equipment from the lessors. All depreciation is paid by the lessees' accounting in different periods. During the period of the lease, the lessees have the usage right of the goods [11, 15].

Thus, the risk should be particularly evaluated and guaranteed. An operating lease refers to a noncapital lease. With an operating lease, the lessors (leasing firms) have the ownership of the leasing subjects (machines and equipment), while the lessees (enterprises) have the usage right of the leasing subjects. Once the lease term expires, ownership of the leasing subjects remains with the lessors. During the rental period, the lessors must undertake the expenditures of renewal, maintenance, and prevention of leasing subjects [11, 12].

Rentals change the consumption patterns of manufacturers and consumers. As purchase has changed into rental service, the original sold product is changed into a service, where consumers can benefit from product functions while ownership belongs to the manufacturer. The manufacturer can meet customer demands of product functions, and reduce product output and sales by providing a service. In this way, the resource consumption and pollutant output can be decreased to achieve the effect of total amount control [11–15].

In modern society, people are concerned about enjoyment and have developed new lifestyles using the rental concept to enjoy lives that are limited by money. New lifestyle groups known as hire groups have thus been constructed. Hire groups enjoy renting items, and they only care about possessing the items for a period of time instead of for the life of the product. With limited cash, consumers can experience unlimited rentals [16–18]. Leasing firms sell services and consumers spend money to satisfy temporary needs instead of receiving ownership. Some products are used rarely during the year. For these products, customers can pay a small amount of money for usage rights that last a few days. They do not need to pay a large amount of money [6–8]. In addition, the same products can be repeatedly used and rented. Thus, rentals are not only good for finance; they also decrease the waste of resources and help protect the environment [1, 13–15].

Such a model of meeting the “environmental protection” demand by “selling service” is in line with the concept of “PSS (product service system).” “PSS” is based on environmental protection and economic considerations [19–22]. It combines product and service to satisfy the consumption demand in order to realize the purpose of dematerialization of the product [23–26]. The system is usually operated by rentals, shared use, or pricing by unit of use. Consumers purchase the product “service,” as provided by this system, rather than the product “substance” [27–31]. Hence, this study introduces the product service concept into the rental development trends of Taiwan, conducts a survey on consumer preferences of rental commodities, and plans to create “Taiwan’s environmentally

friendly rental life.” It is expected to develop products inline with consumer demands and implement the sustainable development of the environment in order to usher in a new era of environmental protection in Taiwan. The purposes of this study are as following.

- (1) Using the above literature review, this study probed into time and the influence of rental consumption groups. Through the investigation on lifestyle, this study explored the life and characteristics of hire groups in Taiwan and analyzed their cognition of rental consumption, behavior, and attitude.
- (2) Through in-depth interviews and questionnaire surveys, this study probed into the rental patterns and product service systems preferred by Taiwan consumers, as well as consumers' views and expectations of the rental industry.

2. Materials and Methods

2.1. Research Framework. In order to probe into lifestyle of rental consumption groups in Taiwan from the perspective of product service systems, this study adopted a literature review, a questionnaire survey on consumer lifestyles, factor analysis, and clustering analysis, in order to recognize the needs of rental consumption groups in Taiwan and generalize the important factors, as shown in Figure 1.

Through a literature review, this study explored theories related to product service systems, rental consumption, sustainable product development, and lifestyles. The first stage of interviews was conducted. Using a questionnaire survey, this study analyzed the types and patterns of rental consumption accepted by the Taiwanese, factors of the leases and lifestyles of rental consumption preferred by different groups, and recognized Taiwanese consumers' expectations and thoughts about the rental industry.

2.2. Research Subjects. This study aimed to probe into Taiwanese consumers' views of the rental industry and generalize the lifestyle of potential rental consumption groups in Taiwan. The subjects were consumers with the cognitive and purchasing capability. Subjects include age 18~55 years old, college educational level, annual income 0.3~1.2 million NTD, occupation respectively labor industry, professional personnel, student and service industry, and residential places from northern, central, and southern of Taiwan. The questionnaire survey was conducted to screen potential hire groups in order to explore their lifestyles.

2.3. Research Design. This study used a questionnaire survey and the investigation included demographics and the subjects' personal basic information. The subjects' consumption behavior of rental goods demonstrated their purchases, consumption cognition, and consumption attitude, as well as factors of their selection of rental consumption. There were five parts in the questionnaire survey.

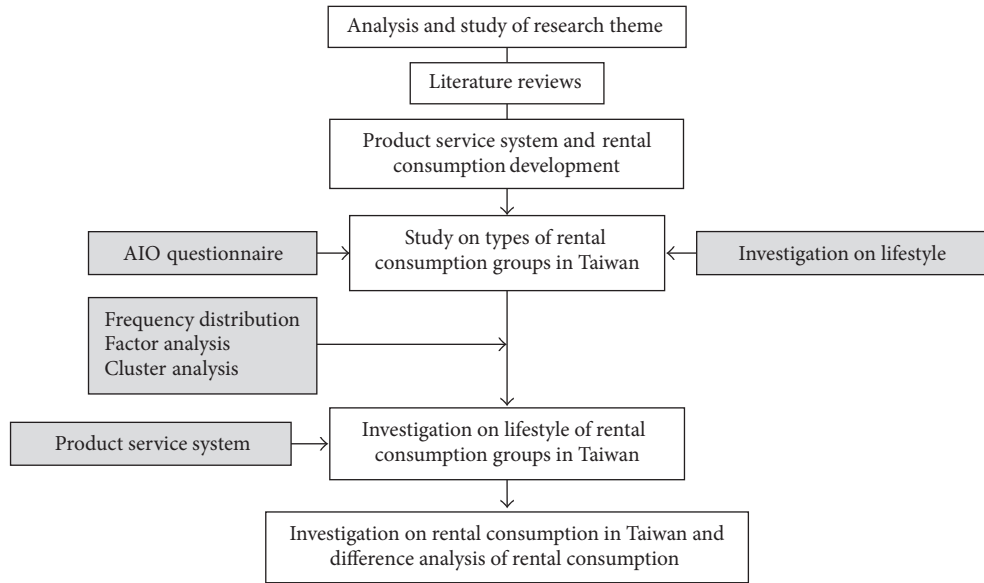


FIGURE 1: Research framework.

TABLE 1: Analysis of the total reliability of the lifestyle scale.

Number of subjects	Cronbach's α	Number of items
198	0.776	31

TABLE 2: KMO and Bartlett's test of lifestyle scale.

Kaiser-Meyer-Olkin measure of sampling adequacy	0.763
Bartlett's test of sphericity	Significance 0.000

First, the demographic variable of the subjects mastered the structure of samples and provided enough information for analysis of problems and interpretation of abilities.

Next, rental consumption behavior of the subjects was used to understand the preference of Taiwanese consumers' rental consumption.

Third part, the awareness of the subjects' rental consumption used the Likert scale five forms on the questionnaire survey. Each question had "strongly agree," "agree," "average," "disagree," and "strongly disagree" with selection of 5~1 points. The contents of the questionnaire included the leasing concepts, the environmental sustainability, and the sustainable rental consumption.

Fourth part, the subjects' attitudes of rental consumption primarily tried to understand the impact factors of rental consumption.

Finally, this study investigated the subjects' rental of goods in the product service system. The questions were designed according to the dimensions of attitude, interest, and Opinion (A.I.O.) to investigate the consumers' lifestyles. By clustering, the subjects' lifestyle types were clustered to

TABLE 3: Eigenvalue of factors, explained variance after rotation, and cumulative explained variance of the lifestyle scale.

Component	Primary eigenvalue		
	Eigenvalue	Explained variance	Cumulative explained variance
1	4.646	14.986	14.986
2	2.313	7.463	22.449
3	2.271	7.325	29.774
4	2.230	7.195	36.969
5	2.176	7.018	43.987
6	1.695	5.467	49.454
7	1.511	4.876	54.329
8	1.416	4.567	58.896

analyze the reactions of different lifestyle and demographic groups in order to find if there were significant rental consumption differences among the groups.

3. Result and Discussion

3.1. Investigation and Analysis on the Lifestyles of Hire Groups

3.1.1. Factor Analysis and Reliability Test of the Lifestyles.

In order to analyze the subjects' different types of lifestyle, by factor analysis, this study simplified 31 questions on the subjects' lifestyles and adopted principal component analysis and varimax in factor analysis for orthogonal rotation, in order to extract the main factors. As to the reliability of the scale of the questionnaire, after reliability analysis, the total

TABLE 4: Component matrix of the lifestyle scale of principal component analysis after rotation.

Questions of lifestyle	Factors							
	Factor 1	Factor 2	Factor 3	Factor 4	Factor 5	Factor 6	Factor 7	Factor 8
Question 19	0.817	-0.124	0.074	0.035	-0.118	0.170	-0.042	0.061
Question 30	0.795	-0.145	0.022	0.044	0.059	-0.008	-0.125	-0.107
Question 10	0.710	0.080	0.000	-0.026	0.007	0.252	-0.237	0.209
Question 1	0.688	0.107	0.062	-0.366	-0.014	0.129	-0.003	-0.024
Question 16	0.688	-0.100	0.139	0.005	0.007	-0.109	-0.134	-0.067
Question 28	0.642	0.102	-0.094	-0.177	-0.010	0.323	0.079	-0.057
Question 20	0.565	-0.074	-0.090	0.141	-0.299	0.279	0.142	0.282
Question 27	0.539	0.149	0.126	0.139	-0.218	-0.329	0.028	-0.074
Question 2	0.515	-0.030	0.313	-0.214	0.016	-0.110	0.309	0.102
Question 13	0.081	0.801	-0.036	-0.032	0.005	0.014	-0.088	0.194
Question 29	-0.058	0.693	0.116	0.144	0.063	0.109	0.064	0.084
Question 14	-0.005	0.643	-0.170	0.323	0.144	0.043	-0.039	-0.261
Question 15	-0.166	0.428	0.038	0.058	0.085	0.066	0.401	-0.091
Question 11	0.005	-0.104	0.650	0.206	0.217	0.052	0.063	0.077
Question 26	0.078	-0.172	0.609	0.193	0.167	0.227	-0.068	-0.060
Question 3	0.428	0.165	0.542	-0.295	-0.092	0.023	-0.141	-0.102
Question 5	0.010	0.380	0.541	-0.370	0.030	0.067	0.021	0.085
Question 12	0.389	0.190	0.398	-0.168	0.166	0.069	0.056	-0.161
Question 25	0.179	0.232	0.389	0.310	0.009	0.314	0.087	-0.293
Question 22	0.014	0.101	-0.071	0.719	0.027	-0.004	0.029	0.007
Question 23	-0.155	0.055	0.172	0.653	-0.019	0.081	0.054	0.084
Question 24	-0.109	0.273	0.067	0.501	0.122	0.053	0.271	-0.275
Question 6	0.019	0.047	0.147	0.101	0.831	0.003	-0.084	-0.026
Question 7	-0.196	0.113	0.163	-0.021	0.732	0.143	-0.082	0.084
Question 31	-0.021	0.077	0.045	0.045	0.659	0.080	0.453	0.140
Question 9	0.312	0.152	0.180	0.118	0.015	0.733	-0.034	0.067
Question 17	0.105	0.038	0.249	-0.065	0.349	0.561	0.276	-0.197
Question 8	0.017	0.201	0.236	0.402	0.166	0.444	-0.205	0.130
Question 4	-0.113	-0.042	-0.019	0.105	-0.062	-0.009	0.773	0.112
Question 21	-0.002	0.112	-0.043	-0.022	0.070	-0.007	0.056	0.806
Question 18	0.029	0.019	0.365	0.148	0.202	0.075	0.260	0.399

reliability was $\alpha = 0.776$, which was higher than 0.7. Thus, the scale of this study was reliable (see Table 1):

$$\alpha = \frac{k}{k-1} \left(1 - \frac{\sum S_i^2}{S^2} \right) = \frac{31}{31-1} \left(1 - \frac{31}{124.497} \right) \quad (1)$$

$$= \frac{31}{30} (0.751) = 0.776.$$

Factor analysis aims to extract common factors of numerous variables in order to simplify the number of variables. The purpose is to represent a great number of variables using few factors while keeping most of the information in the original variables. Before the extraction of factor analysis, this study conducted the KMO measure of sampling adequacy and Bartlett's test of sphericity in order to find if the data is suitable for factor analysis. Kaiser suggested that when the KMO value is higher, it is more effective after factor analysis [32]. A value of at least 0.9 means the effect is extremely appropriate, at least 0.8 means the effect is appropriate, at least

0.7 means the effect is acceptable, and at least 0.6 means the effect is normal. Below 0.5 means the effect is inappropriate. According to Table 2, the KMO = 0.763 and the significance of Bartlett's test of sphericity is $X^2 = 0.000$, indicating that the data were proper:

$$KMO = \frac{\sum_i \sum_{j(i \neq j)} r_{ij}^2}{\sum_i \sum_{j(i \neq j)} r_{ij}^2 + \sum_i \sum_{j(i \neq j)} r_{ij}^2},$$

$$X^2 = \frac{(N-K) \ln(S_p^2) - \sum_{i=1}^K (n_i - 1) \ln(S_i^2)}{1 + (1/3)(k-1) \left(\sum_{i=1}^k (1/(n_i - 1)) - 1/(N-k) \right)}. \quad (2)$$

After the test, principal component analysis was conducted to extract the common factors. A total eigenvalue >1 is the standard. The total explained variance was 58.896%, which matched the standard of being $>40\%$. The least eigenvalue was 1.416, which matched the standard eigenvalue of >1 , as shown in Table 3.

TABLE 5: Meanings of the names of factors.

Factor	Names	Meanings
Factor 1	Fashionable	(i) The subjects are concerned about fashion and change, and they try new things. (ii) They carefully dress themselves to show their extraordinary taste. (iii) They reward themselves by purchasing luxury goods. (iv) They are careful about the quality of the goods.
Factor 2	Stable and cautious	(i) The subjects are more conservative and good at financial management. (ii) They do not have unnecessary dreams or expenses. (iii) They always make plans and are satisfied with their current lives.
Factor 3	Unique taste	(i) The subjects have their own opinions. (ii) They enjoy challenging work and are concerned about the taste of life. (iii) They do not mind using secondhand goods. (iv) Before purchasing goods, they prefer having a trial period, and they believe that they can obtain a life with personal style and unique taste from a flea market.
Factor 4	Strict budgeting	(i) The subjects prefer purchasing goods by the most practical measures. (ii) They do not care about fashion. (iii) They enjoy classic and resistant patterns. (iv) They do not have unnecessary expenses. (v) They save extra money in the banks.
Factor 5	Environmental	(i) The subjects are concerned about the environment and ecology. (ii) They use their own shopping bags, cups, and tableware. (iii) They avoid goods that are only used once. (iv) They treat the environment as a priority when purchasing products.
Factor 6	Interactive consumption	(i) The subjects have frequent interaction. (ii) Besides offering the latest consumption information to relatives and friends, they are careful about green information and recommend environmentally friendly goods. (iii) They engage in a purchase behavior that has the most economic effectiveness. (iv) They use coupons and wait for discount periods to buy goods.
Factor 7	Economic and flexible	(i) The subjects prefer flexible purchases of products. (ii) They are good at paying with credit cards. (iii) They obtain usage rights with little money and treat them as a flexible measure to keep their money. (iv) They prefer rentals instead of buying goods.

TABLE 6: Coefficient of concentration of Ward's method.

Cluster	Coefficient	Incremental value	Percentage
7	948.655	54.442	5.73%
6	1,003.097	63.153	6.29%
5	1,066.250	65.687	6.16%
4	1,131.937	73.396	6.48%
3	1,205.333	79.986	6.63%
2	1,285.319	93.681	7.28%
1	1,379.000		

TABLE 7: Validation result of clustering by judgment analysis.

Coefficient test	Wilks' Lambda	Chi-square	Freedom	Significance
1 to 4	0.066	519.173	28	0.000
2 to 4	0.182	325.848	18	0.000
3 to 4	0.395	177.251	10	0.000
4	0.711	65.154	4	0.000

TABLE 8: ANOVA clustering significance test of 2, 4, and 5 clusters.

7 factors	2 clusters	4 clusters	5 clusters
Fashionable	0.585	0.000	0.000
Stable and cautious	0.000	0.000	0.000
Unique taste	0.000	0.000	0.000
Strict budgeting	0.000	0.000	0.000
Environmental	0.000	0.000	0.000
Interactive consumption	0.042	0.110	0.038
Economic and flexible	0.022	0.000	0.000

TABLE 9: Factors of the lifestyle clusters and means of coefficients.

7 factors	Cluster 1 Simple financial management	Cluster 2 Environment and taste	Cluster 3 Fashionable and flexible	Cluster 4 Careful purchase	Cluster 5 Smart consumption
Factor 1 Fashionable	-0.22001	0.07168	0.80084	-0.36694	-1.14294
Factor 2 Stable and cautious	0.76913	-0.22018	-0.41585	1.10397	-0.72273
Factor 3 Unique taste	-0.45461	0.43147	-0.09925	1.33478	-0.21367
Factor 4 Strict budgeting	0.08988	0.32764	-0.17508	-1.29227	0.42305
Factor 5 Environmental	-0.37356	1.20943	-0.13446	0.12425	-0.64711
Factor 6 Interactive consumption	-0.29853	0.26664	0.02640	0.40808	-0.07634
Factor 8 Economic and flexible	-0.44042	-0.56035	0.53754	0.33632	0.18783
Number of people	52	38	62	15	31
Percentage	26%	19%	31%	8%	16%

Using Varimax $\text{Max } S_{a_i^2}^2 = (1/m) \sum_{j=1}^k (a_{ji}^2 - a_i^{-2})^2$, this study conducted orthogonal rotation and reduced 31 questions into eight factors. According to the significance principle of factor loading proposed by Hair et al. [33], a factor loading that reaches 0.3 is acceptable. The questions used for the factors in this study are shown in Table 4:

$$\text{Max } S_{a_i^2}^2 = \frac{1}{m} \sum_{j=1}^k (a_{ji}^2 - a_i^{-2})^2. \quad (3)$$

The principles for deleting the items were (1) items with a low factor loading; (2) items that included three common factors; (3) factors that only included two or fewer than two items; and (4) items with low reliability [34]. According to the component matrix after rotation in Table 4, Factor 7 and Factor 8 only included one and two items, respectively. The comparison revealed that the factor loading of Factor 7 was lower than that of Factor 8. Thus, Factor 7 was deleted.

By deleting factors having one or fewer than one item, the researcher obtained seven factors. According to the meanings of the items in the factor coefficients shown in Table 4, the factors were named as fashionable, stable and cautious,

unique taste, strict budgeting, environmental, interactive consumption, and economic and flexible, as shown in Table 5.

3.1.2. Lifestyle Clusters and Difference Analysis. The analysis in this section was conducted according to the lifestyle items of the questionnaire. Consumers were divided into different clusters. At the first stage, Ward's method, also known as the minimum variance method $d_{ij} = d(\{X_i\}, \{X_j\}) = \|X_i - X_j\|^2$, was adopted. According to the interval of the squared Euclidean distance, this study judged the maximum increase of total variance and the stage in order to recognize the number of clusters [35]. As shown in Table 6, when the percentage of the coefficient of concentration was reduced from three to two clusters, the change was the most significant. Thus, there should be three clusters:

$$d_{ij} = d(\{X_i\}, \{X_j\}) = \|X_i - X_j\|^2. \quad (4)$$

After the three clusters were decided using Ward's method, this study conducted k-mean clustering analysis and allocated 198 consumers into three lifestyle clusters. According to the results of the three clusters of k-mean

TABLE 10: Distribution of the demographics of different groups.

Item	Cluster 1 Simple financial management Number of people (%)	Cluster 2 Environment and taste Number of people (%)	Cluster 3 Fashionable and flexible Number of people (%)	Cluster 4 Careful purchase Number of people (%)	Cluster 5 Smart consumption Number of people (%)
Gender					
Male	17 (8.6%)	18 (9.1%)	22 (11.1%)	9 (4.5%)	13 (6.6%)
Female	35 (17.7%)	20 (10.1%)	40 (20.2%)	6 (3.0%)	18 (9.1%)
Age					
Less than 18 years old	0 (0.0%)	0 (0.0%)	0 (0.0%)	0 (0.0%)	0 (0.0%)
18–24 years old	18 (9.1%)	5 (2.5%)	8 (4.0%)	10 (5.1%)	8 (4.0%)
25–30 years old	11 (5.6%)	11 (5.6%)	6 (3.0%)	2 (1.0%)	6 (3.0%)
31–40 years old	9 (4.5%)	12 (6.1%)	15 (7.6%)	0 (0.0%)	5 (2.5%)
41–50 years old	8 (4.0%)	8 (4.0%)	23 (11.6%)	1 (0.5%)	7 (3.5%)
51–60 years old	5 (2.5%)	2 (1.0%)	8 (4.0%)	2 (1.0%)	4 (2.0%)
More than 60 years old	1 (0.5%)	0 (0.0%)	2 (1.0%)	0 (0.0%)	1 (0.5%)
Educational level					
Elementary school (and below)	0 (0.0%)	0 (0.0%)	0 (0.0%)	0 (0.0%)	0 (0.0%)
Junior high school	0 (0.0%)	0 (0.0%)	0 (0.0%)	0 (0.0%)	0 (0.0%)
Senior high school and vocational school	3 (1.5%)	3 (1.5%)	8 (4.0%)	0 (0.0%)	1 (0.5%)
University (including college)	35 (17.7%)	22 (11.1%)	36 (18.2%)	10 (5.1%)	18 (9.1%)
Graduate school (and above)	14 (7.1%)	13 (6.6%)	18 (9.1%)	5 (2.5%)	12 (6.1%)
Annual income					
Less than 0.3 million NTD	20 (10.1%)	5 (2.5%)	10 (5.1%)	10 (5.1%)	9 (4.5%)
0.31~0.5 million NTD	7 (3.5%)	9 (4.5%)	9 (4.5%)	2 (1.0%)	5 (2.5%)
0.51~0.8 million NTD	14 (7.1%)	11 (5.6%)	9 (4.5%)	0 (0.0%)	5 (2.5%)
0.81~1 million NTD	5 (2.5%)	6 (3.0%)	13 (6.6%)	1 (0.5%)	4 (2.0%)
1.01~1.2 million NTD	5 (2.5%)	1 (0.5%)	10 (5.1%)	0 (0.0%)	2 (1.0%)
More than 1.21 million NTD	1 (0.5%)	6 (3.0%)	11 (5.6%)	2 (1.0%)	6 (3.0%)
Occupation					
Student	13 (6.6%)	4 (2.0%)	4 (2.0%)	9 (4.5%)	8 (4.0%)
Public official	1 (0.5%)	0 (0.0%)	1 (0.5%)	0 (0.0%)	0 (0.0%)
Service industry	6 (3.0%)	4 (2.0%)	8 (4.0%)	1 (0.5%)	2 (1.0%)
Self-employed	1 (0.5%)	0 (0.0%)	0 (0.0%)	0 (0.0%)	2 (1.0%)
Labor industry	9 (4.5%)	9 (4.5%)	14 (7.1%)	3 (1.5%)	4 (2.0%)
Agricultural, forestry, fishery, and husbandry	0 (0.0%)	0 (0.0%)	0 (0.0%)	0 (0.0%)	0 (0.0%)
Professional personnel	10 (5.1%)	12 (6.1%)	20 (10.1%)	0 (0.0%)	12 (6.1%)
Housewife	0 (0.0%)	0 (0.0%)	1 (0.5%)	0 (0.0%)	0 (0.0%)
Unemployed	1 (0.5%)	1 (0.5%)	0 (0.0%)	0 (0.0%)	0 (0.0%)
Retired	1 (0.5%)	1 (0.5%)	1 (0.5%)	0 (0.0%)	1 (0.5%)
Others	10 (5.1%)	7 (3.5%)	13 (6.6%)	2 (1.0%)	2 (1.0%)
Residential places					
Northern Taiwan	43 (21.7%)	29 (14.6%)	55 (27.8%)	10 (5.1%)	22 (11.1%)
Central Taiwan	5 (2.5%)	7 (3.5%)	2 (1.0%)	4 (2.0%)	7 (3.5%)
Southern Taiwan	3 (1.5%)	2 (1.0%)	4 (2.0%)	1 (0.5%)	1 (0.5%)
Eastern Taiwan	0 (0.0%)	0 (0.0%)	0 (0.0%)	0 (0.0%)	0 (0.0%)
Offshore islands	0 (0.0%)	0 (0.0%)	0 (0.0%)	0 (0.0%)	0 (0.0%)
Other	1 (0.5%)	0 (0.0%)	1 (0.5%)	0 (0.0%)	1 (0.5%)
Total	52 (26.3%)	38 (19.2%)	62 (31.3%)	15 (7.6%)	31 (15.7%)

TABLE 11: Significance of the Pearson chi-square test.

Items	Approximate significance
Gender	0.278
Age	0.003
Educational level	0.630
Annual income	0.002
Occupation	0.086
Residential places	0.318

clustering analysis, in one cluster, there was only one subject. With the division of six clusters, two clusters only had one subject. Thus, this study tried to adopt two, four, and five clusters. However, the clustering precision rate needed to be validated by judgment analysis. Based on Table 7, significance $0.000 < \alpha = 0.05$, and the judgmental capability was significant. This study probed into differences of the factors of the groups and the lifestyle groups using one-way ANOVA $SS_T = \sum(X_i - \mu)^2$, $SS_B = \sum n \times (\mu - \mu)^2$, $SS_W = \sum \sum (X_{gi} - \mu)^2$ and validated the clustering result, as shown in Table 8. According to the result of ANOVA, when there were five clusters, the P values of all factors were $< \alpha = 0.05$. Thus, five clusters are significantly different for seven factors. The different groups were effectively segmented:

$$\begin{aligned}
 SS_T &= \sum (X_i - \mu)^2, \\
 SS_B &= \sum n \times (\mu - \mu)^2, \\
 SS_W &= \sum \sum (X_{gi} - \mu)^2.
 \end{aligned} \tag{5}$$

Finally, the seven factors were divided into five clusters by k-mean clustering, as shown in Table 9. According to the figures, Factor 1 (fashionable) had a significantly positive relation with Cluster 3 and had a significantly negative relation with Cluster 5. Cluster 1 had a positive correlation with Factor 2 (stable and cautious) and Factor 4 (strict budgeting). It had a negative correlation with Factor 1 (fashionable), Factor 3 (unique taste), Factor 5 (environmental), Factor 6 (interactive consumption), and Factor 8 (economic and flexible). Thus, Cluster 1 was more practical and not fashionable, as the subjects did not have unnecessary expenses. Based on the above, Cluster 1 was named simple financial management.

According to Table 9, this study used one-way ANOVA to determine the differences among the groups and factors. According to the characteristics, the clusters were named as follows: Cluster 1: simple financial management; Cluster 2: environment and taste; Cluster 3: fashionable and flexible; Cluster 4: careful purchase; and Cluster 5: smart consumption. After clustering analysis, the cross analysis and chi-square test were conducted to find the significant differences of the groups. The distribution between the group demographics is shown in Table 10.

According to the result of the chi-square test, the lifestyle groups in this study showed a significant difference in age and annual income. The chi-square values of the rest of the items were above the significance level of 0.05, indicating there was no significant difference. In other words, the clusters were not significantly different, as shown in Table 11.

According to the result of the clustering analysis, the demographics of different groups shown in Tables 9 and 10 were compared, as shown in Table 12.

3.2. Investigation on Rental Consumption in the Product Service System. Using the questionnaire survey in the first stage, this study screened potential rental groups. The items of the questionnaire were generalized according to the literatures and included rental consumption behavior, rental consumption cognition, rental consumption attitude, and a lifestyle AIO questionnaire. After integrating the related data, this study treated the result as the criterion of the expected goals. The subjects were consumers with cognitive and purchasing capability. This study focused on consumers above 18 years of age. At the first stage, 206 questionnaires were distributed and 198 valid questionnaires were retrieved. The majority of the questionnaires were online questionnaires, followed by paper-based questionnaires. The aim was to find the rental patterns and types that could be accepted by consumers in Taiwan, as well as the lifestyle factors of the groups that could accept the rental model.

3.2.1. Analysis of the Rental Consumption Behavior in the Product Service System. According to the figures shown in Table 13, 181 subjects had engaged in rental behavior (91.41%). However, 8.59% subjects had never engaged in leasing behavior. According to the responses for the items of the products, common real estate, publications, and transportations had long been associated with the rental business. At least 80% of the subjects had rental experience. Only 20% of the subjects had rented clothing, outdoor items, and cards, which can be rented in many different places. As to the rental of furniture, 15.66% of the subjects had experience. It was inferred that the furniture in rented rooms was considered to be rented furniture, and this was common for the public in Taiwan. As to various assistive devices, which are expensive and rental of the devices is promoted by the government, only 10.61% subjects had rented them. As to baby items that are renewed frequently, only 8.08% of the subjects had rented them. This shows that the subjects were used to purchasing instead of renting such items, not to mention the rental of electric appliances, daily articles, and live objects, which are rare in the market. The above indicated that Taiwanese consumers are not used to renting goods for short-term usage. The implementation of rental business should be significantly improved.

3.2.2. Analysis of Rental Consumption Cognition of the Product Service System. According to the figures shown in Table 14, the subjects agreed with the green effectiveness of leasing and they had a positive attitude. Thus, the development of

TABLE 12: Names and descriptions of clusters.

Number	Names of clusters	Descriptions of clusters
1	Simple financial management	<ul style="list-style-type: none"> (i) The subjects purchase goods by the most practical measures. (ii) They are more conservative and are good at financial management. (iii) They do not have unnecessary dreams nor expenses. (iv) They make plans and they save extra money. (v) They are mostly 18–30 years old and their annual incomes are mostly below 0.3 million NTD. Thus, it was inferred that the cluster includes students. (vi) The second annual income range was 0.51–0.8 million NTD. (vii) Although their salaries are not low, they should work hard. (viii) They live a moderate life in order to fulfill their future plans.
2	Environment and taste	<ul style="list-style-type: none"> (i) The subjects have their own opinions and they enjoy challenging work. (ii) They are concerned about the environment and ecology. (iii) They use personal shopping bags, cups, and tableware. (iv) They value the taste of life. (v) They are mostly 25–40 years old. (vi) Their annual incomes are mostly 31,000–80,000 NTD. (vii) They tend to engage in traditional consumption and are not used to credit cards. (viii) They do not mind using secondhand products. (ix) They are concerned about using trials before purchasing goods. (x) They believe that they can find products with personal style and unique taste in flea markets. (xi) They are careful about environmental protection.
3	Fashionable and flexible	<ul style="list-style-type: none"> (i) The subjects are concerned about fashion and change. (ii) They try new things and dress themselves to demonstrate their extraordinary taste. (iii) They reward themselves with luxurious goods. (iv) They are careful about the quality of goods. (v) They are mostly 31–50 years old and their annual incomes are mostly 0.81–1.21 million NTD (and above). (vi) They are in the middle class to high salary groups. (vii) According to the distribution of their ages, they are still working. Thus, it was inferred that their purchased goods should match their identities to demonstrate the value. (viii) They are good at paying with credit cards. (ix) They obtain the usage rights of products with little money, and this is a measure to keep their current money.
4	Careful purchase	<ul style="list-style-type: none"> (i) The subjects have their own opinions. (ii) They enjoy challenging work. (iii) They are concerned about the taste of life. (iv) They do not mind using secondhand things. (v) They are cautious about making purchases. (vi) They use coupons and wait for discount periods. (vii) However, they do not only buy classic and resistant goods. With extra money and after careful judgment, they will buy the products they like or need instead of saving the money. (viii) They have frequent interaction and often provide the latest consumption information to relatives and friends. (ix) They are concerned about green information and recommend environmentally friendly goods. (x) They are mostly 18–24 years old and their annual incomes are mostly below 0.3 million NTD. Thus, it was inferred that most of them are students. (xi) They do not have economic advantages and they discuss consumption information with each other.
5	Smart consumption	<ul style="list-style-type: none"> (i) The subjects prefer making purchases using the most economic measures. (ii) They do not care about fashion and they buy classic and resistant goods. (iii) They do not have unnecessary expenses. (iv) They save extra money. Most of them are 18–24 and 41–50 years old. (v) Distribution of their annual incomes is extreme. Most of them have less than 0.3 million NTD or more than 1.21 million NTD. Thus, they include students and practical subjects with high salaries. (vi) They are flexible with their consumption. For instance, they pay using credit cards and obtain the usage rights of products using small installments of money. (vii) This is the measure to keep their current money. They do not mind obtaining the usage rights of goods by renting them.

TABLE 13: Scale cross table of the subjects' rental consumption behavior.

Item	Yes		No	
	Frequency	Percentage	Frequency	Percentage
Have you rented things (such as rooms, cars, and books)?	181	91.41%	17	8.59%
If necessary, do you accept renting things?	195	98.48%	3	1.52%
Have you rented real estate (such as rooms or land)?	144	72.73%	54	27.27%
Have you rented electrical appliances (such as cameras, computers, and air conditioners)?	10	5.05%	188	94.95%
Have you rented clothing (such as wedding dresses, luxurious bags, or jewelry)?	46	23.23%	152	76.77%
Have you rented transportation (such as cars, bikes or motorcycles)?	162	81.82%	36	18.18%
Have you rented publications (such as books, DVDs, and music CDs)?	159	80.30%	39	19.70%
Have you rented daily articles (such as thick blankets, window curtains, and carpets)?	1	0.51%	197	99.49%
Have you rented live object (such as plants, pets, or persons to pose as girl/boyfriends)?	1	0.51%	197	99.49%
Have you rented outdoor things (such as camping equipment and luggage)?	51	25.76%	147	74.24%
Have you rented cards (such as membership cards)?	47	23.74%	151	76.26%
Have you rented baby things (such as baby buggies and toys)?	16	8.08%	182	91.92%
Have you rented assistive tools (such as wheelchairs and electric vehicles)?	21	10.61%	177	89.39%
Have you rented furniture (such as tables, chairs, or beds in rented rooms)?	31	15.66%	167	84.34%

TABLE 14: Scale cross table of the subjects' rental consumption cognition.

Item	Strongly agree	Agree	Neutral	Disagree	Strongly disagree	Total
Renting is not a respectable behavior.	0 0.00%	4 2.02%	25 12.63%	133 67.17%	36 18.18%	198 100%
Renting is for only when we cannot afford something.	1 0.51%	19 9.60%	19 9.60%	113 57.07%	46 23.23%	198 100%
Renting is a better bargain than purchasing.	13 6.57%	78 39.39%	77 38.89%	29 14.65%	1 0.51%	198 100%
The use of rented goods is a kind of strict budgeting and saving behavior.	14 7.07%	101 51.01%	68 34.34%	15 7.58%	0 0.00%	198 100%
The repeated use of goods is environmentally friendly, and I will consider leasing.	30 15.15%	119 60.10%	36 18.18%	13 6.57%	0 0.00%	198 100%
Renting and the green consumption of goods are environmentally friendly and they are measures to solve environmental problems.	35 17.68%	121 61.11%	34 17.17%	8 4.04%	0 0.00%	198 100%
I am willing to share the concept of renting and green consumption with my family or friends.	42 21.21%	115 58.08%	40 20.20%	1 0.51%	0 0.00%	198 100%
In order not to waste resources, and for the sustainable development of the earth, it is worthy to change consumption habits (such by using rented goods, shopping at flea markets, and exchanging goods).	59 29.80%	113 57.07%	24 12.12%	2 1.01%	0 0.00%	198 100%
Governments and enterprises should implement and promote rental plans for goods.	48 24.24%	120 60.61%	29 14.65%	1 0.51%	0 0.00%	198 100%

leasing in a product service system could be a new green consumption model.

3.2.3. Analysis on Rental Consumption Attitude of the Product Service System. According to the figures in Table 15, the most significant conditions for consumers to accept rental consumption were low use frequency and high prices of goods. There should be a clear rental contract and process. Renting is not the traditional consumption model in which ownership changes in trading. There are many extended situations. Thus, the subjects worried that the rented goods would not always

be used privately and the conditions were uncertain. They questioned the cleanness and compensation after damage. Leasing firms should be extremely careful about the quality of the rented goods. Clean goods in good condition should not be easily damaged by consumers' common use.

3.3. Difference Analysis of Different Lifestyle Groups on Rental Consumption in the Product Service System. This section explored different groups' rental intention, prices, use frequency, matching of goods, goods propriety, goods renewal, leasing process details, goods exclusiveness, damage of goods,

TABLE 15: Scale cross table of the subjects' rental consumption attitude.

Items	Strongly agree	Agree	Neutral	Disagree	Strongly disagree	Total
Prices of the goods are the factors of my rental selection.	53 26.77%	115 58.08%	21 10.61%	9 4.55%	0 0.00%	198 100%
If the products are not used frequently, I will choose leasing.	65 32.83%	121 61.11%	10 5.05%	1 0.51%	1 0.51%	198 100%
I will consider leasing since I should use (or match) different products in different occasions.	21 10.61%	135 68.18%	33 16.67%	9 4.55%	0 0.00%	198 100%
I will consider leasing since I worry that I will buy the wrong goods.	12 6.06%	86 43.43%	70 35.35%	30 15.15%	0 0.00%	198 100%
I will consider leasing since I can update products at any time.	7 3.54%	81 40.91%	81 40.91%	29 14.65%	0 0.00%	198 100%
If enterprises provide a clear leasing process, I will consider leasing.	22 11.11%	152 76.77%	22 11.11%	2 1.01%	0 0.00%	198 100%
I do not consider leasing since I would like to use new goods.	4 2.02%	34 17.17%	86 43.43%	73 36.87%	1 0.51%	198 100%
I do not consider leasing since I do not have a sense of ownership.	6 3.03%	34 17.17%	72 36.36%	78 39.39%	8 4.04%	198 100%
I do not consider leasing since I worry about compensation.	12 6.06%	64 32.32%	72 36.36%	44 22.22%	6 3.03%	198 100%
I do not consider leasing since I worry about cleanness.	30 15.15%	108 54.55%	39 19.70%	18 9.09%	3 1.52%	198 100%
If I can have additional services other than purchasing, I will choose leasing.	39 19.70%	130 65.66%	23 11.62%	5 2.53%	1 0.51%	198 100%

cleanness of goods, and additional services. Regarding the content of the items, this study conducted cross analysis and chi-square test to find the significant differences among the groups.

According to the figures of the 11 items of different lifestyle groups shown in Table 16, the chi-square test result showed that the chi-square value was below the 0.05 significance level. The items that reached a significant difference were item 2 (prices), item 4 (matching of goods), and item 5 (propriety of goods). The rest of the items were not significantly different and were therefore not discussed.

According to the figures of item 2 (prices), all the clusters agreed that the prices of goods were a factor of choosing to rent. There were two meanings of the result. One was that when the goods are expensive, they are more likely to be rented. The other was that the prices of the rented goods should be advantageous in order to attract the consumers. Noticeably, among Cluster 4, up to 20% of the subjects stated they disagreed. It was inferred that they mostly did not have economic advantages and were supported by their families. They did not have economic pressure. Besides, they were concerned about taste, they did not save all their extra money, and they were more likely to spend money on goods that they liked or needed. After careful consideration, they would pay for certain types of products.

Based on the figures of item 4 (matching of goods), all the lifestyle clusters agreed that they would consider obtaining the usage rights of products by renting them when they had to use (or match) different products in different occasions. This showed that they could rent more expensive goods or

products that are changed frequently (such as luxury bags) to demonstrate their identities.

According to figures of item 5 (propriety of goods), this study realized that more than half of Cluster 4 and Cluster 5 agreed with careful purchases and being concerned about taste and that they did not mind using second-hand goods. They were careful about using trials before purchasing. Cluster of smart consumption is pragmatic when selecting goods and they obtained products by the most economic measures. They did not mind obtaining the usage rights of goods by renting them. Thus, if the products of the rental firms match the characteristics of these two groups, they can treat the groups as the subjects.

4. Conclusions

Due to the importance of consumption, the only way to get rid of the unsustainable development crisis for us is to start from changing the consumption pattern of resource exhaustion which can destroy our living environment. Rental is a consumption pattern which can make the goods used repeatedly. As purchase has been changed into rental service, consumers can benefit from the product functions, but the ownership still belongs to the manufacturer. The manufacturer can not only meet the customer demands of the product functions, but also reduce the product output and selling by providing service. In this way, the resource consumption and pollutant output can be decreased. Selling service can achieve the pattern of environmental appeal, which is exactly

TABLE 16: Distribution of figures of 11 items in different lifestyle groups.

	Items		Cluster 1 Simple financial management	Cluster 2 Environment and taste	Cluster 3 Fashionable and flexible	Cluster 4 Careful purchase	Cluster 5 Smart consumption	Pearson chi-square test significance
1	If necessary, do you accept leasing?	Yes	52 (100.0%)	37 (97.4%)	60 (96.8%)	15 (100.0%)	31 (100.0%)	0.551
		No	0 (0.0%)	1 (2.6%)	2 (3.2%)	0 (0.0%)	0 (0.0%)	
2	The price of goods is the factor of my selection of leasing.	Strongly agree	12 (23.1%)	12 (31.6%)	10 (16.1%)	5 (33.3%)	14 (45.2%)	0.041
		Agree	34 (65.4%)	21 (55.3%)	42 (67.7%)	5 (33.3%)	13 (41.9%)	
		Neutral	5 (9.6%)	3 (7.9%)	8 (12.9%)	2 (13.3%)	3 (9.7%)	
		Disagree	1 (1.9%)	2 (5.3%)	2 (3.2%)	3 (20.0%)	1 (3.2%)	
		Strongly disagree	0 (0.0%)	0 (0.0%)	0 (0.0%)	0 (0.0%)	0 (0.0%)	
3	When goods are not used frequently, I will prefer leasing.	Strongly agree	19 (36.5%)	10 (26.3%)	18 (29.0%)	4 (26.7%)	14 (45.2%)	0.056
		Agree	32 (61.5%)	26 (68.4%)	40 (64.5%)	10 (66.7%)	13 (41.9%)	
		Neutral	1 (1.9%)	2 (5.3%)	4 (6.5%)	0 (0.0%)	3 (9.7%)	
		Disagree	0 (0.0%)	0 (0.0%)	0 (0.0%)	1 (6.7%)	0 (0.0%)	
		Strongly disagree	0 (0.0%)	0 (0.0%)	0 (0.0%)	0 (0.0%)	1 (3.2%)	
4	I consider leasing since I have to use (or match) different products in different occasions.	Strongly agree	6 (11.5%)	3 (7.9%)	1 (1.6%)	3 (20.0%)	8 (25.8%)	0.022
		Agree	40 (76.9%)	24 (63.2%)	44 (71.0%)	10 (66.7%)	17 (54.8%)	
		Neutral	6 (11.5%)	10 (26.3%)	12 (19.4%)	1 (6.7%)	4 (12.9%)	
		Disagree	0 (0.00%)	1 (2.6%)	5 (8.1%)	1 (6.7%)	2 (6.5%)	
		Strongly disagree	0 (0.00%)	0 (0.00%)	0 (0.00%)	0 (0.00%)	0 (0.00%)	
5	I consider leasing since I worry that I will buy the wrong goods.	Strongly agree	6 (11.5%)	0 (0.0%)	0 (0.0%)	3 (20.0%)	3 (9.7%)	0.048
		Agree	20 (38.5%)	16 (42.1%)	30 (48.4%)	6 (40.0%)	14 (45.2%)	
		Neutral	20 (38.5%)	18 (47.4%)	19 (30.6%)	5 (33.3%)	8 (25.8%)	
		Disagree	6 (11.5%)	4 (10.5%)	13 (21.0%)	1 (6.7%)	6 (19.4%)	
		Strongly disagree	0 (0.0%)	0 (0.0%)	0 (0.0%)	0 (0.0%)	0 (0.0%)	
6	I consider leasing since I can update goods at any time.	Strongly agree	1 (1.9%)	1 (2.6%)	1 (1.6%)	1 (6.7%)	3 (9.7%)	0.139
		Agree	23 (44.2%)	14 (36.8%)	25 (40.3%)	6 (40.0%)	13 (41.9%)	
		Neutral	26 (50.0%)	19 (50.0%)	21 (33.9%)	5 (33.3%)	10 (32.3%)	
		Disagree	2 (3.8%)	4 (10.5%)	15 (24.2%)	3 (20.0%)	5 (16.1%)	
		Strongly disagree	0 (0.0%)	0 (0.0%)	0 (0.0%)	0 (0.0%)	0 (0.0%)	
7	If enterprises provide a clear leasing process, I will consider leasing.	Strongly agree	6 (11.5%)	2 (5.3%)	4 (6.5%)	1 (6.7%)	9 (29.0%)	0.110
		Agree	42 (80.8%)	30 (78.9%)	47 (75.8%)	12 (80.0%)	21 (67.7%)	
		Neutral	4 (7.7%)	5 (13.2%)	10 (16.1%)	2 (13.3%)	1 (3.2%)	
		Disagree	0 (0.0%)	1 (2.6%)	1 (1.6%)	0 (0.0%)	0 (0.0%)	
		Strongly disagree	0 (0.0%)	0 (0.0%)	0 (0.0%)	0 (0.0%)	0 (0.0%)	
8-1	I do not consider leasing because I would like to use new products.	Strongly agree	0 (0.0%)	0 (0.0%)	2 (3.2%)	1 (6.7%)	1 (3.2%)	0.307
		Agree	6 (11.5%)	10 (26.3%)	7 (11.3%)	4 (26.7%)	7 (22.6%)	
		Neutral	30 (57.7%)	17 (44.7%)	25 (40.3%)	4 (26.7%)	10 (32.3%)	
		Disagree	16 (30.8%)	11 (28.9%)	27 (43.5%)	6 (40.0%)	13 (41.9%)	
		Strongly disagree	0 (0.0%)	0 (0.0%)	1 (1.6%)	0 (0.0%)	0 (0.0%)	

TABLE 16: Continued.

Items		Cluster 1 Simple financial management	Cluster 2 Environment and taste	Cluster 3 Fashionable and flexible	Cluster 4 Careful purchase	Cluster 5 Smart consumption	Pearson chi-square test significance
8-2	I do not consider leasing since I do not have the sense of ownership.	Strongly agree	1 (1.9%)	1 (2.6%)	2 (3.2%)	2 (13.3%)	0.219
		Agree	5 (9.6%)	9 (23.7%)	7 (11.3%)	4 (26.7%)	
		Neutral	24 (46.2%)	12 (31.6%)	23 (37.1%)	4 (26.7%)	
		Disagree	19 (36.5%)	16 (42.1%)	26 (41.9%)	5 (33.3%)	
		Strongly disagree	3 (5.8%)	0 (0.0%)	4 (6.5%)	0 (0.0%)	
9	I do not consider leasing because I worry about compensation.	Strongly agree	4 (7.7%)	1 (2.6%)	4 (6.5%)	2 (13.3%)	0.810
		Agree	17 (32.7%)	13 (34.2%)	17 (27.4%)	6 (40.0%)	
		Neutral	18 (34.6%)	15 (39.5%)	27 (43.5%)	2 (13.3%)	
		Disagree	11 (21.2%)	9 (23.7%)	12 (19.4%)	5 (33.3%)	
		Strongly disagree	2 (3.8%)	0 (0.0%)	2 (3.2%)	0 (0.0%)	
10	I do not consider leasing because I worry about cleanness.	Strongly agree	5 (9.6%)	5 (13.2%)	9 (14.5%)	3 (20.0%)	0.706
		Agree	31 (59.6%)	23 (60.5%)	31 (50.0%)	8 (53.3%)	
		Neutral	9 (17.3%)	8 (21.1%)	15 (24.2%)	1 (6.7%)	
		Disagree	6 (11.5%)	2 (5.3%)	5 (8.1%)	3 (20.0%)	
		Strongly disagree	1 (1.9%)	0 (0.0%)	2 (3.2%)	0 (0.0%)	
11	If I can have additional services, I will choose leasing.	Strongly agree	14 (26.9%)	6 (15.8%)	8 (12.9%)	3 (20.0%)	0.569
		Agree	34 (65.4%)	25 (65.8%)	41 (66.1%)	9 (60.0%)	
		Neutral	3 (5.8%)	7 (18.4%)	9 (14.5%)	2 (13.3%)	
		Disagree	1 (1.9%)	0 (0.0%)	3 (4.8%)	1 (6.7%)	
		Strongly disagree	0 (0.0%)	0 (0.0%)	1 (1.6%)	0 (0.0%)	

the way of product service system. This study explores the characteristics of rental goods, integrates the green concept in the design and development end, and introduces the concept of product service into the rental consumption trend in Taiwan. As a result, the sustainable product can be developed for the rental consumption to maximize the green effect. This study takes the questionnaire survey to collect various opinions of the consumers to rental consumption and also classifies the Taiwanese consumers into five clusters based on the life styles, and the names of clusters are simple financial management cluster, environment and taste cluster, fashionable and flexible cluster, careful purchase cluster, and smart consumption cluster. Furthermore, this study details the product service rental patterns and types preferred by each cluster, as well as their opinions and expectations of the rental industry. Finally, the following conclusions are obtained from the phenomenon showed in the statistics and research data.

4.1. According to Consumers' Green Consumption Cognition and Attitude toward Environmental Goods, Control the Green Consumption Factors of Rental Goods Development. Green consumption and environmental goods influence each other. In the use of rented goods, environmental effectiveness can

be enhanced by increasing the use rate. Thus, if goods are consumed using a rental model, such action can be seen as green consumption. Consumers agree with this concept; thus, rental goods have environmental implications for consumers. However, consumers have different market characteristics. At the early stage of development of rental products, surveys must be conducted in order to recognize the different subject preferences for goods. At present, consumers in Taiwan worry about situations related to the change of ownership of rental consumption. Thus, if the rental characteristics of goods can be reinforced at the stage of development and if the development of rental goods is guided by the extracted factors, the total value of rented goods can be effectively upgraded.

4.2. In a Rental Market, Market Segmentation Can Be Reinforced by Lifestyle Variables. According to interviews with the enterprises, leasing firms suggested that an important measure to develop rental goods is product market segmentation. This study focused on consumers with purchase capabilities and extracted lifestyle factors by factor analysis in AIO to find 31 items. Through clustering analysis, the factors were divided into five clusters. It was found that the public is willing to acquire the usage rights of products by

rental consumption. Thus, rental consumption in Taiwan can be economically effective. Difference analysis of the lifestyle survey in this study indicated the different cluster preferences in detail. Thus, lifestyle surveys could help probe into rental consumption groups' preferences, could serve as a reference for market segmentation, and allow firms to easily deal with marketing.

4.3. In Development of Rental Consumption Characteristics of Product Service System, Consumers' Opinions Should Be Included in Development Conditions and It Must Reinforce Product Service. As to sustainable goods developed upon rental consumption of product Service System, the main concerns are extension of the product life cycle of components and processed waste returned to the development end. Besides, users' feedback after using the products is also important for the development of the next stage. From consumers' perspective, users use rental goods more frequently, in comparison to goods purchased. It is difficult to predict users' usage. Thus, when developing products, design engineers should be concerned about the new lifestyle of rental goods groups in order to reinforce services of the products. This study generalizes sustainable product development principles of rental consumption of product service system as new rules for developing rental goods. Recycling and usage are particularly critical. Consumers' feedback can be provided by information platform.

4.4. Cost of Cradle-to-Cradle Recycling Pattern Is High: Governmental Assistance and Promotion Will Help Construct Sustainable Consumption Model of Rental Consumption in Product Service System and Influence Consumers' and Enterprises' Selection of the Rental Business Model. According to expert interview and analytical result, in overall green regulations, rental consumption model should particularly modify usage stage and waste recycling stage. It is the result of the change of ownership. However, not all types of firms can accomplish cradle-to-cradle recycling model. Using Aurora Office Furniture as an example, cradle-to-cradle recycling is a huge burden for the enterprise and it will not adopt it. However, the implementation of sustainable goods development of rental consumption of product service system should be assisted by the government and led by large enterprises. It must establish a model rental economy in Taiwan and indirectly influence product selection and operation of consumers and small and medium enterprises in the future.

Acknowledgment

The authors are grateful to the Environmental Protection Administration of China for supporting this research.

References

- [1] N. Yu and L. Ming-Kun, "International development trend of green consumption," *Science Development*, vol. 387, pp. 20–25, 2005.
- [2] P.-C. Lin and Y.-H. Huang, "The influence factors on choice behavior regarding green products based on the theory of consumption values," *Journal of Cleaner Production*, vol. 22, no. 1, pp. 11–18, 2012.
- [3] C. K. Cameron, "What if consumers decided to all "go green"? Environmental rebound effects from consumption decisions," *Energy Policy*, vol. 54, pp. 240–256, 2013.
- [4] M. C. Hung, *Industrial Green Competitiveness Based on Sustainable Goods*, vol. 17, Safety, Health and Environment Today, Industrial Development Bureau, Ministry of Economic Affairs, 2003.
- [5] S. Lorek and J. H. Spangenberg, "Sustainable consumption within a sustainable economy—beyond green growth and green economies," *Journal of Cleaner Production*, vol. 63, pp. 33–44, 20132014.
- [6] H. H. Shu, *Integration and construction of new strategies of environmental goods development and marketing by green consumption and green marketing [M.S. thesis]*, College of Design and Arts, Da-Yeh University, 2008.
- [7] M. Degl'Innocenti and C. Girardone, "Ownership, diversification and cost advantages: evidence from the Italian leasing industry," *Journal of International Financial Markets Institutions and Money*, vol. 22, pp. 879–896, 2012.
- [8] M. R. Gleim, J. S. Smith, D. Andrews, and J. J. Cronin Jr., "Against the green: a multi-method examination of the barriers to green consumption," *Journal of Retailing*, vol. 89, pp. 44–61, 2013.
- [9] W. McDonough and M. Braungart, *Cradle-To-Cradle: Design Proposal of Green Economy*, vol. 21, Yeren, 2008, Translated by the Administrative Center for China's Agenda.
- [10] WCED of UN, *Our Common Future: the World Commission on Environment and Development*, Oxford University Press, 1987.
- [11] K. C. Kao, *The best prevention and maintenance strategy of leasing equipment by failure rate reduction [Ph.D. dissertation]*, Department of Industrial Management, National Taiwan University of Science and Technology, 2009.
- [12] G. Bravo, E. Vallino, A. K. Cerutti, and M. B. Pairotti, "Alternative scenarios of green consumption in Italy: an empirically grounded model," *Environmental Modelling & Software*, vol. 47, pp. 225–234, 2013.
- [13] S. Y. Huang, *History and development of aircraft financial leasing [M.S. thesis]*, Department of Law, Soochow University, 2011.
- [14] T. Chemmanur, Y. Jiao, and A. Yan, "A theory of contractual provisions in leasing," *Journal of Financial Intermediation*, vol. 19, no. 1, pp. 116–142, 2010.
- [15] A. Meneses and F. Mariano, "Capítulo 8—Leasing," *Mercado Financeiro*, pp. 73–79, 2011.
- [16] M. Chater, "Managing the eco-design process," *The Journal of Sustainable Product Design*, vol. 2, no. 2, pp. 48–51, 1997.
- [17] M.-L. Tseng, S. F. (Anthony) Chiu, R. R. Tan, and A. B. Siriban-Manalang, "Sustainable consumption and production for Asia: sustainability through green design and practice," *Journal of Cleaner Production*, vol. 40, pp. 1–5, 2013.
- [18] T. E. Graedel and B. R. Allenby, *Industrial Ecology*, Pearson Education, Saddle Point, NJ, USA, 2nd edition, 2003.
- [19] H. Brezet, "Product-service substitution: examples and cases from the Netherlands, funktions for saljning-product-service systems, stockholm," AFR-Report 299, Swedish Environmental Protection Agency, 2002.
- [20] O. K. Mont, "Clarifying the concept of product-service system," *Journal of Cleaner Production*, vol. 10, no. 3, pp. 237–245, 2002.

- [21] A. Tukker, "Eight types of product-service system: eight ways to sustainability? Experiences from suspronet," *Business Strategy and the Environment*, vol. 13, no. 4, pp. 246–260, 2004.
- [22] F. H. Beuren, M. G. Gomes Ferreira, and P. A. C. Miguel, "Product-service systems: a literature review on integrated products and services," *Journal of Cleaner Production*, vol. 47, pp. 222–231, 2013.
- [23] M. Goedkoop, C. van Haler, H. te Riele, and P. Rommers, "Product service-systems, ecological and economic basics report for Dutch Ministries of Environment (VROM) and Economic Affairs (EZ)," Tech. Rep., 1999.
- [24] L. H. Shih, J. L. Chen, J. C. Tu, and T. C. Kuo, "An integrated approach for product service system development (II): evaluation phase," *Journal of Environmental Engineering and Management*, vol. 16, no. 6, pp. 343–356, 2009.
- [25] B. Yoon, S. Kim, and J. Rhee, "An evaluation method for designing a new product-service system," *Expert Systems with Applications*, vol. 39, no. 3, pp. 3100–3108, 2012.
- [26] Environmental Protection Administration, Executive Yuan, *Study on Enhancement of Product Service System on Resource Use Effectiveness*, Taipei, Taiwan, 2007.
- [27] T. S. Baines, H. W. Lightfoot, S. Evans et al., "State-of-the-art in product-service systems," *Proceedings of the Institution of Mechanical Engineers B*, vol. 221, no. 10, pp. 1543–1552, 2007.
- [28] K. Xing, D. Ness, and F.-R. Lin, "A service innovation model for synergistic community transformation: integrated application of systems theory and product-service systems," *Journal of Cleaner Production*, vol. 43, pp. 93–102, 2013.
- [29] E. Manzini and C. Vezzoli, "A strategic design approach to develop sustainable product service systems: examples taken from the "environmentally friendly innovation" Italian prize," *Journal of Cleaner Production*, vol. 11, no. 8, pp. 851–857, 2003.
- [30] X. Geng, X. Chu, D. Xue, and Z. Zhang, "A systematic decision-making approach for the optimal product-service system planning," *Expert Systems with Applications*, vol. 38, no. 9, pp. 11849–11858, 2011.
- [31] National Science Council, Executive Yuan, *Sustainable Performance Oriented Product Service System (PSS) Selection Tool Development*, 2010.
- [32] H. F. Kaiser, "An index of factorial simplicity," *Psychometrika*, vol. 39, no. 1, pp. 31–36, 1974.
- [33] J. F. Hair et al., *Multivariate Data Analysis*, Prentice Hall, Englewood Cliffs, NJ, USA, 5th edition, 1998.
- [34] M. C. Chen, *The questionnaire on psychological contract of teaching staff in junior high schools [M.S. thesis]*, National Chengchi University, 2006.
- [35] S. Y. Yang, *SPSS Statistical Analysis Practices*, Flag, Taipei, Taiwan, 2011.

Research Article

Rough Set Theory Based Fuzzy TOPSIS on Serious Game Design Evaluation Framework

Chung-Ho Su,^{1,2} Ken T.-K. Chen,³ and Kuo-Kuang Fan¹

¹ Graduate School of Design, National Yunlin University of Science and Technology, 123 University Road, Section 3, Douliou, Yunlin 64002, Taiwan

² Department of Digital Content Application & Management, Wenzao Ursuline University of Languages, 900 Min-Tzu 1st Road, Sanming District, Kaohsiung 80793, Taiwan

³ Department of Animation and Game Design, Shu-Te University, No. 59, Hengshan Road, Yen Chao 82445, Taiwan

Correspondence should be addressed to Chung-Ho Su; mic6033@stu.edu.tw

Received 29 September 2013; Accepted 18 October 2013

Academic Editor: Teen-Hang Meen

Copyright © 2013 Chung-Ho Su et al. This is an open access article distributed under the Creative Commons Attribution License, which permits unrestricted use, distribution, and reproduction in any medium, provided the original work is properly cited.

This study presents a hybrid methodology for solving the serious game design evaluation in which evaluation criteria are based on meaningful learning, ARCS motivation, cognitive load, and flow theory (MACF) by rough set theory (RST) and experts' selection. The purpose of this study tends to develop an evaluation model with RST based fuzzy Delphi-AHP-TOPSIS for MACF characteristics. Fuzzy Delphi method is utilized for selecting the evaluation criteria, Fuzzy AHP is used for analyzing the criteria structure and determining the evaluation weight of criteria, and Fuzzy TOPSIS is applied to determine the sequence of the evaluations. A real case is also used for evaluating the selection of MACF criteria design for four serious games, and both the practice and evaluation of the case could be explained. The results show that the playfulness (C24), skills (C22), attention (C11), and personalized (C35) are determined as the four most important criteria in the MACF selection process. And evaluation results of case study point out that Game 1 has the best score overall (Game 1 > Game 3 > Game 2 > Game 4). Finally, proposed evaluation framework tends to evaluate the effectiveness and the feasibility of the evaluation model and provide design criteria for relevant multimedia game design educators.

1. Introduction

This study aims to provide a system evaluation model for multimedia game design educators selecting the most suitable MACF design from a series of evaluation criteria. The selection of MACF design criteria is regarded as multicriteria problem, including the subjectivity, uncertainty, and fuzziness in the evaluation process.

Based on the above factors, six reasons are proposed for the evaluation. (a) The confirmation of criteria is determined by group experts in which they present subjective and objective considerations. (b) TOPSIS logic is rational and understandable. (c) The judgment rules close to human thinking could be acquired through fuzzy linguistic evaluation. (d) The alternatives could be compared with the objectives and criteria decision-making process. (e) The weights of importance between criteria are taken into account

and included in the comparison. (f) The calculation process is simple and easy to understand [1].

Furthermore, fuzzy Delphi method is utilized for screening the criteria indicators from the literature. The entire fuzzy AHP is used for pairwise comparison of weights, as there are plenty of evaluation criteria in the literatures. It is expected to reduce the large amount of comparisons with AHP and achieve the final sequence. Fuzzy TOPSIS therefore simplifies the process of AHP and rapidly calculates the ideal solution and positive ideal solution. The alternatives are compared with ideal solution and positive ideal solution for the sequence. A project is regarded as the best one when it is close to ideal solution and far away from positive ideal solution. The optimal projects are further sequenced. The remainder of this study is structured as follows Section 2 briefly describes the proposed methods. In Section 3, proposed model for meaningful serious-game flow selection

is presented and the stages of the proposed approach are explained in detail. How the proposed model is used on a real world example is explained in Section 4. In Section 5, conclusions and suggestions are discussed.

2. Related Works

2.1. Rough Set Theory. Rough set theory proposed by Pawlak [2] has been shown as a useful mathematical tool for exploring data patterns [3] and a tool for decision support systems, especially dealing with imprecise, uncertain, and vague information in the decision process. It is used for distinctive classification and recognition, and it has achieved many goals and has been used for machine learning, researching, expert systems, and decision support system and has been widely applied in diverse domains, including finance, manufacturing, medicine, and image processing. In RST [4], a dataset can be described as an information system containing decision rules in the form “if the conditional attributes apply, then the decisional attributes apply.” Chen and Cheng [5] construct hybrid models by using Rough Set (RS) classifiers to provide meaningful decision rules as knowledge-based systems from an intelligent perspective, and offers an alternative method for forecasting credit ratings and assessing the quality of RS classification systems in the global banking industry. Therefore, by using RS to execute selecting important attribute and then classify selecting attributes via intelligent technique.

2.2. Fuzzy Multiple Criteria Decision-Making

2.2.1. Fuzzy Set. Fuzzy set theory is a mathematical theory pioneered by Zadeh [6], which is designed to model the vagueness or imprecision of human cognitive processes. The key idea of fuzzy set theory is that an element has a degree of membership in a fuzzy set [7, 8]. A fuzzy set is defined by a membership function that maps elements to degrees of membership within a certain interval, which is usually the value $[0, 1]$. If the value assigned is zero, the element does not belong to the set (it has no membership). If the value assigned is one, the element belongs completely to the set (it has total membership). Finally, if the value lies within the interval, the element has a certain degree of membership (it belongs partially to the fuzzy set) [9]. Table 1 shows the structure of triangular fuzzy numbers that are used in this paper.

2.2.2. Fuzzy Delphi Method. Fuzzy Delphi Method was proposed by Garriss et al. [10], and it was derived from the traditional Delphi technique and fuzzy set theory. Noorderhaben [11, 12] indicated that applying the Fuzzy Delphi Method to group decision can solve the fuzziness of common understanding of expert opinions. van Laarhoven and Pedrycz [13] proposed the FAHP, which is to show that many concepts in the real world have fuzziness. Therefore, the opinions of decision-makers are converted from previous definite values to fuzzy numbers and membership numbers in FAHP.

TABLE 1: Membership function of fuzzy scale.

Intensity of importance	Definition	Membership function
9	Extremely more importance (EMI)	(8, 9, 10)
7	Very strong importance (VSI)	(6, 7, 8)
5	Strong importance (SI)	(4, 5, 6)
3	Moderate importance (MI)	(2, 3, 4)
1	Equal importance (EI)	(1, 1, 2)

2.2.3. Fuzzy AHP. Satty [14] proposed the analytic hierarchy process (AHP) methodology which was a systematic method developed. It is to solve complex and multicriteria decision problems powerfully. Cheng et al. [15] improve the AHP by Fuzzy theory. Hsieh et al. [16] employed fuzzy analytic hierarchy process (FAHP) method to solve the problem of planning and design tenders selection in public office building. And FAHP method was also applied in the research of Chen et al. [17] to evaluate expatriate assignments. Thus, in this study, due to the fuzziness existed in the part of evaluation criteria, we decide to adopt the RST and FDM to form the primary evaluation criteria of MACF selection, and employ the FAHP to calculate the weight of individual criteria so as to establish the fuzzy multicriteria model of MACF selection criteria.

2.2.4. Fuzzy TOPSIS. Chen and Hwang [18] proposed TOPSIS multiple criteria method to identify solutions from a finite set of alternatives and initially proposed. Hwang and Yoon [19] define the ideal solution and negative ideal solution. The optimal solution should have the shortest distance from the positive ideal solution and the farthest from the negative ideal solution. In recent years, several researchers adopt fuzzy TOPSIS methods and applications to solve the problem and conflict [20–24]. Fuzzy TOPSIS methodology requires preliminarily information about the relative importance of the criteria. This importance is expressed by attributing a weight to each considered criterion. Chen adapted the methodology to calculate the weight of each criterion and to evaluate it by fuzzy AHP [25].

2.3. Learning Theory in Serious Game Design. Serious games have been some attempts to bring in learning effectiveness evaluation models. Garriss et al. [10] presented a far-reaching input-process-output model of instructional games and learning that has implications for the design and implementation of effective instructional games. Prensky [26] proposed digital game-based learning (DGBL) which includes activities that involve learning through solving problems or overcoming challenges posed in games. Specifically, learning arises as a result of the game’s tasks; knowledge is enhanced through the game’s content, and skills are developed while playing the game [27]. The design of digital games is critical in learning. A successful digital game must involve challenge, curiosity and fantasy to increase interest and intrinsic motivation for learning [28], and Added practice and exercise in the game, which can help students to retain information more

easily [29], provide immediate feedback, and activate prior knowledge by requiring players to use previously learned skills in order to advance to higher levels of the game [30].

2.3.1. ARCS Learning Motivation Model. The ARCS model is a problem solving approach to designing the motivational aspects of learning environments to stimulate and sustain students' motivation to learn [31]. There are two major parts to the model. The first is a set of categories representing the components of motivation. The second part of the model is a systematic design process that assists in creating motivational enhancements that are appropriate for a given set of learners. To accurately measure the change in learner motivation, Karoulis and Demetriadis [32] indicated that the ARCS model can be the standard of how much the learning motivation is increased by the game [33]. The four dimensions of ARCS are the following. Attention: attention which increases the learner's curiosity, relevance: establishment of the relevance of the learning content to learners, confidence-feedback to the learner, through the effort and the learning process of self-control, and satisfaction: the satisfaction or reward the learner can gain.

2.3.2. Flow Theory. Csikszentmihalyi [34] proposed the original definition of flow and he defined it as "the holistic experience that people feel when they act with total involvement." Flow describes a state of complete absorption or engagement in an activity and refers to the optimal experience [35]. During the state, people are extremely involved with activity that nothing seems to matter. Csikszentmihalyi [34, 35] summarized the most commonly exhibited factors of flow into nine characteristic dimensions, including clear goals, immediate feedback, potential control, the merger of action and awareness, personal skills well suited to given challenges, concentration, loss of self-consciousness, time distortion, and autotelic experience. The concept has been broad applied in studies such as sports, work, shopping, rock climbing, dancing, games, and others [35].

It is important that the challenge that the player faces in the game matches the player's skill. If challenge is significantly higher than player's skill, the player will feel anxiety. In contrast, if the challenge is significantly lower than player's skill, the player will feel bored. The three-channel model of flow explains the above situation in Figure 1. Therefore, for keeping a player in a flow state, game designers should ensure that while a player's skill increases, the challenges also should become more difficult.

2.3.3. Meaningful Learning. Ausubel [36] proposed meaningful learning strategy with research of cognition and learning. Meaningful learning importance lies in enabling students' acquisition of new knowledge and it is relevant to previous experiences in the personal's information and unique understandings [37]. In recent years, several researches have employed mobile technologies to support the achievement of meaningful learning [38, 39]. Huang et al. [40] design and

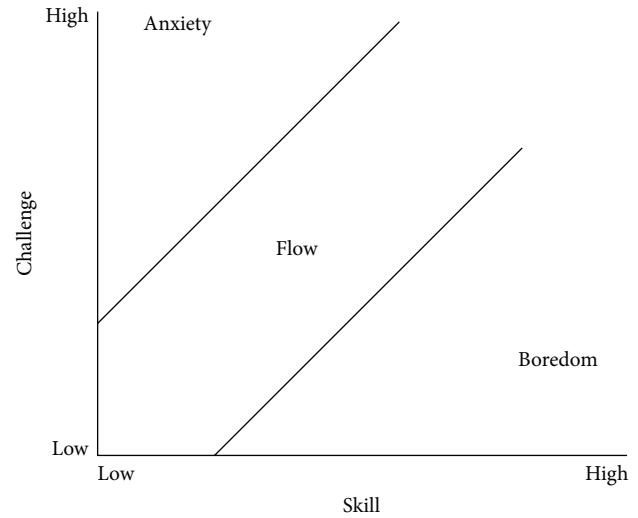


FIGURE 1: Flow.

implement a meaningful learning-based evaluation model for ubiquitous which based on previous study are active, authentic, constructive, cooperative and personal. Several characteristics of u-learning are also linked to attributes of meaningful learning. Therefore, this study adopted these five characteristics of meaningful learning as the evaluation criteria of MACF selection.

2.3.4. Cognitive Load. Cognitive load theory [41] was utilized to measure the cognitive load items. Extraneous cognitive load is the source for the cognitive load when delivering text-book information or presenting to spend learning memory resources for learners. Cognitive load is based on the load when learners understand how to deal with materials [42, 43]. Therefore, cognitive load depends on learners having prior knowledge and learning memory resources. In serious game design, it is usually used as supplementary learning material for enhancing learning achievement. There are three criteria to intrinsic cognitive load from the structure and complexity of the materials for cognitive load. The criteria items are shown in Table 2.

3. The Proposed MACF Evaluation Model

A MACF design evaluation model (Figure 2) is proposed in this study. By integrating group experts' wisdom with AHP and multicriteria decision-making (MCDM) in RST based Fuzzy TOPSIS, three stages are included: (1) Criteria selected by RST and FDM identification of necessary criteria for MACF design by RST and fuzzy Delphi method; (2) Calculating the weights of criteria by Fuzzy AHP; (3) Evaluating and determining the ranking by Fuzzy TOPSIS.

Stage 1 (criteria selected by RST and FDM). MACF design evaluation criteria are first collected through literature, selecting attribute by RST and the hierarchy model identified by experts are screened with Fuzzy Delphi Method.

TABLE 2: Criteria of MACF evaluation model selected by experts using RST and FDM.

Criteria	Sub-criteria	Source	RST core	FDM score (DF > 0.65)				Final
				Min	Max	M	DF	
Meaningful learning (C3)	Active (C31)	[36, 40]	V	3	10	7.63	7.10	V
	Authentic (C32)		V	4	10	7.39	6.87	V
	Constructive (C33)		V	3	9	7.66	7.12	V
	Cooperative (C34)		V	3	8	7.11	6.35	X
	Personalized (C35)		V	4	10	8.61	8.01	V
ARCS motivation (C1)	Attention (C11)	[33]	V	2	9	7.68	7.14	V
	Relevance (C12)		V	3	10	7.33	6.82	V
	Confidence (C13)		V	2	9	7.42	6.90	V
	Satisfaction (C14)		V	2	9	7.29	6.78	V
Cognitive load (C4)	Effort rating (C41)	[41]	X					
	Difficulty rating (C42)		V	5	10	8.39	7.80	V
	Response time (C43)		X					
Flow (C2)	Clear goals (C21)	[34]	V	4	10	8.37	7.78	V
	Skills (C22)	[34, 44]	V	5	10	8.66	8.05	V
	Challenge (C23)	[34, 44]	V	5	10	8.21	7.64	V
	Playfulness (C24)	[45]	V	6	10	8.78	8.17	V
	Novelty (C25)	[46]	X					
	Attractiveness (C26)	[47]	V	4	10	8.13	7.56	V
	Ease of use (C27)	[48]	V	5	10	8.39	7.80	V
	Interactivity (C28)	[49]	X					

Note: V: selected, X: not selected, and DF: defuzzification.

Step 1 (collect the criteria of decision group from related work and RST). RST addresses the continuing problem of vagueness, uncertainty, and incompleteness by applying equivalence classes to partition training instances using lower and upper approximations [50].

Let $B \subseteq A$ and $X \subseteq U$ be an information system. The set X is approximated using information from B and then by constructing the lower and upper approximation sets, which are, respectively,

$$\begin{aligned} BX &= \{ \{x \mid [x]_B \subseteq X \} \}, \\ \overline{BX} &= \{ \{x \mid [x]_B \cap X \neq \emptyset \} \}. \end{aligned} \quad (1)$$

The lower approximation requires the classification of elements in BX as members of set X using knowledge in B . The upper approximation requires the classification of elements in \overline{BX} as possible members of set X using knowledge in B . $BN_B(x) = \overline{B} - \underline{B}$ which is the B -boundary region of set X , comprising those objects that cannot be clearly classified as members of set X using knowledge in B . Set X is considered "rough" with respect to knowledge in B when the boundary region is not empty. The quality of classification of A by B expresses the percentage of objects that can be correctly assigned to set X using attribute B , as follows:

$$\gamma_B(A) = \frac{\sum \text{card}(\underline{BX}_i)}{\text{card}(U)}. \quad (2)$$

If $\gamma_B(A) = 1$, then the decision table is consistent; otherwise, it is inconsistent.

Reduct and core are the two key RST concepts [4, 51]. Given A and $B \in Q$, the reduct is the minimal nonredundant

subset of attributes of the original dataset for $\text{IND}(B) = \text{IND}(A)$, and the reduct can classify the universe with the same quality. The core comprises the most relevant attributes in the original dataset and cannot be removed from an information system. Let $\text{RED}(A)$ denote all reducts of A . The intersection of $\text{RED}(A)$ is a core of A , as it is shown by (3). Pawlak described RST in detail [4, 51] as follows:

$$\text{CORE}(A) = \cap \text{RED}(A). \quad (3)$$

Step 2 (establish the fuzzy positive reciprocal matrix $[\tilde{a}_{ij}]$). The core set of RST is a basic attribute of evaluation for experts. Linguistic variables in a questionnaire are first utilized for finding out the evaluation score of each alternate factor's significance given by the experts. Triangular fuzzy numbers are then used for integrating the experts' opinions to show the fuzziness of significance between factors. The triangular fuzzy number is established with the expert's evaluation values acquired from the questionnaire following the equation \tilde{w}_j, a_j, b_j , and c_j .

The calculation equations are shown as follows.

Assuming the evaluation of the j th factor's significance given by the i th expert, among n experts, being

$$\tilde{W}_{ij} = (a_{ij}, b_{ij}, c_{ij}), \quad i = 1, 2, \dots, n, \quad j = 1, 2, \dots, m, \quad (4)$$

the fuzzy weight ${}_j\tilde{W}_j$ of the j th factor appears,

$$W_j = (\widetilde{a_j, b_j, c_j}), \quad j = 1, 2, \dots, m, \quad (5)$$

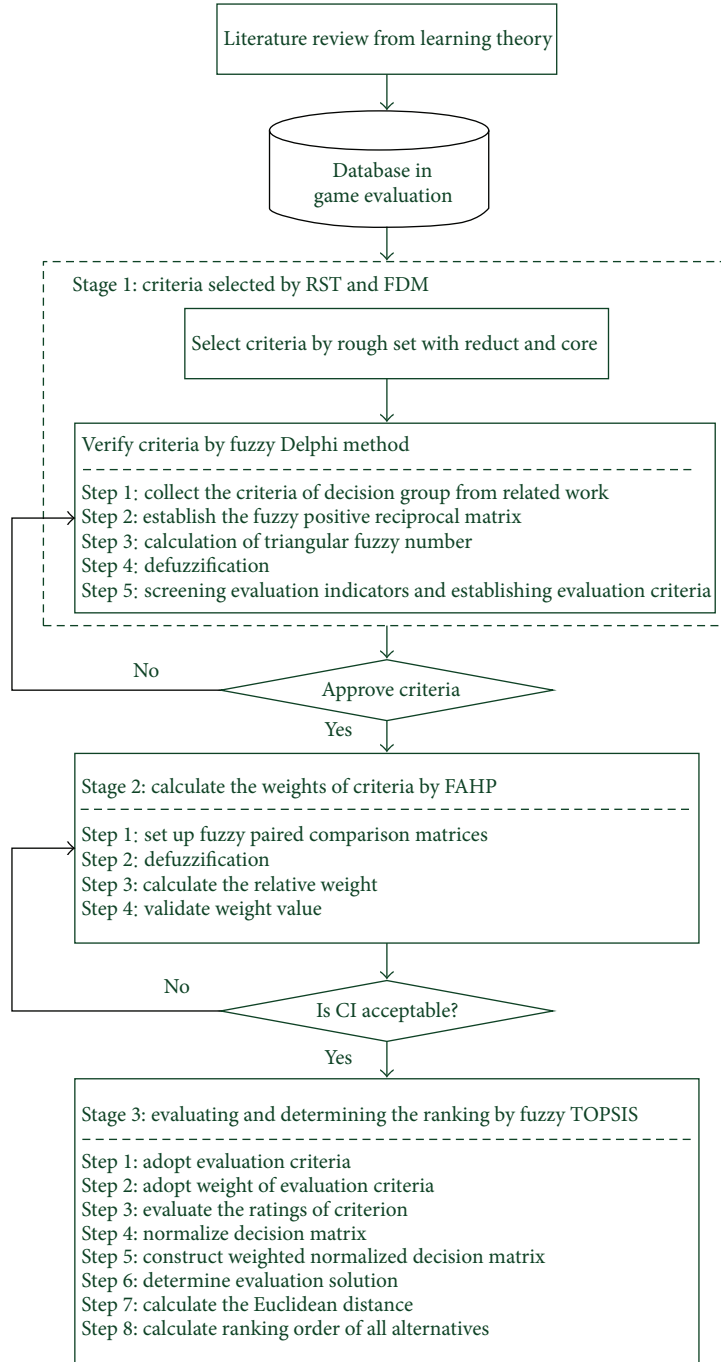


FIGURE 2: Schematic diagram of MACF evaluation model.

where

$$a_j = \text{Min}_i \{a_{ij}\}, \quad b_j = \frac{\{\sum_{i=1}^n b_{ij}\}}{n}, \quad c_j = \text{Max}_i \{c_{ij}\}. \quad (6)$$

Step 3 (calculation of triangular fuzzy number \tilde{w}_k of each criterion significance). The evaluation of each criterion's triangular fuzzy number given by the experts is calculated for the triangular fuzzy number \tilde{w}_k of the alternate factor's significance.

Assuming the evaluation of the j th initial indicator's significance given by the i th expert being $W_{ij} = (a_{ij}, b_{ij}, c_{ij})$, $i = 1, 2, 3, \dots, m$, the fuzzy weight W_j of the j th initial indicator is calculated as below:

$$\tilde{W}_j = (a_j, b_j, c_j), \quad j = 1, 2, 3, \dots, n, \quad (7)$$

where

$$a_j = \text{Min}_j \{a_{ij}\}, \quad b_j = \sqrt[n]{\prod_i^m b_{ij}}, \quad c_j = \text{Max}_j \{c_{ij}\}. \quad (8)$$

\widetilde{W}_j : fuzzy weight, ij : evaluation of the j th initial indicator's significance given by the i th expert, n : number of indicator, m : number of expert.

The total value of the triangular fuzzy number $\widetilde{W}_j = (a_j, b_j, c_j)$ of indicators is organized with defuzzification, proposed by Chen and Hwang [18], to present the consensus of the Delphi members to the indicator evaluation scale.

Step 4 (defuzzification). Center-of-gravity (COG) tends to perform defuzzification the fuzzy weight \widetilde{W}_j of each alternate factor being the actual value S_j . The equation is show as below.

$$S_j = \frac{a_j + b_j + c_j}{3}, \quad j = 1, 2, \dots, m. \quad (9)$$

Step 5 (screening evaluation indicators and establishing evaluation criteria). Finally, a proper factor could be screened from numerous factors by setting the threshold β (determined by Scree test criterion). The screening follows the principles as below.

Situation 1. When $S_j \geq \beta$, accept the j th factor as the evaluation indicator.

Situation 2. When $S_j < \beta$, remove the j th factor.

Practically, the value of threshold β could be determined by Scree test criterion, in which fuzzy numbers (DF_1, DF_2, \dots, DF_n) are first ordered then Linear Graph is drawn, and the Maximum turning point of linear graph scree test is the threshold β .

Stage 2 (calculate the weights of criteria by FAHP). Criteria confirmed by (Fuzzy Delphi Method) FDM are evaluated the hierarchic weight with AHP. The evaluation criteria weights of MACF design formed the matrix through pairwise comparisons.

Step 1 (set up Fuzzy Paired Comparison Matrices). \widetilde{W}_i is the weight of the pairwise comparison matrix \widetilde{A} in each row i

$$\widetilde{Z}_i = \sqrt[n]{(\widetilde{a}_{i1} \oplus \widetilde{a}_{i2} \oplus \dots \oplus \widetilde{a}_{in})}, \quad (10)$$

where n is the number of criteria; then

$$\widetilde{W}_i = \frac{\widetilde{Z}_i}{\widetilde{Z}_1 \oplus \widetilde{Z}_2 \oplus \dots \oplus \widetilde{Z}_n}. \quad (11)$$

Step 2 (defuzzification). \widetilde{W}_i and \widetilde{A} are as follows

$$\widehat{W}_i = \text{Defuzzy}(\widetilde{W}_i) \quad (12)$$

which could be used for calculation with Center-of-gravity

$$a_{\widehat{y}} = \text{Defuzzy}(\widetilde{a}_{\widehat{y}}), \quad (13)$$

where

$$A = [a_{\widehat{y}}]_{n \times n}, \quad \widetilde{A} = [\widetilde{a}_{\widehat{y}}]. \quad (14)$$

Step 3 (calculate the relative weight). The calculation of weight W_i is show as

$$W_i = \frac{\widehat{W}_i}{\sum_{i=1}^n \widehat{W}_i}. \quad (15)$$

Step 4 (validity test of weight). (I) Substitute $AW = \lambda W$ to acquire the eigenvector W'_1 of the weight. The left of the equation AW assumed W'_1 that

$$W'_1 = \lambda W \quad \text{as } AW = \lambda W, \quad (16)$$

$$\begin{bmatrix} W'_1 \\ W'_2 \\ \vdots \\ W'_n \end{bmatrix} = A \begin{bmatrix} W'_1 \\ W'_2 \\ \vdots \\ W'_n \end{bmatrix}. \quad (17)$$

(II) Substitute $AW = \lambda W$ with known A and W for the maximum eigenvalue λ_{\max}

$$\lambda_{\max} = \frac{1}{n} \left[\left(\frac{W'_1}{W_1} \right) + \left(\frac{W'_2}{W_2} \right) + \dots + \left(\frac{W'_n}{W_n} \right) \right]. \quad (18)$$

(III) Calculate the consistency index CI with known λ_{\max}

$$CI = \frac{\lambda_{\max} - n}{n - 1}. \quad (19)$$

(IV) Calculate CR with known CI

$$CR = \frac{CI}{RI}. \quad (20)$$

(V) Consistency test.

Situation 1. When $CR \leq 0.1$ (the pairwise comparison data \widetilde{A} is consistent), the relative weight outputs W_i ($1 \leq i \leq n$).

Situation 2. When $CR > 0.1$ (pairwise comparison data is not consistent), the pairwise comparison empirical analysis is re-proceeded.

Stage 3 (evaluating and determining the ranking by TOPSIS). The decision team would distribute the evaluation criteria weights and determine the optimal alternatives for sequence.

Our overall survey instrument was based on both past literature published surveys (ARCS, flow theory, and meaningful learning and cognitive load) and serious game-based learning. To consider the meaningful serious game flow selection practices in game design evaluation, we built on the MACF selection criteria. We gathered and developed the instruments of serious game design selection criteria from these different sources. All instruments were distributed in 15 critical constructs; all the instruments were represented in Table 2.

A MACF design evaluation with “ m ” alternatives and “ n ” criteria can be expressed in matrix format as given below:

$$y = (f_{ij})_{m \times n} = \begin{matrix} f_1 \\ f_2 \\ \vdots \\ f_m \end{matrix} \begin{pmatrix} x_1 & x_2 & \cdots & x_n \\ f_{11} & f_{12} & \cdots & f_{1n} \\ f_{21} & f_{22} & \cdots & f_{2n} \\ \vdots & \vdots & \ddots & \vdots \\ f_{m1} & f_{m2} & \cdots & f_{mn} \end{pmatrix}, \quad (21)$$

where f_1, f_2, \dots , and f_m are feasible alternatives, X_1, X_2, \dots , and X_n are evaluation criteria, f_{ij} is the performance rating given by the decision-makers to alternative f_i against criterion X_j , and W_j is the weight of criterion X_j .

An algorithm of the fuzzy decision-making method for dealing with the selection of reverse logistics provider is given as follows.

Step 1 (adopts evaluation criteria). Form Stage 1, committee of decision-makers adopts FDM results to identify the evaluation criteria.

Step 2 (adopts weight of evaluation criteria). Form Stage 2, choose the appropriate linguistic variables for the importance weight of the criteria by Fuzzy AHP.

Step 3 (evaluate the ratings of criterion). Use linguistic rating variables to evaluate the ratings of alternatives with respect.

Step 4 (normalized decision matrix). Construct the normalized decision matrix. The normalized value r_{ij} is calculated as,

$$r_{ij} = \frac{f_{ij}}{\sqrt{\sum_{j=1}^n f_{ij}^2}}. \quad (22)$$

Step 5 (construct weighted normalized decision matrix). The weighted normalized U_{ij} is calculated as.

$$U_{ij} = w_j r_{ij}. \quad (23)$$

Step 6 (determine evaluation solution). Determine positive ideal solution (maximum value on each criterion) and negative ideal solution (minimum value on each criterion) from the weighted normalized decision matrix. In the below equation, f^1 is the set of benefit criteria and f^2 is the set of cost criteria:

$$U_I^{*+} = \begin{cases} \max \{u_{ij}\} & \{f_i \in f^1\} & 1 \leq j \leq n \\ \min \{u_{ij}\} & \{f_i \in f^2\} & 1 \leq j \leq n, \end{cases} \quad (24)$$

$$U_I^{*-} = \begin{cases} \max \{u_{ij}\} & \{f_i \in f^2\} & 1 \leq j \leq n \\ \min \{u_{ij}\} & \{f_i \in f^1\} & 1 \leq j \leq n. \end{cases}$$

Step 7 (calculate the euclidean distance). Equations (21), (22) between positive ideal solution and negative ideal solution for each alternative:

$$D^{*+}(X_j) = \sqrt{\sum_{i=1}^m (U_{ij} - U_i^{*+})^2}, \quad (25)$$

$$D^{*-}(X_j) = \sqrt{\sum_{i=1}^m (U_{ij} - U_i^{*-})^2}. \quad (26)$$

Step 8 (calculate ranking order of all alternatives). Calculate the closeness coefficient of each alternative. According to the closeness coefficient, we can understand the assessment status of each alternative and determine the ranking order of all alternatives as follows:

$$C^*(X_j) = \frac{D^{*-}(X_j)}{D^{*+}(X_j) + D^{*-}(X_j)}. \quad (27)$$

4. Implementation of MACF Evaluation Model to Game Design

4.1. Evaluated Game Description

Game 1. Energy education game functions as follows.

Green city is a serious game which was designed for achieving energy education for elementary school. It takes the form of mobile game played within android pad. Each of the game levels and eleven different building locations around Taiwan is instantiated as a team in the game. Each game element has been equipped with real-world energy sensors to measure energy use and this monitoring is the main source for scoring of each team. Additionally, players play simple; fast ecoaction based minigames, take quizzes and learn about energy efficiency from sources on cloud. The actions of a team of players combine to win awards that improve and upgrade the virtual representation of their team building. Figure 3(b) shows that teams cooperate on virtual environment to build the energy city.

Game 2. Software engineering project management game functions as follows [52].

The game situation: the construction of the game, besides the design of the game screen, also includes the situation and character design. The story is set in a computer and internet service company whose clients and complicated equipment are getting more and more. This company therefore wants to develop systems that can answer questions of clients and increase the efficiency. The player must help the company evaluate and develop software, act as different roles in the developing process, and complete different tasks as different roles to complete the software development.

The interface design: the game in this study takes the story background, environment, and age of players into consideration. The game provides five different roles to be chosen. Figure 4(b) shows that every role corresponds to different



FIGURE 3: Game 1: energy education game. (a) Green city game menu; (b) understanding your environment.



FIGURE 4: Game 2: project management game. (a) Discuss a project cost; evaluate a project (b).

situations and tasks, and the player can go through the different roles to learn all different tasks of various positions. In the requirement analysis, this study uses the maze game, which will show the problem sign and player position. When passing a problem sign, the character must stop, and the player must solve the current problem in order to keep going forward. In this task, the multiple choice questions are designed by the meeting record from the game. Besides solving all problems in the maze, Figure 4(a) shows that the player must find a way out in order to increase his interest and keep the player's attention on game-based learning. In this task, the player must distinguish the requirements into functional and nonfunctional. The player has to take an evaluation then he will get the score which will be provided to the teacher for reference.

Game 3. 3D CCGBLS game functions as follows. The learners can understand the operation procedure through game-based simulation of clinical path. With the game-based simulation of Clinical Path, this system is expected to achieve the three objectives. (1) The simulation of various operations allows the player to be familiar with the operation process. (2) The operation simulation allows the player to understand the complication in the operation process. (3) The healthcare information offered in the game could assist the player in acquiring knowledge.

The game provides four different game situation levels to be chosen. Figure 3(a) a doctor that visits patient and talks. In the game of cardiac catheterization, this study uses the first person view control of the game, which will show the situation of view Cardiac Catheterization training. The player must solve all the problem in the game order to keep going forward. In this task, the multiple choice questions are designed by meeting the record from the game. Besides solving all problems in the game, Figure 5(b) shows that the player must find a way out in order to increase his interest and keep the player's attention on game-based learning. In this task, the player must distinguish the emergencies that will be happen occasionally in the 3D-CCGBLS. If the answer is wrong, the health points will decrease by one and the question will reappear and the countdown will be reset in order to give the player the chance to correct the mistake. The player must answer in limited time, to increase the challenge of the game. At the end of the learning phase, the player has to take a learning evaluation; then the learner's learning data will be collected into learner's portfolio by mobile intelligent agent and then he will get the score which will be provided to the teacher for reference.

Game 4. Blood circulation system serious game is called red adventure which functions as follows.



(a)

(b)

FIGURE 5: Game 3: medical education game. (a) Asking clinic situation; (b) cardiac catheterization simulation.



(a)

(b)

FIGURE 6: Game 4: blood circulation system serious game. (a) Red adventure game; (b) blood circulation system menu.

Aiming at the function of blood circulation in human bodies, the learners could log in to the system from the menu in Figure 6(a) and get into the unit practice through the level menu in Figure 6(b) with the main menu and the role selection to enter the unit learning of the circulation system of heart and blood, the circulation system of liver, the circulation system of spleen, and the circulation system of lung.

The game starts on right atrium, going through left lung, left atrium, spleen, liver, right atrium, right lung, and left atrium, where the circulation of blood refers to lung circulation and systemic circulation, returning to the circulation of lung. In addition to the collection of oxygen and carbon dioxide, oxygen or carbon dioxide are released at specific locations in the process, where there are attacks of bacteria and wounds for recovery. Before leaving the learning level of each organ, correctly answering the questions in the games is requested for learning feedback.

4.2. Identification of Necessary Criteria. In this stage, we focused on the analysis of evaluation criteria of MACF selection. Thus, the experts chosen were the professionals in the area related to our study with the experience of serious game design experts. Besides, they should be of rich working experience with the serious game designs and their positions

where at least the rank of department managers should be over 10 years of working experience. In general, the numbers of expert were from three to fifteen [11, 12]. This study was sent out to eleven serious game design experts as questionnaire subjects.

After that we designed the questionnaire in a 9-point fuzzy semantic differential scale; see Table 1. And, we asked the selected experts to answer instrument survey. The selected experts assigned a relative importance to every collected variable with respect to three dimensions of ARCS, flow, and meaningful learning in order to confirm critical constructs as the evaluation criteria of MACF selection. The expert questionnaires were collected, and triangular fuzzy function with respect to every potential variable was established as represented in Table 2.

When selecting the evaluation criteria, it was generally considered important if the relative importance is greater than 65%. According to the above filtering treatment, we obtained from the collected experts' questionnaires, there are 15 important criteria commonly agreed by 11 experts. And, totally 15 instrument items were eliminated. They were listed as shown in Table 2.

According to the experts' decision, evaluation hierarchy of MACF model was built. There are four levels in the decision

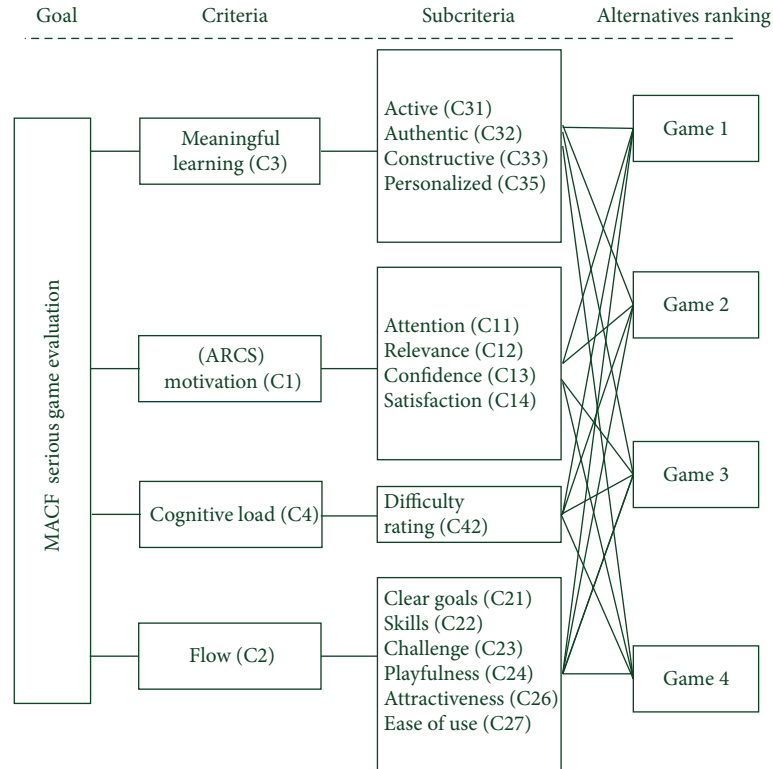


FIGURE 7: Evaluation hierarchy of MACF model.

hierarchy structured for MACF design evaluated criteria (Figure 7). The overall goal of the MACF decision process determined is in the first level of the hierarchy. The criteria are on the second level, subcriteria are on the third level, and evaluated MACF model is on the fourth level of the hierarchy.

4.3. *Calculate the Weights of Criteria.* This stage was employed to calculate the fuzzy weights. The next three steps were shown as follows.

Step 1 (collection). This method was based on the experts' precise value and the synthesized experts' opinions with the geometric mean instead of the fuzzy numbers input directly by experts.

Step 2 (defuzzification). Since the weights of all evaluation criteria were fuzzy values, it was necessary to compute a nonfuzzy value by the process of defuzzification. Through formulas, the defuzzification weight W_i can be obtained.

Step 3 (normalization). In order to effectively compare the relative importance among evaluation criteria, we normalized the obtained weights using formula. They were listed as shown in Table 2.

In the finalization of AHP steps, results are shown in Table 3. From these obtained results, the specialization, interactivity, and the accuracy of MACF selection can be concluded. The results obtained from the computations based on the pairwise comparison matrix are provided in Table 3.

TABLE 3: The summary of evaluation criteria weight.

Criteria	Global weight	Subcriteria	Weight	Total weight
Meaningful learning (C3)	0.25	Active (C31)	0.29	0.073
		Authentic (C32)	0.19	0.048
		Constructive (C33)	0.21	0.053
		Personalized (C35)	0.31	0.078
ARCS motivation (C1)	0.23	Attention (C11)	0.34	0.078
		Relevance (C12)	0.25	0.058
		Confidence (C13)	0.16	0.037
		Satisfaction (C14)	0.25	0.058
Cognitive load (C4)	0.04	Difficulty rating (C42)	1	0.040
Flow (C2)	0.48	Clear goals (C21)	0.1	0.048
		Skills (C22)	0.18	0.086
		Challenge (C23)	0.15	0.072
		Playfulness (C24)	0.27	0.130
		Attractiveness (C26)	0.18	0.086
		Ease of use (C27)	0.12	0.058

Result shows the playfulness (C24), skills (C22), attention (C11), and personalized (C35) which are determined as the four most important criteria in the MACF selection process by fuzzy AHP. Consistency ratio of the pairwise comparison matrix is calculated as $0.068 < 0.1$. So, the weights

TABLE 4: The final evaluation and ranking of alternative.

Criteria	Sub-criteria	Game 1	Game 2	Game 3	Game 4
Meaningful learning (C3)	Active (C31)	0.070	0.057	0.067	0.051
	Authentic (C32)	0.018	0.015	0.017	0.013
	Constructive (C33)	0.162	0.133	0.154	0.131
	Personalized (C35)	0.027	0.022	0.026	0.020
ARCS motivation (C1)	Attention (C11)	0.160	0.131	0.152	0.120
	Relevance (C12)	0.112	0.092	0.106	0.082
	Confidence (C13)	0.051	0.042	0.048	0.032
	Satisfaction (C14)	0.033	0.027	0.031	0.028
Cognitive load (C4)	Difficulty rating (C42)	0.035	0.057	0.045	0.067
Flow (C2)	Clear goals (C21)	0.048	0.039	0.046	0.041
	Skills (C22)	0.032	0.026	0.030	0.028
	Challenge (C23)	0.033	0.027	0.031	0.025
	Playfulness (C24)	0.046	0.045	0.044	0.036
	Attractiveness (C26)	0.030	0.032	0.030	0.023
	Ease of use (C27)	0.040	0.041	0.038	0.031
TOPSIS ranking calculation	D^{**}	0.152	0.147	0.146	0.145
	D^{*-}	0.106	0.068	0.096	0.063
	C^*	0.320	0.189	0.298	0.183
	Ranking	1	3	2	4

are shown to be consistent and they are used in the selection process.

4.4. *Evaluating and Determining the Final Rank of Alternative.* In the following step, decision-makers assessed the quality of the alternative hospital web sites. The same fuzzy scale is used for evaluation as in fuzzy AHP and the decision matrix with alternatives and criteria can be seen with linguistic terms in Table 1. In the case study, there are three game alternatives. After constructing the fuzzy decision matrix and normalized matrix, TOPSIS method expression was used to calculate [25].

The last step of the methodology consists of ranking the selected game project to the ideal solution. The performance indices are computed to rank the alternatives, and the obtained results are given in Table 4. The evaluation results point out that Game 1 has the best score overall (Game 1 > Game 3 > Game 2 > Game 4).

5. Conclusion and Suggestions

Multimedia game design education criteria evaluation refers to the selection of instructional strategies, which could affect the learning effectiveness of game design education. A lot of alternatives should be taken into account evaluating the factors in different game design criteria. In this case, an efficient decision evaluation method is necessary for reinforcing the decision evaluation quality for MACF design.

A system evaluation process for MACF design is proposed in this study, which applies triangular fuzzy numbers to expressing the evaluation linguistics and considering the

subjective judgment and objective analyses. A mixed fuzzy multicriteria decision-making is further applied to completing the group decision evaluation model. The evaluation mode completed the MACF design evaluation based on literature and experts' definitions. The criteria comparisons of the case are preceded by the optimal design sequence.

The criteria weights are acquired by Fuzzy AHP, which provides the calculations of ideal solution and positive ideal solution of Fuzzy TOPSIS in the criteria decision process. Meanwhile, weighted decision evaluation is further calculated according to such weights to generate alternatives and determine the sequence.

The proposed MACF design evaluation decision model has largely enhanced the working efficiency of MACF design education. Fuzzy TOPSIS simplifies the solution of AHP calculating the evaluation process and rapidly generates the results and sequence of decision evaluations. Moreover, the calculation of indicator weights through Fuzzy TOPSIS is important for the evaluation comparison in the case. Different weights could generate the priority sequence of the evaluation results. It shows that the weights are determined through experts' group decision to avoid prejudice, reduce bias in the decision process, and benefit the correctness of criteria evaluation [53].

Most decisions are complex and conflict that decision-makers should consider solving problems with scientific methods. The development of MACF design evaluation decision model could assist game design educators in proposing teaching strategies.

A mixed multicriteria decision-making evaluation model is combined in this study. Although the research model is compared with MACF design, the future research could

revise the criteria and could be utilized for the selection from distinct design course evaluation. Besides, distinct multicriteria decision-making evaluations are used for comparing the priority sequence of decision projects. For instance, the comparison between TPOSI, VIKOR, and ANP could have evaluation decisions be more valuable.

References

- [1] T.-C. Wang and T.-H. Chang, "Application of TOPSIS in evaluating initial training aircraft under a fuzzy environment," *Expert Systems with Applications*, vol. 33, no. 4, pp. 870–880, 2007.
- [2] Z. Pawlak, *Rough Sets: Theoretical Aspects of Reasoning about Data*, Kluwer Academic Publishers, Dordrecht, The Netherlands, 1991.
- [3] S. Greco, B. Matarazzo, and R. Slowinski, "Rough sets theory for multicriteria decision analysis," *The European Journal of Operational Research*, vol. 129, no. 1, pp. 1–47, 2001.
- [4] Z. Pawlak, "Rough sets," *Informational Journal of Computer & Information Sciences*, vol. 11, no. 5, pp. 341–356, 1982.
- [5] Y.-S. Chen and C.-H. Cheng, "Hybrid models based on rough set classifiers for setting credit rating decision rules in the global banking industry," *Knowledge-Based Systems*, vol. 39, pp. 224–239, 2013.
- [6] L. A. Zadeh, "Fuzzy sets," *Information and Control*, vol. 8, no. 3, pp. 338–353, 1965.
- [7] C. V. Negoita, *Expert Systems and Fuzzy Systems*, Benjamin/Cummings, Menlo Park, Calif, USA, 1985.
- [8] H. J. Zimmermann, *Fuzzy Set Theory and Its Applications*, Kluwer Academic Publishers, Boston, Mass, USA, 1985.
- [9] Z. Ayağ, "A fuzzy AHP-based simulation approach to concept evaluation in a NPD environment," *IIE Transactions*, vol. 37, no. 9, pp. 827–842, 2005.
- [10] R. Garris, R. Ahlers, and J. E. Driskell, "Games, motivation, and learning: a research and practice model," *Simulation & Gaming*, vol. 33, no. 4, pp. 441–467, 2002.
- [11] N. Noorderhaven, *Strategic Decision Making*, Addison-Wesley, Boston, Mass, USA, 1995.
- [12] O. Manoliadis, I. Tsolas, and A. Nakou, "Sustainable construction and drivers of change in Greece: a Delphi study," *Construction Management and Economics*, vol. 24, no. 2, pp. 113–120, 2006.
- [13] P. J. M. van Laarhoven and W. Pedrycz, "A fuzzy extension of Saaty's priority theory," *Fuzzy Sets and Systems*, vol. 11, no. 1–3, pp. 199–227, 1983.
- [14] T. Satty, *The Analytic Hierarchy Process*, McGraw-Hill, New York, NY, USA, 1980.
- [15] J.-H. Cheng, C.-W. Chen, and C.-Y. Lee, "Using fuzzy analytical hierarchy process for multi-criteria evaluation model of high-yield bonds investment," in *Proceedings of the IEEE International Conference on Fuzzy Systems*, pp. 1049–1056, Vancouver, Canada, July 2006.
- [16] T.-Y. Hsieh, S.-T. Lu, and G.-H. Tzeng, "Fuzzy MCDM approach for planning and design tenders selection in public office buildings," *The International Journal of Project Management*, vol. 22, no. 7, pp. 573–584, 2004.
- [17] M.-F. Chen, G.-H. Tzeng, and T.-I. Tang, "Fuzzy MCDM approach for evaluation of expatriate assignments," *International Journal of Information Technology and Decision Making*, vol. 4, no. 2, pp. 277–296, 2005.
- [18] S. J. Chen and C. L. Hwang, "Fuzzy multiple attribute decision making methods," in *Fuzzy Multiple Attribute Decision Making: Methods and Applications*, Lecture Notes in Economics and Mathematical Systems, pp. 289–486, Springer, New York, NY, USA, 1992.
- [19] C. L. Hwang and K. Yoon, *Multiple Attribute Decision Making: Methods and Applications*, vol. 186 of *Lecture Notes in Economics and Mathematical Systems*, Springer, New York, NY, USA, 1981.
- [20] C. C. Chang, "The e-hospital website measure architecture approach: integrating internal and external customers' needs in information delivery services," *Asian Journal of Health and Information Sciences*, vol. 2, no. 1–4, pp. 116–131, 2007.
- [21] Z. Gligoric, C. Beljic, and V. Simeunovic, "Shaft location selection at deep multiple orebody deposit by using fuzzy TOPSIS method and network optimization," *Expert Systems with Applications*, vol. 37, no. 2, pp. 1408–1418, 2010.
- [22] Z. Yang, S. Cai, Z. Zhou, and N. Zhou, "Development and validation of an instrument to measure user perceived service quality of information presenting Web portals," *Information & Management*, vol. 42, no. 4, pp. 575–589, 2005.
- [23] H. Zhang, C.-L. Gu, L.-W. Gu, and Y. Zhang, "The evaluation of tourism destination competitiveness by TOPSIS & information entropy—a case in the Yangtze River Delta of China," *Tourism Management*, vol. 32, no. 2, pp. 443–451, 2011.
- [24] J.-H. Huang and K.-H. Peng, "Fuzzy Rasch model in TOPSIS: a new approach for generating fuzzy numbers to assess the competitiveness of the tourism industries in Asian countries," *Tourism Management*, vol. 33, no. 2, pp. 456–465, 2012.
- [25] C.-T. Chen, "Extensions of the TOPSIS for group decision-making under fuzzy environment," *Fuzzy Sets and Systems*, vol. 114, no. 1, pp. 1–9, 2000.
- [26] M. Prensky, *Digital Game-Based Learning*, McGraw-Hill, New York, NY, USA, 2001.
- [27] A. McFarlane, A. Sparrowhawk, and Y. Heald, "Report on the educational use of games: an exploration by TEEM of the contribution which games can make to the education," Tech. Rep., Cambridgeshire, UK, 2002.
- [28] M. D. Dickey, "Engaging by design: how engagement strategies in popular computer and video games can inform instructional design," *Educational Technology Research and Development*, vol. 53, no. 2, pp. 67–83, 2005.
- [29] C. Dondi and M. Moretti, "A methodological proposal for learning games selection and quality assessment," *The British Journal of Educational Technology*, vol. 38, no. 3, pp. 502–512, 2007.
- [30] D. G. Oblinger, "The next generation of educational engagement," *Journal of Interactive Media in Education*, no. 8, pp. 1–18, 2004.
- [31] J. M. Keller, "Motivational design of instruction," in *Instructional-Design Theories and Models: An Overview of Their Current Status*, C. M. Reigeluth, Ed., pp. 386–434, Lawrence Erlbaum Associates, Hillsdale, NJ, USA, 1983.
- [32] A. Karoulis and S. Demetriadis, "The motivational factor in educational games. interaction between learner's internal and external representations in multimedia environments," Research Report, Kaleidoscope NoE JEIRP D21-02-01-F, 2005.
- [33] J. M. Keller, "Development and use of the ARCS model of instructional design," *Journal of Instructional Development*, vol. 10, no. 3, pp. 2–10, 1987.
- [34] M. Csikszentmihalyi, *Beyond Boredom and Anxiety*, Jossey-Bass, San Francisco, Calif, USA, 1975.

- [35] M. Csikszentmihalyi and D. A. Kleiber, "Leisure and self-actualization," in *Benefits of Leisure*, B. L. Driver, P. J. Brown, and G. L. Peterson, Eds., pp. 91–102, Venture, State College, Pa, USA, 1991.
- [36] D. P. Ausubel, *Psychology of Meaningful Verbal Learning: An Introduction to School Learning*, Grune & Stratton, New York, NY, USA, 1963.
- [37] A. B. Rendas, M. Fonseca, and P. R. Pinto, "Toward meaningful learning in undergraduate medical education using concept maps in a PBL pathophysiology course," *The American Journal of Physiology: Advances in Physiology Education*, vol. 30, no. 1, pp. 23–29, 2006.
- [38] P. Karppinen, "Meaningful learning with digital and online videos: theoretical perspectives," *Association for the Advancement of Computing in Education Journal*, vol. 13, no. 3, pp. 233–250, 2005.
- [39] S. Rick and R. A. Weber, "Meaningful learning and transfer of learning in games played repeatedly without feedback," *Games and Economic Behavior*, vol. 68, no. 2, pp. 716–730, 2010.
- [40] Y.-M. Huang, P.-S. Chiu, T.-C. Liu, and T.-S. Chen, "The design and implementation of a meaningful learning-based evaluation method for ubiquitous learning," *Computers & Education*, vol. 57, no. 4, pp. 2291–2302, 2011.
- [41] K. E. DeLeeuw and R. E. Mayer, "A comparison of three measures of cognitive load: evidence for separable measures of intrinsic, extraneous, and germane load," *Journal of Educational Psychology*, vol. 100, no. 1, pp. 223–234, 2008.
- [42] P. Gerjets and K. Scheiter, "Goal configurations and processing strategies as moderators between instructional design and cognitive load: evidence from hypertext-based instruction," *Educational Psychologist*, vol. 38, no. 1, pp. 33–41, 2003.
- [43] A. Renkl and R. K. Atkinson, "Structuring the transition from example study to problem solving in cognitive skill acquisition: a cognitive load perspective," *Educational Psychologist*, vol. 38, no. 1, pp. 15–22, 2003.
- [44] D. L. Hoffman and T. P. Novak, "Marketing in hypermedia computer-mediated environments: conceptual foundations," *The Journal of Marketing*, vol. 60, no. 3, pp. 50–68, 1996.
- [45] R. Agarwal and E. Karahanna, "Time flies when you're having fun: cognitive absorption and beliefs about information technology usage," *MIS Quarterly*, vol. 24, no. 4, pp. 665–694, 2000.
- [46] M.-H. Huang, "Designing website attributes to induce experiential encounters," *Computers in Human Behavior*, vol. 19, no. 4, pp. 425–442, 2003.
- [47] Y. X. Skadberg and J. R. Kimmel, "Visitors' flow experience while browsing a Web site: its measurement, contributing factors and consequences," *Computers in Human Behavior*, vol. 20, no. 3, pp. 403–422, 2004.
- [48] C.-L. Hsu and H.-P. Lu, "Why do people play on-line games? an extended TAM with social influences and flow experience," *Information & Management*, vol. 41, no. 7, pp. 853–868, 2004.
- [49] D. H. Choi, J. Kim, and S. H. Kim, "ERP training with a web-based electronic learning system: the flow theory perspective," *The International Journal of Human-Computer Studies*, vol. 65, no. 3, pp. 223–243, 2007.
- [50] H. M. Abu-Donia, "Multi knowledge based rough approximations and applications," *Knowledge-Based Systems*, vol. 26, pp. 20–29, 2012.
- [51] Z. Pawlak, *Rough Sets: Theoretical Aspects of Reasoning about Data*, vol. 9, Kluwer Academic Publishers, Boston, Mass, USA, 1991.
- [52] C. H. Su and C. H. Cheng, "3D game-based learning system for improving learning achievement in software engineering curriculum," *The Turkish Online Journal of Educational Technology*, vol. 12, no. 2, pp. 1–12, 2013.
- [53] R. U. Bilsel, G. Büyüközkan, and D. Ruan, "A fuzzy preference-ranking model for a quality evaluation of hospital web sites," *International Journal of Intelligent Systems*, vol. 21, no. 11, pp. 1181–1197, 2006.

Research Article

Exploring the Effects of Multidimensional Context on Human Performance in Personal Bookmark Management

Siu-Tsen Shen

Department of Multimedia Design, National Formosa University, 64 Wen-Hua Road, Hu-Wei 63208, Taiwan

Correspondence should be addressed to Siu-Tsen Shen; stshen@nfu.edu.tw

Received 9 September 2013; Accepted 14 October 2013

Academic Editor: Stephen D. Prior

Copyright © 2013 Siu-Tsen Shen. This is an open access article distributed under the Creative Commons Attribution License, which permits unrestricted use, distribution, and reproduction in any medium, provided the original work is properly cited.

This paper presents an exploratory study in comparing the gender difference of how Taiwanese university students interacted and organized their bookmarks under 2D and 3D conceptual prototyping. Participants were asked to execute a set of online tasks for bookmark management and take screenshots to further ground the findings. The results showed that 62% of the female participants preferred the 2D context and there was no significant difference between the 2D and 3D tasks in terms of their time taken, which indicated that they maintained the consistency of their task performance strategy and were not subject to the change of spatial dimension. In contrast, the male participants performed poorly in the 3D context, as opposed to the 2D environment, even though they stated that they preferred the 3D context. A possible explanation for this might be that most of the male participants (mean age 21.8 years, SD = 1.1) are regular 3D game players. Therefore, they tend to unconsciously prefer 3D over 2D. Although the null hypothesis was not disproved, the task time results showed a degree of significance in terms of gender and spatial context differences, which requires further investigation.

1. Introduction

Internet interfaces are no longer a series of static pages linked together by HTML code. A huge range of websites now offer different forms of interaction to engage users, and these can take the form of search engines, online video conferencing, instant messaging, music sharing, personalized blogging, and online shopping and bookings, to name but a few. Users expect websites to meet their needs by collecting and categorizing their data autonomously. This requires web browser developers to generate smarter and more intuitive programs; at present, the best that they can offer is a strictly defined bookmark management system to help users organize data.

In this paper, the author investigates the possibilities of developing 2D and 3D bookmark management prototypes based on the Garden Metaphor [1] and conducts a comparative evaluation of user's performance and preference between 2D or 3D interfaces.

2. Theoretical Background

2.1. Bookmark Management Systems

2.1.1. Browser-Based System of Folders. Bookmarks, known as favorites, or internet shortcuts in Internet Explorer, help users to save their desired links and are an essential component of modern web browsers. The function of bookmarks is to provide the user with the ability to create numerous folders (directories) and subfolders (subdirectories) in order to store, retrieve, and organization information sources. However, the maintenance of bookmarks requires continuous and intensive efforts by naming, sorting, refining, and updating taxonomies. The majority of users find that this process is time consuming and still does not guarantee later information retrieval. To alleviate this problem, the leading browsers such as Google Chrome and Internet Explorer added a search function within the system, whereby typing partial keywords or Uniform Resources Identifiers (URIs) would display an a-priori assumption list.

2.1.2. Tag-Based Systems. There is another kind of bookmark management system called social bookmarking, also known as tagging or folksonomies. This tag-based system is mainly for sharing information within special interest groups either for private or for public purposes. Famous examples are Flickr and Delicious (<http://delicious.com>).

2.1.3. Other Experimental Alternatives. Other web browser developers have extended the concept of the bookmark function in saving links further. PowerBookmarks developed by Li et al. allow bookmarks to be indexed and classified by query [2]. Live bookmarks from RSS feeds have been introduced by Mozilla Firefox since 2004 and could be automatically updated by news sites or blogs. Bookmarklets, which were coined by combining the terms bookmark and applets, are run by JavaScript programs and stored as bookmarks which can be installed by browsing a website and clicking to launch an action [3]. Other types include Weave, Xmarks, and Diigo [4].

These various bookmark management tools aim to help users organize bookmarks more efficiently and effectively. However, they still cannot alleviate the problems of massive piles of unorganized bookmarks and lost bookmarks for unforeseen reasons.

2.2. Related Work on 2D and 3D Desktop Management

2.2.1. 2D Desktop Management. Most current bookmark management systems rely on a hierarchical structure, as well as file management systems. Various examples are different from their visualization presentation and functionality [5–7]. The 2D Lifestreams interface developed by Freeman was a time ordered stream of documents much like a diary of your life, whereby you could store your documents that you created and others sent you. Lifestreams had five major functions, that is, New (for creating documents), Clone (for duplicating documents), Transfer (copying from your stream to others), Find (for a search query and creating a substream), and Summary (by taking a substream and compressing it to a single overview) [8]. More recent documents appeared to be in the front of the screen, while the older ones stayed in the back of the screen. It provided a personal collection of saved documents that could be viewed through filtering based on time.

Ringel et al. had a similar idea for the use of time-centric visualization to display search results from personal emails, files, and bookmarks provided by both public (news headlines, holidays) and personal (date appointments, digital photos) landmark events [9].

Linking File System Browse (LiFSBrowse) used customizable graphical structures in the file system and allowed users to view their files and web pages through querying [10].

Scopeware Vision developed by Mirror World Technologies (NWT) integrated documents and Email messages into addictive streams [11]. Its default screen could show a maximum of 100 of the most recent files and the users could type in keyword search terms such as the file's name, format style, date, and size in thumbnail previews. However,

Scopeware was discontinued in 2004 [12], possibly because of its similar capabilities to the update version of Microsoft's Longhorn release.

Inlight StarTree, also known as the Hyperbolic Tree, provided users with the capability to navigate and explore visual hierarchical relationships for a large collection of different file formats, and drill-down further information of interest within a circular boundary [13].

We may conclude that 2D interfaces have not radically evolved since the introduction of Graphical User Interfaces (GUIs) in the 1980s. The linear, hierarchical structure has been the standard and has been applied extensively to the whole operating system and web applications, such as the file system and bookmark management system. The exploration of alternative 2D information visualization still needs more empirical research to support further development. Therefore, the standardized system has remained largely unchanged and underdeveloped in comparison to 3D systems.

2.2.2. 3D Desktop Management. Over the decades, there have been several predictions of the coming trend in three-dimensional (3D) user interfaces for the desktop. Nevertheless, 3D visualization seems to be restricted to home entertainment, especially the game industry, and its preponderance for first person gaming.

Several attempts to develop 3D bookmark management systems include work by Card et al.—WebBook, and Robertson et al.—Data Mountain. WebBook offered users the ability to save web pages as a book collection in a 3D environment, where users could turn and view the pages and even store them in a bookcase [14]. Data Mountain made use of spatial memory for document management and allowed users to arrange the files in their desired location with 2D iconic viewing layout, that is, thumbnails of web pages, under a 3D desktop environment [15]. It has been said that spatial cognition could aid in information management.

Further, examples include Robertson et al. Cone Tree, and Agarawala and Balakrishnan's Drag'n'Cross. Corn Tree displayed a hierarchical tree structure of information in order to maximize the screen space and could overview the whole structure [16]. Drag'n'Cross simulated a series of our physical actions such as dragging, crossing, and scrubbing on desktop environment to help organize information [17].

Unfortunately, these efforts lack further validation and improvement results. Partially, this might be because of a lack of major leading software developers being not keen to move from 2D to 3D. Therefore, 3D user interface desktop applications have not yet been able to compete with developments in the 3D games industry.

2.3. User Performance and Preference of 2D versus 3D Interface Design. User performance and preference of 2D and 3D interfaces have been discussed in various research papers. Levy et al. found that 3D graphics were preferred in the need of describing and memorizing details, whilst 2D graphics were preferred for the instant feedback and general impressions [18]. Ware and Franck showed that 3D

visualization performed better and more comprehensively than 2D, in terms of information presentation [19]. Cockburn and McKenzie examined the 2D and 3D versions of desktop management based on the concept of Robertson et al. [15], Data Mountain, and indicated that there was a significant preference for 3D, even though the subjects were slightly faster using 2D in storing and retrieving tasks. However, 2D retrieval time was not significant when compared to 3D [20].

Ozok and Komlodi conducted an experiment with 20 subjects who had regular online shopping experience by providing product representations in 2D and 3D (3D low interaction and 3D high interaction). The results showed that the 3D representations, both in low and high interaction, were preferred over the 2D ones, in that they contained more product details, were easy to use, and more fun than the 2D representations [21].

Despite 3D interfaces having certain advantages in terms of the browsing depth of the views and presenting more semantic information, it has been said that they require more computer hardware such as memory cards and a higher resolution of image cards. Perhaps more importantly, they take additional cognitive loading with more complicated instructions in navigation and manipulation [22–25]. 3D spatial semantic mapping provides no advantage and may result in poor performance compared to 2D mapping [26].

In short, the choice of 2D or 3D is highly dependent on which types of tasks are being conducted, which in turn leads to different browsing performance and mapping between 3D input devices, displays, and interaction styles. In the following user studies, we investigate the potential advantages and disadvantages of using 2D and 3D prototypes for a series of bookmarking tasks, which is the extension of Shen and Prior's work on the i-Pot conceptual bookmark management systems [1].

3. User Study Trials

3.1. Test Conditions. Each participant (mean age 21.4 yrs, SD = 1.2) was rewarded with 1000 NT\$ (approx. 33 US\$) for their time. All the participants had previously qualified with intermediate certificate of General English Proficiency Test (GEPT) issued by the Language Training and Testing Center (LTTTC) in Taiwan. The computer used during the tests was running Windows XP SP3 with CPU Intel Pentium 4 (3.20 GHz) 1 GB Ram, using the Google Chrome browser.

3.2. User Study in 2D Prototype. There were a total of 26 students (13 males and 13 females) who took part in this study which was undertaken during 10–31 May, 2012. After a brief introduction and demonstration, the participants were asked to do a series of tasks including creating, deleting, naming a new pot, and changing the color and texture of a new pot (see Supplementary Material at <http://dx.doi.org/10.1155/2013/932586>). They were each given eight (English) websites to bookmark (creating a new leaf) into four specific headline categories, that is, work, social, travel, and health according to a controlled vocabulary protocol. At the end of the test, the participants were asked

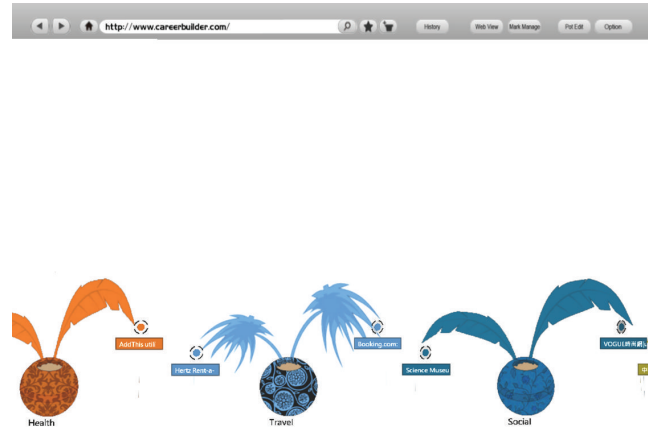


FIGURE 1: 2D i-Pot bookmark management interface.

to find a particular website from the History tree. The time taken for each user's performance was measured and graded on how well they accomplished the tasks. This was followed by a five-point Likert scale satisfaction questionnaire, and the participants were asked to provide their feedback on what they thought of the i-Pot 2D version and which elements they liked most and liked least about the interface and give their reasons for this. Further questions included the user's acceptance of the web browser and participants were asked to provide further suggestions on changes to the design of the 2D i-Pot (see Figure 1).

3.2.1. Results. The mean task time for male participants to complete the test was 191.4 s (SD = 28.5), whilst the mean task time for females was 229.3 s (SD = 57.5). The vast majority of the participants (92%) agreed that the concept of gardening was familiar to them and the information displayed was in a natural and logical order. Most of the participants (88%) thought that the visual icons and layout fitted appropriately to the gardening context, which allowed users to adapt frequent actions and to speed up the interaction. There were 81% of the participants who thought that the visual icons and layout contained relevant information and that the overall design was attractive. The majority of the participants (92%) agreed that the pots, plants, and leaves are logical representational equivalents for folders, files, and documents.

With regard to the functionality of the prototype, most of the participants (73%) found that it was easy to create or delete a new pot. Nevertheless, there was one participant who disagreed (4%) and six participants (23%) who were neutral. Most of the participants (73%) found that it was easy to name a pot. However, there were two participants who disagreed (8%) and five participants (19%) who were neutral. The majority of the participants (93%) considered that it was easy to change the color and texture of the pot. Almost all (96%) of the participants found that it was easy to add a new leaf, while there was one participant (4%) who disagreed. More than half of the participants (62%) thought that the use of the History tree was easy to view their history records,

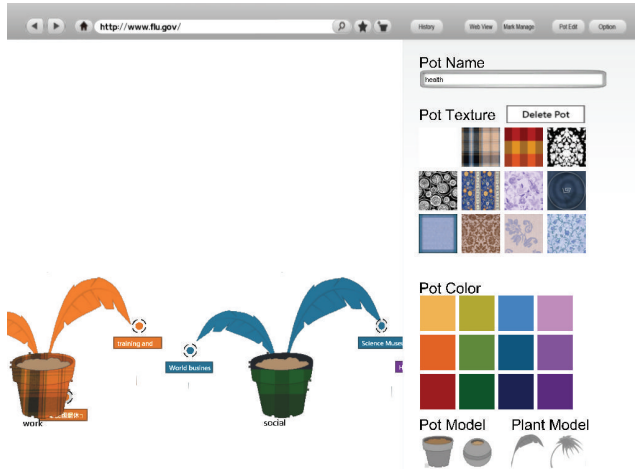


FIGURE 2: 2D i-Pot customizable control panel.

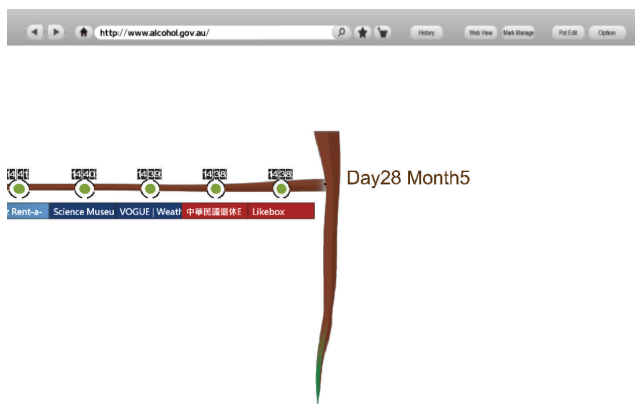


FIGURE 3: 2D History Tree.

whilst there were two participants (8%) who disagreed and eight participants (31%) who were neutral on this point.

3.2.2. Discussion. In general, the 2D i-Pot prototype had a high satisfaction rate. In terms of functionality, there was one participant who found that it was not easy to create or delete a new pot, whilst two participants thought it was not simple to name a pot. The reason for this might be that the function of creating and deleting actions required the user to click on certain buttons on the screen, rather than click on the right key from the mouse directly. The function of naming a pot required the effort of the user to go to the “Pot Edit” to type the name, compared to the existing bookmark management systems that allow the users to directly name/rename the folders or subfolders (see Figure 2). Furthermore, there were two participants who found that it was not easy to view their history records. This could be explained by the fact that the visualization of the History tree was new to them, rather than the traditional lineal lists (see Figure 3).

Most of the participants liked the concept of gardening with its 2D horizontal screen mobility, the selection of different pot styles, plant shapes, colours, and textures, because of

its novelty, visual presentation of realization, and the sense of freedom to customize the elements. Few participants disliked the limitation of 2D horizontal viewing angle, because the limited screen could only show two or three pots, rather than the whole pot collection. The majority of the participants would consider using the beta version of i-Pot web browser, if it was made available. The reasons included the use of multiple colours and textures that allowed the users to distinguish between their bookmarks, the fun visual look, and the novelty factor.

Further suggestions related mostly to technical issues, which included improving the Internet connection speed, adding a blue status bar when linking to the Internet websites, and attaching a background of the screen that makes it more like a real garden setting. Other suggestions involved the adjustment of the web view proportion into a full screen; adjust the My Favorite with pull-down menus, and add more selections of pot styles, plant shapes, colours and textures.

3.3. User Study in 3D Prototype. The same group of 26 students (13 males and 13 females) that took part in the first study also took part in this study which was undertaken in the computer lab during 10–31 May, 2012. After a brief introduction and demonstration, the participants were asked to do a series of tasks including creating, deleting, naming a pot, and changing the colour and texture of a pot (see Supplementary Material). They were each given eight (English) websites to bookmark into four specific headline categories, that is, work, social, travel, and health according to the controlled variable theory. At the end of the test, the participants were asked to find a particular website from the History tree and review their History tree. The time of each user’s performance was measured and graded on how well they accomplished the tasks. This was followed by a five-point Likert scale satisfaction questionnaire, and the participants were asked to provide their feedback on what they thought of the i-Pot 3D version, which elements they liked most, and which they liked least about the interface, and explain the reasons for this. Other questions included the user’s acceptance of this interface, if the web browser based on the Garden Metaphor was made available to them and further suggestions on changing the design of the 3D i-Pot based on the Garden Metaphor.

3.3.1. Results. The average task time for the male participants was 257.5 s (SD = 83.5), whilst the average task time for females was 235.7 s (SD = 58.5). Most of the participants (88%) agreed that the concept of gardening was familiar to them and that the information display was in a natural and logical order. The vast majority of the participants (92%) regarded the visual icons and layout fitted appropriately to the gardening context, which allowed users to adopt frequent actions and speed up the interaction. There were 81% of the participants who thought that the visual icons and layout contained relevant information and the overall design is pleasant. However, there were five participants (19%) who remained neutral on this point. The majority of the participants (96%) agreed that the pots, plants, and leaves

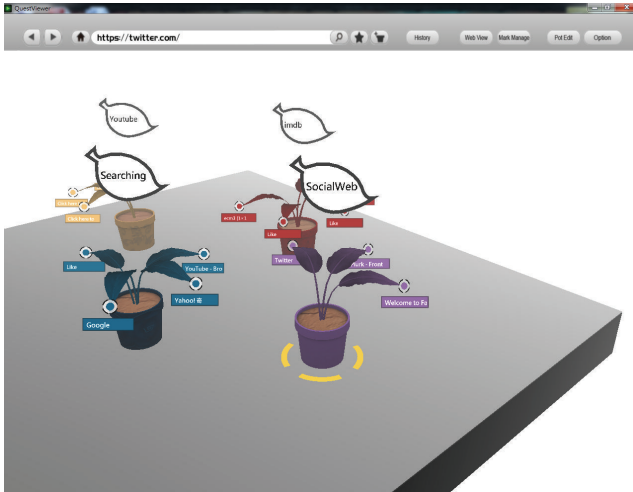


FIGURE 4: 3D i-Pot bookmark management interface.

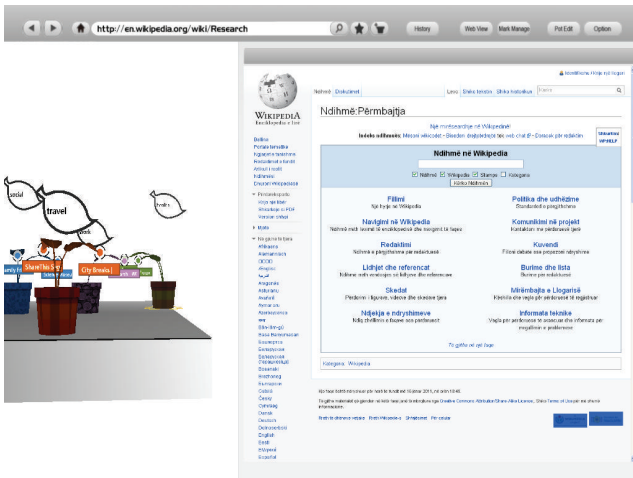


FIGURE 5: 3D i-Pot browsing window split screen.

are logical representational equivalents for folders, files, and documents.

With regard to the functionality of the prototype, more than half of the participants (58%) found that it is easy to create or delete a new pot. Nevertheless, there were eleven participants who remained neutral (42%). Most of the participants (73%) thought that it is easy to name a pot. However, there were two participants who disagreed (8%) and five participants (19%) who were neutral. The majority of the participant (93%) considered that it is easy to change the colour and texture of the pot. There were 73% of the participants who found that it is easy to add a new leaf, while there was one participant (4%) who disagreed. Most of the participants (73%) thought that the use of History tree is easy to view their history records, whilst there was one participant (4%) who disagreed and six participants (23%) who were neutral.

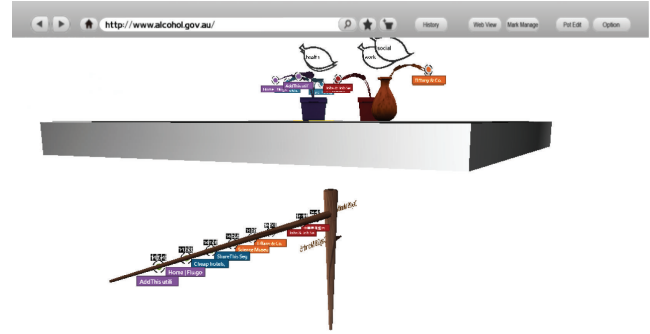


FIGURE 6: 3D History tree.

3.3.2. Discussion. In general, the 3D i-Pot prototype had a high satisfaction rate. In terms of functionality, there were two participants who thought that it was not easy to name a pot. The reason for this might be that the function of naming a pot had required the effort of the user to go to “Pot Edit” to type the name, compared to the existing bookmark management systems that allow the users to directly name/rename the folders or subfolders. Furthermore, there was one participant who found that it was not easy to view their history records. This could be explained by the fact that the visualization of the History tree was new to them, rather than the traditional lineal lists (see Figure 6).

Most of the participants liked the concept of gardening with its 3D easy to manipulate multiple angles (see Figure 4), intuitive spatial management (see Figure 5), the selection of choosing different pot style, colour, and texture, because of its novelty, visual presentation of realization, and the sense of freedom to customize the elements. A few participants disliked the 3D prototype due to the fact that they thought it required a great effort to organize their bookmarks, especially when there was more than twenty pots. The majority of the participants would consider use beta version of i-Pot web browser if it was made available. The reasons included the use of multiple colours and textures that allow the users to locate their bookmarks, the fun visual look, and novel features.

Further suggestions were mostly technical in nature and including improving Internet connection speed, adding a blue status bar when linking to the Internet websites, and attaching a background of the screen that makes it more like a real garden setting such as sky and pebble grounds. Others were the adjustment of the Web View proportion into a full screen, My Favorite with pull-down menus, and more wide selections of pot styles, plant shapes, colour, and texture.

3.4. Overall Summary. The purpose of this study was mainly to observe the participants’ capability to adapt to a new visually oriented bookmark management system, and to see how they migrate and manipulate the elements on the screen, based on their experiential cognitive association knowledge. Even though the researchers did not constrain time, they made sure that each participant had successfully completed the task before the end of the session.

Analysis of the overall results shows some interesting findings as follows (see Figure 7).

TABLE 1: Results of ANOVA statistical analysis.

Source of variation	Sum of squares	d.f.	Mean squares	F
Between	2.9515E + 04	3	9838	2.711
Error	1.7421E + 05	48	3629	
Total	2.0373E + 05	51		

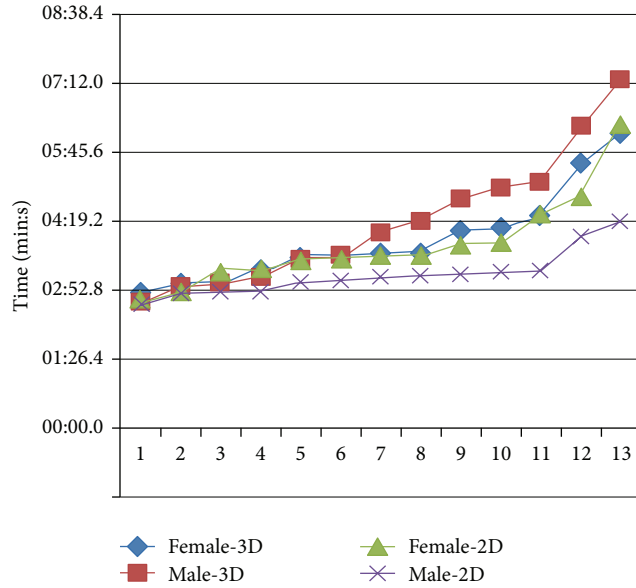


FIGURE 7: Task time analyses for gender and spatial context.

- (1) Males performed the fastest overall in the 2D tasks.
- (2) Males performed the slowest overall in the 3D tasks.
- (3) Females performed broadly the same in both the 2D and 3D tasks.

Figure 8 shows a box plot of the task time performance experimental data across the four subject groups (gender \times spatial context).

3.4.1. One-Way ANOVA Analysis of Task Times. We analyzed the task times of the subjects using a one-way ANOVA test (Table 1); this was conducted using four groups ($Gp = 4$):

- A: female (3D),
- B: male (3D),
- C: female (2D),
- D: male (2D).

Each group consisted of 13 time data points ($N = 13$). The null hypothesis, denoted by H_0 , for the overall F -test for this experiment would be that all four levels of the factor produce the same response, on average. Therefore, there would be no significant difference between gender or the 2D or 3D environments.

The probability of this result, assuming the null hypothesis, is 0.055. In this case, $F_{crit}(3, 48) = 2.8$ at $\alpha = 0.05$. Since $F = 2.711 < 2.80$, the results are on the borderline of

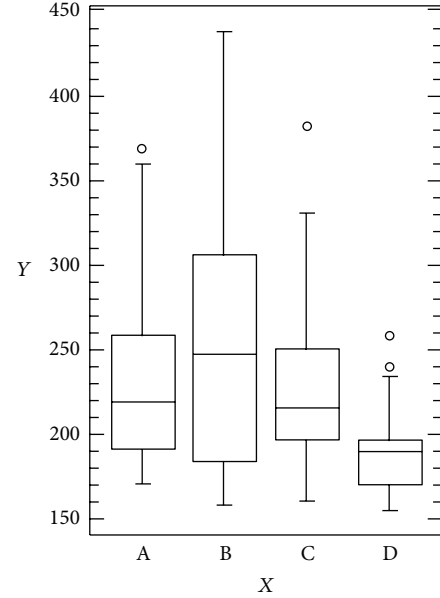
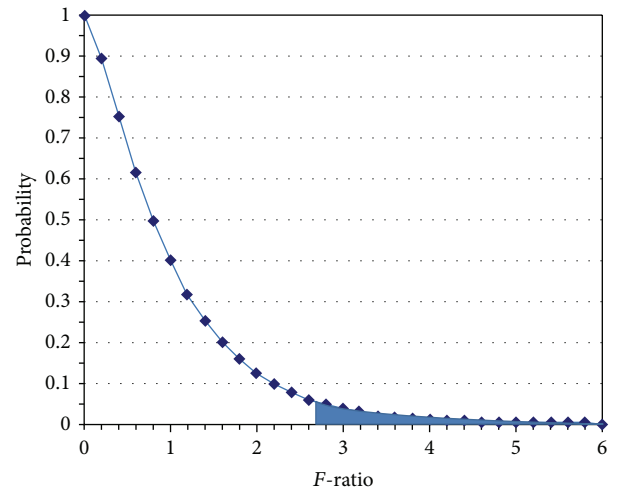


FIGURE 8: Box plot of task time experimental data.

FIGURE 9: F -distribution graph.

significance at the 5% level. One would marginally accept the null hypothesis, concluding that there is evidence that the expected values in the four groups differ and exist on the borderline of statistical significance as can be seen in Figure 9.

3.4.2. User Preferences. When asked about preferences for either the 2D or 3D environment again, the results highlighted some interesting findings as follows.

- (1) The vast majority of males (85%) say that they prefer the 3D environment.
- (2) The majority of females (62%) say that they prefer the 2D environment.

So although most of the male participants say that they preferred using the 3D environment, they were actually much

faster when using the 2D environment. They were even faster than the female participants in this context. The reason to explain this might be that most of the male participants (age 20-21) are the regular 3D game players. Therefore, they tend to prefer 3D rather than 2D unconsciously.

The females on the other hand seem to recognize the benefit of simplicity that the 2D environment gives. Overall, the 2D tasks were completed on average 81 s faster than the 3D tasks across both genders.

Several technical problems were identified such as direct manipulation in pointing and clicking on the specific objects which were not properly been selected both for the 2D and 3D prototype and the overlapping pots on the same location which occur unexpectedly when adding a new pot in 3D. These issues would be rectified in the next stage of the development.

4. Conclusion

This study extends previous work by the authors, demonstrating benefits of the Garden Metaphor when participants performed a series of bookmark management tasks requiring direct manipulations of objects in both the 2D and 3D prototype interfaces.

The i-Pot conceptual prototype aims to provide a personalized organization and bookmark management system. The notion of bookmarks is extended by introducing the concepts and functionality of gardening, such as browsing view, navigation, selection of colors and textures, the plant species, and history tree records.

In general, participants performed faster and with a much reduced standard deviation in the 2D tasks as opposed to the 3D tasks. This finding agreed with previous research as mentioned above [21, 24–26]. It is suggested that this may be due to the familiarity of the users' daily interaction with 2D applications, even with 3D applications such as games, AutoCAD and 3DMax that still rely on 2D direct manipulation of the WIMP.

Results of the testing showed that the male participants performed poorly in the 3D environment, as opposed to the 2D environment, even though they stated that they preferred the 3D environment. This might be due to incongruence between the spatial mapping capability and their presubjective perception. In contrast, 62% of the female participants preferred the 2D environment. However, there was no significant difference between the 2D and 3D tasks in terms of their time taken. This suggests that the female participants' cognitive ability was found not to be influenced between the 2D and 3D context. This may suggest that the female participants maintained the consistency of their task performance strategy and were not subject to the change of spatial dimension.

It may be argued that this does not represent the whole target users, based on such a small sample of participants. However, it is worth noting that these participants all major in multimedia design, a course which demands a highly skillful ability in both 2D and 3D relevant software. Therefore, even

though this was a small sample of users, it still represents valuable data on the subject of user interaction.

Although the null hypothesis was not disproved, the task time results showed a degree of significance in terms of gender and spatial context differences, which requires further investigation. This research indicates a promising and useful application of integrating novel bookmark management systems together with the Garden Metaphor. Many features provided by the i-Pot concept demonstrate creative human computer interaction and rich functionalities.

4.1. Further Work. As stated above, it is intended to further investigate the gender issues raised in this paper. In order to achieve an answer to the central hypothesis (users performance and preference of 2D and 3D interfaces), we plan to involve a larger group of participants. We anticipate that a group size of 100–200 participants would suffice for this purpose.

References

- [1] S. Shen and S. D. Prior, "A fresh look at graphical web browser revisitiation using an organic bookmark management system," in *Cognitively Informed Intelligent Interfaces: Systems Design and Development*, E. M. Alkhalifa and K. Gaid, Eds., pp. 41–55, Information Science Reference IGI Global, Hershey, Pa, USA, 2012.
- [2] W.-S. Li, Q. Vu, D. Agrawal, Y. Hara, and H. Takano, "Power-Bookmarks: a system for personalizable web information organization, sharing, and management," *Computer Networks*, vol. 31, no. 11–16, pp. 1375–1389, 1999.
- [3] Wikipedia, "Bookmark (World Wide Web)," 2012, [http://en.wikipedia.org/wiki/Bookmark_\(World_Wide_Web\)](http://en.wikipedia.org/wiki/Bookmark_(World_Wide_Web)).
- [4] J. Fitzpatrick, "Five best bookmark management tools," 2010, <http://lifelife.com/5540019/five-best-bookmark-management-tools>.
- [5] R. Pircher, "Personal knowledge management: individual, organizational and social perspectives," *Library Review*, vol. 61, no. 2, pp. 165–167, 2012.
- [6] S.-T. Shen and S. D. Prior, "Re-thinking bookmark management—less choice is more efficient," in *Design, User Experience, and Usability: Web, Mobile, and Product Design*, vol. 8015 of *Lecture Notes in Computer Science*, pp. 304–312, Springer, Berlin, Germany, 2013.
- [7] T. M. Skare and B. Bilinski, "System and method for managing bookmark buttons on a browser toolbar," US Patent 8,402,375, 2013.
- [8] E. T. Freeman, *The lifestreams software architecture [Ph.D. thesis]*, Yale University, New Haven, Conn, United States, 1997.
- [9] M. Ringel, E. Cutrell, S. Dumais, and E. Horvitz, "Milestones in time: the value of landmarks in retrieving information from personal stores," in *Proceedings of the 9th IFIP TC13 International Conference on Human Computer Interaction (INTERACT '03)*, IOS Press, Zürich, Switzerland, September 2003.
- [10] S. Ames, "LiFSBrowse: a visual, user environment for the linking file system," Storage Systems Research Center, Baskin School of Engineering, University of California, Santa Cruz, Calif, USA, 2007.
- [11] E. Grevstad, "Scopeware vision review bring clutter and chaos (and maybe your PC) to their knees," 2003, <http://www.small->

- businesscomputing.com/biztools/article.php/2193081/Scopeware-Vision-Review.htm.
- [12] Scopeware and Mirror Worlds Technologies, 2004, <http://web.archive.org/web/20040607060111/>, <http://www.scopeware.com/>.
- [13] Inxight, "Inxight VizServer," Inxight Software Inc, 2006.
- [14] S. K. Card, G. G. Robertson, and W. York, "The WebBook and the Web Forager: an information workspace for the World-Wide Web," in *Proceedings of the SIGCHI Conference on Human Factors in Computing Systems (CHI '96)*, pp. 111–117, ACM, Vancouver, Canada, April 1996.
- [15] G. Robertson, M. Czerwinski, K. Larson, D. C. Robbins, D. Thiel, and M. van Dantzich, "Data mountain: using spatial memory for document management," in *Proceedings of the 11th Annual ACM Symposium on User Interface Software and Technology (UIST '98)*, pp. 153–162, ACM Press, San Francisco, Calif, USA, November 1998.
- [16] G. Robertson, J. D. Mackinlay, and S. K. Card, "Cone trees: animated 3D visualizations of hierarchical information," in *Proceedings of the ACM Conference on Human Factors in Computing Systems (CHI '91)*, ACM Press, New Orleans, La, USA, 1991.
- [17] A. Agarwala and R. Balakrishnan, "Keepin' it real: pushing the desktop metaphor with physics, piles and the pen," in *Proceedings of the SIGCHI Conference on Human Factors in Computing Systems (CHI '06)*, pp. 1283–1292, ACM, Montréal, Canada, April 2006.
- [18] E. Levy, J. Zacks, B. Tversky, and D. Schiano, "Gratuitous graphics? putting preferences in perspective," in *Proceedings of the SIGCHI Conference on Human Factors in Computing Systems (CHI '96)*, pp. 42–49, ACM, Vancouver, Canada, April 1996.
- [19] C. Ware and G. Franck, "Evaluating stereo and motion cues for visualizing information nets in three dimensions," *ACM Transaction on Graphics*, vol. 15, no. 2, pp. 121–139, 1996.
- [20] A. Cockburn and B. McKenzie, "3D or not 3D? evaluating the effect of the third dimension in a document management system," in *Proceedings of the SIGCHI Conference on Human Factors in Computing Systems (CHI '01)*, ACM, Seattle, Wash, USA, 2001.
- [21] A. A. Ozok and A. Komlodi, "Better in 3D? an empirical investigation of user satisfaction and preferences concerning two-dimensional and three-dimensional product representations in business-to-consumer e-commerce," *International Journal of Human-Computer Interaction*, vol. 25, no. 4, pp. 243–281, 2009.
- [22] S. J. Westerman, "A comparison of the cognitive demands of navigating two-versus three-dimensional spatial database layouts," *Ergonomics*, vol. 41, no. 2, pp. 207–212, 1998.
- [23] M. M. Sebrecths, J. V. Cugini, S. J. Laskowski, J. Vasilakis, and M. S. Miller, "Visualization of search results: a comparative evaluation of text, 2D, and 3D interfaces," in *Proceedings of the 22nd Annual International ACM SIGIR Conference on Research and Development in Information Retrieval (SIGIR '99)*, ACM, Berkeley, Calif, USA, August 1999.
- [24] A. Leuski and J. Allen, "Improving interactive retrieval by combining ranked lists and clustering," in *Proceedings of the 6th International Conference on Computer-Assisted Information Retrieval (RIA0 '00)*, ACM, Paris, France, April 2000.
- [25] I. Barshi and A. F. Healy, "The effects of mental representation on performance in a navigation task," *Memory and Cognition*, vol. 30, no. 8, pp. 1189–1203, 2002.
- [26] S. J. Westerman, J. Collins, and T. Cribbin, "Browsing a document collection represented in two- and three-dimensional virtual information space," *International Journal of Human Computer Studies*, vol. 62, no. 6, pp. 713–736, 2005.

Research Article

An Extensive QFD and Evaluation Procedure for Innovative Design

Chang-Tzuoh Wu,¹ Tien-Szu Pan,² Ming-Hui Shao,³ and Chang-Shiann Wu⁴

¹ Department of Industrial Design, National Kaohsiung Normal University, No. 62, Shenjhong Road, Yanchao District, Kaohsiung City 82446, Taiwan

² Department of Electronic Engineering, National Kaohsiung University of Applied Science, 415 Chien Kung Road, Sanmin District, Kaohsiung 80778, Taiwan

³ Department of Industrial Design, National Cheng Kung University, No. 1, University Road, Huwei Township, Tainan City 701, Taiwan

⁴ Department of Information Management, National Formosa University, No. 64, Wunhua Road, Huwei Township, Yunlin County 632, Taiwan

Correspondence should be addressed to Chang-Tzuoh Wu; ctwu@nknucc.nknu.edu.tw

Received 15 September 2013; Accepted 21 October 2013

Academic Editor: Teen-Hang Meen

Copyright © 2013 Chang-Tzuoh Wu et al. This is an open access article distributed under the Creative Commons Attribution License, which permits unrestricted use, distribution, and reproduction in any medium, provided the original work is properly cited.

In this paper, a systematic innovation procedure has been developed based on quality function deployment and extension method. Besides, the evaluation method for design decision making has also been discussed and developed. The major procedure of QFD is to identify the customers' needs for the product and then convert into appropriate technical measures to fulfill the needs based on the company's competitive priorities. The priorities of product characteristics can be obtained by translating important technical measures. According to their characteristics, the prior engineering parameters will be identified and selected as the key requirements to redesign. This paper will focus on the integration of QFD and extension method. With the help of "matter element theory and extension method," customer requirements (CRs) can be transferred into product design attributes more comprehensively and deeply. According to the idea of loss function of Taguchi quality design method, the criteria for design decision making have also been developed in this paper. An innovative design case, bicycle, successfully demonstrates that the proposed design process is feasible and efficient.

1. Introduction

A successful new product development should meet various customer demands. Hence, analyzing customer requirements (the voice of customers) and responding to their needs has now become an important and inevitable task for a company's product development team [1].

Quality function deployment (QFD) is an important quality control theory proposed by the Japanese quality control master Yoji Akao in 1966. It was Akao who first realized the value of this approach in 1969 and wanted to utilize its power during the product design stage so that the product design characteristics could be converted into precise

quality control points in the manufacturing quality control chart [2]. Sullivan, 1986 indicated that quality function deployment (QFD) provides a means of translating customer requirements into the appropriate technical requirements for each stage of product development [3, 4].

Delice and Cüngör, 2009 indicated that, in real world applications, the values of DRs are often discrete instead of continuous. A new QFD optimization approach combining MILP model and Kano model is suggested to acquire the optimized solution from a limited number of alternative DRs, the values of which can be discrete [1]. Garibay et al. (2010) proposed a tool which utilized a combination of the quality function Deployment (QFD)-Kano model to evaluate

service quality. Relevant information may be obtained about issues that should be improved in order to increase customer satisfaction by listening to the voice of the customer (VOC) [5].

Most of the associated researches provide valuable and valid methods to enhance the effect of QFD. Though these studies applied successfully the proposed methods to solve design problems, they focused on local perspective view only. This paper will concentrate on the creative thinking method, “matter element theory and extension method,” with the help of this method to assist in translating customer requirements (CRs) into engineering characteristics (ECs) more deeply and widely.

2. Innovative Design Method

2.1. Quality Function Deployment. QFD is a structured design tool and is defined as “a consumers’ needs oriented tool” which can be used to establish the relationship between customer attributes and design parameters to be quantified through the house of quality and customers’ cognition, finding key design factors in the product to determine the direction of product development and market positioning. As shown in Figure 1, the four-phase approach consists of product planning, part deployment, process planning, and production planning phases [6]. In essence, the product planning phase translates qualitative customer requirements into measurable engineering characteristics and identifies important engineering characteristics. The goal of product planning phase is to translate customer requirements (CRs) into engineering characteristics (ECs) and prioritize their importance. Therefore, the CRs must be acquired from market surveys or customer questionnaires. The acquired information can be used to calculate the relative importance of CRs, calculate the final importance of CRs, and identify the Ecs, so that the final importance of ECs will be calculated and the relationship matrix also be established.

2.2. Matter-Element Analysis and Extension Method. Cai, 1983 developed a powerful tool, matter-element and extension method, to systematically analyze concrete or intangible products. Extension theory is a course to study the extensibility, extent rules, and performing procedure of matter and try to resolve contradictive problems. Extension theory and method are the new science. Their application to the research on conceptual design of the products and innovative design is a new field. The extension method can help people resolve problems separately by decomposing and recombining the problems to search for the feasible solutions.

A matter element can be combined with the other matter elements to form a new one or be decomposed into a few new matter-elements; new matter elements contain qualities that former matter elements do not have. The extension of matter element provides another way of resolving contradiction. Matter element can be used to describe every matter in real world. We use an ordered triad

$$R(N, c, v). \quad (1)$$

The basic element for describing the matter N is called matter element, where N represents the matter; c is the characteristic name; v is N measure about c . Thus, $v = c(N)$.

The extensibility of matter element is the basis of dealing with incompatible problem. It includes divergence, expansibility, conjugate inside the matters, and relativity of matter element. Divergence is to study the possible routes of outward extension. It includes the same matter of matter element, the same characteristics of matter-element, the measure of matter element, the same matter and characteristics of matter element, the same characteristics and measure of matter element, and the same matter and measure of matter-element. Extensibility studies plausibility, integration, and separability of matter element [8, 9].

Replacement, decomposition, addition/deletion, and expansion/contraction are four basic methods for transformation of matter element and conducive to exchanging or to synthesizing different matter element. As shown in Figure 2, general model of extending tree constructed by matter element symbols expresses the divergence in simple way [10, 11].

Study of the internal structure of matter is contributive to solving contradictive problems by using any element of matters. Systems theory, a description of structures of matters, is a science to study matters from system components and internal-external relationships. Through the analysis of a large number of matters, we found that the properties of substance, dynamic, and opposition can also be the research topics of the structure of matters in addition to systemic property. A matter consists of the tangible part and intangible part of substance, both of which should also be considered. As for the dynamic properties, matter has the significant part and potential part. Such as the development of the disease, it generally includes the incubation period and the exacerbation period.

The structure of matter can be described more completely and the nature of variation of the development of matters can also be revealed more deeply while we explore the matter from the point of view of systemic, substance, dynamic, and opposition [7, 12]. Therefore, we proposed the corresponding four pairs of opposing concepts such as real/imaginary, soft/hard, potential/significant, and positive/negative to describe the composition of matters called conjugate of matters.

3. Extensible QFD

Customer needs orientation is the principal spirit of QFD. The conversion between functional quality and engineering design parameters is the important creativity thinking course for the fulfillment of the customer needs oriented innovative design.

The major procedure of QFD is to identify the customers’ needs for the product and then convert into appropriate technical measures to fulfill the needs based on the company’s competitive priorities. The priorities of product characteristics can be obtained by translating important technical measures. According to their characteristics, the prior engineering

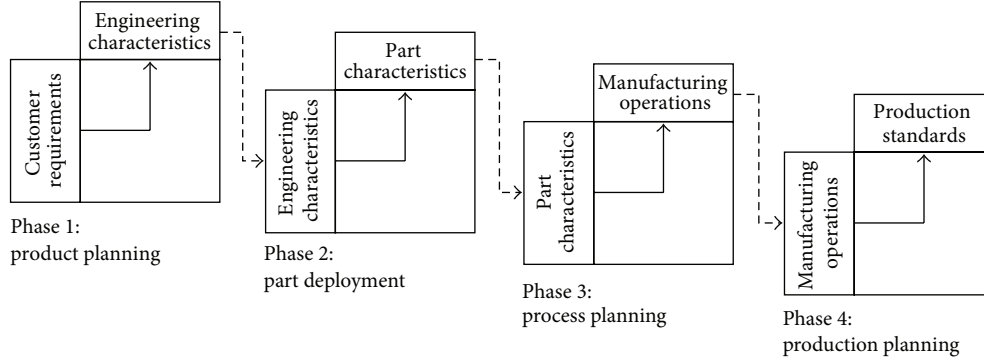


FIGURE 1: Four-phase approach of QFD [7].

parameters will be identified and selected as the key requirements to redesign. Throughout the procedure, the creativity activities with matter-element theory and extension method can be imported or expanded mainly in two parts:

- (1) translating customers' needs into product design attributes (technical measures),
- (2) identifying the corresponding product defect or the parameters needed to be improved.

The use of extensibility of matter element and extension method for the translation of product design attributes and engineering properties can provide effective assistance for the designer to conceive new products comprehensively and deeply. In this research, we will discuss the procedure for improving design attributes by the aids of extensibility of matter element and extension method.

Matter element and matter element with multicharacteristics are defined as follows.

Matter element

$$R = (N(t), c, v(t)), \quad (2)$$

matter element with multicharacteristics

$$R(t) = \begin{bmatrix} N(t) & c_1 & v_1(t) \\ & c_2 & v_2(t) \\ & \vdots & \vdots \\ & c_n & v_n(t) \end{bmatrix} = (N(t), C, V(t)). \quad (3)$$

Based on the divergence of matter element, matter element $R_0(N_0, c_0, v_0)$ can be diverged from one or two of N_0, c_0, v_0 to synthesize different matter elements and build an extending tree. Extending tree, part of rhombus thinking model, is a method for matter to extend outwards to provide multiorientated, organizational and structural considerations, as operating in Figure 2. An event is the interaction of matters and described as event element. Basic elements for describing an event element are constructed by verb (d), name of verb characteristic (b) and u , the corresponding measure about (b).

Event element:

$$I(t) = (d(t), b, u(t)). \quad (4)$$

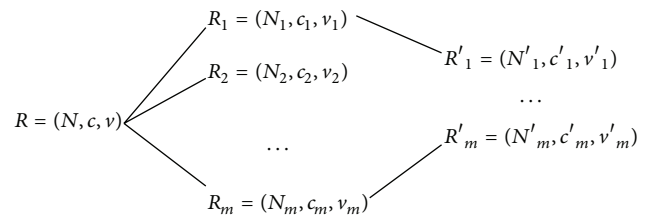


FIGURE 2: Rhombus thinking model.

Multidimensional event element:

$$I(t) = (d(t), B, U(t)). \quad (5)$$

Relationship element is formed by relationship name $s(t)$, characteristics a_1, a_2, \dots, a_n , and corresponding measure values $w_1(t), w_2(t), \dots, w_n(t)$:

$$Q(t) = \begin{bmatrix} S(t) & a_1 & w_1(t) \\ & a_2 & w_2(t) \\ & \vdots & \vdots \\ & a_n & w_n(t) \end{bmatrix} = (S(t), A, W(t)). \quad (6)$$

While solving design problems, diversity, and creativity, the advantages of "extenics" method will be imported by implementing the extensibility of matter element, event element and relationship element. Thus, the solution will not be limited to standard solutions but will be inspired.

3.1. Procedure for Engineering Design Parameters Transformation. Throughout the procedure of QFD, the extensibility of matter element and extension method can be used to assist in translating product functional requirements into engineering design parameters. The following are the steps of creative activities, thus matter element which matter element theory and extension method can be imported or expanded.

Step 1. Define the n -dimensional matter element of product.

Step 2. Determine the m -dimensional requirements matter element.

The m -dimensional characteristics of requirements matter element can be formed by the attributes derived from customers' voices.

Step 3. Determine the functional characteristics set.

Determine the set of functional characteristics of product requirements based on m -dimensional requirements matter element. The corresponding values of the functional characteristic elements should also be determined as the following equation:

$$\begin{aligned} \{c_{\text{function}}\} &= \{c_f\} \\ &= \{(c_f, v_f)\}. \end{aligned} \quad (7)$$

Step 4. Confirm the "hypostatic characteristics."

List all the associated properties of characteristics which can improve the required functions. No matter what, the apparent properties or latent properties will all be considered comprehensively. Thus, the implicit properties for the requirements can be obtained. According to the implicit properties, the "hypostatic characteristics" for the requirements will be derived and confirmed.

Step 5. Solve design problems by using conjugate properties and transformation operation of the elements of "hypostatic characteristics."

According to the requirements of potential function of product, we modify the concepts of design through transformation processes, and thus the new product N possesses the required potential function. Besides, considering the negative value of functional part of product N , negative part of N $ng(c)N$, and the concept can be modified by transform operation to reduce negative effects.

Step 6. Repeat the above processes to achieve a number of programs of product N to develop and expand the concepts of product.

Use basic transformations on the matter element and the transform operation to achieve a variety of new product ideas. The Following is the operation:

$$TR = \prod_{i=1}^n (T_i R_i) = \prod_{i=1}^n \prod_{j=1}^m (T_{ij} R_{ij}). \quad (8)$$

4. Design Evaluation

By using the extensive properties of matter element, many concept design solutions can be obtained. These possible solutions should be checked or evaluated, to filter out as the optimal solutions. Rhombus thinking model is the core method while proceeding optimal innovative design. As shown in Figure 2, "rhombus thinking" is a creative thinking method which diverges first and converges later. The convergent part of Rhombus thinking model is the procedure of evaluation for decision making.

Wang and Zhao, 1998 indicated that "authenticity message discriminant method" and "fuzzy convergence" are feasible extensive decision-making methods. In this paper, an evaluation method has been developed based on HOQ of QFD and Robust design methods [9]. In HOQ, ECs are a list of relevant design characteristics. The absolute importance of ECs can be computed by integrating both the final importance of CRs and the relationship matrix. The corresponding weighting coefficients can be determined based on the weighting values of absolute importance of ECs.

Let $S = \{S_1, S_2, \dots, S_n\}$ be the feasible design solution obtained by extensive innovation, and the corresponding evaluation indices are defined as characteristic set $C = \{C_1, C_2, \dots, C_n\}$; the following is the matter-element model for feasible solutions:

$$R_i = (S_i, C, V_i) = \begin{bmatrix} S_i & C_1 & V_{i1} \\ & C_2 & V_{i2} \\ & \vdots & \vdots \\ & C_n & V_{in} \end{bmatrix} \quad (i = 1, 2, \dots, n), \quad (9)$$

where $V_i = \{V_{i1}, V_{i2}, \dots, V_{in}\}$ are the corresponding values of indices $C = \{C_1, C_2, \dots, C_n\}$ which are determined by experts referring to the feasible solutions. Let the ideal design proposal given by experts express as

$$R^* = (S^*, C, V) = \begin{bmatrix} S^* & C_1 & V_1 \\ & C_2 & V_2 \\ & \vdots & \vdots \\ & C_n & V_n \end{bmatrix}, \quad (10)$$

where $V_j = (V^* - \delta_j, V^* + \delta_j)$ are the value intervals referring to indices C_j .

Based on the definition of loss function of Taguchi method, three characteristics are used to define the criteria of evaluation. The proposed criteria are "nominal-the-best," "smaller-the-better," and "larger-the-better". The following is the definition of dependent function for each required criteria.

- (a) *Nominal-the-Best.* As V^* is the value corresponding to characteristic of ideal design, the dependent function of criteria for "nominal-the-best" can be defined as

$$K(V_j) = \begin{cases} \ln \frac{\delta_j}{|V_j - V^*|} & V^* - \delta_j \leq V_j \leq V^* + \delta_j \\ 0 & \text{others.} \end{cases} \quad (11)$$

- (b) *Smaller-the-Better.* The dependent function of criteria for "smaller-the-better" can be defined as

$$K(V_j) = \ln \frac{\text{Max } V_j - \text{Min } V_j}{V^* - \text{Min } V_j}. \quad (12)$$

- (c) *Larger-the-Better.* The associated dependent function of criteria is defined as

$$K(V_j) = \ln \frac{\text{Max } V_j - \text{Min } V_j}{\text{Max } V_j - V^*}. \quad (13)$$

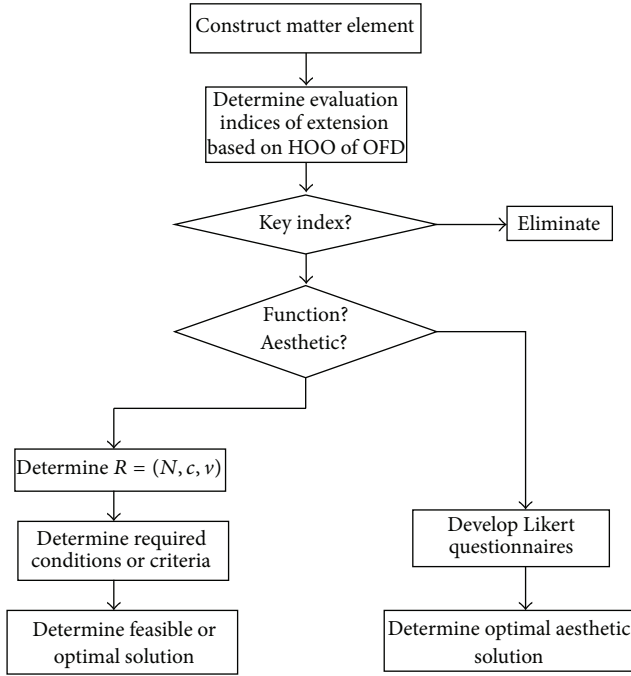


FIGURE 3: Flowchart of evaluation.

The dependent degree between proposed design and ideal design can be calculated by the formula presented above. The flowchart of comprehensive evaluation for the proposed extensive innovation procedure has been presented in Figure 3. There are no explicit formulae for certain characteristics to be evaluated. Aesthetic is the typical characteristic which cannot be evaluated by certain formula. A psychometric scale, Likert scale, is a common suggestion that employs questionnaires to scoring and analyzing the characteristic. Respondents assign their level of agreement or disagreement on a symmetric agree-disagree scale for a series of statements while responding to a Likert questionnaire item. Therefore,

the range catches the intensity of their feelings for a given item. Over the entire range of the scale, a scale can be defined as the simple sum questionnaire responses. Thus, in this research, we suggest that the dependent function for characteristics refers to uncertain scales can be defined as the sum of Likert questionnaire responses.

5. Illustrative Design Case

In this research, design case “bicycle”, the most favorite exercise equipment and transported is adapted to explain and verify feasibility of the proposed innovative procedure. The proposed approach, QFD integrated with extension method, has been used to investigate the users’ needs and relative functional requirements. In the creative course, we make use of the extension method to improve product design attributes and to determine the associated engineering design parameters. The creative solution programs based on customers’ voice will thus be achieved.

5.1. Extensive Processes. Two parts are in this stage of research. First, obtain the needs of bicycle by interviewing the elderly and translate them into product design attributes, and then in the second part, the questionnaire checks for the elderly to pick the important requirements.

In this study, survey candidates are the cycling sport amateurs. In order to avoid some important problems being ignored, the cyclists are included. Gathering respondents’ views and users’ requirements are sorted out as Table 1.

Use extending tree method to assist the establishment of HOO. First, we build the transformation model by extending tree: a matter refers to multicharacteristics; a characteristic is also mapped by matters. Thus, “one matter with multicharacteristics”, “one characteristic maps to multimatters”, “one value maps to multimatters”, “one matter, one value versus multicharacteristics”, “one matter, one characteristic versus multivalues” are the extending propositions of matter element to resolve contradiction.

$$\begin{aligned}
 R_1 &= \left[\begin{array}{c|c} \text{Overall riding comfortable} & \begin{array}{l} \text{comfortable grip} \\ \text{anti-shock} \\ \text{comfortable saddle} \\ \text{ventilatory saddle} \end{array} \\ \cdot & \\ \cdot & \\ \cdot & \end{array} \right] \\
 R_2 &= \left[\begin{array}{c|c} \text{Portability operating} & \begin{array}{l} \text{Light weight} \\ \text{Breaking effort} \\ \text{Operate derailleur smoothly} \\ \text{Chain-link come off the ratchet} \\ \text{and slip gears} \end{array} \\ \text{experience} & \\ \cdot & \\ \cdot & \\ \cdot & \end{array} \right] \\
 R_3 &= \left[\begin{array}{c|c} \text{Flexible adjustment} & \begin{array}{l} \text{Easy to adjust seat post} \\ \text{Quick detach} \end{array} \end{array} \right],
 \end{aligned} \tag{14}$$

and so forth.

We can translate product functional requirements into product design attributes as shown in Table 2.

We derive and confirm the “hypostatic characteristics” from “functional characteristics” and then the corresponding “certain characteristics” will also be derived and confirmed.

TABLE 1: Requirements of bicycle for the sport amateurs.

Portability operating experience
Overall riding comfortable
Cost/price
Flexibility to adjust
Sturdy and durable
Additional functions
Attractive appearance

Then, we use the corresponding four pairs of transformation methods to describe the composition of matters and assist the transformation and extension of matter-elements. For the iso-matter-element, we can use replacement, addition/deletion, expansion/contraction but for the distinct matter-element the applicable methods are addition/deletion, expansion/contraction transformation.

Take the design attributes, (ergonomic, handling, and convenient to pump up tires) and (ergonomic, comfort, and stability of tire pressure), for example. One of the Customers' complaints is that low tire pressure will result in large resistance riding; however, the high tire pressure can easily lead to a puncture or unstable riding. Customers' complaint pointed out that tire pressure seriously affects traffic safety. How to maintain the stability of tire pressure is a noteworthy design problem.

The extension of relationship element of pumping is

$$Q = \begin{bmatrix} \text{Pumping} & \text{Perform type} & \text{Hand pressed} \\ & \text{Air compressed type} & \text{Reciprocating} \\ & \text{Tire type} & \text{Air tire} \\ & \text{Tire pressure control} & \text{No} \\ & & \dots \\ & \vdots & \vdots \end{bmatrix}$$

$$= (s, A, W).$$

(15)

First, we conclude that customers' demands for bicycle tire are safety and comfort. Pumping device is expected to be light and handy. Stable tire pressure device, the customers' demand, indicates two needs "pressure compression" and "pressure relief." Therefore, autopumping system, the latent demand for customers, can be deduced by extensible QFD proposed in this paper.

We consider making the "autopumping device" play the major role of bicycle devices and then design problem becomes "how to pump air into tire during the riding process?" And "how to release pressure while overpumping?" This leads to new design problems based on the new concept. Repeat matter-element extending program and rhombus thinking procedure. Transform the pump device into a new general model by the divergence tree. Therefore, many ideas will be obtained. One of the obtained ideas is using shock absorbers in a suspension system. Shock absorbers usually

TABLE 2: Product design attributes.

Level 1	Level 2	Level 3
Basic function	Specifications	Simplify parts
		Design for assembly
		Weight
	Mechanism	Size
		Driving mechanism
		Breaking mechanism
		Derailleur mechanism
	Safety	Material of frame
		Maintenance
		Breaking performance
Ergonomic	Comfort	Structural strength
		Heat dissipation of saddle
		Suspension performance
		Body dimensions
		Stability of tire pressure
	Handling	Derailleur maneuverability
		Flexible adjustment
		Brake system
		Convenient to pump up tires

consists of two parts: a spring and a damper. The shock absorbers can be redesigned to form the pumping device. The new device, autopumping device as shown in Figure 4, can meet the demand. Rotary compression pump which was placed in the rotary axis of tire is another design example. Therefore, many ideas can be obtained with the help of the extensive QFD. We propose changing the pumping procedure. Autopumping device will be the new design concept we proposed.

Another design case proposed is "wheelchair." We obtained the needs of wheelchair by interviewing the elderly in nursing home and the nurse aides with long experience. Users' requirements are sorted out as Table 3. Thus, "harmful side effects," one of the 39 engineer parameters of TRIZ is what we concerned. We take the "harmful side effects" as the matter-element. By processing the extensive QFD, we try to transform "harmful side effects" to "beneficial side effects." For the elderly, long time in a wheelchair leads to "poor blood circulation" which is one of the "harmful side effects." Thus, a series of cyclic-motion for pedal, such as wave-like motion or vibration type of paddle, seem to be the answer to avoid "poor blood circulation."

6. Conclusions

This study proposes an innovative design and problem-solving process, based on quality function deployment method integrated with extension of matter element. Customers' needs and the priorities of product characteristics can be identified by QFD. This paper proposed the procedure of extensible QFD to transform product functional requirements into engineering design parameters. With the help of

TABLE 3: Requirements of wheelchair for the elderly.

Operation to be effort
Comfortable
Easy to keep clean
Flexibility to adjust
Sturdy and durable
Convenience to get in (off) wheelchair
Additional functions

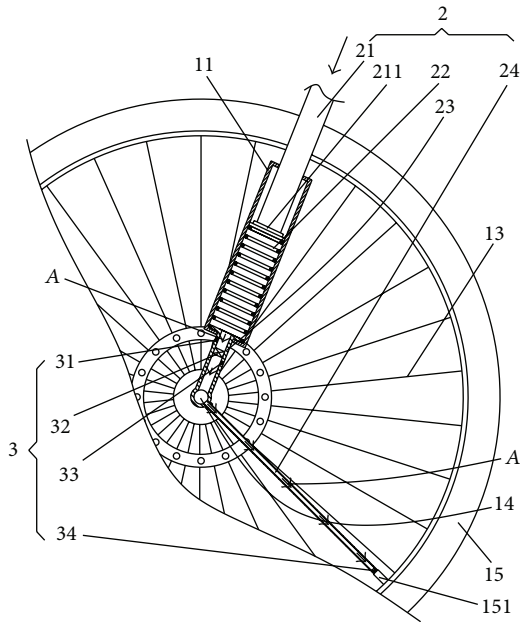


FIGURE 4: Autopumping device.

extension theory, the design proposals can be obtained more widely.

Besides, the evaluation dependent functions for design criteria based on the concepts of Taguchi method have also been proposed. As for the psychological characteristics, Likert questionnaire and scale are suggested to score and analyze such characteristics. Likert scale maybe just a simple measurement method. However, it can provide another way of design evaluation for psychological viewing. Kansei engineering, developed by Mitsuo Nagamachi, aims at the development or improvement of products and services by translating customer's psychological feelings and needs into product's design domain. The authors pay attention to Kansei engineering and hope. The authors pay attention to Kansei engineering and expect to develop another way for evaluation in the future can develop another way for evaluated in the future.

We assess the possibility and advantages to combine quality function deployment with the extension of matter elements. An innovative design case, bicycle, demonstrates the proposed design process. "Convenient to pump up tires" and "stability of tire pressure" are the customers' requirements obtained from the QFD process. By processing the extensible

QFD, autopumping system with overpressure relief device, the latent demand for customers has been deduced. The innovative concept design of "autopumping" demonstrated in this paper won the "IF award" in 2012.

Acknowledgment

This work is supported by the National Science Council, Taiwan, no. NSC 95-2221-E-017-006.

References

- [1] E. K. Delice and Z. Güngör, "A new mixed integer linear programming model for product development using quality function deployment," *Computers and Industrial Engineering*, vol. 57, no. 3, pp. 906–912, 2009.
- [2] A. Hill, "Quality function deployment," in *Gower Handbook of Quality Management*, D. Lock, Ed., chapter 21, pp. 364–386, Gower, Brookeld, Vt, USA, 2nd edition, 1994.
- [3] L. P. Sullivan, "Quality function deployment," *Quality Progress*, vol. 19, no. 6, pp. 39–50, 1986.
- [4] L. P. Sullivan, "The seven stages in company-wide quality control," *Quality Progress*, vol. 19, no. 5, pp. 77–83, 1986.
- [5] C. Garibay, H. Gutiérrez, and A. Figueroa, "Evaluation of a digital library by means of quality function deployment (QFD) and the Kano model," *Journal of Academic Librarianship*, vol. 36, no. 2, pp. 125–132, 2010.
- [6] W. Cai, C. Y. Yang, and W. C. Lin, *Extensive Engineering Method*, Science Press, Beijing, China, 1997.
- [7] Y. Akao, *Quality Function Deployment: Integrating Customer Requirements into Product Design*, Productivity Press, Cambridge, Mass, USA, 1990.
- [8] T. C. Kuo and W. Hsin-Hung, "Fuzzy eco-design product development by using quality function deployment," in *Proceedings of the 4th International Symposium on Environmentally Conscious Design and Inverse Manufacturing (Eco Design '05)*, pp. 422–429, Tokyo, Japan, December 2005.
- [9] W. L. Wang and Y. W. Zhao, "Explore the extensive decision-making of mechanical intelligent CAD," *System Engineering Theory and Practice*, vol. 18, no. 2, p. 114, 1998.
- [10] C. T. Wu, J. R. Chou, and C. S. Wu, "An extensive innovation procedure to quality function deployment for product design," in *Proceedings of the IEEE 19th International Conference on Industrial Engineering and Engineering Management*, pp. 688–692, 2012.
- [11] C. Y. Yang and B. He, "Application of extension method in new product concept," *System Engineering Theory and Practice*, vol. 19, no. 3, p. 120, 1999.
- [12] Y. C. Lee, L. C. Sheu, and Y. G. Tsou, "Quality function deployment implementation based on Fuzzy Kano model: an application in PLM system," *Computers and Industrial Engineering*, vol. 55, no. 1, pp. 48–63, 2008.

Research Article

Analyzing PSU's Performance: A Case from Ministry of Petroleum and Natural Gas of India

Chia-Nan Wang, Lei-Chuan Lin, and Dhanabalan Murugesan

Department of Industrial Engineering and Management, National Kaohsiung University of Applied Sciences (KUAS), Kaohsiung 80778, Taiwan

Correspondence should be addressed to Lei-Chuan Lin; leichuan@mail.mirdc.org.tw

Received 14 September 2013; Accepted 3 October 2013

Academic Editor: Teen-Hang Meen

Copyright © 2013 Chia-Nan Wang et al. This is an open access article distributed under the Creative Commons Attribution License, which permits unrestricted use, distribution, and reproduction in any medium, provided the original work is properly cited.

The high economic growth in the past few years and increasing industrialization coupled with a burgeoning population have created a lot of concern for India's energy scenario. India's crude oil production has not shown significant growth in the last 10 or more years whereas its refining capacity has grown by more than 20% over the last 5 years. Oil consumption is growing at approximately 4.1% per year and natural gas consumption is growing at 68% per year. Therefore, evaluation performances and pushing energy companies to improve become important issues. The purpose of this research is of evaluation the performance of Indian energy industry under multiple different inputs and outputs criteria. The data envelopment analysis (DEA) and grey theory are used to conduct this study. There are total 14 public sector undertakings (PSUs) under this industry and no any private company. However, only 10 of them are mature enough to be published in India stock markets. Therefore, the realistic data of all 10 companies are used for this evaluation. The results demonstrate that Gas Authority of India Limited (GAIL), Chennai Petroleum Corporation Limited (CPCL), and Oil India Limited (OIL) are the top 3 of ranking influences. This integrated numerical study gives a better "past-present-future" insights into evaluation performance in India energy industry.

1. Introduction

According to Vlasblom et al. [1], Indian economy is estimated to grow at 6.9 per cent in 2011-12 as compared to the growth rate of 8.4 per cent in 2010-11. These GDP figures are based on factor cost at constant (2004-5) prices in 2011-12. The growth rate of 6.9 per cent in GDP during 2011-12 has been due to the growth rates of over 8 per cent in the sectors of electricity, gas and water supply, trade, hotels, transport and communication, and financing, insurance, real estate, and business services.

Eichengreen and Tong [2] argue that in 2007 India's share of global output was only 2.2%. Furthermore, rapid trade growth in Asia has been supported by large investment flows. The fact that India has not made any major breakthrough in the field of renewable sources of energy, oil and, natural gas would continue to hold a place of key importance in India's economy.

van Ruijven and van Vuuren [3] said, "India has been growing at a decent rate annually and is committed to accelerating the growth momentum in the years to come. This would

translate into India's energy needs growing many times in the years to come. Hence, there is an emphasized need for wider and more intensive exploration for new finds, more efficient and effective recovery, a more rational and optimally balanced global price regime—against the rather wide upward fluctuations of recent times, and a spirit of equitable common benefit in global energy cooperation."

Performance evaluation is the important approach for enterprises to give incentive and restraint to their operators and it is also an important channel for enterprise stakeholders to get the performance information [4]. There has been numerous and successful research related to data envelopment analysis (DEA) and grey systems theory in various industries going on ranging from products to services and other important fields today. In this research, we will provide some insights after getting combined results of DEA and Grey Systems theory. Using DEA methodologies, we input some performance attributes and classify them as inputs and outputs and then use them for DEA researches. For ranking industries, we have used super SBM method and followed by

MPI for measuring the productivity indexes over the 5 year time frame from March 2008 to March 2012 (latest year).

The Ministry of Petroleum and Natural Gas initiated a new plan called New Exploration Licensing Policy (NELP). It provides an international class fiscal and contract framework for exploration and production of hydrocarbons. In the first seven rounds of NELP from 2000 to 2009, production sharing contracts (PSCs) for 203 exploration blocks have been signed. Under NELP, 70 oil and gas discoveries have been made by private/joint venture (JV) companies in 20 blocks.

The purposes of this study are to rank the companies of the petroleum and natural gas sector public sector undertakings (PSUs), Government of India using Data Envelopment Analysis (DEA) model known as "Slack-based super SMB, Output oriented, Variable returns to scale" by their efficiency score levels, performance score levels, efficiency changes, and productivity index changes over the last 5 consecutive period years (from 2008 to 2012) by means of DEA based MPI (Malmquist Productivity Index).

2. Literature Review

Lahiani et al. [5] mention that in modern era with the development of Indian economy and rapid expansion of trade, the small scale industrial sector has emerged as a vibrant and dynamic segment in the process of industrialization, which is considered not only as a key factor to lift up the per capita income but also as a vital mechanism for a larger transformation of Indian economy.

Nomikos and Pouliasis [6] made an article which tries to assess the utilization efficiency of capacity of Indian rubber industry in terms of econometric framework for the period 1979-80 to 2008-09. The result suggests that there has been declining growth rate of capacity utilization in rubber industry of India during the postreforms period accompanied by declining output growth as well as capacity growth.

Cooper et al. [7] expanded Farrell [8, 9] efficiency measurement concept of multiple inputs and single output to the concept of multiple inputs and multiple outputs, utilized linear combination to convert it to single virtual input and output, estimated efficiency frontier from the ratio of two linear combinations, and measured the relative efficiency of each DMU in CRS, which is between 0 and 1 and can determine whether a DMU is inconstant, increasing or decreasing returns to scale.

Lai and Wei [10] recently have developed a process, based on data envelopment analysis (DEA) to evaluate and rank the relative importance of key performance indices (KPIs). The relative importance of each KPI is evaluated by performance loss measure, and each KPI is weighted according to the measure. Then, the relative performance of each unit is the ratio of weighted output to weighted input based on the common weights.

The super SBM model is adopted by Lo and Lu [11] and they have argued the reasons for using super SMB models. According to them, in contrast to the CCR and BCC measures, which are based on the proportional reduction in input vectors or the increase in output vectors without taking slacks into account, the SBM deals directly with input excesses

and output shortfalls (slacks). The SBM reports an efficiency measure between 0 and 1 and gives an efficiency score of one if and only if the DMU concerned is on the frontier of the production possibility set with no input/output slacks. Furthermore, the SBM model possesses several desirable properties that can properly handle our research interests. For instance, this measure is unit invariant and monotone decreasing with respect to input excesses and output shortfalls; it is determined only by consulting the reference set of the DMUs and is not affected by statistics over the whole data set, and it is closely connected with other measures, for example, those in the CCR and BCC models and the Russell measure. On the other hand, the super efficiency SBM is particularly useful in distinguishing efficient DMUs when the number of DMUs is small compared with the number of evaluation criteria. Liu et al. [12] have studied the power generation efficiency of major thermal power plants in Taiwan during 2004–2006 using the data envelopment analysis (DEA) approach. A stability test was conducted to verify the stability of the DEA model. According to the results, all power plants studied achieved acceptable overall operational efficiencies during 2004–2006, and the combination.

The problem of measuring productive efficiency of an industry is very important to both economic theorist and a policy maker [8].

3. Methodology

3.1. Data Collection. The sample of this study is collected from a market observation posting website in India. This website contains the detailed stock market data of major stock markets like Bombay Stock Exchange (BSE) and National Stock Exchange (NSE). The realistic financial data collected in our study is taken from getting into the individual companies after making sure that they were listed in either of 2 major stock exchanges of India. So in our study, we have probed the required financial statements and the corresponding Evaluation attributes (total assets, total expenses, employee cost, total income, and operating profit were taken for this study) are collected and tabled for data analysis.

Even though there are 14 companies of this industrial segment directly under the control of Government of India, some of them have not been listed on either of the major stock exchanges like Bombay Stock Exchange (BSE) and National Stock Exchange (NSE). Therefore, this study skips those unlisted companies for our study consideration. The final selected companies taken for this research, the type of Industry, or business they are involved in and their stock exchange index numbers are listed in the following table. These following alphabetical order (Table 1) of 10 companies were named DMU1 to DMU10 accordingly. We follow this naming scheme on these companies throughout this study. We follow the same naming scheme even while applying the grey systems theory methods just for the sake of convenience.

According to Ittner and Larcker [13], Five factors, total assets, total expenses, employee cost, total income, and operating profit, are considered as the key financial indicators directly contributing to the performance of the industry.

TABLE 1: List of final selected companies and naming scheme.

Serial no.	Naming scheme	Name	Type of industry or business	Financial index symbols
1	DMU 1	Balmer Lawrie and Company	Packaging	BSE: 523319 NSE: BALMLAWRIE ISIN: INE164A01016
2	DMU 2	Bharat Petroleum Corporation limited (BPCL)	Refineries	BSE: 500547 NSE: BPCL ISIN: INE029A01011
3	DMU 3	Chennai Petroleum Corporation Limited (CPCL)	Refineries	BSE: 500110 NSE: CHENNPETRO ISIN: INE178A01016
4	DMU 4	Engineers India Limited (EIL)	Engineering	BSE: 532178 NSE: ENGINEERSIN ISIN: INE510A01028
5	DMU 5	Gas Authority of India Limited (GAIL)	Oil drilling and exploration	BSE: 532155 NSE: GAIL ISIN: INE129A01019
6	DMU 6	Hindustan Petroleum Corporation (HPCL)	Refineries	BSE: 500104 NSE: HINDPETRO ISIN: INE094A01015
7	DMU 7	Indian Oil Corporation Limited (IOC)	Refineries	BSE: 530965 NSE: IOC ISIN: INE242A01010
8	DMU 8	Oil and Natural Gas Corporation (ONGC)	Oil drilling and exploration	BSE: 500312 NSE: ONGC ISIN: INE213A01029
9	DMU 9	Oil India Limited (OIL)	Oil drilling and exploration	BSE: 533106 NSE: OIL ISIN: INE274J01014
10	DMU 10	Mangalore Refineries and Petrochemicals Ltd. (MRPL)	Refineries	BSE: 500109 NSE: MRPL ISIN: INE103A01014

3.2. *DEA and Nonradial Super Efficiency Model (Super SBM)*. DEA was first proposed in 1978 by Charnes, Cooper, and Rhodes, (CCR) and is based on the technical efficiency measurement theories proposed by Farrell [8], using mathematical programming methods to measure the productivity boundaries of the unit to be evaluated and calculate the relative efficiency of each individual unit. Since the formal definition of the method, several scholars have proposed revisions to the theory and expansions of its application.

In pervious study, the technical efficiency change component of Malmquist productivity index is calculated by CCR score for the two periods. Because the CCR score is a radical measure, it takes no account of slacks. Instead of a radial based model, we now use the slacks based (nonradial) measure of superefficiency model to calculate technical efficiency change. The model takes account of slacks, and it has more accurate measurement.

In this study, a DEA model “Slacks-based measure of super efficiency” was used. This model was developed on “Slacks-based measure of efficiency” (SBM) introduced by Tone [14]. In this model with n DMUs with the input and output matrices $X = (x_{ij}) \in R^{m \times n}$ and $Y = (Y_{ij}) \in R^{s \times n}$, respectively. λ is a nonnegative vector in R^n . The vectors $S^- \in R^m$

and $S^+ \in R^s$ indicate the input excess and output shortfall, respectively. SBM model in fractional form is as follows [14]:

$$\min \rho = \frac{1 - (1/m) \sum_{i=1}^m s_i^- / x_{i0}}{1 + (1/s) \sum_{i=1}^s s_i^- / y_{i0}},$$

$$\text{subject to } \begin{aligned} x_0 &= X\lambda + s^-, \\ y_0 &= Y\lambda - s^+, \\ \lambda &\geq 0, \quad s^- \geq 0, \quad s^+ \geq 0. \end{aligned} \quad (1)$$

Let an optimal solution for SBM be $(p^*, \lambda^*, s^{*-}, s^{*+})$. A DMU (x_0, y_0) is SBM efficient, if $p^* = 1$. This condition is equivalent to $S^{*-} = 0$ and $S^{*+} = 0$, no input excesses and no output shortfalls in any optimal solution. SBM is nonradial and deals with input/output slacks directly. The SBM returns and efficiency measure between 0 and 1.

The best performers have the full efficient status denoted by unity. Tone [15] discriminated these efficient DMUs and ranked the efficient DMUs by superSBM model. Assuming

that the DMU (x_0, y_0) is SBM-efficient, $p^* = 1$, super SBM model is as follows:

$$\begin{aligned} \min \delta &= \frac{(1/m) \sum_{i=1}^m \bar{x}_i / x_{i0}}{(1/s) \sum_{r=1}^s \bar{y}_r / y_{r0}}, \\ \text{subject to } \bar{x} &\geq \sum_{j=1, \neq 0}^n \lambda_j x_j, \\ \bar{y} &\leq \sum_{j=1, \neq 0}^n \lambda_j x_j, \\ \bar{y} &\geq x_0, \bar{y} \leq y_0, \\ \bar{y} \bar{y} &\geq y_0, \lambda \geq 0. \end{aligned} \quad (2)$$

As in many DEA models, it is crucial to consider how to deal with negative outputs in the evaluation of efficiency in SBM models too. However, negative data should have their duly role in measuring efficiency; hence, a new scheme was introduced in DEA-Solver pro 4.1 Manuel and the scheme was changed as follows.

Let us suppose $y_{r0} \leq 0$. It is defined \bar{y}_r^+ and y_{-r}^+ by

$$\begin{aligned} \bar{y}_r^+ &= \max_{j=1, \dots, n} \{y_{rj} \mid y_{rj} > 0\}, \\ \bar{y}_{-r}^+ &= \min_{j=1, \dots, n} \{y_{rj} \mid y_{rj} > 0\}. \end{aligned} \quad (3)$$

If the output r has no positive elements, then it is defined as $\bar{y}_r^+ = y_{-r}^+ = 1$. The term is replaced s_r^+ / y_{r0} in the objective function in the following way. The value y_{r0} is never changed in the constraints.

(1) $\bar{y}_r^+ = y_{-r}^+ = 1$, and the term is replaced by

$$\frac{s_r^+}{y_{-r}^+ (\bar{y}_r^+ - y_{-r}^+) / (\bar{y}_r^+ - y_{r0})}. \quad (4)$$

(2) Consider

$$\frac{s_r^+}{(\bar{y}_{-r}^+)^2 / B (\bar{y}_r^+ - y_{r0})}, \quad (5)$$

where B is a large positive number, (in DEA-Solver $B = 100$).

In any case, the denominator is positive and strictly less than y_{-r}^+ . Furthermore, it is inverse proportion to the distance $\bar{y}_r^+ - y_{r0}$. This scheme, therefore, concerns the magnitude of the nonpositive output positively. The score obtained is units invariant; that is, it is independent of the units of measurement used.

3.3. Malmquist Productivity Index (MPI). Malmquist productivity index of productivity change is a multiplicative composite of efficiency and technical change as the major cause of productivity improvements can be ascertained by comparing the values of the efficiency change and technical change indexes. Put differently, the productivity losses

described can be the result of either efficiency declines, or technique regresses, or both.

The output based Malmquist productivity index is defined as follows [16]:

$$\text{MPI} = \left[\frac{d_o^s(x_t, y_t)}{d_o^s(x_s, y_s)} \times \frac{d_o^t(x_t, y_t)}{d_o^t(x_s, y_s)} \right]^{1/2}, \quad (6)$$

where d_o^s is a distance function measuring the efficiency of conversion of inputs x_s to outputs y_s in the period s . (Note that DEA efficiency is considered a distance measure in the literature as it reflects the efficiency of converting inputs to outputs [17].)

Importantly, if there is a technical change in period t , then

$$\begin{aligned} d_o^t(x_s, y_s) &= \text{Efficiency of conversion of input} \\ &\quad \text{in period } s \text{ to output in period } s \quad (7) \\ &\neq d_o^s(x_s, y_s). \end{aligned}$$

Malmquist productivity index is a geometric average of the efficiency and technical changes in the two periods being considered. Following Grosskopf et al. [17], the Malmquist productivity index in (3.15) in [17] can thus be written as

$$\begin{aligned} \text{MPI} &= \frac{d_o^t(x_t, y_t)}{d_o^s(x_s, y_s)} \left[\frac{d_o^s(x_s, y_s)}{d_o^t(x_s, y_s)} \times \frac{d_o^s(x_t, y_t)}{d_o^t(x_t, y_t)} \right]^{1/2} \\ &= \text{Efficiency change} \times \text{Technical change}. \end{aligned} \quad (8)$$

Malmquist productivity indices were used to estimate changes in the overall productivity of each pharmaceutical company over time. $\text{MPI} > 1$ means that productivity increases; $\text{MPI} = 1$ means that productivity does not change; $\text{MPI} < 1$ indicates that productivity decreases.

Efficiency change is called ‘‘catch-up effect’’ and the efficiency change term relates to the degree to which a DMU improves or worsens its efficiency. Efficiency change > 1 indicates progress in relative efficiency from period s to t , while efficiency change = 1 and efficiency change < 1 , respectively, indicate no change and regress in efficiency.

Technical change is called ‘‘frontier-shift effect’’ (or innovation effect). The technical change term reflects the change in the efficient frontiers between the two time periods. Technical change > 1 stands for technical progress; technical change < 1 shows technical regress.

4. Empirical Result and Analysis

This study utilizes the realistic financial data collected from market observation system for methodology implementation. The latest data was applied for DEA super SBM model. Meanwhile, the least 5 year data was applied for methodology implementation of Malmquist index model as these methods have different purposes on their respective analysis perspectives.

Table 2 specifies the real market data for all companies (DMU’s) for the last year listing data of March 2012. This data

TABLE 2: Initial realistic data of companies: March 2012.

	(I) Total assets	(I) Total expenses	(I) Employee cost	(O) Total income	(O) Operating profit
DMU 1	618.92	2,127.17	140.82	2,337.30	157.03
DMU 2	36,160.30	208,707.72	2,261.07	214,276.35	3,866.85
DMU 3	7,220.90	40,902.51	253.21	41,368.31	401.16
DMU 4	1,844.03	2,982.17	541.69	3,907.79	716.65
DMU 5	26,971.33	34,823.54	678.00	41,270.76	6,070.84
DMU 6	40,601.77	175,513.48	1,583.10	180,585.38	4,046.31
DMU 7	128,200.63	423,238.16	4,980.06	437,172.01	18,443.65
DMU 8	117,456.76	40,036.21	6,796.05	84,199.96	36,570.22
DMU 9	17,731.47	12,549.14	1,517.54	18,669.19	4,674.68
DMU 10	12,980.92	52,307.10	160.64	54,267.87	1613.39

TABLE 3: Statistics of latest information: March 2012.

	Total assets	Total expenses	Employee cost	Total income	Operating profit
Max	83100.12	237990.89	5843.27	252445.87	36570.22
Min	331.27	534.39	83.45	831.47	157.03
Average	24937.781	55698.227	1301.845	62469.481	7656.078
SD	28907.65583	71251.76861	1712.313963	74185.10785	10884.52571

TABLE 4: Correlation coefficient: March 2012 data.

	Total assets	Total expenses	Employee cost	Total income	Operating profit
Total assets	1	0.638691472	0.924470351	0.732162037	0.919705011
Total expenses	0.638691472	1	0.319025867	0.991643276	0.288662319
Employee cost	0.924470351	0.319025867	1	0.43692631	0.986310318
Total income	0.732162037	0.991643276	0.43692631	1	0.409037546
Operating profit	0.919705011	0.288662319	0.986310318	0.409037546	1

TABLE 5: DEA ranking of DMU's latest year (2012).

Rank	DMU	Score
1	DMU 8	2.6875041
2	DMU 10	2.4135548
3	DMU 7	1.5451541
4	DMU 5	1.4015806
5	DMU 9	1.1112872
6	DMU 6	1.0794482
7	DMU 2	1.0257595
8	DMU 4	1
8	DMU 1	1
10	DMU 3	0.3727601

TABLE 6: Important results of DEA. (super SBM from March 2012 data).

No. of DMUs in data	10
No. of DMUs with inappropriate data	0
No. of evaluated DMUs	10
Average of scores	1.363704861
No. of efficient DMUs	9
No. of inefficient DMUs	1
No. of overiteration DMUs	0

will give the clear idea on initial data and its diversity in nature and it also clearly gives a picture on the nature of the data.

Table 3 shows the basic statistical information of the input and output data. This would justify reason that the data can be applicable to basic statistical methods.

Table 4 indicates that both input and output variables are positively correlated even with minor correlation existing between employee costs and operating profit against total expenses indicated as 0.319025867 and 0.288662319, respectively. From these results, we can justify the reason for why we

use these indicators for DEA methodologies. The correlation is also very significant which will affect the performance.

The DEA super SBM model evaluates the efficiency scores as Table 5. It clearly indicates that the DMU 3 has inefficient score of 0.3727601 while the other 9 DMUs have efficiency scores of 1 or more. This means that DMU 3 (Chennai Petroleum Corporation) is considered as inefficient after this analysis.

Table 6 indicates that there is an only one inefficient DMU, DMU3, is become in-efficient after DEA adaptation. This clearly indicates that super SBM can distinguish all DMUs with significant differences on their scoring.

TABLE 7: Consolidated DEA super SBM results for all the periods and ranking.

	March 12		March 11		March 10		March 09		March 08	
DMU 1	1	8	1	8	1	7	1	8	1	8
DMU 2	1.0257595	7	1.1213597	5	1.030814	5	1.0360972	6	1.0422367	6
DMU 3	0.3727601	10	0.7395838	10	0.63242	10	1.0896385	5	1.0201155	7
DMU 4	1	8	1.2386099	4	1.9656867	2	1	8	1	8
DMU 5	1.4015806	4	1.0234648	7	1.0268541	6	0.9320184	10	1.2216315	4
DMU 6	1.0794482	6	1.0377901	6	1.0476469	4	1.145793	4	1.0794482	5
DMU 7	1.5451541	3	1.4350091	3	1.4542432	3	1.4620893	3	1.4464182	3
DMU 8	2.6875041	1	3.4718795	1	3.5388973	1	2.9274643	2	2.8389158	1
DMU 9	1.1112872	5	0.777107	9	0.7559947	9	1.0029777	7	0.8559011	10
DMU 10	2.4135548	2	2.5373827	2	1	7	9.966342	1	1.4899857	2

TABLE 8: Catch-up or efficiency change. (March 2008 to March 2012).

Catch-up	March 08⇒March 09	March 09⇒March 10	March 10⇒March 11	March 11⇒March 12	Average
DMU 1	1	1	1	1	1
DMU 2	0.994109	0.994901	1.087839	1.029747	1.026649
DMU 3	1.068152	0.580394	1.16945	1.500996	1.079748
DMU 4	1	1.965687	0.630116	0.974001	1.142451
DMU 5	0.762929	1.101753	0.996699	1.221724	1.020776
DMU 6	1.061462	0.914342	0.990591	1.005124	0.99288
DMU 7	1.010834	0.994634	0.986774	1.026666	1.004727
DMU 8	1.031191	1.208861	0.981063	0.79588	1.004249
DMU 9	1.171838	0.75375	1.027927	1.169631	1.030787
DMU 10	6.688885	0.100338	2.537383	2.608928	2.983883
Average	1.57894	0.961466	1.140784	1.23327	1.228615
Max	6.688885	1.965687	2.537383	2.608928	2.983883
Min	0.762929	0.100338	0.630116	0.79588	0.99288
SD	1.798363	0.474362	0.509902	0.518266	0.618419

Table 7 shows the DEA efficiency scores for the last 5 years data and ranking of DMUs by their scores. This indicates that the ranking of the industries is tending to change in a very slight manner on yearly basis. However, majority of these companies are maintaining their “efficient” levels even after yearly changes on their financial nature.

Table 8 shows the “efficiency change” of the industries over the year periods of time interval. This reveals that the efficiency changes are not so consistent due to that their nature of their financial management is not really consistently improving or not consistently outperforming DMU over the time yearly frame.

Figure 1 clearly indicates that the “efficiency changes” among the companies over the yearly time frame are exhibiting the inconsistency over the years. However, we can notice some abrupt drop of the efficiency change of DM10 (MRPL) during March 2009 to March 2010. In the following years, it has tended to increase again. But the rest of them have no such big changes even with slight changes by slight increase and decrease. This clearly indicates that the entire industry has not shown much big changes on their catch-up scores during the last 4 years. It is owing to that the financial segment is not much affected even after the global economic recession in 2007-2008.

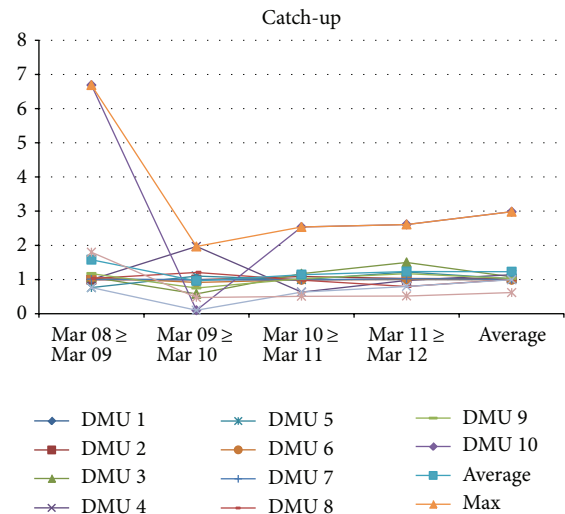


FIGURE 1: Catch-up or efficiency change. (March 2008 to March 2012).

Table 9 and Figure 2 indicated clearly that the companies are tending to change their level of technical changes or their

TABLE 9: Frontier shift or technical change. (March 2008 to March 2012).

Frontier	March 08⇒March 09	March 09⇒March 10	March 10⇒March 11	March 11⇒March 12	Average
DMU 1	0.987134	1	1.009134	0.985076	0.995336
DMU 2	1.003373	0.792531	1.140326	1.207995	1.036056
DMU 3	1.004948	0.818433	1.092449	0.821111	0.934235
DMU 4	0.951497	0.821484	1.29312	0.760486	0.956647
DMU 5	1.086112	0.933236	0.942566	0.940265	0.975545
DMU 6	0.929928	0.800501	1.076819	1.391254	1.049626
DMU 7	0.954895	0.97257	1.041568	1.285798	1.063708
DMU 8	1.083658	1.069626	1.024671	0.887563	1.016379
DMU 9	0.928063	1.093942	0.991948	0.923826	0.984445
DMU 10	0.501099	2.562599	0.673974	0.673993	1.102916
Average	0.943071	1.086492	1.028657	0.987737	1.011489
Max	1.086112	2.562599	1.29312	1.391254	1.102916
Min	0.501099	0.792531	0.673974	0.673993	0.934235
SD	0.165187	0.530562	0.157735	0.234379	0.052098

TABLE 10: Malmquist productivity index (MPI) scores. (March 2008 to March 2012).

Malmquist	March 08⇒March 09	March 09⇒March 10	March 10⇒March 11	March 11⇒March 12	Average
DMU 1	0.987134	1	1.009134	0.985076	0.995336
DMU 2	0.997462	0.788489	1.240491	1.24393	1.067593
DMU 3	1.073437	0.475014	1.277565	1.232484	1.014625
DMU 4	0.951497	1.61478	0.814815	0.740714	1.030451
DMU 5	0.828627	1.028195	0.939455	1.148744	0.986255
DMU 6	0.987084	0.731932	1.066688	1.398383	1.046022
DMU 7	0.965241	0.967351	1.027792	1.320085	1.070117
DMU 8	1.117459	1.293029	1.005266	0.706393	1.030537
DMU 9	1.087539	0.824559	1.01965	1.080536	1.003071
DMU 10	3.351792	0.257125	1.710131	1.7584	1.769362
Average	1.234727	0.898047	1.111099	1.161474	1.101337
Max	3.351792	1.61478	1.710131	1.7584	1.769362
Min	0.828627	0.257125	0.814815	0.706393	0.986255
SD	0.748337	0.38537	0.249313	0.311165	0.236437

innovation effect inconsistently. This is almost like the same effect in the previous “efficiency change” level. Notably, all the companies (DMUs) have very close efficiency scores except some abrupt changes on DMU 10’s efficiency over the beginning years.

Table 10 and Figure 3 are showing the Malmquist Productivity Index (MPI) scores and their changes on a yearly basis. Say for instance, the MPI scores of DMU 4, DMU 5, and DMU 8 are getting better from March 2008 to March 2009. But DMU 1, DMU 7, DMU 8 have also increased their MPI scores but very slightly. And the DMU 2, DMU 3, DMU 6, DMU 9, and DMU 10 have shown a decrement of their productivity index scores.

5. Conclusions and Discussions

The ranking of super SBM model shows the order of performance scores from ONGC in the top position followed by MRPL, IOCL, and GAIL. The lower to higher scores of DEA

scoring order will lie as CPCL, Balmer Lawrie & Refineries Limited, EIL, BPCL, and HPCL. It also shows that CPCL is inefficient DMU, so that it needs a very serious improvement action. Since super SBM model can distinguish the ranking of all DMUs, we would derive a clear decision for improving the performance of less efficiency scored DMUs.

After applying MPI methodology to our data set and calculating the efficiency scores, we have found that all companies in the industry have not shown many abrupt changes on their scores and it is always not consistently good or consistently standing out. So it means that there are not many changes happening on Indian stock markets even with financial crisis in a broad context.

This study provides many significant and noticeable results after applying each methodology for making necessary decisions on the respective concerns. This completed and integrated numerical study gives us better insights through the integration method as it minimizes the methodology limitation problems.

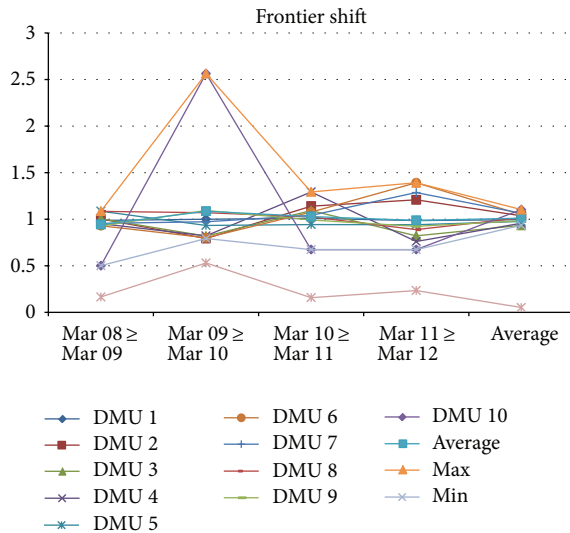


FIGURE 2: Frontier shift or technical change. (March 2008 to March 2012).

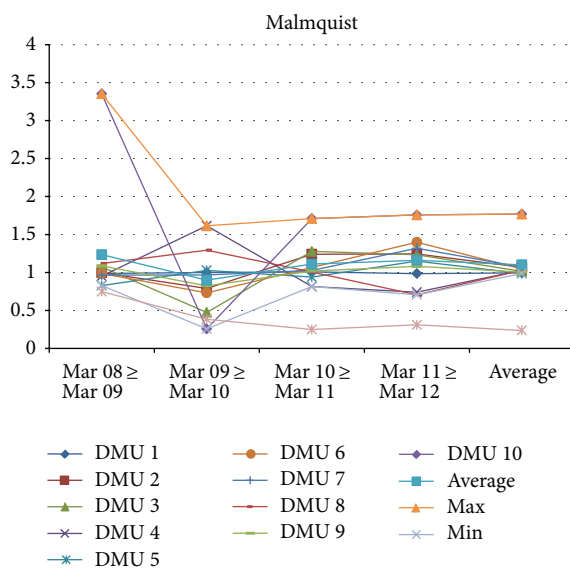


FIGURE 3: Malmquist productivity index (MPI) scores.

It gives better insights in terms of understanding the impact of global economic recession and its consequences in India as it is a core industry of the economy. This also makes this research as a considerable study for global economic outlook planners and researchers.

We suggest that this work could be used as a better model for performance analysis among the decision makers of varied industries. However, the completely integrated performance analysis model needs a detailed reevaluation in terms of the type of Industry that it can be applied to, the nature of the input data, adoptability of data for each method, applicability of each method, and so on. The future directions can also be suggested for including or avoiding different methodologies in this completely integrated model.

Acknowledgments

The authors gratefully acknowledge Dr. Chung Yi Shun from the National Cheng Kung University (NCKU) and Mr. Chuang Yun Chung from the Metal Industries Research & Development Centre (MIRDC) for their comments on earlier versions of the paper.

References

- [1] C. Kroeze, J. Vlasblom, J. Gupta, C. Boudri, and K. Blok, "The power sector in China and India: greenhouse gas emissions reduction potential and scenarios for 1990–2020," *Energy Policy*, vol. 32, no. 1, pp. 55–76, 2004.
- [2] B. Eichengreen and H. Tong, "Is China's FDI coming at the expense of other countries?" *Journal of the Japanese and International Economies*, vol. 21, no. 2, pp. 153–172, 2007.
- [3] B. van Ruijven and D. P. van Vuuren, "Oil and natural gas prices and greenhouse gas emission mitigation," *Energy Policy*, vol. 37, no. 11, pp. 4797–4808, 2009.
- [4] C. Sun, "Assessing Taiwan financial holding companies' performance using window analysis and malmquist productivity index," *African Journal of Business Management*, vol. 5, no. 26, pp. 10508–10523, 2011.
- [5] M. E. H. Arouri, A. Lahiani, A. Lévy, and D. K. Nguyen, "Forecasting the conditional volatility of oil spot and futures prices with structural breaks and long memory models," *Energy Economics*, vol. 34, no. 1, pp. 283–293, 2012.
- [6] N. K. Nomikos and P. K. Pouliasis, "Forecasting petroleum futures markets volatility: the role of regimes and market conditions," *Energy Economics*, vol. 33, no. 2, pp. 321–337, 2011.
- [7] A. Charnes, W. W. Cooper, and E. Rhodes, "Measuring the efficiency of decision making units," *European Journal of Operational Research*, vol. 2, no. 6, pp. 429–444, 1978.
- [8] M. J. Farrell, "The measurement of productive efficiency," *Journal of the Royal Statistical Society A*, vol. 120, no. 3, pp. 253–290, 1957.
- [9] L. Lindholt and S. Glomsrød, "The arctic: no big bonanza for the global petroleum industry," *Energy Economics*, vol. 34, no. 5, pp. 1465–1474, 2012.
- [10] C.-H. Lai and M.-Y. Wei, "A common weighted performance evaluation process by using data envelopment analysis models," in *Proceedings of the IEEE International Conference on Industrial Engineering and Engineering Management (IEEM '07)*, pp. 827–831, Singapore, December 2007.
- [11] S.-F. Lo and W.-M. Lu, "An integrated performance evaluation of financial holding companies in Taiwan," *European Journal of Operational Research*, vol. 198, no. 1, pp. 341–350, 2009.
- [12] Z. Zhu, L. Liu, and J. Wang, "Optimization of China's strategic petroleum reserve policy: a markovian decision approach," *Computers and Industrial Engineering*, vol. 63, no. 3, pp. 626–633, 2012.
- [13] C. D. Ittner and D. F. Larcker, "Are nonfinancial measures leading indicators of financial performance? An analysis of customer satisfaction," *Journal of Accounting Research*, vol. 36, pp. 1–35, 1998.
- [14] K. Tone, "A slacks-based measure of efficiency in data envelopment analysis," *European Journal of Operational Research*, vol. 130, no. 3, pp. 498–509, 2001.
- [15] K. Tone, "A slacks-based measure of super-efficiency in data envelopment analysis," *European Journal of Operational Research*, vol. 143, no. 1, pp. 32–41, 2002.

- [16] D. W. Caves, L. R. Christensen, and W. E. Diewert, "The economic theory of index numbers and the measurement of input, output, and productivity," *Econometrica*, vol. 50, pp. 1393–1414, 1982.
- [17] R. Färe, S. Grosskopf, M. Norris, and Z. Z. Zhongyang Zhang, "Productivity growth, technical progress, and efficiency change in industrialized countries," *The American Economic Review*, vol. 84, no. 1, pp. 66–83, 1994.

Research Article

Vision Servo Motion Control and Error Analysis of a Coplanar XXY Stage for Image Alignment Motion

Hau-Wei Lee¹ and Chien-Hung Liu²

¹ Center of Measurement Standard, Industrial Technology Research Institute, Hsinchu 30011, Taiwan

² Department of Mechanical Engineering, National Chung Hsing University, Taichung 402, Taiwan

Correspondence should be addressed to Chien-Hung Liu; carus@dragon.nchu.edu.tw

Received 27 September 2013; Accepted 10 October 2013

Academic Editor: Teen-Hang Meen

Copyright © 2013 H.-W. Lee and C.-H. Liu. This is an open access article distributed under the Creative Commons Attribution License, which permits unrestricted use, distribution, and reproduction in any medium, provided the original work is properly cited.

In recent years, as there is demand for smart mobile phones with touch panels, the alignment/compensation system of alignment stage with vision servo control has also increased. Due to the fact that the traditional stacked-type $XY\theta$ stage has cumulative errors of assembly and it is heavy, it has been gradually replaced by the coplanar stage characterized by three actuators on the same plane with three degrees of freedom. The simplest image alignment mode uses two cameras as the equipments for feedback control, and the work piece is placed on the working stage. The work piece is usually engraved/marked. After the cameras capture images and when the position of the mark in the camera is obtained by image processing, the mark can be moved to the designated position in the camera by moving the stage and using alignment algorithm. This study used a coplanar XXY stage with $1\mu\text{m}$ positioning resolution. Due to the fact that the resolution of the camera is about $3.75\mu\text{m}$ per pixel, thus a subpixel technology is used, and the linear and angular alignment repeatability of the alignment system can achieve $1\mu\text{m}$ and 5 arcsec, respectively. The visual servo motion control for alignment motion is completed within 1 second using the coplanar XXY stage.

1. Introduction

Visual servo control with digital image processing for optical image alignment has been applied in many processes in recent years, such as MEMS, biochip, semiconductor, LED, LCD, and the popular touch panel. A basic alignment system contains two charge coupled device (CCD) cameras and a high-precision positioning/compensation stage. Kuo et al. presented a precision nanoalignment system using machine vision [1]. The alignment system used a stacked type of compensation stage, which is driven by piezoelectric ceramic motors. The system uses a circle to be the alignment mark and single camera to capture the image. The proposed system can compensate x and y axes' errors and the positional error can be in the range of 60 nm. For an image alignment system, another key point is the recognition of the mark. If the recognition of the mark is insufficient, there may be a misrecognition that influences the alignment quality, and the common mark is cross mark. It may be imagined that if the

mark is a circle, it is likely to be confused with the solder joint in the detection of PCB; if the mark is a straight line, the line of PCB may be misrecognized as the mark. Lin et al. develops a subpixel image matching method CPTRPT [2]. The results show that the translation and rotation mean errors are about 0.03 pixels and 0.1 pixels. Although, the proposed method shows good accuracy, the average run time is 20.5 ms which causes the method to be difficult to be applied on high-speed/real-time alignment. Lee et al. proposed a real time critical dimension measurement of TFT-LCD pattern [3]. The developed system can be used in the TFT-LCD manufacturing and repeatability is less than 30 nm. Pattern searching time is about 12 ms (for $XY\theta$, one time search). The study also proposes an edge detection method, which is simpler than Canny [4]. Huang and Lin used a camera and a stacked XY stage for alignment of XY direction in 2009 [5]. Cross symbol was used as the mark, and the alignment error in steady state was less than $1\mu\text{m}$. In the study, the alignment of $XY\theta$ direction can be finished using

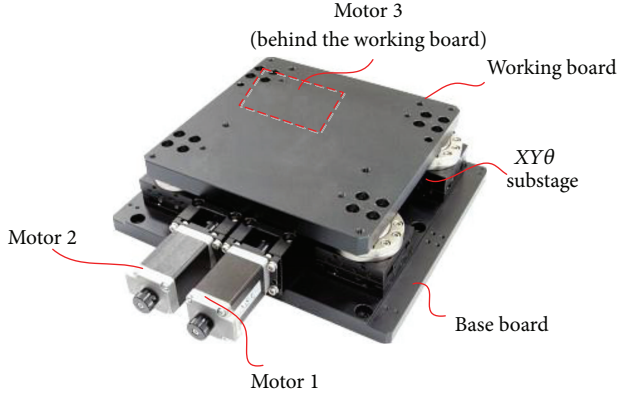


FIGURE 1: Basic structure of coplanar XXY stage.

single camera; however the angular alignment accuracy was worse than two cameras alignment system due to low angular resolution.

The alignment was carried out by stacked $XY\theta$ stage in the past. However, the stacked stage usually has cumulative errors, such as flatness error, parallelism error, and orthogonally error between axes. These errors influence the alignment accuracy as the stacked stage has heavy weight and high gravitational center (compared with coplanar stage). If the acceleration and deceleration of alignment process are too large, it is likely to exceed the stroke because of the inertia (it can be regarded as an inverted pendulum system). In order to solve the above problems, the coplanar $XY\theta$ stage has been widely used in recent years. Using the piezoelectric actuators to construct the coplanar type of stage can be presented in many papers and they showed good positioning accuracy [6–9]. However, for manufacture industrial application like touch panel lamination, a piezoelectric based stage is too expensive and they do not need such an ultrahigh accuracy compensating stage. Yim et al. [10] proposed that a high precision stage for $370 \cdot 470 \text{ mm}^2$ size UV-NIL was modeled as flexible bodies. Both translational and rotational control for misalignment correction were performed using machine vision. Furthermore, each vertical motion of the three and four axis stages was analyzed and compared to each other. In this paper, a coplanar stage as shown in Figure 1 was used to implement visual servo motion control for alignment motion. The kinematic and error analysis were studied and the servo control and image processing were successfully integrated for precision visual servo control.

2. Design of a Coplanar XXY Stage

The coplanar XXY stage (following called XXY stage) is characterized by three actuators on the same plane, so that the gravity center is low. In other words, the moving speed of coplanar XXY stage can be faster than the stacked $XY\theta$ stage, and it is small and light. The main advantage of coplanar XXY stage is being smaller cumulative error of stage composition than the traditional stack-type stage.

2.1. Stage Composition. As shown in Figure 1, the XXY stage consists of four major components.

- (1) Base: the basic base fixes the XXY stage, the parallelism, and flatness verifying reference plane after system assembly.
- (2) Motors: the XXY stage is driven by three stepper motors which are installed on the same plane. The axial direction of Motor 1 and Motor 2 is parallel to the X-direction of the stage; Motor 3 is under the working stage (not displayed in the figure). The axial direction of Motor 3 is parallel to the Y-direction of the stage.
- (3) $XY\theta$ substage: $XY\theta$ substage consists of two small cross roller stages and small rotary stage to have three degrees of motion. The coplanar XXY stage consists of four small $XY\theta$ substages under the working platform. The main purpose of $XY\theta$ substage is to support and to provide constraint conditions for the movement of the XXY stage. In the XXY stage, three motors are connected to three adjacent $XY\theta$ substages by three ball screws, respectively, so each $XY\theta$ substage drives in only one direction (i.e. the others are free moving). There is a $XY\theta$ substage in the XXY stage unconnected to any actuator; the $XY\theta$ substage is called free body in this paper. This kind of component mechanism makes the working platform only with three degrees of motion.
- (4) Working stage: the stage carries work pieces or processed goods. Although each $XY\theta$ substage has cumulative error, when the four $XY\theta$ substages are combined with the stage, only the overall accuracy of the working stage should be considered, suggesting that the accuracy of XXY stage is free from the cumulative error of $XY\theta$ substage. Only the positioning repeatability of each $XY\theta$ substage is required to meet requirements during the stage verification.

2.2. Kinematic of Coplanar Stage. The XXY stage has three-dimensional motion, X, Y, and θ_z as shown in Figure 2. If the linear displacement of stage is represented as $\vec{s} = [\delta_x \ \delta_y]^T$ (unit: mm) and angular displacement of the stage is represented as δ_θ (unit: radius), the displacement of motors is $\vec{m} = [m_1 \ m_2 \ m_3]^T$ (unit: pulse); the basic linearized relation between the stage displacement and the motor displacement is

$$\begin{bmatrix} m_1 \\ m_2 \\ m_3 \end{bmatrix} = \frac{R_m}{\ell_P} \begin{bmatrix} 1 & 0 & k_a \\ 1 & 0 & k_b \\ 0 & 1 & k_c \end{bmatrix} \begin{bmatrix} \delta_x \\ \delta_y \\ \delta_\theta \end{bmatrix}, \quad (1)$$

where R_m is the motor resolution (unit: pulse/rev); ℓ_P is the lead of the ball screw (unit: mm/rev); k_a , k_b , and k_c are the parameters for angle rotation. k_a , k_b , and k_c are related to the distance between the stage center and the XXY stage center connected to the coordinate systems of $\{m_1\}$, $\{m_2\}$, and $\{m_3\}$. For high precision motion control, the kinematic formula must take into account the center deviation of the XXY stage during the motion. If the position vectors between the stage

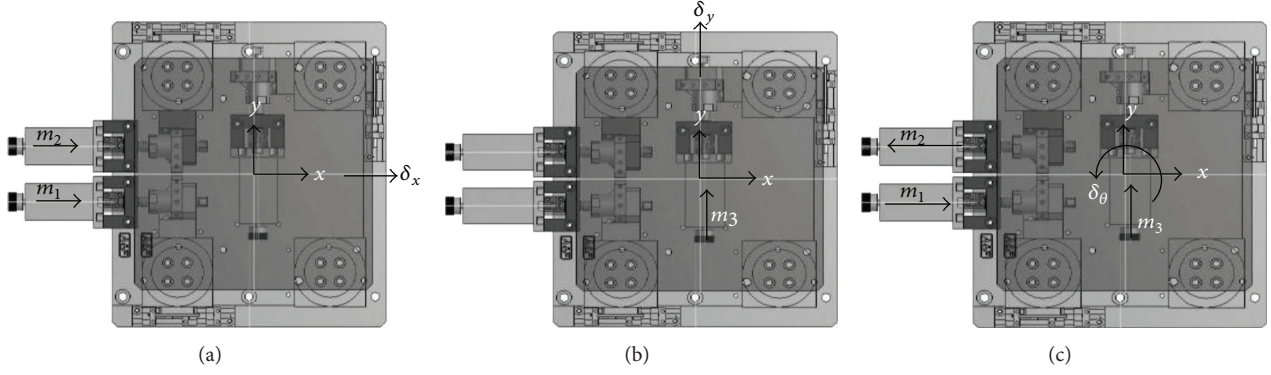
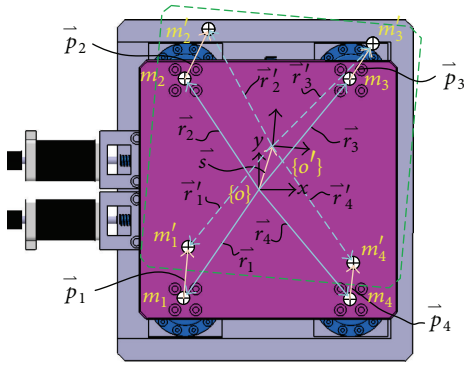

 FIGURE 2: Three-dimensional motion, X , Y , and θ_z : (a) X motion; (b) Y motion; (c) θ_z motion.


FIGURE 3: Coordinate definition of kinematic analysis of XXY stage.

center and i th $XY\theta$ substages center is $\vec{r}_i = [r_{ix} \ r_{iy}]^T$, $i = 1, 2, 3$, and 4 , shown in Figure 3, we have

$$m_i = \vec{t}_i \left(-\vec{r}_i + \vec{s} + \vec{r}_i' \right), \quad (2)$$

$$\vec{r}_i' = \mathbf{R} \cdot \vec{r}_i, \quad (3)$$

$$\mathbf{R} = \begin{bmatrix} \cos \delta_\theta & -\sin \delta_\theta \\ \sin \delta_\theta & \cos \delta_\theta \end{bmatrix}, \quad (4)$$

$$\mathbf{R}_{\text{err}} = \begin{bmatrix} \cos \beta \cos \gamma & \cos \gamma \sin \alpha \sin \beta - \cos \alpha \sin \gamma & \cos \alpha \cos \gamma \sin \beta + \sin \alpha \sin \gamma \\ \cos \beta \sin \gamma & \cos \alpha \cos \gamma + \sin \alpha \sin \beta \sin \gamma & \cos \alpha \sin \beta \sin \gamma - \cos \gamma \sin \alpha \\ -\sin \beta & \cos \beta \sin \alpha & \cos \alpha \cos \beta \end{bmatrix}, \quad (7)$$

$$\mathbf{R}_{pi} = \begin{bmatrix} 1 & 0 & 0 \\ 0 & 1 & 0 \end{bmatrix}. \quad (8)$$

Note that (7) shows the matrix of the angular setup errors of α , β , and γ . In order to expand the displacement vector \vec{s} and distance vector \vec{r}_i to three dimension space, we redefined both as $\vec{s} = [\delta_x \ \delta_y \ 0]^T$ and $\vec{r}_i = [r_{ix} \ r_{iy} \ 0]^T$. Positioning error caused from setup error can be estimated according to sensitivity as in the following equation:

$$\varepsilon(v) = \frac{\partial f_{\text{err}}}{\partial v}, \quad (9)$$

where f_{err} is the kinematic equation with setup error and v is the setup error source. The positioning error due to stage

where \vec{t}_1 and \vec{t}_2 both are $[R_m/\ell_p \ 0]$ and \vec{t}_3 is $[0 \ R_m/\ell_p]$. After linearization of (2), (3), and (4), the parameters of (1) are $k_a = -r_{1y}$, $k_b = -r_{2y}$, and $k_c = r_{3x}$.

2.3. Error Analysis. The XXY stage consists of four $XY\theta$ substages. The setup errors are usually contained when XXY stage is assembled. The setup errors include three straightness errors and three angular errors. As shown in Figure 4, the designed position of the $XY\theta$ substage which is linked with motor 1 is m_1 . However, the actual position of the $XY\theta$ substage is in the position of m_{e1} due to setup error. Let the vector of setup error is $\vec{e}_1 = [e_x \ e_y \ e_z]^T$; we have

$$\vec{r}_{e1} = \vec{r}_1 + \vec{e}_1. \quad (5)$$

According to (2), (3), and (5), we can write

$$\vec{p}_i = \mathbf{R}_{pi} \left[\mathbf{R}_{\text{err}} \left(-\vec{r}_i - \vec{e} + \vec{s} + \mathbf{R} \cdot \vec{r}_i \right) \right], \quad (6)$$

where

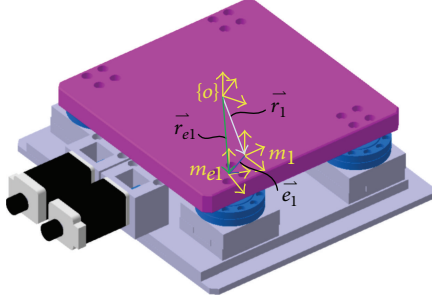


FIGURE 4: Setup error of the XXY stage.

setup error can be estimated by the following equation:

$$E(v) = \varepsilon(v) \times \tau(v), \quad (10)$$

where $\tau(v)$ represents the evaluation value of the estimated error source. To resolve (6), the positioning error estimation result as shown in Table 1. In this estimation, we let $\vec{r}_1 = [-56 \ -74 \ 0]^T$, $\vec{r}_2 = [-56 \ 74 \ 0]^T$, $\vec{r}_3 = [56 \ 74 \ 0]^T$, $\vec{r}_4 = [56 \ -74 \ 0]^T$, $\vec{s} = [2 \ 2 \ 0]^T$, and $\delta_\theta = 2^\circ$. According to (2), we can get that the displacements from $\vec{s} = [0 \ 0 \ 0]$ and $\delta_\theta = 0^\circ$ to the desired position of each $XY\theta$ stage are $\vec{p}_1 = [3.617 \ -0.909]^T$, $\vec{p}_2 = [-1.548 \ -0.999]^T$, and $\vec{p}_3 = [-1.617 \ 2.909]^T$. The estimation results also showed that the setup error sources of e_{x1} , e_{x2} , e_{y3} , e_{z1} , α_i , and β_i do not obviously influence the positioning accuracy. Note that the setup error sources of e_{zi} , α_i , and β_i are related to the parallelism of the base board and the working board. The estimated error trend is as shown in Figure 5.

3. Image Vision Alignment

3.1. Image Alignment. The basic concept of image alignment is shown in Figure 6. The main purpose is to eliminate the spacing distance between the mark and the camera target position, assumed to be $\vec{e}_1 = [x_1 \ y_1]^T$ and $\vec{e}_2 = [x_2 \ y_2]^T$. In an ideal state, the distance D_p between two camera target positions is identical with the distance D_c between two marks. The alignment equation can be derived from Figure 7. Thus, the alignment equation can be obtained similar to (2) to (4) as follows:

$$m_i = \vec{t}_i \left(-\vec{r}_{ai} + \vec{s} + \mathbf{R} \cdot \vec{r}_{ai} \right), \quad (11)$$

$$\vec{r}_{ai} = \vec{r}_i - \vec{v} - \vec{s},$$

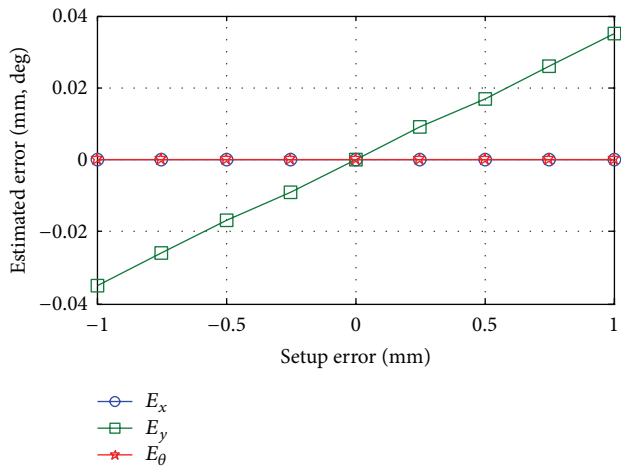
where \vec{v} is the distance vector from $\{O\}$ to the camera target position. As shown, when the XXY stage is used as the alignment stage, the procedure of image alignment is very simple. It is unnecessary to use the stage center as reference point for alignment anymore but to use the position of mark center as the reference point to calculate the displacement of stage. This method is the floating reference point method.

TABLE 1: Estimated glass position error when the camera setup error is existed. (unit: mm, degrees).

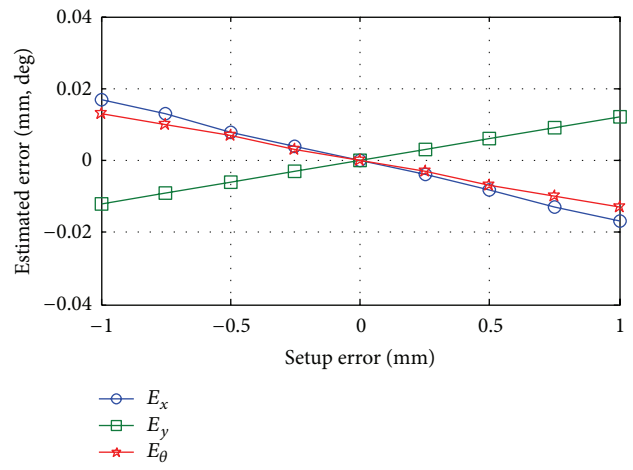
v	$\tau(v)$	Estimated error		
		E_x	E_y	E_θ
m_1				
e_x	± 1	0	0	0
e_y	± 1	∓ 0.017	± 0.013	∓ 0.013
e_z	± 1	0	0	0
α	± 1	0	0	0
β	± 1	0	0	0
γ	± 1	∓ 2.608	± 1.973	± 2.020
m_2	± 1			
e_x	± 1	0	0	0°
e_y	± 1	∓ 0.018	∓ 0.013	± 0.014
e_z	± 1	0	0	0
α	± 1	0	0	0
β	± 1	0	0	0
γ	± 1	0	∓ 0.02	∓ 0.02
m_3	± 1			
e_x	± 1	0	± 0.035	0
e_y	± 1	0	0	0
e_z	± 1	0	0	0
α	± 1	0	0	0
β	± 1	0	0	0
γ	± 1	0	∓ 0.029	0

3.2. Floating Reference Point. Besides the above advantage in alignment, the location mode of floating reference point has its advantage in the replacement of production line. As shown in Figure 8(a), when the traditional fixed stage reference point is used, the work piece center of the next production line should be put on the stage reference point before the production line is changed. In other words, more products represent more replacements. If there is error between the center of work piece and the relative position of stage reference point, the processing quality will be influenced. If the floating center is used, as shown in Figure 8(b), the production line can be changed by keeping to the side; only one replacement is enough for the work pieces in different sizes. As the floating reference point technology can set any position as the reference point, even if there is large offset between the work piece and the center of XXY stage, the alignment function of the stage will not be influenced.

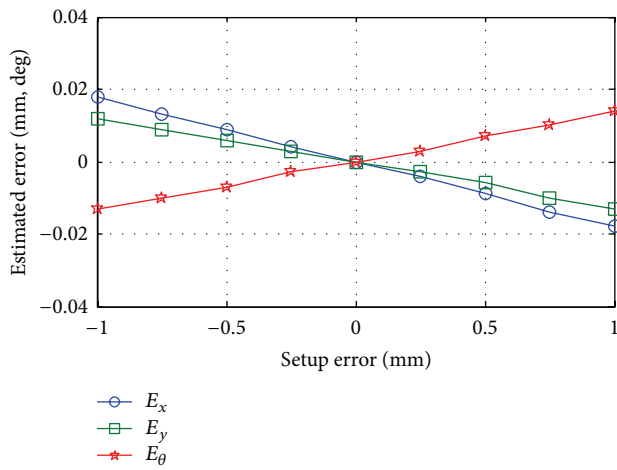
3.3. Mark Recognition. For the image alignment, besides the alignment stage and alignment algorithm, another key point is the mark recognition capability. If the mark recognition is not stable and robust enough, alignment accuracy will decline. In practical application, the changes in external environment and the accuracy of mark recognition are considered. Figure 9 shows different cases: 001 to 004 are general cases, 005 is underexposure, 006 to 009 are overexposure, 0010 to 0013 are incomplete mark, 0014 represents the image without mark, 0015 represents a half of mark out of picture, and 0016 and 0019 represent the photo with noise



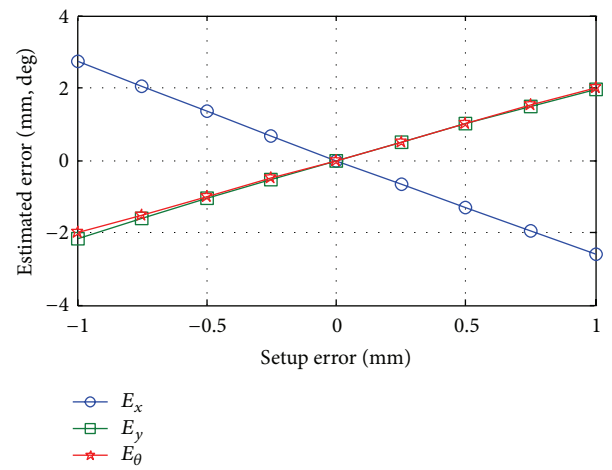
(a)



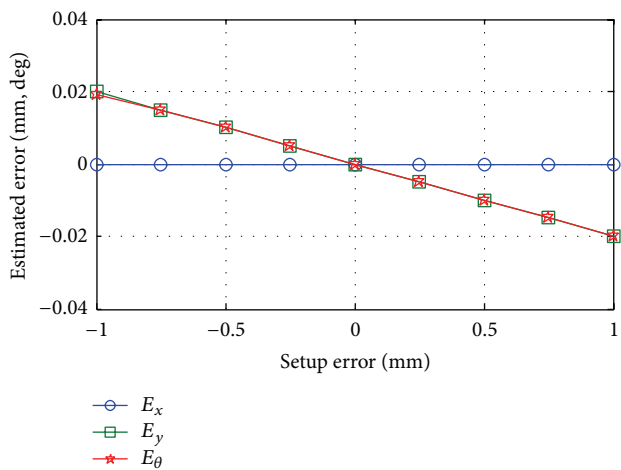
(b)



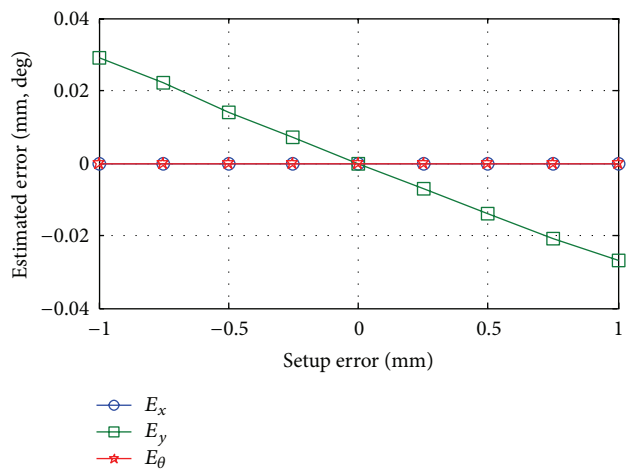
(c)



(d)



(e)



(f)

FIGURE 5: Positioning error estimation results: (a) ex_3 ; (b) ey_1 ; (c) ey_2 ; (d) γ_1 ; (e) γ_2 ; (f) γ_3 .

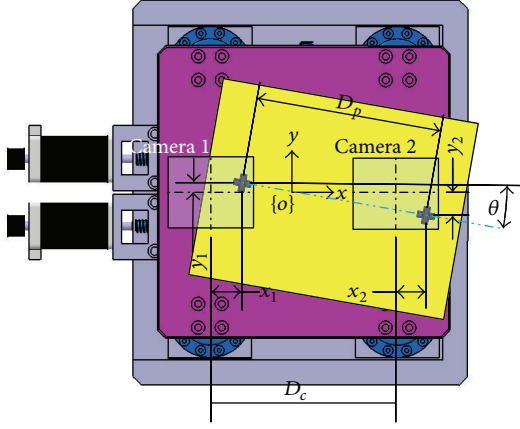


FIGURE 6: Basic concept of image alignment.

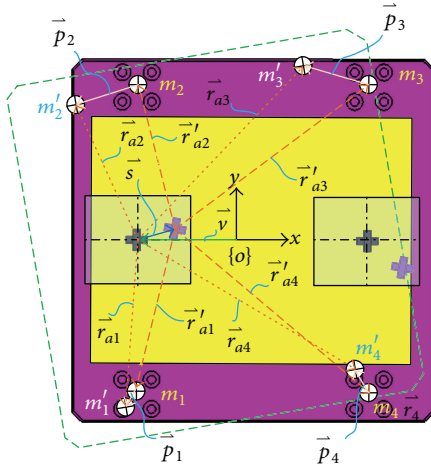


FIGURE 7: Conceptual graph of analysis of image alignment.

images. The above phenomena are probable cases, which have discussed in many studies. Generally, the pattern image must be clear enough, complete, and small orientation angle for high precision alignment. The image processing procedure in this study is described below: during image processing, the actual image (Figure 10(a)) and pattern image (Figure 10(b)) are binarized. The captured image is binarized as shown in Figure 10(c), and then the binary image is smoothed and morphologically processed to obtain a cleaner binary image as shown in Figure 10(d). The binarized image is compared with the pattern image. If they match, the region of interest (ROI) is set, and then the ROI image is subtracted from the pattern image (Figure 10(e)).

Let the image to be searched be denoted by I , the pattern image denoted by T , and the matched score denoted by R . The matched score is evaluated by the following equation:

$$R(x, y) = \sum_x \sum_y [T(x', y') - I(x + x', y + y')]^2. \quad (12)$$

The method above is called square difference matching method. For the case of perfect match, R is zero; otherwise,

R is large when bad matches. If the number of R is smaller than the preset threshold, the sample matching is completed (Figure 10(f)). In order to fasten the mark recognition speed, the image pyramid is used in this study. The original image is denoted by I_0 and the pattern image is denoted by T_0 . The first level image pyramid of original image and pattern image are denoted by I_1 and T_1 , respectively, and the second level are denoted by I_2 and T_2 . The width and height of I_1 and T_1 are half of T_0 and I_0 . The image size of I_2 and T_2 are quadrant of I_0 and T_0 . Thus, the mark recognition time of I_2 is 16 times faster than I_0 . Let the searched mark position be (x_2, y_2) . However, the position is not real mark position on the original image. So, we do mark recognition for I_1 . Now, we do not need to search full image this time. We set a range of interesting (ROI), which is a rectangle area, and the mark recognition is done in the ROI. The ROI starts from the point of $(2x_2 - 0.5W_{T_1} - 1, 2y_2 - 0.5H_{T_1} - 1)$ to the point of $(2x_2 + 0.5W_{T_1} + 1, 2y_2 + 0.5H_{T_1} + 1)$, where W_{T_1} and H_{T_1} are the width and height of T_1 , which means that the area of second mark recognition remains 3×3 . If the position of the second mark recognition is (x_1, y_1) , similarly, we set a ROI for I_0 . The left-top point of the ROI is $(2x_1 - 0.5W_{T_0} - 1, 2y_1 - 0.5H_{T_0} - 1)$ and the width and height of the ROI is $W_{T_0} + 1$ and $H_{T_0} + 1$, respectively. Here, the area of mark recognition for T_0 is still 3×3 . After mark recognition, the mark position (x_0, y_0) can be determined. Image pyramid not only makes the image small but also makes the image large. If we do the procedure above one time, when the processed image size now is the double of the original image, we can get the mark position (x_1', y_1') . To transfer the mark position to the original, the mark position is $(0.5x_1', 0.5y_1')$. In other words, when we large the image N times by image pyramid method; the mark recognition resolution can be increased N times to achieve subpixel resolution. However, large N makes long mark recognition time.

4. System Verification

In this paper, the coplanar XXY stage for system verification is produced by Chiu Yan Technology. The motion control card is NI PCI-7390. The industrial camera is Basler ace1300-30 gm equipped with 1X low distortion telecentric lens. The optical resolution is about $3.75 \mu\text{m}$; the field of view (F.O.V) is $9.6 \text{ mm} \times 7.2 \text{ mm}$. The image is processed by OpenCV. The stage is measured by Keyence GT2-H12K. When the optical system is in alignment, the resolution of optical system is increased by four times by using subpixel; namely, the subpixel processed image resolution is less than $1 \mu\text{m}$, theoretically.

4.1. Synchronism of Stage Location. As the movement of XXY stage in X -direction is resulted from the movement of m_1 and m_2 , when m_1 and m_2 are asynchronous, the stage will have θ displacement. As shown in Figure 11, when the XXY stage moves in X -direction (from 0 mm to 10 mm), the positioning repeatability is about $\pm 1 \mu\text{m}$. The angular error is very small (less than 5 arcsec), and the repeatability is good. The interference in Y -direction is about 0.13%. From

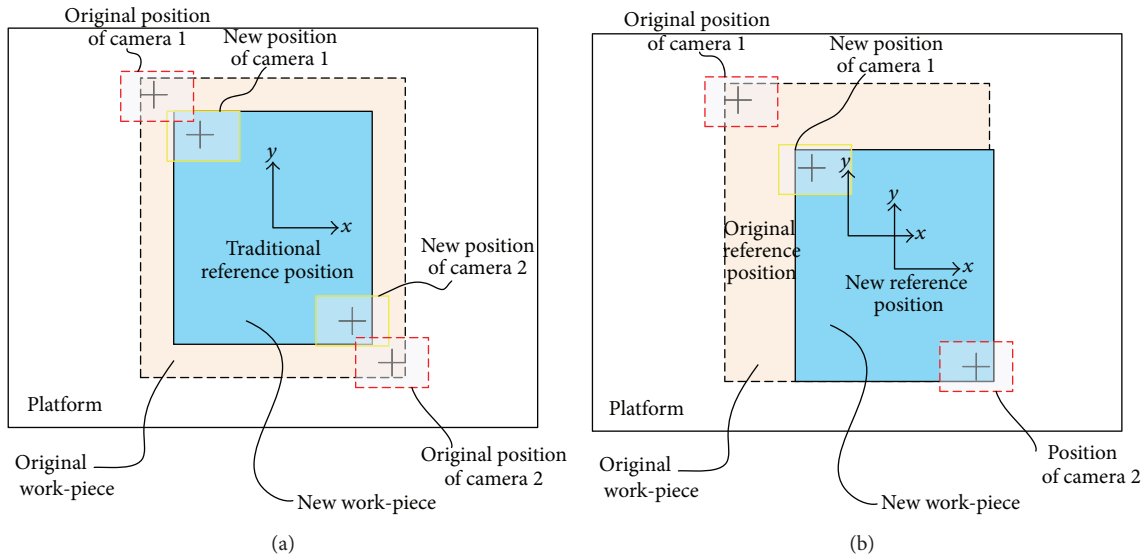


FIGURE 8: Comparison between floating reference point and fixed reference point: (a) fixed reference point; (b) floating reference point.

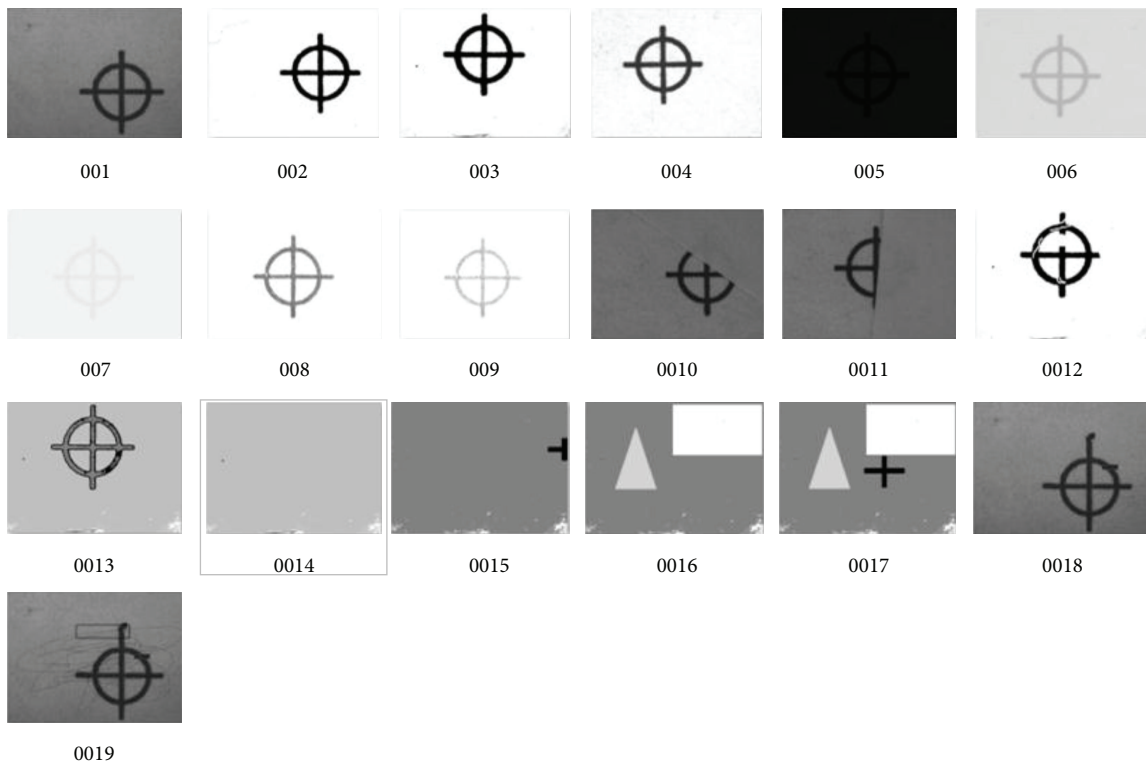


FIGURE 9: Different alignment pattern image with different quality.

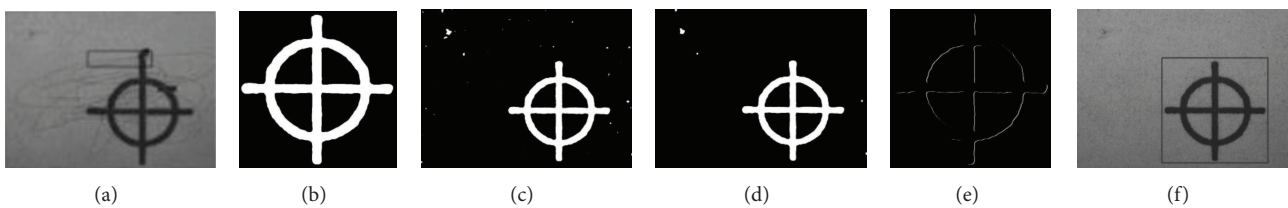


FIGURE 10: Pattern image processing steps. (a) Origin image; (b) pattern image; (c) binarization of origin image; (d) smoothly of the binary image; (e) difference after pattern matched; (f) searched pattern position.

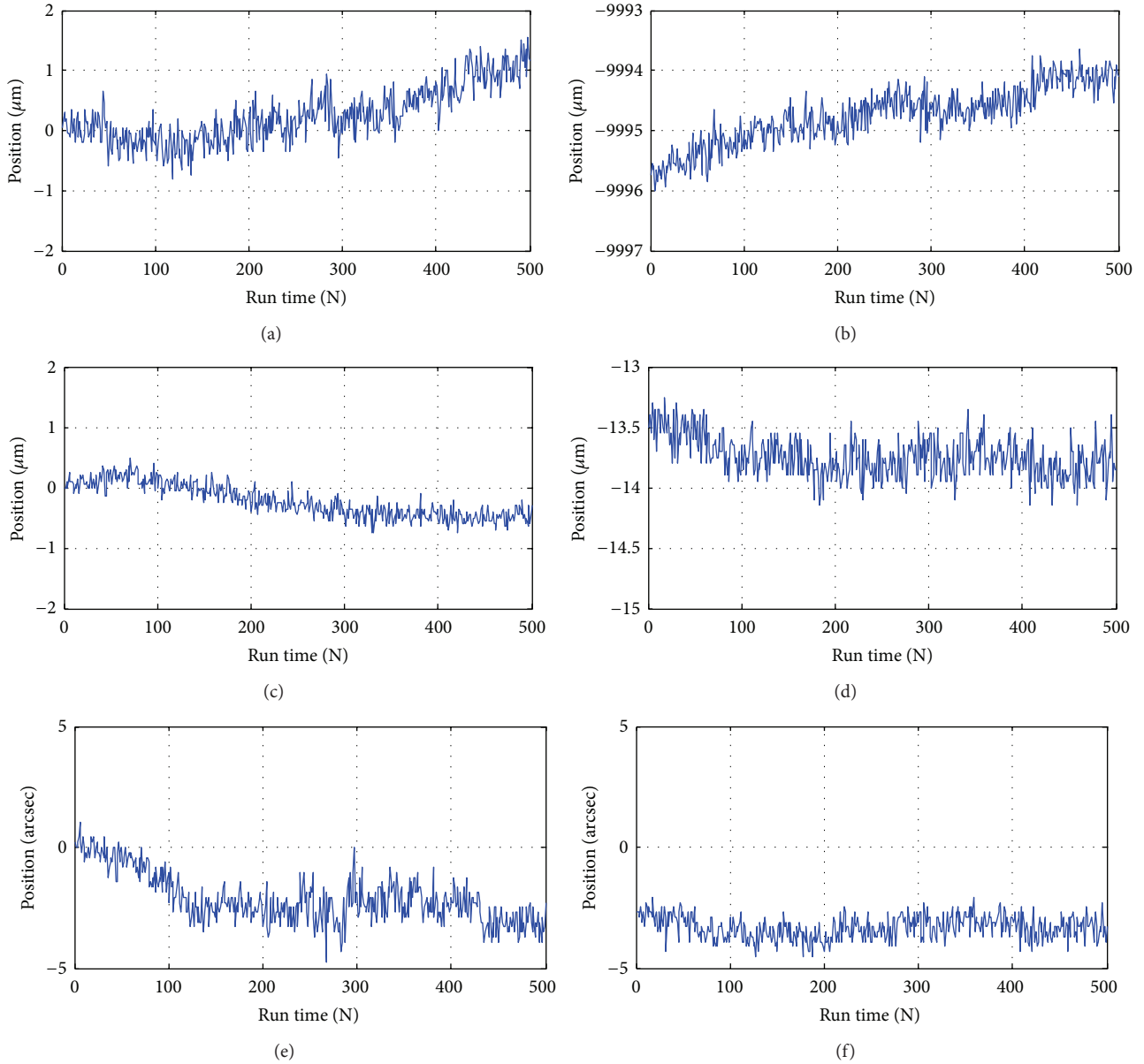


FIGURE 11: The positioning repeatability of X-axial motion of XXY stage: (a) X starting point; (b) X end point; (c) position of Y-axis when X is at starting point; (d) position of y-axis when x is at end point; (e) position of θ -axis when X is at starting point; (f) position of θ -axis when X is at end point.

Figures 11(e) and 11(f) we can see that m_1 and m_2 have good parallelism performance.

The movement of XXY stage in Y-direction is resulted from the movement of m_3 . As shown in Figure 12, when the stage moves in Y-direction (from 0 mm to 10 mm), the positioning repeatability is about ± 2 mm. When Y is at the stroke end, the angular error is about -109 arcsec. The repeatability is still good, and the interference in X-direction is about 0.35%. We conjecture that large positioning error of X-direction is not because of setup error, but because of friction force. As shown in Figure 14, assumption of the desired displacement is δ_y ; Y-direction displacement of motor 2 is less than δ_y due to friction force. The phenomenon is similar to the gantry type of stage. Figure 13 shows the

positioning repeatability of rotation motion; the stage was rotated from 0 degrees to 3 degrees. The angular positioning repeatability is $\pm 0.001^\circ$ (about ± 3 arcsec).

4.2. Floating Reference Point Test. In order to validate the feasibility of floating reference point, the pattern image center captured from CCD1 (mark1) is set as the reference point for movement, as shown in Figure 15. Ideally, the reference center should be not changed when we rotated the stage around the reference center. The top part of Table 2 shows the result of rotation of the stage at negative angles (0.05° each time) when the mark1 is in the initial center position (-319.8 mm, 127.9 mm). The bottom part of Table 2 shows the result of

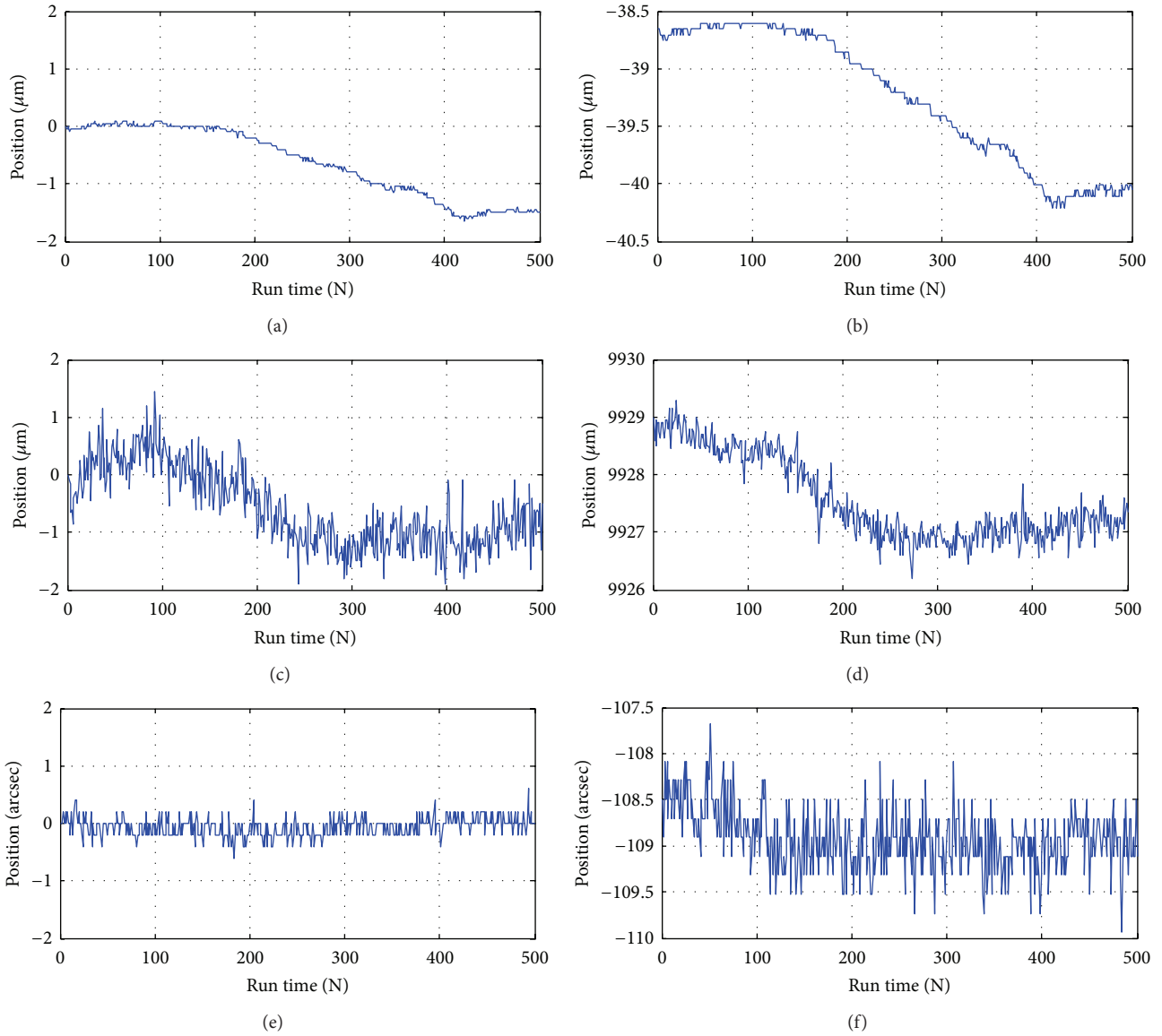


FIGURE 12: The positioning repeatability of Y -axial motion of XXY stage: (a) position of x -axis when Y is at starting point; (b) position of x -axis when Y is at end point; (c) Y starting point; (d) Y end point; (e) position of θ -axis when Y is at starting point; (f) position of θ -axis when Y is at end point.

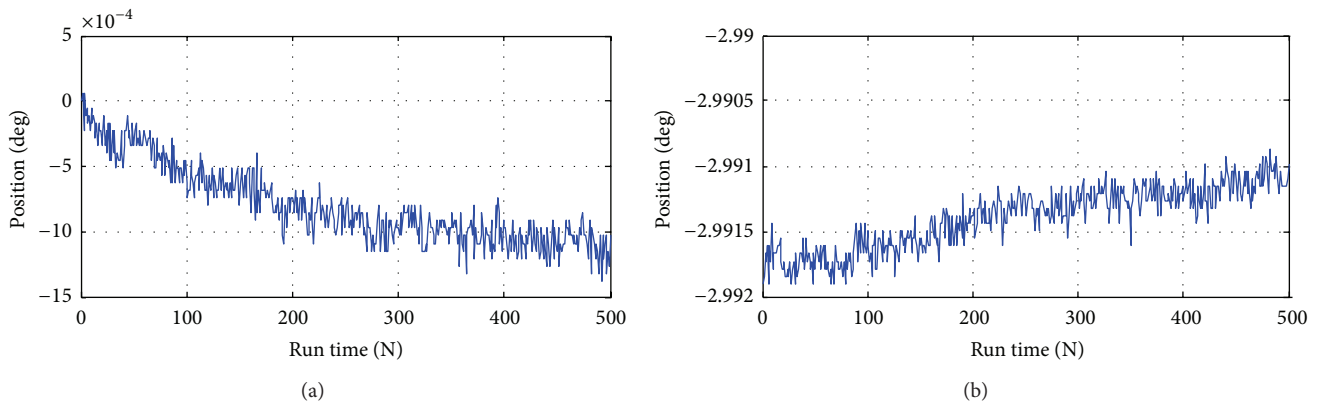


FIGURE 13: The positioning repeatability of rotation motion: (a) θ starting point; (b) θ end point.

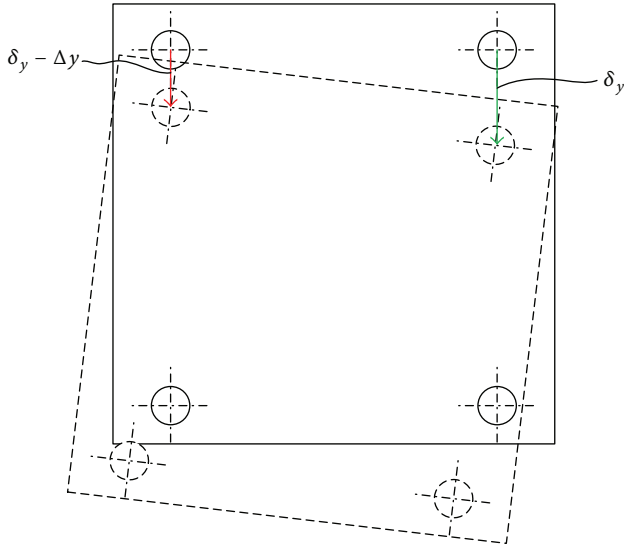


FIGURE 14: Illustration of positioning error due to friction force.



FIGURE 15: Take sample center on CCD1 as reference center.

rotation of the stage at positive angles ($+0.05^\circ$ each time) when mark1 is in the initial center position (0 mm, 0 mm). The results show that the reference center difference amount in X- and Y-directions are about $10 \mu\text{m}$ and $20 \mu\text{m}$.

4.3. Alignment Repeatability Test. The practical optical alignment uses a touch panel tester (capacitive test) produced by Chiuan Yan Technology as the testing machine as shown in Figure 16. The object for alignment was a capacitive type of touch panel glass ($10.5''$, $232 \text{ mm(L)} \times 135 \text{ mm(W)}$). During the test, the stage was randomly moved, in order to move the glass to leave the alignment target point (or alignment reference point), and then started alignment procedure. The preset alignment accuracy was $\pm 1 \mu\text{m}$, and the maximum alignment times were three for each alignment motion. The experimental results are shown in Figures 17 and 18. Each alignment motion of this system was shorter than one second, and each alignment motion could be completed within three times of correction. The alignment accuracy of the system was $\pm 1 \mu\text{m}$ and $\pm 5 \text{ arcsec}$.

5. Conclusions

The paper proposed a visual servo control and image alignment system using a special design coplanar XXY stage. The kinematic analysis and setup error influence were also

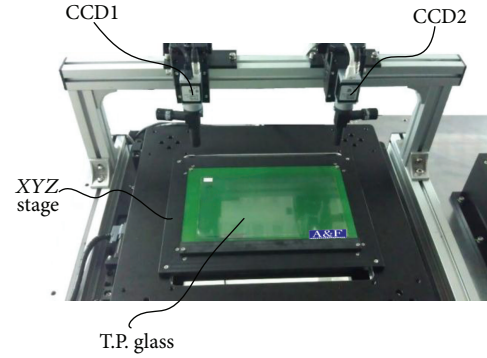


FIGURE 16: Optical alignment system structure.

TABLE 2: Result of floating reference point movement centered on CCD1 sample center.

Rotation angle (degree)	Center position (μm)	
	x	y
-0.5	-326.7	113.7
-0.45	-326.0	116.0
-0.4	-326.7	113.7
-0.35	-326.7	114.4
-0.3	-325.2	119.2
-0.25	-323.3	123.9
-0.2	-322.9	130.2
-0.15	-323.7	130.2
-0.1	-322.9	128.6
-0.05	-321.4	124.7
0	-319.8	127.9
0	0	0
0.05	1.5	0.8
0.1	1.5	1.6
0.15	2.3	3.9
0.2	3.8	2.4
0.25	5.4	2.4
0.3	6.1	6.3
0.35	6.9	4.7
0.4	7.7	7.9
0.45	9.2	14.2
0.5	10.7	17.4

discussed in the paper. A floating reference point based image alignment method was presented for decreasing the influence on each alignment process between the change of the work piece center and the stage reference point. It has better adaptability when the work piece is changed; provided with a stable coplanar XXY stage system, high-precision image alignment can be implemented. Thus, this system also shows good stability. Each alignment motion of this system was shorter than one second, and each alignment motion could

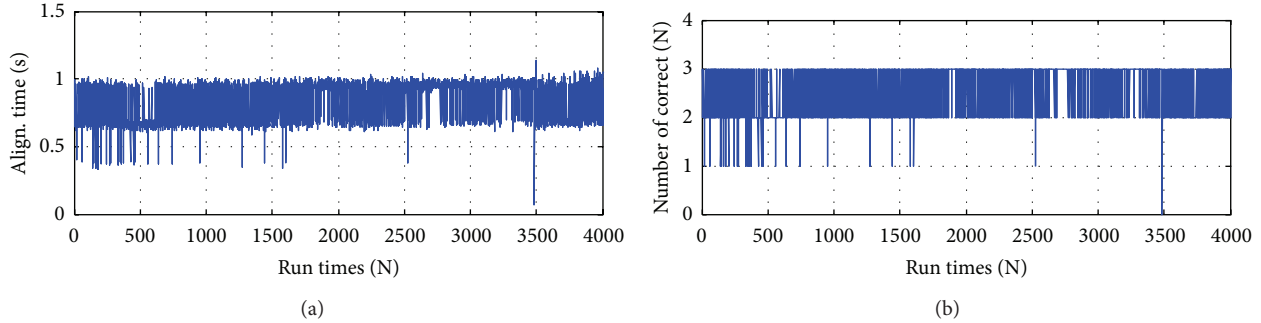


FIGURE 17: Experimental result 1 of positioning repeatability of image alignment (4,000 times of alignment). (a) Alignment completion time; (b) times of alignment completed.

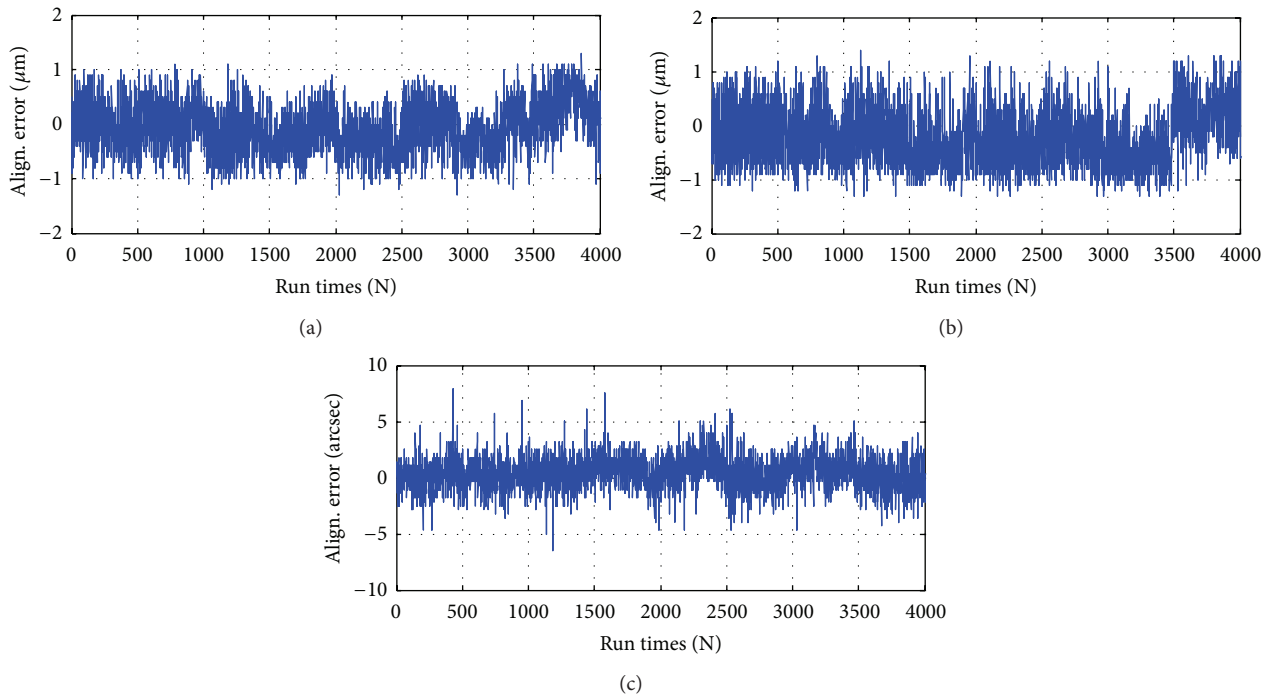


FIGURE 18: Experimental result 2 of positioning repeatability of image alignment (4,000 times of alignment) (a) X-direction; (b) Y-direction; (c) θ -direction.

be completed within three times of correction. The alignment accuracy of the system was $\pm 1 \mu\text{m}$ and $\pm 5 \text{ arcsec}$.

Acknowledgment

The work was supported by National Science Council, Taiwan (NSC. 100-2221-E-005-091-MY3 and NSC 101-2218-E-005-004-).

References

[1] W. M. Kuo, S. F. Chuang, C. Y. Nian, and Y. S. Tarn, "Precision nano-alignment system using machine vision with motion controlled by piezoelectric motor," *Mechatronics*, vol. 18, no. 1, pp. 21-34, 2008.
 [2] Y.-H. Lin, C.-H. Chen, and C.-C. Wei, "New method for sub-pixel image matching with rotation invariance by combining the

parametric template method and the ring projection transform process," *Optical Engineering*, vol. 45, no. 6, Article ID 067202, 2006.
 [3] J.-H. Lee, Y.-S. Kim, S.-R. Kim, I.-H. Lee, and H.-J. Pahk, "Real-time application of critical dimension measurement of TFT-LCD pattern using a newly proposed 2D image-processing algorithm," *Optics and Lasers in Engineering*, vol. 46, no. 7, pp. 558-569, 2008.
 [4] Y.-S. Li, T. Y. Young, and J. A. Magerl, "Subpixel edge detection and estimation with a microprocessor-controlled line scan camera," *IEEE Transactions on Industrial Electronics and Control Instrumentation*, vol. 35, no. 1, pp. 105-112, 1988.
 [5] S.-J. Huang and S.-Y. Lin, "Application of visual servo-control X-Y table in color filter cross mark alignment," *Sensors and Actuators A*, vol. 152, no. 1, pp. 53-62, 2009.
 [6] S. Mori, Y. Sato, A. Sakurada, A. Naganawa, Y. Shibuya, and G. Obinata, "Nano-motion stage for high-speed and precision

- positioning on an X-Y plane," *IEEE Transactions on Magnetics*, vol. 45, no. 11, pp. 4972–4978, 2009.
- [7] C. H. Liu and W.-Y. Jywe, "A four-degrees-of-freedom microstage for the compensation of eccentricity of a roundness measurement machine," *International Journal of Machine Tools and Manufacture*, vol. 44, no. 4, pp. 365–371, 2004.
- [8] W.-Y. Jywe, Y.-R. Jeng, C.-H. Liu et al., "A novel 5DOF thin coplanar nanometer-scale stage," *Precision Engineering*, vol. 32, no. 4, pp. 239–250, 2008.
- [9] C.-H. Liu, W.-Y. Jywe, Y.-R. Jeng, T.-H. Hsu, and Y.-T. Li, "Design and control of a long-traveling nano-positioning stage," *Precision Engineering*, vol. 34, no. 3, pp. 497–506, 2010.
- [10] H. J. Yim, Y. H. Lee, S. H. Lee, J. Il Jeong, and S.-H. Lim, "Multi-layer alignment control of a large area nano-imprinting stage," *Journal of Mechanical Science and Technology*, vol. 23, no. 4, pp. 1094–1097, 2009.

Research Article

An Achievement Prediction Model of Meaningful Learning, Motivation, and Cognitive on SPANI: Partial Least Square Analysis

Kuo-Kuang Fan,¹ Chung-Ho Su,^{1,2} Shuh-Yeuan Deng,¹ and Wei-Jhung Wang¹

¹ Graduate School of Design, National Yunlin University of Science and Technology, 123 University Road, Section 3, Douliou, Yunlin 64002, Taiwan

² Department of Digital Content Application & Management, Wenzao Ursuline University of Languages, 900 Min-Tzu 1st Road, Sanming District, Kaohsiung 80793, Taiwan

Correspondence should be addressed to Kuo-Kuang Fan; fankk@yuntech.edu.tw

Received 7 September 2013; Accepted 10 October 2013

Academic Editor: Teen-Hang Meen

Copyright © 2013 Kuo-Kuang Fan et al. This is an open access article distributed under the Creative Commons Attribution License, which permits unrestricted use, distribution, and reproduction in any medium, provided the original work is properly cited.

This paper employed an SPANI (Shooting Pose Adjustment with Nature Interactions) learning system with achievement prediction model of meaningful learning. Motivation, cognitive, and PLS (Partial Least Square) method was used to analyze the results. Proposed model is focused on information and communication technology teaching mode, meaningful learning, learning motivation, cognitive load, and learning achievement. Theories of SPANI achievement prediction model investigated the learner's degree of meaningful learning, learning motivation, cognitive loading, and learning achievement (Huang et al. 2012, Credé and Phillips 2011, Deleeuw and Mayer 2008, and Peterson et al. 2010). Questionnaire and systems tests were used with 107 valid samples in the samples' record to conduct narrative statistics, inspection of reliability and validity, and PLS of Structural Equation Modeling (SEM). The results show that the developing system is very helpful to learner's learning motivation and learning achievement. And learner's learning motivation, which influences the degree of the cognitive load and learning achievement, has a high relationship. It means, the designers of teaching materials can start with digital content to improve learning motivation and also handle the two important parts which are learning strategy and learning motivation. It can be very helpful in improving teaching quality.

1. Introduction

The use of technology covers a wide range of fields, and it includes the field of education. Technology can improve the quality of education. Digital technology has made many changes in teaching materials and aids and has become the essence of technological change in learning. To make use of the content found on the internet for teaching in synchronous or asynchronous ways, digital tools have been applied widely in recent years. Which kind of circumstances requires the use of the information and communication technology (ICT)? We should consider the most fundamental needs and goals of learners and then determine the appropriate teaching strategies and tools, including the media and even checklists of the learning results of students. Maleki et al. [1] developed the ICT teaching model to investigate the students' learning

in the area of information processing capability and their study pointed out that compared to the use of information and communication technology in a teaching mode, the experimental group had significant differences in learning absorption compared to the control group in this study. Maleki et al. [1] strongly recommended using ICT in teaching and claimed that it can improve student learning absorption and teaching quality.

Information technology is widely believed to be useful for increasing students' learning. However, students vary and the learning outcomes are not all the same. After all, each learners' motivation or cognitive load has differences, as was found in Ausubel and Robinson's [2] study which considered the value of learning new concepts through meaningful learning. The biggest factor which affects learning is the cognitive structure state. Kalyuga et al. [3] also mentioned many studies

that were based on the instructional design to reduce the extraneous cognitive load and give the appropriate cognitive load to assist teaching activities.

In addition to checking the learner's cognitive load, we considered researching whether the design of digital materials can enhance learners' motivation or not. Pintrich et al. [4] developed a measurement tool termed Motivated Strategies for Learning Questionnaire (MSLQ) that can be used to investigate learners' cognition for participation in learning tasks, motivation, and the degree of participation in different learning tasks under different learning strategies.

Similarly, how to test learners' absorption, how to prove that the things we learned have been absorbed, and related research also examined how to test the learner's learning achievement [5–8]. Purdie and Hattie [6] think that learning needs peers to communicate with each other. Also though knowledge has been arranged and absorbed, it still needs to be spoken out to be completely understood. Through the learners' narrations, researchers can examine whether the knowledge has been digested. Thus, if a learner can explain what they have learned to another, then that indicates that the learning has been successful.

For these above reasons, this study is based on the above criteria, and we design a digital program to teach correct shooting postures to serve as the learning material. Then, we use SPANI to analyze the learners' learning motivation, cognitive load, and learning achievements. This is the main motivation of this study.

Below, we will discuss some articles that are related to history, biological exploration, language learning, and geometry. We also examine basketball shooting posture or movements related to basketball. However, the amount of learning attitude research about basketball posture is mostly from overseas and their little research available domestically in this area.

In this study, we focus on meaningful learning, learning motivation, cognitive loading, and learning achievements as the theoretical basis. We discuss the relation between and impact of meaningful learning, learning motivation, the cognitive load, and learning achievements from the digital shooting posture correction learning materials of SPANI. The main purposes are summarized as follows.

- (i) Investigate the learners' association towards learning strategies, learning motivation, and learning achievements of SPANI.
- (ii) Investigate the learners' association towards learning strategies, the cognitive load, and learning achievements of SPANI.
- (iii) Investigate the learners' association towards learning motivation, and the cognitive load of SPANI.

2. Related Work

2.1. Information and Communication Technology Teaching Mode. Currently, the applications of Internet are being used in many fields, including the field of education. Nowadays, teachers not only can upload teaching materials online, but

can even use online teaching programs to instruct students. Through this way of learning, students can learn anytime and anywhere, if they want. It also helps students learn efficiently. Students and teachers should assess their needs and goals as the first consideration. Then they need to decide which teaching materials are most appropriate. Maleki et al. [1] mentioned that information explores the research of student's abilities in dealing with things and learning information which in experimental group of absorbing learning effects has noticeable differences within investigated group of absorbing learning effects. Furthermore, Maleki et al. [1] strongly suggested that people use it in teaching; it can improve students' efficiency of learning and improve the quality of teaching.

2.2. Meaningful Reception Learning. Meaningful reception learning can also be called meaningful learning. In 1963, Ausubel [9] interpreted what the meaning of meaningful reception learning is, based on his investigation about learning and consciousness. He states that encouraging students to make connections with the teaching material they have been taught along with things they have already known is what meaningful learning is all about. Ausubel and Robinson [2] indicated that via the idea of the meaningful reception learning students can achieve greater efficiency in learning because people have basic consciousness about the knowledge in this type of learning. They emphasized that the knowledge of teaching should use key concepts as the central idea and recommends teachers to give students suggestions if they raise the idea about organizing content [2, 9, 10].

2.3. Cognitive Load Theory. According to Sweller [11], there are three sources for the cognitive load as follows. Intrinsic cognitive load from the structure and complexity of the materials. Thus, depending on the complexity of the teaching materials or components in interactive projects, it takes learners different amounts of time to learn memory resources and understand the amount of information in textbooks [12]. Extraneous cognitive load is the source of the cognitive load when delivering textbook information or presenting it in a way to let learners spend learning memory resources in the teaching activities. Germane cognitive load is based on the load when learners understand how to deal with materials [13, 14].

The extraneous cognitive load and the germane cognitive load are usually used in instructional design textbooks when taking how to improve teaching effectiveness and efficiency into consideration. In many studies, these are based on the instructional designing to reduce the extraneous cognitive load and provide appropriate sources to assist in teaching activities [3].

The aim of instructional design is to see whether the degree of the cognitive load is acceptable to the learner or not. The intrinsic cognitive load depends on learners having prior knowledge and learning memory resources. In instructional design, it is unable to control these factors, but the learners can achieve the appropriate level of the cognitive load by the extraneous cognitive and the germane cognitive load.

2.4. Motivated Strategies for Learning Questionnaire. Learners may perform because of motivation, cognition, and learning behavior to select multiple types of academic tasks across different courses (e.g., attend seminars in major courses or select a general education curriculum) or choose different types of learning tasks in the same course (such as prepare a multiple-choice exam or write a glossary report). Every learner in the learning process needs to have self-learning process of situational tests [15]. Empirical research indicates that the self-learning processes and learning mechanisms need a variety of information about the structure of self-measurement, and these must be valid and also a reliable measurement of autonomous learning. Pintrich and colleagues [4] developed a detection method called Motivated Strategies for Learning Questionnaire (MSLQ). The incentive motivation questionnaire is used to investigate learners' cognitive involvement in learning task, and the motivation and degree of participation for learning tasks in different learning strategies.

The learning motivation scale contains 15 dimensions and totally has 81 items in the questionnaire. It is used to investigate whether the students have strong motivation to participate in courses and test learning strategies. The seven point Likert scale is used as the measurement tool. Among the 81 questions, there are eight negative worded items. There are 31 questions. Among these 31 questions, there are six measurement scales to investigate students' oriented motivation in the academic curriculum. These six measurement scales are based on three motivation theories, such as the value component, expectancy component, and affection component [16].

2.5. Learning Achievements. The basis of learning achievement originated from the investigation made by Säljö [17]. In the investigation of Säljö's [17] research, Säljö examined every age group of people and related the meaning of learning to them. Säljö did his investigation to find 5 aspects of learning achievements and has six subjects [18] to discuss the perspective, the learner's process of learning, and finally how learners prove they really understand the knowledge they have learned. The relative investigation also proves the six aspects of learning achievement [5–8].

3. Research Framework

According to Ausubel et al. [10] who proposed the meaningful learning theory, this study will use it as the learning framework combined with Sweller's [19] cognitive load theory. We use Pintrich's et al. [4] measurement tools, which confer the learning conditions which learners have after having used these digital learning materials and uses. Then, we use assessing student's conception of learning [6] as a learner learning achievement for checking and evaluation. This research framework is shown in Figure 1.

3.1. Research Hypotheses. According to the related research, this study proposes the following assumptions.

- (H1) Using proper learning strategies to enhance learning motivation has significant influences.

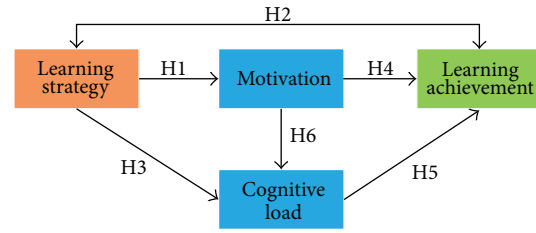


FIGURE 1: Research framework.

- (H2) Using proper learning strategies to enhance learning achievements has significant influences.
- (H3) Using proper learning strategies to enhance the cognitive load has significant inverse influences.
- (H4) Using proper learning motivation to enhance learning achievements has a significant positive relationship.
- (H5) The cognitive load has a significant inverse relationship with learning achievement.
- (H6) Learning motivation has a significant relationship with the degree of the cognitive load process ability.

3.2. Research Subjects and Data. This study focuses on the users of digital learning shooting posture correction materials which were developed specifically for this research. It targets college students as the research subjects to explore the research related to meaningful degree of learning, motivation of learning, cognitive load, effects of learning, and learning achievements when using a digitally designed lesson program to instruct the correct posture while shooting. This study aimed to correct college students' shooting posture for different poses, including the following: standby pose, aim pose, release pose, and shooting pose. This study used judgmental sampling. In order to reduce the incidence of invalid questionnaires, the researcher explained each point or problem that needed any explanation as they came up.

4. System Framework and Description

The system developed in this study uses the Nature Interaction of Shooting Pose Adjustment Program that is used by Nature Interaction (SPANI). It includes a shooting position tutorial and a test for the correct basketball shooting posture. Shooting position tests of shooting postures are designed for both right-handed and left-handed people. SPANI system framework is shown in Figure 2 above.

4.1. System Design. The SPANI system is built on the game engine Unity 3.4.1. We need a database for the information storage of the data we collect on the subjects' shooting posture. This study used C# and JavaScript languages to implement the system requirements. For the hardware identification detection, we used Asus Xtion Pro. Next, we will introduce the processes of the system, the database, and the system interface.

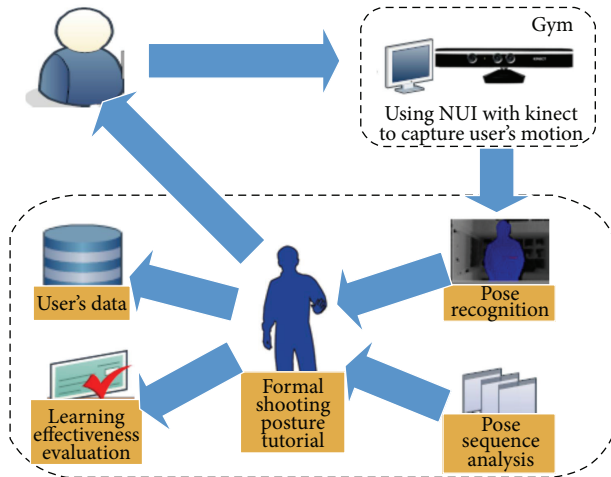


FIGURE 2: SPANI system framework.

We used the local database using MySQL Workbench 5.2 CE, the Unity linked database, and also C# (C-Sharp) language to access the language to load the information.

Images can be divided into foreground and background images, and because of the depth numerical value, a lot of depth sensors define the optimum sensing range to be 0.8 meters to 3.5 meters and the effective angle of depth camera has a 70° angle. The depth sensors have detected the skeleton set of depth numerical values and imported the 3D models to obtain the skeleton information and then they have combined them together. The 3D data can orientate each user's joint depth in an action and then turn that image into the three-dimensional coordinates (X , Y , and Z). The system uses the depth camera to detect when a motion is not correct during the activity and produces three dimensional coordinates. This is the character control. The 3D models in the system are the system which catches a user's three-dimensional coordinate interfaces when he or she is doing the action. Meanwhile, the action's feedback of the 3D model is from the user. In other words, as a user's action changes, the actions of the three-dimensional model will change too.

4.2. Character Control. Use the OpenNI's software development kit (SDK) [20] that was provided specifically for the game engine used in Unity 3D. The software development kit provides the skeleton information correspondence and then makes the 3D modeling software MAYA and joint information including Joint, Inverse Kinematics, and Forward Kinematics into the game engine. Also, the above makes the joint information correspond with the joint information of the software development kit and completes the model and links with OpenNI.

4.3. System Operational Process. According to the basketball shooting position key actions which were mentioned before, they are the standard actions that this research has defined related to basketball free throws. These above mentioned four actions are listed as the key actions, and the name label and

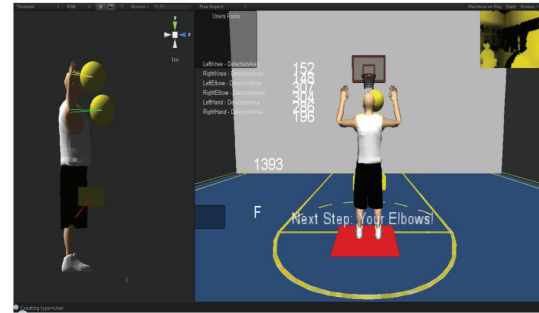


FIGURE 3: Material demonstration.

definitions are used to obtain the three dimensional coordinates' values of the fuzzy set. The position identification procedure pictured in Figure 4 illustrates how this process operates. The Nature Interaction Device utilizes OpenNI to receive preliminary skeleton frame information and orientates each skeleton coordinate with the game engine, and it uses the Trapezoid membership function to judge the standard area. With user's key actions, it will start to check whether the coordinates are in the area of the Trapezoid membership function or not. If it identifies user's actions that have been successful, then it will record user's key actions into the motion sequence that the user has created; if it failed, it will record the results into the motion sequence that the user has created. According to whether the user's key actions are identical to the key motion sequence orders and actions, it will continue to record the user's key actions until all have been completed. Material demonstration is shown in Figure 3.

4.4. Design of Teaching Activities. This section will introduce the design of the teaching activities in this investigation. The investigation is mainly designed for assisting users through interactive instruction to correct the wrong posture when shooting basketballs. Students are not only taking in the knowledge the teacher has taught in class, but are also learning actively. The passive way of learning is not an effective way for students to absorb knowledge or the so called bias or incomplete results. This study hopes to design a student-oriented teaching environment. The previous chapter has introduced the system ability to detect specific joints and detective area. The operating of the study can be accomplished by the depth camera's depth views, which instructs users when their movements are incorrect and when they are correct. In conclusion, users can learn through a physically interactive method to assist learning of the correct posture to shoot a basket.

The teaching activity environment has been developed in an indoor area that provides a large space.

The investigation used the high school physical education and information technology instructions from the Ministry of Education in Taiwan [21] as a reference material. The investigation particularly refers to basketball and is mainly designed to instruct the correct posture to shoot a basket. The design of the teaching activity in the investigation has been

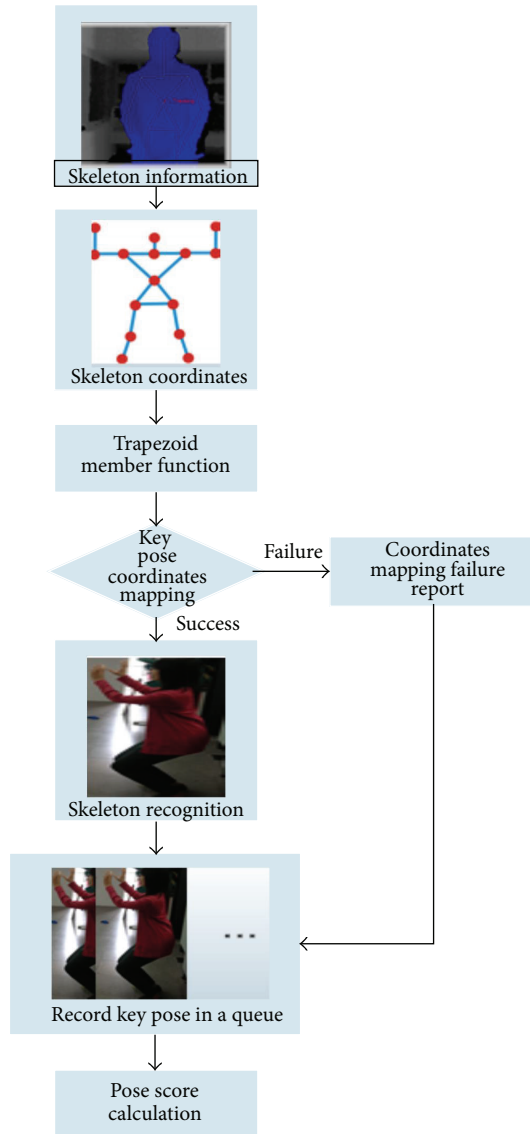


FIGURE 4: Position identification procedure.

divided into 4 scenes. In the teaching activity, users learn through interacting with a depth camera and with a motion-sensing interactive software to carry on the teaching of the correct posture before shooting the basket. At the same time, users can learn through interactive motion sensing to manipulate the character in the material of shooting posture. In the four levels, the study will design teaching goals to initiate the users to accomplish various tasks and how to be successful in learning to shoot a basket with the correct posture. There are four kinds of instructional activities in total. Each of teaching activity has its teaching goal, a way to do the interaction, and finally a way to teach the acquisition of the skills.

Scene 1. Standby pose instructs users to position their joints in the detection area as specified by the system.

This scene of teaching activities is designed to assist users in having the correct posture for the shooting position as a Standby pose. Users are viewed through the depth camera

and have interaction with the virtual characters, and then the users need to adjust their own joints to conform to the view shown in Scene 1, which shows the hand at the waist in the detection area and in front of the knee in the detection area. When users make their posture conform to the instructions, as shown in Scene 1, the system will give them feedback. Users can learn through the feedback and then adjust their joint position again. The essential tips of this program are that it stabilizes breathing and emotions before shooting, and after stabilizing these, the knee are bent slightly in the instructions. This is to instruct users about the power of bent knees to assist the arms in shooting a basketball.

Scene 2. Aim pose instructs users to adjust joints based on the system's specified instructions and places them in the detection area.

This part of the instruction is designed to assist users to prepare certain movements prior to attempting to shoot a basketball. The user interacts with the virtual character in teaching material through the depth camera. The users need to adjust the position of their joints at the same time, in accordance with the instructions presented in Scene 2. The hands need to be in the detection area, in order to accord with the definition in Scene 2 at hand detection in the chest area. The height between the chest and stomach is elbow detection area. The knee detection area is in front of knee. When users do the posture and meet the demands presented in Scene 2, the system will provide feedback. Moreover, the users can readjust their joint positions based on the feedback. The important part of this action is using the eyes to focus on the rim and prepare to shoot a basket. Scrunch up the joints of the elbows, and tighten the angle of the elbows to less than 90° degrees. The reason why users are instructed to tighten the angle of the elbows to less than 90° degrees is because users can shoot the ball with a shorter radius and even make a more stable and effort-saving shot.

Scene 3. Shooting pose instructs users to position their joints in the detection area as specified by the system.

This part of the instruction is designed to assist users to prepare the holding movement. The users position themselves based on the virtual people in the teaching material, according to the depth view provided by the depth camera. The users simultaneously need to adjust the position of their joints, in accordance with the instructions provided in Scene 3 in the detection area, which shows where the hands and head are to be. It also shows the correct height between the shoulders and elbows in the detection area, and the position of the knees is in front of knee. When users do the movements according to the instruction in Scene 3, the system will provide feedback. Moreover, the users can readjust their joints based on this feedback. The important point of this movement is the stretching out of the fingers and holding the ball in the correct way. Instead of using the palm to hold the ball, users should hold the ball with their fingers to control the direction where it will go.

Scene 4. Release pose instructs users to touch the detection block that is specified by the system.

This part of the instructions is designed to assist the users with the correct movements as shooting. The users interact with the virtual character in the teaching material through the depth view provided by the depth camera. The users need to simultaneously adjust the positions of their joints to be in accordance with the instructions provided in Scene 4. When users do the movements correctly according the instructions in Scene 4, the system will provide feedback. Moreover, the users can readjust the positions of their joints according to this feedback. The important part of this movement is to instruct users to properly let the ball rub against their fingertips as it is released, giving the ball backspin, which will increase the chances of successfully making the shot.

5. Outcome Analysis of the Investigation

5.1. Analysis of Pretesting. After completing the design of the questionnaire, there were 34 questions. Furthermore, the questionnaire was tested for validity prior to being used for collecting data. Before conducting the pretesting, the questionnaires needed to be processed through the SPANI system which in this investigation has been designed to instruct students in the proper posture for shooting a basketball. The pretest questionnaires were filled out and returned prior to the actual testing. The administration of the pretesting questionnaires was done with the assistance of other college students. These students, generously, gave their time to assist me with the conduction of the investigation. It took 17 days to finish the pretesting. All the 51 questionnaires were collected on the spot. In order to make sure of the reliability of the questionnaires, I, immediately, put all the questionnaires into SPSS 21.0 system to do the reliability analysis. The measurement of reliability is through Cronbach's α value as the basis. Preadvance deleted out the questions that can improve the Cronbach's α value. Among the meaningful learning, learning motivations, cognitive load, and learning achievement can reach Cronbach's α value which is larger than 0.7. However, the total Cronbach's α value was up to 0.935, and it indicates that no matter whether the Cronbach's α value was only in one aspect for the questions or was for all the aspects, there would be high correlation.

5.2. Analysis Sample of Structure. The questionnaire of this investigation is mainly designed for college students as the research target. This investigation adopts judgmental sampling to take the samples. The distribution of questionnaires was done with the help of my college friend. In each time the experiment was to be done, I describe the purpose of research, introduce the name of the system, make an introduction of the system and finally demonstrate the operation of the system to the research participants. After the users perform the tasks specified by the program, the researcher next would explain how to fill out the questionnaire.

The questionnaires were distributed on the spot. 129 questionnaires were handed out and 129 were collected.

One questionnaire was later omitted because of a missing value, and also 21 questionnaires were later omitted because the answers were not in accord with the previous answers they

TABLE 1: Frequencies and percentage of observed variables.

Variable	Level	Frequency	Percentage
Gender	Female	61	57%
	Male	46	43%
Habit of exercise	Do not have habit of exercise	34	31.8%
	Have the habit of exercise	73	68.2%
	0 times	16	14.9%
	One to two times	66	61.7%
The times of exercise in every week	Three to four times	23	21.5%
	Five to six times	2	1.9%
	more than seven times	0	0%
	30 minutes	45	42.1%
Each exercise time	31–60 minutes	47	43.9%
	61–90 minutes	10	9.3%
	91 minutes or more	5	4.7%

TABLE 2: Latent variable correlations.

Variables	CL	LA	LM	ML
Cognitive load (CL)	0.73			
Learning achieve (LA)	0.15	0.76		
Learning motivation (LM)	0.17	0.71	0.82	
Meaningful learning (ML)	-0.029	0.61	0.71	0.73

had filled in. Finally, there were 107 valid questionnaires, with a percentage of 82.9%.

There are 107 valid samples of the questionnaire. The data from these questionnaires were submitted to personal profile analysis and the following categories were included: gender, exercise habits, weekly exercise frequency, and total time spent exercising each session. Table 1 illustrates the frequencies and percentage of observed variables.

5.3. A Measurement Model of Evaluation. In structural equation modeling (SEM) analysis, the SEM analysis is divided into the measurement model and the structural model. And PLS analysis procedure is divided into two stages: the first stage tests for measurement reliability and validity test analysis and the second stage of the model measurement is a path coefficient to estimate the explanatory power of the model prediction and verification.

5.3.1. Reliability Analysis. PLS measurement models were tested. The terms of reliability included individual items reliability and internal consistency to test the reliability of the sample data. In some facets of internal consistency, the reliability and Cronbach's α composition values have a similar index measurement. The reliability, we suggested, is for values greater than 0.7 degrees [22–25].

Table 4 illustrates that the composite reliability of various research aspects ranged from 0.8521 to 0.9505 in this study, where the composite reliability was higher than the 0.7

TABLE 3: Hypotheses table.

The content of the hypotheses	Result
H1: Using proper learning strategies to enhance learning motivation has significant influences.	Significant
H2: Using proper learning strategies to enhance learning achievements has significant influences.	Significant
H3: Using proper learning strategies to enhance the cognitive load has significant inverse influences.	Significant
H4: Using proper learning motivation to enhance learning achievements has a significant positive relationship.	Significant
H5: The cognitive load has a significant inverse relationship with learning achievement.	Not significant
H6: Learning motivation has a significant relationship with the degree of the cognitive load process ability.	Significant

TABLE 4: Dimension tables of reliability and validity.

Aspect name	Measurable variables	Q.NO	Avg	<i>t</i> -value	CR	AVE	Cronbach's α
Meaningful learning	Active	MeAct2	5.31	4.883	0.91	0.57	0.89
		MeAct3	5.35	8.335			
		MeAu1	5.27	6.808			
	Authentic	MeAu2	4.92	6.959			
		MeAu3	5.27	7.514			
		MeCon1	5.53	6.500			
		MeCon2	5.37	9.526			
Constructive	MeCon3	5.63	5.779				
	Control beliefs	MoCB1	5.71	3.881			
	Intrinsic goal orientation	MoIG1	5.37	7.250	0.85	0.66	0.74
Learning motivation	Task value	MoTV1	5.45	5.773			
	Difficulty rating	CogD1	2.47	7.529			
	Cognitive load	Effort rating	CogE1	3.55	10.713	0.86	0.68
Response time to secondary task		CogR1	4.00	5.073			
Learning achievement	Understanding	AchU1	5.80	5.880			
		AchU4	5.14	7.860			
		AchPC1	5.49	5.644			
		AchPC2	5.78	10.614			
	Personal changes	AchPC3	5.82	9.899	0.95	0.66	0.94
		AchPC4	5.80	8.490			
		AchGI1	5.78	5.392			
		AchGI2	5.88	9.715			
Gain information	AchGI3	5.86	8.490				
	AchGI4	5.86	6.325				

threshold for each dimension of Cronbach's α , and are greater than 0.7, which means that every dimension has good reliability [24, 26, 27].

5.3.2. *Convergent Validity.* Convergent validity refers to the same aspect of the measurement results with a high correlation (measurements of multiple variables are the same aspects as measured degree of compliance). Convergent validity can be tested through composite reliability (CR) and average variance extracted (AVE). According to the recommendation of Fornell and Larcker [23] and Hair et al. [26], the composite reliability should be above 0.7, and the average of Average Variance Extracted, AVE, should be greater than 0.5 shown in Table 2. It represents at least the 50% level for the explanation as the reference index of convergent validity. The composite reliability of the four aspects in this study ranged from 0.8521 to 0.9505; the average variance extracted amount ranged from

0.5754 to 0.6805. All reached the threshold. Hence, these study constructs have convergent validity.

5.4. *Structured Model Evaluation.* Structured Model Evaluation is utilized to estimate path coefficients of research hypothesis which is significance or not. The purpose is to explain the relationship between dependent variables and independent variables. Structural model analysis is also used to view the independent variables, which affect the dependent variable for explanatory power (R^2) and the explanatory power of the model [23, 26, 28, 29].

In this study, the structural model and the relationship between the various aspects of the path coefficients and test results are shown in Tables 5 and 6 and Figure 5. There are motivations, cognitive loads, and learning achievements in the actual usage behavior. The total variance R^2 values for motivation, cognitive load, and learning achievement were

TABLE 5: Effective results of latent variables.

	Learning motivation			Cognitive load			Learning achievements		
	Direct	Indirect	Total	Direct	Indirect	Total	Direct	Indirect	Total
Meaningful learning	0.717	—	0.717	-0.320	0.291	-0.029	0.235	0.386	0.621
Learning motivation	—	—	—	0.406	—	0.406	0.535	0.029	0.564
Cognitive load	—	—	—	—	—	—	0.071	—	0.071

TABLE 6: Path coefficients analysis result.

Hypothesis	Path	Standardized estimates	Standard error	T value
H1	Meaningful learning → learning motivation	0.717	0.0585	12.266**
H2	Meaningful learning → learning achievements	0.235	0.1147	2.048*
H3	Meaningful learning → cognitive load	-0.320	0.143	2.241*
H4	Learning motivation → learning achievement	0.535	0.1326	4.036**
H5	Cognitive load theory → learning achievements	0.071	0.0679	1.043 ^{N.S.}
H6	Learning motivation → cognitive load theory	0.406	0.1473	2.755**

* P values reach the significant standard which is 0.05 ($t \geq 1.6602$); ** P values reach the significant standard which is 0.01 ($t \geq 2.3642$).

^{N.S.} (not significant) P value does not reach the 0.05 significant standard (T value < 1.6602).

51.5%, 8.1%, and 53.9% of the variance, respectively. Through the structural model analysis of PLS, the results showed the following for the system developed for the research: the users' degree of meaningful learning has a significant positive influence on SPANI (Shooting Pose Adjustment with Nature Interactions) learning motivation ($\beta = 0.717$, $P < 0.01$); that is, SPANI has a high degree of meaningful learning for learners. Moreover, SPANI users have higher learning motivation.

It also found that the users' degree of meaningful learning has a significant positive influence on SPANI learning achievement ($\beta = 0.235$, $P < 0.05$). That is, SPANI has a high degree of meaningful learning for learners, and those using SPANI had a higher level of academic achievement.

6. Conclusion and Discussion

This research mainly targets college students as the research subjects. We have investigated college students' behaviors and attitudes of association towards the degree of meaningful learning, learning motivation, cognitive, and learning achievements after using the digital shooting posture correction materials SPANI. Through the information analysis, statistics verification, and investigation, we have proposed hypotheses for this research which can be found in Table 3 and which explain these hypotheses one by one.

6.1. Research Conclusion and Findings. This research mainly targets college students as the research subjects. We have investigated college students' behaviors and attitudes of association towards the degree of meaningful learning, learning motivation, and cognitive and learning achievements after using the digital shooting posture correction materials SPANI.

Subjects' Learning Motivation Positively Influenced by SPANI. The research results show that when SPANI subjects accept

meaningful learning use of learning strategies, it has positive influence on subjects' learning motivation. Hence, SPANI subjects think that to accept SPANI learning strategies is useful to increase learning motivation. Therefore, the research results of Credé and Phillips [15] are supported.

Subjects' Academic Achievements Positively Influenced by SPANI. The research results show that when SPANI subjects accept meaningful learning use of learning strategies, subjects learning achievements will become higher. Hence, SPANI subjects think that to accept SPANI learning strategies is useful to increase learning achievements. Therefore, this research supports the findings of Chang and Ley [30].

Subjects' Cognitive Loads Have Been Negatively Influenced by Using SPANI. The research results show that when SPANI subjects accept meaningful learning use of learning strategies, subject's cognitive load will become lower. Hence, SPANI subjects think that to accept SPANI learning strategies is useful to decrease cognitive load. Our research findings conform with those of Michael Pressley [31], Chang and Ley [30], Binet and Simon [32], and Laidra et al. [33].

SPANI Subjects' Learning Motivation Has a Significantly Positive Relationship with Learning Achievement. The research results show that when SPANI subjects learning motivation increases while using SPANI, their learning achievements will also improve. This point supports the research results of Credé and Phillips [15], Duncan and McKeachie [16], and McClure et al. [34].

SPANI Subjects' Cognitive Loads Do Not Have Significantly Negative Relationship with Learning Achievement. The research results show that SPANI subjects' cognitive load has no significant negative influence on learning achievement when using SPANI. It means that SPANI subjects' cognitive

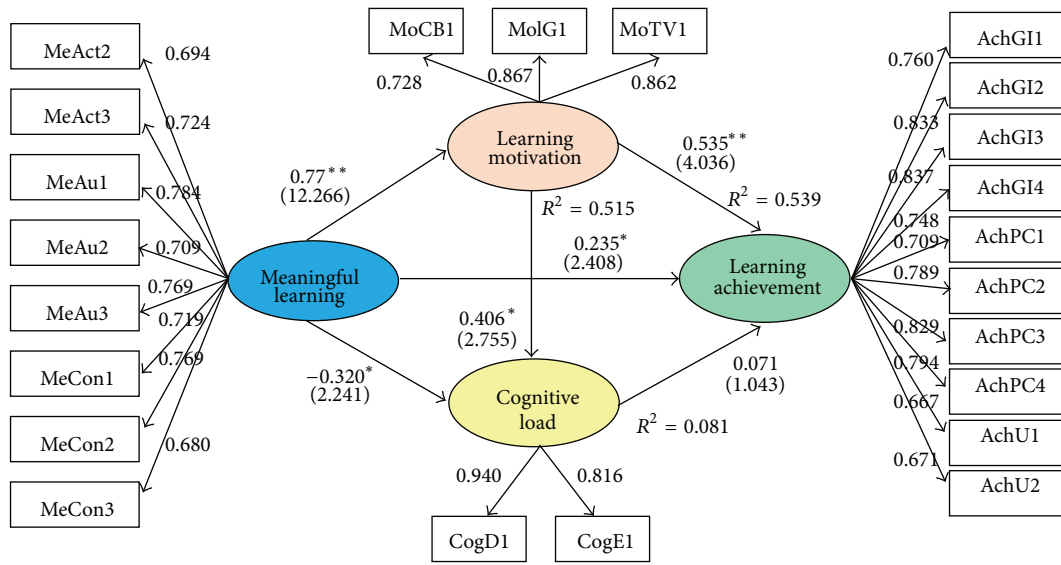


FIGURE 5: Path coefficient and regression in this research.

loads will not directly increase learning achievement. Hence, this point does not support the research results of Binet and Simon [32]; and Laidra et al. [33]

SPANI Subjects' Learning Motivation Has a Significantly Positive Relationship with the Degree of Cognitive Load Process Ability. The research results indicate that SPANI subjects have higher learning motivation towards teaching material. Moreover, their ability to handle the cognitive load when using SPANI increases. Therefore, SPANI subjects' increased learning motivation is useful to increase the ability to handle the cognitive load. This supports the findings of Schnotz [35].

Based on the results of this study, SPANI subjects consider that a cognitive load does not have a significant direct impact on learning achievement. Above we have mentioned, when discussing the system design, that we wanted users to be able to understand and learn how to absorb teaching content in an easy way. On this point, we suggest the subsequent research can conduct a more in-depth exploration of the users' cognitive load, which the digital content materials have given. For example, research could examine more about the cognitive load of digital teaching content and learning effects.

6.2. Implications. To make use of digital content materials is very useful for improving learning attitudes and for improving learning achievements.

In this research, SPANI subjects utilized meaningful learning strategies introduced in this project that were related to learning motivation, cognitive load, and learning achievements. All of our research hypotheses were confirmed. Hence, when using the learning strategies of meaningful learning properly, it can improve SPANI users' learning motivation, reduce the cognitive load, and enhance learning achievement. According to what was mentioned before, Maleki et al. [1]

strongly recommended that making use of information and communication technology (ICT) in teaching can improve students' learning absorption and teaching quality. Certainly, the research results show that using ICT can increase SPANI users' learning motivation and decrease the cognitive load and increase teaching quality. In this research, the users' cognitive load was decreased with using the digital shooting posture correction materials SPANI which can help to improve deficiencies found in traditional curricula for courses related to teaching the correct basketball shooting posture. Moreover, it can increase the users' willingness to learn and motivation, which then increases the willingness of students to voluntarily practice at home.

Learning motivation affects the degree of the cognitive load and learning achievement.

In this study, SPANI subjects who have high motivation were able to handle a higher degree of cognitive loading and also had better performance on learning achievements. Moreover, the above supports the argument which was mentioned with respect to McClure et al's. [34] research. Their research was concerned with how the student's best or worst marks were related to achievement. His research found that learners' learning achievement decided how strong the learners' motivation was. In addition, using digital materials enhanced learners' interests so learners were less likely to feel bored during instruction, and this can further enhance motivation. Besides, the degree of the cognitive load is also related to the learners' motivation: stronger learning motivation leads to a decrease in the cognitive load. When the level of the ability to process cognitive load increases, learners can in turn learn more difficult concepts. Schnotz [35] indicated that learners' investment in learning activities is based on the intensity of their motivation, their attitude toward the subject, and their mental states. Our results supported the

findings of Schnotz [35]. Consequently, we believe that enhancing learning motivation is one important component in designing a comprehensive teaching plan.

In this study, the above mentioned cognitive load did not have a negative influence on learning achievement. This result differs from other researchers' findings. Binet and Simon [32] referred to the use of the cognitive ability to predict learning achievement, and Laidra et al. [33] mentioned that academic achievement is based on the effect of cognitive ability. In this study, SPANI subjects' cognitive load had no significant influence on learning achievement for the following reasons.

- (1) When I designed the interface and the program originally, I based it on design principles stating that users must be able to easily understand and operate the program. The design principles that users can easily understand or operate. The SPANI is referring to design interface of foreign Nature Interaction games as the primary reference.
- (2) Before testers operate the system, they must be able to understand the purpose of the experiment, the content of the program, and the operating instructions of the system. Then, following the experiment, we collected feedback from our subjects. After the experiment, the system will obtain shooting posture grades from student, so student fully understood the contents of this experiment.

In this experiment, the result shows that the cognitive load does not directly affect academic achievement. The reasons could be the two points mentioned above. The high-intensity motivation of learners, it can increase the degree of processing of cognitive load and learning achievements. We found that two of the important roles in teaching design are learning strategy and learning motivation.

References

- [1] H. Maleki, A. Majidi, F. Haddadian, A. M. Rezai, and V. Ali-pour, "Effect of Applying Informant on and Communication Technology (ICT) on learning level and information literacy of students," *Procedia*, vol. 46, pp. 5862–5867, 2012.
- [2] D. P. Ausubel and F. G. Robinson, *School Learning: An Introduction to Educational Psychology*, Holt, Rinehart and Winston, 1969.
- [3] S. Kalyuga, P. Chandler, J. Tuovinen, and J. Sweller, "When problem solving is superior to studying worked examples," *Journal of Educational Psychology*, vol. 93, no. 3, pp. 579–588, 2001.
- [4] P. R. Pintrich, D. Smith, T. Garcia, and W. J. McKeachie, *A Manual for the Use of the Motivated Strategies for Learning Questionnaire*, University of Michigan, Ann Arbor, Mich, USA, 1991.
- [5] A. F. Cliff, "Teacher-learners' conceptions of learning: evidence of a "communalist" conception amongst postgraduate learners?" *Higher Education*, vol. 35, no. 2, pp. 205–220, 1998.
- [6] N. Purdie and J. Hattie, "Assessing students' conceptions of learning," *Australian Journal of Educational and Developmental Psychology*, vol. 2, pp. 17–32, 2002.
- [7] G. M. Boulton-Lewis, F. Marton, D. C. Lewis, and L. A. Wilss, "A longitudinal study of learning for a group of indigenous Australian university students: dissonant conceptions and strategies," *Higher Education*, vol. 47, no. 1, pp. 91–112, 2004.
- [8] M. Makoe, J. T. E. Richardson, and L. Price, "Conceptions of learning in adult students embarking on distance education," *Higher Education*, vol. 55, no. 3, pp. 303–320, 2008.
- [9] D. Ausubel, *The Psychology of Meaningful Verbal Learning: An Introduction to School Learning*, Grune & Stratton, New York, NY, USA, 1963.
- [10] D. P. Ausubel, J. D. Novak, and H. Hanesian, *Educational Psychology: A Cognitive View*, Werbel & Peck, New York, NY, USA, 1978.
- [11] J. Sweller, *Instructional Design in Technical Areas*, ACER Press, Camberwell, Australia, 1999.
- [12] E. Pollock, P. Chandler, and J. Sweller, "Assimilating complex information," *Learning and Instruction*, vol. 12, no. 1, pp. 61–86, 2002.
- [13] P. Gerjets and K. Scheiter, "Goal configurations and processing strategies as moderators between instructional design and cognitive load: evidence from hypertext-based instruction," *Educational Psychologist*, vol. 38, no. 1, pp. 33–41, 2003.
- [14] A. Renkl and R. K. Atkinson, "Structuring the transition from example study to problem solving in cognitive skill acquisition: a cognitive load perspective," *Educational Psychologist*, vol. 38, no. 1, pp. 15–22, 2003.
- [15] M. Credé and L. A. Phillips, "A meta-analytic review of the Motivated Strategies for Learning Questionnaire," *Learning and Individual Differences*, vol. 21, no. 4, pp. 337–346, 2011.
- [16] T. G. Duncan and W. J. McKeachie, "The making of the motivated strategies for learning questionnaire," *Educational Psychologist*, vol. 40, no. 2, pp. 117–128, 2005.
- [17] R. Säljö, *Learning in the Learner's Perspective: Some Commonsense Conceptions Issue 76 of Reports*, Institute of Education, Gothenburg University, Gothenburg, Sweden, 1979.
- [18] F. Marton, G. Dall'Alba, and E. Beatty, "Conceptions of learning," *International Journal of Educational Research*, vol. 19, pp. 277–300, 1993.
- [19] J. Sweller, "Cognitive load during problem solving: effects on learning," *Cognitive Science*, vol. 12, no. 2, pp. 257–285, 1988.
- [20] OpenNI, "OpenNI Unity software development kit (Unity SDK)," 2011, <http://www.openni.org/Downloads/OpenNIModules.aspx>.
- [21] Ministry of Education, "High School Physical education and Information Technology teaching material," 2012, <http://hsmaterial.moe.edu.tw/schema/pe/main.html>.
- [22] J. C. Nunnally, *Psychometric Theory*, McGraw-Hill, New York, NY, USA, 1978.
- [23] C. Fornell and D. F. Larcker, "Evaluating structural equation models with unobservable variables and measurement error," *Journal of Marketing Research*, vol. 18, no. 1, pp. 36–50, 1981.
- [24] R. P. Bagozzi and Y. Yi, "On the evaluation of structural equation models," *Journal of the Academy of Marketing Science*, vol. 16, no. 1, pp. 74–94, 1988.
- [25] W. W. Chin and P. R. Newsted, "Structural equation modeling analysis with small samples using partial least squares," in *Statistical Strategies for Small Sample Research*, R. H. Hoyle, Ed., 1999.
- [26] J. F. Hair, B. Black, B. Babin, R. E. Anderson, and R. L. Tatham, *Multivariate Data Analysis*, Macmillan, New York, NY, USA, 6th edition, 1992.
- [27] I. B. Jum Nunnally, *Psychometric Theory*, McGraw-Hill Humanities, New York, 3rd edition, 1994.

- [28] J. Hulland, "Use of partial least squares (PLS) in strategic management research: a review of four recent studies," *Strategic Management Journal*, vol. 20, no. 2, pp. 195–204, 1999.
- [29] P. A. Pavlou and M. Fygenson, "Understanding and predicting electronic commerce adoption: an extension of the theory of planned behavior," *MIS Quarterly*, vol. 30, no. 1, pp. 115–143, 2006.
- [30] S. L. Chang and K. Ley, "A learning strategy to compensate for cognitive overload in online learning: learner use of printed online materials," *Journal of Interactive Online Learning*, vol. 5, no. 1, pp. 104–117, 2006.
- [31] C. M. Michael Pressley, *Advanced Educational Psychology for Educators, Researchers, and Policymakers*, HarperCollins College Publishers, 1995.
- [32] A. Binet and T. Simon, *The Development of Intelligence in Children*, Williams & Wilkins, Baltimore, Md, USA, 1916.
- [33] K. Laidra, H. Pullmann, and J. Allik, "Personality and intelligence as predictors of academic achievement: a cross-sectional study from elementary to secondary school," *Personality and Individual Differences*, vol. 42, no. 3, pp. 441–451, 2007.
- [34] J. McClure, L. H. Meyer, J. Garisch, R. Fischer, K. F. Weir, and F. H. Walkey, "Students' attributions for their best and worst marks: do they relate to achievement?" *Contemporary Educational Psychology*, vol. 36, no. 2, pp. 71–81, 2011.
- [35] W. Schnotz, "Reanalyzing the expertise reversal effect," *Instructional Science*, vol. 38, no. 3, pp. 315–323, 2010.

Research Article

DSP- and FPGA-Based Stair-Climbing Robot Design

Ming-Shyan Wang, Che-Min Mi, Shih-Yu Wu, and Yi-Ming Tu

Department of Electrical Engineering, Southern Taiwan University of Science and Technology, 1 Nan-Tai Street, Yung Kang District, Tainan 710, Taiwan

Correspondence should be addressed to Ming-Shyan Wang; mswang@mail.stust.edu.tw

Received 15 September 2013; Accepted 3 October 2013

Academic Editor: Teen-Hang Meen

Copyright © 2013 Ming-Shyan Wang et al. This is an open access article distributed under the Creative Commons Attribution License, which permits unrestricted use, distribution, and reproduction in any medium, provided the original work is properly cited.

A stair-climbing robot is equipped with a grasping arm for capturing objects to provide service for the elders. A board based on a digital signal processor (DSP) plays the role of control center to manage all actions of two brushless DC motors for locomotion, two worm gears for torque magnification, and two DC motors for arms' pitching in the main body. The robot is steered by fuzzy logic control (FLC) which integrates the outputs of DC bus current sensor and an inclinometer. There is a CMOS camera for vision used in the robot, and the grasping arm is controlled via the video camera for capturing objects. Simple algorithms of image processing are implemented in the field programmable gate array (FPGA) board that generates the X -axis and Y -axis commands of the grasping arm to capture/load objects. Three walking experiments of the stair-climbing robot to move up and down stairs are shown in the taped pictures from videos. The object tracking and capturing by the grasping arm and camera verifies the proposed design.

1. Introduction

Research on service robots has been attended in recent years. One of the most important reasons is the growing of aging population and decreasing of working population. It is not a long-term way by hiring many foreigners with cheaper payment to work at factories or to take home-caring job for the elder or disabled. As a result, for the latter, home-caring robot is an excellent candidate capable of supporting such an aging society. Specifically, the elders can control the robots directly for service.

The robot designed to directly carry elders up and down stairs needs a large vehicle and the stair rail for moving. The robot "HRP-2" from Harada successfully climbed up 280 mm stairs by grasping the stair rail [1]. The robot "WL-16RII" [2] can walk independently and allow users to build its upper body based on their requirements, such as a walking wheelchair or as a walking support machine that is able to walk up and down stairs carrying or assisting an elder. The developed biped locomotor with Stewart platform legs successfully achieved walking up and down on stairs for 250 mm continuously and carrying 60 kg man on it. Another biped-type robot, for example, "Zero Walker-1" [3], uses its two legs to assist the aged person walking and moving up and down

stairs along the handrail by stepping onto the feet of the robot [4]. However, the aforementioned robots generally need tremendous effect on expense and time. Furthermore, it is very difficult to lift an aged person by human force, and it is not very easy to have a large and heavy-weight lift machine in a normal house.

Generally, the first step of image processing for segmenting the target is background subtraction scheme [5]. Although the background subtraction scheme works fairly well in segment foreground data from nonchanging background but it will still allow objects that are paced into the workspace to be detected as potential objects. As a result, a color (or skin) detector is implemented to further filter the foreground data by converting the RGB (red, green, and blue) form of resultant image into $YCbCr$ (luminance, blueness, and redness) form [5]. Additionally, object tracking has become an important topic in robotics field [6, 7]. Some basic functions such as real time, automation, and robustness to nonideal situations are required for practical object tracking systems. The servo control structure in real-time visual tracking systems usually belongs to the category of "image-based" and "dynamic look and move" [6]. Based on image moments, three different visual predictive control architectures are proposed [7]. However, the proposed system was verified

only by simulation results. A novel two-level scheme for adaptive active visual servoing of a mobile robot equipped with a pan camera was presented in [8]. The designed active visual servoing system shows advantages of a satisfactory solution for the field-of-view problem, global high servoing efficiency, and free of any complex pose estimation algorithm usually required for visual servoing systems. With respect to traditional visual servoing approaches that use geometric visual features, the visual feature used in [9] was the pixel intensity. The proposed approach has been tested in terms of accuracy and robustness via several experimental conditions. A visual servoing strategy based on a novel motion-estimation technique [10] was presented for the stabilization of a nonholonomic mobile robot. The practical exponential stability can be achieved by perturbed linear system theory, despite the lack of depth information.

In the paper, a stair-climbing robot equipped with an arm will be designed to provide the service of carrying objects up and down stairs or patrolling for security. A control board including a digital signal processor (DSP) TMS320F28335 will steer the robot based on the outputs of DC bus current sensor and an inclinometer by fuzzy logic control (FLC). Without background subtraction and complex object tracking schemes, simple algorithms, such as the color filtering and locating center of the detected target, are employed in the robot system. With the aid of a CMOS camera for vision, the robot arm will track, capture, and put back the target object. The field programmable gate array (FPGA) on DE2-70 board will implement the image processing.

The paper is organized as follows for further discussion. Section 2 describes the design steps of the proposed robot, robot mechanism describing each component and the ways of climbing up and going down stairs, DSP-based controller providing all control signals and realizing fuzzy control logic, and the FPGA-based visual servo for tracking and capturing objects. Section 3 presents the experimental results of stair motion and visual servoing. Finally, Section 4 claims our conclusions.

2. Robot Design

There are three steps for the proposed robot design, mechanism, DSP-based controller, and FPGA-based visual servo.

Step I: Mechanism Design. It is well known that the most effective style of movement of a robot on a plane field is the wheel type. As obstacles and stairs exist, crawler-type and leg-type robots become better candidates for application. However, the proposed robot is equipped with roller chains which are attached with polyurethane rubber blocks to generate friction with ground and stairs for climbing up and down. The stair-climbing robot consists of a main body for moving, a front arm and a rear arm for moving up and down stairs. The main body is equipped with two brushless DC motors (BLDCMs) and their drives for locomotion, worm gears for torque amplification, two dc motors to control two arms, and DSP-based board as control center, shown in Figure 1 [11]. The chassis size of the main body is 58.5 cm × 53 cm and each arm is 48 cm × 40 cm such that the maximum length of the robot

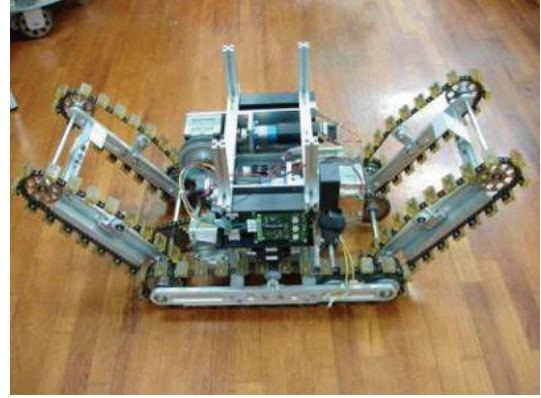


FIGURE 1: Picture of the stair-climbing robot.

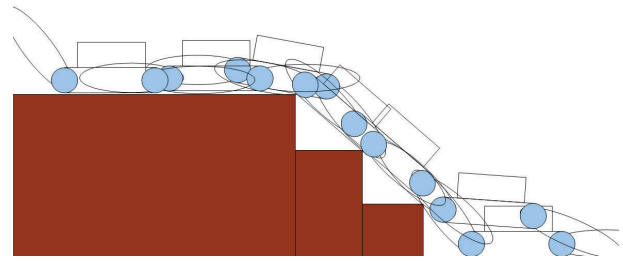


FIGURE 2: Total travel of climbing-up motion.

will be 154.5 cm. The robot is equipped with roller chains attached with rubber blocks used to generate friction with ground and stairs for moving. There are 136 rubber blocks with size of 3 cm × 2 cm × 1 cm attached to the roller chains, 40 for each arm and 56 for main body. The distance between any two plastic blocks is properly arranged to fix the stair brink. The moving direction of the robot is steered based on the speed difference of two BLDCMs and the information from ultrasonic sensors. The robot makes use of friction force between the roller chains/rubber blocks and stairs/ground to climb up. The front arm will be pushed down to flat top so that the main body is lifted. The front arm will be pulled up for next stair-climbing. The rear arm is kept flat during the robot going up. Figure 2 displays total travel of climbing-up motion. Similarly, Figure 3 shows summary of going-down motion.

Step II: DSP-Based Controller Design. DSP provides the pulse-width modulation (PWM) signals of BLDCMs and DC motors and realizes the fuzzy logic rules for speed control.

The i th fuzzy rule in the fuzzy rule-base system is described as [12]

$$R_i: \text{If } x_1 \text{ is } A_{i1} \text{ and } x_2 \text{ is } A_{i2}, \text{ then } y \text{ is } w_i, \quad (1)$$

where w_i , x_j , and A_{ij} , $j = 1, 2$, $i = 1, 2, \dots, n$ are fuzzy output variables, input fuzzy variables, and linguistic variables, respectively. Referring to Figure 4 for i th membership function with isosceles triangle shape, b_{ij} means the length of

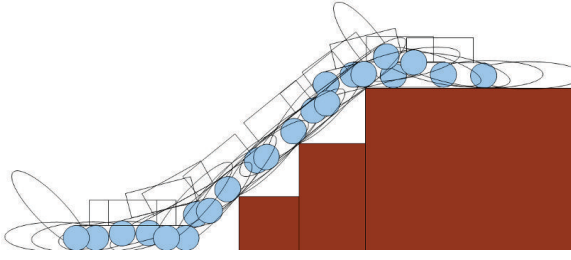
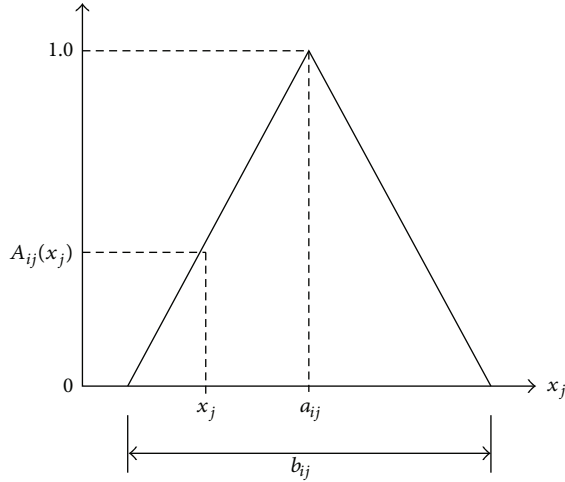


FIGURE 3: Summary of going-down motion.


 FIGURE 4: i th membership function with isosceles triangle shape.

the base and a_{ij} stands for the abscissa of the center of the base. The membership grade of input x_j is calculated by

$$A_{ij}(x_j) = 1 - \frac{2 \cdot |x_j - a_{ij}|}{b_{ij}}, \quad j = 1, 2. \quad (2)$$

The bases of triangular membership function keep same for easily programming. By product operation, the membership grade of the antecedent proposition is calculated as

$$\mu_i = A_{i1}(x_1) \cdot A_{i2}(x_2). \quad (3)$$

Then the output will be

$$y = \frac{\sum_{i=1}^n \mu_i w_i}{\sum_{i=1}^n \mu_i}. \quad (4)$$

Summarily, Table 1 lists the linguistic control rules and Figure 5 displays the design scheme of fuzzy logic control.

Step III: FPGA-Based Visual Servo Design. The grasping multilink arm consists of three couples of gears, three DC motors, four links, and one clasper. Referring to Figure 6, the first DC motor steers the diving gear S_1 and driven gear S_2 to determine the rotating angle. The second motor controls the gears of $S_3, S_{4d}, S_{4u},$ and S_5 together with belts to stretch the length of the arm. S_{4d} and S_{4u} are mounted in the same

TABLE 1: Linguistic control rule table.

θ_m	I			
	ZO	PS	PM	PB
NB	ZO	PS	PM	PB
NM	ZO	PM	PM	PM
NS	ZO	PB	PS	ZO
ZO	ZO	PB	PS	ZO
PS	ZO	PB	PS	ZO
PM	ZO	PS	PM	PM
PB	ZO	PS	PM	PB

shaft and with the same number of gears. Then, the length X can be calculated as

$$X = \cos \theta \times l \times 2, \quad (5)$$

where l is the length of the link. The third motor decides the open angle of the clasper.

The pixel array of CMOS camera THDB-D5M used in the robot consists of a matrix of 2752×2004 pixels addressed by column and row [13, 14]. The 2592×1944 array in the center called active region represents the default output image, surrounded by an active boundary region and a border of dark pixels. Pixels of active region are output in a Bayer pattern format consisting of four ‘‘colors,’’ green1, green2, red, and blue (G1, G2, R, and B) to represent three filter colors [12, 13]. The first row output alternates between G1 and R pixels, and the second row output alternates between B and G2 pixels. The green1 and green2 pixels have the same color filter, but they are treated as separate colors by the data path and analog signal chain.

In order to calculate the R, G, and B intensity of each pixel, we relabel the Bayer pattern by the corresponding column-row address, shown in Figure 7. After analyzing, we summarize each expression of the color intensity for each pixel as follows.

(i) x is even and y is even:

$$R_{(x,y)} = \frac{R_{(x-1,y)} + R_{(x+1,y)}}{\text{Pixel_Count}},$$

$$\text{Pixel_Count} = \begin{cases} 2, & (x-1) > 10, (x+1) < 2681 \\ 1, & \text{others,} \end{cases}$$

$$B_{(x,y)} = \frac{B_{(x,y-1)} + B_{(x,y+1)}}{\text{Pixel_Count}}, \quad (6)$$

$$\text{Pixel_Count} = \begin{cases} 2, & (y-1) > 50, (y+1) < 2002 \\ 1, & \text{others.} \end{cases}$$

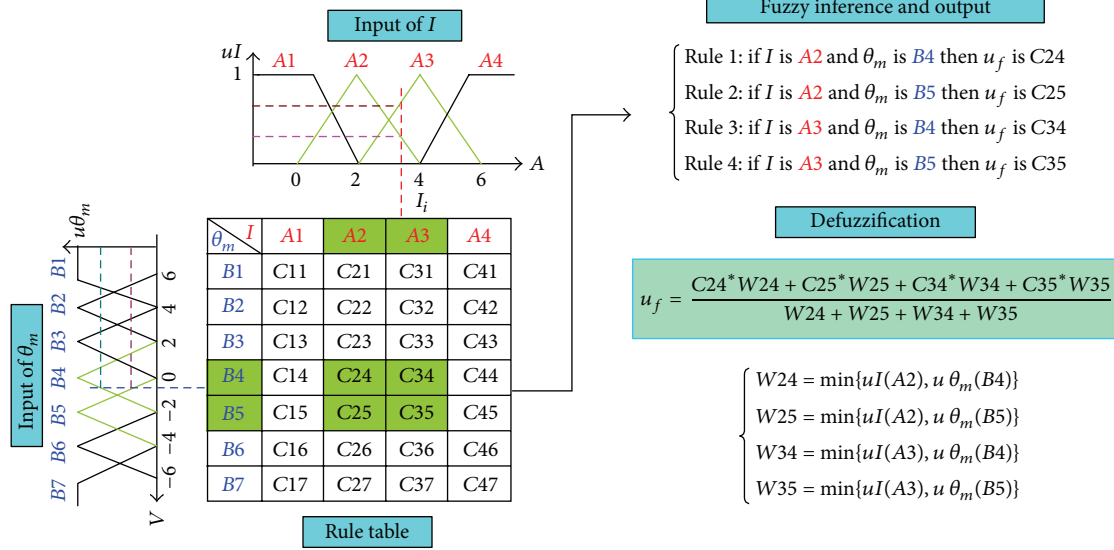


FIGURE 5: Design scheme of fuzzy logic control.

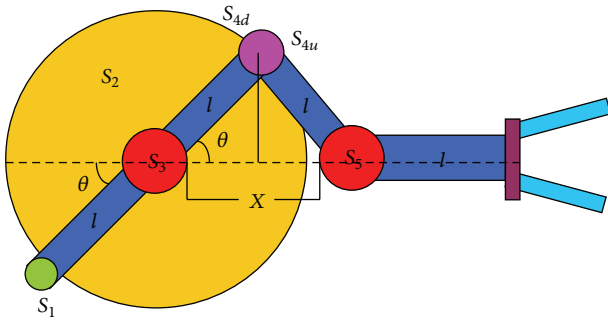


FIGURE 6: Parameter definitions of the grasping arm.

G(14,50)	R(13,50)	G(12,50)	R(11,50)	G(10,50)
B(14,51)	G(13,51)	B(12,51)	G(11,51)	B(10,51)
G(14,52)	R(13,52)	G(12,52)	R(11,52)	G(10,52)
B(14,53)	G(13,53)	B(12,53)	G(11,53)	B(10,53)
G(14,54)	R(13,54)	G(12,54)	R(11,54)	G(10,54)

FIGURE 7: Bayer pattern by the corresponding column-row address.

(ii) x is even and y is odd:

$$G_{(x,y)} = \frac{G_{(x-1,y)} + G_{(x+1,y)} + G_{(x,y-1)} + G_{(x,y+1)}}{\text{Pixel_Count}},$$

$$\text{Pixel_Count} = \begin{cases} 4, & (x-1) > 10, (x+1) < 2618 \\ 3, & \text{others,} \end{cases}$$

$$R_{(x,y)} = \frac{R_{(x+1,y-1)} + R_{(x-1,y-1)} + R_{(x+1,y+1)} + R_{(x-1,y+1)}}{\text{Pixel_Count}},$$

$$\text{Pixel_Count} = \begin{cases} 4, & (x-1) > 10, (x+1) < 2618 \\ 2, & \text{others.} \end{cases}$$

(7)

(iii) x is odd and y is even:

$$G_{(x,y)} = \frac{G_{(x,y-1)} + G_{(x,y+1)} + G_{(x-1,y)} + G_{(x+1,y)}}{\text{Pixel_Count}},$$

$$\text{Pixel_Count} = \begin{cases} 4, & (y-1) > 50, (y+1) < 2002 \\ 3, & \text{others,} \end{cases}$$

$$B_{(x,y)} = \frac{B_{(x-1,y-1)} + B_{(x+1,y-1)} + B_{(x+1,y+1)} + B_{(x-1,y+1)}}{\text{Pixel_Count}},$$

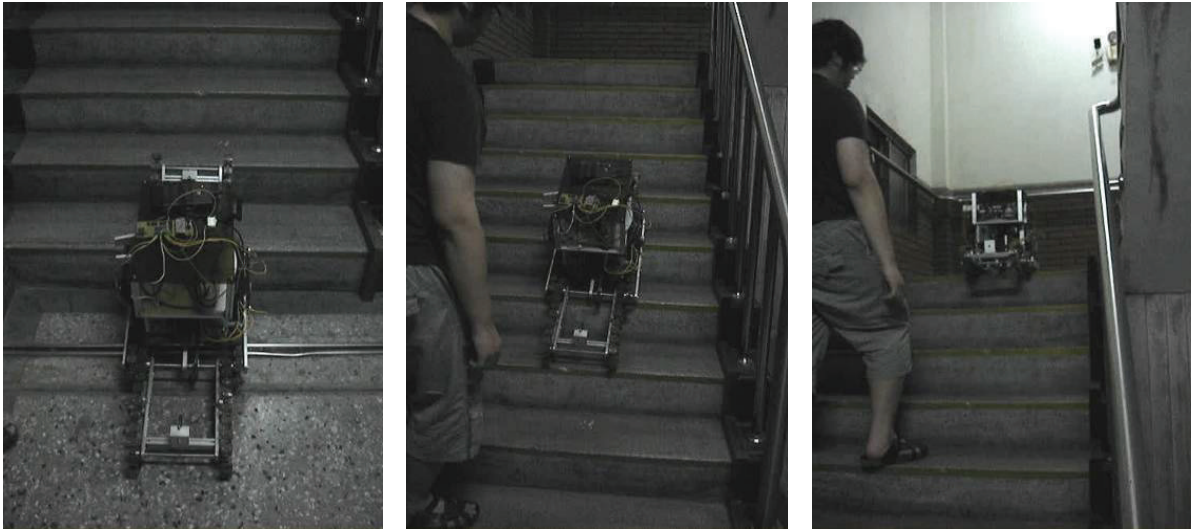
$$\text{Pixel_Count} = \begin{cases} 4, & (y-1) > 50, (y+1) < 2002 \\ 2, & \text{others.} \end{cases}$$

(8)



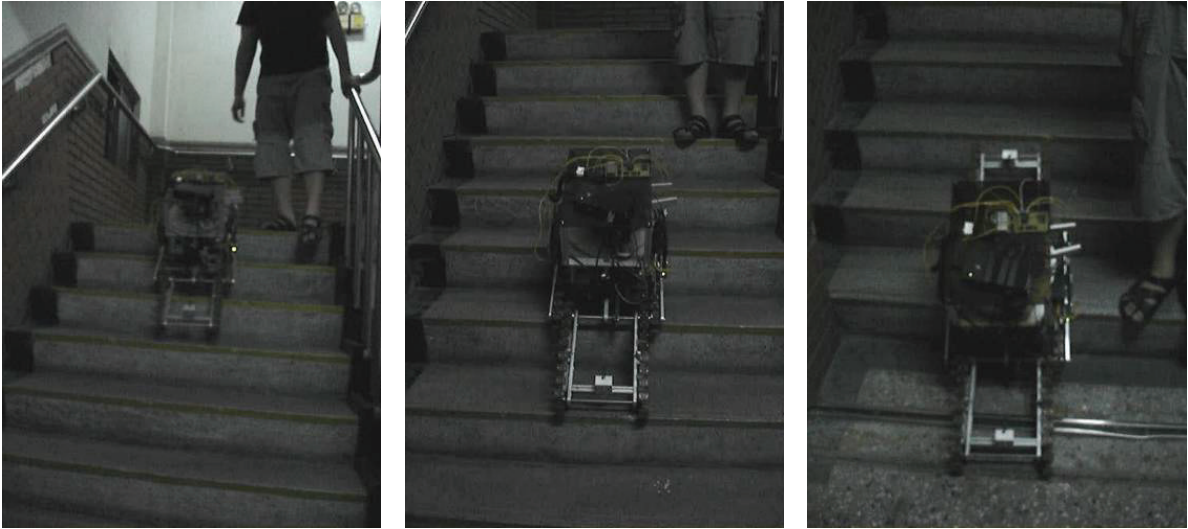
(a) (b)

FIGURE 8: Realized motion of (a) climbing up and (b) going down by wired control.



(a) (b) (c)

FIGURE 9: Realized motion of climbing up by FLC.



(a) (b) (c)

FIGURE 10: Realized motion of going down by FLC.

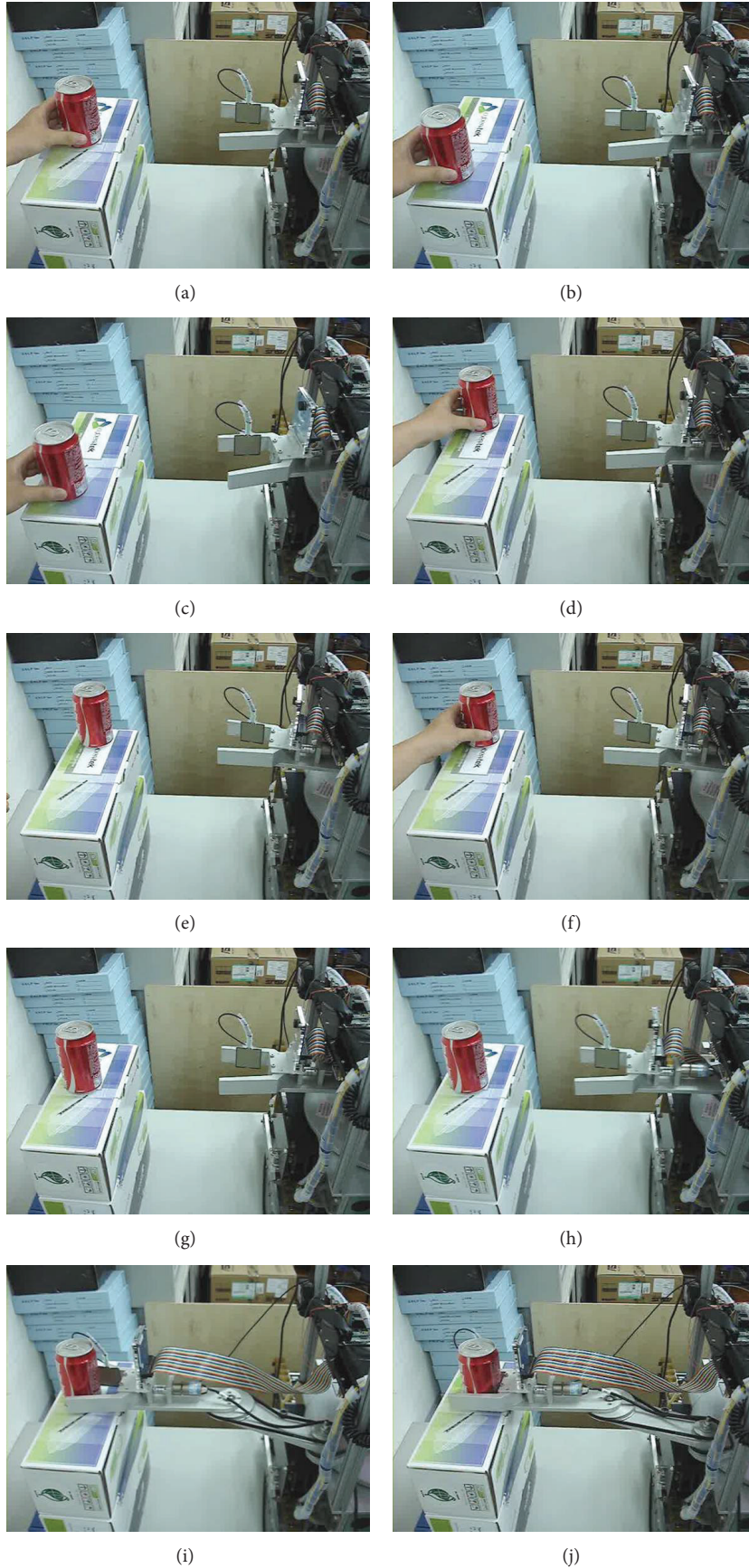


FIGURE II: Continued.

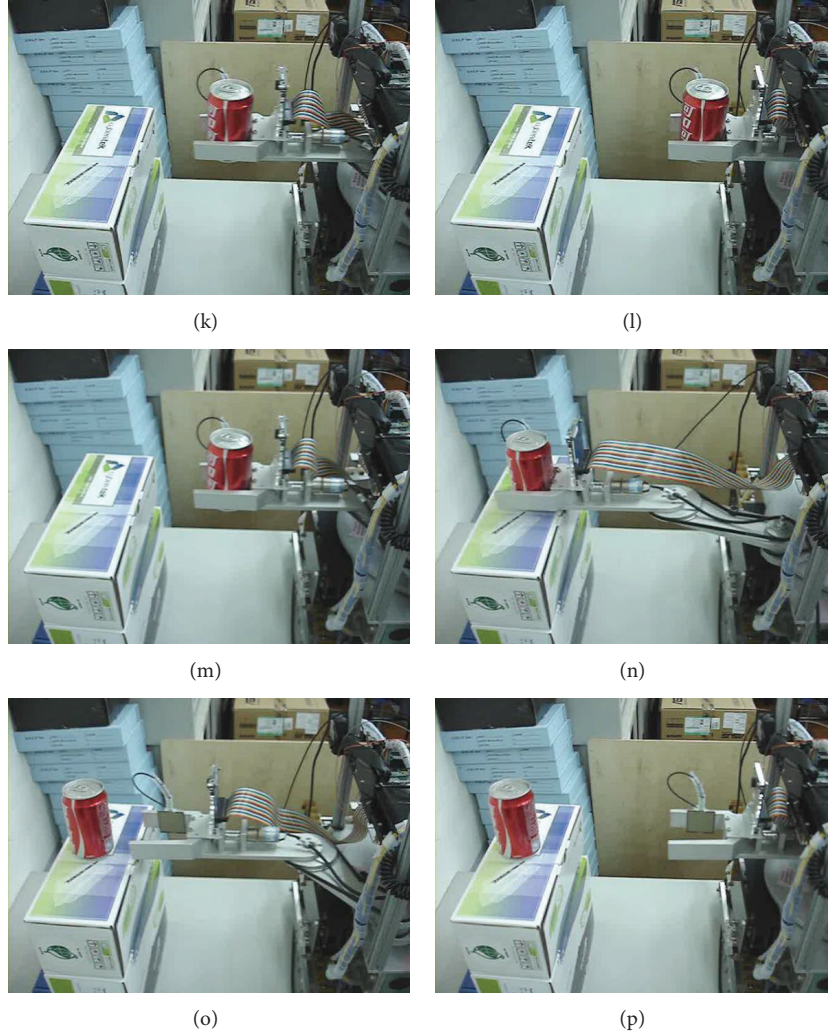


FIGURE 11: The taped pictures of the experimental results on grasping.

(iv) x is odd and y is odd:

$$\begin{aligned} R_{(x,y)} &= \frac{R_{(x,y-1)} + R_{(x,y+1)}}{2}, \\ B_{(x,y)} &= \frac{B_{(x-1,y)} + B_{(x+1,y)}}{2}, \end{aligned} \quad (9)$$

where x and y stand for the column address and row address, respectively.

The image raw data is sent from D5M to DE2-70 board where the FPGA on DE2-70 board will handle image processing and convert the data to RGB format to display on the VGA display [15–17]. As a result, we first capture the image of experiment background to find the ranges of colors of RGB and then define their location regions for color discrimination. In order to reduce the effect of light variation, the image in RGB space will be converted into YC_bC_r space [5]. In addition, the ranges of RGB from D5M are four times of the

general image. So those the transformation can be expressed as

$$\begin{bmatrix} Y \\ C_b \\ C_r \end{bmatrix} = \begin{bmatrix} 0.299 & 0.587 & 0.114 \\ -0.1687 & -0.33126 & 0.5 \\ 0.5 & -0.41869 & -0.08131 \end{bmatrix} \begin{bmatrix} R \\ G \\ B \end{bmatrix} + \begin{bmatrix} 64 \\ 512 \\ 512 \end{bmatrix}. \quad (10)$$

3. Experiment Results

Gear ratio used in the 45 kg stair-climbing robot is 1320 and the rated dc input power and speed of the 200-W BLDCM are 24 V and 9600 rpm. A preliminary experiment that the unloaded robot climbs up and goes down a gradual stair with the rise of 120 mm and depth of 400 mm by wired control is tested. The results of every motion are shown in Figure 8 [11]. It qualifies the designed robot. Then we conduct the second experiment that the robot with loading of one arm moves up and down a steeper stair with the rise of 175 mm and depth

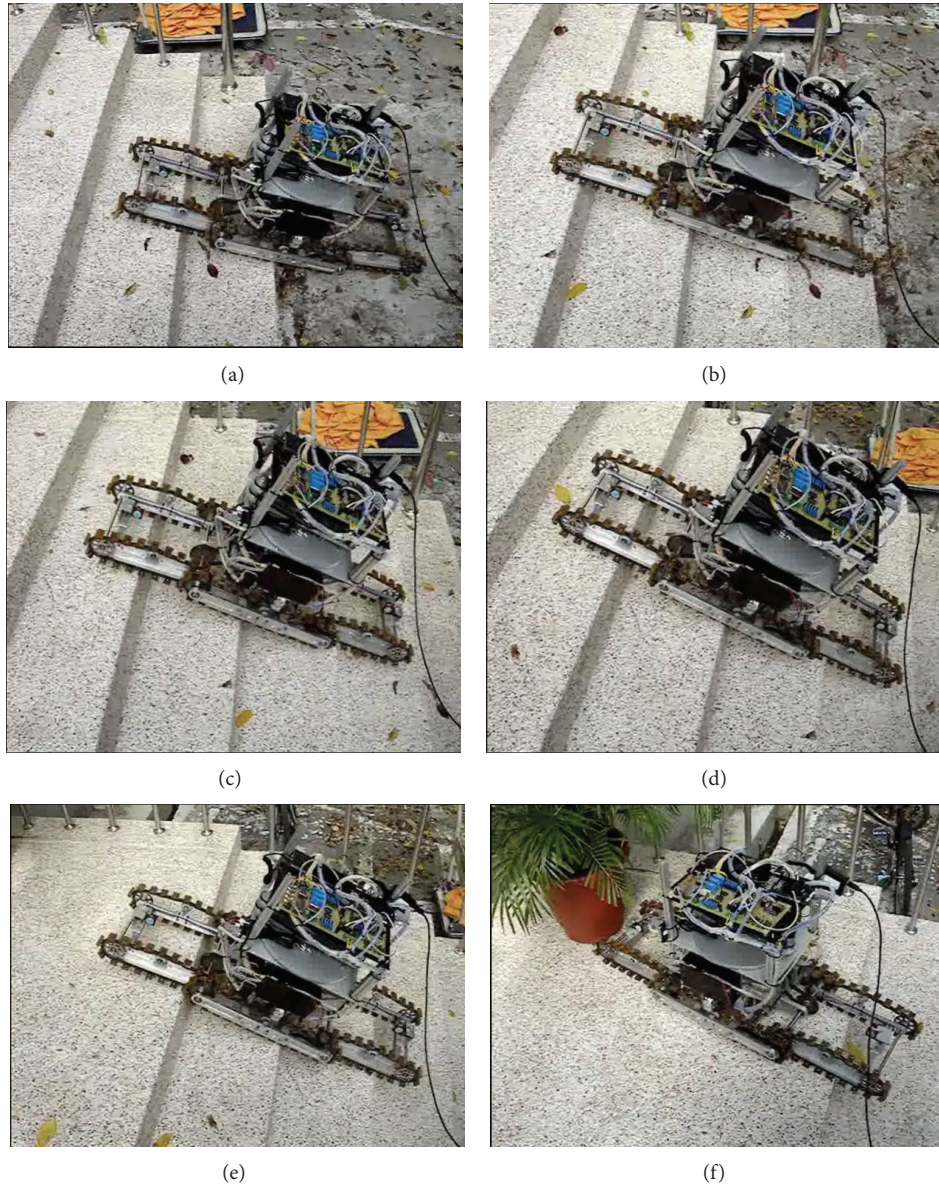


FIGURE 12: Realized motion of climbing up at full loading.

of 280 mm. The taped pictures of the experiment and every motion are shown in Figures 9 and 10, respectively [12].

The third experiment contains image processing and grasping arm motion. In order to prevent target damage while clamping, one pressure sensor is installed inside the clasper. The pressure output after calibrating is sent to DSP for reference. Figure 11 displays the sequentially taped pictures from videos of tracking, capturing the cola can, and putting it back by the robot arm. Figure 11(a) presents the initial status of the experiment. The arm tracks the corresponding direction after the can is shifted left, shown in Figures 11(b) and 11(c). Figures 11(d) and 11(e) depict the right tracking. The arm tracks the can back to central position, shown in Figures 11(f) and 11(g). Then, the robot stretches out the arm for capturing the can and then draws the arm back, presented in Figures

11(h)–11(l). Finally, the robot puts the can back and goes back to the initial status, presented in Figures 11(m)–11(p).

Finally, we conduct the fourth experiment that the robot with all loading moves up a stair with the rise of 150 mm and depth of 300 mm. The taped pictures of the experiment are shown in Figure 12. The climbing-up motion presents variation in proceeding direction. This is due to the plastic bell being almost torn into broken after long time of experimental test. But, it was not found.

4. Conclusion

In the paper, we have developed a stair-climbing robot and completed experiments of moving up/down stairs and object tracking, capturing, and loading. In fact, the stair-climbing

robot can provide service for the elders by capturing the specific object at one floor and then climbing up or down to another floor. In addition, the robot will patrol for security by the CCD camera around the house while more image processing functions are provided.

Acknowledgments

The authors would like to express their appreciation to Ministry of Education and National Science Council, China, under Contract no. NSC 100-2632-E-218-001-MY3, for financial supporting.

References

- [1] K. Harada, H. Hirukawa, F. Kanehiro et al., "Dynamical balance of a humanoid robot grasping an environment," in *Proceedings of the IEEE/RSJ International Conference on Intelligent Robots and Systems*, pp. 1167–1173, Sendai, Japan, October 2004.
- [2] Y. Sugahara, A. Ohta, K. Hashimoto et al., "Walking up and down stairs carrying a human by a biped locomotor with parallel mechanism," in *Proceedings of the IEEE IRS/RSJ International Conference on Intelligent Robots and Systems*, pp. 1489–1494, Alberta, Canada, August 2005.
- [3] Y. Konuma and S. Hirose, "Development of the stair-climbing biped robot 'Zero Walker-1,'" in *Proceedings of the 19th Annual Conference of the Robotics Society of Japan*, pp. 851–852, 2001.
- [4] Y. Takahashi, H. Nakayama, T. Nagasawa et al., "Robotic assistance for aged people," in *Proceedings of the 37th SICE Annual Conference*, pp. 853–858, Chiba, Japan, July 1998.
- [5] A. Malima, E. Özgür, and M. Çetin, "A fast algorithm for vision-based hand gesture recognition for robot control," in *Proceedings of the 14th IEEE Signal Processing and Communications Applications*, pp. 1–4, Antalya, Turkey, April 2006.
- [6] S. Hutchinson, G. D. Hager, and P. I. Corke, "A tutorial on visual servo control," *IEEE Transactions on Robotics and Automation*, vol. 12, no. 5, pp. 651–670, 1996.
- [7] C. Copot, C. Lazar, and A. Burlacu, "Predictive control of nonlinear visual servoing systems using image moments," *IET Control Theory & Applications*, vol. 6, no. 10, pp. 1486–1496, 2012.
- [8] Y. Fang, X. Liu, and X. Zhang, "Adaptive active visual servoing of nonholonomic mobile robots," *IEEE Transactions on Industrial Electronics*, vol. 59, no. 1, pp. 486–497, 2012.
- [9] B. Tamadazte, N. L.-F. Piat, and E. Marchand, "A direct visual servoing scheme for automatic nanopositioning," *IEEE/ASME Transactions on Mechatronics*, vol. 17, no. 4, pp. 728–736, 2012.
- [10] X. Zhang, Y. Fang, and X. Liu, "Motion-estimation-based visual servoing of nonholonomic mobile robots," *IEEE Transactions on Robotics*, vol. 27, no. 6, pp. 1167–1175, 2011.
- [11] M.-S. Wang and Y.-M. Tu, "Design and implementation of a stair-climbing robot," in *Proceedings of the IEEE International Conference on Advanced Robotics and Its Social Impacts*, Taipei, Taiwan, August 2008.
- [12] M.-S. Wang, Y.-S. Kung, and Y.-M. Tu, "Fuzzy logic control design for a Stair-climbing robot," *International Journal of Fuzzy Systems*, vol. 11, no. 3, pp. 174–182, 2009.
- [13] Terasic Company, *THDB-D5M Hardware Specification*, 2008.
- [14] Terasic Company, *TRDB-D5M User Guide*, 2008.
- [15] A. K. Benkhalil, S. S. Sipson, and W. Booth, "Real-time detection and tracking of a moving object using a complex programmable logic device," in *Proceedings of the IEE Colloquium on Target Tracking and Data Fusion*, pp. 1–7, Birmingham, UK, June 1998.
- [16] T. Hamamoto, S. Nagao, and K. Aizawa, "Real-time objects tracking by using smart image sensor and FPGA," in *Proceedings of the International Conference on Image Processing (ICIP '02)*, pp. III/441–III/444, New York, NY, USA, September 2002.
- [17] S.-B. Park, A. Teuner, and B. J. Hosticka, "A motion detection system based on a CMOS photo sensor array," in *Proceedings of the International Conference on Image Processing*, vol. 3, pp. 967–971, Chicago, Ill, USA, October 1998.

Research Article

Fairness Time-Slot Allocation and Scheduling with QoS Guarantees in Multihop WiMAX Mesh Networks

Chien-Yu Wu,¹ Hann-Jang Ho,² Sing-Ling Lee,¹ and Liang Lung Chen¹

¹ *Institute of Computer Science and Information Engineering, National Chung Cheng University, No. 168, Section 1, University Road, Min-Hsiung Township, Chia-yi County 62102, Taiwan*

² *Department of Applied Digital Media, WuFeng University, No. 117, Section 2, Chiankuo Road, Min-Hsiung Township, Chia-yi County 62153, Taiwan*

Correspondence should be addressed to Hann-Jang Ho; hannjangho@gmail.com

Received 17 September 2013; Accepted 9 October 2013

Academic Editor: Teen-Hang Meen

Copyright © 2013 Chien-Yu Wu et al. This is an open access article distributed under the Creative Commons Attribution License, which permits unrestricted use, distribution, and reproduction in any medium, provided the original work is properly cited.

The WiMAX technology has been defined to provide high throughput over long distance communications and support the quality of service (QoS) control applied on different applications. This paper studies the fairness time-slot allocation and scheduling problem for enhancing throughput and guaranteeing QoS in multihop WiMAX mesh networks. For allocating time slots to multiple subscribe stations (SSs), fairness is a key concern. The notion of max-min fairness is applied as our metric to define the QoS-based max-min fair scheduling problem for maximizing the minimum satisfaction ratio of each SS. We formulate an integer linear programming (ILP) model to provide an optimal solution on small-scale networks. For large-scale networks, several heuristic algorithms are proposed for better running time and scalability. The performance of heuristic algorithms is compared with previous methods in the literatures. Experimental results show that the proposed algorithms are better in terms of QoS satisfaction ratio and throughput.

1. Introduction

In recent years, worldwide interoperability for microwave access (WiMAX), the broadband wireless access technology based on IEEE 802.16 standard [1], has received enormous attention in wireless communication networks. Based on IEEE 802.16, WiMAX system has been defined to provide high throughput over long distance and to support the quality of service (QoS) control applied on different applications. The IEEE 802.16 standard supports both the point-to-multipoint (PMP) mode and the mesh mode. In PMP mode, stations are organized as a cellular network, where subscriber stations (SSs) are directly connected to base stations (BSs). Such networks require each SS to be within the communication range of its associated BS, thus greatly limiting the coverage range of the network. In the mesh mode, the mobile stations are connected as an ad hoc network. Moreover, the mobile stations send the packets to the neighbors; the neighbors relay the received packets to the base station. Thus, it is unnecessary to have a direct connection between each mobile station and the base station.

In an IEEE 802.16 mesh network, transmissions can undergo a multihop manner. The standard specifies a centralized scheduling mechanism for the BS to manage the network. Stations will form a routing tree rooted at the BS for the communication purpose. SSs in the network will send request messages containing their traffic demands to the BS to ask for resources. The BS then uses the topology information along with SSs' requests to determine the routing tree and to allocate resources. All next generation cellular wireless systems employ orthogonal frequency division multiple access (OFDMA) based multicarrier technology. An OFDMA frame consists of time slots in the time domain and subchannels in the frequency domain. A time-slot and sub-channel combination, referred to as a tile, is the minimum allocable unit.

In the wireless transmission technology, the schedule for data transmission is a very important research issue. The main purpose of the schedule includes: (1) increasing the network throughput, (2) shorting the scheduled time, (3) providing a guarantee QoS service, and (4) keeping transferring

fairness in the network. Therefore, it is very important to have a good scheduling algorithm in the wireless transmission.

Since current wireless network systems usually use the OFDMA as communication technology, they also plan to provide various QoS services for a large number of users. The high data transfer throughput and QoS assurance have become the main goal of the wireless network [2–4]. To get more efficient bandwidth usage and to provide better QoS services to users of the wireless network, dynamic resource allocation method has been widely studied in [2, 3]. When we consider the real-time service flows, such as VoIP and wireless multimedia communications, their quality of services (QoS) should be satisfied. The real-time connections will periodically transmit or receive a constant amount of traffic.

Recently, several literatures discuss the scheduling scheme for multihop transmissions in WiMAX mesh networks, since the standard protocol usually does not specify any particular scheduling scheme. For example, the throughput and fairness issues have been studied in [5]. However, the previous literature does not guarantee the QoS while considering the fairness scheduling of SSs in real time. It is worth exploring how the well-known fairness schemes such as max-min, max-flow, absolute, and proportional fairness can be implemented in 802.16j networks with the QoS constraint. This paper concentrates on the time-slot allocation and scheduling for WiMAX mesh networks with OFDMA protocol. The goal of this paper is to provide various scheduling schemes which optimize both QoS and fairness of resource allocations for the WiMAX mesh networks. From the experimental results, we show that our proposed schemes are better than the previous work in terms of QoS satisfaction ratio.

This paper applies the concept of max-min fair scheduling to enhance the minimum satisfaction ratio over the WiMAX mesh networks. We propose an ILP model to solve the problem and provide heuristic methods to ensure the QoS priority of scheduling to achieve better overall QoS satisfaction ratio and throughput.

The main contributions of our work are listed below.

- (1) *Propose a heuristic algorithm that can optimize the max-min fair and guarantee QoS.* In our proposed method, QoS requirements are a primary consideration for allocating resources to various SSs. If there are remaining resources after stratifying the QoS requirements, we will then consider the max-min fair scheduling to improve the overall throughput and minimize the satisfaction ratio. In IEEE 802.16j mesh networks, the proposed algorithm can meet the QoS requirements of various SSs in a frame and enhance the network overall QoS satisfaction ratio.
- (2) *Exploit spectral reuse.* The spectral reuse is adopted by our heuristic algorithm to avoid the packets collisions to improve the network throughput and QoS satisfaction ratio.
- (3) *Construct the ILP model.* We construct an integer linear programming model which constraints on the QoS requirements and max-min fairness assignments

for solving the optimization problem in multihop WiMAX mesh networks.

2. Network Model

2.1. MMR Infrastructure. This paper focuses on the time-slot allocation and scheduling on the network system with IEEE 802.16j mobile multihop relay-based (MMR) infrastructure. In accordance with the recommendation of WiMAX standard [6], BS is the root of the tree to assist the transmission of WiMAX mesh networks. The RSs are the intermediate nodes of the tree, and the SSs are the leaf node of the tree.

We mainly focus on the scheduling between the SSs and RSs. Our goal is to find a scheduling method which can meet the QoS requirements of each SS and achieve a fair allocation of network resources. We also study how to allocate subchannels and time slots according to the bandwidth requirements of each SS in a frame. We assign the transmission schedule to maximize the minimum satisfaction ratio over all SSs to get the overall max-min fairness for the multihop relayed WiMAX mesh network.

2.2. Mesh Mode. We focus on the 802.16 mesh network which is composed by one BS and several SSs. The BS is responsible for connecting the back-end network. Each SS transfers data to neighboring SSs without the BS's agreement. The data flow away from the BS is called downlink data flow; conversely, which toward the BS is called uplink data flow. For mesh networks, most studies focus on topology design [7]. In 802.16 mesh networks, some issues are studied for supporting QoS in [8, 9]. Shetiya and Sharma [8] studied the QoS routing problem of Central Scheduling. Hong and Pang [9] considered the multihop scheduling problem with bandwidth and delay constraints. In these researches, different approaches for establishing the routing tree of mesh networks are analyzed, and some issues of time-slot allocation are discussed.

2.3. Spectral Reuse. This paper applies spectral reuse to solve the resource allocation problem for the 802.16 mesh network. The advantage of using spectral reuse is to improve the transmission capacity and the throughput of network. Fu et al. [10] proposed an algorithm to maximize the usage of spectral reuse. Chen et al. [11] studied how to use the spectral reuse to solve the problem of resource allocation.

2.4. Interference Model. Scheduling strategies must ensure that transmissions in each time slot do not collide. There are two types of collision situations in the wireless network environment. They are called Primary Interference and Secondary Interference [12, 13]. Primary Interference occurs in a single time slot of scheduling; the SS cannot do more than one thing. In other words, the SS can only transfer or receive data in a single time slot. Secondary Interference occurs when the originally receiver X turns into the transfer, but the user X is still in the range of the transfer Y . The user X will affect the transmission of the user Y . There are some studies that focus on WiMAX mesh network interference problems [14, 15], Wei et al. [16] proposed an interference-aware multihop

TABLE 1: Parameters and variables table.

Symbol	Description
$G = (V, E)$	Mesh network topology G
V	The set of stations
E	The set of edges
T	The set of time slot in a frame
H	The set of subchannel in each time slot
h	The index parameter of subchannel, $\forall h \in H$
\mathbb{S}	A set of all the SSs
s_i	A subscriber SS i , $\forall s_i \in \mathbb{S}$
\mathbb{R}	Set of all relay stations
r_i	A relay node i , $\forall r_i \in \mathbb{R}$
c_l	The link capacity of each link l , $\forall l \in E$
hp_i	The set of hops from s_i to BS
br_i	The minimum bandwidth requirement of the s_i for guaranteeing QoS
BR_i	The maximum bandwidth requirement of the s_i
λ_i	The actual quantity of node i upload the packet, $\forall i \in \mathbb{S} \cup \mathbb{R}$
σ_i	The actual quantity of node i upload the required tile, $\forall i \in \mathbb{S} \cup \mathbb{R}$
y_i	s_i satisfaction ratio
tr_i	The tile requirement of s_i for transmitting packets from s_i to BS during each hop
TR	The set of tile requirement, $TR = \{tr_i \mid \forall s_i \in \mathbb{S}\}$
$I(\cdot)$	The subset of nodes which will interfere with node or link transceiving
\bar{I}_i	The subset of nodes which will not interfere with s_i 's transceiving
$pa(i)$	The parent of node i on the tree topology
$cd(r)$	The set of children node SSs or RSs of r
$f_{t,h}^l$	A decision variable, which is 1 if link l is assigned with time slot t and subchannel h , and 0 otherwise
OL_i, IL_i	The set of output and input links of node i , respectively

routing algorithm to maximize the degree of use of network bandwidth to maximize the network throughput.

2.5. Fairness Scheduling. Nowadays the related works on WiMAX mesh networks through a network of relay stations scheduling and resource allocation are concerned widely. It is common to study the fairness in many wireless networks in [17–20]. Sayenko et al. [19] studied the proportional fairness and considered the difference between frequency selections with multiuser scheduling problems. Andrews and Zhang [20] proposed a round-robin based scheduling method for IEEE 802.16 BS to ensure QoS requirements of the SS in uplink (UL) and downlink (DL) can be met. But the network bandwidth usage efficiently and bandwidth requirements were not considered in [19, 20].

In this paper, we propose heuristic scheduling algorithms that identify each SS to maximize the minimum satisfaction ratio in the network and, meanwhile, to meet the bandwidth requirements for each SS. We compare the QoS satisfaction ratio, throughput, and min satisfaction ratio with the previous method proposed in [21]. Experimental results show that our method is better in terms of QoS satisfaction ratio.

3. QoS-Based Max-Min Fair Scheduling

3.1. Problem Definition. Based on the WiMAX standard [1], a tree network topology $G = (V, E)$ is given. For readability, the following parameters and variables are listed in Table 1. A BS as the root, a set of subscriber users $\mathbb{S} = \{s_1, s_2, \dots, s_n\}$ as the leaf nodes, and a set of relay stations $\mathbb{R} = \{r_1, r_2, \dots, r_m\}$ as the intermediate nodes. Let the parameter c_l be the link capacity of each link l , $\forall l \in E$. Let the parameter br_i be the minimum bandwidth requirements of each SS s_i during a frame. Let the parameter BR_i be the maximum bandwidth requirements of each SS s_i during a frame. The problem is limited to the following restrictions:

- (1) no spectral reuse for any pair of links which interfere with each other;
- (2) an RS cannot transmit and receive data at the same time;
- (3) the total number of data delivered by an RS to BS during a frame must be equal to the number of data received from its children node during one frame;
- (4) must satisfy the minimum bandwidth requirements of each SS to guarantee QoS.

Therefore, the multihop fair scheduling with QoS control problem is defined as to find a way to schedule the subchannel-time slot (tile) for a scheduling frame. After the tile scheduling, the minimum satisfaction ratio y_i of each s_i will be maximized, and the bandwidth requirements of each s_i will be satisfied to guarantee QoS.

3.2. Integer Linear Programming for the Problem. In [22], it was proved that scheduling with channel capacity is NP-hard. Therefore, our scheduling problem with time-varying channel will be NP-hard. To find an optimal solution, we provide an Integer Linear Programming (ILP) for this problem.

For each node $i \in \mathbb{S} \cup \mathbb{R}$, $\text{pa}(i)$ denotes the parent of node i on the tree topology. For each RS $r \in \mathbb{R}$, the parameter $\text{cd}(r)$ is used to represent the set of children node (SSs or RSs) of r . For each node i in tree network G , the variable $f_{t,h}^l$ denotes that whether the link $l = (i, j)$ is assigned with time-slot t and subchannel h . We refer to the method [23, 24] to verify whether there are interferences between these two edges. $I(l)$ represents the interference link set of link l :

$$\text{Maximize } y \quad (1)$$

$$\sum_{l' \in I(l)} f_{t,h}^{l'} + f_{t,h}^l \leq 1, \quad \forall h \in H, \forall t \in T, \forall l \in \text{OL}_i, \quad (2)$$

$$\forall i \in \mathbb{S} \cup \mathbb{R},$$

$$\sum_{\forall h \in H} \sum_{\forall l \in \text{OL}_r} f_{t,h}^l + \sum_{\forall h \in H} \sum_{\forall l \in \text{IL}_r} f_{t,h}^l \leq 1, \quad \forall t \in T, \quad (3)$$

$$\forall r \in \mathbb{R},$$

$$\sum_{\forall l \in \text{IL}_r} \left(\sum_{\forall h \in H} \sum_{\forall t \in T} f_{t,h}^l \right) \times c_l \quad (4)$$

$$\leq \sum_{\forall l \in \text{OL}_r} \left(\sum_{\forall h \in H} \sum_{\forall t \in T} f_{t,h}^l \right) \times c_l, \quad \forall r \in \mathbb{R},$$

$$\sum_{\forall l \in \text{OL}_i} \left(\sum_{\forall h \in H} \sum_{\forall t \in T} f_{t,h}^l \right) \times c_l \geq \text{br}_i, \quad \forall i \in \mathbb{S}, \quad (5)$$

$$y \leq y_i, \quad \forall i \in \mathbb{S}, \quad (6)$$

$$\text{where } y_i = \frac{1}{\text{BR}_i} \sum_{\forall l \in \text{OL}_i} \left(\sum_{\forall h \in H} \sum_{\forall t \in T} f_{t,h}^l \right) \times c_l, \quad \forall i \in \mathbb{S}, \quad (7)$$

$$f_{t,h}^l = \{0, 1\}, \quad \forall t \in T, \forall h \in H, \forall l \in E. \quad (8)$$

The objective function of QoS-based max-min fair scheduling problem is shown as (1). The goal is to maximize the minimum satisfaction ratio y . The satisfaction ratio y_i is calculated by (7). In (7), the parameter BR_i is the maximum bandwidth requirement of s_i , the parameter c_l is the capacity of link l , and the decision variables $f_{t,h}^l$ are defined in (8). If the time-slot (t, h) is allocated to link l , the value of decision variable $f_{t,h}^l$ is 1. Otherwise, the value of decision variable $f_{t,h}^l$

is 0. The QoS-based max-min fair scheduling problem has four constraints as follows.

- (i) The spectral reuse constraints are shown as (2). For all link l in OL_i , a tile can be used no more than once in each pair of interference links $I(l)$. Where the OL_i is the set of output links of all nodes $i \in \mathbb{S} \cup \mathbb{R}$.
- (ii) The single transceiver constraints are shown as (3). For all time-slot t in T , each RS r in \mathbb{R} cannot transmit and receive data in the same time slot.
- (iii) The flow constraints are shown as (4). All data that are accepted by RS r in a frame will be sent out in the same frame. Where the parameters OL_r and IL_r are the set of output and input links of RS r .
- (iv) The minimum bandwidth requirement constraints are shown as (5). The minimum bandwidth requirements of each s_i must be satisfied to guarantee QoS in a frame.
- (v) The satisfaction ratio constraints are shown as (6). The satisfaction y_i of each s_i will be greater than the variable y .

3.3. Greedy Algorithm for QoS-Based Max-Min Fair Scheduling. Though the ILP solution can be used to obtain optimal solutions for small-sized problem, but if the network scale grows larger, it has large time and space consumption for large-sized network. The heuristics algorithm is needed for better running time in large-sized network. In the following, we designed a heuristic algorithm.

3.3.1. Heuristic Algorithm. The strategy of the proposed heuristic algorithm is smallest total bandwidth requirement first and then applying spectral reuse scheme to assign resource. After QoS of all SSs is guaranteed, the max-min fair scheduling scheme is used to enhance the overall throughput and satisfaction ratio. The proposed heuristic algorithm has four steps as follows.

Step 1 (allocate limited resources to meet the QoS requirements of each SS). At first, the total number of tile requirements ($\text{tr}_i \times \text{hp}_i$) of each s_i is estimated. Then, the resources are allocated to all SSs by Algorithm 2 *QoS_Scheduling()* in increasing order of total tile requirements. Until the resources are not enough allocated or the requirements of all SSs are met, the scheduler will terminate the process of *QoS_Scheduling()*.

Step 2 (increase the number of meeting QoS requirements). If the bandwidth requirements of s_i are not satisfied, the spectral reuse mechanism is used to find available resource for each unmet SS in Algorithm 3 *QoS_Spectral_Reuse()*. The strategy of spectral reuse is to gain tiles from all allocated tiles of s_j ; there is no link between each s_j and the picked s_i . Hence, the satisfaction rate has an opportunity to increase.

Input: $G, \mathbb{S}, \mathbb{R}, H, T, \text{br}, \text{BR}$
Output: $\text{min_satisfaction_ratio}, \text{QoS_satisfaction_ratio}, \text{throughput}$

- (1) Initialization: $\lambda_i \leftarrow 0, \sigma_i \leftarrow 0, \forall s_i \in \text{SS}$;
- (2) for all SS node v_i on G do
- (3) $\text{tr}_i \leftarrow \left\lceil \frac{\text{BR}_i}{c_i} \right\rceil$
- (4) for all RS v_j on the path hp_i from v_i to BS do
- (5) $\text{tr}_i \leftarrow \text{tr}_i + \left\lceil \frac{\text{BR}_i}{c_j} \right\rceil$
- (6) endfor
- (7) endfor
- (8) Sort (TR);
- (9) $A_t \leftarrow |H|, \forall t \in T$
- (10) Set all $\text{ssi.QoSAllocated} = \text{false}$;
- (11) QoS_Scheduling ($G, \mathbb{S}, \mathbb{R}, A, T, \text{TR}, \text{br}, \text{BR}$);
- (12) QoS_Spectral_Reuse ($G, \mathbb{S}, \mathbb{R}, A, T, \text{TR}, \bar{I}, \text{br}, \text{BR}$);
- (13) Maxmin_Scheduling ($G, \mathbb{S}, \mathbb{R}, A, T, Y, \text{BR}$);
- (14) Maxmin_Spectral_Reuse ($G, \mathbb{S}, \mathbb{R}, A, T, Y, \bar{I}, \text{BR}$);

ALGORITHM 1: Heuristic Algorithm.

Output: Y, A

- (1) *Step 1.* Choose a s_i from SS set with the minimal total tile requirement tr_i
- (2) *Step 2.*
- (3) $\text{index} \leftarrow 1$
- (4) for $k = 1 \rightarrow |\text{hp}_i|$
- (5) $\text{req} \leftarrow \left\lceil \frac{\text{br}_i}{c_k} \right\rceil$
- (6) for $t = \text{index} \rightarrow |T|$
- (7) if $A_t \geq \text{req}$
- (8) $A_t \leftarrow A_t - \text{req}; \text{req} \leftarrow 0; k \leftarrow k + 1$
- (9) $\text{index} \leftarrow t; t \leftarrow |T|$
- (10) else
- (11) if $(|T| - t) < (\text{hp}_i - k)$
- (12) free all tiles which allocated to s_i
- (13) $\text{SS} \leftarrow \text{SS} \setminus \{s_i\}$
- (14) go to *Step 1*
- (15) else
- (16) $A_t \leftarrow 0; \text{req} \leftarrow \text{req} - A_t; \text{index} \leftarrow t; t \leftarrow |T|$
- (17) *Step 3.* if all hops of s_i are allocated successfully
- (18) $\mathbb{S} \leftarrow \mathbb{S} \setminus \{s_i\}$
- (19) $\sigma_i \leftarrow \left\lceil \frac{\text{br}_i}{c_i} \right\rceil; \lambda_i \leftarrow \sigma_i \times c_i$;
- (20) for all RS rs_j on the path from s_i to BS do
- (21) $\sigma_j \leftarrow \left\lceil \frac{\text{br}_i}{c_j} \right\rceil; \lambda_j \leftarrow \sigma_j \times c_j$;
- (22) endfor
- (23) $y_i \leftarrow \frac{\lambda_i + \sum_{\forall rs_j \in \text{hp}_i} \lambda_j}{\text{BR}_i \times |\text{hp}_i|}$;
- (24) *Step 4.* if all SSs meet requirement or no sufficient resources can be allocated
- (25) terminate scheduling
- (26) else go to *Step 1*

ALGORITHM 2: QoS-Scheduling ($G, \mathbb{S}, \mathbb{R}, A, T, \text{TR}, \text{br}, \text{BR}$).

Output: Y, A

- (1) *Step 1.* Choose a s_i from SS set with the minimal total tile requirement tr_i
- (2) Recover all allocated tiles of s_j to set $R, \forall s_j \in \bar{I}_i$
- (3) *Step 2.*
- (4) $index \leftarrow 1$
- (5) for $k = 1 \rightarrow |hp_i|$
- (6) $req \leftarrow \left\lceil \frac{br_i}{c_k} \right\rceil$
- (7) for $t = index \rightarrow |T|$
- (8) if $(A_t + R_t) > req$, then
- (9) if $A_t \geq req$
- (10) $A_t \leftarrow A_t - req$
- (11) else
- (12) $A_t \leftarrow 0; R_t \leftarrow R_t - (req - A_t)$
- (13) $req \leftarrow 0; index \leftarrow t; t \leftarrow |T|$
- (14) else if $(|T| - t) < (hp_i - k)$
- (15) free all tiles which allocated to s_i during this step
- (16) $SS \leftarrow SS \setminus \{s_i\}$
- (17) go to *Step 1*
- (18) *Step 3.*
- (19) if the resource is fully allocated successfully to all hops of s_i , then
- (20) $\mathbb{S} \leftarrow \mathbb{S} \setminus \{s_i\}$
- (21) $\sigma_i \leftarrow \left\lceil \frac{br_i}{c_i} \right\rceil; \lambda_i \leftarrow \lambda_i + \sigma_i \times c_i;$
- (22) for all RS rs_j on the path from s_i to BS do
- (23) $\sigma_j \leftarrow \left\lceil \frac{br_i}{c_j} \right\rceil; \lambda_j \leftarrow \lambda_j + \sigma_j \times c_j;$
- (24) endfor
- (25) $y_i \leftarrow \frac{\lambda_i + \sum_{rs_j \in hp_i} \lambda_j}{BR_i \times |hp_i|};$
- (26) *Step 4.* if all SSs meet QoS or no sufficient resources can be allocated, then
- (27) Termination
- (28) else go to *Step 1*

ALGORITHM 3: QoS-Spectral_Reuse ($G, \mathbb{S}, \mathbb{R}, A, T, TR, \bar{I}, br, BR$).

Step 3 (remaining resources to do the max-min fair scheduling). When the first two steps are finished, then some remaining resources are available. Then, the available tiles are allocated to the SSs that have lowest satisfaction, and satisfaction ratio is upgraded by Algorithm 4 *Maxmin.Scheduling()*.

Step 4 (upgrade the min satisfaction ratio). Finally, Algorithm 5 *Maxmin_Spectral_Reuse()* finds out an s_i which has lowest satisfaction ratio among all SSs to increase its satisfaction ratio. Until all the SSs are allocated, available tiles by the spectral reuse mechanism or the satisfaction ratio of s_i are equal to 1. Then, the procedure of scheduling algorithm will be finished.

3.3.2. Scheduling Algorithm Description with an Example. As shown in Figure 1, the networks are composed of one BS, three RSs = $\{r_1, r_2, r_3\}$, and six SSs = $\{s_1, s_2, s_3, s_4, s_5, s_6\}$. The number of maximum bandwidth requirements of each SSs BR_i are $\{10, 10, 8, 8, 8, \text{ and } 10\}$. The bandwidth requirements of SSs br_i are $\{7, 2, 4, 5, 6, \text{ and } 3\}$ for guaranteeing QoS. The capacity of each link c_l is set to 1. The number of time-slots

t is set to 7. The number of subchannels h is set to 3. The interference of each RS and SS is defined as follows:

$$\begin{aligned}
 I(r_1) &= \{s_1, s_2, r_2, r_3\}, & I(r_2) &= \{r_1, r_3, s_3, s_4\}, \\
 I(r_3) &= \{r_2, s_5, s_6\}, & I(s_1) &= \{s_2, r_1\}, & I(s_6) &= \{s_5, r_3\} \\
 I(s_2) &= \{s_1, r_1, s_3\}, & I(s_3) &= \{s_2, r_4, s_4\}, \\
 I(s_4) &= \{s_3, r_2, s_5\}, & I(s_5) &= \{s_4, r_3, s_6\}.
 \end{aligned} \tag{9}$$

At first, the value of $tr_i (= \lceil BR_i/c_i \rceil + \sum_{j \in hp_i \setminus \{s_i\}} \lceil BR_j/c_j \rceil)$ of each s_i is calculated at lines (2)–(7) in Algorithm 1. Then, the value of TR is sorted by increasing order at line (8) in Algorithm 1. The value of parameter A_t is initialized as $|H|$ for all time-slot t .

The limited resources are allocated by Algorithm 2. The s_i is selected with minimum total tile requirement tr_i at line (1) of Algorithm 2. Then, the resources are allocated at lines (2)–(16) of Algorithm 2. After resources allocation are completed, the parameters and variables of the SS and RS will be updated at lines (17)–(23) of Algorithm 2. At lines

Output: Y, A

- (1) *Step 1.*
- (2) Choose a s_i with the smallest satisfaction;
- (3) if $y_i == 1$, then terminate scheduling
- (4) else go to *Step 2*
- (5) *Step 2.*
- (6) $index \leftarrow 1$
- (7) for $k = 1 \rightarrow |hp_i|$
- (8) $req \leftarrow \left\lceil \frac{BR_i}{c_k} \right\rceil - \sigma_k$
- (9) for $t = index \rightarrow |T|$
- (10) if $A_t \geq req$
- (11) $A_t \leftarrow A_t - req; req \leftarrow 0; k \leftarrow k + 1$
- (12) $index \leftarrow t; t \leftarrow |T|$
- (13) else if $A_t < req$
- (14) $A_t \leftarrow 0; tr_i \leftarrow req - A_t$
- (15) else if $(|T| - t) < (|hp_i| - k)$
- (16) free all tiles which allocated to s_i in *Step 2*
- (17) $SS \leftarrow SS \setminus \{s_i\}$
- (18) go to *Step 1*
- (19) *Step 3.*
- (20) if the resource is fully allocated successfully to all hops of s_i , then
- (21) $S \leftarrow S \setminus \{s_i\}$
- (22) $\sigma_i \leftarrow \sigma_i + 1; \lambda_i \leftarrow \lambda_i + c_i; y_i \leftarrow \frac{\lambda_i}{BR_i}$
- (23) for all RS rs_j on the path from s_i to BS do
- (24) $\lambda_j \leftarrow \lambda_j + c_j;$
- (25) $\sigma_j \leftarrow \sigma_j + \left\lceil \frac{\lambda_j}{c_j} \right\rceil;$
- (26) *Step 4.*
- (27) if $y_i = 1$ or S is empty, then
- (28) terminate scheduling
- (29) else go to *Step 1*

ALGORITHM 4: Maxmin_Scheduling ($G, S, \mathbb{R}, A, T, Y, BR$).

(24)–(26) of Algorithm 2 if no available resources are able to allocate to each SS, the procedure goes back to the main algorithm. Otherwise, the scheduler continue to find the next SS which can allocate resources to meet the QoS requirements of the SS. In our example, the total number of tiles is 21. In Algorithm 2, the sequence of s_i will be selected as $\{s_2, s_6, s_3\}$. The value of parameter tr_i is estimated as follows.

$$\begin{aligned} tr_1 &= \left\lceil \frac{BR_1}{c_1} \right\rceil + \sum_{\forall j \in hp_1 \setminus \{s_1\}} \left\lceil \frac{BR_1}{c_j} \right\rceil = 14, \\ tr_2 &= \left\lceil \frac{BR_2}{c_2} \right\rceil + \sum_{\forall j \in hp_2 \setminus \{s_2\}} \left\lceil \frac{BR_2}{c_j} \right\rceil = 4, \\ tr_3 &= \left\lceil \frac{BR_3}{c_3} \right\rceil + \sum_{\forall j \in hp_3 \setminus \{s_3\}} \left\lceil \frac{BR_3}{c_j} \right\rceil = 8, \\ tr_4 &= \left\lceil \frac{BR_4}{c_4} \right\rceil + \sum_{\forall j \in hp_4 \setminus \{s_4\}} \left\lceil \frac{BR_4}{c_j} \right\rceil = 10, \end{aligned}$$

$$tr_5 = \left\lceil \frac{BR_5}{c_5} \right\rceil + \sum_{\forall j \in hp_5 \setminus \{s_5\}} \left\lceil \frac{BR_5}{c_j} \right\rceil = 12,$$

$$tr_6 = \left\lceil \frac{BR_6}{c_6} \right\rceil + \sum_{\forall j \in hp_6 \setminus \{s_6\}} \left\lceil \frac{BR_6}{c_j} \right\rceil = 6.$$

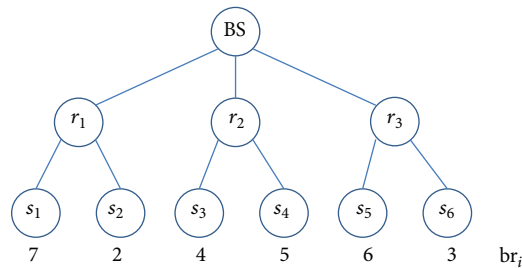
(10)

The scheduling results of Algorithm 2 are shown in Figure 2.

Moreover, if the bandwidth requirements of some SSs are still unsatisfied, the number of SS with QoS guarantee will be raised by Algorithm 3. The bandwidth requirement unsatisfied s_i will be found with the minimum tr_i at line (1) of Algorithm 3. All allocated tiles of $s_j, \forall s_j \in \bar{I}_i$, are recovered to set R at line (2) of Algorithm 3. Then, the spectral reuse strategy is used to maximize satisfaction ratio at lines (3)–(17) in Algorithm 3 for picked s_i . If the available tiles $A_t + R_t$ can meet the requirement of s_i at time slot t for k th hop, the required tiles are allocated at lines (8)–(13) of Algorithm 3. While the requirements of all hops are met, the parameters and variables of the SS and RS will be updated at

Output: Y

- (1) *Step 1.* Choose a s_i with the smallest satisfaction;
- (2) if $y_i = 1$, then terminate scheduling
- (3) else Recover all allocated tiles of s_j to set R , $\forall s_j \in \bar{I}_i$
- (4) go to *Step 2*
- (5) *Step 2.*
- (6) $index \leftarrow 1$
- (7) for $k = 1 \rightarrow hp_i$
- (8) $req \leftarrow tr_i$
- (9) for $t = index \rightarrow |T|$
- (10) if $A_t \geq req$, then
- (11) $A_t \leftarrow A_t - req$; $req \leftarrow 0$; $k \leftarrow k + 1$
- (12) $index \leftarrow t$; $t \leftarrow |T|$
- (13) else
- (14) if $(A_t + R_t) \geq req$, then
- (15) assign req available tiles to k th hop of s_i
- (16) else if $(|T| - t) < (hp_i - k)$, then
- (17) free all tiles which allocated to s_i in *Step 2*
- (18) $\mathbb{S} \leftarrow \mathbb{S} \setminus \{s_i\}$
- (19) go to *Step 1*
- (20) else
- (21) $A_t \leftarrow 0$; $R_t \leftarrow 0$; $req \leftarrow req - A_t$
- (22) *Step 3.* if all hops of s_i are fully allocated successfully, then
- (23) $\sigma_i \leftarrow \sigma_i + 1$; $\lambda_i \leftarrow \lambda_i + c_i$; $y_i \leftarrow \frac{\lambda_i}{BR_i}$;
- (24) for all RS rs_j on the path from s_i to BS do
- (25) $\lambda_j \leftarrow \lambda_j + c_j$;
- (26) $\sigma_j \leftarrow \sigma_j + \left\lceil \frac{\lambda_j}{c_j} \right\rceil$;
- (27) end for
- (28) *Step 4.*
- (29) if $y_i = 1$ or \mathbb{S} is empty, then
- (30) terminate scheduling
- (31) else go to *Step 1*

ALGORITHM 5: Maxmin_Spectral_Reuse ($G, \mathbb{S}, \mathbb{R}, A, T, Y, \bar{I}, BR$).

OFDMA frame:



FIGURE 1: The network topology.

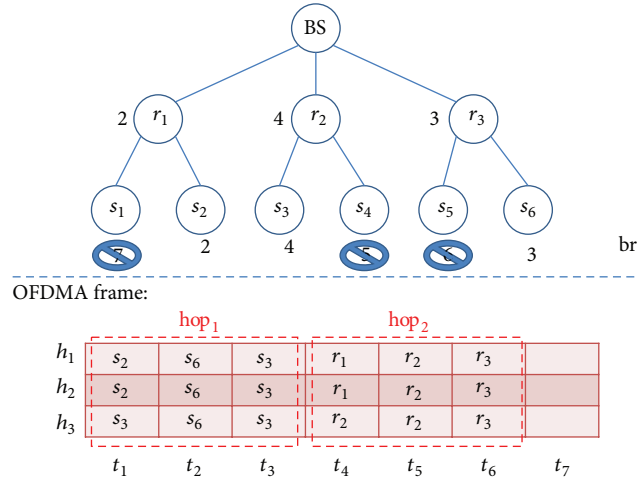


FIGURE 2: The allocation of resources meets the QoS requirements of $s_2, s_3,$ and s_6 .

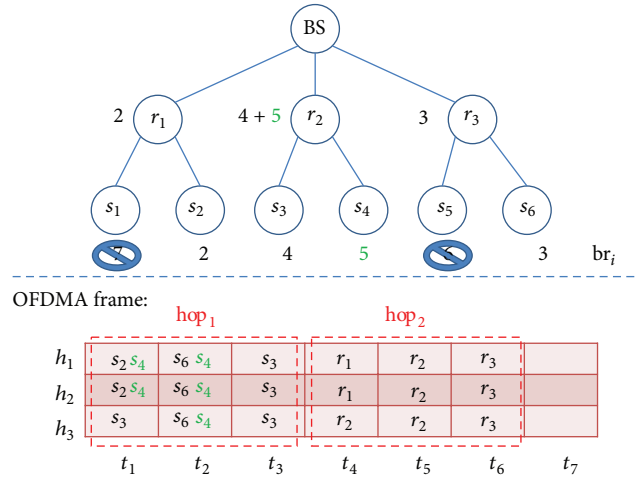


FIGURE 3: s_4 performs the spectral reuse.

lines (18)–(25) in Algorithm 3. Otherwise, all acquired tiles of s_i are freed at line (15) of Algorithm 3. If the resources allocation have not been finished, the scheduler will find out the next one to meet the bandwidth requirements of s_i to guarantee QoS by the spectral reuse strategy. Until the minimum bandwidth requirements of all SSs are satisfied or the available tiles are not enough to allocate, then this step will be terminated. The results of first hop of s_4 are scheduled by spectral reuse strategy of Algorithm 3 as shown in Figure 3. Because the available tiles are insufficient at second hop, s_4 cannot be assigned as shown in Figure 4. Hence, all acquired tiles of s_4 need to be freed. Due to the available tiles which are not enough to assign, this step is terminated.

If the remaining available tiles have not been allocated completely, then these remaining resources can increase the network minimum satisfaction ratio by Algorithm 4. The SS would be picked with lowest satisfaction ratio in sequence at line (2) of Algorithm 4. While the lowest satisfaction ratio is equal to 1, the scheduling of Algorithm 4 is terminated.

Otherwise, the scheduler will check whether there available tiles can be assigned to the s_i at lines (5)–(18) of Algorithm 4, if the resources could be allocated to the SS. After the parameters and variables of SS and RS are updated at lines (19)–(26) of Algorithm 4, the scheduler continue to find out the lowest satisfaction ratio of SS and to assign available tiles to increase satisfaction ratio. Until no available tiles can be allocated or the requirements of all SSs are met, the scheduling procedure is terminated. The max-min fair scheduling is performed with remaining tiles in Algorithm 4. The satisfaction ratio of $\{s_1, s_4, s_5\}$ is 0. Because the second hop has no enough available tiles, the schedule fails for $\{s_1, s_4, s_5\}$. The scheduling results of Algorithm 4 are shown in Figure 5.

Finally, the spectral reuse strategy is operated on the SS which has lowest satisfaction ratio for increasing the minimum satisfaction ratio in Algorithm 5. At line (1) of Algorithm 5, the scheduler pick a s_i that has lowest satisfaction ratio. If the lowest satisfaction ratio equals to 1 at line (2)

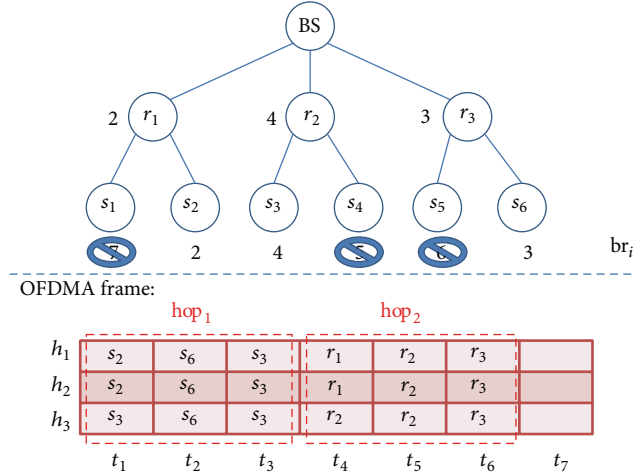


FIGURE 4: When lacking resources, s_4 cannot perform spectral reuse.

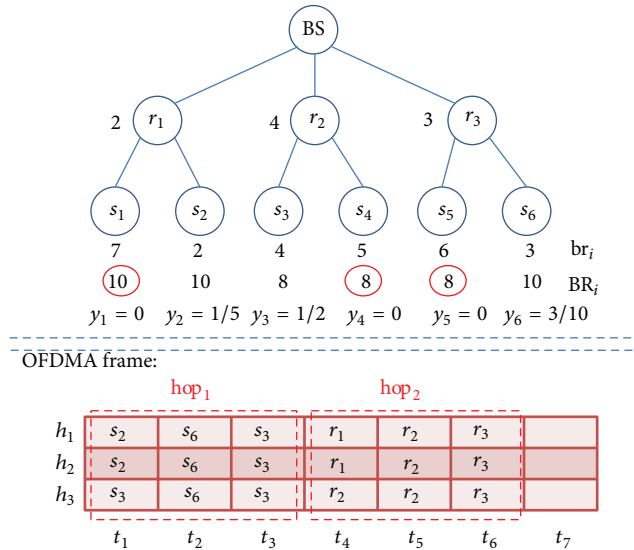


FIGURE 5: No remaining resources can be used to perform max-min fair scheduling.

of Algorithm 5, the scheduling of Algorithm 5 is terminated. Otherwise, all allocated tiles of s_j are recovered to set R , $\forall s_j \in \bar{I}_i$ at line (3) of Algorithm 5. Then, the spectral reuse strategy is used to allocate tiles to s_i for maximizing satisfaction ratio at lines (5)–(21) of Algorithm 5. When the available tiles set A_t enough to assign to k th hop, the tiles of A_t set are firstly allocated at lines (10)–(12) of Algorithm 5. When the set A_t cannot fulfill the req of s_i , both the set A_t and R_t are applied to allocate at lines (13)–(21) of Algorithm 5. When both the set A_t and R_t cannot satisfy the req of s_i at time slot t at line (21) of Algorithm 5, the difference of required tiles would be found at next time slot. If the requirement of all hops cannot be met, all acquired tiles of s_i have to be freed at lines (16)–(19) of Algorithm 5. Then, the scheduler continue to find out next SS until no resources can be allocated. By Algorithm 4, the scheduled satisfaction ratio of $\{s_1, s_4, s_5\}$ is

0. Algorithm 5 enhances satisfaction ratio of $\{s_1, s_4, s_5\}$ to $\{0.1, 0.125, 0.125\}$. The scheduling results of Algorithm 5 are shown in Figure 6.

Finally, we get min satisfaction ratio = 0.1, QoS satisfaction ratio = 0.5, and throughput = 12, as shown in Figure 7.

4. Simulation

In this section, we implement our heuristic algorithms and the algorithm proposed in [21] for performance comparison. We compare three parameters in the experimental results, namely, average minimum satisfaction ratio, average QoS satisfaction ratio, and average throughput.

4.1. Environmental Setup. For experimental environment setting, SS transmission range and interference range are

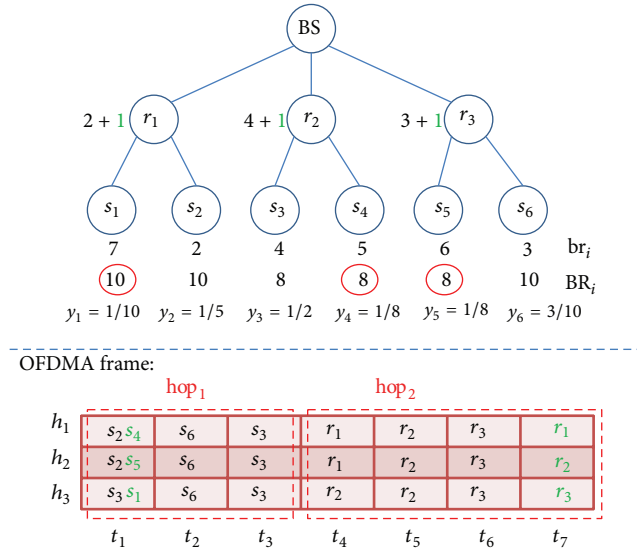


FIGURE 6: Using spectral reuse to perform max-min fair scheduling.

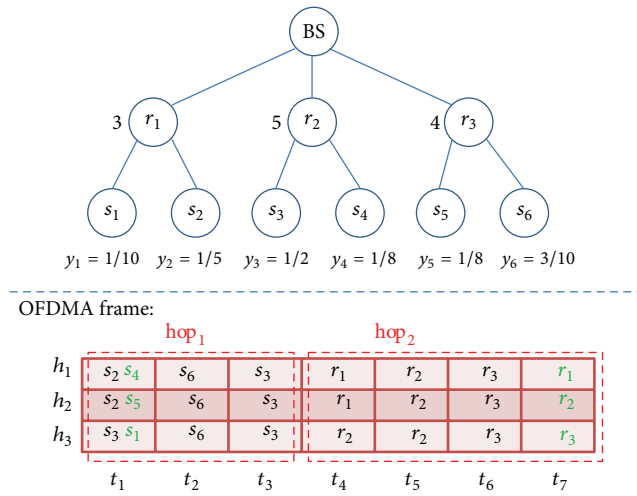


FIGURE 7: The result of example.

set 1000 and 1000; RS and the BS transmission range and interference range are set 1000 and 2000. BS was deployed at the center of the field. Multihop shortest path routing was adopted to obtain the network topology. SS is distributed in the field by random, each data packet requirement and QoS requirement of SS are set randomly among 2 to 8, and the QoS requirements of each SS must be less than or equal to the data packet requirement.

In the beginning, we use our heuristic algorithm and scheduling method of [21] in 1500×1500 square units and deployed 4 RSs to compare with three goals. These three goals are minimum satisfaction ratio, QoS satisfaction ratio, and throughput. For OFDMA setting, the number of time slots and subchannels are 12 and 5 in a frame. Then, we consider another large scale network which has 3000×3000 square units and deploy 16 RSs. For OFDMA setting, time-slots and subchannels number are 48 and 5 in a frame.

4.2. Experiment Results. Then we compare heuristic method with [21] on the experimental results of these two methods by three goals. The three goals are the ratio of average minimum satisfaction, average QoS satisfaction ratio, and average throughput.

When the number of SSs is increasing in Figure 8(a), it will lead to insufficient resources to allocate for all SSs then make min satisfaction ratio decrease. Our method allocates the resources to the proposed QoS requirements of SS at first priority and does the max-min fair allocation scheduling on the remaining resources. We find that the method of [21] is better than our method in terms of average min satisfaction ratio.

When the field changed to 3000×3000 , then 16 RSs are placed for experiment, and the number of SSs increased from 10 to 100. We can find that the number of SSs increased and

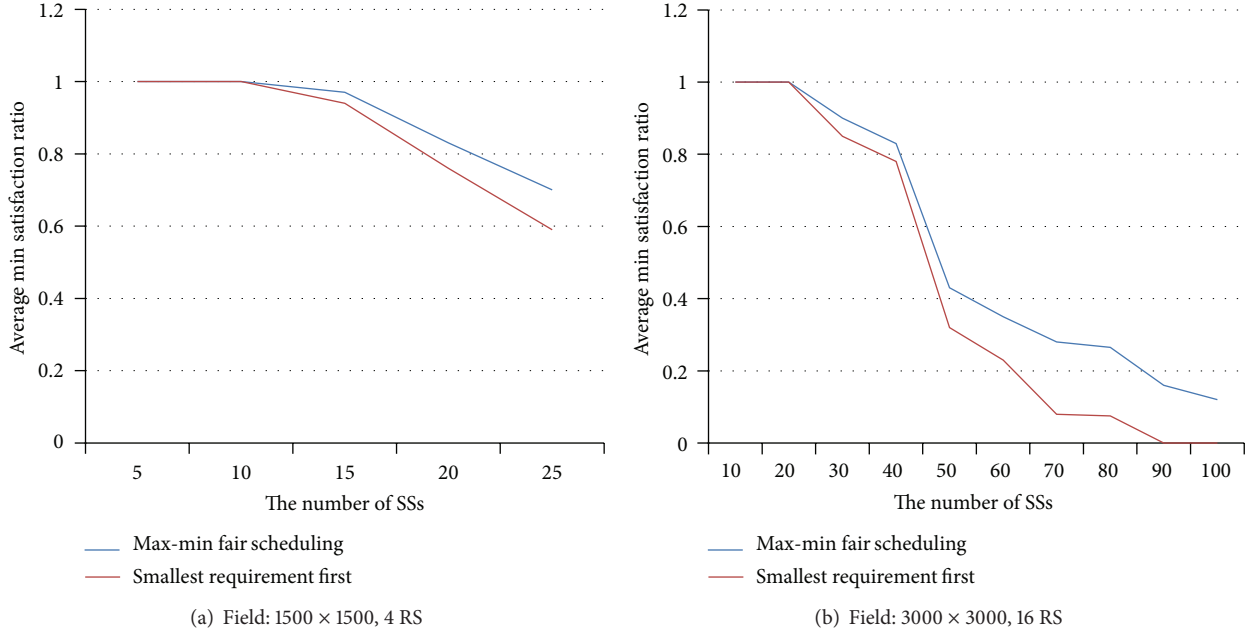


FIGURE 8: Average min satisfaction ratio comparison.

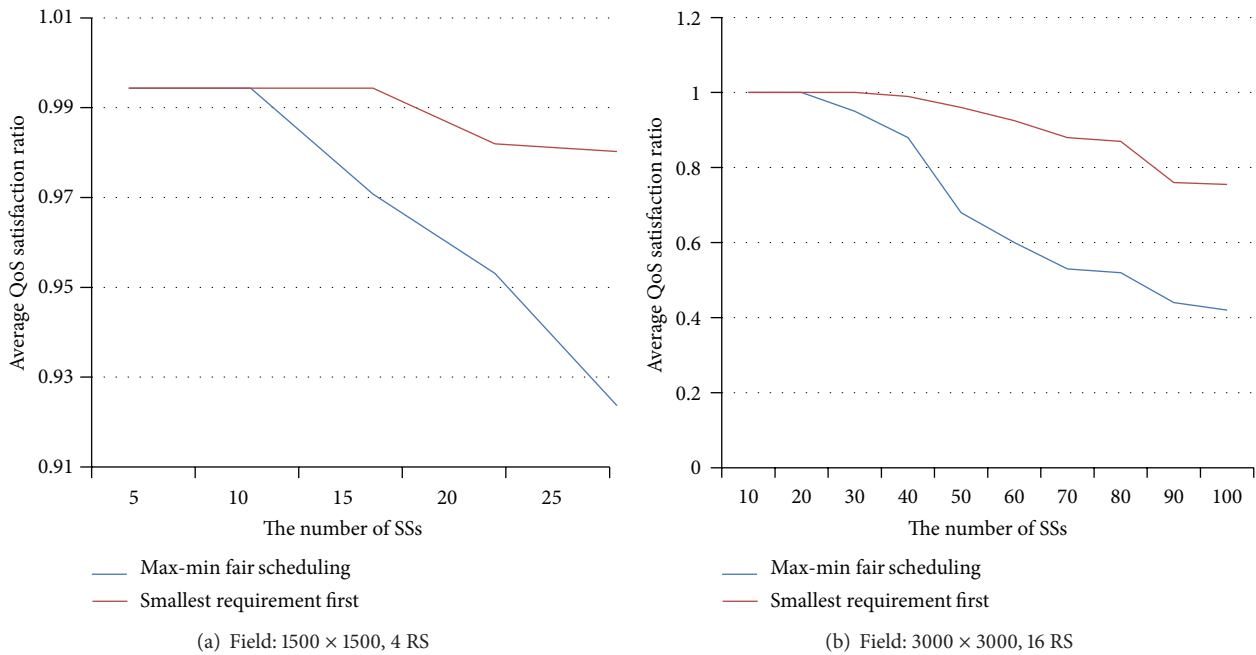


FIGURE 9: Average QoS satisfaction ratio comparison.

the number of hops increased in Figure 8(b), then the overall average min satisfaction ratio will decline obviously.

In Figure 9, our heuristic algorithm will be higher than the method of [21] when comparing with average QoS satisfaction ratio. In order to arrange the QoS requirements in increasing order and allocate resources in increasing order, our heuristic algorithm is better than [21] in terms of QoS satisfaction ratio.

From Figure 10, we can find that the average throughput of the two methods is almost equal. When the number of

hops increase, the average throughput of two methods is also almost equal.

5. Conclusion

In this paper, we study the multihop fairness scheduling problem with QoS control for enhancing throughput and guaranteeing QoS in WiMAX mesh networks. For allocating resource to multiple SSs, fairness is a key concern. The notion of max-min fairness is applied as our metric to define the

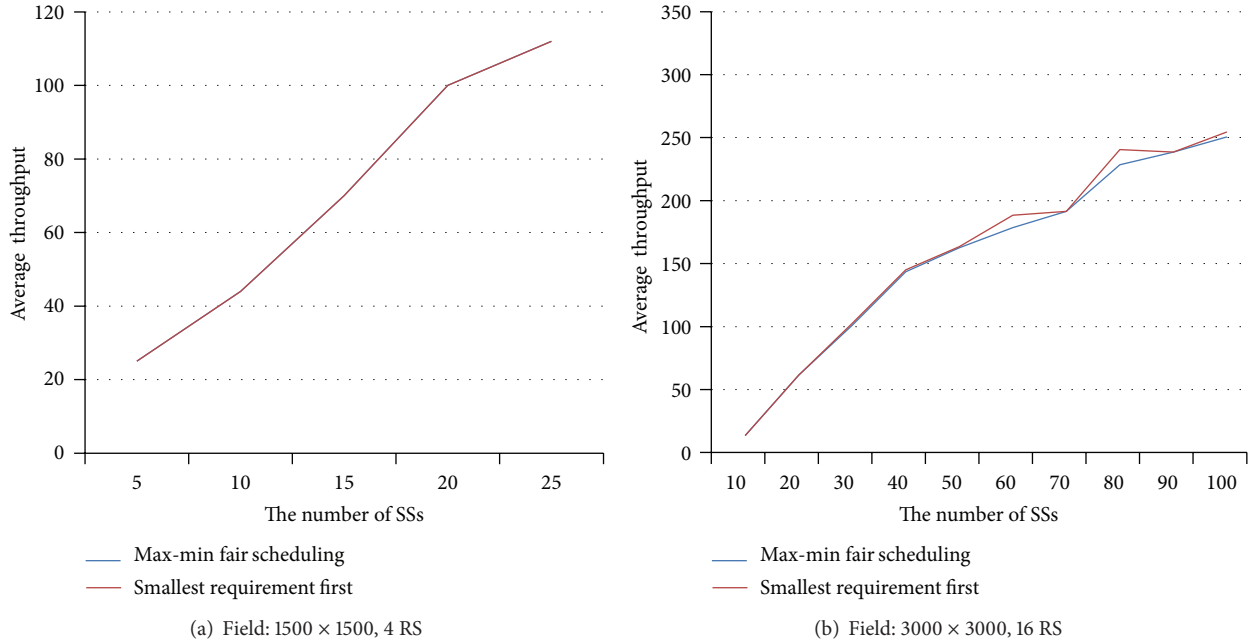


FIGURE 10: Average network throughput comparison.

QoS-based max-min fair scheduling problem for maximizing the minimum satisfaction ratio of each SS. We formulate an integer linear programming (ILP) model to provide an optimal solution on small-scale networks. Although the ILP solution can be used to obtain optimal solutions for small-scale network, it has high operation time and space consumption for large-scale networks.

Therefore, in the paper, several heuristic scheduling algorithms are proposed to maximize both the minimum satisfaction ratio and the QoS satisfaction ratio based on Orthogonal Frequency-Division Multiple Access (OFDMA) model in the networks. The strategy of proposed heuristic algorithm is smallest total bandwidth requirement first and then applying spectral reuse scheme to assign resource. After QoS of all SSs is guaranteed, the max-min fair scheduling scheme is used to enhance the overall throughput and satisfaction ratio. Experimental results show that our method is better than previous work in terms of QoS satisfaction ratio and throughput.

Acknowledgments

This work was supported in part by Taiwan NSC under Grant nos. NSC 102-2221-E-274-004 and NSC 102-2221-E-194-054. The authors would like to thank the reviewers for their insightful comments which helped to significantly improve the paper.

References

- [1] "IEEE 802.16e-2006 Standard, Part 16: Air Interface for Fixed and Mobile Broadband Wireless Access Systems—Amendment for Physical and Medium Access Control Layers for Combined Fixed and Mobile Operation in Licensed Bands," IEEE, 2006.
- [2] G. Li and H. Liu, "Downlink radio resource allocation for multi-cell OFDMA system," *IEEE Transactions on Wireless Communications*, vol. 5, no. 12, pp. 3451–3459, 2006.
- [3] A. Belghith, L. Nuaymi, and P. Maillé, "Pricing of real-time applications in WiMAX systems," in *Proceedings of the 68th Semi-Annual IEEE Vehicular Technology Conference (VTC '08)*, pp. 1–6, September 2008.
- [4] I. G. Fraimis, V. D. Papoutsis, and S. A. Kotsopoulos, "A decentralized subchannel allocation scheme with Inter-cell Interference Coordination (ICIC) for multi-cell OFDMA systems," in *Proceedings of the 53rd IEEE Global Communications Conference (GLOBECOM '10)*, December 2010.
- [5] V. Chandrasekhar, J. G. Andrews, and A. Gatherer, "Femtocell networks: a survey," *IEEE Communications Magazine*, vol. 46, no. 9, pp. 59–67, 2008.
- [6] Y. Kim and M. L. Sichitiu, "Fairness schemes in 802.16j mobile multihop relay networks," in *Proceedings of the 53rd IEEE Global Communications Conference (GLOBECOM '10)*, December 2010.
- [7] V. Gunasekaran and F. C. Harmantzis, "Affordable infrastructure for deploying WiMAX systems: Mesh v. Non Mesh," in *Proceedings of the IEEE 61st Vehicular Technology Conference (VTC '05)*, vol. 5, pp. 2979–2983, June 2005.
- [8] H. Shetiya and V. Sharma, "Algorithms for routing and centralized scheduling in IEEE 802.16 mesh networks," in *Proceedings of the IEEE Wireless Communications and Networking Conference (WCNC '06)*, vol. 1, pp. 147–152, April 2006.
- [9] C.-Y. Hong and A.-C. Pang, "Link scheduling with QoS guarantee for wireless relay networks," in *Proceedings of the 28th Conference on Computer Communications IEEE (INFOCOM '09)*, pp. 2806–2810, April 2009.
- [10] L. Fu, Z. Cao, and P. Fan, "Spatial reuse in IEEE 802.16 based wireless mesh networks," in *Proceedings of the International Symposium on Communications and Information Technologies (ISCIT '05)*, pp. 1311–1314, October 2005.

- [11] L.-W. Chen, Y.-C. Tseng, Y.-C. Wang, D.-W. Wang, and J.-J. Wu, "Exploiting spectral reuse in routing, resource allocation, and scheduling for IEEE 802.16 mesh networks," *IEEE Transactions on Vehicular Technology*, vol. 58, no. 1, pp. 301–313, 2009.
- [12] S. Ramanathan and E. L. Lloyd, "Scheduling algorithms for multihop radio networks," *IEEE/ACM Transactions on Networking*, vol. 1, no. 2, pp. 166–177, 1993.
- [13] I. F. Akyildiz, X. Wang, and W. Wang, "Wireless mesh networks: a survey," *Computer Networks*, vol. 47, no. 4, pp. 445–487, 2005.
- [14] G. Li and H. Liu, "On the capacity of broadband relay networks," in *Proceedings of the Conference Record of the 38th Asilomar Conference on Signals, Systems and Computers*, pp. 1318–1322, November 2004.
- [15] M. K. Awad and X. Shen, "OFDMA based two-hop cooperative relay network resources allocation," in *Proceedings of the IEEE International Conference on Communications (ICC '08)*, pp. 4414–4418, May 2008.
- [16] H.-Y. Wei, S. Ganguly, R. Izmailov, and Z. J. Haas, "Interference-aware IEEE 802.16 WiMax mesh networks," in *Proceedings of the IEEE 61st Vehicular Technology Conference (VTC '05)*, vol. 5, pp. 3102–3106, June 2005.
- [17] L. Tassiulas and S. Sarkar, "Maxmin fair scheduling in wireless networks," in *Proceedings of the IEEE Infocom*, pp. 763–772, June 2002.
- [18] S. C. Liew and Y. J. Zhang, "Proportional fairness in multi-channel multi-rate wireless networks," in *Proceedings of the IEEE Global Telecommunications Conference (GLOBECOM '06)*, December 2006.
- [19] A. Sayenko, O. Alanen, J. Karhula, and T. Hämäläinen, "Ensuring the QoS requirements in 802.16 scheduling," in *Proceedings of the 9th ACM Symposium on Modeling, Analysis and Simulation of Wireless and Mobile Systems (ACM MSWiM '06)*, pp. 108–117, October 2006.
- [20] M. Andrews and L. Zhang, "Scheduling algorithms for multi-carrier wireless data systems," in *Proceedings of the 13th Annual ACM International Conference on Mobile Computing and Networking (MobiCom '07)*, pp. 3–14, September 2007.
- [21] S. Bai, W. Zhang, Y. Liu, and C. Wang, "Max-min fair scheduling in OFDMA-based multi-hop WiMAX mesh networks," in *Proceedings of the IEEE International Conference on Communications (ICC '11)*, June 2011.
- [22] S. Deb, V. Mhatre, and V. Ramaiyan, "WiMAX relay networks: Opportunistic scheduling to exploit multiuser diversity and frequency selectivity," in *Proceedings of the 14th Annual International Conference on Mobile Computing and Networking (MobiCom '08)*, pp. 163–174, September 2008.
- [23] K. Sundaresan, W. Wang, and S. Eidenbenz, "Algorithmic aspects of communication in ad-hoc networks with smart antennas," in *Proceedings of the 7th ACM International Symposium on Mobile Ad Hoc Networking and Computing (MOBIHOC '06)*, pp. 298–309, May 2006.
- [24] Y. Xu, S. Wan, J. Tang, and R. S. Wolff, "Interference Aware routing and scheduling in wireless backhaul networks with smart antennas," in *Proceedings of the 6th Annual IEEE Communications Society Conference on Sensor, Mesh and Ad Hoc Communications and Networks (SECON '09)*, June 2009.

Research Article

Designing a Single-Stage Inverter for Photovoltaic System Application

M. T. Tsai, C. L. Chu, C. M. Mi, J. Y. Lin, and Y. C. Hsueh

Southern Taiwan University of Science and Technology, No. 1, Nan-Tai Street, Yung Kang District, Tainan City 710, Taiwan

Correspondence should be addressed to M. T. Tsai; mttsai@mail.stust.edu.tw

Received 12 September 2013; Accepted 8 October 2013

Academic Editor: Teen-Hang Meen

Copyright © 2013 M. T. Tsai et al. This is an open access article distributed under the Creative Commons Attribution License, which permits unrestricted use, distribution, and reproduction in any medium, provided the original work is properly cited.

This paper focuses on a full-bridge high-frequency isolated inverter which is proposed for distributed photovoltaic power supply application. The researched system consists of a full-bridge high-frequency DC/DC converter with the proposed symmetric phase-shift modulation algorithm to achieve the ZVS switching function and a line frequency unfolding bridge. It replaces the traditional two stages of independent control algorithms with a one-stage control to obtain high conversion efficiency. A TMS 320F2812 digital signal processor-based control technique is used to achieve the desired algorithm function for the grid-connected photovoltaic power system application. The researched system can have two operating methods depending on the applied situation. Finally, a prototype of 300 W with the maximum power point function is settled to verify the proposed idea.

1. Introduction

Recently, renewable energy, such as wind power and photovoltaic cell (PV), feeding the distributed power systems, has been increased and more visible. For PV applications, since the conversion becomes more and more efficient due to the different existing conversion technologies and the decreasing price of the PV modules, it has become suitable for small-scale residential applications with a range below 1kW [1–6]. There are many existing power inverter topologies for interfacing PV modules to the used terminal. Generally, a PV power system can be divided into stand-alone system and grid-connected system depending on whether it is parallel with the utility or not. For the stand-alone system, it usually needs batteries to give a supplement to the insufficient photovoltaic power. Stand-alone system is mainly used in the place without utility source or sparsely populated areas where the utility cannot supply energy with low cost. Grid-connected system is mainly used in the area where the utility can be served. Inverters connected to the grid involve two major functions, one is to ensure that the PV is operated with the maximum power point tracking (MPPT) and the other is to inject a sinusoidal current into the grid [7–11].

Development of grid-connected photovoltaic power supply system is divided into two categories, including centralized converter type and microconverter type [1–5]. The former uses multiple photovoltaic modules for string and/or parallel combination to concentrate the utility; such a framework is usually to adopt a stable DC bus design and it uses a large capacity of electrolyte capacitor to obtain a stable DC voltage; its advantages are more flexible than converter design, but with a worse operation performance for each module, while the latter, oppositely usually uses one or few photovoltaic modules to the utility, and the pulsating DC bus design and a small volume electrolyte capacitor are adopted. Thus, photovoltaic modules can have a better running performance. However, each team of photovoltaic modules requires a special convertor to transfer the energy to the electricity.

A single-stage high-frequency converter topology for decentralized PV systems has been presented in this paper for small-scale residential applications. In contrast to the classic converter topologies the proposed scheme presents a high power density. The researched system consisted of a full-bridge high-frequency DC/DC converter with the proposed symmetric phase-shift modulation algorithm to achieve the ZVS switching function and a DC/AC inverter which can

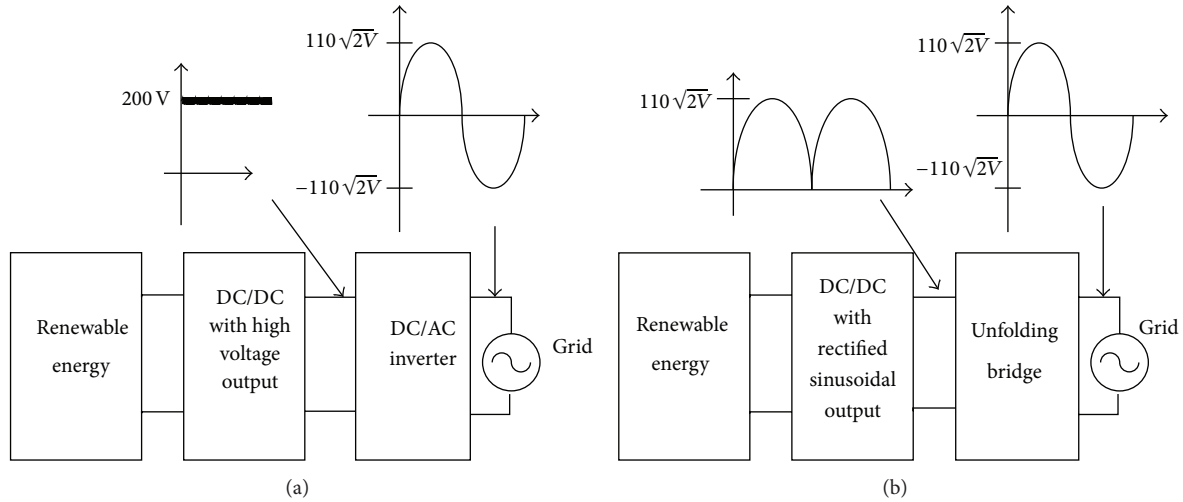


FIGURE 1: (a) Two-stage control-based PV system. (b) Single-stage control-based PV system.

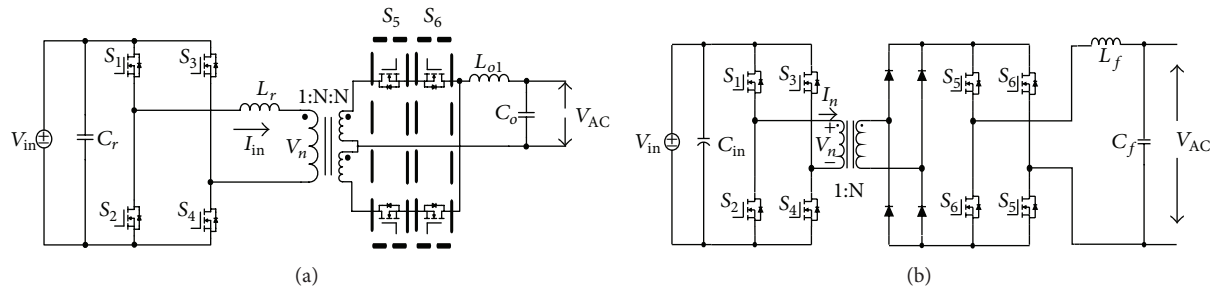


FIGURE 2: (a) The proposed single-stage control-based PV system architecture 1. (b) The proposed single-stage control-based PV system-architecture 2.

have two operating methods depending on the load characteristic. With the proposed control algorithm, it meets the requirement of a high efficiency conversion.

2. System Structure

PV power system is roughly divided into two major categories isolated and nonisolated. This study was to investigate the design of high-frequency isolated structure. For such an architecture, it is basically divided into two control designs depending on the availability large electrolyte capacitor, and can be described as follows.

2.1. Comparison of Two-Stage and Single-Stage Control-Based PV System. Two-Stage control based PV system basically consists of a high-frequency DC/DC stage whose output is connected to a stiff DC bus voltage which is with large electrolyte capacitors. Then the second DC/AC stage operated in sinusoidal pulse-width modulation switching transfers the energy to the utility. It can be shown in Figure 1(a). In contrast to this, the single-stage control based PV system basically consists of a high-frequency DC/DC stage whose output connected to a pulsating DC bus voltage which is with no electrolyte capacitors. Then an unfolding full-bridge inverter

switched in 60 Hz transfers the energy to the utility. It can be shown in Figure 1(b).

2.2. Single-Stage Control Based PV System. The proposed single-stage control based PV system can be implemented in two ways as shown in Figures 2(a) and 2(b). These two architectures have common characteristic of using pulse-link DC-AC converter [6]; therefore, a pulsating waveform presented in its DC output side. The difference between them is that the former's output stage can do the PWM switching in order to implement the nonunit power factor current, while the latter does not have this ability. When parallel to the utility, the control responsibility of both architectures in no change at the first stage, while the second stage is responsible only for low frequency (e.g., 60 Hz) switching to lower the switching losses. Under this situation, feeding a nonunit power current into the main will cause a distorted current waveform, and the distorted current can be solved by a properly PWM switching algorithm for Figure 2(a) but cannot be fitted for Figure 2(b).

This study is focused on a single-stage control based PV system shown in Figure 2, and a symmetric phase-shift control algorithm is adopted to replace the traditional SPWM switching algorithm so as to achieve the zero-voltage

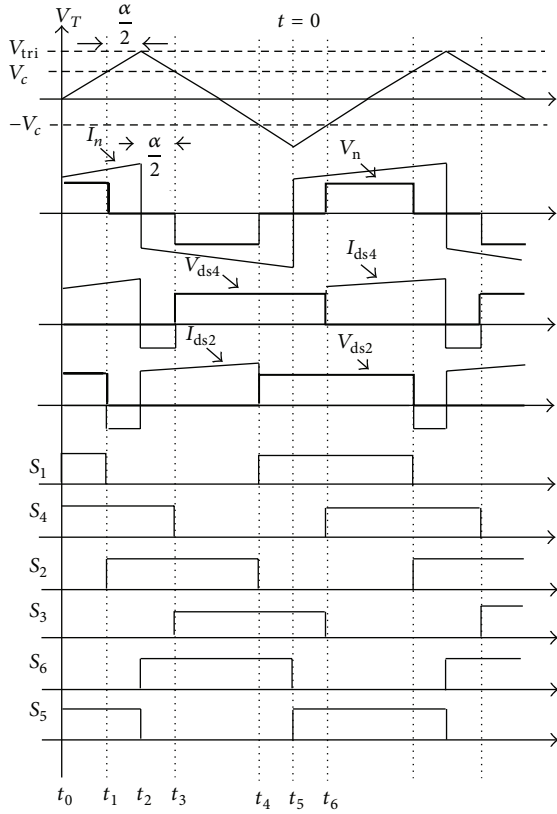


FIGURE 3: The conducting status of Figure 2(a) in stand-alone operation.

switching function. Also, two different switching modes will be introduced to cope with the unity power factor current demand or non-unit power current demand.

3. Symmetric Phase-Shift Control Algorithm

Conventional full-bridge phase-shift converter uses the parasitic capacitance on the switching elements and the leakage inductance existed in the high-frequency transformer to get the zero voltage switching effect. The advantages include reduced switching loss and the switch stress. However, it is suitable for DC/DC converter and cannot satisfy the sine wave output requirement. In response to the requirement achieved by single-stage control, this paper proposes a symmetric phase-shift control to fulfill the DC/AC function. The control algorithm is shown as follows.

In the case of Figure 1(a), the modulation function achieved by $S_1 \sim S_4$ before high frequency transformer, denoted as $H_F(t)$, can be described in (1), where α is denoted as the desired phase shift angle:

$$H_F(t) = \begin{cases} +V_{in}, & \frac{\alpha}{2} \leq t \leq \frac{T_s}{2} - \frac{\alpha}{2}, \\ -V_{in}, & \frac{T_s}{2} + \frac{\alpha}{2} \leq t \leq T - \frac{\alpha}{2}, \\ 0, & \text{elsewhere.} \end{cases} \quad (1)$$

Then, the modulation function achieved by $S_5 \sim S_6$ after high frequency transformer, denoted as $H_B(t)$, can be described as

$$H_B(t) = \begin{pmatrix} 1 & 0 \leq t \leq \frac{T_s}{2} \\ -1 & \frac{T_s}{2} \leq t \leq T_s \end{pmatrix}. \quad (2)$$

Thus, the primary voltage V_n and the control command V_c can be shown as follows:

$$\begin{aligned} V_n &= V_{in} \left(1 - \frac{2\alpha}{T_s} \right), \\ \alpha &= 0, & V_n &= V_{in}, \\ \alpha &= \frac{T_s}{2}, & V_n &= 0, \\ \alpha &= T_s, & V_n &= -V_{in}, \\ V_c &= \left(1 - \frac{2\alpha}{T_s} \right). \end{aligned} \quad (3)$$

To obtain a sinusoidal output, the command $V_{c(t)}$ should be a $\sin \omega t$ waveform; that is:

$$V_c(t) = V_c \sin \omega t. \quad (4)$$

Therefore, the output after $S_5 \sim S_6$ can be expressed as follows:

$$V_o = NV_{in} \frac{V_c}{V_{in}} \sin \omega t. \quad (5)$$

3.1. Stand-Alone Operation. In this situation, the PV inverter should be capable of supplying non-unit power factor current drawn by the load; thus only the structure shown in Figure 2(a) can fulfill the requirement, and Figure 3 shows the conducting status in this operation.

3.1.1. Interval ($t_0 \leq t < t_1$). In this status, S_1 and S_4 are ON; S_2 and S_3 are OFF. The transformer primary voltage is equal to the DC input voltage, and input current flows through the transformer primary side and the switches to form a current loop, making the power from the input source through the transformer to the secondary side, and then through the S_5 to the load. Figure 4(a) shows the energy transfer interval.

3.1.2. Interval ($t_1 \leq t < t_3$). As shown in Figure 4(b) in this status, S_2 and S_4 are ON; S_1 and S_3 are OFF. The energy flows through S_2 and the transformer primary side to form a flywheel current loop, and the transformer primary voltage V_n is in short status. For the transformer secondary, S_5 is ON at $t_1 \leq t < t_2$ and S_6 is ON at $t_2 \leq t < t_3$.

3.1.3. Interval ($t_3 \leq t < t_4$). In this status, S_2 and S_3 are ON; S_1 and S_4 are OFF. The transformer primary voltage is equal to the negative DC input voltage, and input current flows through the transformer primary side and the switches

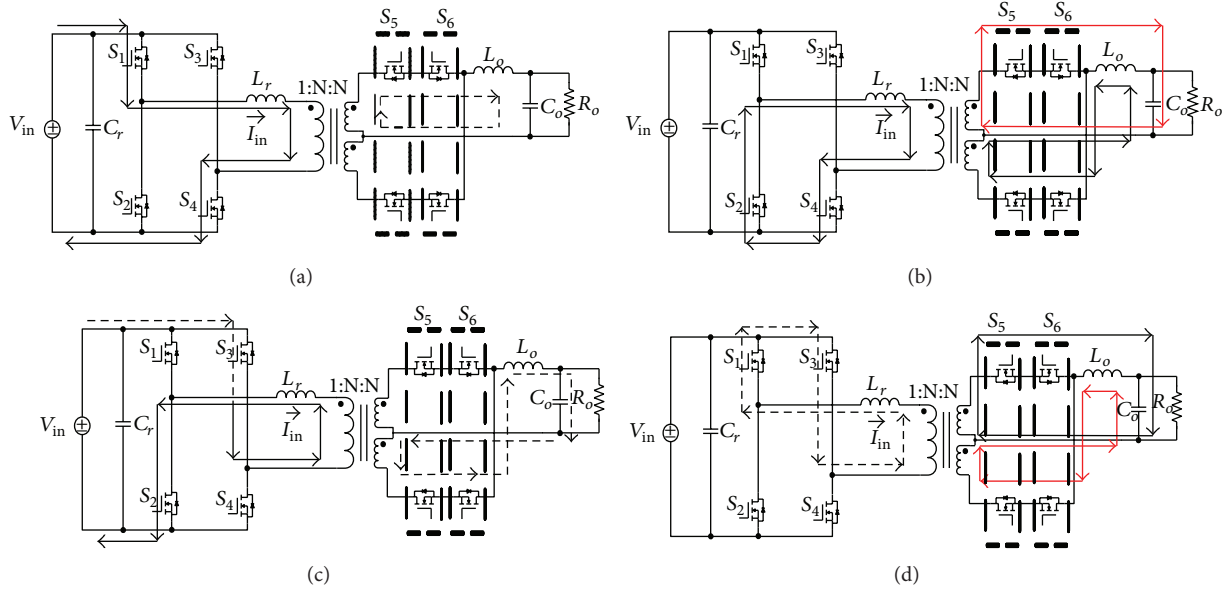


FIGURE 4: (a) Energy transfer interval I. (b) Energy flywheel interval I. (c) Energy transfer interval II. (d) Energy flywheel interval II.

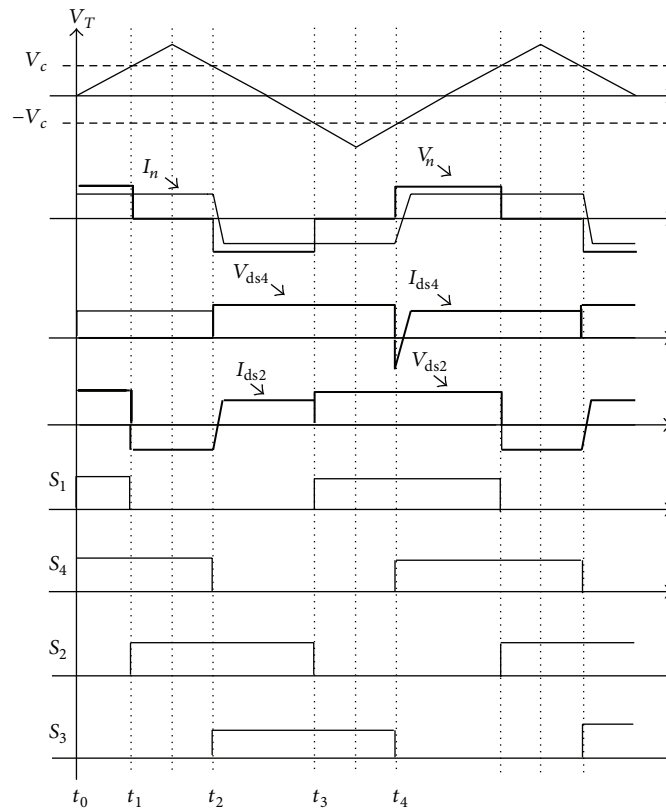


FIGURE 5: The conducting status due to Figure 2(b) structure.

to form a current loop, making the power from the input source through the transformer to the secondary side, and then through the S_6 to the load. Figure 4(c) shows the energy transfer interval.

3.1.4. Interval ($t_4 \leq t < t_6$). As shown in Figure 4(d) in this status, S_1 and S_3 are ON; S_2 and S_4 are OFF. The energy flows through S_1 and the transformer primary side to form a flywheel current loop, and the transformer primary voltage

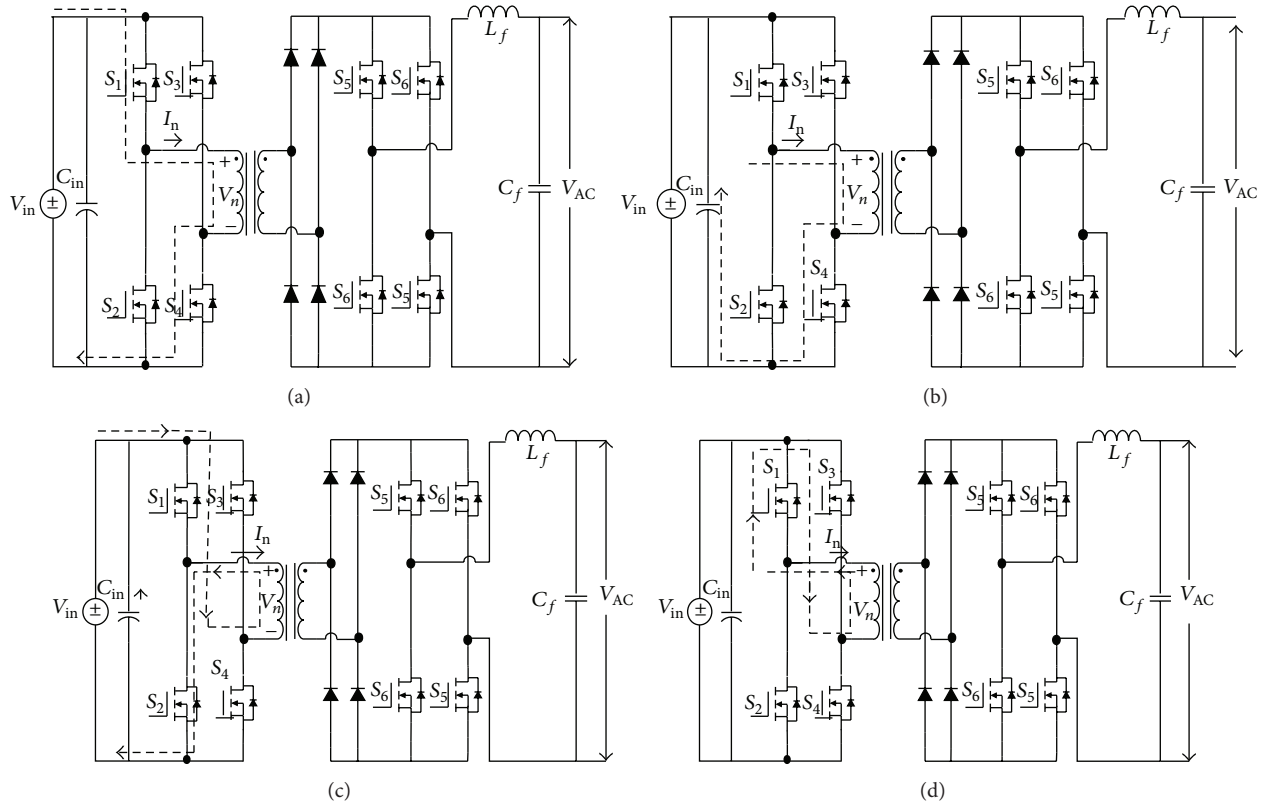


FIGURE 6: (a) Energy transfer interval I. (b) Energy flywheel interval I. (c) Energy transfer interval II. (d) Energy flywheel interval II.

V_n is in short status. For the transformer secondary, S_6 is ON at $t_4 \leq t < t_5$ and S_5 is ON at $t_5 \leq t < t_6$.

3.2. Grid-Connected Operation. In this situation, the PV inverter should be capable of supplying unity power factor current to the utility; thus both the structures shown in Figures 2(a) and 2(b) can fulfill the requirement, where the transformer secondary power switches S_5 and S_6 used as the unfolding bridge and switching at 60 HZ. An example based on Figure 2(b) topology can be shown in Figures 5 and 6, where Figure 5 shows the conducting status in the proposed control algorithm, and Figure 6 shows the four conducting stages.

3.2.1. Interval ($t_0 \leq t < t_1$). As shown in Figure 6(a), in this status S_1 and S_4 are ON; S_2 and S_3 are OFF. The transformer primary voltage is equal to the DC input voltage, and input current flows through the transformer primary side and the switches to form a current loop, making the power from the input source through the transformer to the secondary side, then through the S_5 or S_6 to the load dependent on the positive or negative cycle.

3.2.2. Interval ($t_1 \leq t < t_2$). As shown in Figure 6(b), in this status S_2 and S_4 are ON; S_1 and S_3 are OFF. The energy flows through S_2 and the transformer primary side to form

a flywheel current loop, and the transformer primary voltage V_n is in short status.

3.2.3. Interval ($t_2 \leq t < t_3$). As shown in Figure 6(c), in this status S_2 and S_3 are ON; S_2 and S_4 are OFF. The transformer primary voltage is equal to the negative DC input voltage, and input current flows through the transformer primary side and the switches to form a current loop, making the power from the input source through the transformer to the secondary side, and then through the S_5 or S_6 to the load dependent on the positive or negative cycle.

3.2.4. Interval ($t_3 \leq t < t_4$). As shown in Figure 6(d), in this status S_1 and S_3 are ON; S_2 and S_4 are OFF. The energy flows through S_1 and the transformer primary side to form a flywheel current loop, and the transformer primary voltage V_n is in short status.

3.3. Implementation. A prototype of 300 W due to Figure 2(b) structure has been settled to verify the proposed idea for stand-alone operation and grid-connected operation. The proposed DSP TMS320F2812 processor-based single-stage control block diagram dependent on the operation condition can be shown in Figures 7(a) and 7(b). Figure 7(a) shows the control block diagram for the stand-alone operation, and Figure 7(b) shows the control block diagram for the grid-connected operation. Figure 7(c)

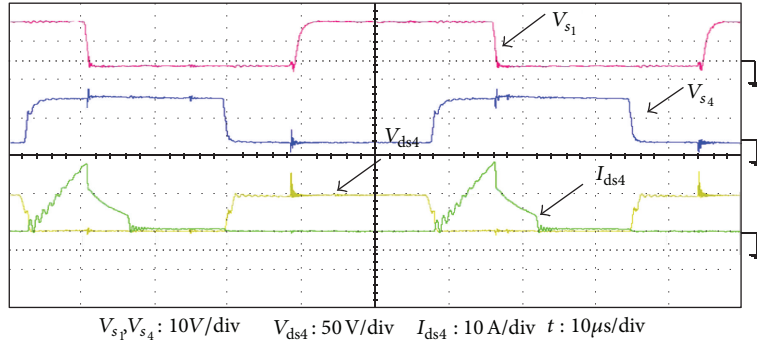
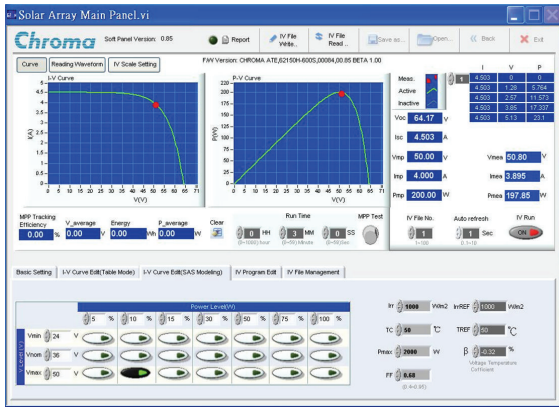
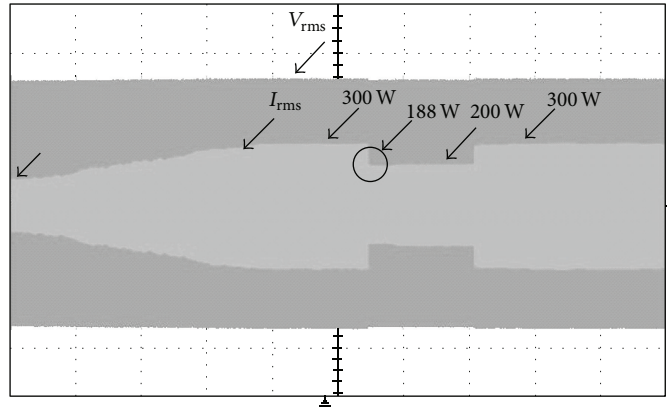


FIGURE 8: The driving signals V_{s1} , V_{s4} , the corresponding voltage V_{ds4} , and current I_{ds4} of S_4 .



(a)



(b)

FIGURE 9: The maximum power point tracking function in the proposed microinverter via a PV emulator manufactured by the Chroma company, (a) the maximum power point operating at 200 W, and (b) the tracking performance due to the PV power change of 300 W–200 W–300 W.

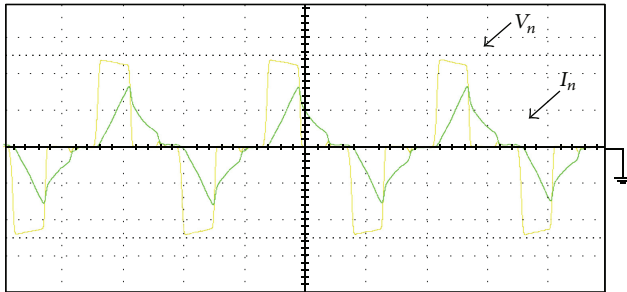


FIGURE 10: The primary input voltage and current of the high-frequency transformer.

shows the current controller, and Figure 7(d) shows the modulation strategy for $S_1 \sim S_4$ used for the grid-connected operation.

4. Simulation and Experimental Results

The system parameters used in the prototype are shown in Table 1.

Figure 8 shows the experimental results, including the driving signals of the switching devices, S_1 , S_4 , and the

TABLE 1: The parameters used in the experimental system.

V_{in}	40~60 V
V_o	110 V _{AC}
$S_1 \sim S_6$	IXTQ69N30
L_f	220 μ F
C_f	2.2 μ F
Switching frequency	18 kHz
Output power	300 W

corresponding voltage waveform and current waveform of S_4 . It shows that the switches can achieve ZVS function.

Figure 9 shows the maximum power point tracking function in the proposed microinverter via a PV emulator manufactured by the Chroma company. The PV output power is set at 200 W. It shows the proposed microinverter is operated at the maximum power related to the set point.

Figure 10 shows the primary input voltage and current of the high frequency transformer. It shows that no bias current existed there.

Figure 11 shows the inverter output voltage and current in the case of stand-alone situation and the grid-connected

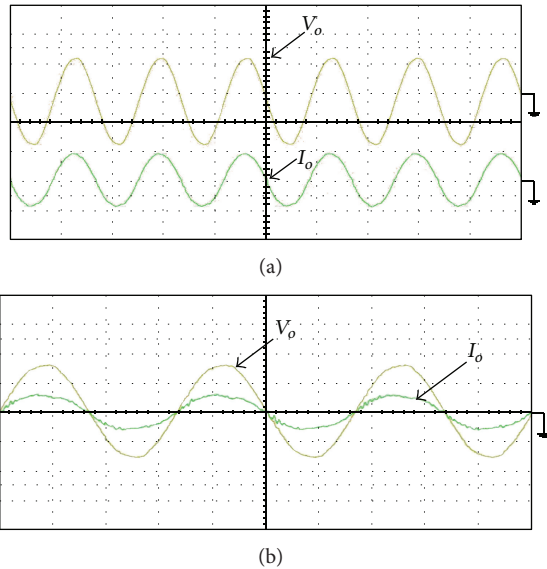


FIGURE 11: The inverter output voltage and current, (a) the stand-alone operation, and (b) the grid-connected operation. V_0 : 100 V/div. I_0 : 5 A/div. t : 2.5 ms/div.

situation. Figure 11(a) shows the stand-alone operation, and Figure 11(b) shows the grid-connected operation. It shows the proposed micro inverter can achieve the inphase current function due to the current control loop, and with low harmonics. The overall system efficiency is about 90%.

5. Conclusion

This paper discusses the steady-state behavior of the single-stage control-based inverter when controlled via a symmetrical phase shift modulation. The single-stage control based algorithm to replace the traditional two-stage control in the micro inverter applications can reduce the system complexity and increase the reliability due to the lack of the electrolytic capacitor. With the use of new symmetrical phase shift control, the ZVS switching performance can be achieved for the proposed micro inverter so as to reduce the switching stress and switching loss and thus improve the inverter's overall efficiency. The theoretical framework is validated by means of computer simulations and experimental results on a 300 W prototype.

Acknowledgment

This work has been supported by National Science Council, Taiwan, under research project NSC101-2221-E-218-040.

References

- [1] R.-J. Wai and W.-H. Wang, "Grid-connected photovoltaic generation system," *IEEE Transactions on Circuits and Systems I*, vol. 55, no. 3, pp. 953–964, 2008.
- [2] S. B. Kjaer, J. K. Pedersen, and F. Blaabjerg, "A review of single-phase grid-connected inverters for photovoltaic modules," *IEEE Transactions on Industry Applications*, vol. 41, no. 5, pp. 1292–1306, 2005.
- [3] Q. Li and P. Wolfs, "A review of the single phase photovoltaic module integrated converter topologies with three different DC link configurations," *IEEE Transactions on Power Electronics*, vol. 23, no. 3, pp. 1320–1333, 2008.
- [4] N. Kasa, T. Iida, and L. Chen, "Flyback inverter controlled by sensorless current MPPT for photovoltaic power system," *IEEE Transactions on Industrial Electronics*, vol. 52, no. 4, pp. 1145–1152, 2005.
- [5] T. Shimizu, K. Wada, and N. Nakamura, "Flyback-type single-phase utility interactive inverter with power pulsation decoupling on the DC input for an AC photovoltaic module system," *IEEE Transactions on Power Electronics*, vol. 21, no. 5, pp. 1264–1272, 2006.
- [6] D. Chen and L. Li, "Novel static inverters with high frequency pulse DC link," *IEEE Transactions on Power Electronics*, vol. 19, no. 4, pp. 971–978, 2004.
- [7] S. Jain and V. Agarwal, "Comparison of the performance of maximum power point tracking schemes applied to single-stage grid-connected photovoltaic systems," *IET Electric Power Applications*, vol. 1, no. 5, pp. 753–762, 2007.
- [8] N. Femia, G. Petrone, G. Spagnuolo, and M. Vitelli, "Optimization of perturb and observe maximum power point tracking method," *IEEE Transactions on Power Electronics*, vol. 20, no. 4, pp. 963–973, 2005.
- [9] A. K. Abdelsalam, A. M. Massoud, S. Ahmed, and P. N. Enjeti, "High-performance adaptive Perturb and observe MPPT technique for photovoltaic-based microgrids," *IEEE Transactions on Power Electronics*, vol. 26, no. 4, pp. 1010–1021, 2011.
- [10] D. Chen and J. Liu, "The uni-polarity phase-shifted controlled voltage mode ac-ac converters with high frequency ac link," *IEEE Transactions on Power Electronics*, vol. 21, no. 4, pp. 899–905, 2006.
- [11] A. K. Abbasi and M. W. Mustafa, "Mathematical model and stability analysis of inverter-based distributed generator," *Mathematical Problems in Engineering*, vol. 2013, Article ID 195038, 7 pages, 2013.

Research Article

FPGA Realization of Sensorless PMSM Speed Controller Based on Extended Kalman Filter

Ying-Shieh Kung,¹ Nguyen Vu Quynh,² Nguyen Trung Hieu,¹ and Jin-Mu Lin¹

¹ Department of Electrical Engineering, Southern Taiwan University of Science and Technology, 1 Nan-Tai Street, Yong-Kang District, Tainan City 710, Taiwan

² Department of Electrical Engineering, Lac Hong University, 10 Huynh Van Nghe Street, Buu Long District, Bien Hoa City 084, Dong Nai Province, Vietnam

Correspondence should be addressed to Ying-Shieh Kung; kung@mail.stust.edu.tw

Received 9 September 2013; Accepted 22 October 2013

Academic Editor: Teen-Hang Meen

Copyright © 2013 Ying-Shieh Kung et al. This is an open access article distributed under the Creative Commons Attribution License, which permits unrestricted use, distribution, and reproduction in any medium, provided the original work is properly cited.

Based on extended Kalman filter (EKF), the design and FPGA implementation of a sensorless control intellectual property (IP) for permanent magnet synchronous motor (PMSM) drive are presented in this paper. Firstly, the mathematical model for PMSM is derived and the vector control is built up. Secondly, the rotor flux angle (FA) and rotor speed which are estimated by using EKF are described. These estimated values are feedbacked to the current loop for vector control and to the speed loop for speed control. Thirdly, the very-high-speed IC hardware description language (VHDL) is adopted to describe the behavior of the sensorless speed control IP which includes the circuits of space vector pulse width modulation (SVPWM), coordinate transformation, EKF, and PI controller. Finally, to evaluate the effectiveness and correctness of the proposed of system, a cosimulation work performed by Simulink and ModelSim is firstly conducted. Then, an experimental system by FPGA chip and motor driving board is set up to further validate the performance of the proposed EKF-based sensorless speed control IP.

1. Introduction

PMSM has been increasingly used in many automation control fields as actuators, due to its advantages of superior power density, high-performance motion control with fast speed, and better accuracy. However, conventional motor control needs a speed sensor or an optical encoder to measure the rotor speed and feedback it to the controller for ensuring the precision speed control. Such sensor presents some disadvantages such as drive cost, machine size, reliability, and noise immunity. In recent years, a sensorless control without position and speed sensors for PMSM drive become a popular research topic in the literature [1–7]. Those sensorless control strategies have sliding mode observer (SMO), extended Kalman filter (EKF), reduced-order EKF, and so forth. The EKF is basically a full-order stochastic observer for the recursive optimum state estimation of a nonlinear dynamic system in real time by using signals that are in noisy environment [7]. Comparing with SMO, EKF can directly

estimate the angular speed and it has high convergence rate which can give a more rapid speed response [5]. However, EKF requires heavy online 4×4 matrix computing; therefore, the complex computation becomes a challenge for a fixed-point processor system. In realization, a fixed-point processor using digital signal processor (DSP) and field programmable gate array (FPGA) both can provide a good solution in this issue. Particularly, FPGA with programmable hardwired feature, fast computation ability, shorter design cycle, embedding processor, low power consumption, and higher density is better for the implementation of the digital system [8, 9] than DSP.

Recently, a cosimulation work by Electronic Design Automation (EDA) Simulator Link has been gradually applied to verify the effectiveness of the Verilog and VHDL code in the motor drive system [10–12]. The EDA Simulator Link [13] provides a cosimulation interface between MATLAB or Simulink and HDL simulators-ModelSim [14]. Using it you

can verify a VHDL, Verilog, or mixed-language implementation against your Simulink model or MATLAB algorithm [13]. Therefore, EDA Simulator Link lets you use MATLAB code and Simulink models as a test bench that generates stimulus for an HDL simulation and analyzes the simulation's response [13]. In this paper, a cosimulation by EDA Simulator Link is applied to sensorless speed control for PMSM drive. The PMSM, inverter, and speed command are performed in Simulink and the EKF algorithm; current vector controller and speed PI controller described by VHDL code are executed in ModelSim. After successful verification in simulation, an FPGA-based experimental system is established with configuration as in Figure 1 for realizing the proposed IP code again, and experiment results will validate the effectiveness of the sensorless speed control system of PMSM drive.

2. System Description of PMSM Drive and Sensorless Speed Control

The sensorless speed control block diagram for PMSM drive is shown in Figure 1. The modeling of PMSM, the EKF-based rotor flux angle (FA) and rotor speed estimation, and the PI controller are introduced as follows.

2.1. Mathematical Model of PMSM. The mathematical model of a PMSM is described, in two-axis d - q synchronous rotating reference frame, as follows:

$$\begin{aligned} \frac{di_d}{dt} &= -\frac{r_s}{L_d}i_d + \omega_e \frac{L_q}{L_d}i_q + \frac{1}{L_d}v_d, \\ \frac{di_q}{dt} &= -\omega_e \frac{L_d}{L_q}i_d - \frac{r_s}{L_q}i_q - \omega_e \frac{\lambda_f}{L_q} + \frac{1}{L_q}v_q, \end{aligned} \quad (1)$$

where v_d, v_q are the d and q axes voltages; i_d, i_q are the d and q axes currents, r_s is the phase winding resistance; L_d, L_q are the d and q axes inductance; ω_e is the rotating speed of magnet flux; and λ_f is the permanent magnet flux linkage.

The current loop control of PMSM drive in Figure 1 is based on a vector control approach. That is, if the i_d is forced to 0, the PMSM will be decoupled, and controlling a PMSM is like controlling a DC motor. After decoupling, the motor's torque is proportional to i_q :

$$T_e = \frac{3N_p}{4} \lambda_f i_q \triangleq K_t i_q. \quad (2)$$

Considering the mechanical load, the overall dynamic equation of PMSM drive system is obtained by

$$J_m \frac{d}{dt} \omega_r + B_m \omega_r = T_e - T_L, \quad (3)$$

where T_e is the motor torque, N_p is pole pairs, K_t is torque constant, J_m is the inertial value, B_m is damping ratio, T_L is the external torque, and ω_r is rotor speed.

2.2. Extended Kalman Filter (EKF). For a motor stochastic nonlinear equation, it can be written in the following form:

$$\dot{x}(t) = f[x(t)] + Bu(t) + \sigma(t), \quad (4)$$

$$y(t) = h[x(t)] + \mu(t), \quad (5)$$

where $x(t)$, $u(t)$, and $y(t)$ are system state, system input, and system output, respectively. The $\sigma(t)$ and $\mu(t)$ represent system noise and measurement noise which are zero-mean white Gaussian distribution with covariance $Q(t)$ and $R(t)$, respectively. Once a nominal solution to a motor nonlinear equation can be found in (4)-(5), the linearized perturbation equation is

$$\delta \dot{x}(t) = F(x(t)) \delta x(t) + B \delta u(t) + \sigma(t), \quad (6)$$

$$\delta y(t) = H(x(t)) \delta x + \mu(t), \quad (7)$$

where the Jacobian and output matrices are defined as follows:

$$F(x(t)) = \left. \frac{\partial f}{\partial x} \right|_{x=x(t)}, \quad (8)$$

$$H(x(t)) = \left. \frac{\partial h}{\partial x} \right|_{x=x(t)}.$$

After discretization with sampling time T_c , (6) becomes

$$\begin{aligned} x(t_n) &= \Phi(t_n, t_{n-1}, x(t_{n-1})) x(t_{n-1}) \\ &+ \int_{t_{n-1}}^{t_n} \Phi(t_n, t_{n-1}, x(t_{n-1})) B d\tau \cdot u(t_{n-1}) + \nu(t_{n-1}), \end{aligned} \quad (9)$$

where $\Phi(t_n, t_{n-1}, x(t_{n-1}))$ is an exponential matrix and its computation can be simplified by

$$\Phi(t_n, t_{n-1}, x(t_{n-1})) \cong I + FT_c. \quad (10)$$

Further,

$$\int_{t_{n-1}}^{t_n} \Phi(t_n, t_{n-1}, x(t_{n-1})) B d\tau \cong BT_c. \quad (11)$$

Therefore, the discrete model of (6)-(7) becomes

$$x(n) = (I + FT_c) x(n-1) + BT_c \cdot u(n-1) + \nu(n-1), \quad (12)$$

$$y(n) = H \cdot x(n) + \xi(n-1), \quad (13)$$

where $t_n = nT_c$ and $t_{n-1} = (n-1)T_c$.

The EKF is an optimal estimator which searches the cost function $J = \sum_{n=1}^m E\{\tilde{x}^2(n)\}$ at the least square sense. The $\tilde{x}(n)$ is defined by $\tilde{x}(n) = \hat{x}(n) - x(n)$, which is the difference of estimation of state $\hat{x}(n)$ and system state $x(n)$. The EKF algorithm is described by the following two-step recursive equations.

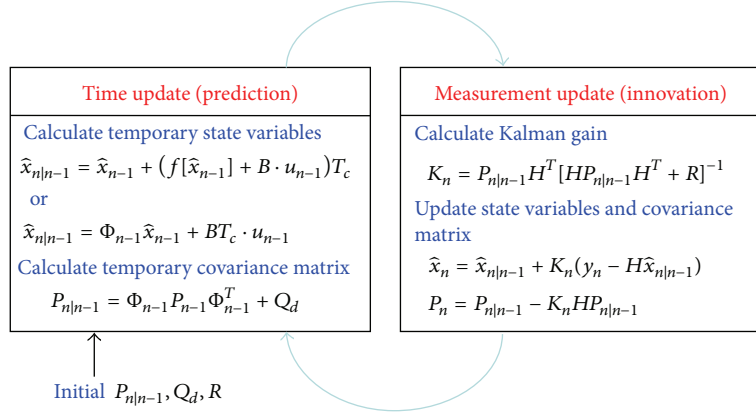


FIGURE 2: Demonstration of the EKF operation.

where $x(t) = [i_\alpha \ i_\beta \ \omega_e \ \theta_e]^T$, $y(t) = [i_\alpha \ i_\beta]$, and $u(t) = [v_\alpha \ v_\beta]^T$. From (8) and (22), the Jacobian and output matrices can be obtained:

$$F(x(t)) = \left. \frac{\partial f}{\partial x} \right|_{x=x(t)} = \begin{bmatrix} -\frac{r_s}{L_s} & 0 & \frac{\lambda_f}{L_s} \sin \theta_e & \frac{\omega_e \lambda_f}{L_s} \cos \theta_e \\ 0 & -\frac{r_s}{L_s} & -\frac{\lambda_f}{L_s} \cos \theta_e & \frac{\omega_e \lambda_f}{L_s} \sin \theta_e \\ 0 & 0 & 0 & 0 \\ 0 & 0 & 1 & 0 \end{bmatrix}, \quad (24)$$

$$H(x(t)) = \left. \frac{\partial h}{\partial x} \right|_{x=x(t)} = \begin{bmatrix} 1 & 0 & 0 & 0 \\ 0 & 1 & 0 & 0 \end{bmatrix}. \quad (25)$$

Further, substituting (24) into (10), the exponential matrix is shown as follows:

$$\begin{aligned} & \Phi(t_n, t_{n-1}, x(t_{n-1})) \\ & \cong I + FT_c \\ & = \begin{bmatrix} 1 - \frac{r_s T_c}{L_s} & 0 & \frac{\lambda_f T_c}{L_s} \sin \theta_e & \frac{\omega_e \lambda_f T_c}{L_s} \cos \theta_e \\ 0 & 1 - \frac{r_s T_c}{L_s} & -\frac{\lambda_f T_c}{L_s} \cos \theta_e & \frac{\omega_e \lambda_f T_c}{L_s} \sin \theta_e \\ 0 & 0 & 1 & 0 \\ 0 & 0 & T_c & 1 \end{bmatrix} \\ & \triangleq \begin{bmatrix} G & 0 & \phi_{13} & \phi_{14} \\ 0 & G & \phi_{23} & \phi_{24} \\ 0 & 0 & 1 & 0 \\ 0 & 0 & T_c & 1 \end{bmatrix}. \end{aligned} \quad (26)$$

As the results, the EKF algorithm in (14)–(19) can be carried out to estimate the state value. The initial values of Q_d , R , and P_0 need to be chosen. Through the recursive calculation, the

state value of $\hat{x}(n) = [\hat{i}_\alpha(n), \hat{i}_\beta(n), \hat{\omega}_e(n), \hat{\theta}_e(n)]^T$ is estimated at each sampling period; then the rotor speed can be derived by

$$\hat{\omega}_r(n) = \frac{\hat{\omega}_e(n)}{N_p}. \quad (27)$$

Finally, a summary for the estimation of rotor FA and rotor speed based on EKF is presented as follows.

Step 1. Set the initial values of Q_d , R , P_0 , and $n = 1$.

Step 2. Measure the values of $i_\alpha(n)$, $i_\beta(n)$, $v_\alpha(n)$, and $v_\beta(n)$ from PMSM system.

Step 3. Estimate the temporary state variables from (14). In addition, refer to (22), and the scalar form of the prediction equation can be expressed as follows:

$$\begin{aligned} \hat{i}_\alpha(n | n-1) &= \left(1 - T_c \frac{r_s}{L_s}\right) \hat{i}_\alpha(n-1) \\ &+ \frac{\hat{\omega}_e(n-1) T_c \lambda_f \sin(\hat{\theta}_e(n-1))}{L_s} \\ &+ \frac{T_c v_\alpha(n-1)}{L_s}, \\ \hat{i}_\beta(n | n-1) &= \left(1 - T_c \frac{r_s}{L_s}\right) \hat{i}_\beta(n-1) \\ &- \frac{\hat{\omega}_e(n-1) T_c \lambda_f \cos(\hat{\theta}_e(n-1))}{L_s} \\ &+ \frac{T_c v_\beta(n-1)}{L_s}, \\ \hat{\omega}_e(n | n-1) &= \hat{\omega}_e(n-1), \\ \hat{\theta}_e(n | n-1) &= \hat{\theta}_e(n-1) + \hat{\omega}_e(n-1) T_c. \end{aligned} \quad (28)$$

Step 4. Calculate the Φ_{n-1} from (26).

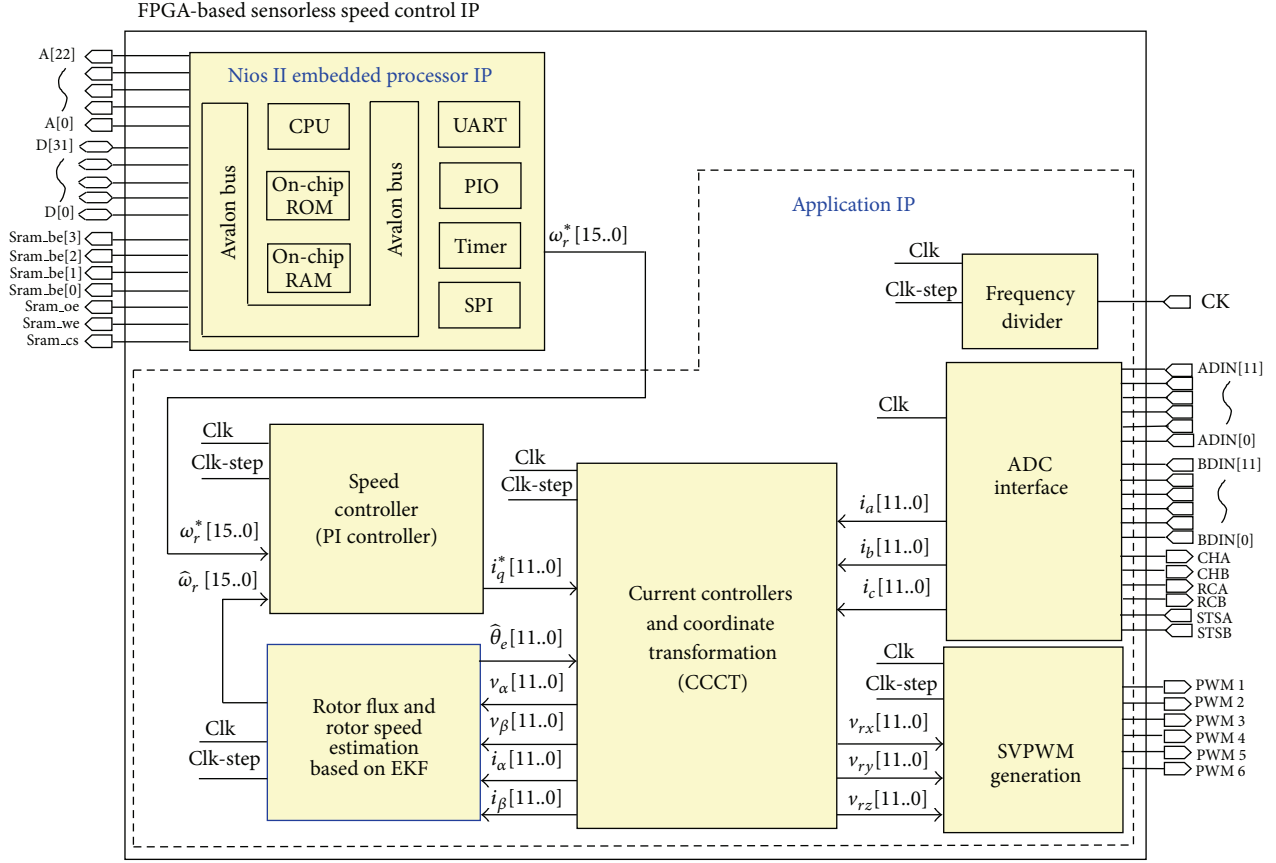


FIGURE 3: Internal architecture of a sensorless speed control IP in FPGA.

Step 5. Obtain the temporary covariance matrix $P_{n|n-1}$ from (16). Because matrix $P_{n|n-1}$ is symmetric matrix by $p_{ij} = p_{ji}$, it can be chosen by the following form:

$$P_{n|n-1} = \begin{bmatrix} P_{11} & P_{12} & P_{13} & P_{14} \\ P_{21} & P_{22} & P_{23} & P_{24} \\ P_{31} & P_{32} & P_{33} & P_{34} \\ P_{41} & P_{42} & P_{43} & P_{44} \end{bmatrix}. \quad (29)$$

Hence, from (16), individual elements of $P_{n|n-1}$ could be updated as follows:

$$\begin{aligned} p_{11} &\Leftarrow G^2 p_{11} + 2G\phi_{14}p_{14} + 2G\phi_{13}p_{13} + 2\phi_{14}\phi_{13}p_{34} \\ &\quad + \phi_{14}^2 p_{44} + \phi_{13}^2 p_{33} + q_{11}, \\ p_{12} &\Leftarrow G^2 p_{12} + G\phi_{14}p_{24} + G\phi_{13}p_{23} \\ &\quad + \phi_{23}(Gp_{13} + \phi_{13}p_{33} + \phi_{14}p_{34}) \\ &\quad + \phi_{24}(Gp_{14} + \phi_{13}p_{34} + \phi_{14}p_{44}), \\ p_{13} &\Leftarrow Gp_{13} + \phi_{13}p_{33} + \phi_{14}p_{34}, \\ p_{14} &\Leftarrow (Gp_{13} + \phi_{13}p_{33} + \phi_{14}p_{34})T_c \\ &\quad + (Gp_{14} + \phi_{13}p_{34} + \phi_{14}p_{44}), \\ p_{22} &\Leftarrow 2G(\phi_{23}p_{23} + \phi_{24}p_{24}) + G^2 p_{22} + \phi_{23}^2 p_{33} \\ &\quad + \phi_{24}^2 p_{44} + 2\phi_{23}\phi_{24}p_{34} + q_{22}, \end{aligned}$$

$$\begin{aligned} p_{23} &\Leftarrow Gp_{23} + \phi_{23}p_{33} + \phi_{24}p_{34}, \\ p_{24} &\Leftarrow (Gp_{23} + \phi_{23}p_{33} + \phi_{24}p_{34})T_c + Gp_{24} \\ &\quad + \phi_{24}p_{44} + \phi_{23}p_{34}, \end{aligned}$$

$$p_{33} \Leftarrow p_{33} + q_{33},$$

$$p_{34} \Leftarrow T_c p_{33} + p_{34},$$

$$p_{44} \Leftarrow p_{44} + T_c^2 p_{33} + 2T_c p_{34} + q_{44}.$$

(30)

Step 6. Calculate the Kalman gain from (19). Using (25) and (29), the formulation is further simplified as follows. Firstly,

$$\begin{aligned} &[HP_{n|n-1}H^T + R]^{-1} \\ &= \begin{bmatrix} 1 & 0 & 0 & 0 \\ 0 & 1 & 0 & 0 \end{bmatrix} \begin{bmatrix} p_{11} & p_{12} & p_{13} & p_{14} \\ p_{21} & p_{22} & p_{23} & p_{24} \\ p_{31} & p_{32} & p_{33} & p_{34} \\ p_{41} & p_{42} & p_{43} & p_{44} \end{bmatrix} \begin{bmatrix} 1 & 0 \\ 0 & 1 \\ 0 & 0 \\ 0 & 0 \end{bmatrix} \\ &\quad + \begin{bmatrix} R_{11} & 0 \\ 0 & R_{22} \end{bmatrix}^{-1} \\ &= \left[\begin{bmatrix} p_{11} & p_{12} \\ p_{21} & p_{22} \end{bmatrix} + \begin{bmatrix} R_{11} & 0 \\ 0 & R_{22} \end{bmatrix} \right]^{-1}, \end{aligned}$$

(31)

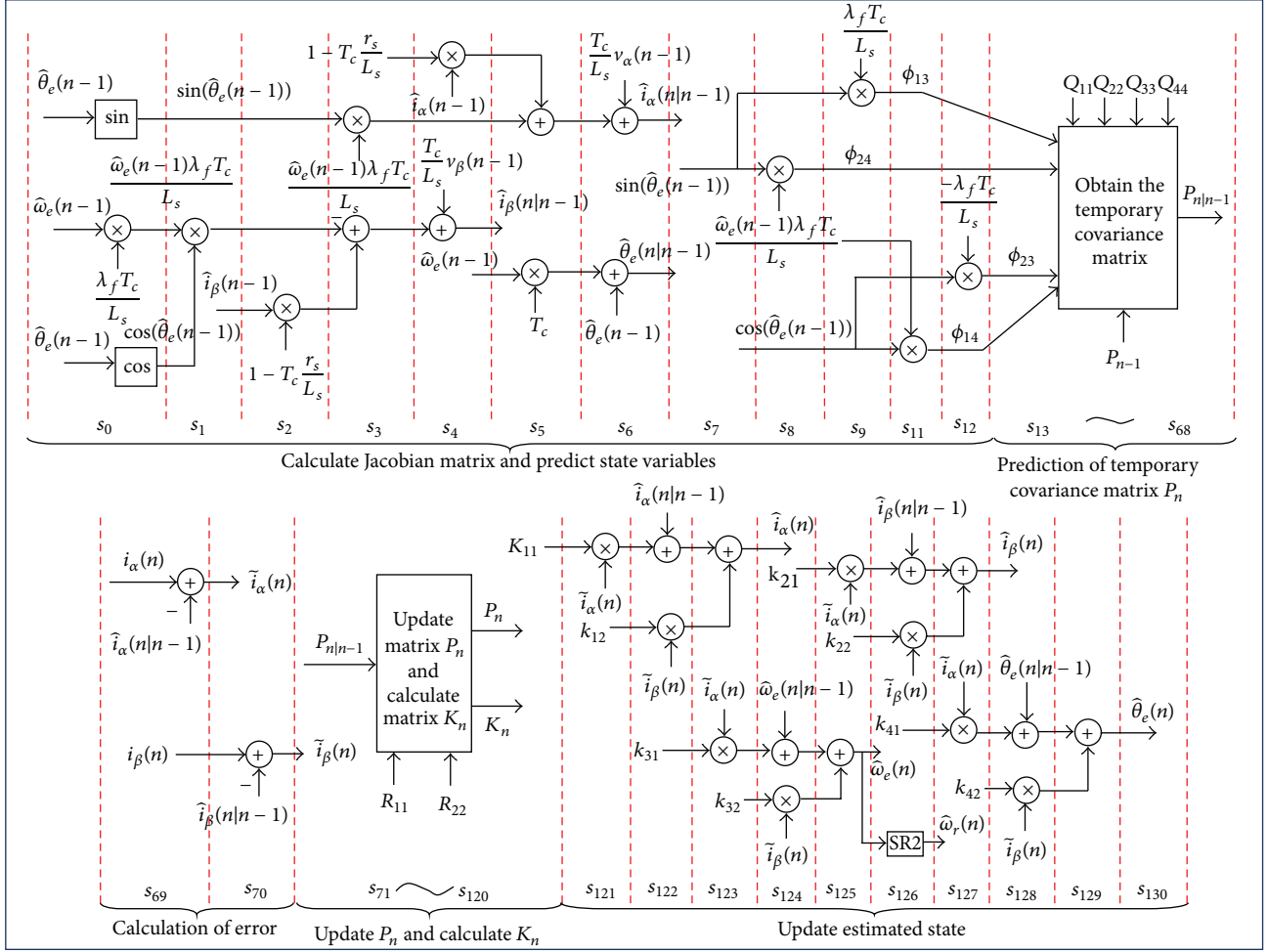


FIGURE 4: State diagram of FSM for describing the EKF-based algorithm.

where R represents the uncertainties of measurement variable which are very difficult to know. Hence, R is often chosen as unity matrix for simplifying the task but does not affect the outcome (31). Since $P_{12} = P_{21}$, (31) can be rewritten in the following form:

$$\begin{aligned} & [HP_{n|n-1}H^T + R]^{-1} \\ &= \frac{1}{P_{11}P_{22} + P_{11} + P_{22} - P_{12}^2 + 1} \begin{bmatrix} P_{22} + 1 & -P_{12} \\ -P_{12} & P_{11} + 1 \end{bmatrix}. \end{aligned} \quad (32)$$

To normalize the input value and to prevent the numerical overflow condition which occurred during computation, (32) is normalized and those values are all divided by 4. Therefore, (32) becomes

$$[HP_{n|n-1}H^T + R]^{-1} = \frac{1}{M} \begin{bmatrix} \frac{P_{22} + 1}{4} & \frac{-P_{12}}{4} \\ \frac{-P_{12}}{4} & \frac{P_{11} + 1}{4} \end{bmatrix} \triangleq \begin{bmatrix} t_{11} & t_{12} \\ t_{21} & t_{22} \end{bmatrix}, \quad (33)$$

where $M = (p_{11}p_{22} + p_{11} + p_{22} - p_{12}^2 + 1)/4$. Then, from (19), the Kalman gain can be calculated by

$$\begin{aligned} K_n &\triangleq \begin{bmatrix} k_{11} & k_{12} \\ k_{21} & k_{22} \\ k_{31} & k_{32} \\ k_{41} & k_{42} \end{bmatrix} \\ &= \begin{bmatrix} p_{11} & p_{12} \\ p_{21} & p_{22} \\ p_{31} & p_{32} \\ p_{41} & p_{42} \end{bmatrix} \begin{bmatrix} t_{11} & t_{12} \\ t_{21} & t_{22} \end{bmatrix} \end{aligned} \quad (34)$$

$$= \begin{bmatrix} p_{11}t_{11} + p_{12}t_{21} & p_{11}t_{12} + p_{12}t_{22} \\ p_{21}t_{11} + p_{22}t_{21} & p_{21}t_{12} + p_{22}t_{22} \\ p_{31}t_{11} + p_{32}t_{21} & p_{31}t_{12} + p_{32}t_{22} \\ p_{41}t_{11} + p_{42}t_{21} & p_{41}t_{12} + p_{42}t_{22} \end{bmatrix}.$$

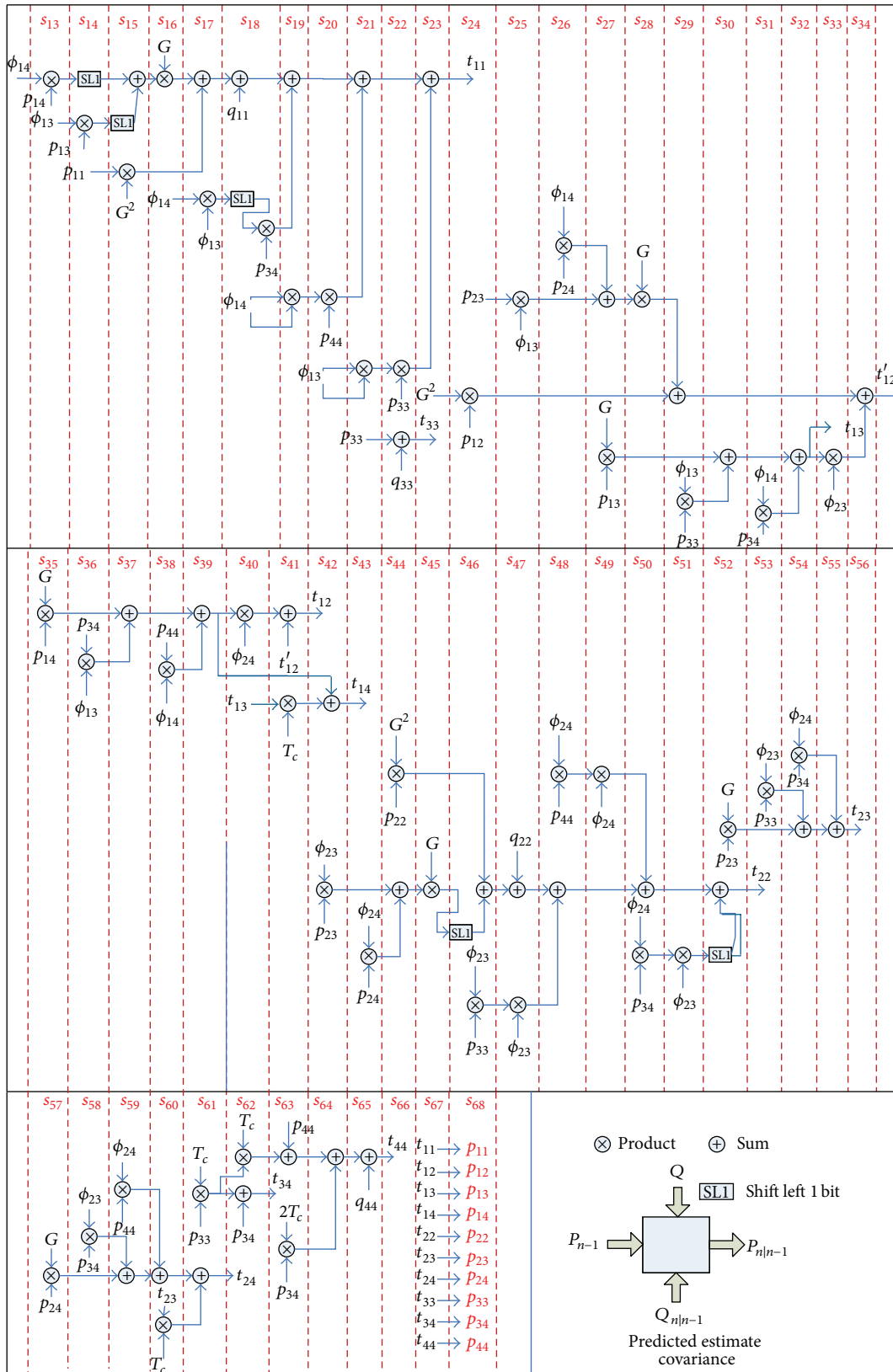


FIGURE 5: State diagram of FSM for prediction of covariance matrix $P_{n|n-1}$.

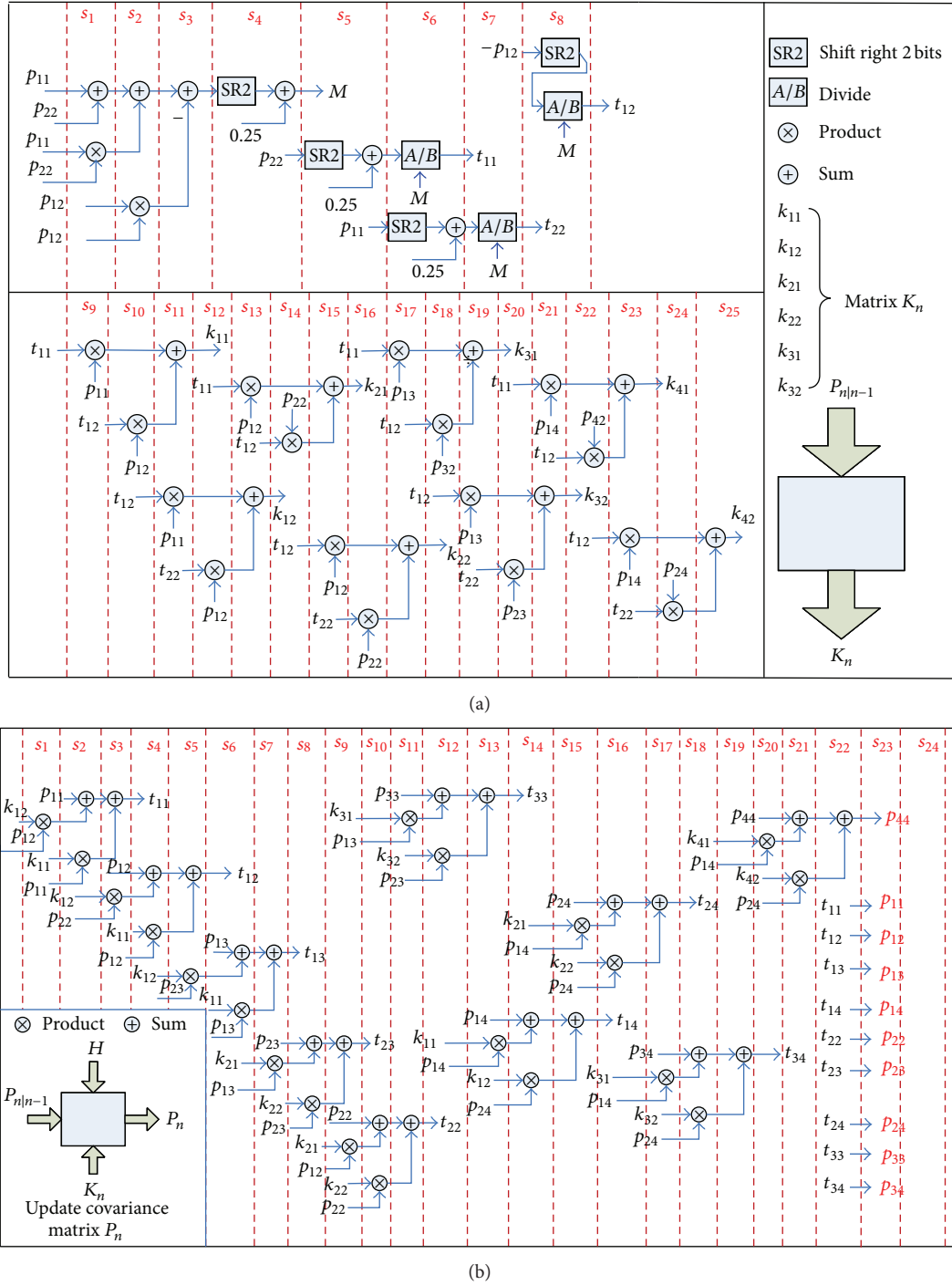


FIGURE 6: State diagram of FSM for (a) the calculation of matrix K_n and (b) the update of covariance matrix P_n .

Step 7. Tune the present state variables from (17), and its scalar form is shown as follows:

$$\hat{i}_\alpha(n) = \hat{i}_\alpha(nm-1) + k_{11}\tilde{i}_\alpha(n) + k_{12}\tilde{i}_\beta(n),$$

$$\hat{i}_\beta(n) = \hat{i}_\beta(nm-1) + k_{21}\tilde{i}_\alpha(n) + k_{22}\tilde{i}_\beta(n),$$

$$\hat{\omega}_e(n) = \hat{\omega}_e(nm-1) + k_{31}\tilde{i}_\alpha(n) + k_{32}\tilde{i}_\beta(n),$$

$$\hat{\theta}_e(n) = \hat{\theta}_e(n | n-1) + k_{41}\tilde{i}_\alpha(n) + k_{42}\tilde{i}_\beta(n),$$

(35)

where k_{ij} is the element in Kalman gain K_n . $\tilde{i}_\alpha(n) = i_\alpha(n) - \hat{i}_\alpha(n | n-1)$ and $\tilde{i}_\beta(n) = i_\beta(n) - \hat{i}_\beta(n | n-1)$.

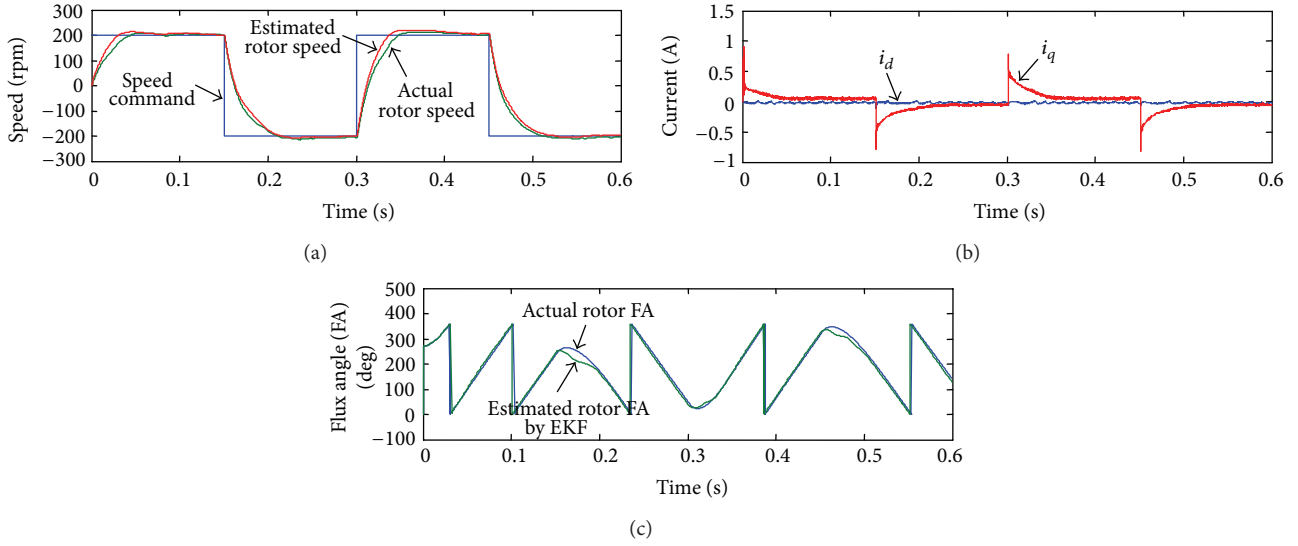


FIGURE 8: PMSM running at low speed (200 rpm) and inverse speed (± 200 rpm) condition. (a) Speed step response, (b) current response, and (c) actual rotor FA and estimated rotor FA.

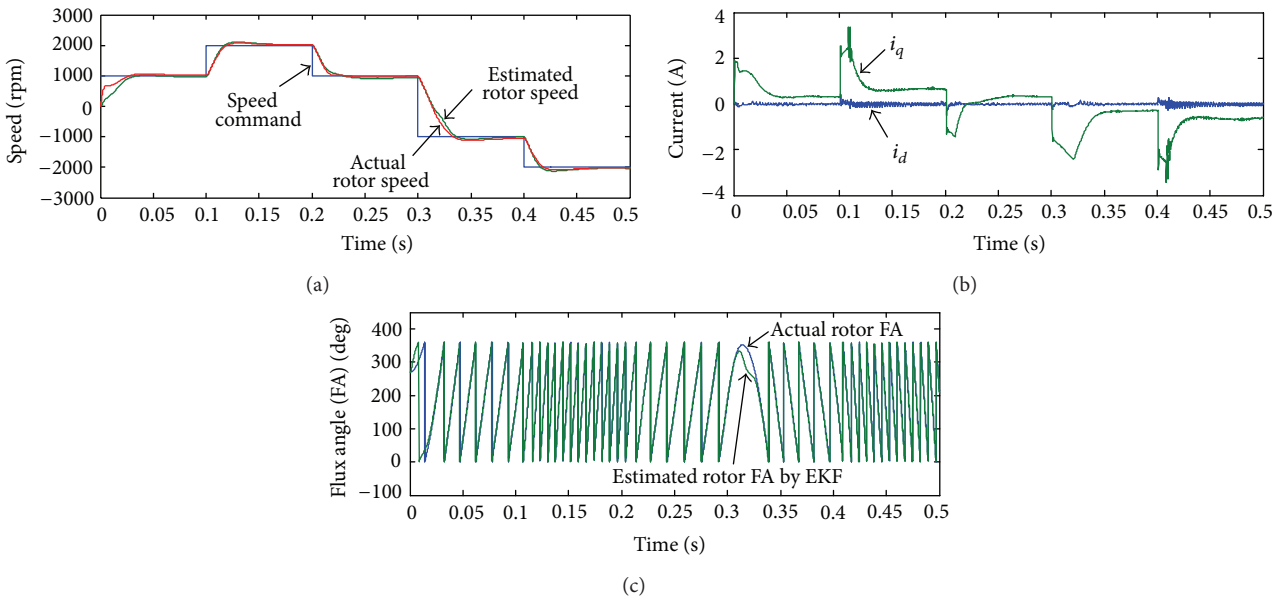


FIGURE 9: PMSM running at wide-range high speed (2000 rpm) and inverse speed (± 1000 rpm) condition. (a) Speed step response, (b) current response, AND (c) actual rotor FA and estimated rotor FA.

the present covariance matrix P_n and calculate the Kalman gain K_n ; $s_{121} \sim s_{130}$ describe the present state tuning as well as executing the computation of rotor FA and rotor speed. According to (30), the computation of temporary covariance matrix $P_{n|n-1}$ in Figure 4 is described in Figure 5. Further, according to (18), (33)-(34), and (36), the update of the present covariance matrix P_n and calculation the Kalman gain K_n in Figure 4 are illustrated in Figure 6. The operation of each step in Figure 4 is 80 ns (12.5 MHz) in FPGA; therefore a total of 131 steps need only 10.48 μ s operation times. The FPGA (Altera) resource usages of EKF-based rotor FA and rotor speed estimation in Figure 4 is 4,158 LEs (logic elements) and 2,890 RAM bits. Additionally, the FPGA

resource usages of the circuits of CCCT, speed PI controller, ADC interface, and SVPWM in Figure 3 are 864 LEs and 24,576 RAM, 2,043 LEs and 0RAM bits, 136 LEs and 0RAM bits, and 1,221 LEs and 0RAM bits, respectively.

4. Simulink/ModelSim Cosimulation and Its Simulation Results

The Simulink/ModelSim cosimulation architecture for sensorless PMSM speed control system is shown in Figure 7. The SimPowerSystem-Blockset in the Simulink executes the PMSM and the IGBT-based inverter. The EDA simulator link for ModelSim executes the cosimulation using VHDL code

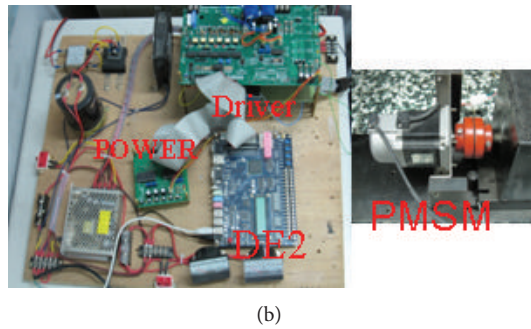
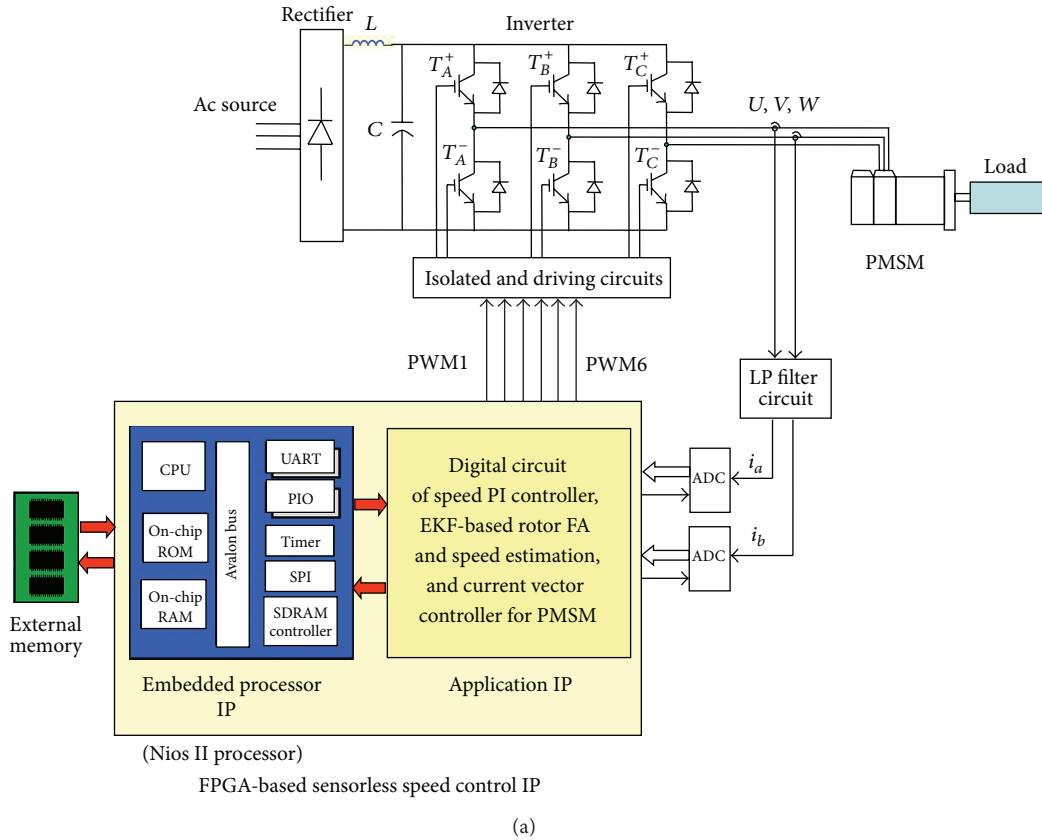


FIGURE 10: Experimental system (a) with block diagram and (b) in real system.

running in ModelSim program. It executes the function of the sensorless speed controller by three works. The work-1 to work-3 of ModelSim in Figure 7, respectively, perform the function of speed loop PI controller, the function of current controller and coordinate transformation (CCCT) and SVPWM, and the function of EKF-based rotor FA and rotor speed estimation. The sampling frequency in current control loop and EKF-based estimation algorithm is designed with 16 kHz, but in speed control loop is 2 kHz. The clocks of 50 MHz and 12.5 MHz will supply all works of ModelSim. The FPGA (Altera) resource usages of work-1 to work-3 are 2,043 LEs and 0 RAM bits, 2,085 LEs and 24,576 RAM bits, and 4,158 LEs and 2,890 RAM bits, respectively.

In simulation, the designed PMSM parameters used in Figure 7 are as follows: pole pairs are 4, stator phase resistance is 1.3Ω , stator inductance is 6.3 mH, inertia is $J = 0.000108 \text{ kg}\cdot\text{m}^2$, and friction factor is $F = 0.0013 \text{ N}\cdot\text{m}\cdot\text{s}$. PI gains in speed control loop are designed with $K_p = 0.2442$ and $K_i = 0.00458$. To evaluate the proposed controller performance, PMSM running at low speed (200 rpm) and inverse speed (from 200 rpm to -200 rpm or vice versa) condition is firstly considered, and its simulation results regarding as the speed step response, the current response as well as the actual rotor flux angle (FA) and the estimated rotor flux angle are shown in Figure 8. It shows that the motor speed gives a good dynamic response performance with a

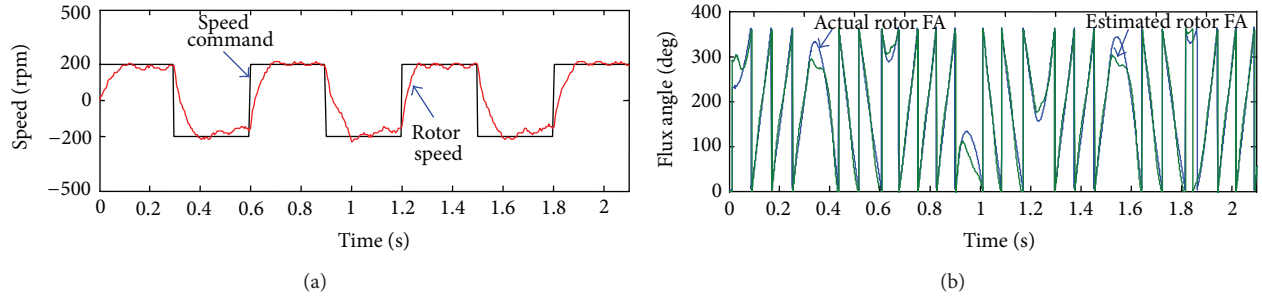


FIGURE 11: (a) Step speed response of actual rotor speed and estimated rotor speed and (b) actual rotor FA and estimated rotor FA.

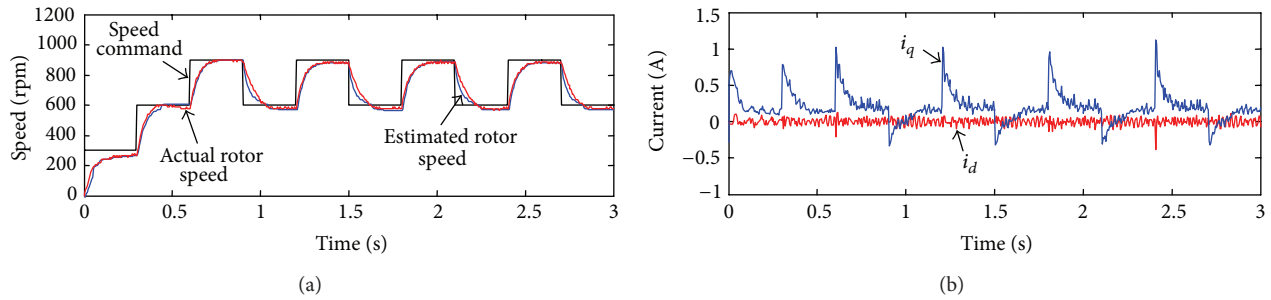


FIGURE 12: (a) Step speed response of actual rotor speed and estimated rotor speed and (b) current response.

little overshoot and 25 ms rising time. It also shows that the estimated rotor speed can track actual rotor speed well. Figure 8(b) shows a successful vector control because i_d is controlled to zero. Figure 8(c) shows that the estimated rotor FA can fast track the actual rotor FA even in the inverse speed command condition. Further, another simulation case while the PMSM running at wide-range high speed (from 0 rpm \rightarrow 1000 rpm \rightarrow 2000 rpm \rightarrow 1000 rpm \rightarrow -1000 rpm \rightarrow -2000 rpm) and inverse speed (from 1000 rpm to -1000 rpm) condition is tested, and its simulation results are shown in Figure 9. It presents that not only at speed tracking but also at rotor FA tracking, the estimated value adopted by EKF method can give a good follow to the real rotor value. However, except in the initial condition, the actual rotor speed gives a fast step response by 18 ms rising time, near 0 mm steady-state value, and maximum 17.5% overshoot.

5. Experimental System and Results

After confirming the correctness of the proposed EKF-based sensorless control IP by simulation, the VHDL codes are directly applied to the experimental FPGA-based sensorless PMSM drive system. The block diagram and real experimental system are depicted in Figure 10. The main devices include a PMSM, a DE2 board with Altera CycloneII FPGA, a motor driver, and a power supplier. The parameters of the PMSM are $r_s = 0.63 \Omega$, $L = 2.77$ mH, and 4 pole pairs. The input voltage, continuous current, rating torque, rating speed, and continuous power of the PMSM are 220 V, 12 A, 2.3 N·m, 3000 rpm, and 750 W, respectively. The Altera CycloneII EP2C35 chip adopted in the design possesses 33,216 LEs, maximum 475 available I/O pins, 483,840 RAM, and 35

embedded multipliers. The chip can be embedded with a Nios II multicore processor that is equipped with several 32-bit CPU, flexibility of core size, 1 to 16 Mbytes of flash memory in the available memory chip, 1 Mbyte SRAM, 16 M byte SDRAM, and 4 Gbytes memory outside of the chip. In implementation, except the VHDL codes of CCCT, EKF, and PI controller, the VHDL code of ADC interface circuit should be added and integrated and then downloaded into FPGA. The PI gains of speed control loop in experiment are designed with $K_p = 0.512$ and $K_i = 0.021$.

In the experimental case, PMSM running at low speed (200 rpm) and inverse speed (from 200 rpm to -200 rpm or vice versa) condition are firstly considered, and its experiment results regarding the speed step response as well as the actual rotor FA and the estimated rotor FA are shown in Figure 11. Figure 11(a) shows that the motor speed gives a good dynamic response performance with a little oscillation and overshoot and it has 15 ms rising time. Figure 11(b) shows that the estimated FA can fast track the actual rotor FA even in the inverse speed command condition. Further, another experimental case while the PMSM running at medium speed (from 0 rpm \rightarrow 300 rpm \rightarrow 600 rpm \rightarrow 900 rpm \rightarrow 600 rpm \rightarrow 900 rpm) condition is evaluated, and its experiment results are shown in Figure 12. The Figure 12(a) presents a fast speed tracking with 15 ms rising time and no occurrence of overshoot condition. Figure 12(b) shows a successful vector control due to the i_d being controlled to zero. Therefore, from the simulation results in Figures 8 and 9 and the experimental results in Figures 11 and 12, it is demonstrated that the EKF-based estimation algorithm used in sensorless PMSM drive and the behavior description by using VHDL are effective and correct.

6. Conclusions

This study has presented a sensorless PMSM drive based on EKF and successfully demonstrated its performance through cosimulation by using Simulink/ModelSim and implementation by using FPGA. In realization aspect, the VHDL is used to describe the behavior of EKF algorithm, and FSM is used to reduce the FPGA resource usage; therefore, it only needs 4,158 LEs and 2,890 RAM bits. In computational power aspect, the operation time to complete the computation of EKF algorithm is only 10.48 μ s, which is less than the 62.5 μ s (16 KHz) sampling time in current control loop. In simulated and experimental results, it shows that the use of EKF in sensorless PMSM drive can accurately estimate the rotor FA and rotor speed, and it can give a good step response performance in case of low speed control, inverse speed control, and high speed control as well.

Acknowledgment

This work was supported by the National Science Council of China under Grant no. NSC 101-2221-E-218-039.

References

- [1] V. C. Ilioudis and N. I. Margaris, "PMSM sensorless speed estimation based on sliding mode observers," in *Proceedings of the 39th IEEE Annual Power Electronics Specialists Conference (PESC '08)*, pp. 2838–2843, June 2008.
- [2] S. Chi, Z. Zhang, and L. Xu, "Sliding-mode sensorless control of direct-drive PM synchronous motors for washing machine applications," *IEEE Transactions on Industry Applications*, vol. 45, no. 2, pp. 582–590, 2009.
- [3] V. Delli Colli, R. di Stefano, and F. Marignetti, "A system-on-chip sensorless control for a permanent-magnet synchronous motor," *IEEE Transactions on Industrial Electronics*, vol. 57, no. 11, pp. 3822–3829, 2010.
- [4] S. Bolognani, R. Oboe, and M. Zigliotto, "Sensorless full-digital pmsm drive with ekf estimation of speed and rotor position," *IEEE Transactions on Industrial Electronics*, vol. 46, no. 1, pp. 184–191, 1999.
- [5] M. C. Huang, A. J. Moses, and F. Anayi, "The comparison of sensorless estimation techniques for PMSM between extended Kalman filter and flux-linkage observer," in *Proceedings of the 21st Annual IEEE Applied Power Electronics Conference and Exposition (APEC '06)*, pp. 654–659, March 2006.
- [6] W. Wang, M. Zhang, and Q. Wu, "Application of reduced-order extended kalman filter in permanent magnet synchronous motor sensorless regulating system," in *Proceedings of the International Conference on Digital Manufacturing and Automation (ICDMA '10)*, pp. 271–274, December 2010.
- [7] J.-S. Jang, B.-G. Park, T.-S. Kim, D. M. Lee, and D.-S. Hyun, "Parallel reduced-order extended Kalman Filter for PMSM sensorless drives," in *Proceedings of the 34th Annual Conference of the IEEE Industrial Electronics Society (IECON '08)*, pp. 1326–1331, November 2008.
- [8] Y.-S. Kung and M.-H. Tsai, "FPGA-based speed control IC for PMSM drive with adaptive fuzzy control," *IEEE Transactions on Power Electronics*, vol. 22, no. 6, pp. 2476–2486, 2007.
- [9] L. Idkhajine and E. Monmasson, "Design methodology for complex FPGA-based controllers—application to an EKF sensorless AC drive," in *Proceedings of the 19th International Conference on Electrical Machines (ICEM '10)*, pp. 1–6, September 2010.
- [10] H.-H. Chou, Y.-S. Kung, N. Vu Quynh, and S. Cheng, "Optimized FPGA design, verification and implementation of a neuro-fuzzy controller for PMSM drives," *Mathematics and Computers in Simulation*, vol. 90, pp. 28–44, 2013.
- [11] Y. S. Kung and T. H. Nguyen, "Simulink/Modelsim Co-simulation of EKF-based Sensorless PMSM drives," in *Proceedings of IEEE International on Power Electronics and Drive Systems (PEDS '13)*, pp. 709–713, 2013.
- [12] Y. Li, J. Huo, X. Li, J. Wen, Y. Wang, and B. Shan, "An open-loop sin microstepping driver based on FPGA and the co-simulation of modelsim and simulink," in *Proceedings of the International Conference on Computer, Mechatronics, Control and Electronic Engineering (CMCE '10)*, pp. 223–227, August 2010.
- [13] The Mathworks, "Matlab/Simulink Users Guide, Application Program Interface Guide," 2004.
- [14] Modeltech, "ModelSim Reference Manual," 2004.

Research Article

Minimum Porosity Formation in Pressure Die Casting by Taguchi Method

Quang-Cherng Hsu and Anh Tuan Do

Department of Mechanical Engineering, National Kaohsiung University of Applied Sciences, 415 Chien-Kung Road, 80778 Kaohsiung City, Taiwan

Correspondence should be addressed to Anh Tuan Do; 1099403120@kuas.edu.tw

Received 17 September 2013; Accepted 15 October 2013

Academic Editor: Teen-Hang Meen

Copyright © 2013 Q.-C. Hsu and A. T. Do. This is an open access article distributed under the Creative Commons Attribution License, which permits unrestricted use, distribution, and reproduction in any medium, provided the original work is properly cited.

Die casting process is significantly used in the industry for its high productivity and less postmachining requirement. Due to light weight and good formability, aluminum die casting plays an important role in the production of transportation and vehicle components. In the current study of die casting for Automobile starter motor casing, the following issues are focused: shot piston simulation, defect analysis, and, finally, the use of the Taguchi multiquality analytical method to find the optimal parameters and factors to increase the aluminium ADC10 die casting quality and efficiency. Experiments were conducted by varying molten alloy temperature, die temperature, plunger velocities in the first and second stage, and multiplied pressure in the third stage using L_{27} orthogonal array of Taguchi method. After conducting a series of initial experiments in a controlled environment, significant factors for pressure die casting processes are selected to construct an appropriate multivariable linear regression analysis model for developing a robust performance for pressure die casting processes. The appropriate multivariable linear model is a useful and efficient method to find the optimal process conditions in pressure die casting associated with the minimum shrinkage porosity percent.

1. Introduction

High pressure die casting for nonferrous casting applications is increasingly used in the foundries today as an economically viable casting process. High pressure die casting (HPDC) process has been widely used to manufacture a large variety of products with high dimensional accuracy and productivities. It has a much faster production rate in comparison to other methods and it is an economical and efficient method for producing components with low surface roughness and high dimensional accuracy. All major aluminium automotive components can be processed with this technology.

High Pressure Die Casting process is rapid and depends on many factors. So, to capture the problem it requires a lot of time and experience including testing and simulation. The conventional trial and error based die design and process development is expensive and time consuming. Such a procedure also might lead to higher casting rejections. The HPDC castings production process has many defects, such

as shrinkage porosity, misrun, cold-shut, blister, scab, hot-tear. Several previous studies of defects in aluminum alloy by the method of HPDC and disability solutions (Shen et al. 2007 [1], Dargusch et al. 2006 [2], Verran et al. 2006 [3], Mousavi Anijdan et al. 2006 [4], Tsoukalas et al. 2004, 2008 [5, 6]). However, the study to optimize aluminum alloy casting process in the condition of production casting factory is essential. This study focused on analysis of shrinkage porosity defect with mold design and put into production casting by foundry factory conditions.

Shrinkage porosity is one of the most common defects leading to rejection of aluminium die casting, often only showing up after much value has been added to the casting via operations such as machining, polishing, and coating. The added value of the casting at the point of rejection can be very high. If you find out the causes and how to reduce the defects of castings will be of great significance in reducing the production cost of die casting. However, optimizing the conditions to render aluminium die castings of minimum

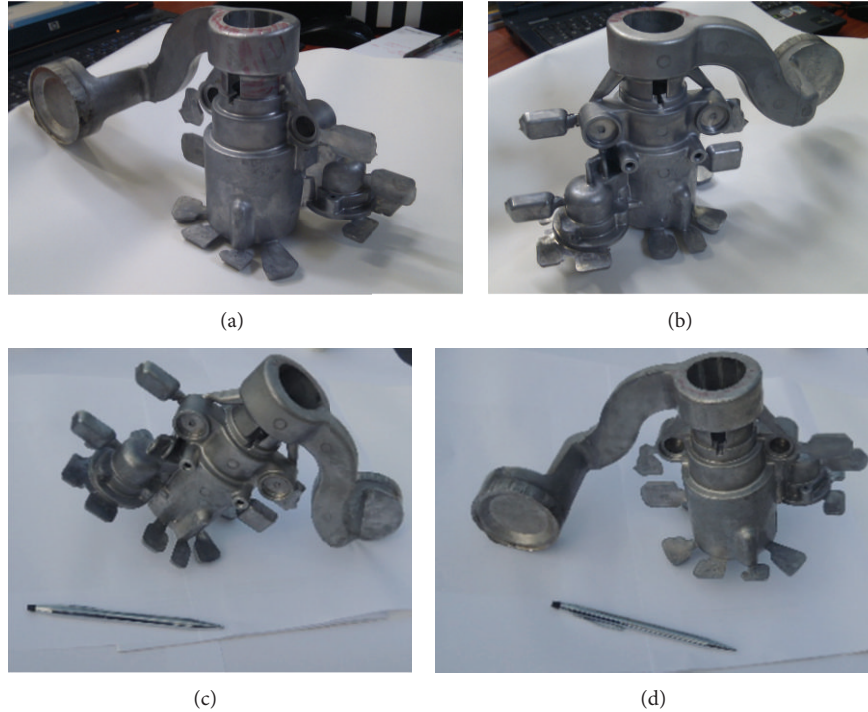


FIGURE 1: Casting image.

porosity percent is costly and time consuming, because many experiments are necessary to find the optimal parameters.

Taguchi method is one of the efficient problems solving tools to upgrade the performance of products and processes with a significant reduction in cost and time involved. Taguchi's parameter design offers a systematic approach for optimization of various parameters with regard to performance, quality, and cost (Syracos 2003 [7], Taguchi 1986 [8]).

2. Materials and Methods

The die casting part product of this study is provided through aluminium die casting factory, so the casting body no changes. A major factor in the successful development of castings is the design of the die and design of gates, biscuit, and runner system. A well-designed gating and runner system should avoid turbulence in metal flow and to reduce incidence of inclusions and air entrapment in the casting. The die design is required to avoid solidification related defects like shrinkage, micro-porosities, hot-tear and so forth. Die design process is very much dependent on the experience and skill of the design engineer. The die for this study is the result of collaboration between the foundry factory and Department of Mechanical Engineering-National Kaohsiung University of Applied Sciences. The casting with full of the gating, runner system and biscuit, is shown in Figure 1. The die casting is designed in CATIA V5R19 software, shown in Figure 2. Moreover, the die casting material selection is very important. The nature of the material will directly affect the quality of the casting and die casting parameters configuration, this study selects casting material as the aluminium alloy

TABLE 1: Chemical composition of the alloy ADC10 used in the experiment.

Element	Si	Fe	Cu	Mg	Mn	Ni	Zn	Sm
wt%	7.5~9.5	1.3	3.0~4.0	0.1	0.5	0.5	3	0.35

ADC10. The chemical composition of the aluminum alloy used in the experimental procedure is given in Table 1.

Shrinkage porosity formation in pressure die casting is the result of a so much number of parameters. Figure 3 shows a cause and effect diagram that was constructed to identify the casting process parameters that may affect die casting porosity (Tsoukalas et al. 2004, 2008 [5, 6]). In this case, holding furnace temperature, die temperature, plunger velocity in the first stage, plunger velocity in the second stage, and multiplied pressure in the third stage were selected as the most critical in the experimental design. The other parameters were kept constant in the entire experimentation. The range of holding furnace temperature was selected as 640~700°C, the range of die temperature as 180~260°C, the range of plunger velocity in the first stage as 0.05~0.35 m/s and in the second stage as 1.5~3.5 m/s, and the range of multiplied pressure in the third stage was chosen as 200~280 bars. The selected casting process parameters, along with its ranges, are given in Table 2.

Taguchi method based design of experiment has been used to study the effects of five casting process parameters (holding furnace temperature: A, die temperature; B, plunger velocity in the first stage; C, plunger velocity in the second stage; D, multiplied pressure in the third stage; E, on an

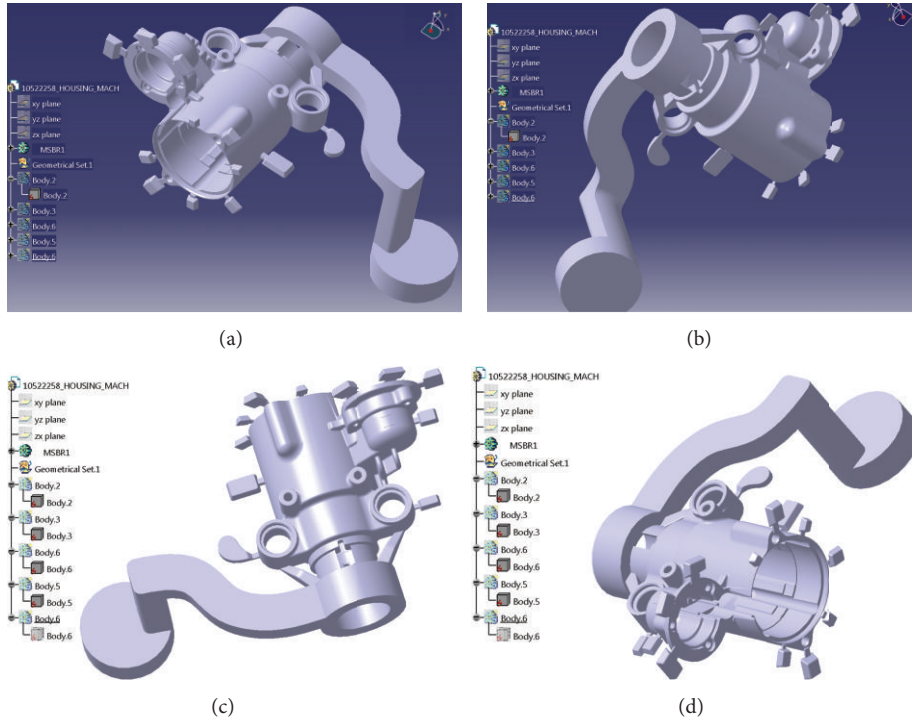


FIGURE 2: Part product is designed by CATIA software.

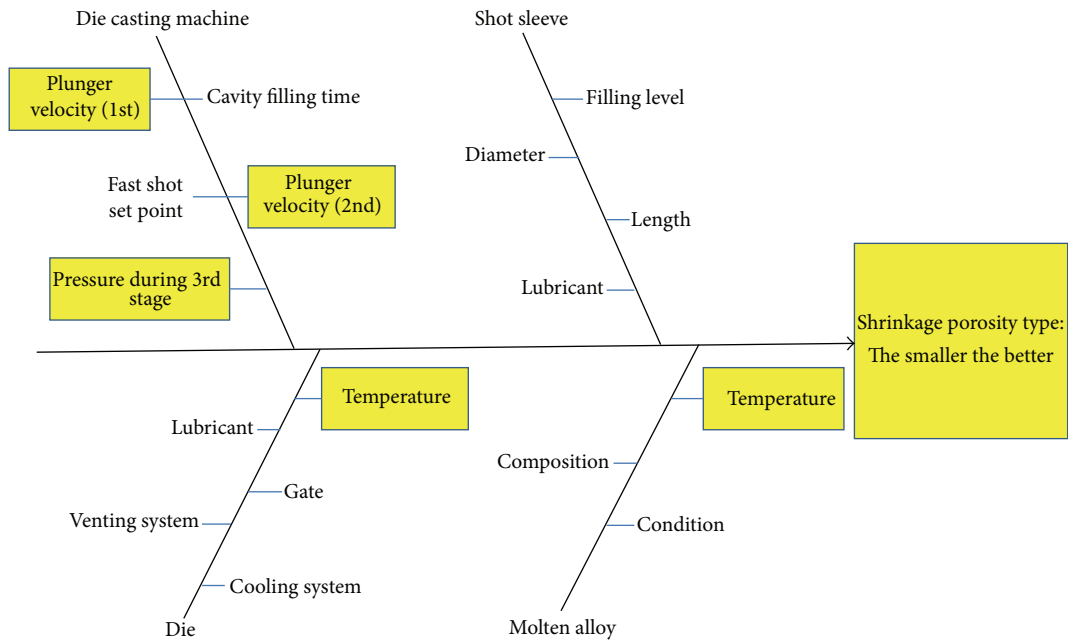


FIGURE 3: Cause and effect diagram.

TABLE 2: The parameter and its value at three levels.

Process parameters	Parameters range	Level 1	Level 2	Level 3
Holding furnace temperature (°C)	640~700	640	670	700
Die temperature (°C)	180~260	180	220	260
Plunger velocity, 1st stage (m/s)	0.05~0.35	0.05	0.2	0.35
Plunger velocity, 2nd stage (m/s)	1.5~3.5	1.5	2.5	3.5
Multiplied pressure (bars)	200~280	200	240	280

TABLE 3: Experimental layout using an L_{27} orthogonal array.

Trials	Holding furnace temperature A	Die temperature B	Plunger velocity 1st stage C	Plunger velocity 2nd stage D	Multiplied pressure E
1	1	1	1	1	1
2	1	1	2	2	2
3	1	1	3	3	3
4	1	2	1	2	2
5	1	2	2	3	3
6	1	2	3	1	1
7	1	3	1	3	3
8	1	3	2	1	1
9	1	3	3	2	2
10	2	1	1	2	3
11	2	1	2	3	1
12	2	1	3	1	2
13	2	2	1	3	1
14	2	2	2	1	2
15	2	2	3	2	3
16	2	3	1	1	2
17	2	3	2	2	3
18	2	3	3	3	1
19	3	1	1	3	2
20	3	1	2	1	3
21	3	1	3	2	1
22	3	2	1	1	3
23	3	2	2	2	1
24	3	2	3	3	2
25	3	3	1	2	1
26	3	3	2	3	2
27	3	3	3	1	3

important output parameter (Shrinkage porosity). For selecting appropriate orthogonal array, degree of freedom (number of fair and independent comparisons needed for optimization of process parameters is one less than the number of levels of parameter) of the array is calculated.

In the experimental layout plan with five factors and three levels using L_{27} orthogonal array, 27 experiments were carried out to study the effect of casting input parameters, shown in Table 3. The input parameters are installed in the ProCAST software to conduct 27 simulation experiments.

Computer simulation procedure-based process development and die design can be used for rapid process development and die design in a shorter time. Such a computer simulation based procedure, often using FINITE ELEMENT ANALYSIS based software systems, can improve the quality and enhance productivity of the enterprise by way of faster development of new product. Analysis software is used as a ProCAST commercial with finite element method analysis for a casting process. In this study, all parameters can be able to affect the analysis process, choice of material is aluminum alloy die casting ADC10, and cold chamber die

casting method with molding material is H13. FEM based simulation software systems help the designer to visualize the metal flow in the die cavity, the temperature variation, the solidification progress, and the evolution of defects such as shrinkage porosity, cold-shut, hot-tear.

ProCAST a FEM simulation-based virtual casting environment for analysis of the casting process is used as a tool for die design and process optimization. ProCAST with Visual-Viewer module can provide temperature field, thermal cracking, flow field, solidification time, and shrinkage analysis. This paper focused on the analysis of shrinkage porosity by ProCAST software base on parameters input from Table 3.

The analysis of defects simulated by ProCAST software with Visual-Viewer module can detect many types of disabilities casting. The defective products do not necessarily reflect the loss of the original function, for example, the internal pore trims acceptable. However, with large structural castings, defect analysis of this study focuses on maximum porosity in the selection casting, and the important parts of the casting shrinkage analysis (an important component), casting defect analysis are described as follows.

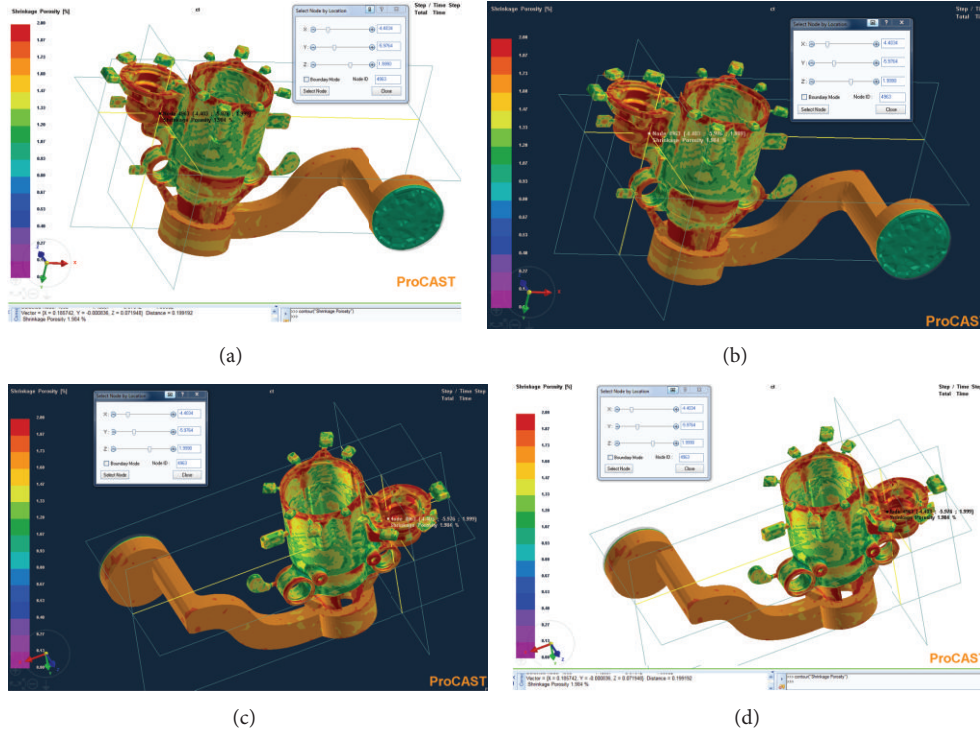


FIGURE 4: Casting measurement area.

The Solid Fraction. Solid fraction may be available shrinkage prediction casting position, the present study is in accordance with the theory prediction of defect, and ProCAST manual referred to in the final period of solidification. Shrinkage solid fraction prone is greater than 0.7, here as the reference value of 0.7 solid fractions. When the solid fraction area is below this value and the area around the solid phase rate is rather than this value, we can predict this area shrinkage porosity occurred.

Maximum Porosity. The maximum porosity analysis using the Shrinkage Porosity function of the Visual-Viewer comes defined in the manual. According to the ProCAST user manual shrinkage definition and with the solid fraction, it can be used to analyse the basis of the maximum porosity.

Shrinkage Analysis. For the amount of inspection shrinkage casting part used for the Visual-Viewer module function for quantitative analysis. In each experiment we took five elements with the coordinates determined at the important positions in the working conditions of automobile starter motor casing. Each experiment was repeated five times in order to reduce experimental errors, as shown in Figure 4. Data from 27 experiments with five sampling times in each simulation are summarized as in Table 4. From this table, we conducted quality characteristics analysis.

Quality Characteristics. The parameter design study involves control and noise factors. The measure of interactions between these factors with regard to robustness is signal-to-noise (S/N) ratio. S/N characteristics formulated for three

different categories are as follows: the bigger the better, and the smaller the better, the nominal the best. This paper focused on studying the effects of five input parameters (A, B, C, D, E) to defect shrinkage porosity in the process of casting, so the criteria “the smaller the better” is selected.

The smaller the better (for making the system response as small as possible) is as follows:

$$\frac{S}{N_s} = -10 \log \left(\frac{1}{n} \sum_{i=1}^n y_i^2 \right), \quad (1)$$

where n is the number of sampling (Each experiment was repeated five times sampling, so that $n = 5$), y_i : value of Shrinkage porosity at each time sampling.

The responding graph shown in Figure 5 learned that the best combination for this study with shrinkage porosity defect value minimum is $A_3B_3C_3D_1E_3$.

Process Parameter Optimization Using MVLRL. The objective of the process optimization is to select the optimal control variables in aluminium die casting process in order to obtain the minimum porosity. In this work, the fitness function used in the optimization procedure was based on the MVLRL model.

Multivariable Linear Regression Analysis. In most cases, the form of the relationship between the response and the independent variables is usually unknown. Multiple linear regression (MLR) is a method used to model the linear relationship between a dependent variable and one or more

TABLE 4: Shrinkage porosity results of the L_{27} array design. (Full table).

Trials	Holding Furnace Temperature A	Die temperature B	Plunger velocity 1st stage C	Plunger Velocity 2nd stage D	Multiplied Pressure E	Shrinkage porosity (%)					MSD	S/N	
						Repetition 1	Repetition 2	Repetition 3	Repetition 4	Repetition 5			Average
1	640	180	0.05	1.5	200	1.973	1.988	1.984	1.978	1.954	1.9754	3.902346	-5.91326
2	640	180	0.2	2.5	240	1.912	1.893	1.948	1.908	1.912	1.9146	3.666021	-5.64195
3	640	180	0.35	3.5	280	1.846	1.853	1.814	1.813	1.828	1.8308	3.352095	-5.25316
4	640	220	0.05	2.5	240	1.862	1.867	1.861	1.878	1.871	1.8678	3.488716	-5.42666
5	640	220	0.2	3.5	280	1.793	1.804	1.761	1.764	1.775	1.7794	3.166541	-5.00585
6	640	220	0.35	1.5	200	1.916	1.908	1.912	1.887	1.903	1.9052	3.629888	-5.59893
7	640	260	0.05	3.5	280	1.786	1.797	1.754	1.757	1.768	1.7724	3.141679	-4.97162
8	640	260	0.2	1.5	200	1.909	1.903	1.889	1.898	1.893	1.8984	3.603973	-5.56782
9	640	260	0.35	2.5	240	1.852	1.859	1.82	1.819	1.836	1.8372	3.375568	-5.28347
10	670	180	0.05	2.5	280	1.799	1.81	1.767	1.77	1.781	1.7854	3.18793	-5.03509
11	670	180	0.2	3.5	200	1.957	1.968	1.971	1.951	1.965	1.9624	3.851068	-5.85581
12	670	180	0.35	1.5	240	1.857	1.864	1.825	1.824	1.841	1.8422	3.393965	-5.30707
13	670	220	0.05	3.5	200	1.924	1.935	1.923	1.928	1.909	1.9238	3.701079	-5.68328
14	670	220	0.2	1.5	240	1.803	1.814	1.771	1.774	1.785	1.7894	3.202229	-5.05452
15	670	220	0.35	2.5	280	1.751	1.744	1.713	1.731	1.725	1.7328	3.002778	-4.77523
16	670	260	0.05	1.5	240	1.796	1.807	1.764	1.767	1.778	1.7824	3.177227	-5.02048
17	670	260	0.2	2.5	280	1.738	1.726	1.724	1.745	1.715	1.7296	2.991629	-4.75908
18	670	260	0.35	3.5	200	1.881	1.878	1.898	1.893	1.903	1.8906	3.574461	-5.53211
19	700	180	0.05	3.5	240	1.876	1.871	1.895	1.887	1.893	1.8844	3.551052	-5.50357
20	700	180	0.2	1.5	280	1.755	1.743	1.741	1.762	1.732	1.7466	3.050725	-4.84403
21	700	180	0.35	2.5	200	1.921	1.901	1.956	1.916	1.928	1.9244	3.703644	-5.68629
22	700	220	0.05	1.5	280	1.708	1.696	1.694	1.715	1.685	1.6996	2.888753	-4.6071
23	700	220	0.2	2.5	200	1.864	1.898	1.881	1.876	1.885	1.8808	3.537532	-5.487
24	700	220	0.35	3.5	240	1.825	1.832	1.793	1.792	1.807	1.8098	3.275642	-5.15296
25	700	260	0.05	2.5	200	1.856	1.861	1.855	1.872	1.865	1.8618	3.466338	-5.39871
26	700	260	0.2	3.5	240	1.814	1.821	1.782	1.781	1.796	1.7988	3.235948	-5.10001
27	700	260	0.35	1.5	280	1.692	1.694	1.706	1.683	1.712	1.6974	2.881274	-4.59585

TABLE 5: The results after analysing by Intercooled Stada 8.2 software.

(a)

. reg Fx A B C D E				
Source	SS	df	MS	Number of obs = 27 $F(5, 21) = 146.74$
Model	0.155044498	5	0.0310089	Prob > F = 0.0000
Residual	0.004437799	21	0.000211324	R-squared = 0.9722 Adj R-squared = 0.9655
Total	0.159482297	26	0.006133935	Root MSE = 0.01454

(b)

Fx	Coef.	Std. Err.	t	P > t	[95% Conf. Interval]	
A	-0.0008844	0.0001142	-7.74	0.000	-0.001122	-0.0006469
B	-0.00083	0.0000857	-9.69	0.000	-0.0010081	-0.0006519
C	-0.0305925	0.7284277	-0.042	0.000	-0.0780965	0.0169114
D	0.0175444	0.0034264	5.12	0.000	0.0104189	0.02467
E	-0.0020122	0.0000857	-23.49	0.000	-0.0021904	-0.0018341
_cons	3.054569	0.0820708	37.22	0.000	2.883893	3.225244

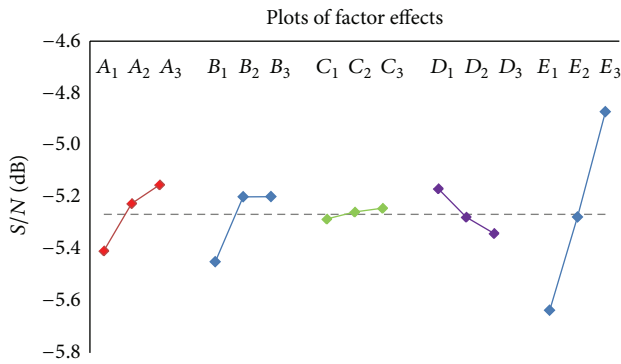


FIGURE 5: S/N Response graphs.

B (°C): Die temperature,

C (m/s): Plunger velocity 1st stage,

D (m/s): Plunger velocity 2nd stage,

E (bars): Multiplied pressure during the third phase.

The results after analysing by Intercooled Stada 8.2 Software as shown in Table 5.

The final MVLR model equation for porosity after substituting regression coefficients is as follows:

$$F(x) = 3.054569 - 0.8844 * 10^{-3}A - 0.83 * 10^{-3}B - 0.03059C + 0.01754D - 0.00201E. \quad (4)$$

independent variables. MLR is based on least squares: the model is fitted such that the sum-of-squares of differences of observed and predicted values is minimized.

Let $x_1; x_2; \dots; x_r$ be a set of r predictors believed to be related to a response variable Y . The linear regression model for the j th sample unit has the form

$$Y_j = \beta_0 + \beta_1 x_{j1} + \beta_2 x_{j2} + \dots + \beta_r x_{jr} + \epsilon_j, \quad (2)$$

where ϵ is a random error and the $\beta_i, i = 0, 1, \dots, r$ are unknown regression coefficients.

In this paper, there are five independent variables and one dependent variable. The relationships between these variables are of the following form:

$$F(x) = \beta_0 + \beta_1 A + \beta_2 B + \beta_3 C + \beta_4 D + \beta_5 E. \quad (3)$$

In which

$F(x)$: Dependence variable,

A (°C): Holding furnace temperature,

3. Results and Discussion

We applied multivariable linear regression analysis (MVLR) to seek the optimal parameter in the casting process of independent parameter variables in this study. A stationary point for the optimal performance was obtained by using the multivariable linear regression method in this linear regression equation, and the result is presented in Figure 6. A very good fit was observed and substantiated by the coefficient of determination, $R^2 = 0.9722$. That is, the R^2 value indicates that the polynomial model explains almost 97.22% of variability in the casting process.

Figure 6 shows the efficacy of the optimization scheme by comparing the MVLR results with the experimental values. There is a convincing agreement between experimental values and predicted values for shrinkage porosity percent.

Matlab code for finding optimization shrinkage porosity value.

```

clc;
clear all;
close all;
f = @(x) 3.054569-0.8844e-3*x(1)-0.83e-3*x(2)-...
        0.03059*x(3) + 0.01754*x(4)-0.00201*x(5);
options = optimset('GradObj', 'on');
[x,fval,exitflag,output] = ...
fmincon(f,[670;220;0.2;2.5;240],[[],[],[],[]],[600;180;0.05;1.5;
200],[700;260;0.35;3.5;280],[],optimset('Display','iter'));
x
fval

```

ALGORITHM 1

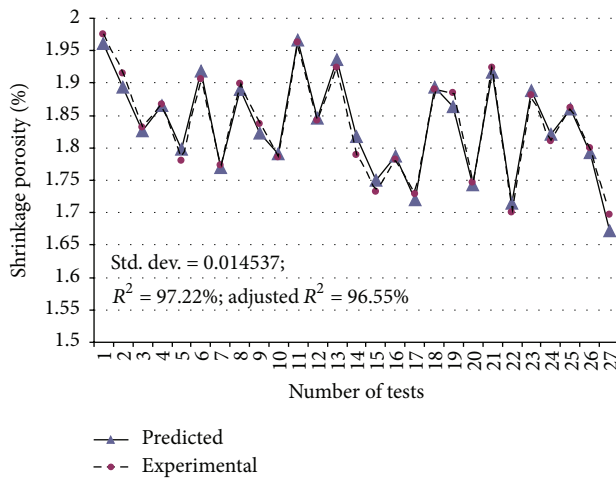


FIGURE 6: Experimental and predicted values of shrinkage porosity percent.

Program in Matlab (see Algorithm 1).

Results after running in Matlab are as follows:

$$\begin{aligned}
 x = 700.0000 & \quad \text{so that} \rightarrow A = 700^{\circ}\text{C} \\
 260.0000 & \quad B = 260^{\circ}\text{C} \\
 0.3500 & \quad C = 0.35 \text{ m/s} \\
 1.5000 & \quad D = 1.5 \text{ m/s} \\
 280.0000 & \quad E = 280 \text{ bar} \\
 fval = 1.6725 & \quad \text{Shrinkage porosity : } 1.6725\%.
 \end{aligned} \tag{5}$$

By the Program in Matlab, we are known as the best combination in the 27 experimental configurations.

This result is similar to quality characteristics and is the best combination for this study $A_3B_3C_3D_1E_3$.

4. Conclusion

In this paper, the optimum process parameters values predicted for casting of minimum shrinkage porosity

(1.6725%) and the best combination parameters given as follows:

holding furnace temperature 700°C ,
 die temperature 260°C ,
 plunger velocity, 1st stage 0.35 m/s ,
 plunger velocity, 2nd stage 1.5 m/s ,
 multiplied pressure 280 bar .

The model proposed in this paper gives satisfactory results in the optimization of pressure die casting process. The predicted values of the process parameters and the calculated are in convincing agreement with the experimental values.

The experiments which are conducted to determine the best levels are based on "Orthogonal Arrays," and are balanced with respect to all control factors and yet are minimum in number. This in turn implies that the resources (materials, saving time, and money) required for the experiments are also minimized.

References

- [1] C. Shen, L. Wang, and Q. Li, "Optimization of injection molding process parameters using combination of artificial neural network and genetic algorithm method," *Journal of Materials Processing Technology*, vol. 183, no. 2-3, pp. 412–418, 2007.
- [2] M. S. Dargusch, G. Dour, N. Schauer, C. M. Dinnis, and G. Savage, "The influence of pressure during solidification of high pressure die cast aluminium telecommunications components," *Journal of Materials Processing Technology*, vol. 180, no. 1–3, pp. 37–43, 2006.
- [3] G. O. Verran, R. P. K. Mendes, and M. A. Rossi, "Influence of injection parameters on defects formation in die casting Al12Si1,3Cu alloy: experimental results and numeric simulation," *Journal of Materials Processing Technology*, vol. 179, no. 1–3, pp. 190–195, 2006.
- [4] S. H. Mousavi Anijdan, A. Bahrami, H. R. Madaah Hosseini, and A. Shafyei, "Using genetic algorithm and artificial neural network analyses to design an Al-Si casting alloy of minimum porosity," *Materials and Design*, vol. 27, no. 7, pp. 605–609, 2006.
- [5] V. D. Tsoukalas, S. A. Mavrommatis, N. G. Orfanoudakis, and A. K. Baldoukas, "A study of porosity formation in pressure die casting using the Taguchi approach," *Journal of Engineering Manufacture*, vol. 218, no. 1, pp. 77–86, 2004.

- [6] V. D. Tsoukalas, "Optimization of porosity formation in AlSi₃Cu₃ pressure die castings using genetic algorithm analysis," *Materials and Design*, vol. 29, no. 10, pp. 2027–2033, 2008.
- [7] G. P. Syrcos, "Die casting process optimization using Taguchi methods," *Journal of Materials Processing Technology*, vol. 135, no. 1, pp. 68–74, 2003.
- [8] G. Taguchi, *Introduction to Quality Engineering*, Asian Productivity Organization, UNIPUB, 1986.

Research Article

A Data Transmission Technique for Personal Health Systems

Jih-Fu Tu¹ and Chih-yung Chen²

¹ Department of Electronic Engineering, St. John's University, Tamsui 251, Taiwan

² Department of Information Management, St. John's University, Tamsui 251, Taiwan

Correspondence should be addressed to Jih-Fu Tu; tu@mail.sju.edu.tw

Received 14 September 2013; Accepted 10 October 2013

Academic Editor: Teen-Hang Meen

Copyright © 2013 J.-F. Tu and C.-y. Chen. This is an open access article distributed under the Creative Commons Attribution License, which permits unrestricted use, distribution, and reproduction in any medium, provided the original work is properly cited.

We used the modular technique to design a personal health data transmitter (PHDT) that is composed of the following components: (1) the core is an embedded signal chip, (2) three kinds of transmutation modules such as USB, RF, and UART, (3) an I²C interface is used to acquire the users data, and (4) through Internet it links to the cloud server to store the personal-health data. By the experiment, we find that the modular manner is feasible, stable of functional, integral, and accurate, while it is exploited to design the PHDT. For the experiment, we present each module algorithm to find that our system is very helpful to people.

1. Introduction

Recently, personal health management has become one of the popular research topics. For instance, to acquire and measure the personal health signal, the techniques of personal health data transmission, personal health data record manner, embedded biomedical analysis platform, and so forth. Shu [1] used mixed signal to design the system functions in the signal chip PSoC and then exploited NI USB-6251 and Tektronix TDS3054e scope to verify the functional module the authors finally linked the sensors to this PSoC to accomplish miniaturization and modular measurement system [2–5].

In this paper, we integrate the personal medical measurement instruction and the cloud server to support the transmission of the personal health data by Internet. In this result, we create a central information management and data sharing storage. This work is made from a module manner, in which we support an automatic PHDT that can rapidly and easily link to the cloud server to transmit personal health data. We also employ a mobile to substitute the personal computer and to access the personal health data via the Internet.

In the recent years, the previous works aimed at storing the physiology signals and then sending them to the remote information center that is either PC or server. So, the end users cannot employ a simplified manner to send the personal health measurement data to the cloud server [6, 7].

The wireless network electric appliances are developed for peoples, home, enterprise, and so forth. Therefore, the near-distance wireless communication protocol becomes very important to them [8, 9]. Thus, most of short distance wireless communication protocols and techniques are estimated in the free-pay ISM bandwidth [1, 10].

The rest of this paper is organized as follows. In Section 2, we introduce the short distance transmitting technologies. The structure of the PHDT is constructed in Section 2. We make the module algorithms and the characteristics in Section 3. The system functions are verified in Section 4. Finally, we make the summaries in Section 5.

2. The Infrastructure of PHDT

Figure 1 illustrates the structure of personal health data transformer (PHDT) in which the MCU is used as central control core. The personal medicine data can be transmitted by one of RF, USB, or UART modules to a personal health data buffer. The recorded data through the I²C module inputs to the users data buffer. The MCU indicates the IP of the user and initials the network module to connect to the cloud server. Finally, the user can exploit the user ID, and password to login the server to transmit the personal health data to the cloud server.

Three kinds of input/output interfaces are offered in the transmitter as follows.

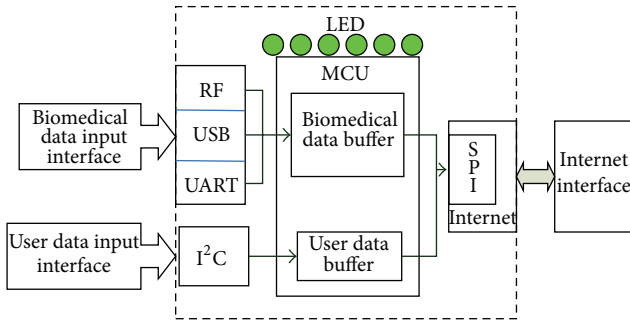


FIGURE 1: Transmitter system block diagram.

- (1) Personal health data input interface is composed of three modules, which are
 - (i) RF module: it supports wireless method to transmit the personal health data in channel;
 - (ii) USB module: it supports USB method to transmit the personal health data in channel;
 - (iii) UART module: it is an expandable data transform interface and classifies four types, UART to RS-232, UART to RS-485, UART to Zigbee, and UART to Bluetooth. We also employ this UART interface to connect RS-232 to PC and to service.
- (2) User data input interface is composed of an I²C and an alternation transmitted interface. The user data card supports different users and replaces the user data transform module, to acquire the primary data of user in the transmitted channel.
- (3) Internet module supports a data transmitted interface between transmitter and network.

2.1. MCU Module. The core of MCU module is achieved in PIC24FJ128GB106 [11]. This chip has an embedded USB 2.0 OTG, 128 KB core memory, 16384-byte data memory, and several communication interfaces such as UART, SPI, and I²C.

The main job of MCU module is to integrate the overall modules and to control each module. In order to fairly control each module, we exploit the polling manner by taking turn for each module. The specifications of MCU modules are described as follows.

- (1) MCLR chip reset circuit is operated while the SW1 is turning on. At the same time, the MCLR immediately issues a *Reset* signal to reboot the MCU.
- (2) ICSP chip online circuit has 6 pins to connect to the PICkit3 recorder. We can directly upgrade the driver of MCU via an online PCB.
- (3) XTAL is an external crystal circuit and the operation frequency is 16 MHz.

2.2. Network Module. Figure 2 shows the network transform module, which is composed of two parts, hardware and software.

- (1) Hardware:
 - (i) network chip control circuit,
 - (ii) network connection circuit embedded transformer.
- (2) Software:
 - (i) network chip driver,
 - (ii) small scalar TCP/IP protocol level *uIP* [12],
 - (iii) the application program includes DHCP client, DNS client, and FTP clients.

The previous characteristics are described as follows.

- (1) Network driver is used to control network chip; it also can write the external packages to the sent buffer of network chip.
- (2) *uIP* protocol is used during the package transmission in Internet, and it is necessary to add IP and TCP headers. So, we use the TCP/IP function while the job has been accomplished. Therefore, we can transplant the *uIP* protocol and handle the TCP/IP of a small scalar embedded system.
- (3) The network application program includes
 - (i) DHCP which client is realized by the *dhcp.c*. The DHCP client can acquire and obtain an IP address, gateway, and DNS from DHCP server;
 - (ii) the DNS client functions which are realized by the *resolv.c* to acquire the cloud server IP address;
 - (iii) FTP client which accomplishes the ftp function through the *client.c*.

The data is transmitted by the transmitter and the product that is presented as follows. First, the MCU is set in a polling manner to query each peripheral device whether package be handled or not. If it is true, the control right passes to *uIP*. What the package will deliver that is dependent on *UIP_APPCALL()* or *UIP_UDP_APPCALL()*; hence, the application program takes over the data transmission process.

The network module is constructed in ENC424J600. The network control circuit is combined of a four-line SPI interface and an ENC424J600's interrupt request.

The control programs of AVR MCU and ENC424J600 are modified to fit the PIC24FJ128GB106 [11] in order to control the drivers. We also edit a system level interface program, *network.c*, which includes the interface subroutines between MCU module and network module that are listed in Table 1.

2.3. *uIP* Protocol. *uIP* is proposed by Adam Dunkels and it is a free open source code for small scalar TCP/IP protocol [12], in which he had deeply described the transplant process for porting *uIP*1.0 linking to LPC23xx/24xx. The process of *uIP* transplant is described as follows.

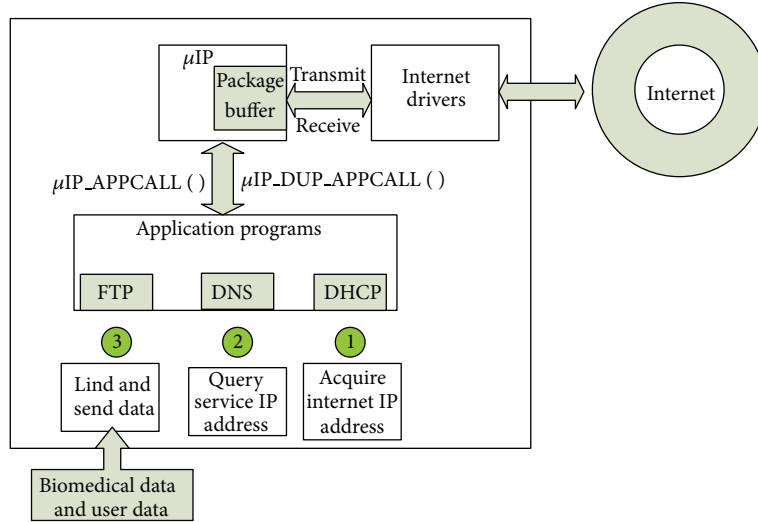


FIGURE 2: Network module structure.

TABLE 1: The sun-routines of network interface.

network_init()	Initializing the network chip
network_read()	Reading a received package
network_send()	Sending a network package
network_get_MAC()	Acquire the MAC address
network_set_MAC()	Setting the MAC address

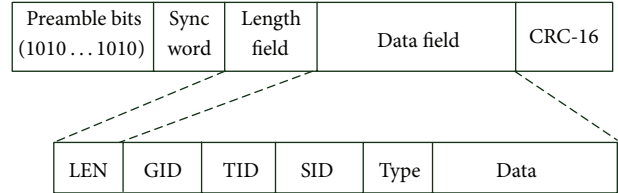


FIGURE 3: The formal package in RF module.

(1) Transplant timer:

- (i) at first, we complete the *clock_init(void)* function to initialize system clock module;
- (ii) and then the *clock_time_t* and *clock_time(void)* functions support a referred system clock.

(2) We transplant network chip driver to complete the network module interface.

(3) Adding *uip.c*:

- (i) we create *uipapp.c* to realize the return function of *uip_appcall()* and *udp_appcall()*; then
- (ii) we define the return-function in *uipapp.h*. It is added to *UIP_APPCALL* and *UIP_UDP_APPCALL*. Furthermore, we add them into the *uip_arp.c*.

(4) Adding the *dhcp.c* is to test the *uIP* function. At the same time, the DHCP server can acquire IP address, too.

2.4. RF Module. In order to obtain lower power consumption in near-distance transmission, we employ the 2.4 GHz ISM bandwidth in RF module. It is implemented by CC2500 RF controller, and a 4-wire SPI is used to connect between MCU and CC2500.

For most peoples at home, the basic request is a wireless network in short distance. So, we exploit a broadcast method

as the wireless network topology. The wireless network is recognized by the GID to detect whether the same network group or not. In the same GID, the network is composed of several members which are detected by the different SID. So, in the same group members have unique SID. In this working network, a master in central and its SID are 255. The rest members are set to the slave transmitter. The master uses polling manner to query whether the slave (i.e., medicine measurement instrument) transmits data or not. In order to implement the previous works, the RF module supports the following four subroutines:

- (i) *ccInit()*: initials RF module to set GID and SID;
- (ii) *ccSendPkg()*: sends data package via RF;
- (iii) *ccGetPkg()*: reads RF data package;
- (iv) *RFProc()*: is the main program of RF module.

The format of data package in RF module is defined in Figure 3, where the LEN indicates data length and the data field includes group ID (GID), target ID (TID), source ID (SID), data classify (TYPE), and transmitted data (DATA).

In RF module, the main program will call the *SaveData()* subroutine during data receiving. When a data packet is received firstly to recognize the GID, if the TID equals SID, then the package will be received.

2.5. USB Module. Most of medicine measurement instruments have the USB interface. For this reason, the transmitter

must own a USB host. In this work, the USB software is based on Microchip USB stack and we use the *USBConfig.exe* tool to complete the USB. In this module, we support a *usbmain()* subroutine of system level to call the *usbmain()* subroutine; while the device receives data by the USB, it will trig the *SaveData()* subroutine to handle the data receiving works.

2.6. UART Module. For most commercial products, they offer a UART interface as a converter such as Bluetooth to UART and Zigbee to UART. In this paper, we support two types of UART modules, UART1 and UART2, that are described as follows.

The UART1 is connected to an external RS232 interface. Then the transmitter can easily link this RS232 to the PC and connects to the superterminal.

We use the *UARTProc()* function to manage the UART2 and exploit an interrupt scheme to handle the received data. When data is received by UART2, immediately the *SaveData()* subroutine is called to trig the data reception process.

The UART2 module has VDD and GND to support the power to Zigbee. The MCU's UART2 directly connects to the Zigbee to realize the wireless work; there are from UART2's RX2 to Zigbee's TX1 and from UART2's TX2 to Zigbee's RX1.

2.7. I²C Module. Another important advantage of transmitter is a plug-in manner to the user. When the I²C module is used, the necessary power of user data card is supported by the VDD, GND of I²C, and the SCL3, and SDA3 of I²C is connected to the 24LCXX EEPROM's SCL and SDA, respectively. We use the *IDProc()* subroutine to handle the I²C module and initial the user input request.

2.8. LED Module. The LED module is used to indicate the operation status during transmission. The signals of each LED are defined as in Table 2. We also support four subroutines to control the LED, which are

- LEDInit()*: initials LED module,
- LEDON()*: turns on the LED,
- LEDOFF()*: turns off a specific LED,
- LEDTGL()*: turns on/off the specific LED.

3. Algorithms

In advance, we build up a practicality integration development environment (IDE) to verify and support our assumption. For the PCB of the physical devices, we use the KiCad [13] to do, and the experiment PCB is shown in Figure 4.

The system verification work has two stages, individual module function and system integration function.

- (1) The individual module function.
 - (i) UART module function,
 - (ii) I²C module function,
 - (iii) USB module function,

TABLE 2: LED indication.

LED1	Personal data input over
LED2	Insert internet line
LED3	Link to internet
LED4	Insert USB devices
LED5	USB data read
LED6	Data transmitting
LED7	Power on

- (iv) RF module function,
- (v) network module function.

(2) In system integration function stage, users can select one of the input channels.

- (i) RF transmitter + personal data card,
- (ii) medicine measurement instrument + personal data card,
- (iii) Zigbee transmitter + personal data card.

3.1. Main Function. Before the individual module function is verified, we must build a main program in terminal. So, we insert the calling operation in the main program to call module function. The main program is shown as in Algorithm 1.

3.2. UART Function. In this paper, we support two UART modules which are UART1 and UART2. The UART1 is used as a terminal to present the system operation message. In advance, we must confirm the UART circuit correctness. And then the transmitter is able to connect PC via the RS-232.

The UART2 is connected to the Zigbee transmitter. The UART2 also is one of the input channels of the personal medicine data. The works are among UART1 and UART2 as follows.

- (1) First, the UART2 issues a request to send data in a fixed interval time.
- (2) During data receiving stage, a received signal is sent from UART1 to the other transmitter.
- (3) Finally, the "data accepted" is issued from UART1 while being accomplished.

If we want to let the UART2 operate, we only insert the *UARTProc()* subroutine into the main program and the process is shown in Algorithm 2.

3.3. I²C Function. The I²C module is done by inserting the *IDProc()* subroutine into the main loop that is shown in Algorithm 3.

3.4. USB Function. We need to insert the *usbmain()* subroutine into the main program to implement the USB module. It is shown in Algorithm 4.

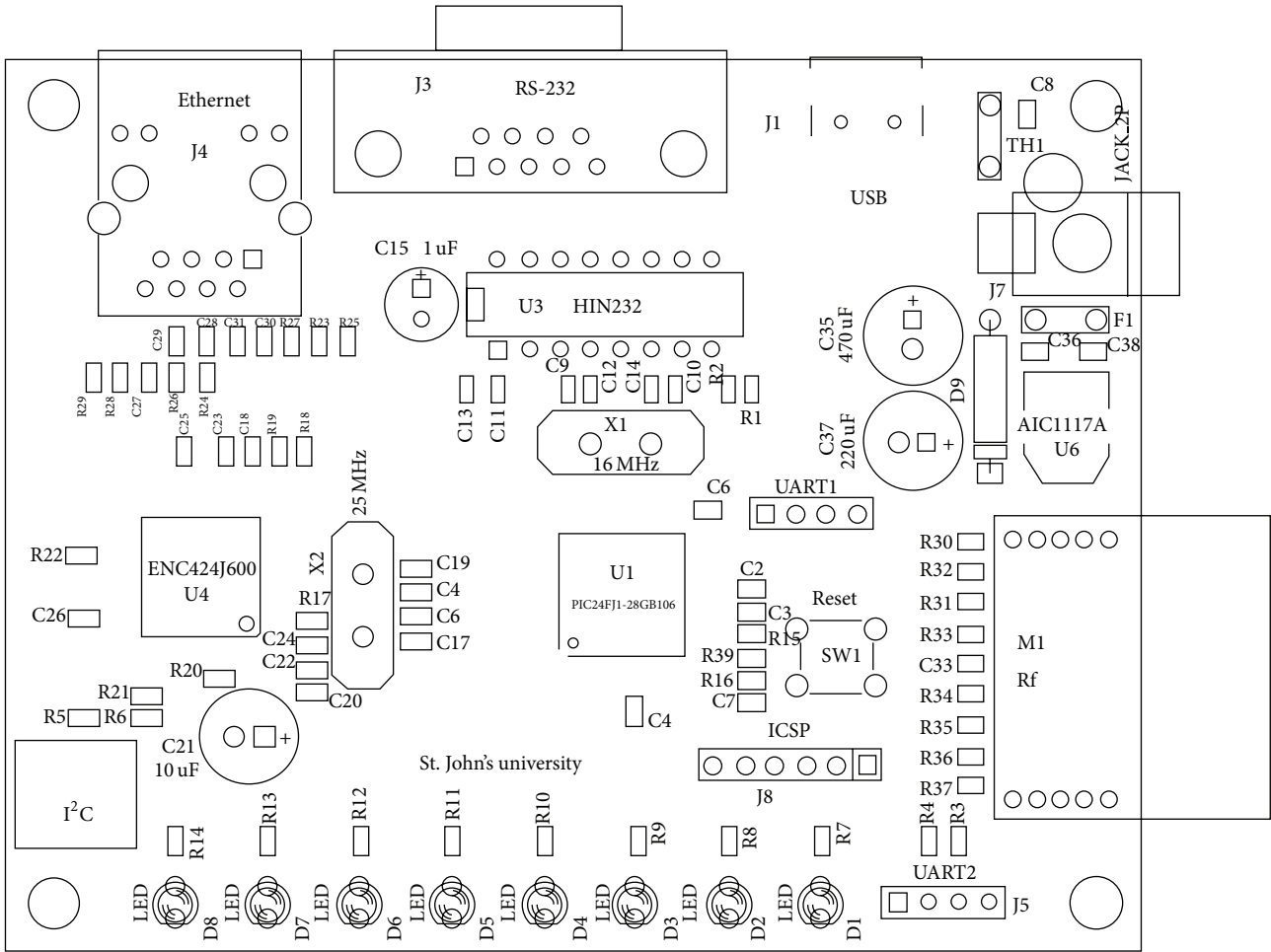


FIGURE 4: The implemented PCB.

```

int main (void)
{
    Init(); //system initialization
    //--- Main Loop ----
    while(1){
        Timer1Proc(); //call the system Timer module functions
    }
}
    
```

ALGORITHM 1

```

//--- Main Loop ----
while(1){
    Timer1Proc(); // system Time
    UARTProc(); //UART2 module handle
    function
}
    
```

ALGORITHM 2

```

//--- Main Loop ----
while(1){
    Timer1Proc(); // system Timer
    IDProc(); //I2C module handle function
    uipmain(); //ETHERNET module handle function
}
    
```

ALGORITHM 3

```

//--- Main Loop ---
while(1){
Timer1Proc(); // system Time
usbmain(); //USB module handle function
}

```

ALGORITHM 4

```

//--- Main Loop ----
while(1){
Timer1Proc(); // system Timer
IDProc(); //I2C module handle function
uipmain(); //Network module handle function
}

```

ALGORITHM 6

```

//--- Main Loop ----
while(1){
Timer1Proc(); // system Timer
RFProc(); //RF module handle function }

```

ALGORITHM 5

```

USER: 8860100002011000008
PASSWD: 1234567887654321
URL: ftp.ecaretek.com
UART1: Baudrate 57600
UART2: Baudrate 38400
UART2: request
UART2: request
UART data is linked. . .
Machine name: GM06L
Product: Glucose
1, 2009, 11, 30, 13, 50, Lo., mg_dL
2, 2009, 11, 30, 13, 45, Lo., mg_dL
3, 2009, 11, 30, 13, 43, 68, mg_dL
4, 2009, 11, 30, 13, 40, 37, mg_dL
5, 2009, 11, 30, 13, 27, 36, mg_dL
6, 2009, 11, 30, 13, 27, Lo., mg_dL
7, 2009, 11, 29, 13, 27, 33, mg_dL
8, 2009, 11, 28, 13, 27, 55, mg_dL

```

Box 1: Data transmission via UART2.

3.5. RF Function. For implementing the RF function, we need to insert the *RFProc()* subroutine into the main program that is shown in Algorithm 5.

3.6. Network Function. The work of network module is made from the following steps:

- (1) trig the network chip,
- (2) set the parameters of the dynamic host configuration protocol (DHCP) to acquire the network, and
- (3) make sure the IP of personal data card is accepted by the cloud server.

In order to implement the previous processes, we insert the *IDProc()* and *uipmain()* subroutines into the main program to implement the network module that is shown in Algorithm 6.

In this paper, we use the *Packetyzer* network package acquirement analysis tool to verify network module and to acquire DHCP query product.

4. System Function

As a reason, the transmitter has three types of data input channels, RF, USB, and UART, in order to prevent the data from being transmitted by different channels simultaneously. We exploit a software scheme to handle the personal health data in the collector. For personal health data collector maintaining, it is realized by the *SaveData()*, where we can receive a primary data from RF, USB, and UART2. After the primary data is processed, a signal is sent by the *call()* subroutine to notice the data being “accepted,” “unaccepted,” or “completed.” By this way, it is helpful to the software development and maintenance.

The personal health measurement instruction instrument using USB transform wire and transmitter connects to physical level verify manner follow the personal medicine data input different channels, exploiting the following operation model to verify.

- (i) RF transmitter + personal data card,
- (ii) health measurement instrument + personal data card,
- (iii) Zigbee transmitter + personal data card.

We use the *Filezilla FTP* transform software to upload/download the file to/from server. Both uploading and downloading the personal health data are via the UART2 channel. The result is shown in Box 1.

5. Conclusions

We use three normal interfaces, such as USB, UART, and RF to implement the purposed device. This paper issues a personal health data transformer, RF interface, and acquirement of the user personal health measurement data. Adding a replacement personal data card, we can, according to the data card, access the user accord, password, and server IP. For this reason, we can transmit the personal health data via the network sent to transform the cloud server and to crate the personal healthy information file.

The advantages of the personal health data transformer (PHDT) are listed as follows.

- (1) We used wireless technology directly to connect PHDT to acquire the records from personal health measurement.
- (2) Substitutable user data card: the user’s data card records the following data: user ID, password, and

server IP. The substitutable design manner allows dissimilar users with higher speed to replace the user data.

- (3) Internet transform functions: we can use the PHDT to acquire dynamic IP address. By the DNS address, we recognize the query cloud server IP address and enter into the cloud server by a dynamic FTP. Therefore, the measured records of personal health are delivered to cloud server to estimate the personal health information.

References

- [1] K. L. Shu, *A study of embedded platform of bio-medical signal measurement [M.S. thesis]*, Nantai Techniques University, Tainan, Taiwan, 2007.
- [2] A. Z. Alkar and U. Buhur, "An internet based wireless home automation system for multifunctional devices," *IEEE Transactions on Consumer Electronics*, vol. 51, no. 4, pp. 1169–1173, 2005.
- [3] M. B. Huang, *Brain Wave Recorder with USB Interface Module [M.S. thesis]*, ChoYn University.
- [4] Microchip Cop., "USB embedded host stack," Microchip Application Note AN1140, 2008.
- [5] K. Römer and F. Mattern, "The design space of wireless sensor networks," *IEEE Wireless Communications*, vol. 11, no. 6, pp. 54–61, 2004.
- [6] E. Callaway, P. Gorday, L. Hester et al., "Home networking with IEEE 802.15.4: a developing standard for low-rate wireless personal area networks," *IEEE Communications Magazine*, vol. 40, no. 8, pp. 70–77, 2002.
- [7] K.-I. Hwang, J. In, N. Park, and D.-S. Eom, "A design and implementation of wireless sensor gateway for efficient querying and managing through world wide web," *IEEE Transactions on Consumer Electronics*, vol. 49, no. 4, pp. 1090–1097, 2003.
- [8] J.-D. Lai, *A embedded platform of bio-medical with wireless [M.S. thesis]*, Jao-Ton University, 2008.
- [9] H. Z. Lee, *Regular report of foods in home carewith RFID [M.S. thesis]*, Asia University, Taichung, Taiwan.
- [10] E. F. Liu, *A transform system for body temperature and blood press with wireless [M.S. thesis]*, Asia University, Taichung, Taiwan, 2010.
- [11] Microchip Cop., "PIC24FJ256GB110 Family Data Sheet," <http://www.microchip.com/wwwproducts/Devices.aspx?dDocName=en531079>.
- [12] NXP Semiconductors, AN10799, "Porting uIP1.0 to LPC23xx/24xx V2," NXP Semiconductors, 2009.
- [13] Microchip Cop., "PICkit 3 In-Circuit Debugger," <http://www.microchip.com/pickit3/>.

Research Article

Numerical Analysis of Indoor Sound Quality Evaluation Using Finite Element Method

Yu-Tuan Chou¹ and Shao-Yi Hsia²

¹ Department of Applied Geoinformatics, Chia Nan University of Pharmacy & Science, Tainan 717, Taiwan

² Department of Mechanical and Automation Engineering, Kao Yuan University, Kaohsiung 821, Taiwan

Correspondence should be addressed to Shao-Yi Hsia; syhsia@cc.kyu.edu.tw

Received 30 September 2013; Accepted 2 November 2013

Academic Editor: Teen-Hang Meen

Copyright © 2013 Y.-T. Chou and S.-Y. Hsia. This is an open access article distributed under the Creative Commons Attribution License, which permits unrestricted use, distribution, and reproduction in any medium, provided the original work is properly cited.

Indoors sound field distribution is important to Room Acoustics, but the field suffers numerous problems, for example, multipath propagation and scattering owing to sound absorption by furniture and other aspects of décor. Generally, an ideal interior space must have a sound field with clear quality. This provides both the speaker and the listener with a pleasant conversational environment. This investigation uses the Finite Element Method to assess the acoustic distribution based on the indoor space and chamber volume. In this situation, a fixed sound source at different frequencies is used to simulate the acoustic characteristics of the indoor space. This method considers the furniture and decoration sound absorbing material and thus different sound absorption coefficients and configurations. The preliminary numerical simulation provides a method that can forecast the distribution of sound in an indoor room in complex situations. Consequently, it is possible to arrange interior furnishings and appliances to optimize acoustic distribution and environmental friendliness. Additionally, the analytical results can also be used to calculate the Reverberation Time and speech intelligibility for specified indoor space.

1. Introduction

Economic development in human society has been more demanding in terms of quality of life, particularly in relation to noise issues. Noise is defined as undesirable sound or sound with inappropriate timing and location. Noise thus includes sound that interferes with talking and listening and may include sound with a potential to damage hearing. In modern living environments, noise is ubiquitous and includes pile driving and hammering on construction sites, vehicle engines and horns, and mechanical sounds associated with printing, underground factories, or other industrial activities. Noise quality of vehicles and electric appliances causes stress, and noise problems associated with public construction, which can affect a citizen's health and damage quality of life, are also emphasized. This makes it necessary to understand noise characteristics and then select a favorable engineering control to protect people against noise. Current domestic research on the evaluation of interior sound fields rarely considers the evaluation of environmental

noise, and distinct approaches are applied to test and evaluate different noise sources. Noise evaluation indices and sound field simulation are commonly employed for interior sound field analyses. In a residential study, Huang and Lai [1] measured existing noise environments, including volume and location analyses of various noise sources, and found that the allowance for interior noise ranged between 30 dB(A) and 40 dB(A) in foreign countries. Hsieh [2] discussed real cases involving air-conditioning noise in auditoriums in Taiwan and discovered that most did not conform to permit standards for background noise. The main problem was that air conditioners were excessively noisy when activated and 14 dB(A) higher than when switched off. Hsieh et al. [3] discussed the present situation of background noise in cultural centers and the objective measurement of background noise, specifically air-conditioning in the main building. The results demonstrated that air conditioners were the major background noise source in 95% of cases. Chen and Chung [4] introduced the acoustic characteristics of a newly built studio, including the design and measurement results of

Reverberation Time, air soundproofing, and floor sound insulation, and discussed the design feasibility. Chiang et al. [5] analyzed the impulse responses measured in three theater types using Hyper Signal to measure the physical parameters of acoustic competence and compared how enclosure affected that acoustic competence. Chang et al. [6] used the jury testing to establish an evaluation procedure for human hearing perception in indoor space. They carried out this testing in three types of residential spaces and built a reasonable sound quality assessment method. Vorlander [7] reviewed the concept and implementations of room simulation methods. He found that a better prediction of Reverberation Times can be derived by using the theory of error propagation of uncertainties.

Among various methods used in discussions of simulation, the Finite Element Method is commonly utilized in research analyses. It tends to obtain solutions by simplifying complex problems, such as those involving complex and irregular boundary conditions and loads. Huang and Yang [8] developed a prediction model to calculate the sound pressure level in a small space. The FEM is employed to solve the indoor sound field and obtain good quantitative sound characteristics at low frequency. Aretz and Vorlander [9, 10] presented series of papers on the realistic simulation of car audio sound in car passenger compartments using a combined Finite Element (FE) and Geometrical Acoustics (GA) approach. The simulations are conducted for the whole audible frequency range with the loudspeakers of the car audio system as the sound sources. Their study clearly points out the strengths and weaknesses of the applied methods depending on the considered frequency range and material characteristics.

This study analyzes the characteristics of interior sound fields with fixed capacity and sound sources. The effects of shape, absorption property, and room boundary on sound delivery are analyzed to determine the improvement of interior noise. The research results can be used in the predesign of interior architecture to improve interior noise, decrease construction costs, and improve living quality.

2. Basic Theory

2.1. Basic Theory of Interior Sound. Sound comprises pressure change that resulted from the vibration of objects or molecules (the sound source), which, transmitted through water, air, or other media (communication path), becomes mechanical energy detected by human ears (the sound body). The waveform of sound comprises the mathematical and physical characteristics of sine waves, including frequency, wavelength, time lapse, and phase angle. Sound volume is normally represented using the physical quantity of sound pressure, with the unit of measurement being decibels (dB), and is related to an object's vibration. Volume is the subjective perception of human ears of the amplitude, which differs from the definition in physics.

The sound discrimination ability of human ears exhibits nonlinear characteristics and is sensitive to distinct frequency. The general auditory frequency of human ears

appears at 20-20 kHz. Sound pressure and sound intensity are normally used to measure sound as the perception of loudness changes with frequency. In this case, noise level meters are generally equipped with different weighted noise levels, A, B, and C, where weighted noise level A most closely resembles the human ear.

W. C. Sabine spent five years seeking to improve acoustics in university lecture halls and developed the famous Reverberation Theory, which defined Reverberation Time (RT) to present reflection time for a direct sound to decay 60 dB. He further explained the relations between the shape, size, and decoration of a room, which could improve the quality of interior listening environment, as well as Reverberation Time, which became the determinant of Room Acoustics [11]. After the production of an indoor sound source, the interior sound field achieved the static state and then constantly reflected sound when the sound source was stopped to prevent immediate disappearance of the sound. The situation whereof the sound did not immediately disappear was called Reverberation, and the period for which it persisted was called the Reverberation Time. Reverberation Time in the design of Room Acoustics is generally known as Regulated Reverberation Time, which is defined as the time required for stable sound pressure attenuating 60 dB, T_{60} (or reducing the sound energy density down to the millionth static sound energy density). Clarity refers to the ability of the audience to clearly discriminate the parts and notes (music) and accurately hear the syllables (language) when the sound (language or music) is transmitted to them. Clearness and reverberation are two aspects of a single phenomenon and are inversely related to each other. Consider

$$T_{60} = \frac{0.049 V}{-S \ln(1 - a)}, \quad (1)$$

where T_{60} is the Reverberation Time (sec), V is the room capacity (cubic feet), a is the average room surface absorption coefficient, and S is the total room reflection surface (square feet).

Three sound waves are transmitted in interior sound environments. Direct sound indicates that the sound source is directly transmitted to the receiving point without influence from interior interfaces [11, 12]. Reflected sound describes the reflected sound in circumstances where the time delay is less than 50 ms. Reverberant sound describes the situation where sound is constantly reflected, where length and attenuation are considered the key factors in Room Acoustic design.

When analyzing indoor acoustic simulation, the coupling of fluid and a structure is generally taken into account [13]. Meanwhile, the dynamic equation for a structure and Navier-Stokes equation for flow are also calculated and analyzed. Assuming fluid being compressible and nonviscous, average velocity being zero, and average pressure and density being uniform, the continuous equations could be simplified as an acoustic wave equation in the kinematic equation for fluid. Consider

$$\frac{1}{c^2} \frac{\partial^2 P}{\delta t^2} - \nabla^2 P = 0, \quad (2)$$

where c is the velocity of sound of fluid, P is the the acoustic pressure, and t is the time. In consideration of the harmonic change of acoustic pressure with frequency, it is assumed that

$$P = \bar{P}e^{j\omega t}, \quad (3)$$

where \bar{P} stands for the amplitude of acoustic pressure and ω is the frequency. Equation (2) could be simplified as Helmholtz equation as follows:

$$\frac{\omega^2}{c^2}\bar{P} + \nabla^2\bar{P} = 0. \quad (4)$$

Since the spillover effect of viscous energy of fluid is ignored, the lossless wave equation could be proceeded spatial discretization when combining with the structure dynamic equation. The original differential operator ∇ could be transformed into the matrix operator as follows:

$$\nabla \cdot (\quad) = \{L\}^T = \left[\frac{\partial}{\partial x} \quad \frac{\partial}{\partial y} \quad \frac{\partial}{\partial z} \right]. \quad (5)$$

2.2. Applying Finite Element Method to Sound Field Analysis. This study establishes the Finite Element Method as the model used for interior sound field analysis. With the development of CAE during recent decades, the Finite Element Method (FEM), Boundary Element Method (BEM), and Finite Differential Method (FDM) have been developed for different applications. Finite Element Analysis (FEA), being widely utilized, was based on Hamilton's Variation Principle, which was defined as the total energy required to achieve extreme values in neighboring areas. Based on this definition, analyses can be performed to calculate the sum energy, and the Euler-Lagrange differential equation can be derived using differential calculus. The governing equation is a simultaneous multivariate partial differential equation where an accurate solution can be obtained by given simple shape, boundary condition, and material property of the domain. Nevertheless, this approach only yields approximate solutions when applied in the real world.

Finite Element Method is composed of nodes and elements and replaces the original engineering systems. Additionally, a complete FEM contains the boundary conditions of constraints and external loads of an engineering system. This study uses ANSYS to simulate the sound field distribution under fixed noise sources in an interior space, where sound sources can be indoor fan or air-conditioner noise, and the floor, surroundings, and air can be the media that consider the absorption characteristics. The simulation results can be used to clarify the changes in sound field characteristics, such as frequency, location, and intensity of sound sources in distinct interior space and boundary reflections.

The strong form governing equation will be converted to weak form for obtaining the discrete algebraic equation. Multiplying (2) by a virtual change in pressure δP ,

the differential form is transformed into a ranged volume integral using Galerkin method as follows:

$$\begin{aligned} \int_{\text{vol}} \frac{1}{c^2} \delta P \frac{\partial^2 P}{\partial t^2} d(\text{vol}) + \int_{\text{vol}} (\{L\}^T \delta P) (\{L\} P) d(\text{vol}) \\ = \int_S \{n\}^T \delta P (\{L\} P) d(S), \end{aligned} \quad (6)$$

where vol is the volume of the scope of analysis, S is the curve of the coverage, $\{n\}$ is the positive vector of the curve, and the curve S is the interface in the coupling of fluid structures. In the simplification assumption, the momentum equation of fluid forms a pressure gradient on the surface of the structure, resulting in a positive acceleration on the surface. The relations appear as

$$\{n\}^T (\{L\} P) = -\rho_0 \{n\}^T \cdot \frac{\partial^2 \{u\}}{\partial t^2}, \quad (7)$$

where $\{u\}$ is the displacement vector of the structure on the interface and ρ_0 is the fluid density. Substituting (6) into (5), it shows

$$\begin{aligned} \int_{\text{vol}} \frac{1}{c^2} \delta P \frac{\partial^2 P}{\partial t^2} d(\text{vol}) + \int_{\text{vol}} (\{L\}^T \delta P) (\{L\} P) d(\text{vol}) \\ = - \int_S \rho_0 \delta P \{n\}^T \frac{\partial^2 \{u\}}{\partial t^2} d(S). \end{aligned} \quad (8)$$

In the solution process with Finite Element Method, the physical quantity of the points in the scope of analysis could be approximated with the following shape functions for the elements. Consider

$$\begin{aligned} P &= \{N\}^T \{P_e\}, \\ u &= \{N'\}^T \{u_e\}, \end{aligned} \quad (9)$$

where $\{N\}$ is the shape function of pressure, $\{N'\}$ is the shape function of displacement, $\{P_e\}$ is the pressure vector of a node, and $\{u_e\} = \{u_{x_e}\}, \{u_{y_e}\}, \{u_{z_e}\}$ is the composition of vector of node displacement. The differential shape function with the differential operator $\{L\}$ is shown as

$$[B] = \{L\} \{N\}^T. \quad (10)$$

Substituting it with (8), the following equation is acquired:

$$\begin{aligned} \frac{1}{c^2} \int_{\text{vol}} \{N\} \{N\}^T d(\text{vol}) \{\ddot{P}_e\} + \int_{\text{vol}} [B]^T [B] d(\text{vol}) \{P_e\} \\ + \rho_0 \int_S \{N\} \{n\}^T \{N'\}^T d(S) \{\ddot{u}_e\} = \{0\}. \end{aligned} \quad (11)$$

Equation (11) could be simplified as

$$[M_e^P] \{\ddot{P}_e\} + [K_e^P] \{P_e\} + \rho_0 [R_e] \{\ddot{u}_e\} = \{0\}, \quad (12)$$

where $[M_e^P] = (1/c^2) \int_{\text{vol}} \{N\} \{N\}^T d(\text{vol})$ is the fluid mass matrix, $[K_e^P] = \int_{\text{vol}} [B]^T [B] d(\text{vol})$ is the fluid stiffness matrix, $\rho_0 [R_e] = \rho_0 \int_S \{N\} \{n\}^T \{N'\}^T d(S)$ is the coupling mass matrix.

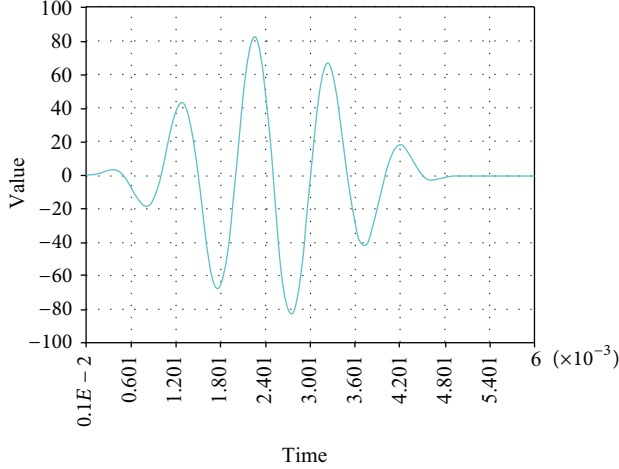


FIGURE 1: Delivery of pulse sound pressure at the 0.001 sec.

Equation (12) presents the wave equation of fluid, and the dynamic equation of a structure is shown as

$$[M_e] \{\dot{u}_e\} + [C_e] \{\dot{u}_e\} + [K_e^P] \{u_e\} = \{F_e\} + \{F_e^{Pr}\}, \quad (13)$$

where $\{F_e^{Pr}\}$ is the pressure load of fluid, which, with pressure integrals, is shown as below. Consider

$$\begin{aligned} \{F_e^{Pr}\} &= \int_S \{N^i\} P \{n\} d(S) \\ &= \int_S \{N^i\} \{N^T\} \{n\} d(S) \{P_e\} = [R_e] \{P_e\}. \end{aligned} \quad (14)$$

Equations (12) to (14) could be organized as

$$\begin{aligned} \begin{bmatrix} [M_e] & [0] \\ [M^{fs}] & [M_e^P] \end{bmatrix} \begin{Bmatrix} \{\ddot{u}_e\} \\ \{\ddot{P}_e\} \end{Bmatrix} + \begin{bmatrix} [C_e] & [0] \\ [0] & [C_e^P] \end{bmatrix} \begin{Bmatrix} \{\dot{u}_e\} \\ \{\dot{P}_e\} \end{Bmatrix} \\ + \begin{bmatrix} [K_e] & [K^{fs}] \\ [0] & [K_e^P] \end{bmatrix} \begin{Bmatrix} \{u_e\} \\ \{P_e\} \end{Bmatrix} &= \begin{Bmatrix} \{F_e\} \\ \{0\} \end{Bmatrix}, \end{aligned} \quad (15)$$

where $[M^{fs}] = \rho_0 [R_e]$, $[K^{fs}] = -[R_e]$.

The internal approximate values of the elements could be calculated with (15). The matrix equation of the scope of analysis could be acquired by integrating all elements for further calculating the pressure and displacement.

3. Implementation and Procedure

Working environment is the main influence on human productivity and health that improves interior environments to reduce personnel costs through simulations that minimize loss. The Finite Element Method transforms the engineering system into the Finite Element System for the simulation and analyses. Among the acoustic parameters, the absorption coefficient is one of the main factors and is used to quantify the absorption competence for the reference and the application of soundproofing engineers interested in calculating attenuated volume. The absorption coefficient is

Nodal solution
Stop = 1
PUB = 1
Time = 0.100E - 05
PRES (AVG)
RSES = 0
DMX = 0.116E - 12
SMN = -0.186E - 13
SMX = 0.670E - 13

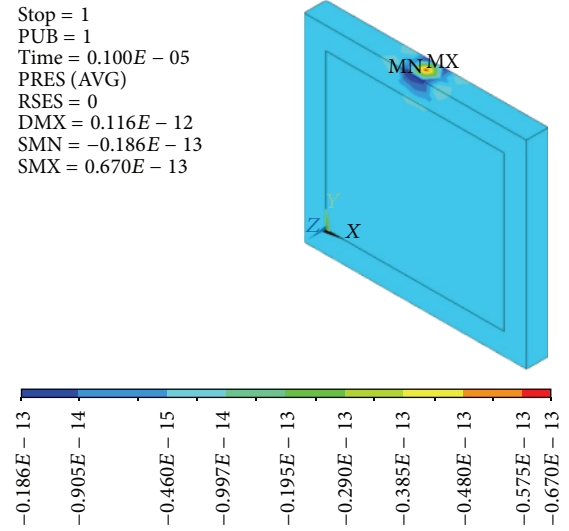


FIGURE 2: Stereo diagram of sound field before the diffusion at 1×10^{-6} sec.

Nodal solution
Stop = 1
PUB = 1
Time = 0.100E - 04
PRES (AVG)
RSES = 0
SMN = -0.497E - 03
SMX = 0.213E - 03

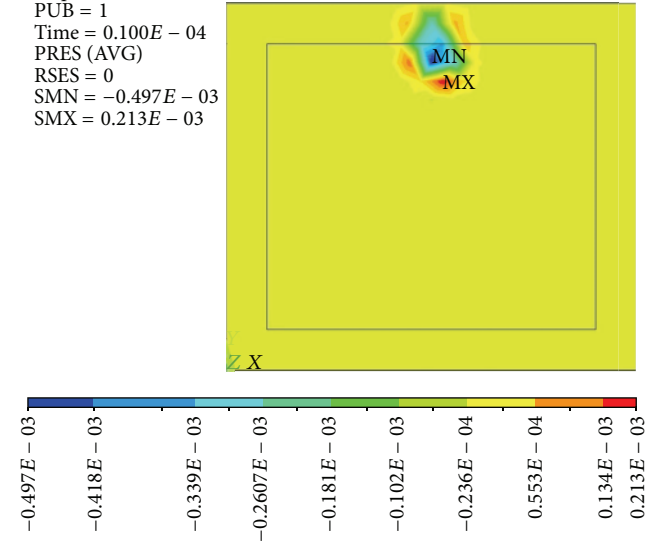


FIGURE 3: Sound field distribution after 1×10^{-5} sec.

the competence indicator of absorption materials. When the sound is transmitted to absorption materials, the sound is partially reflected and partially absorbed, as the commonly used porous absorption materials present a loose structure that allows easy sound penetration. Furthermore, absorption materials are generally fitted on thick structures like walls and metal plates that sound does not easily penetrate but from which is easily reflected. Small E_t often ignores that the absorption coefficient is simplified as $a = E_a/E_t$. Furthermore, the absorption coefficient ranges from 0.0 to 1.0, where higher value indicates the material has better absorption. In contrast, materials with worse absorption are reflective, where $a = 1.0$ presents complete absorption and

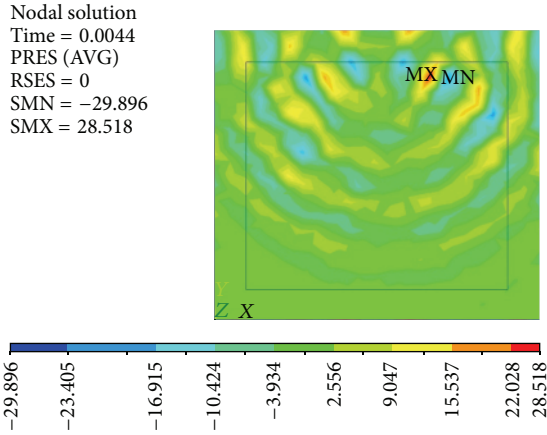


FIGURE 4: Boundary reflection with the delivery time 0.0044 sec.

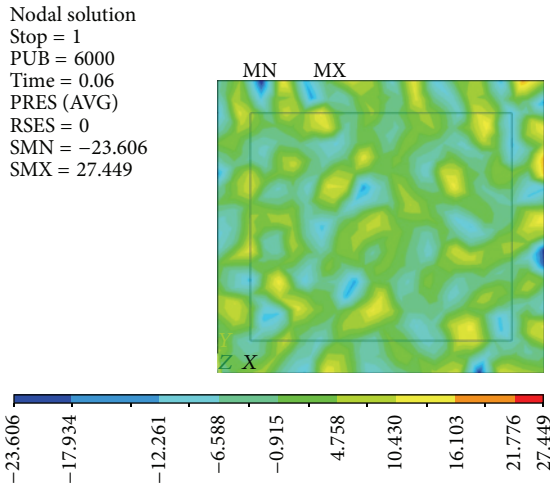


FIGURE 5: Stable state of sound pressure after several reflections.

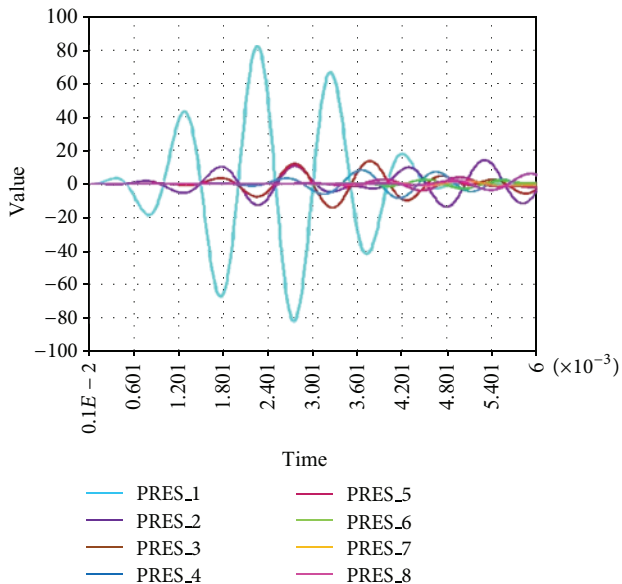


FIGURE 6: Sound decay phenomena along the perpendicular direction of the sound source.

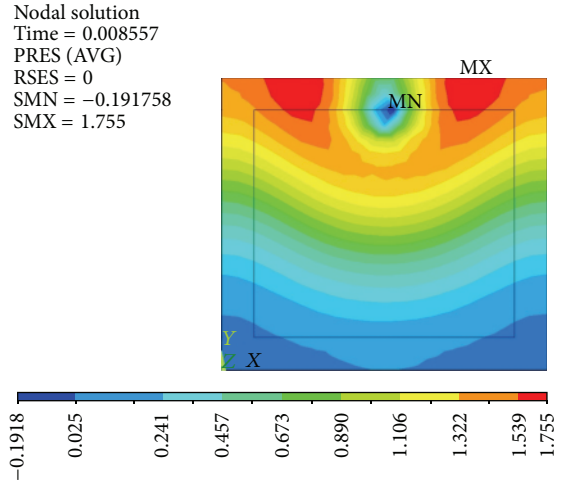


FIGURE 7: Sound pressure distribution of the fan noise for propagating to the ground.

TABLE 1: Input parameters for this research analysis.

Properties	Air	Wall
Length (m)	2.13	2.74
Width (m)	0.31	0.31
Height (m)	2.44	3.05
Density (kg/m ³)	1.29	2600
Velocity (m/sec)	335.28	3100
Absorption coefficient	~0..	0.04–0.70

$a = 0.0$ indicates complete reflection. Nonetheless, complex sound diffusion exists in the interior sound field, such as the interior surface and in the reflection of objects, such that changes of interior sound field are difficult to estimate.

Finite Element Analysis precedes the simulation in the environment with existing room arrangement, room capacity, and fixed sound sources and discusses the effects of room boundary on Reverberation Time of interior language under distinct frequency. In the analysis, the room shape and materials influence the reflection, diffraction, and scattering of sound and allow organization of the transmission in the space and the acquisition of interior data such as room size and absorption materials used on walls. The software is utilized to obtain the sound pressure distribution and Reverberation Time indoors. The results can be compared with the measured value of interior sound pressure to improve interior noise. The research results can also be used in preanalyses to improve the interior noise. Such measures not only can effectively reduce construction costs, but also can improve living quality. Table 1 lists the input parameters used in the present research analysis.

4. Simulation Results and Discussion

Finite Element Analysis is applied to analyze the interior sound field with fixed capacity and sound sources. The effects of room shape, absorption characteristics, and boundary are

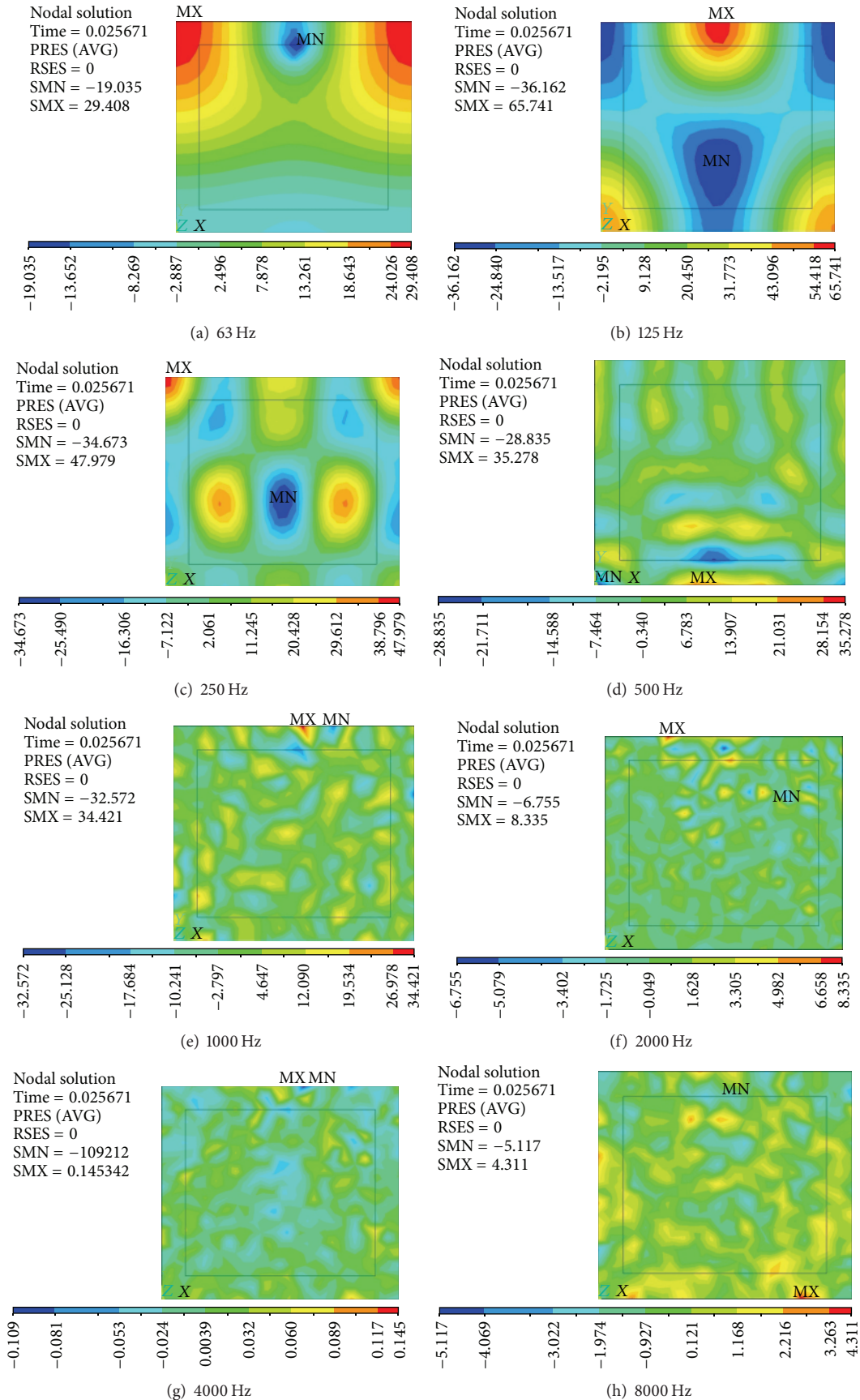


FIGURE 8: Sound pressure distributions for different frequencies at time 0.02567 sec.

also analyzed. Table 1 lists the input data. To simplify the analysis model, the room length is assumed to exceed the width and height, simply considering the wave propagation of the central cross-section. The boundary thus is simply expressed as the boundaries of the width and height, with length being excluded. Two cases are studied for investigating the sound quality of indoor space. General characteristics of sound propagation at specified frequencies are analyzed in the first case. The rest shows the indoor sound quality evaluation for an electric fan and motor put into the space.

4.1. Characteristics of Indoor Sound Propagation. In this case, the analysis is unsuitable for the corners at the length direction. Figure 1 shows that the input frequency of sound pressure 1 kHz and the induced length is five times that of the wavelength of the pulse wave under wave propagation at a distinct time. The ear-wave frequency response curve demonstrates that human ears respond differently to loudness at distinct frequencies. That is, human ears have different sensitivities to frequency, where the response to receiving the sound pressure 1 kHz is consistent with the actual sound pressure. Consequently, 1 kHz is used in the present analysis. The reason for the induced length being five times the wavelength may be that the length is considered the complete minimum pulse wave and thus that it is easier to identify the relevant physical parameters for the loudness competence. The setting computational duration for each step is 10^{-6} sec, where the sound pressure is distributed in tiny sections and the instant sound pressure diffusion is observable.

Figure 2 illustrates the wave propagation after the sound pressure is increased for 1×10^{-6} sec for the elements in the middle of the analysis. Figure 3 denotes the wave propagation for 1×10^{-5} sec. When comparing with the Figure 2, it is easy to understand the phenomenon of the sound wave propagating from top to bottom direction. Figure 4 shows the wave delivery for 0.0044 sec, where the wave reflection is visible on the left and right boundaries. Figure 5 illustrates the sound pressure distribution at time 0.05 sec, where the distribution of several reflected sound pressures in the room can be obtained when the sound pressure diffuses from the top and constantly reflects after passing the boundary. Figure 6 shows the sound pressure decay along the perpendicular direction of the sound source. It can be founded that higher sound decay exists at the far away sound source.

4.2. Indoor Sound Quality Evaluation for the Existence of an Electric Fan and Motor. When an indoor space existing a fluid machine, such as pump, fan, or air condition, the induced sound source for different frequency should be considered. For an electric fan and motor, the sound pressure of several frequencies is listed in Table 2 [14]. The corresponding sound distribution can be obtained using the ANSYS software. Figure 7 illustrates the pressure distribution at frequency 63 Hz when the sound propagates to the ground. The 0.008557 sec travelling duration can be derived from the simulation process. Next, Figure 8 shows the pressure distribution of different frequencies (63, 125, 250, 500, 1000, 2000, 4000, and 8000 Hz) at time 0.02567 sec. Since the frequency

TABLE 2: Sound pressure levels of an electric fan and motor.

Frequency (Hz)	Fan (dB)	Motor (dB)
63	84.6	49.0
125	81.6	53.0
250	83.6	57.0
500	84.6	61.0
1000	82.6	61.0
2000	79.6	57.0
4000	77.6	53.0
8000	67.6	49.0

varies at the same time, different pattern of distribution is represented.

The analysis data can be applied to evaluate the relevant physical parameters of the loudness component, including the interior sound quality analysis of the Reverberation Time required for the sound pressure at the fixed location attenuating to 60 dB, with (1).

5. Conclusion

Using the frequency 1 kHz and the induced time of five complete cycles of the pulse wave, this study analyzes the interior wave propagation. ANSYS analysis considers the boundary reflection, coupling, and the absorption characteristics of materials. The simulation results demonstrate the characteristics of interior wave propagation, as well as the superposition characteristics following boundary contact. The fluid machine sound source is also examined for obtaining the sound distribution of various amplitudes and frequencies. It can be further applied to the predesign analysis of interior architecture to improve interior noise and effectively reduce the construction costs and increase quality of life.

References

- [1] S. B. Huang and J. P. Lai, "Research on noise limit of building boundary-noise of residential equipment," in *Proceedings of the Annual Meeting and 15th Symposium of Acoustical Society of the Republic of China*, Tainan, Taiwan, 2002.
- [2] Y. Y. Hsieh, "Property analysis of air-conditioner noise in auditoriums in Taiwan," in *Proceedings of the Annual Meeting and 16th Symposium of Acoustical Society of the Republic of China*, pp. 238–242, Taipei, Taiwan, 2003.
- [3] H. R. Hsieh, J. P. Lai, Y. Y. Hsieh, and T. R. Wu, "Investigation and analysis of current indoor noise in cultural centers," in *Proceedings of the Annual Meeting and 13th Symposium of Acoustical Society of the Republic of China*, Tainan, Taiwan, 2000.
- [4] C. W. Chen and C. C. Chung, "Acoustic property of a newly built studio," in *Proceedings of the Annual Meeting and 13th Symposium of Acoustical Society of the Republic of China*, Tainan, Taiwan, 2000.
- [5] W. H. Chiang, Y. K. Hsu, and C. C. Tsai, "Acoustic measurement of courtyard-type traditional Chinese theater," in *Proceedings of the Annual Meeting and 16th Symposium of Acoustical Society of the Republic of China*, pp. 279–284, Taipei, Taiwan, 2001.

- [6] S. H. Chang, H. W. Wu, and C. F. Hung, "A sound quality study of house hold electrical appliances by iury test in indoor space," *The Open Acoustics Journal*, vol. 6, pp. 11–19, 2013.
- [7] M. Vorlander, "Computer simulations in room acoustics: concepts and uncertainties," *Journal of the Acoustical Society of America*, vol. 133, no. 3, pp. 1203–1213, 2013.
- [8] X. F. Huang and Z. X. Yang, "Prediction of the sound pressure level in a small room," *Applied Mechanics and Materials*, vol. 409–410, pp. 699–702, 2013.
- [9] M. Aretz and M. Vorlander, "Combined wave and ray based room acoustic simulations of audio systems in car passenger compartments, part I: boundary and source data," *Applied Acoustics*, vol. 76, pp. 82–99, 2014.
- [10] M. Aretz and M. Vorlander, "Combined wave and ray based room acoustic simulations of audio systems in car passenger compartments, part II: comparison of simulations and measurements," *Applied Acoustics*, vol. 76, pp. 52–65, 2014.
- [11] K. C. Huang, *Effects of interior decoration and sound source on sound field [M.S. dissertation]*, National Pingtung University of Science and Technology, Pingtung, Taiwan, 2008.
- [12] T. Y. Liu and C. H. Li, "Calculation and experiment comparison of acoustic field clarity and reverberation time," in *Proceedings of the Annual Meeting and 19th Symposium of Chinese Society of Sound and Vibration*, 2006.
- [13] "Environmental Protection Administration, Executive Yuan, Basic principles of noise and the control materials handbook".
- [14] S.-Y. Hsia, S.-M. Chiu, and J.-W. Cheng, "Sound field analysis and simulation for fluid machines," *Advances in Engineering Software*, vol. 40, no. 1, pp. 15–22, 2009.

Research Article

An Innovative Design Methodology KKBDCA for Affective Product Development

Kun-Chieh Wang¹ and Fang-Rong Ju²

¹ Department of Computer-Aided Industrial Design, Overseas Chinese University, Taichung, Taiwan

² Institute of Technological Product Design, Ling Tung University, Taichung, Taiwan

Correspondence should be addressed to Kun-Chieh Wang; simplyoung0104@gmail.com

Received 15 September 2013; Accepted 13 October 2013

Academic Editor: Teen-Hang Meen

Copyright © 2013 K.-C. Wang and F.-R. Ju. This is an open access article distributed under the Creative Commons Attribution License, which permits unrestricted use, distribution, and reproduction in any medium, provided the original work is properly cited.

This study proposes an innovative design scheme, called KKBDCA (Kano model, Kansei engineering, Base information, Design developing, Creativity thinking, and quality Assurance) for developing affective products. Firstly, a modified Kano model is proposed to link the customer's overall satisfaction and customer's partial preferences. Secondly, the KE together with appropriate quantification theory is used to establish the mapping relationship between design elements and customers' preferences. Then, a prototype of product with high customer satisfaction index (CSI) is selected from the product database as design reference. Thirdly, through the operation of BDCA design procedure, a new style of product is performed. Finally, verification is done to the new designed product and a satisfying evaluation result is obtained. The proposed integrated scheme may be used as a design methodology to explore new product style that satisfies customers' needs in overall aspects.

1. Introduction

The factors that influence the willing of consumers to purchase a certain product are multiphases, such as psychological, economic, and social. These factors usually change with time and different customers have their own motivation to make purchase decision. Among these factors, there is one deterministic factor that never changes: the customers' preferences.

Customer's preference or sensation is hard to be expressed and even hard to quantify, and there were lots of ways proposed to express human's preference about a product, such as words, physiological response (e.g., heart rate, EMG, and EEG), people's behaviors and actions, and facial and body expressions [1, 2]. Among these different ways of measuring human's affection or Kansei (Japanese word), the most common way is through words. This method has been successfully applied in many product design studies [3–8]. However, only one single word or even multiple words are not sufficient to describe customer's preference. Moreover, improper consideration of the Kansei words may lead to vital results when designing products matching customers' requirements.

In general, the purchase decision of a customer is directly controlled by his overall satisfaction about the product, not his partial preference. And, how much influence of the individual sensation on the overall satisfaction is still not clear.

To link the customer's overall satisfaction with individual sensation, a modified Kano's model is proposed by this study. Originally speaking, the Kano model [9] is a 2D diagram in order to display three groups of qualitative wants and needs of customers. These three groups include basic needs, performance needs, and motivational needs as shown in Figure 1. The basic needs curve (must-be requirement) of Kano model shows that if customers expect more satisfaction with receiving products and services, it cannot satisfy customers. The excitement needs curve (one-dimensional requirement) shows that whenever the product has a higher performance, customers receive more satisfaction. The performance needs curve (attractive requirement) indicates the fact that non-fulfillment of performance requirements in the product will cause dissatisfaction, but complete and suitable fulfillment of them will be followed by customers' satisfaction.

The next problem is how to convert the customers' preferences into product design elements and eventually design

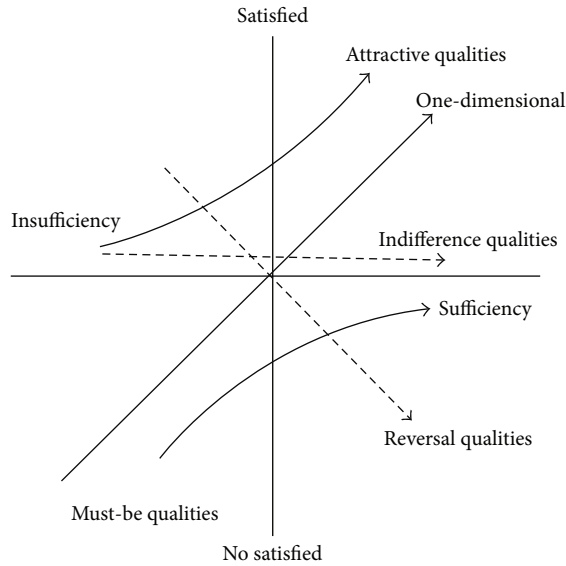


FIGURE 1: The Kano model.

an innovative product satisfying customers. To concretely translate the customer preference into product design elements, many methodologies were proposed in the past, such as quality function development (QFD) and matrix approach [10, 11]. Specifically, a popular methodology to translate consumers' psychological feelings about a product into perceptual design elements is the "Kansei Engineering" (KE) [1, 2]. It uses the "adjective words (Kansei words)" to describe the human preference and builds proper model to map these words into product design elements. Based on this mapping model, designers may easily evaluate product design style and design suitable product style meeting the given Kansei words. The Kansei engineering has been successfully applied in the field of product design [9, 12–14] to explore the relationship between the feeling of the consumers and the design elements of the product. Examining these studies, it is found that they did not extend the Kansei engineering scheme to really design a product and evaluate the design results from the viewpoint of customer satisfaction. In other words, the application of Kansei engineering scheme was so far limited and only used for evaluating the customer preference to existed products. Regarding this, this study attempts to develop an innovative design procedure, named BDCA, to compensate the insufficiency of KE.

In summary, our study will not only include the traditional Kansei engineering procedure to build a suitable model to connect the design features with customer preference (Kansei words) but also extend both upstream to include customer satisfaction (using the modified Kano model) and downstream to include the innovation procedure of product design. Furthermore, an overall customer satisfaction index is proposed to objectively evaluate the new design results from the viewpoint of customer preference. The manipulation procedures (Step 1 to Step 8) are shown in Figure 2 and explained as follows. (1) Firstly, we propose a modified Kano model to link the customer Kansei with customer satisfaction (Step 1 to Step 4). (2) Secondly, the Kansei engineering scheme

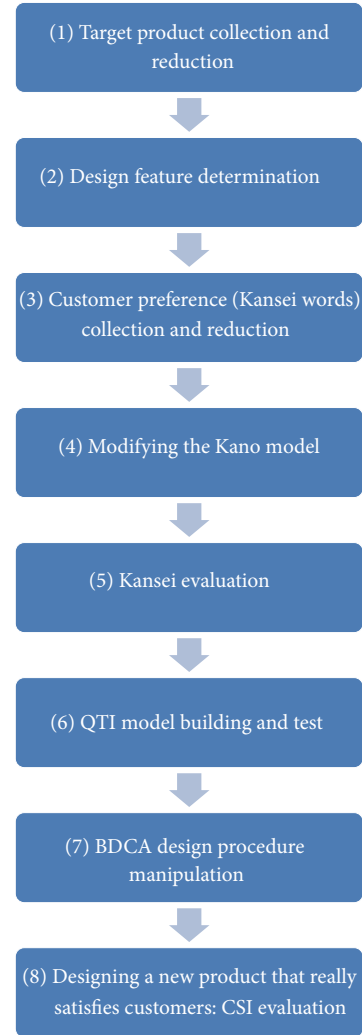


FIGURE 2: The KKBDCA innovative product design procedure based on customer satisfaction.

together with the QT I is used to map the design elements into customer Kansei (Steps 5 and 6). (3) Thirdly, using the high-weighting design elements as basis, an illustrative new style of digital camera is thus designed. (4) Then, the BDCA design procedure is introduced to design a new product (Step 7). (5) Eventually, a customer satisfaction index (CSI) is proposed to give a final evaluation on judging the goodness of the new designed product (Step 8).

2. Methodology

2.1. The Modified Kano Model. In order to link the customers' partial preferences with their overall satisfaction about a product, the aforementioned Kano's model is modified as follows. First, the above three categories of customer needs remain unchanged. Second, the horizontal axis is modified from "manner of product and service" into "customer's Kansei about products (adjective words)." This modification establishes a bridge between customer's individual Kansei and customer's overall satisfaction. Through this modified

Kano model, designers may easily understand what category the customer preference belongs to and how much influence it has on the customer satisfaction.

2.2. The Kansei Engineering. According to Nagamachi [2], there are six types of KE technique categorized as follows: (1) Type I: category classification, (2) Type II: Kansei engineering system, (3) Type III: Kansei engineering modeling, (4) Type IV: hybrid Kansei engineering, (5) Type V: virtual Kansei engineering, and (6) Type VI: collaborative Kansei engineering. In this study, we are focusing on Type III. The major work of the KE modeling (TYPE III) is to establish a proper model that connects people's psychological feelings with perceptual design elements of a product. Meanwhile, to complete the KE modeling work, the popular Quantitative Theory Type I [15] is used to build the relationship of product design elements and Kansei words. The entire manipulation procedure, including five steps, is described as follows.

Step 1. Initially, products within a specifically domain are described from two perspectives: a semantic perspective (image space) and a physical perspective (design space). These two descriptions span one space each, which in some cases can be defined mathematically as a vector space [16].

Step 2. Data in these two spaces are analyzed and reduced using statistical methods [17] such as K-Means method (KM), Kawakita Jirol method (KJ), multi-dimensional scaling method (MDS), hierarchical cluster analysis (HCA), and factor analysis (FA).

Step 3. Subsequently, the interactions between these two spaces are analyzed to realize their behavior. A final Kansei evaluation of questionnaire survey (product feature elements versus product images) is accomplished by proper subjects.

Step 4. Then the QT1 is applied to establish the relationship between product feature elements and product images. The weightings of every design attribute on different Kansei words are examined as the modification basis for designing future product.

Step 5. To evaluate the performance of our proposed integrated schemes, a validity test for the modeling is conducted.

2.3. The Quantification Mapping Model. The Quantitative Theory Type I is a multiple regression analysis scheme for deducing the relationship between a quantitative variable and qualitative variables. Here the quantitative variable, also the dependent variable, is set as the Kansei word, and the qualitative variables, also the independent variables, are set as design parameters. The mapping results are expressed in terms of the partial correlation coefficients (PCCs). The value of PCC indicates the relative importance of each design parameter to each Kansei word. Furthermore, the correlation between the observed value and predicted value of the dependent variables, expressed as R , is calculated. The coefficient of multiple determinations is R^2 . This parameter explains the linearity

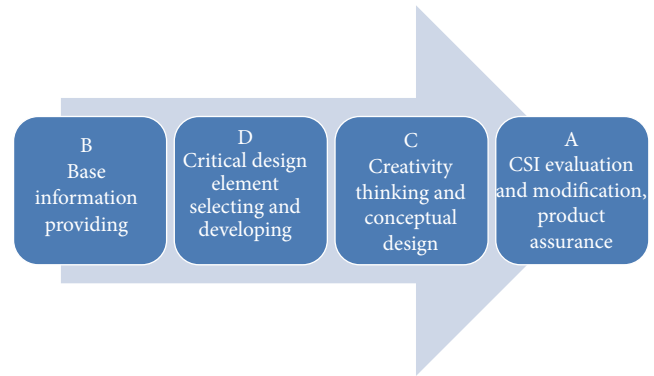


FIGURE 3: The BDCA design procedure.

extent between the dependent variables and independent variable.

2.4. The BDCA Design Procedure. This study proposes a design procedure, called KKBDCa, to design a product based on the results obtained from the Kano model and the Kansei engineering. The remained BDCA means base information, design developing, creativity thinking, quality assurance, as shown in Figure 3. This procedure includes four steps. Firstly, we select the highest CSI value sample as the design reference. Then, we examine the variation influence of all design elements on each Kansei word and think about their relationship. Secondly, we extract the commonly high influential elements of each of design categories for all three quality-sufficiency Kansei words, according to the results from the modified Kano model and Kansei engineering manipulation. Thirdly, we execute the creativity thinking work and perform the conceptual design. Fourthly, we introduce the questionnaire survey to the obtained prototype and calculate its CSI value. Then, we modify the prototype to obtain a new model of product which may catch current customers' overall satisfaction.

3. Results and Discussion

Here we choose the digital camera as the experimental target, but the proposed methodologies can be applied to other similar products with various design elements. The experimental study involves 30 subjects. Each has more than 3 years of experience in using digital camera. The following is the manipulation processes of the customer-satisfaction-based KE technique applying to the innovative design of a digital camera.

3.1. Product Information

3.1.1. Sample Collection. To identify the design elements of digital cameras, we first selected 159 digital cameras of various makers and models, which entered the market during 2006–2011. Totally 60 styles of digital cameras, excluding those using for specific purposes or styles with too exaggerated outlook, were chosen to represent the space of product. These

samples were represented in pictures that had been done as similar as possible in contrasts, sizes, and soon to be comparable in the experiment. The pictures were also of good quality and shading to represent the three dimensional shapes of the products. We then asked the subjects to classify these 60 digital camera samples into 2~10 groups based on their similarity degree, using Kawakida Jirou method. This method was introduced by Kawakida Jirou in 1953 [18] for classifying ideas, concepts, or objects into several groups by their similarity degree. All participants were skilled in visualization and capable of considering three-dimensional shapes from pictures. Then, we built a similarity matrix from the previously obtained separation result. The similarity matrix was transformed into a dissimilarity matrix and analyzed by the multidimensional scaling (MDS) scheme. To determine the most appropriate dimensionality for the data, we examined 9 different dimensional spaces (ranging from 2 to 10 dimensions). A result of 6-dimensions with stress of 0.04912 was suggested here, since a commonly used measure of fit in MDS is "stress", which is the square root of a normalized residual sum of squares. A smaller stress value indicates a better fit (an empirical suggested stress value is 0.05 [17]). Thus, the 6 dimensional spaces were appropriate. Finally, the hierarchical cluster analysis (HCA) was performed based on the MDS result.

Furthermore, the representative of each group was obtained via the K-means clustering scheme. This scheme calculates the distance of individual sample to its group center of gravity and eventually the sample which has the smallest distance can be visualized as the group representative. For instance, the samples and their representative of group 2, including the calculated distances to their group center of gravity, are obtained and shown in Table 1.

3.1.2. Product Feature. Distinguished from the usual way that only considered the form style as the design parameter, this study, more meaningfully, extends the design elements to include three design categories: hardware appearance design, form style, and color type. Regarding this, a detailed design analysis, including the morphological analysis, is performed to extract the design features from the 6 representatives and their group samples. The result is listed in Table 2 which shows the obtained 3 categories of design features and 11 associated design elements (denoted as X1~X11). Each design element has its own different variation, numbering from 1 to 4.

3.2. Product Image. This study uses the Kansei words (image words) to describe the consumer's psychological feeling and perception about the image of a product. The following is the details to extract the representatives of image words.

3.2.1. Image Collection. A total of 60 Kansei adjective words describing the integral feeling of collected digital cameras were chosen from magazines, literature, manuals, experts, experienced users and product catalogs. And after deleting those too exaggerated, similar, or overlapping words, eventually a total of 24 low-level Kansei words was built up.

TABLE 1: The sample classification results: samples of Group 2 and their representative.

Sample no.	Group	Distance
p.28	2	0.787
p.52	2	0.719
p.95	2	0.887
p.108	2	0.922
p.109	2	0.825
p.112	2	0.737
p.128	2	1.001
p.146	2	0.745
p.150 (representative)	2	0.710
p.153	2	0.782



p.: product.

Bold font means the data of representative of Group 2.

3.2.2. High-Level Kansei Words. To extract the representative image words for describing the consumers' perception about the collected digital cameras, a designed questionnaire interview was done to the subjects. A result of three final high-voted high-level Kansei words of product images was obtained as follows: usability (Y_1), aesthetics (Y_2), and innovation (Y_3).

3.3. Quality Sufficiency of Image. Based on the proposed modified Kano model, (1) the vertical axis is set as the overall customer satisfaction about a product and denoted as CSI and (2) the horizontal axis is set as the quality-sufficiency high-level Kansei words, denoted as $Y_1 \sim Y_3$, which represent the proper feelings (preferences) of consumers about the selected products. To determine the contribution extent as well as classification of each quality-sufficiency Kansei word to the overall customer satisfaction, a questionnaire survey was done to 30 subjects. The major question is how much influence will happen (range: $-5 \sim 5$) if the extent of Kansei word is increased by one unit. The obtained mean influence weighting of Y_1 , Y_2 , and Y_3 on customer satisfaction is $W_1 = 1.3$, $W_2 = 0.47$, and $W_3 = 1.16$ and it can be classified as attractive, one-dimensional, and one-dimensional quality, respectively (shown in Table 3).

3.4. Mathematic Mapping Model

3.4.1. Sample Evaluation. The Kansei evaluation questionnaire is done to 30 subjects for evaluating their preference

TABLE 2: Design feature decomposition.

Design attribute	Design element	Type I	Type II	Type III	Type IV
Hardware design	Power (X1) key	Pushing-on type (X11)	Turning-on type (X12)	Sliding-on type (X13)	
	Picturing switch button (X2)	Wheel (X21) 	Touch screen (X22) 	Combined with the function key (X23) 	
	Function Key type (X3)				
	Screen size (X4)	3.5" (X41) X51	3" (X42) X52	2.7" (X43)	2.5" (X44)
	Len type (X5)				
Form style	Upper face (X6)	X61 	X62 	X63 	X64 
	Front face (X7)	X71 	X72 	X73 	X74 
	Side face (X8)	X81 	X82 		
	Color type	Front face: brightness (X9) No (X91)	Low (X92)	Medium (X93)	High (X94)
	Front face: hue (X10)	No (X101)	Low (X102)	Medium (X103)	High (X104)
	Rear face: color (X11)	Same with front face (X111)	Black (X112)	Silver (X113)	

TABLE 3: The relationship between customer satisfaction and customer preference.

Quality-sufficiency image	Y_1 (usability)	Y_2 (aesthetics)	Y_3 (innovation)
Influence on CSI (weighting)	$W_1 = 1.3$	$W_2 = 0.47$	$W_3 = 1.16$
Kano category	Attractive quality	One-dimensional quality	One-dimensional quality

about the collected 60 samples using the 7-scale semantic differential scheme. The obtained average score of $Y_1 \sim Y_3$ is listed in Table 4. Further, the CSI value of each sample is calculated from the formula $CSI = \sum_{i=1}^3 W_i Y_i$, and it is found that the N15 sample has the highest rank of customer satisfaction. This sample may be used as the basis of conceptual design so as to further design an innovative product.

3.4.2. *Model Building.* Based on the results of sample feature decomposition, together with the obtained Kansei credits of every sample listed in Table 4, the linear relationship between

design elements and Kansei words can be built via QT1. The obtained results of the partial correlation coefficients (PCCs), which mean the relative importance of every design element on the Kansei image, are listed in Table 5.

(i) For Y_1 (usability).

It is seen that there is no influence on Y_1 for design parameters X12, X23, X31, X42, X51, X62, X71, X93, X104, and X111, since their PCCs are all zero. Further, X32, X33, X34, X81, and X82 have relatively high positive influences on Y_1 (the higher the better), since their coefficients are all greater than 0.3. On the other hand, X13, X21, and X52 have significantly reverse influences on Y_1 (the lower the better), since their coefficients are all smaller than -0.3 .

(ii) For Y_2 (aesthetics).

Design parameters X12, X23, X31, X42, X51, X62, X72, X93, X104, and X111 have no influence (zero PCC) on Y_2 . High positive weighting (greater than 0.3) are found in design parameters: X33, X34, X81, X82, X102, X112, and X113. It is noted that the design parameters X33, X34, X81, and X82 have commonly positive influences on both Y_1 and Y_2 . High reverse weighting (smaller than -0.3) is found in design parameters: X13, X21, X22, X44, X63, and X74.

TABLE 4: The Kansei evaluation result (mean value) of all samples.

Samples	Y_1	Y_2	Y_3	CSI	Rank
N01	4.35	4.17	3.79	12.011	35
N02	4.44	3.52	3.46	12.416	25
N03	3.68	3.52	3.46	10.452	58
N04	5.21	4.81	4.96	14.787	4
N05	4.90	4.31	4.43	13.535	15
N06	4.35	4.68	4.23	12.761	20
N07	4.33	4.55	3.87	12.257	31
N08	4.60	4.35	4.80	13.593	13
N09	4.91	4.34	4.57	13.724	11
N10	4.30	4.42	4.06	12.377	27
N11	3.38	3.34	2.99	9.432	60
N12	3.58	4.15	3.51	10.676	55
N13	5.07	4.50	4.34	13.740	10
N14	4.98	4.68	4.82	14.265	8
N15	4.98	4.94	5.65	15.350	1
N16	3.66	4.19	3.44	10.718	54
N17	4.39	3.58	3.37	11.299	45
N18	3.74	3.80	3.79	11.044	50
N19	5.60	4.94	4.02	14.265	7
N20	3.81	3.89	3.43	10.760	52
N21	4.51	4.44	3.36	11.847	38
N22	5.14	4.83	4.87	14.601	6
N23	5.25	5.35	4.78	14.884	3
N24	3.96	3.69	3.32	10.734	53
N25	5.07	4.33	4.27	13.579	14
N26	3.75	4.11	3.90	11.331	43
N27	3.94	4.15	3.62	11.272	46
N28	4.41	4.46	4.11	12.597	22
N29	4.20	3.46	2.92	10.473	57
N30	4.32	3.79	3.46	11.411	42
N31	4.91	3.89	3.44	12.202	33
N32	4.22	3.53	2.93	10.544	56
N33	4.67	4.04	3.78	12.355	29
N34	5.63	4.74	4.38	14.628	5
N35	4.63	3.88	3.78	12.227	32
N36	4.43	4.73	4.75	13.492	16
N37	4.43	3.70	3.39	11.430	41
N38	3.61	4.23	4.00	11.321	44
N39	3.57	4.11	4.05	11.271	47
N40	3.59	4.28	4.41	11.794	40
N41	3.81	3.27	3.26	10.272	59
N42	4.46	4.43	4.43	13.019	18
N43	4.19	4.34	4.95	13.229	17
N44	4.35	4.68	4.23	12.761	21
N45	4.45	4.66	3.85	12.441	24
N46	4.44	4.52	4.41	13.021	19
N47	3.99	4.34	4.46	12.400	26
N48	4.31	4.24	4.02	12.259	30
N49	4.39	4.11	3.61	11.826	39
N50	5.07	4.54	4.22	13.620	12
N51	3.74	4.21	3.75	11.191	48

TABLE 4: Continued.

Samples	Y_1	Y_2	Y_3	CSI	Rank
N52	5.13	4.70	4.25	13.808	9
N53	3.89	4.01	3.64	11.164	49
N54	5.29	4.15	5.23	14.894	2
N55	4.33	4.35	3.66	11.919	36
N56	4.55	4.12	3.98	12.468	23
N57	3.63	4.24	3.61	10.899	51
N58	4.17	4.17	3.88	11.882	37
N59	4.55	4.18	3.86	12.357	28
N60	4.28	3.91	4.02	12.065	34

(iii) For Y_3 (innovation).

Design parameters X12, X23, X31, X42, X51, X62, X71, X93, X104, and X111 have no influence (zero PCC) on Y_3 . High positive weighting (greater than 0.3) is found in design parameters X11, X13, X32, X33, X34, X102, and X112. It is noted that the design parameters X33 and X34 have commonly and significantly positive influences on all three Kansei words. High reverse weighting (smaller than -0.3) is found in design parameters X21, X22, X61, X63, X73, X74, X81, and X82. It is noted that the design parameters X21, X22, X63, and X74 have commonly and significantly reverse influences on both Y_2 and Y_3 .

3.4.3. Verification. To identify the modeling accuracy, other four samples (different from the 60 training samples), numbering T01, T02, T03, and T04, are randomly chosen from the sample population. These samples are decomposed first, and through questionnaire survey, the Kansei credits are obtained. Then the CSI value of each sample is calculated using the previously obtained Kano weighting for each quality-sufficiency Kansei word. The results including the final customer satisfaction ranking are listed in Table 6. It is found that although the predicted and experimental sample CSI values are slightly different, the ranking orders are the same. This result is obviously satisfying.

3.5. New Product Creation. Basically, the Kansei engineering is used to deal with customers' preference about products in the past. Also, the obtained design features of the target product are past events. Certainly, the current or future design of a product should be different from the past one. However, the KE modeling results do provide valuable design trace and may give us a guide for designing a future product. The following is the manipulation of the proposed BDCA design process to design an innovative future product based on the past-obtained KE results.

3.5.1. The BDCA Procedure

Step 1 (B—base information providing). Examining the PCCs of all design elements to three quality-sufficiency Kansei words, it is found that the most influential design factors for each design category are (1) X11 for category X1,

TABLE 5: The QTI mapping result: relationship between Kansei words and design elements.

Design elements	Y_1	Y_2	Y_3
X1			
X11	-0.140	0.166	0.471
X12	0.000	0.000	0.000
X13	-0.318	-0.498	0.767
X2			
X21	-0.710	-0.417	-0.395
X22	0.244	-0.897	-0.395
X23	0.000	0.000	0.000
X3			
X31	0.000	0.000	0.000
X32	0.346	0.249	0.323
X33	1.092	1.235	0.940
X34	1.071	1.622	0.380
X4			
X41	-0.028	-0.215	-0.041
X42	0.000	0.000	0.000
X43	0.144	-0.198	-0.112
X44	-0.027	-0.565	-0.137
X5			
X51	0.000	0.000	0.000
X52	-0.353	-0.130	0.158
X6			
X61	0.020	-0.096	-0.325
X62	0.000	0.000	0.000
X63	0.004	-0.886	-0.927
X64	-0.223	-0.281	0.213
X7			
X71	0.000	0.000	0.000
X72	0.109	-0.145	0.061
X73	-0.011	0.050	-0.552
X74	-0.147	-0.554	-0.345
X8			
X81	0.620	0.342	-0.302
X82	0.580	0.483	-0.582
X9			
X91	0.262	0.115	0.286
X92	-0.049	-0.254	-0.174
X93	0.000	0.000	0.000
X94	-0.087	-0.009	-0.231
X10			
X101	-0.030	-0.288	-0.118
X102	0.138	0.331	0.332
X103	-0.024	0.269	0.084
X104	0.000	0.000	0.000

(2) X22 for category X2, (3) X33 and X34 for category X3, (4) X44 for category X4, (5) X52 for category X5, (6) X63

TABLE 5: Continued.

Design elements	Y_1	Y_2	Y_3
X11			
X111	0.000	0.000	0.000
X112	-0.084	0.308	0.445
X113	-0.295	0.490	0.299
C (constant)	3.814	3.884	3.972
R^2	0.889	0.592	0.688

TABLE 6: The CSI value and ranking of products from prediction and experiment.

	Sample T01	Sample T02	Sample T03	Sample T04
Prediction				
CSI	12.259	13.558	13.450	10.812
Ranking	3	1	2	4
Experiment				
CSI	11.977	13.628	13.186	11.023
Ranking	3	1	2	4

for category X6, (7) X73 for category X7, (8) X82 for category X8, (9) X91 for category X9, (10) X101 for category X10, and (11) X112 for category X11. These important design parameters give us a guide to design a good product satisfying customer needs. The enhancement of these design parameters may lead to an increase of CSI.

Further, it is crucial to offer an useful design reference in order to construct a new product prototype. Regarding this, this study proposes that the product having the highest CSI credit may be selected as a design reference, for example, the sample N15 (shown in Table 7). So far the preparation work before designing a prototype has been completed. The next step is to properly select design elements and creatively alter them.

Step 2 (D—critical design element selecting and developing). Based on the chosen high-score sample N15, we now change the type of design elements with zero or negative PCC and keep the other unchanged. It is noting that design elements with zero or negative PCC mean they have no or reverse influence on customer’s preference. Therefore, they should be considered as the key design parameters to be changed first in order to create a new product style that can rapidly promote customers’ preferences. Creative thinking can be actuated now from these key elements.

Step 3 (C—creativity thinking and conceptual design). After mature consideration, the creative alteration is done to the previously suggested key design elements. With the help of software SolidWorks, a conceptual design of new prototype is performed. The three-dimensional sketch of the new conceptually digital camera is shown in Figure 4.

Step 4 (A—CSI evaluation and modification, product Assurance). After several times of modification based on the aesthetics consideration and human usage of hereafter possible

TABLE 7: The design reference: the sample with high CSI score.



Sample N15		Weightings		
Design category	Design elements	PCC (Y_1)	PCC (Y_2)	PCC (Y_3)
X1	X11	-0.140	0.166	0.471
X2	X23	0.000	0.000	0.000
X3	X33	1.092	1.235	0.940
X4	X42	0.000	0.000	0.000
X5	X51	0.000	0.000	0.000
X6	X62	0.000	0.000	0.000
X7	X72	0.109	-0.145	0.061
X8	X81	0.620	0.342	-0.302
X9	X91	0.262	0.115	0.286
X10	X102	0.138	0.331	0.332
X11	X112	-0.084	0.308	0.445
Kansei word credits (Y_1, Y_2, Y_3)		$Y_1 = 4.98$	$Y_2 = 4.94$	$Y_3 = 5.65$
CSI			15.350	

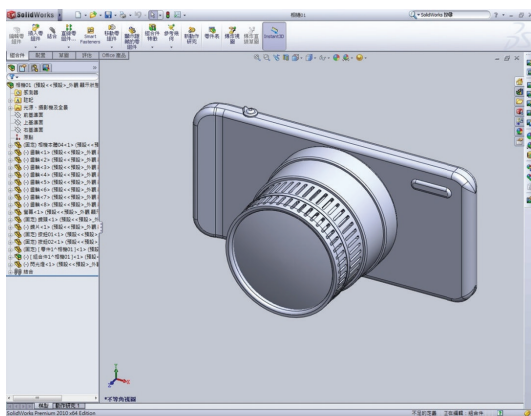


FIGURE 4: The prototype of a new design camera.

TABLE 8: Verification of the new designed camera.

Product	Y_1	Y_2	Y_3	CSI
Design reference (N15)	$Y_1 = 4.98$	$Y_2 = 4.9442$	$Y_3 = 5.6548$	15.350
New design (KKBDC A)	$Y_1 = 6.222$	$Y_2 = 5.511$	$Y_3 = 5.756$	17.356
Enhancement	24.94%	11.46%	1.79%	13.01%

3.5.2. *Verification.* To evaluate the design results through the operation of the proposed KKBDC A design scheme, an investigation is done to 30 subjects to evaluate the quality-sufficiency customers' preferences. The obtained results are shown in Table 8. Comparing the CSI value of new designed camera with the original sample (No. p15), it is found that a 13% increase in CSI is obtained. This reveals that a satisfying result is attended while using the proposed innovative KKBDC A product design procedure.

manufacturing process, the final model of a new digital camera is obtained, as shown in Figure 5.



FIGURE 5: The final new designed product based on KKBDCA process.

4. Conclusion

This study aims to provide a design methodology to approach customer satisfaction more closely so as to rise up the possibility of customer's decision for buying the designed merchant. The proposed methodology, called KKBDCA, includes the modified Kano model, the Kansei engineering, the Quantum Theory I, and an innovative design procedure BDCA. A major conclusion is drawn as follows.

- (1) Firstly, in the Kano model, the horizontal coordinate variables, that is, the quality factors, were modified as customer preferences (i.e., Kansei words). These influential quality factors were found as usability, aesthetics, and innovation. Then their weighting on customer satisfaction and Kano's classification were determined according to the questionnaire survey results.
- (2) In Kansei manipulation, the target products, digital cameras, were collected and classified. Totally 60 effective samples were obtained and divided into 6 categories. Eleven design features of cameras were drawn from these sample representatives. According to the Kansei evaluation results of product design features with respect to each Kansei word for the 60 samples, the QTI mapping model was built. Then a verification test was performed, and a good prediction result was obtained.
- (3) In the last stage, an innovative product design procedure was proposed. Based on the viewpoints of low-weighting (including zero and negative weighting), design elements should be highly modified so as to more effectively and rapidly enhance customer satisfaction, and a brand new camera was thus designed. Meanwhile, to identify our proposed design procedure, a verification test for the overall customer satisfaction was done and a satisfying result was obtained.

The proposed integrated procedure not only extends the past Kansei evaluation results to really designing a new product but also provides a more effective approach to meet the customer satisfaction.

References

- [1] M. Nagamachi, "Kansei engineering: a new ergonomic consumer-oriented technology for product development," *International Journal of Industrial Ergonomics*, vol. 15, no. 1, pp. 3–11, 1995.
- [2] M. Nagamachi, *Introduction of Kansei Engineering*, Japan Standard Association, Tokyo, Japan, 1996.
- [3] S. Ishihara, K. Ishihara, M. Nagamachi, and Y. Matsubara, "An automatic builder for a Kansei Engineering expert system using self-organizing neural networks," *International Journal of Industrial Ergonomics*, vol. 15, no. 1, pp. 13–24, 1995.
- [4] S. S. Guan and Y. C. Lin, "A study on the color and style collocation of mobile phones using neural network method," *Journal of Chinese Institute of Industrial Engineers*, vol. 18, no. 6, pp. 84–94, 2001.
- [5] B. B. Nadia, "Kansei mining: identifying visual impressions as patterns in images," in *Proceedings of the International Conference IFSA/NAFIPS*, Vancouver, Canada, 2001.
- [6] K. C. Wang, "User-oriented product form design evaluation using integrated Kansei engineering scheme," *Journal of Convergence Information Technology*, vol. 6, no. 6, pp. 420–438, 2011.
- [7] M. G. Helander and M. P. Tham, "Hedonomics—affective human factors design," *Ergonomics*, vol. 46, no. 13-14, pp. 1269–1272, 2003.
- [8] S. Baek, M. Hwang, H. Chung, and P. Kim, "Kansei factor space classified by information for Kansei image modeling," *Applied Mathematics and Computation*, vol. 205, no. 2, pp. 874–882, 2008.
- [9] H.-Y. Chen and Y.-M. Chang, "Extraction of product form features critical to determining consumers' perceptions of product image using a numerical definition-based systematic approach," *International Journal of Industrial Ergonomics*, vol. 39, no. 1, pp. 133–145, 2009.
- [10] D. Clausing, *Total Quality Development: A Step-by-Step Guide to World-Class Concurrent Engineering*, ASME Press, New York, NY, USA, 1994.
- [11] R. T. K. Fung and Popplewell, "The analysis of customer requirements for effective rationalization of product attributes in manufacturing," in *Proceedings of the 3rd International Conference on Manufacturing Technology*, pp. 287–296, Hong Kong, 1995.
- [12] X. Chen, C. J. Barnes, T. H. C. Childs, B. Henson, and F. Shao, "Materials' tactile testing and characterisation for consumer products' affective packaging design," *Materials and Design*, vol. 30, no. 10, pp. 4299–4310, 2009.
- [13] C.-C. Yang, "Constructing a hybrid Kansei engineering system based on multiple affective responses: application to product form design," *Computers and Industrial Engineering*, vol. 60, no. 4, pp. 760–768, 2011.
- [14] M.-S. Huang, H.-C. Tsai, and T.-H. Huang, "Applying Kansei engineering to industrial machinery trade show booth design," *International Journal of Industrial Ergonomics*, vol. 41, no. 1, pp. 72–78, 2011.
- [15] C.-C. Chen and M.-C. Chuang, "Integrating the Kano model into a robust design approach to enhance customer satisfaction

with product design,” *International Journal of Production Economics*, vol. 114, no. 2, pp. 667–681, 2008.

- [16] C. E. Osgood, P. H. Tannenbaum, and G. J. Suci, *The Measurement of Meaning*, University of Illinois Press, Urbana, Ill, USA, 1957.
- [17] J. B. Kruskal, “Multidimensional scaling by optimizing goodness of fit to a nonmetric hypothesis,” *Psychometrika*, vol. 29, no. 1, pp. 1–27, 1964.
- [18] N. Cross, *Engineering Design Methods: Strategies for Product Design*, John Wiley & Sons, Chichester, UK, 2000.

Research Article

An Objective Approach to Identify Spectral Distinctiveness for Hearing Impairment

Yeou-Jiunn Chen¹ and Jiunn-Liang Wu²

¹ Department of Electrical Engineering, Southern Taiwan University of Science and Technology, Tainan 710, Taiwan

² Department of Otolaryngology, College of Medicine, National Cheng Kung University, Tainan 701, Taiwan

Correspondence should be addressed to Yeou-Jiunn Chen; chenyj@mail.stust.edu.tw

Received 14 September 2013; Accepted 10 October 2013

Academic Editor: Teen-Hang Meen

Copyright © 2013 Y.-J. Chen and J.-L. Wu. This is an open access article distributed under the Creative Commons Attribution License, which permits unrestricted use, distribution, and reproduction in any medium, provided the original work is properly cited.

To facilitate the process of developing speech perception, speech-language pathologists have to teach a subject with hearing loss the differences between two syllables by manually enhancing acoustic cues of speech. However, this process is time consuming and difficult. Thus, this study proposes an objective approach to automatically identify the regions of spectral distinctiveness between two syllables, which is used for speech-perception training. To accurately represent the characteristics of speech, mel-frequency cepstrum coefficients are selected as analytical parameters. The mismatch between two syllables in time domain is handled by dynamic time warping. Further, a filter bank is adopted to estimate the components in different frequency bands, which are also represented as mel-frequency cepstrum coefficients. The spectral distinctiveness in different frequency bands is then easily estimated by using Euclidean metrics. Finally, a morphological gradient operator is applied to automatically identify the regions of spectral distinctiveness. To evaluate the proposed approach, the identified regions are manipulated and then the manipulated syllables are measured by a close-set based speech-perception test. The experimental results demonstrated that the identified regions of spectral distinctiveness are very useful in speech perception, which indeed can help speech-language pathologists in speech-perception training.

1. Introduction

Hearing loss would seriously degrade a subject's speech perception, thereby affecting the development of articulation ability. It then reduces speech intelligibility and affects speech and language development, learning, and communication. Recently, assistive listening devices such as hearing aids or cochlear implants could help subjects with hearing loss utilize their residual hearing and develop their speech perception [1–7]. To facilitate this process, speech-language pathologists (SLPs) have to provide speech-perception training that could increase subject's ability to distinguish one syllable from another. In clinical practice, SLPs manually enhance the distinguishable acoustic cues and extensively use them in speech-perception training. However, it is a time-consuming and expensive process. Thus, it is beneficial for SLPs in speech-perception training if the regions of spectral distinctiveness between two syllables can be identified automatically.

When a speech wave propagates on the basilar membrane, it is characterized as time-spectral patterns. Then, unique perceptual cues, which are the basic units for speech perception, can be identified. Therefore, the relation between the acoustic cues and perceptual units is a key problem for speech perception [8–10]. In the last decade, the relation had been examined [11–18] and the results show that the main factors of acoustic cues are duration, stress, and spectral distinctiveness.

SLPs generally increase the duration and stress of a syllable to teach a subject how to distinguish one syllable from another. Duration and stress can be simply manipulated by speech techniques [19]. However, the spectral distinctiveness between two syllables is very difficult to be identified. In clinical practice, SLPs have to repeatedly pronounce a syllable by enhancing the volume of part segment of a syllable. However, it is a complicated task for SLPs to manually enhance spectral distinctiveness of a syllable. In order to

identify the regions of spectral distinctiveness, Li et al. proposed a psychoacoustic method in three dimensions: time, frequency, and intensity [20]; still it is a time-consuming process. Moreover, it is difficult to apply to other languages. Hence, to automatically identify the regions of spectral distinctiveness is very important for hearing impairment in speech-perception training.

In this study, an objective approach to identify the regions of spectral distinctiveness is proposed. The mel-frequency cepstrum coefficients (MFCCs) are selected as analytical parameters and used to represent the characteristics of acoustic signal. The mismatch between two syllables in time domain is handled by dynamic time warping; thereby, an optimal matching condition could be obtained. To accurately estimate the spectral similarity, filter bank is applied to find the spectral components of different frequency bands. For the speech signal in each frequency band, the MFCCs are also extracted to represent the acoustical characteristics. According to the optimal matching condition, the spectral distinctiveness of each frequency band between two syllables can be estimated easily by using Euclidean metrics. Finally, the morphological gradient operator is developed to automatically identify the regions of spectral distinctiveness. Moreover, in order to evaluate the accuracy of identified regions of spectral distinctiveness, an acoustic cue manipulation is proposed in this study.

The rest of this paper is organized as follows. Section 2 describes the objective approach to identify spectral distinctiveness including feature extraction, spectral distinctiveness estimation, and spectral distinctiveness identification. Besides, the acoustic cue manipulation is introduced. Section 3 then describes a series of experiments to examine the performance of our approach. Finally, conclusions are drawn in Section 4, along with recommendations for future research.

2. Materials and Methods

In this section, the proposed objective approach to identify the regions of spectral distinctiveness between two syllables (as shown in Figure 1) is introduced. Firstly, the MFCCs are extracted from the input speech signals and the filtered speech signals. Secondly, the distance between the MFCCs of two syllables is computed and used to find the consonant-vowel boundary. This approach also adopts the dynamic time warping to find an optimal matching condition between two input syllables. Thirdly, according to the optimal matching condition, the spectral distinctiveness of each frequency band can be easily estimated by using Euclidean metric. Finally, a morphological gradient operator is applied to automatically identify the regions of spectral distinctiveness. To examine the proposed approach, an acoustic cues manipulation is also proposed to manipulate the regions of spectral distinctiveness. These procedures are illustrated serially in the following subsections.

2.1. Feature Extraction. Analytical parameters which can accurately represent a speech signal play an important

role in objective measurement of spectral distinctiveness. Since, MFCCs had been widely used in speech processing, especially speech recognition [21], they are very suitable for accurately representing not only a speech signal but also speech signals in different frequency bands. The procedure to extract MFCCs from a speech signal is illustrated as follows:

- (1) taking the Fourier transform of frames windowed from input speech signal;
- (2) mapping the powers of the spectrum onto the mel scale which is defined as

$$m = 2595 \log_{10} \left(1 + \frac{h}{700} \right), \quad (1)$$

where h is the frequency (Hz) in linear domain;

- (3) using triangular overlapping windows to get the power spectrum in mel scale;
- (4) taking the logs of the powers at each of the mel frequencies which is denoted as f ;
- (5) taking the discrete cosine transform of the mel log powers which is defined as

$$c(u) = \alpha(u) \sum_{x=0}^{N-1} f(x) \cos \left(\frac{\pi(2x+1)u}{2N} \right), \quad (2)$$

where N is the length of window size and $\alpha(u)$ is defined as

$$\alpha(u) = \begin{cases} \sqrt{\frac{1}{N}}, & \text{for } u = 0; \\ \sqrt{\frac{2}{N}}, & \text{for } u \neq 0; \end{cases} \quad (3)$$

- (6) finally, MFCCs are composed of amplitudes of the resulting spectrum, $c(u)$.

In Mandarin, a syllable can be decomposed into an INITIAL and a FINAL. INITIALs consist of consonants or semivowels, and FINALs consist of vowels or vowels plus one of the two nasal sounds. Thus, two syllables represented as $s_i = c_i v$ and $s_j = c_j v$ are used to estimate the regions of spectral distinctiveness. Let $O_i = o_{i1} o_{i2} o_{i3}, \dots, o_{in_i}$ and $O_j = o_{j1} o_{j2} o_{j3}, \dots, o_{jn_j}$, respectively, represent the MFCCs of s_i and s_j , in this study.

In addition, a filter bank is adopted to separate the input signal into multiple components, which are the acoustical characteristics of frequency bands. For the k th frequency band, the corresponding MFCCs of s_i and s_j are also extracted and denoted as $O_i^k = o_{i1}^k o_{i2}^k o_{i3}^k, \dots, o_{in_i}^k$ and $O_j^k = o_{j1}^k o_{j2}^k o_{j3}^k, \dots, o_{jn_j}^k$, respectively.

2.2. Spectral Distinctiveness Estimation. In order to estimate the spectral distinctiveness between two syllables, the mismatch should be dealt; thereby, the difference in frequency bands can be easily estimated by using Euclidean metric. Therefore, the dynamic time warping algorithm is adopted to

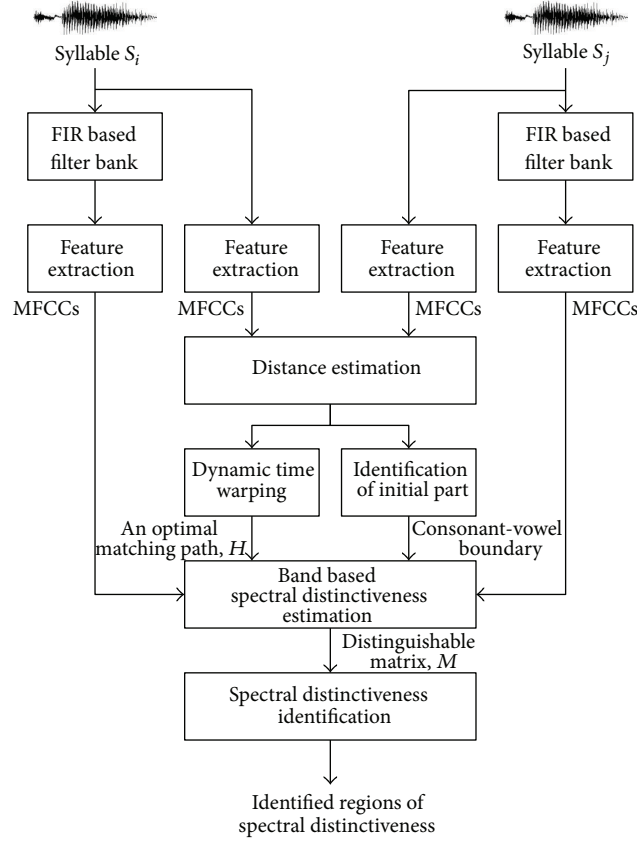


FIGURE 1: The flowchart of the objective approach to identify the regions spectral distinctiveness.

compare two sequences O_i , and O_j ; thereby, a plane spanned by O_i and O_j is considered as a distance matrix D , which is written as

$$D(O_i, O_j) = \begin{bmatrix} d_{11} & \cdots & d_{1n_j} \\ \vdots & \ddots & \vdots \\ d_{n_i1} & \cdots & d_{n_i n_j} \end{bmatrix}, \quad (4)$$

where d_{qr} is the Euclidean distance between o_{iq} and o_{jr} . The matching condition indicating the correspondence between the time axes of O_i and O_j can be represented a sequence of lattice points on the plane D and written as

$$H = \{(h_1^i, h_1^j), (h_2^i, h_2^j), (h_3^i, h_3^j), \dots, (h_n^i, h_n^j)\}, \quad (5)$$

where h_r^q is the r th matching pair in s_q . The H is the best matching condition and then the dynamic time warping algorithm is described as shown in Algorithm 1.

In the dynamic time warping algorithm, the variable is used to store a path, which reaches at lattice point (a, b) with minimum accumulative distance. The minimum accumulative distance is stored in variable $DTW(a, b)$. Since the durations are quite different for each INITIAL, the boundary condition should be ignored in this study. Hence, the path of the lattice point at first row and column goes through its previous lattice point at the step 1. In order to stop

the backtrack for finding the optimal path, $\text{path}(1, 1)$ is set to be $(0, 0)$. In addition, monotony and continuity condition is applied to be concerned in the matching condition at step 2. It means that the search space of lattice point (a, b) includes three lattice points: $(a - 1, b)$, $(a - 1, b - 1)$ and $(a, b - 1)$. At step 3, a simple method is implemented to find an optimal matching condition H by backtracking from lattice point (n_i, n_j) .

According to the optimal matching condition H and a distinguishable matrix for syllable s_i , $M(s_i)$, can be estimated as

$$M(s_i) = \begin{bmatrix} m_1^F & m_2^F & \cdots & m_{n_i-1}^F & m_{n_i}^F \\ m_1^{F-1} & m_2^{F-1} & \cdots & m_{n_i-1}^{F-1} & m_{n_i}^{F-1} \\ \vdots & \vdots & \ddots & \vdots & \vdots \\ m_1^2 & m_2^2 & \cdots & m_{n_i-1}^2 & m_{n_i}^2 \\ m_1^1 & m_2^1 & \cdots & m_{n_i-1}^1 & m_{n_i}^1 \end{bmatrix}, \quad (6)$$

where F is the number of filter bands and m_t^f is the distance for frame t at f th frequency band. m_t^f can be defined as

$$m_t^f = \frac{1}{\#c} \sum_{c \ni (t,c) \in H} \text{Dist}(o_{it}^f, o_{jc}^f), \quad (7)$$

where $\#c$ is the number of frames in O_j which is matched with frame t in O_i .

```

Step 1. Initialization
  DTW(1, 1) =  $d_{11}$ 
  Path(1, 1) = (0, 0)
  For  $a = 2$  to  $n_i$ 
    DTW( $a$ , 1) =  $d_{a1} + \text{DTW}(a - 1, 1)$ 
    Path( $a$ , 1) = ( $a - 1$ , 1)
  End For
  For  $b = 2$  to  $n_j$ 
    DTW(1,  $b$ ) =  $d_{1b} + \text{DTW}(1, b - 1)$ 
    Path(1,  $b$ ) = (1,  $b - 1$ )
  End For
Step 2. Iteration
  For  $a = 2$  to  $n_i$ 
    For  $b = 2$  to  $n_j$ 
      DTW( $a$ ,  $b$ ) =  $d_{ab} + \min_{v \in \{(a-1), b), (a, (b-1)), ((a-1), (b-1))\}} \{d_v\}$ 
      Path( $a$ ,  $b$ ) =  $\arg \min_{v \in \{(a-1), b), (a, (b-1)), ((a-1), (b-1))\}} \{d_v\}$ 
    End For
  End For
Step 3. Backtracking and Termination
  The optimal (minimum) distance is  $\text{DTW}(n_i, n_j)$ .
  The optimal matching path  $H$  is found by simple backtracking from  $\text{Path}(n_i, n_j)$ .
   $H = \emptyset$ 
   $lp = (n_i, n_j)$ 
  While  $lp \neq (0, 0)$  Do
     $H = H \cup lp$ 
     $lp = \text{Path}(lp)$ 
  End While

```

ALGORITHM 1: The dynamic time warping algorithm.

2.3. *Spectral Distinctiveness Identification.* The spectral distinctiveness between two syllables is estimated; thereby, the regions of spectral distinctiveness should be identified from the distinguishable matrix M . Recently, the grayscale morphological gradient operator is a powerful and fast technique for both contour detection and region based segmentation [22]. Thus, it can be successfully used to detect the regions of spectral distinctiveness. To obtain the regions of spectral distinctiveness from M , the morphological gradient operator is used and defined as

$$MG(f) = \frac{1}{n} \sum_{i=1}^n (((f \oplus b_i) - (f \ominus b_i)) \oplus b_{i-1}), \quad (8)$$

where n is the scale of morphological gradient operator and b_i denotes the group of square structuring elements.

In (8), the symbols \oplus and \ominus are the grayscale dilation and grayscale erosion, which are defined as follows:

$$(M \oplus b)(s, t) = \max \left(M(s - x, t - y) - \frac{b(x, y)}{(s - x)} \mid (t - y) \in D_f, (s, y) \in D_b \right),$$

$$(M \ominus b)(s, t) = \max \left(M(s - x, t + y) - \frac{b(x, y)}{(s + x)} \mid (t + y) \in D_f, (s, y) \in D_b \right), \quad (9)$$

where b is a flat structuring element. D_f and D_b are the domains of M and b , respectively. According to (9), the grayscale opening and closing then can be derived as

$$\begin{aligned} f \circ b &= (f \ominus b) \oplus b, \\ f \bullet b &= (f \oplus b) \ominus b. \end{aligned} \quad (10)$$

2.4. *Acoustic Cues Manipulation.* The accuracy of identify regions of spectral distinctiveness was examined in this subsection. Therefore, the power of the spectrogram of these regions should be manipulated to examine that a syllable is converted to another. Thus, a speech modification procedure based on short-time Fourier transform (STFT) is proposed to analyze a speech sound and then synthesize an enhanced speech sound [23].

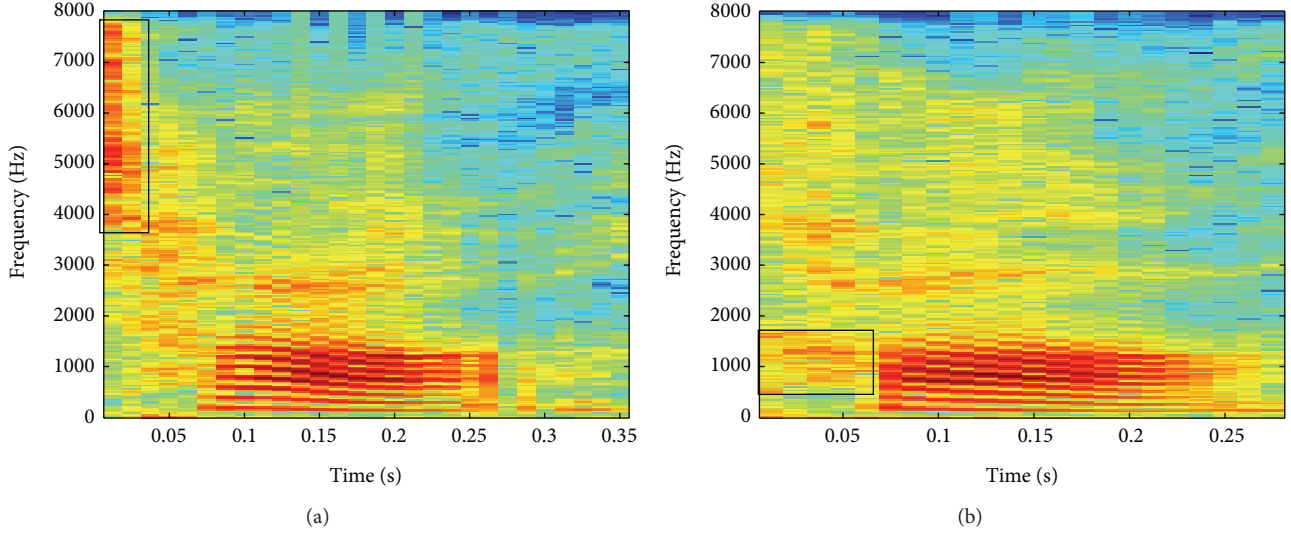


FIGURE 2: The spectrograms of (a) /ta/ and (b) /ka/.

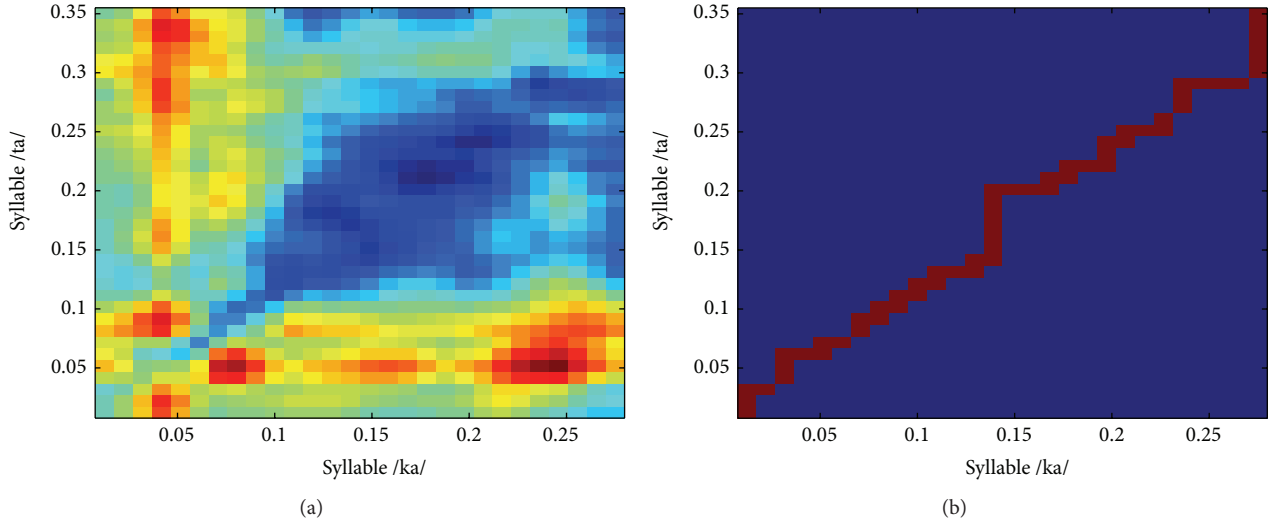


FIGURE 3: The results of (a) distance matrix and (b) optimal matching condition.

Let $x[n]$ denote the speech signal at sample times n . A Hamming window $w[n]$ is used to divide $x[n]$ into N point overlapping frames, which can be written as

$$x[m, n] \equiv w[n] x[mR - n], \quad (11)$$

where R is the step size and is defined as $N/4$. Therefore, the resulting STFT coefficients $X[m, k]$ can be derived as

$$X[m, k] = \sum_{n=0}^{N-1} x[m, n] e^{-j2\pi kn/N}. \quad (12)$$

To improve the accuracy of modification, the windowed speech is zero-padded before performing the Fourier transform.

The region of spectral distinctiveness is then modified by multiplying a specific gain $M[m, k]$. Specifically, $M[m, k] = 0$

indicates feature removal, $0 < M[m, k] < 1$ corresponds to feature attenuation, and $M[m, k] > 1$ represents feature enhancement. Thus, the modified speech spectrum can be written as

$$\tilde{X}[m, k] = X[m, k] \cdot M[m, k]. \quad (13)$$

Generally, the gain is expressed in dB as

$$G = 20 \log_{10}(M[m, k]). \quad (14)$$

According to $\tilde{X}[m, k]$, the single frame signal is recovered by applying an inverse Fourier transform, which is defined as follow:

$$\tilde{x}[m, n] = \frac{1}{N} \sum_{k=0}^{N-1} \tilde{X}[m, k] e^{j2\pi kn/N}. \quad (15)$$

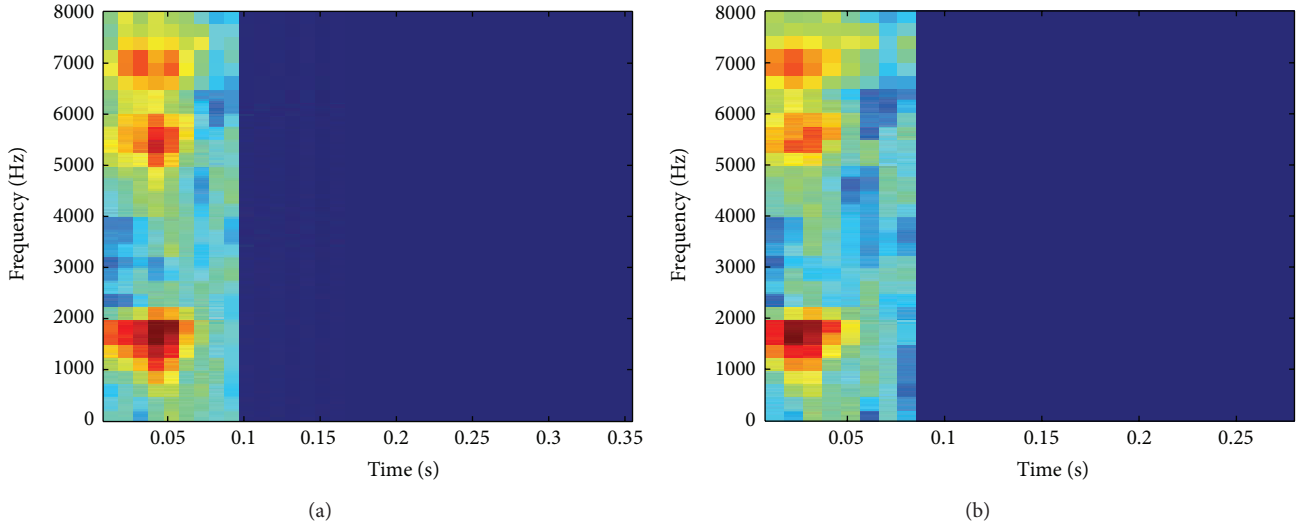


FIGURE 4: The results of distinguishable matrix for (a) /ta/ and (b) /ka/.

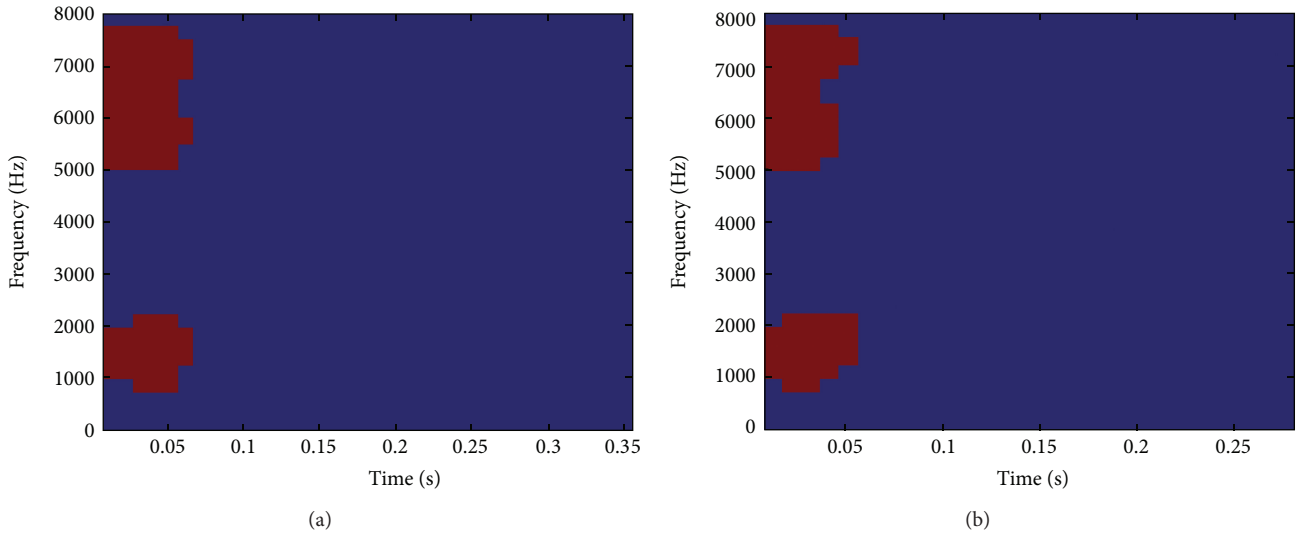


FIGURE 5: The identified regions of spectral distinctiveness for (a) /ta/ and (b) /ka/.

Finally, an overlap-add synthesis is used to generate the modified speech $\tilde{X}[n]$ in time domain, which can be written as

$$\tilde{X}[n] = \sum_{m=-M_0}^0 \tilde{X}[mR, n]. \quad (16)$$

3. Results and Discussions

To evaluate the proposed approach, a close-set based speech-perception test on stop consonants was performed in this study. The speech stimuli, including the syllables /da, ga, ka, ba, pa, ta/, were chosen from the University of Pennsylvania's Linguistic Data Consortium (LDC) LDC2005S22. The detailed experimental results are shown as follows.

3.1. Results of Manipulating /ta/ and /ka/. In this subsection, the syllables /ta/ and /ka/ were used to illustrate the results of the proposed approach. First, the regions of spectral distinctiveness were manually identified to check the results of our approach. The spectrograms of /ta/ and /ka/ were shown in Figure 2. It is obvious that /ta/ has high-frequency burst above 4 k Hz (marked as black rectangle) and /ka/ has a low-frequency burst about 1 k Hz (marked as black rectangle). These two regions should be very important to distinguish /ta/ from /ka/.

Second, the results of distance matrix and dynamic time warping algorithm are examined here. The distance matrix D estimated from /ta/ and /ka/ is shown in Figure 3(a). In this figure, the FINALS of /ta/ and /ka/ are the same; then the distances between the speech segments of FINALS are very small. The distances between the speech segments of FINALS

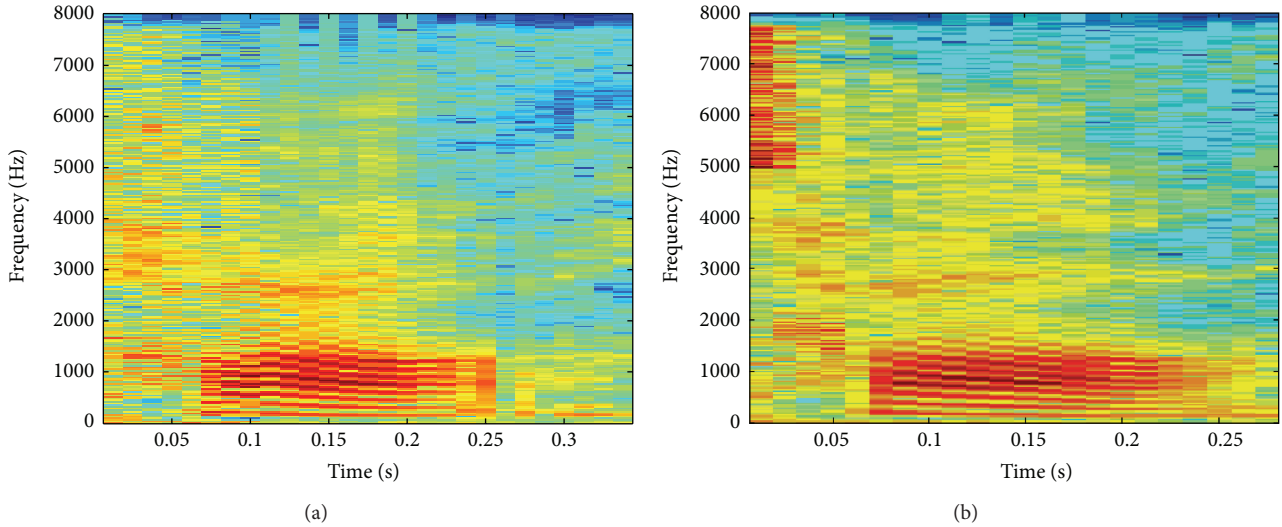


FIGURE 6: The spectrograms of manipulated syllables (a) /ta → ka/ and (b) /ka → ta/.

and those of INITIALs are much large. Further, the speech segments of INITIALs for /ta/ and /ka/ are also quite different. Obviously, there exists an optimal path in 45-degree. In Figure 3(b), the optimal matching path can be successfully detected by dynamic time warping algorithm. It demonstrates that the mismatch between two syllables in time domain can be handled in our approach. Besides, the first frame and the third frame of /ka/ match with three frames of /ta/; thus, the first frame and the third frame of /ka/ should be duplicated three times when /ka/ is manipulated as /ta/. It also shows that our approach can be applied to correctly increase the duration of a syllable.

Third, the spectral distinctiveness between /ta/ and /ka/ measured by our approach is validated with manually identified results. Therefore, with the optimal matching path (shown in Figure 3(b)), the MFCCs of /ta/ and /ka/ in different frequency bands were adopted to estimate the spectral distinctiveness. The results were normalized in time domain and shown in Figure 4. Comparing Figures 4 and 2, it is obvious that the differences in spectrogram are precisely estimated. By selecting a suitable threshold in morphological gradient operator, the regions of spectral distinctiveness for /ta/ and /ka/ can be identified (shown in Figure 5), which are very similar to the expected regions (shown in Figure 2).

Finally, the regions of spectral distinctiveness should be manipulated to examine the accuracy by a subject. According to the identified regions in Figure 5, the acoustic cues manipulation was applied to modify /ta/ and /ka/. /ta/ and /ka/ were converted to /ka/ (denoted as /ta → ka/) and /ta/ (denoted as /ka → ta/), respectively. Then, the spectrograms of /ta → ka/ and /ka → ta/ were shown in Figure 6. Comparing Figure 6(a) with Figure 2(b), the spectral energy about 1 k Hz had been relatively decreased. Comparing Figure 6(b) with Figure 2(a), the spectral energy above 4 K increases. Therefore, /ta/ and /ka/ are heard as /ka/ and /ta/, respectively. So, the identified regions really play an important role in distinguishing one syllable from another.

3.2. Experimental Results of Subject Evaluation. In this subsection, the results of manipulated syllables are used to examine the identified regions of spectral distinctiveness. Seven males and three females (college students, age about 30 years) were asked to participate in this study. Each token with and without manipulation was randomly presented to each subject 5 times. The speech stimuli were played at the most comfortable level (around 70 dB SPL) for the listeners. The parameters of gain G in (14) were set to be 3 dB, 6 dB, 9 dB, and 12 dB. After each presentation, subjects responded to the stimulus by clicking on one of two buttons labeled with syllables. The detailed results in recognition rate (%) are shown in Table 1. The experimental results show that the recognition rate is over 86%. Moreover, the average recognition rates of manipulated syllables are 89.53%, 91.27%, 92.87%, and 92.80% for G which is 3 dB, 6 dB, 9 dB, and 12 dB, respectively. When the gain G is set to be 9 dB, it can achieve the best recognition rate. Then, speech intelligibility is distorted for the larger gain.

To objectively compare these results, the syllables without manipulation were also used and the results are shown in Table 2. The average of recognition rate is 94.93% which is very similar to that of syllables with manipulation ($G = 9$ dB). It means that a syllable can be heard as another syllable by manipulating these regions of spectral distinctiveness. Hence, the identified regions of spectral distinctiveness really play an important role in speech perception. SLPs then can apply the identified regions of spectral distinctiveness to help a subject with hearing loss increase his/her ability to distinguish one syllable from another; thereby, the process of speech-perception training then can be facilitated.

4. Conclusions

In this study, an objective approach is proposed to identify the regions of spectral distinctiveness between two syllables. The MFCCs are appropriate to represent not only the speech

TABLE 1: The recognition rates (%) of syllables with identified regions enhanced by (a) 3 dB, (b) 6 dB, (c) 9 dB, and (d) 12 dB.

		(a)					
Manipulated syllable	Target syllable						
	da	ga	ka	ba	pa	ta	
da	—	88	90	90	88	90	
ga	92	—	94	84	86	88	
ka	88	86	—	90	92	96	
ba	96	96	90	—	92	92	
pa	84	88	88	86	—	90	
ta	90	90	88	86	88	—	

		(b)					
Manipulated syllable	Target syllable						
	da	ga	ka	ba	pa	ta	
da	—	88	90	90	88	90	
ga	94	—	94	92	96	88	
ka	88	96	—	90	92	96	
ba	96	96	90	—	92	94	
pa	90	88	88	90	—	90	
ta	96	90	88	90	88	—	

		(c)					
Manipulated syllable	Target syllable						
	da	ga	ka	ba	pa	ta	
da	—	90	92	92	90	92	
ga	94	—	94	92	96	92	
ka	94	96	—	90	94	96	
ba	96	96	90	—	94	94	
pa	90	94	92	90	—	92	
ta	96	90	94	90	94	—	

		(d)					
Manipulated syllable	Target syllable						
	da	ga	ka	ba	pa	ta	
da	—	90	92	92	90	92	
ga	94	—	94	92	96	92	
ka	94	96	—	90	92	96	
ba	96	96	92	—	92	94	
pa	90	94	92	90	—	92	
ta	96	90	94	90	94	—	

signal but also the speech components in different frequency bands. In addition, the use of the dynamic time warping overcomes the mismatch between two speech signals in time domain. According to the optimal matching condition, the spectral distinctiveness of each frequency band between two syllables is easily estimated by using Euclidean metrics. The regions of spectral distinctiveness are precisely identified by morphological gradient operator. The experimental results demonstrate that the identify regions play an important role in distinguishing one syllable from another. In the future, the regions of spectral distinctiveness should be automatically

TABLE 2: Recognition rates (%) of syllables without manipulation.

Testing syllable	Competitive syllable					
	da	ga	ka	ba	pa	ta
da	—	94	92	94	92	92
ga	96	—	96	96	94	96
ka	94	96	—	94	96	94
ba	94	94	92	—	98	96
pa	92	96	96	94	—	92
ta	96	94	92	92	94	—

enhanced and extensively used in speech-perception training; then it can efficiently reduce the loading of SLPs and facilitate the process of developing speech perception.

Acknowledgment

The authors would like to thank the National Science Council of the Republic of China, Taiwan, for financially supporting this work under Contract NSC 102-2221-E-218-001.

References

- [1] S. Hintea, P. Faragó, M. N. Roman, G. Oltean, and L. Feștilă, "A programmable gain amplifier for automated gain control in auditory prostheses," *Journal of Medical and Biological Engineering*, vol. 31, no. 3, pp. 185–192, 2011.
- [2] P. M. Bollard, P. M. Chute, A. Popp, and S. C. Parisier, "Specific language growth in young children using the clarion cochlear implant," *The Annals of Otolaryngology, Rhinology and Laryngology*, vol. 177, pp. 119–123, 1999.
- [3] R. T. Vieira, N. Brunet, S. C. Costa, S. Correia, B. G. Aguiar Neto, and J. M. Fechine, "Combining entropy measures and cepstral analysis for pathological voices assessment," *Journal of Medical and Biological Engineering*, vol. 32, no. 6, pp. 429–436, 2012.
- [4] T. A. Meyer, M. A. Svirsky, K. I. Kirk, and R. T. Miyamoto, "Improvements in speech perception by children with profound prelingual hearing loss: effects of device, communication mode, and chronological age," *Journal of Speech, Language, and Hearing Research*, vol. 41, no. 4, pp. 846–858, 1998.
- [5] N. Tye-Murray, L. Spencer, and G. G. Woodworth, "Acquisition of speech by children who have prolonged cochlear implant experience," *Journal of Speech and Hearing Research*, vol. 38, no. 2, pp. 327–337, 1995.
- [6] J. L. Wu and H. M. Yang, "Speech perception of mandarin Chinese speaking young children after cochlear implant use: effect of age at implantation," *International Journal of Pediatric Otorhinolaryngology*, vol. 67, no. 3, pp. 247–253, 2003.
- [7] J. F. Yu, C. K. Chen, S. R. Wang et al., "Activation of the auditory cortex in subjects with unilateral sensorineural hearing impairment in response to hearing their own names," *Journal of Medical and Biological Engineering*, vol. 30, no. 4, pp. 215–219, 2010.
- [8] H. Fletcher and R. Galt, "Perception of speech and its relation to telephony," *Journal of the Acoustical Society of America*, vol. 22, pp. 89–151, 1950.
- [9] J. B. Allen, "Harvey Fletcher's role in the creation of communication acoustics," *Journal of the Acoustical Society of America*, vol. 99, no. 4 I, pp. 1825–1839, 1996.

- [10] J. B. Allen, *Articulation and Intelligibility*, Morgan and Claypool, LaPorte, Colo, USA, 2005.
- [11] A. Cristia, G. L. McGuire, A. Seidl, and A. L. Francis, "Effects of the distribution of acoustic cues on infants' perception of sibilants," *Journal of Phonetics*, vol. 39, no. 3, pp. 388–402, 2011.
- [12] S. Anand, R. Shrivastav, J. M. Wingate, and N. N. Chheda, "An acoustic-perceptual study of vocal tremor," *Journal of Voice*, vol. 26, no. 6, pp. 811.e1–811.e7, 2012.
- [13] J. E. Lupo, K. Koka, J. L. Thornton, and D. J. Tollin, "The effects of experimentally induced conductive hearing loss on spectral and temporal aspects of sound transmission through the ear," *Hearing Research*, vol. 272, no. 1-2, pp. 30–41, 2011.
- [14] S. Bouton, P. Colé, and W. Serniclaes, "The influence of lexical knowledge on phoneme discrimination in deaf children with cochlear implants," *Speech Communication*, vol. 54, no. 2, pp. 189–198, 2012.
- [15] M. Steinschneider and Y. I. Fishman, "Enhanced physiologic discriminability of stop consonants with prolonged formant transitions in awake monkeys based on the tonotopic organization of primary auditory cortex," *Hearing Research*, vol. 271, no. 1-2, pp. 103–114, 2011.
- [16] T. Kendall and V. Fridland, "Variation in perception and production of mid front vowels in the U.S. southern vowel shift," *Journal of Phonetics*, vol. 40, no. 2, pp. 289–306, 2012.
- [17] I. Grichkovtsova, M. Morel, and A. Lacheret, "The role of voice quality and prosodic contour in affective speech perception," *Speech Communication*, vol. 54, no. 3, pp. 414–429, 2012.
- [18] B. E. Lobdell, J. B. Allen, and M. A. Hasegawa-Johnson, "Intelligibility predictors and neural representation of speech," *Speech Communication*, vol. 53, no. 2, pp. 185–194, 2011.
- [19] Y. C. Huang, C. H. Wu, and Y. T. Chao, "Personalized spectral and prosody conversion using frame-based codeword distribution and adaptive CRE," *Proceedings of the IEEE Transactions on Audio, Speech, and Language Processing*, vol. 21, no. 1, pp. 51–61, 2013.
- [20] F. Li, A. Menon, and J. B. Allen, "A psychoacoustic method to find the perceptual cues of stop consonants in natural speech," *Journal of the Acoustical Society of America*, vol. 127, no. 4, pp. 2599–2610, 2010.
- [21] Y. J. Chen, "Identification of articulation error patterns using a novel dependence network," *IEEE Transactions Biomedical Engineering*, vol. 58, no. 11, pp. 3061–3068, 2011.
- [22] K. Parvati, B. S. Prakasa Rao, and M. M. Das, "Image segmentation using gray-scale morphology and marker-controlled watershed transformation," *Discrete Dynamics in Nature and Society*, vol. 2008, Article ID 384346, 8 pages, 2008.
- [23] Y. J. Chen and J. L. Wu, "A novel speech enhancement using forward-backward minima-controlled recursive averaging," *Journal of the Chinese Institute of Engineers*, 2013.

Research Article

Developments of Machine Learning Schemes for Dynamic Time-Wrapping-Based Speech Recognition

Ing-Jr Ding, Chih-Ta Yen, and Yen-Ming Hsu

Department of Electrical Engineering, National Formosa University, No. 64, Wunhua Road, Huwei Township, Yunlin County 632, Taiwan

Correspondence should be addressed to Chih-Ta Yen; chihtayen@gmail.com

Received 13 September 2013; Accepted 22 October 2013

Academic Editor: Teen-Hang Meen

Copyright © 2013 Ing-Jr Ding et al. This is an open access article distributed under the Creative Commons Attribution License, which permits unrestricted use, distribution, and reproduction in any medium, provided the original work is properly cited.

This paper presents a machine learning scheme for dynamic time-wrapping-based (DTW) speech recognition. Two categories of learning strategies, supervised and unsupervised, were developed for DTW. Two supervised learning methods, incremental learning and priority-rejection learning, were proposed in this study. The incremental learning method is conceptually simple but still suffers from a large database of keywords for matching the testing template. The priority-rejection learning method can effectively reduce the matching time with a slight decrease in recognition accuracy. Regarding the unsupervised learning category, an automatic learning approach, called “most-matching learning,” which is based on priority-rejection learning, was developed in this study. Most-matching learning can be used to intelligently choose the appropriate utterances for system learning. The effectiveness and efficiency of all three proposed machine-learning approaches for DTW were demonstrated using keyword speech recognition experiments.

1. Introduction

Vocal and visual information that can be used as communication media to allow machines to interact with people has attracted considerable attention in the development of intelligent human-machine interaction devices [1]. Regarding the vocal aspect, the object of the information process is the voice uttered by speakers. The machines require equipment, such as a microphone (or an array of microphones that are widely used in mobile devices), to capture speech sequences that serve as the audio input from which the configuration of the surroundings, and even the status or situation reflected by the context, must be established such that the machine is claimed to be able to listen. A series of analyses must then be performed on the collected audio streams to enable speech recognition.

Automatic speech recognition (ASR) techniques have been widely used in numerous practical applications in recent years [2]. With the maturity and growth of handheld smartphone device applications, the ASR function is attracting much attention and becoming an essential application program in most mobile equipment. ASR also plays a key role in the field of speech processing. Considering ASR, proper uses

of speech pattern recognition techniques, such as speaker recognition, speaker verification, and audio event detection and classification, are being determined in the industry chain.

ASR techniques are classified into two categories: model-based and feature-based methods. Model-based speech recognition involves using a statistical model for recognizing the input testing utterance produced by a speaker. The hidden Markov model (HMM) [3], artificial neural network (ANN) [4], and support vector machine (SVM) [5] are frequently used computational models for performing speech recognition tasks. By contrast, feature-based speech recognition does not involve adopting a statistical model. Establishing (or training) a classification model in advance is not required for feature-based speech recognition, and therefore, this method is generally considered a conceptually simple and direct recognition technique. Dynamic time-wrapping (DTW), which belongs to the dynamic programming category, is a type of feature-based speech recognition [6]. DTW is essentially a type of optimal algorithm and has been widely used to solve numerous optimal problems, including speech recognition. Although DTW has only recently been used for speech recognition, DTW is still a prevalent and indispensable

technique because of its simplicity and inexpensive computation [7].

DTW is one of the mainstream techniques used in speech recognition, and related studies on improving DTW speech recognition have been conducted in recent years [8–11]. Most of these DTW-related studies have either developed improved template-matching algorithms [8, 9] or provided modified schemes for a DTW operation optimization framework [10, 11] for increasing the robustness of the recognition system. In [8], a partial sequence-matching method that involves using an unbounded DTW algorithm was proposed. In [9], the effectiveness of an improved end-point detection algorithm with reduced start- and end-points was validated using simulations. In the study conducted by [10], a feedback method for establishing a database of matching templates was presented. Chen et al. [11] systematically analyzed an optimal warping window size for DTW. Although several studies on improving the performance of DTW speech recognition have been conducted, developing DTW machine learning schemes by using utterances produced by a test speaker for tuning the recognition system is rare. Speaker learning functions for speech recognition, including DTW recognition, are crucial and necessary. Uttered voice data from a test speaker produce abundant information for adjusting the recognition system. By constantly tuning the DTW speech recognition system according to the utterances obtained from a test speaker, the system becomes speaker dependent and can maintain satisfactory recognition accuracy even when encountering unknown speakers. In general, speaker learning techniques for ASR are adopted in model-based speech recognition, particularly in HMM speech recognition. In HMM speech recognition, machine learning is also known as speaker adaptation [12–15]. However, these speaker learning methods are rarely observed in the field of feature-based speech recognition techniques. DTW, which is considered the representative of feature-based speech recognition techniques, displays an increase in recognition performance with well-designed speaker learning schemes.

Thus, machine learning schemes for DTW speech recognition were developed by using uttered data obtained from a test speaker. Supervised and unsupervised learning methodologies for DTW speech recognition are thoroughly explored in this paper. Regarding supervised learning, two learning methods for DTW were proposed in this study: incremental learning and priority-rejection learning. Regarding unsupervised learning, the most-matching learning method was developed, which extends the supervised priority-rejection learning to include a double-checking processing procedure of automatically verifying learning data. In summary, the three proposed machine learning methods for DTW speech recognition in this study have several advantages compared with those without the following

- (i) DTW speech recognition can be combined with system learning using data derived from a test speaker;
- (ii) speaker-dependent DTW behaves similarly to the HMM model-based technique, and

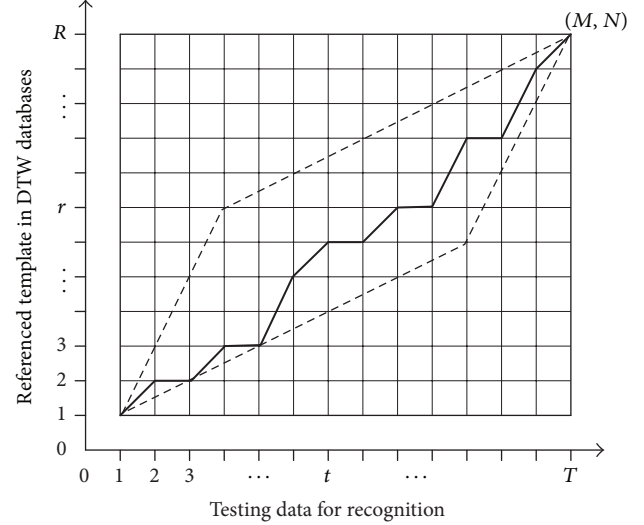


FIGURE 1: Template-matching operations on DTW speech recognition.

- (iii) additional robustness is provided to be adaptive in ordinary recognition environments, such as encountering an unknown test speaker.

2. DTW Speech Recognition

This section presents the conventional DTW speech recognition procedure without using any learning strategies. DTW, categorized into dynamic programming techniques, is a nonlinear warping algorithm that combines time-warping and appropriate template-matching calculations [6]. Figure 1 illustrates how the DTW algorithm was used to search for an optimal path between the testing data and the reference template. As illustrated in Figure 1, when computing the similarity degree between the testing data and the reference template, the low distortion between the two of them suggests a high similarity degree. The operation of DTW speech recognition is subsequently explained in this section. The testing utterance is composed of T frames and an arbitrary frame (a feature vector), denoted by t . The reference template consists of R frames and the arbitrary frame, indicated as r . The distortion between the T and R frames can be represented as $d[T(t), R(r)]$. The starting-point is $(T(1), R(1)) = (1, 1)$ and the end-point is $(T(M), R(M)) = (T, R)$. Based on these DTW operational settings, the DTW distance from the optimal comparison path can be derived using (1). The arbitrary frame t in the testing data is generally not equal to the arbitrary frame r in the indices reference template

$$(\text{optimal}) D = \min \sum_{m=1}^M d(T(m), R(m)). \quad (1)$$

Assuming that the point $(T(0), R(0)) = (0, 0)$ and $d(0, 0) = 0$, the accumulated distance that selects the optimal source path can be represented as follows:

$$\min D(t, r) = \min_{(t-1, r-1)} \{ \min D(t-1, r-1) + d(t, r) \}, \quad (2)$$

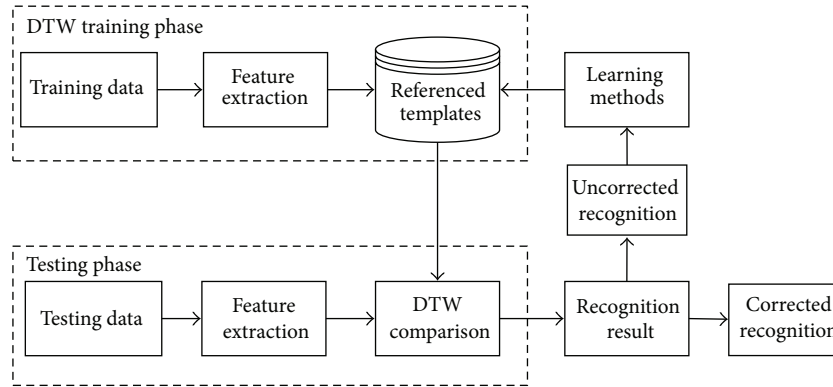


FIGURE 2: Frameworks of DTW speech recognition with machine learning.

where $\min D(t, r)$ is the shortest distance from the starting position to position (t, r) . In Figure 1, the solid, black line represents the DTW optimal matching path with the distance derived using (2). The dotted line is the global path search constraint that was used to effectively reduce the searching time for acquiring an overall optimal path on DTW operations.

3. Proposed Machine Learning Approaches for DTW Speech Recognition

The DTW technique cannot maintain satisfactory recognition performance levels in an ordinary recognition testing environment in which the uttered data from a test speaker is unmatched to the recognition system. Performing machine learning on DTW recognition may effectively resolve this phenomenon. Figure 2 illustrates the DTW recognition procedure combined with machine learning. As observed in Figure 2, the main contribution of this study is developing a method that can be used to continually adjust the DTW recognition system to become familiar with a speaker and then achieve outstanding recognition performance. The following subsection presents the proposed learning methods of DTW: incremental learning, priority-rejection learning, and most-matching learning.

3.1. Incremental Learning. The proposed incremental learning method for DTW is a supervised learning strategy. The supervisor (usually a system developer) monitors the overall speech recognition process. The system supervisor decides whether the test utterance should be returned to the DTW recognition system for learning according to the DTW recognition scores. The parameter D , which denotes the distortion of the entire comparison path in (1), is used to evaluate the DTW recognition score. If the system supervisor decides to perform the learning operation, the test utterance is considered to be a new template equipped with an appropriate label and added to the module of key word templates. This machine learning task should be conducted when the test utterance is incorrectly recognized. After learning, the updated DTW template set is closer to the uttered data derived from the test speaker and, therefore, the error recognition numbers are decreased. Figure 3 illustrates the processing flow of

the incremental learning scheme on DTW. To explain this learning scheme further, a pseudocode of the proposed DTW incremental learning method is presented in Pseudocode 1. As observed in Pseudocode 1, when performing incremental learning on DTW, the primary operations are

- (1) to label the learning data;
- (2) to add the learning data index into the referenced pattern index database; and
- (3) to add the feature of the learning data into the reference templates.

Thus, incremental learning provides a direct and conceptually simple learning technique. The primary disadvantage of incremental learning is that a large module of templates (reference template database in Figure 3) is presented for recognition comparisons because of numerous incorrectly recognized utterances found, which increases the number of computations on template matching and subsequently produces a heavy load of reference templates for real-time recognition responses.

3.2. Priority-Rejection Learning. To accelerate the computation of incremental learning using a large-scale reference template database and also maintain excellent recognition performance, an improved incremental learning scheme, priority-rejection learning, was further developed in this study and is presented in this section.

Priority-rejection learning offers the advantage of an invariant reference template database and can also immediately update content records in the template database when an utterance acquired from the test speaker is added into the template database for system learning. Figure 4 presents the processing procedure of the developed priority-rejection learning approach. As presented in Figure 4, after performing DTW recognition, two tasks were conducted. One task was to establish the recognition result among all of the possible template keyword candidates according to the DTW comparison scores, and the other was to record the value of the computed distance parameter, parameter D in (1), of each template keyword candidate. Priority-rejection learning, which involves processes that are similar to those used in incremental learning, is also a type of

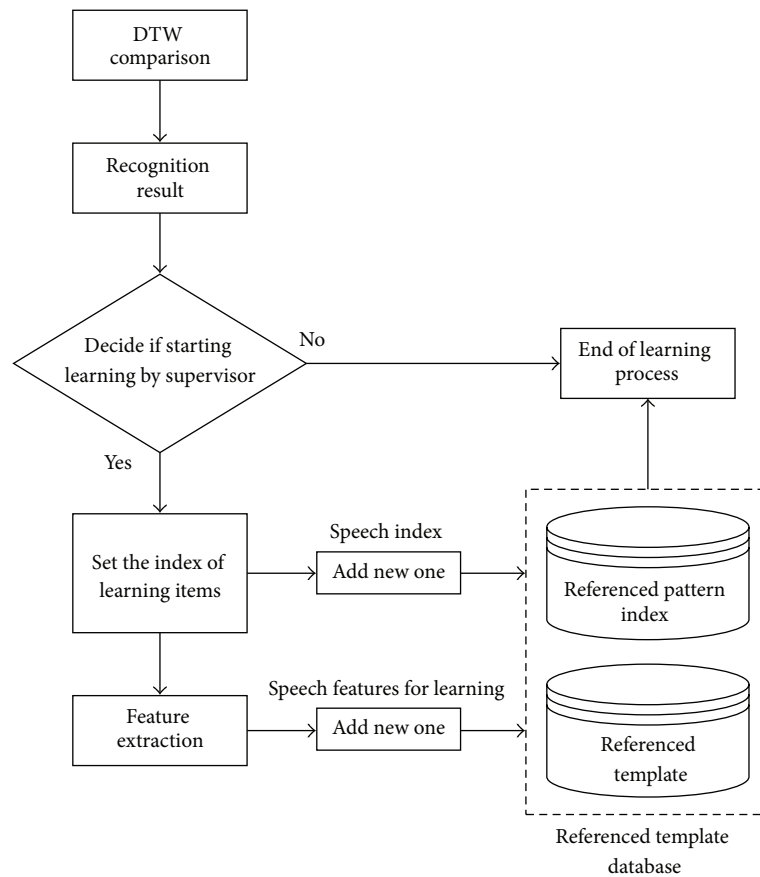


FIGURE 3: The proposed incremental learning method for DTW speech recognition.

```

Procedure DTW_Incremental_Learning ();
/*DTW recognition process*/
Perform DTW template matching;
Output recognition result before learning;
/* A decision of DTW system learning made by a supervisor */
If (Decision == "YES") then
  /* Correct recognition and then start the learning process */
  Label the recognition result and set the index  $i$ ;
  /*  $i$  is a relative index in referenced templates database */
  If ( $i$  setting == TRUE) then
    Convert the testing data to be the learning data;
    Feature extraction;
    Add  $i$  into the referenced pattern index;
  End If
  For each frame  $t$  ( $t = 1$  to total frames  $N$  of the learning data)
    Add features $_t$  into reference templates;
  End For
  /* End of learning process */
Else
  /* End of learning process (No learning) */
End If
  
```

PSEUDOCODE 1: The pseudocode of proposed incremental learning.

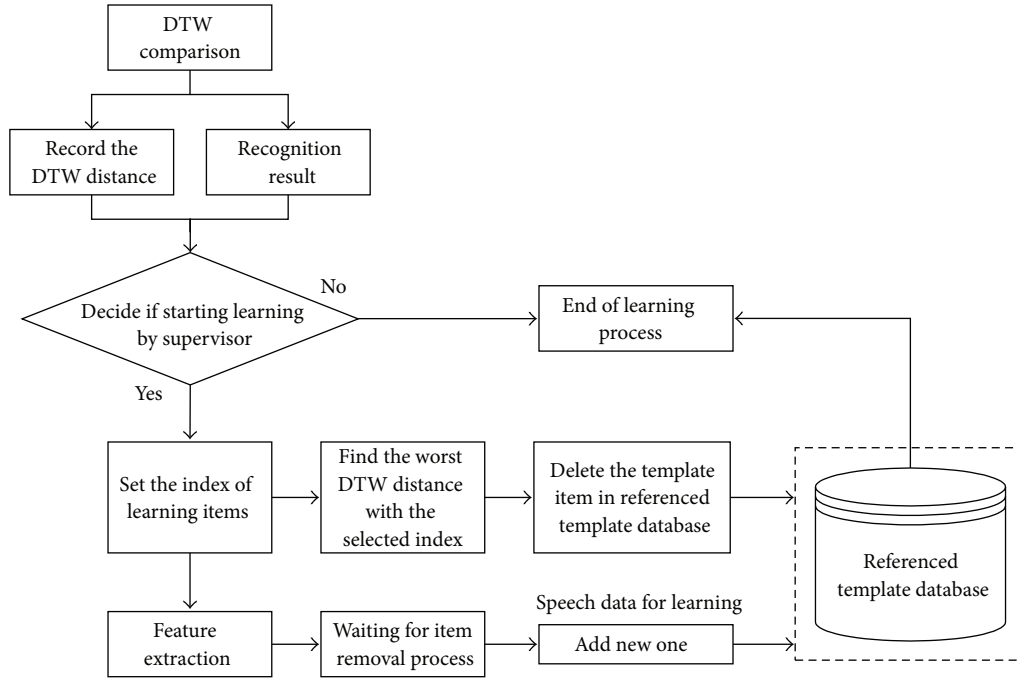


FIGURE 4: The developed priority-rejection learning method for DTW speech recognition.

supervised learning strategy. If the system supervisor decides to adjust the recognition system by using the test utterance, the learning target keyword template is first set. All of the keyword templates in the database with the same label as the target keyword template are subsequently removed. Following this step, the keyword template is removed from the system database to maintain the size of the reference template database after adding the test utterance to the database and subsequently establish a new reference template. In the reference template removal process, the determination policy of this study was to select the reference template with the lowest DTW comparison scores. The reference template that produces the highest value of parameter D is the least similar to the testing utterance, which causes correspondingly low DTW comparison scores to be produced. To explain the developed learning scheme further, a pseudocode of the proposed priority-rejection learning approach for DTW is presented in Pseudocode 2. As observed in Pseudocode 2, when performing priority-rejection learning on DTW, the main operations are

- (1) to search for the template item with the worst DTW distance;
- (2) to remove the identified item from the reference template database; and
- (3) to perform the primary incremental learning operations.

3.3. Most-Matching Learning. Unsupervised learning is an appropriate learning scheme for practical online speech recognition applications. This paper proposes an unsupervised learning method, namely, the most-matching learning

method, for DTW speech recognition. Most-matching learning is an extended version of the supervised priority-rejection learning method. The primary distinction between priority-rejection learning and most-matching learning is the decision-making scheme design of the recognition system adjustments for the test utterance. In contrast to the supervised learning scheme used in the priority-rejection learning method, the DTW speech recognition system involving most-matching learning uses an unsupervised learning scheme that determines whether the test utterance is appropriate for automatically performing system learning without any supervisors. The proposed most-matching learning method is illustrated in Figure 5. The continuous function blocks covered in the dashed line were integrated into a double-checking process, which verifies whether the test utterance was used in the learning process to update the DTW reference template database. In addition to the double-checking process, the operational functions in Figure 5 are almost similar to those of the priority-rejection learning method.

The double-checking process used in the most-matching learning method contains two fundamental steps to verify the test utterances produced by the speaker. The first step is to check if the calculated DTW score of Top-1 (indicating the reference template that is most similar to the test utterance) is greater than the predefined threshold T . If the score is lower than the value of T , the most-matching learning algorithm is immediately aborted because of the substandard test utterance. Otherwise, the most-matching learning process continues and then begins the second checking process. At the second checking step, reference templates with the same label as that of the Top-1 reference template are identified among the 10 highest DTW computational scores

```

Procedure DTW_Priority_Rejection_Learning ();
/*DTW recognition process*/
Perform DTW template matching and store DTW distance;
Output recognition result before learning;
/* A decision of DTW system learning made by a supervisor */
If (Decision == "YES") then
  /* Correct recognition and then start the learning process */
  Label the recognition result and set the index i;
  /* i is a relative index in referenced templates database */
  If (i setting == TRUE) then
    For each n
      /* n is numbers of the estimated DTW-distance with i */
      Search the worst (the largest) DTW-distance;
    End For
    Return the template item with the worst DTW-distance;
    /* Removal process */
    Delete the found template item with the worst DTW- distance in the database;
    /* Process of learning data */
    Convert the testing data to be the learning data;
    Feature extraction;
    If (Removal process finished == TRUE) then
      Add i into the referenced pattern index;
      For each frame t (t = 1 to total frames N of the learning data)
        Add featurest into reference templates;
      End For
    End If
  End If
  /* End of learning process */
Else
  /* End of learning process (No learning) */
End If

```

PSEUDOCODE 2: The pseudocode of priority-rejection learning.

(Top-1 to Top-10) of the reference templates. If the number of searched reference templates (including the Top-1 reference template) is higher than a predefined value N , most-matching learning dictates that DTW recognition system learning be conducted. Otherwise, most-matching learning is aborted. The settings for the T and N values are established in an empirical procedure. The optimal values of thresholds T and N can be derived using a simple and direct trial-and-error testing procedure. To explain the unsupervised learning scheme further, a pseudocode of the most-matching learning approach for DTW is presented in Pseudocode 3. The primary functions performed using the most-matching learning method are summarized as follows:

- (1) to feed the learning data into an unsupervised double-checking process; and
- (2) to perform the primary operations of priority-rejection learning if the learning data are accepted.

4. Experiments and Results

The experiments on DTW speech recognition involving the three proposed machine learning techniques were performed using a small vocabulary recognition application in which the test speaker was requested to utter a phrase for recognition

TABLE 1: Small-sized vocabulary keywords settings in DTW speech recognition.

Index of keywords	Keywords (in Chinese)
1	回家
2	請開燈
3	請關燈
4	開門
5	關門

testing. All of the uttered data were recorded in an office using a close-talking microphone. The speech signal was sampled at 44.1 kHz and recorded with monochannel settings and 16 bit resolution. The analysis frames were 20 ms wide with a 10 ms overlap. For each frame, a 10-dimensional cepstral vector was extracted. Table 1 presents the small vocabulary database that was composed of five keyword patterns. Each of the test speakers was asked to provide utterances that served as training data for establishing the DTW reference template database. Each of the five reference templates in Table 1 acquired 10 copies from the test speakers. Fifty reference templates were present in the database for DTW speech recognition. The recognition testing experiments for

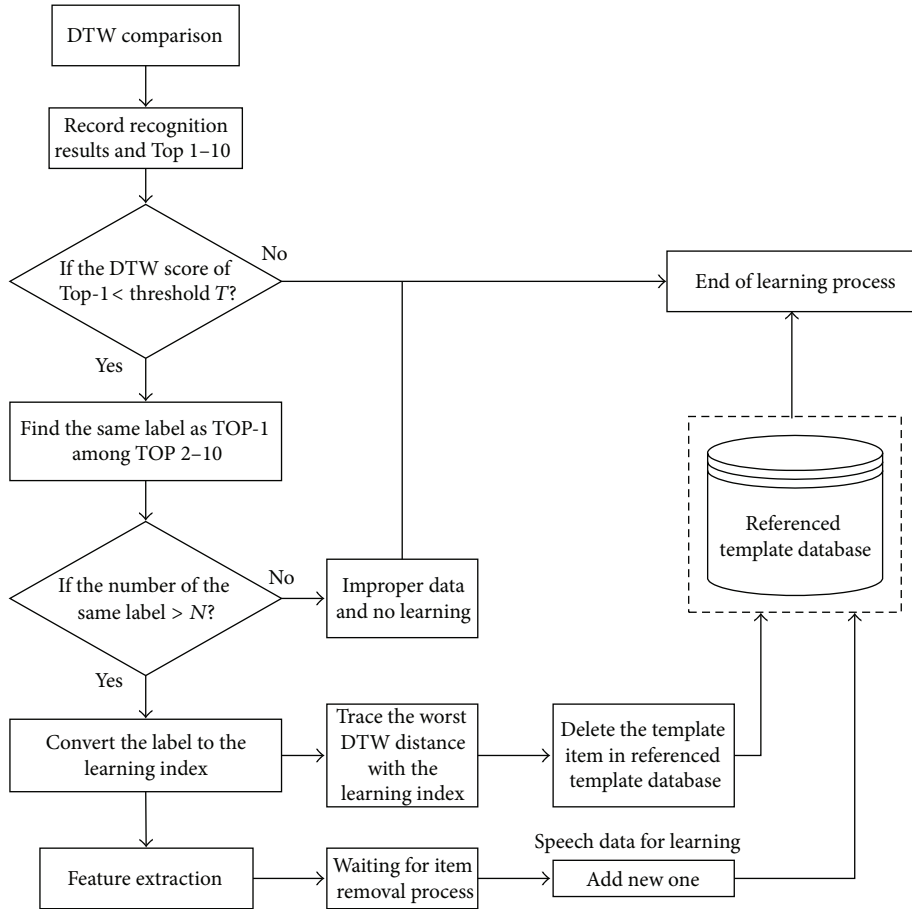


FIGURE 5: The presented most-matching learning method for DTW speech recognition.

TABLE 2: Recognition performances of inside testing DTW speech recognition.

Index of keywords	Recognition rates
Index 1	100%
Index 2	100%
Index 3	100%
Index 4	100%
Index 5	100%

evaluating the three proposed learning methods for DTW comprised two parts: inside testing and outside testing.

Table 2 presents the experimental results of performing inside testing using DTW speech recognition on the keyword patterns listed in Table 1. As shown in Table 2, the recognition accuracy of each template item reached 100% and, therefore, no learning was required.

In the outside testing recognition experiments, the utterances used to test the DTW speech recognition system completely differed from those used for establishing the DTW reference template database. Unique utterances were acquired from the test speakers. In addition, the utterances used as the learning data for the proposed learning methods were also obtained from the same test speakers. The baseline

TABLE 3: Recognition rates of outside testing DTW speech recognition (baselines without any learning).

Index of keywords	Baselines (no learning) Recognition rates
Index 1	96%
Index 2	80%
Index 3	70%
Index 4	62%
Index 5	66%
Average	74.8%

recognition rates of each reference template in the database are presented in Table 3. The data in Table 3 indicate a distribution from the highest recognition rate, 96%, to the lowest recognition rate, 62%, which suggests that the overall recognition performance was not ideal. The average recognition rate produced using conventional DTW speech recognition without any learning was 74.8%. The performance evaluations of DTW speech recognition combined with the proposed incremental learning method are presented in Table 4. As shown in Table 4, after performing five learning iterations, a recognition rate improvement was apparent. The

```

Procedure DTW_Most_Matching_Learning ();
Initialize the values of thresholds  $T$  and  $N$  to be constants;
/* DTW recognition process */
Perform DTW template matching;
Record DTW-distances of recognition results of Top-1 to Top-10;
/* Decide if starting learning by the unsupervised method */
If (DTW score of Top-1 < Threshold  $T$ ) then
/* Start learning */
  For each result label of Top- $t$  ( $t = 2$  to 10)
    Search the same label as Top-1 among Top 2-10;
  End For
If (Numbers of the same labels as that of Top-1 >  $N$ ) then
  Convert the label of Top-1 to the learning index  $i$ ;
  If ( $i$  setting == TRUE) then
    For each  $n$ 
      /*  $n$  is the number of the DTW-distance with  $i$  */
      Search the worst (the largest) DTW-distance;
    End For
    Return the template item with the worst DTW-distance;
    /* Removal Process */
    Remove the template item with the worst DTW-score in the database;
    /* Process of learning data */
    Feature extraction;
    If (Removal process finished == TRUE) then
      Add  $i$  into the referenced pattern index;
      For each frame  $t$  ( $t = 1$  to total frames  $N$  of the learning data)
        Add features $_t$  into reference templates;
      End For
    End If
  End If
Else
  /* Improper data and no learning */
End If
Else
  /* End of learning process (No learning) */
End If

```

PSEUDOCODE 3: The pseudocode of most-matching learning.

TABLE 4: Recognition results of DTW speech recognition with incremental learning.

Index of keywords	Recognition rates after incremental learning (supervised learning)		
	One time	Two times	Five times
Index 1	96%	98%	100%
Index 2	84%	88%	94%
Index 3	80%	92%	96%
Index 4	64%	66%	76%
Index 5	66%	68%	72%
Average	78%	82.4%	87.6%

TABLE 5: Recognition results of DTW speech recognition with priority-rejection learning.

Index of keywords	Recognition rates after priority-rejection learning (supervised learning)		
	One time	Two times	Five times
Index 1	96%	96%	98%
Index 2	90%	90%	92%
Index 3	82%	86%	94%
Index 4	68%	68%	72%
Index 5	68%	66%	70%
Average	80.8%	81.2%	85.2%

third template item exhibited the greatest recognition rate improvement, which was 26% (from 70% to 96%). The recognition rate of the first item reached 100% after completing the fifth incremental learning. Table 5 shows the performance of the priority-rejection learning method when applied to DTW

speech recognition. As shown in Table 5, after completing five learning iterations, the first template item exhibited the highest recognition rate, 98%, which is a nearly 100%, of incremental learning. Regarding the increase in the recognition rate after performing priority-rejection learning, as

TABLE 6: Comparisons of incremental learning and priority-rejection learning methods on DTW computation time.

Learning times	Incremental learning method			
	No learning	One time	Two times	Five times
DTW computation time (sec.)	0.594	0.609	0.718	0.828
Learning times	Priority-rejection method			
	No learning	One time	Two times	Five times
DTW computation time (sec.)	0.594	0.609	0.609	0.609

TABLE 7: Recognition results of DTW speech recognition with most-matching learning (settings of thresholds: $T = 300$ and $N = 4$).

Index of keywords	Recognition rates after most-matching learning (unsupervised learning)		
	One time	Two times	Five times
Index 1	100%	100%	98%
Index 2	86%	86%	90%
Index 3	66%	64%	66%
Index 4	62%	62%	60%
Index 5	66%	68%	58%
Average	76%	76%	74.4%

the incremental learning, the third template item achieved the most improvement, 24% (from 70% to 94%), which was still slightly lower than 26% of incremental learning. The finding that the priority-rejection learning performance is inferior compared with that of incremental learning is completely reasonable and correct because priority-rejection learning maintains a fixed reference template database (50 templates in this scenario), and the reference template database of incremental learning gradually increases after learning. Table 6 presents a comparison of incremental learning and priority-rejection learning computational speed. As observed in Table 6, priority-rejection learning was superior to incremental learning because priority-rejection learning requires fewer template-matching comparison operations. The performance of unsupervised most-matching learning is shown in Tables 7 and 8 with various threshold settings for parameters T and N . Using unsupervised most-matching learning is evidently less favorable than using incremental learning or priority-rejection learning. Although most-matching learning is operated without a supervisor, the recognition performance still improved after learning in most situations. However, under circumstances in which DTW speech recognition encountered substandard test utterances for most-matching learning, the recognition performance was dissatisfactory and the recognition rate was substantially lower than the baseline (e.g., the recognition rates of the third template item listed in Tables 7 and 8 were lower than the baseline after unsupervised learning operations were conducted). DTW speech recognition achieved the highest average recognition rate of 76.4%, which was higher than the baseline of 74.8%, when the unsupervised learning method was used.

TABLE 8: Recognition results of DTW speech recognition with most-matching learning (settings of thresholds: $T = 400$ and $N = 4$).

Index of keywords	Recognition rates after most-matching learning (unsupervised learning)		
	One time	Two times	Five times
Index 1	98%	96%	98%
Index 2	84%	88%	90%
Index 3	72%	68%	58%
Index 4	62%	64%	54%
Index 5	66%	66%	58%
Average	76.4%	76.4%	71.6%

5. Conclusion

This study focused on DTW-based speech recognition for developing machine learning schemes in recognition systems. Two categories of learning mechanisms, supervised and unsupervised learning, used for DTW speech recognition were thoroughly explored in this paper. Regarding supervised learning, this study proposed two methods, incremental learning and priority rejection learning, for performing DTW. Both incremental learning and priority-rejection learning are conceptually simple and improve the recognition accuracy of conventional DTW. Regarding unsupervised learning, the most-matching approach was developed for DTW in this study. The most-matching approach was based on the concept that priority-rejection learning can automatically perform DTW system learning without any human supervisors. DTW that applies any of the three proposed learning methods uses processes that are similar to those used in model-based speech recognition and can adjust the recognition system properly by using the utterances produced by the speaker.

References

- [1] F. Harashima and S. Suzuki, "State-of-the-art intelligent mechatronics in human-machine interaction," *IEEE Industrial Electronics Magazine*, vol. 4, no. 2, pp. 9–13, 2010.
- [2] S. K. Gaikwad, B. W. Gawali, and P. Yannawar, "A review on speech recognition technique," *International Journal of Computer Applications*, vol. 10, no. 3, pp. 16–24, 2010.
- [3] L. R. Rabiner, "A Tutorial on hidden Markov models and selected applications in speech recognition," *Proceedings of the IEEE*, vol. 77, no. 2, pp. 257–286, 1989.

- [4] A. K. Paul, D. Das, and M. M. Kamal, "Bangla speech recognition system using LPC and ANN," in *Proceedings of the IEEE 7th International Conference on Advances in Pattern Recognition (ICAPR '09)*, pp. 171–174, Kolkata, India, February 2009.
- [5] A. Ganapathiraju, J. E. Hamaker, and J. Picone, "Applications of support vector machines to speech recognition," *IEEE Transactions on Signal Processing*, vol. 52, no. 8, pp. 2348–2355, 2004.
- [6] H. Sakoe and S. Chiba, "Dynamic programming algorithm optimization for spoken word recognition," *IEEE Transactions on Acoustics, Speech, and Signal Processing*, vol. 26, no. 1, pp. 43–49, 1978.
- [7] P. G. N. Priyadarshani, N. G. J. Dias, and A. Punchihewa, "Dynamic time warping based speech recognition for isolated Sinhala words," in *Proceedings of IEEE International Midwest Symposium on Circuits and Systems*, 2012.
- [8] X. Anguera, R. Macrae, and N. Oliver, "Partial sequence matching using an unbounded dynamic timewarping algorithm," in *Proceedings of the IEEE International Conference on Acoustics, Speech, and Signal Processing (ICASSP '10)*, pp. 3582–3585, Dallas, Tex, USA, March 2010.
- [9] Y.-S. Lin and C.-P. Ji, "Research on improved algorithm of DTW in speech recognition," in *Proceedings of the International Conference on Computer Application and System Modeling (ICCASM '10)*, vol. 9, pp. V418–V421, Taiyuan, China, October 2010.
- [10] X. Chen, J. Huang, Y. Wang, and C. Tao, "Incremental feedback learning methods for voice recognition based on DTW," in *Proceedings of International Conference on Modeling, Identification and Control*, 2012.
- [11] Q. Chen, G. Hu, F. Gu, and P. Xiang, "Learning optimal warping window size of DTW for time series classification," in *Proceedings of International Conference on Information Sciences, Signal Processing and their Applications*, 2012.
- [12] C.-H. Lee, C.-H. Lin, and B.-H. Juang, "A study on speaker adaptation of the parameters of continuous density hidden Markov models," *IEEE Transactions on Signal Processing*, vol. 39, no. 4, pp. 806–814, 1991.
- [13] C. J. Leggetter and P. C. Woodland, "Maximum likelihood linear regression for speaker adaptation of continuous density hidden Markov models," *Computer Speech and Language*, vol. 9, no. 2, pp. 171–185, 1995.
- [14] R. Kuhn, J.-C. Junqua, P. Nguyen, and N. Niedzielski, "Rapid speaker adaptation in eigenvoice space," *IEEE Transactions on Speech and Audio Processing*, vol. 8, no. 6, pp. 695–706, 2000.
- [15] B. K.-W. Mak and R. W.-H. Hsiao, "Kernel eigenspace-based MLLR adaptation," *IEEE Transactions on Audio, Speech and Language Processing*, vol. 15, no. 3, pp. 784–795, 2007.

Research Article

Optimization of Microextrusion Preforming Using Taguchi Method

Shao-Yi Hsia

Department of Mechanical & Automation Engineering, Kao-Yuan University, Kaohsiung 821, Taiwan

Correspondence should be addressed to Shao-Yi Hsia; syhsia@cc.kyu.edu.tw

Received 15 September 2013; Accepted 22 October 2013

Academic Editor: Teen-Hang Meen

Copyright © 2013 Shao-Yi Hsia. This is an open access article distributed under the Creative Commons Attribution License, which permits unrestricted use, distribution, and reproduction in any medium, provided the original work is properly cited.

Micropin head geometry significantly influences surface contact and electrical conductivity. In this paper, the preforming process of extrusion is investigated to establish it as a viable process for microforming. Here, the numerical simulations using DEFORM-3D software are used to examine the effect of performance and pin shape on the extrusion of microbrass pins with a minimum diameter of 0.88 mm under several design parameters. These parameters are planned with the Taguchi method and help to discover better conditions for the minimum extrusion loads. For obtaining the required parameters to enable the finite element software, a compression test is first performed to determine the true stress and true strain curve of the materials. The result acquired from the experiment is compared with the simulation outcome and verified the accuracy. The consequences show that the optimal microextrusion forming conditions appear on stage rod length 0.015 mm, extruding angle 60°, upper front-end taper 60°, and bottom stage angle 60° to minimize the forming load, and the dimensions of the deformed micropin reveal a good identification with the simulation. The study hence shows a potential tool for the combination of Taguchi method and finite element software to analyze the microforming process in the fastener industry.

1. Introduction

With the gradually increasing emphasis on microforming and the rapid development of the semiconductor, optoelectronics, communication, and 3C industries, the direction of product development is towards multifunctions and decreasing of size. For example, parts of common 3C products like mobile phones, digital cameras, and notebooks are becoming miniaturized, with lightness, thinness, shortness, and smallness all being significant trends. Assembly parts such as microconnectors, micromotor, microsprings, and microgear require the use of microforming as a production and processing technology, where metal forming possesses higher processing efficiency, superior quality stability, and lower costs than other processing technologies. Consequently, the development of new micrometal forming technology continues to be strongly emphasized. Nevertheless, the processing technology for the parts of micro-sized products is different from it with traditional processing, including the grain size of metal materials, surface friction effect, geometric shape, isotropy of materials, flow stress strain, experimental equipment and

the manufacturing of die, and the precise orientation of the relative positions between dies and materials. Moreover, materials with smaller grain sizes appear to have higher hardness and strength after the product being miniaturized to the degree that it is not easily formed. From the aspect of microshaping, materials with smaller grain size can easily fill in small cavity and benefit from the forming of complex microparts. Such an effect is called size effect.

Wu and Hsu [1] identified the best design parameters using DEFORM-2D to simulate precise bevel gear in 2002. Appropriate chamfering of corners and tapers could assist materials to flow and decrease forming pressure. Syu [2] used finite element software to analyze axisymmetric forge forming in 2002 and discussed the effects of die parameters on formability. They concluded that die inclination angle and fillet size did not strongly influence forming load but did influence extruded height and width. In the study, larger inclination angle and smaller fillet condition were used to stimulate the extrusion of the larger height and width. Finally, the die inclination angle, reverse fillet radius, and forming strain were represented using a 3D contour map to

observe the distribution tendency. Chen et al. [3] designed a microterminal component with 0.6 mm (diameter) \times 1.0 mm (depth) \times 0.125 mm (inner thickness) and planned five-stage forming (facial dressing, head upsetting, perform, backward extrusion, and size finishing) based on formability of copper alloy in 2005. The finite element simulation software, DEFORM-2D, was further applied to simulate the forming process to provide a reference die design for use in production. The research outcomes demonstrated that lubricant and air easily accumulated in the fillet in a cavity, contributing to unfavorable surface quality of perform fillet after formation. Consequently, such air and lubricant could be excluded by dividing the cavity and adding taper grooves. In terms of die processing, poor processing precision could cause numerous small features (0.05~0.1 mm fillet) in microforming, contributing to unsuccessful forming, centric deviation, and raw edges. More precise processing technology is thus necessary for die processing. Gau et al. [4] discussed size effect with experiments in 2006 and found that the intensity resulted from yield strength and tensile strength of materials and the flow stress and formability of aluminum and copper pole pair could be presented with T/D (plate thickness/average grain size). When $T/D > 1$, the yield and tensile strength decreased with decreasing T/D , while the yield and bending deviation increased with decreasing T/D . Finally, it was indicated that the formability would get worse with decreasing T/D when the plate thickness was not taken into account. With closed dies, Hu et al. [5] applied finite element analysis to simulating the forge forming of change gears in 2007 that the fillet size would affect the stress and material flow. Focusing on magnesium alloy AZ31, Yoon et al. [6] investigated the effects of various backward extrusion gaps and forward diameter on forward and backward processes at 200°C and forecast cracks on the products using the finite element software, DEFORM-2D, in 2008. The research outcomes demonstrated that material tended to flow in the shear direction when outside diameter of the punch head approached the forward diameter and the product cracks were likely to appear on the fillet at the contact between the material and the following channel. Sun et al. [7] utilized the animation simulation and finite element software (DEFORM-3D) for simulating the multistage cold forging of stainless automotive battery fastener backward extrusion process in 2013. In this paper, the CAD drawing was made by Inventor 3D software, and then the STL file was imported to DEFORM-3D software to do the settings of preprocess and simulation analysis. Effective stress, effective strain, velocity field, and forging force had also been shown in this study. Finally, the actual manufacture measurement results were compared with simulation datum to verify the analysis acceptance. Mori et al. [8] presented the results of experiments conducted to investigate the friction coefficient existing at a brass-steel interface. The research discussed the size effects in friction conditions that exist during microextrusion. In the regime of dimensions of the order of a few hundred microns, these size effects tend to play a significant role in affecting the characteristics of microforming processes. In this study, a series of frictional experiments was conducted using a stored-energy Kolsky bar. Tests were conducted using brass samples of a small grain size

(32 μm) and a large grain size (211 μm) at low contact pressure (22 MPa) and high contact pressure (250 MPa) to see whether there was any change in the friction conditions due to these parameters. The main conclusion of these experiments was that the friction coefficient did not show any significant dependence on the material grain size, interface pressure, or area of contact. Cao et al. [9] investigated the extrusion process for micropins and its numerical simulation, and the process of extrusion is investigated to establish it as a viable process for microforming. In this paper, the effect of grain size is investigated by using workpieces heat-treated to produce grain sizes varying from 32 mm up to 211 mm. At the same time, a new method, the Reproducing Kernel Element Method (RKEM), had recently been developed to address the limitations of the FEM (e.g., remeshing issue), while maintaining FEM's advantages. The new RKEM method was used to simulate the micro-extrusion problem and compared with that obtained from the FEM and the experimental result.

Present research on microforming is relatively less in Taiwan. A development technology for developing stabler and rapid micro-metal elements being able to enhance the precision and production efficiency becomes a critical issue. Extrusion is regarded as the commonest metal forming process with deep potential for analyses. This investigation discusses the relevant parameters in microforming pin extrusion, including the effects of die shape on processing. These experimental values are compared with the simulation results.

2. Research Method and Framework

2.1. Research Method. Using the finite element software, DEFORM-3D, to analyze the formability, 3D SolidWorks is applied as the platform to simulate forward microextrusion forming and die design (Figure 1). The procedure begins from the production of workpiece. Simple compression tests can obtain the material parameters for simulations and experiments. Finally, the differences are compared. This investigation discusses the effects of various performance geometries and micropin designs (Figure 2) on material filling in forming. During the first stage forming, an angle (ϕ) is introduced to the material, and a stage rod length (h) is then extended with end flow to optimize the material filling and decrease the forming load during the second stage forming. Product shape during the second stage forming becomes a front-end taper (α) and bottom stage angle (β) shown in Figure 2 for the effects on the filling in the extrusion under different factors and to optimize the design.

2.2. Finite Element Method. Among various methods used in discussions of metal forming, the Finite Element Method is commonly utilized in research analyses. It tends to obtain solutions by simplifying complex problems, such as those involving complex and irregular boundary conditions and loads. As the solutions are merely approximations, rather than accurate solutions, the present numerical solutions are inaccurate. DEFORM-3D, with ordinary application and adaptive geometric shape, exhibits greater practicality

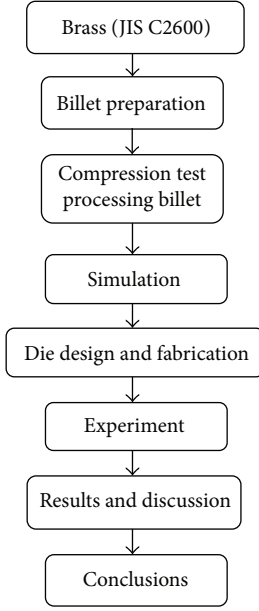


FIGURE 1: Flowchart of study.

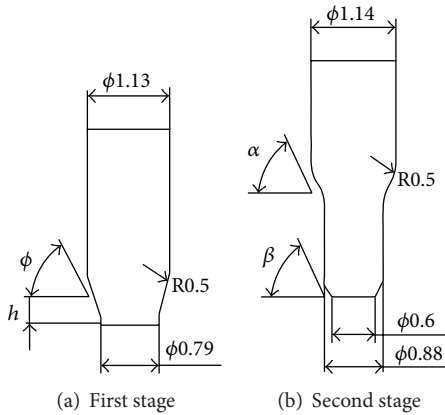


FIGURE 2: Key dimensions in preform shape and final product.

and performance advantages in terms of forming load, stress/strain distribution, material distortion, temperature distribution, and velocity field and hence is used in this investigation. The calculation aims to satisfy the equilibrium equation, constitutive equation, geometric compatibility equation, yield criterion, and boundary conditions. Since metal forming is a complicated deforming behavior, the assumption of boundary conditions and material characteristics in Finite Element Analysis being accurate and reasonable would largely affect the analysis results. For simplifying the complexity of plastic processing and reducing the computational time, the suitable assumptions are adopted to analyze in this case. They are listed as below.

(1) *The Material Is Assumed to Have the Homogeneity and Isotropy.* Cylindrical workpieces are utilized for simulating the microextrusion forming in order to simplify and reduce the analysis complexity. In this study, the workpiece is

assumed to be homogeneous and isotropic, but with ignoring the effects of directions that von Mises should be taken into account in the stress yield.

(2) *Yield Criterion.* Generally, von Mises yielding criterion is adopted as material plastic rule. It provides the relationship between the material yield condition and 3D stress states. All three axial principal stresses can be expressed as the effective stress shown in (1) as

$$\bar{\sigma} = \frac{1}{\sqrt{2}} [(\sigma_1 - \sigma_2)^2 + (\sigma_2 - \sigma_3)^2 + (\sigma_3 - \sigma_1)^2]^{1/2} \quad (1)$$

von Mises presents that the effective stress reaches the yield strength (Y) of material, the plastic deformation occurs. Equation (2) is expressed as

$$\bar{\sigma} = \frac{1}{\sqrt{2}} [(\sigma_1 - \sigma_2)^2 + (\sigma_2 - \sigma_3)^2 + (\sigma_3 - \sigma_1)^2]^{1/2} = Y. \quad (2)$$

(3) *Rigid-Plastic Mode.* Since the deformation of formed pieces is large in the forming process, the elastic deformation of formed pieces can be ignored but merely considered in the plastic deformation. The upper and the lower molds are assumed as the rigid body, which will not deform because of pressure. The variation principle of von Mises is used as the finite element for the rigid-plastic material, and the functional is shown as follows [10]:

$$\pi = \int_V \bar{\sigma} \dot{\epsilon} dV - \int_{S_F} \bar{t}_i v_i dS, \quad (3)$$

where the equivalent strain rate is the surface force. The first variation of the functional is acquired by the basic finite element as

$$\delta\pi = \int_V \bar{\sigma} \delta\dot{\epsilon} dV + k \int_V \dot{\epsilon}_V \delta\dot{\epsilon}_V dV - \int_{S_F} \bar{t}_i v_i dS, \quad (4)$$

where k is the penalty constant and $\dot{\epsilon}_V$ is the volumetric strain rate.

(4) *Constant Temperature Mode.* The forming temperature is kept at the room temperature, and the temperature resulted from the plastic deformation of formed pieces in the cold forming process is small than the effects of the local temperature which is ignored [11].

(5) *Friction Model.* The cold forming processing of fasteners reveals high contact pressure that the constant shear friction model is utilized for the interface friction, the constant shear friction factor is regarded as the interface friction coefficient, and the interface friction between the mold and the work remains constant in the process.

2.3. *Stress-Strain Curve.* To enable the finite element software, DEFORM, to simulate forward microextrusion, simple compression tests are first performed to determine the true stress-true strain curve of the materials. Electric press, with compression function, is used to perform the tests.

The maximum force of the punch head is 5,000 Kg, with 1% error (JP-5400). The simple compression test sheet is implemented using ASTM E9-89 rules, with the diameter-height ratio of 2:3. The compression rate for the tests is 0.01 mm/s, and the brass pin applies to diameter 1.1 mm and height 1.65 mm. The upper and lower flat dies are used for the compression tests, in which the material for the flat die is SKD11 with heat processing and burnishing processing. Molybdenum disulfide (MoS_2) grease is added to reduce the friction effect. The sheet is compressed to 90% depth to enable the grease to evenly flow out on sheet compression. In this case, the contact surface of the die is determined through favorable interface lubrication, and the load-displacement curve during compression is then obtained using a computer to calculate the true stress-strain curve. The equations of true stress and true strain are shown as follows:

$$\sigma = \frac{F}{(\pi \times D \times H_0) / H} \quad (5)$$

$$\varepsilon = \ln \left(\frac{H_0}{H} \right),$$

where σ is the true stress, F the punch load, D the pin diameter, H_0 the pin original height, H the pin compressed height, and ε the true strain.

2.4. Simulation of Forward Microextrusion. When the finite element software, DERORM-3D, is used to simulate forward microextrusion of workpiece, the differences between the simulated stage process and the experimental process are discussed, and the reaction of the punch head when the effective stress strain, material flow, and simulated estimated materials result from the extrusion forming is assessed for the standard of punch head and die intensity during die design. DEFORD-3D is applied to simulate the forward extrusion of brass (C2600). Since the forming is axisymmetric, the model is merely 1/6 constructed, appropriate boundary conditions are set, rigid plastic is used for the work, the total grid number for the finite element is approximately 15,000, the punch head speed is 0.12 mm/s, and the friction factor between objects is 0.12. A brief summarization of the analysis conditions is denoted in Table 1, and the simulation steps are shown as follows. (1) SolidWorks is utilized for drawing the required die (cavity, upper punch, and lower ejector), which is further transformed into STL files. (2) The STL files are imported into DEFORD 3D, the punch head and die are set on the suitable positions shown in Figure 4 and the grid division is defined. (3) The true stress-strain curve obtained from compression tests shown in Figure 3 is regarded as the basis of the material character. (4) The compression stroke and the punch head speed are defined. (5) The friction between objects applies to constant friction factor.

2.5. Taguchi's Optimization Experiment

(1) *Taguchi's Orthogonal Array.* Taguchi's Orthogonal Array describes the creation of a pair of parameters from all levels at two column intervals in the experimental table, where each composition presents the same frequency. The Classical

TABLE 1: Analysis conditions in FEM simulation.

Workpiece	Brass (JIS C2600)
Flow stress	$\sigma = 721.46e^{0.4606}$
Workpiece/die	Rigid plastic body/rigid body
Symmetric mesh	1/6
Mesh number	10,000~15,000
Punch speed (mm/sec)	0.1 mm/sec
Frictional factor	Constant frictional factor/0.12

Orthogonal Array is named after $L_a(b^c)$ and presents that the experiment contains c factors, each of which has b levels for an experiment. Orthogonal Array compromises on experimental cost and precision, and fewer experiments are needed to achieve useable statistical information. Nevertheless, Orthogonal array experiments are *not* full factorial experiments. The "bias" cannot be completely eliminated, but is acceptable as not all levels of compositions appear on the orthogonal array. The optimal composition therefore might not be in the experimental group.

(2) *Signal-to-Noise Ratio (S/N Ratio).* S/N ratio is often used as the quality index in the Taguchi method, showing the effects of errors on the process or product level. According to different quality characteristics, various S/N ratio formulas would appear, including nominal-the-best, smaller-the-better, and larger-the-better. Only smaller-the-better is applied in this study for the minimum extrusion loads, where smaller-the-better S/N ratio is shown as follows:

$$S/N_{SB} = -10 \log \left[\frac{\sum_{i=1}^n (y_i)^2}{n} \right], \quad (6)$$

where y_i presents the experimental values, and n the number of experimental times.

(3) *Factor Response Table.* The response table and response diagram of each factor are constructed after the experiment for understanding the effects on the target function. Based on the S/N ratio of each factor in the same level to calculate the mean, the effects of the factor level on the results are listed in a table and transformed into an auxiliary response diagram as

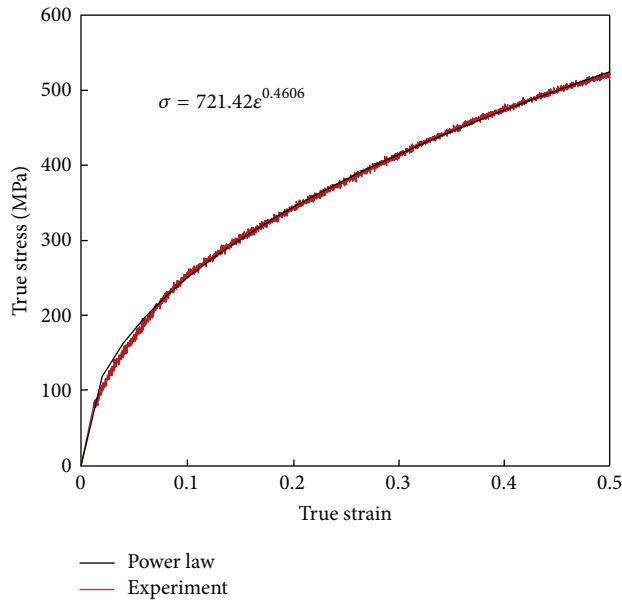
$$M_{ij} = \frac{\sum_{k=1}^N S/N_{ijk}}{N}, \quad (7)$$

where M_{ij} is the mean S/N ratio of the experiment with i factor and j level, k the k th S/N ratio with i factor and j level, and N the number of experiments with i factors and j level.

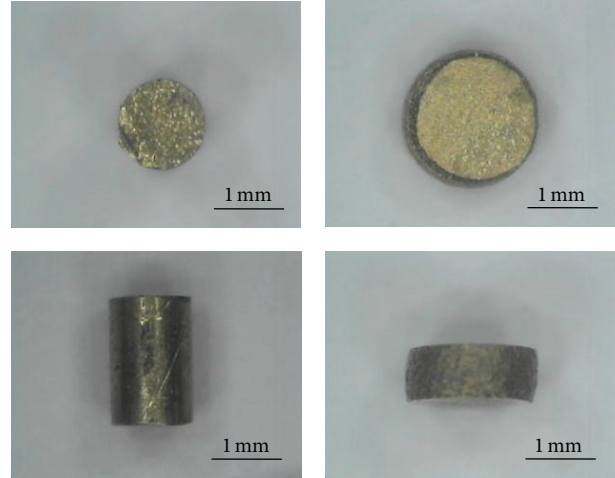
A number of simulations are planned with the Taguchi method in designing the geometric of optimal microextrusion dies for discovering the better conditions for the minimum extrusion loads.

3. Simulation and Experiment

3.1. FEM Simulation. By following Table 2 planned with the Taguchi method, an angle (ϕ) and rod length (h) are used to



(a) True-stress and true-strain curve



(b) Original and deformed brass pin

FIGURE 3: Simple compression tests of the material.

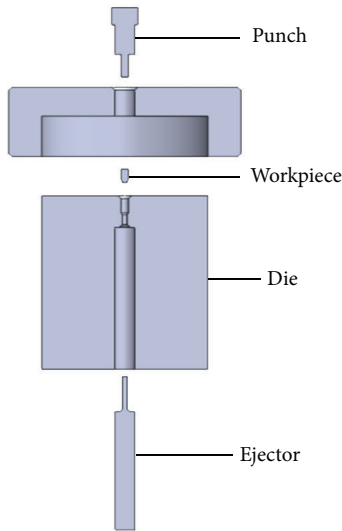


FIGURE 4: Schematic diagram of die construction.



FIGURE 5: Die components.

TABLE 2: Die parameters and factors of Taguchi method.

Factors	Specifics	Level 1	Level 2	Level 3
A	h (mm)	0.05	0.1	0.2
B	ϕ (Deg.)	45	50	60
C	α (Deg.)	45	60	75
D	β (Deg.)	0	30	60

design the first stage forming, and a front-end taper (α) and bottom stage angle (β) are used for the second stage forming. All of the four factors have three levels and will be used to discuss the effects on the filling in the extrusion under different factors and to optimize the design. To simplify the simulation quantity, 9 sets of Taguchi's orthogonal arrays $L_9(3^4)$ are applied to acquiring the minimum extrusion loads. Consequently, based on S/N ratio, response table or response diagram can hence be utilized for finding the optimal designing conditions.

3.2. Die Design and Experiment. This study designs forward microextrusion die (Figures 4 and 5). By locating a punch head in the cavity, the movement uses a plate to extrude the punch head, the materials are formed into the required shape, and the product is ejected. The orientation of the punch head and cavity can be ignored. The die components include the punch head, upper module, cavity, and ejector. The punch head has diameter 1.13 mm, with SKH9 high-speed steel as the material; JIS SKD 11 is selected as the material of the upper module and guides the positioning of the punch head and cavity; the tungsten carbide (WC) module is embedded in the cavity, where the tungsten carbide module is subjected to inward stress to offset the outward stress on the cavity during

forging so as to reduce the overall stress and improve die life; the tool steel, JIS SKD11, strengthened by heat processing is used for the rest of the forms; SKH9 is selected for the ejector, which displays both ejection and forming effects.

The completed die is installed on the electric press platform for a microextrusion forming experiment. The experimental load and stroke data are obtained via an interface and recorded on a computer. The experimental procedure used in micropin forming is as follows (Figure 4). (a) The cavity is placed on the lower module and takes the form of a composite cavity. (b) The workpiece is evenly covered with lubricant and located in the cavity. (c) The upper module corresponds to the cavity. (d) The punch head is located on top of the workpiece and oriented with the cavity. (e) The press stroke is calculated and the data are obtained.

4. Results and Discussions

By simulating the forming punch head of a brass micropin with minimum diameter 0.88 mm, the effects of performance design and pin shape on the cavity extrusion filling under different factors are experimentally verified. The first forming stage aims to extrude angle (ϕ) on the workpiece with forward extrusion and to extend a stage rod length (h) to improve material filling and reduce forming load during the second forming stage. During the second stage, the geometric shape of the product is changed to an upper front-end taper (α) and the bottom stage angle (β), and the effects on filling during extrusion forming are discussed, under the factors, for design optimization.

According to Taguchi's orthogonal array $L_9(3^4)$, nine experiments and nine different symbols represent each simulation result. On Table 2, the workpiece is extended in the stage rod lengths (h), 0.05 mm, 0.1 mm, and 0.2 mm, and extruded with the angles (θ), 45°, 50°, and 60°. Regarding the design of second forming stage, the angles α and β are changed to simulate the filling differences with restricted forming load, where α is conducted with 45°, 60°, and 75°, and β is also conducted with 0°, 30°, and 60°. Table 3 represents the DEFORM-3D simulation results of forming loads and smaller-the-better S/N ratio according to (6). Table 4 shows the factor response table of S/N ratio on forming loads, which was calculated from the simulation results in Table 3. The level values listed under column present the effects of variability, and the variability among different levels could be regarded as the effect of controlling factors on S/N . The range in the table shows the maximum range of variability, where the larger variability in rank is more important in the design optimization. Hence, Table 4 shows that stage rod length (h) is the largest factor in the experimental results, followed by bottom stage angle (β), upper front-end taper (α), and extruding angle (ϕ). As the S/N ratio is expected to be smaller-the-better, the optimal experimental settings for minimum extrusion load showed the conditions of A1B3C2D3. This implies stage rod length 0.015 mm, extruding angle 60°, upper front-end taper 60°, and bottom stage angle 60°. The quality characteristics shown in Figure 6 are the response graph according to Table 4, where

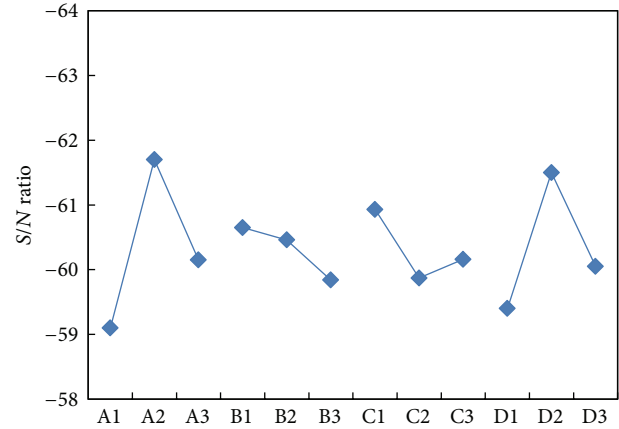


FIGURE 6: The response graph of S/N ratio in different levels.

TABLE 3: Simulation layout and results using the modified $L_9(3^4)$ orthogonal array.

Set	A	B	C	D	Loads (N)	S/N
1	1	1	1	1	904	-59.12
2	1	2	2	2	998	-59.98
3	1	3	3	3	812	-58.19
4	2	1	2	3	1165	-61.33
5	2	2	3	1	1092	-60.76
6	2	3	1	2	1415	-63.02
7	3	1	3	2	1190	-61.51
8	3	2	1	3	1077	-60.64
9	3	3	2	1	823	-58.31

the x -axis A1 represented the reaction with controlling factor A and level number 1. The y -axis represented the S/N ratio of forming load. The notation in this figure is similar with that in Table 4. It means that A and D are significant factors, and B and C have light influence on a number of simulations. Figure 7 indicates the effective stress, effective strain, and velocity of the workpieces on the different forming series. The maximum values of effective stress and strain always occur on the corner or bottom of the deformed micropins. As shown in Figure 7, there are the two maximum effective stresses 1,600 MPa on stage 1 and 1,800 MPa on stage 2 due to a larger deformation. The similar tendency is also obtained on the maximum effective strains 5.3 and 6.4 for different stages. The corresponding microstructures of the second deforming stage on the top right corner, middle right corner, and bottom right corner are shown in Figure 8. These microstructures are obtained by metallographic test on 100 times and 200 times. Due to the larger deformations on middle and bottom corners, the grain shapes of the two positions became long and narrow. It is opposite to the top side that seems to have a nearly original grain shape. The figure also denotes that the deforming tendency of the middle right corners is counterclockwise corresponding to the velocity fields shown in Figure 8.

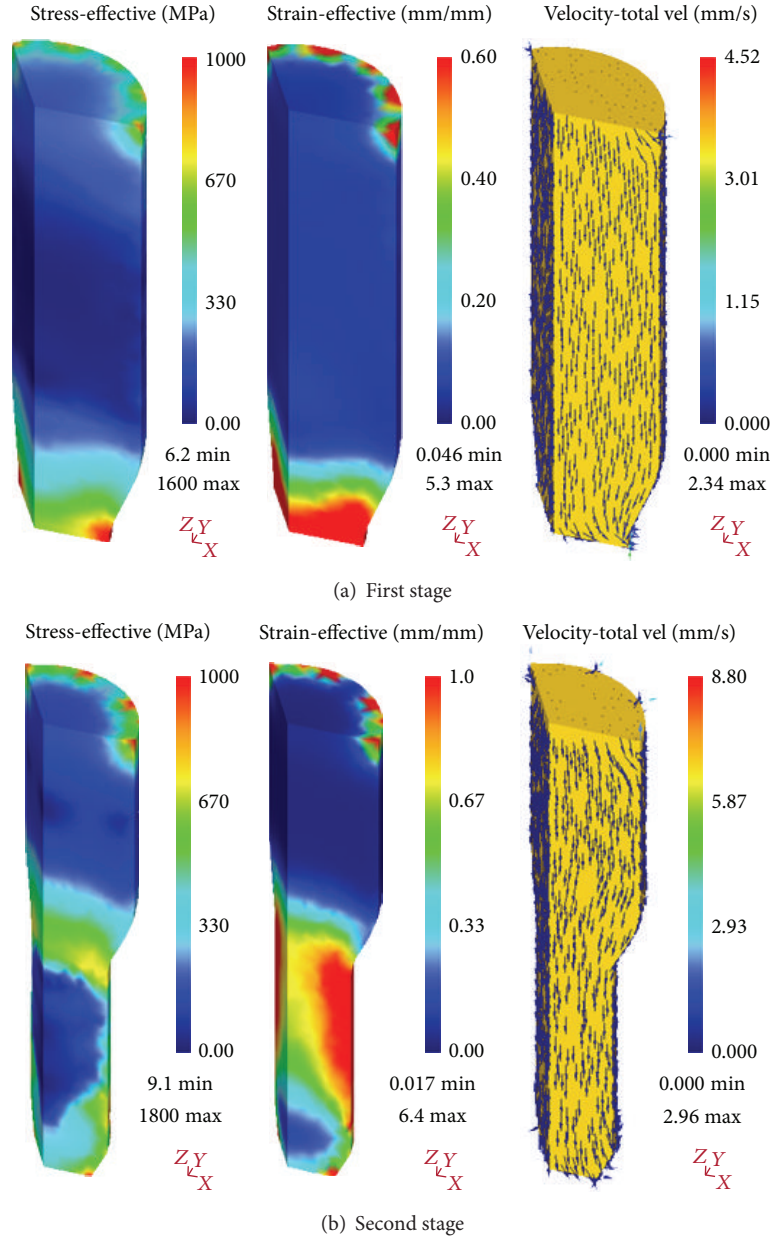


FIGURE 7: Stress-effective, strain-effective, and velocity of extrusion in 3D.

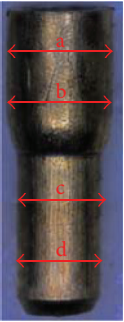
TABLE 4: Response table of punch load in different levels of S/N ratio.

	A	B	C	D
Level 1	-59.10	-60.65	-60.93	-60.05
Level 2	-61.70	-60.46	-59.87	-61.50
Level 3	-60.15	-59.84	-60.16	-59.40
Range	2.60	0.82	1.06	2.10
Rank	1	4	3	2

Comparison of the simulation and experimental results shown in Figure 9 reveals no significant difference. Table 5

shows mean and standard deviation (SD) values on the basis of three micropins for second stage. In this table, two diameters 1.14 mm and 0.88 mm and four measurement positions of the deformed micropin are used to verify the satisfactory results. All SD values are from 0.001 to 0.006 mm. When considering the relations of stroke load, Figure 10 indicates the situation of the two stages in three cases: the experiment result, the simulation of the rigid die, and the elastic-plastic die. Although the simulation load would suddenly rise when die is set as a rigid body, which is different from the experimented forming load, they always have the same tendency. When the die cavity is filled with the raw material, the increased drag force quickly induces the major stroke load in all cases. As a result, Figure 10 implies that the die is set as a

TABLE 5: Dimensions of the deformed micropin.

	Position	Measurement (mm)			Mean \pm SD (mm)	Standard dimension (mm)
		a	b	c		
	a	1.133	1.149	1.145	1.142 ± 0.0068	1.14 ± 0.01
	b	1.121	1.133	1.124	1.126 ± 0.0051	
	c	0.880	0.879	0.882	0.880 ± 0.0013	0.88 ± 0.01
	d	0.877	0.870	0.876	0.874 ± 0.0031	

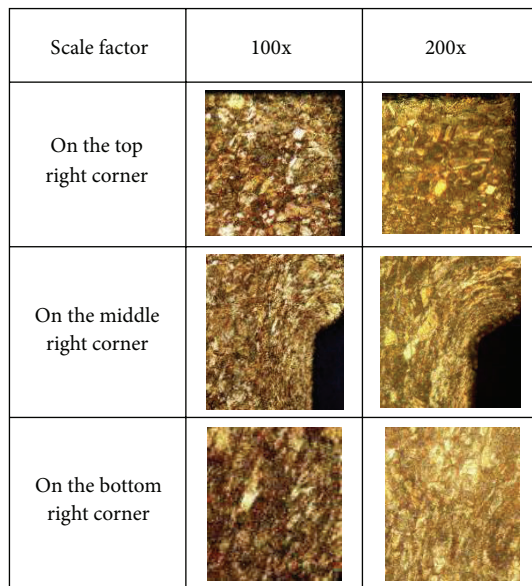
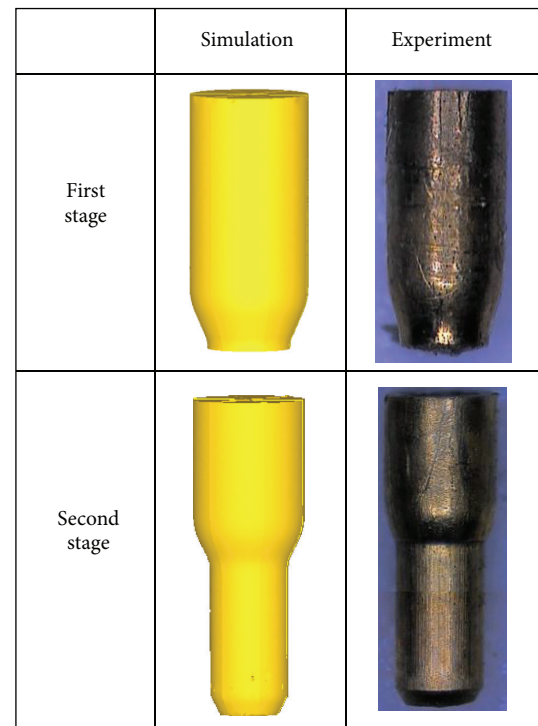


FIGURE 8: Microstructure of deformed brass sample.

flexible body in the simulation, and the simulated stroke-load tendency is close to the experimental result.

5. Conclusion

This study simulates the forming punch head of brass micropin with minimum diameter 0.8 mm. Under various factors, the effects of performance design and pin shape on cavity extrusion filling are experimentally verified. The process is completed using two-stage forming. The first stage, performance of forming, produces a stage rod with a workpiece through forward extrusion. The second stage then completes the cavity filling. Besides performance, namely, the design of stage rod, the effects of pin shape on the process are also considered. The research outcomes are summarized below.

FIGURE 9: Predicted results and extruded products ($h = 0.05$ mm, $\phi = 60^\circ$, $\alpha = 60^\circ$, and $\beta = 60^\circ$).

- (1) This study shows a potential tool on the combination of Taguchi method and DEFORM-3D software to simulate the microforming process.
- (2) The stage rod length is the largest factor in the experimental results, followed by bottom stage angle, upper front-end taper, and extruding angle.
- (3) The forming conditions of optimal microextrusion appear on stage rod length 0.015 mm, extruding angle 60° , upper front-end taper 60° , and bottom stage angle 60° .
- (4) The dimensions of the deformed micropin reveal a good identification with the simulation.

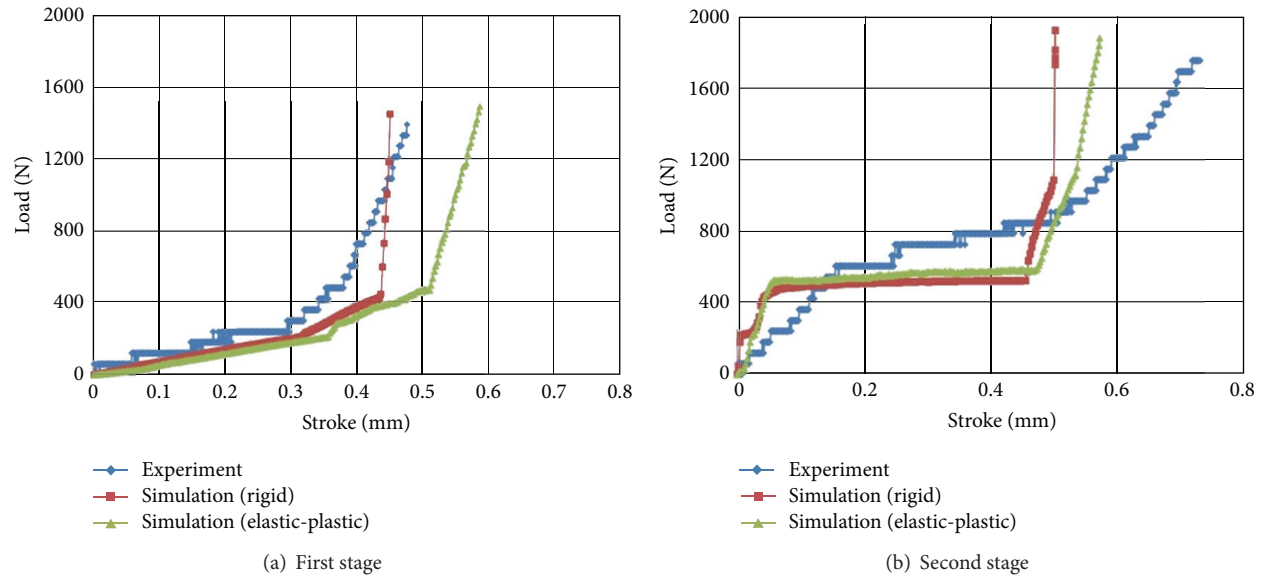


FIGURE 10: Predicted and measured loads.

Satisfactory results are obtained in this research. It hence proposes a good analysis technology to manufacture successfully the microsized fastener for the industry.

References

- [1] C.-Y. Wu and Y.-C. Hsu, "The influence of die shape on the flow deformation of extrusion forging," *Journal of Materials Processing Technology*, vol. 124, no. 1-2, pp. 67–76, 2002.
- [2] H. S. Syu, "A study on precision forging of bevel gear by using finite element method," Report on the outcome of the National Science Council Research Project, 2003.
- [3] Y. A. Chen, C. F. Wu, and H. C. Tsai, "The development of the micro terminal of battery con-tact device for mobile phone," *Forging*, vol. 13, pp. 52–57, 2004.
- [4] J.-T. Gau, C. Principe, and J. Wang, "An experimental study on size effects on flow stress and formability of aluminum and brass for microforming," *Journal of Materials Processing Technology*, vol. 184, no. 1-3, pp. 42–46, 2007.
- [5] C. Hu, K. Wang, and Q. Liu, "Study on a new technological scheme for cold forging of spur gears," *Journal of Materials Processing Technology*, vol. 187-188, pp. 600–603, 2007.
- [6] D. J. Yoon, S. J. Lim, H. G. Jeong, E. Z. Kim, and C. D. Cho, "Forming characteristics of AZ31B magnesium alloy in bidirectional extrusion process," *Journal of Materials Processing Technology*, vol. 201, no. 1-3, pp. 179–182, 2008.
- [7] M.-C. Sun, G.-Y. Tzou, and L.-A. Zheng, "Processing animation simulation and FEM analysis of multi-stage cold forging of stainless automotive battery fastener," *Indian Journal of Engineering & Materials Sciences*, vol. 20, pp. 219–224, 2013.
- [8] L. F. Mori, N. Krishnan, J. Cao, and H. D. Espinosa, "Study of the size effects and friction conditions in microextrusion—part II: size effect in dynamic friction for brass-steel pairs," *Journal of Manufacturing Science and Engineering*, vol. 129, no. 4, pp. 677–689, 2007.
- [9] J. Cao, N. Krishnan, Z. Wang, H. Lu, W. K. Liu, and A. Swanson, "Microforming: experimental investigation of the extrusion process for micropins and its numerical simulation using RKEM," *Journal of Manufacturing Science and Engineering*, vol. 126, no. 4, pp. 642–652, 2004.
- [10] K. H. Huebner and E. A. Thornton, *Finite Element Method*, Hsiao Yu-an Publishing, Taipei, Taiwan, 1984, translated by C.-C. Wang.
- [11] S. Isogawa, I. Mori, and Y. Tozawa, "Determination of basic data for numerical simulation," *The Japan Society for Technology of Plasticity*, vol. 38, no. 5, pp. 480–485, 1997.

Research Article

Construction of the Control System of Cleaning Robots with Vision Guidance

Tian-Syung Lan,¹ Long-Ji Yeh,² Min-Chie Chiu,³ and You-Xiang Hwang²

¹ Department of Information Management, Yu Da University of Science and Technology, Miaoli 36143, Taiwan

² Department of Mechanical Engineering, Tatung University, Taipei 104, Taiwan

³ Department of Mechanical and Automation Engineering, Chung Chou University of Science and Technology, Changhua 510, Taiwan

Correspondence should be addressed to Tian-Syung Lan; tslan888@yahoo.com.tw

Received 15 September 2013; Revised 16 October 2013; Accepted 16 October 2013

Academic Editor: Teen-Hang Meen

Copyright © 2013 Tian-Syung Lan et al. This is an open access article distributed under the Creative Commons Attribution License, which permits unrestricted use, distribution, and reproduction in any medium, provided the original work is properly cited.

The study uses Kinect, modern and depth detectable photography equipment to detect objects on the ground and above the ground. The data collected is used to construct a model on ground level, that is, used lead automatic guiding vehicle. The core of the vehicle uses a PIC18F4520 microchip. Bluetooth wireless communication is adopted for remote connection to a computer, which is used to control the vehicles remotely. Operators send movement command to automatic guiding vehicle through computer. Once the destination point is identified, the vehicle lead is forward. The guiding process will map out a path that directs the vehicle to the destination and void any obstacles. The study is based on existing cleaning robots that are available. Aside from fixed point movement, through data analysis, the system is also capable of identifying objects that are not supposed to appear on the ground, such as aluminum cans. By configuring the destination to aluminum cans, the automatic guiding vehicle will lead to a can and pick it up. Such action is the realization of cleaning function.

1. Introduction

Since the first robot made its appearance in the 1960s, there has been significant development progress in the past 40 years [1, 2]. On the other hand, with the advancement of computer processing power, the maturity of wireless transmission technology, and the popularity of personal mobile devices, consumer electronic devices have become a normality and can be seen everywhere [3]. In addition, the advancement of processor's commutation capacity allows technologies that were originally researched in labs, such as machine vision and virtual reality, can be applied to consumer products. This brings a wide range of possibilities, such as cleaning robot, human imitation robot, agriculture robot, service robot, underwater robot, medical robot, military robot, and entertaining robot [4, 5]. The technologies used within these automatic guiding robots, such as robot control technology, sensor technology, multirobot coordination technology, and communication technology, are being applied for practical use in a growing number of situations [6–8].

The research objective of this study focuses on how to use digital processing technology to develop home-use intelligent vacuum cleaner. Image segmentation is an important process in digital processing technology. The research focuses on cleaning robots and how its image guidance can be enhanced by applying the depth detection capability by using the modern detection device of Kinect.

2. System Structure

2.1. Master Robot System Structure Planning. The purpose of the system is to construct a robot group in which individuals are capable of share cleaning workloads automatically. Figure 1 illustrates the master robot's system structure. The master robot takes the lead and commands all slave robots. The number of slave robots is adjustable based on the task range and other demands. By adopting many slave robots of the same type, the robots can share workloads and speed up the task time required. The master robot system equips

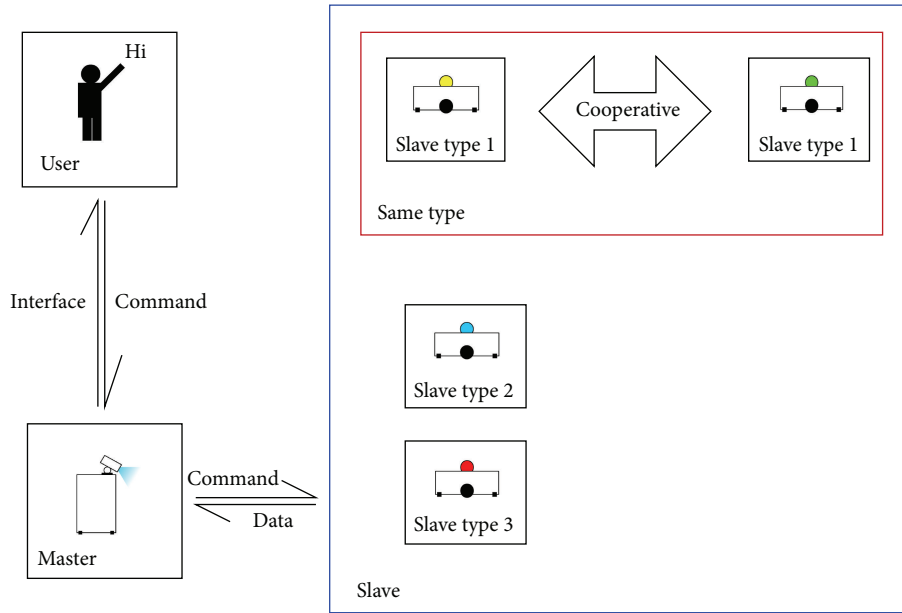


FIGURE 1: System structure of a master robot.

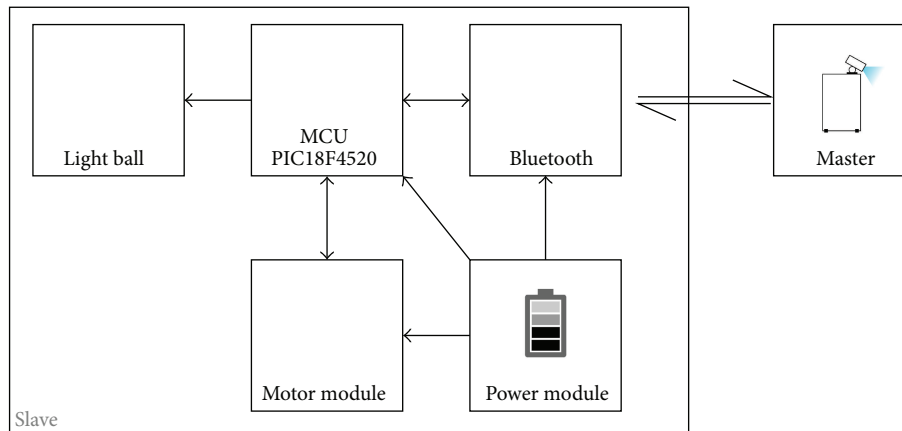


FIGURE 2: Hardware structure of a slave robot.

Bluetooth and Wi-Fi wireless communication. The communication between master and slave robots is conducted via wireless communication. Communication type includes commands, reporting project progress, malfunction reports, and other data transmissions.

2.2. *Hardware Design of Slave Robots.* The hardware structure of slave robots is shown in Figure 2. Microprocessor PIC18F4520 works as the central processor. It conducts wireless communication via Bluetooth module, which receives commands sent by master robot and sends back status reports. The slave robot illustrated in this study is an experimental prototype. The device carries only the basic accessories that are required for slave robot to move according to master robot's command. The robot does not have the capability for exploration and cleaning. Slave robot structure includes processing center, Bluetooth module, power module, movement module, and light ball module.



FIGURE 3: Bluetooth module.

2.3. *Bluetooth Module.* The Bluetooth module used on slave robots is ZX-BLUETOOTH, which is shown in Figure 3. Its Bluetooth capability only contains the slave mode and not the

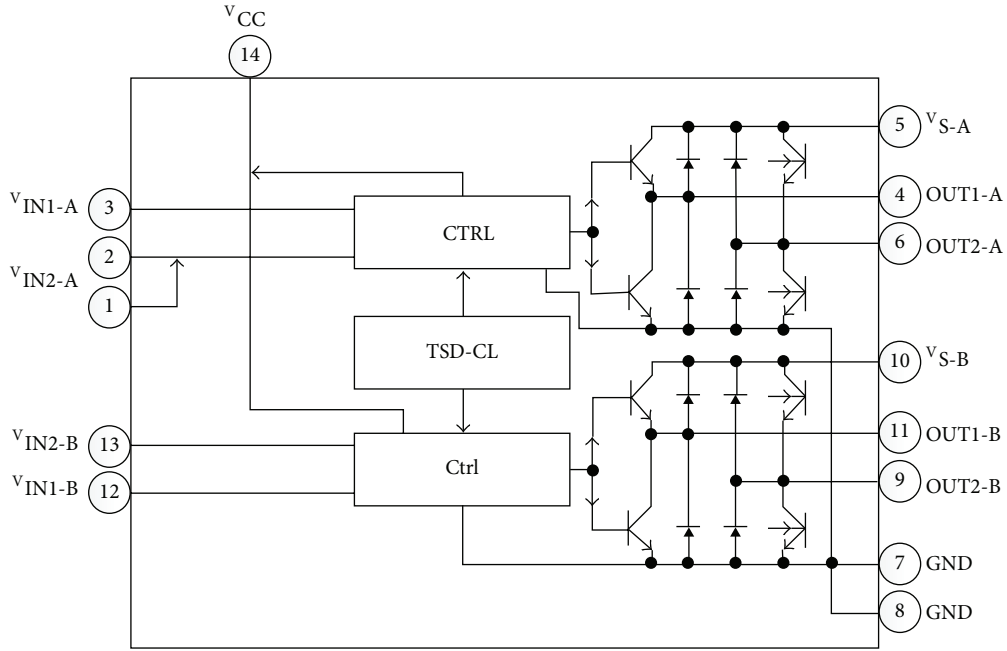


FIGURE 4: TA7279 block diagram.

master mode. Serial data can be transmitted via Tx and Rx pin for input and output.

2.4. Movement Module. DC motor controller TA7279P is used as movement module. The module controls motor rotation. Two DC motors are used as the power source of the automatic guiding vehicle. Each TA7279P is equipped with two sets of H Bridge, which is shown in Figure 4. The PWM output of microprocessor also contributes to the adjustment of motor speed.

2.5. Light Ball Module. The main purpose of light ball module is to indicate the current status by its color. It can also help in allowing the master robot to detect the position of the slave robot. The master robot detects the light via its camera. Therefore the light ball is positioned at the top of the slave robot to avoid being blocked by robot body or other obstacles. The red, green, and blue LED are installed inside the light ball and can provide 8 different colors of light. The master robot uses the light to identify different slave robots. The color can also help operator understand slave robots' status.

3. Figures Processing

3.1. Depth Test. The position of infrared projector and the recording camera is positioned at different level. According to the experiment results as shown in Table 1, objects must be at least 0.5 m away from the camera to generate stable results on depth. When the distance is close to 0.5 m, the depth resolution is up to 1 mm. As distance increases, the resolution

TABLE 1: Kinect distance test result.

Actual distance (cm)	Value
50	396
50.1	397
50.2	398
50.3	400
50.32	401
50.4	402
51.03	409
51.06	410
51.1	411
51.15	412
51.3	413
51.5	414
145	849
150	857
155	864
160	872
165	878
170	885

decreases gradually as shown in Figure 5. When the object distance reaches 4 meters, the resolution is reduced to about 50 mm.

3.2. Accelerometer Angle Test. Accelerometers are built in all three axes of Kinect. Their purpose is to measure the acceleration speed from all angles. The association between accelerometer and gravity can be used to deduct the horizontal level of Kinect. If the device is not fully parallel with

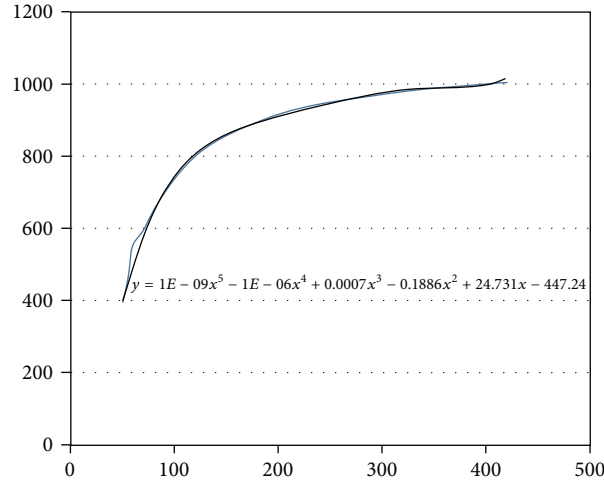


FIGURE 5: Kinect distance test result.

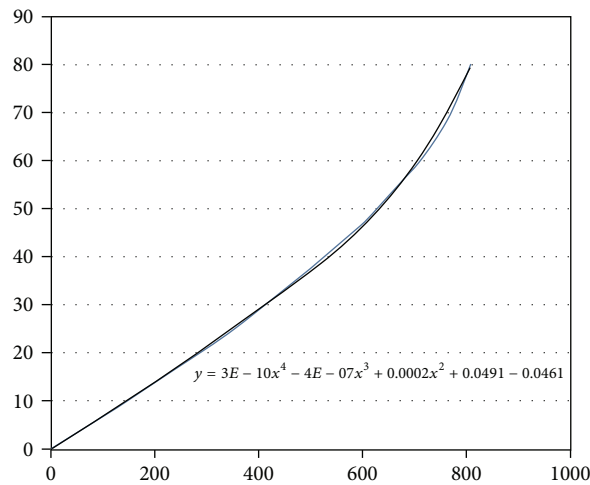


FIGURE 6: Acceleration speed test result.

ground level, the angle that forms by the two is called “dip angle.” Table 2 and Figure 6 display the acceleration speed measured by accelerometer when Kinect is positioned in different angles against the ground level.

4. Guiding Path Design and Slave Robot Guidance

4.1. Guiding Path Design. Before deciding on a guiding path, the master robot needs to draw up a map and locate the coordinates of slave robots. The slave robots are guided by the master robot to reach the indicated positions, which are decided by the operator. The designed path is based upon the map drawn by the master robot and the position function built within slave robots. These two required steps must be decided before the experiment begins. The map layout and the position of the slave robots are marked out. The operator decides on slave robots destination point and begins path planning.

TABLE 2: Accelerometer test result.

Angle	Value
0	4
10	145
20	290
30	417.3333
45	580
60	710.6667
70	769
80	806
90	810.6667

4.2. Slave Robot Guidance. Once the path is set, master robot sends the command to slave robots and guides them to the destination as shown in Figure 7. Slave robots are only capable of rotating and moving forward. Path direction is presented as combinations of angles and distance. After the figures are readjusted by angle encoder or slave robots’ correction adjustment, the numbers are sent to slave robot’s

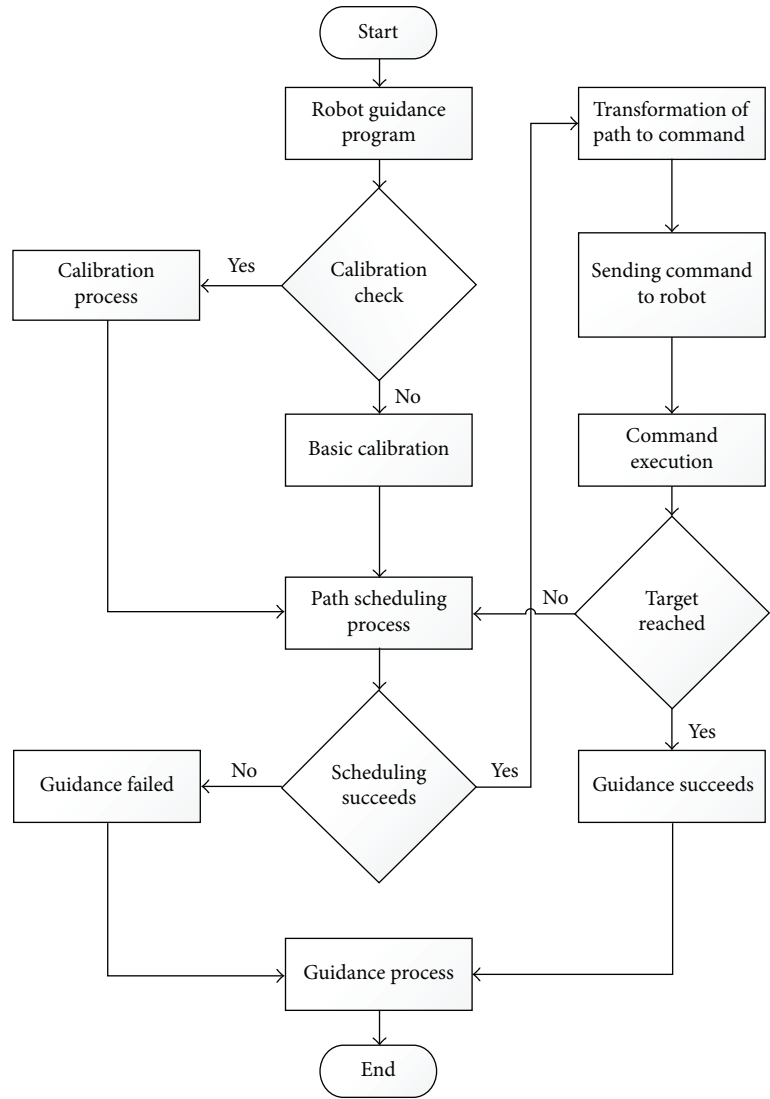


FIGURE 7: Slave robot guidance flowchart.

task scheduler. Slave robots perform tasks according to task sequence. Once all tasks are carried out, operators check to see if the device has reached the destination.

In Figure 8(a), red block is preset destination. Once the destination is set, slave robots start to perform tasks. First is motion adjustment. Figures 8(b) to 8(d) show the standard actions during the adjustment. The slave robots move forward for 5 seconds, make a 3-second right turn, and move forward for another 2 seconds. After the motion adjustment, the slave robot will head toward the destination. Figure 8(f) shows that the slave robot reaches the destination. Figure 8(g) is what the operator observes on the computer screen.

5. Results and Discussion

Video recorders are easily affected by external lights. Therefore, the depth of the surrounding is taken into consideration during data analysis. This will avoid any possible decision errors that are caused by objects brightness, which sometimes

may be too bright to affect the environment. During the object search, the main objective is to check if the depth value taken by infrared camera is different from the pre-constructed map data. The differences will be marked out.

6. Conclusions

The development of an automatic guiding vehicle guidance system is based on the infrared ray within Kinect. Digital processing and roadmap planning were used to map out the test area and construct guiding path. Bluetooth modules are used to help the master robot guide slave robots within Kinect recorder’s detectable distance. Through the design, the slave robots are able to avoid obstacles and reach the destination point.

The research can be extended to adding cleaning tools, such as clamps used to pick up aluminum can, on slave robots. Master robots detects aluminum can and guides slave robots to pick up the aluminum can, or sorting out the cans



FIGURE 8: Operation procedure.

from other materials. Another research direction is to use the motion capture device of Kinect and the microphone array feature to replace tradition user experience that is carried out with computer screens and mouse. Operators can stand in front of the master robot, making commands through motion, hand gesture, and voice control. For example, the operator points to the aluminum can and speaks the word “clean.” The master robot can detect the operator’s current action and the vector value extended from the arm to find the can’s coordinates. Slave robots can be sent out to execute the task.

References

- [1] E. R. Benson, J. F. Reid, and Q. Zhang, “Machine vision-based guidance system for agricultural grain harvesters using cut-edge detection,” *Biosystems Engineering*, vol. 86, no. 4, pp. 389–398, 2003.
- [2] Z. Hunaiti, V. Garaj, and W. Balachandran, “A remote vision guidance system for visually impaired pedestrians,” *Journal of Navigation*, vol. 59, no. 3, pp. 497–504, 2006.
- [3] M. P. Heilbrun, P. McDonald, C. Wiker, S. Koehler, and W. Peters, “Stereotactic localization and guidance using a machine vision technique,” *Stereotactic and Functional Neurosurgery*, vol. 58, no. 1–4, pp. 94–98, 1992.
- [4] J. Billingsley and M. Schoenfisch, “The successful development of a vision guidance system for agriculture,” *Computers and Electronics in Agriculture*, vol. 16, no. 2, pp. 147–163, 1997.
- [5] N. D. Tillett and T. Hague, “Computer-vision-based hoe guidance for cereals—an initial trial,” *Journal of Agricultural Engineering Research*, vol. 74, no. 3, pp. 225–236, 1999.
- [6] E. R. Benson, J. F. Reid, and Q. Zhang, “Machine vision-based guidance system for an agricultural small-grain harvester,” *Transactions of the American Society of Agricultural Engineers*, vol. 46, no. 4, pp. 1255–1264, 2003.
- [7] S. Han, Q. Zhang, B. Ni, and J. F. Reid, “A guidance directrix approach to vision-based vehicle guidance systems,” *Computers and Electronics in Agriculture*, vol. 43, no. 3, pp. 179–195, 2004.
- [8] C.-C. J. Ho and N. H. McClamroch, “Automatic spacecraft docking using computer vision-based guidance and control techniques,” *Journal of Guidance, Control, and Dynamics*, vol. 16, no. 2, pp. 281–288, 1993.

Research Article

Influential Factors and Strategy of Sustainable Product Development under Corporate Social Responsibility in Taiwan

Jui-Che Tu,¹ Pi-Lien Chiu,^{1,2} Yu-Chen Huang,¹ and Chuan-Ying Hsu³

¹ Graduate School of Design Doctoral Program, National Yunlin University of Science and Technology, Yunlin County 640, Taiwan

² Department of Product Design, Tung-Fang Design Institute, Kaohsiung 829, Taiwan

³ Department of Business Administration, Dayeh University, Changhua City 515, Taiwan

Correspondence should be addressed to Jui-Che Tu; tujc@yuntech.edu.tw

Received 28 September 2013; Accepted 16 October 2013

Academic Editor: Teen-Hang Meen

Copyright © 2013 Jui-Che Tu et al. This is an open access article distributed under the Creative Commons Attribution License, which permits unrestricted use, distribution, and reproduction in any medium, provided the original work is properly cited.

This study aimed to adopt the perspective of corporate social responsibility (CSR) to explore the intention of sustainable product development in Taiwan, as well as leading to the creation of influential factors that affect corporate sustainable product development intention. In this research, the induction analysis was conducted to understand the implementation of sustainable product development, and this was supplemented with questionnaire surveys and in-depth interviews to evaluate developmental intention. In addition, principal component analysis was used for factor analysis and content analysis in the 6 W expression method, leading to the creation of the influential factors. The research results have demonstrated that the factors affecting the intention of corporate sustainable product development include having a sustainable design and a development purpose, a corporate development purpose, sustainable development concepts, a sustainable design value, a sustainability concept, and a manufacturing process quality. For sustainable product development, corporate social responsibility needs to be most concerned with the added value of products, regulation requirements, and accommodation of the industrial chain, costs, and quality.

1. Introduction

In modern society, the concept of sustainable development is based on three factors, which are economic development, environmental conservation, and social justice. While pursuing new economic development models, the long-term sustainable development should not be neglected for short-term individual benefits. In economic development, the environmental load should be balanced and buffered, and the natural resources and environments needed by human beings should be well protected, instead of abusing environmental resources. Development should be accompanied by contribution to the society; thus, there should be a balanced model of sustainable development based on the economy, environment, and society in order to accomplish sustainable development in human society [1, 2].

As corporate social responsibility (CSR) is gradually valued, firms usually have to deal with difficult problems regarding green issues in corporate sustainable development. Regarding environmental pollution caused by 3C electronic

products in particular, firms should try to undertake CSR, while simultaneously achieving greater successful and stable sustainable development in design. Since the issues of global warming and climatic change become important, countries around the globe value the importance of constructing green civilization, and related measures of environmental protection become more complete [3]. The establishment of environmentally friendly green industry policies, finance policies, and tax policies and the enhancement of laws of environmental protection and complete management system result in harmony between human beings and nature, and they are important policies for the present and future of different countries [4, 5]. Therefore, while the government actively reviews overall economic direction and implements new tax reform, firms should more positively implement sustainable development and product sustainable development design.

The corporate cognition and practice of social responsibility have evolved from a narrow to a broad sense. In Europe, Japan, and the USA, the concept of the corporate social

citizen has become common. However, in Taiwan, the concept of CSR is still new. Therefore, when overseas cognition of CSR makes progress, firms in Taiwan are still at the level of charities and fundamental associations [6, 7]. Regarding firms' difficulties in implementation of sustainable development, 53.4% of firms suggest the lack of a guidance mechanism, 50.9% suggest that costs are too high, 38.8% suggest the existence of ambiguous governmental laws, and 35.3% indicate a lack of related professional knowledge. As to corporate sustainable development policy in regards to green business policy, 90.5% of firms suggest the importance of resource recovery, 83.6% use energy-saving devices, and 61.2% identify with the improvement of production [8].

Regarding positive development upon CSR, firms should not only be familiar with international laws and have significant support and guidance from government, but they should also possess the concepts of sustainable development, positive professional sustainable development, and responsive ability. However, firms sometimes cannot fulfill this responsibility due to a lack of management time and the traditional profit-oriented concept of business [9, 10], and they tend to be passive and careless regarding sustainable development. However, nowadays, with green trends, sustainable products should be based on the concerns of development procedures, including material selection, manufacturing, innovation, assembly, transportation, dismantling, and recycling. Firms should try to obtain a balance in sustainable development within this trend in order to enhance corporate image in the market after product sustainable development [11–13].

For successful sustainable development, at the decision-making stage, firms must consider the impact on the environment, the direction after green product manufacturing, and the resulting waste. They must notice the demonstration of CSR and the increase of public consciousness of sustainability [14]. Therefore, in sustainable development, besides the sustainable perspective, they should consider the issues important for consumers and future trends, including corporate social image, positive attitude, and acceptance regarding corporate sustainable development in order to further recognize the important trend of sustainable development [15–17]. Firms must then explore the different degrees of implementation in decision-making of sustainable development, developmental intention, and difference, which will not only enhance firms' sustainable product development intention but will also solve the problems encountered during development. Therefore, firms, consumers, and social environments will be sustainable and developed by mutual dependency [18–20]. This study will analyze and conduct cross-comparison on the investigation of CSR, the degree of corporate product sustainable development, and the factors. Finally, the researcher constructs influential factors and strategy of sustainable product development as the criterion for the implementation of other related firms. Thus, based on the above analysis, this study aimed to explore correlation and effects of current corporate-developed sustainable products and the effects of sustainable product development intention.

Using interviews, this study probed into CSR and the current situation of corporate sustainable product development. In addition, it analyzed and conducted cross-comparisons of

the impact factors. Finally, a coping model was constructed for corporate sustainable product development. The findings can serve as references for the implementation of corporate development of sustainable products.

2. Research Structure and Method

2.1. Research Structure. This study first reviewed their literatures related to CSR and sustainable product development in order to explore the correlation between CSR and sustainable product development. Secondly, using a questionnaire survey and in-depth interviews, this study investigated current sustainable product development under CSR and conducted an intention survey. SPSS was used to practice frequency distribution and factor analysis in order to establish factor analysis of the factors of sustainable product development under CSR. Content analysis of 6 W was conducted to explore the current sustainable product development under CSR. Finally, the results of the above two surveys and the literature review were generalized to propose future development intentions of sustainable product development under CSR and to construct an interactive influential model of sustainable product development under CSR (Figure 1).

2.2. Research Subjects. In order to explore the current situation and intentions of sustainable product development under CSR, the factors of different dimensions are investigated in this study. The research subjects investigated were experts in product design, management, and marketing as well as design strategy in the most representative and large-scale enterprises among the 3C industries in Taiwan such as ASUSTeK Computer, Inc. (ASUS), Chi Mei Optoelectronics Corporation, Hewlett-Packard Development Company (HP), and National Council for Sustainable Development Network, as illustrated in Table 1, and these top four enterprises all practice a CSR system. The research subjects include four senior product designers, three product marketing managers, and one development strategy director. A questionnaire survey and in-depth interviews were conducted to acquire in-depth and valid data. In addition, a number of representative research institutes from the National Council for Sustainable Development Network are also interviewed to obtain information and suggestions.

2.3. Data Collection Procedure. In order to recognize the current situation and intentions of corporate sustainable product development under CSR, this study collected data using a questionnaire survey and in-depth interviews. The questionnaire design includes three parts. Part 1 was the subjects' basic information, Part 2 was an investigation of the current sustainable development situation, and Part 3 was an investigation of sustainable product development intentions. The questionnaire aimed to determine the factors of the corporate subjects' sustainable product development under CSR with the purpose that acquiring factors of sustainable product development can explore relationship between the current situation of sustainable product development and the increase of intention by corporate researchers. Finally,

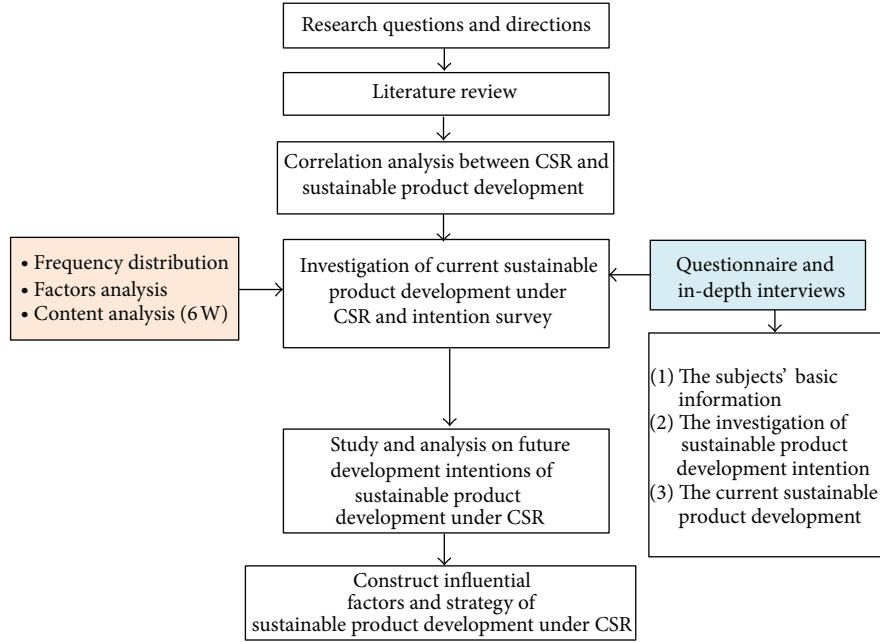


FIGURE 1: Research structure.

TABLE 1: Research subjects' backgrounds.

No.	Name of corporation/council	Subjects	People	Years	Specialty
1	ASUS	Product designers	2	10 and 12	Product development and design
		Managers	1	10	Product marketing
2	Chi Mei Optoelectronics Corporation	Product designers	1	8	Product development and design
		Managers	1	12	Product marketing and plan management
3	HP	Product designers	1	10	Product development and design
		Managers	1	15	Product marketing
4	National Council for Sustainable Development Network	Director	1	9	Sustainable development strategy

this study developed the factor analysis as a resource of sustainable product development to be used as a reference for future coping models of corporate sustainable product development.

2.4. *Data Analysis.* After collecting data using the above methods, in order to thoroughly recognize the corporate subjects' views toward sustainable product development under CSR and the current situation, this study adopted SPSS to analyze the data of the questionnaire survey and conduct frequency distribution and principal component analysis. The analysis was based on 18 items of sustainable product development intention (Table 2). This study extracted the impact factors of sustainable product development intention, acquired their weights and rankings using SPSS, and recognized the implied design development points from the data.

In order to thoroughly interpret the interviews with the enterprises, this study conducted content analysis, which is a

research method that uses objective, systematic, and quantitative descriptions of the content. It includes the characteristics of objectivity, systematicness, quantitiveness, and manifestness [21]. Consider the following.

- (1) *Objectivity.* Data interpretation and coding do not totally rely on the researcher's explanation. They are based on consistent and systematic rules in order to guarantee the consistent results of different persons at different times.
- (2) *Systematicness.* The main purpose is to show the truth. It is the other side of objectivity. The research step design should be based on precise rules. With systematic coding rules, research reliability can be guaranteed.
- (3) *Quantitiveness.* The text can be transformed into figures. In other words, qualitative data is transformed into quantitative data. Quantitative applications are based on the measurements and items which are

TABLE 2: Questions of sustainable product development intention.

No.	Questions
1	In the development of all products, sustainable development is the priority.
2	Besides product costs, product profits, environmental protection, and maximum social welfare are secondary concerns.
3	Sustainable product development makes products different.
4	To identify with the view that sustainable design is valuable.
5	Sustainable design products are developed since the quality is guaranteed.
6	Products are developed for sustainable design.
7	Sustainable products are developed for CSR.
8	When prices are the same, products of sustainable design will be developed.
9	The sustainability of products is not important. We only develop products with the highest profits.
10	Firms will develop the products because of the sustainability.
11	The main value of your sustainable products is profit.
12	The main values of sustainable products are based on environmental protection and social welfare.
13	The increase of sustainable product development intention is based on governmental laws and corporate development planning.
14	The concern is the practicability of products and pollution, and the sustainability of products is not important.
15	Brand image will influence your sustainable development.
16	The increase of sustainable product development intention is based on the increase of talents and professional knowledge.
17	The sustainable products differ from the design and products of other brands.
18	In the era of CSR, the value of sustainable product design is the most significant.

generally the frequency, percentage, chi-square value, and population tests, such as the t -test, regression, and factor analysis.

- (4) *Manifestness*. It studies the content of propagation and the effect. Content can be implied by various symbols or words. In other words, something is hidden in the propagation. After the data are screened and interpreted, the hidden meanings will be shown.

The above characteristics matched the data analysis of this study. Thus, by content analysis of 6 W, this study analyzed the qualitative data of the in-depth interviews. The content analysis and the 6 W were used to find the message to the receivers, why and how the message was sent, and the effect of the message (Table 3) in order to completely interpret the environmental backgrounds of the subjects and the meanings [22].

3. Research Analysis and Results

3.1. Intentions of Sustainable Product Development under CSR. In this study, a total of 12 questionnaires were distributed, and there were 12 returns. The principal component factor analysis technique is employed for extracting firms' factors of sustainable product development intention under CSR. Factor analysis is used to uncover the latent dimensions of a set of variables. It reduces attribute space from a larger number of variables to a smaller number of factors. The mathematical framework of the principal component factor analysis is to be presented as follows.

Assuming a set of p new variables, each variable can be represented as a linear transformation of q common factors f_j and specific factors ε_i . Consider the following:

$$\begin{aligned}
 x_1 &= \mu_1 + l_{11}f_1 + l_{12}f_2 + \cdots + l_{1q}f_q + \varepsilon_1, \\
 x_2 &= \mu_2 + l_{21}f_1 + l_{22}f_2 + \cdots + l_{2q}f_q + \varepsilon_2, \\
 x_3 &= \mu_3 + l_{31}f_1 + l_{32}f_2 + \cdots + l_{3q}f_q + \varepsilon_3, \\
 &\vdots \\
 x_p &= \mu_p + l_{p1}f_1 + l_{p2}f_2 + \cdots + l_{pq}f_q + \varepsilon_p,
 \end{aligned} \tag{1}$$

where $q < p$ and l_{ij} is the factor loading which represents the loading or weights of the i th variable on the j th common factor, and it is given as follows:

$$l_{ij} = \frac{w_{ij}\sqrt{\lambda_j}}{s_i}, \tag{2}$$

where w_{ij} is the weights of the i th variable on the j th common factor, λ_j is the eigenvalue of the j th common factor, and s_i is the standard deviation of the i th variable. Factor loading represents the correlation between a specific observed variable and a specific factor, and higher value means a closer relationship.

The linear transformations as illustrated in (1) can be expressed in terms of matrix form as

$$X = \mu + LF + \varepsilon, \tag{3}$$

TABLE 3: 6 W of content analysis.

Item	Definition	Explanation
Who	Study on message sources	The author's capability, characteristics or ideology, and value system.
What	Message content	To study the change of content in different places and at different times, as well as the relationship between the authors' characteristics and content and the content matching external criteria.
Whom	Message receiver	To find whether there are different propagation implications for different message receivers.
How	Skill of message propagation	Subjects are not limited to words.
What effect	Message effect	To study the effect after message propagation.
Why	Reason of message propagation	To study the author's motives.

where

$$\begin{aligned}
 X &= \begin{bmatrix} x_1 \\ x_2 \\ x_3 \\ \vdots \\ x_p \end{bmatrix}, & \mu &= \begin{bmatrix} \mu_1 \\ \mu_2 \\ \mu_3 \\ \vdots \\ \mu_p \end{bmatrix}, \\
 L &= \begin{bmatrix} l_{11} & l_{12} & l_{13} & \cdots & l_{1q} \\ l_{21} & l_{22} & l_{23} & \cdots & l_{2q} \\ l_{31} & l_{32} & l_{33} & \cdots & l_{3q} \\ \vdots & \vdots & \vdots & \ddots & \vdots \\ l_{p1} & l_{p2} & l_{p3} & \cdots & l_{pq} \end{bmatrix}, & (4) \\
 F &= \begin{bmatrix} f_1 \\ f_2 \\ f_3 \\ \vdots \\ f_p \end{bmatrix}, & \varepsilon &= \begin{bmatrix} \varepsilon_1 \\ \varepsilon_2 \\ \varepsilon_3 \\ \vdots \\ \varepsilon_p \end{bmatrix}.
 \end{aligned}$$

The matrix L is called the factor loading matrix or factor pattern matrix. Meanwhile, the following assumptions are defined:

$$\begin{aligned}
 E(F) &= 0, & \text{Cov}(F) &= \Phi, \\
 E(\varepsilon) &= 0, & \text{Cov}(\varepsilon) &= \Psi, & (5) \\
 \text{Cov}(F, \varepsilon) &= 0,
 \end{aligned}$$

where specific factors ε_i , $i = 1, 2, \dots, p$, are assumed uncorrelated and the expected values are 0 such that $E(\varepsilon_i) = 0$, for all i . The variances of these specific factors can be defined as the normal distribution of ψ_i , $i = 1, 2, \dots, p$, such that

$$\Psi = \begin{bmatrix} \psi_1 & 0 & 0 & \cdots & 0 \\ 0 & \psi_2 & 0 & \cdots & 0 \\ 0 & 0 & \psi_3 & \cdots & 0 \\ \vdots & \vdots & \vdots & \ddots & \vdots \\ 0 & 0 & 0 & \cdots & \psi_p \end{bmatrix}. \quad (6)$$

For the common factors, $\text{Cov}(F)$ is the covariance matrix and is equal to

$$\begin{aligned}
 \text{Cov}(F) &= \sigma(F, F) = E(FF^T) \\
 &= \Phi = \begin{bmatrix} \phi_{11} & \phi_{12} & \phi_{13} & \cdots & \phi_{1q} \\ \phi_{21} & \phi_{22} & \phi_{23} & \cdots & \phi_{2q} \\ \phi_{31} & \phi_{32} & \phi_{33} & \cdots & \phi_{3q} \\ \vdots & \vdots & \vdots & \ddots & \vdots \\ \phi_{q1} & \phi_{q2} & \phi_{q3} & \cdots & \phi_{qq} \end{bmatrix}, & (7)
 \end{aligned}$$

where F^T is the transpose of the vector F . Generally, vector μ is assumed to be 0, the common factors f_i , $i = 1, 2, \dots, q$, are assumed to be uncorrelated, and the variance of each factor is 1 since the variance is a special case of the covariance when the two variables are identical such that $\sigma(F, F) = \sigma^2(F)$ and $\Phi = I$, where I is an identity matrix.

Similarly, the covariance matrix of the new variables can be defined as [23]

$$\begin{aligned}
 \text{Cov}(X) &= \sigma(X, X) = E(XX^T) \\
 &= E[(LF + \varepsilon)(LF + \varepsilon)^T] \\
 &= E[LF(LF)^T + \varepsilon(LF)^T + LF\varepsilon^T + \varepsilon\varepsilon^T] \\
 &= LE(FF^T)L^T + E(\varepsilon F^T)L^T + LE(F\varepsilon^T) + E(\varepsilon\varepsilon^T) \\
 &= L\Phi L^T = \begin{bmatrix} \sigma_1^2 & 0 & 0 & \cdots & 0 \\ 0 & \sigma_2^2 & 0 & \cdots & 0 \\ 0 & 0 & \sigma_3^2 & \cdots & 0 \\ \vdots & \vdots & \vdots & \ddots & \vdots \\ 0 & 0 & 0 & \cdots & \sigma_p^2 \end{bmatrix}, & (8)
 \end{aligned}$$

where σ_i^2 , $i = 1, 2, \dots, p$, are the eigenvalues λ_i , $i = 1, 2, \dots, p$, of covariance matrix $\text{Cov}(F)$, which represent the contribution of the common factors to the new variables.

Based on the discussion presented in the previous paragraphs, the common factor extracting criterion adopted

TABLE 4: Factors of sustainable product development intention under CSR.

Names of factors	Eigenvalues	Variance explained (in %)	Number
Sustainable development purpose	5.930	22.964	6.8.10.12.13.17
Corporate development purpose	4.205	18.724	2.7.14.15.18
Corporate sustainable development	2.766	17.350	1.4.9
Sustainable development value	2.028	14.188	3.11
Sustainable development activity	1.498	11.303	16.6
Sustainable product quality	1.334	8.948	5

is called the Kaiser criterion which decides the principal components for use by simply selecting the factors with greater than 1 eigenvalues. Consequently, 6 most influential factors are extracted from 18 items of sustainable product development intention as the common factors which participate in further analysis.

In order to facilitate the interpretation of these extracted components that are considered relevant, a rotation procedure which is essential in giving factors meaning is usually followed. The rotating approach has been suggested as it simplifies the component structure and therefore makes its interpretation easier and more reliable. The rotation can be explained as a variety of methods used to further analyze initial components, aiming to make the pattern of loadings clearer and more well-defined, thus revealing a simple structure of the initial information [24]. Among the rotation approaches, Promax rotation method is much more efficient, and it is commonly applied on the large factoring processes.

The Promax rotation with Kaiser normalization and a Kappa parameter of 4 is employed in this research. The Promax rotation computes best orthogonal solution and then relaxes orthogonality constraints to gain simplicity in the interpretation. The amount of relaxation is determined by a parameter called Kappa. The Kappa value of 4 was adopted as it is the most efficient amount of rotation that allows the factors to be correlated [25].

To rotate a factor pattern is to apply a nonsingular linear transformation to the unrotated factor pattern matrix. An optimal transformation is usually defined as a minimization or maximization procedure of a simplicity function. For the Promax rotation, the simplicity function employed is the sum of squared differences between the rotated factor pattern and the target matrix in which the entries are raised to some power (typically between 2 and 4) to make the structure of the loadings become bipolar. The optimal transformation is obtained by minimizing this simplicity function with respect to the choices of all possible transformations [26]. The simplicity function being optimized can be defined as [27]

$$f = c_1 (H - Q) + c_2 (V - Q), \quad (9)$$

where

$$H = \sum_i \left(\sum_j b_{ij}^2 \right)^2, \quad V = \sum_j \left(\sum_i b_{ij}^2 \right)^2, \quad (10)$$

$$Q = \sum_j \sum_i b_{ij}^4,$$

and c_1 and c_2 are constants, b_{ij} represents an element of the rotated pattern matrix, $(H - Q)$ represents variable (row) parsimony, and $(V - Q)$ represents factor (column) parsimony. Thus, the relative importance of both the variable parsimony and the factor parsimony is adjusted using the constants c_1 and c_2 [27]. For rotations with Kaiser normalization, the definition of b_{ij} is replaced by b_{ij}/h_i , where h_i is the communality estimate of the i th variable and is given as follows:

$$h_i^2 = l_{i1}^2 + l_{i2}^2 + \dots + l_{iq}^2 = \sum_{j=1}^q l_{ij}^2. \quad (11)$$

As shown in (11), communality is the total influence on a single observed variable from all of the factors associated with it. It is equal to the sum of all the squared factor loadings for all of the factors related to the observed variable as defined in (11).

It can be discovered that, in oblique rotation such as Promax rotation, both a factor pattern matrix and a structure matrix are obtained. The structure matrix is simply the factor loading matrix as in orthogonal rotation, representing the variance in a measured variable explained by a factor on both unique and common contributions basis. Therefore, the factors with factor loading above the threshold of 0.4 are adopted and are given factors meanings in this study.

On the other hand, total variance explained indicates how much of the variability in the data has been modeled by the extracted factors. It can be discovered that the factor loadings for the principal component factor analysis are larger in absolute values as are the communalities, and, as a consequence, the total variance explained is also greater. The performed analysis has demonstrated that the cumulative total variance explained is 86.457%.

Employing SPSS and principal component factor analysis, this study extracted the firms' factors of sustainable product development intention under CSR, which were based on 18 items of sustainable product development intention. The results are illustrated in Table 4. As demonstrated in Table 4, the researchers Zaltman and Burger [28] have suggested that, as long as the eigenvalues of selected factors are greater than 1, the factor loadings in absolute values are over 0.30, the cumulative total variance explained is above 40%, and the obtained results of the factor analysis are feasible. Therefore, the obtained analysis results have demonstrated the feasibility of this study.

Based on the above data analysis, the impact factor rankings of the firms' sustainable product development intention

TABLE 5: Factors of sustainable development purpose.

Number	Questions of sustainable product development intention	Factor coefficient
06	Products are developed for sustainable design.	0.851
08	When prices are the same, products of sustainable design will be developed.	0.837
10	Firms will develop the products because of the sustainability.	0.779
12	The main values of sustainable products are based on environmental protection and social welfare.	0.746
13	The increase of sustainable product development intention is based on governmental laws and corporate development planning.	0.653
17	The sustainable products differ from the design and products of other brands.	0.463

TABLE 6: Factors of corporate development purpose.

Number	Questions of sustainable product development intention	Factor coefficient
02	Besides product costs, product profits, environmental protection, and maximum social welfare are secondary concerns.	0.734
07	Sustainable products are developed for CSR.	0.748
14	The concern is the practicability of products and pollution, and the sustainability of products is not important.	0.673
15	Brand image will influence your sustainable development.	0.673
18	In the era of CSR, the value of sustainable product design is the most significant.	0.435

under CSR were as follows: (1) factors of sustainable development purpose; (2) factors of corporate development purpose; (3) factors of corporate sustainable development; (4) factors of sustainable development value; (5) factors of sustainable development activity; and (6) factors of sustainable product quality. Thus, according to the rankings, the key factor of sustainable product development for firms was sustainable development purpose, which refers to value-added services, profits, and brand image in the development. The second factor was corporate development purpose, which focuses on strategies of corporate development, governmental regulations, and international laws. The effect of manufacturing quality on development was the lowest. The factors were illustrated as follows.

(1) *Factors of Sustainable Development Purpose.* According to Table 5, the factors included six items. The results showed that the top three were the following: “06. Products are developed for sustainable design;” “08. When prices are the same, products of sustainable design will be developed;” and “10. Firms will develop the products because of the sustainability”. The lowest was “17. The sustainable products differ from the design and products of other brands.” Thus, based on the rankings, firms were concerned about the sustainable design of products the most. Table 7 lists the factors of the sustainability of products and prices, otherwise known as the sustainable development purpose.

(2) *Factors of Corporate Development Purpose.* According to Table 6 results of the factor analysis, the top four factors were the following: “07. Sustainable products are developed for CSR” (Factor coefficient 0.748); “02. Besides product costs, product profits, environmental protection, and maximum social welfare are secondary concerns” (Factor coefficient

0.734); “15. Brand image will influence your sustainable development” (Factor coefficient 0.673); and “14. The concern is the practicability of products and pollution, and the sustainability of products is not important” (Factor coefficient 0.673). The lowest factor was “18. In the era of CSR, the value of sustainable product design is the most significant” (Factor coefficient 0.435). According to the rankings, the firms focused on the image value of sustainable product development based on CSR. Besides the product costs, profits, environmental protection, and maximum social welfare were secondary concerns. This is known as the corporate development purpose.

(3) *Factors of Corporate Sustainable Development.* According to Table 7 factor analysis results, the top two factors were the following: “04. To identify with the view that sustainable design is valuable” (Factor coefficient 0.802), and “01. In the development of all products, sustainable development is the priority” (Factor coefficient 0.708). The lowest factor was “09. The sustainability of products is not important. We only develop products with the highest profits” (Factor coefficient 0.417). Thus, according to the rankings, the firms identified with the value of sustainable design, and they treated sustainable development as the priority. This is known as corporate sustainable development.

(4) *Factors of Sustainable Development Value.* According to Table 8 factor analysis results, the top two factors were the following: “18. In the era of CSR, the value of sustainable product design is the most significant” (Factor coefficient 0.802) and “03. Sustainable product development makes products different” (Factor coefficient 0.708). The lowest factors were the following: “11. The main value of your sustainable products is profit” (Factor coefficient 0.417) and “14. The concern is

TABLE 7: Factors of corporate sustainable development.

Number	Questions of sustainable product development intention	Factor coefficient
01	In the development of all products, sustainable development is the priority.	0.708
04	To identify with the view that sustainable design is valuable.	0.802
09	The sustainability of products is not important. We only develop products with the highest profits.	0.417

TABLE 8: Factors of sustainable development value.

Number	Questions of sustainable product development intention	Factor coefficient
03	Sustainable product development makes products different.	0.708
11	The main value of your sustainable products is profit.	0.417
14	The concern is the practicability of products. Pollution and the sustainability of products are not important.	0.417
18	In the era of CSR, the value of sustainable product design is the most significant.	0.802

the practicability of products. Pollution and the sustainability of products are not important" (Factor coefficient 0.417). According to the rankings, the firms suggested that, in the era of CSR, the value of sustainable product development is the most significant. Sustainable product development makes products different. This is known as the sustainable development value.

(5) *Factors of Sustainable Development Activity.* According to Table 9 factor analysis results, the top factor was: "16. The increase of sustainable product development intention is based on the increase of talents and professional knowledge" (Factor coefficient 0.501). The lowest factor was "06. Products are developed for sustainable design" (Factor coefficient 0.428). Thus, according to the rankings, the firms were concerned about professional knowledge of sustainable development and the increase of talents. This is known as sustainable development activity.

(6) *Factors of Sustainable Product Quality.* According to Table 10 factor analysis results, the top factor was "05. Sustainable design products are developed since the quality is guaranteed" (Factor coefficient 0.768). The lowest factor was "03. Sustainable product development makes products different" (Factor coefficient 0.423). Thus, according to the rankings, the firms considered sustainable products as a guarantee of quality. This is known as sustainable product quality. Consider the following.

3.2. *Effects of Sustainable Product Development under CSR.* This study adopted a literature review and interviews to generalize eight results of sustainable product development under CSR by content analysis of 6 W. The content analysis is shown in Table 11.

- (1) CSR aims to change firms' past profit-oriented concepts and suggests that it is good for firms to develop products according to the new concept of sustainable development. However, their concerns are prices, profit ratio, environmental protection, necessities, market demand, and recycling.
- (2) Certification of sustainable product seals is influential and should be concerned about the requirements of

regulations, cooperation of industrial chains, cost, and quality. Thus, regarding consumption, the functional and intrinsic value of products can be more important than the priority of sustainable products. Therefore, during development, firms should be concerned with the functions and added value of products, as well as environmental materials, security, human factor engineering, maintenance (reduction of waste), and so forth.

- (3) Firms are essentially business units; thus, when developing new product, they must treat profits as the priority instead of CSR. However, in the product development process, design and development can be changed according to various factors. Thus, in the introduction of sustainable product development, the factor of firms' maximum profits will be overall manufacturing, materials, supply chains, and design processes. The concept of CSR can be introduced during this process.
- (4) CSR relatively influences sustainability and manufacturing processes of products. However, as suggested above, it depends on firm managers to include environmental protection in the development and manufacturing processes in order to meet related regulations. Thus, in design and development, such regulations will encounter more obstacles. The construction of brands and corporate responsibilities are important indicators of CSR.
- (5) Brand value is the main purpose for firms to develop CSR. Therefore, effects on consumers' identification and demand indirectly enhance firms' sustainable product development; however, implementation can be difficult. Corporate transportation should not rely on a single execution. Sustainable development can be implemented by guidance and assistance of government.
- (6) Construction of corporate brand image, word-of-mouth brands of sustainable products, construction of products, and service quality are the key factors of consumers' opinions of sustainable products; thus,

TABLE 9: Factors of sustainable development activity.

Number	Questions of sustainable product development intention	Factor coefficient
06	Products are developed for sustainable design.	0.428
16	The increase of sustainable product development intention is based on the increase of talents and professional knowledge.	0.501

TABLE 10: Factors of sustainable product quality.

Number	Questions of sustainable product development intention	Factor coefficient
05	Sustainable design products are developed since the quality is guaranteed.	0.768
03	Sustainable product development makes products different.	0.423

consumers perceive that the purpose of firms' development of sustainable products is to increase overall social benefits. In addition, consumers demand good bargains of less economic cost, which will be one of the critical issues in the future corporate developments.

- (7) The basic factors for the development of sustainable products are technical support, cooperation of industrial chains, and economic benefits. The priority is to deal with the authority of product quality and business owners' concepts. Moreover, the effects of market demand and brand image should be of concern.
- (8) Firms' current scope of sustainable development is limited to energy saving, environmental protection, recycling, environmental protection of materials, green manufacturing, maintenance, high added value, and so forth, which are the dimensions of product development. However, the sustainability of overall corporate development is more important. In other words, CSR will be the future trend.

3.3. Influential Factors and Strategy of Sustainable Product Development under CSR. After extracting the factors of sustainable product development intention under CSR and developing the rankings (Table 4), based on the impact factors and in-depth interviews, this study extracted the internal and external major factors of sustainable product development intention under CSR. This could help corporate development decision makers to make the best decision model in sustainable product development according to the factors. In general, corporate development decision models are based on product materials, profits, and costs as the criteria of development decisions. By introducing factors of sustainable product development under CSR generated by this study, the major factors of corporate sustainable product development could be developed. According to Figure 2, in the sustainable development purpose of sustainable product development intention under CSR, the major factors of corporate internal development intention were the reduction of actual costs, the enhancement of corporate image, and the added value for products. The major factor of corporate external development intention was the application for governmental subsidies. As to the corporate development purpose, the major factors

of corporate internal development intention were corporate transformation actions and the construction of sustainable brands. The major factors of corporate external development intention were the corporate development strategy and restrictions of governmental laws. As to corporate sustainable development, the major factor of corporate internal development intention was the construction of internal concepts. The major factor of corporate external development intention was the promotion of sustainable development. As to the sustainable development value, the major factor of corporate internal development intention was the development of sustainable design. The major factor of corporate external development intention was future market demand. Regarding sustainable development activity, the major factors of corporate internal development intention were the development of sustainable design and the promotion of sustainable concepts. The major factor of corporate external development intention was the cooperation of the supply chains. Finally, as to the sustainable product quality, the major factors of corporate internal development intention were the innovation of product services and the enhancement of product quality. The major factor of corporate external development intention was innovation system construction.

According to the previously mentioned 18 main factors of corporate internal and external sustainable development intentions, as well as the interview content, the researcher obtained the internal factors of sustainable product development (Figure 3) and the external factors of sustainable product development (Figure 4) under CSR. As to sustainable product development under CSR, the internal decision factors referred to employee stimulation, image improvement, innovation capability, cost reduction, and quality enhancement. The external decision factors referred to law making and bans, market demand, social environment, supply chains (suppliers), and trading associations. Apparently, in the future, firms should promote sustainable concepts in the organizations, actively cultivate sustainable talents, and enhance employees' self-sustainability in order to encourage the employees. By the establishment of sustainable brands, firms can have an active transformation and effectively enhance their corporate image. They can promote sustainable design development and innovative product services and reinforce innovation capability. They can carefully consider the reduction of actual costs and increase the added value in

TABLE II: Content analysis of 6 W.

6 W questions	Who	What	Whom	How	What effect	Why
How does CSR influence sustainable product development? What are the key points or criteria in the introduction?	CSR	To change firms' past concept of profits. Sustainable products are declared as good actions and new concepts.	Corporate	Necessity of profits and environmental protection are compared. Recycling of the products.	To change corporate development and divide sustainable development from profits as a priority.	We choose the products in order to survive.
What are the factors of sustainable product development in the product development process? What is the relationship with design development?	Sustainable product development	Regulations must be concerned. Cooperation of industrial chains. Concerns of cost and quality.	Corporate	Functions, added value, and materials of products should be environmental, safe, based on human factor engineering, and able to be maintained.	Functions of products will be influenced. Actual value will be higher than the priority of green products.	For the restriction of regulations.
How does CSR influence current sustainable product development? Does it change the design?	CSR	The sustainable development process will not be influenced significantly.	Sustainable product design	Profit is the priority. In the development process, some factors will change the design. The process is inevitable.	Change the firms that treat profits as the priority.	The implementation of CSR will be the niche in the future.
What are the factors of CSR? What are the effects on the sustainable product development and the manufacturing process?	CSR	In order to construct brands, firms must recognize the additional responsibility, safety, and necessity.	Corporate	Environmental protection should be included in the product development and manufacturing process. It must match the regulations.	It will certainly influence the product sustainability and manufacturing process.	Product development and manufacturing processes must match related regulations.
What are the factors needed to develop sustainable products for CSR? What can be the obstacles in practice?	CSR	Value of CSR and consumers' identification with CSR.	Sustainable product development	The implementation must be difficult. Firms do not necessarily value CSR. They treat profits as the priority. Thus, they must rely on governmental promotion and practice of laws.	Firms that treat profit as a priority will turn to CSR.	CSR is the trend of the future, and firms can obtain value besides the profits.
What are the messages received by consumers from successful sustainable products?	Sustainable product	Consumers can buy products at a good bargain.	Consumer	Based on CSR, firms are expected to have measures related to production and price adjustment or to treat the development of CSR in a broader sense.	Construction of corporate brand image, construction of word-of-mouth of sustainable products, and construction of quality of products and services.	When they are concerned about society, they are more likely to be accepted by consumers. They can enhance their reputation and create brand image.

TABLE II: Continued.

6W questions	Who	What	Whom	How	What effect	Why
What are the factors of sustainable products?	Sustainable product	Energy conservation, reclaim, resolve, green manufacturing, maintenance, and high value added.	Corporate	Monitoring of the product chain and energy-saving system of products.	The downstream supply chain must follow governmental laws and corporate policy, change the original system, and adopt the development of energy saving and carbon reduction.	For the restrictions of governmental regulations, firms must follow the rules.
In current corporate development sustainable products, what are the success factors of product development?	Sustainable product development	The basic factors of sustainable product development are technical standards, cooperation of industrial chains, economic benefits, and business owners' concepts.	Corporate	Guarantee of quality, subjectivity of firms, and market demand.	Promotion of quality and functions of products.	Creation of brand image.
What are the aspects that do not accomplish the goals of sustainable product development?						
What are the problems?						

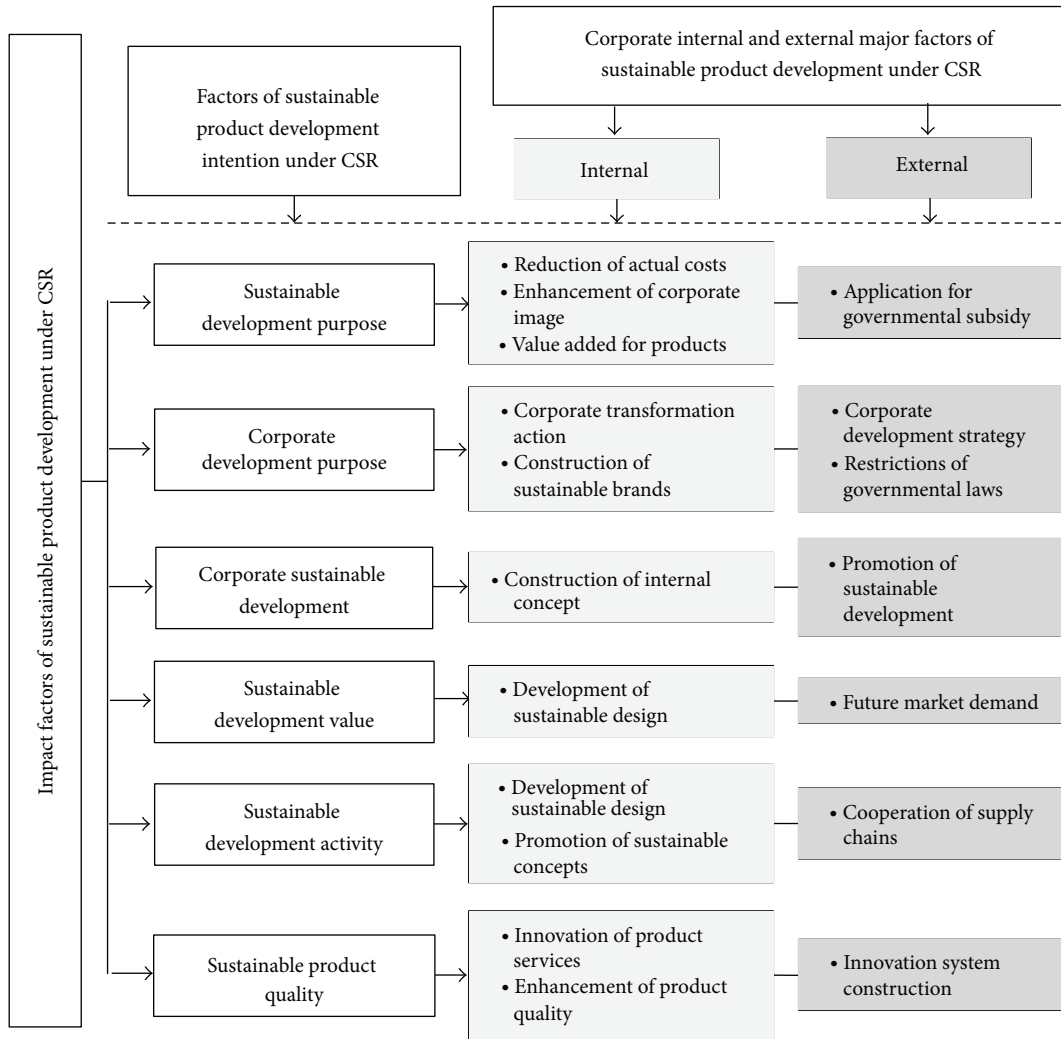


FIGURE 2: The impact factors of sustainable product development under CSR.

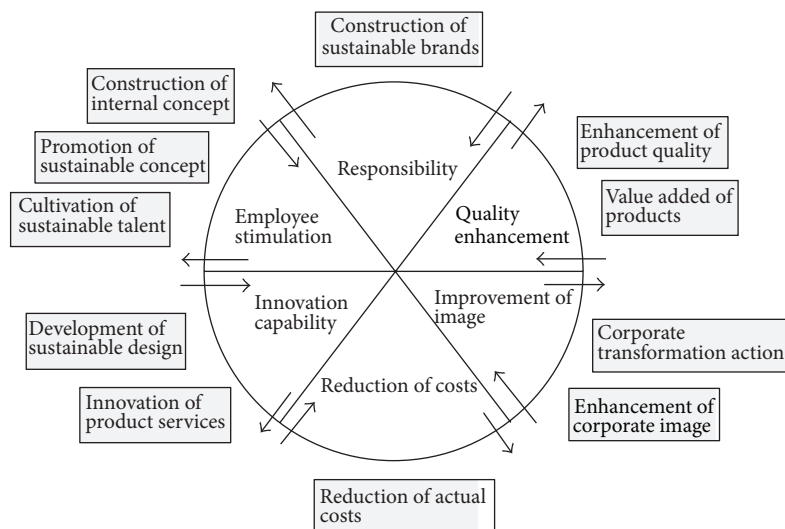


FIGURE 3: The internal factors of sustainable product development under CSR.

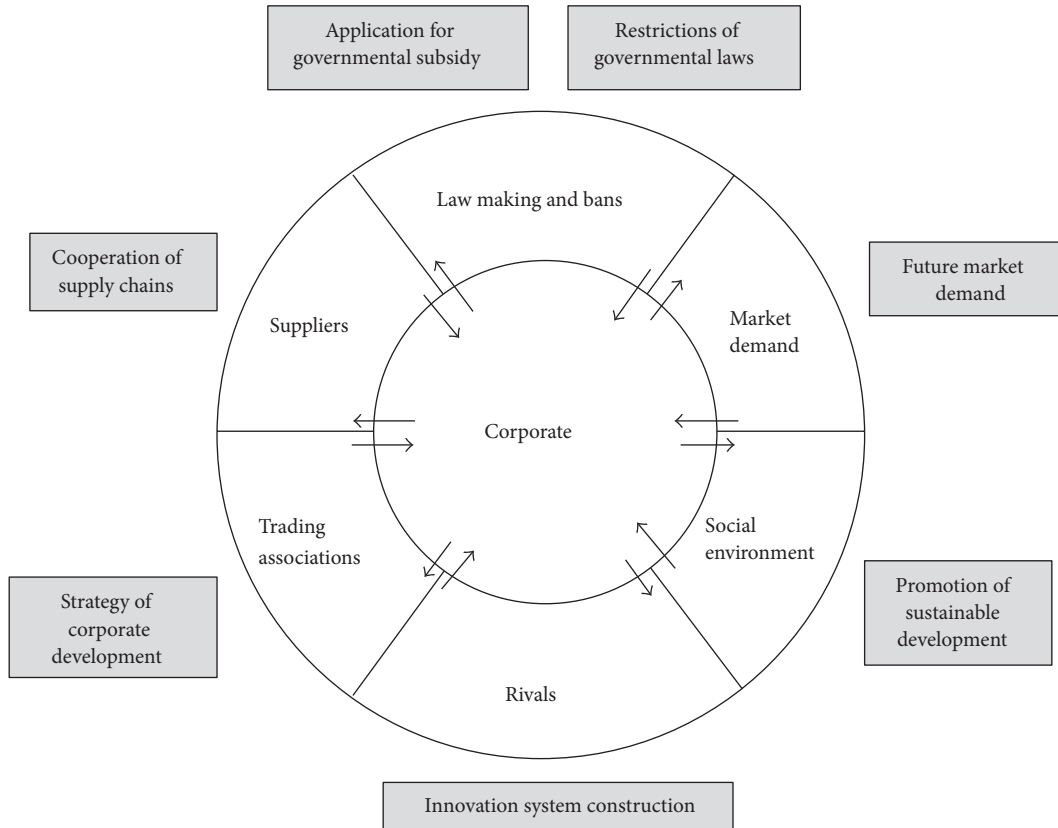


FIGURE 4: The external factors of sustainable product development under CSR.

order to save development costs. Finally, by improving product quality, overall corporate quality can be strengthened. In addition, firms rely on external factors, such as the implementation of governmental regulations and the applications for governmental subsidies. They can match future market demand and the overall supply chain to plan corporate sustainable development strategies, and they can actively implement innovation systems and sustainable development to accomplish sustainable product development under CSR.

4. Conclusions

With the rise of CSR, firms should pursue more sustainable operational rules. As to corporate development, sustainable product development has become the mainstream in the recent years. The reason is that the development of small and medium enterprises is rapid and prevailing. There are different types of corporate development. The effect of environmental change on convenience and efficiency on people is the most significant. However, due to the perspective of CSR and the uncertainty of sustainable development, firms' intention for sustainable product development is usually influenced. Apparently, environmental laws and corporate development strategy are the significant criteria of corporate sustainable development. If firms can effectively control these sustainable development factors, they will enhance their

development intention for corporate sustainable development. This study expected that the coping model of sustainable product development constructed under CSR could serve as a reference for the sustainable development of small and medium enterprises in Taiwan. Based on the results, we conclude the paper with the following.

- (1) Regarding current sustainable product development under CSR, firms must adjust development policies between sustainable development and profits to accomplish the goal of mutual benefits. It is suggested that, in sustainable development, firms should first be concerned about the requirement of laws, cooperation of industrial chains, cost, quality, and proper practice of incidents or activities of CSR. They can thus construct corporate brand image and word-of-mouth for sustainable products and quality service.
- (2) Regarding sustainable product development intentions under CSR, firms concern about sustainable development purpose the most, meaning value added, profit, and brand image during development. The second is corporate development purpose, which emphasizes corporate development strategy, legal regulations of government, and international laws; the third is the concept of sustainable development, including employees' concepts of sustainability, which

mostly refers to positive concepts of sustainable development.

- (3) Regarding the trend of sustainable product development under CSR, internal corporate environment management and corporate sustainable development are moderated by attitude toward CSR, meaning a more active attitude. In addition, relationships between internal environment management and positive performance are influenced by attitudes toward CSR. Sustainable development performance is better, such as management, improvement of corporate internal environments, and enhancement of environmental performance, which can lower energy consumption, waste, and cost of fines for environmental accidents.
- (4) In the development of sustainable business, firms can mainly practice internal reform with the support of external reform in order to cultivate sustainable talents, promote sustainable concepts, improve corporate image, follow the regulations, cooperate with the overall supply chain, follow corporate transformation development, and follow the responsive policies of governmental laws. As to CSR, the relationship between corporate internal environment management and corporate sustainable development is moderated by attitude toward CSR. Those with a more active attitude toward CSR have a better performance of sustainable development. In addition, the relationship between internal environment management and positive performance is influenced by the attitude toward CSR. When the attitude toward CSR is more active, there will be a more positive performance of sustainable development.

References

- [1] I. C. Pirnea, M. Olaru, and C. Moisa, "Relationship between corporate social responsibility and social sustainability," *Economy Transdisciplinarity Cognition*, vol. 14, no. 1, pp. 36–43, 2011.
- [2] U. Ubius and R. Alas, "The impact of corporate social responsibility on the innovation climate," *Engineering Economics*, vol. 23, no. 3, pp. 310–318, 2012.
- [3] C. Y. Hsu, C. C. Liang, and F. Y. Ye, "Ownership structure and corporate social responsibility," in *Proceedings of the Corporate Finance Academic Conference*, National Kaohsiung First University of Science and Technology, Kaohsiung, Taiwan, May 2010.
- [4] T. H. Koh and W. C. Fang, "The effects of corporate social responsibility on purchase intention: the mediating effects of brand attachment and brand image," *Journal of Business Administration*, vol. 94, pp. 41–68, 2012.
- [5] A. Kolk and R. van Tulder, "International business, corporate social responsibility and sustainable development," *International Business Review*, vol. 19, no. 2, pp. 119–125, 2010.
- [6] D. Krumwiede, A. M. Hackert, J. Tokle, and R. J. Vokurka, "The practice of corporate social responsibility in different countries: a study of firms in Canada, Hungary, Italy, Lebanon, Taiwan and the United States," *International Journal of Management*, vol. 29, no. 1, pp. 389–403, 2012.
- [7] K.-T. Hsu, "The advertising effects of corporate social responsibility on corporate reputation and brand equity: evidence from the life insurance industry in Taiwan," *Journal of Business Ethics*, vol. 109, no. 2, pp. 189–201, 2012.
- [8] National Council for Sustainable Development Network [NCSDN], 2007, <http://nsdn.epa.gov.tw/INDEX.ASP>.
- [9] W. C. Wei and Y. H. Chuage, "An empirical study of the relationship among corporate social responsibility, corporate image, consumer's attitude and behavioral intentions," *International Journal of Lisrel*, vol. 2, no. 2, pp. 1–21, 2009.
- [10] A. Lindgreen and V. Swaen, "Corporate social responsibility," *International Journal of Management Reviews*, vol. 12, no. 1, pp. 1–7, 2010.
- [11] J. C. Tu and T. F. Kao, "Relationship between attitude toward green consumption and corporate social responsibility," *Ling Tung Journal*, vol. 30, pp. 73–110, 2011.
- [12] G. Campopiano, A. de Massis, and L. Cassia, "The relationship between motivation and actions in corporate social responsibility: an exploratory study," *International Journal of Business & Society*, vol. 13, no. 3, pp. 325–341, 2012.
- [13] A. D. Jayal, F. Badurdeen, O. W. Dillon Jr., and I. S. Jawahir, "Sustainable manufacturing: modeling and optimization challenges at the product, process and system levels," *CIRP Journal of Manufacturing Science and Technology*, vol. 2, no. 3, pp. 144–152, 2010.
- [14] C. Y. Hsu and C. C. Lin, "The impact of controlling shareholder on corporate social responsibility," in *Proceedings of the Taiwan Conference on Business and Information*, Graduate School of Information Management, Taipei University, Taipei, Taiwan, April 2011.
- [15] B. Y. Zhou, "The correlation analysis between corporate social responsibility and corporate operating performance," *Journal of Chinese Economic Research*, vol. 10, no. 2, pp. 17–29, 2012.
- [16] R. Virvilaite and U. Daubaraitė, "Corporate social responsibility in forming corporate image," *Engineering Economics*, vol. 22, no. 5, pp. 534–543, 2011.
- [17] J. Golovachev, O. Budde, and D. Kellmerein, "Technology and Innovation radars: effective Instruments for the development of a sustainable innovation strategy and successful product launches," *International Journal of Innovation & Technology Management*, vol. 7, no. 3, pp. 229–236, 2010.
- [18] C. Yu, C. C. Yu, Y. S. Cheng, T. F. Yu, and P. J. Lee, "A study of the relationships among employees' perception of corporate social responsibility, organizational commitment and turnover intention," *Journal of National Taipei University of Technology*, vol. 42, no. 2, pp. 147–173, 2009.
- [19] A. B. Carroll and K. M. Shabana, "The business case for corporate social responsibility: a review of concepts, research and practice," *International Journal of Management Reviews*, vol. 12, no. 1, pp. 85–105, 2010.
- [20] J. K. Hall, G. A. Daneke, and M. J. Lenox, "Sustainable development and entrepreneurship: past contributions and future directions," *Journal of Business Venturing*, vol. 25, no. 5, pp. 439–448, 2010.
- [21] M. W. DiStaso and D. S. Bortree, "Multi-method analysis of transparency in social media practices: survey, interviews and content analysis," *Public Relations Review*, vol. 38, no. 3, pp. 511–514, 2012.
- [22] L. Yang, Z. G. Hu, J. Long, and T. Guo, "Ontology modeling and semantic information service of expert domain," *Journal of Chinese Computer Systems*, vol. 8, pp. 1730–1735, 2012.

- [23] W. J. Krzanowski, *Principles of Multivariate Analysis*, vol. 3 of *Oxford Statistical Science Series*, chapter 7.1, The Clarendon Press Oxford University Press, New York, NY, USA, 1988.
- [24] V. Bountziouka and D. B. Panagiotakos, "The role of rotation type used to extract dietary patterns through principal component analysis, on their short-term repeatability," *Journal of Data Science*, vol. 10, no. 1, pp. 19–36, 2012.
- [25] A. B. Costello and J. W. Osborne, "Best practices in exploratory factor analysis: four recommendations for getting the most from your analysis," *Practical Assessment Research & Evaluation*, vol. 10, no. 7, pp. 1–9, 2005.
- [26] R. I. Jennrich, "Standard errors for obliquely rotated factor loadings," *Psychometrika*, vol. 38, pp. 593–604, 1973.
- [27] C. B. Crawford and G. A. Ferguson, "A general rotation criterion and its use in orthogonal rotation," *Psychometrika*, vol. 35, no. 3, pp. 321–332, 1970.
- [28] G. Zaltman and P. Burger, *Marketing Research: Fundamentals and Dynamics*, Dryden Press, Hinsdale, Ill, USA, 1975.

Research Article

Study on the Wind Environment of the Architecture Communities: Traditional Typical Min Nan Human Settlements' Case

Yuan Miao^{1,2} and Shang-Chia Chiou³

¹ Graduate School of the Design Doctoral Program, National Yunlin University of Science and Technology, Douliu 640, Taiwan

² Tan Kah Kee College, Xiamen University, Zhangzhou, Fujian 363105, China

³ Department of Architecture and Interior Design, National Yunlin University of Science and Technology, Douliu 640, Taiwan

Correspondence should be addressed to Yuan Miao; qq28256@gmail.com

Received 15 September 2013; Accepted 10 October 2013

Academic Editor: Teen-Hang Meen

Copyright © 2013 Y. Miao and S.-C. Chiou. This is an open access article distributed under the Creative Commons Attribution License, which permits unrestricted use, distribution, and reproduction in any medium, provided the original work is properly cited.

In contrast to the modern urban planning, which can be done in short period in terms of the spatial qualified design, the traditional tribe needs longer period in terms of the villagers' sense of community. The selection of location, planning, and construction reveals the wisdom of the former people's use of the resourceful life experience. First, the paper employs PHOENICS to simulate the wind environments of two most representative patterns of rural settlements in the southern area of Southern Fujian, China. This was made to compare the different conditions caused by settlements of various architectural groups. Second, the engineering and construction aspects of settlements—such as the width of roads and building structures—will be further analyzed and examined as case study in attempt to discover the favorable environmental factors for generating winds as well as the construction dimension of the settlement, such as the road width and the architectural design. Finally, the paper tends to conclude with an energy conservation strategy applied to the construction of modern communities which has low density and small group buildings.

1. Introduction

The worldwide environmental deterioration and the energy and resource crisis have recently attracted widespread attention among the people around the globe. The construction of the architecture always needs to consume a great amount of regular resources. Hence, how to make the best use of the natural renewable resources to reduce the consumption of energy in building has become the main task in the architectural design circle. In the past, most research was devoted to the building and its subsidiary environment. Rarely was the research conducted to discuss how to use the natural energy—such as the wind power—in the construction dimension of the settlement. On the other hand, the research was usually pertaining more to the overall energy conservation measures in the traditional settlements based on their experiences, and less to a comprehensive research of quantitative calculation. The reasonable layout of building groups in

modern residential district is conducive to the formation of good natural ventilation environment and regional climate in cities [1, 2]. Based on the CDF method, this paper provides analysis on the relationship between traditional settlement wind environment and microclimate environment [3–5] and discusses the construction of residential district in modern cities from the perspective of architecture and urban design.

1.1. Research Objects. Under the cultural background which includes immigration history, there are two most representative patterns of rural settlements in Southern Fujian, China: determinant-ordered structure and circular-spread structure. Determinant-ordered structure values the defensive functions of building and mainly forms building groups with orderliness in the spacious plains to form enclosed spaces. For the example of determinant-ordered structure, see Dai Mei Village, Longhai Country, Zhangzhou City, Fujian (Hereinafter referred to as Village A) in Figure 1.



FIGURE 1: Dai Mei Village. (source: Google map).



FIGURE 2: Hillside Village. (source: Google map).

Circular-spread structures mostly appear in the hillside section and the central loci of Circular-spread structures are ancestral hall and temple (Figure 2). The living building gradually spread from the central loci, which values the worship of ancestors and gods. To see the example of circular-spread structure; see, Hillside Village, Longhai Country, Zhangzhou City, Fujian (Hereinafter referred to as Village B) in Figure 1. These two patterns of settlement spaces are derived from different historic background and thus could express obvious meaning of cultural identity.

1.2. Research Methods and Steps. PHOENICS serves more as commonly-used software, less as software specifically used; it is widely applied for the calculation of “flow” and “heat” in various fields. Thus the optimization settings is the prime concern as the simulation of settlement patterns was put into application. The methods and steps can be summarized as follows.

- (1) First, complete the environment setting before simulation, and then output the results of simulation and analysis.
- (2) Compare the function of wind environments.
- (3) Examine the reason why certain villages offer good wind environment and good wind effects.
- (4) Offer suggestions and strategies for modern living communities.

2. The Numerical Simulation and Calculation of Wind Environment

2.1. The Environment Setting before Simulation

2.1.1. The Selection of the Mathematical Model. The winds flowing within the settlements are sometimes incompressible and low-speed turbulence [6]. Hence, the standard and generally-used mathematic model was applied to the present research: $k - \epsilon$ model. The advantages of $k - \epsilon$ model are low costs of calculation tools, low fluctuation while calculation,

and high accuracy [7]. According to Tao’s research [8] on the numerical heat transfer, all controlled differential equation elements—including continuity equation, momentum equation, K equation, and ϵ equation—are defined as follows.

- (1) Turbulent viscosity coefficient $\eta_t = c_\mu \rho k^2 / \epsilon$.
- (2) Continuity equation $\partial(\rho u_i) / \partial x_i = 0$.
- (3) Momentum equation $\partial(\rho u_i u_j) / \partial x_i = (\partial / \partial x_i)(\eta_{\text{eff}}(\partial u_j / \partial x_i)) - \partial_p / \partial x_j + (\partial / \partial x_i)(\eta_{\text{eff}}(\partial u_i / \partial x_j))$.
- (4) K equation $\partial(\rho u_i k) / \partial x_i = (\partial / \partial x_i)[(\eta + \eta_t / \sigma_k)(\partial_k / \partial x_i)] - \rho \epsilon + \eta_t(\partial u_j / \partial x_i + \partial u_i / \partial x_j)(\partial u_j / \partial x_i)$.
- (5) ϵ equation $\partial(\rho u_i \epsilon) / \partial x_i = (\partial / \partial x_i)[(\eta + \eta_t / \sigma_\epsilon)(\partial_\epsilon / \partial x_i)] - c_2(\rho \epsilon^2 / k) + (c_1 \epsilon \eta_t / k)(\partial u_j / \partial x_i + \partial u_i / \partial x_j)(\partial u_j / \partial x_i)$.

2.1.2. Selection of Physical Model. The traditional settlement architecture community is not high and is relatively smaller sized. The design of the architecture may lead to local microclimate, such as the space of courtyard and the shape of the roof. To reduce the statistical variations, the cubical model of the architect should be taken into consideration and made to undergo the configurative simulation model, especially the form of the slope roof which can easily cause impact on the direction of the wind. Hence, it is imperative that the model is necessary to as to obtain constructed in accordance with the original traditional roof form and design.

2.2. Simulate Wind Environments

2.2.1. Set Up Models. CAD was adopted to draw the 3-dimension substantial graphics of village pattern in STL format and introduce the graphics into PHOENICS (Figures 3 and 4).

2.2.2. Setting Up Climate Condition. The climate parameters about winds in the location of building groups were used as analogous boundary conditions (Table 2).

TABLE 1: Climate parameters about winds in Zhangzhou city.

City	Summer		Winter	
Zhangzhou city	Wind speed: 1.6 (m/s)	Wind direction: northerly winds	Wind speed: 1.6 (m/s)	Wind direction: southerly wind

Source: Practical design manual for heating and air conditioning (1st edition).

TABLE 2: The relation between human's feeling and wind speeds.

Range of wind speeds (m/s)	People's feeling
<1.0	Cannot feel any wind
1.0~5.0	Comfortable
5.0~10.0	Uncomfortable and the activities are influenced
10.0~15.0	Uncomfortable and the activities are severely influenced
15.0~20.0	Cannot tolerate
>20.0	Dangerous

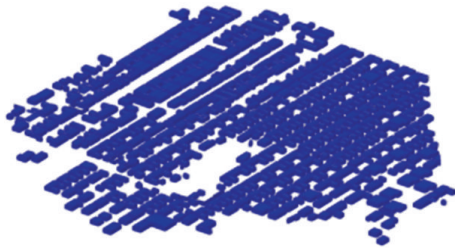


FIGURE 3: CAD3D model for Village A.

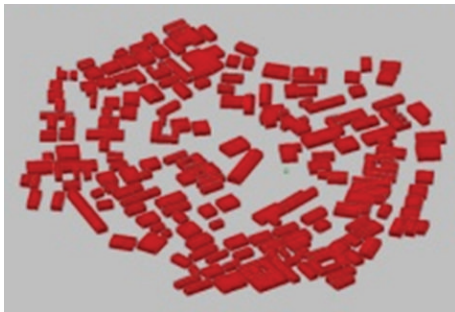


FIGURE 4: CAD3D model for Village B.

2.2.3. Comparison of Wind Environments. Consider the following.

- (1) Introduction of the STL model (Figures 5 and 6).
- (2) To adjust the size of calculated areas; the areas that buildings cover are smaller than 3% of overall areas of calculated region. First, targeted building was chosen as the center and made to set the height of building as H . The targeted building was used as the center and the region within a radius of $5H$, which serves as the calculated region. The calculation area above the building proves greater than $3H$.

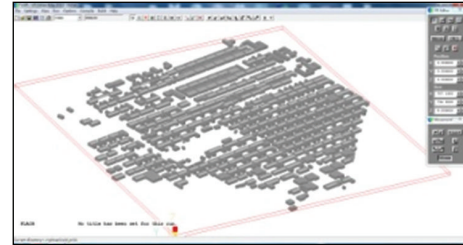


FIGURE 5: Model graphics for Village A.

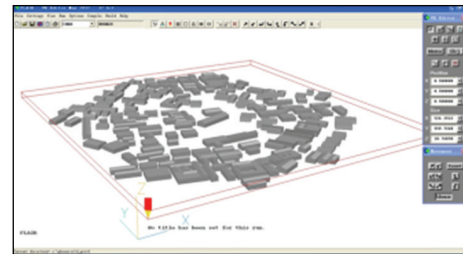


FIGURE 6: Model graphics for Village B.

- (3) To adjust the amounts of grids. The appropriate grids were divided in terms of the side length of buildings. The key observation region mainly exceeds above the third grids and the higher grids counted from the ground (Figures 7 and 8).
- (4) To set up parameters. "Calculation model", "Parameters for fluids", and "Calculation for step length" were set up (Figure 9).
 - (1) Calculation model. As the definition of controlled differentiation equation chosen in this project was concerned, KEMODLd was selected as the model of this research to undergo fluids calculation.
 - (2) Parameters for fluids. Physical parameters of the air flow such as pressure and temperature could be set in this interface.
 - (3) Calculation for step length. As the errors fall below 0.1% and the calculation come to convergence, the calculation ends.
- (5) To set up the boundary conditions of wind environments. In terms of the wind speeds and wind directions of the two villages, this item was set and made. Wind speeds could be seen in Table 1, used to compare the different heat works of the two villages, which belongs to the hot summer and cold winter climate environment. The leading directions of summer

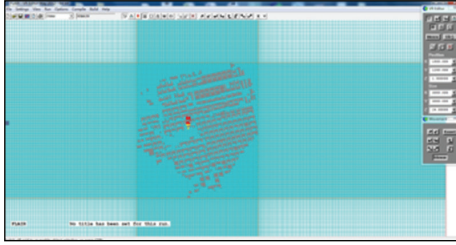


FIGURE 7: The grid setting of XY plane and Z axis of Village A.



FIGURE 8: The grid setting of XY plane and Z axis of Village B.



FIGURE 9: Parameters for fluids.

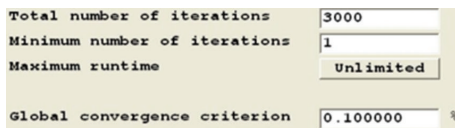


FIGURE 10: Calculate step length.

and winter to undergo calculations were thus chosen (Figures 10 and 11).

- (6) Solutions for calculations. The Curve on the left frame demonstrates instant values such as wind pressure, wind speed, and so forth. The curve in the right frame suggests the curve of residuals after subtraction. This indicates that the calculation results of this time minuses the calculation results of the previous time (Figures 12 and 13).
- (7) Simulation results. The analog results could be divided into two parts. The first indicates that the village was regarded as the object of the overall wind environment (Figure 14). The second suggests that the local wind environment formed by certain buildings was taken as the object of the overall wind environment (Figure 15). Advantages of the two above mentioned parts could be separately demonstrated as well as mutually complementary. Bigger body mass and longer calculation periods are the two characteristics of the results in Part One. However, the results of Part One is easy for observing how the flow-in and flow-out direction of monsoons in the village exerts significant impact upon the formation of the whole wind

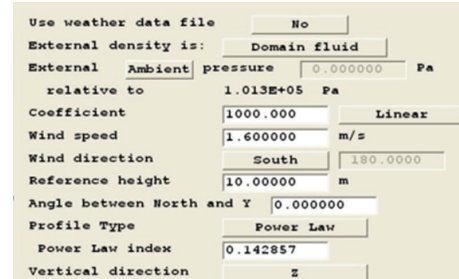


FIGURE 11: Parameters for winds.

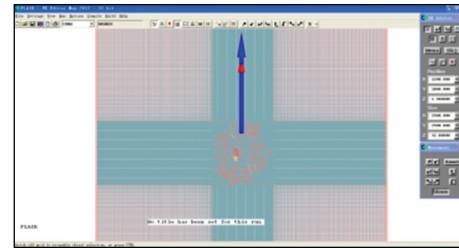


FIGURE 12: Direction of the wind.

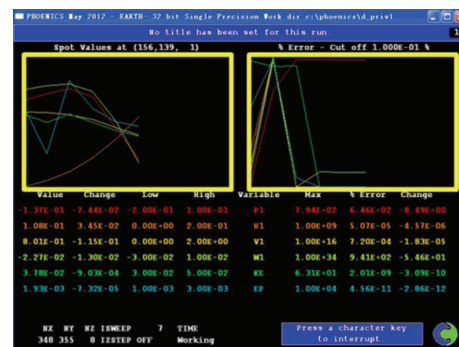


FIGURE 13: Solutions for calculations.

environment as well as internal distribution of different wind field. The results of Part Two were easy for observing single building's inner and outer natural ventilation conditions influenced by wind environment.

2.3. Comparative Research. As the requirement of Evaluation Standard of the Green Building in Fujian (DBJ/T 13-118-2010) and the climate characteristics (hot summer and cold winter) indicate, summer and winter were chosen as the main seasons for evaluation. Assumedly, if the wind speeds of the pedestrian zone around the building fell lower than 5.0 m/s (1.5 meters in attitude, counted from the ground), it would not influence people's fundamental requirements about normal outdoor activities. The index for evaluating whether the natural ventilation of the outdoor of building group is the wind speed measured at 1.5 m in attitude counting from the ground. The fewer strong-wind regions with wind speeds higher than 5 m/s and lower than 1.0 m/s in the main entrance of the wind, the better wind environment would be defined in

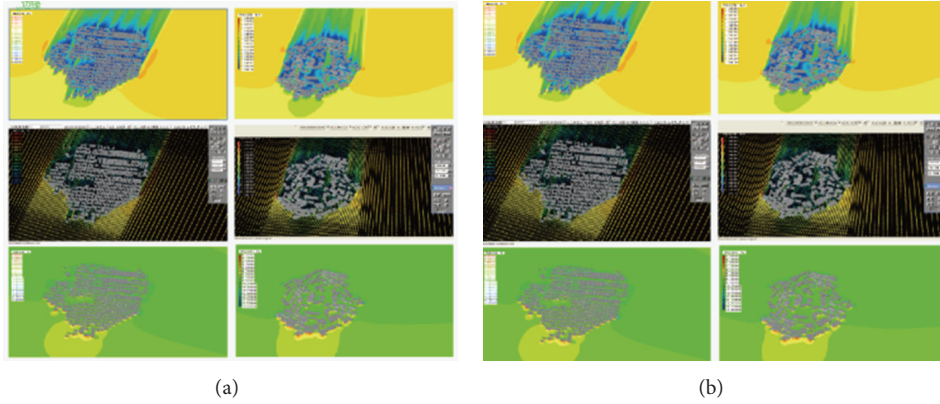


FIGURE 14: Simulation results about two villages' wind speeds and pressure influenced by summer monsoon and winter monsoon.

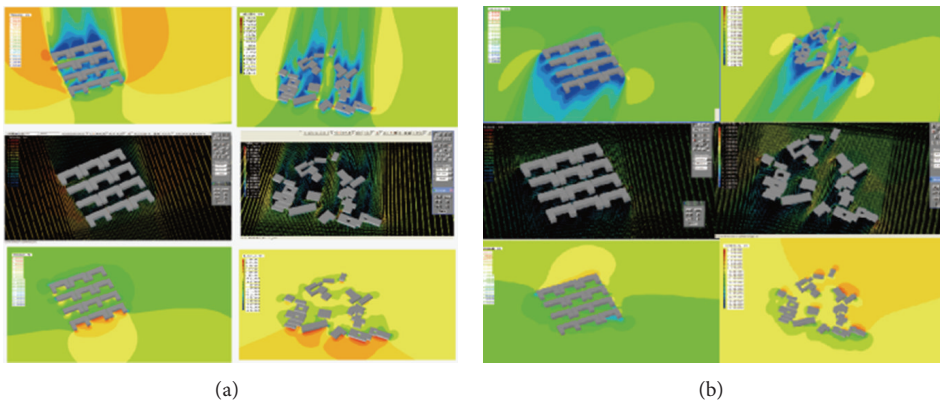


FIGURE 15: Simulation results about the wind speeds and pressure of the two local typical building groups influenced by summer monsoon and winter monsoon.

the region (Table 2). As the standard of DBJ/T13-118-2010 and the color table with the unit values accessory to software system (Figure 16) indicate, the wind environments of village A and village B could be taken to access.

2.4. Assessment on the Wind Environments of Settlements

Wind Speed. As the winter monsoon of the prevailing wind direction is concerned, the highest wind speed in Village A is 1.1 m/s and the highest wind speed in Village B is 2.4 m/s; when considering the summer monsoon as the prevailing wind direction, the highest wind speed in Village A is 1.6 m/s and the highest wind speed in Village B is 1.5 m/s. Overall, both villages' wind speeds of outdoor pedestrian areas and activity areas in winter, summer, and transition seasons are lower than 5 m/s. Hence, the condition of natural ventilation is favorable and could live up to the requirement of comfort. Nevertheless, in contrast to village A, there are obvious differences between the calm zone (Figure 17) and strong wind (Figure 18) zone in village B. As the faces of the building in village B is irregular, part of the building groups face to the winter monsoon surface and back to the summer monsoon surface. Strong wind areas are more vulnerable to fire hazards.

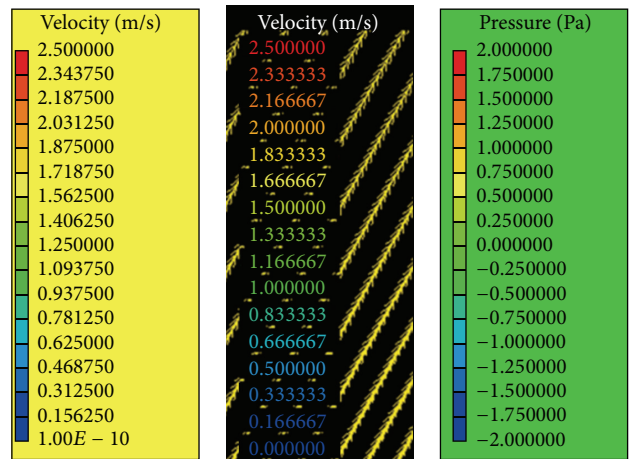


FIGURE 16: Units of wind speed, wind vector, and wind pressure.

Wind Direction. As there remain to be fewer differences between the wind vectorgraphs that show the wind environments influenced by the southern monsoon and the northern monsoon, as Figure 19 indicates, it is valid to suggest that, compared with village B, the variation of wind vectors in

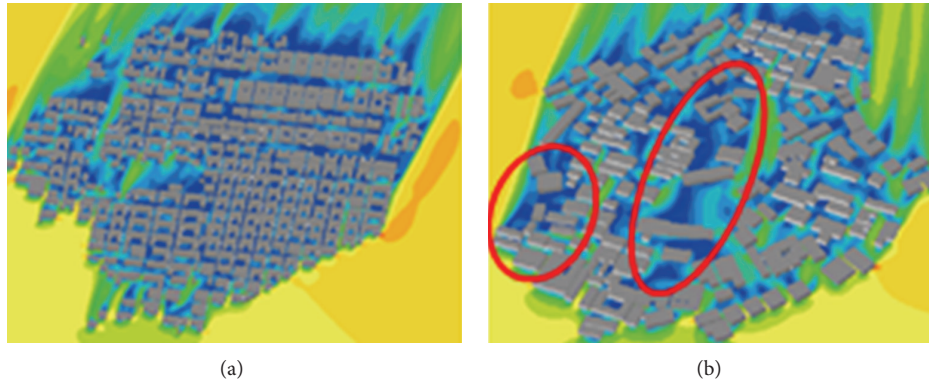


FIGURE 17: Wind speed simulations of Village A and Village B in summer.

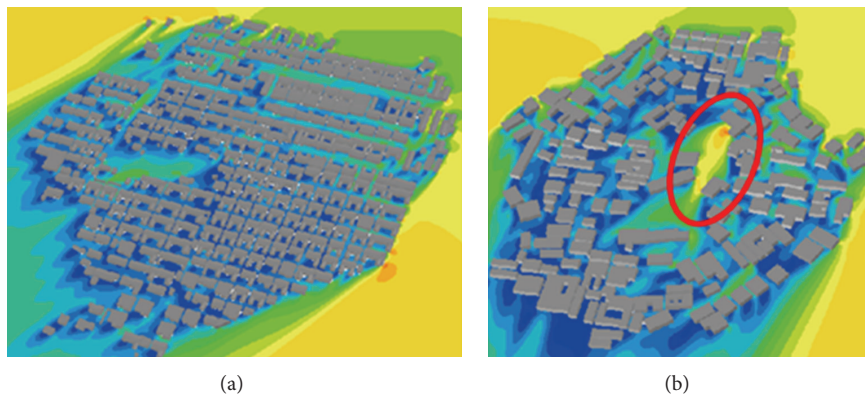


FIGURE 18: Wind speed simulations of Village A and Village B in winter.

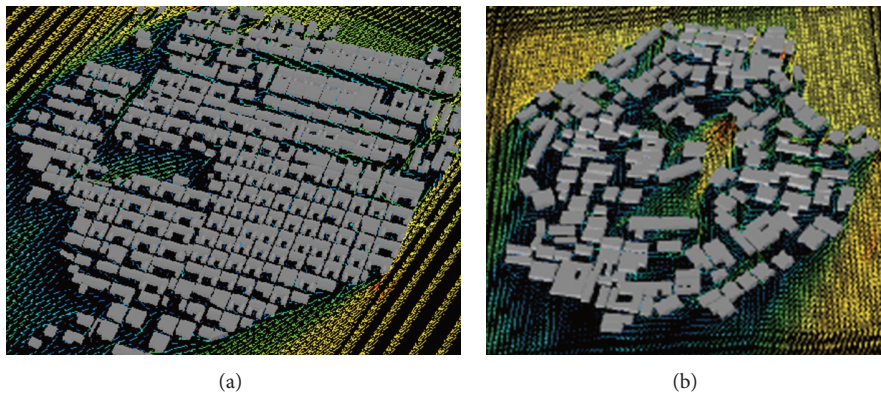


FIGURE 19: Winter monsoon wind vectorgraphs of village A and village B.

village A is smaller. Also, the trends of the air volumes rarely change and owing to the regular and ordered direction, it is easier for the guidance of wind direction. The trends of wind vectors in village B could be seen through the distinctions between the hierarchical color gradients, as there are obvious different hierarchies. The values of numerical differences fall between 2.5~0.15 and the wind direction diverge disorderly, which is against the indoor natural ventilation that takes advantage of the windward sides as gable walls.

Wind Pressure. As Figure 20 indicates, we could know that the in village A, the wind pressures in the northeast is higher and in village B, there are no high wind pressure areas. Nonetheless, high wind pressure values would not form strong wind areas and would form winds according to the pressure differences in the neighboring areas. Thus, according to the color table with the unit values, we calculate the differences between the neighboring wind pressures and find that village B is 1.0 Pa and village A is 0.3 Pa. Hence, there are higher



FIGURE 20: Wind pressure graphics of Village A and Village B in winter.

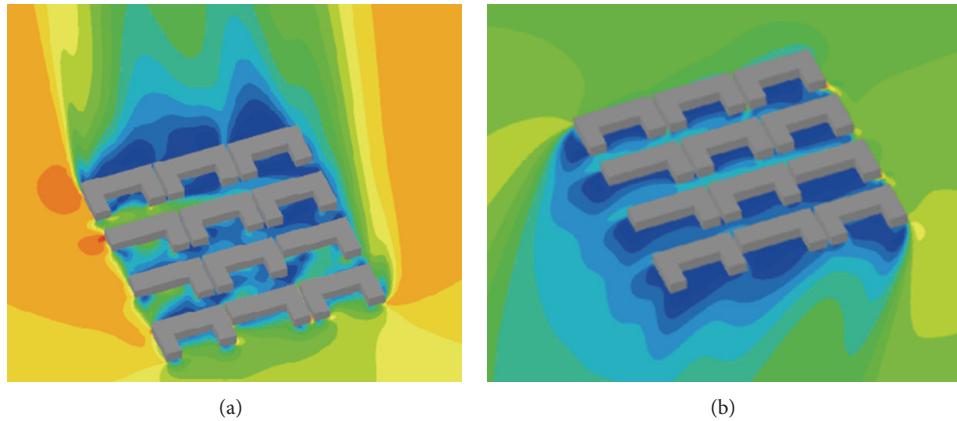


FIGURE 21: Wind speed simulations of the villagers A's building groups with determinant-ordered structures in winter and summer.

probabilities for village B to form cold and strong winds in winter.

2.5. The Outdoor Wind Environment of Building Group. Both the indoor and outdoor areas are the environments that villagers mainly use and are important venues for activities. The local wind environments formed by the building groups should be separately investigated to further understand the details of wind environments through observation data. The typical building group features determinant-ordered structures in village A and typical building group feature circular-spread structures in village B to undergo comparison analyses.

The choice of the building group case is considering the morphological features of the two typical settlements. So, the building group locates in the main inlet and outlet of the settlements and intensive distribution areas. Settlement A distributes with the same form of the building group, they have not manifest differences. Settlement B has a layout of reflection form, so we take the building group which is near the center position as an example, which have the structural features of the circle.

Wind Speed Graphics. The distribution of outdoor winter wind fields in the two villages and the highest wind speed is 1.6 m/s. The wind speed values in the main areas all situate within the range of feeling comfortable. There are obviously stronger winds in the center of the bag-shaped neighborhoods in village B and also fall within the comfortable range

of 5 m/s. But, as the figure demonstrates, the configuration of building that contributes a lot to the formation of calm zones can be revealed. The building configurations of three-section compounds in village A are favorable to form the weak wind field in winter (Figures 21 and 22).

Wind Vectorgraphs. Consistent with the the overall wind vector graphics of the settlement, obvious differences remain on the trends and flowing amounts between Village A and Village B. The vector values of Village A are about 0.6 and the vector values of Village B are fluctuating between 0.2~2.0. In contrast to irregular structures, determinant-ordered structures are more likely to form gentle winds. The fluctuations of winds in Village B are relatively proven to be more obvious.

Wind Pressure. Research objects and neighboring environments pose great influences on the values of wind pressures. Thus, the intercepted spaces of parts of Village A and Village B does not appear proper to undergo wind pressure analysis; it is more proper for taking the overall wind pressure of the settlement as a premise (Figure 23).

2.6. Summary. A comparison can be recapped as follows. Village A forms better wind environments under the climate condition of Fujian and Minnan that characterize hot summer and cold winter. Determinant-ordered structures could control the gentle trends of wind vectors. The overall structures of the settlement are favorable to form the premise of

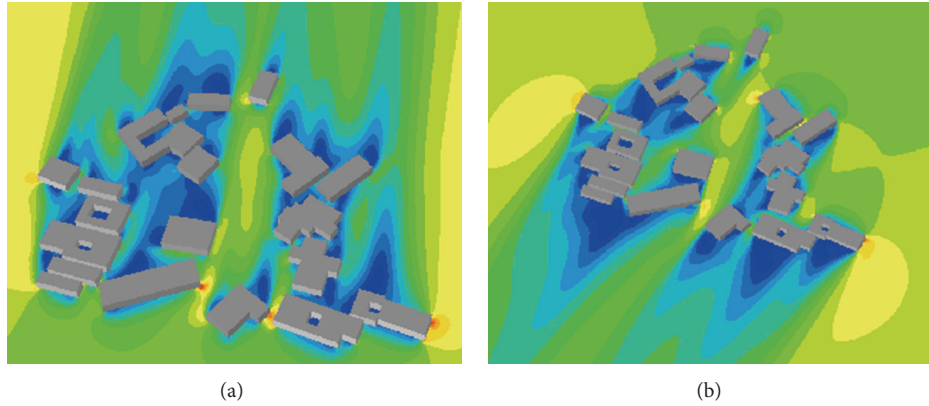


FIGURE 22: Wind speed simulations of the villagers B's building groups with irregular structures in winter and summer.

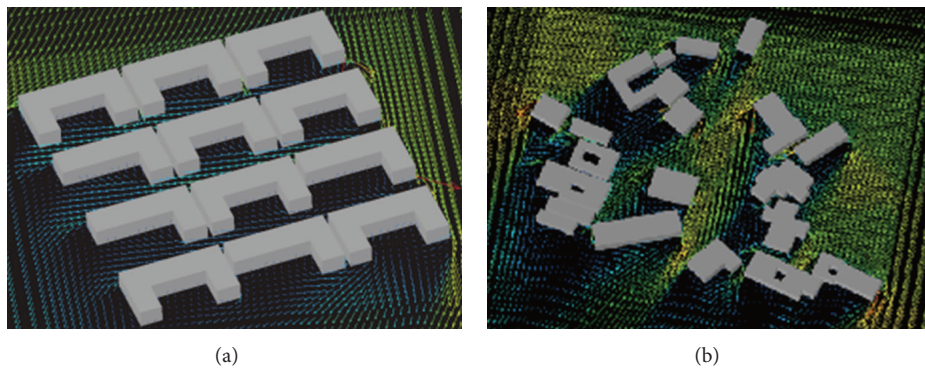


FIGURE 23: The winter monsoon vector diagrams of village A and village B.



FIGURE 24: The structures of Dai Mei Village, Longhai Country, Zhangzhou City, Fujian.



FIGURE 25: The broad transverse road in Dai Mei Village.

natural ventilation that flow across the buildings. The faces and configurations of the buildings are proven to be more difficult to form calm zones on the entrance surface of building in the winter. However, Village B's capacity for forming the calm zones is proven to be relatively weaker.

3. Spatial Pattern Analysis on Village A

Various definitions remain for space in different subjects. In this research, the space is the focus of the research, and it is formed by the construction and engineering. Hence, the investigation about the environments influenced by the artificial engineering such as the faces of the buildings and roads will be emphatically examined. In conducting the field work and making survey in Village A, the following points about

the formation of wind environments in the settlement are accrued.

3.1. Street Structure. The structure of Dai Mei Village (Village A) is determinant-ordered, multilevel depth, and connected with organic environment around (Figure 24). The roads are wide in the front and narrow in both sides and with broader road in the southern side of the building, which ranges from 8 to 12 meters (Figure 25). The western side and eastern side of the roads are narrower, ranging from 1 to 4 meters (Figure 26).

In Minnan, prevailing northwest winds reign in winter and prevail over southeast winds in summer. In the attempt



FIGURE 26: The narrow longitudinal road in Dai Mei Village.

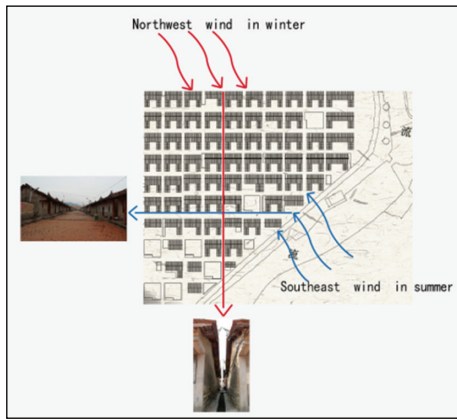


FIGURE 27: The relation between the monsoon in winter and summer and building style of settlement in Dai Mei Village.

of planning the construction of Dai Mei Village, the comb-styled structure of the roads was designed to guide the winds and to provide optimal capacity for the adaptation of climate condition (Figure 27). The southeast sides are open and wide, which make it easy for the entrance of southeast monsoon in the summer and could lower the indoor temperatures through natural ventilation. The building structures in the northwest direction are relatively enclosed and are easy to reduce the entrance of cold winds from the northwest sides. This could also reduce the energy consumption for heat preservation in winter.

3.2. The Strategy for the Layout of the Building. The determinant-ordered structure in Dai Mei Village is favorable for guiding the entrance of the southern winds in summer. However, this form of structure remains too unitary for the building in the living communities. Thus, PHOENICS was adopted to simulate and calculate the wind environments formed by other structures derived from determinant-ordered structure (Figure 28). We find that the transversal dislocation and longitudinal dislocation favors the guidance of southeast winds in summer (Figure 29).

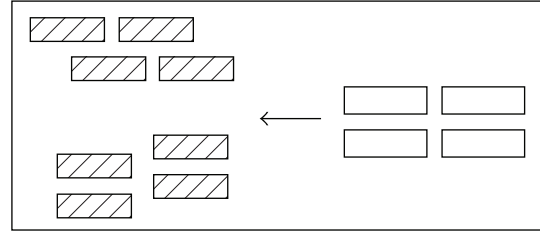


FIGURE 28: Two figures derived from determinant-ordered structure.

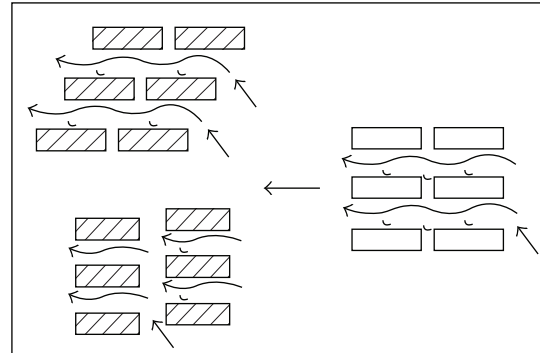


FIGURE 29: Simplified illustration about wind vector.

3.3. Architecture Forms. In Dai Mei Village, the distances between the buildings in the eastern and western directions make the streets narrower. The narrow streets surrounded by the two-sided high walls are commonly known as “ventilation lane” or “cool lane” [9]. In general, the walls would be exposed to the sunshine and would absorb lots of heat and would radiate heat to the indoor and thus cause the high temperatures in the indoor. But the intense built building in Dai Mei Village could shade each other and most of the walls in east-west direction basically are not influenced by the sunshine from the west, which could avoid the disadvantageous results caused by heat accumulation.

As the villagers in Dai Mei Village are consanguinity in the same clan, the relationships between the villagers are close. Consensus are made between villagers that every home would set a door on the end elevation of the building. Once all the doors on the end elevation of the building are opened, a circulating ventilation pipeline in east-west direction could be formed (Figures 30 and 31).

The configuration of higher front surface and lower back surface (Figure 32) is favorable to block cold northern winds and also form relatively weaker reflow winds. This proves to be advantageous for natural ventilation. Multiple layers of parallel-ordered buildings could form bigger areas for wind shadow and could influence the effects of natural ventilation.

3.4. To Build Altitude Strategy. The narrow distances between the walls of two building bring the access to the formation of the long and narrow ventilation space in northern-southern direction. This kind of building structures provides active ventilation, which could reduce the radiated heat from sun



FIGURE 30: The narrow ventilation lane is the best place to enjoy the cool air in Dai Mei Village.



FIGURE 31: There are doors in the east-west direction of all buildings.

and form the convection condition that connects the lanes and the indoor to make the living place shaded and cool. Of course, modern residences could not allow too close spacing or distance between building walls. Nevertheless, it is totally feasible to take advantage of the building groups for forming ventilation lane. It should be avoided to make the long axis of the house vertical to the prevailing wind direction in winter. By doing this, the negative effects caused by the front-row houses on back-row houses could be reduced and form good air convection (Figure 33).

4. Conclusion

By means of analog calculation of computing fluid dynamics, it is possible to suggest that the determinant-ordered structures formed by the engineering and construction of living houses and streets in Dai Mei Village could provide good natural wind environments. It is advantageous for the passing through of southeast winds in summer and the blocking the cold northwest wind in winter. To recap, the three main characteristics of the structures in the settlement are described as follows.

(1) *Comb-Styled Structures*. The neat and ordered streets are parallel to the prevailing direction in summer. While gusting, the narrow lanes and streets could enhance the wind speeds,

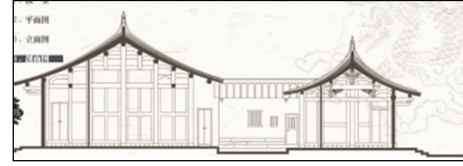


FIGURE 32: The altitude differences between the front and the back of the single building.

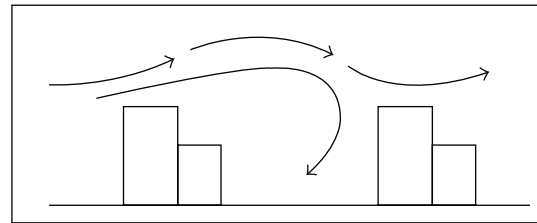


FIGURE 33: The altitude of the building groups in the community.

which is favorable for lowering the temperatures. Without winds, the high-intensity cold air in the shaded lane and low-intensity hot air outside the lanes would form convection and the convection. It could improve the heat environment of the living houses.

(2) *High Walls and Narrow Lanes*. The aspect ratio of narrow lane is huge and there are also eaves on the walls that could shade the sun to reduce temperature. Owing to the small areas exposed to sun and low-temperature air, the outdoor cool lane could thus be formed. Cool lanes are those wind paths with smaller cross-sectional areas. These cross-sectional areas could accrue the wind speed and lower the wind pressure. The hotter airs in the rooms connected to the cool lanes could be brought to the cool lane. The cooler air in the cool lane would supplement to the room, which could achieve the goal of ventilation.

(3) *Southern Wind Hallway*. The roads in front and in back of the house are broad and the lanes in both the right and the left of the house are narrow. This brings access to the southern winds to enter the south face of houses with three-section compound structure in summer.

Chinese modern city including office buildings, public buildings, and high-rise apartments tends to develop towards high-rise buildings. According to energy saving strategy of wind environment which this paper concerns, which is under the background of traditional low-rise residential areas, therefore, this design strategy is applied to local rural areas and urban villa residential areas.

5. Future Work

The results of the design strategy have already been transformed into a design program to take apart in the Residence Design Competition of Fujian village in 2009 (Figure 34); and the design program adapted from this research results was awarded with Excellent Planning Award and Champion of



FIGURE 34: The design program of Minnan rural house in regions that is hot in summer and warm in winter.

Building category. The following research can investigate how wind environments influence the heat environment of settlements.

References

- [1] L. Yang and Y. Li, "Thermal conditions and ventilation in an ideal city model of Hong Kong," *Energy and Buildings*, vol. 43, no. 5, pp. 1139–1148, 2011.
- [2] R. Priyadarsini, W. N. Hien, and C. K. Wai David, "Microclimatic modeling of the urban thermal environment of Singapore to mitigate urban heat island," *Solar Energy*, vol. 82, no. 8, pp. 727–745, 2008.
- [3] Y. Tominaga, A. Mochida, R. Yoshie et al., "AIJ guidelines for practical applications of CFD to pedestrian wind environment around buildings," *Journal of Wind Engineering and Industrial Aerodynamics*, vol. 96, no. 10–11, pp. 1749–1761, 2008.
- [4] A. R. Azli, H. Aya, I. Naoki, and T. Jun, "Analysis of airflow over building arrays for assessment of urban wind environment," *Building and Environment*, vol. 59, pp. 56–65, 2013.
- [5] B. Givoni, "Comfort, climate analysis and building design guidelines," *Energy and Buildings*, vol. 18, no. 1, pp. 11–23, 1992.
- [6] T. E. Jiru and G. T. Bitsuamlak, "Application of CFD in modelling wind-induced natural ventilation of buildings—a review," *International Journal of Ventilation*, vol. 9, no. 2, pp. 131–147, 2010.
- [7] F. Wang and Y. Q. Xiao, "Simulation and evaluation of building cluster's wind environment with PHOENICS software," *Shandong Architectural Engineering Journal*, vol. 20, no. 5, pp. 39–42, 2005.
- [8] W. Q. Tao, *Numerical Heat Transfer*, Xi'an Jiao Tong University Press, 2001.
- [9] P. Daven, "The relationship of wind structure to wind loading," in *Proceeding of the Symposium on Wind Effect on Building and Structures*, pp. 54–102, London, UK, 1965.

Research Article

The Use of a Brain Computer Interface Remote Control to Navigate a Recreational Device

Shih Chung Chen,¹ Aaron Raymond See,¹ Yeou Jiunn Chen,¹
Chia Hong Yeng,¹ and Chih Kuo Liang²

¹ Department of Electrical Engineering, Southern Taiwan University of Science and Technology, Yung Kang District, Tainan City 71005, Taiwan

² Department of Electrical Engineering, National Taitung College, Taitung City 95045, Taiwan

Correspondence should be addressed to Shih Chung Chen; scchen1960@gmail.com

Received 15 September 2013; Accepted 21 October 2013

Academic Editor: Teen-Hang Meen

Copyright © 2013 Shih Chung Chen et al. This is an open access article distributed under the Creative Commons Attribution License, which permits unrestricted use, distribution, and reproduction in any medium, provided the original work is properly cited.

People suffering from paralysis caused by serious neural disorder or spinal cord injury also need to be given a means of recreation other than general living aids. Although there have been a proliferation of brain computer interface (BCI) applications, developments for recreational activities are scarcely seen. The objective of this study is to develop a BCI-based remote control integrated with commercial devices such as the remote controlled Air Swimmer. The brain is visually stimulated using boxes flickering at preprogrammed frequencies to activate a brain response. After acquiring and processing these brain signals, the frequency of the resulting peak, which corresponds to the user's selection, is determined by a decision model. Consequently, a command signal is sent from the computer to the wireless remote controller via a data acquisition (DAQ) module. A command selection training (CST) and simulated path test (SPT) were conducted by 12 subjects using the BCI control system and the experimental results showed a recognition accuracy rate of 89.51% and 92.31% for the CST and SPT, respectively. The fastest information transfer rate demonstrated a response of 105 bits/min and 41.79 bits/min for the CST and SPT, respectively. The BCI system was proven to be able to provide a fast and accurate response for a remote controller application.

1. Introduction

The effect of a neurodegenerative disease or a spinal cord injury suffered from an accident has caused the loss of quality of life for millions of people around the world. One important reason is that they have reduced capabilities in communicating normally with people and their external environments. In order to better provide for the needs of these individuals, developments of high technology assistive devices have seen an increase in proliferation in recent years. These devices are used to help the patients cope with daily tasks such as eating, dressing, living, and mobility, among others. A field about psychologically healing that has only recently been considered is entertainment for the patients. New forms of entertainment were developed through the use of a brain computer interface (BCI). BCI is essentially a means of extracting several features from the scalp potential,

or electroencephalography (EEG), with the aid of external devices. These assistive devices provide patients a distinct method to communicate with the outside world [1]. The game of chess was reinvented to make use of BCI control wherein EEG is used to determine which piece to move [2]. Previous developments on BCI made use of event-related potential (ERP) associated in time with either physical or mental occurrence.

ERP often includes the μ and β rhythms, slow cortical potential, P300-evoked potential, and the steady-state visual-evoked potential (SSVEP) [1]. A form of slow cortical potential is the visual evoked potential (VEP), in which a visual stimulus, such as an alternating checkerboard pattern, is displayed on the screen to elicit evoked potential [3]. In a previous article the research group developed a BCI-controlled LEGO page-turner that uses VEP technology. It was able to produce a high recognition rate in turning

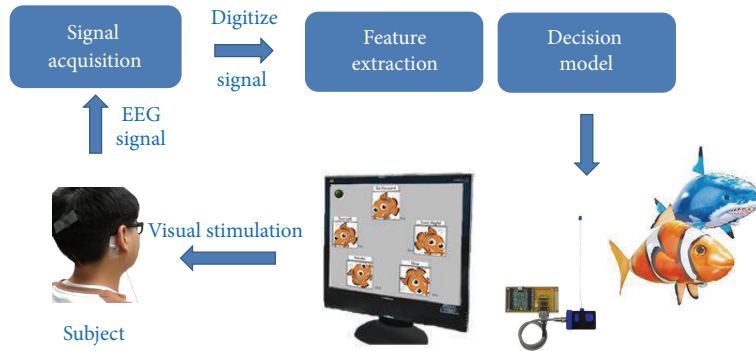


FIGURE 1: System architecture of the proposed BCI remote control.

the page of a book to the left or right. However, the duration for each trial was about 7 to 12 seconds [4]. In order to reduce the response time and increase the signal-to-noise ratio (SNR) in future projects, BCI researchers are shifting to the use of SSVEP. SSVEP is an oscillatory wave that appears in the occipital leads of the EEG in response to visual stimuli modulated at a certain frequency. It can involve the use of pattern-reversed checkerboard or flickering LEDs [3].

The frequency of the SSVEP matches that of the stimulus and its harmonics [1, 3]. The uses of LED and SSVEP were implemented in several ways, such as moving a cursor location or selecting a certain target. In larger cases such as a QWERTY keyboard spelling system, SSVEP requires the number of stimulating frequencies to be larger than that of the displayed characters [5]. In congruence with a previous study on an alternative sleep EEG electrode placement [6], the coherence of different frequency stimuli and its effect on the EEG signal at different electrode placements is also a topic of interest in this field of study.

In this paper, we propose the integration of a remote control entertainment device to a noninvasive BCI system. Throughout the years, remote control devices are one kind of the most popular toys by both children and adults alike. And in recent years a commercial remote control toy called the Air Swimmer gained popularity due to its unique concept of having a flying fish controlled with the standard remote control. Controlling the toy can be done with ease by normal people, but for those with certain disorders even this form of entertainment can be cumbersome. Therefore, the current research aims to develop a BCI remote control for the Air Swimmer and evaluate its performance. Subsequently, the proposed BCI system is based on the theory of steady state evoked potentials (SSVEP). It states that when a person stares at an oscillating visual stimulus the brain will produce a corresponding response and this response can then be used to create a BCI command. It utilizes lights or flickering boxes on a computer interface to induce SSVEP. As an object flickers at a certain frequency, it instigates a response in the visual cortex at the frequency stimulus or its harmonics. Hence, a set of frequencies can be used to perform different commands [7, 8].

The rest of this paper is organized as follows. Section 2 describes the BCI remote control and the application protocol to test the system. It also includes the methodological approach to identify spectral response including feature extraction, decision modeling, and translation command. Section 3 then describes the results of a series of experiments to examine the performance of our approach. Finally, conclusions are drawn in Section 4, and possible improvements for future development of this work are discussed.

2. Methods

The system architecture of the proposed BCI-based remote control system for recreational purposes is shown in Figure 1. The BCI system presented thereafter includes the remote control system with the following processes: visual stimulation, signal acquisition, signal preprocessing, feature extraction, decision model, and translational commands. First, the subjects need to focus on the flickering box that is marked with the desired icon displayed on an LCD screen. Second, electroencephalographic (EEG) signals are extracted using a single electrode from the occipital area of the subject's head. Third, the EEG signals acquired are preprocessed to remove unnecessary drifts, trends, and noise. The signal undergoes baseline correction and a series of filtering methods prior to analysis. Fourth, the computations of the power spectra of the EEG signal's different harmonic bands are performed. Fifth, a decision model is used to determine the required response that will then be translated to a command signal. Sixth, the hardware module control is discussed and lastly experimental procedures are stated.

2.1. Visual Stimulation. Visual stimulation was performed to elicit SSVEP. A 24" LCD monitor displaying the flickering boxes simulated by a program was used. The boxes were arranged and placed at different locations across the screen with the concern of reducing interference between frequencies. A program is designed to make the boxes flickering at frequencies between 6 Hz–10 Hz with 1 Hz increments. The corresponding commands are as follows: (a) 6 Hz (dive), (b) 7 Hz (left turn), (c) 8 Hz (swim forward), (d) 9 Hz (right turn), and (e) 10 Hz (elevate).

2.2. Signal Acquisition. The visual stimulation elicits signals on the visual cortex of the brain. Concurrently, EEG signals are simultaneously read from the occipital region of the subject's head by a data acquisition device. Signal acquisition was conducted with the use of Ag-Cl electrodes connected to an EEG amplifier using the NuAmps EEG amplifier by Neuroscan Company. The EEG cap has a total of 40 electrodes and sampling frequency can be set at 125/250/1000 Hz. The device also makes use of a 22-bit analog to digital converter. EEG recordings were acquired from the Oz channel with reference placed at A2. The subjects were required to sit at a distance of 55 cm from the monitor, measured from the subject's nasion to the screen of the BCI interface. The raw data of the EEG signals were then transmitted to a personal computer to perform further analysis and eventually control the Air Swimmer. Next, the EEG signal is then temporarily saved in a buffer array. The purpose of this buffer is to accumulate the real-time EEG signal to form an array size of 1000 samples before being processed. After the sampled data is processed, the buffer array is cleared.

2.3. Signal Preprocessing. In order to accurately/perceptively represent the EEG signal, x , the drift phenomenon of EEG signal should be removed. An exponentially modified Gaussian function based on nonlinear curve fit model is used and defined as

$$f(x) = y_0 + \frac{A}{t_0} \exp \left[\frac{1}{2} \left(\frac{w}{t_0} \right)^2 - \frac{x - x_c}{t_0} \right] \times \left[\frac{1}{2} + \frac{1}{2} \operatorname{erf} \left(\frac{z}{\sqrt{2}} \right) \right], \quad (1)$$

where y_0 is the offset from the y -axis and A is the amplitude of the data set. x_c is the center of the data while w is the width of the function. t_0 is the modification factor and z is defined as

$$z = \frac{x - x_c}{w} - \frac{w}{t_0}. \quad (2)$$

The erf function in (1) represents an error function and can be defined as

$$\operatorname{erf}(z) = \frac{2}{\sqrt{\pi}} \int_0^z \exp(-u^2) du. \quad (3)$$

After removing the drift phenomenon of the EEG signal x , a 2nd order band-pass filter with cut-off frequencies between 5 and 30 Hz is used to limit the frequency range of the EEG signals to the subject's responses on visual stimulation. In order to smooth the signal and reduce noise, the Savitzky-Golay filter, $\bar{g}(t)$, is adopted to preserve its fundamental features and is defined as

$$\bar{g}(t) = \sum_{i=-n_L}^{n_R} c_i \times f(t+i), \quad (4)$$

where n_L and n_R are the number of points the signal is smoothed before and after each considered time point t , respectively. c_i are the weighting coefficients of filter, which can keep higher moments [9, 10].

2.4. Feature Extraction. To determine the subject's selection, the power spectrum of the preprocessed EEG signal is $\bar{g}(t)$ calculated. The power spectrum is calculated by using fast Fourier transform (FFT) [11] which is defined as

$$\Psi_d = \frac{1}{N} \sum_{n=0}^{N-1} \bar{g}_n \exp^{j(2\pi/N)nd}, \quad d \in \{0, 1, \dots, N-1\}, \quad (5)$$

where \bar{g}_n is the discrete form of the continuous signal $\bar{g}(t)$ and N is the length of the data. Then the power spectrum is calculated as

$$E = \lim_{T \rightarrow \infty} \frac{1}{2T} \int_{-T}^T \Psi(t)^2 dt. \quad (6)$$

In order to determine the target frequency, the energy at frequency bins 6 Hz, 7 Hz, 8 Hz, 9 Hz, and 10 Hz is selected as the feature k which will be used in the decision model to arbitrate the desired selection.

2.5. Decision Model. A threshold is set to exclude the possibility of unnecessary peak occurrence during the initial EEG acquisition. The subjects are first exposed to the different flickering boxes and their initial responses to the stimuli are recorded. The threshold is set by obtaining the mean of the peaks from each frequency band after undergoing the preliminary EEG measurement. The selected features are required to meet the predefined threshold before any command will be sent to the remote controller.

The decision model is used to determine the command selection from feature k and is defined as

$$\hat{w} = \arg \max_{w_i} P(w_i | k), \quad (7)$$

where w_i is the model and x is the set of data. According to Bayesian theory, (7) can be derived as

$$\hat{w} = \arg \max_{w_i} \frac{P(w_i)}{P(k)} P(k | w_i). \quad (8)$$

Since $P(k)$ is constant to all other models and $P(w_i)$ is assumed to be a uniform distribution, $P(k)$ and $P(w_i)$ would not affect the result of (8). Therefore, (8) can be rewritten as

$$\hat{w} = \arg \max_{w_i} P(w_i | k). \quad (9)$$

In this study, the $P(w_i | k)$ is assumed to have the form of a Gaussian probability density function in the m -dimension space and is defined as

$$P(k) = \frac{1}{(2\pi)^{m/2} |\Sigma|^{1/2}} \exp^{-(1/2)(k-\mu)^T \Sigma^{-1}(k-\mu)}, \quad (10)$$

where $\mu = \lambda[k]$ is the mean value and Σ is the variance defined as

$$\Sigma = \lambda [(k - \mu)^2]. \quad (11)$$

It is readily seen that for $m = 1$ the multivariate Gaussian coincides with the univariate one. Afterwards, the location of the maximum peak is determined as the selection of the subject and a command is sent through the DAQ and transmitted to the reconfigured remote control.

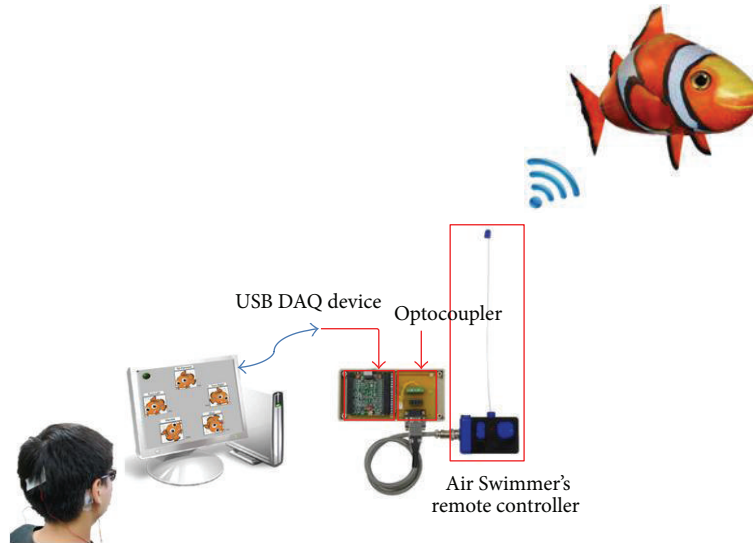


FIGURE 2: Reconfigured Air Swimmer remote controller connected to a computer via a DAQ device and commands are sent through an RF signal to the receiving end underneath the flying fish.

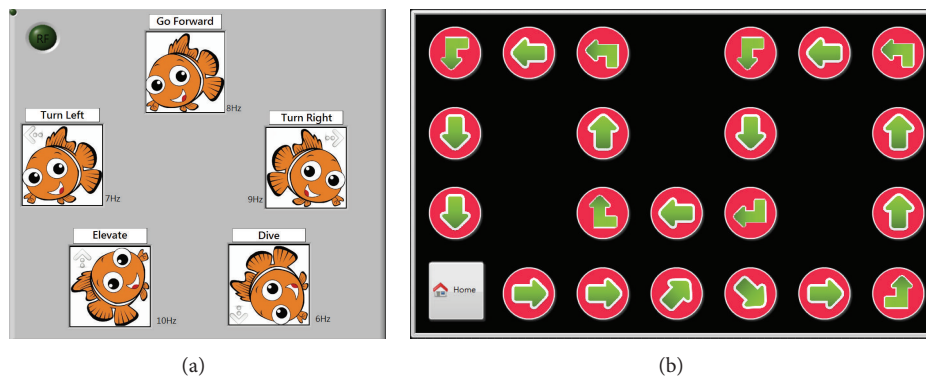


FIGURE 3: The experiments were conducted using (a) flickering boxes that are distributed in a star shape for visual stimulation to efficiently separate the 5 frequencies and (b) the simulated pathway for the subjects to follow.

2.6. Hardware Module. The remote control module was reconfigured to be able to accept input from a computer. The hardware module includes a USB data acquisition (DAQ) device and an optocoupler for data transmission. The DAQ is required to convert the digital command output from the computer to an analog input for the remote control. However, in order to reduce the transmission interference, an optocoupler was included as a bridge between the DAQ and remote control. Furthermore, modifications were also made on the input connection of the original remote control circuit board to control the Air Swimmer as shown in Figure 2. Command to the Air Swimmer is then sent via radio frequency transmission.

2.7. Experimental Design for the BCI Remote Control. To validate the proposed BCI remote control system, the subjects performed 2 different experiments, namely, command selection training (CST) and simulated path testing (SPT).

The graphic user interface for the visual stimulation and a simulated path are shown in Figure 3.

2.7.1. Command Selection Training (CST). The CST aims to determine the subject's initial response to SSVEP stimulation. First, the CST requires the subjects to continuously look at a designated flickering box. The trial ends when the subject triggers 30 responses. After each trial the user is required to rest for 2 minutes with eyes closed. These steps are repeated until all 5 different command frequencies have been tested. The program counts the number of correct and wrong selections and calculates the accuracy of the subject. The time for each trial is also recorded for use in further analysis.

2.7.2. Simulated Path Testing (SPT). After undergoing CST, the performances of the subjects in using the system were tested. A simulated path was developed for the subjects to follow. Arrows chain on a separate graphic user interface

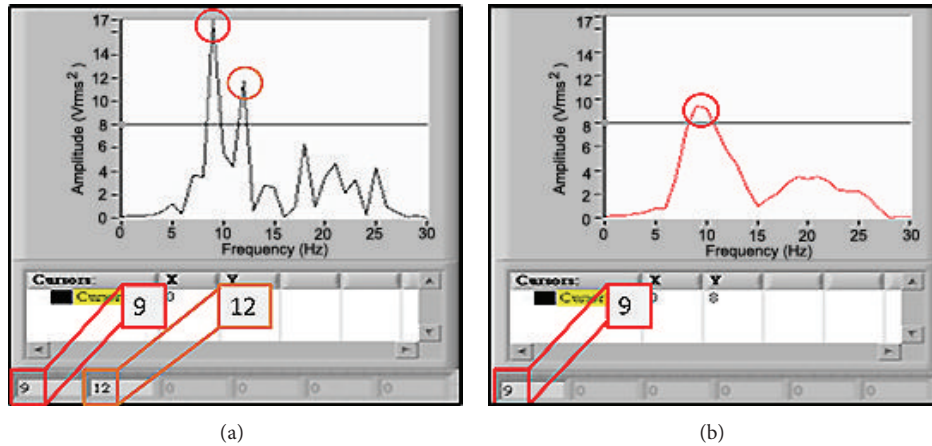


FIGURE 4: Results of the feature extraction showing (a) multiple peaks detected and (b) single peak after performing moving average.

(GUI) serves as a guideline on which command should be selected. Subsequently, an audio command is provided to assist the subjects on the designated command. The arrow will be turned on with a green color when a correct input is made. However, if the wrong input is sent, the arrow will remain off and dark and will require the subject to make another input until the correct selection has been made. The program counts the number of correct and wrong selections and calculates the accuracy of the subject. The time for the whole trial was also recorded for use in further analysis. Moreover, after a correct selection is made, a delay was introduced by stopping the flickering boxes and letting the subject rest for 3 seconds to reduce the probability of having residual frequency from the previous selection.

3. Experimental Results

To evaluate the proposed BCI remote control system, 12 subjects (10 males and 2 females) were asked to participate in the experiments. The average age of the group is 20.9 and 21.5 years olds for males and females, respectively. In addition, they have normal or corrected-to-normal vision and had no history of any neurological or psychological disorders.

3.1. System Limitation. The first step for users to adapt to an SSVEP system is by training the brain with the set of frequencies that will be used in the experiment. During the course of the experiment it was noted that different users exhibited different responses to the same set of frequencies. Some of the subjects were removed from the study due to several reasons: strong electrocardiograph (ECG) signals were detected at the Oz region and poor response to SSVEP. Since the study only made use of a single channel EEG, independent component analysis cannot be used to remove the noise caused by the ECG signal. Subsequently, the frequencies which are adaptive to SSVEP system were divided into three main frequency bands composed of low (1–12 Hz), medium (12–30 Hz), and high (30–60 Hz) [12]. The limitation of the study includes the use of low frequency range due to the limitation of the refresh rate of the LCD screen and

the number of flickers the computer can handle in real time. The subjects exhibited response to low frequencies as that of [5, 13]. Nevertheless, some of the subjects were not accustomed to low frequency and their EEG signals reflected minimal response. It was challenging to recognize the EEG feature of the subject and thus some of the initial subjects discontinued the experiments and were not included in the results. In order to correct the trigger level, the threshold was adjusted for each subject in accordance to the mean of the peak responses at different frequencies. Subsequently, the Savitzky-Golay method was also useful in the smoothing signal as it preserves the fundamental features including the maxima, minima, width of the peaks, and others [10].

3.2. Peak Detection and Control Command. The control command is sent when the specific frequency response exceeds the given threshold. However, during the experiment body movements and unconscious jitters produced unwanted noise on the signal. It would result in irrelevant peaks that interfere with the peak threshold detection as shown in Figure 4(a).

The solution chosen for the peak interference was the use of moving average. The purpose of moving average is to reduce the noise in the signal, increasing peak identification and reducing the random noise. It is optimal for this process due to its simple theory and fast calculation time [14]. In the current research the Henderson 7-term method was used. In the event that more than one peak exceeds the threshold, a possible misjudgment will cause error in the command selection. Through the use of the decision model mentioned above, the peak frequency is ascertained. Consequently, the position of the resulting peak is recorded for the command process. Once the correct peak is determined, the computer would then send the control signal to the remote control via the self-developed control module. It should also be noted that a control command is only sent if only a single peak is determined as shown in Figure 4(b).

3.3. BCI Performance Evaluation. The performance of the remote control system will be assessed by calculating the

TABLE 1: Results of the command selections made during the training experiments showing the accuracy, total time, and ITR of each subject.

Subject no.	Command selections (correct/total)					Accuracy (%)	Time (s)	ITR (bits/min)
	Left	Right	Forward	Elevate	Dive			
1	30/30	30/30	29/30	30/30	30/30	99.30	198	104.98
2	28/30	17/30	25/30	20/30	25/30	76.70	620	28.40
3	30/30	26/30	25/30	25/30	30/30	90.70	1578	12.31
4	30/30	30/30	29/30	30/30	30/30	99.30	671	30.98
5	29/30	27/30	26/30	28/30	30/30	93.30	288	68.86
6	30/30	29/30	28/30	20/30	29/30	90.70	523	37.16
7	21/30	24/30	23/30	25/30	30/30	82.00	424	43.04
8	30/30	30/30	30/30	18/30	25/30	88.70	522	36.67
9	30/30	29/30	27/30	25/30	30/30	94.00	250	79.73
10	30/30	25/30	30/30	25/30	29/30	92.70	636	31.02
11	30/30	29/30	30/30	22/30	30/30	94.00	824	24.19
12	26/30	17/30	20/30	16/30	30/30	72.70	968	17.74

information transfer rate (ITR). In this study we used the parameters of bit rate, selections per minute (SPM), and time to determine the ITR. This method had been widely used to quantify the speeds of developed BCI systems [13, 15, 16]. The ITR calculation used in this study is the Wolpaw method based on the formula presented in [16] and is defined as

$$B_t = \log_2 N + p \log_2 p + (1 - p) \log_2 \left[\frac{1 - p}{N - 1} \right], \quad (12)$$

where p is the accuracy of the classification and N is the number of selections. B_t is presented as bits per trial. In this study, the number of selections (N) is equivalent to the number of flickering boxes ($N = 5$).

The classification accuracy p is computed by taking the correct selection commands divided by the total number of selections. Like in most BCI studies, it can be considered that each box, flickering at different frequencies, is assumed to have an equal probability of being positively classified.

ITR is usually calculated in terms of bits/min (bpm) and is calculated using

$$\text{ITR} = \frac{60}{T} \cdot S_N \cdot B_t, \quad (13)$$

where T is the total selection time in seconds, S_N is the number of selections, and B_t is the bit rate.

3.4. Experimental Results of the BCI Remote Control System. The CST experiment was conducted to train and understand the subject's brain response to the different set of flickering frequencies. It was also a baseline to determine how accurate and fast the response of each subject is to visual stimulation. The results of the CST experiment are summarized in Table 1. After performing a total of 30 correct selections for each of the 5 commands, it is evident that a large disparity was manifested between the subjects. It was observed that the fastest response time shown during the training was that of subject 1 with an average time of 1.32 seconds per command while still maintaining the accuracy of 99.3% and an ITR of 105 bits/min. In contrast, subject 4 may have the same

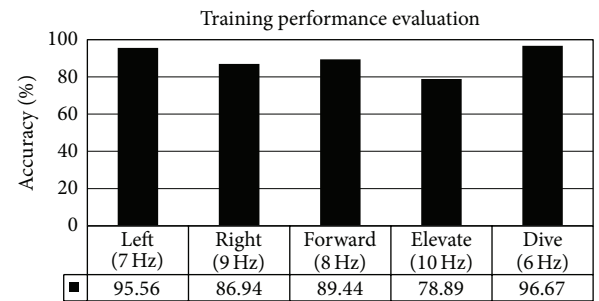


FIGURE 5: Average accuracy of the different command selection in the training experiments by all the subjects.

accuracy but the response time was 3.4 times slower than that of subject 1 causing significantly lower ITR of 30.98 bits/min. It was observed that although some of the subjects have an accuracy of more than 90% the response time it took to accomplish the task was 8 times slower than the best time as manifested by subject 3.

Overall, the subjects were able to achieve an average classification accuracy of 89.51% for the whole training experiments with a mean of 4.16 seconds per command. It can also be noted that the average ITR of the group is 42.92 bits/min.

Based on the results it was discovered that although the subject is only required to focus on a single flickering box there were still some instances wherein the wrong responses were produced. The erroneous results could be the effect of the other boxes flickering simultaneously near the desired frequency. It was then observed that the subjects are highly sensitive to the first 4 frequencies from 6 Hz to 9 Hz but have a slightly lower sensitivity at the 10 Hz (elevate) selection as shown in Figure 5.

The summarized results of the SPT experiment are shown in Table 2. The subjects were required to activate all the commands correctly, thus the similarity in the number of correct selections. It is also evident that a larger total number of selections can be deduced as the occurrence of multiple

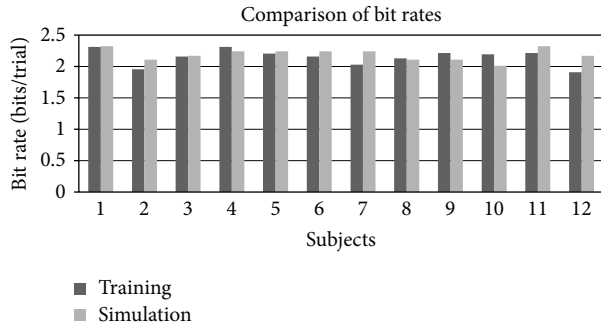


FIGURE 6: Comparison of bit rates during training and simulated experiment.

TABLE 2: Experimental results of the simulated path.

Subject	Selections (correct/total)	Accuracy (%)	Duration (s)	ITR
1	21/21	100.00	70	41.79
2	21/24	87.50	120	25.31
3	21/23	91.30	339	8.83
4	21/22	95.45	204	14.49
5	21/22	95.45	134	22.07
6	21/22	95.45	195	15.16
7	21/22	95.45	149	19.84
8	21/24	87.50	280	10.85
9	21/24	87.50	155	19.59
10	21/26	80.77	178	17.62
11	21/21	100.00	96	30.48
12	21/23	91.30	122	24.54

errors during the selection progress. The average accuracy is calculated to be 92.31% with an average time of 7.45 s. The average ITR was 20.88 bits/min. It was observed that the bit rate for each subject is relatively the same during the CST and SPT experiments as shown in Figure 6. However, more experiments will be conducted to determine the learning process and how to improve the bit rate of the subjects.

The experiments were then compared with the ITR results of the system from previous SSVEP studies that made use of LCD screen with frequencies in the low and medium frequency bands [10]. Results were satisfactory with some subject's exhibiting results close to those of the best performing ITRs in previous studies. The average bit rate for both the CST and SPT was 31.9 bits/min and an average accuracy of 90.91% with both tests performed by the 12 subjects. Subsequently, the current application is also more convenient due to the use of only a single channel EEG as compared to multiple channels used in previous studies such as [5, 10, 15]. In comparison to the research of [13], the bit rate of their BCI spelling system was 37.62 bits per minute and an accuracy of 92.25%. Their system focuses mainly on 3 out of the 5 commands available. Studies investigated by Zhu et al. showed ITR ranging from 7.5 bits/min to 68 bits/min [12]. The peaks amplitudes of the SSVEP were observed

to be large near the 10 Hz range that concurs with the study of [17]. One inherent disadvantage of the frequencies used in this study is that it falls between 5 and 25 Hz which is considered as uncomfortable compared to its higher frequency counterparts. Concurrently, the use of flash and pattern reversal stimuli within a 20 Hz interval from 5 and 25 Hz can elicit epileptic seizures and the subjects got tired more easily [18]. The task of integrating the BCI system with the remote control device offers a wide range of opportunities to entertainment devices that can help improve the quality of life of the disabled patients.

4. Conclusions

In this paper, we have successfully integrated a BCI remote-control system with a remote controlled device in the form of Air Swimmer that exhibited high accuracy and with a fast response time. It should be noted that in order to achieve high accuracy and fast response time, the subjects were trained prior to the simulated test. It can be deduced that evaluating the performance of the subject while using the BCI system requires time and training as current results of the CST and SPT showed minute change. The resulting ITR was within the range of BCI systems using LCD screens. The performance of the system using only a single channel EEG showed an average ITR of 32 bits/min while performing at an average above 90% accuracy as compared to other multielectrode BCI. In the future a more convenient EEG acquisition device could be developed and integrated with an external device that contains the visual stimulators and also a standalone signal processing module would provide a practical and convenient method for future BCI remote controls. Improvements on the feature extraction method through the use of statistical analysis will also be done to reduce misclassification.

Acknowledgment

The authors would like to thank the National Science Council for funding this project under Grant no. NSC-100-2632-E-218-001-MY3.

References

- [1] J. Wolpaw, N. Birbaumer, D. McFarland, G. Pfurtscheller, and T. Vaughan, "Brain-computer interfaces for communication and control," *Clinical Neurophysiology*, vol. 113, pp. 767–791, 2002.
- [2] P. Morias, *Playing Chess by Thinking: Brain Computer Interfaces over EEG*, 2012, <http://bciovereeeg.blogspot.tw/2012/04/playing-chess.html>.
- [3] J. V. Odom, M. Bach, C. Barber et al., "Visual evoked potentials standard," *Documenta Ophthalmologica*, vol. 108, no. 2, pp. 115–123, 2004.
- [4] S. C. Chen, W. J. Hong, Y. C. Chen, S. C. Hsieh, and S. Y. Yang, "The page turner controlled by BCI," in *Proceedings of the IFMBE 6th World Congress of Biomechanics (WCB '10)*, vol. 31, pp. 1534–1537, Singapore, August 2010.

- [5] H. J. Hwang, J. H. Lim, Y. J. Jung, H. Choi, S. W. Lee, and C. H. Im, "Development of an SSVEP-based BCI spelling system adopting a QWERTY-style LED keyboard," *Journal of Neuroscience Methods*, vol. 208, no. 1, pp. 59–65, 2012.
- [6] S. C. Chen, A. R. See, C. J. Hou et al., "Coherence validation of alternative sleep EEG electrode placements using wavelet transform," *Journal of Medical and Biological Engineering*, 2013.
- [7] H. Cecotti, "Spelling with non-invasive brain-computer interfaces—current and future trends," *Journal of Physiology*, vol. 105, no. 1–3, pp. 106–114, 2011.
- [8] F.-B. Vialatte, M. Maurice, J. Dauwels, and A. Cichocki, "Steady-state visually evoked potentials: focus on essential paradigms and future perspectives," *Progress in Neurobiology*, vol. 90, no. 4, pp. 418–438, 2010.
- [9] A. Savitzky and M. J. E. Golay, "Smoothing and differentiation of data by simplified least squares procedures," *Analytical Chemistry*, vol. 36, no. 8, pp. 1627–1639, 1964.
- [10] P. Martinez, H. Bakardjian, and A. Cichocki, "Fully online multicommand brain-computer interface with visual neurofeedback using SSVEP paradigm," *Computational Intelligence and Neuroscience*, vol. 2007, Article ID 94561, 9 pages, 2007.
- [11] "The fundamentals of FFT-based signal analysis and measurement in LabVIEW and LabWindows/CVI," National Instruments, 2012, <http://www.ni.com/white-paper/4278/en/>.
- [12] D. Zhu, J. Bieger, G. Garcia Molina, and R. M. Aarts, "A survey of stimulation methods used in SSVEP-based BCIs," *Computational Intelligence and Neuroscience*, vol. 2010, Article ID 702357, 12 pages, 2010.
- [13] H. Cecotti, "A self-paced and calibration-less SSVEP-based brain-computer interface speller," *IEEE Transactions on Neural Systems and Rehabilitation Engineering*, vol. 18, no. 2, pp. 127–133, 2010.
- [14] R. M. Rangayyan, *Biomedical Signal Analysis: A Case-Study Approach*, Wiley-Interscience, New York, NY, USA, 2002.
- [15] S. M. T. Müller, W. C. Celeste, T. F. Bastos-Filho, and M. SarcinelliFilho, "Brain-computer interface based on visual evoked potentials to command autonomous robotic wheelchair," *Journal of Medical and Biological Engineering*, vol. 30, no. 6, pp. 407–416, 2010.
- [16] I. Volosyak, "SSVEP-based Bremen-BCI interface—boosting information transfer rates," *Journal of Neural Engineering*, vol. 8, no. 3, Article ID 036020, 2011.
- [17] D. Regan, *Human Brain Electrophysiology: Evoked Potentials and Evoked Magnetic Fields in Science and Medicine*, Elsevier, Amsterdam, The Netherlands, 1989.
- [18] R. S. Fisher, G. Harding, G. Erba, G. L. Barkley, and A. Wilkins, "Photic- and pattern-induced seizures: a review for The Epilepsy Foundation of America Working Group," *Epilepsia*, vol. 46, no. 9, pp. 1426–1441, 2005.

Research Article

Empirical Analysis of Server Consolidation and Desktop Virtualization in Cloud Computing

Bao Rong Chang,¹ Hsiu-Fen Tsai,² and Chi-Ming Chen³

¹ Department of Computer Science and Information Engineering, National University of Kaohsiung, 81148 Kaohsiung, Taiwan

² Department of Marketing Management, Shu Te University, 82445 Kaohsiung, Taiwan

³ Department of Computer Science and Information Engineering, National University of Kaohsiung, 81148 Kaohsiung, Taiwan

Correspondence should be addressed to Bao Rong Chang; brchang@nuk.edu.tw

Received 11 September 2013; Accepted 10 October 2013

Academic Editor: Teen-Hang Meen

Copyright © 2013 Bao Rong Chang et al. This is an open access article distributed under the Creative Commons Attribution License, which permits unrestricted use, distribution, and reproduction in any medium, provided the original work is properly cited.

Physical server transitioned to virtual server infrastructure (VSI) and desktop device to virtual desktop infrastructure (VDI) have the crucial problems of server consolidation, virtualization performance, virtual machine density, total cost of ownership (TCO), and return on investments (ROI). Besides, how to appropriately choose hypervisor for the desired server/desktop virtualization is really challenging, because a trade-off between virtualization performance and cost is a hard decision to make in the cloud. This paper introduces five hypervisors to establish the virtual environment and then gives a careful assessment based on C/P ratio that is derived from composite index, consolidation ratio, virtual machine density, TCO, and ROI. As a result, even though ESX server obtains the highest ROI and lowest TCO in server virtualization and Hyper-V R2 gains the best performance of virtual machine management; both of them however cost too much. Instead the best choice is Proxmox Virtual Environment (Proxmox VE) because it not only saves the initial investment a lot to own a virtual server/desktop infrastructure, but also obtains the lowest C/P ratio.

1. Introduction

Well-known public large-size cloud and private enterprise-owned cloud are currently leading cloud computing and services, for example, Amazon AWS, Google App Engine, and Windows Azure in public cloud and Salesforce.com and EMC² in private cloud. In contrast, small-to-medium sized enterprises (SMEs), educational institutes, and social groups are also very eager to pursue the services they want based on virtual server in cloud (VSiC) [1] architecture due to cost reduction, performance escalation, and security improvement. With this service, the operational costs for the information system can be drastically reduced and it can quickly increase the competitiveness of its information system, which is sustained by the following advantages: centralized monitoring, quick management, dynamic optimization, and efficient backup.

Technically, unexpected situations with service-type servers, such as websites, databases, AP servers, and file servers, bring much trouble for enterprises. Once a service

stops its function, it can cause faulty data, stalled production lines, and interrupted operation procedures, leading to multiple losses. However, a physical host has problems of promptness of service transfer to another host, restarting the service, and inability to update data in real time. The hardware, information, and data will be obstacles for enterprises to overcome.

To solve the issues mentioned above, virtual machine management system or hypervisor [2], such as VMware ESX/ESXi Server, Microsoft Hyper-V R2 [3], and Proxmox virtual environment (Proxmox VE) [4], is able to deliver the virtual machine services for virtual server/desktop infrastructure with high availability in computing, secured networking, and consolidated storage. With this approach, users make it possible to adopt low cost thin clients (a low-end PC or PDA) to link to the system for the services [5], reducing IT purchasing cost and saving computation power because thin client devices are easier to setup where the chances of malfunction, heat crash, and computer virus are considerably

low. In addition, easy to use through wireless mobile computing environment gains peoples' attraction a lot.

As the virtualization architecture expands continuously, network storage services have become part of the virtualization architecture. Openfiler [6] is a storage management system used for disk read/write accessing in a shared storage among several virtual machines or servers in enterprises. It is a free and conducive system that supports both network-attached storage (NAS) [7] and storage area network (SAN) [7] functions. As installed, it can be managed via web browsers in conjunction with iSCSI shared storage (IPSAN) [7] technique to provide file accessing on cloud computing servers. One can also use logical unit number (LUN) [8] through iSCSI to complete the placement of block accessing for virtual machines that are created by VMware or Hyper-V. This paper will evaluate the performance of accessing to block storage area network with Openfiler.

The goal in this paper also wants to clarify a credibility of cost and benefits on infrastructure virtualization. Speaking of virtualization cost and benefits, we will give the exploration of total cost of ownership (TCO) and return on investment (ROI) individually in the following statements. ROI [9] related to two factors, savings and investment, is equal to savings/investment, where investment represents the sum of incremental investment in transition from physical to virtual (new servers, shared storage, software licenses & support, services and training, etc.). In addition to investment, TCO [10] yet includes IT administration and downtime cost. Apparently, ROI and TCO can be properly undertaken well according to how big infrastructure has been virtualized. In terms of virtualization, how many infrastructures can be virtualized that intuitively depend on the ratio of the virtual machines per core (VMs/core), the so-called consolidation ratio [11]. The consolidation ratio is a measurement unit that virtualization vendors use with extreme prudence to provide a rough idea of the server consolidation level that can be achieved on their hypervisors. Virtual infrastructure as we know has been classified into server virtualization and desktop virtualization. We will explore the consolidation ratio and TCO/ROI for both server and desktop virtualizations in this study.

In addition, how to appropriately choose the virtual machine management (i.e., hypervisor) for the desired server/desktop virtualization is a really tough problem of a trade-off between performance and cost before making the decision to deploy virtual server in cloud (VSIC) as a new IT. Given five hypervisors used to establish VSICs, this paper introduces a composite index to represent the evaluated functional performance as well as formulates a proper equation to stand for the estimated virtualization cost so that a C/P ration will conclude a careful assessment about a variety of VSICs discussed in this paper.

2. Structure of Virtual Machine and Shared Storage

The purpose of this session is to setup five different virtual servers in cloud (VSIC) and provide an appropriate assessment for every virtual machine monitor (i.e., hypervisor).

TABLE 1: Hypervisor architecture.

VMM	Hypervisor architecture
VMware ESXi 5.0 (Redhat Linux)	Bare-metal/monolithic
MS Hyper-V R2 (Windows Server 2008)	Bare-metal/microkernel
Proxmox VE* (Debian)	Hosted
KVM* (Ubuntu Enterprise Server)	Hosted
Xen* (Cent OS)	Bare-metal/microkernel

*Open source.

These assessments can provide an optimal solution for SMEs, schools, and social groups. This research will setup and implement five heterogeneous virtual machine management systems which are (a) vSphere ESX/ESXi, (b) Hyper-V R2, (c) Proxmox virtual environment, (d) Ubuntu KVM [12], and (e) CentOS Xen [13], where they are shown in Figures 1, 2, 3, 4, and 5, respectively. Moreover, five heterogeneous hypervisors all link to a shared storage Openfiler through LAN, which is a type of IPSAN storage as shown in Figure 6.

Noted that vSphere ESX/ESXi Server, Hyper-V Server 2008 R2, or CentOS-based Xen required at least a stand alone machine for installation, Ubuntu Enterprise Server has to at least include 2 physical machines (Cloud Controller and Node Controller) and Proxmox VE at least a master or optionally adding multiple nodes as well.

As shown in Table 1, hypervisor includes all kinds of virtual machine architectures and types, hence referred to as heterogeneous virtual server in cloud. Virtual machine architectures are divided into hosted architecture, such as (a) and (b), and bare-metal architecture, such as (c), (d), and (e); its types are classified into paravirtualization, such as (d) and (e), full-virtualization, such as (a), (b), and (c), and hardware-assisted virtualization for all of them. This is because the new x86 machines, regardless of 32-bit or 64-bit, now support Intel VT-x and AMD-V virtual instructions.

3. Formulation of Consolidation Ratio and TCO/ROI

The aim of this section is first to understand the consolidation ratio of VMware ESX server as well as TCO/ROI evaluated at VMware TCO/ROI calculator [14]. Consolidation ratio means the number of VMs running in a server concurrently depending on the number of workloads and the average number of VMs per core. The max consolidation ratio per VMware ESX server is by default calculated as 1.5 VMs per core multiplied by the total number of cores per server [15]. That is, it gives 12:1 in ESX's server favor. Based on Taneja Group observations early in 2009 [16] during testing as well as their familiarity with a broad range of virtual server infrastructures, they claimed there are many realistic workloads under which ESX4 gains a 2:1 VM density advantage comparing with Hyper-V R2 and XenServer 5.5. Thus, we extensively proposed to analyze VM density according to a VMware official document for EXS server [14] and a testing report from consulting services [16] such that the consolidation ratio for the other hypervisors can be obtained.

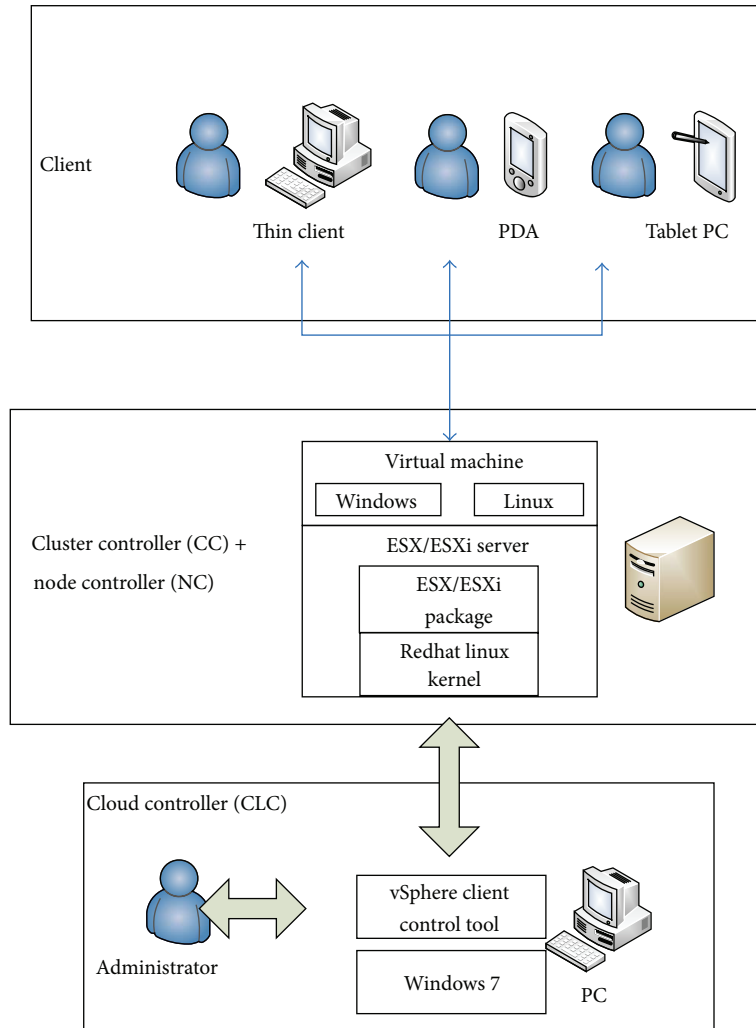


FIGURE 1: vSphere ESX/ESXi server.

On the other hand, the ROI required for the transition to virtual infrastructure evaluates the percent of total saving/total cost, where total saving consists of capital expenditure, operational expenditure, and downtime cost; total cost is composed of new servers, storage, network storages, software license & support, server, and training [14]. TCO is the costs associated with operation of datacenter which include capital expenditure (servers, storage, and switches), operational expenditure (power & cooling, infrastructure administration labors, and rack space), and business agility (planned downtime, unplanned downtime, and business downtime) [14]. Furthermore, the TCO/ROI for the other hypervisors has been estimated carefully according to VM density and the ratio of ESX normalized performance index to anyone.

4. Empirical Analysis Method

With respect to the performance evaluation for the virtual machine monitor, a variety of guest OS and two well-known

test tools are adopted in this study. PassMark PerformanceTest 7.0 (at http://www.passmark.com/download/pt_download.htm) is applied to the test of virtual machine performance for the Windows series guest OS like Windows XP, Windows 7, and Windows Server 2003, and UnixBench 5.1.3 (at <http://byte-unixbench.google-code.com/files/UnixBench5.1.3.tgz>) is employed for Linux series guest OS like Ubuntu. According to evaluated performance score for each virtual infrastructure server, we derived the respective scores into a composite index, each hypervisor on (1) and (2), and sequentially normalized to be a value ranging from 0 to 1 on (3), where we refer to this as a normalized composite index related to virtual machine performance. In (1), WS_i is a test score for various guest Windows OSs (e.g., Win XP, Win Server 2003, and Win 7) running in a VM, and accordingly, WS_{mean} represents a mean test score for various guest OSs; in (2), LS_{mean} stands for a mean test score for a guest Linux OS (e.g., Ubuntu and CentOS); in (3), CI_{vm} means a VM composite index for a specific hypervisor, and two coefficients λ_1 and λ_2 act as a

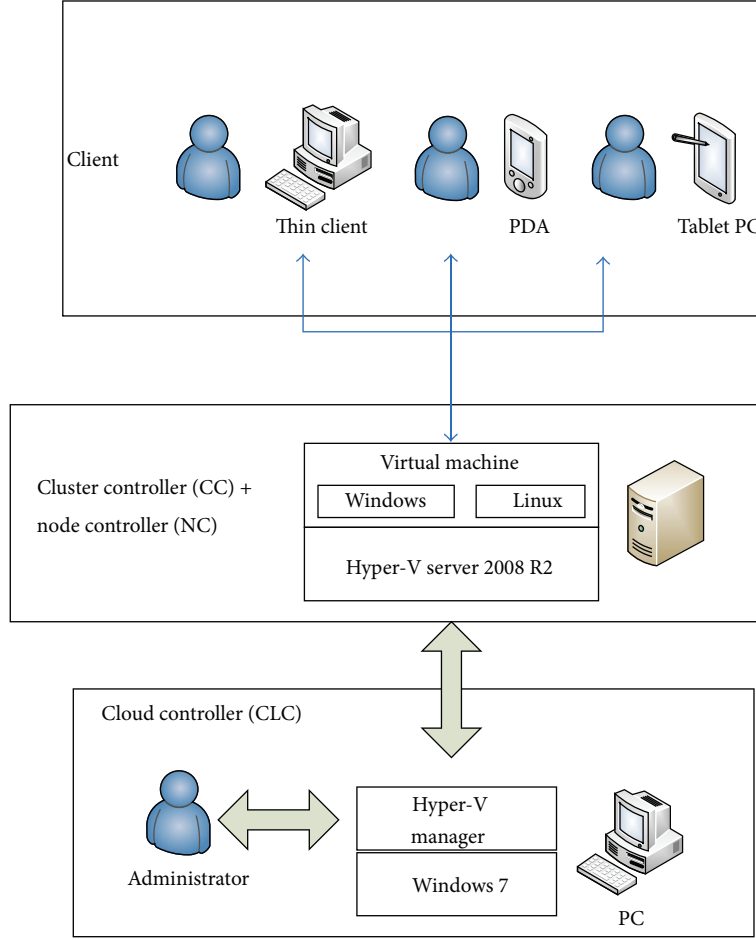


FIGURE 2: Hyper-V Server 2008 R2 server.

weighted average; in (4), \overline{CI}_{vm_k} represents a normalized VM composite index for a specific hypervisor. Consider

$$WS_{mean} = \frac{\sum_{i=1}^N WS_i}{N}, \quad (1)$$

$$LS_{mean} = \frac{\sum_{j=1}^M LS_j}{M}, \quad (2)$$

$$CI_{vm} = \lambda_1 \cdot LS_{mean} + \lambda_2 \cdot WS_{mean} \quad (3)$$

s.t. $\lambda_1 + \lambda_2 = 1,$

$$\overline{CI}_{vm_k} = \frac{CI_{vm_k}}{CI_{vm_{ESX}}}. \quad (4)$$

In order to achieve virtual infrastructure together with a shared storage, we first have to establish a set of block storage area network system called Openfiler and then mount shared storage to each virtual server. After that, we go for the performance evaluation of accessing block storage by using Linux hdparm command [17] to test disk reading speed. Likewise, we do the same thing as the above mentioned procedure to develop a composite index on (5) and its normalized composite index on (6) associated with storage-accessing speed performance. Finally, we derive the composite index

for total on (7) and a normalized one on (8). In (5), CS_{mean} is a mean test score for cache read speed performance on a guest Linux OS in a VM, DS_{mean} a mean test score for disk read speed performance, and CI_{sa} a storage-accessing speed composite index; in (6), \overline{CI}_{sa_k} stands for a normalized storage-accessing speed composite index for a certain hypervisor; in (7), CI represents a composite index for a certain hypervisor for overall, and in (8), \overline{CI} represents a normalized composite index. In terms of average, three sets of coefficients indicated by ν_1/ν_2 , w_1/w_2 , and η_1/η_2 are designated to act as a weighted average for equation in (5), (7), and (8), respectively. Consider

$$CI_{sa} = \nu_1 \cdot CS_{mean} + \nu_2 \cdot DS_{mean} \quad (5)$$

s.t. $\nu_1 + \nu_2 = 1,$

$$\overline{CI}_{sa_k} = \frac{CI_{sa_k}}{CI_{sa_{ESX}}}, \quad (6)$$

$$CI = w_1 \cdot CI_{vm} + w_2 \cdot CI_{sa} \quad (7)$$

s.t. $w_1 + w_2 = 1,$

$$\overline{CI} = \eta_1 \cdot \overline{CI}_{vm} + \eta_2 \cdot \overline{CI}_{sa} \quad (8)$$

s. t. $\eta_1 + \eta_2 = 1.$

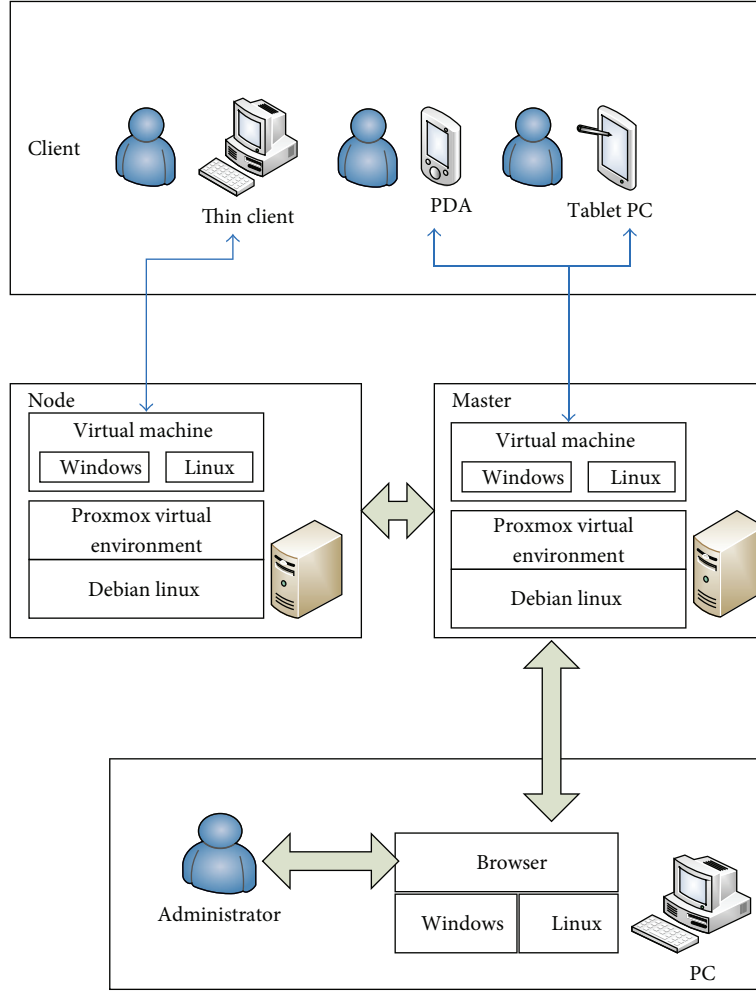


FIGURE 3: Proxmox virtual environment server.

In this paper, we mainly conduct a credibility of cost and benefits before and after infrastructure virtualization. Speaking of cost and benefit, we will explore the consolidation ratio and TCO/ROI of both server consolidation and desktop virtualizations as mentioned above. VMware ESX server is first chosen to evaluate its consolidation ratio and estimate TCO/ROI at VMware calculator webpage. The consolidation ratio and TCO/ROI of both server and desktop virtualizations for the other hypervisors will be proportional to both its VM density (major part) and the ratio of ESX normalized composite index to alternative one (minor part). We broke the costs about capital expenditure, operational expenditure, and business agility into 13 items. Technically the table as listed in Table 2 gives us an insight to realize which item highly concerned with the VM density and/or normalized performance index ratio, which are derived from TCO/ROI calculation. Moreover, a formula for calculating the expenditure of TCO/ROI has been derived on (9) where VMD_{ESX} represents VM density for ESX server and $VMD_{hypervisor}$ for the other hypervisors; $Cost_{ESX}$ stands for the expenditure for ESX server and $Cost_{hypervisor}$ for the other hypervisors. There is no the initial cost of software package for Proxmox VE,

Ubuntu KVM, and CentOS Xen due to open source software. However, the initial cost of ESX server software package (approximate US\$ 12,668) is greater than that of Hyper-V R2 (approximate US\$ 6,000). Consider

$$\begin{aligned}
 Cost_{hypervisor} = & \left(\alpha \cdot \left(1 - \frac{VMD_{hypervisor}}{VMD_{ESX}} \right) \right. \\
 & \left. + \beta \cdot \left(1 - \frac{CI_{hypervisor}}{CI_{ESX}} \right) \right) \\
 & \cdot Cost_{ESX} + \text{initial cost} \quad (9)
 \end{aligned}$$

$$\text{s.t. } 0 \leq \alpha \leq 1$$

$$0 \leq \beta \leq 1$$

$$\alpha + \beta = 1.$$

5. Experimental Results and Discussion

There are three experiments and the discussion presented in the following subsections.

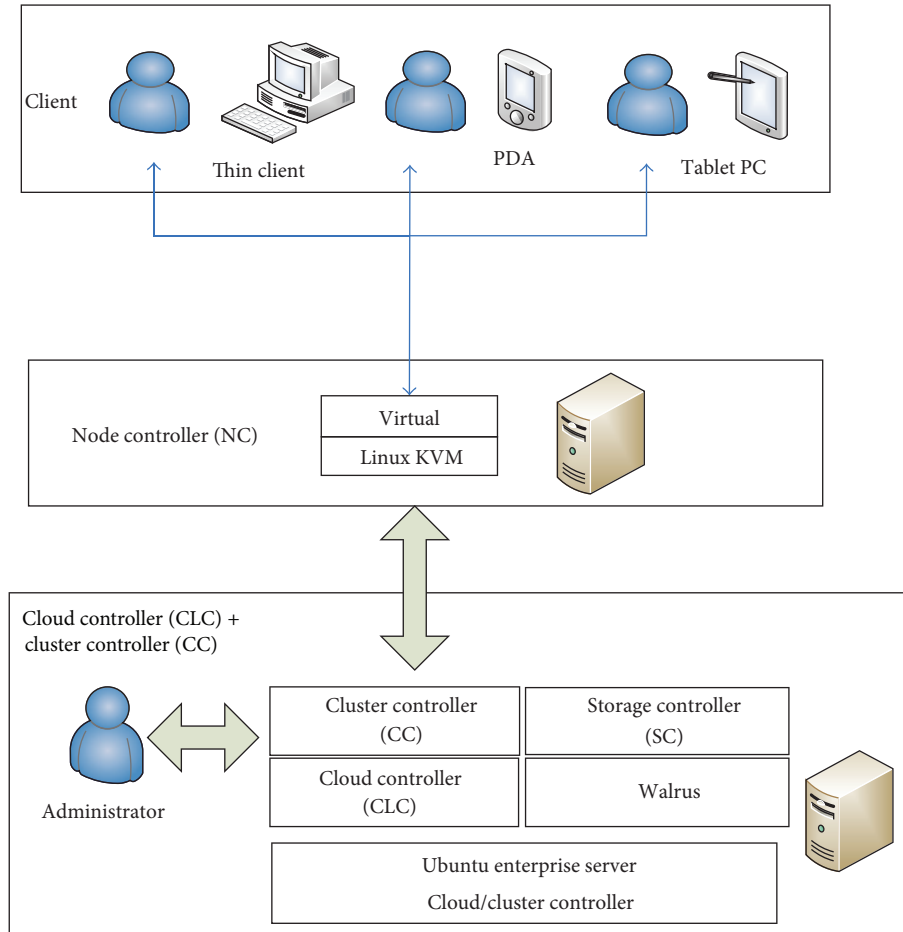


FIGURE 4: Ubuntu KVM server.

5.1. Assessment of Virtual Machine Performance. The server hardware specification is listed in Table 3.

The resulting score is an average of various scores from test items, for example, CPU, memory, storage, network, and 2D graph. In the experiment, two testing softwares (PassMark PerformanceTest 7.0 and UnixBench 5.1.3) are applied to evaluate the virtual machine performance for hypervisors such as ESXi 5.0, Hyper-V R2, Proxmox VE, Ubuntu Enterprise Server KVM, and CentOS Xen. A summary of the virtual machine performances is shown in Table 4 as well as Figures 7 and 8.

Different guest OS is installed separately on each virtual machine and adds up to 5 VMs in each predetermined virtual machine monitor (one of the above-mentioned hypervisors). They are divided into Windows series and Linux series guest OSs. After that, the testing software will be taken to analyze a set of target items as mentioned above.

5.2. Performance Evaluation of VM Accessing Shared Storage. In the experiment, according to the same server hardware specification as mentioned above, Openfiler storage device is separately mounted onto five virtual servers in cloud to test disk-accessing speed. Tests carried out two disk-accessing

speed indicators, (a) timing cached reads (MB/sec) and (b) timing buffered disk reads (MB/sec) [18]. A summary of storage-accessing speed performances is shown in Table 5 as well as Figures 7 and 8.

5.3. Estimation of Consolidation Ratio and TCO/ROI. This part goes to the estimation of the consolidation ratio and TCO/ROI for each virtual server infrastructure as mentioned above. We choose VMware ESXi server as a benchmark and use VMware TCO/ROI calculator to yield its server/desktop consolidation ratio and TCO/ROI quantity. VMware ESXi exceeds 2 times the workload capacity per server for the competitive hypervisors such as hypervisor-V R2, XenServer 5.5, and the others [16]. Accordingly, we assumed ESXi achieved 2:1 VM density per server advantage over the other hypervisors in this study. Thus, ESXi achieved the consolidation ratio 12:1 in server virtualization as well as 96:1 in desktop virtualization because of 1.5 VM per core; instead the other hypervisors result in 6:1 in server virtualization as well as 48:1 in desktop virtualization. We estimate that TCO/ROI for alternative hypervisor is greatly proportional to its VM density (i.e., major part of estimation) and additionally adds somewhat fluctuations or changes to the evaluation of TCO

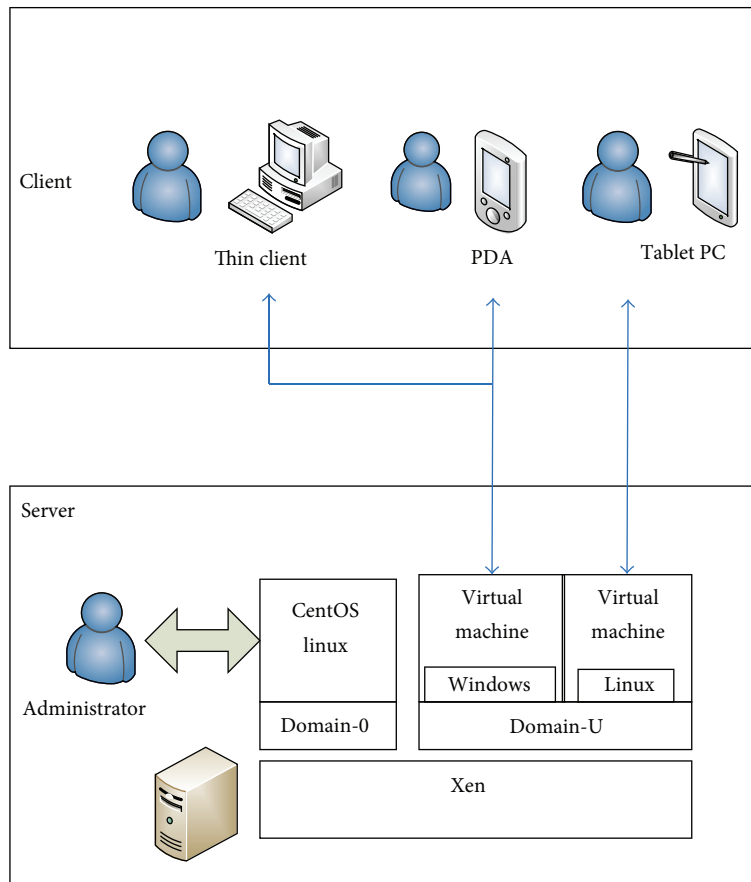


FIGURE 5: CentOS Xen server.

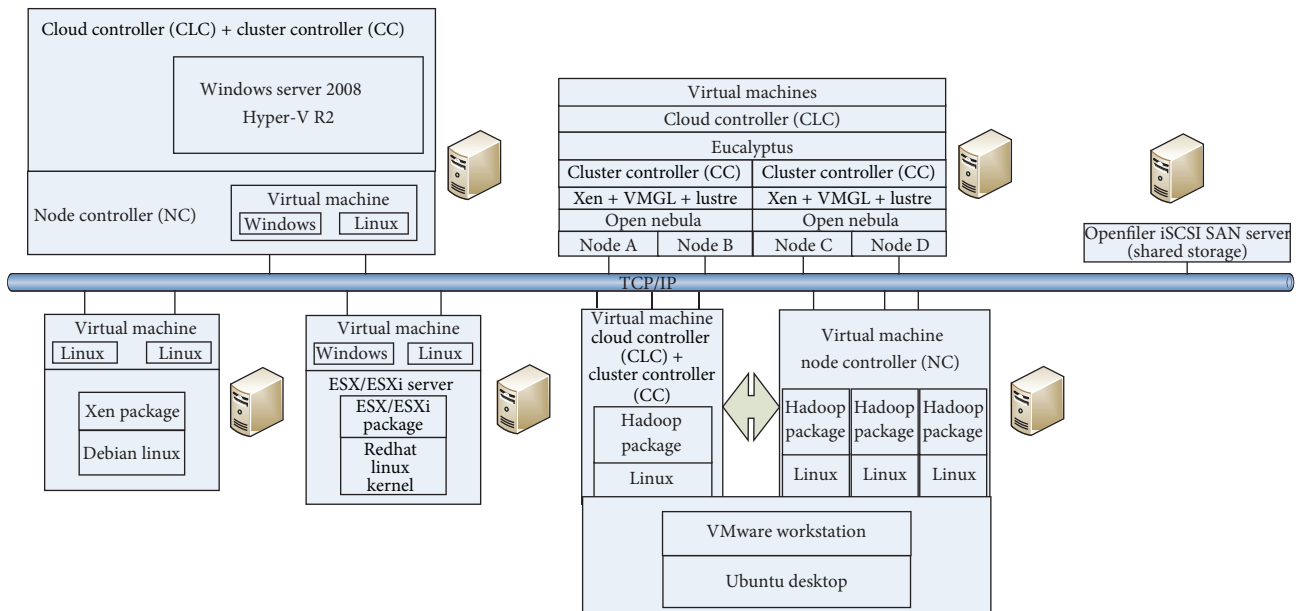


FIGURE 6: Virtual server in cloud and a shared storage with Openfiler.

TABLE 2: Cost affected by VM density and performance composite index ratio.

Cost	VM density (workload counts)	Performance composite index ratio
Capital expenditure		
Client HW + MS VDA	✗	✗
Server HW	✓	✗
Storage HW	✗	✗
Networking and security HW	✓	✗
Hypervisor SW + SnS	✓	✗
Operational expenditure		
Infrastructure admin	✓	✓
Power and cooling	✓	✓
Rack space and office spaces	✓	✗
Services + Training	✗	✗
Business agility		
Planned downtime	✗	✗
Unplanned downtime	✗	✗
Business downtime	✓	✓
Other + Tax	✓	✗

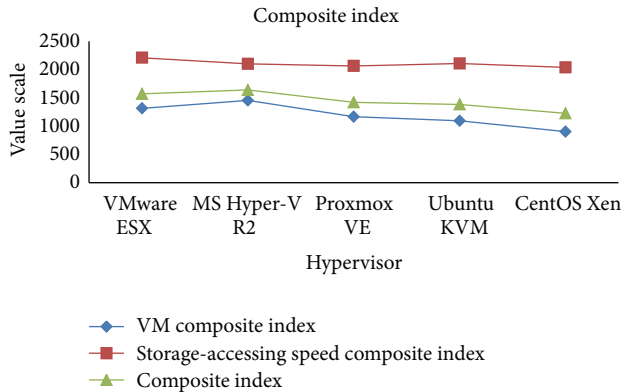


FIGURE 7: Composite index distribution.

part based on the ratio of ESXi normalized composite index to alternative one (i.e., minor part of estimation). In the experiment, we have deployed up to 50, 100, 150, 200, 250, and 300 workloads for the transition to their respective server virtualization with a 5-year duration. A summary of TCO/ROI calculation for 5 years is shown in Figures 9 and 10 in server virtualization as well as Figures 11 and 12 in desktop virtualization.

5.4. Cost Estimation for Server/Desktop Virtualization. According to the cost formula on (9), this part gives the operation cost for server/desktop virtualization so that the ratio of cost to performance (C/P ratio) for various virtual machine managements (hypervisors) is able to carry out the goal of the assessment in this paper. With a basis cost

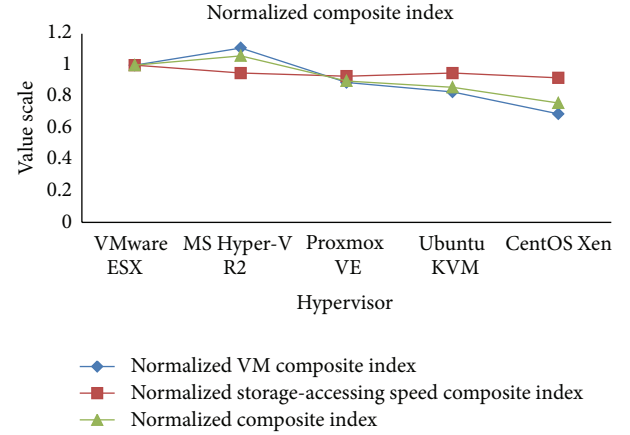


FIGURE 8: Normalized composite index distribution.

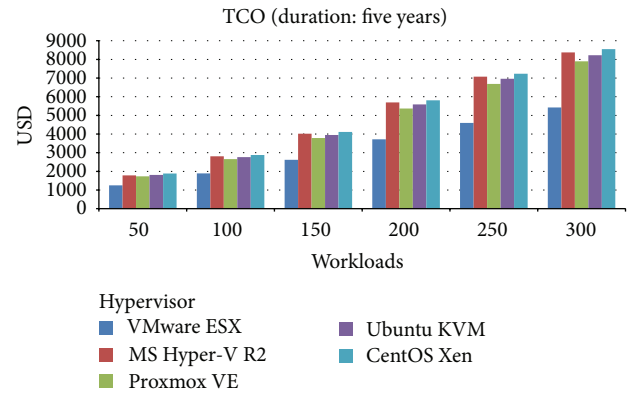


FIGURE 9: TCO histogram of server consolidation.

of vSphere ESX server indicated in (9), the operation cost computation to Hyper-V R2, Proxmox virtual environment, Ubuntu KVM, and CentOS Xen are conducted to disclose the real assessment of virtual server/desktop infrastructure. In terms of VM performance as indicted in (7) and (8), the composite index presents how the function of VM and its related storage-accessing speed perform in the various hypervisors, and the results are shown in Figures 7 and 8 as well. As we can see in Figure 13, a $Cost_{\text{hypervisor}}$ divides \overline{CI} and yields the C/P ratio with varying coefficients α/β , and the summary is also listed in Table 6. Even though Hyper-V R2 gains the best performance, Proxmox VE obtains the best choice in this study due to the lowest C/P ratio.

5.5. Discussion. In terms of VM performance and its storage-accessing speed as shown in Figures 7 and 8, Hyper-V R2 gains the best performance overall because of the highest composite index. As shown in Figures 9 and 10 in the server virtualization, the best choice is to take 150 workloads with ESX server because this combination will achieve the highest ROI and the lowest TCO over the duration of 5 years. However, when we look at desktop virtualization as shown

TABLE 3: Comparison of VM performance of hypervisor.

Hardware specification	CPU	Memory	Hard disk	Network card
Server	Intel(R) Core(TM) i7-2600 CPU 3.40 GHz × 2	ASint DDRIII 8G-1600 × 2	Seagate Barracuda 7200 1TB	RTL8169SC B7C33A5 GB29 TAIWAN (TG-3269)
Shared storage	Intel E5620 CPU 2.4 GHz * 1	8 GB DDRIII RAM	1TB SATA HDD	RTL8169SC B7C33A5 GB29 TAIWAN (TG-3269)

TABLE 4: Comparison of VM performance of hypervisor.

VM performance	Unix bench 5.1.3		Pass mark performance test 7.0			Composite index	Normalized composite index
	Ubuntu	CentOS	Win XP	Win Server 2003	Win 7		
ESXi 5.0	1540.7	1550.3	1026.4	1126.1	1108.8	1316.3	1
Hyper-V R2	1619	1629	1213.4	1328.3	1318.9	1455.4	1.11
Proxmox VE	1411.8	1427.3	1013.3	750.9	976.4	1166.7	0.89
KVM	1411	1427	730	688.4	902.7	1096.4	0.83
Xen	1094.6	1084.7	700	597	860.3	904.2	0.69

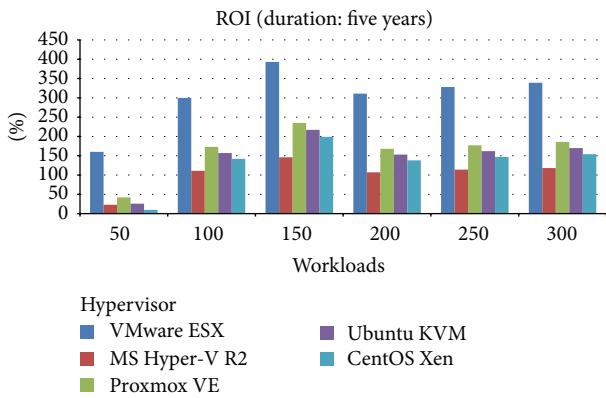


FIGURE 10: ROI histogram of server consolidation.

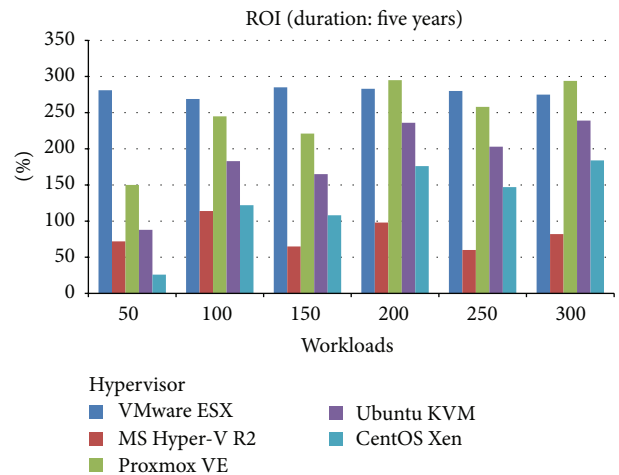


FIGURE 12: ROI histogram of desktop virtualization.

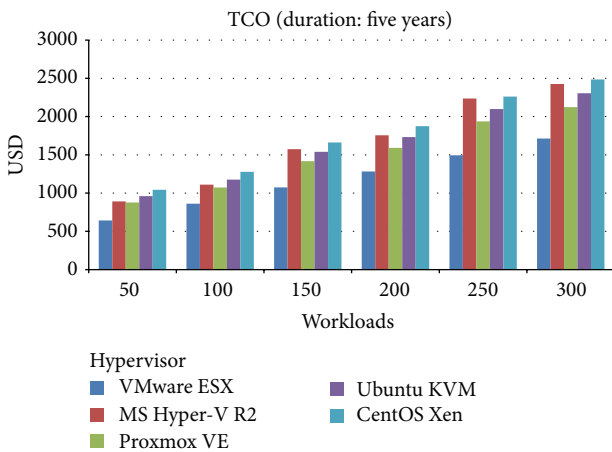


FIGURE 11: TCO histogram of desktop virtualization.

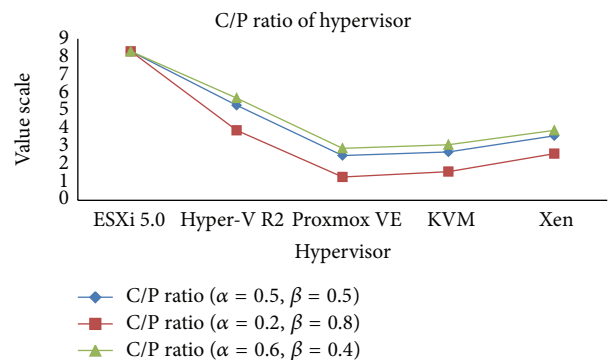


FIGURE 13: C/P ratio of hypervisor.

TABLE 5: Comparison of storage-accessing speed performance.

Storage-accessing speed performance	Timing cached reads (MB/sec)	Timing buffered disk reads (MB/sec)	Composite index	Normalized composite index
ESXi 5.0	11007.21	11.16	2210.4	1
Hyper-V R2	10475.72	9.33	2102.6	0.95
Proxmox VE	10287.88	9.98	2065.6	0.93
KVM	10503.85	9.75	2108.6	0.95
Xen	10160.47	9.55	2039.7	0.92

TABLE 6: C/P ratio of hypervisor (cost unit: US\$).

Hypervisor	Composite index	Operation cost	C/P ratio	Operation cost	C/P ratio	Operation cost	C/P ratio
		$\alpha = 0.5, \beta = 0.5$		$\alpha = 0.2, \beta = 0.8$		$\alpha = 0.6, \beta = 0.4$	
ESXi 5.0	1517.8	12,667	8.3	12,667	8.3	12,667	8.3
Hyper-V R2	1640.3	8,656	5.3	6,449	3.9	9,391	5.7
Proxmox VE	1423.5	3,560	2.5	1,896	1.3	4,115	2.9
KVM	1385.6	3,718	2.7	2,149	1.6	4,241	3.1
Xen	1228.6	4,373	3.6	3,197	2.6	4,765	3.9

in Figures 11 and 12, Proxmox VE outperforms the others to achieve the best ROI over a 5-year duration, even though its TCO is a little bit less than ESX's TCO. In addition, Proxmox VE would not only be the best choice to save the initial investment to own a virtual server infrastructure with better ROI in desktop virtualization, but it also obtains the lowest C/P ratio. This paper does not mention the security issue for virtual machines, which is related to access control [19] and cryptograph in VMs [20]. It can be explored in the further work.

6. Conclusions

The objective of this paper is to explore several critical issues of virtual server/desktop infrastructure such as server consolidation, virtualization performance, virtual machine density, total cost of ownership (TCO), and return on investments (ROI). Thus, this paper introduces five distinct well-known hypervisors installed in VSIC and has proceeded with an empirical analysis of server consolidation and desktop virtualization. As a result, even though ESX server gets the highest ROI and the lowest TCO in server virtualization and Hyper-V R2 gains the best performance over all, both of them cost too much; instead Proxmox VE would not only be the best choice to save the initial investment to own a virtual server infrastructure with better ROI in desktop virtualization, but also it obtains the lowest C/P ratio. We drew the conclusion that Proxmox VE outperforms the other hypervisors operating in the virtual server/desktop infrastructure.

Acknowledgment

This work is supported by the National Science Council, Taiwan, under Grant no. NSC 100-2221-E-390-011-MY3.

References

- [1] B. R. Chang, H. F. Tsai, and C. M. Chen, "Evaluation of virtual machine performance and virtualized consolidation ratio in cloud computing system," *Journal of Information Hiding and Multimedia Signal Processing*, vol. 4, no. 3, pp. 192–200, 2013.
- [2] J. Hardy, L. Liu, C. Lei, and J. X. Li, "Internet-based virtual computing infrastructure for cloud computing," in *Principles, Methodologies, and Service-Oriented Approaches For Cloud Computing*, chapter 16, pp. 371–389, IGI Global, Hershey, Pa, USA, 2013.
- [3] Y. Haga, K. Imaeda, and M. Jibu, "Windows server 2008 R2 hyper-V server virtualization," *Fujitsu Scientific and Technical Journal*, vol. 47, no. 3, pp. 349–355, 2011.
- [4] A. Kovari and P. Dukan, "KVM & OpenVZ virtualization based IaaS open source cloud virtualization platforms: openNode, proxmox VE," in *Proceedings of IEEE 10th Jubilee International Symposium on Intelligent Systems and Informatics*, pp. 335–339, 2012.
- [5] S. M. S. Kimball and C. Bisciglia, "Cluster computing for web-scale data processing," *ACM SIGCSE Bulletin*, vol. 40, no. 1, pp. 116–120, 2008.
- [6] F. Guthrie, S. Lowe, and M. Saidel-Keesing, *VMware vSphere Design*, John Wiley & Sons, New York, NY, USA, 2011.
- [7] D. Sacks, "Demystifying DAS, SAN, NAS, NAS Gateways, Fibre Channel, and iSCSI," *IBM Storage Networking*, pp. 3–7, 2001.
- [8] I. Yakti and W. A. Salameh, "iSCSI (internet small computer system interface) for your startup," *International Journal of Information and Communication Technology Research*, vol. 20, no. 3, 2012.
- [9] J. M. Kurz, "Beyond ROI," *Value Management*, pp. 1–7, 2012.
- [10] M. Kornevs, V. Minkevica, and M. Holm, "Cloud computing evaluation based on financial metrics," *Information Technology and Management Science*, vol. 15, no. 1, pp. 87–92, 2013.
- [11] A. Beloglazov and R. Buyya, "Optimal online deterministic algorithms and adaptive heuristics for energy and performance efficient dynamic consolidation of virtual machines in Cloud

- data centers,” *Concurrency and Computation*, vol. 24, no. 13, pp. 1397–1420, 2012.
- [12] S. Simanta, G. A. Lewis, E. J. Morris, K. Ha, and M. Satyanarayanan, “Cloud computing at the tactical edge,” *Software Engineering Institute* 680, 2012.
- [13] B. K. Kim, K. W. Hur, J. H. Jang, and Y. W. Ko, “Feedback scheduling for realtime task on Xen virtual machine,” *Communications in Computer and Information Science*, vol. 266, no. 2, pp. 283–291, 2011.
- [14] VMware TCO/ROI Calculator, VMware, <http://roitco.vmware.com/vmw/>.
- [15] Frequently Asked Questions, *Report of VMware ROI TCO Calculator, Version 2.0*, VMware, 2013.
- [16] TANEJA Group Technology Analysis, “Evaluating the ESX 4 Hypervisor and VM Density Advantage,” *Technology Validation*, pp. 1–12, 2009.
- [17] M. Tabuchi, K.-I. Itoh, Y. Nomura, and H. Taniguchi, “Design and evaluation of a system for running two coexisting linux systems,” *Electronics and Communications in Japan*, vol. 90, no. 9, pp. 56–68, 2007.
- [18] M. Aboutabl, A. Agrawala, and J. D. Decotignie, “Temporally determinate disk access (extended abstract): an experimental approach,” *ACM SIGMETRICS Performance Evaluation Review*, vol. 26, no. 1, pp. 280–281, 1998.
- [19] S. Prabhakar, S. Pankanti, and A. K. Jain, “Biometric recognition: security and privacy concerns,” *IEEE Security and Privacy*, vol. 1, no. 2, pp. 33–42, 2003.
- [20] R. L. Krutz and R. D. Scott Lowe Vines, *Cloud Security: A Comprehensive Guide to Secure Cloud Computing*, John Wiley & Sons, New York, NY, USA, 2010.

Research Article

Analyzing Taiwan IC Assembly Industry by Grey-Markov Forecasting Model

Lei-Chuan Lin and Shan-Yau Wu

Department of Industrial Engineering and Management, National Kaohsiung University of Applied Sciences, Kaohsiung 80778, Taiwan

Correspondence should be addressed to Lei-Chuan Lin; leichuan@mail.mirdc.org.tw

Received 14 September 2013; Revised 19 October 2013; Accepted 20 October 2013

Academic Editor: Teen-Hang Meen

Copyright © 2013 L.-C. Lin and S.-Y. Wu. This is an open access article distributed under the Creative Commons Attribution License, which permits unrestricted use, distribution, and reproduction in any medium, provided the original work is properly cited.

This study utilizes the black swan theorem to discuss how to face the lack of historical data and outliers. They may cause huge influences which make it impossible for people to predict the economy from their knowledge or experiences. Meanwhile, they cause the general dilemma of which prediction tool to be used which is also considered in this study. For the reason above, this study uses 2009 Q1 to 2010 Q4 quarterly revenue trend of Taiwan's semiconductor packaging and testing industry under the global financial turmoil as basis and the grey prediction method to deal with nonlinear problems and small data. Under the lack of information and economic drastic changes, this study applies Markov model to predict the industry revenues of GM(1,1) and DGM(1,1) results. The results show that the accuracy of 2010 Q1–Q3 is 88.37%, 90.27%, and 91.13%, respectively. Besides, they are better than the results of GM(1,1) and DGM(1,1) which are 86.51%, 77.35%, 75.46% and 73.77%, 74.25%, 59.72%. The results show that the prediction ability of the grey prediction with Markov model is better than traditional GM(1,1) and DGM(1,1) facing the changes of financial crisis. The results also prove that the grey-Markov chain prediction can be the perfect criterion for decision-makers judgment even when the environment has undergone drastic changes which bring the impact of unpredictable conditions.

1. Introduction

Financial turmoil has huge influences on varieties of industries, like the black swan theorem which produces a great deviation and causes adverse reactions [1]. In Taiwan, semiconductor production capacity accounts for more than half of the global semiconductor manufacturing market, and the IC packaging and testing accounts for the global foundry capacity of over 60%. The speed and environment of new products replacing older market create the competitiveness of related industries in Taiwan. The black swan theorem will produce outliers. This study found that the way to remove the deviation would be more difficult to predict regression or other methods of forecasting future trends accurately.

The grey method proposed by professor Long can provide very good prediction under short-time historical data [2]. Among the method, GM(1,1) provides suitable reference tools to decision-makers in the changing and competitive environment. In the previous researches, grey theory applied to the economic, financial, engineering, and other fields

reached ideal results [3–5]. For example, Ken and Li [6] used a different grey prediction model which included traditional GM(1,1), RGM(1,1), and Tan's GM(1,1), and he used chained convenience stores sales patterns as backgrounds for model selection. Hung et al. [7] also used GM(1,1) to predict under incomplete information. Compared with two prediction models of Egli and Walfisch-bertoni [8], it had proved that the GM(1,1) rolling model produced the lowest error. Lin and Yang [9] used GM(1,1) to predict Taiwan semiconductor optoelectronics industry, and the average residual is less than 10%, which proves the high accuracy of grey prediction to semiconductor industry. But the financial crisis causes excessive fluctuations in random sequence and it easily leads to the condition of inadequate accuracy. If it is applied to the Taiwan semiconductor packaging and testing industry revenue data, it will cause the lack of precision because of deficiencies historical data message with random fluctuations, which also increases the difficulty in using general prediction tools in this paper.

Markov (Markov-chain) is generally used in the forecasting model on a random time series, and it is a dynamic system which is based on the transition between the states and all the random factors to reflect the impact [7]. Although it is very suitable for handling random variation problems, it still needs enough raw data to determine the probability of state transitions. Hence, this study uses Markov theory to improve GM(1,1) and reduce the variation when historical data increase and financial crisis happens. By evaluating accuracy, the prediction effect of Markov model can be improved [3].

2. Grey System Theory

Yin [10] has investigated during the time span of 1996 to 2011, the earliest year when the database was available to the best possible full text availability to date. The paper points out that there were 482 publications that met the selection criteria of "grey relational analysis" or "gray relational analysis" topic search. It is seen that the grey system theory is one of the most popular forecasting methods. Ken and Li [6] applied grey system as a module to help predicting sales revenue of convenience chain stores in Taiwan. They do get more accuracy on their prediction. Also, Huang et al. [11] predict the silkworm cocoon yield in china base on the grey-Markov forecasting model. The findings show that grey-Markov has more accuracy than other forecasting model. Meanwhile, Hsu and Chen [12] compared various statistical methods based on the suitability of short-term forecasting. They got similar findings.

3. Methodology

3.1. GM(1,1) and DGM(1,1) Grey Forecasting Model. GM(1,1) is a type of prediction model, the analysis steps are listed below.

Step 1. The original sequence is defined as

$$X^{(0)} = (x_1^{(0)}, x_2^{(0)}, \dots, x_n^{(0)}). \quad (1)$$

Step 2. Use 1-AGO to decrease the randomness of sequence and define the 1-AGO as

$$X^{(1)} = (x_1^{(1)}, x_2^{(1)}, \dots, x_n^{(1)}), \quad (2)$$

where $x_k^{(1)} = \sum_{i=1}^k x_i^{(0)}$, $k = 1, 2, \dots, n$.

Step 3. Establish a first-order differential equation

$$\frac{dX^{(1)}}{dt} + aX^{(1)} = u. \quad (3)$$

Step 4. From (3), we can get

$$\hat{x}^{(1)}(k+1) = \left(x^{(0)}(1) - \frac{u}{a}\right) e^{-ak} + \frac{u}{a}, \quad k \geq 0, \quad (4)$$

$$\hat{a} = \begin{bmatrix} a \\ u \end{bmatrix} = (B^T B)^{-1} B^T Y,$$

where

$$B = \begin{bmatrix} -\frac{1}{2(x_1^{(0)} + x_2^{(0)})} & 1 \\ -\frac{1}{2(x_2^{(0)} + x_3^{(0)})} & 1 \\ \vdots & \vdots \\ -1 & 1 \\ \frac{1}{2(x_{n-1}^{(0)} + x_n^{(0)})} & 1 \end{bmatrix} = \begin{bmatrix} -z^{(1)}(2) & 1 \\ -z^{(1)}(3) & 1 \\ \vdots & \vdots \\ -z^{(1)}(n) & 1 \end{bmatrix}, \quad (5)$$

$$Y = \begin{bmatrix} x^{(0)}(2) \\ x^{(0)}(3) \\ \vdots \\ x^{(0)}(n) \end{bmatrix}.$$

Step 5. Use 1-AGO to get the real prediction data

$$\hat{x}(k+1) = \hat{x}^{(1)}(k+1) - \hat{x}^{(1)}(k). \quad (6)$$

Step 6. From Step 5, a trend curve equation can be formed

$$\hat{Y}(k) = \hat{x}^{(0)}(k+1) = g e^{-ak}, \quad (7)$$

where $g = (x^{(0)}(1) - (b/a) - e^a x_{(1)}^{(0)} + e^a (b/a))$.

DGM(1,1) discrete grey forecasting model is the dynamic cycle rolling model; it is from original sequence by GM(1,1). Use this result of DGM(1,1) model to become the first stage of forecasting value that is needed. Comparative forecasting value and actual value are examined in order to get error value and accuracy.

3.2. Partition of States by Markov-Chain Forecasting Model.

The values of $X^{(0)}(k+1)$ are distributed in the region of the trend curve $\hat{Y}(k)$ that may be divided into a convenient number of contiguous intervals. When $X^{(0)}(k+1)$ falls in interval i , one of S such intervals, it may be regarded as corresponding to a state E_i , and E_i can be signified as follows:

$$E_i = [E_{1i}, E_{2i}], \quad (8)$$

where $i = 1, 2, \dots, S$ and S is the amount of states

$$\begin{aligned} E_{1i} &= \hat{Y}(k) + A_i, \\ E_{2i} &= \hat{Y}(k) + B_i, \end{aligned} \quad (9)$$

where $\hat{Y}(k)$ is time function, E_i is in the i state, E_{1i} and E_{2i} are time varying, and A_i and B_i are fixed value, depending on the original data.

3.3. Calculation of State Transfer Probability. In Markov-chain series, the changing probability from E_i to E_j can be presented as follows:

$$P_{ij}(m) = \frac{M_{ij}(m)}{M_i} \quad (i, j = 1, 2, \dots, S), \quad (10)$$

where $P_{ij}(m)$ is the transition probability of state E_j transferred from state E_i for m steps (in this paper, 1 step stands for 1 quarter), m is the number of transition steps each time, $M_{ij}(m)$ is the number of original data of state E_j transferred from state E_i for m steps, and M_i is the number of original data points in state E_i .

The state transition probability matrix $R(m)$ is as follows:

$$R(m) = \begin{bmatrix} P_{11}(m) & P_{12}(m) & \cdots & P_{1j}(m) \\ P_{21}(m) & P_{22}(m) & \cdots & P_{2j}(m) \\ \vdots & \vdots & \ddots & \vdots \\ P_{j1}(m) & P_{j2}(m) & \cdots & P_{ij}(m) \end{bmatrix} \quad (11)$$

$(i, j = 1, 2, \dots, S).$

The state transition probability $P_{ij}(m)$ reflects the transition rules of a system. The state transition probability matrix $R(m)$ describes the probability of transition from state i to j . Generally, it is necessary to observe the one-step transition matrix $R(1)$. Supposing the object to be forecasted is in state E_Q ($1 \leq Q \leq S$), row Q in matrix $R(1)$ should be considered. If $\max P_{Qj}(1) = P_{QL}(1)$ ($j = 1, 2, \dots, S; 1 \leq Q \leq S$), then what will most probably happen in the system at the next moment is the transition from state E_Q to state E_L . It is difficult to determine the future transition of the state; if two or more transition probabilities in the row Q of matrix $R(1)$ are the same, the transition probability matrix of two-step transition matrix $R(2)$ or multistep transition matrix $R(m)$, where $m \geq 3$, should be considered [4].

3.4. Calculate the Forecasting Data. After the determination of the future state transition of a system, that is, the determination of grey elements E_{1i}, E_{2i} , the changing interval of the forecast value is between E_{1i} and E_{2i} . The most probable forecast value, $\hat{Y}(k+1)$, is considered to be the middle value of the determined state interval; that is,

$$\hat{Y}(k+1) = \frac{1}{2(E_{1i} + E_{2i})} = \hat{Y}(k) + \frac{1}{2(A_i + B_i)}. \quad (12)$$

3.5. Accuracy Inspection Analysis of Forecasting Ability. Numerous methods exist for judging forecasting model accuracy, and no single recognized inspection method exists for forecasting ability. MAPE is often used to measure forecasting accuracy. Smaller MAPE value indicates better forecasting ability

$$\text{MAPE} = \frac{1}{n} \sum \frac{|\text{Actual} - \text{Forecast}|}{\text{Actual}} \times 100, \quad (13)$$

$n = \text{Forecasting number of step.}$

Evaluation of MAPE forecasting ability is divided as forecasting ability is evaluated as follows:

- (i) <10 excellent forecasting ability,
- (ii) 10~20 good forecasting ability,
- (iii) 20~50 reasonable forecasting ability,
- (iv) >50 poor forecasting.

TABLE 1: The IC assembly industry revenue of Taiwan from 2007 Q1 to 2010 Q3.

Number	Year	Amount
1	2007 Q1	39,317,687
2	2007 Q2	42,373,477
3	2007 Q3	49,468,262
4	2007 Q4	50,574,715
5	2008 Q1	43,602,058
6	2008 Q2	46,390,298
7	2008 Q3	48,554,800
8	2008 Q4	36,766,363
9	2009 Q1	28,271,646
10	2009 Q2	40,941,246
11	2009 Q3	47,782,022
12	2009 Q4	49,296,071
13	2010 Q1	48,204,412
14	2010 Q2	53,435,639
15	2010 Q3	54,287,889

Unit: million NTDs.

4. Results and Analyses

There are many factors which could influence the Taiwan economy, such as the country's culture, the government's policy, and the industry framework. Some factors are clear, and others are not clear. But semiconductor still is the major supporting in Taiwan.

IC Industry Situation in Taiwan. Taiwan Semiconductor Manufacturing Company (TSMC) and United Microelectronics Corporation (UMC) are the first and second in worldwide ranking, with a combined market share exceeding 50%. IC assembly industry total product value is the first of the worldwide [13].

Table 1 shows the historical data series of the IC assembly industry Revenue of Taiwan from 2007 Q1 to 2010 Q3, but fluctuating randomly. So this paper forecasts and analyzes IC assembly industry revenue by Grey-Markov forecasting model.

4.1. Build the GM(1,1) Grey Forecasting Model. Using the data of the IC assembly industry revenue of Taiwan from 2007 Q1 to 2010 Q3, in Table 1 and (1)–(7) for model building, the GM(1,1) model of IC assembly industry revenue yield is

$$\hat{Y}(k) = \hat{x}^{(0)}(k+1) = 46389938e^{-0.00887984k} \quad (k = 1, 2, 3, \dots, k), \quad (14)$$

where k is the series number of the quarter and $k = 1$ means 2007*Q1.

4.2. Partition of States by Markov-Chain Forecasting Model. According to the actual data, four states, that is, four contiguous intervals, are established about the curve of $X^{(0)}(k+1)$.

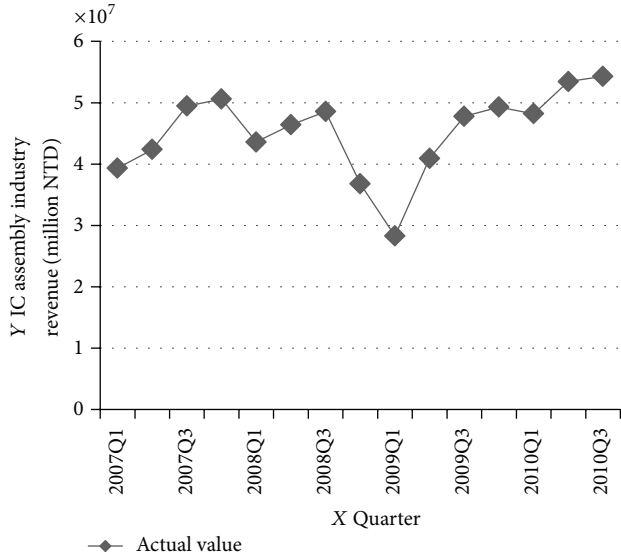


FIGURE 1: The curve of the IC assembly industry revenue in Taiwan.

According to (8)-(9), the four states intervals can be got as follows:

$$\begin{aligned}
 E_1: E_{11} &= \hat{Y}(k) - 1.08\bar{Y} & E_{21} &= \hat{Y}(k) - 0.28\bar{Y} \\
 E_2: E_{12} &= \hat{Y}(k) - 0.28\bar{Y} & E_{22} &= \hat{Y}(k) \\
 E_3: E_{13} &= \hat{Y}(k) & E_{23} &= \hat{Y}(k) + 0.28\bar{Y} \\
 E_4: E_{14} &= \hat{Y}(k) + 0.28\bar{Y} & E_{24} &= \hat{Y}(k) + 1.08\bar{Y},
 \end{aligned}
 \tag{15}$$

where \bar{Y} denotes the average value of the historical IC assembly industry revenue of Taiwan from 2007 Q1 to 2009 Q4. Figure 1 shows the historical data series and the states intervals.

4.3. Calculation of State Transition. The number of the historical data in every interval can be gotten as follows:

$$M_1 = 1, \quad M_2 = 3, \quad M_3 = 7, \quad M_4 = 1, \tag{16}$$

where M_i denotes the number of the historical data in the interval i and $i = 1, 2, 3, 4$. The numbers of one-step transiting to E_1, E_2, E_3 , and E_4 from E_3 are as follows:

$$M_{31} = 0, \quad M_{32} = 1, \quad M_{33} = 4, \quad M_{34} = 1. \tag{17}$$

Next $M_{ij}(1)$, where $i = 1, 3, 4$ and $j = 1, 2, 3, 4$, can be calculated in the same way. Then calculate the one-step transition probability to every states interval and present them in the transition matrix $R(1)$ as follows:

$$R(1) = \begin{bmatrix} \frac{0}{1} & \frac{0}{1} & \frac{1}{1} & \frac{0}{1} \\ \frac{1}{3} & \frac{0}{3} & \frac{2}{3} & \frac{0}{3} \\ \frac{0}{7} & \frac{1}{7} & \frac{4}{7} & \frac{1}{7} \\ \frac{0}{1} & \frac{0}{1} & \frac{1}{1} & \frac{0}{1} \end{bmatrix}. \tag{18}$$

4.4. Calculate the Forecast Value. According to (12), the date of IC assembly industry revenue in 2010 Q1 is calculated; that is,

$$\begin{aligned}
 \hat{Y}(13) &= \frac{1}{2(E_{13} + E_{23})} \\
 &= \frac{1}{2(55555326 + 52066442)} = 53810904.
 \end{aligned}
 \tag{19}$$

As Table 1 shows, the actual IC assembly industry revenue in Taiwan in 2010 Q1 is 48204412 million NTD. So the precision of the forecasting is 88.37 percent.

By the same method, the IC assembly industry revenue in 2010 Q2 and Q3 can be calculated, the forecast value of 2010 Q2 is 58,636,460 million NTD, and that of 2010 Q3 is 59105003 million NTD. So the forecasting precisions are 90.27% and 91.13%.

4.5. Comparison of Forecast Value between the Grey-Markov, GM(1,1), and DGM(1,1) Forecasting Model. First build a GM(1,1) Grey forecasting model to forecast the IC assembly industry revenue from 2010 Q1 to Q3. And utilize GM(1,1) to build and construct a 5 DGM(1,1) rolling modeling, forecasting in the same way. Then the forecasting results are presented and the results that are forecasted by Grey-Markov model are presented in Table 2.

The forecast value of Grey-Markov forecasting models is more precise than GM(1,1) grey forecasting model in Figure 2. It is showed that the Grey-Markov forecasting model is better for forecasting the IC assembly industry revenue in Taiwan. Figure 2 is showed that even if it causes the random array to fluctuate too big to face the influence that Financial turmoil, the forecasting curve of GM(1,1), DGM(1,1), and Grey Markov, the Grey-Markov forecasting models are still fit for the predication of the IC assembly industry revenue in Taiwan.

5. Conclusions and Discussions

Grey Markov prediction model is a hybrid model which mixes traditional grey prediction and Markov-chain, with fewer limitations which not need to complicate matrix operations. By the empirical analysis, we can prove the ability with the advantages of short-term forecasts, and by using GM(1,1), most future trends can be reflected. Indeed, the Markov probability matrix can extract the information provided by historical data to response to fluctuation system. Even when facing inconsistent fluctuating events, such as the financial crisis, it still gain a high accuracy [12].

In addition to revenue, the impact of IC packaging and testing industry in Taiwan also includes the country economy, industrial structure, policies of government, and even the climate, culture, and other relevant issues. These indicators are followed by specific historical data trend of random fluctuations which are suitable for grey Markov model. It is best to be applied to big fluctuation time-series problems, but outliers often appear in the scope of expectations. According to past experience, it is often impossible for anyone to believe

TABLE 2: Comparison of forecast values with three different methods.

Year		Reality amount	GM(1,1)	DGM(1,1)	Gray-Markov
2010 Q1	V	48,204,412	41700971	60847214	53810904
	E		13.49%	26.23%	11.63%
	P		86.51%	73.77%	88.37%
2010 Q2	V	53,435,639	41332312	67197053	58636460
	E		22.65%	25.75%	9.73%
	P		77.35%	74.25%	90.27%
2010 Q3	V	54,287,889	40966912	76155527	59105003
	E		24.54%	40.28%	8.87%
	P		75.46%	59.72%	91.13%

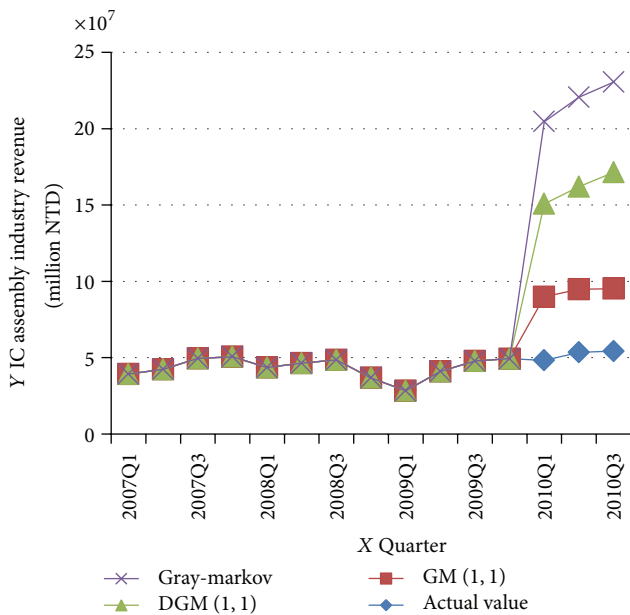


FIGURE 2: The forecasting curve of three different methods.

the possibility of their emergence. With the tremendous impact, we easily fall into the Black Swan myth because of human nature, and let it becomes hard explained and unpredictable.

When enterprise decision-makers make decisions for a major future investment, there must be a risk management mechanism; however, the reference data toward decision making always depend on historical data. For future industry prediction, there are many methods which can be used, but most of them can only reach accurate prediction in normal behavior. In the past market which included drastic uncontrollable factor's changes, instant dropping data could be recognized as special cases or outliers which would not be calculated. But the results may be distorted due to limited or insufficient data. Therefore, this study applied Markov prediction, which includes fewer complicated calculation and higher accuracy, to help the important references and make better investment portfolio decision.

Acknowledgments

The authors gratefully acknowledge Dr. Chung, Yi Shun from National Cheng Kung University (NCKU) and Mr. Chuang,

Yun Chung from Metal Industries Research & Development Centre (MIRDC), for their comments on earlier versions of the paper.

References

- [1] N. Nicholas, "The black swan: the impact of the highly improbable," *Journal of the Management Training Institut*, vol. 36, no. 3, p. 56, 2008.
- [2] D. Ju-Long, "Control problems of grey systems," *Systems and Control Letters*, vol. 1, no. 5, pp. 288–294, 1982.
- [3] H. Y. B. Yidan, "Grey-Markov forecasting model and its application," *Systems Engineering-Theory & Practice*, vol. 4, p. 12, 1992.
- [4] Z. Jun, S. Jianming, and F. Yingjun, "The grey model MGM (1, n) and its application," *Systems Engineering-Theory & Practice*, vol. 5, pp. 109–113, 1997.
- [5] Y. He and M. Huang, "A grey-Markov forecasting model for the electric power requirement in China," in *Proceedings of the Advances in Artificial Intelligence: 4th Mexican International Conference on Artificial Intelligence (MICAI '05)*, pp. 574–582, Springer, 2005.
- [6] M.-L. Ken and Y.-B. Li, "A study of applying grey predictive module into sales revenue prediction of convenience chain stores an investigation of 7-Eleven and familymart," *Journal of Grey System*, vol. 12, no. 3, pp. 139–146, 2009.
- [7] K.-C. Hung, K.-P. Lin, F.-Y. Hsu, C.-K. Wang, and J.-C. Lin, "Grey model with rolling mechanism for radio-wave path-loss forecasting in suburban environment," *Journal of Grey System*, vol. 13, no. 2, pp. 49–53, 2010.
- [8] G. L. Siqueira, E. A. Vasquez, R. A. Gomes, C. B. Sampaio, and D. A. Borghi, "Comparison between propagation measurements and coverage prediction models for small urban cells," in *Proceedings of the Global Telecommunications Conference—Communications: The Key to Global Prosperity (GLOBECOM '96)*, vol. 2, pp. 1182–1186, IEEE, London, UK, November 1996.
- [9] C.-T. Lin and S.-Y. Yang, "Forecast of the output value of Taiwan's opto-electronics industry using the Grey forecasting model," *Technological Forecasting and Social Change*, vol. 70, no. 2, pp. 177–186, 2003.
- [10] M.-S. Yin, "Fifteen years of grey system theory research: a historical review and bibliometric analysis," *Expert Systems with Applications*, vol. 40, no. 7, pp. 2767–2775, 2013.
- [11] L. Huang, P. Jin, Y. He et al., "Prediction of silkworm cocoon yield in china based on grey-Markov forecasting model," in *Proceedings of the Advances in Artificial Intelligence: 5th Mexican International Conference on Artificial Intelligence (MICAI '06)*, pp. 505–512, Springer, 2006.

- [12] C.-C. Hsu and C.-Y. Chen, "Applications of improved grey prediction model for power demand forecasting," *Energy Conversion and Management*, vol. 44, no. 14, pp. 2241–2249, 2003.
- [13] C.-C. Lou, T.-P. Lee, S.-C. Gong, and S.-L. Lin, "Effects of technical innovation on market value of the U.S. semiconductor industry," *Technological Forecasting and Social Change*, vol. 77, no. 8, pp. 1322–1338, 2010.

Research Article

An Indoor Video Surveillance System with Intelligent Fall Detection Capability

Ming-Chih Chen and Yang-Ming Liu

Department of Electronic Engineering, National Kaohsiung First University of Science and Technology, Kaohsiung City 811, Taiwan

Correspondence should be addressed to Ming-Chih Chen; mjchen@nkfust.edu.tw

Received 12 September 2013; Accepted 8 October 2013

Academic Editor: Teen-Hang Meen

Copyright © 2013 M.-C. Chen and Y.-M. Liu. This is an open access article distributed under the Creative Commons Attribution License, which permits unrestricted use, distribution, and reproduction in any medium, provided the original work is properly cited.

This work presents a novel indoor video surveillance system, capable of detecting the falls of humans. The proposed system can detect and evaluate human posture as well. To evaluate human movements, the background model is developed using the codebook method, and the possible position of moving objects is extracted using the background and shadow eliminations method. Extracting a foreground image produces more noise and damage in this image. Additionally, the noise is eliminated using morphological and size filters and this damaged image is repaired. When the image object of a human is extracted, whether or not the posture has changed is evaluated using the aspect ratio and height of a human body. Meanwhile, the proposed system detects a change of the posture and extracts the histogram of the object projection to represent the appearance. The histogram becomes the input vector of K-Nearest Neighbor (K-NN) algorithm and is to evaluate the posture of the object. Capable of accurately detecting different postures of a human, the proposed system increases the fall detection accuracy. Importantly, the proposed method detects the posture using the frame ratio and the displacement of height in an image. Experimental results demonstrate that the proposed system can further improve the system performance and the fall down identification accuracy.

1. Introduction

In Taiwan, falls represent the second leading accidental cause of death among elderly people. The rate of falling down among the elderly ranges from roughly 15% to 40% annually, and the incidence of falling increases as they grow older. Most falls lead to hospitalization of the elderly, residing in nursing homes, and barriers to daily activities. Elderly people most commonly fall in the bathroom, toilet, living room, and bedroom. Therefore, the ability to detect the falling of elderly people quickly would decrease the rate of injuries and reduce medical treatment costs. The damage degree of falls among the elderly is often decided by the time of discovery, transport, and emergency medical services. Developing electronic technologies facilitates the integration of sensors, computer vision, and the increasingly popularity of the wireless network. Such integrated applications can help the elderly to avoid potentially dangerous situations. This automatic system also reduces neglect among individuals and achieves zero-distance medical treatment.

The rest of this paper is organized as follows. Section 2 surveys previous design methods for detecting human falls. Section 3 then introduces the proposed system design. Next, Section 4 summarizes the experimental results of the proposed system and compares them with those of other ones. Conclusions are finally drawn in Section 5, along with recommendations for future research.

2. Related Work

Recognizing human behaviors using computer vision techniques is actively researched in various fields. A simple method detects a fall by analyzing the aspect ratio of the bounding box of a moving object [1-5]. Another design [6] evaluates whether or not a fall occurs by using motion history image and the ratio and angle of ellipse. In posture recognition, a commonly used feature vector is the projection histogram, in which the pixel number of row- and column-wise foreground objects is calculated, followed by a comparison with stored posture templates to evaluate the human

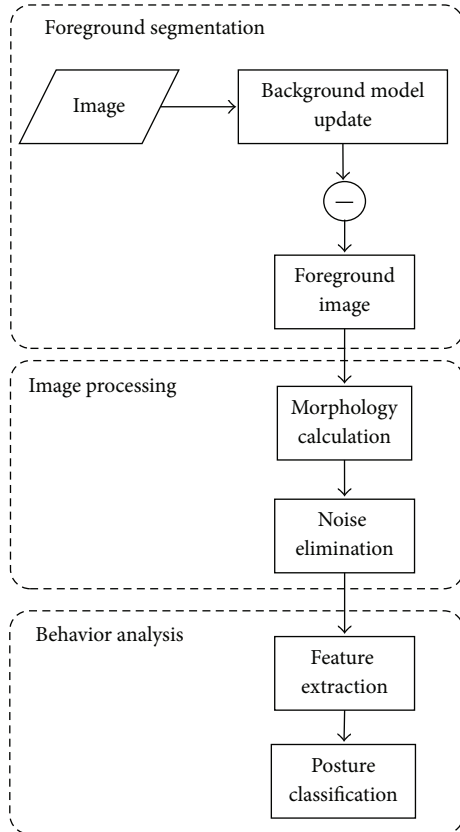


FIGURE 1: Proposed system architecture.

posture [2, 3, 7–12]. Another design [13] incorporates a fall detection method which uses combination of ellipse and skin color matches for head localization. The centroid of the feet area is identified by using the head location and medial axis. During the fall detection phase, a scene image is divided into equal-sized blocks. These blocks are then categorized into head, floor, and neutral ones. When the vertical displacement of a human head exceeds a threshold, whether the location of a human head lies in the floor block must be determined to evaluate whether or not a fall occurs.

Another design [14] identifies the centroid of a foreground object by using the 3D model of the human body and also identifies the floor plane by using the random sample consensus (RANSAC) plane detection algorithm. The system can detect whether the fall event occurs or not by calculating the distance between the centroid of human body and floor plane judge. Despite this, the above systems expend a significant amount of resources when calculating posture recognition. This work presents a novel indoor video surveillance system to recognize the falls by spending fewer resources and achieving a higher accuracy rate compared with previous ones.

3. Proposed System Architecture

Figure 1 shows the system framework, which consists of foreground segmentation, image processing, and behavior

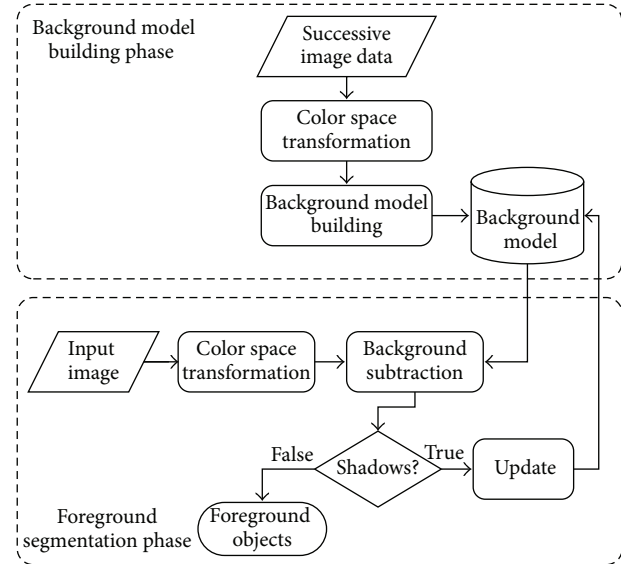


FIGURE 2: Foreground segmentation flow.

analysis. The proposed system first obtains the segmentation of moving objects by using the background subtraction method and the image processing technique to eliminate noise interference. When the moving objects are identified, the postures of these detected objects are recognized using behavior analysis.

3.1. Foreground Segmentation. While a vision surveillance system heavily emphasizes how to detect moving objects, the segmentation accuracy of moving objects can improve the performance of further analysis (e.g., object extraction or posture analysis). Figure 2 shows the proposed foreground segmentation flow. The flow first collects successive images and then transforms them into hue, saturation, and value (HSV) color space and builds the preliminary background model. When a new image is inputted, the background subtraction method described in [1] extracts the foreground image and removes shadows by using the shadow detection method. Finally, the background model is updated, owing to background subtraction.

3.2. Image Processing. When a foreground image is identified, some noises appear in the image or some holes appear in moving objects. Additionally, the morphology model is used to eliminate some small noise interference and fill holes of moving objects. Moreover, large noises are eliminated by using the information of each foreground object boundaries and foreground object area to distinguish between larger noises and regions of interest. Figure 3 shows the above procedure.

3.3. Behavior Analysis. The proposed system finally recognizes the posture of each foreground object. Features of each foreground object are first extracted for further analysis and

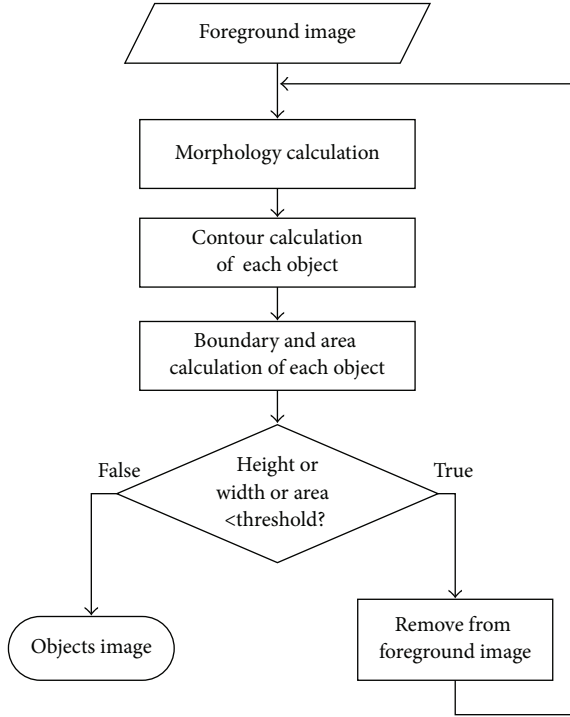


FIGURE 3: Image processing flow.

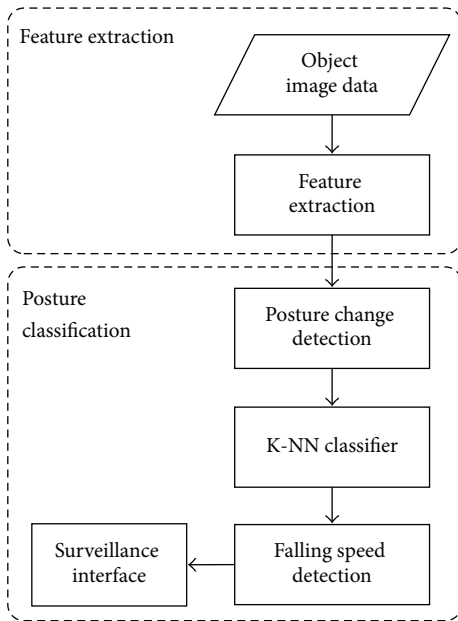


FIGURE 4: Behavior analysis flow.

classification. The classifier uses the K-Nearest Neighbor (K-NN) algorithm and combines it with posture change detection. When a change event of the posture is detected, the proposed system recognizes which posture is changed by using the K-NN based classifier. Finally, the foreground object between the real fall and only a supine position is discriminated by using the falling speed. Figure 4 shows the detailed processes of behavior analysis.

3.3.1. Feature Extraction. Extracting useful feature information in a foreground image is of priority concern in recognition processes. The proposed system extracts three main features, as described in the following.

(a) *Projection Histograms.* The horizontal and vertical projection histogram of foreground objects is derived by calculating the pixel number of row- and column-wise foreground objects. Since projection histograms vary according to location of foreground objects in the scene, the normalization step must be performed by using the discrete fourier transform (DFT) method described in [2]. By assuming that the image size is $N \times M$ pixels, the normalization step is as follows.

Step 1. Calculate the horizontal and vertical projection histogram of foreground objects:

$$\begin{aligned} \text{HZ}(y) &= \left| \left\{ (x_p, y_p) \in F, y_p = y \right\} \right|, \\ \text{VT}(x) &= \left| \left\{ (x_p, y_p) \in F, x_p = x \right\} \right|. \end{aligned} \quad (1)$$

Step 2. Apply DFT to $\text{HZ}(y)$ and $\text{VT}(x)$:

$$\begin{aligned} \text{DFT}_{\text{HZ}(h)} &= \frac{1}{N} \sum_{i=1}^N \text{HZ}(i) e^{-2j\pi(hi/N)}, \quad h = 0, 1, \dots, N-1, \\ \text{DFT}_{\text{VT}(v)} &= \frac{1}{M} \sum_{i=1}^M \text{VT}(i) e^{-2j\pi(vi/M)}, \quad v = 0, 1, \dots, M-1. \end{aligned} \quad (2)$$

Step 3. Normalize based on the following formula:

$$\begin{aligned} \text{NDFT}_{\text{HZ}(h)} &= \frac{|\text{DFT}_{\text{HZ}(h)}|}{|\text{DFT}_{\text{HZ}(1)}|}, \quad h = 2, \dots, 50, \\ \text{NDFT}_{\text{VT}(v)} &= \frac{|\text{DFT}_{\text{VT}(v)}|}{|\text{DFT}_{\text{VT}(1)}|}, \quad v = 2, \dots, 50. \end{aligned} \quad (3)$$

In (2), magnitudes of these DFT coefficients decay for large values of h and v . The first fifty significant DFT coefficients are selected and normalized by (3). The normalized magnitudes of fifty significant DFT coefficients of different postures are obtained by the above equations. After the above three steps are performed, the normalization of posture is completed.

(b) *Variance of Aspect Ratio in the Human Body.* The boundary of foreground objects is described using the bounding box. In most works [2, 5, 6, 9, 14, 15], the discrimination between normal state and fall state uses the ratio of human body. By using the variance in the ratio of the human body, the proposed system detects whether or not the posture has changed. Variance in the aspect ratio can be calculated as follows:

$$R(t) = \frac{w(t)}{h(t)}, \quad (4)$$

$$\mu_r(t) = (1 - \alpha) \mu_r(t-1) + \alpha R(t), \quad (5)$$

$$\sigma_r(t) = R(t) - \mu_r(t-1). \quad (6)$$

In (4), the parameters $w(t)$, $h(t)$ denote width and height of the bounding box at current time t , respectively, and $R(t)$ represents the ratio of width and height. In (5), the value $\mu_r(t)$ refers to the mean value of the aspect ratio at current time t and value $\mu_r(t-1)$ denotes the mean value of the aspect ratio at previous time $(t-1)$. Value α is the updated parameter. Value $\sigma_r(t)$ in (6) represents the variance value of aspect ratio at current time t . The variance is small if an individual does not change his or her posture. Otherwise, the variance is large if an individual changes his or her posture. When the variance exceeds a threshold, which posture has changed is determined using the K-NN based classifier.

(c) *Variance of Height in the Human Body.* Whether or not the posture has changed when using the variance in human body height is worthwhile to detect because that height varies according to different postures or image resolutions. Variance of height is calculated as follows:

$$\mu_h(t) = (1 - \alpha) \mu_h(t-1) + \alpha H(t), \quad (7)$$

$$\sigma_h(t) = H(t) - \mu_h(t-1). \quad (8)$$

In (7), values $H(t)$ and $\mu_h(t)$ denote the height and mean value of human height at current time t , respectively, while value $\mu_h(t-1)$ represents the mean value of the height at previous time $(t-1)$. Also, value α refers to the updated parameter. In (8), value $\sigma_h(t)$ denotes the mean value of height at current time t . Notably, the variance is small if an individual does not change his or her posture. Otherwise, the variance is large if an individual changes his or her posture. When the variance exceeds a threshold, which posture has changed is determined using the K-NN based classifier.

3.3.2. Posture Classification. The proposed posture classification system has two major components: K-NN classifier and falling speed detection. The system first detects whether or not the posture has changed by using the features of the aspect ratio and human body height. When a posture change is detected, exactly which posture has changed is recognized using the K-NN based classifier. Otherwise, the system selects the recent output in the classifier as the current output. Figure 5 shows the posture change detection. K-NN algorithm consists of two phases: offline training and classification. As described in [9], the algorithm trains the posture model based on five posture types, with each type having three templates. Figure 6 shows the five postures of standing, sitting, bending, lying, and lying toward. The five images are retrieved from the video surveillance and processed after eliminating the background interference.

During the classification phase, the distance between the current frame and the stored template i of posture j can be calculated by (9). The winning posture is taken by a majority vote. When the posture is lying towards the camera, the height test is conducted to distinguish between bending posture and lying towards posture. When the posture is lying or lying towards the camera, the falling speed is used to

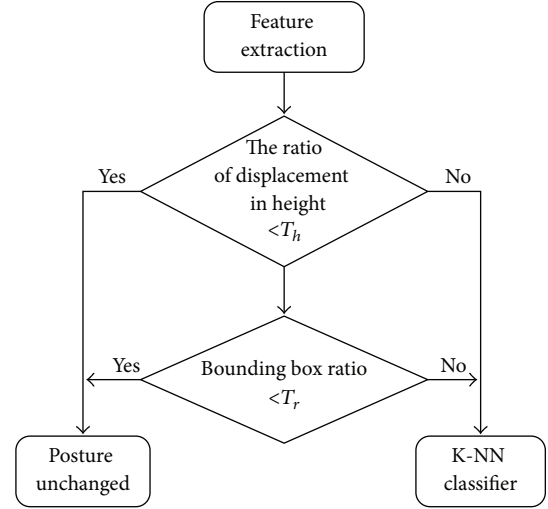


FIGURE 5: Posture change detection flow.

distinguish between a real fall and an individual in a supine position:

$$S_{i,j} = \sqrt{\sum_{y=0}^M (\text{HZ}^v(y) - \text{HZ}_{i,j}^v(y))^2 + \sum_{x=0}^N (\text{VT}^v(x) - \text{VT}_{i,j}^v(x))^2}, \quad (9)$$

where $\text{HZ}^v(y)$ denotes the horizontal projection of the current frame; $\text{HZ}_{i,j}^v(y)$ represents the horizontal projection of the stored template i of posture j ; $\text{VT}^v(x)$ refers to the vertical projection of the current frame; $\text{VT}_{i,j}^v(x)$ denotes the vertical projection of the stored template i of posture j ; and $S_{i,j}$ represents the distance between the current frame and the stored template i of posture j .

(1) *Test of Height.* The shape of lying towards posture occasionally resembles that of a bending posture, necessitating a method to distinguish between these two postures. A previous design [9] distinguishes between standing and lying towards postures by using the angle of bounding box. This work presents a novel method by using the mean ratio of the height in standing and lying towards postures to distinguish between them. The method is described in what follows:

$$\begin{aligned} \text{lying_toward,} & \quad \text{if } \frac{H(t)}{\mu_{\text{stand}}(t)} < T, \\ \text{bending,} & \quad \text{else,} \end{aligned} \quad (10)$$

where $H(t)$ denotes the height of a lying towards posture; $\mu_{\text{stand}}(t)$ represents the mean of the height in a standing posture, T is threshold, and its value ranges from around 0.4 to 0.5.

(2) *Test of Falling Speed.* A human occasionally lies without falling. To distinguish between these two postures, this work

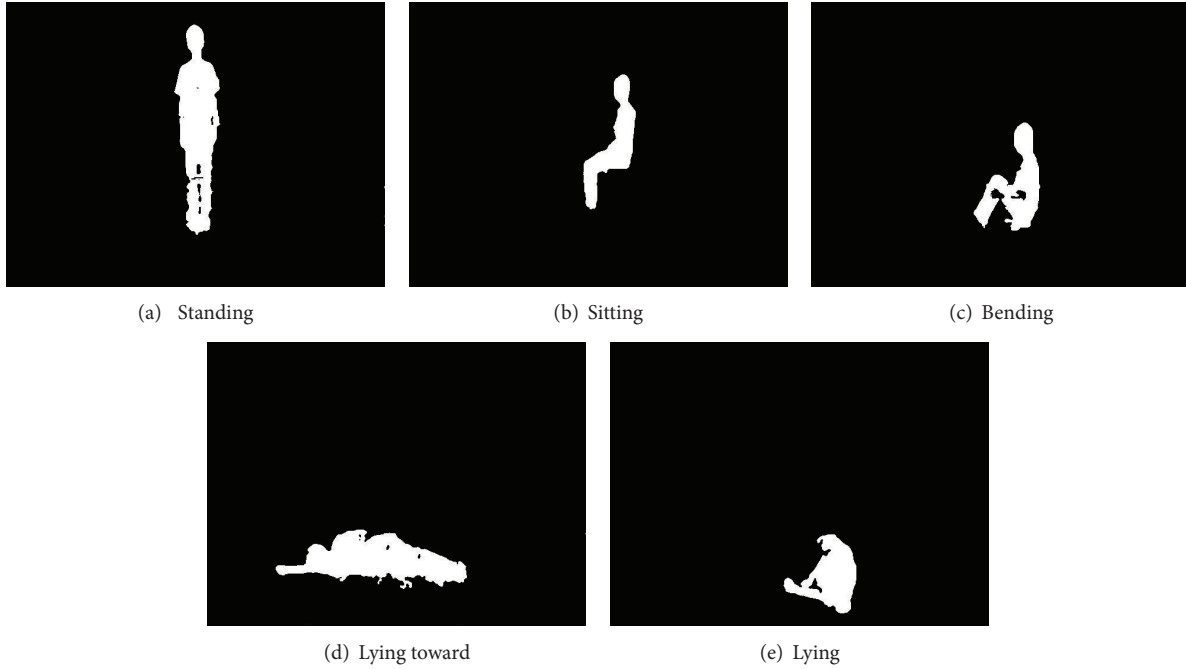


FIGURE 6: Five postures defined in our system.

adopts the method in [9], which uses temporal information including the last time t_{stand} of standing posture and the time t_{lying} of a lying posture. When the difference of time is less than threshold T , we can infer that a real fall occurs as follows:

$$\begin{aligned} &\text{fall,} && \text{if } t_{\text{lying}} - t_{\text{stand}} < T, \\ &\text{lying,} && \text{else.} \end{aligned} \tag{11}$$

4. Experimental Results

While implemented by OpenCV library and Visual C++ 2008, the proposed system runs on an Intel Core i7 3.4 GHz laptop PC with 8 GB memory. To evaluate the system performance and accuracy, the experimental environment is an indoor place with a single and fixed camera. The distance between the individual and the camera is approximately 4-5 meters. The experiment is conducted by observing the video and noting the detection results to determine whether or not the current image is classified accurately.

4.1. Comparison of Different Methods in Terms of Execution Time. To reduce the computational cost and stabilize the classifier output, this work also develops a posture change detection method to overcome these problems. Figure 7 compares the classifier output with and without the posture change detection approach. According to this figure, the output fluctuates less with the posture change detection method. Equation (12) defines the execution speed. The execution speed refers to how much time that a recognition algorithm

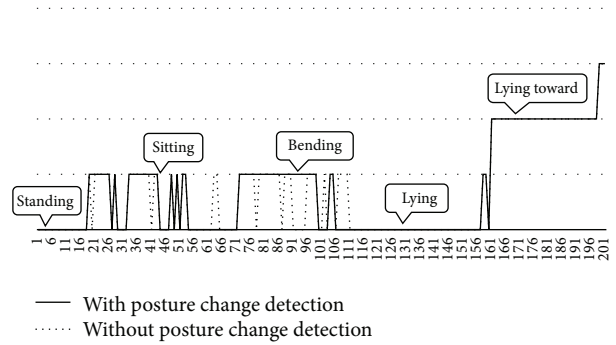


FIGURE 7: Comparison between output of classifier with and without posture change detection.

needs to finish a frame, regardless of whether or not the recognition is accurate:

$$\text{Execution speed (ms/frame)} = \frac{\text{Totally Execution time}}{\text{frames}}. \tag{12}$$

Table 1 compares different scenarios of the execution speed. Although the design in [5] has the shortest average execution time, owing to that it does not need to build the background model in this algorithm, the algorithm sacrifices the recognition accuracy of other postures. The design in [9] requires more execution time to build the background model than the proposed design.

4.2. Comparison of Different Methods in Terms of Recognition Rate. In our video clips, eight subjects of different heights

TABLE 1: Comparison of different methods in terms of the execution time.

Scenario	Method		
	Nasution and Emmanuel [9]	Silapasuphakornwong et al. [5]	Ours
Video 1 (ms)	85.25	15.00	54.26
Video 2 (ms)	88.00	15.40	60.26
Video 3 (ms)	99.34	15.27	73.23
Video 4 (ms)	111.23	15.66	82.77
Average execution time (ms)	95.96	15.33	67.63

TABLE 2: Recognition rates for various postures in the proposed system.

Posture	Recognition			
	N_a	N_c	N_f	R (%)
Standing	1459	1432	27	98.15
Sitting	419	391	28	93.31
Bending	634	603	31	95.11
Lying	297	297	0	100.00
Lying toward	236	216	20	91.53
Fall down	514	476	38	92.60

and weights were asked to participate in the project. The image resolution is 640×480 pixels. Four of the video clips were taken to train the templates of the classifier, and the remaining ones were taken to evaluate the system performance. In the posture change detection method, the threshold for the aspect ratio of the human body was set to 0.1, and the threshold for the height ratio of the human body was set to 0.15. In the height test, the threshold was set to 0.45. Table 2 summarizes the experimental results of the recognition rate for five postures in the proposed system, where N_a denotes the number of images for various postures; N_c represents the number of accurately detected images; N_f refers to the number of falsely detected images; and R denotes the recognition rate. According to this table, the best recognition appears in the lying posture with an accuracy rate of 100%, and the worst case appears in the supine posture with an accuracy rate of 91.53%.

Table 3 compares different algorithms in terms of the recognition rate. This table reveals that the design in [5] has the best execution time to complete the recognition of a frame. However, its recognition rate is extremely low especially in the bending posture with only a recognition rate of 9.30%. The design fails to recognize two postures (i.e., the sitting and supine postures) owing to the lack of background model. The design in [9] has higher recognition rates in the sitting and supine postures compared with others, because it has a more efficient foreground segmentation algorithm. According to Table 1, the design in [9] sacrifices the execution time for increasing the recognition accuracy. The worst case scenario for the posture recognition appears in the standing and binding postures. Their recognition rates are 76.56% and 63.25%, respectively. The proposed method can achieve 98.15% and 95.11% for recognizing the two postures. By using the average execution time of 95.96 ms, although the design

in [9] recognizes a frame, the proposed system uses only 67.63 ms to perform the same recognition. The proposed design can detect an individual falling down with an accuracy rate of 92.60%. In terms of execution time and recognition rate, the proposed system performs better than previous designs.

4.3. Performance Comparisons with Different Methods. This work also evaluates the performance of different fall detection methods by using a video recorded with three individuals, who participated in the project with different heights and weights. Our video clips contain 100 fall events and 100 false fall events. Two widely used criteria in fall detection systems are adopted here for comparisons [2, 6, 9, 15], as shown in the following:

$$\begin{aligned} \text{Sensitivity (\%)} &= \frac{TP}{TP + FN} \times 100\%, \\ \text{Specificity (\%)} &= \frac{TN}{TN + FP} \times 100\%, \end{aligned} \quad (13)$$

where the parameters TP, FP, FN, TN defined in (13) can be expressed as shown in Table 4.

Parameter TP refers to a subject having experienced a fall event, and the detection system can detect it accurately; however, a system having failed to detect a fall of a subject is denoted by parameter FN. Parameter TN denotes a subject having experienced a false fall, and the system can recognize it accurately. An event in which a subject experiences a false fall yet the system recognizes a fall as having occurred is denoted by parameter FP. These four parameters are used to calculate the times of the four possible recognitions. The criterion sensitivity refers to the accuracy rate of a system that can recognize the falls under all of the fall events in a video. The criterion specificity denotes the accuracy rate of a system that can recognize the false falls under all of the false fall events in a video. Table 5 reveals that the proposed system has a sensitivity of 96% and a specificity of 97%. This work has implemented the methods of Nasution and Emmanuel [9] and Rougier et al. [6], respectively. According to Table 6, the method in [9] has a higher sensitivity and specificity than those of the method in [6]. Nevertheless, the proposed system performs better than the two previous designs.

5. Conclusions

This work designs an indoor video surveillance system with fall detection capability. The proposed system can also detect

TABLE 3: Comparison of different methods in terms of recognition rate.

Posture	Method		
	Nasution and Emmanuel [9] (%)	Silapasuphakornwong et al. [5] (%)	Ours (%)
Standing	76.56	95.68	98.15
Sitting	99.28	None	93.31
Bending	63.25	9.30	95.11
Lying	66.00	100.00	100.00
Lying toward	100.00	None	91.53
Fall down	None	None	92.60

TABLE 4: Parameter definitions in (8) and (9).

System recognition	Fall incident	
	Occurs	Does not occur
Positive	TP	FP
Negative	FN	TN

TABLE 5: Experimental results of our system with four possible recognitions.

System recognition	Fall Incident	
	Occurs	Does not occur
Positive	94	3
Negative	6	97

TABLE 6: Comparison of fall detection methods.

Criterion	Method		
	Nasution and Emmanuel [9]	Rougier et al. [6]	Ours
Sensitivity (%)	83	40	94
Specificity (%)	88	63	97

and evaluate a human posture. An attempt is also made to improve the overall system performance by developing three methods to reduce the execution time for recognition and increase the recognition rate of human postures. The first method utilizes the mean ratio of the height in standing and supine postures to distinguish between these two postures. By using the posture change detection, the second method reduces the computational cost and stabilizes the classifier output. By using the height of a human body, the third method distinguishes between the bending and supine postures. Experimental results indicate that the proposed design can further reduce the execution time and increase the recognition rate of human postures. Additionally, the proposed system can achieve a recognition rate higher than 90% for each posture. Moreover, the proposed system can also detect the fall down with the accurate rate of 92.60%. Performance comparisons reveal that the proposed system performs better than previous designs. Efforts are underway in our laboratory to incorporate capabilities of multiobject tracing and face recognition in the proposed system.

Acknowledgments

This work is supported in part by Taiwan's Ministry of Education under Project no. 101B-09-027.

References

- [1] K. Kim, T. H. Chalidabhongse, D. Harwood, and L. Davis, "Real-time foreground-background segmentation using codebook model," *Real-Time Imaging*, vol. 11, no. 3, pp. 172–185, 2005.
- [2] H. Foroughi, B. S. Aski, and H. Pourreza, "Intelligent video surveillance for monitoring fall detection of elderly in home environments," in *Proceedings of the 11th International Conference on Computer and Information Technology (ICCIT '08)*, pp. 219–224, Khulna, Bangladesh, December 2008.
- [3] H. Foroughi, A. Rezvanian, and A. Pazirae, "Robust fall detection using human shape and multi-class support vector machine," in *Proceedings of the 6th Indian Conference on Computer Vision, Graphics and Image Processing (ICVGIP '08)*, pp. 413–420, December 2008.
- [4] B. Huang, G. Tian, and X. Li, "A method for fast fall detection," in *Proceedings of the 7th World Congress on Intelligent Control and Automation (WCICA '08)*, pp. 3613–3618, Chongqing, China, June 2008.
- [5] P. Silapasuphakornwong, S. Phimoltares, C. Lursinsap, and A. Hansuebsail, "Posture recognition invariant to background, cloth textures, body size, and camera distance using morphological geometry," in *Proceedings of the International Conference on Machine Learning and Cybernetics (ICMLC '10)*, pp. 1130–1135, Shangdong, China, July 2010.
- [6] C. Rougier, J. Meunier, A. St-Arnaud, and J. Rousseau, "Fall detection from human shape and motion history using video surveillance," in *Proceedings of the 21st International Conference on Advanced Information Networking and Applications Workshops (AINAW '07)*, pp. 875–880, May 2007.
- [7] I. Haritaoglu, D. Harwood, and L. S. Davis, "GHOST: a human body part labeling system using silhouettes," in *Proceedings of the 14th International Conference on Pattern Recognition*, vol. 1, pp. 77–82, August 1998.
- [8] I. Haritaoglu, D. Harwood, and L. S. Davis, "W4: real-time surveillance of people and their activities," *IEEE Transactions on Pattern Analysis and Machine Intelligence*, vol. 22, no. 8, pp. 809–830, 2000.
- [9] A. H. Nasution and S. Emmanuel, "Intelligent video surveillance for monitoring elderly in home environments," in *Proceedings of the IEEE 9th International Workshop on Multimedia Signal Processing (MMSP '07)*, pp. 203–206, Crete, Greece, October 2007.

- [10] F. Xie, G. Xu, Y. Cheng, and Y. Tian, "Human body and posture recognition system based on an improved thinning algorithm," *IET Image Processing*, vol. 5, no. 5, pp. 420–428, 2011.
- [11] M. Yu, S. M. Naqvi, A. Rhuma, and J. Chambers, "One class boundary method classifiers for application in a video-based fall detection system," *IET Computer Vision*, vol. 6, no. 2, pp. 90–100, 2012.
- [12] K. Ozcan, A. K. Mahabalagiri, M. Casares, and S. Velipasalar, "Automatic fall detection and activity classification by a wearable embedded smart camera," *IEEE Journal on Emerging and Selected Topics in Circuits and Systems*, vol. 3, no. 2, pp. 125–136, 2013.
- [13] M. Shoaib, R. Dragon, and J. Ostermann, "View-invariant fall detection for elderly in real home environment," in *Proceedings of the 4th Pacific-Rim Symposium on Image and Video Technology (PSIVT '10)*, pp. 52–57, November 2010.
- [14] G. Diraco, A. Leone, and P. Siciliano, "An active vision system for fall detection and posture recognition in elderly healthcare," in *Proceedings of the Design, Automation and Test in Europe Conference and Exhibition (DATE '10)*, pp. 1536–1541, Dresden, Germany, March 2010.
- [15] N. Noury, A. Fleury, P. Rumeau et al., "Fall detection—principles and methods," in *Proceedings of the 29th Annual International Conference of IEEE-EMBS, Engineering in Medicine and Biology Society (EMBC '07)*, pp. 1663–1666, Lyon, France, August 2007.

Research Article

A Novel Cloud Computing Algorithm of Security and Privacy

Chih-Yung Chen¹ and Jih-Fu Tu²

¹ Department of Information Management, St. John's University, 499 Section 4, Tam King Road, Tamsui District, New Taipei City 25135, Taiwan

² Department of Electronic Engineering, St. John's University, 499 Section 4, Tam King Road, Tamsui District, New Taipei City 25135, Taiwan

Correspondence should be addressed to Chih-Yung Chen; yung@mail.sju.edu.tw

Received 12 September 2013; Accepted 12 October 2013

Academic Editor: Teen-Hang Meen

Copyright © 2013 C.-Y. Chen and J.-F. Tu. This is an open access article distributed under the Creative Commons Attribution License, which permits unrestricted use, distribution, and reproduction in any medium, provided the original work is properly cited.

The emergence of cloud computing has simplified the flow of large-scale deployment distributed system of software suppliers; when issuing respective application programs in a sharing clouds service to different user, the management of material becomes more complex. Therefore, in multitype clouds service of trust environment, when enterprises face cloud computing, what most worries is the issue of security, but individual users are worried whether the privacy material will have an outflow risk. This research has mainly analyzed several different construction patterns of cloud computing, and quite relevant case in the deployment construction security of cloud computing by fit and unfit quality, and proposed finally an optimization safe deployment construction of cloud computing and security mechanism of material protection calculating method, namely, Global Authentication Register System (GARS), to reduce cloud material outflow risk. We implemented a system simulation to test the GARS algorithm of availability, security and performance. By experimental data analysis, the solutions of cloud computing security, and privacy derived from the research can be effective protection in cloud information security. Moreover, we have proposed cloud computing in the information security-related proposals that would provide related units for the development of cloud computing security practice.

1. Introduction

Cloud computing provides service of several different service types, namely, software as a service (SaaS), platform as a service (PaaS), and infrastructure as a service (IaaS) [1]. Each pattern in risk of control and benefit will differ from each other, the protection right of privacy in cloud computing is an important subject [2], and the traditional encryption solution was unable to provide effective privacy protection mechanism of the cloud environment [3]. For example, the user of cloud service response pays close attention to individual or company related information, whether under the condition that possibly the material owner does not know the circumstances of the matter provided to other people usages [4]. The right of privacy in traditional software development is not a main issue but in the protection right of privacy regarding the cloud computing is a big challenge at present, because these materials usually in unencrypted form are deposited on a machine, but the owner of the material possibly contains the different organization operators, enhancement divulging

commercial sensitive information, and possible loss in privacy material [5]; therefore, protection of individual secret and sensitive information stores up in the clouds is very important. When establishing the cloud computing service system carries on the information security risk control, one must consider all type factors and promotes user the level of trust in the laws condition, needs to analyze and take the gauge of the system in principle of design of each stage [6].

Clouds computing on the Internet is an important development application; the cloud serves the user without hardware master control power [7], the user by the application service that the cloud service provides, processing and depositing material, for example, credit card, account dense, and personal preference profile, picture conduct calendar, finance and health, and other materials. Characteristics of cloud computing are to provide the service of data storage, processing, and platform use flow to global users, but the result of this material set will be material privacy protection, causing the common reason for the enterprise or individual not being willing to use the cloud service solution package.

Furthermore, the security of cloud computing material still has many problems not yet solved, at present there is not a good and effective test method for cloud computing material of privacy right system [2], and different types of cloud computing service need a different data safety protection solution. The objective of this research is mainly the hope to establish a research model of cloud computing to discuss the fit and unfit quality relations of material protection and to analyze which application of cloud computing service needs to be protected, including the following several parts: (1) establishing a research model for cloud arithmetic system construction privacy material protection; (2) discussing fit and unfit quality relations of cloud service material protection and traditional material protection; (3) discussing some applications of cloud computing service type. Which type of news needs to be protected? (4) Analysis result provides relevant unit to referring to, in order to help it in the future research, and contribute to the practical realm.

2. Related Works

2.1. The Operation Principle of Clouds Computing. The cloud computing system is mainly comprised of the software service supplier (SaaS), the platform service supplier (PaaS), and the network infrastructure construction supplier (IaaS) [8]; the typical operation principle is shown in Figure 1.

By Google Cloud Computing Trends analysis chart (Figure 2) it can be seen that in the trend of cloud computing the well-respected degree has grown year by year, the products of the database manufacturer are joining the function of the cloud computing to support the database (e.g. Oracle now operates a cloud computing platform (EC2) service directly in Amazon) [9], therefore, deposits along with more and more materials in the clouds service, expansion that the issue of data safety will also continue, because these materials usually contain the company or individual related important sensitive news.

2.2. Management Style of Cloud Computing. The hardware device of cloud computing can be provided by internal cloud or the exterior third party organization entrusted with the clouds (TTP Cloud), the cloud computing is possibly limited in sole organizations and agencies Private Cloud (private cloud) or many organizations and agencies share the public cloud (Public Cloud) [11, 12].

2.3. Privacy Right Issues

2.3.1. What Is Privacy Right? The private right of privacy is a fundamental human right, coming from the current UN Universal Declaration of Human Rights and European human rights convention, including various types of privacy rights, for example, May control with right of own relevant information [13]. Regarding how to protect the personal privacy not to be encroached upon and harmed became important discussion of privacy right on safe presented [14–16].

2.3.2. Privacy Right Risk of Cloud Computing. As shown in an investigation that was done by Pew Internet in 2008 [4],

69% of Internet users use the online mail service in US, stores up material in the network, or uses homepage application program, such as the copy clerk distributed processing. These users are using the clouds to operate an actual emerging construction; the user through the equipment (PC, NB ...) connects to Internet downloading application program processing material and deposit material in cyberspace, Table 1 explains various cloud application services for the proportion that Internet user uses, and may understand why the clouds computing will issue the right of privacy risk.

In this section, we explain the concrete right of privacy issues in cloud computing, analyze the different clouds service case to explain that the request degree of each right of privacy under the different conditions was possibly different, and provide the comprehensive appraisal of the privacy risk of cloud computing. The main right of privacy risk is as follows [6]: (1) Individual user of cloud service: Runs counter to individual wish, was forced or convinced to provide the personal data, or makes them feel uncomfortable in other ways. (2) Enterprise or organization user in cloud service: Does not observe the policy and legislation of enterprise, loses prestige. (3) Clouds platform implementer: exposition of Sensitive information in storage platform (possibly for cheating goal), the faith of legal liability, influence goodwill and deficient user. (4) Clouds ASP: Does not abide by the law, loses prestige, uses the background program to store up personal data in the clouds, that is, the material is used in the non-clouds service. (5) Material level: Revelation personal data.

2.4. The Security Requirements of Different Levels. We need to consider the security problem level classification as follows [7]: (1) server deposit security, (2) Internet deposit security, (3) database deposit security, (4) material privacy security, and (5) program deposit security.

3. Research Methodology

3.1. Research Supposition. This research of the nature of cloud computing and challenge concept of privacy rights proposes that the research supposition of several possibilities in cloud computing services needs protected material type as follows. (1) Individual identification information can be used to distinguish or find individual material. (2) Sensitive information: health, tendency, religious belief or race material, union members, or others are considered as the personal information. (3) To be considered as sensitive information, for example, the biological information or the image data that the public places monitoring device are filmed. (4) User preference uses computer ancillary equipment collection material—like printer, behavior material—such as viewing habit, the digital content, and the user had visited recently the historic information of websites or products. (5) Unique identification equipment, using the only characteristics of hardware, may correspond to trace the equipment of user, for example, IP address, RFID label type material. (6) Transaction material, for example, electronic commerce material contains the order material of the user. These materials possibly have the sensitive information, for example, user

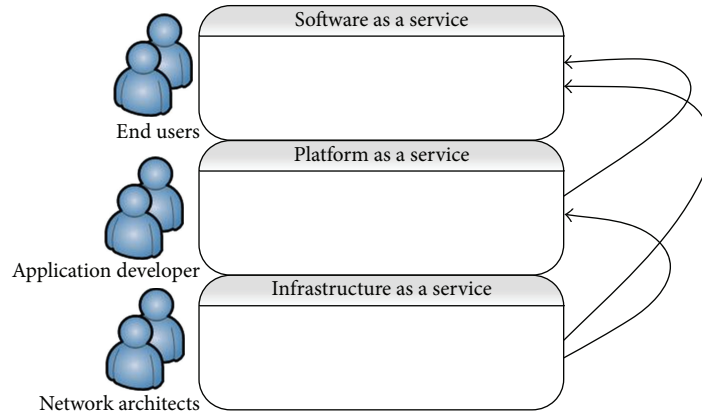


FIGURE 1: Composition and operation principle of clouds computing.

TABLE 1: The Internet network user uses the cloud service of questionnaire of all kinds of application offered.

All kinds of application clouds service—the Internet network user uses service of all kinds of application (%)	
Use Webmail service, for example, Hotmail, Gmail, or Yahoo! Mail	56%
Online to store the personal photo	34%
Use the Online application program, for example, Google Documents or Adobe Photoshop Express	29%
Online to store the personal film	7%
Online to pay and store the computer file	5%
Online to back up the hard disk	5%



FIGURE 2: Cloud Computing Trends [10].

material or credit card number and any latent, or increase the infringement privacy of the security loophole.

3.2. *Range of Research.* This research’s main discussion and analysis issue of data safety and privacy right of cloud computing service, through comparative analysis proposes a suggestion of cloud computing optimization model. The usability and test relevant question of cloud computing service are not in this range of study.

3.3. *Optimization Model.* This research proposes a cloud computing optimization model according to the comparison analysis method as shown in Figure 3 in the processing of the solution of privacy protection and in the security issue. This research suggests to establish Global Authentication Register

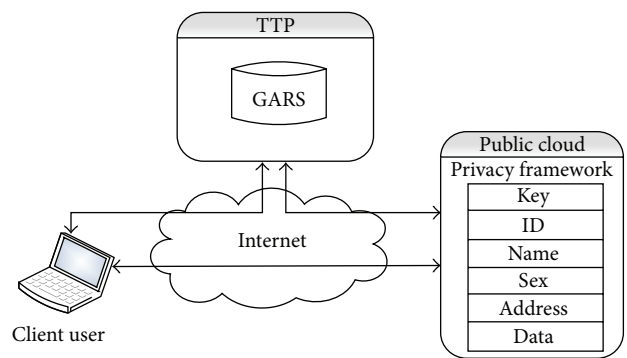


FIGURE 3: Optimization model of cloud computing.

System (GARS) on third party clouds of trust (TTP), provides the subscriber’s premises and clouds both sides separately carries out a disposable registration certification service, but Public Cloud part establishes right of privacy frame and model in the public cloud, and the encryption mechanism uses the GARS calculating method of this research and makes processing and protection on the privacy material and security.

3.4. *Data Transmission Flow.* Figures 4 and 5 are subscriber’s premise/clouds and TTP proof procedure data transmission flow chart.

The Calculating Method Parameter Definitions.

- C: Client.
- S: Server.

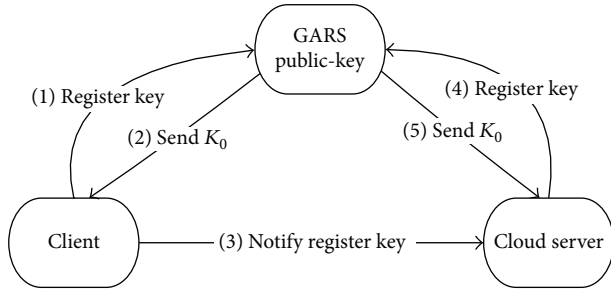


FIGURE 4: Optimization model of cloud computing (initialization).

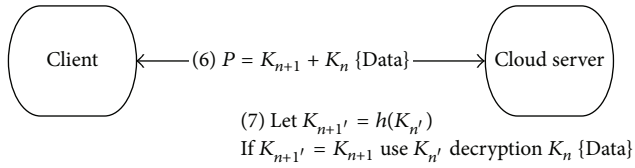


FIGURE 5: Optimization model of cloud computing (after TTP authorizes).

K_n : Authentication basis code. (K_0 obtains initial authentication basis code by GARS).

H : Hash Function.

$K_{n+1} = h(K_n)$: Encryption key (transmission end).

$K_{n+1}' = h(K_{n'})$: Encryption key (receiving end).

$P = K_{n+1} + K_n\{\text{Data}\}$: Encryption seal material (Package).

The GARS Calculating Method. GARS calculating method steps are as follows.

Step 1. The client sends out Request Register Key to GARS. C-TTP: Request Register Key.

Step 2. GARS transmits one group of Key: K_0 to give Client. TTP-c: Send Public Key: K_0 .

Step 3. Client informs Cloud Server Register Key. C-s: Notify Register Key.

Step 4. Cloud Server sends out Request Register Key to GARS. S-ttp Request Register Key.

Step 5. GARS transmits the same group Key: K_0 to give Cloud Server. TTP-s: Send Register Key.

Step 6. The subscriber's premise uses K_0 to produce one group of authentication encryption Key: K_1 ($K_1 = h(K_0)$) transmission encryption material ($P = K_1 + K_0\{\text{Data}\}$) to Cloud Server. $C \rightarrow S: K_{n+1} = h(K_n), P = K_{n+1} + K_n\{\text{Data}\}$ (Initial Value: 0).

Step 7. Cloud Server receives the encryption material and uses original $K_{n'}$ Hash Function to obtain K_{n+1}' , confirmation comparison Step 6 K_{n+1} weather is equal to Step 7 K_{n+1}' ; if equal, then it uses K_n to decipher the material. S: use K_n

Create K_{n+1}' ($K_{n+1}' = h(K_n)$). If $K_{n+1}' = K_{n+1} \implies$ Identify C then use K_n decryption $K_n\{\text{Data}\}$ S-c: $K_{n+1} = h(K_n), P = K_{n+1} + K_n\{\text{Data}\}$.

Note. (1) If the Server end must transmit material to return to the Client end, then similarly use Steps 6 and 7, Server and Client role exchange.

(2) If material authentication mistake, by the subscriber's premise were decided whether needs to duplicate the Step 1 to Step 5 to authenticate. And the GARS calculating method flow is shown in Figure 6.

4. Results and Discussion

The previous section introduced the research method of the main system function operation and GARS calculating flow in detail. To confirm that research of the present paper is feasible and effective, therefore in this section, we simulate to make the reality of GARS flow and analyze to discuss different flows by the empirical datum and result. In the system environment test, and experiment, the implementation of the present paper contains three flow function of main operation in the GARS flow and uses the testing tool record flow operation time needing comparative data.

Figure 7 is Client/Server both sides authenticate Http Response Time after authentication; we may see that it takes approximately 7 seconds to carry out the analog transmission material 50 times response time to complete.

Figure 8 is the general three parties authenticate Http Response Time; we may see that it takes 33 seconds to carry out the analog transmission material 50 times response time to complete.

Figure 9 is GARS one time authenticates Http Response Time; we may see that it takes 22 seconds to carry out the analog transmission material 50 times response time to complete.

4.1. Experimental Data Analysis. Through the above experimental data, we may see one time authentication of GARS flow simplified flow time of TTP authentication each time. Obviously we may see the result of simplified authentication flow, the condition of abbreviated execution step, and the execution time reduced relatively. From this we may confirm the design of GARS to have good execution efficiency. By way of the above results analysis of experimental data is stated as follows. (1) Client/Server/TTP one time authentication flow (5 steps): data are made by the simulation implementation in carrying out 50 times Client/Server to TTP authentication flow in which the finish time is 22 seconds, and authentication time on average is 0.44 second each time. (2) Client/Server both sides authentication flow (2 steps): after carrying out TTP authentication, Client/Server does not need to make the authentication with TTP again so long as carries out Client/Server both sides authentication flow in carrying out 50 times Client/Server both sides authentication flow in which the finish time is 8 seconds, and authentication time on average is 0.16 second each time. (3) Client/Server/TTP tripartite authentication flow (7 steps): this empirical datum

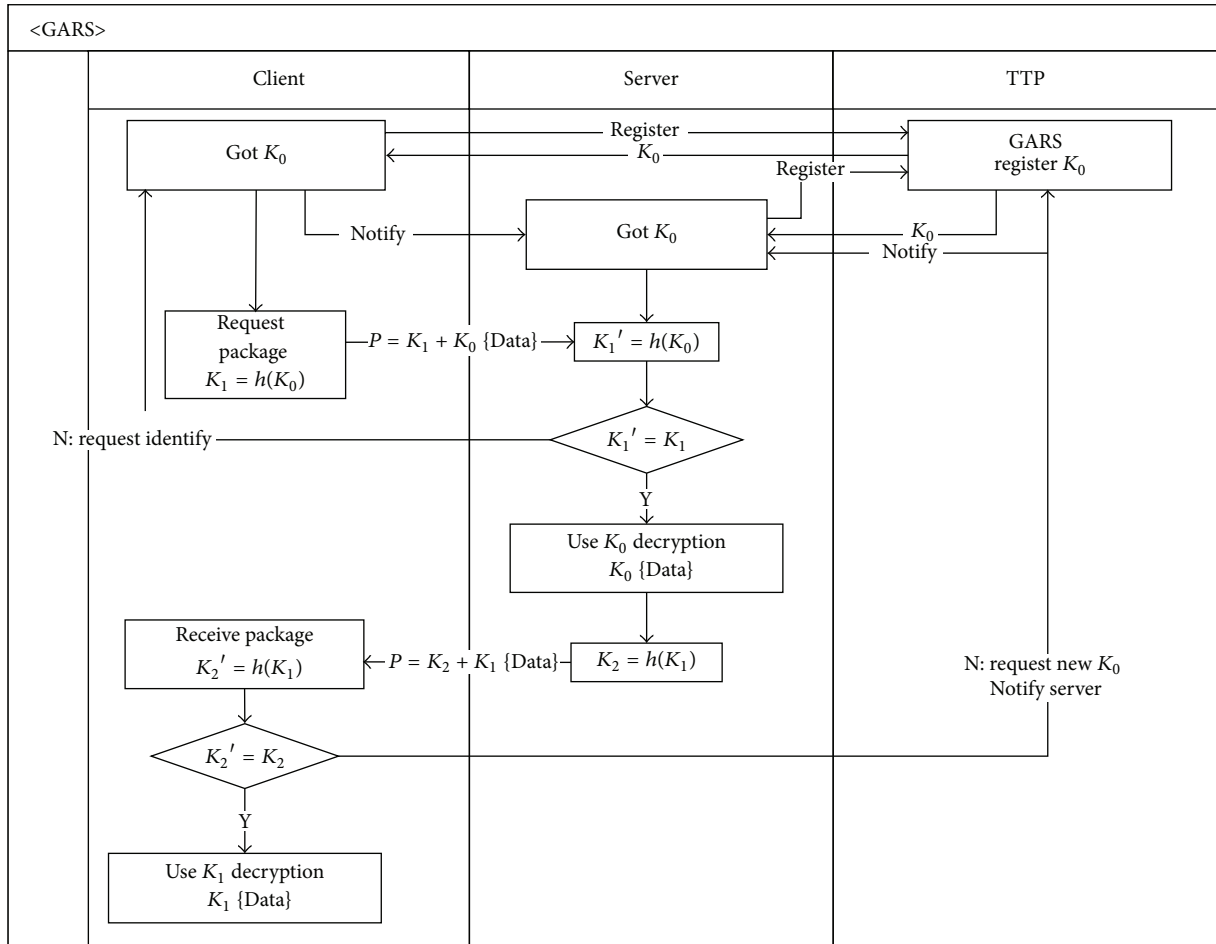


FIGURE 6: GARS algorithm flow diagram.

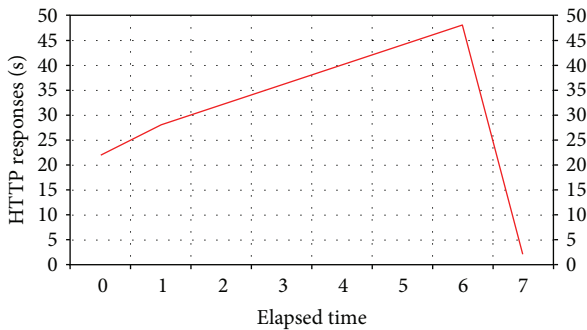


FIGURE 7: Both sides authenticate Http Response Time.

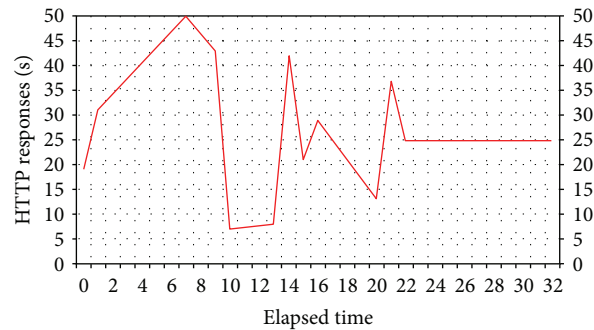


FIGURE 8: The three parties authenticate Http Response Time.

needs to carry out the time needed of tripartite authentication for the simulation in which each time is 33 seconds, and authentication time on average is 0.66 second each time.

4.2. *Experimental Data Comparison.* By the above data analysis results, the present procedure is to take tripartite authentication flow, and each time authentication must authenticate to TTP; this research takes one time authentication procedure to transmit data in carrying out both sides authentication

flow. By the data it was shown that the latter (present research) surpasses the former (present general procedure) in carrying out the potency. Therefore, by assessment of experimental data analysis, if authentication flow needs the tripartite authentication way of TTP authentication by each time, execution time is longer after being compared with the GARS one time authentication. Therefore, it can have fast potency performance in carrying out both sides authentication flow.

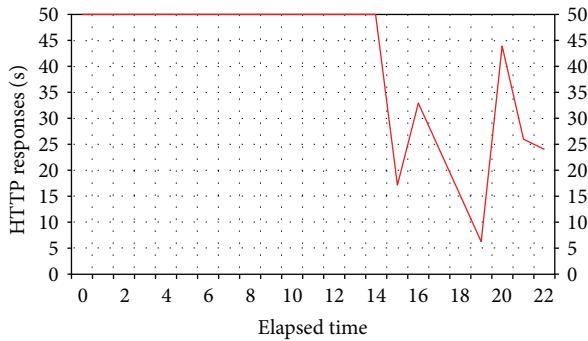


FIGURE 9: Authenticates Http Response Time one time.

5. Conclusions

In this research we proposed an effective feasible cloud material protection algorithm (GARS) which takes the technical theory of symmetrical encryption as the foundation, applies GARS in the information security of cloud computing. GARS has used the third party authentication mechanism trust, contains using Hash function and AES/DES data encryption technology characteristics, and coordinates the completed GARS flow to effectively protect security of cloud material and readability of stolen material. This research promotes and improves privacy right and security capital issue in cloud computing and provides in capital security procedure of relevant unit when develops cloud computing for reference. By the experiment it was shown that the data encryption way of GARS utilization can protect the material security, in potency, because after GARS carrying out one time authentication, only needs user and cloud make both sides authentication flow; it has the obvious performance in the potency with currently general procedure of the authentication flow. By way of the result of analysis discussion, we may know usability of this algorithm, and in cloud service security issue, it improves and strengthens cloud security relevant question using GARS.

References

- [1] M. Armbrust, A. Fox, R. Griffith et al., *Above the Clouds: A Berkeley View of Cloud Computing*, 2011.
- [2] L. Gu and S.-C. Cheung, "Constructing and testing privacy-aware services in a cloud computing environment—challenges and opportunities," in *Proceedings of the 1st Asia-Pacific Symposium on Internetware (Internetware '09)*, October 2009.
- [3] M. Jensen, J. Schwenk, N. Gruschka, and L. L. Iacono, "On technical security issues in cloud computing," in *Proceedings of the IEEE International Conference on Cloud Computing (CLOUD '09)*, pp. 109–116, September 2009.
- [4] J. B. Horrigan, "Use of cloud computing applications and services," Pew Internet & American Life Project Memo, 2008.
- [5] M. Mowbray and S. Pearson, "A client-based privacy manager for cloud computing," in *Proceedings of the 4th International ICST Conference on Communication System Software and Middleware (COMSWARE '09)*, Dublin, Ireland, June 2009.
- [6] S. Pearson, "Taking account of privacy when designing cloud computing services," in *Proceedings of the ICSE Workshop on Software Engineering Challenges of Cloud Computing (CLOUD '09)*, pp. 44–52, Vancouver, Canada, May 2009.
- [7] B. R. Kandukuri, P. V. Ramakrishna, and A. Rakshit, "Cloud security issues," in *Proceedings of the IEEE International Conference on Services Computing (SCC '09)*, pp. 517–520, September 2009.
- [8] L.-J. Zhang and Q. Zhou, "CCOA: cloud computing open architecture," in *Proceedings of the IEEE International Conference on Web Services (ICWS '09)*, pp. 607–616, Los Angeles, Calif, USA, July 2009.
- [9] Amazon Elastic Compute Cloud—EC2, <http://aws.amazon.com/ec2/>.
- [10] Cloud Computing Trends, <http://trends.google.com/trends>.
- [11] L. Robert and G. Yunhong, *On the Varieties of Clouds for Data Intensive Computing*, 2009.
- [12] Wikipedia, CloudComputing, http://en.wikipedia.org/wiki/Cloud_computing#cite_note-idc-28.
- [13] The Royal Academy of Engineering, *Dilemmas of Privacy and Surveillance: Challenges of Technological Change*, 2007.
- [14] D. J. Solove, "A taxonomy of privacy," *University of Pennsylvania Law Review*, vol. 154, no. 3, pp. 477–564, 2006.
- [15] E. Bertino, *Privacy-Preserving, Digital Identity Management for Cloud Computing*, 2010.
- [16] M. Mowbray and S. Pearson, "A client-based privacy manager for cloud computing," in *Proceedings of the 4th International ICST Conference on Communication System Software and Middleware (COMSWARE '09)*, Dublin, Ireland, June 2009.

Research Article

Traffic Noise Propagating from Vibration of Railway Wagon

Shao-Yi Hsia¹ and Yu-Tuan Chou²

¹ Department of Mechanical and Automation Engineering, Kao Yuan University, Kaohsiung 821, Taiwan

² Department of Applied Geoinformatics, Chia Nan University of Pharmacy and Science, Tainan City 717, Taiwan

Correspondence should be addressed to Shao-Yi Hsia; syhsia@cc.kyu.edu.tw

Received 15 September 2013; Accepted 22 October 2013

Academic Editor: Teen-Hang Meen

Copyright © 2013 S.-Y. Hsia and Y.-T. Chou. This is an open access article distributed under the Creative Commons Attribution License, which permits unrestricted use, distribution, and reproduction in any medium, provided the original work is properly cited.

Traffic noise has become a serious environmental hazard as more cars are purchased and driven. To help objectively and subjectively reduce perceived noise load, methods to analyze traffic noise offer an important means of creating a design to reduce noise output from main sources and transmission routes. Acoustic analysis using BEASY and dynamic analysis using ANSYS are conducted to forecast noise at a distance of 15 m from a railway wagon travelling at 100 km/h. This noise is based on structural vibration only and it excludes other noise sources from the railway wagon. The simulation results demonstrate that the overall noise at 15 m from a railway wagon car is 85.1 dB(L) from linear energy weighting calculation and 72.9 dB(A) from the A-weighting calculation. In this study, noise level propagating from vibration of the railway wagon is measured or calculated using A-weighting filter to simulate the frequency response of the human ear. The study results can be useful to factories, companies, or organizations and can provide an important resource and help reduce traffic noise. This can be achieved by predetermining the test location and structure configuration and adapting local planning and thus preventing excessive traffic noise in residential areas.

1. Introduction

Noise pollution is one of the negative issues of environmental pollution in metropolitan areas and is one of the most detrimental agents. It is estimated that over half of the world's population is exposed to unacceptable noise levels. In general, the major noise source is from road transportation followed by aircraft and railway noise; therefore many countries have regulations and laws to control noise emission limits for vehicles in order to reduce traffic noise. In recent years in some countries, new restricted rules were enacted for controlling city road traffic noise. The recognition of road traffic noise as one of the main sources of environmental pollution led to designed models and devices that enable us to predict traffic noise levels. Several models have been developed from fundamental variables such as the traffic flow, speed of vehicles, and sound emission levels using regression analysis of experimental data [1–4].

Facing the worsening pollution caused by every day traffic, the EU has set a goal to solve this problem and has been trying different ways to lower the traffic noise to a healthier level for the people who are regularly affected by

the long-term average noise levels in its 6th Environmental Action Program [5]. Unpleasant, frequent, and long-lasting traffic noise can cause many health issues psychologically and physically, to name a few, such as fear, uncertainty, mild anger, and even hearing loss. In densely populated areas, traffic is the single most important source of noise annoyance [6, 7]. Traffic noise prediction models are required as aids in designing highways and various types of roads and often are also very helpful to reduce the existing unbearable noise conditions. Traffic noise prediction models in the 1950s and 1960s were designed to predict a single vehicle sound pressure level (L_p) at the roadside. These models were based on constant speed experiments, the predicted levels then being expressed as functions of speed and with zero acceleration.

This report highlights the scale and scope of the traffic noise problem, which focuses on road and rail transport, for example, a wagon traveling at 100 km/hour. At the beginning, the frequency response should be derived from the time history of the measured velocity for the wagon. Then, a boundary element method was used to simulate the noise distribution of the wagon. The objective of the analysis was to predict the noise level at 15 m away from the wagon when it

is passing by at 100 km/hour and when it is empty. In conclusion, a number of recommendations for action were given and recorded.

2. Sound Field Simulation for Railway Wagon

In this simulation, the sound source intensity and propagation are separated for analysis using the Finite Element (FEM) and Boundary Element (BEM) methods, respectively. Noise analysis is examined using two commercial softwares. The sound source is obtained from ANSYS simulation. The increasing sound is calculated using BEASY simulation.

2.1. Sound Source Identification. When analyzing acoustic simulation, the coupling of fluid and a structure is generally taken into account. Meanwhile, the dynamic equation for a structure and Navier-Stokes equation for flow are also calculated and analyzed. Assuming fluid being compressible and nonviscous, average velocity being zero, and average pressure and density being uniform, the continuous equations could be simplified as an acoustic wave equation in the kinematic equation for fluid as follows:

$$\frac{1}{c^2} \frac{\partial^2 p}{\partial t^2} - \nabla^2 p = 0, \quad (1)$$

where c is the velocity of sound of fluid, p is the acoustic pressure, and t is the time. In consideration of the harmonic change of acoustic pressure with frequency, it is assumed that

$$p = \bar{p}e^{j\omega t}, \quad (2)$$

where \bar{p} stands for the amplitude of acoustic pressure and ω stands for the angular frequency. Equation (1) could be simplified as Helmholtz equation, as shown below:

$$\frac{\omega^2}{c^2} \bar{p} + \nabla^2 \bar{p} = 0. \quad (3)$$

Once the vibration velocity of structure is known, the acoustic pressure can be obtained using a mathematical transformation. For plane acoustic waves, the specific acoustic impedance Z is simply a function of the fluid properties. Consequently, the relation between the acoustic velocity u and acoustic pressure p is represented by

$$p = Zu = \rho cu, \quad (4)$$

where ρ represents the mass density.

2.2. Boundary Element Method for Acoustic Simulation. When considering the noise source, the linear wave equation form (4) propagation through an elastic medium governs can be rewritten as

$$\nabla^2 u = \frac{1}{c^2} \frac{\partial^2 b}{\partial t^2} + b, \quad (5)$$

where $b(x, t)$ is the noise source.

Similar to (2), (5) can be expressed as time harmonic and can be transferred to the modified Helmholtz equation

as follows:

$$\nabla^2 u + k^2 u = b, \quad (6)$$

where $k = \omega/c$ denotes the wave number. Equation (6) at the specified angular frequency ω can be expressed in matrix form as [8]

$$HP = GV + B, \quad (7)$$

where H and G are frequency dependent coefficients, P and V are the pressure and velocity, and B denotes a body force vector.

3. Analysis Model

People react differently to noise from a passing train versus noise from road traffic. The passage of a train has a defined beginning and end within a specified duration. On the other hand, urban traffic noise is more or less continuous, particularly at rush hour and in a busy city. Moreover, railway noise typically occurs some distance from human habitation, and since the passage of each train lasts only a short period it does not normally carry a risk of hearing damage, since the ambient noise level is restored. Railway noise also produces a different physical response to other traffic noise sources. Understanding the nature of railway noise requires understanding railway bed construction, including its tie-and-ballast design. The ties generally comprise treated wood strips, while the weight/base is crushed rock piled and placed beneath the ties on drained and graded ground. The ties distribute the weight from the tracks, and several noise sources were identified to be associated with the passage of a train like the following: (a) wheel/rail interaction, (b) car coupler contact, and (c) vibration of structural parts of the railroad car. The cause of wheel-rail noise is generally thought to be wheel and rail structural vibrations excited by a combination of the wheel and rail surface roughness. On the other hand, vibration of structural parts refers to the transport structures to be subjected to loads that vary in both time and space. In this research, the vibration of the structural parts of the car, for example, the bogie pivots, is measured and shown to be the main cause of noise. Figure 1 shows the geometry and the initial FE mesh. A flowchart about the analysis process is shown in Figure 2. The first step in measuring the noise level at 15 m is to locate the sound source of the car. According to the new LW3 profiles over the track factored to just meet QR track category 6, the velocity histories of train's pivot points are calculated for 100 km/h railway wagon speed and shown in Figure 3. Consequently, the noise history record of the bogie pivots stimulated in this study are listed as follows:

- (a) time in seconds and output interval 1/20,000th sec,
- (b) lateral velocity in body over the leading bogie pivot in m/s,
- (c) lateral velocity in body over the trailing bogie pivot in m/s,

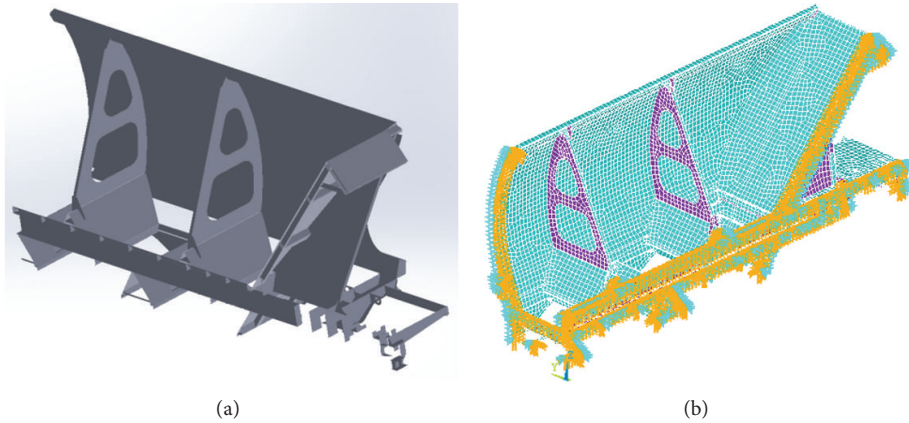


FIGURE 1: 1/4 configuration of the railway wagon.

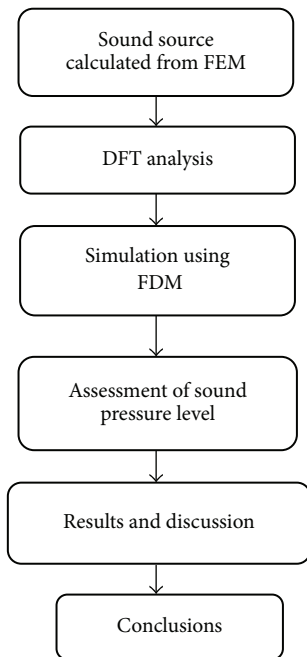


FIGURE 2: Flowchart of analysis process.

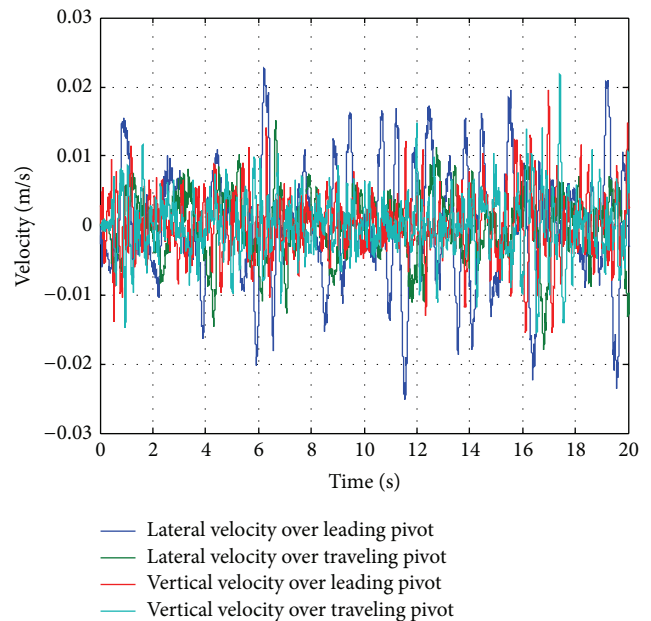


FIGURE 3: Velocity histories of train's pivot points.

- (d) vertical velocity in body over the leading bogie pivot in m/s,
- (e) vertical velocity in body over the trailing bogie pivot in m/s.

This study considers velocity response of four locations, namely, the lateral and vertical velocities of the leading and trailing pivots. The time interval for each point is 0.0005 seconds and 65,536 points are shown. Regarding sound transmission, the frequency response should be significant based on the time history of the velocity. Furthermore, the Discrete Fourier Transform (DFT) is applied using MATLAB software to yield the velocity responses.

Since the time interval is 0.0005 seconds, the calculated frequency can be obtained ranging from 0 to 1,000 Hz.

The unstudied information does not have adequate data resolution to obtain a higher frequency response. Acoustic analysis reveals the sound frequency is spread across a wide range, meaning it is unnecessary to analyze each frequency. The 1/3 octave frequency thus is frequently used to derive the transmission characteristics. Therefore, the velocity excitations listed in Table 1 were applied to the bogie pivot points.

Once the vibration velocity of structure is known, the acoustic pressure can be obtained using a mathematical transformation. For plane acoustic waves, the specific acoustic impedance Z is simply a function of the fluid properties. Consequently, the relation between the acoustic velocity u and acoustic pressure p is represented by (4). Various quantities are used in acoustics, including acoustic pressure and intensity. For example, an undamaged human ear can detect

TABLE 1: Lateral and vertical velocities at 1/3 octave over leading and trailing pivot.

Frequency (Hz)	Lat.vel.over ldg.pivot (m/s)	Lat.vel.over tlg.pivot (m/s)	Vert.vel.over ldg.pivot (m/s)	Vert.vel.over tlg.pivot (m/s)
20	$7.62E - 04$	$3.46E - 05$	$6.36E - 04$	$3.43E - 04$
25	$1.18E - 04$	$2.11E - 05$	$1.42E - 04$	$4.96E - 05$
31.5	$1.92E - 04$	$2.45E - 06$	$1.85E - 04$	$3.35E - 05$
40	$7.51E - 05$	$3.80E - 06$	$4.29E - 05$	$4.28E - 06$
50	$2.69E - 05$	$5.05E - 06$	$5.70E - 05$	$1.46E - 05$
63	$3.82E - 05$	$1.76E - 06$	$4.88E - 05$	$1.15E - 05$
80	$1.46E - 05$	$1.75E - 06$	$1.91E - 05$	$4.19E - 06$
100	$1.05E - 05$	$7.02E - 07$	$7.18E - 06$	$1.27E - 06$
125	$5.18E - 06$	$6.90E - 07$	$4.34E - 06$	$8.14E - 07$
160	$3.96E - 06$	$2.85E - 07$	$1.18E - 06$	$1.62E - 08$
200	$2.46E - 06$	$2.02E - 07$	$5.73E - 07$	$7.91E - 08$
250	$1.58E - 06$	$1.30E - 07$	$4.25E - 07$	$4.33E - 08$
315	$9.64E - 07$	$8.71E - 08$	$2.57E - 07$	$1.51E - 08$
400	$6.26E - 07$	$5.48E - 08$	$1.66E - 07$	$1.24E - 08$
500	$4.15E - 07$	$3.62E - 08$	$1.04E - 07$	$5.95E - 09$
625	$2.86E - 07$	$2.45E - 08$	$6.57E - 08$	$5.04E - 09$
800	$1.97E - 07$	$1.66E - 08$	$4.88E - 08$	$3.47E - 09$
1,000	$1.46E - 07$	$1.28E - 08$	$3.42E - 08$	$2.07E - 09$

TABLE 2: Lateral and vertical sound levels at 1/3 octave over leading and trailing pivot.

Frequency (Hz)	Lat.pres.over ldg.pivot (dB)	Lat.pres.over tlg.pivot (dB)	Vert.pres.over ldg.pivot (dB)	Vert.pres.over tlg.pivot (dB)
20	105.7	79.0	104.2	98.9
25	92.1	76.8	93.2	84.2
31.5	97.8	60.3	97.4	82.6
40	91.7	66.0	87.4	68.0
50	84.8	70.2	91.3	79.5
63	89.8	63.0	91.9	79.4
80	83.6	64.9	85.9	72.6
100	82.6	59.1	79.3	64.1
125	78.4	60.9	76.8	62.3
160	78.2	55.3	67.7	30.4
200	76.0	54.3	63.4	46.1
250	74.1	52.4	62.7	42.8
315	71.8	50.9	60.3	35.7
400	70.1	49.0	58.6	36.1
500	68.5	47.3	56.4	31.6
625	67.2	45.9	54.4	32.1
800	66.1	44.6	54.0	31.0
1,000	65.4	44.3	52.8	28.5

sounds with an acoustic pressure as low as $20 \mu\text{Pa}$ and can withstand sounds with a sound pressure as high as 20 Pa for a few minutes. Additionally, it was found that the response of the human ear to sound depends more on the ratio of the intensity of one sound to another, rather than on the difference in the intensity. Consequently, this analysis uses a logarithmic sound pressure level (dB). Combining (4) and the concept of relation between sound pressure and acoustic velocity can obtain the acoustic sources of the bogie pivot points, which are listed in Table 2. In this table, ρc is $408 \text{ Pa}\cdot\text{s}/\text{m}$ due to the air characteristic.

In rail transport design of structures intended to mitigate noise, it is frequently necessary to estimate the sound pressure level produced from the noise source of the wagon. This investigation examined the BEASY acoustic software, which can be used to predict noise emission from the sound field around a moving railway wagon. Generally, it is essential to predict not only overall noise level, but also the noise spectrum or sound pressure level in each octave band. Knowledge of the sound pressure level spectrum enables prediction of the A-weight sound level, which is important in determining compliance with noise regulations.

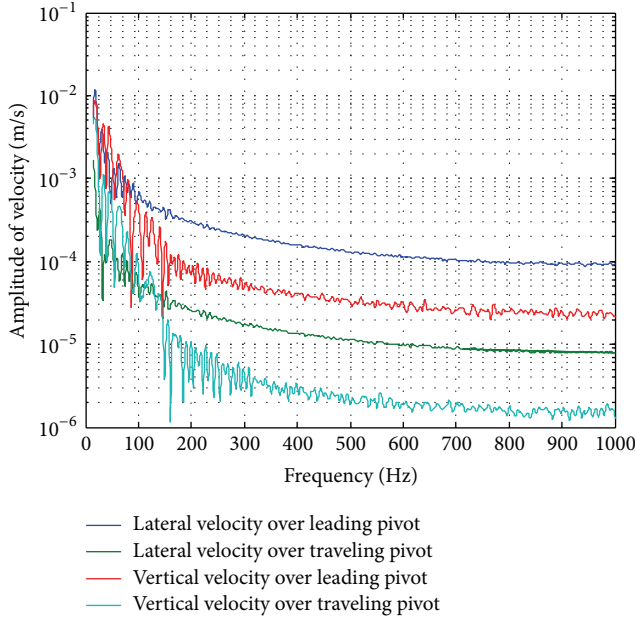


FIGURE 4: Vibration amplitude of velocity versus frequency for four wheels.

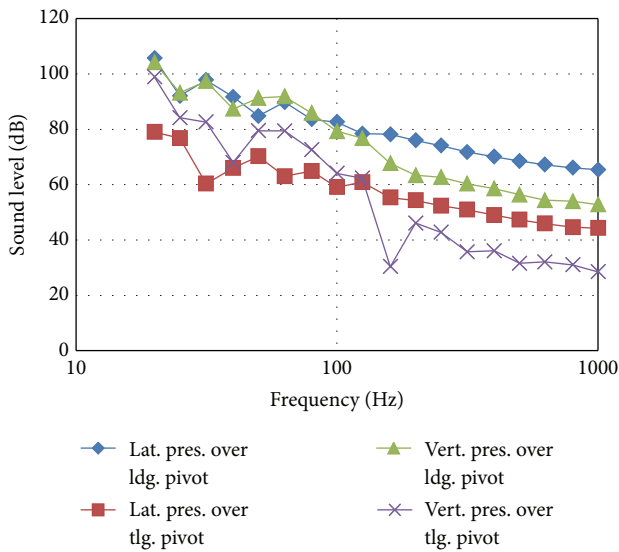


FIGURE 5: Sound source of the train's pivot points at 1/3 octave frequency.

4. Results and Discussion

The vibration velocity at 1/3 octave frequency of the car over leading and trailing pivots is analyzed by applying MATLAB software as shown in Table 1. Figure 3 shows detailed information on the vibration data, and Figure 4 shows the FFT result. Structural vibration influences the sound source on the car. The pressure level of the sound source is calculated by (4) and can be converted to dB level at 1/3 octave frequency, as listed in Table 2. Table 2 clearly shows that the maximum value of the sound source is 105.7 dB at 20 Hz on the lateral

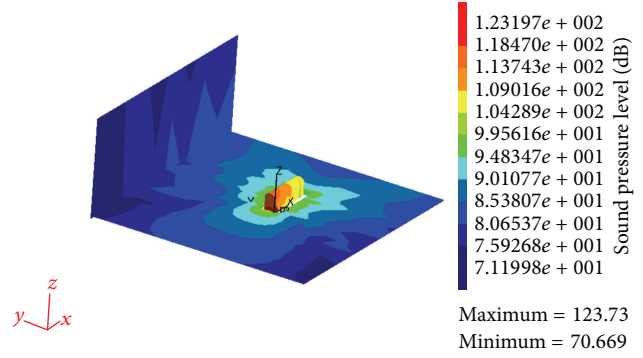


FIGURE 6: Lateral pressure of the leading pivot at 100 Hz from distance of 15 m.

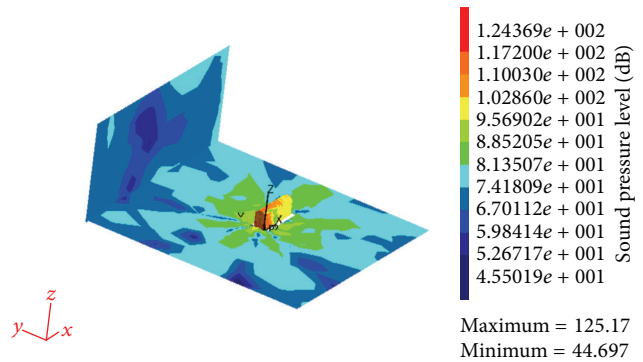


FIGURE 7: Lateral pressure of the leading pivot at 500 Hz from distance of 15 m.

leading pivot. The values of the sound source on the leading pivots exceed those on the trailing pivots. Figure 5 shows the spectrum across 1/3 octave of the sound source for various cases. The figures show that the lowest frequencies are always maximized for the four cases and then decay along the higher frequencies. The frequencies also differ most during 31.5 to 50 Hz. The profile of a car is modeled using BEASY software and the sound source from Table 2 is inserted on the leading and trailing pivots to reproduce the sound field. For acoustic analysis, the sound field of the car is indicated on the attachment, and Table 3 lists the predicted noise level at 15 m. For further information on the acoustic distribution around the car, three simulations of the lateral pressure of the leading pivot at 100 Hz, 500 Hz, and 1000 Hz, as listed in Table 3, are shown in Figures 6, 7, and 8. The red color in the figures represents the high sound pressure level distribution, and the blue area denotes the low sound pressure level. The sound pressure level is shown in dB on the bar chart beside the sound field distribution profile. These figures also showed that the red color is concentrated in the center of the car. This phenomenon demonstrates that high level sound pressure surrounds the car. The results in Figures 6–8 also clearly demonstrate that the noise gradually reduces with distance. This means that the sound pressure depends on distance from the source. Some further interesting facts regarding the higher frequency, for example, 1000 Hz, are shown in

TABLE 3: Sound pressure levels at 1/3 octave over leading and trailing pivot at 15 m.

Frequency (Hz)	Lat.pres.over ldg.pivot (15 m, dB)	Lat.pres.over ldg.pivot (15 m, dB)	Vert.pres.over ldg.pivot (15 m, dB)	Vert.pres.over tlg.pivot (15 m, dB)	Combined noise level (15 m, dB)	Combined noise level (15 m, dBA)
20	82.1	55.3	80.6	75.2	84.2	33.7
25	70.0	54.7	71.1	62.2	73.5	28.8
31.5	75.3	58.4	75.5	60.7	78.5	39.1
40	69.8	44.0	65.4	46.0	71.1	36.5
50	64.2	69.6	70.7	58.9	73.7	43.5
63	69.3	42.9	71.8	59.2	73.7	47.5
80	65.5	47.2	68.1	54.8	70.0	47.5
100	69.7	46.2	66.4	51.3	71.3	52.2
125	72.0	54.5	70.4	55.9	74.3	58.2
160	62.0	39.1	51.5	14.2	62.4	49.0
200	67.9	46.2	55.3	38.1	67.9	57.0
250	64.2	42.5	52.8	32.9	64.2	55.6
315	56.6	36.3	45.7	21.1	56.7	50.1
400	75.0	53.9	63.5	39.6	75.1	70.3
500	61.8	40.6	47.7	22.7	61.8	58.6
625	57.1	35.7	49.8	19.9	57.8	55.9
800	70.2	48.8	58.1	35.2	70.2	69.4
1000	60.5	39.4	47.9	23.5	60.5	60.5
Overall noise level					85.1	72.9

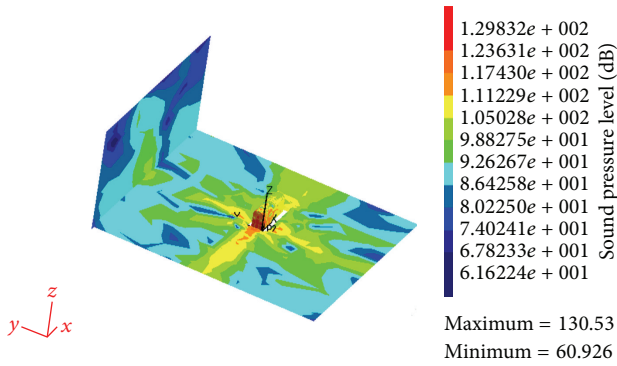


FIGURE 8: Lateral pressure of the leading pivot at 1000 Hz from distance of 15 m.

Figure 8. This figure shows the energy variation outside the car compared with Figures 6 and 7. This phenomenon means that the small wavelength radiates energy more easily at high frequency.

Figure 9 illustrates the noise level spectrum across 1/3 octave for various cases using the simulation results listed in Table 3. When the observer is located at a distance that exceeds one-third of the car length, the car appears closer as a point source and the radiation generates a spherical wave. Consequently, the acoustic pressure varies inversely with distance from the car, since the acoustic power is constant given zero energy dissipation. The acoustic power thus becomes spread over a larger area as the sound wave departs the

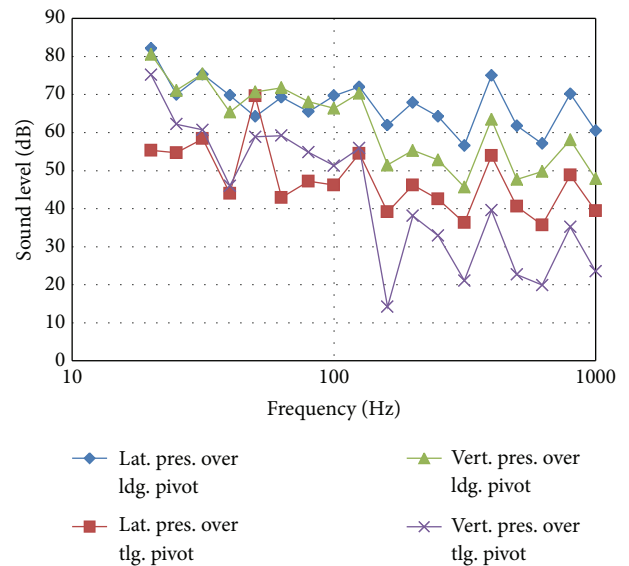


FIGURE 9: Noise level of the train's pivot points from the distance of 15 m.

source, causing an inverse decrease in the acoustic intensity proportionally with the square of the calculated distance from the observer to the car. Most frequencies decrease their acoustical pressures when comparing Figure 5. The acoustical field illustrated in the figure also indicates higher noise levels at 500 Hz and 1000 Hz.

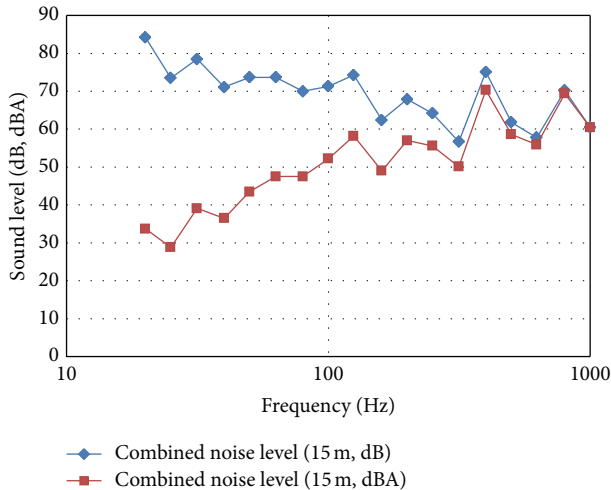


FIGURE 10: The 1/3 octave spectra of linear and A-weighting noise level at 15 m.

Table 3 reveals that the combined noise level is 85.1 dB(L) from the linear weighting of energy and 72.9 dB(A) from the A-weighting filtered noise. dB(A) is the most commonly used measurement of community noise and is measured or calculated using the A-weighting filter to simulate the frequency response of the human ear. Figure 10 plots the linear weighting and A-weighting filter of combined noise level listed in the second to fourth column of Table 3. Originally, the A-weighting was designed to correspond to the response of the human ear to a pressure level of 72.9 dB(A) at all frequencies. Since the human ear does not respond as strongly to low-frequency sounds, noise at low frequencies is generally less damaging or annoying than sound at high frequencies. The large negative weighting factor for low-frequency sound reflects this. Hence, A-weighting line has a lower noise level compared to linear weighting line for frequencies of 20 Hz to 800 Hz shown in Figure 10.

5. Conclusion

The overall noise calculated 15 m from a car is 85.1 dB(L) from 20 to 1,000 Hz based on the linear energy weighting calculation and 72.9 dB(A) based on the A-weighting calculation. dB(A) is the metric most commonly used to noise level when assessing impact on a community. Noise is measured or calculated using the A-weighting filter to simulate the frequency response of the human ear. This method of calculating noise is based solely on structural vibrations. The analysis excluded other noise sources on the train that may contribute to total noise, such as aerodynamic noise, interior noise, drive system noise, rail-wheel noise, and so on. Furthermore, calculations were based on just one carriage, though in a real world situation neighboring carriages would contribute to noise at the measurement point and increase total noise level. The overall noise level calculated by linear weighting thus will exceed 85 dB. However, A-weighting noise is 72.9 dB(A) and the overall noise considering all noise sources may still be below 85 dB at 15 m from a passing train.

References

- [1] B. M. Ross and T. Wolde, "Noise from traffic as a worldwide policy problem," *Noise Control Engineering Journal*, vol. 49, no. 4, pp. 159–161, 2001.
- [2] R. D. Stefano and B. Morri, "A statistical model for predicting road traffic noise based on poisson type traffic flow," *Noise Control Engineering Journal*, vol. 49, no. 3, pp. 137–143, 2001.
- [3] C. M. Steele, "Critical review of some traffic noise prediction models," *Applied Acoustics*, vol. 62, no. 3, pp. 271–287, 2001.
- [4] B. Li, S. Tao, R. W. Dawson, J. Cao, and K. Lam, "A GIS based road traffic noise prediction model," *Applied Acoustics*, vol. 63, no. 6, pp. 679–691, 2002.
- [5] L. C. E. den Boer and A. A. Schrotten, "Traffic noise reduction in Europe, solution for environment," Report on Economy and Technology, 2007.
- [6] B. Li, S. Tao, and R. W. Dawson, "Evaluation and analysis of traffic noise from the main urban roads in Beijing," *Applied Acoustics*, vol. 63, no. 10, pp. 1137–1142, 2002.
- [7] Ö. Gündoğdu, M. Gökdağ, and F. Yüksel, "A traffic noise prediction method based on vehicle composition using genetic algorithms," *Applied Acoustics*, vol. 66, no. 7, pp. 799–809, 2005.
- [8] S.-Y. Hsia, S.-M. Chiu, and J.-W. Cheng, "Sound field analysis and simulation for fluid machines," *Advances in Engineering Software*, vol. 40, no. 1, pp. 15–22, 2009.

Research Article

Thrust Reduction of Magnetic Levitation Vehicle Driven by Long Stator Linear Synchronous Motor

Wan-Tsun Tseng

Department of Electrical Engineering, National Yunlin University of Science & Technology, 123 University Road, Section 3, Douliou, Yunlin 64002, Taiwan

Correspondence should be addressed to Wan-Tsun Tseng; tsengwt@yuntech.edu.tw

Received 10 September 2013; Accepted 20 October 2013

Academic Editor: Teen-Hang Meen

Copyright © 2013 Wan-Tsun Tseng. This is an open access article distributed under the Creative Commons Attribution License, which permits unrestricted use, distribution, and reproduction in any medium, provided the original work is properly cited.

The propulsion technology of long stator linear synchronous motors is used to drive high-speed maglev trains. The linear synchronous motor stator is divided into sections placed on guideway. The electric power supplies to stator sections in which the train just passes in change-step mode for long-distance operation. However, a thrust drop will be caused by change-step machinery for driving magnetic vehicle. According to the train speed and vehicle data, the change-step mode has three types of operation, namely premature commutation, simultaneous commutation, and late commutation. Each type of operation has a different thrust drop which can be affected by several parameters such as jerk, running speed, motor section length, and vehicle data. This paper focuses on determining the thrust drop of the change-step mode. The study results of this paper can be used to improve the operation system of high-speed maglev trains.

1. Introduction

High-speed maglev systems for public transportation have been introduced for a long time. Typical examples are the Transrapid series in Germany [1–4] and the MLX series in Japan [5–7]. Both propulsion systems operate with long stator linear synchronous motors [8–11]. Although the maglev system in Germany can already go into commercial operation, the improvement of propulsion technology is still ongoing.

The propulsion system of the high-speed maglev train is devised to operate in different modes, depending on whether it is used in a short- or long-distance line. The propulsion system needs a high thrust to accelerate the train at startup so that the stator sections are connected using a three-step structure. This three-step structure consists of three sets of converter and power-cable systems [10, 12]. In contrast to the three-step structure, however, a change-step structure requires only two. In order to reduce investment costs of substations, the propulsion system of the maglev train will be designed to use the change-step mode when the train travels at a constant speed [13, 14]. In addition, stator winding loss can also be reduced significantly because power is only supplied to the segment over which the train just passes.

Therefore, when the train is about to leave the current stator section, the power supply should be switched off timely. And the power must be transferred to the next stator section. Such a process can result from turning off and on line switches (vacuum breakers) along the guideway.

Since the stator current should be adjusted up or down during stator section changing, the thrust will also be affected. Such thrust reduction can lead to a speed drop because the propulsion energy is reduced. Therefore, determining the thrust reduction has become an important issue for driving a maglev train using the change-step mode. Influential parameters on thrust are jerk, running speed, stator section length, and vehicle data. Among them, the jerk (in the unit of m/s^3) and running speed are most important. These influential parameters will be quantified in the following analysis.

2. Description of Change-Step Mode

The change-step mode is used to reduce line power losses, to improve the utilization of the installed power capacity of substations, and to increase the availability of the drive system

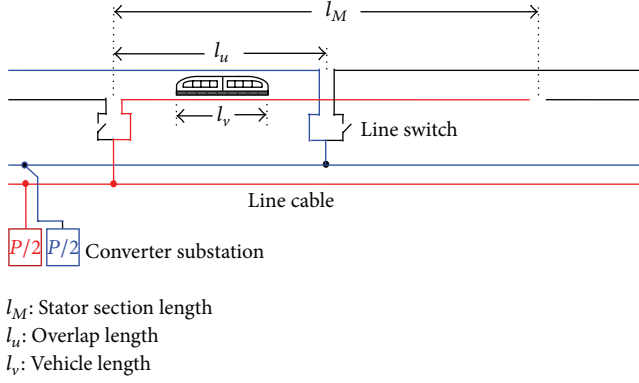


FIGURE 1: Propulsion system in change-step mode.

accordingly. The principal design of the change-step structure is depicted in Figure 1. The long stator motor sections at both sides of the guideway are installed in a staggered manner [9, 14]. The overlap length l_u must be longer than one train in length l_v for minimizing the thrust losses due to a stator section change. The linear motor sections on the left- and right-side of the guideway are supplied by independent power sources. The electric power from the substation can be transferred through line switches to the corresponding stator motor sections where a train is located, as shown in Figure 1. If the train is leaving a section, the present stator current must be adjusted to zero and the line switch connected to that stator section will be opened subsequently. After the current stator section has been disconnected from the power source, the new stator section can receive the power by closing its associated line switch. And, then, the stator current of the newly connected stator section will be increased to a full load condition to drive the vehicle. This process repeats when the train travels for every change from a current stator section to the next.

3. Three Operation Modes

Based on various needs of commercial operations, the travel time between start point and destination is made flexible so that the maglev train Transrapid is not driven at the same speed for every trip constantly. According to the boundary condition of every trip, three different change-step modes can be classified by comparing the change time t_C and commutation time t_K as follows:

- (i) premature commutation, $t_C < t_K$,
- (ii) simultaneous commutation, $t_C = t_K$, or
- (iii) late commutation, $t_C > t_K$.

The process of alternating the stator current between down and up is termed *commutation* and the corresponding time is referred to as commutation time t_K . And the elapsed time from the beginning to the end of a change is defined as the change time t_C .

Among the three modes, considering the reference speed v_S under simultaneous commutation ($t_C = t_K$) is quite

reasonable, because we can determine the type of commutation in comparison with this speed. However, the case of the simultaneous commutation is relatively rare, because the operating speed usually deviates from the reference speed. If the train speed is greater than the reference speed of simultaneous commutation, premature commutation is used. On the contrary, when the train is moving slower than the reference speed of simultaneous commutation, late commutation should be taken. To obtain the reference speed of simultaneous commutation, the change time t_C and commutation time t_K must be calculated first. Letting l_v be the vehicle length, the change time and commutation time can take from (1) and (2), respectively

$$t_C = \frac{l_v}{v} \quad (1)$$

$$t_K = \frac{F_N}{mr} + t_s, \quad (2)$$

where m is the vehicle mass, the switch time t_s remains constant for 500 ms, r is the limited jerk, and F_N represents the rated thrust that is created by the corresponding running resistance. Given $t_C = t_K$, the reference speed v_S of simultaneous commutation can be found from the following equation:

$$\frac{l_v}{v_s} = \frac{F_N}{m \cdot r} + t_s. \quad (3)$$

The running resistance of the maglev train Transrapid is composed of three parts, namely linear generator F_{LG} [15], eddy current from guidance F_E [15], and aerodynamic resistance F_A [16], as expressed in (4)–(7)

$$F_{LG} = 0 \text{ [kN]}, \quad v < 100 \text{ km/h} \quad (4)$$

$$F_{LG} = n_c \left(\frac{3.6P_{LG}}{v} - 0.2 \right) \text{ [kN]}, \quad 100 \text{ km/h} \leq v \leq 500 \text{ km/h} \quad (5)$$

$$F_E = n_c \left[0.1 \sqrt{\frac{v}{3.6}} + 0.02 \left(\frac{v}{3.6} \right)^{0.7} \right] \text{ [kN]}. \quad (6)$$

$$F_A = 0.216 \cdot 10^{-3} \left(\frac{0.53n_c}{2} + 0.3 \right) (v + \Delta v)^2 \text{ [kN]}. \quad (7)$$

Parameters in (4)–(7) are defined as follows: v : train speed in km/h, Δv : side wind speed in km/h, P_{LG} : output power of linear generator in kW, n_c : the total number of cars. F_N depends on v^{-1} , $v^{0.5}$, $v^{0.7}$ and v^2 , so v_S can be numerically solved from (3). Note that v_S is not fixed but varies when different vehicle data are in use. With reference to the reported information of vehicle TR-09 [17], where a car is 50 tons and 25 m long on average, reference speeds for different vehicles are listed in Table 1.

4. Calculation of Thrust Drop

For a maglev train running at a constant speed, the change step mode operation provides a periodic thrust drop. The

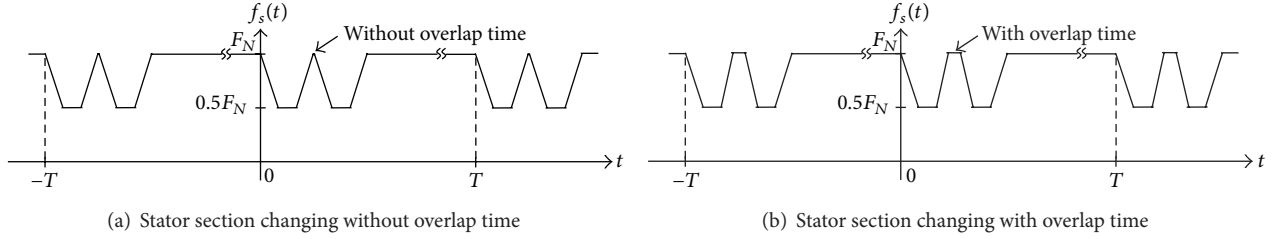
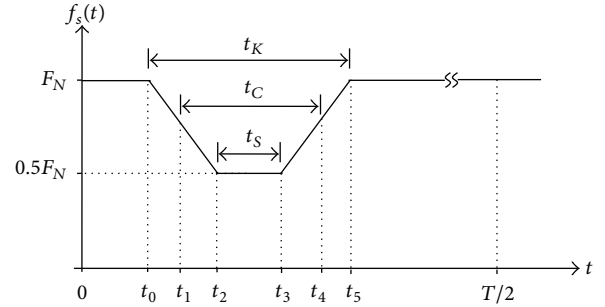


FIGURE 2: Periodic thrust drop in change-step mode.

 TABLE 1: Reference speed v_s .

Jerk (m/s^3)	v_s (km/h)			
	4-car	5-car	6-car	8-car
0.1	200	233	261	306
0.2	267	333	339	394
0.3	307	351	388	451
0.4	336	384	425	494
0.5	359	410	454	529


 FIGURE 3: Thrust time curve at the premature commutation type ($t_C < t_K$).

overlap time t_u can be obtained by overlap length l_u shown in Figure 1. As mentioned in Section 2, the overlap length is set between vehicle length l_v and half of the stator section length l_M . If $l_u = l_v$, the overlap time is defined as zero ($t_u = 0$, as shown in Figure 2(a)). Figure 2(b) indicates that the overlap time is greater than zero. The period T of thrust time curve depends on travel speed and stator section length and can be determined by (8)

$$T = \frac{l_M}{v}. \quad (8)$$

The thrust drop is a negative effect of the maglev train operating in change-step mode. It should be as small as possible. In order to know the influence on the thrust drop, the arithmetic value of the thrust can be calculated according to (9)

$$F_{\text{av}} = \frac{1}{T} \int_{-T/2}^{T/2} f_s(t) dt. \quad (9)$$

From Section 3, the calculation of the average thrust can be divided into three parts, namely premature commutation ($t_C < t_K$), simultaneous commutation ($t_C = t_K$), and late commutation ($t_C > t_K$).

4.1. Thrust Drop under Premature Commutation. Because the thrust time curve is a periodic function, the average thrust can be calculated from half of a period. In this case, the thrust

time curve is shown in Figure 3. The thrust time function can be represented by (10)

$$f_s(t) = \begin{cases} F_N, & 0 \leq t \leq t_0 \\ \frac{F_N}{2} \left(1 + \frac{t - t_2}{t_0 - t_2} \right), & t_0 < t \leq t_2 \\ \frac{F_N}{2}, & t_2 < t \leq t_3 \\ \frac{F_N}{2} \left(1 + \frac{t - t_3}{t_5 - t_3} \right), & t_3 < t \leq t_5 \\ F_N, & t_5 < t \leq \frac{T}{2}, \end{cases} \quad (10)$$

where t_0 is the time point for turning down of the stator current and t_1 is the beginning of stator section changing. The other parameters are defined in Section 3. During the stator section changing, the train thrust will be also changed and causes a jerk. The jerk $r(t)$ at premature commutation can be expressed in (11)

$$r(t) = \begin{cases} 0, & 0 \leq t \leq t_0 \\ \frac{F_N}{2m(t_0 - t_2)}, & t_0 < t \leq t_2 \\ 0, & t_2 < t \leq t_3 \\ \frac{F_N}{2m(t_5 - t_3)}, & t_3 < t \leq t_5 \\ 0, & t_5 < t \leq \frac{T}{2}. \end{cases} \quad (11)$$

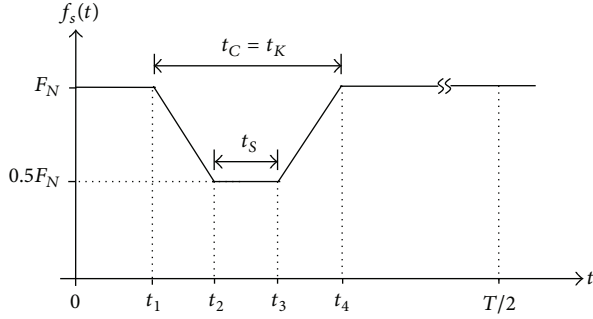


FIGURE 4: Thrust time curve at the simultaneous commutation type ($t_C = t_K$).

The arithmetic thrust F_{av} can be calculated with reference to (9)–(11) and Figure 3 as (12)

$$F_{av} = F_N \left[\frac{v}{l_M} \left(\frac{l_M}{v} - t_s - \frac{F_N}{2mr} \right) \right]. \quad (12)$$

Obviously, the arithmetic thrust F_{av} depends on parameters jerk r , speed v , mass of vehicle m , and motor stator section length l_M .

4.2. Thrust Drop under Simultaneous Commutation. The calculation of the arithmetic value of the thrust in this case is the same as at premature commutation. Comparing Figures 3 and 4, we can find that the thrust curves are almost identical. Only the change time and commutation time are different. From Figure 4, the time function of thrust $f_s(t)$ and jerk $r(t)$ are formulated in (13) and (14), respectively

$$f_s(t) = \begin{cases} F_N, & 0 \leq t \leq t_1 \\ \frac{F_N}{2} \left(1 + \frac{t-t_1}{t_1-t_2} \right), & t_1 < t \leq t_2 \\ \frac{F_N}{2}, & t_2 < t \leq t_3 \\ \frac{F_N}{2} \left(1 + \frac{t-t_3}{t_4-t_3} \right), & t_3 < t \leq t_4 \\ F_N, & t_4 < t \leq \frac{T}{2} \end{cases} \quad (13)$$

$$r(t) = \begin{cases} 0, & 0 \leq t \leq t_1 \\ \frac{F_N}{2m(t_1-t_2)}, & t_1 < t \leq t_2 \\ 0, & t_2 < t \leq t_3 \\ \frac{F_N}{2m(t_4-t_3)}, & t_3 < t \leq t_4 \\ 0, & t_4 < t \leq \frac{T}{2}. \end{cases} \quad (14)$$

With reference to (9), (13), and (14), the arithmetic thrust F_{av} at premature commutation can also be calculated from (12)

4.3. Thrust Drop under Late Commutation. If the train travels slower than the reference speed v_s , the change-step mode

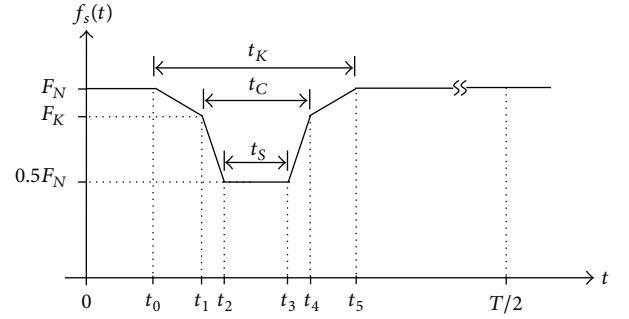


FIGURE 5: Thrust time curve at late commutation ($t_C > t_K$).

is operated with late commutation. In this case, the thrust time curve for one time stator section changing is shown in Figure 5 and the time function is in (15)

$$f_s(t) = \begin{cases} F_N, & 0 \leq t \leq t_0 \\ F_K + (F_N - F_K) \left(\frac{t-t_1}{t_0-t_1} \right), & t_0 < t \leq t_1 \\ \frac{F_N}{2} + \left(F_K - \frac{F_N}{2} \right) \left(\frac{t-t_2}{t_1-t_2} \right), & t_1 < t \leq t_2 \\ \frac{F_N}{2}, & t_2 < t \leq t_3 \\ \frac{F_N}{2} + \left(F_K - \frac{F_N}{2} \right) \left(\frac{t-t_3}{t_4-t_3} \right), & t_3 < t \leq t_4 \\ F_K + (F_N - F_K) \left(\frac{t-t_4}{t_5-t_4} \right), & t_4 < t \leq t_5 \\ F_N, & t_5 < t \leq \frac{T}{2}. \end{cases} \quad (15)$$

In Figure 5, the force F_K is the thrust at commutation beginning of the stator current. It can be determined by (16)

$$F_K = \frac{F_N}{2} \left(2 - \frac{t_1-t_0}{t_C} \right). \quad (16)$$

The jerk $r(t)$ at late commutation is expressed in (17)

$$r(t) = \begin{cases} 0, & 0 \leq t \leq t_0 \\ \frac{F_N - F_K}{m} \left(\frac{1}{t_0-t_1} \right), & t_0 < t \leq t_1 \\ \frac{2F_K - F_N}{2m} \left(\frac{1}{t_1-t_2} \right), & t_1 < t \leq t_2 \\ 0, & t_2 < t \leq t_3 \\ \frac{2F_K - F_N}{2m} \left(\frac{1}{t_4-t_3} \right), & t_3 < t \leq t_4 \\ \frac{F_N - F_K}{m} \left(\frac{1}{t_5-t_4} \right), & t_4 < t \leq t_5 \\ 0, & t_5 < t \leq \frac{T}{2}. \end{cases} \quad (17)$$

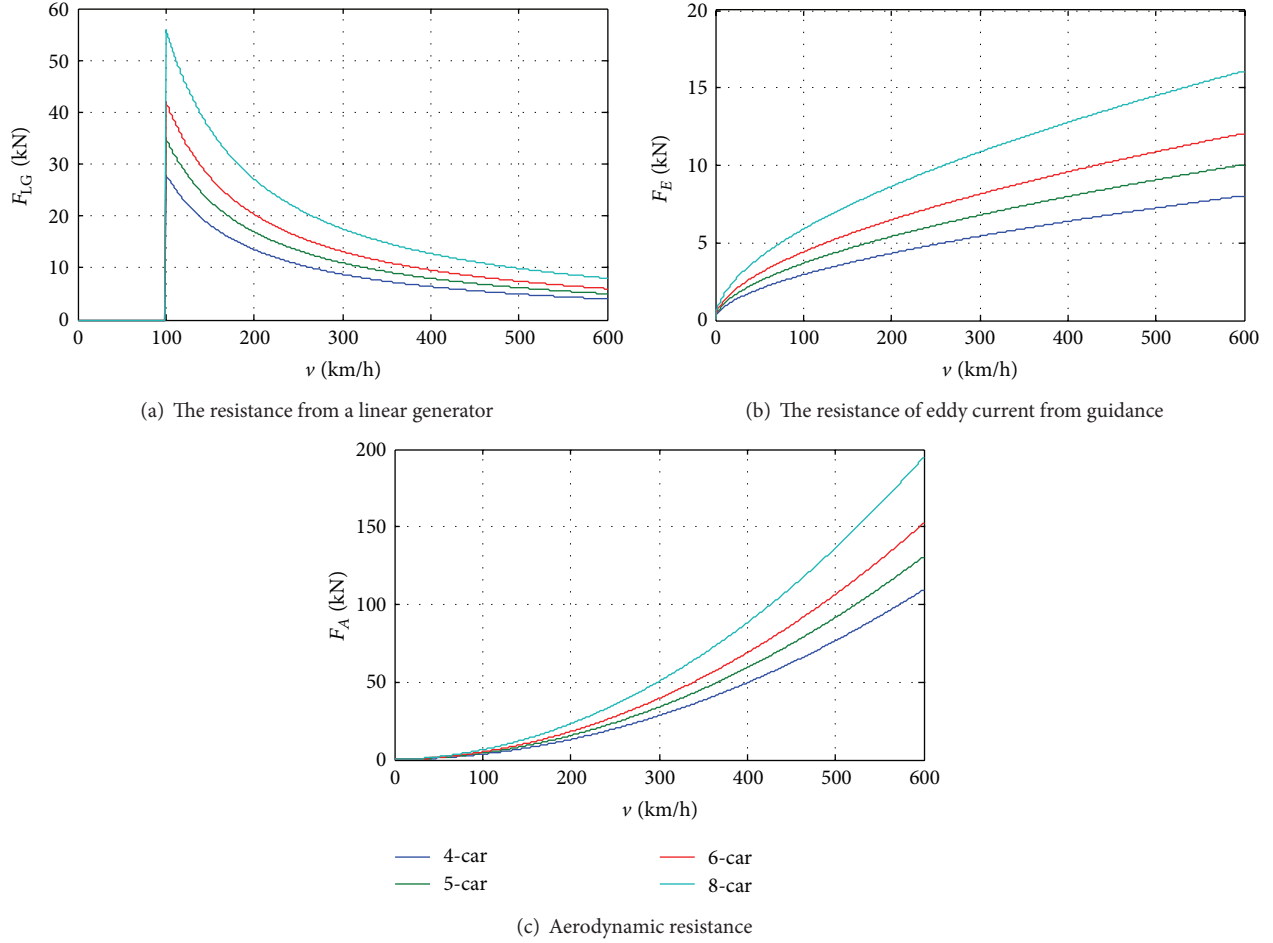


FIGURE 6: Three different running resistances of maglev trains.

Similarly, the arithmetic thrust can be calculated according to (9), (16), and (17) as (18)

$$F_{av} = F_N \cdot \frac{v}{l_M} \times \left\{ \frac{v}{vF_N - 2mrl_v} \left(mrt_s - \frac{mrl_v}{v} + F_N \right) \cdot \left[\frac{F_N}{2mr} - \frac{1}{2} \left(\frac{l_v}{v} - t_s \right) \right] + \frac{l_M}{v} - \frac{F_N}{2mr} - t_s \right\}. \quad (18)$$

It is obvious that (18) provides one more influential parameter (i.e., l_v) than (12) does. The reason for this result is the train has two different jerks during the stator section changing period. The first jerk takes place if the vehicle is leaving the present stator section without reducing or increasing the stator current. The second jerk occurs when the stator current is adjusted from full-load to zero or reversely. The duration of this jerk depends on the vehicle length.

5. Results and Discussion

In the following quantitative analyses, the influential parameters on thrust including train speed, jerk, and stator section length are selected as variables. In general, the train speed is set from 300 to 500 km/h because a maglev vehicle travels more appropriately for a long distance commercial line under this speed limitation. The jerk can be reasonably chosen between 0.1 and 0.5 m/s^3 . However, the decision of a proper jerk depends on driving comfort. And, the stator section length can be selected with reference to the test facility Emsland in Germany between 900 and 1350 m in change-step mode [13]. The train mass is represented by vehicle cars. For the long distance commercial line, a maglev train is favorably made by 4, 5, 6, or 8 cars in accordance with the number of passengers. As the last parameter, switch time is set to 500 ms as mentioned in Section 3. In order to obtain the corresponding thrust F_N , the running resistance must be determined first.

5.1. Running Resistance. As in Section 3, the three parts of the running resistance of the maglev train can be calculated from (5)–(7). And, the results are shown in Figures 6(a)–6(c). Figure 6(a) shows the running resistance from a linear

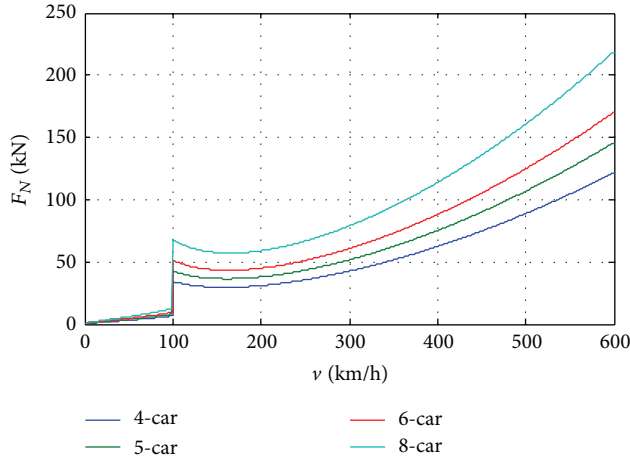


FIGURE 7: The total running resistance of maglev trains.

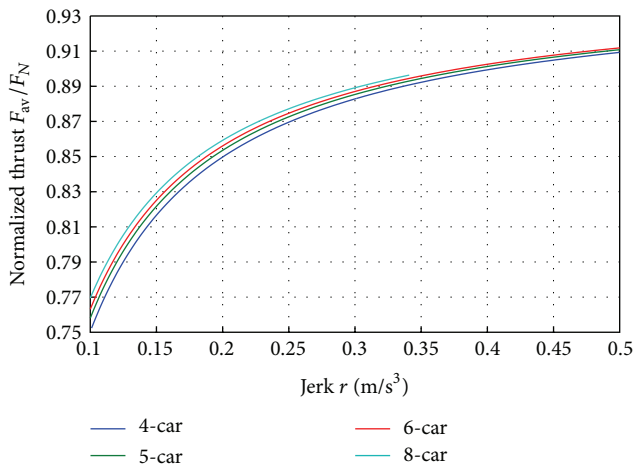


FIGURE 8: Arithmetic thrust as a function of jerk under $t_C < t_K$ ($v = 470$ km/h, $l_M = 1280$ m).

generator. It appears when the train speed reaches 100 km/h. This means that the linear generator has come into service until the train speeds up to 100 km/h. The resistance of eddy current from guidance and the aerodynamic resistance are represented in Figures 6(b) and 6(c), respectively.

Comparing Figures 6(a)–6(c), it is good to know that the aerodynamic resistance is dominant when the train travels at a high speed (>300 km/h). The total running resistance is shown in Figure 7 and indicates the required thrust to drive the maglev train.

5.2. Thrust Losses. Theoretical analysis of thrust during stator section changing was completed in Section 4. Because the jerk and the train speed are the most important influential parameters on thrust, the following analyses will be based on these two parameters. The calculation results at premature commutation are shown in Figures 8 and 9. For the ease of reading, the average thrust will be normalized with rated thrust. Figure 8 presents the influence of the jerk on the arithmetic thrust F_{av} . Figure 9 shows the arithmetic thrust

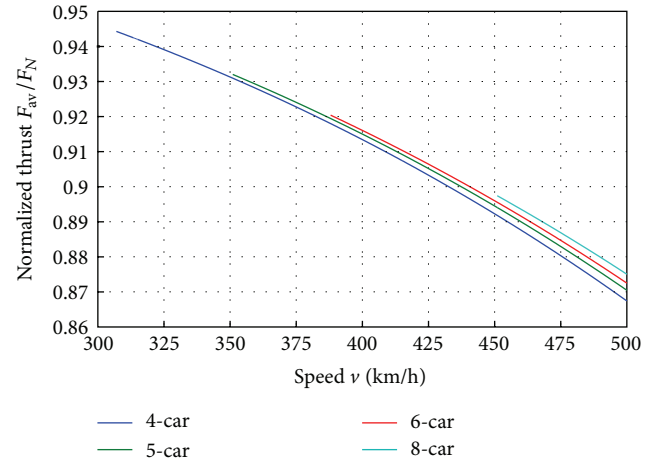


FIGURE 9: Arithmetic thrust as a function of speed under $t_C < t_K$ ($r = 0.3$ m/s³, $l_M = 1280$ m).

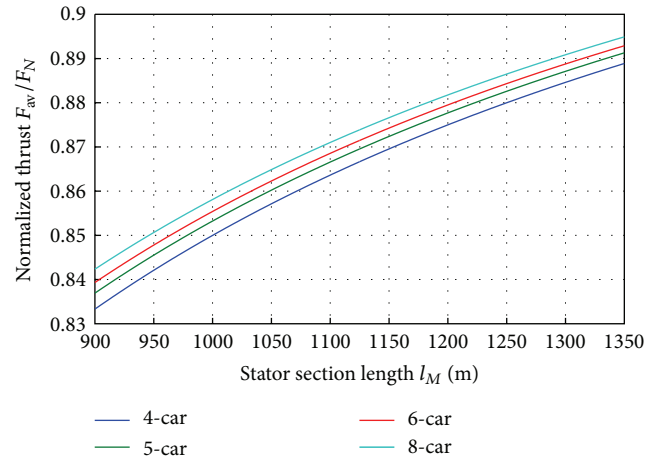


FIGURE 10: Arithmetic thrust as a function of stator section length under $t_C < t_K$ ($r = 0.3$ m/s³, $v = 470$ km/h).

F_{av} as a function of speed. From the calculation results, we know that the thrust drop becomes larger when the travel speed is higher. Among them, the parameter jerk r is the most important factor because the thrust drop becomes larger with a smaller jerk under premature commutation. However, the thrust drop and jerk are in conflict with each other. One must find a compromise between them, especially at high speeds. In addition, the stator section length also affects thrust losses. The influence of stator section length on thrust is shown in Figure 10. The thrust losses become smaller, when the stator section length is longer. However, a longer stator section can lead to less efficiency of the linear synchronous motor. Therefore, a compromise between thrust and efficiency is required.

The calculation of thrust under simultaneous commutation type is the same as in premature commutation type. The variation of thrust in this case is similar to premature commutation. In fact, the simultaneous commutation type rarely occurs in actual operation because a maglev train

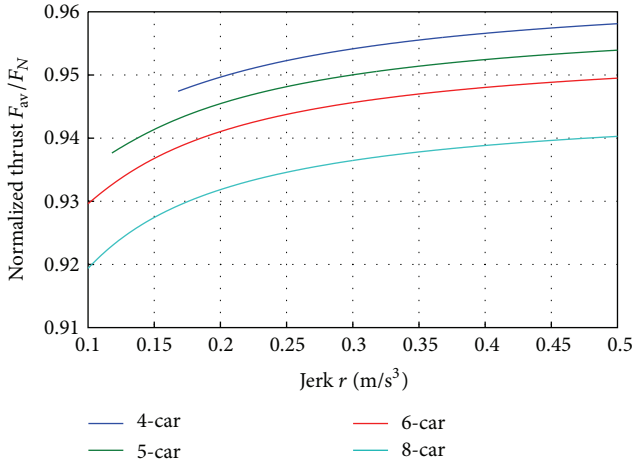


FIGURE 11: Arithmetic thrust as a function of jerk under $t_C > t_K$ ($v = 280$ km/h, $l_M = 1280$ m).

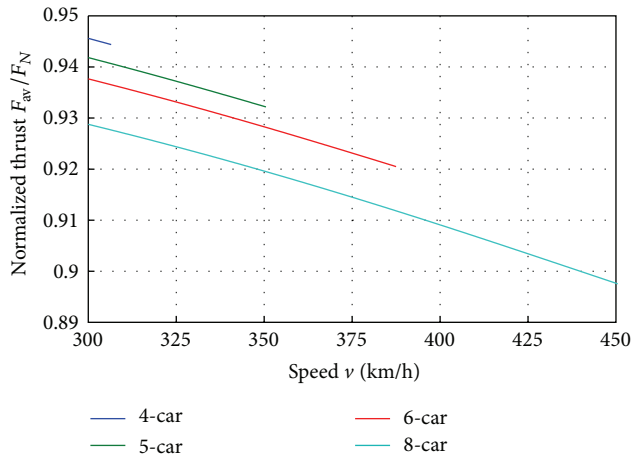


FIGURE 12: Arithmetic thrust as a function of speed under $t_C > t_K$ ($r = 0.3$ m/s³, $l_M = 1280$ m).

with a selected jerk has only one speed for simultaneous commutation (see Table 1). In general, this speed is not equal to the operating speed.

From (18), the calculated results of the average thrust under late commutation are presented in Figures 11, 12, and 13, suggesting a higher average thrust in comparison with premature commutation type. The reason for this phenomenon is that the late commutation is better applied to lower speed. In addition, the late commutation has lower thrust losses with fewer train cars under the same jerk and stator section length. In other words, the maglev train operated in late commutation type is suitable for fewer cars. Conversely, a longer maglev train is better for premature commutation type.

6. Conclusions

The propulsion technology of high-speed maglev systems using the change-step mode has been described in this paper.

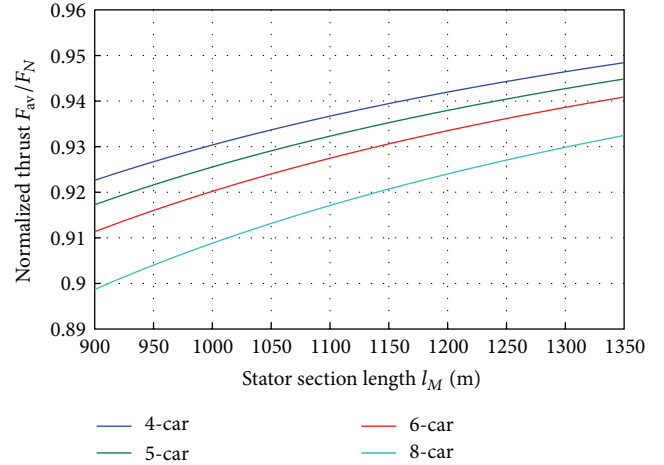


FIGURE 13: Arithmetic thrust as a function of stator section length under $t_C > t_K$ ($r = 0.3$ m/s³, $v = 300$ km/h).

The thrust losses of the change-step mode for each commutation type are also calculated. The operational parameters have different potency on thrust. Among these parameters, the limited jerk and running speed affect the thrust evidently. For lower thrust losses, the maglev train should travel at high speed with more cars, conversely, at low speed for fewer cars. For example, if a maglev train travels with speed 470 km/h and jerk 0.3 m/s³ under premature commutation, the 8-car combination has the lowest thrust losses. Similarly, the 4-car combination obtains the lowest thrust losses when a train runs at a speed of 280 km/h and jerk 0.3 m/s³ under late commutation. These calculated results can provide a better solution for operating the high-speed maglev train. In addition, the thrust losses that were studied in this paper can lead to a speed drop of maglev trains. This is also a disadvantage by using the proposed change-step mode. Concerning how thrust losses affect the speed of maglev trains, it is the research issue in the future.

Acknowledgments

This work was supported by the National Yunlin University of Science and Technology and by the National Science Council of Taiwan under Grant NSC 100-2221-E-224-003. The author also wishes to express his appreciation to Ya-Tong Chang for drawing the diagrams.

References

- [1] W. Leonhard, R. G. Rhodes, and J. H. Rakels, "Technical alternatives for a Maglev system," *Electronics and Power*, vol. 24, no. 4, pp. 293–296, 1978.
- [2] H. Yaghoubi, "The most important Maglev applications," *Journal of Engineering*, vol. 2013, Article ID 537986, 19 pages, 2013.
- [3] A. Cassat and M. Jufer, "MAGLEV projects technology aspects and choices," *IEEE Transactions on Applied Superconductivity*, vol. 12, no. 1, pp. 915–925, 2002.

- [4] W. W. Dickhart, "Status of transrapid Maglev," in *Electro International*, pp. 613–617, 1991.
- [5] H.-W. Lee, K.-C. Kim, and J. Lee, "Review of Maglev train technologies," *IEEE Transactions on Magnetics*, vol. 42, no. 7, pp. 1917–1925, 2006.
- [6] K. Davey, "Analysis of an electrodynamic Maglev system," *IEEE Transactions on Magnetics*, vol. 35, no. 5, pp. 4259–4267, 1999.
- [7] M. Ono, S. Koga, and H. Ohtsuki, "Japan's superconducting Maglev train," *IEEE Instrumentation and Measurement Magazine*, vol. 5, no. 1, pp. 9–15, 2002.
- [8] R. Hellinger and P. Mnich, "Linear motor-powered transportation: history, present status, and future outlook," *Proceedings of the IEEE*, vol. 97, no. 11, pp. 1892–1900, 2009.
- [9] B. M. Perreault, "Optimizing operation of segmented stator linear synchronous motors," *Proceedings of the IEEE*, vol. 97, no. 11, pp. 1777–1785, 2009.
- [10] H. Ikeda, S. Kaga, Y. Osada et al., "Development of power supply system for Yamanashi Maglev test line," in *Proceedings of the Power Conversion Conference*, vol. 1, pp. 37–41, Nagaoka Japan, August 1997.
- [11] T. Sakamoto and T. Shiromizu, "Propulsion control of superconducting linear synchronous motor vehicle," *IEEE Transactions on Magnetics*, vol. 33, no. 5, pp. 3460–3462, 1997.
- [12] R. Fischperer, *Magnetschnellbahn für den schnellen Regionalverkehr Optimierung des Langstatorantriebs und der Energieversorgung [Ph.D. thesis]*, Technische Universität Berlin, Berlin, Germany, 2006.
- [13] R. Fürst, *Anwendungsnahe Dimensionierung und messtechnische Überprüfung von Langstator-Linearmotoren für Magnetschnellbahnen [Ph.D. thesis]*, Technische Universität Berlin, Berlin, Germany, 1993.
- [14] X. Wang, H. Liu, and S. Zhang, "High performance propulsion control of magnetic levitation vehicle long stator linear synchronous motor," in *International Conference on Electrical Machines and Systems (ICEMS '11)*, pp. 20–23, August 2011.
- [15] R. Schah, P. Jehle, and R. Naumann, *Transrapid und Rad-Schienen-Hochgeschwindigkeitsbahn, Ein gesamtlicher Systemvergleich*, Springer, Berlin, Germany, 2006.
- [16] P. Mnich, "Die Bahnen und die Magnetechnik in Japan und Deutschland," *ETR—Eisenbahntechnische Rundschau*, vol. 46, no. 12, pp. 816–824, 1997.
- [17] R. D. Thornton, "Efficient and affordable Maglev opportunities in the united states," *Proceedings of the IEEE*, vol. 97, no. 11, pp. 1901–1921, 2009.

Research Article

A Karaoke System with Real-Time Media Merging and Sharing Functions for a Cloud-Computing-Integrated Mobile Device

Her-Tyan Yeh,¹ Juing-Shian Chiou,² and Ting-Jun Zhou¹

¹ Department of Information and Communication, Southern Taiwan University of Science and Technology, No. 1 Nan-Tai Street, Yongkang District, Tainan 710, Taiwan

² Department of Electrical Engineering, Southern Taiwan University of Science and Technology, No. 1 Nan-Tai Street, Yongkang District, Tainan 710, Taiwan

Correspondence should be addressed to Juing-Shian Chiou; jschiou@mail.stust.edu.tw

Received 12 September 2013; Accepted 16 October 2013

Academic Editor: Teen-Hang Meen

Copyright © 2013 Her-Tyan Yeh et al. This is an open access article distributed under the Creative Commons Attribution License, which permits unrestricted use, distribution, and reproduction in any medium, provided the original work is properly cited.

Mobile devices such as personal digital assistants (PDAs), smartphones, and tablets have increased in popularity and are extremely efficient for work-related, social, and entertainment uses. Popular entertainment services have also attracted substantial attention. Thus, relevant industries have exerted considerable efforts in establishing a method by which mobile devices can be used to develop excellent and convenient entertainment services. Because cloud-computing technology is mature and possesses a strong computing processing capacity, integrating this technology into the entertainment service function in mobile devices can reduce the data load on a system and maintain mobile device performances. This study combines cloud computing with a mobile device to design a karaoke system that contains real-time media merging and sharing functions. This system enables users to download music videos (MV)s from their mobile device and sing and record their singing by using the device. They can upload the recorded song to the cloud server where it is merged with real-time media. Subsequently, by employing a media streaming technology, users can store their personal MVs in their mobile device or computer and instantaneously share these videos with others on the Internet. Through this process, people can instantly watch shared videos, enjoy the leisure and entertainment effects of mobile devices, and satisfy their desire for singing.

1. Introduction

The vigorous development of information and communication technologies and the increased use of the Internet have led network technologies to be integrated into people's daily lives. The proportion of people using mobile application services has dramatically increased following the popularization of mobile devices. Despite the global economic recession of recent years, major technological and telecommunication companies have maintained positive stances toward the smart phone and mobile business service markets, believing that these markets present substantial potential for development.

Recently, cloud-computing technology has developed rapidly, attracting considerable attention from numerous companies, enterprises, and users. This technology is highly effective in that it can handle computations for massively complex systems on the Internet, thereby enabling remote

service providers to process a vast amount of information within a short period of time. Cloud computing exhibits excellent computing performance similar to that of a supercomputer.

Increasing numbers of people have focused on the mobile web for mobile devices. According to the Institute for Information Industry, a survey on the mobile Internet penetration rate among Taiwanese citizens showed that since 2010 the rate has increased rapidly, at a pace of more than 10% per year. In the first quarter of 2013, the penetration rate reached almost 50%, as shown in Figure 1.

Advancements in Internet technology and mobile devices have rendered video streaming one of the most popular application services. This technology offers services such as entertainment video sharing and live Internet television. Users can browse the channel directory to obtain information regarding the channel content and choose the content or

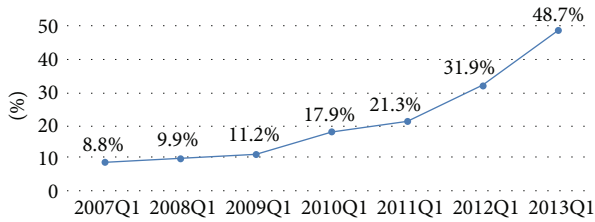


FIGURE 1: The trend of Taiwan's mobile Internet penetration rate (data source: Institute for Information Industry).

the program they wish to view. Currently, numerous websites provide free or paid online video services (e.g., YouTube, Vimeo, and I'mTV), where users can watch videos wherever and whenever they desire.

Singing-related talent shows have received considerable attention worldwide. People can participate in the entire selection process from initial auditions through to the finals, during which each process is broadcast on television. Currently, popular large-scale singing talent shows include American Idol, The Voice, The Voice of China, and Taiwan's One Million Star and Super Idol. The distribution of these shows has increased the viewership of associated television channels and become a common topic of discussion among various communities. The increased popularity of television talent shows has also potentially raised people's interest in singing, prompting them to frequently organize social events with friends at karaoke establishments (hereafter referred to as KTV). According to a 2011 Survey on the Music Industry in Taiwan announced by the Bureau of Audiovisual and Music Industry Development, MOC in 2012, the revenue of the Taiwanese karaoke industry was estimated to be NT\$ 843 million. For the majority of consumers, singing at KTVs is not only a form of leisure and entertainment but also an activity in which people can easily interact and socialize with others. Singing enables people to release their emotions and relieve stress. People generally practice singing techniques to achieve their goal of becoming a celebrity, and they select singing as their basic form of entertainment. Even without going to KTVs, people can casually hum or sing songs whenever they desire.

In an era where modern technologies are vigorously developing, establishing a method in which to integrate various forms of entertainment with fast-growing and commonly used mobile devices has raised considerable awareness. This study combines cloud computing and a mobile device to design a karaoke system that is integrated with real-time media merging and sharing functions, thereby entertaining users with a singing-related application service. This service was established based on the cloud-computing framework. The application program enables users to sing into their mobile devices, which simultaneously records and uploads their voice to the cloud server. In this process, the noises that interfere with the recording are eliminated. This system also allows them to merge their song recordings with a music video (MV) and share their personal MVs with others. Overall, users can create and store their personal MVs, which

can be synchronized and shared with others on the Internet. This study provides the following contributions.

- (1) Users can attain entertainment goals without being limited by time and location with their mobile phone and Internet access. Through their cloud-computing-integrated mobile device, they can sing and share their creations with other users.
- (2) Audio and video media can be merged and immediately shared.
- (3) Users can merge their song recordings with an MV or with a self-developed video to create personal MVs.
- (4) Consequently, through their mobile devices, people can sing heartily without having to visit KTVs, experience the enjoyment of friends and relatives' gatherings without having to attend, and feel the pleasure of being a singer.

2. Literature Review

2.1. Cloud Computing. Cloud computing has received the attention of numerous companies and users in recent years. By using this technology, users can store their data or application programs in cloud, from which they can download or share the stored data with others on the Internet. Essentially, cloud-computing service is accessible and available online regardless of the time and location [1–4].

Cloud computing excels in calculation processing in that it allows remote service providers to process a vast amount of information within a short period of time. Therefore, it has excellent computing performance similar to that of a super computer. Furthermore, through Internet connections, this technology facilitates the collaboration and services between the service provider and its clients. Currently, numerous companies are actively adopting the cloud-computing service technology for internal and external use to reduce costs and enhance the competitiveness of the given company.

2.2. Internet Video Sharing. Internet video sharing functions have increased in popularity and are incorporated into numerous applications. For example, YouTube and Vimeo are two well-known applications. Previously, Live Video was only provided by Internet service providers; presently, this application can be personalized, enabling users to instantly broadcast videos they wish to share with others on the Internet whenever and wherever they desire. It also provides audiences with real-time services. Because of this transformation, general citizens, celebrities, politicians, and business celebrities are able to share self-produced videos and interesting clips in their personal and video blogs.

2.3. Video Streaming Technology. The advancement of broadband Internet technology has prompted users to frequently use multimedia streaming services on the Internet [5–9]. The development of high-speed Internet has also rendered the provision of real-time multimedia services on the Internet feasible. Users no longer need to spend prolonged periods of time downloading an entire file or store large files in hard

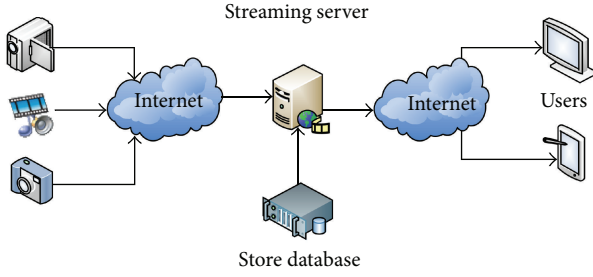


FIGURE 2: The framework of a media streaming system.

drives. By using the Internet, the server end can constantly transmit files, and, in turn, the user can receive the file while watching the video. Figure 2 presents the framework of the media streaming system, which can transfer media files or live broadcasts in the server. Popular media sharing websites adopt this type of streaming technology for online transmissions.

Real-time transport protocol (RTP) is a streaming communication protocol commonly used to control video and audio files [10]. Real time streaming protocol (RTSP) is a communication protocol designed to remotely control multimedia playbacks [11]. Additionally, it is a multimedia streaming protocol used to control audios and videos and is frequently used in conjunction with RTP. This study streamed data to instantly merge and share videos by using the RTSP approach, which enables the packet to transmit data without interruptions and allows users to smoothly render the audio and media content.

2.4. Noise Elimination. Digital signal processing is a critical aspect in information technology. Nowadays, people generally listen to music using a CD or an MP3 file format, which are classified as digital signals. Professional singers typically record and produce music in a fully equipped recording studio, which is designed to isolate external noise interferences and record the most original sound. However, general citizens have no access to these professional studios. Background noise is often recorded when singing using general microphones or at KTVs. Therefore, background environmental noises must be attenuated when using mobile devices to record singing.

Spectral subtraction is an effective speech enhancement technique for processing speech frequencies. In 1979, Boll [12] proposed a spectral subtraction method to reduce noise signals [12]. The spectral subtraction algorithm is simple, fast, and effective, requires few calculation steps, and can enhance the signal-to-noise ratio (SNR) of a sound signal. Assuming a noise corrupted input signal $y(n)$, clean speech signal $s(n)$, and noise signal $w(n)$, the signal influenced by noise can be expressed as follows:

$$y(n) = s(n) + w(n). \quad (1)$$

Therefore, an original clean speech signal can be considered a corrupted input signal minus noise:

$$|s(t)|^2 = |y(t)|^2 - |w(t)|^2. \quad (2)$$

To reduce a speech signal, Boll [12] modified the basic spectral subtraction method:

$$|\hat{s}(t)|^2 = |y(t)|^2 - \lambda|\hat{w}(t)|^2. \quad (3)$$

λ is calculated below, where SNR is expressed in decibels (dBs):

$$\lambda = \lambda_0 - \frac{3}{20}\text{SNR} \quad -5 \text{ dB} \leq \text{SNR} \leq 20 \text{ dB}. \quad (4)$$

In reality, noise frequency in a noisy environment is irregular. To examine the effects of noise on speech signals, Bero-uti proposed a method that segments speech signals into multiple frequency bands [13]. The equation can thus be rewritten as follows:

$$|\hat{s}_i(t)|^2 = |y_i(t)|^2 - \lambda_i|\hat{w}_i(t)|^2, \quad (5)$$

where λ_i is calculated as follow:

$$\lambda_i = \begin{cases} 4.75 & \text{SNR}_i \leq -5 \text{ dB} \\ 4 - \frac{3}{20}(\text{SNR}) & -5 \text{ dB} \leq \text{SNR}_i \leq 20 \text{ dB} \\ 1 & \text{SNR}_i \geq 20 \text{ dB}. \end{cases} \quad (6)$$

The equation below represents nonlinear spectral subtraction, which is used to reduce high-SNR-subtracted instantaneous power spectrum and enhance low-SNR-subtracted instantaneous power spectrum, where $|s_i(t)|$ denotes the enhanced speech signal, $|y_i(t)|$ denotes the noise speech signal, and $l_i(t)$ represents the estimate dependent on noise signals:

$$|s_i(t)| = |l_i(t)| \times |y_i(t)|, \quad (7)$$

$$l_i(t) = \frac{w_i(t)}{|\hat{y}_i(t)|},$$

$$|w_i(t)| = |\hat{y}_i(t)| - |\hat{w}_i(t)|.$$

To eliminate musical noise, Berouti also proposed a spectral subtraction with the oversubtraction method, asserting that the subtraction quantity of noise spectral amplitude should be inversely related to SNR. Audios with louder speech should be subtracted with softer audios:

$$|\hat{s}_i(t)|^2 = \begin{cases} |\hat{s}_i(t)|^2 & \\ = |y_i(t)|^2 - \alpha(\text{SNR})|w(t)|^2, & |\hat{s}_i(t)|^2 > \beta|w(t)|^2 \\ \beta|w(t)|^2, & \text{otherwise,} \end{cases} \quad (8)$$

where $0 < \beta \ll 1$ is a constant and $\alpha(\text{SNR}) \geq 1$ can be calculated as follows:

$$\alpha(\text{SNR}) = \alpha_0 + \text{SNR} \frac{1 - \alpha_0}{\text{SNR}_i}, \quad (9)$$

where $\alpha_0 \geq 1$ and $\text{SNR}_i \geq \text{SNR}$; therefore, when speech signal is weak (i.e., low SNR), $\alpha(\text{SNR})$ increases. The amplitude of the noise spectrum is oversubtracted, and the musical noise is eliminated by using $\beta|w(t)|^2$ in place of the subtracted result.

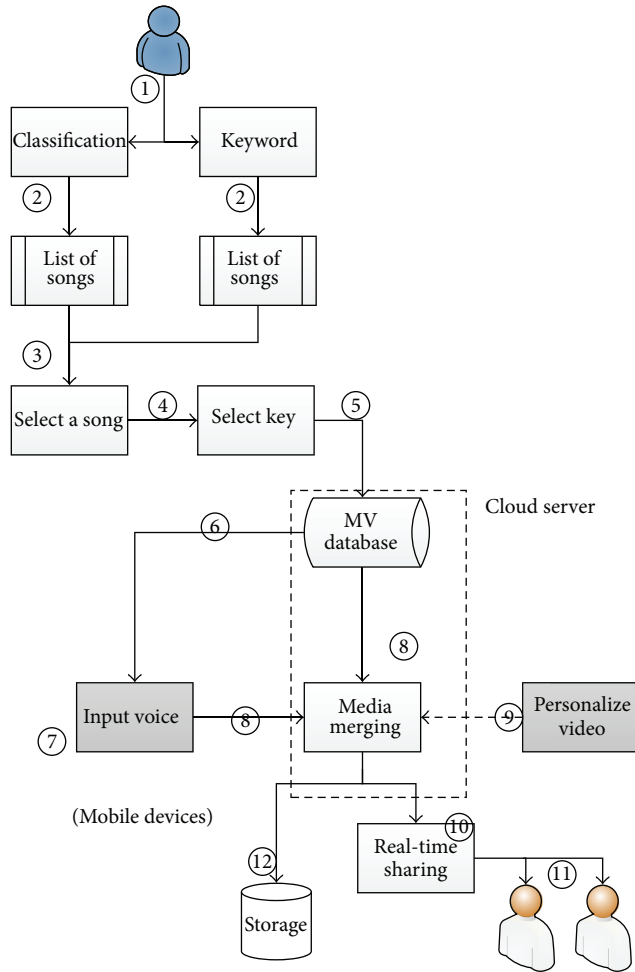


FIGURE 3: System architecture.

3. Karaoke System with Real-Time Media Merging and Sharing Function

3.1. System Framework. During leisure time, people often organize social events with friends at KTVs. The increased popularity of television talent shows has potentially increased people's desires to become a celebrity. The majority of these people select singing as their basic form of entertainment, which is conveniently available. This study combined cloud computing and a mobile device to design an application system that allows instant singing and sharing; thus, users can sing wherever they are and instantly share their recorded singings with others by using a cloud-computing-integrated mobile device that is connected to the Internet. Furthermore, the recordings can be merged with MVs and self-developed videos, thereby permitting users to feel the pleasure of being a singer. Figure 3 exhibits the system framework.

A description of the procedures that occur when users have completed downloading and installing the system application program into their personal device is outlined as follows.

- (1) According to the interface display, users can enter the song selection mode and select the "Select Songs by Classification" option to choose from the subcategories of the songs (e.g., Chinese, Taiwanese, and English songs, male and female singers, rock and roll, sentimental songs, and hip hop music) for the music file they wish to sing and search in the "Search Songs" selection by inputting keywords relevant to the songs.
- (2) The system shows results in the "Select Songs by Classification" or "Search Songs" function, displaying the possible list of songs for users to select and verify.
- (3) Users select the music file they intend to sing.
- (4) The system displays the option for selecting tunes; users can choose "male key" or "female key" based on their ability or preference.
- (5) Once the user has selected the desired song and tune, the application program searches for the song and tune file from the MV database in the cloud server.
- (6) Subsequently, the MV file relevant to the selected song and tune is streamed to users' mobile device.
- (7) The mobile device begins receiving the MV file of the selected song, while users are able to sing the song through the mobile device.
- (8) While the user sings, the system synchronously uploads the input speech/voice signal in the mobile device to the application program in the cloud server, where the voice is processed and subsequently merged with the MV file in the database.
- (9) If users do not wish to merge their recordings with the MV files in the database, they can select their personal videos (images or motion pictures) stored in the mobile device to merge with their voice signals.
- (10) The merged media file can be shared instantly through the use of the Internet.
- (11) Other users can watch the merged video from their mobile devices or personal computers. The transmission process used in this process also involves a media streaming technology.
- (12) Users can also store their completed works or upload and share them directly on social networking websites such as YouTube and Facebook.

3.2. Instant Video Merging. For cloud servers to process real-time media merging, a real-time media merging server must be installed in the cloud server. When users sing through their mobile device, the voice signal is first uploaded into the cloud server for background noise elimination to reduce noise interferences, thereby attaining a crisp and clear sound. Upon receiving the processed signals, the real-time media merging server in the cloud server obtains the MV file of the selected song from the MV database to merge the video and audio signals in the streamed media file with the uploaded and processed audio stream. If users do not wish to merge their recordings with the videos in the MV database, they

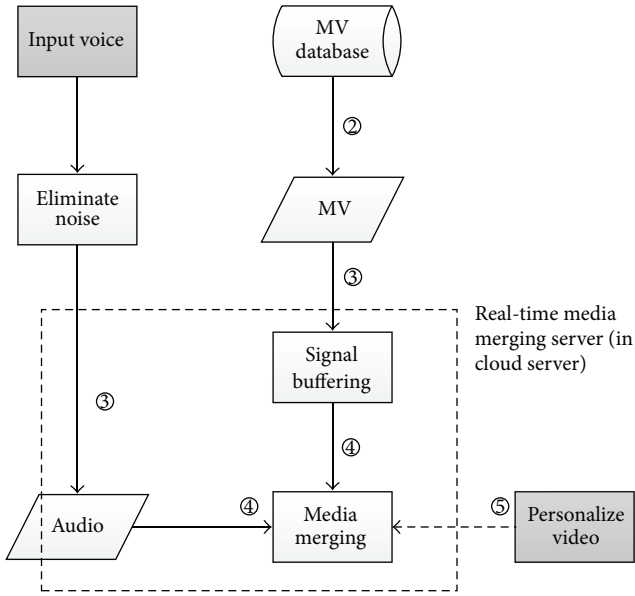


FIGURE 4: Real-time media merging framework.

can select their personal videos (images or motion pictures) stored in the mobile device and upload them to the real-time media merging server in the cloud server while they sing. Figure 4 presents the real-time merging framework.

The merging process is summarized as follows.

- (1) When users sing through their mobile device, the voice signal is first uploaded into the cloud server for background noise elimination, which is explained in Section 3.2.1.
- (2) The system retrieves the MV media file of the song that has been sung from the MV database in the cloud server.
- (3) When the real-time media merging server installed in the cloud server receives the processed signal (i.e., noise eliminated), the merging server begins to extract MV media files from the database and buffer the signal of the media file of the user’s song.
- (4) Upon streaming the media MV of the song singing in progress, the system merges the buffered video and audio signals with the uploaded and processed audio stream.
- (5) If users do not wish to merge their recordings with the videos in the MV database, they can select their personal videos (images or motion pictures) stored in the mobile device and upload them to the merging server in the cloud server, where merging is simultaneously conducted.

3.2.1. Noise Elimination and Signal Buffering. Background noise is often recorded when singing using mobile devices. This is in contrast to the recordings by professional singers, who typically record and produce music in fully equipped recording studios which are designed to isolate external noise

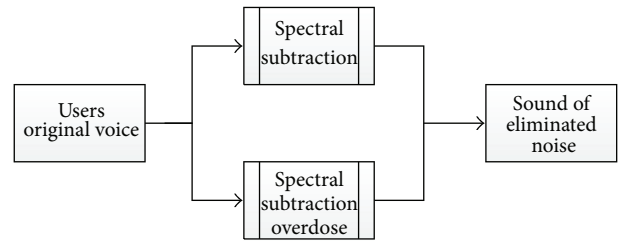


FIGURE 5: Noise elimination.

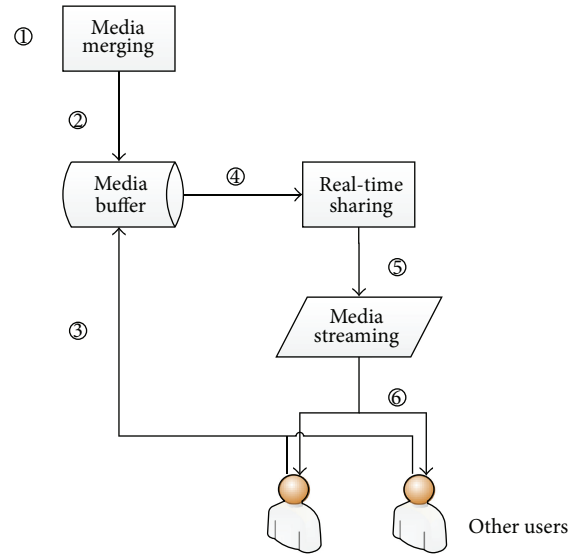


FIGURE 6: Real-time media sharing framework.

interferences and record the most original sound. Background environmental noises must be attenuated when using mobile devices to record singing. The study designed the karaoke system based on the methods outlined in Section 2.4, including the spectral subtraction method proposed by Boll [12] and the spectral subtraction with oversubtraction method proposed by Berouti. These methods were used for processing sound signals to eliminate noise. Figure 5 presents the workflow for noise elimination.

3.3. Real-Time Media Sharing. Among the numerous services provided in mobile devices, entertainment services are extensively used and extremely popular. These services not only entertain users and serve as a mean for users to release stress but also provide mobile Internet for them to interact with others. The system designed in this study allows users to sing through their mobile device, records their singing, and instantly merges the recording with a media file. Users can then share the content of their merged file with others through an online media streaming technology. Consequently, other users can watch the shared file through their mobile device or computer, thereby enabling them to experience the fun similar to that when singing at KTVs. Figure 6 presents the real-time media sharing framework.

When a song is merged with a media file, the system stores the merged file in the “Media Storage” section of the cloud server. Other users can then connect to the system cloud server and download this file to their mobile device or computer by using the media streaming download service provided in the “media storage” section. RTSP is a multimedia streaming protocol used to control audios and videos. Additionally, it permits multiple streaming demand control, which not only reduces the network traffic at the cloud server end but also supports multiple rendering. Therefore, with regard to real-time media sharing, this study adopted the RTSP approach to perform online streaming, thereby permitting packets to transmit data without interruptions. Consequently, users can easily connect to the server and render the selected media content.

This process is outlined as follows.

- (1) The system performs media merging as outlined in Section 3.2.
- (2) The merged file is stored in the “Media Storage” section and transmitted for real-time sharing.
- (3) Other users must connect to the “Media Storage” section in the system cloud server before they can watch the content of the merged medial file.
- (4) Once connected, real-time media sharing is implemented by reading the media content stored in the “Media Storage” section.
- (5) Media streaming is used as the technology for transmitting online media.
- (6) By using the Internet and adopting a media streaming approach, multiple users can simultaneously and instantly watch the media content.

4. System Analysis and Comparison

This study combined cloud computing and a mobile device to design a media sharing system; thus, users can sing wherever they are and instantly share their recorded songs with others by using their cloud-computing-integrated mobile device that is connected to the Internet. Furthermore, the recordings can be merged with MVs and self-developed videos, thereby allowing users to feel the pleasure of being a singer. This section outlines the analysis on the performance and features of the developed system and a comparison of the advantages of this system with traditional KTV.

4.1. Application in Mobile Devices. Because of the rapid development of mobile devices and their high rate of penetration, this study primarily employed a mobile device to operate the system. The main reasons and goals for using a mobile device are described as follows.

- (1) Mobile devices are light and portable. Through years of development, such devices contain numerous functions and have become a crucial part of people’s lives.
- (2) Entertainment-based programs available in mobile devices are widely used and extremely popular and

have received substantial attention. The developed system not only provides users with an entertainment service and serves as a mean for users to release stress but also enables users to interact with others on the Internet.

- (3) Because of the convenience and portability of mobile devices, by using this system, users can simply install the application program to sing whenever and wherever they want. They can also share their media file (containing recordings of their singing) with others, thereby achieving the goal of using entertainment services in their mobile device.

4.2. Applying Cloud-Computing Technology. This study developed the karaoke system based on cloud computing technology. The main reasons and goals for using this technology are described as follows.

- (1) Cloud computing excels in the calculation processing and can process large computing programs into numerous small subprograms on the Internet. Therefore, numerous application programs operate based on this technology.
- (2) Cloud computing can compute and analyze large programs, reduce system load in users’ mobile devices, and increase the computing performance of the mobile device.
- (3) The cloud server established at the cloud end provides several functions: store MVs and media files (which contain users’ recorded singing that is merged with a MV), eliminate noise, merge real-time media, search songs, and generate lists of recommended songs.
- (4) By using the cloud computing technology, users can share media files with others on the Internet. Thus, regardless of the location, users can remotely experience fun and pleasure.

4.3. System Performance. In this study, a karaoke system integrated with real-time merging and sharing functions was designed. This system was developed by integrating cloud computing into a mobile device and operates by using real-time media merging and sharing technology. Through this approach, the rate of using entertainment services in mobile devices can be enhanced, which subsequently increases the convenience of singing. Thus, users can sing and share their singing with others. Compared with the traditional karaoke system, the system developed in this study is more suitable for users of the current era in which digital information technology is extremely popular. Moreover, the traditional KTV market is approaching saturation. Therefore, the potential of this study’s system for future development is considerably high. In contrast to the online music platform, KKBOX, this study’s system not only serves as a karaoke option but also possesses real-time media merging and sharing functions. This system is also integrated with advantageous functions identical to those of the KKBOX. Thus, if combined with the KKBOX, the value of the system developed in this study

TABLE 1: A comparison of the advantages.

	Traditional KTV	The integrated KTV system
Location and temporal limitations	Yes	No
Singing-related and facility costs	High	Low
Maintenance cost	High	Low
Online instant sharing	No	Yes
Remote entertainment	No	Yes
Produce personalized music media	No	Yes
Potential for development	Low	High
The capability of being integrated with other platforms	No	Yes

can be further enhanced. Table 1 presents the comparison of the advantages between the traditional KTV and this study's system.

5. Conclusion

This study investigated a method by which people's leisure and entertainment activities and cloud computing technology can be integrated into mobile devices, which are rapidly advancing and are frequently used, thereby creating a new type of service. Subsequently, this study designed a karaoke system integrated with real-time merging and sharing functions, allowing users to enjoy a singing-related application service regardless of the time and location. This service was established based on the cloud computing framework. The application program enables users to sing through their mobile device and upload the recorded singing to the cloud server where background noises within the recording are eliminated. Additionally, this program provides a service whereby users' singing can be merged with MV media, thus permitting users to possess personal MVs, which can then be shared with others on the Internet for others to watch. This study provides the following contributions.

- (1) Users can attain entertainment goals without being limited by time and location with their mobile phone and Internet access. Through their cloud-computing-integrated mobile devices, they can sing and share their creations with other users.
- (2) Audio and video media can be merged and immediately shared.
- (3) Users can merge their song recordings with a MV or with a self-developed video to create personal MVs.
- (4) Consequently, through their mobile devices, people can sing heartily without having to visit KTVs, experience the enjoyment of friends and relatives' gatherings without having to attend, and feel the pleasure of being a singer.

The current market for traditional KTV is approaching saturation. The system designed and developed in this study can effectively facilitate the expansion of the current KTV market, which is reaching saturation. It is more suitable for users of the current era in which digital information technology is extremely popular. Furthermore, the system facilitates the transformation of the current lifestyle into a mobile-based entertainment lifestyle. Therefore, in addition to visiting KTV establishments, people who wish to sing are also provided with a more convenient and immediate alternative. Overall, the availability of the system developed in this study can ultimately reduce the infrastructure and maintenance costs, which would subsequently decrease the manpower demands and costs.

Acknowledgment

This work is partially supported by the National Science Council of Taiwan under the Grants NSC 101-2221-E-218-052, NSC 102-2221-E-218-017, and NSC 100-2632-E-218-001-MY3.

References

- [1] H. Chih-Kai, *Dynamic adjustment mechanism of the virtual machine computing resource in the cloud computing [M.S. thesis]*, 2010.
- [2] N. Fernando, S. W. Loke, and W. Rahayu, "Mobile cloud computing: a survey," *Future Generation Computer Systems*, vol. 29, pp. 84–106, 2013.
- [3] M. Chen, W. Cai, and L. Ma, "Cloud computing platform for an online model library system," *Mathematical Problems in Engineering*, vol. 2013, Article ID 369056, 7 pages, 2013.
- [4] S. H. Kang and K. Lee, "Emerging materials and devices in spintronic integrated circuits for energy-smart mobile computing and connectivity," *Acta Materialia*, vol. 61, pp. 952–973, 2013.
- [5] D. Xiao-dan, H. Qing, L. Yong-hong, and Y. Hong, "The system construction and the implementation of QOS control mechanism in intelligent streaming media," *International Conference on Solid State Devices and Materials Science*, vol. 25, pp. 808–813, 2012.
- [6] G. Sebestyen, A. Hangan, K. Sebestyen, and R. Vachter, "Self-tuning multimedia streaming system on cloud infrastructure," in *International Conference on Computational Science*, pp. 1342–1351, 2013.
- [7] J. Chen, R.-M. Wang, L. Li, Z.-H. Zhang, and X.-S. Dong, "A distributed dynamic super peer selection method based on evolutionary game for heterogeneous P2P streaming systems," *Mathematical Problems in Engineering*, vol. 2013, Article ID 830786, 9 pages, 2013.
- [8] A. A. Hasan, "Magnetohydrodynamic stability of streaming jet pervaded internally by varying transverse magnetic field," *Mathematical Problems in Engineering*, vol. 2013, Article ID 325423, 12 pages, 2012.
- [9] S. Chen, Z. Shi, H. Lin, and L. Huang, "H.264 coding stream transfer based on mediastreamer framework," in *Proceedings of the 2nd International Conference on MultiMedia and Information Technology (MMIT '10)*, pp. 262–265, April 2010.
- [10] Peterson, L. Larry, and B. S. Davie, *Computer Networks 2007*, Morgan Kaufmann, 4 edition, 2007.
- [11] RFC 2326, Real Time Streaming Protocol (RTSP), IETF, 1998.

- [12] S. F. Boll, "A spectral subtraction algorithm for suppression of acoustic noise in speech, Acoustics, Speech and Signal Processing," pp. 200–203, 1979.
- [13] M. Berouti, R. Schwartz, and J. Makhoul, "Enhancement of speech corrupted by acoustic noise," in *Proceedings of the IEEE International Conference on Acoustics, Speech, and Signal Processing (ICASSP '79)*, vol. 97, pp. 208–211, 2002.

Research Article

Low-Cost Design of an FIR Filter by Using a Coefficient Mapping Method

Ming-Chih Chen and Hong-Yi Wu

Department of Electronic Engineering, National Kaohsiung First University of Science and Technology, Kaohsiung City 811, Taiwan

Correspondence should be addressed to Ming-Chih Chen; mjchen@nkfust.edu.tw

Received 14 September 2013; Accepted 9 October 2013

Academic Editor: Teen-Hang Meen

Copyright © 2013 M.-C. Chen and H.-Y. Wu. This is an open access article distributed under the Creative Commons Attribution License, which permits unrestricted use, distribution, and reproduction in any medium, provided the original work is properly cited.

This work presents a novel coefficient mapping method to reduce the area cost of the finite impulse response (FIR) filter design, especially for optimizing its coefficients. Being capable of reducing the area cost and improving the filter performance, the proposed mapping method consists of four steps: quantization of coefficients, import of parameters, constitution of prime coefficients with parameters, and constitution of residual coefficients with prime coefficients. Effectiveness of the proposed coefficient mapping method is verified by selecting the 48-tap filter of IS-95 code division multiple access (CDMA) standard as the benchmark. Experimental results indicate that the proposed design with canonical signed digit (CSD) coefficients can operate at 86 MHz with an area of 241,813 μm^2 , leading to a throughput rate of 1,382 Mbps. Its ratio of throughput/area is 5,715 Kbps/ μm^2 , yielding a higher performance than that of previous designs. In summary, the proposed design reduces 5.7% of the total filter area, shortens 25.7% of the critical path delay, and improves 14.8% of the throughput/area by a value over that of the best design reported before.

1. Introduction

Digital signal processing applications are common in home entertainment systems, television sets, high-fidelity audio equipment, and information systems. The digital filter is an important component in mathematical operations on a sampled, discrete-time signal to enhance the certainty of a signal. The digital filter is characterized by its transfer function. Two digital filters are infinite impulse response (IIR) and finite impulse response (FIR) filters. The IIR filter consists of a transfer function with feedback mode, and the FIR filter consists of the function with nonfeedback mode. Commonly found in image processing, audio processing, and wireless communications, FIR filter applications are characterized by a linear phase, arbitrary magnitude, and relatively easy implementation. The filter hardware consists of adders, subtractors, shifters, and registers. Many related works [1–9] attempt to reduce the number of these required components in filter implementation, especially for the optimization of coefficients' realization. Experimental results demonstrate that the proposed coefficient mapping method performs better than previous designs in terms of area ratio.

The rest of this paper is organized as follows. Section 2 briefly describes previous researches for filter optimization. Section 3 then describes the coefficient mapping method. Next, Section 4 summarizes the experimental results and compares them with those of other previous designs. Conclusions are finally drawn in Section 5, along with recommendations for future research.

2. Background

2.1. Digital FIR Filter. Digital filters generally vary in coefficients, based on their specifications. The design of coefficients in a filter can be divided into four portions: coefficient selection, coefficient identification, searching algorithm, and coefficient quantization.

(1) Coefficient Selection. Typically determined by a set of filter specifications, coefficient selection must consider the number of taps, bit width, and filter complexity. According to the different complexities of coefficients, different algorithms are used to find the common subexpressions (CSs) and eliminate them for obtaining the best area reduction.

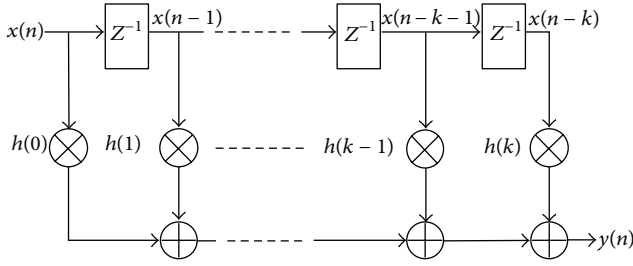


FIGURE 1: Filter architecture of a direct form.

(2) *Coefficient Identification.* Coefficients must be encoded to determine the area cost of a filter and the frequency of extracting common subexpressions. In coefficient encoding, the common expression is binary encoding. However, this encoding method causes more 1's signals in data expression and more calculations in hardware implementation. Hence, optimizing more coefficients [10, 11] involves using the canonic signed digit (CSD) expression to eliminate many 1's signals and using less common subexpressions.

(3) *Searching Algorithm.* The searching algorithm can find more common subexpressions to reduce the area cost of filter. Although many works [1–9, 12, 13] have attempted to find as many common subexpressions as possible, a more complex algorithm may not yield a higher performance, especially in coefficients with a low complexity.

(4) *Coefficient Quantization.* Coefficient quantization is an effective means of reducing the number of logic gates while implementing a filter. When the coefficients are quantized for implementation, the commonly used rounding method causes a deviation in the time and frequency responses of the implemented filter from the ideal response. Sensitivity of the filter response is of priority concern when quantizing the coefficients.

2.2. *Optimization of the FIR Filter.* The equation of FIR filter can be expressed as (1), and its transferred function can also be expressed as (2):

$$y(n) = \sum_{k=0}^{N-1} h(k) x(n-k), \quad (1)$$

$$H(z) = \sum_{n=0}^{N-1} h(n) z^{-n}. \quad (2)$$

Parameter n in (1) and (2) is expressed as the number of taps. This parameter is related to the output of a filter system and its frequency responses. Two implementation methods used for a filter are direct and cascade architectures. Here, the direct architecture is of priority concern, especially for enhancing the frequency responses of a filter with all zeros. The direct architecture can also be divided into direct and transposed forms. The direct form consists mainly of multipliers, adders, and registers. Figure 1 shows the architecture of the direct form. An n -tap filter with a direct form requires n copies of a multiplier, $n-1$ copies of an adder, and n copies of a register.

Coefficients $h(0)$ – $h(k)$ can be expressed as binary numbers. The binary expressions for the coefficients can be found with the common subexpressions (CSs) between them. In previous researches [1–9], there are three common subexpression elimination (CSE) methods including horizontal, vertical, and mixed searching methods. The method in [1] uses CSD expressions [2] for the coefficients and uses horizontal searching algorithm to find the CSs including $(1, 0, 1)$, $(1, 0, -1)$, $(1, 0, 0, 1)$, and $(1, 0, 0, -1)$. This method first optimizes the CS with the highest appearance until no CS can be extracted. In [3, 7], this method also uses CSD expressions, yet uses vertical search to find the CSs, including $(1, -1)$ and $(-1, 1)$. By modifying the vertical searching method in [8], the method in [4] first uses horizontal search to extract the CSs including $(1, 0, 1)$, $(1, 0, -1)$, $(1, 0, 0, 1)$ and $(1, 0, 0, -1)$, which is expressed in CSD format. Thereafter, this method performs a vertical search to extract the CSs, including $(1, 0, 1)$ and $(-1, 0, 1)$.

In addition to using two horizontal methods and one vertical searching method to extract the CSs, the method in [5] also uses a multiplier-adder block (MAB) and structure adder (SA) to construct the CSs and their residues. Besides finding two CSs with the same appearances, the method in [6] extracts the CS with a smaller bit width. A previous work [8] developed two methods for extracting the CSs in CSD format. The first method analyzes the CSs with 3-, 4-, and 5-bit by performing the statistics of their appearances. The second method searches the coefficients up to down and extracts the CSs between them by using vertical search. The method in [9] proposes a rule in which the depth of logic gates cannot be increased by performing the horizontal search in the same way as in [4] and the vertical search in the same way as in [8].

Following implementation of the above searching methods, the CSs can be extracted and the same CSs can be used for calculation only once. Calculation times of the filter are reduced due to the extractions. These searching methods can also reduce the required number of adders and subtractors. To verify the different searching methods, the 48-tap filter of IS-95 CDMA is selected as the benchmark.

3. Proposed Coefficient Mapping Method

The mapping method divides the coefficients into two parts: primary coefficients and remaining coefficients. The parameters that are set up in the algorithm are Q_h and Q_p . The constitution of coefficients has two steps: constitution of primary coefficients and calculation of multiple relations between the primary and remaining coefficients. The operation steps of the mapping method are described as follows.

Step 1. Normalize the n -tap coefficients c_i by multiplying 2^m . The normalized results are $h_i = c_i \times 2^m$, for $0 \leq i \leq n-1$.

Step 2. Separate normalized coefficients h_i into two parts, H_1 and H_2 :

$$\begin{aligned} H_1 &= \{h_j\}, & 0 \leq j \leq \frac{n}{2} - 1, \\ H_2 &= \{h_k\}, & \frac{n}{2} \leq k \leq n-1. \end{aligned} \quad (3)$$

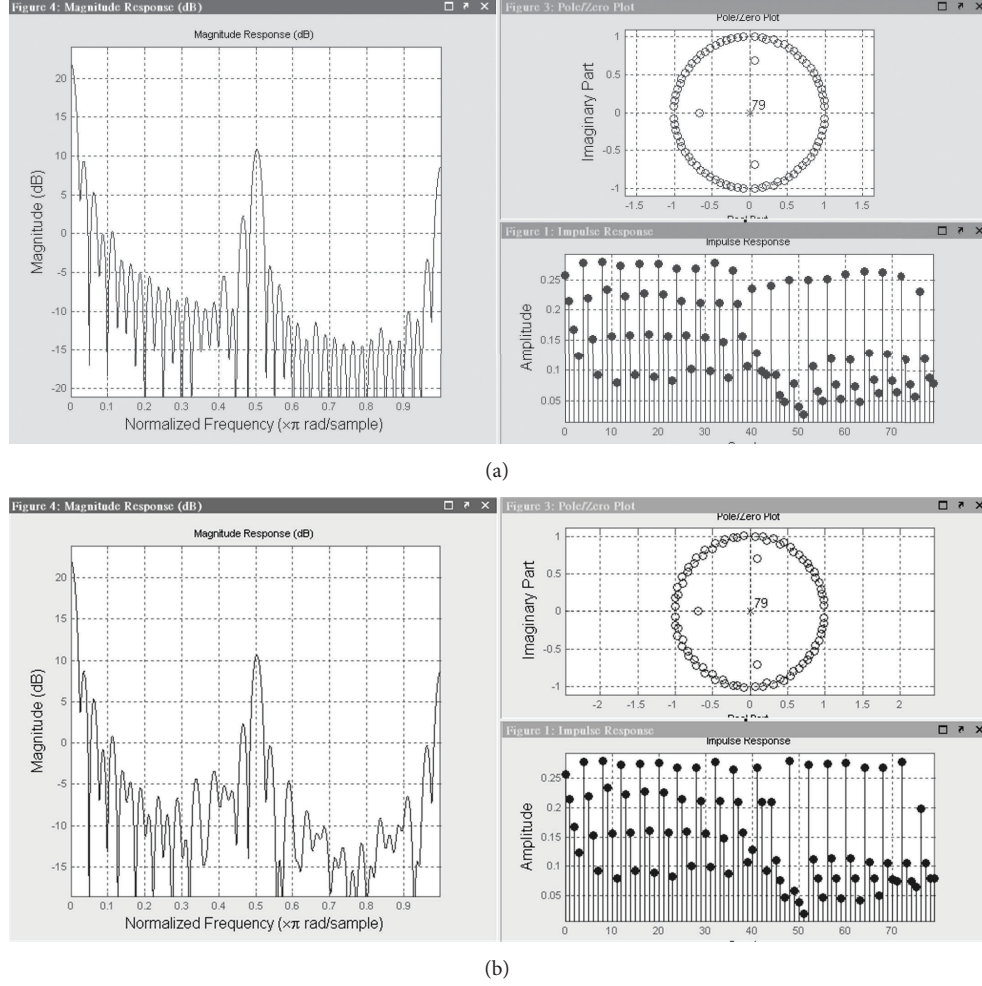


FIGURE 2: (a) Frequency responses, poles and zeros distributions of the original filter. (b) Frequency responses, poles and zeros distributions of the modified filter.

Step 3. Quantize h_j and h_k based on Q_h . Equations (4) and (5) show the relations between Q_h , h_j , and h_k

$$h_j = Q_h(S_{h,j}) \times \Delta h_j, \quad (4)$$

$$h_k = Q_h(S_{h,k}) \times \Delta h_k. \quad (5)$$

Parameters Δh_j and Δh_k are the variances after performing the quantization. Let $h'_j = Q_h(S_{h,j})$ and let $h'_k = Q_h(S_{h,k})$. Equations (4) and (5) thus become the following equations separately:

$$h_j = h'_j \times \Delta h_j, \quad (6)$$

$$h_k = h'_k \times \Delta h_k. \quad (7)$$

Step 4. Find a multiple value $p_{k,j}$ that is between h_k and h_j , and find a multiple value $p'_{k,j}$ that is between h'_k and h'_j .

The relations are shown as

$$h_k = p_{k,j} \times h_j \implies p_{k,j} = \frac{h_k}{h_j}, \quad (8)$$

$$h'_k = p'_{k,j} \times h'_j \implies p'_{k,j} = \frac{h'_k}{h'_j}. \quad (9)$$

Step 5. Quantize $p'_{k,j}$ based on Q_p . Equation (10) shows the relation between Q_p and $p'_{k,j}$. Parameter $\Delta p_{k,j}$ denotes the variance after performing the quantization:

$$p'_{k,j} = Q_p(S_{p,k,j}) \times \Delta p_{k,j}. \quad (10)$$

Let $p''_{k,j} = Q_p(S_{p,k,j})$, and (11) shows the relation between $p'_{k,j}$ and $p''_{k,j}$:

$$p'_{k,j} = p''_{k,j} \times \Delta p_{k,j}. \quad (11)$$

Step 6. Constitute h'_k and substitute (11) with (9). The relation between h'_k , h'_j , and $p'_{k,j}$ becomes

$$h'_k = p''_{k,j} \times h'_j \times \Delta p_{k,j}. \quad (12)$$

TABLE 1: New coefficients after performing the mapping method ($Q_h = 32, Q_p = 0.25$).

Group	Sign	Coefficient		Error rate (%)
		h_j, h_k (original coefficient)	h'_j, h'_k (new coefficient)	
H_1				
c_0	-	829	832 (32 × 26)	0.36
c_1	-	1120	1120 (32 × 35)	0.00
c_2	-	1172	1184 (32 × 37)	1.01
c_3	-	548	544 (32 × 17)	0.74
c_4	+	708	704 (32 × 22)	0.57
c_5	+	2128	2144 (32 × 67)	0.75
c_6	+	2982	2976 (32 × 93)	0.20
c_7	+	2684	2688 (32 × 84)	0.15
c_8	+	1215	1216 (32 × 38)	0.08
H_2				
c_9	-	721	832 (832 × 1)	13.3
c_{10}	-	1990	1960 (1120 × 1.75)	1.53
c_{11}	-	1677	1776 (1184 × 1.5)	5.57
c_{12}	+	258	272 (544 × 0.5)	5.15
c_{13}	+	2765	2816 (704 × 4)	1.81
c_{14}	+	4157	4288 (2144 × 2)	3.06
c_{15}	+	3098	2976 (2976 × 1)	4.10
c_{16}	-	421	672 (2688 × 0.25)	37.4
c_{17}	-	4560	4560 (1216 × 3.75)	3.09

Step 7. Revert the parameters h_j and h_k by substituting (9) and (12) with (7). Equations (13) and (14) show the relations as follows:

$$h_j = Q_h (S_{h,j}) \times \Delta h_j \implies h_j = h'_j \times \Delta h_j, \quad (13)$$

$$\begin{aligned} h_k &= Q_h (S_{h,j}) \times Q_p (S_{p,k,j}) \times \Delta p_{k,j} \times \Delta h_k \\ \implies h_k &= h'_j \times p''_{k,j} \times \Delta p_{k,j} \times \Delta h_k. \end{aligned} \quad (14)$$

Let $h''_k = h'_j \times p''_{k,j}$, and (14) is then modified to

$$h_k = h''_k \times \Delta p_{k,j} \times \Delta h_k. \quad (15)$$

According to the variance, the calculation error and correct rates can be expressed as

$$e_i = \begin{cases} 1 - \Delta & \text{if } \Delta \leq 1, \\ \Delta - 1 & \text{if } \Delta > 1, \end{cases} \quad (16)$$

$$a_i = 1 - e_i. \quad (17)$$

Substitute the variances of h_k and h_j into (16). The error rate e_i can be obtained, for $0 \leq i \leq n - 1$.

For example, this work selects 18 coefficients c_0 - c_{17} from 48-tap IS-95 CDMA to perform the mapping method. The coefficients are

$$\begin{aligned} c_0 &= -0.025299, & c_1 &= -0.034179, \\ c_2 &= -0.035766, & c_3 &= -0.016723, \\ c_4 &= 0.021606, & c_5 &= 0.064941, \\ c_6 &= 0.091003, & c_7 &= 0.081909, \\ c_8 &= 0.037078, & c_9 &= -0.022003, \\ c_{10} &= -0.060729, & c_{11} &= -0.051177, \\ c_{12} &= 0.007873, & c_{13} &= 0.084381, \\ c_{14} &= 0.126861, & c_{15} &= 0.094543, \\ c_{16} &= -0.012847, & c_{17} &= -0.143463. \end{aligned} \quad (18)$$

Before performing the mapping method, this work first sets up two parameters in which Q_h equals 32 and Q_p equals 0.25 to reduce the hardware design complexity. After Steps 1, 2, 3, 4, 5, 6, and 7 of the proposed method are performed, Table 1 lists the generated h_i values. Figure 2(a) shows the frequency responses, poles, and zeros distributions of the original filter. Figure 2(b) shows the behaviors of the filter with modified coefficients after applying the proposed mapping method. The behaviors in Figures 2(a) and 2(b) are approximately the same with each other.

TABLE 2: Performance comparison of various 48-tap filter designs for generating 16-bit outputs.

Methods	Architecture level		Info.		
	Area no. of add., sub., and reg.	Area (μm^2)	Critical path delay (ns)	Throughput (Mbps)	Throughput/area ($\text{Kbps}/\mu\text{m}^2$)
Binary	(220, 0, 48)	300284	12.61	1268	4225
CSD	(88, 74, 48)	299622	12.08	1324	4421
Paško et al. [1]	(76, 22, 48)	271357	15.08	1061	3910
Jang and Yang [3]	(72, 70, 48)	295567	15.27	1047	3545
Vinod et al. [4]	(62, 34, 48)	274025	14.32	1117	4077
Choo et al. [5]	(67, 24, 48)	259104	14.18	1128	4355
Takahashi and Yokoyama [6]	(78, 22, 48)	273902	15.28	1047	3823
Mahesh and Vinod [7]	(88, 0, 48)	255450	15.58	1271	4979
Kato et al. [8]	(64, 26, 48)	264240	14.46	1106	4187
Vinod et al. [9]	(62, 34, 48)	260976	14.25	1122	4303
Our method with binary format	(66, 0, 48)	244547 (4.3%)	11.45 (26.5%)	1397 (9.9%)	5713 (14.7%)
Our method with CSD format	(23, 33, 48)	241813 (5.3%)	11.58 (25.7%)	1382 (8.7%)	5715 (14.8%)

4. Experimental Results

For comparison, Table 2 lists various 48-tap filter designs for IS-95 CDMA. These filters can generate 16-bit output data at one clock cycle. The table shows the architecture- and gate-level information of the filters. The area cost of the architecture-level includes how many adders, subtractors, and registers are used for implementation. Gate-level information includes the area cost, critical path delay, throughput, and throughput per area. In the architecture-level, analysis results indicate that the original filter with binary coefficients has the largest area cost among other designs. The design in [7] has the smallest summation for calculating the number of adders and subtractors. More than having the smallest area cost, the proposed design also achieves the highest throughput and ratio of throughput per area in the gate-level synthesis among other designs.

Table 2 lists two filter designs: the coefficients expressed with binary and CSD formats. In the architecture-level, the proposed filter with CSD coefficients has the smallest summation for calculating the number of adders and subtractors. The proposed filter only requires a total of 56 adders and subtractors which are the smallest amounts among the previous designs. The best design is the method in [7], which has an area of $255,450 \mu\text{m}^2$ and achieves a throughput/area of $4,979 \text{ Kbps}/\mu\text{m}^2$. The proposed design with CSD coefficients can operate at 86 MHz with an area of $241,813 \mu\text{m}^2$, leading to a throughput rate of 1,382 Mbps. Its ratio of throughput/area is $5,715 \text{ Kbps}/\mu\text{m}^2$, which is the highest performance among the previous designs. In summary, the proposed design reduces 5.7% of the total filter area, shortens 25.7% of the critical path delay, and improves 14.8% of the throughput/area compared with the best design in [7].

5. Conclusions

This work has developed a novel filter design with coefficient mapping method. The proposed method can reduce the area

cost by finding the primary coefficients and using them to construct the remaining coefficients. The proposed method can also use several coefficients and construct all of the filter coefficients. Experimental results demonstrate that the proposed design with binary or CSD coefficients can more significantly reduce the area cost and improve the ratio of throughput/area compared with previous designs. Implementation results further demonstrate that the proposed design has the highest throughput with the lowest area cost.

Acknowledgment

This work is supported in part by the National Science Council of Taiwan under Grants NSC 99-2221-E-327-046.

References

- [1] R. Paško, P. Schaumont, V. Derudder, S. Vernalde, and D. Đuračková, "A new algorithm for elimination of common subexpressions," *IEEE Transactions on Computer-Aided Design of Integrated Circuits and Systems*, vol. 18, no. 1, pp. 58–68, 1999.
- [2] R. M. Hewlitt and E. S. Swartzlander Jr., "Canonical signed digit representation for FIR digital filters," in *Proceedings of the IEEE Workshop on Signal Processing Systems (SIPS '00)*, pp. 416–426, October 2000.
- [3] Y. Jang and S. Yang, "Low-power CSD linear phase FIR filter structure using vertical common sub-expression," *Electronics Letters*, vol. 38, no. 15, pp. 777–779, 2002.
- [4] A. P. Vinod, E. M.-K. Lai, A. B. Premkumar, and C. T. Lau, "FIR filter implementation by efficient sharing of horizontal and vertical common subexpressions," *Electronics Letters*, vol. 39, no. 2, pp. 251–253, 2003.
- [5] H. Choo, K. Muhammad, and K. Roy, "Complexity reduction of digital filters using shift inclusive differential coefficients," *IEEE Transactions on Signal Processing*, vol. 52, no. 6, pp. 1760–1772, 2004.
- [6] Y. Takahashi and M. Yokoyama, "New cost-effective VLSI implementation of multiplierless FIR filter using common

- subexpression elimination,” in *Proceedings of the IEEE International Symposium on Circuits and Systems (ISCAS '05)*, pp. 1445–1448, May 2005.
- [7] R. Mahesh and A. P. Vinod, “A new common subexpression elimination algorithm for realizing low-complexity higher order digital filters,” *IEEE Transactions on Computer-Aided Design of Integrated Circuits and Systems*, vol. 27, no. 2, pp. 217–229, 2008.
- [8] K. Kato, Y. Takahashi, and T. Sekine, “A new horizontal and vertical common subexpression elimination method for multiple constant multiplication,” in *Proceedings of the 16th IEEE International Conference on Electronics, Circuits and Systems (ICECS '09)*, pp. 124–127, December 2009.
- [9] A. P. Vinod, E. Lai, D. L. Maskell, and P. K. Meher, “An improved common subexpression elimination method for reducing logic operators in FIR filter implementations without increasing logic depth,” *Integration, the VLSI Journal*, vol. 43, no. 1, pp. 124–135, 2010.
- [10] C.-H. Chang and M. Faust, “On ‘a new common subexpression elimination algorithm for realizing low-complexity higher order digital filters,” *IEEE Transactions on Computer-Aided Design of Integrated Circuits and Systems*, vol. 29, no. 5, pp. 844–848, 2010.
- [11] D. Shi and Y. J. Yu, “Design of linear phase FIR filters with high probability of achieving minimum number of adders,” *IEEE Transactions on Circuits and Systems I*, vol. 58, no. 1, pp. 126–136, 2011.
- [12] A. Shahein, Q. Zhang, N. Lotze, and Y. Manoli, “A novel hybrid monotonic local search algorithm for FIR filter coefficients optimization,” *IEEE Transactions on Circuits and Systems*, vol. 59, no. 3, pp. 616–627, 2011.
- [13] B. Y. Kong and I. C. Park, “FIR filter synthesis based on interleaved processing of coefficient generation and multiplier-block synthesis,” *IEEE Transactions on Computer-Aided Design of Integrated Circuits and Systems*, vol. 31, no. 8, pp. 1169–1179, 2012.

Research Article

Implementation of Fall Detection and Localized Caring System

Ming-Chih Chen,¹ Yi-Wen Chiu,² Chien-Hsing Chen,³ and Ei-Jo Chen¹

¹ Department of Electronic Engineering, National Kaohsiung First University of Science and Technology, Kaohsiung City 811, Taiwan

² Department of Social Work and Service Management, Tatung Institute of Commerce and Technology, Chiayi 612, Taiwan

³ Department of Information Technology, Meiho University, Pingtung 912, Taiwan

Correspondence should be addressed to Ming-Chih Chen; mjchen@nkfust.edu.tw

Received 13 September 2013; Accepted 12 October 2013

Academic Editor: Teen-Hang Meen

Copyright © 2013 Ming-Chih Chen et al. This is an open access article distributed under the Creative Commons Attribution License, which permits unrestricted use, distribution, and reproduction in any medium, provided the original work is properly cited.

We propose the fall detection and localized caring system to effectively detect the postures of a human and provide a service of remote connection with health care center. Especially, when elderly people fall down, they often need to be hospitalized. The system can inform the care center automatically through the wireless sensor network and send the rapid information of the incident for their family through the mobile phone. It also provides the location of incident for immediate rescue by dispatching medical staff from the center. The experimental results show that our system achieves the accurate rate of 99.9% for detecting a human fall and provides the care services effectively.

1. Introduction

According to the statistics in Taiwan, fall is the top second accidental cause of death happened in elderly people. The rate of falling down is about 15% to 40% every year, and the times of fall will increase along with their age. Most of the fall will cause the elderly people to be hospitalized or to reside in nursing home, and it will also cause the barriers of their daily activities. The risk factors of fall were found to be significantly associated with their osteoporosis disease, chronic disease, and so on. Even the slight fall will cause the most danger to elderly people.

The damage degree of fall for elderly people is often decided by the time of discovery, transport, and emergency medical service. The development of electronic technologies let the integration of sensors and wireless network become more and more popular. The automatic system management reduces the neglect from people and realizes the zero-distance medical treatment. A design deploys several infrared and temperature sensors in a room for detecting the fall of a human by receiving the information from sensors and performing detection algorithm [1].

More accelerometers and related circuits are used [2–12], and more costs are needed when the system is designed.

A portable device with two-axis accelerometer is worn on a shank for detecting the fall [2], and two similar designs use the same detection method but put the device on the waist [3, 4]. In 2009, a special design puts two devices with three-axis accelerometers on the chest and thigh separately for observing the changes under different postures [5]. The fall detection method in [6] uses a barometric pressure sensor with an accelerometer to improve the recognition accuracy. A new design puts eight accelerometers in the washable pullover for detecting the motions of the torso and the upper body [8]. A hidden-Markov-model-(HMM-) based method is used to detect and predict a fall event [10]. The method in [11] uses two accelerometers and four surface electromyography sensors to effectively detect the human fall.

Our design uses only one accelerometer and achieves the fall detection with high accuracy. The system will be deployed in the long-term care institution. It can deliver the falling information through the connection of wireless sensor network (WSN), Ethernet, and Internet. The elderly people wear a fall detection device to detect the activities. If the fall situation is happened, the wearing device sends the falling message to the unit of medical treatment automatically. The design of such system can increase the living time of sufferers and reduce the rate of death due to the fall.

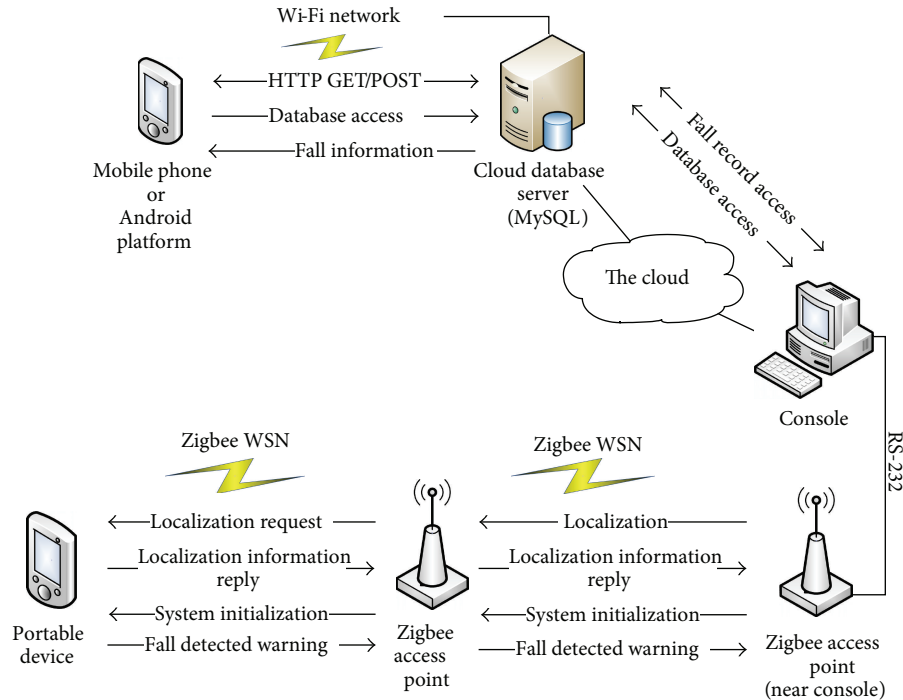


FIGURE 1: Proposed caring system architecture.

The implementation of our caring system includes hardware (HW) and software (SW) platforms that are described in Section 2. Sections 3 and 4 introduce the detailed HW and SW implementation, respectively. The experimental results are involved in Section 5, and the conclusion is given in Section 6.

2. Proposed Caring System Architecture

Our caring system architecture uses three kinds of networks including wireless sensor network, 802.11 wireless network (also called Wi-Fi), and Internet. As Figure 1 shows, the system architecture includes portable device, Zigbee access point, console, cloud database server, and mobile phone. The portable device in this system can detect the fall automatically and transmit the warning message to the nursing station through the Zigbee access point.

When a user wears the portable device but falls under the cover of wireless sensor network, the device automatically transmits the fall message to the console deployed in the nursing station. The station dispatches a nurse to find the user according to the indoor localization function and provide the required services according to the case history searched from the cloud database server. The system also informs the destined family of the user via mobile phone and shows the information of the rescue processes such as the time of fall, the arriving time of the nurse, the time of taking medical treatment, and so on.

Figure 1 also shows the communication information between two adjacent devices. For example, the portable device should communicate with Zigbee access point, especially the fall happens. The access point delivers the request

of localization and system initialization from the console and the localization information and the warning of fall console to the console. The console also searches, records, and updates the case history in the database of MySQL.

The cloud sever performs three kinds of programs including the network connection program with the console and mobile phone and the users' database. When the system is utilized in a medium or small care institution, the cloud server could combine with the console and perform it in the nursing station. Figure 1 shows a caring network which utilizes cloud database server for managing a large number of institutions. One of the institutions connects the fall detection subsystem with the cloud database server through the console setup in the institution. The centralized database management can reduce the system costs effectively and manage the case history of users efficiently. Our caring system is suitable for each type of care institutions.

3. Proposed System Hardware Platform

In this system, there are two hardware designs including portable device worn by user and Zigbee access point deployed in the environment. The portable device is utilized to autodetect the fall of user as shown in Figure 2. It consists of a microcontroller unit (MCU), a three-axis accelerometer, a Zigbee WSN module, and a buzzer. The ARM9 MCU receives the analog signals from the accelerometer, performs the fall detection algorithm, and sends the warning message through Zigbee module if the user falls. The powers of all modules are supplied by a 1000 mA Polymer Lithium-Ion battery via a 5 V to 3.3 V voltage regulator. The battery has stable, slim, and extremely light characteristics which are suitable for



FIGURE 2: The portable device.



FIGURE 3: The circuit board of the Zigbee access point.

the portable device. The prototype of the portable device is embedded in a box with the dimensions of $8 \times 4 \times 2.5 \text{ cm}^3$. The device can operate over one month on standby mode or continuously transmit fall information over 500 times in the experiment.

Figure 3 shows the circuit board of Zigbee access point. It consists of two modules including an ARM9 MCU and a Zigbee module. The Zigbee module is placed in the front of the board and is utilized to transfer the information between portable devices and the console. The Zigbee access point is deployed in the ceiling or upper side of the room and supplies the power by a wall adapter power supply with 5 V DC. The deployment of the access point needs to consider its signal attenuation in an environment with multicorner or shelter. The Zigbee access point connects with the console through the COM or USB port. The RS-232 communication protocol is performed between the console and the circuit board. The circuit board only uses Zigbee module for the wireless communication with other Zigbee access points, but it does not need a MCU to control the Zigbee. The console controls the Zigbee directly by sending commands through RS-232 protocol.

The appropriate deployment of access points in an institution contributes to the well performance of the localization function. The localization function can be performed by the

triangulation method [13]. For example, the console sends the command to localize a user with a fixed portable device. The identification (ID) number of the portable device is known from the search of the database. The console broadcasts the request through all the access points. The portable device will receive the request from the near access points. The values of received signal strength indicator (RSSI) measured between the portable device and the near access points will be transmitted to the console. The console performs the triangulation method to calculate the distance between the nearest three access points. The estimated location of the user will be shown in the graphic interface of the caring system. From our experiment, we observe that the triangulation method can provide an approximate location in the visible range after adding the consideration of signal attenuation.

4. Proposed System Software Platform

Figure 4 shows the graphic user interface of the caring system. The interface is written by Borland C++. The left upper side of the interface shows the map of interior space in the institution. When a user wears a portable device and comes into the cover area of the wireless sensor network, the location of the user will be shown in the map. The nurse can point to the location of the user, and the system can show the user's essential information including his or her photo, name, sex, birthday, and blood type in the right upper side. The bottom of the interface shows the serial number of user's device and the plane position of the user.

The nurse can also find the user's detailed information in the next page including his case history and emergency contact person. The system can set different authorities of each staff in the institution for protecting user's information and also record which staff uses the database, his login/logout time, and executed commands against the database.

The database records user's information in the cloud server or in the console depending on the selection from institution. The design of the database utilizes MySQL which is an open source relational database management system (RDBMS). The database provides multiuser access through wire, wireless, and 3G networks. It also allows the administrator to gather statistics and perform analyses by extracting their physiological information, care histories, the locations of fall, and so on. The danger zones in the institution for the residents also can be found and improved after analyzing the information of fall related.

5. Experimental Results

5.1. Experimental Results of Our Fall Detection Algorithm. The data flow of our fall detection algorithm is shown in Figure 5. How to detect the fall accurately is the most important issue in the caring system. There are five types of the fall happened when people fall including falling forward, falling backward, falling leftward, falling rightward, and falling slowly. The experiment selects fifty people to wear the portable device which performs the fall detection algorithm for verifying the accuracy of fall detection. They perform fifty times for each

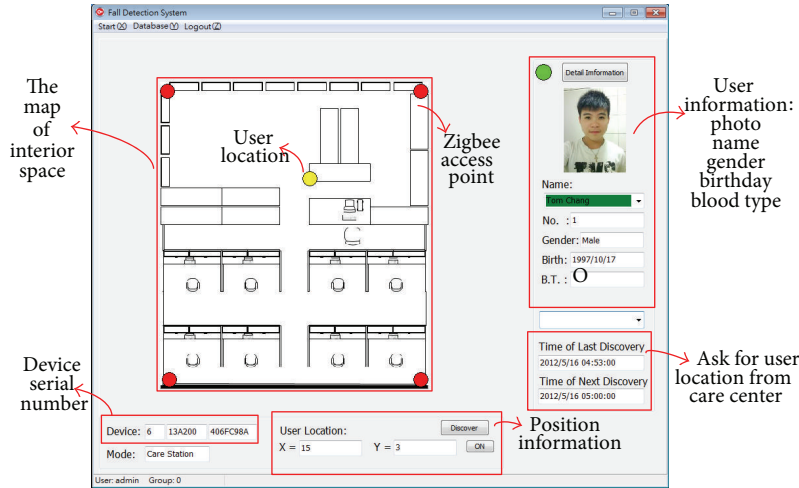


FIGURE 4: The user interface of caring system.

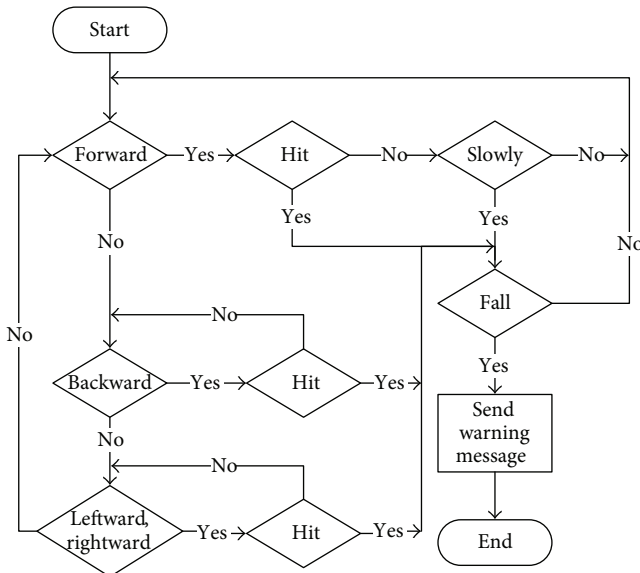


FIGURE 5: The fall detection algorithm.

fall type and the same times for each movement type. 12,500 times of falls and 12,500 times of movements are performed in the experiment.

Table 1 shows the experimental results by recording the hit or miss when a fall happened. We observe that the algorithm achieves the accurate rate of 100% in judging falling forward, falling leftward, and falling slowly. And the algorithm also achieves the accurate rate of 99.8% in judging falling backward, and the accurate rate of 99.9% in judging falling rightward. The algorithm also performs the judgment of different movements in Table 2. For example, there are five times of judgment misses in performing 2,500 times of jumps. The recognition accuracy of 100% is achieved in the judgments of running, going upstairs or downstairs, and lying down. For solving the miss of fall detection, a button is designed for emergency call on the portable device, and the caring system performs the indoor localization function per

TABLE 1: Experimental results of different fall types.

Fall type	Forward	Backward	Leftward	Rightward	Slowly
Hit (times)	2,500	2,495	2,500	2,498	2,500
Miss (times)	0	5	0	2	0
Accuracy (%)	100%	99.8%	100%	99.9%	100%

ten minutes to monitor the location of the user. These two methods can deal with the miss of fall detection effectively in our experiment.

5.2. Performance Comparisons with Different Methods. This work also evaluates the performance of different fall detection methods by using three widely used criteria in fall detection systems. Two major criteria are adopted for performance comparisons in [6, 7, 11] as shown in

$$\text{sensitivity (\%)} = \frac{TP}{TP + FN} \times 100\%, \tag{1}$$

$$\text{specificity (\%)} = \frac{TN}{TN + FP} \times 100\%,$$

where the parameters TP, FP, FN, and TN defined in (1) can be expressed as shown in Table 3.

Parameter TP refers to a subject having fallen, and the detection system can detect it accurately; on the other hand, a system having failed to detect a fall of a subject is denoted by parameter FN. Parameter TN denotes a subject having experienced a false fall, and the system can recognize it correctly. An event in which a subject experiences a false fall yet the system recognizes it as a fall is denoted by parameter FP. These four parameters are used to calculate the times of the four possible recognition events. The criterion *sensitivity* refers to the correct rate of a system that can recognize the falls under all of the fall events. The criterion *specificity* denotes the correct rate of a system that can recognize the false falls under all of the false fall events.

TABLE 2: Experimental results of special movements.

Movement type	Run	Jump	Go upstairs or downstairs	Lie down	Collide
Hit (times)	2,500	2,495	2,500	2,500	2,497
Miss (times)	0	5	0	0	3
Accuracy (%)	100%	99.8%	100%	100%	99.9%

TABLE 3: Comparison of fall detection methods.

Method	Bianchi et al. [6]	Aziz and Robinovitch [7]	Cheng et al. [11]	Ours
Criterion				
Recognition accuracy (%)	96.9	97	95	99.9
Sensitivity (%)	97.5	96	95.3	99.9
Specificity (%)	96.5	98	97.7	99.9

Table 3 reveals that the proposed system has a sensitivity of 99.9% and a specificity of 99.9%. This work has been compared with the methods of Bianchi et al. [6], Aziz and Robinovitch [7], and Cheng et al. [11], respectively. According to Table 3, the method in [7] has a higher recognition accuracy and specificity than those of the methods in [6, 11]. Nevertheless, the proposed system performs better than the three previous designs.

6. Conclusions

In this paper, we design a localized caring system with the capability of fall detection. The fall detection algorithm proposed in the system can achieve an average accurate rate of 99.9% for detecting the fall down. The system allows residents in a care institution to wear a portable device which can reduce more damages from their falls due to the fall detection of high accuracy. The system also enables the localization function to help the nurse to find someone or take care of the residents. The design of cloud database server can record more information of the residents and help the administrator to perform analyses based on different classes of records. The system provides efficient and effective caring services for a care institution.

Acknowledgment

This work is supported in part by Taiwan's Ministry of Education under Project no. 101B-09-027.

References

- [1] A. Sixsmith and N. Johnson, "A smart sensor to detect the falls of the elderly," *IEEE Pervasive Computing*, vol. 3, no. 2, pp. 42–47, 2004.
- [2] K. T. Song and Y. Q. Wang, "Remote activity monitoring of the elderly using a two-axis accelerometer," in *Proceedings of the CACS Automatic Control Conference*, pp. 1–6, 2005.
- [3] T. Zhang, J. Wang, L. Xu, and P. Liu, "Fall detection by wearable sensor and one-class SVM algorithm," *Lecture Notes in Control and Information Sciences*, vol. 345, pp. 858–863, 2006.
- [4] C. Doukas, I. Maglogiannis, P. Tragas, D. Liapis, and G. Yovanof, "Patient fall detection using support Vector Machines," *IFIP International Federation for Information Processing*, vol. 247, pp. 147–156, 2007.
- [5] Q. Li, J. A. Stankovic, M. A. Hanson, A. T. Barth, J. Lach, and G. Zhou, "Accurate, fast fall detection using gyroscopes and accelerometer-derived posture information," in *Proceedings of the 6th International Workshop on Wearable and Implantable Body Sensor Networks (BSN '09)*, pp. 138–143, June 2009.
- [6] F. Bianchi, S. J. Redmond, M. R. Narayanan, S. Cerutti, and N. H. Lovell, "Barometric pressure and triaxial accelerometry-based falls event detection," *IEEE Transactions on Neural Systems and Rehabilitation Engineering*, vol. 18, no. 6, pp. 619–627, 2010.
- [7] O. Aziz and S. N. Robinovitch, "An analysis of the accuracy of wearable sensors for classifying the causes of falls in humans," *IEEE Transactions on Neural Systems and Rehabilitation Engineering*, vol. 19, no. 6, pp. 670–676, 2011.
- [8] G. Yongli, O. S. Yin, and P. Y. Han, "State of the art: a study on fall detection," *World Academy Science, Engineering and Technology*, vol. 62, pp. 294–298, 2012.
- [9] Y. W. Bai, S. C. Wu, and C. L. Tsai, "Design and implementation of a fall monitor system by using a 3-axis accelerometer in a smart phone," *IEEE Transactions on Consumer Electronics*, vol. 58, no. 4, pp. 1269–1275, 2012.
- [10] L. Tong, Q. Song, Y. Ge, and M. Liu, "HMM-based human fall detection and prediction method using tri-axial accelerometer," *IEEE Sensors Journal*, vol. 13, no. 5, pp. 1849–1856, 2013.
- [11] J. Cheng, X. Chen, and M. Shen, "A framework for daily activity monitoring and fall detection based on surface electromyography and accelerometer signals," *IEEE Journal of Biomedical and Health Informatics*, vol. 17, no. 1, pp. 38–45, 2013.
- [12] W. C. Cheng and D. M. Jhan, "Triaxial accelerometer-based fall detection method using a self-constructing cascade-AdaBoost-SVM classifier," *IEEE Journal of Biomedical and Health Informatics*, vol. 17, no. 2, pp. 411–419, 2013.
- [13] C. C. Pu, *Development of a new collaborative ranging algorithm for RSSI indoor location tracking in WSN [Ph.D. thesis]*, Dongseo University, Busan, South Korea, 2009.

Research Article

An 8-Bit ROM-Free AES Design for Low-Cost Applications

Ming-Chih Chen and Wei-Ting Li

Department of Electronic Engineering, National Kaohsiung First University of Science and Technology, Kaohsiung City 811, Taiwan

Correspondence should be addressed to Ming-Chih Chen; mjchen@nkfust.edu.tw

Received 13 September 2013; Accepted 14 October 2013

Academic Editor: Teen-Hang Meen

Copyright © 2013 M.-C. Chen and W.-T. Li. This is an open access article distributed under the Creative Commons Attribution License, which permits unrestricted use, distribution, and reproduction in any medium, provided the original work is properly cited.

We have presented a memory-less design of the advanced encryption standard (AES) with 8-bit data path for applications of wireless communications. The design uses the minimal 160 clock cycles to process a 128-bit data block. For achieving the requirements of low area cost and high performance, new design methods are used to optimize the MixColumns (MC) and Inverse MixColumns (IMC) and ShiftRows (SR) and Inverse ShiftRows (ISR) transformations. Our methods can efficiently reduce the required clock cycles, critical path delays, and area costs of these transformations compared with previous designs. In chip realization, our design with both encryption and decryption abilities has a 29% area increase but achieves 4.85 times improvement in throughput/area compared with the best 8-bit AES design reported before. For encryption only, our AES occupies 3.5 k gates with the critical delay of 12.5 ns and achieves a throughput of 64 Mbps which is the best design compared with previous encryption-only designs.

1. Introduction

The AES algorithm has been widely used in data transmission in wireless communications [1–3] and RFID applications [4, 5]. The AES design with ASIC chip(s) can achieve the requirements of low cost and high performance. The design with low area cost usually also results in low power consumption. The area reduction of designing the AES can be achieved by optimizing the architectures of its subfunctions [4, 6–11], sharing the same operations of subfunctions [6, 9, 10, 12], and reducing the data path of overall architectures [1, 2, 4–7, 10, 12–15]. The feature of inherently iterative AES algorithm can be exploited to reduce the data path of overall architecture. The data path design of AES can be shrunk to 8-bit versions [1, 2, 4–7, 10, 12, 13] for reducing the area cost. The ASIC design of 8-bit AES reported in [5] has the smallest area cost compared with other versions but also leads to the lowest performance since more clock cycles are needed in encryption and decryption. For the objective of reducing the area cost but still keeping the acceptable performance, the proposed AES uses 8-bit data path and minimum clock cycles to perform the encryption/decryption processes.

For the portability of AES in different platforms and CMOS technologies, our AES uses pure combination logic to design the overall circuit without any memory blocks.

The new proposed design methods in major transformations led to the reduction of area cost in AES but still keep the high throughput that meets the requirements of wireless communications. The experiment results show that our AES design has better performance/area ratio compared with previous designs. The remainder of this paper is organized as follows. Section 2 briefly describes the AES algorithm and its transformations. The new designs of transformations and overall AES architecture are proposed in Section 3. Section 4 describes experimental results and comparisons with other previous designs. Finally, conclusions are given in Section 5.

2. AES Algorithm

2.1. AES Algorithm. The AES algorithm for 8-bit data path that processes a 128-bit data block will take at least 160 rounds. The encryption processes perform ShiftRows (SR), SubBytes (SB), MixColumns (MC), and AddRoundKey (ARK) transformations. A separate KeyExpansion (KE) unit is required to generate the K th round key for each ARK. The decryption process has three reversed transformations, InvShiftRows (ISR), InvSubBytes (ISB), and InvMixColumns (IMC), and one ARK. The normal rounds perform the four inversed transformations. The round keys operated in the decipher

process are the reverse of the round keys generated in each round in the cipher process.

2.2. AES Transformations. Four kinds of transformations and one key generation unit in the AES algorithm are described as follows.

(a) *SB/ISB Transformations.* The transformations are non-linear substitution operations where each byte of the input state is computed with multiplicative inverse (MI) in $GF(2^8)$ and followed by an affine transformation (AF) over the same field. Similarly, the ISB transformation performs the inverse affine transformation (IAF) followed by the operation of MI in $GF(2^8)$.

(b) *MC/IMC Transformations.* The transformations operate column-by-column on the 4×4 byte array and treat each column as four-term polynomial with coefficients over $GF(2^8)$. The MC transforms each column to a new one by multiplying it with a constant polynomial $a(x) = \{03\}x^3 + \{01\}x^2 + \{01\}x + \{02\}$ modulo $x^4 + 1$. The IMC operation is a multiplication of each column with $b(x) = a^{-1}(x) = \{0B\}x^3 + \{0D\}x^2 + \{09\}x + \{0E\}$ modulo $x^4 + 1$.

(c) *SR/ISR Transformations.* The SR transformation rotates the last three rows of the state to the left by one, two, or three bytes depending on the row numbers. The ISR rotates them in the inverse direction of the SR.

(d) *ARK Transformation.* In each round, the ARK transformation performs an addition of the state with the round key using a bitwise XOR operation.

(e) *KE Unit.* In each round, the KE unit generates a new 128-bit round key for the XOR operation with the state in the ARK transformation.

3. Design of Our AES Architecture

3.1. Designs of Major Transformations. The optimization of separate transformations focuses on two major transformations, SR and MC, and their inverses, ISR and IMC. The designs of these transformations are described as follows.

(a) *The Design of SR/ISR Unit.* In this paper, we propose a combined SR/ISR design as shown in Figure 1. It uses twelve 8-bit registers for receiving and storing data from MC or ARK units. The output sequences are generated after performing the SR rotations. Equation (1) shows the original 4 by 4 state matrix and the output state matrix after the SR rotations. The original states in the first row after performing the SR are unchanged. The states in the second, third, and fourth rows are rotated by right shifting one, two, and three positions, respectively,

$$\begin{pmatrix} S_{12} & S_8 & S_4 & S_0 \\ S_{13} & S_9 & S_5 & S_1 \\ S_{14} & S_{10} & S_6 & S_2 \\ S_{15} & S_{11} & S_7 & S_3 \end{pmatrix} \Rightarrow \begin{pmatrix} S_{12} & S_8 & S_4 & S_0 \\ S_1 & S_{13} & S_9 & S_5 \\ S_6 & S_2 & S_{14} & S_{10} \\ S_{11} & S_7 & S_3 & S_{15} \end{pmatrix}. \quad (1)$$

Original Input States Output States After SR

For completing the rotation sequences, several multiplexers are added in Figure 1. The states are inputted to the SR unit

by the sequences of their state number. Therefore, the state S_0 is the first one that is inputted to the SR in the first clock cycle, and the state S_{15} is the last input to the SR in the sixteenth clock cycle. The output sequences of the states in the first row are unchanged after performing the SR rotations. The input state S_0 , S_4 , and S_8 are stored in register $R8$, $R4$, and $R0$, respectively, after several clock cycles. The state S_{12} is stored in register $R0$ after outputting the state S_0 from register $R8$. In the second row, the first state S_1 is delayed to the last one and other states S_5 , S_9 , and S_{13} bypass the state S_1 using the multiplexer. These three states are outputted before the state S_1 .

The states S_2 and S_6 in the third row are delayed behind states S_{10} and S_{14} after the rotation of the third row. In the fourth row of original state matrix, the state S_{15} is the last one but becomes the first output state of that row after performing the SR. Similarly, the ISR performs the rotations in the inverse direction of the SR by using the multiplexers to bypass some states for outputting the correct sequences. The design in [13] is the best method to solve the SR and ISR rotations reported so far, but our design can reduce four 8-bit registers and shorten the critical path delay of the unit.

(b) *The Design of MC/IMC Unit.* In our AES design, the MC, and IMC units are separated to reduce the complexity of the data paths. Equation (2) shows four input states S_0 , S_1 , S_2 , and S_3 that multiply constant values $\{03\}$, $\{02\}$, $\{01\}$, and $\{01\}$, respectively, in Galois Field $GF(2^8)$ for generating output states S'_0 to S'_3 . The equation also shows that the constant values in the second, third, and fourth rows are rotated to left by one, two, and three positions corresponding to the first row

$$\begin{pmatrix} S'_0 \\ S'_1 \\ S'_2 \\ S'_3 \end{pmatrix} = \begin{pmatrix} 02 & 03 & 01 & 01 \\ 01 & 02 & 03 & 01 \\ 01 & 01 & 02 & 03 \\ 03 & 01 & 01 & 02 \end{pmatrix} \times \begin{pmatrix} S_0 \\ S_1 \\ S_2 \\ S_3 \end{pmatrix}. \quad (2)$$

Output States After MC Constant Matrix Original States

As shown in Figure 2, our MC design uses eight 8-bit registers to store the states and uses two multiplication units ($\{02\} \times X$) and ($\{03\} \times X$) for performing the multiplication in (2). These two multiplication units are realized by simple bit-level XOR operations. The MC design uses two levels of registers. The four registers in the first level receive data from the MC or the ARK units. The second-level registers prepare calculation operations for the outputs. For example, the result of output state S'_0 is calculated as $(\{02\} \times S_0 + \{03\} \times S_1 + \{01\} \times S_2 + \{01\} \times S_3)$. The states S_1 , S_2 , S_3 , and S_4 are inputted to registers $R4$, $R5$, $R6$, and $R7$, respectively, after four clock cycles. In the next cycle, the four states are stored in registers $R0$ – $R3$, respectively, and perform the multiplications ($\{02\} \times R0$) and ($\{03\} \times R1$). The MC unit outputs the states S'_0 – S'_3 in the subsequent four clock cycles. At the same time, the next four states are inputted to registers $R4$ – $R7$ and wait for performing the multiplication with the constant matrix. The MC unit needs sixteen clock cycles to complete the calculation of a 128-bit state. The design in [1, 4–7, 14, 15] is the best method to solve the MC and IMC operations reported before, but our design can further reduce twenty-four 8-bit registers and shorten the critical path delay of the MC unit. The similar

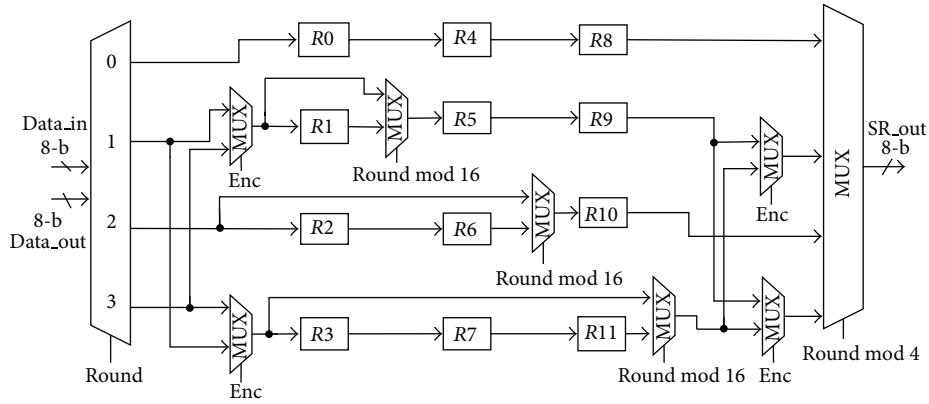


FIGURE 1: Proposed combined SR/ISR architecture.

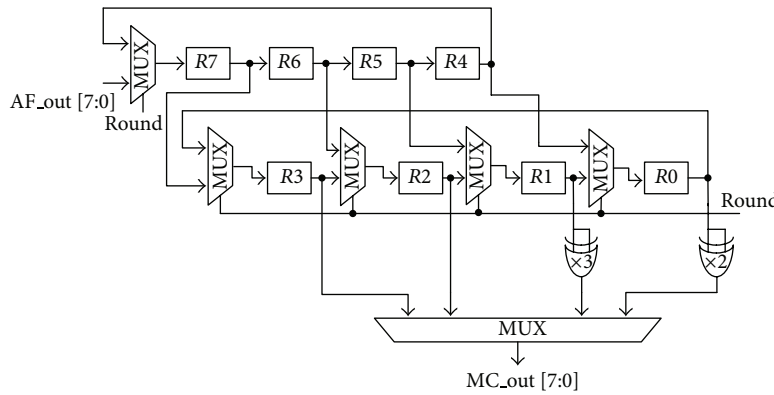


FIGURE 2: Proposed MC architecture.

optimization results are also obtained in the design of IMC unit.

3.2. *The Design of Overall Architecture.* We realized iterative AES architecture designs using TSMC 0.18 μm cell library. Figure 3 shows the 8-bit AES processor architecture. A plaintext block and the encryption key are loaded to the AES through the 8-bit input ports *data.in* and *key.in*. The *enc* signal is used to select the encryption or decryption processes. The SB can be realized by the calculation of Multiplicative Inverse (MI) in $\text{GF}((2^4)^2)$ and Affine Transformation (AF) units. The ISB can be realized by the same MI calculation with SB and inversed affine transformation (IAF) units. For reducing the area cost of the combined implementations of SB/ISB units, the MI logic is usually shared. The key expansion unit is used to generate and output the required 8-bit round key to the ARK. Since the round keys are in reverse order in decryption, the inverse cipher process can start only after generating the last round key. Afterward, the key expansion with the same round keys can be executed concurrently with the decryption process.

4. Experimental Results

In Table 1, various 8-bit AES designs in different technologies are listed for comparison. The designs in [1, 4, 7, 14] only have

the encryption ability. The design in [4] is the encryption-only version of the previous design [5], for application in radio frequency identification (RFID). The design in [5] adopts the clock gating method to reduce the power consumption. One pipeline stage is used to reduce the critical path delay in the SB/ISB design. The SR/ISR units are implemented by random access memory (RAM). In [7], the encryption-only design merges the ARK and SR operations by using four pipeline stages to generate the correct output order of the computed state. The design in [1] provides a low power AES design for the RFID application. It uses gated clock design to reduce unwanted switching activity, the same approach as in [5]. Good and Benaissa [14] proposed a low power/area AES chip design that provides a series of finite-field doubling, tripling, and XOR operations to perform the MC transformation. It also adopts separate data and key memories, the same approach as in [1], for parallel processing the state and round key.

In Table 1, we provide two kinds of implementation information of our AES design including AES with encryption ability and AES with encryption/decryption abilities in the chip level. The chip design is used to compare with other chip results that have their circuits fabricated.

We observe that most realizations are encryption only due to the fast verification of their designs. Most realizations of 8-bit data path AES require more clock cycles to compute

TABLE 1: Performance comparison of different 8-bit AES designs.

Design	Tech. (um)	Mode	Max. clock freq. (MHz)	Clock cycles	Area (k-gates)	Max. throughput (Mbps)	Max. throughput/area (Mbps/k-gates)	Power consumption
Feldhofer et al. [4] (Syn.)	0.35	Enc only	0.1	992	3.628	0.013	0.0036	26.9 uW at 100 KHz
Kaps and Sunar [7] (Syn.)	0.13	Enc only	0.5	534	4.07	0.12	0.0295	23.85 uW at 500 KHz
Kim et al. [1] (Syn.)	0.25	Enc only	0.1	870	3.9	0.015	0.0038	4.85 uW at 100 KHz
Feldhofer and Wolkerstorfer [5] (chip)	0.35	Both	80	Enc: 1,032 Dec: 1,165	3.4	9.9	2.91	4.5 uW at 100 KHz 1.5 V
Good and Benaissa [14] (chip)	0.13	Enc only	12	356	5.5	4.31	0.78	99 uW at 12 MHz 0.8 V
Ours (chip)	0.18	Enc only	80	160	3.5	64	18.3	65 uW at 80 MHz 1.8 V
Ours (chip)	0.18	Both	60	160	4.4	48	10.9	93 uW at 60 MHz 1.8 V

*Tech.: technology; Syn.: synthesis; Freq.: frequency.

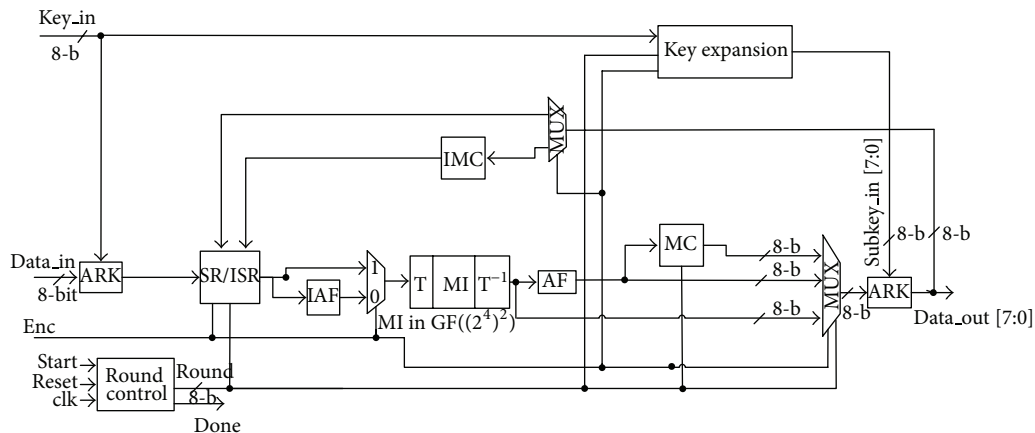


FIGURE 3: Proposed AES architecture.

a 128-bit data block, resulting in smaller throughput rate. Therefore, most realizations are suitable for those applications with low frequency and throughput rate requirement, such as RFID. On the other hand, our design with higher throughput can be used in applications such as 802.11 series wireless network. Our AES design with only encryption ability occupies 3.5 k gates with the critical delay of 12.5 ns. The major improvement of our AES in this version is to minimize the required number of clock cycles and critical path delay for processing MC and SR operations by our architecture designs.

The area cost and critical path delay of our AES are similar with the best design in [5]. But our design can achieve a throughput of 64 Mbps which is the best design compared with previous encryption-only designs. The area cost of our AES design with both encryption and decryption abilities

increases about 29%, but the throughput improves 4.85 times compared with the best design in [5]. From the experimental results, we also observe that our AES design has the best normalized performance of throughput per gate compared with other previous designs.

5. Conclusions

In this paper, we have presented new design methods of AES transformations and their architecture. The major transformations, SR/ISR and MC/IMC, dominate the required clock cycles and path delays for processing the data encryption and decryption. We presented two design methods that can efficiently optimize these transformations, and the proposed architecture design can improve the throughput but keep low area cost compared with other previous designs. The design

is suitable for area-limited applications that require high throughput, such as wireless communications. The implementation results demonstrate that the proposed design has the highest throughput with low area cost.

Acknowledgments

This work is supported in part by Taiwan's Ministry of Education under Project no. 101B-09-027. One of the authors would like to thank Professor Shen-Fu Hsiao for providing the comments.

References

- [1] M. Kim, J. Ryou, Y. Choi, and S. Jun, "Low power AES hardware architecture for radio frequency identification," in *Advances in Information and Computer Security*, vol. 4266 of *Lecture Notes in Computer Science*, pp. 353–363, Springer, Berlin, Germany, 2006.
- [2] O. Song and J. Kim, "An efficient design of security accelerator for IEEE 802.15.4 wireless sensor networks," in *Proceedings of the 7th IEEE Consumer Communications and Networking Conference*, pp. 1–5, January 2010.
- [3] Y. T. Tsou, C. S. Lu, and S. Y. Kuo, "MoteSec-aware: a practical secure mechanism for wireless sensor networks," *IEEE Transactions on Wireless Communications*, vol. 12, no. 6, pp. 2817–2829, 2013.
- [4] M. Feldhofer, S. Dominikus, and J. Wolkerstorfer, "Strong authentication for RFID systems using the AES algorithm," in *Cryptographic Hardware and Embedded Systems—CHES 2004*, vol. 3156 of *Lecture Notes in Computer Science*, pp. 357–370, Springer, Berlin, Germany, 2004.
- [5] M. Feldhofer and J. Wolkerstorfer, "Strong crypto for RFID tags—a comparison of low-power hardware implementations," in *Proceedings of the IEEE International Symposium on Circuits and Systems*, pp. 1839–1842, May 2007.
- [6] T. Good and M. Benaissa, "AES on FPGA from the fastest to the smallest," in *Cryptographic Hardware and Embedded Systems—CHES 2005*, vol. 3659 of *Lecture Notes in Computer Science*, pp. 427–440, Springer, Berlin, Germany, 2005.
- [7] J. P. Kaps and B. Sunar, "Energy comparison of AES and SHA-1 for ubiquitous computing," in *Emerging Directions in Embedded and Ubiquitous Computing*, vol. 4097 of *Lecture Notes in Computer Science*, pp. 372–381, Springer, Berlin, Germany, 2006.
- [8] W.-T. Huang, C. H. Chang, C. W. Chiou, and S.-Y. Tan, "Non-XOR approach for low-cost bit-parallel polynomial basis multiplier over $GF(2^m)$," *IET Information Security*, vol. 5, no. 3, pp. 152–162, 2011.
- [9] M. M. Wong, M. L. D. Wong, A. K. Nandi, and I. Hijazin, "Composite field $GF(((2^2)^2)^2)$ Advanced Encryption Standard (AES) S-box with algebraic normal form representation in the subfield inversion," *IET Circuits, Devices and Systems*, vol. 5, no. 6, pp. 471–476, 2011.
- [10] T. A. Pham, M. S. Hasan, and H. Yu, "Area and power optimisation for AES encryption module implementation on FPGA," in *Proceedings of the 18th International Conference on Automation and Computing*, pp. 1–6, September 2012.
- [11] M. M. Wong, M. L. D. Wong, A. K. Nandi, and I. Hijazin, "Construction of optimum composite field architecture for compact high-throughput AES S-Boxes," *IEEE Transactions on Very Large Scale Integration Systems*, vol. 20, no. 6, pp. 1151–1155, 2012.
- [12] J. Chu and M. Benaissa, "Low area memory-free FPGA implementation of the AES algorithm," in *Proceedings of the 22nd International Conference on Field Programmable Logic and Applications*, pp. 623–626, August 2012.
- [13] H. Li and J. Li, "A new compact architecture for AES with optimized ShiftRows operation," in *Proceedings of IEEE International Symposium on Circuits and Systems*, pp. 1851–1854, May 2007.
- [14] T. Good and M. Benaissa, "692-nW advanced encryption standard (AES) on a 0.13- μm CMOS," *IEEE Transactions on Very Large Scale Integration Systems*, vol. 18, no. 12, pp. 1753–1757, 2010.
- [15] K. Thongkhome, C. Thanavijitpun, and S. Choomchuay, "A FPGA design of AES core architecture for portable hard disk," in *Proceedings of the 8th International Joint Conference on Computer Science and Software Engineering*, pp. 223–228, May 2011.

Research Article

Impacts of Light Rail Transit Tram on the Voltage and Unbalance of the Distribution System

Cheng-Ting Hsu, Hung-Ming Huang, Tsun-Jen Cheng, and Lian-Jou Tsai

Department of Electrical Engineering, Southern Taiwan University of Science and Technology, Tainan 710, Taiwan

Correspondence should be addressed to Tsun-Jen Cheng; chengtj@mail.stust.edu.tw

Received 10 September 2013; Accepted 4 October 2013

Academic Editor: Teen-Hang Meen

Copyright © 2013 Cheng-Ting Hsu et al. This is an open access article distributed under the Creative Commons Attribution License, which permits unrestricted use, distribution, and reproduction in any medium, provided the original work is properly cited.

This paper presents the three-phase voltage and unbalance analysis for the distribution system with the loading of a light rail transit (LRT) tram. To investigate the dynamic responses of the system voltage and current, this paper adopts the Alternative Transients Program (ATP) software to model and simulate a multigrounded four-wire distribution system with an LRT loading. Two different definitions about unbalance are used to evaluate the problem. In this paper, the traction supply substation (TSS) with a single-phase transformer configuration is designed first for providing the electric power to the trams of LRT. However, it may result in the significant neutral line current and unbalance phenomenon to deteriorate the power quality of the distribution system. A Le-Blanc connection transformer in the TSS is therefore proposed to solve the problems.

1. Introduction

Many counties and cities in the world are keen on planning light rail transit (LRT) system to meet the growing demand of public transportation. The LRT takes the advantages of low cost, low noise, low pollution, mature technology, short construction period, and easy maintenance. In addition, it may utilize electrical power from distribution systems of power grid because of its lower power requirements than the traditional railway and mass rapid transit systems. In general, it is very suitable to use the LRT as the public transport of the metropolitan areas and a variety of urban transport connections [1–3]. The tram of LRT is a heavy and irregular load, and it carries many power electronic equipment; the power quality of the distribution system can inevitably be affected [4, 5]. For the distribution system with the LRT, it may cause voltage fluctuation, unbalance, and harmonic and other power quality issues. To ensure the power quality, utilities have published many limits on these issues.

The traction power substation (TSS) supplies the LRT with either alternating current (AC) or direct current (DC) electric power. Mostly, the AC power may cause three-phase unbalance problem, while the DC power supply will generate

a harmonic problem. In this paper, the AC supply systems are considered, and the three-phase unbalance problem is the main investigation issue. This study case is based on a typical Taiwan Power Company (Taipower) 11.4 kV distribution feeder with four-wire and multigrounded system [6]. And the ATP [7] software is applied to establish the selected distribution feeder and the different AC power supply structures of the LRT. After that, it is used to execute three different operating scenarios. The instantaneous three-phase voltage and current and neutral line current are therefore simulated to calculate unbalance. By the way, two different definitions, the negative sequence unbalance ratio and unbalance factors [8], are both adopted for evaluating the three-phase unbalance of the distribution system.

2. LRT Impacts on the Unbalance of the Distribution Systems

Three-phase voltages (V_A , V_B , and V_C) can be decomposed into three separate phase sequence (V_1), the negative phase sequence (V_2), and the zero-phase sequence (V_0) components, as shown in (1). It is well known that only the positive

phase sequence exists in the balanced system. Consider

$$\begin{bmatrix} V_0 \\ V_1 \\ V_2 \end{bmatrix} = \frac{1}{3} \begin{bmatrix} 1 & 1 & 1 \\ 1 & a & a^2 \\ 1 & a^2 & a \end{bmatrix} \begin{bmatrix} V_A \\ V_B \\ V_C \end{bmatrix}, \quad (1)$$

where $a = 120\angle 0^\circ$. Negative sequence unbalance in a three-phase system is defined as the ratio of the magnitude of the negative sequence component to the magnitude of the positive sequence component, while the zero sequence unbalance is defined as the magnitude of the zero sequence component to the magnitude of the positive sequence component, expressed as a percentage [8]. This definition can be applied for either voltage or current as shown in the following:

$$\begin{aligned} d_2 (\%) &= \frac{V_2}{V_1} \times 100\%, \\ d_0 (\%) &= \frac{V_0}{V_1} \times 100\%, \\ m_2 (\%) &= \frac{I_2}{I_1} \times 100\%, \\ m_0 (\%) &= \frac{I_0}{I_1} \times 100\%. \end{aligned} \quad (2)$$

In addition, three-phase voltage unbalance factor (VUF) and current unbalance factor (IUF) can also be defined as the ratio of the maximum deviation of a voltage or current from the average value to the average value, expressed in percentage, using phase-to-phase voltage or current as follows:

$$\begin{aligned} \text{VUF} (\%) &= \frac{\text{Max}(|V_{\text{avg}} - V_{AB}|, |V_{\text{avg}} - V_{BC}|, |V_{\text{avg}} - V_{CA}|)}{V_{\text{avg}}} \\ &\times 100\%, \\ \text{IUF} (\%) &= \frac{\text{Max}(|I_{\text{avg}} - I_{AB}|, |I_{\text{avg}} - I_{BC}|, |I_{\text{avg}} - I_{CA}|)}{I_{\text{avg}}} \\ &\times 100\%, \end{aligned} \quad (3)$$

where

$$V_{\text{avg}} = \frac{V_{AB} + V_{BC} + V_{CA}}{3}, \quad I_{\text{avg}} = \frac{I_{AB} + I_{BC} + I_{CA}}{3}. \quad (4)$$

The voltage and current unbalance ratio limitations are set with different provisions according to different types of load duration by different institutions. In general, the voltage service of negative sequence unbalance (d_2) is less than 3%. The current unbalance can be considerably higher, especially when single-phase loads are present [8]. For the rail systems in Taiwan, the value is limited to 1% and 1.2% for one day and 15 minute measurement period, respectively.

3. Le-Blanc Connection Transformer

A single-phase power supply for LRT will give rise to the problem of three-phase unbalance. In general, this problem can be improved by using the static var compensators (SVC) or a special connection of transformers, such as the Le-Blanc transformer connection. The purpose of the Le-Blanc transformer connection is to convert a three-phase system into two single-phase systems with symmetrical primary current. Figure 1 shows the wiring diagram of the Le-Blanc transformer [9]. The secondary outputs of two single-phase voltages, V_m and V_t , have the characteristics of equal magnitude and 90 degrees phase shift. N_1 and N_2 are the number of winding turns at primary and secondary, respectively. Figure 2 gives the voltage vector diagram of the transformer.

The relations of the primary and secondary voltages of the Le-Blanc transformer can be written as

$$\begin{aligned} V_m &= \frac{1}{\sqrt{3}} \frac{N_2}{N_1} (V_B + V_C - 2V_A), \\ V_t &= \frac{N_2}{N_1} (V_B - V_C). \end{aligned} \quad (5)$$

The primary currents of the transformer are given by

$$\begin{aligned} I_A &= I_{AB} - I_{CA}, \\ I_B &= I_{BC} - I_{AB}, \\ I_C &= I_{CA} - I_{BC}. \end{aligned} \quad (6)$$

Also, the primary and secondary currents are dependent and can be expressed as

$$\begin{aligned} I_{CA} &= \frac{1}{\sqrt{3}} \frac{N_2}{N_1} I_m - \frac{1}{3} \frac{N_2}{N_1} I_t, \\ I_{BC} &= \frac{2}{3} \frac{N_2}{N_1} I_t, \\ I_{AB} &= -\frac{1}{\sqrt{3}} \frac{N_2}{N_1} I_m - \frac{1}{3} \frac{N_2}{N_1} I_t. \end{aligned} \quad (7)$$

Substituting (7) into (6) will result in

$$\begin{aligned} I_A &= -\frac{2}{\sqrt{3}} \frac{N_2}{N_1} I_m, \\ I_B &= \frac{1}{\sqrt{3}} \frac{N_2}{N_1} I_m + \frac{N_2}{N_1} I_t, \\ I_C &= \frac{1}{\sqrt{3}} \frac{N_2}{N_1} I_m - \frac{N_2}{N_1} I_t. \end{aligned} \quad (8)$$

Furthermore, the relation of voltages and currents at the secondary side can be expressed as

$$I_m = Y_m V_m, \quad I_t = Y_t V_t, \quad (9)$$

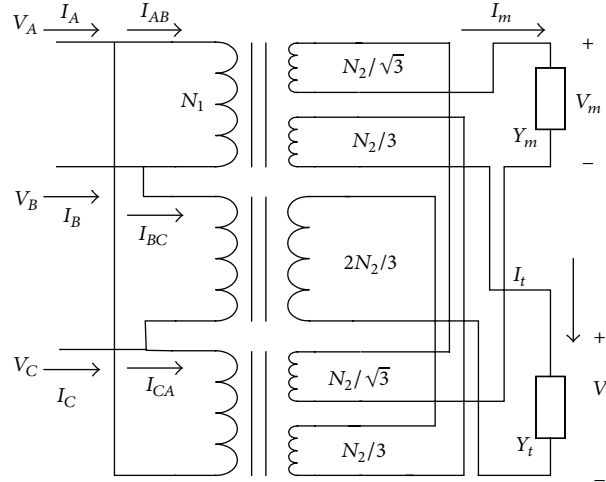


FIGURE 1: The Le-Blanc transformer connection diagram.

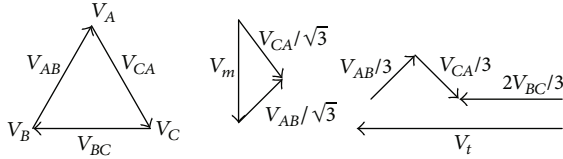


FIGURE 2: The Le-Blanc transformer voltage vector diagram.

where Y_m and Y_t are the admittances of the loading at secondary side. The primary line currents are thus obtained by substituting (9) into (8) as follows:

$$\begin{aligned} I_A &= -\frac{2}{\sqrt{3}} \frac{N_2}{N_1} Y_m V_m, \\ I_B &= \frac{1}{\sqrt{3}} \frac{N_2}{N_1} Y_m V_m + \frac{N_2}{N_1} Y_t V_t, \\ I_C &= \frac{1}{\sqrt{3}} \frac{N_2}{N_1} Y_m V_m - \frac{N_2}{N_1} Y_t V_t. \end{aligned} \quad (10)$$

It is found that the sum of the primary line currents must be zero, which keeps three-phase balanced, regardless of the load at the secondary side.

4. Distribution System and LRT Modeling

Figure 3 shows the equivalent model of a multigrounded four-wire distribution system by the ATP software. The 69 kV high voltage side of the distribution substation is simplified as an ideal three-phase source with a short circuit capacity of 1000 MVA. The test feeder is fed by a 69 kV/11.4 kV, 25 MVA power transformer sited in the distribution substation. The primary feeders and laterals are all overhead construction and their parameters are listed in Table 1. In addition, there are 13 distribution transformers to serve the customers that are distributed along the test feeder. The active power and reactive power consumption of the customers in the feeder

TABLE 1: Line parameters.

Impedance	Conductor			
	Feeder		Lateral	
	Phase	Neutral	Phase	Neutral
Resistance (Ω/km)	0.131	0.209	0.945	0.945
Resistance (Ω/km)	0.364	0.382	0.355	0.355

are 4560 kW and 3420 kvar, respectively. Besides, a capacitor bank with a rating capacity of 2100 kvar is installed at the end terminal of the feeder. It is assumed that the test distribution system is operated under balanced condition. The grounding resistance of the neutral point of the substation power transformer and the grounding points along the neutral wire are assumed to be 1 ohm and 25 ohm, respectively.

The electrical power of the tram must be fed from the TSS. The site of the TSS is 300 m from the distribution substation along the feeder. Figure 4 shows the TSS with a single-phase transformer to supply the tram. In Figure 5, the transformer is replaced with the proposed Le-Blanc transformer connection, which converts a three-phase power into two single-phase powers to supply the tram. The AC power voltage is further step down by the transformer installed at the tram and is rectified into DC power then. Finally, it is converted into controllable voltage and frequency AC power to drive the induction motors with a total capacity of 720 kW for the tram.

5. Voltages and Unbalance Analysis

This section is to explore the influence of unbalance, voltage drop, and the neutral line current variation on the three-phase four-wire multi-grounding distribution feeder system with AC power supply to the tram.

5.1. Case 1: Original System. This case executes the relative analysis without considering the tram loading. First, the ATP software is applied to obtain the power system responses.

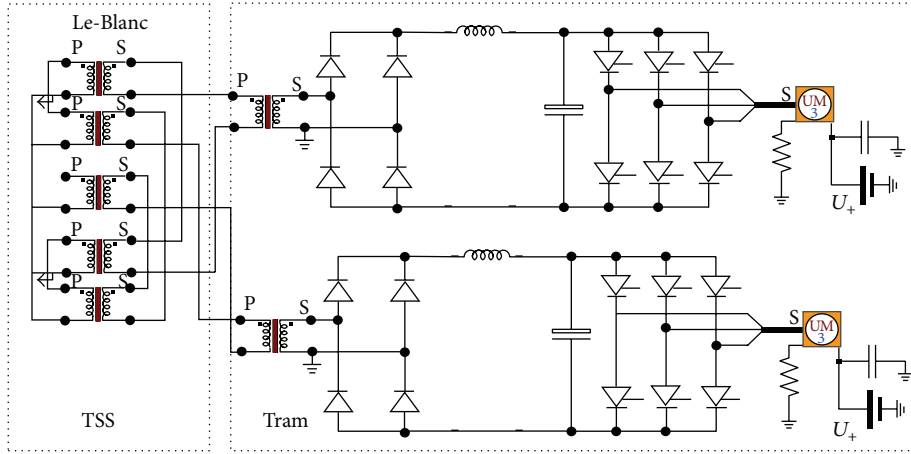


FIGURE 5: A TSS with the Le-Blanc transformer connection.

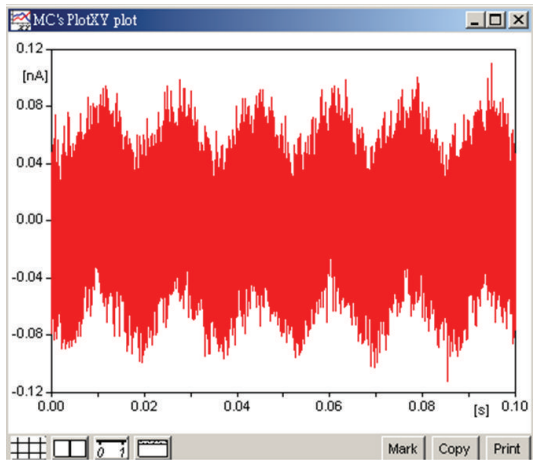


FIGURE 6: Instantaneous neutral line current at substation terminal for Case 1.

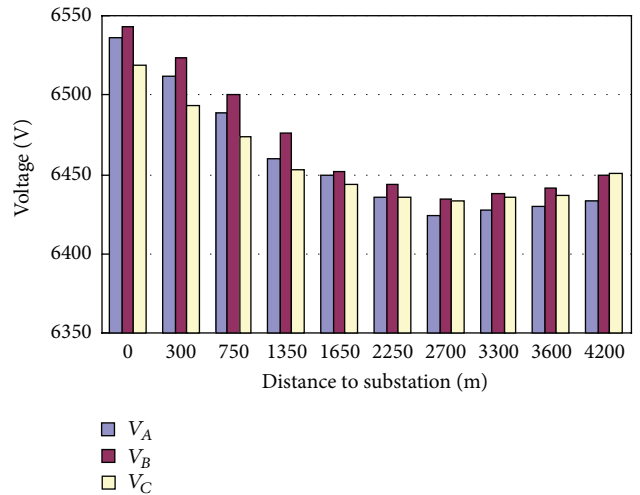


FIGURE 8: Three-phase voltage magnitudes at different feeder sites for Case 2.

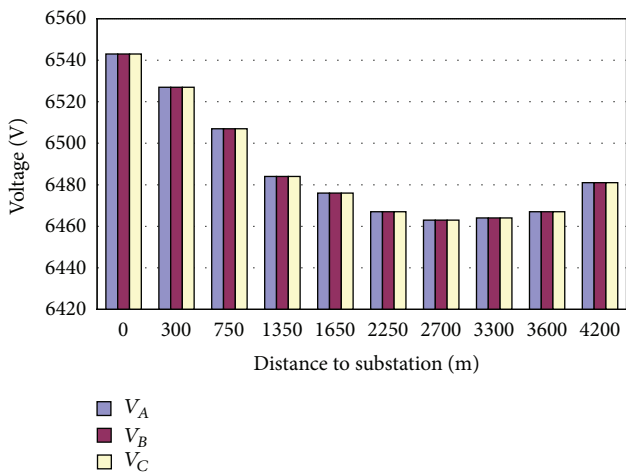


FIGURE 7: Three-phase voltage magnitudes at different feeder sites for Case 1.

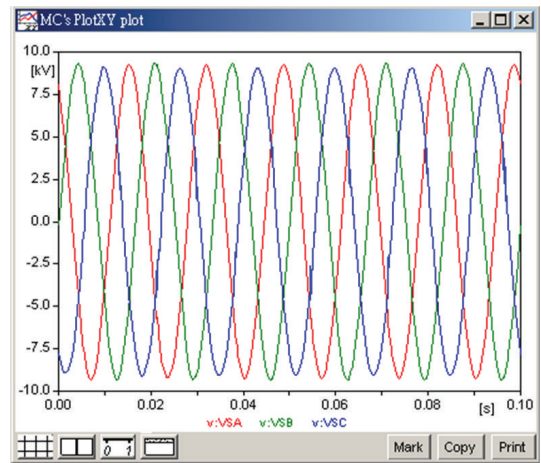


FIGURE 9: Instantaneous three-phase voltages at substation terminal for Case 2.

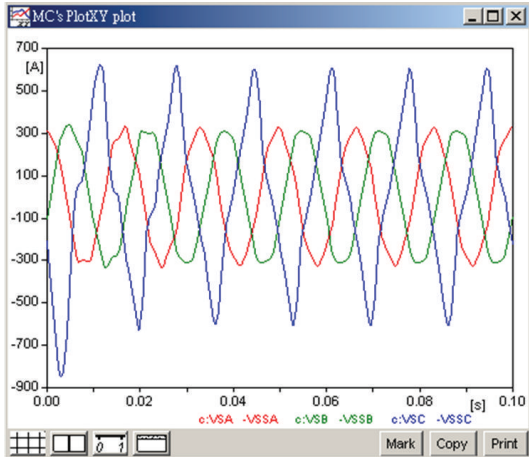


FIGURE 10: Instantaneous three-phase currents at substation terminal for Case 2.

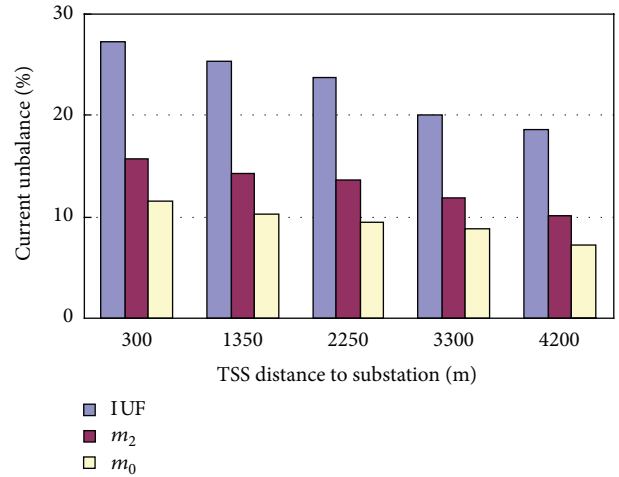


FIGURE 13: Current unbalance at substation terminal with different TSS sites for Case 2.

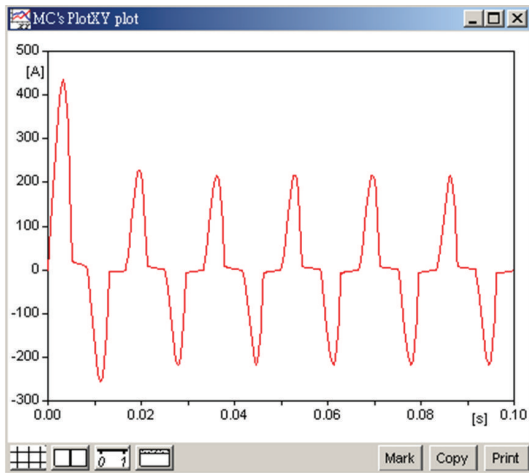


FIGURE 11: Instantaneous neutral line current at substation terminal for Case 2.

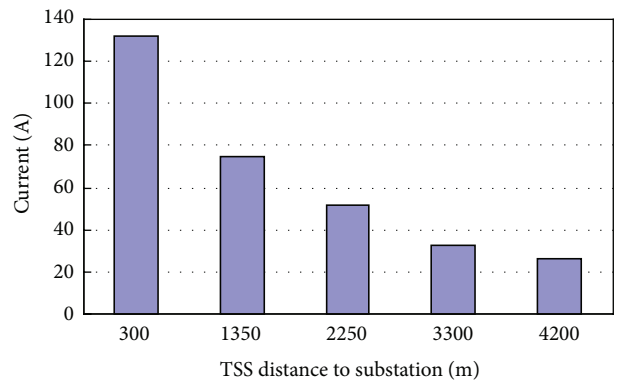


FIGURE 14: Neutral current at substation terminal with different TSS sites for Case 2.

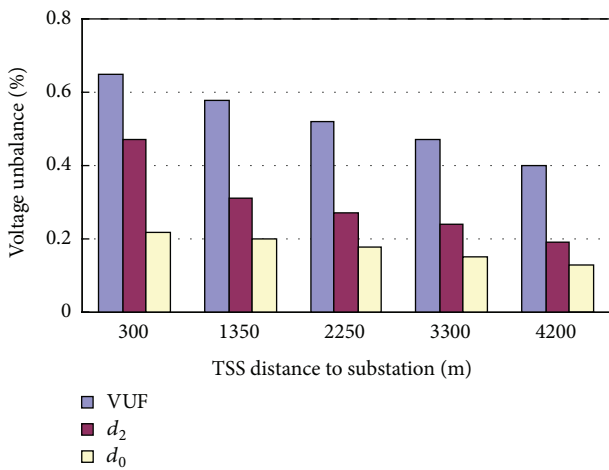


FIGURE 12: Voltage unbalance at substation terminal with different TSS sites for Case 2.

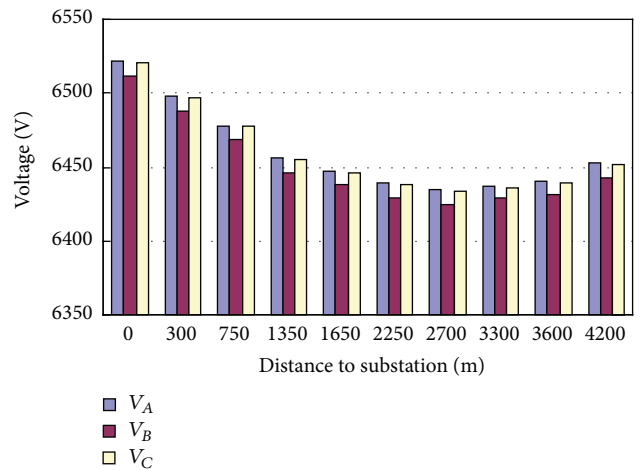


FIGURE 15: Three-phase voltage magnitudes at different feeder sites for Case 3.

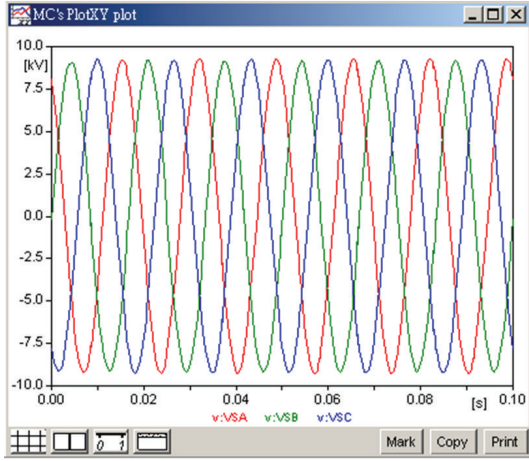


FIGURE 16: Instantaneous three-phase voltages at substation terminal for Case 3.

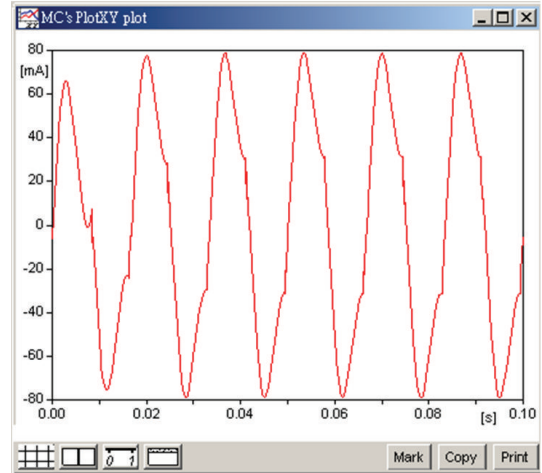


FIGURE 18: Instantaneous neutral line current at substation terminal for Case 3.

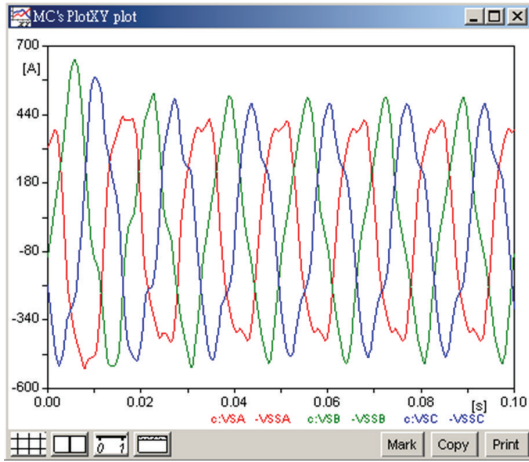


FIGURE 17: Instantaneous three-phase currents at substation terminal for Case 3.

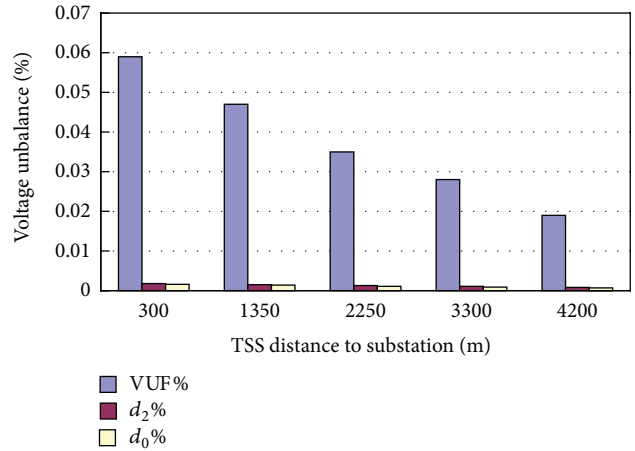


FIGURE 19: Voltage unbalance at substation terminal with different TSS sites for Case 3.

Figure 18. In this case, the voltage unbalances are calculated as $VUF = 0.059\%$, $d_2 = 0.0018\%$, and $d_0 = 0.0016\%$, and the current unbalances are obtained as $IUF = 0.06\%$, $m_2 = 0.0105\%$, and $m_0 = 0.0127\%$ at the secondary side of the substation.

Figures 19 and 20 depict the voltage and current unbalance as the TSS is in different locations away from the secondary side of the substation. The voltage unbalances are calculated as $VUF = 0.035\%$, $d_2 = 0.0013\%$, and $d_0 = 0.001\%$ when the TSS is located at a distance of 2250 m from the secondary side of the substation, and the current unbalances are obtained as $IUF = 0.0043\%$, $m_2 = 0.0092\%$, and $m_0 = 0.01\%$. The voltage unbalances are calculated as $VUF = 0.019\%$, $d_2 = 0.0008\%$, and $d_0 = 0.0007\%$ as the TSS is installed at the 4200 m point away from the secondary side of the substation, and the current unbalances are determined as $IUF = 0.0027\%$, $m_2 = 0.0074\%$, and $m_0 = 0.007\%$. Figure 21 illustrates the neutral line currents for different locations of the TSS. The neutral line currents are 73.5 mA, 26.4 mA,

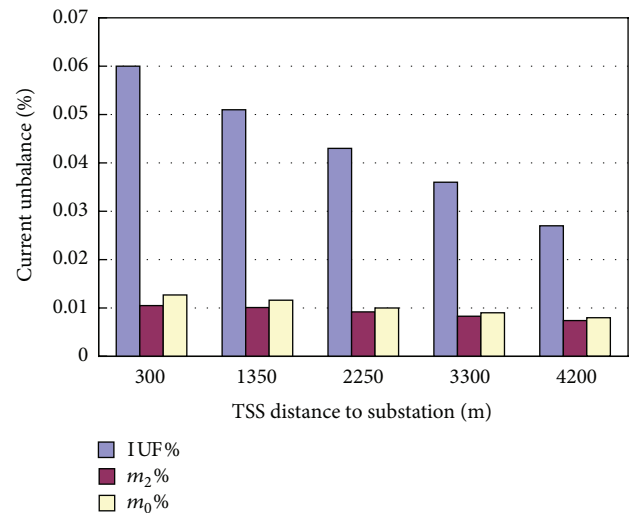


FIGURE 20: Current unbalance at substation terminal with different TSS sites for Case 3.

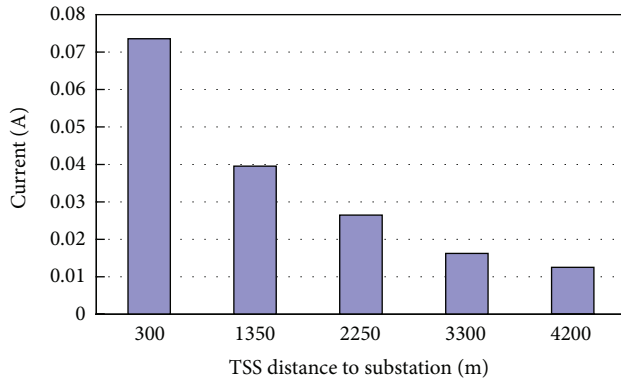


FIGURE 21: Neutral current at substation terminal with different TSS sites for Case 3.

and 12.5 mA when the TSS is located at 300 m, 2250 m, and 4200 m points, respectively.

6. Conclusions

For the original test system, it is a three-phase balance system. However, the neutral line current flowing through the substation transformer is increased to 132 A when the TSS of the LRT adopts a single-phase transformer to supply the tram. In addition, the negative voltage and current sequence unbalances at the secondary side of the substation are obtained as 0.47% and 15.7%, respectively. To improve the poor power quality phenomenon, the TSS with the proposed Le-Blanc connection transformer is then used. It is found that the neutral line current flowing through the transformer and the negative voltage sequence unbalance decreases to the values of 0.074 A and 0.002%, respectively. It is concluded that the proposed TSS design has a significant effect on three-phase unbalances reduction for the distribution system with an LRT loading.

Acknowledgment

This work is supported by the NSC of Taiwan (NSC 102-3113-P-214-001).

References

- [1] P. Neroth, "Waiting for nowait—engineering transport," *Engineering and Technology*, vol. 4, no. 10, pp. 28–31, 2009.
- [2] L. Li, H. Zhang, X. Wang, W. Lu, and Z. Mu, "Urban transit coordination using an artificial transportation system," *Proceedings of the IEEE Transactions on Intelligent Transportation Systems*, vol. 12, no. 2, pp. 374–383, 2011.
- [3] J. Fishelson, D. Freckleton, and K. Heaslip, "Evaluation of automated electric transportation deployment strategies: integrated against isolated," *IET Intelligent Transport Systems*, vol. 7, no. 3, pp. 337–344, 2013.
- [4] Z. Shu, S. Xie, K. Lu et al., "Digital detection, control, and distribution system for co-phase traction power supply application," *Proceedings of the IEEE Transactions on Industrial Electronics*, vol. 60, no. 5, pp. 1831–1839, 2013.

- [5] P. E. Sutherland, M. Waclawiak, and M. F. McGranaghan, "System impacts evaluation of a single-phase traction load on a 115-kV transmission system," *Proceedings of the IEEE Transactions on Power Delivery*, vol. 21, no. 2, pp. 837–844, 2006.
- [6] T. H. Chen and W. C. Yang, "Analysis of multi-grounded four-wire distribution systems considering the neutral grounding," *IEEE Transactions on Power Delivery*, vol. 16, no. 4, pp. 710–717, 2001.
- [7] ATP Draw version 1.0 Users Manual, SINTEF TR A4790, 1998.
- [8] IEEE PES Transmission and Distribution Committee, "IEEE recommended practice for monitoring electric power quality," IEEE Std 1159, 2009.
- [9] B.-K. Chen and B.-S. Guo, "Three phase models of specially connected transformers," *IEEE Transactions on Power Delivery*, vol. 11, no. 1, pp. 323–330, 1996.

Research Article

Performance Enhancement of Optical CDMA by Differential-Phase Method for Radio-over-Fiber Transmissions

Hsu-Chih Cheng,¹ Chih-Ta Yen,² and Ing-Jr Ding²

¹ Department of Electro-Optical Engineering, National Formosa University, Yunlin County 632, Taiwan

² Department of Electrical Engineering, National Formosa University, Yunlin County 632, Taiwan

Correspondence should be addressed to Chih-Ta Yen; chihtayen@gmail.com

Received 8 September 2013; Accepted 7 October 2013

Academic Editor: Teen-Hang Meen

Copyright © 2013 Hsu-Chih Cheng et al. This is an open access article distributed under the Creative Commons Attribution License, which permits unrestricted use, distribution, and reproduction in any medium, provided the original work is properly cited.

The study proposes the differential-phase optical code-division multiple-access (OCDMA) network for radio-over-fiber (RoF) transmissions, and the characteristics are numerically analyzed. The network coder/decoders (codecs) are structured on the basis of arrayed-waveguide-grating (AWG) routers with complementary Walsh-Hadamard (CWH) signature codes. In the proposed system, the network requires only two AWG routers to accomplish spectral encoding of radio base station (RBS) and decoding of control station for the complementary keying, thus resulting in a simpler and low cost system. Performance analyses are evaluated with the dominant noise of phase-induced intensity noise (PIIN) in spectral code OCDMA network. By the proposed AWG-based OCDMA with the differential-phase scheme, it is possible to establish interference-free and low crosstalk beat noise RoF systems.

1. Introduction

The millimeter-wave radio-over-fiber (RoF) system has drawn much attention on the realization of broadband radio access services recently. This is because of RoF technology can resolve the scarcity of available radio frequency (RF) resource problem [1–5]. It will become an important network access scheme other than the fiber-to-the-home (FTTH) technology. As a configuration of RoF network, microcells are connected by optical fibers among radio base stations (RBS) and central control station (CS).

Optical code-division multiple-access (OCDMA) is one candidate scheme for RoF network access technique that allows multiple users in local area networks (LANs) to access the same fiber channel asynchronously without delay or scheduling. This property is also powerful for RoF access because of its asynchronous access, flexibility, and transparency for various radio air interfaces.

In general, traditional incoherent OCDMA uses unipolar sequences as signature codes, and the coded method is usually based on the time domain. However, it is a problem to suppress multiple-access interference (MAI), and the code length of the codes is always long to support simultaneous

users in the systems. In the recent researches, spectral amplitude coding (SAC) scheme [4–11] of OCDMA becomes more popular because of the MAI-elimination and low cost set up components of incoherent optical sources and optical filter in the system. There are many code families that can be used in SAC-OCDMA network such as maximal-length sequence (M-sequence) codes [8], Walsh-Hadamard codes [9–11], modified quadratic congruence (MQC) codes [6], and modified PN codes [4].

The SAC-OCDMA network codecs can be constructed with fiber Bragg grating (FBG) devices [6, 7], but the physical size of FBG arrays will become impractical when the number of network users becomes large. The other kind of implementation option uses arrayed waveguide grating (AWG) router as codec on OCDMA network [11]. It needs mirrors and circulators to code the data, which loses the power and increases the system cost. The two-dimensional (2D) wavelength/time spreading OCDMA system in [12] implements multidimensional codes utilizing AWG multiplexers and fiber delay lines. This scheme is limited by the multiple-access interference (MAI) and is not easy to be implemented for analog RoF network. The other kind of digital OCDMA network [8] with AWG codec is proposed.

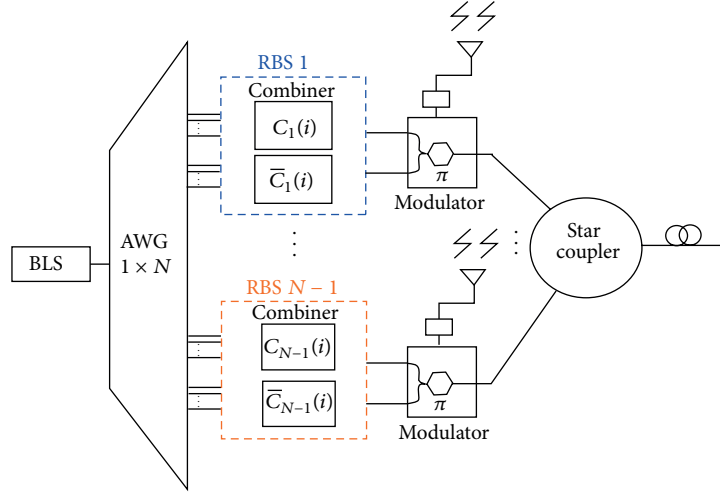


FIGURE 1: The proposed RBS transmitters and AWG encoders.

Unfortunately, it will increase the crosstalk beat noise [13, 14] when the number of active users becomes large. In spectrum-based coding OCDMA system, the number of simultaneous active users is limited to the beat noise or calls phase-induced intensity noise (PIIN). It accumulated at balanced photodetector (PD) during decoding process. In this study, we propose the interference-free RoF system structured with AWG routers [15], differential-phase intensity modulators coded with complementary Walsh-Hadamard (CWH) codes in the transmitter and balanced photodetector scheme in the receiver. The scheme can reduce the physical size of the coder and is also constructed without any sampling technique and aliasing canceller. The carrier-to-noise (CNR) ratio of proposed scheme with CWH code is superior to conventional SAC with M-sequence and Walsh-Hadamard code about 7.7 dB in RoF system.

The remainder of this paper is organized as follows. In Section 2, spectral encoding scheme using CWH code is described. In Section 3, the system encoder and decoder are presented. Section 4 evaluates performance of the proposed system in terms of CNR ratio and bit-error-rate conditions for PIIN. Finally, conclusions are presented in Section 5.

2. Spectrum Coding Scheme with the Complement Walsh-Hadamard Code

The unipolar Walsh-Hadamard code sequences $\mathbf{C}_k = (c_k(0), c_k(1), \dots, c_k(N-1))$ are (0, 1) sequences of length N assigned as the signature code for RBS k , where $k \in \{0, 1, \dots, N-1\}$, and the periodic correlation between \mathbf{C}_k and \mathbf{C}_j is defined as

$$R_{cc}(k, j) = \sum_{i=0}^{N-1} c_k(i) c_j(i). \quad (1)$$

We assume that complementary spectral $\bar{\mathbf{C}}_k = (\bar{c}_k(0), \bar{c}_k(1), \dots, \bar{c}_k(N-1))$, where $\bar{\mathbf{C}}_k(i) = 1 - \mathbf{C}_k(i)$ for $i =$

$0, 1, \dots, N-1$. The periodic correlation between $\bar{\mathbf{C}}_k$ and \mathbf{C}_j can be expressed as

$$R_{\bar{c}c}(k, l) = \sum_{i=0}^{N-1} \bar{c}_k(i) c_j(i). \quad (2)$$

According to the property of code families that $R_{\bar{c}c}(k, j) = R_{cc}(k, j) = 0$ for $k \neq j$, that can reject the influence of MAI coming from other RBSs.

In the proposed differential-phase scheme using CWH code, the RBS k will send codeword \mathbf{C}_k (for in-phase radio signal k) and its complement codeword $\bar{\mathbf{C}}_k$ (for out-of-phase radio signal k) at the same time. Thus by combining the orthogonal property of \mathbf{C}_k and $\bar{\mathbf{C}}_k$ codes to get phase diversity of radio signal, CNR will increase approximately 7.7 dB comparing with traditional coding single phase technologies. Each RBS requires only two AWG router and combiners to implement spectral encoding and decoding, respectively. Therefore, the fiber radio system using AWG router with CWH codes can be realized.

3. System Description

The proposed SAC-OCDMA system utilizes broadband light sources (BLSs) and AWG routers. Complementary keying is employed for each radio signal by directing the light from incoherent sources to input port of AWG encoder, and then AWG router output ports are connected to combiners according to codeword \mathbf{C}_k and its complement codeword $\bar{\mathbf{C}}_k$ to generate the amplitude spectrum of transmitted radio signal.

Figure 1 shows the proposed differential-phase transmitters and AWG encoders. In each RBS transmitter, differential-phase intensity modulator is performed when the radio signal of each RBS is used to analog or digital modulation. A BLS spectrum is filtered for one free spectral range (FSR) of the AWG router. The codeword \mathbf{C}_k which takes the in-phase radio signal k and $\bar{\mathbf{C}}_k$ which takes the out-of-phase radio

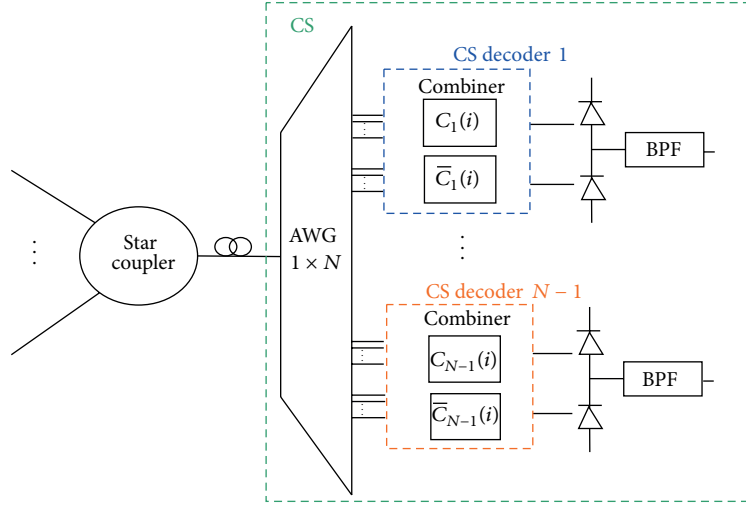


FIGURE 2: The proposed CS receiver and AWG decoders.

signal k will be transmitted when the BLS is directed into the first input port of the AWG router in the transmitter k . The advantage of complementary encoding is accomplished with only one AWG router for each RBS.

After the encoding process, the coded spectra of C_k and \bar{C}_k become the optical carriers to take the in-phase radio signal and out-of-phase radio signal simultaneously via differential-phase intensity modulator. All coded optical signals of each RBS then collected by the star coupler and broadcasted to the CS.

The radio signal $r_k(t)$ at the transmitter has the form

$$r_k(t) = a_k(t) \cos(2\pi f_{rf} t), \quad (3)$$

where f_{rf} is the carrier frequency of the radio signal and $a_k(t)$ is the complex envelope with a bandwidth B_{rf} .

The received optical signal spectrum \mathbf{S} is the summation of all RBSs' transmitted signal spectrum as follows:

$$\begin{aligned} \mathbf{S} &= (s_0, s_1, \dots, s_{N-1}) \\ &= \sum_{k=0}^{N-1} \{ [1 + m r_k(t)] C_k + [1 - m r_k(t)] \bar{C}_k \}, \end{aligned} \quad (4)$$

where m is modulation index and $r_k(t)$ is the k th RBS's radio signal.

The AWG router-based decoders are shown in Figure 2. The star coupler is connected to the decoder's AWG router, which distributes received signals to the balanced PDs of each CS decoder to realize differential decoding process. Taking CS decoder k as the example, connections from output ports of the AWG router to combiners are determined by the C_k codeword and its complement codeword \bar{C}_k . The received signal \mathbf{S} coming from the star coupler is connected to the AWG router directly; it can reduce the loss by using the split device and can also suppress the crosstalk beat noise of AWG router [8] because it is only connected to one input port. The balanced PD of RBS k will receive $\mathbf{S}C_k$ in the upper arm of PD

and $\mathbf{S}\bar{C}_k$ in the lower arm of PD. After correlation subtraction of $\mathbf{S}C_k - \mathbf{S}\bar{C}_k$ is performed in the balanced PD, the radio signal for the RBS k will be extracted, and other RBSs' interferences are rejected.

4. Performance Analysis and Discussion

The performance of the proposed 2D OCDMA system is limited by shot, thermal, and PIIN noises, particularly when the received power is high. PIIN results from the beating of incoherent light fields during the direct detection of square-law PDs, and its magnitude depends essentially on the state of polarizations (SOPs) and spectra of the optical signals. To simplify the current system performance analysis, the following assumptions are made.

- (i) The power spectral density (PSD) of each light source is ideally flat over the optical bandwidth $\nu_o + \Delta\nu/2$, where ν_o is the central optical frequency and $\Delta\nu$ is the common optical source bandwidth in hertz.
- (ii) Sufficient chip time width delays exist between the arrivals of successive pulses.
- (iii) Each coding chip has an identical spectral width of $\Delta\nu/N$.
- (iv) The chip streams from each RBS are synchronous.
- (v) T_F is set equal to $1/(2B_{rf})$.
- (vi) The transmitted radio signal that is set to the time-average power $\langle r_k^2(t) \rangle$ equals one half (i.e., $\langle r_k^2(t) \rangle = 1/2$).

The light source spectrum of each RBS is assumed to be unpolarized and ideal flat over a bandwidth $\Delta\nu$ Hz with magnitude $P_{sr}/\Delta\nu$, where P_{sr} is the effective power from a

single source at the receiver. The instantaneous PSD of the received optical signals at star coupler can be written as

$$s(\nu, t) = \frac{P_{sr}}{\Delta\nu} \sum_{k=1}^K \sum_{i=1}^N \left\{ [1 + mr_k(t)] C_k(i) + [1 - m(t)] \bar{C}_k(i) \right\} \Pi(i), \quad (5)$$

where

$$\begin{aligned} \Pi(i) = & u \left[\nu - \nu_0 - \frac{\Delta\nu}{2N} (-N + 2i - 2) \right] \\ & - u \left[\nu - \nu_0 - \frac{\Delta\nu}{2N} (-N + 2i) \right], \end{aligned} \quad (6)$$

and $u(\nu)$ is the unit step function.

The instantaneous PSD of the upper PD and lower PD for CS decoder l can be written as

$$\begin{aligned} G_1(\nu, t) &= \frac{P_{sr}}{\Delta\nu} \sum_{k=1}^K \sum_{i=1}^N \left\{ [1 + r_k(t)] C_k(i) + [1 - r_k(t)] \bar{C}_k(i) \right\} \\ &\quad \times C_l(i) \Pi(i), \end{aligned} \quad (7)$$

$$\begin{aligned} G_2(\nu, t) &= \frac{P_{sr}}{\Delta\nu} \sum_{k=1}^K \sum_{i=1}^N \left\{ [1 + r_k(t)] C_k(i) + [1 - r_k(t)] \bar{C}_k(i) \right\} \\ &\quad \times \bar{C}_l(i) \Pi(i). \end{aligned}$$

In (7), $G(\nu, t)$ is assumed to be the single sideband instantaneous PSD of the source.

The input current to the BPF can be written as

$$\begin{aligned} i_o(t) = & i_o(t) - i_1(t) i_{S_{k,l}}(t) \\ & + i_{MAI}(t) + i_{PIIN}(t) + i_{shot}(t) \\ & + i_{thermal}(t), \end{aligned} \quad (8)$$

where $i_{S_{k,l}}(t)$, $i_{MAI}(t)$, $i_{PIIN}(t)$, $i_{shot}(t)$, and $i_{thermal}(t)$ are the desired signal, the interference, the PIIN noise, the shot noise, and the thermal noise, respectively.

In the proposed RoF system, differential-phase intensity modulator is employed to suppress the noise of nonlinearity during optical-electrical conversion process. We consider the worst case of proposed system when all RBSs transmit the maximum radio power, and it will cause the most noise power of PIIN. The PIIN power now becomes the dominant noise in our proposed RoF system.

To simplify the calculation, the radio signals are assumed as to be nonmodulated carriers which have the autocorrelations function $R_{r_k}(\tau)$ and are expressed as

$$R_{r_k}(\tau) = \frac{1}{2} \cos(2\pi f\tau). \quad (9)$$

The variation of the photocurrent caused as a result of PIIN is given by:

$$\langle I_{PIIN}^2 \rangle = E \left[I^2 (1 + P^2) B \tau_c \right], \quad (10)$$

where E is the expectation operator, I is the average photocurrent, B is the noise-equivalent electrical bandwidth of the receiver, and τ_c is the coherence time of the source expressed as

$$\tau_c = E \left\{ \frac{\int_0^\infty G^2(\nu, t) d\nu}{\left[\int_0^\infty G(\nu, t) d\nu \right]^2} \right\}, \quad (11)$$

and the degree of polarization (DOP), P , is defined as

$$P^2 = \frac{(\langle s_1 \rangle^2 + \langle s_2 \rangle^2 + \langle s_3 \rangle^2)}{\langle s_0 \rangle^2}, \quad (12)$$

where s_0 , s_1 , s_2 , and s_3 are Stoke parameters used to express the state of polarization (SOP). The bracket $\langle \cdot \rangle$ in (12) denotes the average value of the parameter over wavelength, time, or space. It is well known that the DOP is dependent on not only the light source but also the distance traveled by the optical signal in long haul network transmissions.

Since the noises at the upper and lower PDs are independent, the power of the noise sources in the output photocurrent can be written as

$$\langle I_{PIIN}^2 \rangle = BR^2 E \left[\int_0^\infty G_0^2(\nu, t) d\nu + \int_0^\infty G_1^2(\nu, t) d\nu \right]. \quad (13)$$

The power of the differential-phase system's PIIN which exists in the photocurrent of the decoder is given by

$$\langle I_{PIIN}^2 \rangle = \frac{BR^2 P_{sr}^2 K(K+3)}{4\Delta\nu(P^2+1)}. \quad (14)$$

The SAC-OCDMA systems with flat PSD of light sources in the coded bandwidth, performance is mainly limited by PIIN [6–11] due to light from the incoherent sources interfering at the PDs especially when the received power is large.

Finally, the CNR due to the effect of PIIN for conventional single-phase and the proposed differential-phase modulation schemes can be calculated as follows:

$$\begin{aligned} \text{CNR}_{\text{Single-phase}} &= \frac{(I_1 - I_2)^2}{\sigma_{PIIN}^2} = \frac{\Delta\nu}{6K(K+1)(P^2+1)B}, \quad (15) \\ \text{CNR}_{\text{Differential-phase}} &= \frac{(I_1 - I_2)^2}{\sigma_{PIIN}^2} = \frac{\Delta\nu}{K(K+3)(P^2+1)B}, \quad (16) \end{aligned}$$

where I_1 and I_2 are two average photocurrents of the upper photodiode and lower photodiode at the CS decoder.

Figure 3 plots the variation of the CINR with the number of simultaneous RBSs as a function of the length of several codes. It is clear that CNR performance of differential-phase

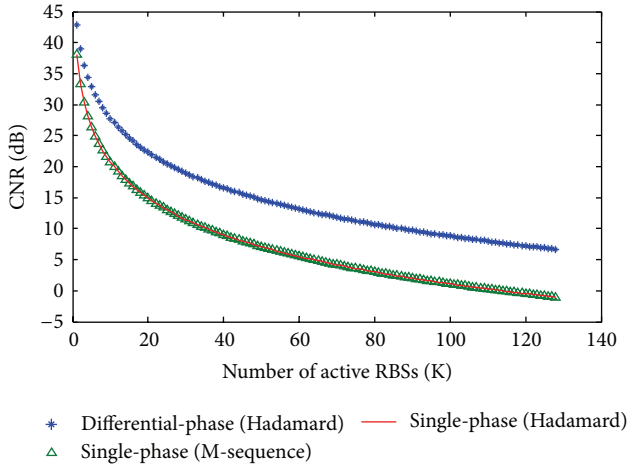


FIGURE 3: CNR versus number of active RBSs for different code families.

SAC-OCDMA with CWH code is superior to conventional single-phase SAC-OCDMA with Hadamard code and M-sequence code about 7.7 dB in large active RBSs scenario. The parameters of incoherent broadband sources used here have linewidth 60 nm, center wavelength 1550 nm, and the noise-equivalent electrical bandwidth of the receiver $B = 80$ MHz (for the bit rate 155 Mb/s).

The CNR of the conventional single-phase system degrades more significantly than that of the proposed differential-phase system, particularly with a large number of RBSs. The reason for this is that the PIIN effect becomes much larger since in the SAC-based OCDMA system, when a large number of RBSs transmit their coding patterns simultaneously, more wavelengths beat together during the direct detection by the square-law PDs. Besides, the performance in SAC-OCDMA system cannot be improved by increasing code length.

A common unpolarized amplified spontaneous emission (ASE) source can be used in the current differential-phase system because the scheme considers only the source power but not phase or polarization. However, on the long-haul transmissions over RoF network, the DOP effect must be addressed. In general, CNR can be improved by positioning a scrambler in front of balanced photodetector to eliminate the polarization-dependent effect of the detector. The scrambler theoretically removes the polarization sensitivity of the photodetector in the proposed RoF scheme; hence the average values of s_1 , s_2 , and s_3 in (12) approach zero, and the DOP is significantly decreased. In other words, the scrambler theoretically removes the polarization sensitivity of the photodetector in the proposed RoF scheme. In order to analyze the BER performance with variance of DOP (i.e., the DOP varies in the range 0 to 1) was assumed to represent the influence of polarization following long haul transmission.

As is shown in Figure 4, the BER performance of the proposed differential-phase scheme is characterized by an

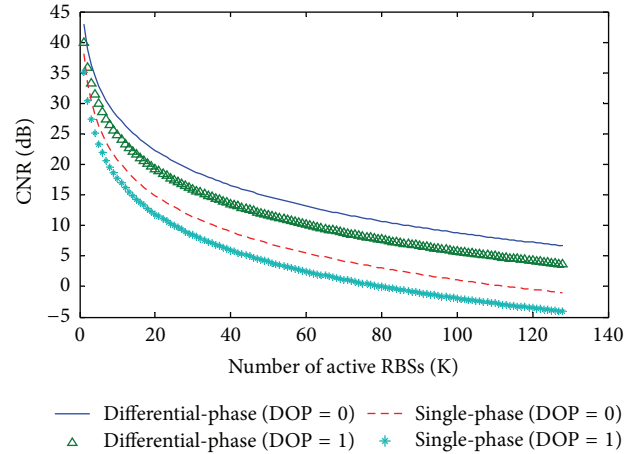


FIGURE 4: CNR performance with degree of polarization (DOP).

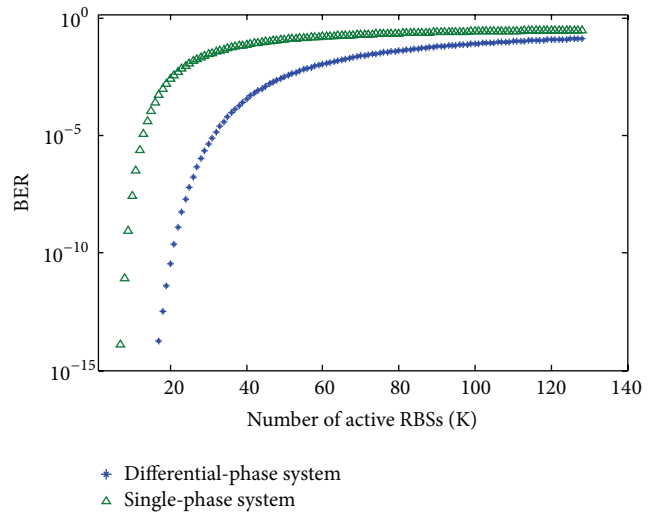


FIGURE 5: BER versus number of active RBSs for different modulation schemes.

upper bound of $P = 1$ for the worst case and a lower bound of $P = 0$ for the ideal case with the same assumption of Figure 3. Compared to the average DOP of 1 for the worst case, the CNR of the proposed differential-phase scheme is improved about 7.7 dB when the number of RBSs is 120. We can also find that the proposed differential-phase system even in high SOP condition is still performing better performance than single-phase system in the transmission links.

By assuming all the interference terms to be Gaussian distributed, the conditional BER can be calculated from amplitude shift keying (ASK) modulation; that is, on employing $BER = 0.5 \operatorname{erfc}(\sqrt{CINR}/8)$, we can obtain the relation BER and the number of active RBSs as a function of the length. Figure 5 plots the variation of the BER with the number of active RBSs as a function of the length of differential-/single-phase systems. It can be seen that the BER of the conventional OCDMA network using single-phase scheme is worse than that of the differential-phase technology particularly in a large number of RBSs conditions. The reason for this is that

when a large number of RBSs transmit their coding patterns simultaneously, more wavelengths beat together during the direct detection by the square-law PDs, the PIIN becomes the dominate noise degrading BER performance, and hence performance in SAC-OCDMA system cannot be improved by increasing code length of Hadamard codes. The BER performance of differential-phase scheme can support more than 19 active RBSs than single-phase scheme when the BER is 10^{-5} . After BPF process, the transmitted signal power becomes the dominant issue to improve system performance.

5. Conclusion

The study proposes an AWG router-based OCDMA networks embedded with signal phase diversity scheme for RoF systems. The advantages of MAI and crosstalk beat noise effect in AWG routers can be suppressed by designed codec structure. In the case of ideal system constructed by the flattened source, each RBS requires only two AWG routers for spectral encoding and decoding processes; thus filter mismatch between network coders and decoders can be mitigated. Also, unlike FBG-based system, AWG router scheme exhibits no round-trip time delay problem. Besides, AWG router-based codecs lies in that it has no accumulation of insertion loss when the total number of RBSs is increased. The CNR and BER of the proposed system are numerically analyzed by taking the dominate noise of PIIN into account. The result shows that the CNR of the proposed differential-phase system is superior 7 dB than other conventional single-phase OCDMA schemes in RoF system. The tradeoff on complementary codes in the study between system complexity and performance can be considered in different RoF links; hence the system flexibility is increased. In conclusion, the proposed system achieves a higher performance than a conventional RoF OCDMA scheme and can be implemented using a simple configuration comprising conventional low cost BLSs and compact optical components, rendering the overall system both cheap and straightforward.

Acknowledgment

This work was supported in part by the National Science Council under Grant no. NSC-102-2221-E-150-002.

References

- [1] Z. Ahmed, D. Novak, R. B. Waterhouse, and H.-F. Liu, "37-GHz fiber-wireless system for distribution of broad-band signals," *IEEE Transactions on Microwave Theory and Techniques*, vol. 45, no. 8, pp. 1431–1435, 1997.
- [2] C. T. Yen, H. C. Cheng, and I. J. Ding, "Hybrid analog/digital wavelength-time optical CDMA systems in radio-over-fiber transmissions," *The Journal of Supercomputing*, 2013.
- [3] C. T. Yen, H. C. Cheng, Y. T. Chang, and W. B. Chen, "Performance analysis of dual unipolar/bipolar spectral code in optical CDMA systems," *Journal of Applied Reserch and Technology*, vol. 11, no. 2, pp. 235–241, 2013.
- [4] B. K. Kim, S. Park, Y. Yeon, and B. W. Kim, "Radio-over-fiber system using fiber-grating-based optical CDMA with modified PN codes," *IEEE Photonics Technology Letters*, vol. 15, no. 10, pp. 1485–1487, 2003.
- [5] C. T. Yen, "Optical code-division multiple-access embedded with a polarisation diversity scheme for radio-over-fibre transmissions," *IET Optoelectronics*, vol. 6, no. 3, pp. 131–139, 2012.
- [6] Z. Wei, H. M. H. Shalaby, and H. Ghafouri-Shiraz, "Modified quadratic congruence codes for fiber Bragg-grating-based spectral-amplitude-coding optical CDMA systems," *Journal of Lightwave Technology*, vol. 19, no. 9, pp. 1274–1281, 2001.
- [7] J. F. Huang and D. Z. Hsu, "Fiber-grating-based optical CDMA spectral coding with nearly orthogonal M-sequence codes," *IEEE Photonics Technology Letters*, vol. 12, no. 9, pp. 1252–1254, 2000.
- [8] C. C. Yang, J. F. Huang, and S. P. Tseng, "Optical CDMA network codecs structured with M-sequence codes over waveguide-grating routers," *IEEE Photonics Technology Letters*, vol. 16, no. 2, pp. 641–643, 2004.
- [9] M. Kavehrad and D. Zaccarin, "Optical code-division-multiplexed systems based on spectral encoding of noncoherent sources," *Journal of Lightwave Technology*, vol. 13, no. 3, pp. 534–545, 1995.
- [10] E. D. J. Smith, R. J. Blaikie, and D. P. Taylor, "Performance enhancement of spectral-amplitude-coding optical CDMA using pulse-position modulation," *IEEE Transactions on Communications*, vol. 46, no. 9, pp. 1176–1185, 1998.
- [11] J.-F. Huang, C.-C. Yang, and S.-P. Tseng, "Complementary Walsh-Hadamard coded optical CDMA coder/decoders structured over arrayed-waveguide grating routers," *Optics Communications*, vol. 229, no. 1–6, pp. 241–248, 2004.
- [12] Y. T. Chang, J. F. Huang, L. W. Chou, C. C. Wang, C. T. Yen, and H. C. Cheng, "Adaptive modified time-spreading and wavelength-group-hopping embedded M-sequence code for improved confidentiality over synchronous networks," *Optical Engineering*, vol. 50, no. 5, Article ID 055001, 2011.
- [13] H. Takahashi, K. Oda, and H. Toba, "Impact of crosstalk in an arrayed-waveguide multiplexer on $N \times N$ optical interconnection," *Journal of Lightwave Technology*, vol. 14, no. 6, pp. 1097–1105, 1996.
- [14] D. Castleford, A. Nirmalathas, D. Novak, and R. S. Tucker, "Optical crosstalk in fiber-radio WDM networks," *IEEE Transactions on Microwave Theory and Techniques*, vol. 49, no. 10, pp. 2030–2035, 2001.
- [15] H. Takahashi, K. Oda, H. Toba, and Y. Inoue, "Transmission characteristics of arrayed waveguide $N \times N$ wavelength multiplexer," *Journal of Lightwave Technology*, vol. 13, no. 3, pp. 447–455, 1995.

Research Article

Strategic Bidding Behaviors in Nondecreasing Sponsored Search Auctions

Chen-Kun Tsung,¹ Hann-Jang Ho,² and Sing-Ling Lee¹

¹ *Institute of Computer Science and Information Engineering, National Chung Cheng University, No. 168, Section 1, University Road, Min-Hsiung Township, Chia-yi County 62102, Taiwan*

² *Department of Applied Digital Media, WuFeng University, No. 117, Section 2, Chiankuo Road, Min-Hsiung Township, Chia-yi County 62153, Taiwan*

Correspondence should be addressed to Hann-Jang Ho; hannjangho@gmail.com

Received 23 September 2013; Accepted 9 October 2013

Academic Editor: Teen-Hang Meen

Copyright © 2013 Chen-Kun Tsung et al. This is an open access article distributed under the Creative Commons Attribution License, which permits unrestricted use, distribution, and reproduction in any medium, provided the original work is properly cited.

To realize the specific results in the sponsored search auctions, most advertisers submit particular bid prices. The bidding behaviors with specific purposes are called as the strategic bidding. However, some strategic bidding behaviors will result in negative effects, such as the elimination of the equilibrium and the payment increase for some advertisers. The bidding behaviors with negative results are termed as the vindictive bidding. We survey four strategic bidding behaviors which include a rational bidding and three vindictive bidding strategies. In this paper, we study the relationship between the effects resulted by the vindictive bidding and the valuations of the vindictive advertisers. In our experiments, the search engine provider (SEP) is benefited by all vindictive bidding behaviors, and the increment of the SEP's revenue is proportional to the degree of the vindictiveness. Bidding vindictively without sacrificing the own utility improves the advertiser's utility with high probability. Moreover, we observe that the SEP's revenue is improved by the following situations. First, the vindictive advertiser with low valuation in the keywords with high market value results in more SEP's revenue than that in the keywords with low market value. The second case is to raise the bidding competition between advertisers.

1. Introduction

When an Internet user submits a keyword query to the SEP, such as Google or Yahoo, the user will receive a web page including the search results and some advertisements. Combining the search service and the advertising is called the sponsored search auction (SSA) [1, 2] or the keyword auction [3–5]. Figure 1 is an example of the SSA service provided by Yahoo. The user queries the keyword Taiwan tour agency and then receives the web page. The center area includes the search results while the area with red box is the advertisements recommended by Yahoo. The advertising area includes some slots, and each slot displays some information of an advertisement including a title, a hyperlink connected to the source web page, and a brief description. Because the recommended advertisements are related to the input keywords, the advertising information is useful for the readers. Therefore, most Internet users accept the advertisements recommended by the SSAs.

Most SSAs consider the pay-per-click and the generalized second price (GSP) as the pricing mechanisms [6, 7]. The pay-per-click indicates that each advertiser pays for advertising only when the Internet user clicks the advertisement. The GSP charges each winner the essential price of winning the slot; that is, each payment equals to the next-ranked bid value rather than the claimed bid price. The pricing mechanism improves the advertising effectiveness, and consequently many advertisers prefer to promote their products via the SSAs. Therefore, the SSAs become major incoming of the SEPs [6, 7].

Some advertisers attempt to realize the specific outcomes by submitting particular bid values, and that is called as the strategic bidding. For example, to realize the outcomes with maximum utility, Bu et al. proposed the forward-looking bidding strategy [4], and Cary et al. introduced the balanced bidding strategy [5]. Both bidding strategies guarantee the equilibrium outcome (The equilibrium is

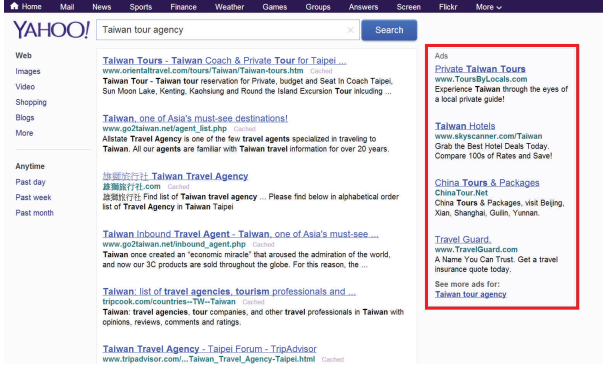


FIGURE 1: An example of the SSA provided by Yahoo! with the keyword phrase: Taiwan tour agency.

a steady state that all participants are not benefited by any unilateral deviation [8]. This implies that all participants satisfy with the equilibrium outcome simultaneously. The equilibrium is applied to measure the outcome quality. For example, Yan et al. find the Nash equilibrium in the optimal bandwidth scheduling problem [9].), where the SEP's revenue is identical to that obtained in the Vickrey-Clarke-Groves auction [10]. Because most advertisers aim at maximizing the obtained utility, we treat the bidding behaviors of maximizing the utilities as the *rational bidding*.

However, not all strategic bidding behaviors are rational. For example, some advertisers apply the flaw of the GSP to manipulate the payments of other advertisers rather than to maximize their own utility. This kind of bidding strategies is called the *vindictive bidding* [2].

In the GSP, each payment equals to the next-ranked bid value. So, submitting the price between the previous-ranked and the next-ranked bid values will win the same slot if other advertisers do not update their bid values. The vindictive bidding utilizes this property to manipulate the competitor's payments. We use the example shown in Table 1 to describe the vindictive bidding. For convenience, we use a *round* to indicate that every time the SSA receives a keyword query. Suppose three advertisers $\{ad_1, ad_2, ad_3\}$ compete for two slots $\{sl_1, sl_2\}$. The bids are denoted by b_1, b_2 , and b_3 , where $b_1 > b_2 > b_3$. ad_1 and ad_2 are the winners of sl_1 and sl_2 , respectively. Based on the pricing rule of the GSP, ad_1 pays b_2 , ad_2 pays b_3 , and ad_3 pays zero. Supposing b_1 and b_3 are fixed, ad_2 wins sl_2 by proposing any price between b_1 and b_3 . If ad_2 bids b_2^+ , where $b_1 > b_2^+ > b_2$, ad_2 still wins sl_2 and pays b_3 , but the payment of ad_1 is increased from b_2 to b_2^+ . Obviously, raising the price from b_2 to b_2^+ is a vindictive bidding. In the following context, ad_2 is called as the vindictive advertiser while ad_1 is the target advertiser.

The major objective of the vindictive bidding is to maximize the payment of the target advertiser. Some negative effects that resulted from the vindictive bidding are observed. For the target advertisers, the utilities are decreased because the payments are raised by the vindictive bidding. For the outcome stability, the equilibrium is eliminated in some cases [2]. In this paper, investigating the effects that resulted from the vindictive bidding is our major

TABLE 1: Example of the vindictive bidding in a SSA.

Terms	ad_1	ad_2	ad_3
Occupied slot	sl_1	sl_2	Nothing
Bid price in the current round	b_1	b_2	b_3
Bid price in the next round	b_1	b_2^+ (where $b_1 > b_2^+ > b_2$)	b_3

objective, where the vindictive advertisers have different valuations.

The strategic bidding behaviors that we considered include the rational bidding and the vindictive bidding. According to the studies of Bu et al. [2], we survey three vindictive bidding behaviors: the malicious bidding, the selective bidding, and the conservative bidding. Note that the malicious, selective, and conservative advertisers represent the bidders who utilize the malicious, selective, and conservative bidding strategies to determine the bid values. The malicious advertisers always try to maximize the payments of the target advertisers. They have higher degree of the vindictiveness than other vindictive bidding advertisers. The selective advertisers bid vindictively only if they miss their desire positions. The bidding behaviors of the conservative advertisers are similar to that of the selective advertisers, but the utilities of the conservative advertisers are never sacrificed for bidding vindictively.

We study the effects of the vindictive bidding in an English auction-based SSA: the nondecreasing sponsored search auction (NDSSA) [1]. The English auction is widely applied in the real world application and the electronic marketing because of the easy implementation. Moreover, various outcomes can be realized by adjusting the auction parameters. Thus, considering the NDSSA is close to real world behaviors and helps us to understand the effects resulted from the vindictive bidding.

Increasing target advertisers' payments is the major objective of the vindictive advertisers. Obviously, the vindictive bidding increases SEP's revenue and decreases the utilities of the target advertisers. However, we are interested in the relationship between the negative effects resulted from the vindictive bidding and the valuations of the vindictive advertisers. To focus on the negative effects resulted from the vindictive bidding, we consider only one vindictive advertiser in each simulation instance. According to our experiment results, the SEP's revenue is proportional to the degree of the vindictiveness. When the advertisers have stronger vindictiveness, the SEP will gain more revenue. On the other hand, advertisers' utilities are reduced by the vindictive bidding in most instances. Only conservative behaviors improve the utilities in some instances because the utility is not sacrificed for the vindictive bidding. The advertiser with small valuation without bidding vindictively has no idea how to win any slot, but they may earn the last slot by adopting the selective bidding. The advertisers with low valuation should consider the slightly vindictive bidding strategy. In summary, even if bidding vindictively increases

competitors' payments, vindictive advertisers may also lose a part of the utility in most instances.

2. Related Works

There are two English auction-based SSAs: the generalized English auction [6] and the NDSSA [1]. The generalized English auction considers full processes of the English auction to rank advertisers. When the valuations are very close to each other; the generalized English auction requires huge time to determine ranking results. In real world SSAs, most Internet users do not wait to receive a web page for a long time. Therefore, the NDSSA is more appropriate than the generalized English auction in practice because the NDSSA utilizes the rank-by-bid strategy to determine the ranking results.

Many strategic bidding strategies are studied. For example, the forward-looking bidding strategy proposed by Bu et al. [4], the multibidding strategy proposed by Bu et al. [11], the balanced bidding strategy proposed by Cary et al. [5], and some vindictive bidding strategies [2]. The bidding strategies can be classified by the rational bidding and the vindictive bidding. The rational bidding aims to maximize the own utility while the vindictive bidding focuses on maximizing the competitors' payments.

In the SSAs with complete information, the SEP can utilize some mechanisms to prevent the negative effects resulted from the vindictive bidding. For example, the Vickrey-Clarke-Groves auction guarantees the incentive compatibility, so the vindictive bidding is the dominated strategy [12–14]. However, not all information in the real world SSAs is common knowledge. Most advertisers do not expose their valuations and adopted bidding strategies to other advertisers and the SEP. So, it is hard to capture the vindictive advertisers. Moreover, the effects resulted from the vindictive advertisers with various valuations and the interactions of the advertisers adopting different bidding strategies are still unclear.

3. Preliminaries

3.1. Auction Model. Consider a repeated SSA which focuses on a specific keyword. The search result page consists of K advertising slots. Each slot sl_j includes a click-through-rate (CTR) θ_j which is the click probability that the Internet users click the advertisement on sl_j . We assume that the slot rearranged in a better position will receive more clicks; that is, $\theta_1 > \theta_2 > \dots > \theta_K$. Suppose N advertisers participate in the auction, where $K < N$. As a keyword query arrives, each advertiser ad_i submits a bid b_i to declare the maximum payment per click. When an Internet user clicks the advertising link of ad_i , ad_i receives the income v_i which is named as the valuation. We assume that ad_i wins sl_i . According to the pricing rule of the GSP, the payment of ad_i denoted by p_i is equal to the next-ranked bid price; that is, $p_i = b_{i+1}$. Given the bid profile $b = \{b_1, b_2, \dots, b_N\}$, the expected utility of ad_i is $u_i(b) = (v_i - p_i) \times \theta_i$. SEP's expected revenue comes from the sum of advertisers' payments, that is, $\sum_{s=1}^K b_{s+1} \times \theta_s$.

In the real world applications, the valuations and the bidding strategies adopted by advertisers are private information. Thus, the SEP or the advertisers do not know who is the vindictive advertiser. Note that the bid profile and the payment profile are public only if the auction result is announced. This implies that each advertiser does not access the bid values of other advertisers when computing a new bid price.

3.2. Nondecreasing Sponsored Search Auction. The NDSSA is an English auction-based mechanism [1]. Similar to the English auction, the NDSSA considers the minimum increase price (MIP) to indicate the lower bound of the bid value for all updated bids. The SEP should determine two parameters of the NDSSA: an initial MIP value and an MIP adjusting strategy. The initial MIP value indicates the minimum bid increment in the second round (there is no restriction for submitting the bid price in the first round). The MIP adjusting strategy recomputes the MIP value that will be applied in the next round after obtaining the auction result in each round.

The MIP restricts the bid prices. Submitting the following bid prices is allowed.

Rule 1. The same value as that proposed in the last round.

Rule 2. A price higher than the last one plus the MIP value.

To focus on the effects resulted from the vindictive bidding, we consider the fixed-MIP as our MIP adjusting strategy. The fixed-MIP uses the initial MIP value throughout the auction. In other words, the MIP is not changed until the NDSSA is restarted every day.

When an Internet user issues a keyword query, the NDSSA selects N advertisers as the candidates for advertising. Each candidate is asked to propose the bid value b_i which is verified by the MIP. We assume that all bids are legal. Then, all candidates are ranked in the decreasing order of the bid values. First K highest candidates are claimed as the winners. Eventually, the allocation result and the new MIP value will be announced to each advertiser. Note that we consider the fixed-MIP, each advertiser knows the MIP setting in each round. If the SEP adopts the other MIP adjusting strategies, the new MIP is announced in the end of each round.

If we follow the bidding restriction applied in [1], some vindictive bidding behaviors are restricted. For example, the price difference between the current bid value and the previous-ranked bid value is smaller than the MIP value. The vindictive advertiser can only bid the price higher than that proposed by the previous-ranked advertiser. This bid update is not the vindictive bidding. So, the third feasible bid price is considered.

Rule 3. Each ad_i has an opportunity to raise the bid without the MIP constraint, but ad_i cannot update the bid price in the future.

4. Bidding Behaviors

According to the aspect of the game theory [8], rational advertisers aim at maximizing the obtained utility. However,

the vindictive advertisers prefer to increase the payments of the target advertisers. Based on the studies on [2, 4], we consider a rational bidding and three vindictive bidding behaviors. If the vindictive advertiser wins the top slot, that is, he/she does not have any competitor, the bid price will not be updated in the next round.

4.1. Rational Advertiser. Rational advertisers try to maximize the expected utility $u_i(b)$. The bid price is updated only if winning the previous-ranked slot improves $u_i(b)$. For example, the forward-looking bidding behaviors [4] and the greedy bidding strategies [5] are rational bidding. Given the MIP value x , the bidding behavior of the rational advertiser in the NDSSA is shown in equality (1) where $b_{-i} = \{b \setminus b_i\}$, $\forall i > 1$. If winning sl_{i-1} results in higher utility, ad_i will bid submit a higher price, and b_i otherwise:

$$BH_i^r(b) = \begin{cases} b_i, & \text{if } u_i(b_{i-1} + 0.1, b_{-i}) \leq u_i(b) \\ \max(b_{i-1} + 0.1, b_i + x), & \text{otherwise.} \end{cases} \quad (1)$$

4.2. Selective Advertiser. Selective advertisers retaliate against the target advertiser only if the desire position is not obtained. When ad_i is benefited by winning the previous-ranked slot but the MIP is too high to update the bid price, that is, $b_i + x > v_i$, a vindictive action takes place. The bid value is increased to $(b_{i-1} - 0.1)$ to maximize the payment of the target advertiser. When $v_{i-1} < v_i$, ad_i can propose a higher bid value than b_{i-1} if the previous-ranked slot is benefited to ad_i . So, $v_{i-1} > v_i$ is the essential condition for the selective bidding strategies. The selective bidding is defined in equality (2) for each $i > 1$.

$$BH_i^s(b) = \begin{cases} b_{i-1} - 0.1, & \text{if } u_i(b_{i-1} + 0.1, b_{-i}) > u_i(b), \\ b_i + x > v_i, & v_{i-1} > v_i, \\ BH_i^r(b), & \text{otherwise.} \end{cases} \quad (2)$$

4.3. Conservative Advertiser. Selective advertisers may receive negative utility if $BH_i^s(b) = b_{i-1} - 0.1 > v_i$. The conservative bidding strategy does not sacrifice the utility for the vindictive bidding. This implies that the conservative advertisers do not overbid, and the utility can be protected. The conservative bidding strategy is formulated in the following equality:

$$BH_i^c(b) = \begin{cases} \min\{b_i - 0.1, v_i\}, & \text{if } u_i(b_{i-1} + 0.1, b_{-i}) > u_i(b) \\ b_i + x > v_i, \\ BH_i^r(b), & \text{otherwise.} \end{cases} \quad (3)$$

4.4. Malicious Advertiser. The malicious advertiser ad_i is most vindictive than above advertisers. The objective of the malicious advertisers is to maximize the payments of the target advertiser without respect to the own utility. So, ad_i

always bids $(b_{i-1} - 0.1)$. The bid price of the malicious advertiser $BH_i^m(b)$ is shown in the equality

$$BH_i^m(b) = b_{i-1} - 0.1, \quad \forall i > 1. \quad (4)$$

5. Experiments

5.1. Parameters Settings. We consider $K = 6$ and $N = 9$, and no advertiser will depart from the auction. Referring to the experiment settings in [3], the valuation instances are determined by the uniform distribution, triangular distribution, normal distribution, exponential distribution, and Pareto distribution within 1 and 50. The valuations are sorted in the decreasing order in each instance. We generate five initial bid profiles by four normal distributions with different standard deviation and one random distribution. We use Zipf's distributions [3] to generate CTR instances (from the studies of [3, 15], most click behaviors can be simulated by Zipf's distribution and the geometrically decreasing sequence with different parameters. For the big value of α , the CTR gap between two successive slots is smaller than that of the small value of α . This implies that the bigger values of α result in the keywords with lower market value, and vice versa). Given the parameter α , where $\alpha \in \mathcal{R}^+$, the CTR value under Zipf's distribution is shown in the equality

$$\theta_j \propto \frac{1}{j^\alpha}, \quad \forall \alpha \in \mathcal{R}^+. \quad (5)$$

The initial MIP values are set from 1 to 49 with the fixed-MIP strategy. Because the maximum valuation is 50 in our simulations, no advertiser can update bid prices if the initial MIP value is higher than 50. The maximum initial MIP value is set to be 49 to prevent the case that all advertisers can not update bids throughout the auction.

We observe the relationship between the effects resulted from the vindictive bidding and the valuations of the vindictive advertisers. The advertisers with higher valuations win a slot in high probability than the advertisers with lower valuations. Consider that the vindictive advertisers having different valuations are essential. In our simulations, we assume that each advertiser is a vindictive bidder in each auction. Therefore, each auction is performed ten times (including one case with all rational advertisers and nine cases that one vindictive advertiser is in each case).

5.2. Search Engine Revenue. We first evaluate the SEP's revenue under the vindictive bidding consideration. To simplify the problem scale, we consider one vindictive advertiser in each instance. The result is shown in Figure 2. The SEP's revenue is averaged by the results captured from all combinations of valuation, CTR, and initial bid prices. The horizontal axis denotes the index of the vindictive advertiser, and the vertical axis represents the SEP's revenue. The benchmark is the SEP's revenue obtained when all advertisers are rational.

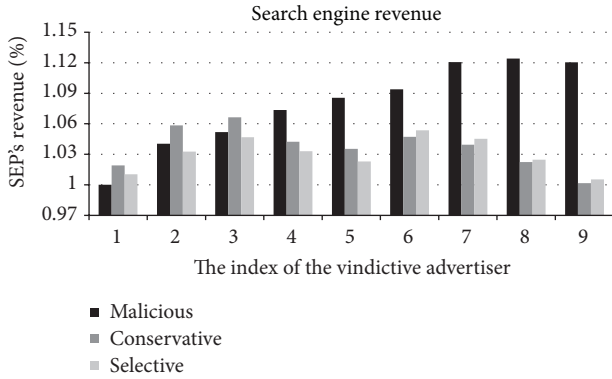


FIGURE 2: The comparison between the rational and the vindictive advertisers for SEP's revenue.

Observation 1. The SEP's revenue is inversely proportional to the valuation of the malicious advertiser.

The malicious advertiser always retaliates against the target advertiser. In the worst case, the malicious advertiser occupies the next-ranked slot of the advertiser with maximum valuation. Because any vindictive behavior will not bid higher than the previous-ranked bid price, the bid update is stopped at the second slot. Therefore, the malicious advertiser with lower valuation produces higher SEP's revenue.

Observation 2. The malicious advertiser with highest valuation does not vary the SEP's revenue.

When the malicious advertiser wins the first slot, no advertiser is in front of the first slot. The vindictive advertiser will not raise his/her bid price. Thus, SEP's revenue is not varied by the malicious advertiser with the highest valuation.

Observation 3. For the winners, the SEP gains more revenue from conservative advertisers than selective advertisers. The opposite results occur for losers.

The bid value of the conservative advertiser is bound by the valuation, while it is not considered by the selective advertisers. The selective losers, that is, ad_7 , ad_8 , and ad_9 , result in higher SEP revenue than conservative losers because no loser can win the target slot. The selective losers continuously retaliate to the sixth winner even though overbidding, but this is not considered by the conservative advertisers. Then, the SEP gains more revenue from selective losers than conservative losers.

For the winners, the SEP receives more revenue from the conservative advertisers than the selective advertisers. Because the previous-ranked advertiser may have a lower valuation than the selective advertiser, the selective advertisers do not bid vindictively frequently. So, the conservative winners contribute more SEP's revenue than the selective winners.

5.3. Utility of Vindictive Advertisers. Next, we focus on the relationship between advertisers' utilities and the valuation

of the vindictive advertiser. We use the ratio of the vindictive advertiser's utility to that of the rational advertiser. The results obtained from the malicious, selective, and conservative advertisers are shown in Figures 3(a), 3(b), and 3(c), respectively. In each figure, the horizontal axis denotes the index of the vindictive advertiser. The vertical axis represents the ratio of the instances that the vindictive advertiser's utility is better than, the same as, or worse than that of the rational advertiser. In Figure 3(a), for example, the third advertiser has more utility by adopting the malicious bidding than the rational bidding in 20% of the instances.

Observation 4. Malicious advertisers are benefited in only a few instances (20% instances at most).

The objective of the malicious advertisers is to maximize the payments of the target advertisers without caring about their own utilities. So, the utility reduce is in expectation. The result in Figure 3(a) matches that in Figure 2. Since the SEP's revenue completely comes from the sum of advertisers' payments, the SEP is benefited when the advertiser's utility is decreased, and vice versa.

Observation 5. In most instances, the utility of the selective winners is equal to that of the rational advertiser. On the other hand, the selective losers receive more utility than the selective winners in high probability.

Similar to the discussion in Observation 3, the selective winners and the rational winners obtain the same utility in more than 60% of instances. Since the NDSSA considers the GSP as the pricing strategy, the selective advertiser's valuation may be higher than that of the target advertiser. Therefore, the vindictive bidding does not occur frequently. The selective losers continuously propose vindictive bid values because the target slot is not obtained. When the selective losers and the target advertiser raise prices and move forward a slot simultaneously, the selective loser obtains the last slot. So, the utility of the selective loser is improved. Eventually, the selective losers have more opportunities than rational losers to win the target slots.

Observation 6. The advertiser's utility is slightly improved by the conservative bidding.

The bid value of the conservative advertiser is bound by the valuation. The overbidding does not take place, so the utility of the conservative advertiser is better than that of the malicious advertiser. Therefore, slightly bidding vindictively improves the advertiser's utility in some instances, and no overbidding is necessary for improving the utility under the vindictive bidding consideration.

In summary, bidding vindictively without turning back results in high payment increment for the target advertiser. But, the utilities of the malicious advertisers are also be decreased by their vindictive bidding behaviors. The selective advertisers can save the utilities in most instances. For the conservative advertisers, although the utility is protected, the auction results are hard to be predicted in terms of the utility.

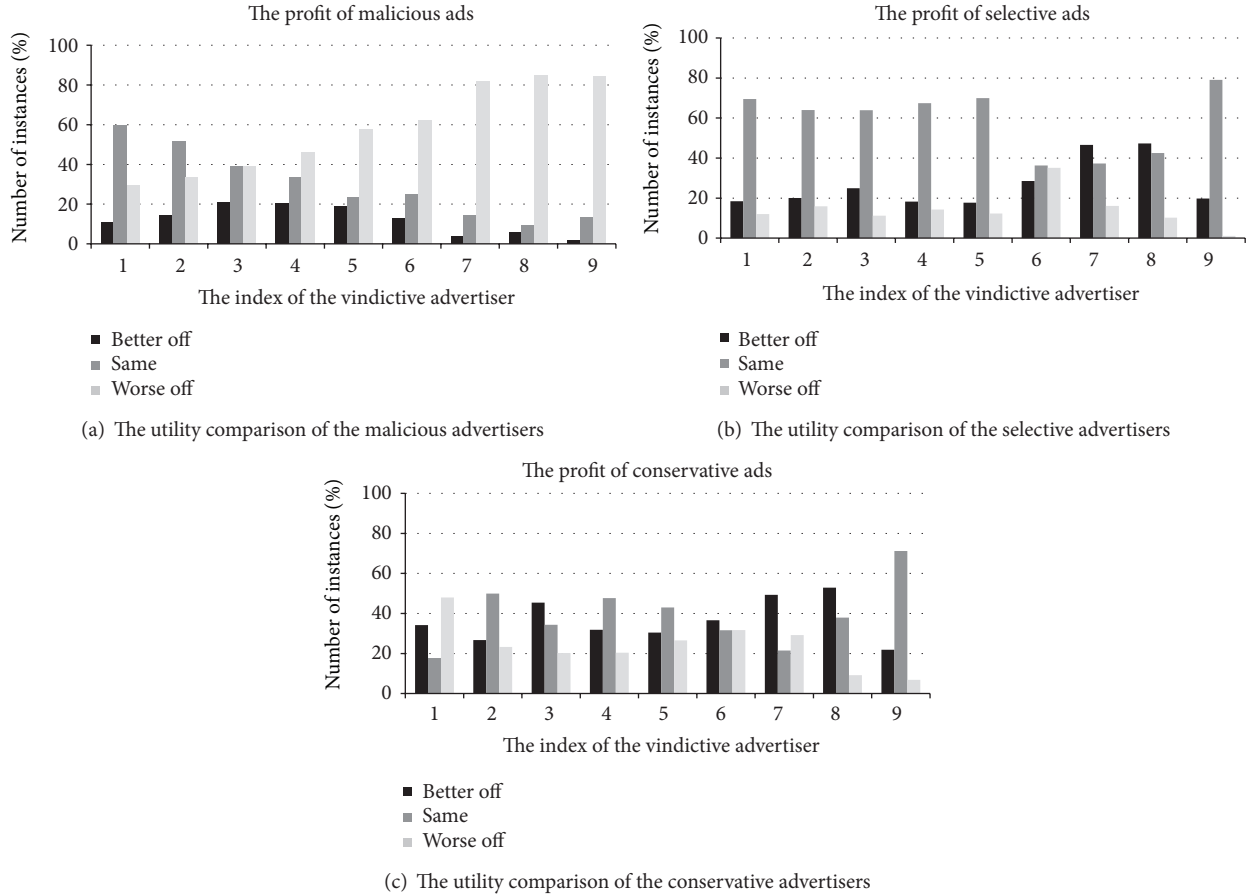


FIGURE 3: Advertisers' utilities obtained by different vindictive bidding strategies.

5.4. *The Effects Resulted from the Vindictive Bidding in Different Keywords.* In this experiment, we observe the relationship between different keyword phrases and the SEP's revenue when one vindictive advertiser is considered. The simulation results are shown in Figure 4. The horizontal axis denotes the CTR distributions that are produced by different values of α . Higher value of α results in smaller CTR gap between two successive slots and that represents the keyword phrases with lower market value. The vertical axis represents the SEP's revenue which is normalized by that obtained from the rational bidders. The winners are drawn by solid lines while the losers are illustrated by the dashed lines. Although the sixth advertiser is still a winner, we use the dashed line to represent it because he/she is affected by the vindictive losers.

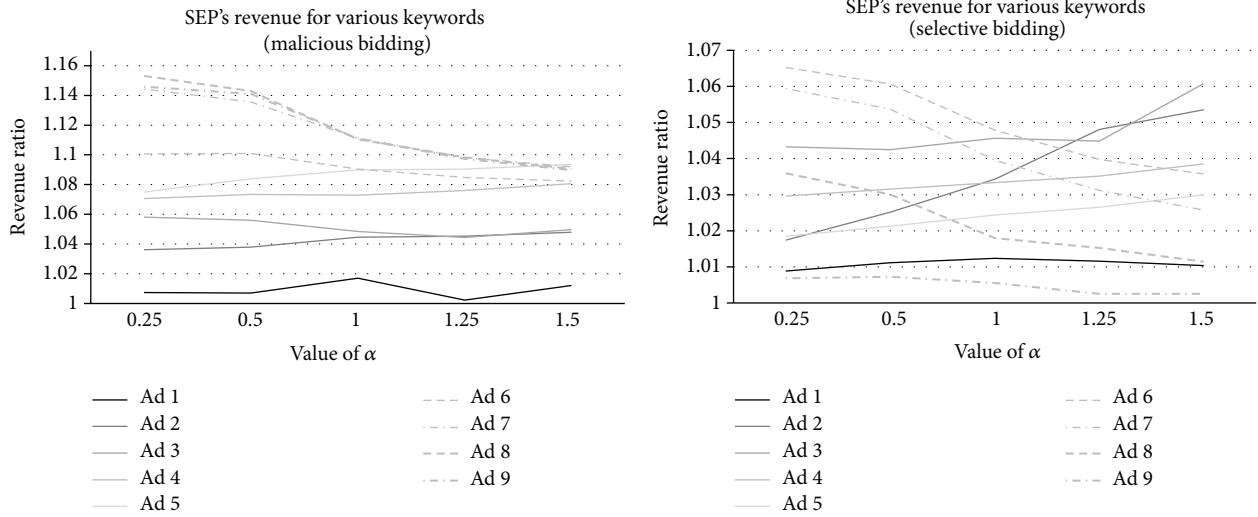
Observation 7. For the losers, the improvement of the SEP's revenue in the keywords with high market value is much more than that with low market value. The opposite result is obtained for the winners.

From Figure 4, the tendencies of the losers' curves are descending. However, the tendencies of the winners' curves are not varied dramatically except for the second advertiser. The instances with small values of α represent the keywords

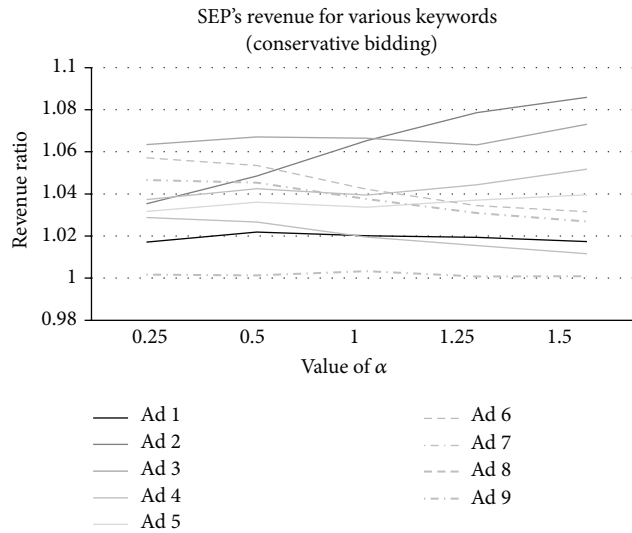
with high market values. So, in the last slot, the CTR with the small value of α is higher than that with high value of α , and vice versa. In other words, the last slot with small value of α is more valuable than that with high value of α . Therefore, it is reasonable that the improvement of the SEP's revenue for the keywords with high market value is higher than that for the keywords with low market value.

On the other hand, the variance of the revenue improvement for the SEP is small for most vindictive advertisers. This implies that different keyword phrases do not vary the revenue improvement for the SEP too much. Because the objective of the vindictive bidding is to maximize the payments of the target advertiser. The price of the vindictive bidding depends on the bid value proposed by the target advertiser. So, the relationship between the keyword phrases and the revenue improvement of the SEP is not very close for the winners.

5.5. *The Effects Resulted from the Vindictive Bidding in Different Minimum Increase Prices.* In this simulation, we evaluate the relationship between the initial MIP settings and the SEP's revenue. The simulation result is illustrated in Figure 5. The horizontal axis denotes the initial MIP setting. The vertical



(a) The revenue variance of the SEP for one malicious advertiser (b) The revenue variance of the SEP for one selective advertiser



(c) The revenue variance of the SEP for one conservative advertiser

FIGURE 4: SEP's revenue comparisons with different vindictive bidding strategies for various keyword phrases.

axis represents the SEP's revenue which is normalized by that obtained from the rational advertisers.

Observation 8. The amount of the SEP's revenue raised by the malicious advertisers is higher than that resulted from other vindictive advertisers.

From Observations 1 and 2, the improved amount of the SEP's revenue is proportional to the degree of the vindictiveness. Therefore, the SEP will receive more revenue when the vindictive advertiser adopts the bidding strategy with stronger vindictiveness.

Observation 9. Before the initial MIP 42, the SEP's revenue is proportional to the initial MIP values. The opposite results are derived as the initial MIP is bigger than 42.

By increasing the initial MIP value, the bidding competition is raised. Simultaneously, the vindictiveness is also raised. So, the improvement of the SEP's revenue is raised as increasing the initial MIP setting.

From Figure 5, the revenue improvement is at a watershed in the initial MIP 42. According to our input data, the maximum gap between the valuation and the initial bid price is 44. This implies that no advertiser can update the bid value if the initial MIP is set to be higher than 44. So, it is rational that the watershed of the SEP's revenue presents before the initial MIP 44. However, the vindictive advertiser still can bid vindictively by the third bidding restriction that we relaxed in Section 3.2. So, this is why the SEP's revenue is more than that obtained by rational bidders in the initial MIP values higher than 42.

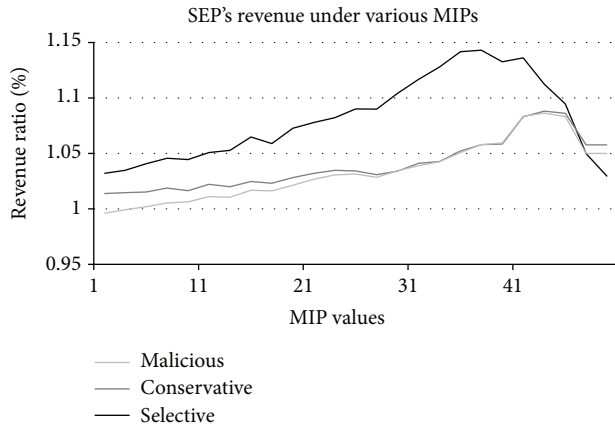


FIGURE 5: The revenue comparison for the SEP given various initial MIP settings.

6. Conclusion

The vindictive bidding occurs frequently in the real world SSAs. We survey three well-defined vindictive bidding strategies and one rational bidding behavior. Our major objective is to analyze the effects resulted from the vindictive bidding for the aspects of the advertisers and the SEP, where the vindictive advertisers have different valuations. According to our simulation results, the SEP is benefited by all kinds of vindictive bidding behaviors. This means that rational advertiser's payment is increased by the vindictive bidding. On the other hand, the degree of the vindictiveness affects the advertiser's utility. The utility of the advertiser with high vindictiveness is reduced in most instances. Advertisers' utilities are improved in some instances only if submitting the bids with slightly vindictive prices. Therefore, even though vindictive bidding increases the competitor's payment, the advertisers adopting vindictive bidding behaviors also lose a part of the utilities.

The effects of vindictive bidding behaviors are studied in this paper. In our simulation, we notice that the advertiser is benefited by slightly vindictive bidding behavior in some situations. Understanding the conditions where vindictive bidding behavior is beneficial for the advertiser's utility is our next objective.

Acknowledgments

This work was supported in part by Taiwan NSC under Grants no. NSC 102-2221-E-274 -004 and NSC 102-2221-E-194-054-. The author would like to thank reviewers for their insightful comments which helped to significantly improve the paper.

References

[1] C. Tsung, H. Ho, and S. Lee, "Analysis of stable prices in non-decreasing sponsored search auction," in *Proceedings of the 13th International Workshop on Agent-Mediated Electronic Commerce*, pp. 84–96, 2011.

[2] T.-M. Bu, L. Liang, and Q. Qi, "On robustness of forward-looking in sponsored search auction," *Algorithmica*, vol. 58, no. 4, pp. 970–989, 2010.

[3] M. Naldi, G. D'Acquisto, and G. F. Italiano, "The value of location in keyword auctions," *Electronic Commerce Research and Applications*, vol. 9, no. 2, pp. 160–170, 2010.

[4] T.-M. Bu, X. Deng, and Q. Qi, "Forward looking Nash equilibrium for keyword auction," *Information Processing Letters*, vol. 105, no. 2, pp. 41–46, 2008.

[5] M. Cary, A. Das, B. Edelman et al., "Greedy bidding strategies for keyword auctions," in *Proceedings of the 8th ACM Conference on Electronic Commerce (EC '07)*, pp. 262–271, June 2007.

[6] B. Edelman, M. Ostrovsky, and M. Schwarz, "Internet advertising and the generalized second-price auction: selling billions of dollars worth of keywords," *American Economic Review*, vol. 97, no. 1, pp. 242–259, 2007.

[7] Y. Narahari, D. Garg, R. Narayanam, and H. Prakash, *Game Theoretic Problems in Network Economics and Mechanism Design Solutions*, Springer, 2009.

[8] N. Nisan, T. Roughgarden, E. Tardos, and V. V. Vazirani, *Algorithmic Game Theory*, Cambridge University Press, 2007.

[9] X. Yan, H. Li, L. Wang, and P. Shen, "Optimal bandwidth scheduling of networked learning control system based on mash theory and auction mechanism," *Mathematical Problems in Engineering*, vol. 41, no. 4, pp. 617–631, 2013.

[10] H. R. Varian, "Position auctions," *International Journal of Industrial Organization*, vol. 25, no. 6, pp. 1163–1178, 2007.

[11] T.-M. Bu, X. Deng, and Q. Qi, "Multi-bidding strategy in sponsored search auctions," *Journal of Combinatorial Optimization*, vol. 23, no. 3, pp. 356–372, 2012.

[12] W. Vickrey, "Counterspeculation, auctions, and competitive sealed tenders," *Journal of Finance*, vol. 16, no. 1, pp. 8–37, 1961.

[13] E. H. Clarke, "Multipart pricing of public goods," *Public Choice*, vol. 11, no. 1, pp. 17–33, 1971.

[14] T. Groves, "Incentives in teams," *Econometrica*, vol. 41, no. 4, pp. 617–631, 1973.

[15] J. Feng, H. K. Bhargava, and D. M. Pennock, "Implementing sponsored search in web search engines: computational evaluation of alternative mechanisms," *INFORMS Journal on Computing*, vol. 19, no. 1, pp. 137–148, 2007.

Research Article

An Innovative Direct-Interaction-Enabled Augmented-Reality 3D System

Sheng-Hsiung Chang¹ and Tsair-Chun Liang²

¹ Department of Optoelectronic Engineering, Far East University, Tainan 744, Taiwan

² Graduate Institute of Electrical Engineering, National Kaohsiung First University of Science and Technology, Kaohsiung 811, Taiwan

Correspondence should be addressed to Sheng-Hsiung Chang; joec358@gmail.com

Received 10 September 2013; Accepted 9 October 2013

Academic Editor: Teen-Hang Meen

Copyright © 2013 S.-H. Chang and T.-C. Liang. This is an open access article distributed under the Creative Commons Attribution License, which permits unrestricted use, distribution, and reproduction in any medium, provided the original work is properly cited.

Previous augmented-reality (AR) applications have required users to observe the integration of real and virtual images on a display. This study proposes a novel concept regarding AR applications. By integrating AR techniques with marker identification, virtual-image output, imaging, and image-interaction processes, this study rendered virtual images that can interact with predefined markers in a real three-dimensional (3D) environment.

1. Introduction

Recently, augmented-reality (AR) techniques have been widely applied in modern technology, allowing developers to incorporate computer-generated virtual images into actual footage that was recorded using a camera. Thus, AR is observed in numerous applications and fields [1–7] such as advertising, films, visual conferences, education, and smart phones.

Previously, integrated real-space and virtual images using AR techniques could only be viewed on a display [8]. For example, Milgram proposed a see-through and monitor-based AR display method that required a display to enable interaction and defined markers and virtual image as indirect interactions. Recent AR products, such as Google Glass, are also see-through methods. The AR system developed in this study differs from those methods because this system enables direct-interaction functionality. This functionality is achieved by using a system-imaging device, which renders virtual images that overlap predefined real space. In addition, the proposed system is in compliance with the three characteristics proposed by Azuma, who stated that AR applications must combine real and virtual elements, be interactive in real time, and operate in three-dimensional (3D) environment [9].

2. The Direct-Interaction 3D System Design

In the application process of AR techniques, this study designed a direct-interaction system that enables direct interactions between real and virtual environments, as shown in Figure 1. The figure depicts a user holding a marker that is used to interact with the AR system. When the camera and computer identify the shape of the marker, the virtual image of the marker overlays the real space by applying image structuring. The user can then directly observe the interaction between the marker and virtual imagery. To achieve this direct interaction, optical principles must be carefully applied to the reimaging structure. The design concepts of the proposed system are explained in the following section.

2.1. The Interactive Design. The interactive structure designed in this study is based on a 3D display technique (Taiwan Patent Publication number I28830 [10]) invented by the research team. By integrating AR application concepts and the 3D display technique, the researchers could design a display system that features direct-interaction functionalities. As shown in Figure 2, the structure of the display system primarily comprises two function types, specifically, an AR identification and interaction function and a virtual-imaging function. In Figure 2, components 1 and 2 are reflective mirrors

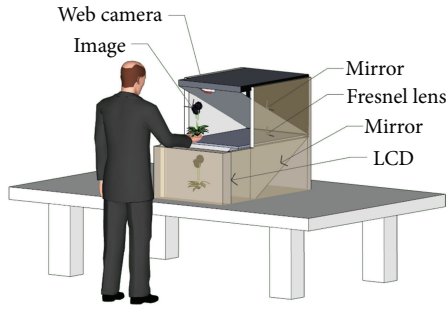


FIGURE 1: The innovative AR direct-interaction 3D system.

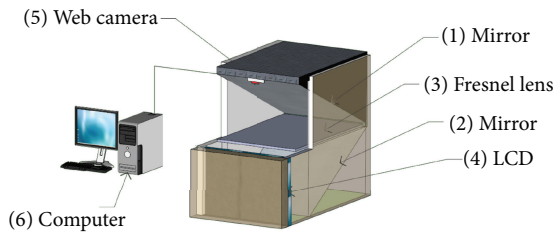


FIGURE 2: The structure of the direct-interaction 3D system.

and component 3 is a Fresnel lens. Integrating these three components enables the system to render virtual images into a real-space platform. Component 4 is a virtual-image display that not only presents virtual images but also presents viewable 3D images. Component 5 is a camera that is used to extract the marker of the real space. A computer (component 6) is used to process the images captured by the imaging system (components 1, 2, and 3) and create virtual images. These images are then projected in a predefined location in which the marker can be used to interact with the real-time AR image directly. The size of the proposed structure is primarily based on two factors, namely, the focal length of the Fresnel lens and the size of the image display (component 4).

2.2. The Optical Design. In this study, component 4 was a flat display instead of a 3D device. This device produces flat images similar to those of conventional indirect-interaction AR systems. To project these images in a real space, the display position and the influence of the Fresnel lens on image quality must be considered. Figure 3 depicts a conceptual diagram of the images generated by using the interactive structure. In the figure, O represents the flat images provided by the display, I represents the generated image, M1 and M2 denote the reflective mirrors placed at 45° angles, L represents an optical condenser, and f denotes the focal length. The mirror image effect is eliminated by using a double-mirror setup (M1 and M2), and inverse images are prevented because the

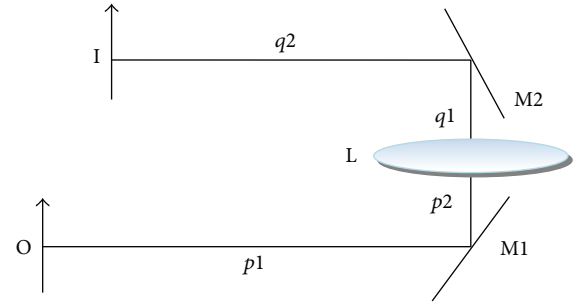


FIGURE 3: A conceptual diagram of the imaging process in the interactive structure.

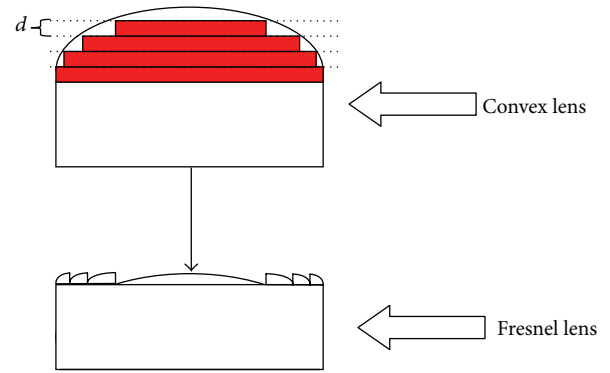


FIGURE 4: The conversion of a convex lens to a Fresnel lens.

angled placement of the mirrors is equivalent to a 180° rotation effect.

The relative positions of O and I are expressed according to the following:

$$\frac{1}{p_1 + p_2} + \frac{1}{q_1 + q_2} = \frac{1}{f}. \quad (1)$$

When the image is magnified to $m = 1$, the optimal image quality is obtained. Because $m = (q_1 + q_2)/(p_1 + p_2)$, $p_1 + p_2 = q_1 + q_2$ is observed in the system structure. When the design of the structure is symmetrical, then $p_2 = q_1$ and $p_1 = q_2$. In addition, the size of I is similar to that of O. In this instance, (1) can be rewritten as

$$\frac{1}{p_1 + p_2} + \frac{1}{p_1 + p_2} = \frac{1}{f}, \quad (2)$$

where $p_1 + p_2 = q_1 + q_2 = 2f$. In this study, the focal length of the optical condenser was $f = 20$ cm; therefore, $p_1 = p_2 = q_1 = q_2 = 20$ cm.

In Figure 3, L represents the optical condenser. Considering generation capacity and component availability, a Fresnel lens was used as a substitute for conventional optical condensers. However, based on diffraction theory, the quality of the final product generated by using a Fresnel lens is different compared to that of a conventional optical condenser. The reason for these differences is demonstrated by the data shown in Figure 4. In this figure, the diffraction potential of

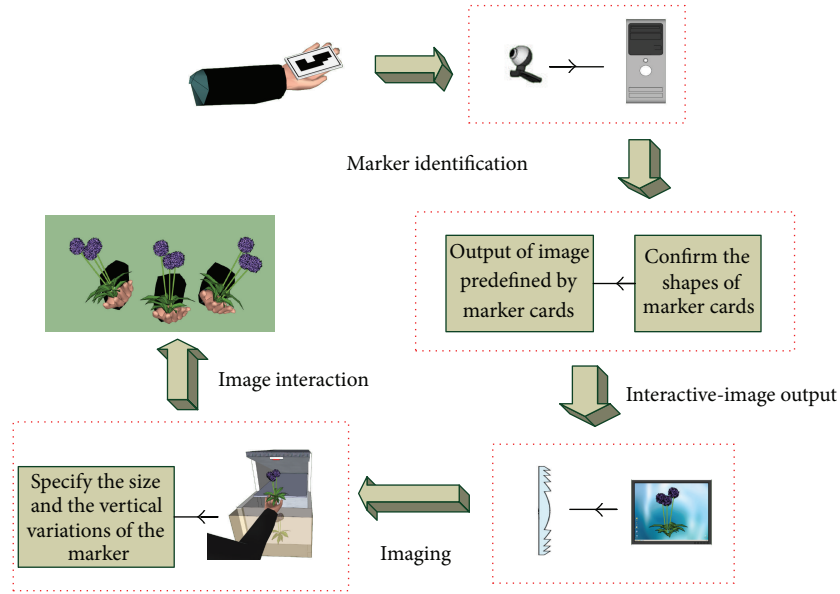


FIGURE 5: The operational principles of the innovative AR direct-interaction system.

a convex lens was stratified and each layer had a thickness of d (the red rectangles in Figure 4). When the red rectangles were removed, the shape of the light wavefront was unaffected and did not affect the imaging results. Thickness d can be obtained by using the following reasoning: let d represent the thickness of the lens medium. The optical wavelength (λ) traveling a distance of d in space corresponds to a phase shift of Φ_1 , whereas that traveling a distance of d in the lens medium corresponds to Φ_2 . Therefore, the difference between phase shifts is Φ . If the reflective index of the lens medium is n , then

$$\begin{aligned}\Phi_1 &= \frac{2\pi d}{\lambda}, \\ \Phi_2 &= \frac{2\pi d}{\lambda/n}.\end{aligned}\quad (3)$$

When $\Phi = \Phi_2 - \Phi_1 = 2n\pi$, then $m = 1, 2, 3, \dots$

The wavefronts of the mentioned light waves are identical. After traveling a distance of d , the wavefronts of the light waves remain identical. Thus, when $m = 1$, the minimum thickness of the reduced lens can be expressed as follows:

$$d = \frac{\lambda}{n-1}.\quad (4)$$

However, the curved surfaces of common Fresnel lenses are imperfect unlike those presented in Figure 4, because the design and manufacturing of these lenses typically involve a second-order manufacturing process. This process sacrifices the microstructures within the lenses [11], thereby substantially reducing the thickness, weight, and size of the lens at the cost of quality degradation. This study adopted a Fresnel lens as the imaging component and used a convex lens for comparing the quality differences.

3. Testing

By integrating the mentioned structural designs and optical principles, this study developed an innovative direct-interaction AR system. Based on the operational principles presented in Figure 5, the proposed system was used to render virtual images into the real space, and the predefined marker was used to interact spontaneously with the system.

3.1. Marker Identification. To render virtual images in 3D environments and enable direct-interaction functionalities, the researchers adopted AR techniques. A camera and computer were used to complete the identification process of the marker cards (Figure 5). The marker cards used in this study were created in black and white, which was easier for the computer to identify. However, other objects could also be used in the identification process.

3.2. Interactive-Image Output. The camera captured the shapes of the marker cards, and the AR design program (VIZARD) was used to identify and confirm the shapes. In the AR program design, a predefined marker representing a 3D bouquet was used. After confirming the shape of the marker, the system produced a predefined 3D bouquet. The shape and angle of the 3D bouquet varied according to the shape and size of the marker determined by the AR system, subsequently producing images at different angles and sizes. In the AR program design, X and Y mirrored the symmetric setting of the 3D bouquet on the liquid crystal display (LCD) and did not require adjustment because of the corresponding positions of the two reflective mirrors (Figure 2) and the two reflecting and single-diffracting processes.

3.3. Imaging. The image displayed on the LCD was rendered onto a marker by using the Fresnel lens in the imaging system.

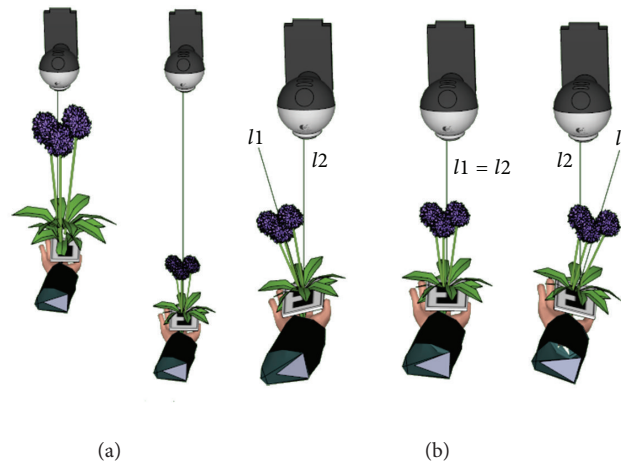


FIGURE 6: The interaction between the marker and the camera.

As previously explained by (1), when $m = 1$, the imaging of M2 is rendered at q_2 , that is, the initial position of the marker. Because component 4 is not a 3D display (Figure 2), the objects were considered flat, and thus a flat image was produced. This restricted the marker identification and display position; that is, the 3D bouquet in this test could only be displayed as a flat image.

3.4. Image Interaction. The 3D bouquet can be illustrated using the Autodesk 3ds Max software. When the image is rendered at the marker, the AR program specifies that the camera captures a specific size and determines the vertical variations of the marker, subsequently displaying the size of the marker. Based on Figure 6(a), when the distance between the marker and camera becomes great, the bouquet becomes small; conversely, at short distances, a large bouquet is displayed.

As established in the AR program, when a specific point on the marker presents a vertical line of l_1 at the central point of the camera, the 3D bouquet becomes perpendicular on the marker card. Thus, when the surface of the marker card changes line angles l_2 and l_1 , the bouquet rotates because the surface of the marker card is rotating, as shown in Figure 6(b). These results indicated that the marker card directly interacts with the predefined image.

4. Conclusions

This study successfully rendered virtual images into the real space and enabled the virtual images to interact with real-time objects. This achievement is a novel application in AR techniques. By integrating the proposed handheld 3D image-interaction structure with an image display and marker identification, AR techniques can successfully be applied to the real space, thereby enabling actual objects to be involved in real-time and direct interaction with virtual images.

References

- [1] M. Billinghurst, H. Kato, and I. Poupyrev, "The MagicBook: a transitional AR interface," *Computers and Graphics*, vol. 25, no. 5, pp. 745–753, 2001.
- [2] J. Liang and M. Green, "JDCAD: a highly interactive 3D modeling system," *Computers and Graphics*, vol. 18, no. 4, pp. 499–506, 1994.
- [3] M. T. Cook and A. Agah, "A survey of sketch-based 3-D modeling techniques," *Interacting with Computers*, vol. 21, no. 3, pp. 201–211, 2009.
- [4] T. Ha, Y. Lee, and W. Woo, "Digilog book for temple bell tolling experience based on interactive augmented reality," *Virtual Reality*, vol. 15, no. 4, pp. 295–309, 2011.
- [5] M. Masry, D. Kang, and H. Lipson, "A freehand sketching interface for progressive construction of 3D objects," *Computers and Graphics*, vol. 29, no. 4, pp. 563–575, 2005.
- [6] E. Sachs, A. Roberts, and D. Stoops, "3-Draw: a tool for designing 3D shapes," *IEEE Computer Graphics and Applications*, vol. 11, no. 6, pp. 18–26, 1991.
- [7] O. Bimber, L. M. Encarnação, and A. Stork, "Multi-layered architecture for sketch-based interaction within virtual environments," *Computers and Graphics*, vol. 24, no. 6, pp. 851–867, 2000.
- [8] P. Milgram, H. Takemura, A. Utsumi, and F. Kishino, "Augmented reality: a class of displays on the reality-virtuality continuum," in *Telem manipulator and Telepresence Technologies*, pp. 2351 of *Proceedings of SPIE*, pp. 282–292, November 1994.
- [9] R. T. Azuma, "A survey of augmented reality," *Presence: Teleoperators and Virtual Environments*, vol. 6, no. 4, pp. 355–385, 1997.
- [10] C. S. Hsiung, "A 3-D display apparatus," Taiwan Patent, Application no. 094131371, Publication no. I288830, August 2007.
- [11] J. N. Mait, "Design of binary-phase and multiphase Fourier gratings for array generation," *Journal of the Optical Society of America A*, vol. 7, no. 8, pp. 1514–1528, 1990.

Research Article

Design and Analysis of a Novel Speed-Changing Wheel Hub with an Integrated Electric Motor for Electric Bicycles

Yi-Chang Wu and Zi-Heng Sun

Department of Mechanical Engineering, National Yunlin University of Science & Technology, Yunlin 640, Taiwan

Correspondence should be addressed to Yi-Chang Wu; wuyc@yuntech.edu.tw

Received 9 September 2013; Accepted 10 October 2013

Academic Editor: Teen-Hang Meen

Copyright © 2013 Y.-C. Wu and Z.-H. Sun. This is an open access article distributed under the Creative Commons Attribution License, which permits unrestricted use, distribution, and reproduction in any medium, provided the original work is properly cited.

The aim of this paper is to present an innovative electromechanical device which integrates a brushless DC (BLDC) hub motor with a speed-changing wheel hub stored on the rear wheel of an electric bicycle. It combines a power source and a speed-changing mechanism to simultaneously provide functions of power generation and transmission for electric bicycles. As part of the proposed integrated device, the wheel hub consists of a basic planetary gear train providing three forward speeds including a low-speed gear, a direct drive, and a high-speed gear. Each gear is manually controlled by the shift control sleeve to selectively engage or disengage four pawl-and-ratchet clutches based on its clutching sequence table. The number of gear teeth of each gear element of the wheel hub is synthesized. The BLDC hub motor is an exterior-rotor-type permanent-magnet synchronous motor. Two-dimensional finite-element analysis (FEA) software is employed to facilitate the motor design and performance analysis. An analysis of the power transmission path at each gear is provided to verify the validity of the proposed design. The results of this work are beneficial to the embodiment, design, and development of novel electromechanical devices for the power and transmission systems of electric bicycles.

1. Introduction

An electric bicycle is a bicycle with an integrated electric motor which can be used for urban transportation, propulsion, and recreation. Except for those with direct-driven hub motors, electric bicycles are typically equipped with speed-changing devices to mechanically adjust the rotational speed of the rear wheel. Since the efficiency of an electric motor is related to its rotational speed, an electric bicycle further provides a mechanical speed-changing device for transmission enabling the electric motor to operate in its most efficient state and, hence, leads to longer periods of use before the battery needs to be charged. As can be seen in the existing products [1], the electric motor and the speed-changing device of an electric bicycle, which are, respectively, used for power generation and transmission, make up individual electrical and mechanical devices. The driving power generated by the electric motor is mostly transmitted from the front chain-wheel at the crankset to the rear sprocket installed on the rear wheel via a chain mechanism. The main

drawback of such a conventional design is the lengthy power transmission path from the electric motor to the speed-changing device using a sprocket and chain mechanism, which may cause additional mechanical energy losses due to friction. A second drawback is the cumbersome workspace arrangement due to the individual design of the electric motor and the speed-changing device. Hence, the integration of the electric motor and the speed-changing device for electric bicycles is worth studying. Upon investigating existing electric bicycles, we found that they usually employ the rear derailleur system as the mechanical speed-changing device to provide a set of speed ratios. Unfortunately, the derailleur, the chain, and sprockets are all exposed to the elements. Rain and mud usually stick to the shifter and may damage the derailleur. Therefore, the derailleur mechanism needs to be regularly maintained. In contrast, the speed-changing wheel hub, which is implemented with a planetary gear train and a speed-changing control mechanism, is immune to contamination due to the protection of the hub shell. Such a kind of internal transmission hub for electric bicycles

has the unique advantages of compact size, good reliability, and high efficiency [2–4]. One special feature of the speed-changing wheel hub is that it can change gear ratios when the rear wheel is not rotating. This can be very useful for a commuter with frequent stop-and-go riding in urban areas. Because the speed-changing wheel hub generally has a long maintenance-free life, it is the subject of ongoing research by commercial organizations and academic institutions. As for the power source of electric bicycles, several types of electric motors, including brush DC motors, induction motors, reluctance motors, and brushless permanent-magnet motors, are employed in existing products for traction. Among these electric motors, brushless DC (BLDC) motors have attracted increasing interest due to the characteristics of high efficiency, low cost of maintenance, light weight, easy speed control, and low noise and vibration [5, 6]. Due to these reasons, the BLDC motor and the speed-changing wheel hub are designated as the objects of this study. In addition, the integration of the BLDC motor and the speed-changing wheel hub for electric bicycles may offer new opportunities to overcome the above shortcomings of existing products.

The purpose of this paper is to develop a novel electromechanical device by combining an electric motor with a speed-changing wheel hub for electric bicycles to overcome the drawbacks of traditional designs. An integrated design that combines an exterior-rotor BLDC hub motor within a three-speed wheel hub resulting in a compact power generation and transmission device is introduced. The configuration, operational principles, and qualitative features of the proposed design are addressed. A clutching sequence table is synthesized to provide three forward speeds. The embodiment design of a speed-changing wheel hub, that comprises a basic planetary gear train and a speed-changing control mechanism, is presented. Besides, a 350 W, 3-phase, 12-pole/18-slot BLDC hub motor with an exterior-rotor configuration is designed as part of the integrated device, and the electromagnetic torque of this motor is calculated by finite-element analysis (FEA). Finally, the power transmission path at each speed is illustrated to verify the feasibility of the integrated device.

2. A Novel Design Concept

By integrating a 3-phase, 12-pole/18-slot exterior-rotor BLDC hub motor within a three-speed wheel hub, an electromechanical device with a compact structure is proposed. This integrated device is stored on the rear wheel of the electric bicycle. Figures 1(a), 1(b), and 1(c), respectively, show an exploded view, a cutaway view, and a longitudinal sectional view of the proposed design concept. For the three-speed wheel hub, it consists of two degrees-of-freedom (DOF) basic planetary gear train, which is the main body of the wheel hub and a speed-changing control mechanism to carry out a power source impartation. The basic planetary gear train is the simplest geared mechanism in the planetary gear train family, which comprises a stationary hub shaft (Member 0) mounted to the rear fork of the electric bicycle, a planet gear (Member 4) engaged with a sun gear (Member 1) and a ring

gear (Member 2), and a planet arm (Member 3) to maintain a constant distance between the sun gear (Member 1) and the planet gear (Member 4). The sun gear (Member 1), the ring gear (Member 2), and the planet arm (Member 3) all rotate about the stationary hub shaft (Member 0); they are called coaxial links. Only coaxial links can be used as the input, output, or fixed links of a transmission due to the engineering reality [7, 8]. To obtain a predictable output with this two-DOF planetary gear train, two independent inputs, including one input link and one fixed link, are required. The sun gear (Member 1) is designated as the fixed link since it is mounted to the stationary hub shaft (Member 0). The ring gear (Member 2) or the planet arm (Member 3) serves as the input link or the output link. Once the ring gear (Member 2) is designated as the input link, then the planet arm (Member 3) becomes the output link, and vice versa. The speed-changing control mechanism consists of a shift control sleeve (Member 8) to selectively control the engagement or the disengagement of two one-way clutches, including an input pawl-and-ratchet clutch (Member C_{i3}) and an output pawl-and-ratchet clutch (Member C_{o2}), and a compression spring (Member 13) attached to the right side of the shift control sleeve (Member 8). As illustrated in Figure 2, the right side of the shift control sleeve (Member 8) disposes of a plurality of keys to transfer the rotational power from the rotor yoke (Member 6). In the middle of the shift control sleeve (Member 8), a circular flange is configured to control the engagement or the disengagement of an output pawl-and-ratchet clutch (Member C_{o2}). The left side of the shift control sleeve (Member 8) circularly disposes of pawls which are used to engage with the ratchet arranged in the inner periphery of the planet arm (Member 3) to form an input pawl-and-ratchet clutch (Member C_{i3}). The activation of clutches C_{o2} and C_{i3} is controlled by the axially relative position of the shift control sleeve (Member 8) and the stationary hub shaft (Member 0). The main components of the exterior-rotor BLDC hub motor are a rotor (Member 6) and a stator (Member 5). Twelve permanent magnets (Member 7) are affixed to the inner surface of the rotor yoke (Member 6) to prevent the magnets from flying apart, especially in high-speed applications. In contrast to a traditional interior-rotor BLDC motor, the relatively large rotor diameter increases the moment of inertia, which in turn helps maintain a constant rotational speed. The rotor yoke (Member 6) is engaged with the ring gear (Member 2) by an input pawl-and-ratchet clutch (Member C_{i2}) and is engaged with the shift control sleeve (Member 8) by a plurality of keys on the shift control sleeve (Member 8) and slots on the rotor yoke (Member 6). The stator (Member 5) has eighteen stator slots around which 3-phase winding coils are wound. Both the rotor yoke (Member 6) and the stator (Member 5) are comprised of a lamination of magnetic steel slices to reduce the eddy current losses. In addition, Member 9 is the hub shell of the integrated device, Member 10 is a cover integrated with a bearing seat, Member 11 is the right-side ball bearing, Member 12 is the left-side ball bearing, and Members 14 and 15 are pins for the planet gear (Member 4) and pawls of one-way clutches, respectively. Each speed of the integrated device is governed by the engagement and disengagement of four pawl-and-ratchet clutches C_{i2} ,

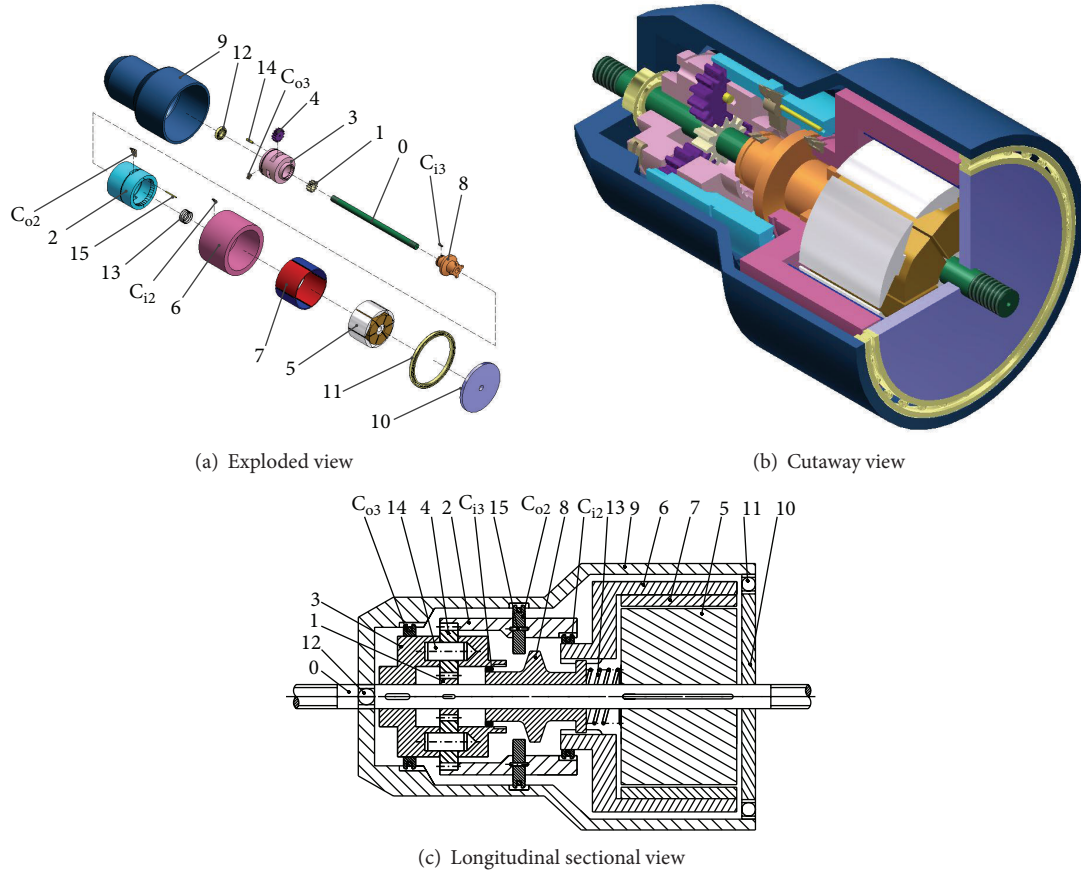


FIGURE 1: A novel electromechanical device in which a three-speed wheel hub integrates with an exterior-rotor BLDC hub motor.

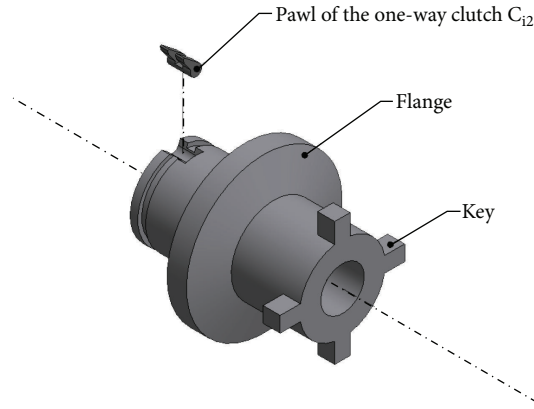


FIGURE 2: A shift control sleeve (Member 8) of the speed-changing control mechanism of the integrated device.

C_{o2} , C_{i3} , and C_{o3} for proper control of the power transmission path based on the clutching sequence table presented in the following section.

In contrast to individual designs of power generation and transmission systems of existing electric bicycles, the proposed integrated design has the following significant features. (1) The BLDC motor, integrated with a three-speed wheel hub, reduces the use of a chain mechanism and related mechanical fasteners. Fewer mechanical components may

decrease production cost, improve the reliability, and make the power and transmission systems more compact and lightweight. (2) The length of the power transfer path from the electric motor to the speed-changing device installed on the rear wheel has shrunk, which also reduces the required space for installation. (3) The proposed design provides three forward speeds. It enables the electric motor to operate in its most efficient state due to the mechanically adjustable speed of the rear wheel by the speed-changing wheel hub.

3. Design of a Three-Speed Wheel Hub

For a 5-link, 2-DOF basic planetary gear train, the related functional schematic is illustrated in Figure 3. The sun gear (Member 1) is adjacent to the planet gear (Member 4) with an external gear pair (Joint a), while the planet gear (Member 4) is adjacent to the ring gear (Member 2) with an internal gear pair (Joint b). A fundamental circuit consists of two meshing gears i and j and one carrier k to maintain a constant center distance between the two gears, which is symbolically denoted as $(i, j)(k)$ [9, 10]. Two fundamental circuits are identified as $(1, 4)(3)$ and $(2, 4)(3)$, respectively. The corresponding fundamental circuit equations are

$$\begin{aligned} \omega_1 - \gamma_{41}\omega_4 + (\gamma_{41} - 1)\omega_3 &= 0, \\ \omega_2 - \gamma_{42}\omega_4 + (\gamma_{42} - 1)\omega_3 &= 0, \end{aligned} \tag{1}$$

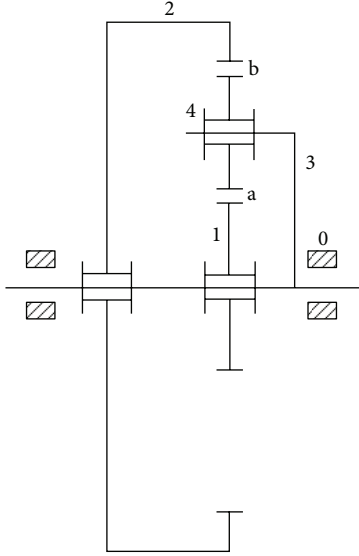


FIGURE 3: A functional schematic of a 5-link, 2-DOF basic planetary gear train.

where ω_i is the angular speed of link i and gear ratios $\gamma_{41} = -Z_4/Z_1$ and $\gamma_{42} = +Z_4/Z_2$. The positive sign of the gear ratio represents an internal gear pair, and the negative sign depicts an external gear pair. The symbol Z_i is the number of teeth on gear i . By eliminating ω_4 from (1), the kinematic equation of a basic planetary gear train is

$$\omega_1 - \gamma_{24}\gamma_{41}\omega_2 + (\gamma_{24}\gamma_{41} - 1)\omega_3 = 0, \quad (2)$$

where the gear ratio $\gamma_{24} = 1/\gamma_{42}$. As mentioned in Section 2, the sun gear (Member 1) is designated as the fixed link, while the ring gear (Member 2) or the planet arm (Member 3) serves as the input link or the output link for the proposed speed-changing wheel hub. Therefore, three different arrangements are listed in Table 1. The speed ratio (SR) is defined as the ratio of the input link speed to the output link speed, while the SR formula can be derived from the kinematic equation shown in (2). It is found that the SR formulas of Case 1 and Case 2 are reciprocal. Since the SR of Case 1 is greater than one, that is, $(\gamma_{24}\gamma_{41} - 1)/\gamma_{24}\gamma_{41} > 1$, it is an underdrive. The SR of Case 2 is less than one; that is, $0 < \gamma_{24}\gamma_{41}/(\gamma_{24}\gamma_{41} - 1) < 1$; it is an overdrive. The SR of Case 3 is equal to one; it is a direct drive. Therefore, the proposed three-speed wheel hub provides an underdrive for the low-speed gear (Gear I), a direct drive (Gear II), and an overdrive for the high-speed gear (Gear III). We let the SR of Gear I be 4/3 for the low-speed driving; that is, $(\gamma_{24}\gamma_{41} - 1)/\gamma_{24}\gamma_{41} = 4/3$; then, we have $3Z_1 = Z_2$. Due to the limited installation space of the rear fork, the minimum number of teeth of sun gear Z_1 is selected as 18 to avoid gear interference, when the module is equal to 1. Because the number of teeth of planet gear Z_4 does not affect the SR, the minimum number of teeth of planet gear Z_4 is also selected as 18. A set of feasible solutions for the number of teeth on the sun gear, planet gear, and ring gear are $Z_1 = 18$, $Z_4 = 18$, and $Z_2 = 54$, respectively. For the direct drive, the input link can be designated as the ring gear (Member 2) or

TABLE 1: Speed ratio at each speed of the three-speed wheel hub.

Case	Fixed link	Input link	Output link	SR formula
I	1	2	3	$(\gamma_{24}\gamma_{41} - 1)/\gamma_{24}\gamma_{41}$
II	1	3	2	$\gamma_{24}\gamma_{41}/(\gamma_{24}\gamma_{41} - 1)$
III	1	2 (3)	2 (3)	1

the planet arm (Member 3). Based on the engineering reality, the power transmission path from the rotor (Member 6) of the BLDC motor to the hub shell (Member 9) via the ring gear (Member 2) is shorter than that via the planet arm (Member 3). Due to this, the input link of Gear II is selected as the ring gear (Member 2). The related clutching sequence table and the SR of each gear of the proposed three-speed wheel hub are shown in Table 2, where the symbol ‘‘X’’ denotes that the corresponding clutch is engaged. It is noted that only one clutch is engaged while another is simultaneously disengaged during speed ratio changes, so, the proposed three-speed wheel hub is operated with a single clutch-to-clutch shaft. This is an important feature for a mechanical wheel hub to shift smoothly from one speed to another.

4. Design of an Exterior-Rotor BLDC Hub Motor

The design of a BLDC hub motor is an iterative process, where many unknown parameters are involved. One important task is to check whether the electromagnetic torque of the hub motor is sufficient to propel an electric bicycle. In general, the rated torque about of 15 Nm is required for an electric bicycle. A 350 W, 3-phase, 12-pole/18-slot BLDC hub motor with an exterior-rotor configuration has been designed as part of the integrated device for use in electric bicycles. Figure 4 illustrates the geometry of the designed BLDC hub motor that contains a cross-sectional view and related geometric parameters. Table 3 shows the rated conditions, magnet’s material properties, and design results for the exterior-rotor BLDC hub motor. The permanent magnet is selected as the neodymium-iron-boron (NdFeB) BNPI2. The winding configurations of each phase for the BLDC hub motor are schematically shown in Figure 5. A two-dimensional FEA package Ansoft/Maxwell has been employed in the magnetic field analysis and electromagnetic torque calculation of the hub motor. The flux density distribution within the air gap is shown in Figure 6. We can find that the dips in the air gap flux density occur at 15 and 42 mechanical degrees, which are caused by stator slot openings. The pulsation of the air gap flux density is pronounced under a fixed region near the dips, which may be induced by the flux concentrating effect. Figure 7 shows the three-phase flux linkage waveforms of this BLDC hub motor obtained from the software simulation. The period of the flux linkage waveform is equal to 360 electrical degrees, that is, 60 mechanical degrees for this hub motor with 6 magnet pole pairs. The waveforms of the three-phase back-EMF constant without multiplying the number of coils are presented in Figure 8. It can be found

TABLE 2: A clutching sequence table of the proposed three-speed wheel hub.

Gear	Clutch				SR
	C_{i2}	C_{o2}	C_{i3}	C_{o3}	
Low-speed gear (Gear I)	X			X	1.33
Direct drive (Gear II)	X	X			1.00
High-speed gear (Gear III)		X	X		0.75

TABLE 3: Rated conditions, magnet's material properties, and design results for an exterior-rotor BLDC hub motor.

Items	Symbol	Values
Rated conditions		
Rated power (W)	P_R	350
Rated speed (rpm)	ω_R	300
Magnet's material properties (NdFeB BNP12)		
Remanence (T)	B_r	0.76
Relative permeability	μ_r	1.26
Coercivity (A/m)	H_c	-480000
Direction of magnetization	—	Parallel
Magnet thickness (mm)	l_m	2
Magnet arc (degree)	θ_m	27
Design results		
Number of phases	N_{ph}	3
Number of magnet poles	P	12
Number of armature slots	S	18
Air-gap length (mm)	g	0.5
Slot opening (mm)	W_s	2.6
Inner radius of rotor (mm)	R_{ri}	50.5
Outer radius of rotor (mm)	R_{ro}	60
Inner radius of stator (mm)	R_{si}	20
Outer radius of stator (mm)	R_{so}	50
Tooth width of stator (mm)	w_{tb}	7
Shoe depth (mm)	d_1	2
Shoe ramp (degree)	d_2	0
Number of coils per armature tooth (turn)	N_c	54
Stack length (mm)	L	80
Rated phase current (A)	i_{ph}	8.3

that a concave portion, which is caused by the stator slot opening on the stator, occurs on the flat top of the back-EMF constant waveform. The back-EMF constant waveform of each phase is similar to a trapezoidal wave shape, so each phase current of this motor is suitable to operate with square-wave excitation, as shown in Figure 9. The electromagnetic torque generated by this BLDC hub motor based on the FEA simulation is demonstrated in Figure 10. The average electromagnetic torque of this BLDC hub motor is 19.67 Nm, which is sufficient to propel an electric bicycle.

5. Analysis of Power Transmission Path

The validity for the operation of the integrated device at each gear can be checked by analyzing the related power

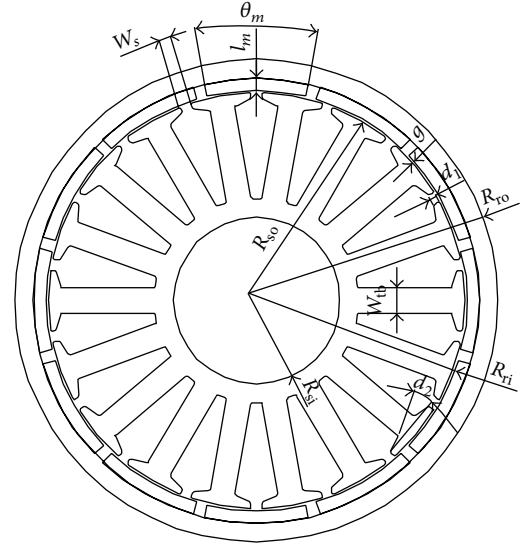


FIGURE 4: Cross-section and geometric parameters of the BLDC hub motor.

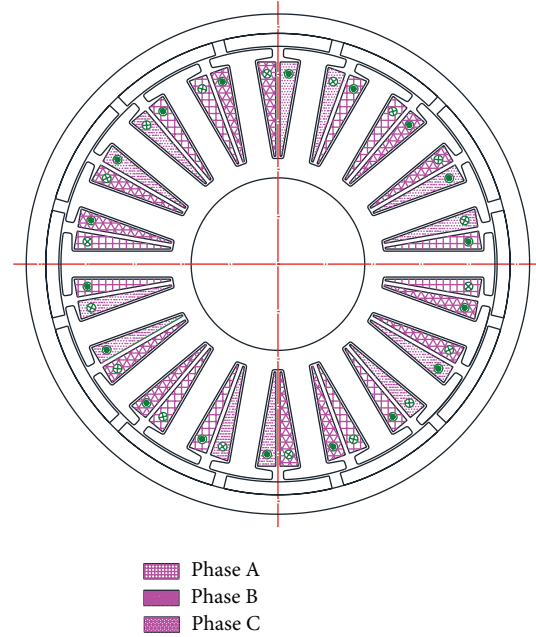


FIGURE 5: Winding configurations of each phase for the BLDC hub motor.

transmission path. At a low-speed gear (Gear I), pawl-and-ratchet clutches C_{i2} and C_{o3} are simultaneously engaged according to the clutching sequence table, shown in Table 2. The shift control sleeve (Member 8) is in its left position. The pawl of clutch C_{o2} is controlled by the flange of the shift control sleeve (Member 8) to be unengaged, as sketched in Figure 11, while clutch C_{i3} is also controlled to be unengaged. The power from the rotor yoke (Member 6) of the BLDC hub motor is transmitted via clutch C_{i2} to the ring gear (Member 2), the planet gear (Member 4), the planet arm (Member 3), clutch C_{o3} , and finally, to the hub shell (Member 9), as shown

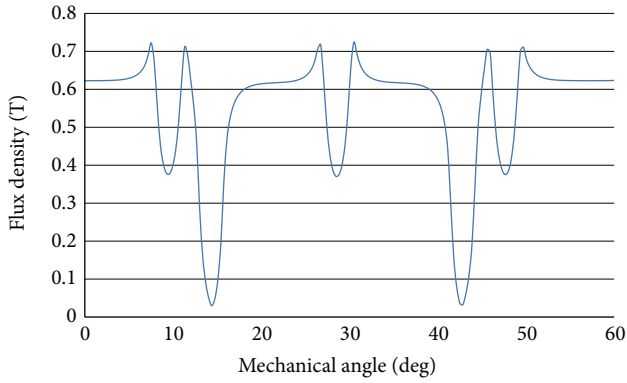


FIGURE 6: Air gap flux density of the BLDC hub motor.

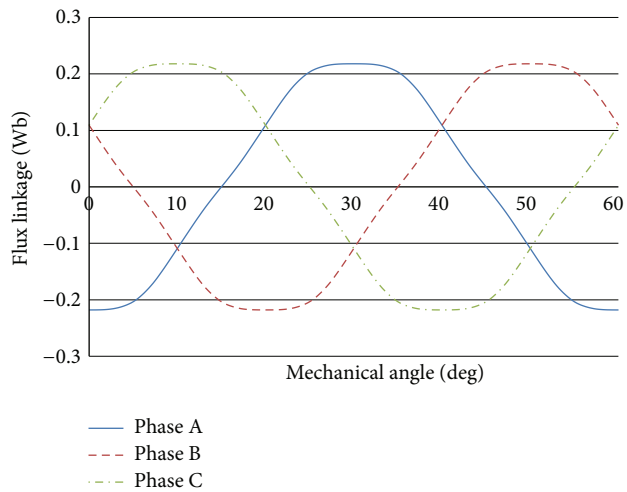


FIGURE 7: Three-phase flux linkage waveforms of the BLDC hub motor.

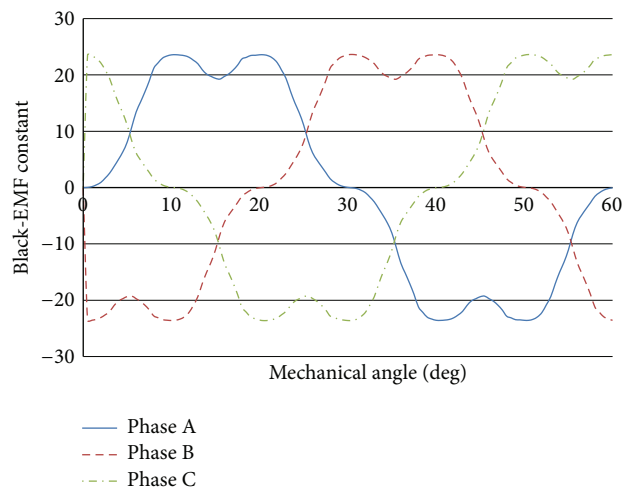


FIGURE 8: Three-phase back-EMF constant waveforms of the BLDC hub motor.

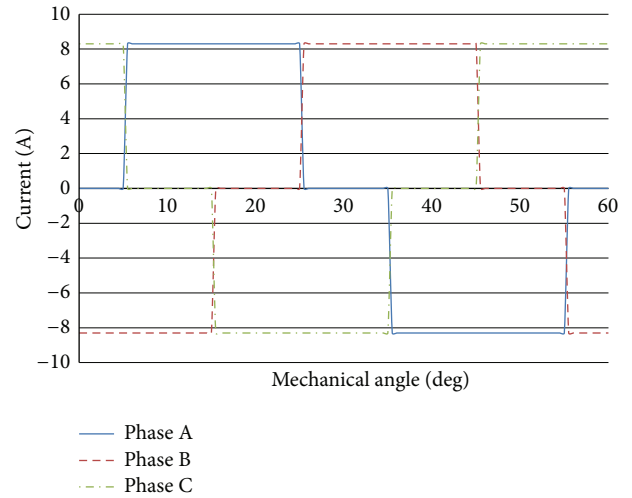


FIGURE 9: Three-phase excitation current waveforms of the BLDC hub motor.

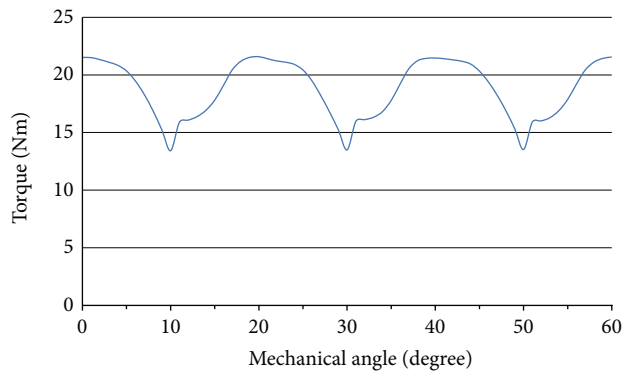


FIGURE 10: Electromagnetic torque generated by the BLDC hub motor.

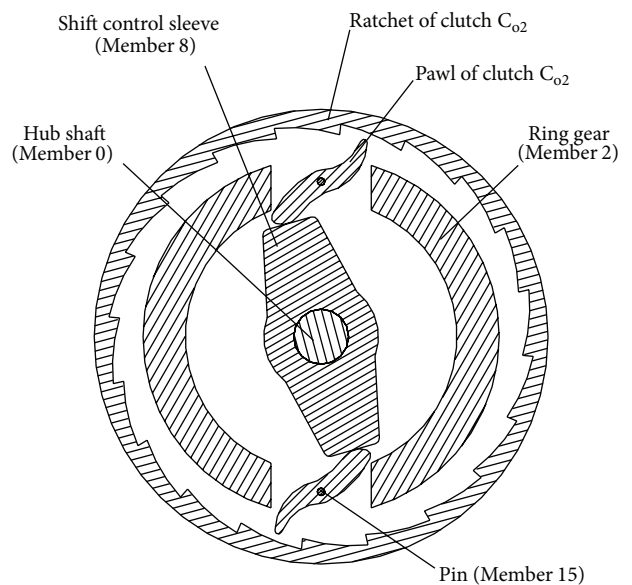


FIGURE 11: The pawl of clutch C_{o2} is controlled by the flange of the shift control sleeve to be unengaged.

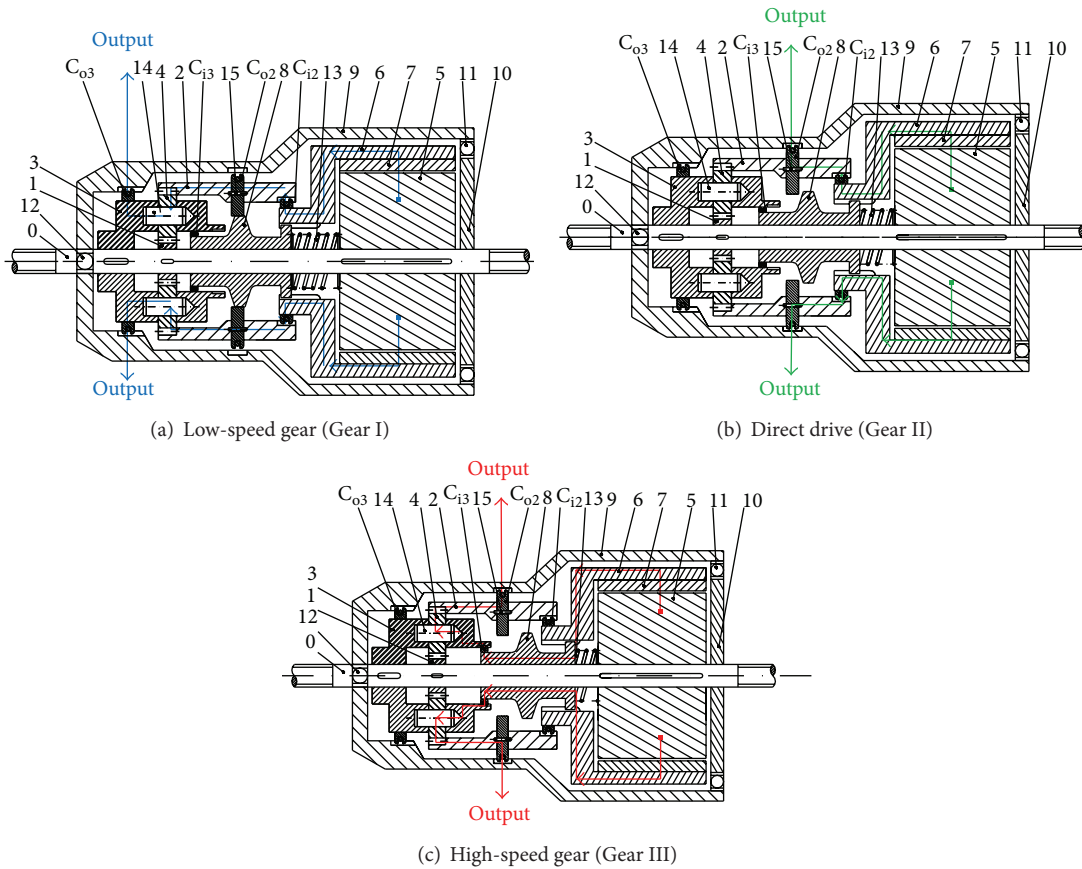


FIGURE 12: Power transmission path at each gear of the integrated device.

in Figure 12(a). At the direct drive (Gear II), the shift control sleeve (Member 8) is axially shifted to the middle position along the stationary hub shaft. Since the pawl of clutch C_{o2} is no longer controlled by the flange of the shift control sleeve (Member 8), it is engaged with the ratchet portion on the hub shell (Member 9) due to the action of a torsion spring stored at a pin (Member 15), as shown in Figure 13. At Gear II, only clutch C_{i3} is controlled to be unengaged. The power from the rotor (Member 6) of the BLDC hub motor at this speed is transmitted via clutch C_{i2} , the ring gear (Member 2), clutch C_{o2} , and then, directly to the hub shell (Member 9), as shown in Figure 12(b). When the shift control sleeve (Member 8) is further shifted to the right position, the integrated device is at a high-speed gear (Gear III). The pawl of clutch C_{i3} on the shift control sleeve (Member 8) is engaged with the ratchet on the planet arm (Member 3), thereby activating clutch C_{i3} . Since the rotational speed of the ring gear (Member 2) is faster than that of the planet arm (Member 3) at Gear III, clutch C_{o2} is engaged. As shown in Figure 12(c), the power from the rotor (Member 6) of the BLDC hub motor is transmitted via the shift control sleeve (Member 8), clutch C_{i3} , the planet arm (Member 3), the planet gear (Member 4), the ring gear (Member 2), clutch C_{o2} , and finally, to the hub shell (Member 9). Based on the above analyses, three forward speeds of the proposed design can be successfully achieved.

6. Conclusion

A novel electromechanical device integrating an electric motor within a speed-changing wheel hub is presented for electric bicycle applications. A 5-link, 2-DOF planetary gear mechanism is employed to provide three forward speeds, including an underdrive ($SR = 1.33$), a direct drive ($SR = 1.00$), and an overdrive ($SR = 0.75$). A speed-changing control mechanism is designed and installed within the planetary gear mechanism to manually control four pawl-and-ratchet clutches, which govern the power transmission path at each gear. A set of feasible solutions for the number of gear-teeth of the planetary gear mechanism is further synthesized based on the fundamental circuit equations. A 350 W, 3-phase, 12-pole/18-slot BLDC hub motor with an exterior-rotor configuration is designed as the power source of the integrated device by using commercial finite-element analysis package Ansoft/Maxwell. The average electromagnetic torque of this BLDC hub motor is 19.67 Nm, which is sufficient for electric bicycle applications. Such an integrated device overcomes inherent drawbacks of existing products. Although the proposed device integrates an exterior-rotor BLDC motor with a basic planetary gear train, it can be extended to the integration of other types of electric motors with a multispeed wheel hub for providing better output performance and more forward speed ratios.

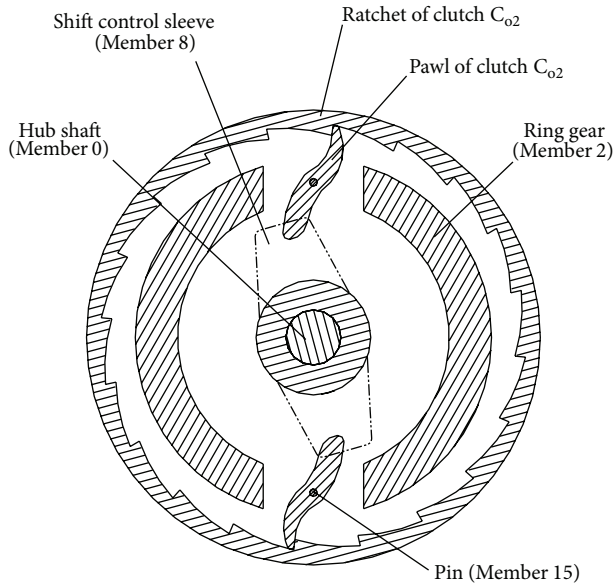


FIGURE 13: The pawl of clutch C_{02} engaged with the ratchet portion on the hub shell.

Acknowledgment

The authors are grateful to the National Science Council (Taiwan) for supporting this research under Grant NSC 102-2221-E-224-016-MY2.

References

- [1] *Giant Bicycles Catalog*, Giant Bicycle, Taipei, Taiwan, 2013.
- [2] Y. C. Wu and P. W. Ren, "Design and analysis of a multispeed transmission hub," *INFORMATION*, vol. 16, no. 9(B), pp. 7003–7014, 2013.
- [3] C.-H. Hsu and Y.-C. Wu, "Automatic detection of embedded structure in planetary gear trains," *Journal of Mechanical Design, Transactions of the ASME*, vol. 119, no. 2, pp. 315–318, 1997.
- [4] Y. C. Wu and S. L. Lin, "Conceptual design of a 16-speed bicycle drive hub," *Applied Mechanics and Materials*, vol. 52–54, pp. 279–284, 2011.
- [5] Z. Q. Zhu, D. Howe, and C. C. Chan, "Improved analytical model for predicting the magnetic field distribution in brushless permanent-magnet machines," *IEEE Transactions on Magnetics*, vol. 38, no. 1, pp. 229–238, 2002.
- [6] B. Han, S. Zheng, and X. Liu, "Unbalanced magnetic pull effect on stiffness models of active magnetic bearing due to rotor eccentricity in brushless DC motor using finite element method," *Mathematical Problems in Engineering*, vol. 2013, Article ID 745912, 10 pages, 2013.
- [7] C.-H. Hsu and R.-H. Huang, "Systematic design of six-speed automatic transmissions with an eight-link two-DOF Ravigneaux gear mechanism," *Journal of Mechanical Design, Transactions of the ASME*, vol. 131, no. 1, Article ID 0110041, 8 pages, 2009.
- [8] W. H. Hsieh, "Kinetostatic and mechanical efficiency studies on cam-controlled planetary gear trains—part I theoretical analysis," *Indian Journal of Engineering and Materials Sciences*, vol. 20, no. 3, pp. 191–198, 2013.

- [9] F. Freudenstein and A. T. Yang, "Kinematics and statics of a coupled epicyclic spur-gear train," *Mechanism and Machine Theory*, vol. 7, no. 2, pp. 263–275, 1972.
- [10] L.-C. Hsieh and H.-S. Yan, "Generalized kinematic analysis of planetary gear trains," *International Journal of Vehicle Design*, vol. 13, no. 5-6, pp. 494–504, 1992.

Research Article

Fast Facial Detection by Depth Map Analysis

Ming-Yuan Shieh and Tsung-Min Hsieh

Department of Electrical Engineering, Southern Taiwan University of Science and Technology, Tainan 710, Taiwan

Correspondence should be addressed to Ming-Yuan Shieh; myshieh@mail.stust.edu.tw

Received 15 September 2013; Accepted 17 October 2013

Academic Editor: Teen-Hang Meen

Copyright © 2013 M.-Y. Shieh and T.-M. Hsieh. This is an open access article distributed under the Creative Commons Attribution License, which permits unrestricted use, distribution, and reproduction in any medium, provided the original work is properly cited.

In order to obtain correct facial recognition results, one needs to adopt appropriate facial detection techniques. Moreover, the effects of facial detection are usually affected by the environmental conditions such as background, illumination, and complexity of objectives. In this paper, the proposed facial detection scheme, which is based on depth map analysis, aims to improve the effectiveness of facial detection and recognition under different environmental illumination conditions. The proposed procedures consist of scene depth determination, outline analysis, Haar-like classification, and related image processing operations. Since infrared light sources can be used to increase dark visibility, the active infrared visual images captured by a structured light sensory device such as Kinect will be less influenced by environmental lights. It benefits the accuracy of the facial detection. Therefore, the proposed system will detect the objective human and face firstly and obtain the relative position by structured light analysis. Next, the face can be determined by image processing operations. From the experimental results, it demonstrates that the proposed scheme not only improves facial detection under varying light conditions but also benefits facial recognition.

1. Introduction

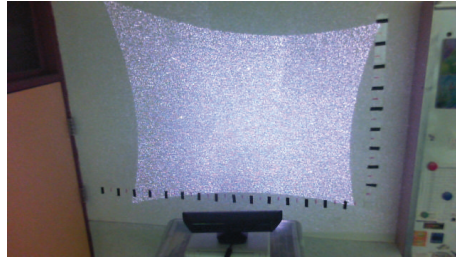
The processes of digital image processing such as detection and recognition are similar to those of human vision. To enhance the effectiveness of digital image processing, numerous approaches focus on 3D image processing methodology especially depth map scan and related topics. To make closer interaction between human and device, the game console Wii released by Nintendo in 2006 had raised the studies on detections of pose, gesture, action and motion, and related topics. Further on 3D detection, the Kinect released by Microsoft is a motion sensing device as a game console for Xbox 360 and Windows PCs. By the Kinect, users just need to swing their hands, legs, or body and then can interactively control game role players. The new idea inspires numerous players and researchers to invest in 3D scanning, motion detection and interaction and related approaches.

The first success of Kinect is its depth map scan which let users easily determine the depth of every object from a screen. From the technical documents provided from the PrimeSense Ltd. [1], in the light coding solutions, the Kinect generates near-IR light to code the scene and then uses a standard off-the-shelf CMOS image sensor to read the coded

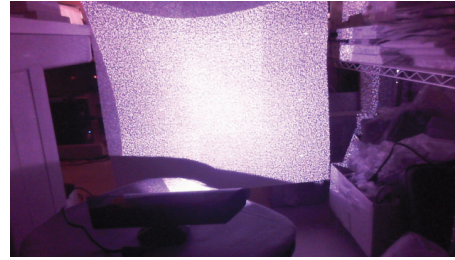
light back from the scene. In which, the near-IR emitter diverges an infrared beam through a diverging lens and then the beam is projected on the surfaces in the form of uniform squares scattered as formed structured light planes. Then, the monochrome CMOS image sensor detects and recognizes the structured light map and then results in the depth map. Since near-infrared light is invisible and unaffected by ambient light, to diverge near-infrared light to detect distance is very suitable.

Besides, many similar studies [2–7] on structured light coding are proposed. In [2], Albitar et al. proposed a monochromatic pattern for a robust structured light coding which allows a high error rate characterized by an average Hamming distance higher than 6. Tong et al. present an up-to-date review and a new classification of the existing structured light techniques in [4].

Generally, to integrate two or more cameras/image sensors as a stereo vision device is a common technology for 3D capture. Another aspect, during these years numerous researchers focus on 3D scanning. Unlike 3D camera that collects color information about surfaces, 3D scanner collects depth/distance information about surfaces. These two aspects



(a) The speckle pattern projected on the surface from distance of 1.6 m (in a common room)



(b) The speckle pattern projected on the surface from distance of 0.5 m (in a dark room)

FIGURE 1: Test of the speckle patterns projected from different distances.

both provide useful information for stereo vision but also lack others [5]. That is why Kinect [6, 7] integrates an infrared projector and a monochrome CMOS camera as the depth sensor to collect distance information and adopts a RGB camera as the image sensor to collect color information for full 3D motion capture and facial recognition.

For advanced security, to detect and recognize biological characteristics such as fingerprint, face, voice, and iris, has become a commonly used technology. Among these biometric identification technologies, face identification is the most widely used. Since good recognition must follow good detection in face identification processes, how to detect the objective faces became a major topic, in which the depth map of image objects will be an important factor because if the object is far away from the camera then its image in size will be smaller than original without zooming. It means that if the depth map and the 2D image are considered simultaneously, then the facial detection and recognition will become easy.

Nowadays, there are numerous approaches on facial detection and recognition. The common technologies of facial recognition consist of Eigenface, Fisherface, waveletface, EGM (Elastic Graph Matching), PCA (Principal Component Analysis), LDA (Linear Discriminant Analysis), Haar wavelet transform, and so on. It is worthy noted that most approaches develop the theory and algorithms on 2D image processing. There are many approaches [6–11] that focus on 3D integrated face reconstruction and recognition, in which the depth map becomes as an important factor. For instance, in the approach [8], Burgin et al. extend the classic Viola-Jones face detection algorithm [9] which considers depth and color information simultaneously while detecting faces in an image. The studies proposed by Rodrigues et al. in [10] discuss an efficient 2D to 3D facial reconstruction and recognition scheme.

In this paper, the human facial features of configuration and movement are estimated by using Haar wavelet transform. The features will be considered as patterns for facial detection and recognition. To determine skin color range, geometric relationships of features, and eigenfaces as patterns, the system will conclude the facial appearance and features to the most similar pattern. Then, the interface will show the meaning of the facial expression.

2. Structured Light Based Depth Map Analysis

In Kinect system, there are two speckle patterns that could appear on the camera: one is the primary speckle coming from the diffuser (projected on the object) and the other is the secondary speckle formed during the imaging due to the lens aperture and object material roughness. It only concentrates in primary speckle. The primary speckle pattern, produced by the diffuser and diffractive optical element (DOE) and then projected on the surface, varies with z -axis, in which the PrimeSense Ltd. calls the speckle pattern structured light. Based on the extended depth of field (EDoF), DOE is the embodiment of astigmatic optical element, which has different focus for different angle direction. Besides, DOE is designed to reduce the divergence angle so that light intensity would vary slower with distance.

Figure 1(a) shows the speckle pattern projected when the distance between the surface and the device is 1.60 m; Figure 1(b) displays the speckle pattern projected in a dark room from the distance of 0.5 m. Moreover, in order to test how the speckle pattern is generated by an infrared light source, one can modify the webcam: LifeCam Cinema (Microsoft, as shown in Figure 2(a)) by removing the filter of infrared light. As shown in Figures 2(b) and 2(c), there indicate the speckle patterns of the projection surfaces captured by the modified webcam where the infrared light is emitted from a remote control and the Kinect respectively. Notice that the infrared light source of the Kinect, emits a pyramidal speckle pattern.

In this paper, the detectable range of objects is the distances from 60 cm to 10 m and in front of the Kinect. By integrating a Kinect and its depth map analysis, the proposed system aims to improve the effectiveness of facial detection. The diagram of proposed scheme is as shown in Figure 3. At first, the Kinect emits a near-IR light beam which is then projected on surfaces and forms a speckle pattern. The speckle pattern is captured as a grayscale image by a monochrome CMOS camera of the Kinect. The grayscale image is then processed by histogram thresholding and transferred to a binarized image containing the contours of objectives. Next, by using median filter operation, the minor image blocks will be eliminated. Finally, after the following steps of edge detection and ellipse detection, the objective facial blocks will be determined.



(a) The webcam of infrared filter removed



(b) The speckle pattern from a remote control



(c) The speckle pattern from a Kinect

FIGURE 2: The test of speckle patterns emitting from different infrared light sources.

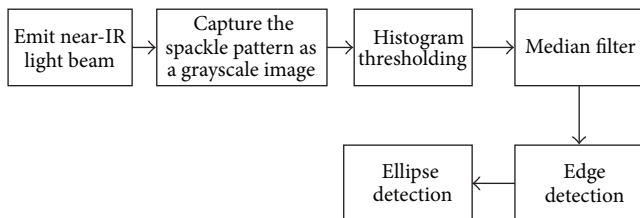


FIGURE 3: The diagram of facial detection by the depth map analysis of Kinect.

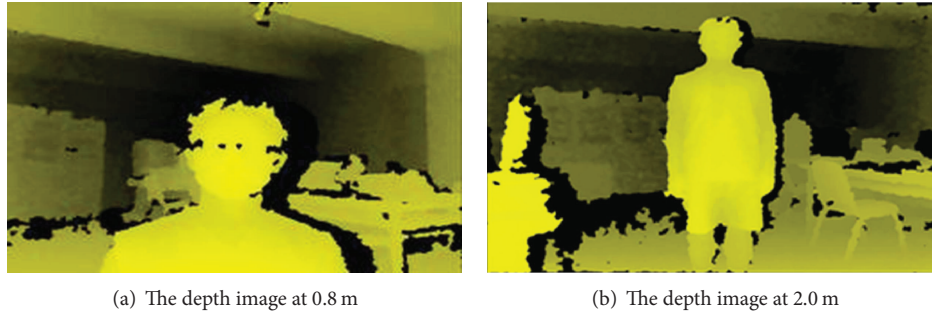
Facial image preprocessing is an important aspect of the facial detection and facial recognition. The images are sensitive to ambient conditions such as the brightness of ambient light, resolution and characteristics of the image device, and signal noises. There will be noise, distortion, low contrast, and other defects occurring during facial detection processes. In addition, the captured distance and direction of objectives, focal size, and so forth might make face blocks be with different sizes and locations in the image.

To ensure that all the objective faces in the image can be detected with consistent features such as size, aspect, contour, and position of facial blocks, it needs to do suitable image preprocessing. The common image preprocessing methods include facial position correction (rotation, cropping, and

scaling), facial image enhancements, geometric normalization, grayscale normalization, and so forth, in which in order to get good facial recognition must follow to get upright positions of facial images; the facial image enhancement is to improve the facial images and then results in clearer images and the images in uniform size and conditions are more conducive to the image processing for facial detection and recognition. The necessary image preprocessing of facial detection will be discussed below.

2.1. Light Coding. A typical structured light measurement method is to project a known light pattern into the 3D scene viewed by camera(s) and/or by means of the triangle measurement and geometry relations computation and then can determine the contours of objective surfaces. Similarly, the PrimeSense Ltd. calls the above technology in Kinect “light coding,” which means the speckle spots on the projection are able to be coding to represent the depths of surfaces. That is, the objects will be marked in the same light code because of their similar depth through structured light measurement and determination. Such processing results in a depth map as shown in Figure 4. It is noted that the original grayscale images have been transferred into yellow grayscale ones in this paper in order to display more significantly.

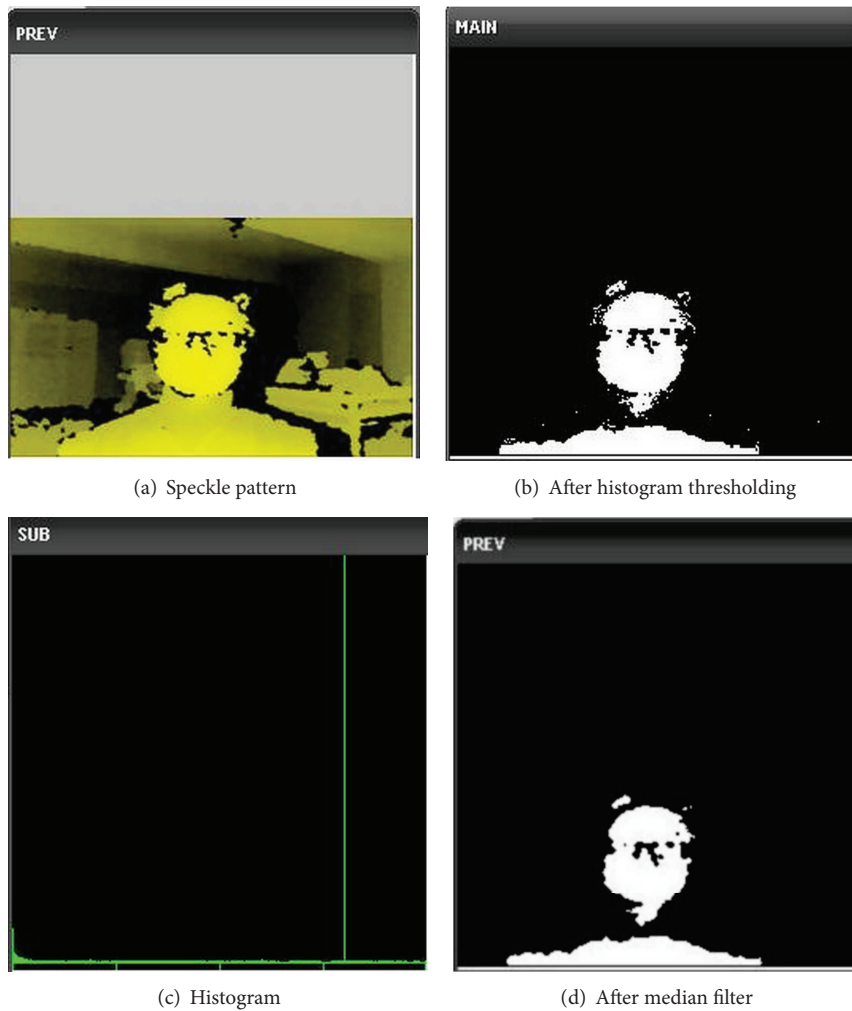
2.2. Histogram Thresholding and Median Filter. There are many noises or unexpected blocks in the grayscale image and



(a) The depth image at 0.8 m

(b) The depth image at 2.0 m

FIGURE 4: The depth maps determined after light coding.



(a) Speckle pattern

(b) After histogram thresholding

(c) Histogram

(d) After median filter

FIGURE 5: The image preprocessing by filters.

need to be removed. Firstly, the image can be in binarization by histogram thresholding operation. Then, the noises in the binary image can be filtered by median filter operation. After these two steps of image preprocessing as shown in Figure 5, the objective facial blocks will be split from the original image successfully.

However, the threshold of binarization is difficultly decided by a constant. From Figures 6(a) to 6(d), it is seen

that there need to be different thresholds in different depths. One can observe these figures and if to look at the point of 0.5% height in histogram, the possible thresholds 209, 215, 219, and 220 in the depths 0.6 m, 0.8 m, 1.0 m, and 1.2 m can be approximated by the formula of their respective depth as the follows:

$$\text{Threshold} = 219 + (\text{depth} - 1) * 2.5. \quad (1)$$

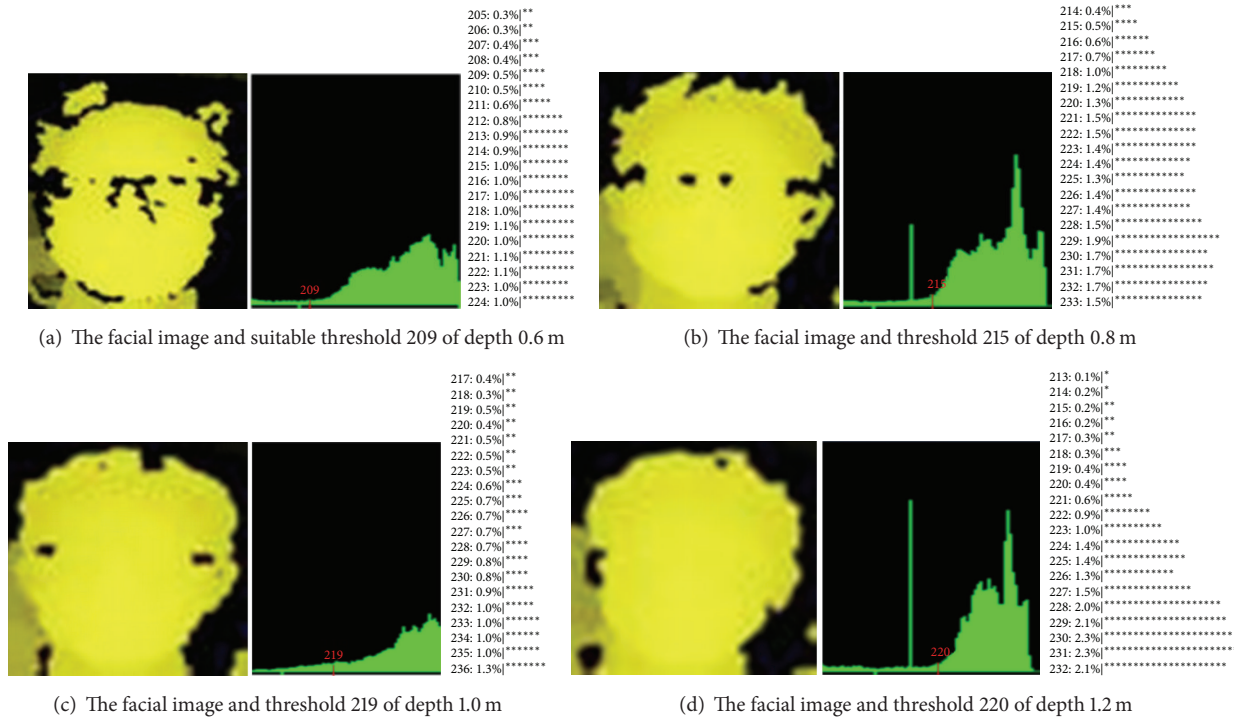


FIGURE 6: Different thresholds need to be given for different depth maps.

The estimated thresholds by (1) will become 209, 214, 219, and 224.

2.3. Edge Detection and Ellipse Detection. The resultant image after median filter shows the objective block including face and part of body. To execute gradient computation for edge detection (Figure 7(a)) and then to match the block to an ellipse model in axis ratio of 1.2 (a common face) for ellipse detection (Figure 7(b)), the objective facial block is determined as shown in Figure 7(c).

2.4. The Advantages of Adopting Structured Light Analysis. The facial detection based on structured light analysis starts from the grayscale image which is a monochrome image of the speckle pattern. Besides, the foundation processes of the speckle pattern are almost unaffected from ambient light which results in more reliable detection. It benefits the objective detection be superior to being influenced in dusky or bright or inconstant illumination. Moreover, the computations in such monochrome way also cost lower than those while dealing with color image detection. Thus, the proposed scheme is suitably adopted for fast facial detection facing different even bad illumination conditions.

3. Haar-Like Facial Detection

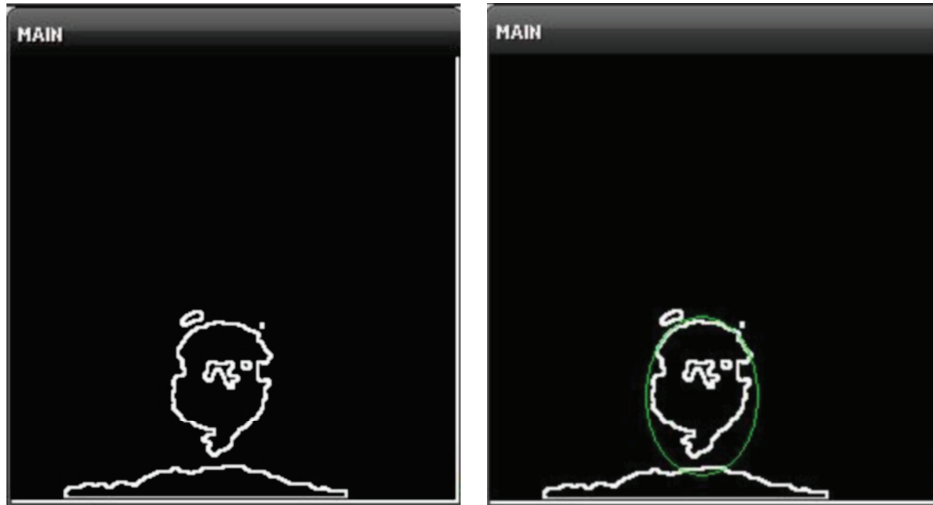
The concept of Haar-like features was firstly proposed by Papageorgiou et al. in 1998 [12] and then widely used in object recognition [12–15]. They intended to adopt Haar wavelet transfer algorithms to deal with the facial detection of upright

faces but found there were certain limitations existing in the application. In order to obtain the best spatial resolution, they proposed 3 kinds and 3 types of characteristics. In [13], Viola and Jones have made an expansion based on these foundations, who propose 2 kinds and 4 types of characteristics defined as 3-rectangle features and 4-rectangle features.

The rapid object detection based on Haar-like features [11, 13] is proposed by Viola and Jones in which there are three characteristics as follows:

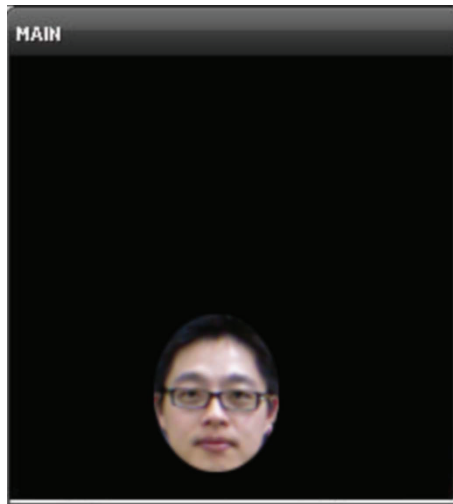
- (1) the use of integral images achieves the fast characteristic computation;
- (2) constructing a classifier by the method of AdaBoost [14] to collect few important characteristics;
- (3) Using a boosted cascade of simple features, it enhances the detection by focusing on useful features.

In the studies in [13], Viola and Jones proposed the concept of integral images and the theory based on the AdaBoost real-time facial detection. They construct an upright facial classifier which is based on 200 characteristics concluded after classifying 4,916 artificial faces in the size of 24×24 and 3,500,000 inhuman faces. From these two examples of rectangular characteristic model, the AdaBoost facial classifier can achieve 95% detection rate; moreover in 14804 inhuman face examinations, the proposed scheme achieved 100% false positive rate. To adopt a boosted cascade of classifiers, it improves the effectiveness of facial detection and reduces the computation time because the inhuman faces will be passed in real-time human facial detection.



(a) After edge detection by gradient computations

(b) After ellipse detection



(c) The resultant facial detection

FIGURE 7: The image processing for facial detection.

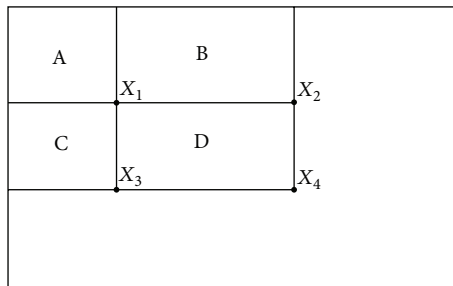
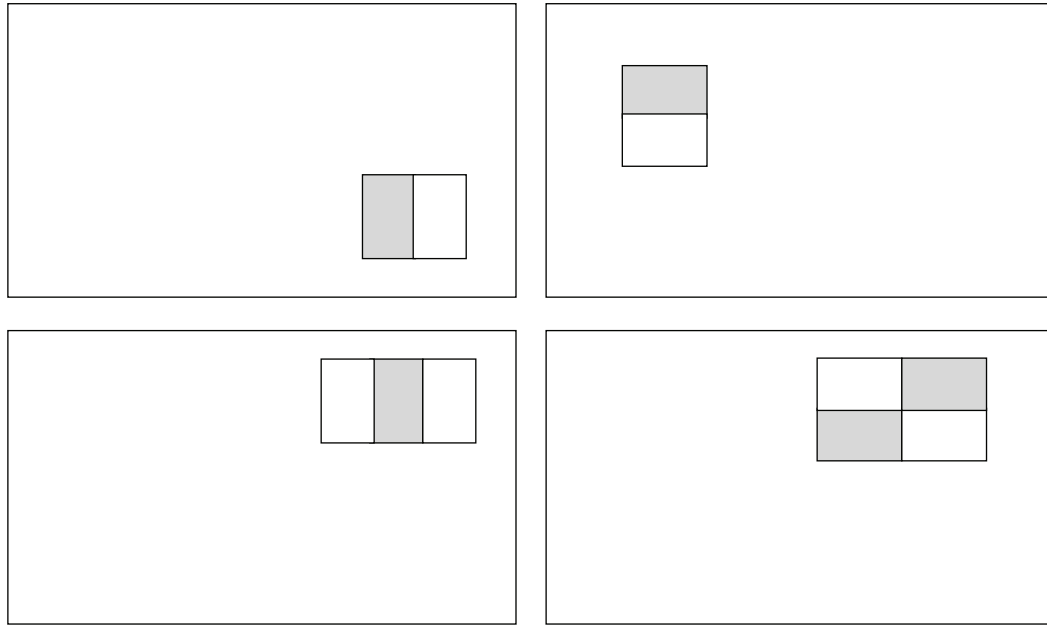


FIGURE 8: The diagram of determining an integral image.

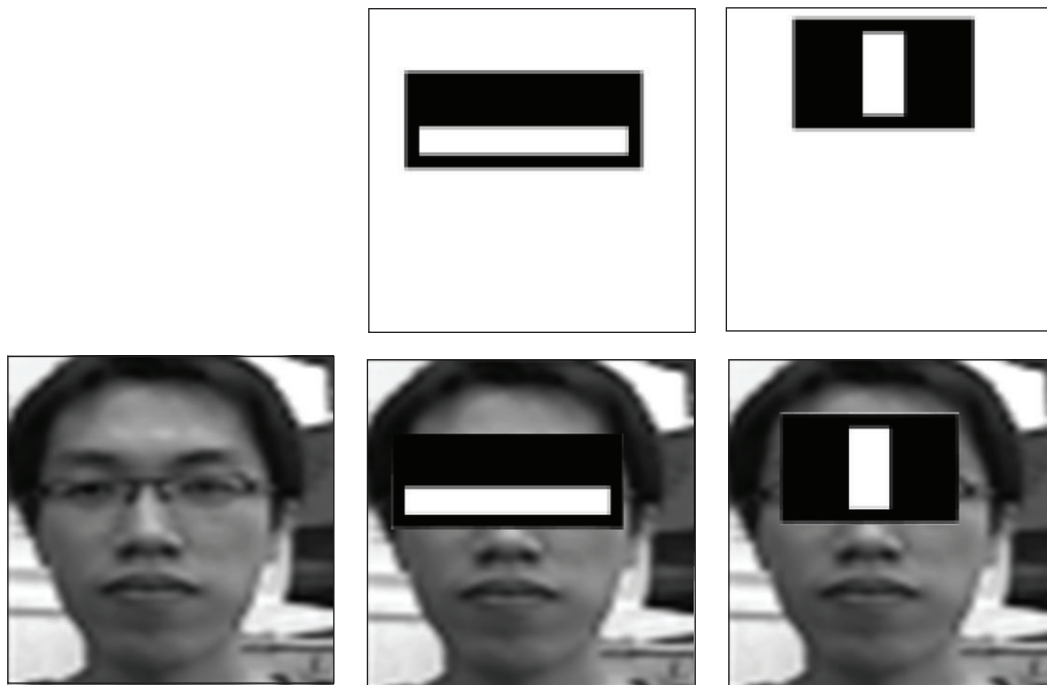
3.1. *Integral Image.* Because there are usually more than ten thousand training samples in a rectangular image to represent the features, for instance, if one needs to count the total of pixels in any rectangle, the computation will be huge and time-consuming. The concept of integral image is to count

the sum of features in the rectangle, which is then defined as the new image value of respective pixel.

For instance, in Figure 8, the value X_1 represents the total of the pixels in the rectangular A as a feature and the values X_2 , X_3 , and X_4 indicate the total of the pixels in



(a) Four types of basic rectangle features proposed by Viola and Jones.



(b) To find out a face by Haar-like features

FIGURE 9: The concepts of the Haar-like rectangle features.

the rectangular $A + B$, $A + C$, and $A + B + C + D$, respectively. Then one can easily get the total of the pixels in rectangular D by $X_4 + X_1 - (X_2 + X_3)$. It indicates that if the integral image could be determined firstly then the computation cost of features will be reduced through integral image than from original image.

3.2. Rectangular Feature, Weak Classifier, and AdaBoost Algorithm. The AdaBoost algorithm is one iteration generation

method, which aims to combine those with meaningful classified features among numerous weak classifiers as a new strong classifier, in which, a weak classifier refers to whose performance is better than ones of the stochastic classifiers. In the definitions proposed by Viola and Jones, the Haar-like features are mainly formed by the basic rectangle blocks of 2~3 white-black sections as shown in Figure 9(a). For facial detection, one can adopt the obvious differences on illumination existing in facial features as Haar-like features,

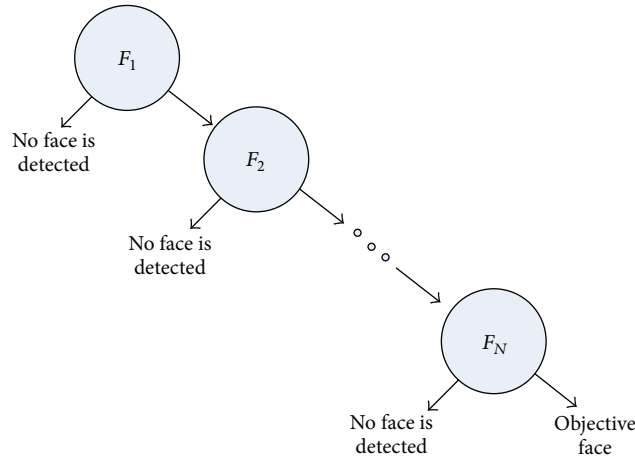


FIGURE 10: The diagram of a cascade of boosted classifiers.

such as in Figure 9(b), to find out the location of the objective face in a facial image.

3.3. Boosted Classifiers Cascade. The cascade of boosted classifiers, as shown in Figure 10, is working with Haar-like features. It needs to be trained with a few hundred sample views of a particular object such as a face, called positive examples, which are scaled to the same size (maybe 20×20), and negative examples, arbitrary images of the same size.

After a classifier is trained, it can be applied to a region of interest (of the same size as used during the training) in an input image. The classifier outputs a “1” if the region is likely to show the face and “0” otherwise. To search for the object in the whole image one can move the search window across the image and check every location using the classifier. The classifier is designed so that it can be easily “resized” in order to be able to find the objects of interest at different sizes, which is more efficient than resizing the image itself. So, to find an object of an unknown size in the image the scan procedure should be done several times at different scales.

3.4. Haar-Like Feature-Based Cascade Classifier. The cascade in the classifier means that the resultant classifier consists of several simpler classifiers (stages) that are applied subsequently to a region of interest until at some stage the candidate is rejected or all the stages are passed. The word “boosted” means that the classifiers at every stage of the cascade are complex themselves and they are built out of basic classifiers using one of four different boosting techniques (weighed voting). The basic classifiers are decision tree classifiers with at least 2 leaves.

The feature used in a particular classifier is specified by its shape, position within the region of interest and the scale (this scale is not the same as the scale used at the detection stage, though these two scales are multiplied). For example, in the case of the third line feature the response is calculated as the difference between the sum of image pixels under the rectangle covering the whole feature (including the two white stripes and the black stripe in the middle) and the sum of

the image pixels under the black stripe multiplied by 3 in order to compensate for the differences in the size of areas. The sums of pixel values over a rectangular region are calculated rapidly using integral images.

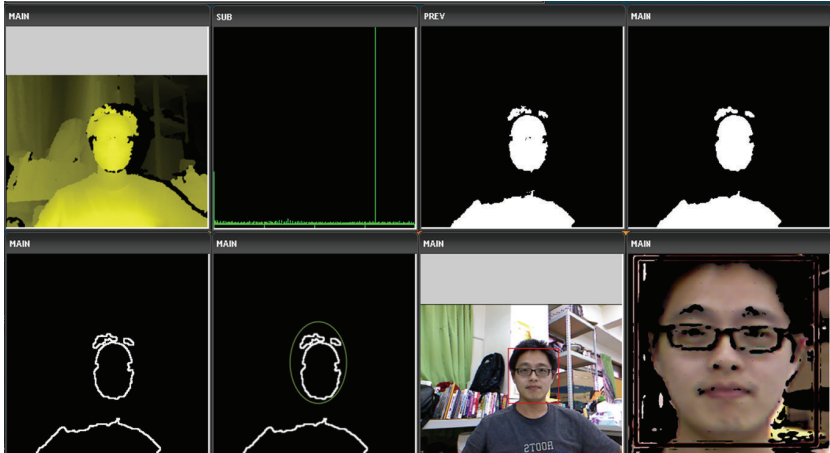
4. Results and Discussion

The detection experiments are executed by using a Kinect, the depth sensing device produced by Microsoft Corp. It emits invisible infrared light beams through a diffuser to be scattered on detected surface. The speckles projected on the surface are detected by the CMOS camera of Kinect as a depth image which could display 3D scene and be used to determine 3D poses and motions.

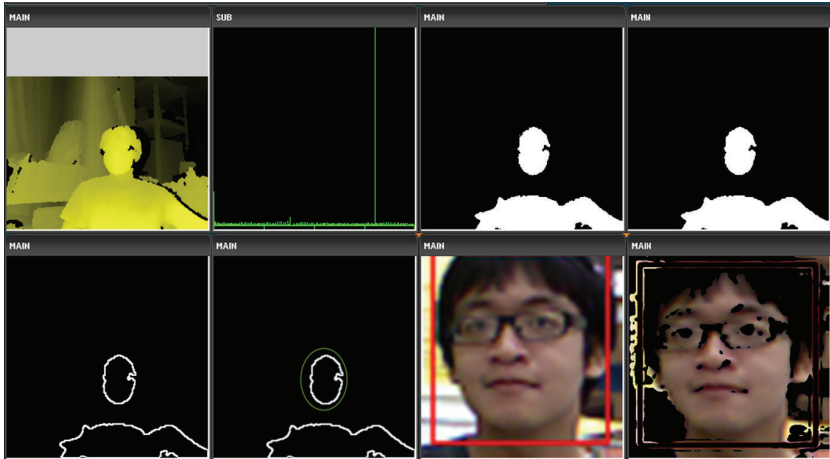
Figure 11 displays three cases of real facial detections. Each subfigure contains 8 experimental results, from top to bottom and left to right, and there are the speckle pattern, the histogram, the binarized image after thresholding, the image after median filter, the image after edge detection, the facial block after ellipse detection, the image after Haar-like facial detection, and the resultant image after skin segmentation. Even in complex background, the experimental results still demonstrate the feasibility of proposed scheme. From the data after over 5,000 pattern (inhuman face included) tests, the average of successful facial detection rate is 95.3%. If only counts the human face tests, the success rate will be reduced into 85.7%. It is necessary to recover in skin segmentation.

5. Conclusion

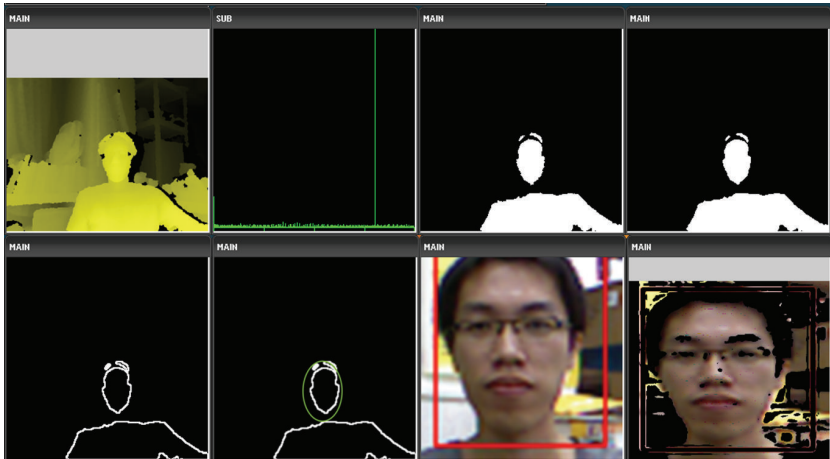
The proposed scheme consists of three subsystems, the first part is the structured light based depth sensing system, the second is the depth map analysis system, and the third is the Haar-like feature based cascade classifier. The structured light device provides the depth maps and helps the system to detect the human face by proposed fast facial detection. The Haar-like feature-based cascade classifier then makes good and fast facial detection. The proposed facial detection scheme based on depth map analysis is proven to obtain



(a) Case 1



(b) Case 2



(c) Case 3

FIGURE 11: The experimental results of real facial detection based on Haar-like features.

better effectiveness of facial detection and recognition under different environmental illumination conditions. From the experimental results, even in complex background, it still demonstrates the feasibility of proposed scheme.

Acknowledgment

This work is supported by the National Science Council, Taiwan, under Grant nos. NSC101-2221-E-218-029 and NSC100-2632-E-218-001-MY3.

References

- [1] PrimeSense/Solution, <http://www.primesense.com/solutions/technology/>.
- [2] C. Albitar, P. Graebing, and C. Doignon, "Robust structured light coding for 3D reconstruction," in *Proceedings of the 11th IEEE International Conference on Computer Vision (ICCV '07)*, pp. 1–6, October 2007.
- [3] C. Je, K. H. Lee, and S. W. Lee, "Multi-projector color structured-light vision," *Signal Processing*, vol. 28, no. 9, pp. 1046–1058, 2013.
- [4] J. Tong, J. Zhou, L. Liu, Z. Pan, and H. Yan, "Scanning 3D full human bodies using kinects," *IEEE Transactions on Visualization and Computer Graphics*, vol. 18, no. 4, pp. 643–650, 2012.
- [5] G. Vogiatzis and C. Hernández, "Self-calibrated, multi-spectral photometric stereo for 3d face capture," *International Journal of Computer Vision*, vol. 97, no. 1, pp. 91–103, 2012.
- [6] G. Fanelli, M. Dantone, J. Gall, A. Fossati, and L. V. Gool, "Random forests for real time 3D face analysis," *International Journal of Computer Vision*, vol. 101, no. 3, pp. 437–458, 2013.
- [7] T. Leyvand, C. Meekhof, Y.-C. Wei, J. Sun, and B. Guo, "Kinect identity: technology and experience," *Computer*, vol. 44, no. 4, Article ID 5742015, pp. 94–96, 2011.
- [8] W. Burgin, C. Pantofaru, and W. D. Smart, "Using depth information to improve face detection," in *Proceedings of the 6th ACM/IEEE International Conference on Human-Robot Interaction (HRI '11)*, pp. 119–120, March 2011.
- [9] Z. Ren, J. Meng, and J. Yuan, "Depth camera based hand gesture recognition and its applications in Human-Computer-Interaction," in *Proceedings of the 8th International Conference on Information, Communications and Signal Processing (ICICS '11)*, pp. 1–5, December 2011.
- [10] J. Rodrigues, R. Lam, and H. du Buf, "Cortical 3D face and object recognition using 2D projections," *International Journal of Creative Interfaces and Computer Graphics*, vol. 3, no. 1, pp. 45–62, 2012.
- [11] P. Viola and M. J. Jones, "Robust real-time face detection," *International Journal of Computer Vision*, vol. 57, no. 2, pp. 137–154, 2004.
- [12] C. P. Papageorgiou, M. Oren, and T. Poggio, "A General framework for object detection," in *Proceedings of the 6th IEEE International Conference on Computer Vision*, pp. 555–562, January 1998.
- [13] P. Viola and M. Jones, "Rapid object detection using a boosted cascade of simple features," in *Proceedings of the IEEE Computer Society Conference on Computer Vision and Pattern Recognition*, vol. 1, pp. 1511–1518, December 2001.
- [14] T. Susnjak, A. L. C. Barczak, and K. A. Hawick, "Adaptive cascade of boosted ensembles for face detection in concept drift," *Neural Computing and Applications*, vol. 21, no. 4, pp. 671–682, 2012.
- [15] A. Ehlers, F. Baumann, and B. Rosenhahn, "Exploiting object characteristics using custom features for boosting-based classification," in *Image Analysis*, vol. 7944 of *Lecture Notes in Computer Science Volume*, pp. 420–431, 2013.

Research Article

A Novel Dual-Electrode Plug to Achieve Intensive Electric Field for High Performance Ignition

Chih-Lung Shen, Jye-Chau Su, and Tsair-Chun Liang

Department of Electronic Engineering, National Kaohsiung First University of Science and Technology, Kaohsiung City 82445, Taiwan

Correspondence should be addressed to Chih-Lung Shen; clshen@ccms.nkfust.edu.tw

Received 10 September 2013; Accepted 13 October 2013

Academic Editor: Teen-Hang Meen

Copyright © 2013 Chih-Lung Shen et al. This is an open access article distributed under the Creative Commons Attribution License, which permits unrestricted use, distribution, and reproduction in any medium, provided the original work is properly cited.

A thorough analysis of electric field is carried out so as to verify that a novel dual-electrode plug can build intensive electric field and can improve the main drawbacks of feeble electric field and low ignition efficiency of the traditional plug. With intensive electric field, the proposed novel plug can achieve high performance ignition, resulting in fuel saving and exhaust reduction. Gauss law is applied for electric field analysis to show that intensive electric field can be built by the novel plug. Then, according to Faraday law a lower-voltage ignition feature accomplished by the plug is discussed. Compared with traditional plug, the novel dual-electrode plug has the following advantages. (1) Much higher energy density is built between the plug electrodes, lowering ignition voltage requirement. (2) Electromagnetic interference (EMI) problem caused by high ignition voltage is readily resolved. (3) Ignition time delay can be improved. (4) The feature to save fuel consuming is achieved. (5) The exhaust of CO and HC is reduced significantly. Practical measurements are fulfilled to validate the electric field analysis and to demonstrate the features of the proposed dual-electrode plug.

1. Introduction

Recently, the world is facing the threat of global warming due to the heavy use of fossil fuels and other greenhouse gases which result in a substantial increase of carbon dioxide. There are 24% of carbon dioxide emissions across the world, which is produced by the transportation tools. Mostly, it is produced from motor vehicles because of the use of fossil fuel [1]. In order to reduce the emission pollution from transportation tools, one has to understand how an electrical field is built by the spark plug and how a time delay is caused by the spark plug. In general, the operation of a vehicle engine can be divided into four steps: (1) intake, (2) compression, (3) explosive combustion, and (4) exhaust.

In an engine ignition cycle [2, 3], the engine power comes from which the explosion of the spark plug ignites the compressed mixed gas, and then the piston pushes the crankshaft rotation to generate power output. When the cross-section of the electrodes of the spark plug is too large, the spark arc will not concentrate at a point easily. Thus, this is difficult to start the engine and is prone to cause

an incomplete combustion, resulting in exhaust pollution. Moreover, it needs a higher ignition voltage to produce a critical electrical field for the plug. A higher ignition voltage will cause a more serious EMI problem. Besides, if a plug needs a high ignition voltage, it has to take longer time for voltage accumulation, leading to time delay for igniting. Figure 1 illustrates that an optimal igniting time locates at the 10 degrees of crankshaft.

Therefore, the establishment of the ignition voltage and electric field [4–6] for a spark plug is very important. In this paper, with the application of Maxwell equations [7, 8], we propose a dual-electrode enhanced electric field plug for combustion engines. The proposed plug not only can build a more intensive ignition electric field and can produce a spark arc in time.

2. The Proposed Plug Structure

To ignite the proposed spark plug, a corresponding block diagram of the ignition system is shown in Figure 2, in which

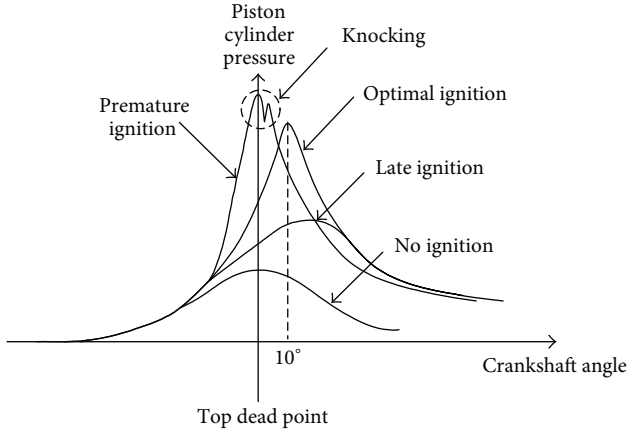


FIGURE 1: The relationship between crankshaft position and the combustion chamber pressure.

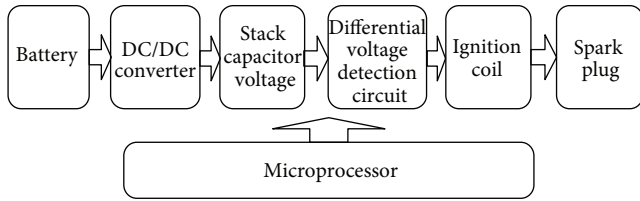


FIGURE 2: A block diagram of electronic ignition system.

the DC/DC converter can be implemented by a switch-mode converter [9–15]. In this paper, the flyback-type converter is adopted to fulfill high voltage generation. In the following, we will deal with the electric field analysis and ignition voltage discussion.

2.1. Principle of Dual-Electrode Plug with Enhanced Electric Field. Figure 3 illustrates the structure of the output of an ignition system. According to Ampere theorem, one can know that charges will flow to the spark plug electrodes and then build an electrical field. When the electric field between the spark plug electrodes reaches the critical electrical field E_C , charges release energy and produce arc sparkle to ignite mixed gas for generating power [16]. In addition, the current and output charge of a high voltage ignition coil at each ignition time interval can be expressed as follows:

$$\Delta q = i(t) \Delta t, \tag{1}$$

where Δq is the total charge supplied to the plug.

2.2. Critical Electric Field Built by Traditional Plug. Figure 4 shows the structure of a traditional spark plug, in which a Gaussian cylindrical shell is selected. The positive electrode is placed at the middle of the spark plug electrodes. In Figure 4, A_1 is the cross-section of the positive electrode, V_i is the voltage of the positive electrode, V_f is the voltage of the negative electrode, d is the distance between the plug

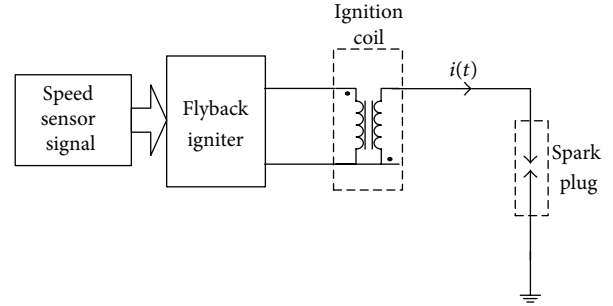


FIGURE 3: A simplified diagram to express the structure of the output of the ignition system.

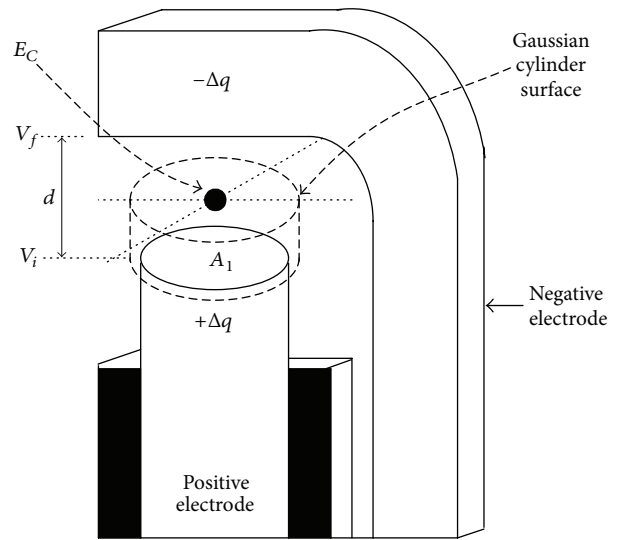


FIGURE 4: The structure of the traditional spark plug.

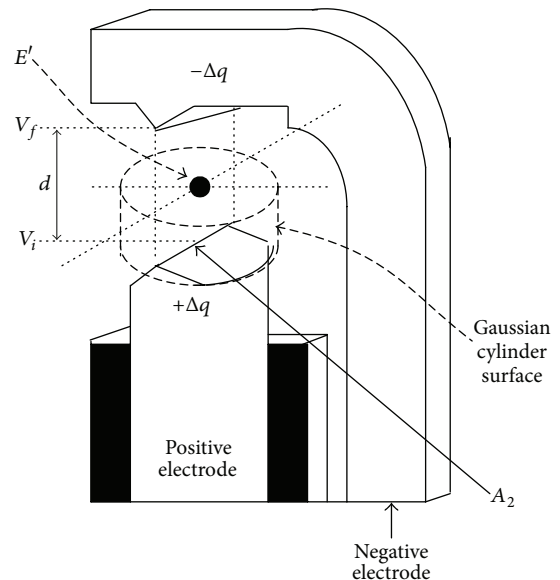


FIGURE 5: The structure of the proposed spark plug.

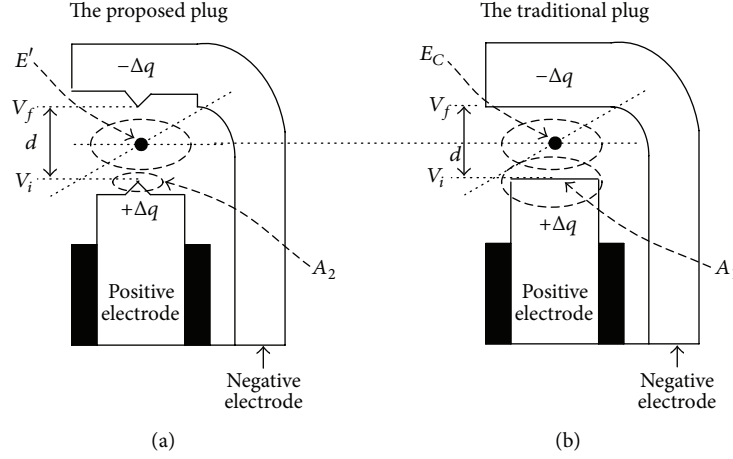


FIGURE 6: The side views of the proposed plug (a) and the traditional plug (b).

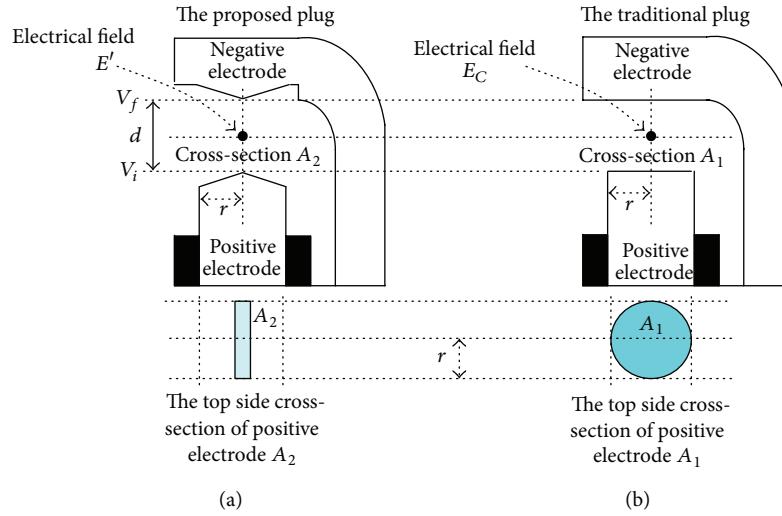


FIGURE 7: Expressing the key parameters of the proposed plug (a) and the traditional one (b).

electrodes, and $-\Delta q$ is the induced charge by $+\Delta q$. A critical electric field, E_C , is calculated as follows:

$$\epsilon_0 \oint \vec{E} \cdot d\vec{A} = q, \quad (2)$$

where ϵ_0 is the permittivity of free space. The critical electrical field E_C established between the two electrodes is

$$E_C = \frac{\Delta q}{\epsilon_0 A_1}. \quad (3)$$

From Faraday law, one can obtain

$$\oint \vec{E} \cdot d\vec{s} = -\frac{d\Phi_B}{dt} = -V. \quad (4)$$

The ignition voltage established between the two electrodes is

$$\oint \vec{E}_C \cdot d\vec{s} = E_C d = -V_1, \quad (5)$$

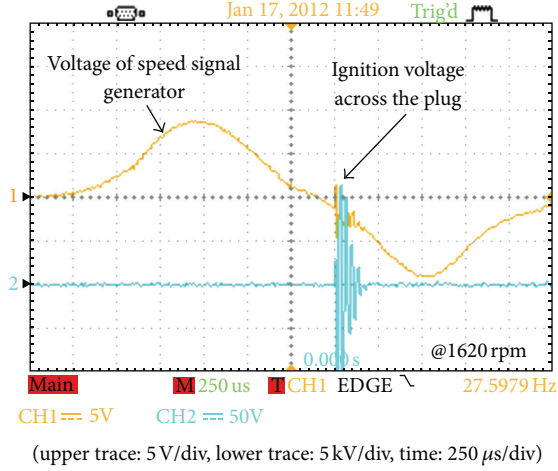
where V_1 is determined by

$$V_1 = -E_C d = -\frac{d\Delta q}{\epsilon_0 A_1}. \quad (6)$$

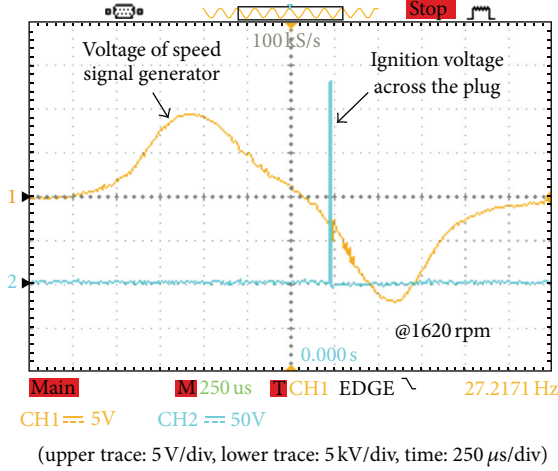
According to (3) and (6), if the cross-section of the spark plug electrodes, A_1 , is reduced without changing the electrodes distance, the ignition electrical field will be established faster.

2.3. Electric Field Built by Proposed Plug. Figure 5 shows the structure of the proposed spark plug, in which the cross-section of the spark plug electrodes, A_2 , is reduced as a shape of sharp knife, and the positive electrode faces the negative electrode with their sharp end. With the same way, a Gaussian cylindrical shell is selected and an electrical field, E' , is calculated as

$$E' = \frac{\Delta q}{\epsilon_0 A_2}. \quad (7)$$



(a)



(b)

FIGURE 8: The waveforms of ignition timing under the speed of about 1620 rpm: (a) traditional plug and (b) the proposed plug.

From Faraday law, the relationship holds

$$\oint \vec{E} \cdot d\vec{s} = -\frac{d\Phi_B}{dt} = -V. \quad (8)$$

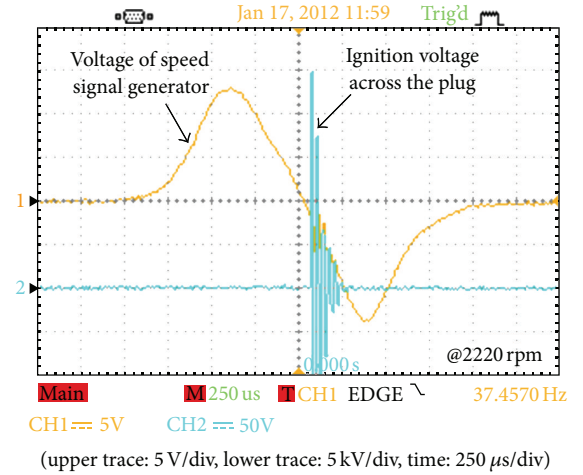
The ignition voltage that is established between the two electrodes is

$$\oint \vec{E}' \cdot d\vec{s} = E'd = -V_2, \quad (9)$$

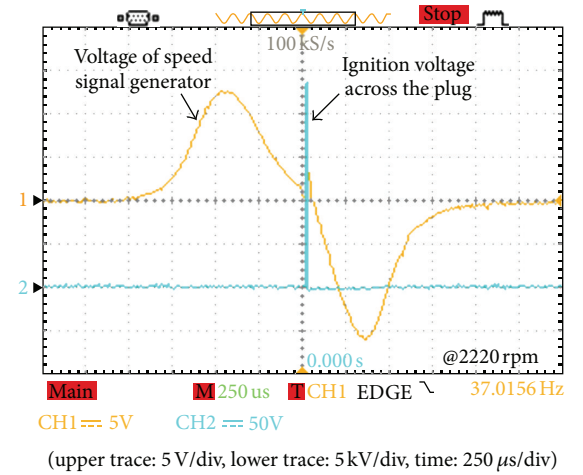
where the V_2 can be calculated by

$$V_2 = -E'd = -\frac{d\Delta q}{\epsilon_0 A_2}. \quad (10)$$

2.4. Comparisons of the Electric Field and Ignition Voltage. The side views of the proposed plug and traditional plug are placed in line horizontally in order to distinguish the magnitude of key parameters. Figure 6 shows the side views. The electric fields in the spark plug of traditional plug and the



(a)



(b)

FIGURE 9: The waveforms of the ignition timing under the speed of about 2200 rpm: (a) traditional plug and (b) the proposed plug.

proposed plug are in (3) and (7), respectively. If (7) is divided by (3), one can find

$$E' = \frac{A_1}{A_2} E_C. \quad (11)$$

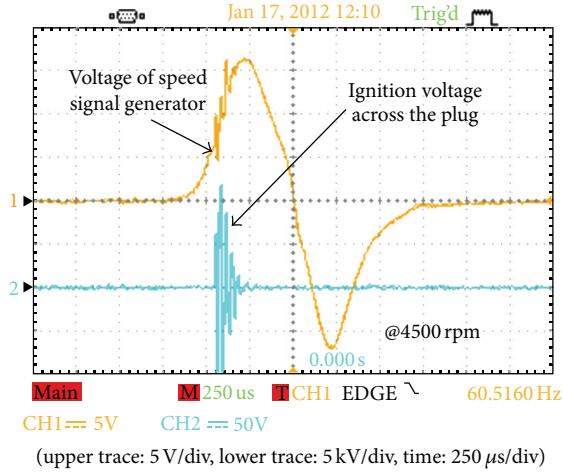
Since $A_2 < A_1$; then $E' > E_C$. The E_C is estimated by

$$E_C = \frac{\Delta q}{\epsilon_0 A_1} = \frac{i(t) \Delta t}{\epsilon_0 A_1} = \frac{i(t) \Delta t'}{\epsilon_0 A_2}. \quad (12)$$

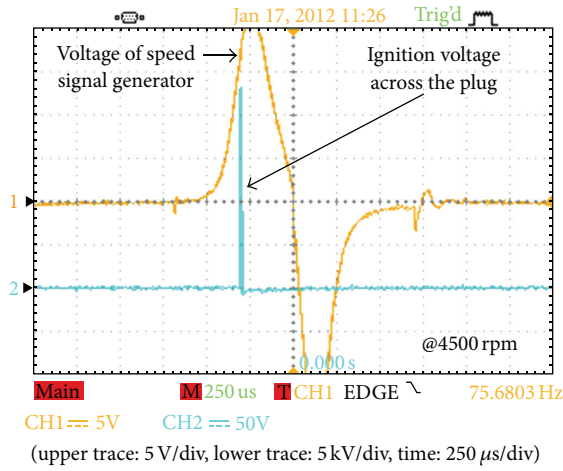
Thus, the following yields

$$\Delta t' < \Delta t. \quad (13)$$

This derivation shows that the electrical field E' is established faster than E_C and the ignition charges are concentrated in a smaller cross-section. It results in an improvement of engine combustion efficiency. The voltages across the spark plug created by the proposed plug and traditional plug are



(a)



(b)

FIGURE 10: The waveforms of the ignition timing under the speed of about 4500 rpm: (a) traditional plug and (b) the proposed plug.

shown in (6) and (10), respectively. As $E' > E_C$, from (6) and (10), it can be obtained that

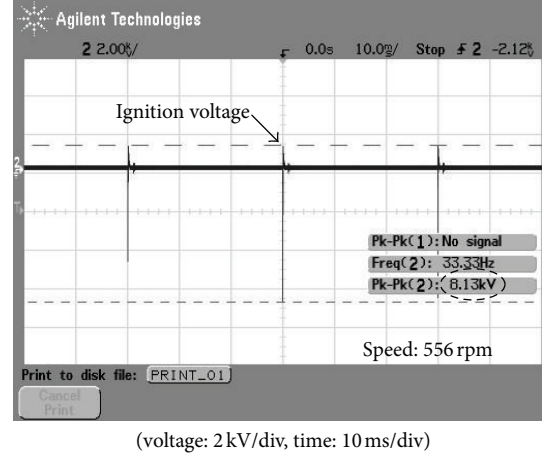
$$V_2 < V_1. \quad (14)$$

This reveals that the proposed plug can reduce the ignition voltage as well as EMI issue.

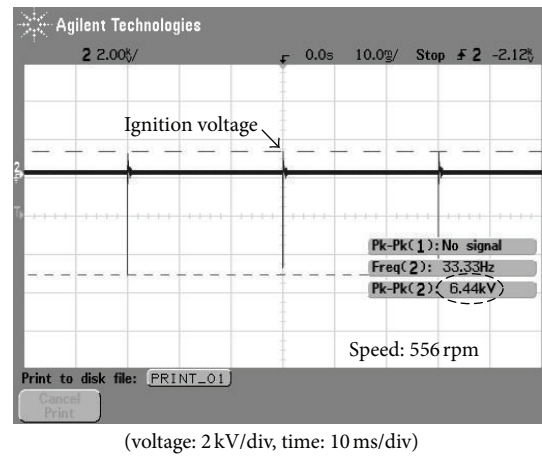
3. Experimental Results

To verify the functionality of the proposed spark plug, real-car test is carried out, and practical measurement is fulfilled. In order to complete the contrast test, key parameters of the proposed novel dual-electrode plug and the traditional one are listed in the following. A corresponding figure is also illustrated in Figure 7.

- (1) The radius of the positive electrode is $r = 1.2$ mm.
- (2) The distance between positive electrodes is $d = 1.4$ mm.



(a)



(b)

FIGURE 11: The waveforms of the ignition voltages under the speed of about 556 rpm: (a) traditional plug and (b) the proposed plug.

- (3) The top cross section of positive electrode of the traditional plug $A_1 = 3.77$ mm².
- (4) The top cross section of positive electrode of the proposed plug $A_2 = 2.40$ mm².

In the test, a flyback-type capacitor discharging igniter is used as the plug driver. Figures 8, 9, and 10 show that the proposed plug has the feature of less time delay at the vehicle speed close to 1620 rpm, 2220 rpm, and 4500 rpm, respectively. Figures 11, 12, and 13 show the ignition voltages measured from traditional plug and the proposed plug. It can be found that the proposed plug needs much smaller ignition voltage than that of the traditional one at the speeds of 556, 838, and 1380 rpm, in turns.

4. Conclusion

In this paper, a novel dual-electrode spark plug for combustion engines is proposed, which can obtain an enhanced electric field to lower ignition voltage and EMI issue. As a result, fuel consumption and exhaust pollution can be readily

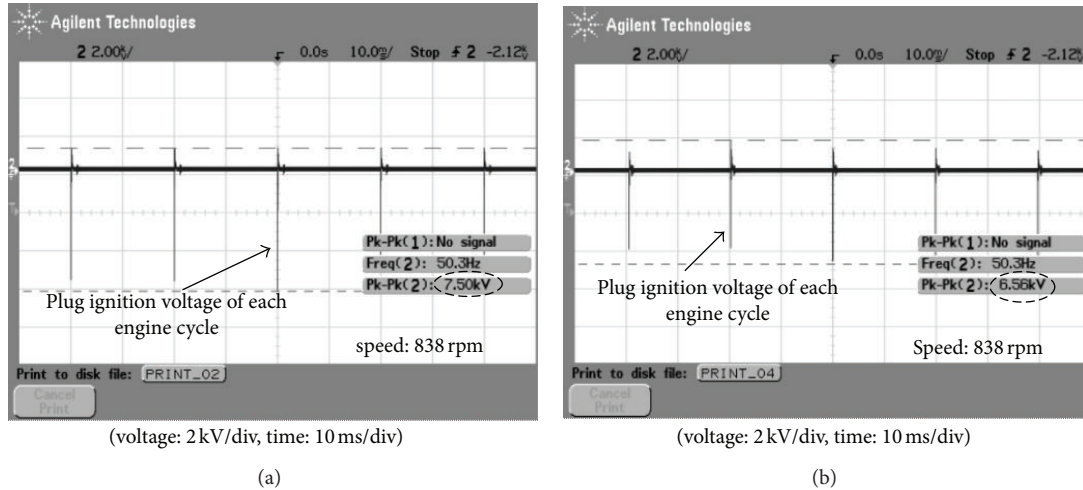


FIGURE 12: The waveforms of the ignition voltages under the speed of about 838 rpm: (a) traditional plug and (b) the proposed plug.

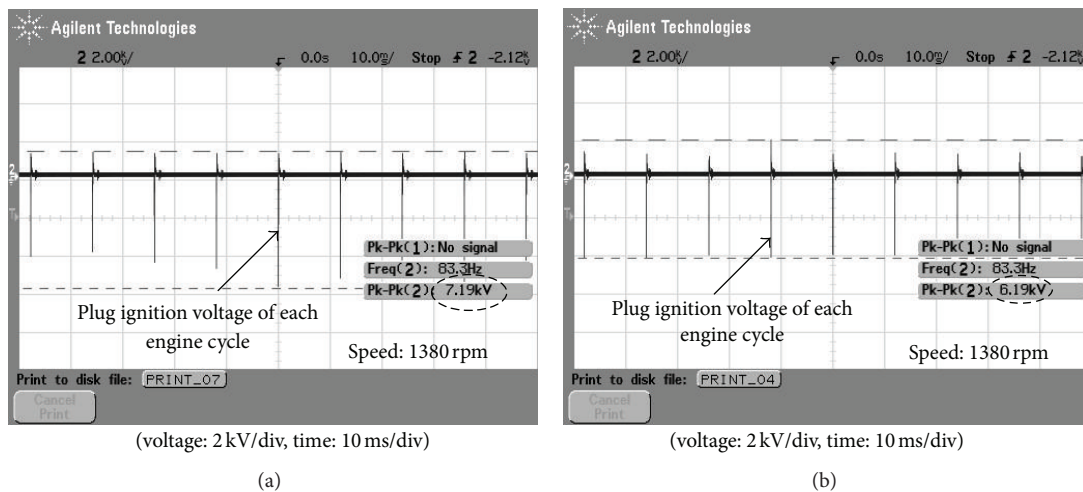


FIGURE 13: The waveforms of the ignition voltages under the speed of about 1380 rpm: (a) traditional plug and (b) the proposed plug.

alleviated. The electric field built in the proposed plug and the corresponding ignition voltage are discussed by Gauss law and Faraday law. To verify the excellent performance of the plug, real-car test is carried out. The proposed plug and a traditional plug are installed in an engine vehicle in turn. At a different speed, the measured results reveal that the proposed plug can lead to lower ignition voltage and have exact igniting timing.

References

- [1] R. Hawley, "Urban energy needs and the environment," *Engineering Science and Education Journal*, vol. 5, no. 2, pp. 89–95, 1996.
- [2] J. B. Vance, B. C. Kaul, S. Jagannathan, and J. A. Drallmeier, "Output feedback controller for operation of spark ignition engines at lean conditions using neural networks," *IEEE Transactions on Control Systems Technology*, vol. 16, no. 2, pp. 214–228, 2008.
- [3] E. Hellstrom, A. Stefanopoulou, and L. Jiang, "Cyclic variability and dynamical instabilities in auto-ignition engines with high residuals," *IEEE Transactions on Control Systems Technology*, vol. 21, no. 5, pp. 1527–1536, 2013.
- [4] W. Langeslag, R. Pagano, K. Schetters, A. Strijker, and A. van Zoest, "VLSI design and application of a high-voltage-compatible SoC-ASIC in bipolar CMOS/DMOS technology for AC-DC rectifiers," *IEEE Transactions on Industrial Electronics*, vol. 54, no. 5, pp. 2626–2641, 2007.
- [5] Z. J. Shen and S. P. Robb, "A dual-voltage self-clamped IGBT for automotive ignition applications," *IEEE Electron Device Letters*, vol. 22, no. 5, pp. 239–241, 2001.
- [6] M. Jia, Q. Howard Zhang, and D. B. Min, "Pulsed electric field processing effects on flavor compounds and microorganisms of orange juice," *Food Chemistry*, vol. 65, no. 4, pp. 445–451, 1999.
- [7] H. S. Bhat and B. Osting, "Kirchhoff's laws as a finite volume method for the planar Maxwell equations," *IEEE Transactions on Antennas and Propagation*, vol. 59, no. 10, pp. 3772–3779, 2011.

- [8] O. Ouchetto, H. Ouchetto, S. Zouhdi, and A. Sekkaki, "Homogenization of Maxwell's equations in lossy bi-periodic metamaterials," *IEEE Transactions on Antennas and Propagation*, vol. 61, no. 8, pp. 4214–4219, 2013.
- [9] C.-T. Tsai and C.-L. Shen, "High efficiency current-doubler rectifier with low output current ripple and high step-down voltage ratio," *IEEJ Transactions on Electrical and Electronic Engineering*, vol. 8, no. 2, pp. 182–189, 2013.
- [10] H. Yoshino, K. Sato, A. Tomago, and I. Yamauchi, "Development of a corona discharge detector for flyback transformers," *IEEE Transactions on Consumer Electronics*, vol. 23, no. 1, pp. 114–119, 1977.
- [11] F. Forest, E. Labouré, T. A. Meynard, and J.-J. Huselstein, "Multicell interleaved flyback using intercell transformers," *IEEE Transactions on Power Electronics*, vol. 22, no. 5, pp. 1662–1671, 2007.
- [12] N. P. Papanikolaou and E. C. Tatakis, "Minimisation of power losses in PFC flyback converters operating in the continuous conduction mode," *IEE Proceedings*, vol. 149, no. 4, pp. 283–291, 2002.
- [13] R. Watson, F. C. Lee, and G. C. Hua, "Utilization of an active-clamp circuit to achieve soft switching in flyback converters," *IEEE Transactions on Power Electronics*, vol. 11, no. 1, pp. 162–169, 1996.
- [14] C.-L. Shen and S.-H. Yang, "Multi-input converter with MPPT Feature for wind-PV power generation system," *International Journal of Photoenergy*, vol. 2013, Article ID 129254, 13 pages, 2013.
- [15] C.-L. Shen and K.-K. Chen, "Single-stage coupled-inductor Sepic-type HB-LED driver with soft-switching for universal line input," *Mathematical Problems in Engineering*, vol. 2012, Article ID 593568, 17 pages, 2012.
- [16] S. J. Beebe, P. M. Fox, L. J. Rec, K. Somers, R. H. Stark, and K. H. Schoenbach, "Nanosecond pulsed electric field (nsPEF) effects on cells and tissues: apoptosis induction and tumor growth inhibition," *IEEE Transactions on Plasma Science*, vol. 30, no. 1, pp. 286–292, 2002.

Research Article

Delay Pressure Detection Method to Eliminate Pump Pressure Interference on the Downhole Mud Pressure Signals

Yue Shen,¹ Ling-Tan Zhang,¹ Shi-Li Cui,¹ Li-Min Sheng,² Lin Li,² and Yi-Nao Su²

¹ School of Science, China University of Petroleum, Qingdao 266580, China

² Drilling Technology Research Institute, CNPC, Beijing 100195, China

Correspondence should be addressed to Yue Shen; sheny1961@aliyun.com

Received 12 September 2013; Accepted 12 October 2013

Academic Editor: Teen-Hang Meen

Copyright © 2013 Yue Shen et al. This is an open access article distributed under the Creative Commons Attribution License, which permits unrestricted use, distribution, and reproduction in any medium, provided the original work is properly cited.

The feasibility of applying delay pressure detection method to eliminate mud pump pressure interference on the downhole mud pressure signals is studied. Two pressure sensors mounted on the mud pipe in some distance apart are provided to detect the downhole mud continuous pressure wave signals on the surface according to the delayed time produced by mud pressure wave transmitting between the two sensors. A mathematical model of delay pressure detection is built by analysis of transmission path between mud pump pressure interference and downhole mud pressure signals. Considering pressure signal transmission characteristics of the mud pipe, a mathematical model of ideal low-pass filter for limited frequency band signal is introduced to study the pole frequency impact on the signal reconstruction and the constraints of pressure sensor distance are obtained by pole frequencies analysis. Theoretical calculation and numerical simulation show that the method can effectively eliminate mud pump pressure interference and the downhole mud continuous pressure wave signals can be reconstructed successfully with a significant improvement in signal-to-noise ratio (SNR) in the condition of satisfying the constraints of pressure sensor distance.

1. Introduction

In measurement while drilling (MWD), various downhole signals will be transmitted to the surface in real time for instructing the drilling operation. One of the most common methods of transmitting the measured downhole information to the surface is through mud pressure pulses produced by mechanical modulation of a mud siren in MWD tools and transmitted at acoustic speed in the mud flow. The mud siren generates mud continuous pressure wave signals with complex modulation methods to produce higher data rates. When transmitting the mud pressure signals, there will be a lot of pressure noise and interference, among which the mud pressure fluctuation generated by the mud pump contributes to the largest influence. The mud pump pressure interference is related to the pump stroke rate which includes fundamental component and harmonic component. When the mud pump is in imbalance operation mode caused by sealing problem or in abnormal working status, some higher harmonic amplitude will become very large. Although the

pressure dampers are equipped on mud pump pipe, the pressure fluctuation generated by mud pump reaches or exceeds the downhole signal strength detected in the stand pipe [1]. These higher harmonics will enter the frequency band of mud pressure signal and thereby create great interference that cannot be eliminated by conventional signal processing method, leading to the great decrease of signal-to-noise ratio (SNR) of signal and affecting extraction of the MWD signals. Many studies had been done to eliminate the pump interference. Marsh and others proposed the matched filter method which treated mud pump interference as random noise and calculated the autocorrelation coefficient to eliminate the mud pump pressure interference [2]. However, the pump interference is a kind of system interference rather than random noise, so the conclusions of the method needed further discussion. Brandon and others proposed an adaptive compensation method which uses extracted interference component in the signal and automatically adjusts strength of the interference component to eliminate the pump pressure interference impact on the signal [3], but the effect was

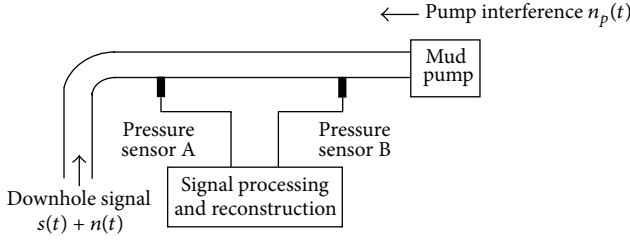


FIGURE 1: Mud pressure detection system.

limited. Some literatures [4–7] introduced the delay pressure detection technique and built a mathematical model, being fitted to the single-frequency signal with pressure sensors distance of quarter signal wavelength, for eliminating the mud pump pressure interference. Because components of many frequencies are contained in mud continuous pressure wave signals, the mathematical model presented in those literatures cannot be applied in reconstruction of actual mud continuous pressure wave signals. Based on transmission path analysis of mud pump pressure interference and downhole mud pressure signals, the authors established the mathematical model in time domain for processing mud continuous pressure wave signals according to the fundamental mathematical principle of delay pressure detection method and then studied the reconstruction method of mud continuous wave signals in both time domain and frequency domain and constraints of the distance between pressure sensors.

2. Mathematical Model of Delay Pressure Detection

The delay pressure detection method uses two pressure sensors being some distance apart on the mud pipe to detect and process the mud pressure signal; Figure 1 shows the schematic figure of mud pressure signal detection system. Two pressure sensors, A and B, having distance L_0 between each other, are equipped in a straight pipe between wellhead and mud pump. The pressure signals received by two sensors contain downhole signal (mud pressure signal) $s(t)$, downhole random noise $n(t)$, and mud pump pressure interference $n_p(t)$. The transmission direction of pump pressure interference is opposite to that of downhole signal. Suppose that the propagation velocity of the mud pressure wave is c_0 and the pressure wave transmission time between sensors A and B is $\tau_0 = L_0/c_0$.

Considering the mud pipe between sensors A and B as a linear system, its frequency response can be described as

$$H(j\omega) = |H(j\omega)| \cdot e^{-j\omega\tau_0}, \quad (1)$$

where $|H(j\omega)|$ is modulus of frequency domain transfer function of the mud pipe between pressure sensors A and B.

Suppose that $h(t)$ is unit impulse response of the linear system $H(j\omega)$. When the signal is being transmitted through

the linear system [8], signals received by the pressure sensors A and B can be expressed as

$$\begin{aligned} p_A(t) &= s(t) + n(t) + h(t) * n_p(t), \\ p_B(t) &= h(t) * [s(t) + n(t)] + n_p(t). \end{aligned} \quad (2)$$

We can get convolution of $h(t)$ with $p_B(t)$ as

$$h(t) * p_B(t) = h(t) * h(t) * [s(t) + n(t)] + h(t) * n_p(t). \quad (3)$$

Equation (3) means that $p_B(t)$ is transmitted through a linear system with unit impulse response $h(t)$ again. Because $h(t)$ contains delayed time $\tau_0 = L/c_0$, the physical meaning of (3) is that $p_B(t)$ will be detected after delayed time τ_0 .

Subtracting the formula in (3) from $p_A(t)$, we can get the delay pressure detecting signal as follows:

$$\begin{aligned} p_A(t) - h(t) * p_B(t) &= s(t) + n(t) \\ &\quad - h(t) * h(t) * [s(t) + n(t)]. \end{aligned} \quad (4)$$

In (4), the pump pressure interference item $n_p(t)$ has been eliminated.

After Fourier transform of the formula in (4), we can get spectral density function of the downhole signal as

$$S(j\omega) + N(j\omega) = H'(j\omega) [P_A(j\omega) - P_B(j\omega) \cdot H(j\omega)], \quad (5)$$

where $H'(j\omega) = 1/(1 - H(j\omega) \cdot H(j\omega))$ can be applied to reconstruct the downhole signal.

3. Signal Reconstruction Based on Time-Domain Differential Equation

According to (5), the time-domain solution of the system frequency response can be described as the reconstruction of the downhole signal after the delay pressure detecting signal $p_A(t) - h(t) * p_B(t)$ is passed through a signal recovering system with frequency transfer function $H'(j\omega)$.

Considering that the maximum frequency of mud continuous pressure wave signal in transmission will be dozens of hertz (Hz), the signal frequency is lower and limited. In limited frequency band, the signal attenuation in amplitude will keep unchangeable when mud continuous pressure wave signal passes the straight pipe between pressure sensors A and B, so the pipe can be seen as an undistorted transmission system and regarded as an ideal low-pass filter. The frequency domain transfer function of the system can be described as

$$H(j\omega) = aG(\omega) e^{-j\omega\tau_0}, \quad (6)$$

where a is the signal attenuation coefficient and $G(\omega)$ is unit gate function with ω_b as unilateral bandwidth. According to the unit impulse response of ideal low-pass filter [9], the unit impulse response of system $H(j\omega)$ can be described as

$$h(t) = \frac{a\omega_b}{\pi} \cdot \frac{\sin[\omega_b(t - \tau_0)]}{\omega_b(t - \tau_0)} = \frac{a\omega_b}{\pi} \text{Sinc}[\omega_b(t - \tau_0)]. \quad (7)$$

After reciprocal transformation of $H'(j\omega)$, we can get

$$H_1(j\omega) = \frac{1}{H'(j\omega)} = \frac{Y_1(j\omega)}{X_1(j\omega)} = 1 - H(j\omega) \cdot H(j\omega). \quad (8)$$

Then

$$Y_1(j\omega) = X_1(j\omega) - H(j\omega) \cdot H(j\omega) \cdot X_1(j\omega). \quad (9)$$

Because transfer functions of $H_1(j\omega)$ and $H'(j\omega)$ are reciprocal, so their input and output functions are inverse of each other.

Substituting input function $x(t)$ and output function $y(t)$ of $H'(j\omega)$ for output function $y_1(t)$ and input function $x_1(t)$ of $H_1(j\omega)$ in (9), there will be

$$x(t) = y(t) - \left(\frac{a\omega_b}{\pi}\right)^2 \text{Sinc}(\omega_b t) * \text{Sinc}(\omega_b t) * y(t - 2\tau_0). \quad (10)$$

Thus, the time-domain solution of the output function of $H'(j\omega)$ can be built as

$$y(t) = x(t) + \left(\frac{a\omega_b}{\pi}\right)^2 \text{Sinc}(\omega_b t) * \text{Sinc}(\omega_b t) * y(t - 2\tau_0), \quad (11)$$

where $x(t)$ is delay pressure detecting signal and can be expressed as $x(t) = p_A(t) - h(t) * p_B(t)$ and $y(t) = s(t) + n(t)$ is reconstructed downhole signal.

Converting the continuous-time system to Z-system of discrete-time and setting $z = e^{j\omega T_s}$, $k = 2\tau_0/T_s$, and $t = NT_s$, we can get the Z-transform of $H'(j\omega)$ as

$$H'(z) = \frac{1}{1 - |H(z)|^2 z^{-k}}, \quad (12)$$

where T_s is the sampling period and N is the number of sample sequences.

According to digital filter theory, $H'(z)$ is a k -order infinite impulse response (IIR) filter system [10] and its frequency domain response, being similar to the low-pass filter with sharp cut-off characteristic, strengthens with k . When $H(z)$ is an ideal low-pass transmission, the output of $H'(z)$ is a differential equation and can be expressed as

$$y(N) = x(N) + \left(\frac{a\omega_b}{\pi}\right)^2 \text{Sinc}(\omega_b N) * \text{Sinc}(\omega_b N) * y(N - k). \quad (13)$$

Equations (13) and (11) have the same structure, so the essence of signal reconstruction process in time domain is to make the delay pressure detecting signal pass through a closed-loop delay feedback system with recursive structure.

4. Signal Reconstruction and Pole Frequency Analysis Based on Inverse Fourier Transform

The straight pipe between pressure sensors A and B will cause pressure signal attenuation. According to the transmission

characteristics of mud pressure wave [11], the attenuation coefficient of pressure signal or the amplitude ratio of mud pipe can be described as

$$a = e^{-L_0/D} \quad (14)$$

with

$$D = \frac{d}{2} \sqrt{\frac{K_l}{\pi f \mu [1 + \psi((K_l d)/Ee) + \beta_g((K_l/K_g) - 1) + \beta_s((K_l/K_s) - 1)]}},$$

$$\psi = \frac{1}{1 + (e/d)} \left[\left(1 - \frac{\sigma}{2}\right) + 2\frac{e}{d}(1 + \sigma) \left(1 + \frac{e}{d}\right) \right], \quad (15)$$

where L_0 is the pipe length between pressure sensors A and B, D is the attenuation index, β_g is the volume fraction of gas in mud, β_s is the volume fraction of solids in mud, K_g is the bulk modulus of gas in mud, K_l is the bulk modulus of liquid in mud, K_s is the bulk modulus of solid in mud, E is the bulk modulus of the mud pipe, d is the internal diameter of the mud pipe, e is the wall thickness of the mud pipe, σ is the Poisson's ratio of the mud pipe, μ is the kinematic viscosity of mud, and f is signal frequency.

Because the mud pipe forms an ideal low-pass filter in the limited band $\omega < \omega_b$, (5) can be transformed into

$$S(j\omega) + N(j\omega) = \frac{[P_A(j\omega) - P_B(j\omega) \cdot H(j\omega)]}{1 - a^2 G^2(\omega) \cdot e^{-j2\omega\tau_0}}. \quad (16)$$

After inverse Fourier transform of (16), we can get the time-domain solution of (16):

$$y(t) = s(t) + n(t)$$

$$= \frac{1}{2\pi} \int_{-\infty}^{+\infty} \frac{[P_A(j\omega) - P_B(j\omega) \cdot H(j\omega)]}{1 - a^2 G^2(\omega) \cdot e^{-j2\omega\tau_0}} e^{j\omega t} d\omega. \quad (17)$$

Suppose that the mud is water-based mud. The computational conditions are listed as follows [12]: internal diameter of the mud pipe is 108.6 mm, wall thickness of the mud pipe is 9.2 mm, the mud kinematic viscosity is 20 mPa · s, the pipe Poisson's ratio is 0.3, volume fraction of gas in mud is 0.5%, volume fraction of solid in mud is 15%, the mud pipe bulk modulus is 210 GPa, and bulk modulus of water in mud is 2.04 GPa, bulk modulus of solid in mud is 16.2 GPa. If signal frequency of mud continuous pressure wave is $f < f_b = 40$ Hz, when the distance between pressure sensors A and B is less than 18 m, the pressure signal attenuation coefficient will be $a > 0.988$ by numerical calculation. This means that transmission loss of mud pressure wave signal is very small and the attenuation coefficient will be close to 1 when the two sensors are nearer to each other.

When $a = 1$, the transfer function of downhole signal reconstruction system can be expressed as

$$H'(j\omega) \Big|_{\omega < \omega_b} = \frac{1}{1 - G^2(\omega) \cdot e^{-j2\omega\tau_0}}$$

$$= \frac{1}{1 - \cos(2\omega\tau_0) + j \sin(2\omega\tau_0)}. \quad (18)$$

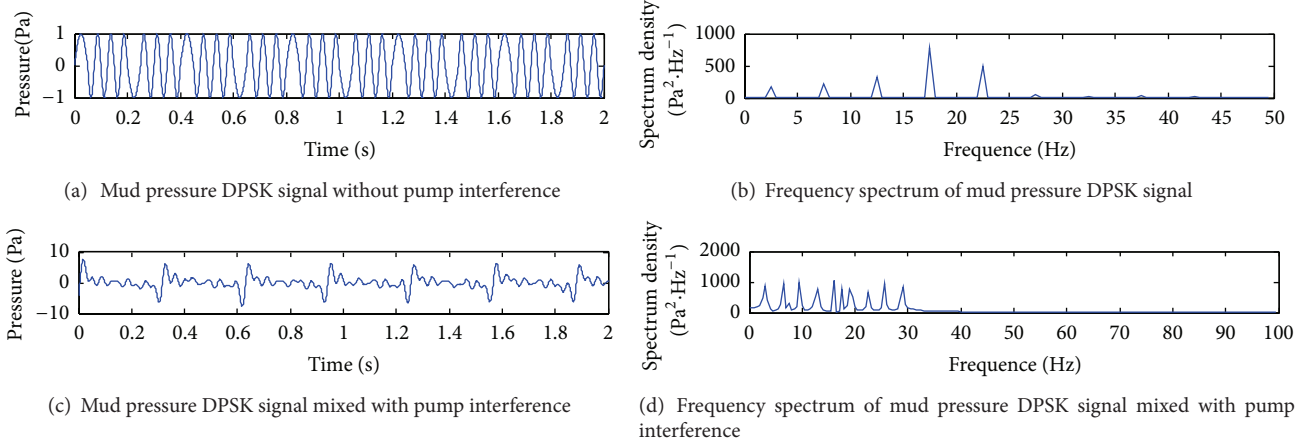


FIGURE 2: Mud pressure DPSK signal mixed with pump interference.

By analyzing (18), there will be generated pole in the condition of $2\omega\tau_0 = 2m\pi$ ($m = 1, 2, 3, \dots$) and the corresponding pole frequency is $f_0 = m/2\tau_0$.

If the maximum frequency of mud pressure signal spectrum is f_{\max} , there is $f_{\max} < f_b$. When the corresponding pole frequency falls into the passband of ideal low-pass filter, the pole frequency will be very likely to enter signal spectrum and generate great interference in the reconstruction of downhole signal. To avoid such situation, all the pole frequency values should be greater than the passband frequency of ideal low-pass filter. That is, $f_0 = m/2\tau_0 > f_b$.

Suppose that $m = 1$ and $\tau_0 < 1/2f_b$; we can get the constraints of distance between pressure sensors:

$$L_0 = \tau_0 c_0 < \frac{c_0}{2f_b}. \quad (19)$$

Propagation velocity of the mud pressure wave in the mud pipe can be calculated according to the literature [13]. Take the mud pressure DPSK (differential phase shift keying) signal with carrier wave frequency of 24 Hz for example, the maximum frequency of signal spectrum is 36 Hz. When $f_b = 40$ Hz, we have $\tau_0 < 1/80$ s. Furthermore, if the mud pressure wave velocity is $c_0 = 1280$ m/s, the corresponding distance between pressure sensors is $L_0 = \tau_0 c_0 < 16$ m.

5. Numerical Simulation of Signal Reconstruction

The numerical simulation takes mud pressure DPSK signal as an example. According to the mathematical model of mud pressure DPSK signal [14], the signal can be formulated as $s(t) = A_c \sin[2\pi f_c t - f(t)]$. In the formula, carrier frequency is $f_c = 20$ Hz, signal amplitude is $A_c = 1$ Pa, and data code is $C = [1 \ 1 \ 1 \ 1 \ 1 \ 1 \ 1 \ 1 \ 1]$. By analyzing the power spectral of mud pressure DPSK signal, the maximum frequency of signal spectrum is $f_{\max} = 30$ Hz and the signal power is $P_s = (A_c/\sqrt{2})^2 = 0.5 \text{ Pa}^2$. Mud pump interference simulates multifrequency pressure pulsation generated by triplex pump with pump impulse rate 64 r/min, and the fundamental wave frequency is $f_1 = 3 \times 64/60 = 3.2$ Hz with

harmonic orders 2 to 9. Therefore, the frequency changing range of pump interference is from 3.2 Hz to 28.8 Hz. Suppose that the fundamental wave and every harmonic wave amplitude are $A_i = 1$ Pa. The corresponding power density of fundamental wave or every harmonic wave is an impact function $S(f) = (A_i/\sqrt{2})^2 \delta(f - f_i)$ and the average power of the pump interference is

$$\begin{aligned} P_n &= \int_{-\infty}^{+\infty} S(f) df = \int_{-\infty}^{+\infty} \left(\frac{A_i}{\sqrt{2}} \right)^2 \delta(f - f_i) df \\ &= \sum_{i=1}^9 \frac{A_i^2}{2} = 4.52 \text{ Pa}^2. \end{aligned} \quad (20)$$

Therefore, the SNR of signal mixed with the pump interference is $P_s/P_n = 0.11$ when downhole noise is set to $n(t) = 0$.

Figure 2 shows the signal waveform and the signal spectrum mixed with mud pump interference. It can be seen that the mud pressure DPSK signal is completely submerged in the pump interference in time domain and the signal spectrum is completely covered by mud pump interference frequencies.

Suppose that the signal acts on the $H'(j\omega)$ at $t = 0$, $H'(j\omega)$ has zero state response only, and the system output before $t = 0$ is $y(0^-) = 0$. Simulation result of the reconstructed signal by MATLAB programming is shown in Figure 3. It can be seen that the mud pump interference is eliminated after delay pressure detection from Figure 3(a); the reconstructed signal in Figures 3(b) and 3(c) are consistent with the mud pressure DPSK signal in Figure 2(a). In Figure 3(b), the numerical calculation result shows that the SNR of reconstructed mud pressure DPSK signal under condition of $\tau_0 = 3.91$ ms is 72.4, which is about 657 times higher than that of existing pump interference. Numerical calculation and analysis show that the SNR of reconstructed mud pressure DPSK signal will be affected by the delayed time τ_0 in time domain and the influence is listed in Table 1. The reason is that the set value of $y(0^-) = 0$, participating in the recursive computation in (11), will be increased with the delayed time τ_0 ,

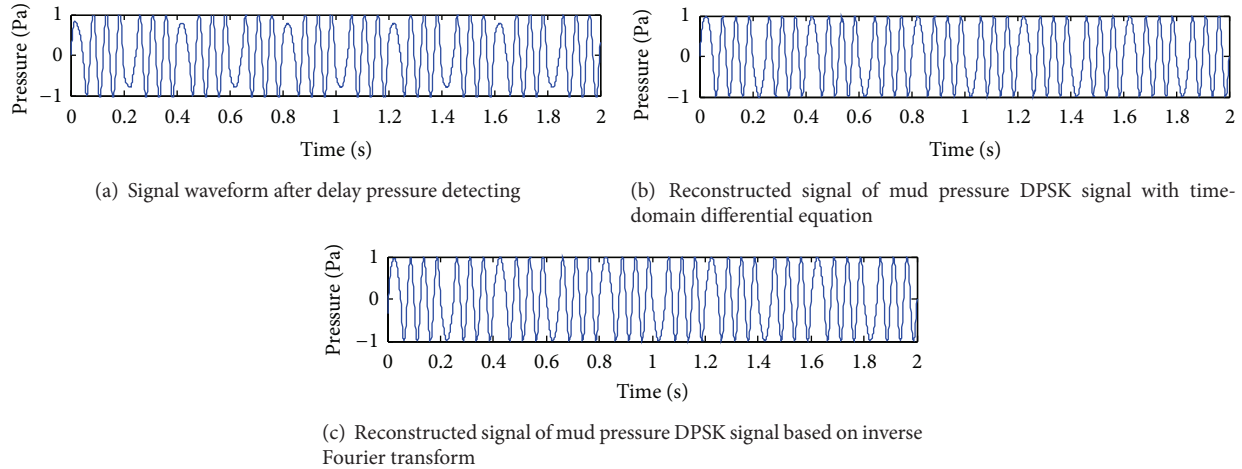


FIGURE 3: Reconstruction of mud pressure DPSK signal.

TABLE 1: SNR of reconstructed mud pressure DPSK signal.

Delayed time τ_0 (ms)	SNR of reconstructed mud pressure DPSK signal
0.98	72.6
1.95	72.6
2.93	72.5
3.91	72.4
4.89	72.1
5.86	70.5

but the influence is not notable. In Figure 3(c), the reconstructed mud pressure DPSK signal based on inverse Fourier transform method has no distortion in whole waveform and is better than the signal reconstructed by time-domain differential equation method in quality. However, both reconstruction methods can reconstruct downhole signal effectively.

Numerical simulation shows that if downhole noise is added to DPSK signal, the reconstructed signals based on the two reconstruction methods are the linear superposition of DPSK signal and downhole noise, which is consistent with theoretical analysis of (11) and (17).

6. Conclusions

(1) Theoretical analysis and numerical simulation show that delay pressure detection method can effectively eliminate mud pump interference and realize reconstruction or recovery of mud continuous pressure wave signals with greater SNR.

(2) To avoid the pole frequency entering into the signals frequency band in signal reconstruction, the distance between pressure sensors should be determined according to the highest signal frequency and the minimum wave velocity.

(3) According to the mathematical principle analysis of delay pressure detection method, it is only applied to eliminate special interference (mud pump pressure interference) whose transmitting direction is opposite to that of the

downhole signal. For mud continuous pressure wave signal which is seriously affected by mud pump interference, this method has some inspiration effect on solving the problem of mud pump pressure interference.

Acknowledgments

This work was supported by the Project of National Natural Science Foundation of China (no. 51274236) and the Project of High-tech Research and Development Program of China (no. 2006AA06A101).

References

- [1] R. Hutin, R. W. Tennent, and S. V. Kashikar, "New mud pulse telemetry techniques for deepwater applications and improved real-time data capabilities," in *Proceedings of the SPE/IADC Drilling Conference*, vol. 67762 of *SPE*, pp. 73–82, March 2001.
- [2] J. L. Marsh, E. C. Fraser, and A. L. Holt Jr., "Measurement-while-drilling mud pulse detection process: an investigation of matched filter responses to simulated and real mud pressure pulses," in *Proceedings of the Petroleum Industry Applications of Microcomputers*, *SPE*, pp. 119–17787, June 1988.
- [3] T. L. Brandon, M. P. Mintchev, and H. Tabler, "Adaptive compensation of the mud pump noise in a measurement-while-drilling system," *SPE Journal*, vol. 4, no. 2, pp. 128–133, 1999.
- [4] B. A. Montaron, J.-M. D. Hache, and B. Voisin, "Improvements in MWD telemetry: 'the right data at the right time,'" in *Proceedings of the Asia Pacific Oil and Gas Conference*, vol. 25356 of *SPE*, pp. 337–346, February 1993.
- [5] C. A. Martin, R. M. Philo, D. P. Decker, and T. M. Burgess, "Innovative advance in MWD," in *Proceedings of the Drilling Conference*, vol. 27516 of *SPE*, pp. 787–796, February 1994.
- [6] C. Klotz, P. Bond, I. Wasserman, and S. Priegnitz, "A new mud pulse telemetry system for enhanced MWD/LWD applications," in *IADC/SPE Drilling Conference*, vol. 112683 of *SPE*, pp. 949–953, Orlando, Fla, USA, March 2008.
- [7] M. R. Foster and B. J. Patton, "Apparatus for improving signal-to-noise ratio in logging-while-drilling system," U. S. Patent, 3742443, 1973.

- [8] X. J. Sun and B. J. Wang, *Principles of Communication*, Publishing House of Electronics Industry, Beijing, China, 2001.
- [9] D. Z. Wu, *Signals and Linear Net Analysis*, Higher Education Press, Beijing, China, 1980.
- [10] Z. Y. Wu, *Digital Signals Processing*, Higher Education Press, Beijing, China, 2004.
- [11] Y. Shen, J. Zhu, Y. Su, L. Sheng, and L. Li, "Transmission characteristics of the drilling fluid pressure quadrature phase shift keying signal along a directional wellbore," *Acta Petrolei Sinica*, vol. 32, no. 2, pp. 340–345, 2011.
- [12] Y. Shen, C. Li, J. Zhu, Y.-N. Su, and L. Li, "Numerical modeling and characteristics analysis of drilling fluid pressure MPSK signals," *Journal of China University of Petroleum*, vol. 34, no. 5, pp. 77–83, 2010.
- [13] X. S. Liu and Y. N. Su, "Study on transmission velocity of mud pulse signal," *Petroleum Drilling Techniques*, vol. 28, no. 5, pp. 24–26, 2000.
- [14] Y. Shen, Y. N. Su, G. S. Li et al., "Transmission characteristics of DPSK mud pressure signals in a straight well," *Petroleum Science and Technology*, vol. 29, no. 12, pp. 1249–1256, 2011.

Research Article

A Study of Developing a System Dynamics Model for the Learning Effectiveness Evaluation

Tian-Syung Lan,¹ Yu-Hua Lan,² Kai-Ling Chen,³ Pin-Chang Chen,¹ and Wen-Cheng Lin¹

¹ Department of Information Management, Yu Da University of Science and Technology, Miaoli 36143, Taiwan

² Center for General Education and Core Curriculum, Tamkang University, New Taipei City 25137, Taiwan

³ Department of Leisure Recreation and Travel Management, Toko University, Chiayi 61363, Taiwan

Correspondence should be addressed to Pin-Chang Chen; chenpc@ydu.edu.tw

Received 15 September 2013; Accepted 14 October 2013

Academic Editor: Teen-Hang Meen

Copyright © 2013 Tian-Syung Lan et al. This is an open access article distributed under the Creative Commons Attribution License, which permits unrestricted use, distribution, and reproduction in any medium, provided the original work is properly cited.

This study used the research method of system dynamics and applied the Vensim software to develop a learning effectiveness evaluation model. This study developed four cause-and-effect chains affecting learning effectiveness, including teachers' teaching enthusiasm, family involvement, school's implementation of scientific activities, and creative teaching method, as well as the system dynamics model based on the four cause-and-effect chains. Based on the developed system dynamic model, this study performed simulation to investigate the relationship among family involvement, learning effectiveness, teaching achievement, creative teaching method, and students' learning interest. The results of this study verified that there are positive correlations between family involvement and students' learning effectiveness, as well as students' learning effectiveness and teachers' teaching achievements. The results also indicated that the use of creative teaching method is able to increase students' learning interest and learning achievement.

1. Introduction

When entering the third grade in elementary school, students are facing the new challenge in the learning of "science and technology" subject. Because the learning motivation and learning method of science and technology are significantly different from those of other fields, it is necessary to investigate the learning effectiveness of the "science and technology" subject [1]. Many variables may affect students' learning effectiveness of science and technology. The research architecture of this study included four parts that affect learning effectiveness, which are teachers' teaching enthusiasm, family involvement, school's implementation of scientific activities, and creative teaching method. Each of the above subsystems is mutually connected with one another to develop cause-and-effect relationships [2, 3].

Most of the past studies on the issues concerning the learning of science and technology of elementary schools are static studies, which cannot assess the postimplementation policies [4, 5]. This study used Vensim software to develop the framework of a systemic model from the perspective of system dynamics and performed dynamic simulation for

analysis and explanation. This study investigated the learning effectiveness of science and technology based on system dynamic model.

This study elevated the previous static studies to a dynamic level. The suggestions proposed based on the simulation results can serve as reference for educators and policymakers in the academic community. It is hoped that this study can help in improving the learning motivation and learning effectiveness of science and technology of students and apply the model-based concepts to different learning fields to further extend such concepts to other relevant studies.

2. Research Method

This study used the research methods of system dynamics and the specific package software Vensim software for system dynamics to develop the model and executed system dynamics equations to perform analyses and discussions.

System dynamics is a system analysis theory created by Forrester in 1968 [6]. System dynamics used the feedback characteristic of information in the system to develop

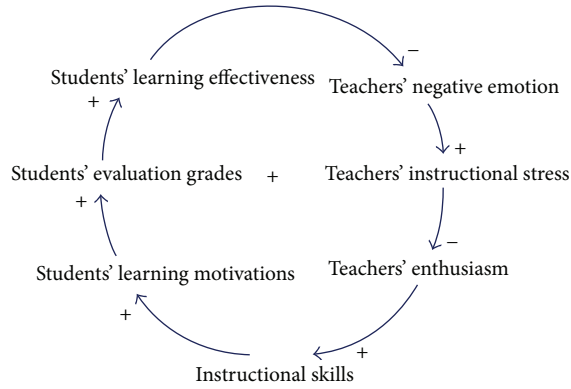


FIGURE 1: Cause-and-effect chain diagram of teacher's teaching enthusiasm and students' learning effectiveness.

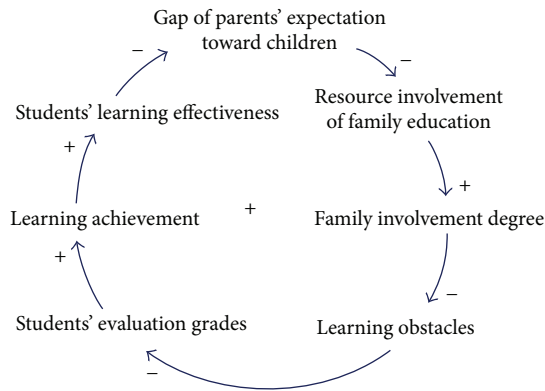


FIGURE 2: Cause-and-effect chain diagram of family involvement and learning effectiveness.

model equations, simulate, and predict the implementation of various policies to achieve the objective of improvement [7]. System dynamics excels in the processing of high-level, nonlinear, and time-varying issues, and it can still be used for investigation under the condition of absence of data [8].

Vensim software is the software developed by Ventana Inc. for model development of system dynamics. It uses various graphics as interface to constitute a complete system dynamics model [9]. The cause-and-effect relationships among various factors can be explained. Its major function is to perform simulation, analysis, and prediction based on the model [10].

3. Cause-and-Effect Chain

This study developed four cause-and-effect chains affecting learning effectiveness, including teachers' teaching enthusiasm, family involvement, school's implementation of scientific activities and creative teaching method.

During the teaching process, the better the teacher-student interaction is, the better the behavioral performance of students is. As long as teachers give proper expectation to students according to their abilities, their high learning motivation can be triggered, their learning effectiveness will

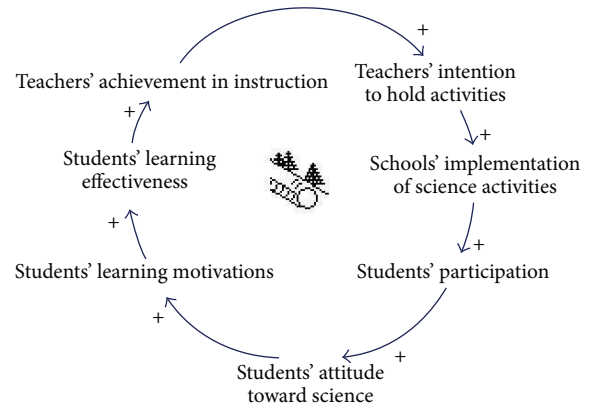


FIGURE 3: Cause-and-effect chain diagram of school's implementation of scientific activities and learning effectiveness.

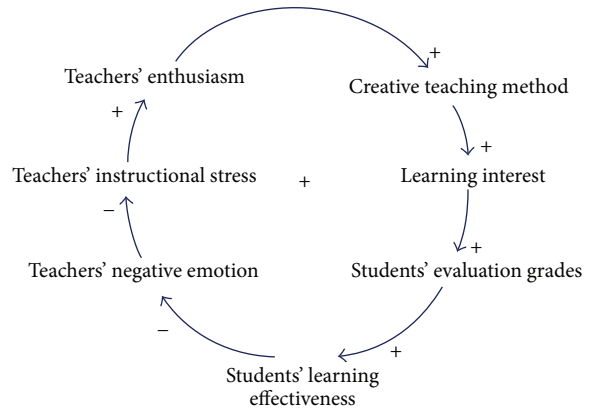


FIGURE 4: Cause-and-effect chain diagram of creative teaching method and learning effectiveness.

become better, and teachers-students relationship will be improved to inspire teachers' teaching enthusiasm. Based on the above, the cause-and-effect chain diagram of relevant factors affecting teachers' teaching enthusiasm and students' learning effectiveness is drawn, as shown in Figure 1.

If parents are willing to spend more time accompanying children to learn, the learning obstacles of science and technology encountered by children will be reduced. Once learning obstacles are reduced, students' learning motivation will be enhanced to further affect their academic performance, learning achievement, and learning effectiveness. This study develops the cause-and-effect chain diagram of relevant factors affecting family involvement and learning effectiveness, as shown in Figure 2.

The scientific activities implemented by schools are mainly instructed by science and technology subject teachers. The success of such activities and the performance of students are subject to the intention and involvement of instructors. The higher the teacher's intention to hold activities is, the better the students' performance is. In this way, students' learning motivation can be triggered and enhanced, and their learning effectiveness can also be improved. This study develops the cause-and-effect chain diagram of relevant factors

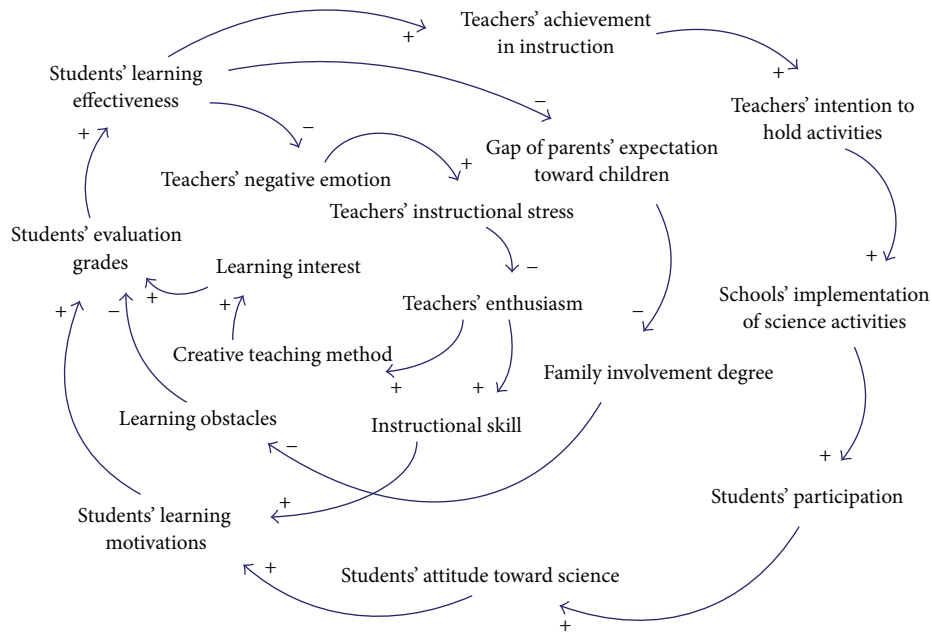


FIGURE 5: Cause-and-effect chain diagram of learning science and technology.

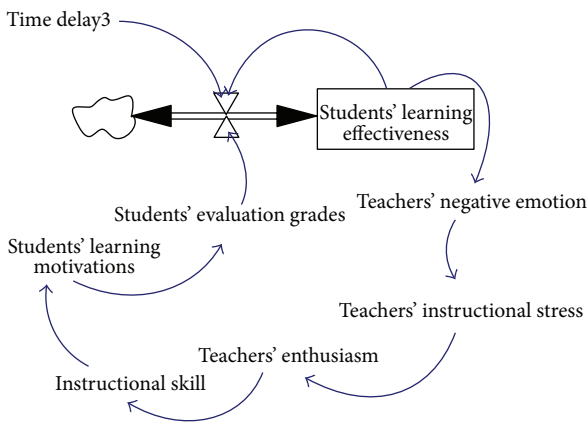


FIGURE 6: System dynamics model of teachers' teaching enthusiasm and students' learning effectiveness.

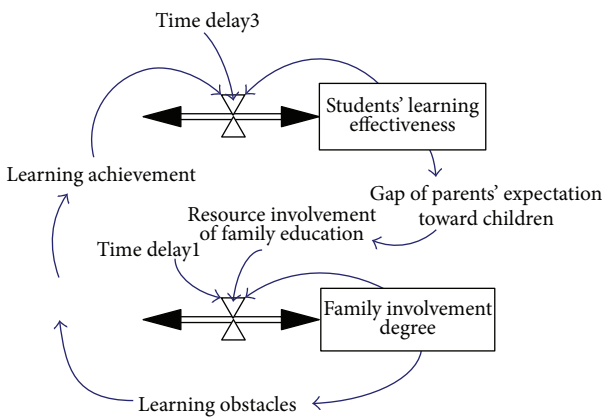


FIGURE 7: System dynamics model of family involvement and learning effectiveness.

affecting schools' implementation of scientific activities and learning effectiveness, as shown in Figure 3.

Teaching methods have constantly changed and evolved with the progress of time. With the technology of teaching aids and materials, creative teaching method has been constantly created. New teaching method will increase students' learning interest, trigger their learning motivation, develop their scientific attitude, and improve their learning achievements and learning effectiveness. This study develops the cause-and-effect chain diagram of factors affecting creative teaching method and learning effectiveness, as shown in Figure 4.

Based on the four cause-and-effect chain diagrams above, this study develops the cause-and-effect chain diagram of relevant factors affecting the learning effectiveness of science and technology, as shown in Figure 5.

4. System Dynamics Model

This study developed the system dynamics model based on the cause-and-effect chain diagrams, which are discussed as follows.

In the learning field of science and technology, teachers need sufficient teaching enthusiasm to encourage themselves to change teaching method and strategies and further trigger students' learning motivation and improve their learning intention. This study develops the system dynamics model of the relationship between teaching enthusiasm and learning effectiveness, as shown in Figure 6.

Parents' educational attitude toward the learning of various subjects will affect students' learning condition. During family involvement in children's education, other factors will intervene with the learning of science and technology. The major one is the assignment time of other subjects. This

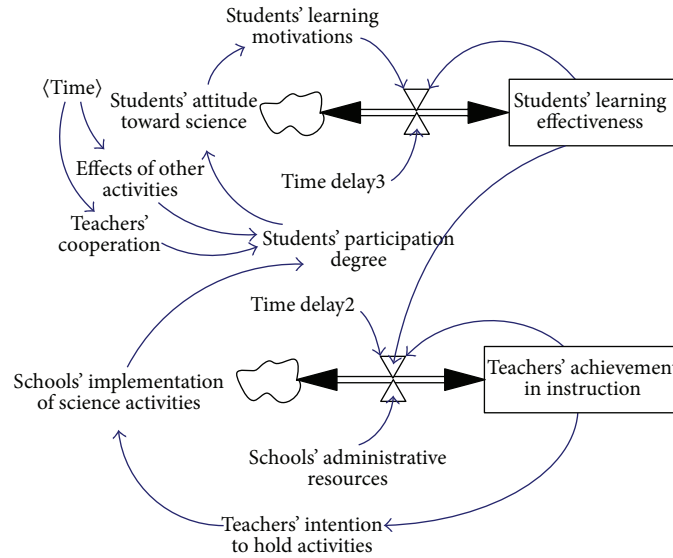


FIGURE 8: System dynamics model of school's implementation of scientific activities and learning effectiveness.

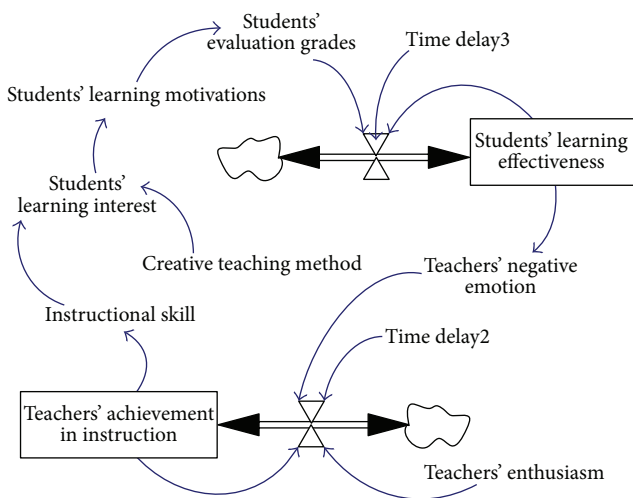


FIGURE 9: System dynamic model of creative teaching and learning effectiveness.

study develops the system dynamics model of the relationship between family involvement and learning effectiveness, as shown in Figure 7.

School's implementation or participation in scientific activities has a significant effect on students' learning motivation and learning effectiveness. Therefore, teachers' intention to hold or cooperate with activities affects students' scientific attitude and learning effectiveness. This study develops the system dynamic model of the relationship between school's implementation of scientific activities and learning effectiveness, as shown in Figure 8.

Creative teaching method can arouse the interest of students and trigger their learning motivation. In addition, creative teaching method can also change students' scientific attitude. This study develops the system dynamics model

of the relationship between creative teaching method and learning effectiveness, as shown in Figure 9.

Based on the four system dynamics models above, this study integrated the four sub-models to develop the system dynamics model of science and technology, as shown in Figure 10.

5. Results and Discussion

Based on the developed system dynamic model, this study performed simulation to investigate the relationship among family involvement, learning effectiveness, teaching achievement, creative teaching method, and students' learning interest.

- (1) Family involvement and students' learning effectiveness: the simulation of this system mainly investigated the relationship between family involvement and learning effectiveness. According to the simulation results, in the short term, there is a steady increase, as well as ups and downs, in family involvement, and so is learning effectiveness. In the long term, there is a highly positive correlation between them. In other words, the higher the family involvement is, the higher the students' learning effectiveness is, as shown in Figure 11.
- (2) Students' learning effectiveness and teachers' teaching achievements: the simulation of this system mainly investigates the relationship between students' learning effectiveness and teachers' teaching achievements. The results showed that there is a positive correlation between students' learning effectiveness and teachers' teaching achievements. The higher the teaching achievement is, the higher the students' learning effectiveness is, as shown in Figure 12.

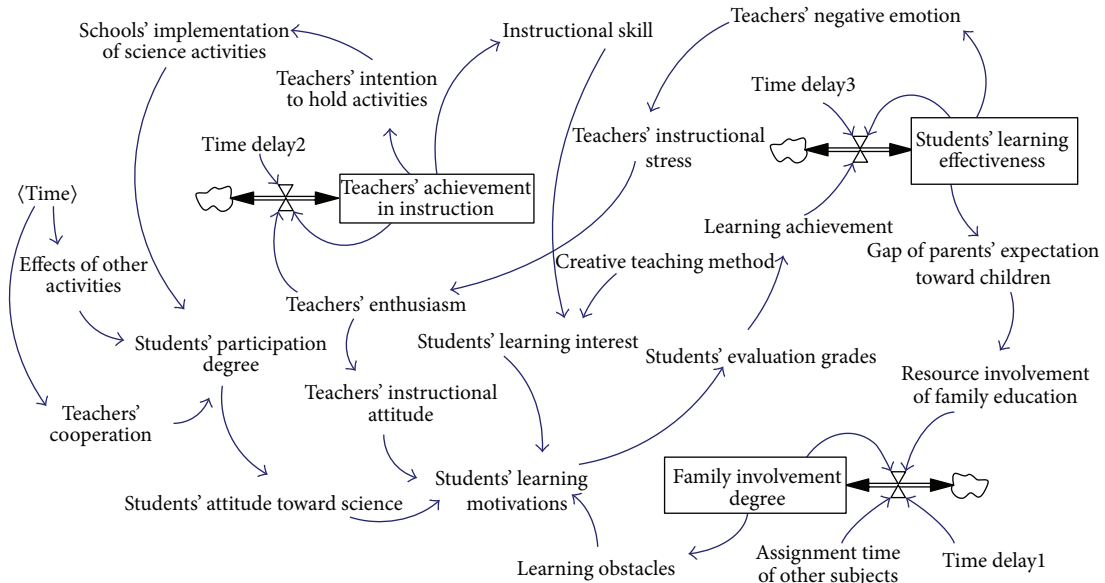


FIGURE 10: System dynamics model of learning science and technology.

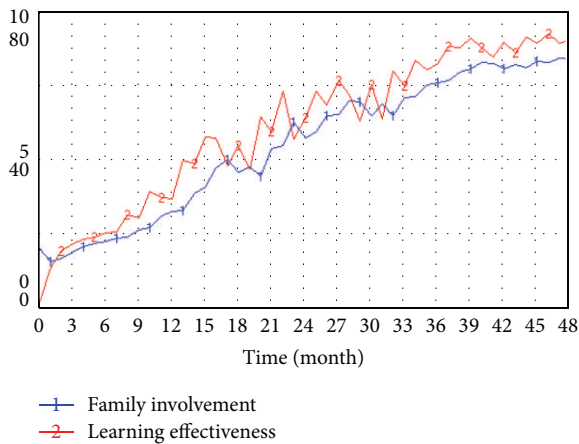


FIGURE 11: Analysis of family involvement and learning effectiveness.

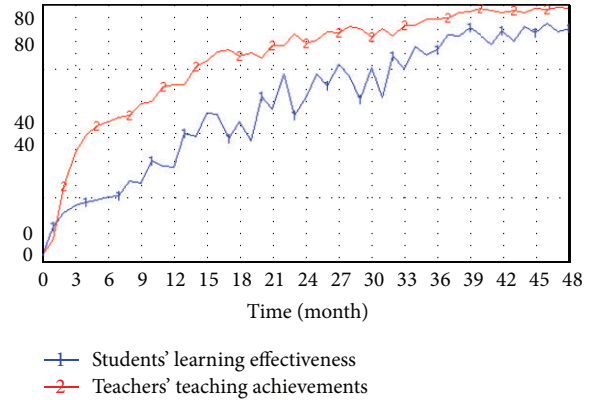


FIGURE 12: Analysis of students' learning effectiveness and teachers' teaching achievements.

(3) Effect of creative teaching method on students' learning interest: the simulation of this system mainly investigates the relationship between creative teaching method and students' learning interest. The use of creative teaching method can trigger students' learning interest. Apparently, in the beginning of learning science and technology, the use of different creative teaching methods can immediately arouse students' interest, as shown in Figure 13.

6. Conclusion

This study verified that there is a highly positive correlation between family involvement and students' learning effectiveness. In other words, family plays an important role in students' learning, and the role of parents is particularly

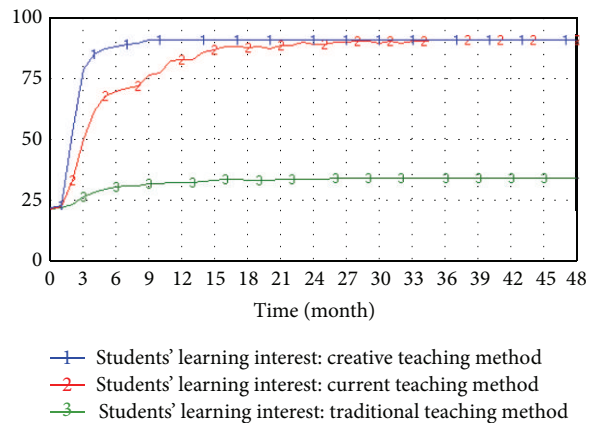


FIGURE 13: Analysis of the effect of creative teaching method on students' learning interest.

important. The learning of science and technology in elementary schools is different from the reading, speaking, listening, and writing of language, the comprehension and calculation of mathematics, or the memorization and induction of social science. Instead, it is the integration of learning approaches of various fields. Higher family involvement, lower obstacles encountered in the field of science and technology, and parents willing to help children complete their assignment in science and technology are beneficial to students, which can further improve their learning effectiveness.

This study also verified that there is a positive correlation between students' learning effectiveness and teachers' teaching achievements. Teachers can handle their teaching content and teaching method to obtain a sense of achievement from the gradual progress in learning effectiveness of students. Their sense of achievement is usually higher than students' learning effectiveness. Once teachers obtain a good sense of achievement, their teaching enthusiasm will be higher. They will maintain their teaching enthusiasm and aggressively engage in teaching. Under such an atmosphere, students' learning effectiveness will be better as well.

This study also indicated that the difference in teaching method has an effect on students' learning interest. The traditional narrative teaching has become outdated. However, there are still teachers using such a teaching method, which cannot arouse the learning interest of students at all. In the current learning environment filled with information and diversification, traditional teaching should have been eliminated and replaced by various newly arising teaching methods. The most popular teaching method at present is e-whiteboard, which has been used for three years. Teachers' use of e-whiteboard is attractive to students, which can significantly increase learning interest, as well as the enthusiasm for science and technology to further improve learning effectiveness. In the current learning environment filled with information and diversification, students' learning has changed, so teachers' teaching methods have to change as well. If teachers can use proper aids and other creative teaching methods during the use of e-whiteboard, students' learning interest will be increased and their learning achievements will be improved.

References

- [1] S. S. Liaw, "Investigating students' perceived satisfaction, behavioral intention, and effectiveness of e-learning: a case study of the blackboard system," *Computers and Education*, vol. 51, no. 2, pp. 864–873, 2008.
- [2] J. Gosen and J. Washbush, "A review of scholarship on assessing experiential learning effectiveness," *Simulation and Gaming*, vol. 35, no. 2, pp. 270–293, 2004.
- [3] G. L. Karns, "Learning style differences in the perceived effectiveness of learning activities," *Journal of Marketing Education*, vol. 28, no. 1, pp. 56–63, 2006.
- [4] A. Lau and E. Tsui, "Knowledge management perspective on e-learning effectiveness," *Knowledge-Based Systems*, vol. 22, no. 4, pp. 324–325, 2009.
- [5] M. Wrzesien and M. A. Raya, "Learning in serious virtual worlds: evaluation of learning effectiveness and appeal to students in the e-junior project," *Computers and Education*, vol. 55, no. 1, pp. 178–187, 2010.
- [6] J. W. Forrester, *Principles of Systems*, MIT Press, Cambridge, Mass, USA, 1968.
- [7] J. D. Sterman, *Business Dynamics: Systems Thinking and Modeling for a Complex World*, Irwin McGraw-Hill, Boston, Mass, USA, 2000.
- [8] M. Wu and H. Yan, "Simulation in software engineering with system dynamics: a case study," *Journal of Software*, vol. 4, no. 10, pp. 1127–1135, 2009.
- [9] N. Helfrich and W. Schade, "Bringing distributed software development to SD modelling with vensim," in *Proceedings of the 26th International Conference of the System Dynamics Society*, Athens, Greece, July 2008.
- [10] R. L. Eberlein and D. W. Peterson, "Understanding models with vensim," *European Journal of Operational Research*, vol. 59, no. 1, pp. 216–219, 1992.

Research Article

A Fast Image Stitching Algorithm via Multiple-Constraint Corner Matching

Minchen Zhu,¹ Weizhi Wang,² Bingham Liu,¹ and Jingshan Huang³

¹ College of Mathematics and Computer Science, Fuzhou University, Fuzhou, Fujian 350108, China

² College of Civil Engineering, Fuzhou University, Fuzhou, Fujian 350108, China

³ School of Computing, University of South Alabama, Mobile, AL 36688, USA

Correspondence should be addressed to Bingham Liu; lbh@fzu.edu.cn

Received 8 September 2013; Accepted 30 September 2013

Academic Editor: Artde Donald Kin-Tak Lam

Copyright © 2013 Minchen Zhu et al. This is an open access article distributed under the Creative Commons Attribution License, which permits unrestricted use, distribution, and reproduction in any medium, provided the original work is properly cited.

Video panoramic image stitching is in general challenging because there is small overlapping between original images, and stitching processes are therefore extremely time consuming. We present a new algorithm in this paper. Our contribution can be summarized as a multiple-constraint corner matching process and the resultant faster image stitching. The traditional Random Sample Consensus (RANSAC) algorithm is inefficient, especially when stitching a large number of images and when these images have quite similar features. We first filter out many inappropriate corners according to their position information. An initial set of candidate matching-corner pairs is then generated based on grayscale of adjacent regions around each corner. Finally we apply multiple constraints, e.g., their midpoints, distances, and slopes, on every two candidate pairs to remove incorrectly matched pairs. Consequently, we are able to significantly reduce the number of iterations needed in RANSAC algorithm so that the panorama stitching can be performed in a much more efficient manner. Experimental results demonstrate that (i) our corner matching is three times faster than normalized cross-correlation function (NCC) rough match in traditional RANSAC algorithm and (ii) panoramas generated from our algorithm feature a smooth transition in overlapping image areas and satisfy human visual requirements.

1. Introduction

To stitch images and form a video panoramic image, the similarity of overlapping regions among adjacent images needs to be calculated in the first place. State-of-the-art algorithms for image registration (sometimes also referred to as “image alignment”) can be classified into intensity-based, frequency domain-based, and feature-based ones [1–7]. Intensity-based algorithms usually involve a large amount of computation and therefore are not appropriate for image alignment when there is image rotation and scaling. On the other hand, algorithms based on frequency-domain are in general faster and can handle well small translation, rotation, and scaling. Unfortunately, the performance of frequency domain-based algorithms will be degraded when dealing with scenarios where smaller overlapping regions exist. Feature-based algorithms utilize a small number of invariant points, lines, or edges to align images. One significant advantage of these algorithms is that the computational

complexity will be reduced due to less information that needs to be processed. Additionally, feature-based algorithms are robust to changes in image intensity. However, there is one serious issue identified for many existing algorithms. Most of these algorithms make use of an exhaustive search that is based on template matching. As a result, the computation, although already decreased to some extent, is still intensive, which does not meet the real-time requirement usually found in video panorama stitching.

We present in this paper a new algorithm to handle the aforementioned challenge. Our algorithm is motivated by the observation that adjacent images usually have small overlapping and small difference of translation, rotation, and scaling between each other. The proposed algorithm is based upon our innovative multiple-constraint corner matching. First, we filter out large numbers of candidate corners according to their position information. We then generate an initial set of matching-corner pairs based on grayscale of each corner's adjacent regions. Finally, multiple constraints, for example,

their midpoints, distances, and slopes, will be applied on every two candidate pairs to remove incorrectly matched pairs. Consequently, we are able to significantly reduce the number of iterations that are needed in conventional Random Sample Consensus (RANSAC) algorithm [8]. As a result, the video panoramic image stitching can be performed a lot more efficiently.

The rest of this paper is organized as follows. Section 2 introduces in detail our methodology; Section 3 describes experimental results; and Section 4 concludes with future research directions.

2. Methodology

2.1. Corner Selection. Harris algorithm [2] detects corners through the differential of the corner score and the autocorrelation matrix. Suppose that an image has an intensity of $I(x, y)$ and an image patch over the area $w(x, y)$ is shifted by (u, v) the intensity change, $E(u, v)$, of the pixel (x, y) can then be calculated by (1) where $M = \begin{bmatrix} A & C \\ C & B \end{bmatrix} = w(x, y) \otimes \begin{bmatrix} I_x^2 & I_x I_y \\ I_x I_y & I_y^2 \end{bmatrix}$ ($I(x)$ and $I(y)$ are partial derivatives of the pixel, respectively, and w is the Gaussian function to filter noises). One has

$$E(u, v) = [uv] M \begin{bmatrix} u \\ v \end{bmatrix}. \quad (1)$$

The corner response function is defined in (2) with k in the range of $[0.04, 0.06]$. Any pixels whose R value is greater than a threshold, λ , can be selected as candidate corners:

$$R = \det(M) - k(\text{trace}(M))^2. \quad (2)$$

Note that λ depends on characteristics of actual images, size and texture for example; Usually λ is determined indirectly: pixels are sorted in a descending order of their R values; then the first Sum pixels are selected as corners.

Harris detector only involves the first order difference and filtering operations of pixel grayscale, with low computational complexity. A large number of corners can be detected in regions with rich texture, whereas fewer corners will be selected in regions with less texture information. Therefore, selected corners are not evenly distributed; that is, corners tend to cluster around regions with richer texture. Zhao et al. proposed an algorithm in [9] where they fragmented the original image into several regions. A fixed number of corners with top R values were selected in each region as candidate corners; all such candidate corners (a total of Sum) were then sorted in their R values. Finally a scaling parameter, k , whose range is $(0, 1)$, was applied to finalize the corner selection, that is, generating a total of $k \times \text{Sum}$ corners. To assure that each region contains some finalized corners, this algorithm iteratively applied different k values in an ascending order and the iteration was terminated as soon as there was at least one finalized corner for each region. Because of its ability to select corners with relatively high quality, we adopt this algorithm when selecting Harris corners from adjacent images to be stitched.

2.2. Multiple-Constraint Corner Matching. The traditional RANSAC algorithm is inefficient, especially when stitching a large number of images and when these images have quite similar features. Thus, it does not meet the real-time requirement commonly found in video panorama stitching. Note that in the field of video panorama stitching, more often than not, adjacent images have highly similar features with each other, that is, small difference of translation, rotation, and scaling between each other. Based on this insight, we propose to apply multiple constraints on candidate matching-corner pairs to remove incorrectly matched pairs. As such, we can significantly reduce the number of iterations needed in RANSAC algorithm.

2.2.1. Create a Corner Similarity Matrix between Adjacent Images. Suppose that the image I has a resolution of $W \times H$, and the k th corner in I is denoted by I_k (with coordinates $I_k \cdot x$ and $I_k \cdot y$, and intensity $I(x_k, y_k)$). One corner from the left image (I_l^l) and another corner from the right image (I_j^r) can be matched with each other if the following conditions are satisfied: (i) the difference between y coordinates of these two corners is no greater than $H/3$; (ii) the x coordinate of the left corner is greater than or equal to that of the right corner; and (iii) there is a high intensity correlation between two corners. Accordingly, we utilize (3) to calculate pairwise corner similarity and create a similarity matrix between adjacent images I^l and I^r :

$$\text{sim}(i, j) = \begin{cases} |\text{NCC}(I_i^l, I_j^r)| & \text{if } |I_i^l \cdot y - I_j^r \cdot y| < \lambda_h, \\ & I_i^l \cdot x \geq I_j^r \cdot x, \\ 0 & \text{else.} \end{cases} \quad (3)$$

In (3), λ_h is the threshold of the difference between y coordinates of two corners, and normalized cross-correlation (NCC) function is the one described in [10]. Suppose that the similarity window size is $(2w + 1) \times (2w + 1)$; NCC is then calculated as

$$\begin{aligned} \text{NCC}(I_i^l, I_j^r) &= \frac{\sum_{u=-w}^w \sum_{v=-w}^w D_l(i, u, v) \cdot D_r(j, u, v)}{\sqrt{\sum_{u=-w}^w \sum_{v=-w}^w D_l(i, u, v)^2 \cdot \sum_{u=-w}^w \sum_{v=-w}^w D_r(j, u, v)^2}}, \end{aligned} \quad (4)$$

where

$$\begin{aligned} D_l(i, u, v) &= I^l(x_i + u, y_i + v) - \bar{I}_i^l, \\ D_r(j, u, v) &= I^r(x_j + u, y_j + v) - \bar{I}_j^r, \end{aligned} \quad (5)$$

and \bar{I}_i^l and \bar{I}_j^r are the mean intensity of windows around corners I_i^l and I_j^r , respectively. In addition, we further filter out corner pairs with low similarity using (6), where λ_n is the similarity threshold (a real number that is greater than 0.5):

$$\text{sim}(i, j) = \begin{cases} \text{sim}(i, j) & \text{if } \text{sim}(i, j) > \lambda_n, \\ 0 & \text{else.} \end{cases} \quad (6)$$

In brief, we use (3) and (6) to calculate pairwise corner similarity, $\text{sim}(i, j)$, resulting in a similarity matrix between two adjacent images.

2.2.2. Generate an Initial Set of Matching-Corner Pairs. A set of indexes of matching-corner pairs is generated by the following procedure: in each row of the similarity matrix obtained previously, we find the column index so that the corresponding cell in the matrix has the maximum value for that row, and the pair of (*row index*, *column index*) is added into the set. After we process all rows in the matrix, we will obtain a set of index pairs, L^l . Such a procedure is formally described in (7), where Sum_l is the predefined total number of corners in the left image I^l :

$$L^l = \{(i, j) \mid \forall i \in [1, \text{Sum}_l], \quad (7)$$

$$s(i, j) = \max(s(i, :)), s(i, j) \neq 0\}.$$

Similarly, we can obtain another set of index pairs, L^r , by searching the maximum row index for each column. Equation (8) is a formal description of this procedure, where Sum_r is the predefined total number of corners in the right image I^r :

$$L^r = \{(i, j) \mid \forall j \in [1, \text{Sum}_r], \quad (8)$$

$$s(i, j) = \max(s(:, j)), s(i, j) \neq 0\}.$$

In general, Sum_l in (7) and Sum_r in (8) can take different values. In our algorithm we use the same value for these two parameters. Now we compare two sets, L^l and L^r . If a row index and a column index happen to have each other as the other component in a pair, their similarity will be adjusted to 1. That is, if two corners mutually find their “best” match as each other, such a pair will have an updated similarity value of 1. Equation (9) formalizes this procedure of similarity adjustment:

$$\text{sim}_{\text{updated}}(i, j) = \begin{cases} 1 & \text{if } (i, j) \in L^l \cap L^r, \\ \text{sim}(i, j) & \text{else.} \end{cases} \quad (9)$$

Finally we generate an initial set of matching-corner pairs, L , by a union of L^l and L^r , shown in (10). Note that this initial set of pairs is already reduced in size compared with NCC rough match in traditional RANSAC algorithm because as shown in (3) we have already filtered out some inappropriate corners according to their positions in respective regions (i.e., their coordinate values). One has

$$L = L^l \cup L^r = \{(l, r) \mid (l, r) \in L^l \text{ or } (l, r) \in L^r\}. \quad (10)$$

2.2.3. Apply Multiple Constraints on Matching-Corner Pairs. Consider two initial matching-corner pairs in Figure 1, (l_m, r_m) and (l_n, r_n) , along with their respective midpoints, that is, l_{mn} between l_m and l_n and r_{mn} between r_m and r_n . Let δ_m and \bar{m} be the slope and length of the segment formed by l_m and r_m , respectively, and let δ_n and \bar{n} be the slope and length of the segment formed by l_n and r_n , respectively. We design

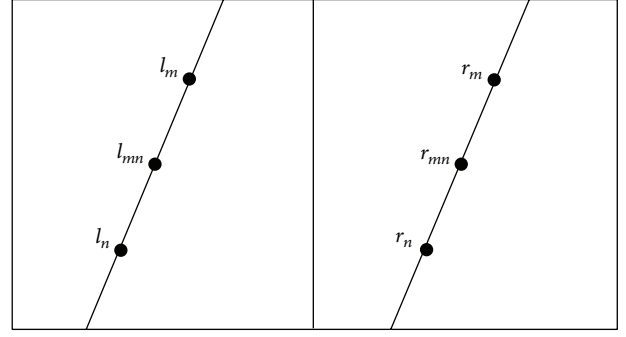


FIGURE 1: Two initially matching-corner pairs.

three constraints to be applied to these two matching-corner pairs, as follows:

$$\begin{aligned} \text{constraint 1: } & |\delta_m - \delta_n| < \lambda_\delta, \\ \text{constraint 2: } & |\bar{m} - \bar{n}| < \lambda_d, \\ \text{constraint 3: } & |\text{NCC}(I_{l_{mn}}^l, I_{r_{mn}}^r)| > \lambda_n. \end{aligned} \quad (11)$$

The intuition of (11) is that, between two matching pairs, not only the intensity of their respective midpoints (constraint 3) should be correlated, but also the slope (constraint 1) and length (constraint 2) of the segments formed between these two pairs should be similar with each other as well. According to multiple constraints specified in (11), we calculate pairwise similarity between every two initial matching pairs using (12) and generate a matrix D of size $K \times K$, with K being the cardinality of L generated in (10). One has

$$D(m, n) = \begin{cases} \frac{\text{sim}_{\text{updated}}(l_m, r_m) + \text{sim}_{\text{updated}}(l_n, r_n) + |\text{NCC}(I_{l_{mn}}^l, I_{r_{mn}}^r)|}{3}, & \text{if satisfying all 3 constraints} \\ 0 & \text{else.} \end{cases} \quad (12)$$

2.2.4. Generate the Final, Reduced Set of Matching-Corner Pairs. Among a total of K initial matching-corner pairs, according to (13), we search for a special pair, t , which has the strongest correlation with all other pairs:

$$t = \underset{i \in [1, K]}{\text{argmax}} \left(\sum_{j=1}^K D(i, j) \right). \quad (13)$$

Then we refer back to the matrix D generated previously and find out all initial matching pairs that have some correlation with the aforementioned special pair, t ; that is, an initial matching-corner pair will be output to the final, further reduced set as long as the cell in D corresponding to this pair and the special pair t has a nonzero value. Equation (14) formally specifies this final selection step, and the resultant set T is the finalized, reduced set of matching-corner pairs. Note that the size of T is further reduced from that of L , and we explained earlier that L is already reduced in size

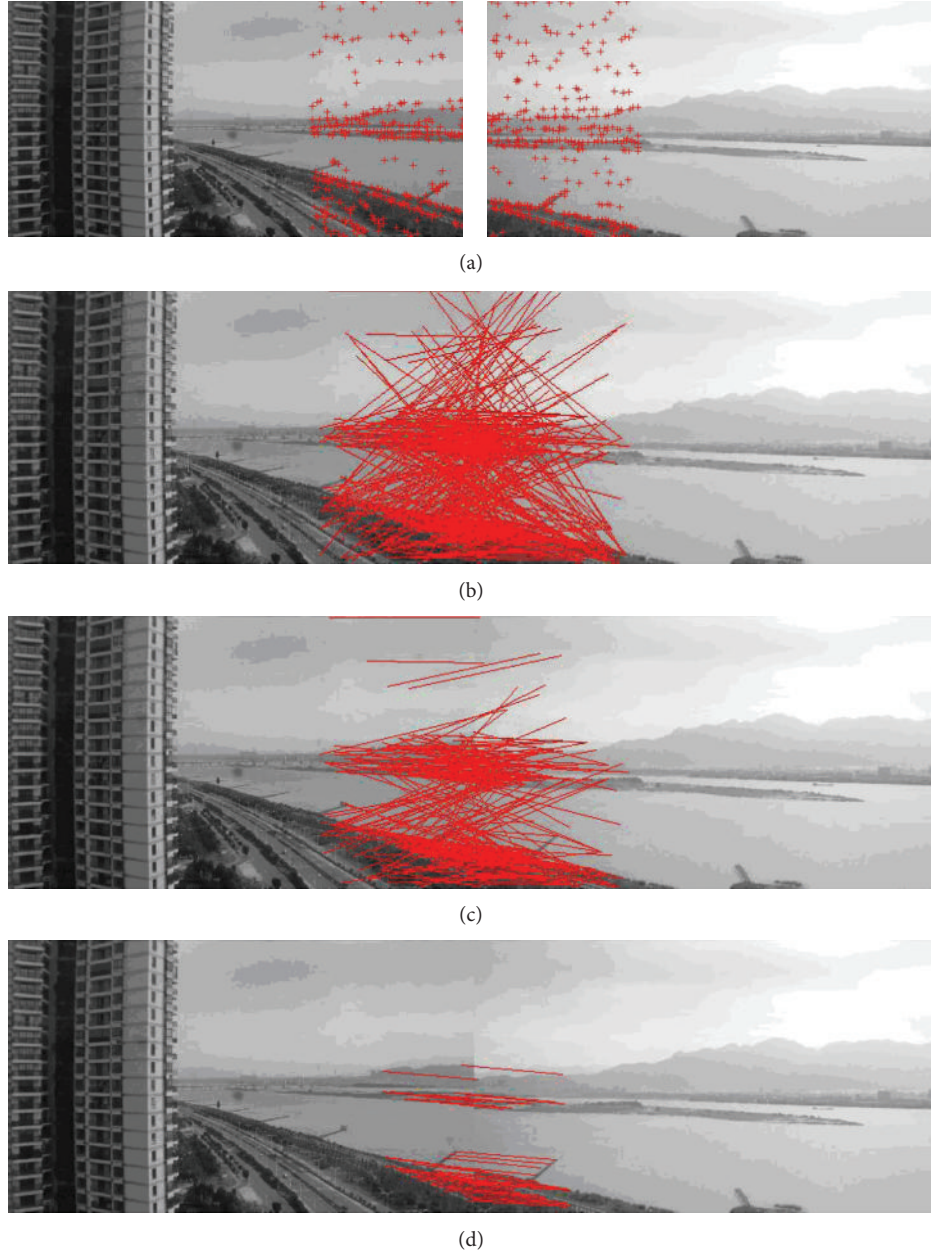


FIGURE 2: Experiments on corner matching.

compared with NCC rough match in traditional RANSAC algorithm:

$$T = \{l \mid \forall l \in L, D(t, l) \neq 0\}. \quad (14)$$

2.3. Image Stitching. After we obtain a reduced set of matching-corner pairs between two original images to be stitched, we select one as the reference image and calculate the affine transformation parameters using RANSAC algorithm. Based on these parameters we map pixel coordinates in the other image into the coordinate system of the reference image. The light conditions may vary among different cameras; therefore, the panorama to be generated may be inconsistent in terms of its intensity. To obtain a smooth

transition in overlapping areas among images to be stitched, we utilize the weighted-sum method introduced in [10] to perform a gradual fading-in and fading-out image stitching process to generate the final video panoramic image.

3. Experimental Results and Analysis

3.1. Experimental Environment and Parameter Setup. Experimental Environment and Parameter Setup are as follows: PC: CPU E2200 + 2.2 GHz, 4 GB memory, Matlab 7.0; image resolution: 1280×720 .

Various parameters described earlier in Section 2 were set as follows. Note that the setting of these experimental

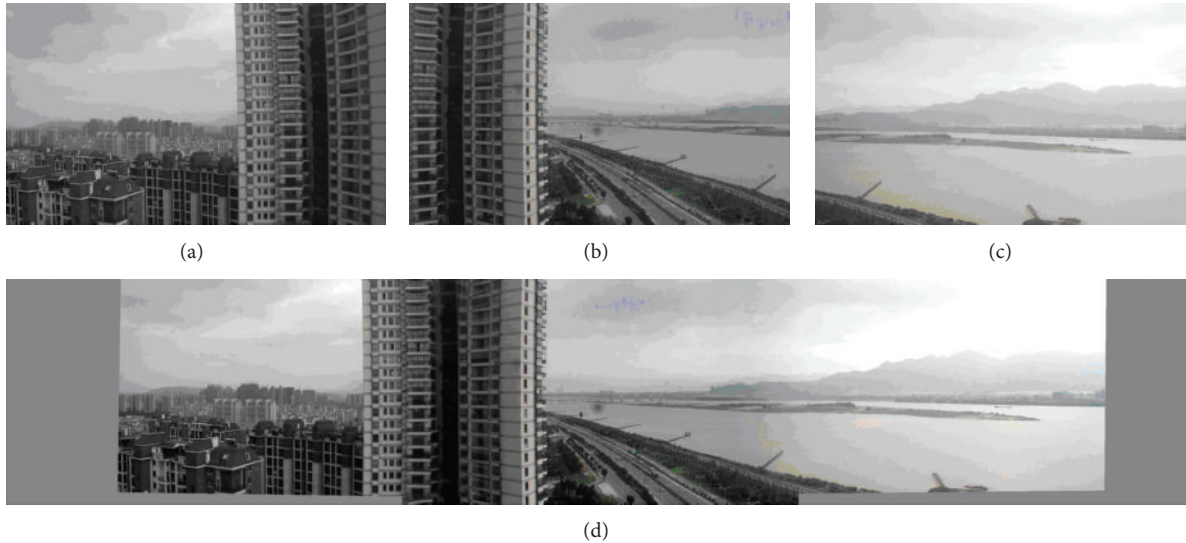


FIGURE 3: Experiments on image stitching.

parameters was based upon our previous experience from numerous experiments.

- (i) The difference of y coordinates of adjacent cameras was not greater than $H/3$; that is, λ_h in (3) was set to $H/3$;
- (ii) The horizontal overlapping was not great than $W/3$;
- (iii) The original image was segmented into regions of size 80×80 , and the number of corners for each region was set to six;
- (iv) The similarity threshold, λ_s , in (6) was set to 0.75, and the similarity window size in (4) was set to 7×7 ; that is, w was set to three.

3.2. Evaluation on Corner Matching. The experimental results are demonstrated in Figure 2. Two original images with corners selected using algorithm in [9] are exhibited in Figure 2(a). We chose the right one-third region of the left image and the left one-third region of the right image as two regions to perform corner matching. So we had a total of 45 ($= (H/80) \times ((W/3)/80)$) segmented regions, and the total number of corners is 270 ($= 6 \times 45$). The total number of matching-corner pairs from NCC rough match in traditional RANSAC algorithm was 388 (Figure 2(b)), whereas the total numbers of initial and finalized matching-corner pairs from our algorithm were 332 (Figure 2(c)) and 35 (Figure 2(d)), respectively. This result verified our earlier discussion in Section 2.2; that is, the initial set of pairs is already reduced in size compared with NCC rough match in traditional RANSAC algorithm because as shown in (3) we have already filtered out some corners according to their positions in respective regions (i.e., their coordinate values). Note that most of the 35 matching pairs in Figure 2(d) were correct ones. In addition, as demonstrated in Table 1, our multiple-constraint corner matching was three times faster than NCC rough match in traditional RANSAC algorithm. The reason

TABLE 1: Efficiency comparison between traditional RANSAC and our algorithm.

	NCC rough match in traditional RANSAC	Our initial matching	Multiple- constraint matching
Number of matching pairs	388	332	35
Time spent (s)	8.74	2.30	2.94

for us to obtain a much shorter matching process is that traditional RANSAC algorithm needs to calculate the NCC function, which is very time consuming, for *all pairwise combinations* of corners, whereas in our algorithm only a *small number of combinations* need to be considered. To be more specific, (3) ignores all corners that do not meet the position requirement, and we further avoid NCC calculation if two initial pairs do not satisfy the first two constraints specified in (11). More experimental results can be found at the following project Web link: <http://www.soc.southalabama.edu/~huang/ImageStitching/ExperimentResults.rar>.

3.3. Evaluation on Image Stitching. The experimental results are demonstrated in Figure 3. We performed both the regional Harris corner selection and multiple-constraint corner matching between Figures 3(a) and 3(b) and between Figures 3(b) and 3(c), respectively. After we obtained two finalized sets of matching-corner pairs, we selected Figure 3(b) as the reference image and calculated the affine transformation parameters as discussed earlier in Section 2.3. We then mapped pixel coordinates in Figures 3(a) and 3(c) into the coordinate system of Figure 3(b), respectively. Finally we performed a gradual fading-in and fading-out image stitching process. The final result in Figure 3(d) clearly demonstrated that (i) our corner matching was accurate; (ii) we obtained a smooth transition in

overlapping areas among images to be stitched; and (iii) the panorama generated satisfied human visual requirements. Similarly, more experimental results can be found at the following link: <http://www.soc.southalabama.edu/~huang/ImageStitching/ExperimentResults.rar>.

4. Conclusions

We presented an innovative algorithm to handle challenges in video panoramic image stitching, for example, small overlapping regions and extremely time-consuming stitching processes. Our contribution can be summarized as (i) a multiple-constraint corner matching and (ii) a more efficient image stitching process. To overcome the inefficient corner matching in traditional RANSAC algorithm, we first filtered out a large number of corners according to their position information. We then generated an initial set of matching-corner pairs based on grayscales of adjacent regions around each corner. Finally we applied multiple constraints on every two candidate pairs to remove incorrectly matched pairs. We were able to significantly reduce the number of iterations needed in RANSAC algorithm, resulting in a much more efficient panorama stitching process. Experimental results (both those that were detailed in this paper itself and those additional ones in the Web link provided) demonstrated that (i) our corner matching is three times faster than traditional RANSAC matching and (ii) panoramas generated from our algorithm feature a smooth transition in overlapping image areas and satisfy human visual requirements.

One possible future research direction is to investigate on automatically determining the total number of corners according to the image texture information. Another interesting future work is to handle the motion ghost challenge during image stitching.

Acknowledgment

This research was supported by the Project of Fujian Province under Grant nos. 2011Y0040, 2012J01263, and 2013J01186.

References

- [1] E. De Castro and C. Morandi, "Registration of translated and rotated images using finite Fourier transforms," *IEEE Transactions on Pattern Analysis and Machine Intelligence*, vol. 9, no. 5, pp. 700–703, 1987.
- [2] C. G. Harris and M. Stephen, "A combined corner and edge detector," in *Proceedings of the 4th Alvey Vision Conference*, pp. 147–151, Manchester, UK, 1998.
- [3] Z. Li, "A quick image stitching algorithm for images with overlapping borders," *Computer Engineering*, vol. 26, no. 5, pp. 37–38, 2000.
- [4] A. Chalechale, G. Naghdy, and A. Mertins, "Sketch-based image matching using angular partitioning," *IEEE Transactions on Systems, Man, and Cybernetics Part A*, vol. 35, no. 1, pp. 28–41, 2005.
- [5] Q. Zhu, B. Wu, and Z.-X. Xu, "Seed point selection method for triangle constrained image matching propagation," *IEEE Geoscience and Remote Sensing Letters*, vol. 3, no. 2, pp. 207–211, 2006.
- [6] Y. Zhang, G. Gao, and K. Jia, "A fast algorithm for cylindrical panoramic image based on feature points matching," *Journal of Image and Graphics*, vol. 14, no. 6, pp. 1188–1193, 2009.
- [7] S. Cao, J. Jiang, G. Zhang, and Y. Yuan, "Multi-scale image mosaic using features from edge," *Computer Research and Development*, vol. 48, no. 9, pp. 1788–1793, 2011.
- [8] H. Yu and W. Jin, "Evolution of research on digital image mosaics methods," *Infrared Technology*, vol. 31, no. 6, pp. 348–353, 2009.
- [9] W. Zhao, S. Gong, C. Liu, and X. Shen, "A self-adaptive Harris corner detection algorithm," *Computer Engineering*, vol. 34, no. 10, pp. 212–214, 2008.
- [10] J. Wang, J. Shi, and X. Wu, "Survey of image mosaics techniques," *Application Research of Computers*, vol. 25, no. 7, pp. 1940–1943, 2008.

Research Article

Investigation of Dispersion and Performance Based on Ring Cavity by Birefringent Interleaver for DWDM Transmission Systems

Tsair-Chun Liang and Chun-Ting Chen

Graduate Institute of Electrical Engineering, National Kaohsiung First University of Science and Technology, Kaohsiung City 811, Taiwan

Correspondence should be addressed to Tsair-Chun Liang; tcliang@nkfust.edu.tw

Received 10 September 2013; Accepted 7 October 2013

Academic Editor: Teen-Hang Meen

Copyright © 2013 T.-C. Liang and C.-T. Chen. This is an open access article distributed under the Creative Commons Attribution License, which permits unrestricted use, distribution, and reproduction in any medium, provided the original work is properly cited.

We theoretically investigate a 25 GHz multichannel filter based on ring cavity birefringent optical interleaver for dense wavelength division multiplexing (DWDM) transmission systems. The simulation tool used in this work is the Advanced System Analysis Program (ASAP) optical modeling software. We improve the dispersion performance by employing $\lambda/6$ and $\lambda/4$ wave plates as birefringent compensators for interleavers. The new structure exhibits a high performance with nearly zero ripple, a channel isolation greater than 102 dB, and a passband utilization of 86% within the C-band. The research results illustrate that our modified scheme can improve the dispersion of more than 76.6% in comparison with the previous studies of optical interleaver with birefringent crystal and ring cavity structures.

1. Introduction

In the recent years, with the rapid growth of internet and the maturity of multimedia conferencing, dense wavelength division multiplexing (DWDM) [1, 2] has emerged as a vital component for optical fiber networks. And how to increase the number of channels is an important issue [3]. One way to increase the channels number is to widen the usable wavelength bandwidth in low-loss region of the used single-mode fiber [4, 5]. Another way to increase the channels number is to narrow the channel spacing. Several techniques have been engaged in DWDM systems with channel spacing of less than 0.8 nm [6, 7]. A spectral interleaver is capable of separating a set of channels into two sets at twice the channel spacing [8, 9]. An optical interleaver has been verified as an effective technique in increasing channel counts by doubling or quadrupling the number of optical channels when the channel spacing is in the range of 0.2 nm (25 GHz). Nevertheless, the greatest shortcoming of conventional interleavers is an inferior dispersion.

In this paper, we improve the dispersion performance by employing $\lambda/6$ and $\lambda/4$ wave plates as birefringent compensators for Sagnac-interferometer-based flat-top birefringent

optical interleaver employing a ring cavity as a phase-shift element, which was proposed by Lee et al. [10]. The simulation tool used in this work is the Advanced System Analysis Program (ASAP) optical modeling software [11]. And the interleaver design model is configured based on the actual component parameters.

2. Configuration of the Proposed Birefringent Interleaver

Figure 1 depicts the configuration of ring cavity birefringent interleaver. For this scheme, an optical circulator, a polarization beam splitter (PBS), two birefringent crystals (YVO_4 has the length of 30 mm), a triangular-shape prism (transmission 91.4%; refraction index 1.6), and four highly reflective mirrors (reflectivity 99.8%) are used. In this structure, we proposed two $\lambda/4$ wave plates and two $\lambda/6$ wave plates as dispersion compensators employed in the ring cavity to ensure excellent flat-top spectral passband. The YVO_4 birefringent crystal is used for appropriate retardance of interference. The $\lambda/6$ and $\lambda/4$ wave plates are engaged to rotate the beam polarization state by 30 and 45 degrees, respectively.

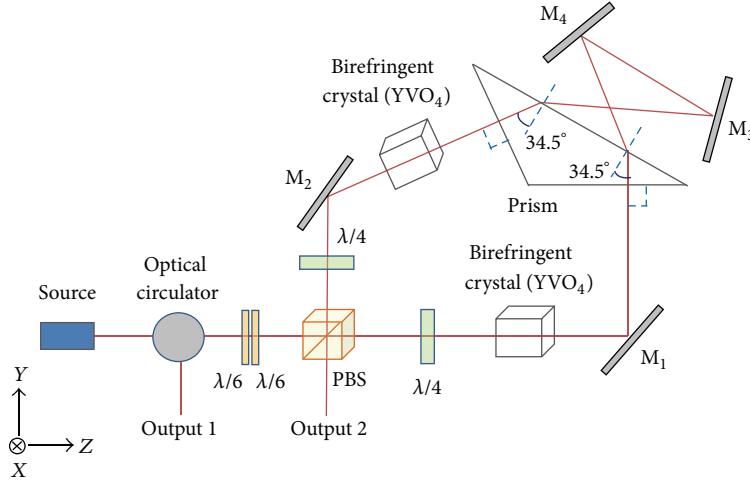


FIGURE 1: Configuration of the proposed ring cavity birefringent interleaver.

The input signal of unpolarized light in the 1530–1565 nm wavelength range (C-band) with a channel spacing of 0.2 nm is considered. When the input signal was transmitted through the PBS, the s-component propagates along the loop in the clockwise direction and the p-component propagates along the loop in the counterclockwise direction. As a result, the beams inside the birefringent crystals consist of both the ordinary wave and the extraordinary wave with equal amplitudes. As the beams propagate inside the birefringent crystals, a phase retardation exists between these two waves at the end of the crystals. These beams, consisting of both ordinary wave (o-ray) and extraordinary wave (e-ray), are then directed toward the ring cavity which is configured by a prism and two mirrors (M_3 and M_4).

In the two birefringent crystals, the ordinary wave corresponds to s-wave, while the extraordinary wave corresponds to p-wave. The prism interface of the ring cavity exhibits different Fresnel reflectivities for these two polarization components (s and p) of the beam. Due to the different reflectivities, these two polarization components experience different phase shifts upon transmitting (or reflecting) through the ring cavity. Through the ring cavity, these two components of the beam incur further phase retardation from the birefringent crystal before they are mixed and recombined by the PBS.

3. Computer Simulation

The air-prism interface is aligned perpendicularwise to the light beams, as shown in Figure 1. And the prism is cut into a triangular shape to provide an appropriate angle of incidence so that the desired Fresnel reflectivities, R_o and R_e , are obtained. R_e and R_o are the reflectivities of the air-prism interface for the e-ray and the o-ray. In this work, the optimum incident angle is near 34.5° , and, at this angle of incidence, the reflectivities are $R_o = 17.01\%$ and $R_e = 8.39\%$. The normalized intensity of one of the output ports can be expressed as follows [12, 13]:

$$I = \frac{I_0}{2} \left[I_0 + \cos \left(\frac{2\pi}{\lambda} (n_e - n_o) L + (\phi_e - \phi_o) \right) \right], \quad (1)$$

where I_0 is the intensity of the unpolarized incident beam, L is the length of the two birefringent crystals, ϕ_e and ϕ_o are the phase shifts of the beam for the e-ray and the o-ray, respectively, upon reflection from the ring cavity, and $\Delta n (=n_e - n_o)$ is the refractive index difference of n_e and n_o . Chromatic dispersion compensation [14] is the most deserving in our study because the dispersion is the parameter which restricts the transmission distance of DWDM systems. The polarization azimuth angle of the birefringent crystal [15, 16] is obtained by $\lambda/4$ wave plates ($\lambda/4$ at 45°) and $\lambda/6$ wave plates ($\lambda/6$ at 30°). Then, the output group delay after compensation can be viewed as the average group delay from two modes, $\tau(\omega) = [\tau_e(\omega) + \tau_o(\omega)]/2$, and can be shown as in (2), where $\omega = 2\pi c/\lambda$ is the optical angular frequency, $T = L_R/c$ is the round-trip time in the ring cavity, L_R is the round-trip optical path of the ring cavity, and d_1 and d_2 are the round-trip phase shifts of $\lambda/4$ wave plates and $\lambda/6$ wave plates, respectively. The group velocity dispersion (GVD) is given by $D(\lambda) = d\tau/d\lambda$ (ps/nm) and can be obtained as in (3). Consider the following:

$$\begin{aligned} \tau(\omega) &= \frac{T}{2} \left\{ (1 - R_o) \times \left(1 + R_o - 2\sqrt{R_o} \cos \left(\left(\frac{2\pi}{\lambda} \right) L_R \right) \right)^{-1} \right. \\ &\quad + \left(1 - \left(\frac{R_e}{(d_1^2 + d_2^2)} \right) \right) \\ &\quad \times \left(1 + \left(\frac{R_e}{(d_1^2 + d_2^2)} \right) - 2 \left(\frac{R_e}{(d_1^2 + d_2^2)} \right)^{1/2} \right. \\ &\quad \left. \left. \times \cos \left(\left(\frac{2\pi}{\lambda} \right) L_R \right) \right)^{-1} \right\}, \end{aligned} \quad (2)$$

$$\begin{aligned} D(\lambda) &= \frac{2\pi L_R T \sin \left((2\pi/\lambda) L_R \right)}{\lambda^2} \end{aligned}$$

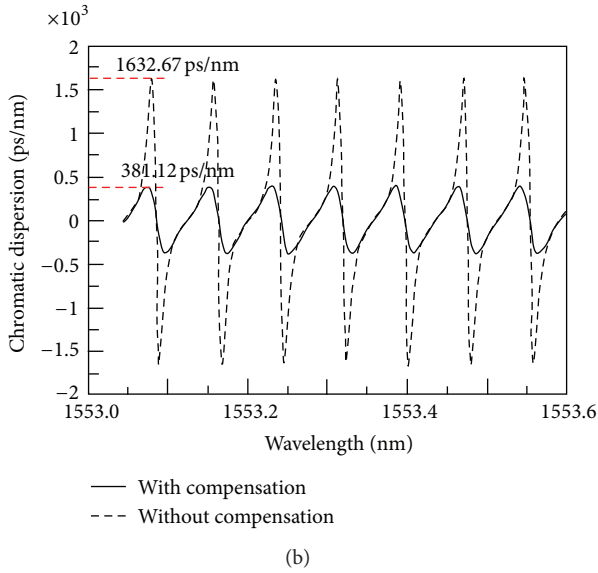
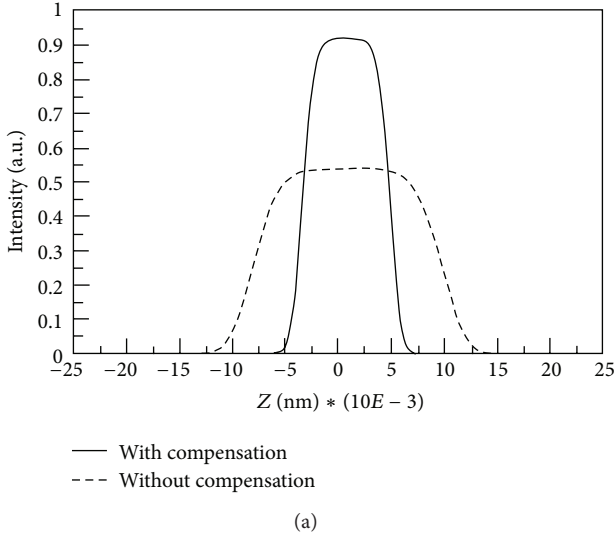


FIGURE 2: The optical spectral (a) signal intensity of one of the output ports and (b) chromatic dispersion characteristics of partial C-band, with and without compensation.

$$\begin{aligned}
 & \times \left\{ (R_o)^{1/2} (1 - R_o) \times \left(\left[1 + R_o - 2(R_o)^{1/2} \right. \right. \right. \\
 & \quad \left. \left. \left. \times \cos \left(\left(\frac{2\pi}{\lambda} \right) L_R \right) \right]^2 \right)^{-1} \right. \\
 & \quad + \left(\frac{(R_e)}{(d_1^2 + d_2^2)} \right)^{1/2} \left(1 - \left(\frac{R_e}{(d_1^2 + d_2^2)} \right) \right) \\
 & \quad \times \left(\left[1 + \left(\frac{(R_e)}{(d_1^2 + d_2^2)} \right) - \frac{2(R_e)}{(d_1^2 + d_2^2)^{1/2}} \right. \right. \\
 & \quad \left. \left. \times \cos \left(\left(\frac{2\pi}{\lambda} \right) L_R \right) \right]^2 \right)^{-1} \left. \right\}.
 \end{aligned}$$

(3)

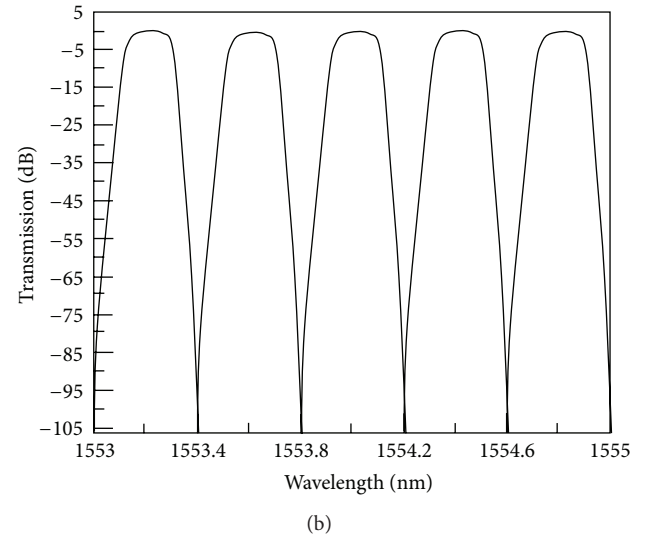
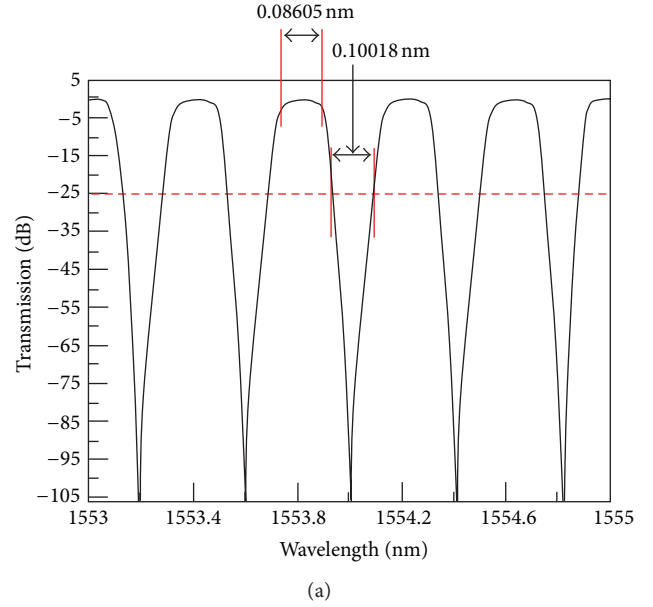


FIGURE 3: The relative transmission power of partial C-band: (a) output port 1 (odd channels) and (b) output port 2 (even channels).

According to (1) and (3), calculated by the simulation software ASAP, we can get normalized intensity of the output channels and their chromatic dispersion. Figure 2(a) shows the calculated spectral output power of one channel. The optical intensities of with- and without-compensation schemes are 0.91 a.u. and 0.553 a.u., respectively. Figure 2(b) shows the chromatic dispersion of partial C-band comparison between with- and without-compensation schemes of 25 GHz channel spacing. The research results illustrate that our modified scheme can improve the dispersion of more than 76.6% ($= (1632.67 - 381.12) / 1632.67$) in comparison. The channel isolation of the interleaver with compensators is greater than 102 dB, and the calculated results of the stopband and channel isolation of a 25 GHz channel spacing application are shown in Figure 3. The 25 dB stopband was found to be 0.10018 nm, the 0.5 dB wide passband was found

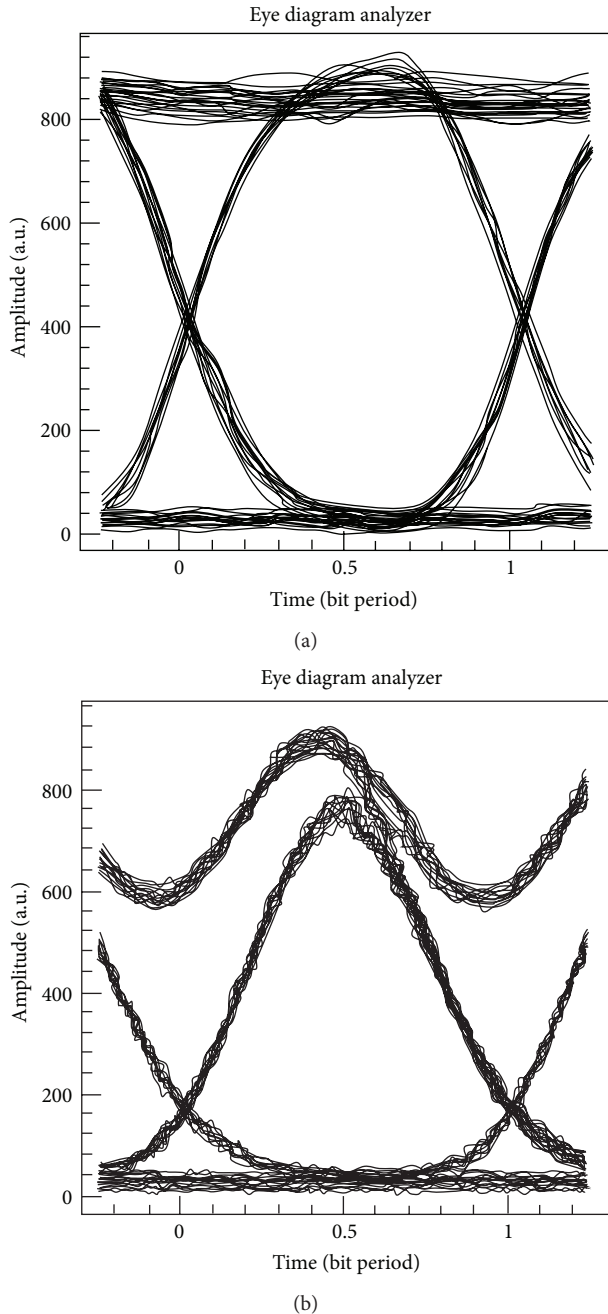


FIGURE 4: The eye diagrams by PRBS $2^{31}-1$ for 10 Gb/s application: (a) with compensation and (b) without compensation.

to be 0.08605 nm, and the passband utilization was 86% ($=0.08605 \text{ nm} / 0.10018 \text{ nm}$) within the C-band. Figure 4 shows the eye diagrams for 10 Gb/s application of with- and without-compensation schemes by pseudorandom binary sequence (PRBS) ($2^{31}-1$).

4. Conclusions

We have investigated the characteristics of a flat-top 25 GHz optical interleaver based on ring cavity architecture with

and without dispersion compensation elements. We found that the ring cavity birefringent interleaver with two $\lambda/4$ wave plates and two $\lambda/6$ wave plates as birefringent compensators exhibited a 0.5 dB passband larger than 10.75 GHz (0.08605 nm), a 25 dB stopband greater than 12.52 GHz (0.10018 nm), and a channel isolation higher than 102 dB. The benefit of this interleaver is that it utilizes the Fresnel principle to achieve precise reflectivities. Unlike dielectric mirrors with thin-film coatings, the reflectivities of the Fresnel reflection are insensitive to wavelength variations in the transmission band. The uniform reflectivities are essential to ensure the same performance over the entire C-band. In particular, the novel interleaver can simultaneously produce the excellent performance of chromatic dispersion that achieved an improvement of 76.6% when compared to the currently available interleaver without wave plates as birefringent compensators, which was proposed by Lee et al. [10]. This modified interleaver may find important applications in DWDM systems and transmission networks.

Acknowledgment

This work was partly supported by the National Science Council of the Republic of China, under Contracts nos. NSC 101-2221-E-327-032 and NSC 102-2622-E-327-005-CC3.

References

- [1] R. Saunders, "Coherent DWDM technology for high speed optical communications," *Optical Fiber Technology*, vol. 17, no. 5, pp. 445–451, 2011.
- [2] Y. C. Chi, C. J. Lin, S. Y. Lin, and G. R. Lin, "The reuse of downstream carrier data erased by self-feedback SOA for bidirectional DWDM-PON transmission," *Journal of Lightwave Technology*, vol. 30, pp. 3096–4643, 2012.
- [3] R. Casellas, R. Munoz, J. M. Fabrega et al., "GMPLS/PCE control of flexi-grid DWDM optical networks using CO-OFDM transmission," *Journal of Optical Communications and Networking*, vol. 4, pp. B1–B10, 2012.
- [4] T.-C. Liang, Y.-K. Chen, J.-H. Su et al., "Optimum configuration and design of 1480-nm pumped L-band gain-flattened EDFA using conventional erbium-doped fiber," *Optics Communications*, vol. 183, no. 1–4, pp. 51–63, 2000.
- [5] M. Matsuura, M. Taguchi, and N. Kishi, "S, C, L-band signal transmission using a widely tunable optical clock generator," *Optics Communications*, vol. 281, no. 21, pp. 5423–5428, 2008.
- [6] S. Zirak-Gharamaleki, "Narrowband optical filter design for DWDM communication applications based on Generalized Aperiodic Thue-Morse structures," *Optics Communications*, vol. 284, no. 2, pp. 579–584, 2011.
- [7] Z. Zhou, S. L. Xiao, T. Qi, P. Q. Li, M. H. Bi, and W. S. Hu, "25-GHz-spaced DWDM-PON with mitigated rayleigh backscattering and back-reflection effects," *IEEE Photonics Journal*, vol. 5, no. 4, Article ID 7901407, 2013.
- [8] G. R. Bhatt, R. Sharma, U. Karthik, and B. K. Das, "Dispersion-free SOI interleaver for DWDM applications," *Journal of Lightwave Technology*, vol. 30, no. 1, pp. 140–146, 2012.
- [9] N. Kumar, M. R. Shenoy, and B. P. Pal, "Flattop all-fiber wavelength interleaver for DWDM transmission: design analysis, parameter optimization, fabrication and characterization

- recipe," *Optics Communications*, vol. 281, no. 20, pp. 5156–5164, 2008.
- [10] C.-W. Lee, R. Wang, P. Yeh, and W.-H. Cheng, "Sagnac interferometer based flat-top birefringent interleaver," *Optics Express*, vol. 14, no. 11, pp. 4636–4643, 2006.
- [11] ASAP (Advanced Systems Analysis Program), Breault Research Organization, Tucson, Ariz, USA.
- [12] S. Cao, J. Chen, J. N. Damask et al., "Interleaver technology: comparisons and applications requirements," *Journal of Lightwave Technology*, vol. 22, no. 1, pp. 281–289, 2004.
- [13] B. B. Dingel and M. Izutsu, "Multifunction optical filter with a Michelson-Gires-Tournois interferometer for wavelength-division-multiplexed network system applications," *Optics Letters*, vol. 23, no. 14, pp. 1099–1101, 1998.
- [14] L. Wei and J. W. Y. Lit, "Design optimization of flattop interleaver and its dispersion compensation," *Optics Express*, vol. 15, no. 10, pp. 6439–6457, 2007.
- [15] J. Zhang, L. Liu, and Y. Zhou, "Novel and simple approach for designing lattice-form interleaver filter," *Optics Express*, vol. 11, pp. 2217–2224, 2003.
- [16] M. Oguma, T. Kitoh, Y. Inoue et al., "Compact and low-loss interleaver filter employing lattice-form structure and silica-based waveguide," *Journal of Lightwave Technology*, vol. 22, no. 3, pp. 895–902, 2004.

Research Article

Design and Implementation of a High-Voltage Generator with Output Voltage Control for Vehicle ER Shock-Absorber Applications

Chih-Lung Shen and Tsair-Chun Liang

Department of Electronic Engineering, National Kaohsiung First University of Science and Technology, Kaohsiung 824, Taiwan

Correspondence should be addressed to Chih-Lung Shen; clshen@ccms.nkfust.edu.tw

Received 10 September 2013; Accepted 6 October 2013

Academic Editor: Teen-Hang Meen

Copyright © 2013 C.-L. Shen and T.-C. Liang. This is an open access article distributed under the Creative Commons Attribution License, which permits unrestricted use, distribution, and reproduction in any medium, provided the original work is properly cited.

A self-oscillating high-voltage generator is proposed to supply voltage for a suspension system in order to control the damping force of an electrorheological (ER) fluid shock absorber. By controlling the output voltage level of the generator, the damping force in the ER fluid shock absorber can be adjusted immediately. The shock absorber is part of the suspension system. The high-voltage generator drives a power transistor based on self-excited oscillation, which converts dc to ac. A high-frequency transformer with high turns ratio is used to increase the voltage. In addition, the system uses the car battery as dc power supply. By regulating the duty cycle of the main switch in the buck converter, the output voltage of the buck converter can be linearly adjusted so as to obtain a specific high voltage for ER. The driving system is self-excited; that is, no additional external driving circuit is required. Thus, it reduces cost and simplifies system structure. A prototype version of the actual product is studied to measure and evaluate the key waveforms. The feasibility of the proposed system is verified based on experimental results.

1. Introduction

In a vehicle suspension system, the shock system is installed between the carriage and the tires. The shock system mainly consists of springs and a shock absorber. When the car is driven on an uneven road, the springs provide support between the carriage and the tires. The shock absorber reduces the oscillation energy in the springs and prevents the energy produced from vertical oscillation from being transferred to the carriage. This improves stability and comfort during the drive. There are advantages and disadvantages of having a shock absorber with different damping factors. If the damping factor is high, then more protection is offered when controlling the car and turning the car; however, with a lower damping factor, more comfort is provided to the passengers. If the shock absorber is able to continuously adjust the damping force, optimal suspension could be achieved when driving the car.

To improve the stability when driving, major motor companies currently use methods including gas springs controlled by microcomputers, digital control systems, or active oil pressure control system to build controllable suspension systems for different road conditions. The system structure and the control mechanism can be quite complicated. To overcome the disadvantages mentioned above, electrorheological (ER) fluids are used as the working fluid in shock absorbers [1–3]. The intensity of electric field is used to control the behavior of the ER fluid, as well as to adjust the damping factor in the shock absorber [4–7]. This is a simple method. ER fluids are formed of electrically polarizable suspended particles. Suspension fluids can be made by a variety of materials: silicone oil, cooling oil, kerosene, and so forth. Suspended particles can include macromolecule materials such as ion-exchange resin, starch, and microfiber granules. When changes in the external electric field occur, ER fluids can transform between a liquid state and solid

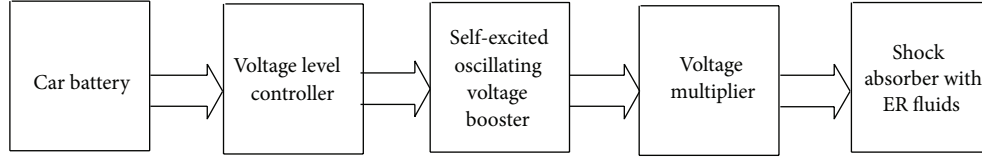


FIGURE 1: System diagram of the proposed high-voltage generator to supply ER shock absorber.

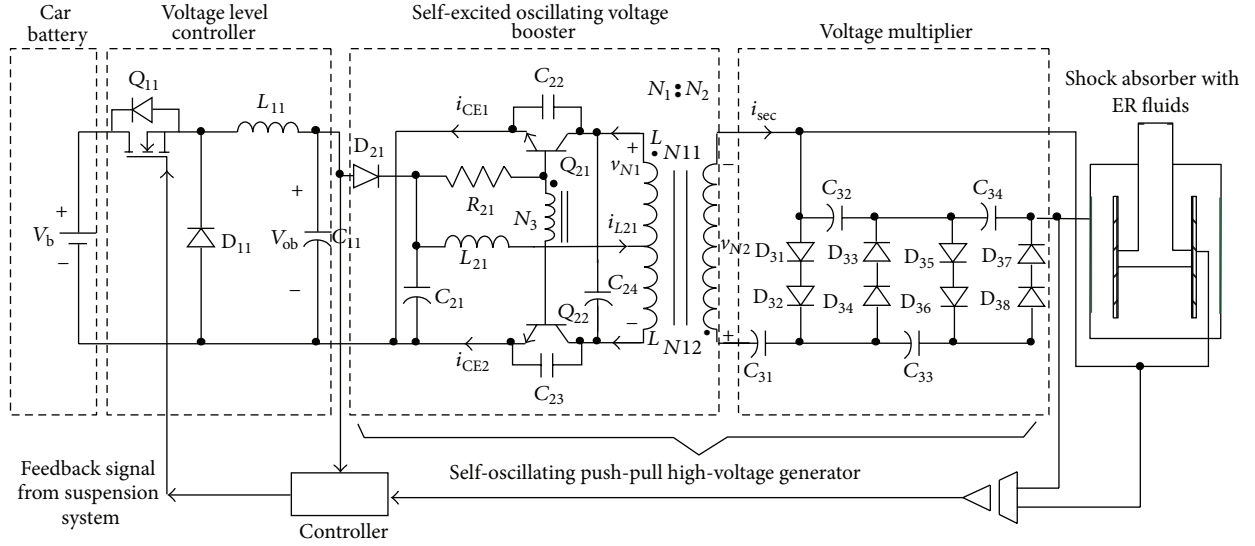


FIGURE 2: Main power circuit of the proposed high-voltage generator to supply ER shock absorber.

state within a few milliseconds. The transformation process is reversible. ER fluids can be applied in the clutch, hydraulic pump, robotic arms, oscillation damper, and so forth and seem to be a promising trend for future motor applications [8, 9].

Switching-mode power converters are widely used to process electricity energy. For example, buck type is adopted for stepping down input voltage [10–13], while push-pull configuration is suitable for dc/ac applications [14–19]. In our study, we use a self-excited high-voltage generator to create a high-voltage dc electric field to control the physical property of the ER fluids. The input dc power source for the high-voltage generator is from the car battery. As previously stated, no external dc power source is required. In addition, a dc/dc buck converter is used to adjust the input dc level for the high-voltage generator. This replaces the conventional linear power supply. The proposed shock absorber with the high-voltage generator has the following advantages: low cost, simple structure, linear control, and high efficiency for power transformation.

2. System Structure

The system diagram for the proposed self-excited high-voltage generator for shock absorbers with ER fluids is shown in Figure 1. It mainly includes car battery, voltage level controller, self-excited oscillating voltage booster, voltage multiplier, and shock absorber with ER fluids. The voltage

level controller transforms the voltage from the car battery within a controlled output range of 0 to 12 volts. A buck converter is used in our study. The self-excited oscillating voltage booster has a push-pull converter structure. It takes the dc voltage from the buck converter and drives the power transistor using self-excited oscillation. Thus, dc voltage is therefore transformed into ac. A high-frequency transformer is then used to increase the voltage. The voltage multiplier, instead of active-type voltage booster so as to lower cost and volume [20, 21], converts the ac from the high-frequency transformer into dc potential. Then, the output voltage of the voltage multiplier is supplied to the shock absorber. The main power circuit of the proposed high-voltage generator is shown in Figure 2.

3. Operation Principle

As shown in Figure 2, the buck-type voltage level controller reduces the 12 volts from the car battery to a desired voltage level by controlling the duty ratio of the active power switch component, Q_{11} . Using volt-second balance criterion, at steady-state operation, the relationship between the input voltage of the buck converter, V_b , and the output voltage, v_{ob} (voltage across capacitor C_{11}), can be obtained as

$$d = \frac{v_{ob}}{V_b}, \quad (1)$$

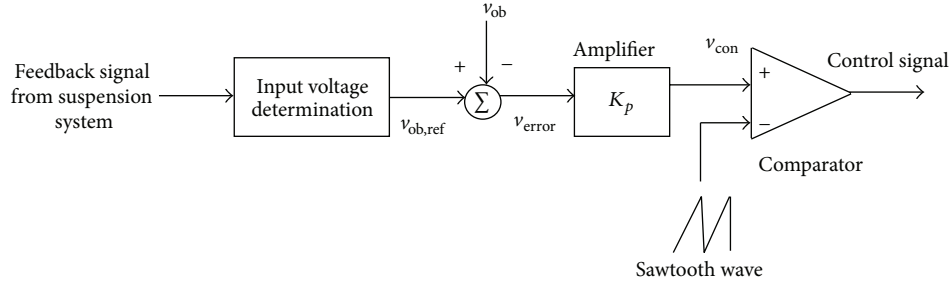


FIGURE 3: The control block diagram of the voltage level controller.

where d is the switching duty cycle. It is observed from (1) that voltage across C_{11} can be changed by controlling the switching duty cycle. This in turn adjusts the intensity of the electric field of the ER shock absorber. As shown in Figure 3, feedback signals from the suspension system determine the reference input voltage of the self-excited oscillating voltage booster, $v_{ob,ref}$. We then compare the reference voltage with the actual voltage, v_{ob} . After magnifying the errors, we can obtain the controlling signal, v_{con} . This controlling signal, v_{con} , is compared with a sawtooth waveform to determine the controlling signal for the active switch, Q_{11} . If we suppose the peak value of the sawtooth waveform is V_{sp} , then

$$v_{ob} = \frac{V_b}{V_{sp}} v_{con}. \quad (2)$$

Since V_b and V_{sp} are constant, from (2) it can be observed that v_{ob} and v_{con} are proportional to each other. In the voltage level controller, the voltage ripple Δv_{ob} is generated on C_{11} when the active switch is switching. If the voltage ripple is too large, a significant impact on the high-voltage generator will occur. Therefore, the switching frequency, f_s , for the voltage level controller must be much greater than the oscillating frequency, f_o , of the self-excited oscillator. In addition, C_{11} should be greater than $C_{11,min}$, which is determined by

$$C_{11,min} = \frac{(1 - d_{min})}{f_s^2 L_{11}} \left(\frac{v_{ob}}{\Delta v_{ob}} \right)_{max}. \quad (3)$$

The self-excited high-voltage generator consists of two parts: the self-excited oscillating voltage booster and the voltage multiplier. The self-excited oscillating voltage booster derived from a Royer-type resonant oscillator [22]. With the feature of iron saturation in the transformer, it alternately drives two power transistors and converts dc into ac. Then, with the use of a high turns ratio transformer, the booster steps up the voltage. The voltage multiplier adjusts the secondary output voltage of the transformer into dc voltage and stacks voltage to a high level. The high-level voltage is transmitted through the electric poles to the shock absorber. The time that both Q_{21} and Q_{22} conduct simultaneously is very short and is negligible. Therefore, the self-excited high-voltage generator can be divided into the following two primary working modes.

Mode 1 [$t_1 - t_2$]. Transistor Q_{21} is on and Q_{22} is off. The voltage across Q_{21} , v_{CE1} , is zero. Inductors L_{21} and C_{23} are resonant.

The voltage of C_{23} is a sinusoid wave. Output voltage from the high-frequency generator is a negative half-wave.

Mode 2 [$t_1 - t_3$]. The high-frequency transformer saturates. Coil N_3 drives transistor Q_{22} but Q_{21} is off. The voltage across Q_{22} , v_{CE2} , is zero. The inductance of the high-frequency transformer resonates with the capacitors, C_{24} and C_{22} . The voltage across C_{22} is a sinusoid wave. The output voltage from the high-frequency generator is a positive half-wave.

According to the operation of the proposed high-voltage generator, the secondary current i_{sec} can be expressed as

$$i_{sec}(t) = K_1 \sin(\omega_p t + \varphi) + \frac{nC_{31}}{2(n^2C_{31} + C_{23})} i_{L21}, \quad (4)$$

where

$$n = \frac{N_2}{2N_1}, \quad (5)$$

$$\varphi = \tan^{-1} \frac{i_{L21}}{2[nv_{C_{23}}(0) - v_{C_{31}}(0)]} \cdot \sqrt{\frac{n^2C_{31}L_{N2}}{C_{23}(n^2C_{31} + C_{23})}}, \quad (6)$$

$$K = \sqrt{\frac{n^2C_{31}^2 i_{L21}^2}{4(n^2C_{31} + C_{23})^2} + \frac{C_{31}C_{23}(nv_{C_{23}}(0) - v_{C_{31}}(0))^2}{L_{N2}(n^2C_{31} + C_{23})}}. \quad (7)$$

In (7), L_{N2} stands for magnetizing inductance looking into the secondary of the high-frequency transformer. Figure 4 shows the corresponding waveforms for both working mode 1 and working mode 2, including the transistor base currents i_{B1} and i_{B2} , the collector-emitter currents i_{CE1} and i_{CE2} , and the collector-emitter voltages v_{CE1} and v_{CE2} .

4. Experimental Result

A prototype is built to assess the feasibility of the proposed structure. The related data and waveforms are measured and evaluated. In order to avoid the skin effect which causes temperature increase in the high-frequency transformer as well as the surrounding components, a multiwire-wound transformer is used to lower the operating temperature and to increase current capacity. In addition, if the turns of the

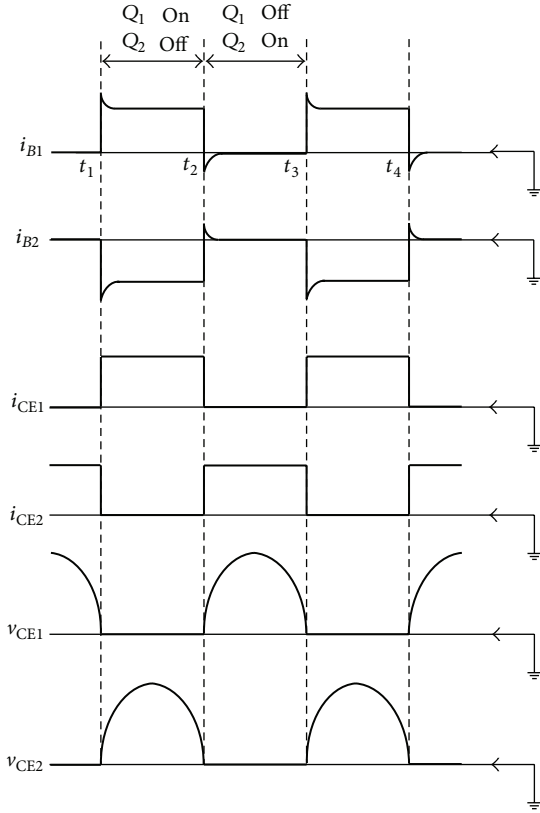


FIGURE 4: Conceptual key waveforms of the proposed high-voltage generator for ER shock absorber.

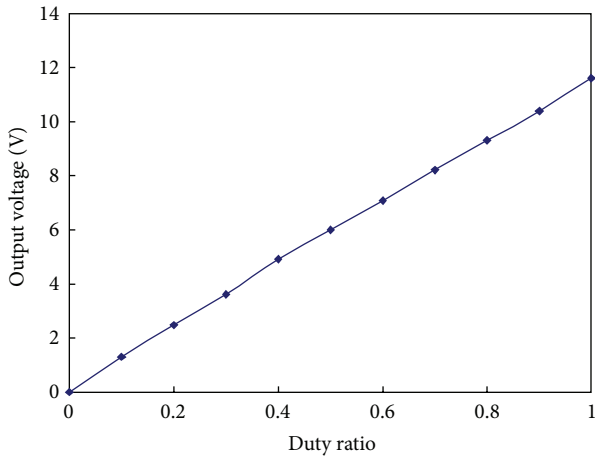


FIGURE 5: Measured result: relationship between output voltage and duty ratio of the voltage level controller.

transformer winding increase, transformer wire resistance will increase, which increases the temperature of the transformer. This can also be alleviated by using the multiwire-wound transformer.

In order to verify that the output voltage of the voltage level controller can be linearly adjusted by controlling the duty ratio of the active switch Q_{11} , the relationship between the duty and output voltage is measured, which is shown in

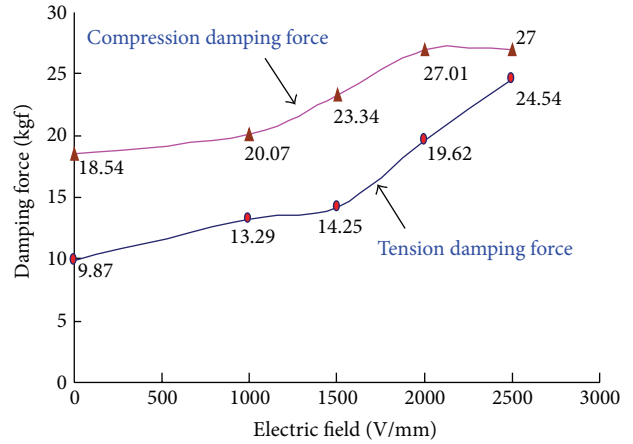


FIGURE 6: Measured result: relationship between damping force and intensity of electric field.

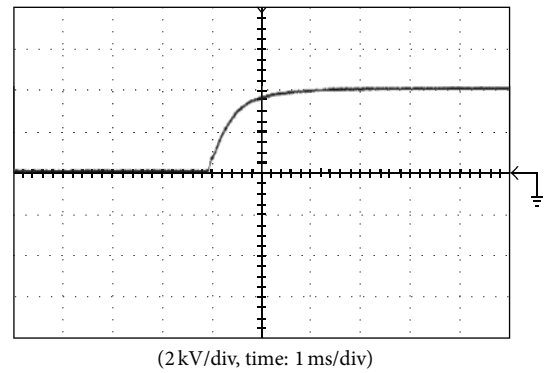


FIGURE 7: Measured waveform while output voltage changes from 0 V to 4 kV.

Figure 5. It can be observed that we can linearly adjust the output voltage by changing the duty cycle. In Figure 6 the relationship between the damping force in the shock absorber with ER fluids and the intensity of the electric field is shown. The corresponding desired voltages for the electric poles are between 0 to 4 kV. Figure 7 shows the dynamic response when voltage supplied on the electric poles in the shock absorber was changed from 0 and 4 kV. As changed from 4 kV to 0 V, Figure 8 shows the corresponding response. From Figures 7 and 8, it can be seen that the self-excited high-voltage generator proposed in this study can rapidly step up or down voltage, supplying the suspension system with the desired damping force. Figure 9 shows the relationship between the input voltage and the output voltage of the self-excited high voltage generator. It reveals that the supply voltage on ER shock absorber can be linearly changed by adjusting the input voltage.

5. Conclusion

In tradition, ER-absorber driver is carried out by linear power supply, which has the apparent drawbacks of low efficiency,

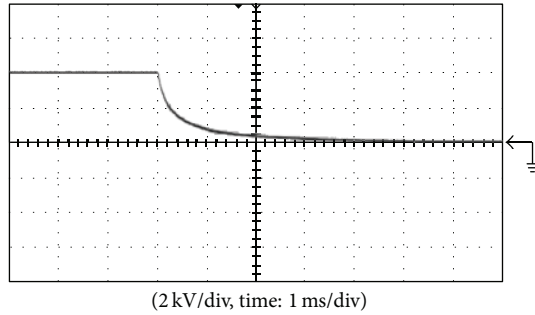


FIGURE 8: Measured waveform while output voltage changes from 4 kV to 0 V.

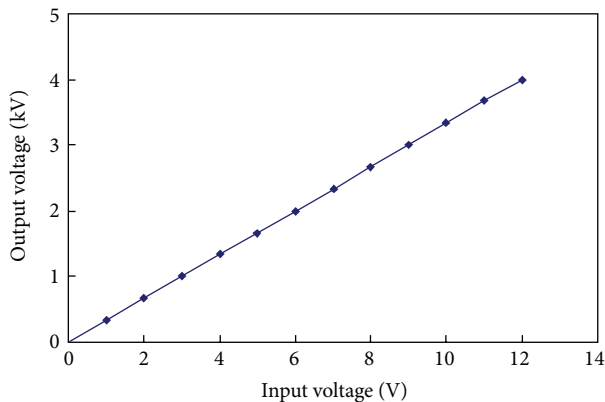


FIGURE 9: Measured results: relationship between output voltage and input voltage of the voltage booster.

large volume, and heavy weight. In this paper, switching-mode technique is applied to the design for ER driver and a self-excited push-pull-based high-voltage generator is proposed. In the proposed ER driver, a controlled voltage output can be obtained in order to control the damping force in a shock absorber. The high-voltage generator is powered by car battery. That is, no additional dc power supply is required. A buck converter is used to control the input dc level of the voltage booster. With the control of the duty ratio of the buck converter, we can obtain a high output voltage proportional to the duty ratio, which simplifies voltage control mechanism. The proposed system has the main advantages of having simple structure, low cost, easy control, high reliability and rapid response and being a compact product. A hardware prototype is constructed to verify the feasibility of the proposed ER high-voltage driver.

References

- [1] T. R. Weyenberg, J. W. Piolet, and N. K. Petek, "The development of electrorheological fluids for an automotive semi-active suspension system," *International Journal of Modern Physics B*, vol. 10, no. 23-24, pp. 3201-3209, 1996.
- [2] A. Crowson, "Smart materials and structures: an army perspective," in *Recent Advances in Adaptive and Sensory Materials and Their Applications*, p. 811, CRC Press, 1992.
- [3] Z. P. Shulman, R. G. Gorodkin, E. V. Korobko, and V. K. Gleb, "The electrorheological effect and its possible uses," *Journal of Non-Newtonian Fluid Mechanics*, vol. 8, no. 1-2, pp. 29-41, 1981.
- [4] J. Nikitzuk, B. Weinberg, and C. Mavroidis, "Rehabilitative knee orthosis driven by electro-rheological fluid based actuators," in *Proceedings of the 2005 IEEE International Conference on Robotics and Automation*, pp. 2283-2289, April 2005.
- [5] W. A. Bullough and N. Jakeman, "Electro-rheological (ER) devices—properties, performance and applications," in *Proceedings of the 1998 IEE Colloquium on Limited Motion Electrical Actuation Systems*, pp. 4/1-4/4, October 1998.
- [6] T. Yakoh and T. Aoyama, "Application of electro-rheological fluids to flexible mount and damper devices," in *Proceedings of the 26th Annual Conference of the IEEE on Industrial Electronics Society*, vol. 3, pp. 1815-1820, October 2000.
- [7] C. Xu, Y. Wang, and S. Lou, "Research on semi-active control of engine vibration basing on Electro-Rheological(ER) technology," in *Proceedings of the 6th World Congress on Intelligent Control and Automation*, pp. 5129-5133, June 2006.
- [8] Y. Kakinuma, T. Yakoh, T. Aoyama, H. Anzai, and K. Isobe, "Development of gel-structured electro-rheological fluids and their application to mechanical damper elements," in *Proceedings of the 8th IEEE International Workshop on Advanced Motion Control*, pp. 541-545, March 2004.
- [9] D. J. Peel, R. Stanway, and W. A. Bullough, "Dynamic modelling of an ER vibration damper for vehicle suspension applications," *Smart Materials and Structures*, vol. 5, no. 5, pp. 591-606, 1996.
- [10] C. T. Tsai and C. L. Shen, "High step-down interleaved buck converter with active-clamp circuits for wind turbine," *Energies*, vol. 5, no. 12, pp. 5150-5170, 2012.
- [11] X. Du, L. Zhou, and H. Tai, "Double-frequency buck converter," *IEEE Transactions on Industrial Electronics*, vol. 56, no. 5, pp. 1690-1698, 2009.
- [12] C. Tsai and C. Shen, "Interleaved soft-switching buck converter with coupled inductors," *WSEAS Transactions on Circuits and Systems*, vol. 10, no. 3, pp. 93-103, 2011.
- [13] B. Chittibabu, S. R. Samantaray, N. Saraogi, M. V. A. Kumar, R. Sriharsha, and S. Karmaker, "Synchronous buck converter based PV energy system for portable applications," in *Proceedings of the 2nd IEEE Students' Technology Symposium*, pp. 335-340, January 2011.
- [14] H. Ma, L. Chen, and Z. Bai, "An active-clamping current-fed push-pull converter for vehicle inverter application and resonance analysis," in *Proceedings of the 2012 IEEE International Symposium on Industrial Electronics*, pp. 160-165, May 2012.
- [15] S. Manikandan and S. Venkatasubramanian, "Implementation of high efficiency current-fed push-pull converter using soft switching technique," in *Proceedings of the 2012 ICCEET International Conference on Computing*, pp. 273-278, March 2012.
- [16] Y. H. Kim, S. C. Shin, J. H. Lee, Y. C. Jung, and C. Y. Won, "Soft-switching current-fed push-pull converter for 250-W AC module applications," *IEEE Transactions on Power Electronics*, vol. 29, no. 2, pp. 863-872, 2013.
- [17] J. S. Glaser and J. M. Rivas, "A 500-W push-pull Dc-dc power converter with a 30-MHz switching frequency," in *Proceedings of the 25th Annual IEEE Applied Power Electronics Conference and Exposition (APEC '10)*, pp. 654-661, February 2010.
- [18] Y. Wang, Q. Liu, J. Ma, L. Chen, and H. Ma, "A new ZVCS resonant voltage-fed push-pull converter for vehicle inverter application," in *Proceedings of the 2013 IEEE International Symposium on Industrial Electronics*, pp. 1-6, May 2013.

- [19] T. C. Lim, B. W. Williams, S. J. Finney, H. B. Zhang, and C. Croser, "Energy recovery snubber circuit for a dc-dc push-pull converter," *IET Power Electronics*, vol. 5, pp. 863–872, 2012.
- [20] Y. Zhao, X. Xiang, W. Li, X. He, and C. Xia, "Advanced symmetrical voltage quadrupler rectifiers for high step-up and high output-voltage converters," *IEEE Transactions on Power Electronics*, vol. 28, no. 4, pp. 1622–1631, 2013.
- [21] C. Pan, C. Lai, M. Cheng, and C. Lee, "High efficiency high step-up converter module for DC microgrid systems," in *Proceedings of the IEEE International Conference on Sustainable Energy Technologies (ICSET '10)*, pp. 1–7, December 2010.
- [22] G. H. Royer, "A switching transistor DC to AC converter having an output frequency proportional to the DC input voltage," *AIEE Transactions I*, vol. 74, pp. 322–326, 1955.